arXiv:2403.03147v1 [gr-qc] 5 Mar 2024

The resonant history of gravitational atoms in black hole binaries

Giovanni Maria Tomaselli,[1] Thomas F.M. Spieksma[2] and Gianfranco Bertone[1]

[1] *Gravitation Astroparticle Physics Amsterdam (GRAPPA), University of Amsterdam, Science Park 904, 1098 XH Amsterdam, The Netherlands*

[2] *Niels Bohr International Academy, Niels Bohr Institute, Blegdamsvej 17, 2100 Copenhagen, Denmark*

Abstract

Rotating black holes can produce superradiant clouds of ultralight bosons. When the black hole is part of a binary system, its cloud can undergo resonances and ionization. These processes leave a distinct signature on the gravitational waveform that depends on the cloud's properties. To determine the state of the cloud by the time the system enters the band of future millihertz detectors, we study the chronological sequence of resonances encountered during the inspiral. For the first time, we consistently take into account the nonlinearities induced by the orbital backreaction and we allow the orbit to have generic eccentricity and inclination. We find that the resonance phenomenology exhibits striking new features. Resonances can "start" or "break" above critical thresholds of the parameters, which we compute analytically, and induce dramatic changes in eccentricity and inclination. Applying these results to realistic systems, we find two possible outcomes. If the binary and the cloud are sufficiently close to counter-rotating, the cloud survives in its original state until the system enters in band; otherwise, the cloud is destroyed during a resonance at large separations, but leaves an imprint on the eccentricity and inclination. In both scenarios, we characterize the observational signatures, with particular focus on future gravitational wave detectors.

Contents

1 Introduction **1**

2 Setup **4**

3 Resonance phenomenology **6**
- 3.1 Two-state resonances 6
- 3.2 Resonances on eccentric and inclined orbits 7
- 3.3 Backreaction on the orbit 9
- 3.4 Floating orbits 10
  - 3.4.1 Adiabatic or non-adiabatic 10
  - 3.4.2 Evolution of eccentricity and inclination 12
  - 3.4.3 Resonance breaking 15
- 3.5 Sinking orbits 18

4 Three types of resonances **19**
- 4.1 Hyperfine resonances 20
- 4.2 Fine resonances 21
- 4.3 Bohr resonances 21

5 Resonant history of the cloud **23**
- 5.1 General behavior 23
- 5.2 Evolution from a $|211\rangle$ initial state 26
- 5.3 Evolution from a $|322\rangle$ initial state 29

6 Observational signatures **32**
- 6.1 Direct signatures of the cloud 32
- 6.2 Indirect signatures: impact on binary parameters 33

7 Conclusions **35**

A Hyperfine resonances and angular momentum **37**

B General resonance breaking **38**

C Ionization at resonance **39**

D $|211\rangle \to |200\rangle$ resonance **41**

References **42**

1 Introduction

The advent of gravitational-wave (GW) astronomy has opened up new opportunities to test fundamental physics. One promising avenue focuses on the environments surrounding black holes (BH). When a binary inspirals inside a sufficiently dense medium, the orbital motion is modified, and the resulting GW signal is affected accordingly [1]. Intermediate to extreme mass ratio inspirals form the perfect testbed for this phenomenon, as (1) the perturbation from the companion is not strong enough to completely disrupt the environment and (2) the binary spends many orbital cycles *in band* allowing environmental effects to build up throughout the inspiral.[1] Future GW detectors such as LISA or the Einstein Telescope will be able to probe these types of binaries [3–5], and potentially infer properties of the evironment from the waveform with great accuracy [6–16]. This area of research has recently attracted conspicuous interest.

One intriguing type of environment is comprised of ultralight bosons. Such particles are predicted from high energy physics as a possible solution to the strong CP problem (i.e., the QCD axion [17–19]), but they can also arise from string compactifications [20, 21] and have been proposed as possible dark matter candidates [22–25]. As it turns out, rotating BHs are unstable against perturbations of the boson field. In particular, when the Compton wavelength of the bosonic field is comparable to the size of the BH, an efficient energy and angular momentum extraction from the BH is possible. Consequently, a "cloud" is formed around the BH, often referred to as a "gravitational atom". This process is termed *superradiance* and has been studied extensively in the literature [26–29]. While superradiance occurs for bosons of any spin, in this work we focus on scalars, due to their simplicity and stronger theoretical motivation. As no couplings to other standard model particles are required, GWs form the ideal tool to study gravitational atoms, especially since they have been shown to exhibit a rich phenomenology in binary systems [30–38].

In particular, in previous works [31, 33], it was found that during a binary inspiral the cloud induces not only secular effects such as dynamical friction or accretion, but also resonant behavior. At certain *resonance frequencies*, where the orbital frequency of the binary matches the energy difference between two eigenstates of the cloud, the gravitational perturbation from the companion is resonantly enhanced and a full transfer from one state to another can be induced. The accompanied change in the angular momentum of the cloud must then be compensated for by the binary. Depending on the nature of the resonance, this leads to *floating* or *sinking* orbits, where the cloud releases or absorbs angular momentum from the binary and hence the inspiral is either stalled or sped-up. Consequently, a potentially detectable dephasing is left in the GW signal. The orbital frequency at which these resonances happen can be predicted, and thus they serve as a direct and unique probe of the properties of the cloud. In addition to their floating or sinking nature, resonances can be divided into three different types, depending on the energy difference between the eigenstates involved. These are called hyperfine, fine or Bohr resonances, which occur in this chronological order. The former two happen "early" in the inspiral (at radii far larger than the cloud's radius), and are all of the floating type. These will thus only affect

[1] Although the impact of the environment is less strong, one can also look for environmental effects in the equal mass ratio case using the already available LIGO-Virgo data [2].

the GW signal *indirectly*: the binary frequency is too low for GW detectors to pick up the signal, but the resonance can change the late-time evolution of the system. Conversely, Bohr resonances happen "late" in the inspiral (at radii comparable with the cloud's radius) and can be either floating or sinking. As these happen while the signal is in band, they can affect the GW signal *directly*.

Due to the exciting observational signatures, various works have studied these resonances. However, to date, they have all made simplifying assumptions, which turn out to crucially alter the behavior of the system. This includes ignoring the backreaction from the resonance [39], assuming a quasi-circular and equatorial orbit, or including just the strongest multipole of the gravitational perturbation [30, 40–43]. A nonzero eccentricity was only considered in [44], yet at a time when the behavior of the resonances had still not been fully understood. In this work, we relax all of the aforementioned assumptions to study resonances in gravitational atoms in full generality, and use this to determine the evolution of the cloud-binary system throughout the inspiral. Crucially, by studying the nonlinear system, we find that there exists a critical threshold above which an *adiabatic* floating resonance is initiated. Below the threshold, there is a negligible transfer, or a *non-adiabatic* resonance. Furthermore, we discover mechanisms that induce a *resonance breaking*, shutting down the transition before it is complete: these are due to the decay of the state excited by the resonance, or to a slow time variation of the parameters. Additionally, we allow for generically inclined and eccentric orbits and study how resonances impact the orbital parameters: while the eccentricity is forced towards fixed points, the inclination angle is always tilted towards a co-rotating configuration. Finally, we take into account the impact of ionization [34–36] in the evolution of the system and include all relevant multipoles.

Using these results, we lay out, for the first time, a systematic study of resonances for realistic parameters, focusing on intermediate and extreme mass ratios. Starting from states commonly populated by superradiance, we evolve the binary taking into account energy losses from both GWs and ionization. By doing so, we determine the resonant evolution of the cloud and the impact of the resonances on the binary's orbit. We find that, for generic orbital configurations, the cloud is often destroyed early in the inspiral. This is due to floating resonances that transfer the cloud to states that decay much quicker than the duration of the resonance. However, when the orbital inclination is within a certain interval centered around a counter-rotating configuration, all hyperfine and fine floating resonances are either non-adiabatic or break prematurely, allowing the cloud to survive until it enters the Bohr regime. Conversely, we find that all sinking resonances for typical parameters have a negligible impact on the cloud. A schematic illustration of these conclusions is given in Figure 1.

To accurately model a binary inspiral in a non-vacuum spacetime, one needs to combine secular effects, such as dynamical friction, with resonant behavior. In a recent work [36], we studied the former, whose associated energy losses can be much larger than those emitted by GWs. In this work, we combine these results with the resonant behavior, to obtain a self-consistent treatment of binary inspirals in a gravitational atom. We hope these two works serve as a guideline towards future studies in a fully relativistic setup, which should be able to describe correctly even the final stages of the inspiral. Recent work on this [37] has already shown encouraging progress and new insights in the rich phenomenology of the problem.

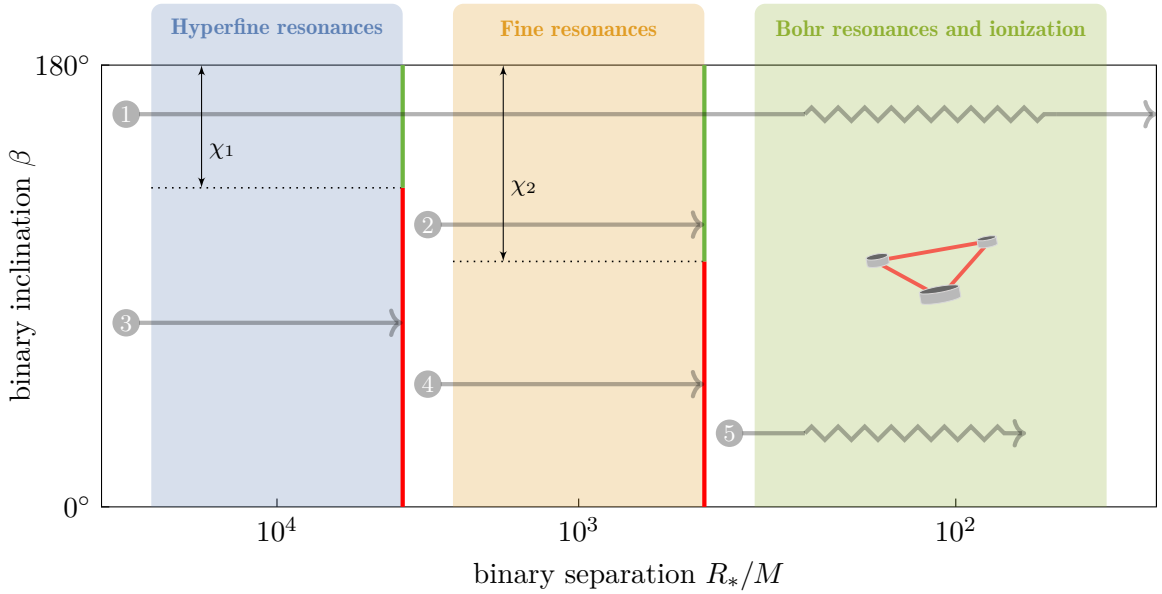


Figure 1: Illustration of the possible outcomes of the resonant history of the cloud-binary system. The inspiral starts with the cloud in its initial state, either $|211\rangle$ or $|322\rangle$. Only systems ①–② whose inclination angle is within intervals χ_1 and χ_2 from the counter-rotating ($\beta = 180°$) configuration are able to move past the hyperfine and fine resonances with the cloud still intact (green vertical lines). These later give rise to observational signatures in the form of ionization and Bohr resonances. Others ③–④ are destroyed by the hyperfine or fine resonances (red vertical lines). Binary systems that form at small enough separations may be able to skip early resonances ⑤.

Outline The outline of the paper is as follows. In Section 2, we briefly review our setup and introduce necessary definitions and equations. Then, in Section 3, we study resonances at the nonlinear level, determining when they are adiabatic and when they break, and extending the framework to eccentric and inclined orbits. In Section 4, we discuss the different types of resonances. Then, in Section 5, we turn to a realistic setting and unveil the full history of the cloud and binary as function of the parameters. In Section 6, we discuss the observational signatures this leads to. We conclude in Section 7. Appendices A, B, C and D contain technical details.

Notation and conventions We work in natural units, $G = \hbar = c = 1$. The larger BH has a mass M and dimensionless spin $\tilde{a}$, with $0 \leq \tilde{a} < 1$. The mass and radial distance of the smaller object are denoted by $M_* \equiv qM$ and R_*, where q is the mass ratio, while the orbital frequency is Ω and the mass of the cloud is M_c. The gravitational fine structure constant is $\alpha = \mu M$, where μ is the mass of the scalar field. We write most of our results in an explicit scaling form, with respect to the following set of benchmark parameters: $M = 10^4 M_\odot$, $M_c = 0.01M$, $q = 10^{-3}$ and $\alpha = 0.2$. The eigenstate of the cloud before encountering a resonance will be denoted by $|n_a \ell_a m_a\rangle$, while any other eigenstate involved in the resonance by $|n_b \ell_b m_b\rangle$. The cloud's wavefunction will then be expanded in as a linear superposition of energy eigenstates as $|\psi\rangle = c_a |a\rangle + \sum_b c_b |b\rangle$.

Code availability The code used in this work and in [36] is publicly available on GitHub.

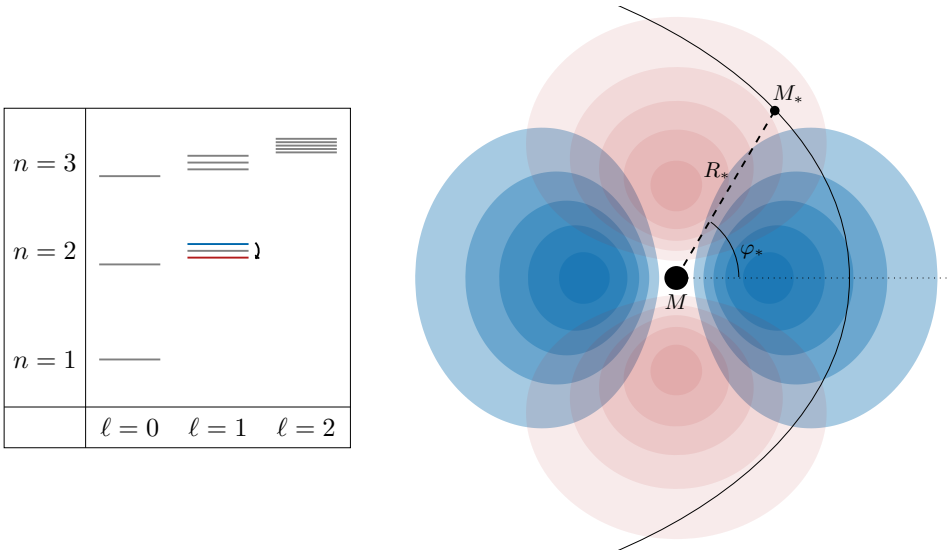


Figure 2: Schematic illustration of the cloud-binary system. The primary object of mass M is surrounded by a superradiantly grown scalar cloud of mass M_c. The secondary object of mass M_* perturbs it through its gravitational potential, causing a mixing between different states of the cloud. The blue and red regions are a faithful representation of the mass densities of the states $|211\rangle$ and $|21\,{-1}\rangle$ on the equatorial plane, but the BH size is not to scale. In the box, we show the bound state spectrum of the gravitational atom for the first few values of n.

2 Setup

The goal of this section is to lay down our framework. We closely follow a previous work [36], and thus we refer the reader there for more details.

Via BH superradiance, bosonic fields can extract energy and angular momentum from rotating BHs, analogous to the Penrose process. The key condition for this process to occur is that the boson's frequency $\omega_{\rm B}$ is smaller than the angular velocity of the event horizon Ω_H, i.e., $\omega_{\rm B} < m\Omega_H$, where m is the azimuthal quantum number in the BH frame. If the boson is massive, the superradiantly amplified waves can get trapped around the BH, allowing their number to grow exponentially. In particular, when the gravitational radius of the BH (r_g) and the Compton wavelength of the field (λ_c) are of the same order, i.e.,

$$\alpha \equiv \frac{r_g}{\lambda_c} = \mu M \lesssim 1\,, \tag{2.1}$$

this growth becomes efficient on astrophysical timescales and a "cloud" of particles can build up around the BH. The system is then often referred to as a "gravitational atom".

In this work, we will stay in the non-relativistic limit, where the Klein-Gordon equation reduces to a Schrödinger equation and thus its solution are the hydrogenic eigenfunctions, defined as

$$\psi_{n\ell m}(t,\mathbf{r}) = R_{n\ell}(r)Y_{\ell m}(\theta,\phi)e^{-i(\omega_{n\ell m}-\mu)t}\,, \tag{2.2}$$

where n, ℓ and m are the principal, angular momentum and azimuthal quantum numbers, respectively. These satisfy the usual relations, $n > \ell$, $\ell \geq 0$ and $\ell \geq |m|$, while $Y_{\ell m}$ are the spherical harmonics and $R_{n\ell}$ the hydrogenic radial functions.

Due to the dissipative nature of the BH horizon, the eigenstates of the cloud, written as $|n\ell m\rangle$, are only quasi-stationary and have complex eigenfrequencies, i.e., $\omega_{n\ell m} = (\omega_{n\ell m})_{\rm R} + i(\omega_{n\ell m})_{\rm I}$. A certain eigenstate or *mode* is superradiant when $(\omega_{n\ell m})_{\rm I} > 0$, which can only happen if $m > 0$. The fastest growing mode is $|n\ell m\rangle = |211\rangle$ and the maximum mass the cloud can obtain is approximately $M_{\rm c} = 0.1M$ [45–47].

The energy of different modes is defined through the real part of the eigenfrequency which, in the limit $\alpha \ll 1$, reads [48]

$$\epsilon_{n\ell m} \equiv (\omega_{n\ell m})_{\rm R} = \mu\left(1 - \frac{\alpha^2}{2n^2} - \frac{\alpha^4}{8n^4} - \frac{(3n-2\ell-1)\alpha^4}{n^4(\ell+1/2)} + \frac{2\tilde{a}m\alpha^5}{n^3\ell(\ell+1/2)(\ell+1)} + \mathcal{O}(\alpha^6)\right). \quad (2.3)$$

As we will see later, it is useful to define different types of energy splittings: we say that two states have a *Bohr* ($\Delta n \neq 0$), *fine* ($\Delta n = 0$, $\Delta\ell \neq 0$) or *hyperfine* ($\Delta n = 0$, $\Delta\ell = 0$, $\Delta m \neq 0$) splitting. A schematic illustration of the bound state spectrum of the gravitational atom is shown in Figure 2.

We work in the reference frame of the central BH with mass M, where $\mathbf{r} = \{r, \theta, \phi\}$ and the coordinates of the companion with mass $M_* = qM$ are $\mathbf{R}_* = \{R_*, \theta_*, \varphi_*\}$. In our conventions, the gravitational perturbation from the companion in the Newtonian approximation is defined as

$$V_*(t, \mathbf{r}) = -\sum_{\ell_*=0}^{\infty}\sum_{m_*=-\ell_*}^{\ell_*} \frac{4\pi q\alpha}{2\ell_*+1} Y_{\ell_* m_*}(\theta_*, \varphi_*) Y^*_{\ell_* m_*}(\theta, \phi)\, F(r)\,, \quad (2.4)$$

where

$$F(r) = \begin{cases} \dfrac{r^{\ell_*}}{R_*^{\ell_*+1}}\Theta(R_* - r) + \dfrac{R_*^{\ell_*}}{r^{\ell_*+1}}\Theta(r - R_*) & \text{for } \ell_* \neq 1\,, \\ \left(\dfrac{R_*}{r^2} - \dfrac{r}{R_*^2}\right)\Theta(r - R_*) & \text{for } \ell_* = 1\,. \end{cases} \quad (2.5)$$

On a generic orbit, the perturbation (2.4) induces a mixing between the cloud's bound state $|n_b\ell_b m_b\rangle$ and another state $|n_a\ell_a m_a\rangle$ through the matrix element [31, 33]

$$\langle n_a\ell_a m_a|V_*(t, \mathbf{r})|n_b\ell_b m_b\rangle = -\sum_{\ell_*, m_*} \frac{4\pi\alpha q}{2\ell_*+1} Y_{\ell_* m_*}(\theta_*, \varphi_*)\, I_r(t)\, I_\Omega(t)\,, \quad (2.6)$$

where I_r and I_Ω are integrals over radial and angular variables, respectively. The following *selection rules* need to be satisfied in order for I_Ω to be nonzero

$$\text{(S1)} \qquad m_* = m_b - m_a\,, \quad (2.7)$$

$$\text{(S2)} \qquad \ell_a + \ell_* + \ell_b = 2p, \qquad \text{for } p \in \mathbb{Z}\,, \quad (2.8)$$

$$\text{(S3)} \qquad |\ell_b - \ell_a| \leq \ell_* \leq \ell_b + \ell_a\,. \quad (2.9)$$

Furthermore, we will often expand the spherical harmonic $Y_{\ell_* m_*}$ appearing in (2.6) in terms of the form $Y_{\ell_* g}(\pi/2, 0)$ (where g is a summation index), which is zero whenever ℓ_* and g have opposite parity.

3 Resonance phenomenology

As first shown in [33], while the companion perturbs the cloud at a slowly increasing frequency, transitions between modes are induced, analogous to the ones described in quantum mechanics by Landau and Zener [49, 50]. This process can exert a strong backreaction on the orbit, giving rise to "floating" and "sinking" orbits. In this section, we study these transitions for generic orbits and at the nonlinear level, by including the backreaction in the frequency evolution self-consistently. The general results found here will be applied to realistic cases in Section 5, where they will be crucial in determining the evolution of the cloud-binary system.

In Section 3.1 we review the setup and the well-known results, which we extend to inclined and eccentric orbits in Section 3.2. Then, in Section 3.3 we include the backreaction, thus coupling the resonating states to the evolution of the binary parameters. The phenomenology of the resulting nonlinear system is explored in Section 3.4 and Section 3.5, for the floating and sinking cases respectively.

3.1 Two-state resonances

The matrix element (2.6) of the gravitational perturbation V_* between two states $|a\rangle = |n_a \ell_a m_a\rangle$ and $|b\rangle = |n_b \ell_b m_b\rangle$ is an oscillatory function of the true anomaly of the orbit φ_*,

$$\langle a|V_*(t)|b\rangle = \sum_{g\in\mathbb{Z}} \eta^{(g)} e^{ig\varphi_*} \,. \tag{3.1}$$

On equatorial co-rotating quasi-circular orbits, the only nonzero term is $g = m_b - m_a \equiv \Delta m$ (on counter-rotating orbits, g has opposite sign), and the coefficients $\eta^{(g)}$ only depend on time through $\Omega(t)$. Restricting our attention to the two-state system, the Hamiltonian is thus

$$\mathcal{H} = \begin{pmatrix} -\Delta\epsilon/2 & \eta^{(g)} e^{ig\varphi_*} \\ \eta^{(g)} e^{-ig\varphi_*} & \Delta\epsilon/2 \end{pmatrix} , \tag{3.2}$$

where $\Delta\epsilon = \epsilon_b - \epsilon_a$ is the energy difference between $|b\rangle$ and $|a\rangle$. As in [33], it is useful to rewrite (3.2) in a *dressed* frame, where the fast oscillatory terms $e^{ig\varphi_*}$ are traded for a slow evolution of the energies. This is done by means of a unitary transformation,

$$\begin{pmatrix} c_a \\ c_b \end{pmatrix} = \begin{pmatrix} e^{ig\varphi_*/2} & 0 \\ 0 & e^{-ig\varphi_*/2} \end{pmatrix} \begin{pmatrix} \tilde{c}_a \\ \tilde{c}_b \end{pmatrix} , \tag{3.3}$$

where $c_j = \langle j|\psi\rangle$ (with $j = a, b$) are the Schrödinger frame coefficients, while $\tilde{c}_a$ and $\tilde{c}_b$ are the dressed frame coefficients. Because $|c_i|^2 = |\tilde{c}_i|^2$, we will drop the tildes in the following discussion. In the dressed frame, the Schrödinger equation reads

$$\frac{\mathrm{d}}{\mathrm{d}t}\begin{pmatrix} c_a \\ c_b \end{pmatrix} = -i\mathcal{H}_{\mathrm{D}} \begin{pmatrix} c_a \\ c_b \end{pmatrix} , \qquad \mathcal{H}_{\mathrm{D}} = \begin{pmatrix} -(\Delta\epsilon - g\Omega)/2 & \eta^{(g)} \\ \eta^{(g)} & (\Delta\epsilon - g\Omega)/2 \end{pmatrix} . \tag{3.4}$$

When $\Omega(t) \equiv \dot{\varphi}_*$ is specified, (3.4) determines the evolution of the population of the two states.

Without including the backreaction of the resonance on the orbit, $\Omega(t)$ is exclusively determined by external factors, such as the energy losses due to GW emission or cloud ionization,

which induce a frequency chirp. These effects typically have a nontrivial dependence on Ω itself, widely varying in strength at different points of the inspiral. However, the resonances described by (3.4) are restricted to a bandwidth $\Delta\Omega \sim \eta^{(g)}$. This is typically narrow enough to allow us to approximate the external energy losses, as well as any other Ω-dependent function, with their value at the resonance frequency

$$\Omega_0 = \frac{\Delta\epsilon}{g} \,. \tag{3.5}$$

Around Ω_0, we can linearize the frequency chirp and write $\Omega = \gamma t$. For concreteness, in this section we will assume that external energy losses are only due to GW emission, in which case

$$\gamma = \frac{96}{5} \frac{q M^{5/3} \Omega_0^{11/3}}{(1+q)^{1/3}} \,. \tag{3.6}$$

It is particularly convenient to rewrite the Schrödinger equation in terms of dimensionless variables and parameters:

$$\frac{\mathrm{d}}{\mathrm{d}\tau} \begin{pmatrix} c_a \\ c_b \end{pmatrix} = -i \begin{pmatrix} \omega/2 & \sqrt{Z} \\ \sqrt{Z} & -\omega/2 \end{pmatrix} \begin{pmatrix} c_a \\ c_b \end{pmatrix} \,, \tag{3.7}$$

where the frequency chirp now reads $\omega = \tau$, and we defined

$$\tau = \sqrt{|g|\gamma}\, t \,, \qquad \omega = \frac{\Omega - \Omega_0}{\sqrt{\gamma/|g|}} \,, \qquad Z = \frac{(\eta^{(g)})^2}{|g|\gamma} \,. \tag{3.8}$$

The initial conditions at $\tau \to -\infty$ we are interested in are those where only one state is populated, say $c_a = 1$ and $c_b = 0$. The only dimensionless parameter of (3.7) is the so-called "Landau-Zener parameter" Z, which determines uniquely the evolution of the system and its state at $\tau \to +\infty$. In fact, the populations at $\tau \to +\infty$ can be derived analytically and are given by the Landau-Zener formula:

$$|c_a|^2 = e^{-2\pi Z} \,, \qquad |c_b|^2 = 1 - e^{-2\pi Z} \,. \tag{3.9}$$

For $2\pi Z \gg 1$ the transition can be classified as *adiabatic*, meaning that the process is so slow that the cloud is entirely transferred from $|a\rangle$ to $|b\rangle$. Conversely, for $2\pi Z \ll 1$, the transition is *non-adiabatic*, with a partial or negligible transfer occurring.

There is one final remark to be made before we proceed. Dealing with two-state transitions is a good approximation as long as the frequency width of the resonance, $\Delta\Omega \sim \eta^{(g)}$, is much narrower than the distance (in frequency) from the closest resonance. The latter becomes extremely small for hyperfine resonances, especially on generic orbits, where g can take values different from Δm. In some cases formula (2.3) can indeed return an exact degeneracy of two resonances, up to $\mathcal{O}(\alpha^5)$. We have thoroughly checked, by numerical computation of the eigenfrequencies up to $\mathcal{O}(\alpha^6)$, that in all realistic cases the resonances are indeed narrow enough for the two-state approximation to hold.

3.2 Resonances on eccentric and inclined orbits

We now extend the treatment of Section 3.1 to orbits with nonzero eccentricity or inclination, explaining what changes for the resonant frequencies and the overlap coefficients $\eta^{(g)}$.

Let us start with eccentric co-rotating orbits. In the quasi-circular case, equation (3.1) manifestly separates a "fast" and a "slow" motion: the former originates from φ_* varying over the course of an orbit, while the latter is due to the dependence of the coefficients $\eta^{(g)}$ on $\Omega(t)$ (and can be safely neglected). It will be helpful to work with a variable that performs the same trick on eccentric orbits: the *mean anomaly*

$$\tilde{\varphi}_*(t) = \int^t \Omega(t')\,\mathrm{d}t' \,. \tag{3.10}$$

Because φ_* itself is an oscillating function of $\tilde{\varphi}_*$, we can write

$$\langle a|V_*(t)|b\rangle = \sum_{g\in\mathbb{Z}} \tilde{\eta}^{(g)} e^{ig\tilde{\varphi}_*} \,, \tag{3.11}$$

where the coefficients $\tilde{\eta}^{(g)}$ only depend on time through $\Omega(t)$. For simplicity, in the following discussion we will drop the tildes, with the different definition of $\eta^{(g)}$ for nonzero eccentricity left understood.

For a given eccentricity $\varepsilon \neq 0$, multiple terms of (3.11), each corresponding to a different value of g, can be nonzero. As a consequence, a resonance between two given states can be triggered at different points of the inspiral, at the frequencies $\Omega_0^{(g)} = \Delta\epsilon/g$, for any integer g (provided that it has the same sign as $\Delta\epsilon$). The numerical evaluation of the coefficients $\eta^{(g)}$ requires to Fourier expand V_* in the time domain, at the orbital frequency $\Omega = \Omega_0^{(g)}$. This can be done with techniques similar to [36], where the same matrix element was evaluated between a bound and an unbound state. The coefficient $\eta^{(\Delta m)}$ is special because it is the only one with a finite, nonzero limit for $\varepsilon \to 0$, where it reduces to its circular-orbit counterpart. For all other values of g, instead, $\eta^{(g)}$ vanishes for $\varepsilon \to 0$. Even at moderately large ε, the coefficient $\eta^{(\Delta m)}$ remains significantly larger than all the others

Let us now look at circular but inclined orbits. Here, the Fourier coefficients $\eta^{(g)}$ acquire a dependence on the inclination angle β, where $\beta = 0$ and $\beta = \pi$ correspond to the co-rotating and counter-rotating scenarios. The functional dependence can be readily extracted by evaluating the perturbation (2.4) using the the identity [51]

$$Y_{\ell_* m_*}(\theta_*, \varphi_*) = \sum_{g=-\ell_*}^{\ell_*} d^{(\ell_*)}_{m_*,g}(\beta) Y_{\ell_* g}\left(\frac{\pi}{2}, 0\right) e^{ig\Omega t} \,. \tag{3.12}$$

Here, $d^{(\ell_*)}_{m_*,g}(\beta)$ is a Wigner small d-matrix and is responsible for the angular dependence of the coupling, $\eta^{(g)} \propto d^{(\ell_*)}_{m_*,g}(\beta)$. Its functional form takes on a simple expression in many of the physically interesing cases, as we will discuss explicitly in Section 4. We thus see that inclined orbits also trigger resonances at $\Omega = \Omega_0^{(g)} = \Delta\epsilon/g$, but this time g can only assume a finite number of different values. Similar to the eccentric case, $g = \Delta m$ is special, because it is the only case where $d^{(\ell_*)}_{m_*,g}(\beta)$ does not vanish for $\beta \to 0$, as the resonance survives in the equatorial co-rotating limit. Similarly, in the counter-rotating case $\beta \to \pi$, the only surviving value is $g = -\Delta m$.

Similar techniques can be applied in the eccentric *and* inclined case, where the overlap can be expanded in two sums, each with its own index, say g_ε and g_β. We do not explicitly compute $\eta^{(g)}$ in the general case, as the understanding developed so far is sufficient to move forward and characterize the phenomenology in realistic cases.

3.3 Backreaction on the orbit

We now include the backreaction on the orbit, allowing for generic nonzero eccentricity *and* inclination. During a resonance, the energy and angular momentum contained in the cloud change over time: this variation must be compensated by an evolution of the binary parameters, the (dimensionless) frequency ω, eccentricity ε and inclination β. In turn, this backreaction impacts the Schrödinger equation (3.7), which directly depends on ω. The result is a coupled nonlinear system of ordinary differential equations, describing the co-evolution of the cloud and the binary, which we derive in this section.

To describe the evolution of ω, ε and β we need three equations. These are the conservation of energy and of two components of the angular momentum: the projection along the BH spin and the projection on the equatorial plane. The conservation of energy reads

$$\frac{\mathrm{d}}{\mathrm{d}t}\left(E+E_{\rm c}\right)=-\gamma f(\varepsilon)\,\frac{qM^{5/3}}{3(1+q)^{1/3}\Omega_0^{1/3}}\,, \tag{3.13}$$

where γ was defined in (3.6) and the binary's and cloud's energies are

$$E=-\frac{qM^{5/3}\Omega^{2/3}}{2(1+q)^{1/3}}\,,\qquad E_{\rm c}=\frac{M_{\rm c}}{\mu}(\epsilon_a|c_a|^2+\epsilon_b|c_b|^2)\,, \tag{3.14}$$

while the function

$$f(\varepsilon)=\frac{1+\frac{73}{24}\varepsilon^2+\frac{37}{96}\varepsilon^4}{(1-\varepsilon^2)^{7/2}} \tag{3.15}$$

quantifies the dependence of GW energy losses on the eccentricity [52, 53]. Similarly, the conservation of the angular momentum components requires

$$\frac{\mathrm{d}}{\mathrm{d}t}\left(L\cos\beta+S_{\rm c}\right)=-h(\varepsilon)\gamma\,\frac{qM^{5/3}}{3(1+q)^{1/3}\Omega_0^{4/3}}\cos\beta\,, \tag{3.16}$$

$$\frac{\mathrm{d}}{\mathrm{d}t}\left(L\sin\beta\right)=-h(\varepsilon)\gamma\,\frac{qM^{5/3}}{3(1+q)^{1/3}\Omega_0^{4/3}}\sin\beta\,. \tag{3.17}$$

where

$$L=\frac{qM^{5/3}}{(1+q)^{1/3}}\frac{\sqrt{1-\varepsilon^2}}{\Omega^{1/3}},\qquad S_{\rm c}=\frac{M_{\rm c}}{\mu}(m_a|c_a|^2+m_b|c_b|^2)\,, \tag{3.18}$$

and

$$h(\varepsilon)=\frac{1+\frac{7}{8}\varepsilon^2}{(1-\varepsilon^2)^2}\,. \tag{3.19}$$

Before proceeding, there are two issues the reader might worry about. First, depending on the resonance, the spin of the cloud during the transition might also have equatorial components, and should thus appear in (3.17). Second, the BH spin breaks spherical symmetry, therefore the equatorial projection of the angular momentum should not be conserved. Clearly, in the Newtonian limit this is not a problem, but one might still question whether it is consistent to treat within this framework hyperfine resonances, whose very existence is due to a nonzero BH spin in the first place. We address both these issues in Appendix A, where we justify our assumptions, and proceed here to study the dynamics of the previous equations.

Equations (3.13), (3.16) and (3.17) can be put in a dimensionless form as follows,

$$\frac{\mathrm{d}\omega}{\mathrm{d}\tau} = f(\varepsilon) - B\frac{\mathrm{d}|c_b|^2}{\mathrm{d}\tau}\,, \tag{3.20}$$

$$C\frac{\mathrm{d}}{\mathrm{d}\tau}\sqrt{1-\varepsilon^2} = \sqrt{1-\varepsilon^2}\left(f(\varepsilon) - B\frac{\mathrm{d}|c_b|^2}{\mathrm{d}\tau}\right) + B\frac{\Delta m}{g}\frac{\mathrm{d}|c_b|^2}{\mathrm{d}\tau}\cos\beta - h(\varepsilon)\,, \tag{3.21}$$

$$C\sqrt{1-\varepsilon^2}\frac{\mathrm{d}\beta}{\mathrm{d}\tau} = -B\frac{\Delta m}{g}\frac{\mathrm{d}|c_b|^2}{\mathrm{d}\tau}\sin\beta\,, \tag{3.22}$$

where we defined the dimensionless parameters

$$B = \frac{3M_\mathrm{c}}{M}\frac{\Omega_0^{4/3}((1+q)M)^{1/3}}{q\alpha\sqrt{\gamma/|g|}}(-g)\,, \qquad C = \frac{3\Omega_0}{\sqrt{\gamma/|g|}}\,. \tag{3.23}$$

The Schrödinger equation (3.7) remains unchanged, but it should be kept in mind that Z now depends on ε and β through $\eta^{(g)}$ (instead, the dependence on ω can still be neglected if the resonance is narrow enough).

The parameter B controls the strength of the backreaction. As can be seen from (3.20), a positive $B > 0$ (i.e., $g < 0$ and $\Delta\epsilon < 0$) will slow down the frequency chirp, giving rise to a *floating* orbit and generally making the resonance more adiabatic. Conversely, $B < 0$ (i.e., $g > 0$ and $\Delta\epsilon > 0$) induces *sinking* orbits and makes resonances less adiabatic. By extension, we will refer to floating resonances and sinking resonances to denote the type of backreaction they induce.

3.4 Floating orbits

Backreaction of the floating type ($B > 0$) turns out to be the most relevant case for realistic applications, so we make a detailed study of its phenomenology here. When the backreaction is strong, the evolution of the system exhibits a very well-defined phase of floating orbit. We are then concerned with three aspects.

1. Under what conditions is a floating resonance initiated? We answer this question with a simple analytical prescription, which is found and discussed in Section 3.4.1.

2. How does the system evolve during the float? This is addressed in Section 3.4.2, where we study the evolution of the eccentricity and inclination.

3. When does a floating resonance end? In Section 3.4.3 we show that several phenomena can *break* (and end) the resonance before the transition from $|a\rangle$ to $|b\rangle$ is complete, and compute accurately the conditions under which this phenomenon happens.

3.4.1 Adiabatic or non-adiabatic

From Section 3.1, we know that if $B = 0$, then a fraction $1 - e^{-2\pi Z}$ of the cloud is transferred during the resonances. For $2\pi Z \gg 1$, this value is already very close to 1. Adding the backreaction does not change this conclusion: the resonance stays adiabatic and a complete transfer from $|a\rangle$ to $|b\rangle$ is observed. Assuming for simplicity quasi-circular orbits ($\varepsilon = 0$), the duration of the floating orbit can be easily read off (3.20):

$$\Delta t_\mathrm{float} = \frac{B}{\sqrt{|g|\gamma}} = \frac{3M_\mathrm{c}}{M}\frac{\Omega_0^{4/3}((1+q)M)^{1/3}}{q\alpha\gamma}(-g)\,. \tag{3.24}$$

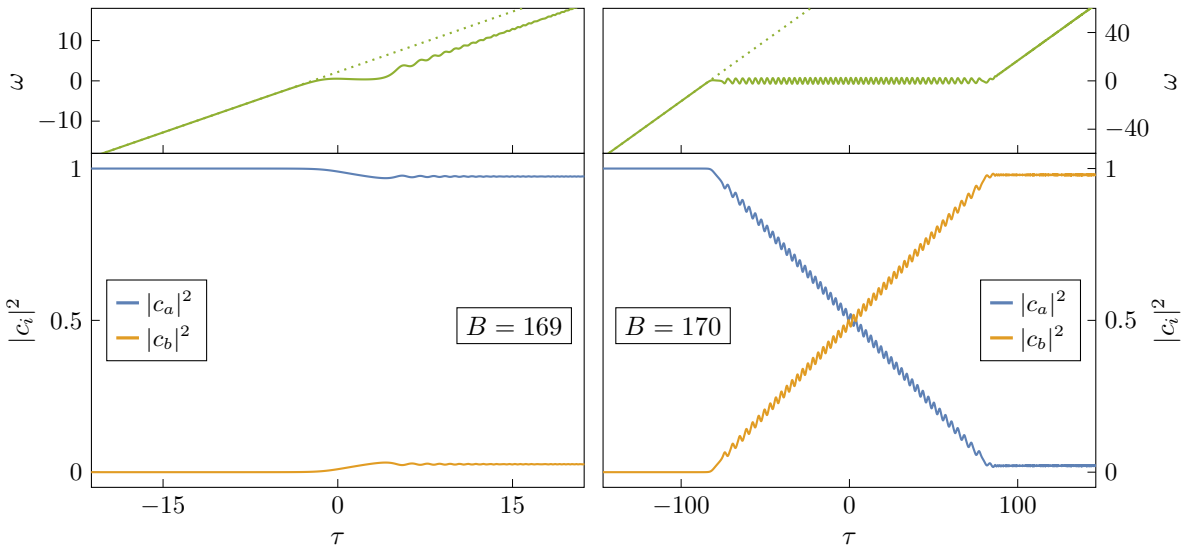


Figure 3: Numerical solution of the nonlinear system (3.7)-(3.20). In both panels we set $Z = 0.001$, whereas we choose the values of B to be 169 (*left panel*) and 170 (*right panel*), slightly below or above the adiabaticity threshold (the limit value of ZB differs slightly from the one given in (3.25), due to finite-Z corrections). In the left panel, a non-adiabatic transition is observed. Conversely, in the right panel, we find an adiabatic transition and the consequent formation of a floating orbit, whose duration matches the predicted $\Delta t_{\text{float}} = B/\sqrt{|g|\gamma}$. The dotted lines represent the evolution of ω in absence of backreaction.

This is independent of the strength of the perturbation $\eta^{(g)}$, and corresponds to the time it takes for the external energy losses to dissipate the energy of the two-state system. For nonzero eccentricity instead, one must integrate $f(\varepsilon)$ over time to determine the duration of the float.

The situation for $2\pi Z \ll 1$ is in principle much less clear: with $B = 0$ the resonance would be non-adiabatic, but backreaction tends to make it more adiabatic. Let us once again restrict to quasi-circular orbits for simplicity. By careful numerical study of equations (3.7) and (3.20), we find that the long-time behavior of the system is predicted by the parameter ZB alone. Depending on its value, two qualitatively different outcomes are possible:

$$\text{if} \quad 2\pi Z \ll 1 \quad \text{and} \quad \begin{cases} ZB < 0.1686\ldots & \longrightarrow \quad \text{very non-adiabatic,} \\ ZB > 0.1686\ldots & \longrightarrow \quad \text{very adiabatic.} \end{cases} \tag{3.25}$$

In the upper case, a negligible fraction of the cloud is transferred and the time evolution of ω is almost exactly linear. Conversely, in the bottom case, the cloud is entirely transferred from $|a\rangle$ to $|b\rangle$ and ω is stalled for an amount of time Δt_{float} given by (3.24), during which it oscillates around zero. Intermediate behaviors are not possible, unless the value of ZB is extremely fine tuned. The two cases are illustrated in Figure 3.

We can give an approximate derivation of the previous result as follows. As long as $|c_b|^2$ is small enough, the backreaction term in (3.20) is negligible, hence ω evolves linearly and the final populations approximate the Landau-Zener result (3.9), giving $|c_b|^2 \approx 2\pi Z$. As the unbackreacted transition happens in the time window $|\tau| \lesssim 1$, we see from (3.20) that the backreaction becomes

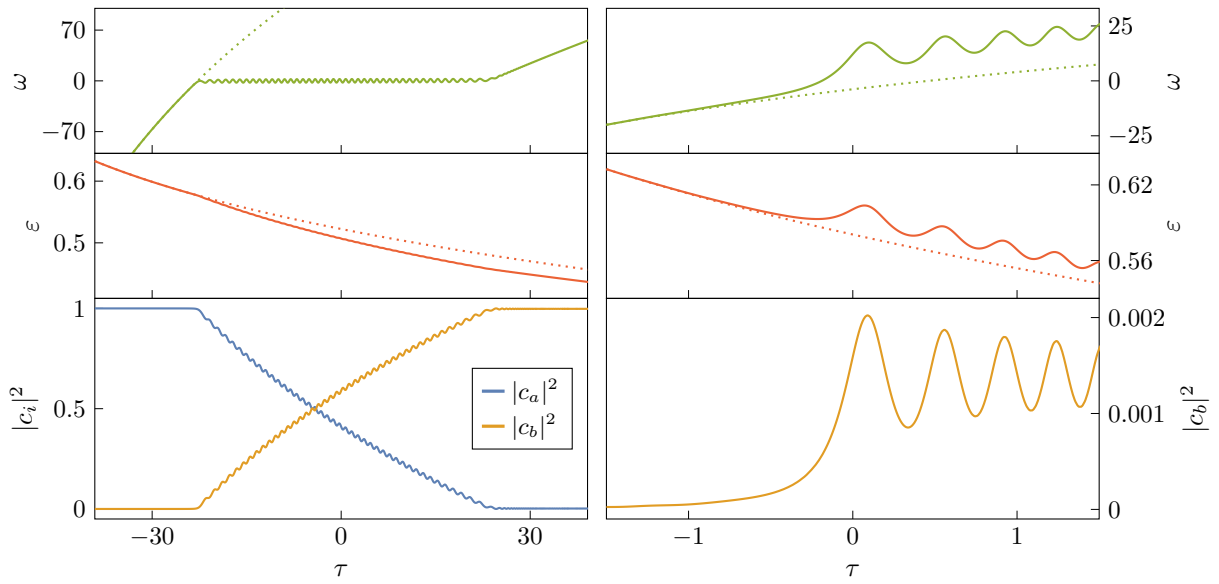


Figure 4: Floating (*left panel*) and sinking (*right panel*) resonances on eccentric orbits, with $\Delta m/g = 1$. We display the value of the frequency ω, the eccentricity ε and the populations $|c_a|^2$ and $|c_b|^2$ as function of τ, obtained by solving equations (3.7), (3.20) and (3.21) with $\beta = 0$ numerically. The parameters used for the floating case are $Z = 0.03$, $B = 250$, $C = 1000$, while for the sinking case we used $Z = 0.01$, $B = -10000$, $C = 100$. The dotted lines represent the evolution of ω and ε in absence of backreaction. Even though the impact of the resonance on the eccentricity might look mild, the effect is actually dramatic when seen as function of ω, as shown in Figure 5.

significant when $1 \lesssim B \cdot 2\pi Z \implies ZB \gtrsim 1/(2\pi) \approx 0.159\ldots$ Given the minimal numerical difference between this coefficient and the one given in (3.25), for simplicity we will often write the relevant condition for an adiabatic resonance simply as $2\pi ZB \gtrless 1$. The slow-down effect on the evolution of $\omega(\tau)$ enjoys a positive-feedback mechanism: the slower ω evolves, the more the transition is adiabatic, meaning that $|c_b|^2$ is larger, which further slows down $\omega(\tau)$, and so on. This explains why no intermediate behaviors are observed: once the backreaction goes over a certain critical threshold, the process becomes self-sustaining.

The picture outlined so far changes slightly when the eccentricity is nonzero. First, if the binary had a constant eccentricity ε_0, we could simply replace $\gamma \to \gamma f(\varepsilon_0)$ to conclude that the critical threshold for adiabaticness becomes

$$2\pi ZB \gtrless f(\epsilon_0)^{3/2}\,. \tag{3.26}$$

When the eccentricity is allowed to vary starting from the initial value ε_0, equation (3.26) still correctly predicts whether the system enters a floating orbit phase. However, the transfer might no longer be complete, as the resonance might *break*. This aspect will be discussed in Section 3.4.3.

3.4.2 Evolution of eccentricity and inclination

The left panel of Figure 4 shows a numerical solution of the coupled nonlinear equations (3.7), (3.20), (3.21) and (3.22), for an equatorial co-rotating ($\beta = 0$) but eccentric ($\varepsilon \neq 0$) system, undergoing a floating orbit with $g = \Delta m$. The state dynamics is largely similar to what we

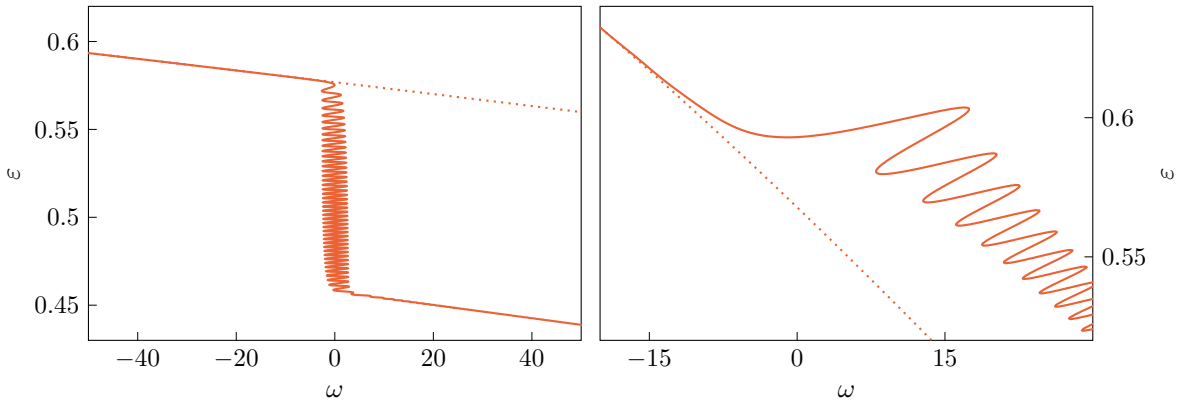


Figure 5: Same resonances as in Figure 4, but now the evolution of eccentricity is shown as function of the frequency, for floating (*left panel*) and sinking (*right panel*) orbits. The dashed lines represent the vacuum evolution.

described in Section 3.4.1. The most interesting new effect concerns the evolution of the eccentricity, which can be seen to decrease during the float, at a rate faster than the circularization provided by GW emission. The same numerical solution is shown as function of frequency in Figure 5.

The evolution of the eccentricity during a float can be studied analytically by plugging $\mathrm{d}\omega/\,\mathrm{d}\tau \approx 0$ in equations (3.21) and (3.22), which become

$$C\frac{\mathrm{d}}{\mathrm{d}\tau}\sqrt{1-\varepsilon^2} = \frac{\Delta m}{g} f(\varepsilon)\cos\beta - h(\varepsilon)\,, \tag{3.27}$$

$$C\sqrt{1-\varepsilon^2}\frac{\mathrm{d}\beta}{\mathrm{d}\tau} = -\frac{\Delta m}{g} f(\varepsilon)\sin\beta\,. \tag{3.28}$$

For resonances with $\beta = 0$ and $g = \Delta m$, such as the one shown in Figures 4 and 5, a small-ε expansion leads to the following solution:

$$\varepsilon(t) \approx \varepsilon_0\, e^{-\frac{22}{18}\gamma t/\Omega_0}\,. \tag{3.29}$$

This result should be compared to the GW-induced circularization in absence of backreaction,

$$\varepsilon(t) \approx \varepsilon_0\, e^{-\frac{19}{18}\gamma t/\Omega_0}\,. \tag{3.30}$$

Therefore, not only is the orbit stalled at $\Omega(t) \approx \Omega_0$ for a potentially long time, given in (3.24), during which the eccentricity keeps reducing; but it also goes down at a faster rate than in the vacuum, as can be seen comparing (3.29) with (3.30). The longer the resonance, the more the binary is circularized.

This result holds for co-rotating resonances with $g = \Delta m$, which are the only ones surviving in the small-ε limit and usually have the largest coupling $\eta^{(g)}$ even at moderately large eccentricities. The dynamics is different in other cases. Remaining in the equatorial co-rotating case ($\beta = 0$), eccentric binaries can also undergo (usually weaker) resonances where $g \neq \Delta m$. In this case, (3.27) has a different behavior: if $|\Delta m/g| < 1$, there is a fixed point $\bar{\varepsilon} > 0$ such that if $\varepsilon < \bar{\varepsilon}$ then

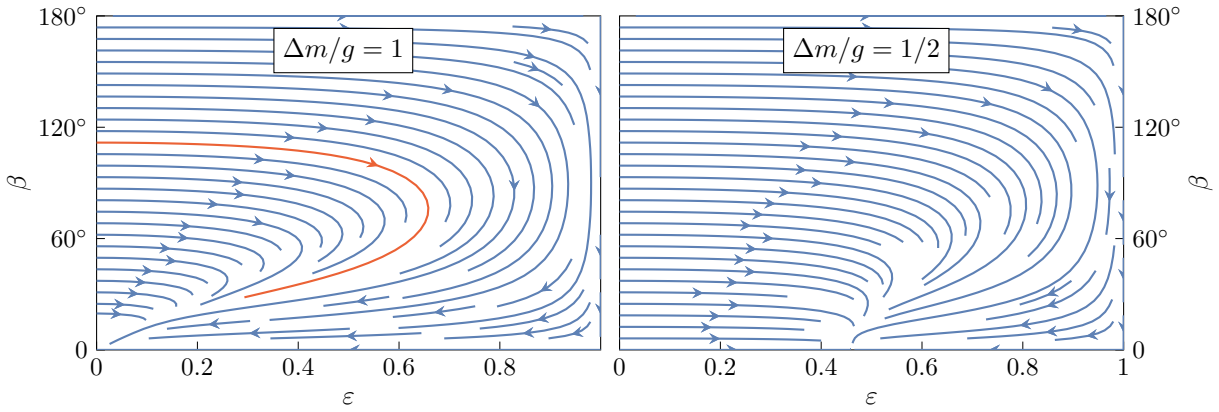


Figure 6: Flow in the eccentricity-inclination plane (ε, β) determined by equations (3.21) and (3.22) under the assumption that the system is on a floating orbit, i.e., $\mathrm{d}|c_b|^2/\,\mathrm{d}\tau = f(\varepsilon)/B$, for two different values of $\Delta m/g$. The highlighted arrow [red] roughly depicts the trajectory followed by the system in Figure 7.

ε increases, while if $\varepsilon > \bar{\varepsilon}$ then ε decreases. For example, for $\Delta m/g = 1/2$, we have $\bar{\varepsilon} \approx 0.46$ and the eccentricity approaches the fixed point according to

$$\varepsilon(t) \approx 0.46 + (\varepsilon_0 - 0.46) e^{-3.49\gamma t/\Omega_0} \,. \tag{3.31}$$

Floating resonances with $|\Delta m/g| > 1$ will instead circularize the binary even quicker than (3.29). As ε decreases, however, so does Z: eventually, the perturbation becomes too weak and the resonance stops, generically leaving the cloud in a mixed state as the inspiral resumes. This aspect will be discussed in Section 3.4.3.

The possibilities described so far are a particular case of the general dynamics, which includes the evolution of the inclination β. The flow induced by equations (3.27) and (3.28) in the (ε, β) plane is shown in Figure 6, where the dynamics on the x axis is described by equations (3.29) (*left panel*) and (3.31) (*right panel*). Perhaps the most striking feature of Figure 6 is the fact that the system is violently pulled away from inclined circular orbits (y axis). In fact, $\mathrm{d}\varepsilon/\,\mathrm{d}\tau$ diverges for $\varepsilon \to 0$ and finite β, meaning that the validity of equations (3.27) and (3.28) must somehow break down in that limit. The explanation for this behavior is that it is inconsistent to assume that the system undergoes an adiabatic floating resonance on inclined circular orbits: eccentricity *must* increase before the onset of the resonance. This is precisely the behavior observed in Figure 7, where equations (3.7), (3.20), (3.21) and (3.22) are solved numerically starting from $\varepsilon_0 = 0$ and $\beta_0 \neq 0$. If $2\pi ZB > f(\varepsilon_0)^{3/2}$, then the system enters the floating orbit and starts to follow the trajectories shown in Figure 6. The total "distance" in the (β, ε) plane travelled by the system by the time the transition completes depends on a single dimensionless parameter,

$$D \equiv \frac{B}{C} = \frac{\gamma \Delta t_{\rm float}}{\Omega_0} \,. \tag{3.32}$$

However, it is also possible that the transition stops before fully completing, as shown in Figure 7 (*right panel*). This is the subject of Section 3.4.3.

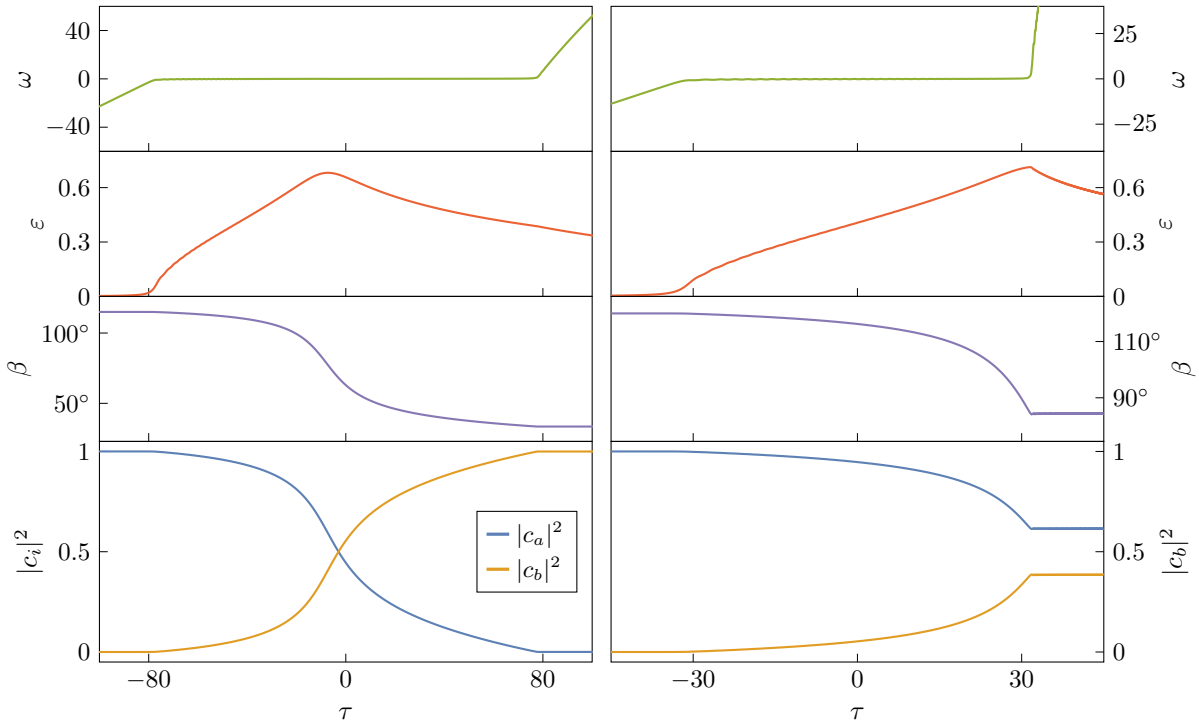


Figure 7: Numerical solution of equations (3.7), (3.20), (3.21) and (3.22) with parameters $Z = 0.001$, $B = 1000$, $D = 4/3$ and $g = \Delta m$. For simplicity we ignore that in realistic cases Z depends on the eccentricity, and we keep it constant instead. The system is initialized with eccentricity $\varepsilon_0 = 0$. A complete transition is achieved when the initial inclination is $\beta_0 = 115°$ (*left panel*), while a "broken resonance" is observed when $\beta_0 = 120°$ (*right panel*), with the float abruptly ending when (3.39) is satisfied. In both cases, the system follows the trajectories indicated in Figure 6 until the resonance ends or breaks.

3.4.3 Resonance breaking

When some parameters are allowed to vary with time, the floating orbit dynamics described in Section 3.4.1 and 3.4.2 features a new phenomenon, which we call *resonance breaking*, and has been shown already in Figure 7 (*right panel*). The goal of this section is to determine analytically under which conditions a floating resonance breaks. Three different cases of parameter variation are encountered in realistic scenarios.

1. The binary eccentricity ε changes with time, as seen in Figure 7. The eccentricity is the only binary parameter that appears explicitly in (3.7) and (3.20), while a change in β only acts through a variation of Z.

2. As a consequence of changing ε and β, the strength of the perturbation $\eta^{(g)}$, and thus the Landau-Zener parameter Z, changes as well.

3. The total mass of the cloud changes with time if state $|b\rangle$ has $(\omega_{n\ell m})_{\rm I} \neq 0$: as a consequence, the Schrödinger equation (3.7) is modified to

$$\frac{\mathrm{d}}{\mathrm{d}\tau}\begin{pmatrix} c_a \\ c_b \end{pmatrix} = -i\begin{pmatrix} \omega/2 & \sqrt{Z} \\ \sqrt{Z} & -\omega/2 - i\Gamma \end{pmatrix}\begin{pmatrix} c_a \\ c_b \end{pmatrix}, \tag{3.33}$$

where $\Gamma \equiv (\omega_{n\ell m})_{\rm I}/\sqrt{\gamma/|g|}$, and care must be paid in the definition of B.

All three effects come with two possible signs, one of which "weakens" the resonance and potentially breaks it, while the other "reinforces" it: in the first category we have the increase of eccentricity, the decrease of Z and the cloud decay ($\Gamma < 0$).[2]

To understand under what conditions a resonance breaks, it is insightful to study the evolution of ω during the float. To zeroth order, ω is identically zero, but Figures 3, 4 and 7 hint towards a nontrivial dynamics to higher order, with small oscillatory features of varying frequency. Let us try to find an equation of motion for the sole ω, in the vanilla case with $\mathrm{d}\varepsilon/\,\mathrm{d}\tau = \mathrm{d}Z/\,\mathrm{d}\tau = \Gamma = 0$, where no resonance break is expected. By taking the derivative of (3.20) and repeatedly using Schrödinger's equation, we find

$$\frac{\mathrm{d}^2\omega}{\mathrm{d}\tau^2} = -B\frac{\mathrm{d}|c_b|^2}{\mathrm{d}\tau^2} = -2ZB(1-2|c_b|^2) + \sqrt{Z}B(c_a^* c_b + c_a c_b^*)\omega\,. \tag{3.34}$$

Remarkably, the equation of motion obeyed by ω closely resembles a harmonic oscillator whose (squared) frequency is $-\sqrt{Z}B(c_a^* c_b + c_a c_b^*)$. It is thus natural to study this quantity: by directly applying Schrödinger's equation, we find

$$\sqrt{Z}\frac{\mathrm{d}}{\mathrm{d}\tau}(c_a^* c_b + c_a c_b^*) = \omega\frac{\mathrm{d}|c_b|^2}{\mathrm{d}\tau}\,. \tag{3.35}$$

We notice that equations (3.34) and (3.35) form a closed system of ordinary differential equations (because in the vanilla case $|c_b|^2 = (\tau-\omega)/B$), through which it is possible to prove mathematically a number of interesting properties of the system, such as the fact that at small Z the evolution is entirely determined by ZB, as thoroughly described in Section 3.4.1.

For the scope of this section it is however sufficient to assume that the quantity $c_a^* c_b + c_a c_b^*$ evolves slowly during a float, with a timescale of $\Delta t_{\rm float}$, similar to $|c_b|^2$. Equation (3.34) can then be solved in a WKB approximation as

$$\omega \approx \frac{2\sqrt{Z}(1-2|c_b|^2)}{c_a^* c_b + c_a c_b^*} + \frac{A\,Z^{-1/8}B^{-1/4}}{(-c_a^* c_b - c_a c_b^*)^{1/4}}\cos\left(Z^{1/4}B^{1/2}\int_0^\tau \sqrt{-c_a^* c_b - c_a c_b^*}\,\mathrm{d}\tau' + \delta\right), \tag{3.36}$$

where A is a constant and δ is a phase. As the fast oscillations average out, we can plug the first, non-oscillatory, term of (3.36) into (3.35) and integrate to find $c_a^* c_b + c_a c_b^* \approx -\sqrt{1-(1-2|c_b|^2)^2}$. The resulting solution for ω,

$$\omega \approx -\frac{2\sqrt{Z}(1-2|c_b|^2)}{\sqrt{1-(1-2|c_b|^2)^2}} + \text{oscillatory terms}\,, \tag{3.37}$$

is well-behaved for the entire duration of the float, only diverging before ($|c_b|^2 = 0$) or after ($|c_b|^2 = 1$) the resonance.

The same analytical approach can be applied to the cases mentioned above, with varying ϵ or Z, or $\Gamma \neq 0$. A "master equation", where all three effects are turned on at the same time, is derived and shown in Appendix B. Here, we find it more illuminating to study them one at a

[2] The superradiant amplification of state $|b\rangle$, that is, $\Gamma > 0$, is never encountered for floating resonances anyway.

time. The outcome in realistic cases may then be approximated by only retaining the strongest of the three effects.

When the eccentricity is not a constant, the time derivative of (3.20) contains the additional term $\mathrm{d}f(\varepsilon)/\,\mathrm{d}\tau$. As a result, the equation of motion for ω and the expression of $c_a^* c_b + c_a c_b^*$ are both modified. The final result, which has been thoroughly checked against numerical solutions of the full system (3.7)-(3.20)-(3.21)-(3.22), is

$$\omega \approx \frac{\frac{\mathrm{d}f(\varepsilon)}{\mathrm{d}\tau} - 2ZB(1-2|c_b|^2)}{\sqrt{ZB^2(1-(1-2|c_b|^2)^2) - (f(\varepsilon)^2 - f(\varepsilon_0)^2)}} + \text{oscillatory terms}\,. \tag{3.38}$$

If ε increases from its initial value ε_0, the denominator can hit zero before the transition is complete, and the resonance breaks. The population remaining in state $|a\rangle$ and the binary eccentricity at resonance breaking satisfy

$$4ZB^2(|c_a|^2 - |c_a|^4) = f(\varepsilon)^2 - f(\varepsilon_0)^2\,, \tag{3.39}$$

which can be compared with the numerical solution in Figure 7 (*right panel*). Despite the simplicity of (3.39), a numerical integration is still needed, in principle, to determine ε as function of $|c_a|^2$, and so whether a resonance will break. We can however make a simple conservative estimate by noting that the left-hand-side can be at maximum ZB^2. If the system follows a trajectory in the (ε, β) plane (cf. Figure 6) that significantly increases its eccentricity, such that

$$f(\varepsilon) > \sqrt{Z}B \tag{3.40}$$

at some point, then the resonance must necessarily break.

If instead Z is allowed to vary while ε is kept constant, new terms appear when taking the time derivative of the Schrödinger equation (used in the second equality of (3.34)), and (3.36) becomes a damped harmonic oscillator. Similar to the previous case, the resonance breaks when $c_a^* c_b + c_a c_b^* = 0$, which is equivalent to

$$4ZB^2(|c_a|^2 - |c_a|^4) = f(\varepsilon)^2\left(1 - \frac{Z}{Z_0}\right), \tag{3.41}$$

see Figure 8 (*left panel*). Analogous considerations as before can be applied to extract from (3.41) the approximate point of resonance breaking without performing a numerical integration.

Taking into account a nonzero decay width Γ, while keeping ϵ and Z constant, requires more care. Because $|c_a|^2 + |c_b|^2$ is no longer a constant, equation (3.20) is now written as

$$\frac{\mathrm{d}\omega}{\mathrm{d}\tau} = f(\varepsilon) - \frac{B}{\Delta\epsilon}\left(\epsilon_a \frac{\mathrm{d}|c_a|^2}{\mathrm{d}\tau} + \epsilon_b \frac{\mathrm{d}|c_b|^2}{\mathrm{d}\tau} + 2\Gamma\epsilon_b|c_b|^2\right) = f(\varepsilon) + B\frac{\mathrm{d}|c_a|^2}{\mathrm{d}\tau}\,, \tag{3.42}$$

where the constant parameter B is computed according to (3.23), using the value of the mass of the cloud before the start of the resonance. Furthermore, due to the modified Schrödinger equation, formula (3.35) becomes

$$\sqrt{Z}\frac{\mathrm{d}}{\mathrm{d}\tau}(c_a^* c_b + c_a c_b^*) = -\omega\frac{\mathrm{d}|c_a|^2}{\mathrm{d}\tau} - \Gamma\sqrt{Z}(c_a^* c_b + c_a c_b^*)\,. \tag{3.43}$$

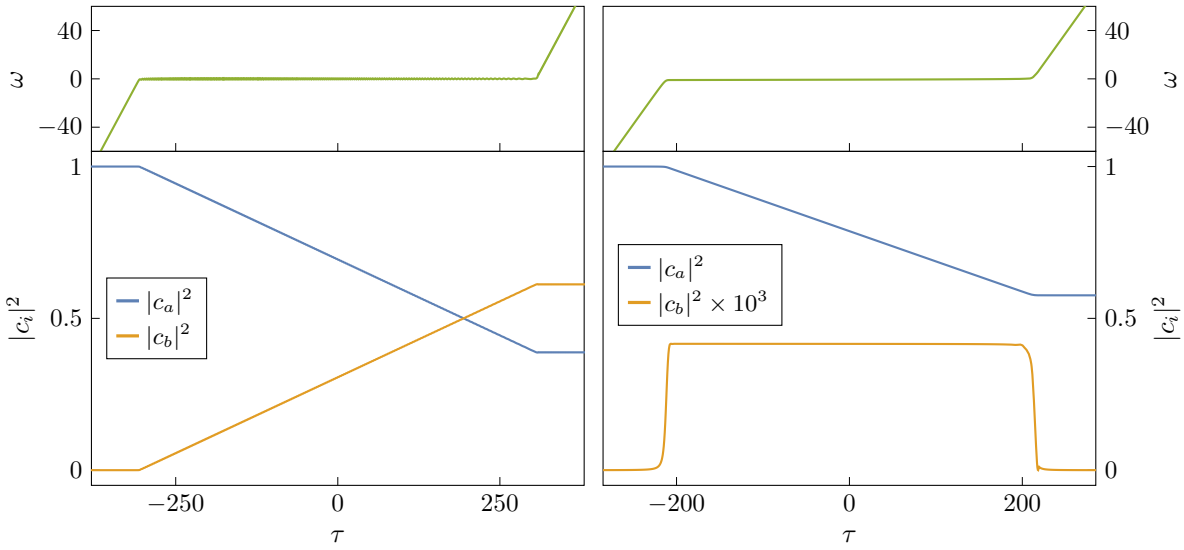


Figure 8: Numerical solution of equations (3.7) and (3.20) with (initial) parameters $Z = 0.001$ and $B = 1000$. A Z-breaking occurs when Z is slowly reduced over time, with the resonance ending when (3.41) is satisfied (*left panel*). A Γ-breaking is observed when Z is kept fixed but state $|b\rangle$ is given a nonzero decay width $\Gamma = 1.2$, with the resonance ending when (3.45) is satisfied (*right panel*).

As we will show later (cf. Figure 10), in almost all realistic cases state $|b\rangle$ decays much faster than the duration of the resonance, i.e., $\tau_{\text{decay}} \equiv (2\Gamma)^{-1} \ll B$. As a consequence, its population $|c_b|^2$ during a floating orbit stays approximately constant, at a value $|c_b|^2 = f(\varepsilon)/(2\Gamma B)$, where the state decay is balanced by the transitions from $|a\rangle$ to $|b\rangle$. As this saturation value is typically very small, we will neglect it. Under this assumption, we can solve (3.43) as

$$c_a^* c_b + c_a c_b^* \approx \sqrt{\frac{2ZB|c_a|^2 - \Gamma}{\Gamma Z B^2}}\,, \tag{3.44}$$

and conclude that the resonance breaks when the remaining population in the initial state is

$$|c_a|^2 \approx \frac{\Gamma}{2ZB}\,, \tag{3.45}$$

see Figure 8 (*right panel*). Resonances where this quantity is larger than 1 do not exhibit a floating orbit at all, showing an "immediate" breaking.

We refer to the three types of resonance breaking as ε-breaking, Z-breaking and Γ-breaking. A summary of the respective conditions is given below.

ε-breaking	Z-breaking	Γ-breaking
$f(\varepsilon) \gtrsim \sqrt{Z}B$	$Z/Z_0 \lesssim 1 - ZB^2/f(\varepsilon)^2$	$\lvert c_a\rvert^2 \lesssim \Gamma/(2ZB)$

3.5 Sinking orbits

Let us now turn our attention to sinking orbits, corresponding to $B < 0$, where backreaction tends to make the resonance less adiabatic. This case turns out to not be as dramatically relevant as

floating orbits for the resonant history of the system. However, it is important for direct GW signatures. For this reasons, we will only study the aspects of it with observational consequences.

All the observable sinking resonances have $2\pi Z \ll 1$. In this case, the final population in state $|b\rangle$, as predicted by (3.9), is very small, and this quantity is further reduced by the backreaction. In the regime where this correction is dominant, we can find a rough approximation for the total population transferred by only keeping the backreaction term in (3.20). Further assuming $|c_a|^2 \approx 1$ and $\dot{c}_b \approx 0$, we can substitute in the second component of (3.7) and obtain $|c_b|^2 \approx (Z/B^2)^{1/3}$, where we assumed for simplicity quasi-circular orbits.[3] This result is confirmed by numerical tests, modulo a multiplicative factor: we find

$$B \ll -\frac{1}{Z}, \qquad |c_b|^2 \approx 3.7 \left(\frac{Z}{B^2}\right)^{1/3}. \tag{3.46}$$

This formula is accurate for $2\pi Z \ll 1$ and provides a slight under-estimate of the final population for moderately large Z.

Sinking orbits backreact on the orbit by increasing both the orbital frequency and the binary eccentricity, as shown in Figure 4 and 5 (*right panels*). At the same, time both Ω and ε feature long-lived oscillations after the resonance. These oscillations slowly die out, so that a "jump" in the Ω and ε is the only mark left after a long time. The non-monothonic behavior of Ω was already observed in [33], where it was also speculated that sinking orbits could yield large eccentricities (becoming "kicked orbits"). Our results confirm that the oscillations are not an artifact of having considered quasi-circular orbits and further show that the increase of the eccentricity is also not monothonic. However, for the realistic cases analyzed in Section 5, the increase in eccentricity due to sinking orbits turns out to be negligible.

4 Three types of resonances

Resonances can be divided in three distinct categories, depending on the energy splitting between the two states, as computed from (2.3). *Hyperfine* resonances occur between states with same n and ℓ but different m; they have the smallest energy splitting and thus occur the earliest in the inspiral, as the corresponding resonant orbital frequency is smallest. Then, *fine* (same n, different ℓ) and *Bohr* resonances (different n) follow, the latter having the largest splittings. The tools developed in Section 3 apply to all of them: the character of a resonance is only determined by the parameters $2\pi Z$ and B, its impact on eccentricity and inclination is quantified by D, and its duration (in case it is a floating resonance) is $\Delta t_{\rm float}$. In principle, the recipe to determine the co-evolution of the binary and the cloud is clear: (1) pick the earliest resonance, (2) determine its character and backreaction by computing Z, B, D and $\Delta t_{\rm float}$, (3) update the state of binary and cloud accordingly, (4) move to the next resonance and repeat. We will indeed execute this algorithm in Section 5. To be as generic as possible and explore a wide parameter space, it will prove useful to find the scalings of the relevant quantities with M, $M_{\rm c}$, q, α and $\tilde{a}$. Different types of resonances have different scalings, so we analyze them here systematically.

[3] The validity of the assumption will become clear in Section 5.

4.1 Hyperfine resonances

Let us start with hyperfine resonances. From (2.3), we see that the energy splitting (and thus the resonant frequency) scales as $\Omega_0 \propto M^{-1}\alpha^6\tilde{a}$. The corresponding orbital separation is $R_0 \propto M\alpha^{-4}\tilde{a}^{-2/3}$. This strong α-dependence places hyperfine resonances at distances parametrically much larger than the cloud's size. At such large orbital separations, the cloud's ionization is very inefficient, and thus the only significant mechanism for energy loss is the GW emission. As this too is a very weak effect, other phenomena might potentially be relevant, including astrophysical interactions connected to the binary formation mechanism. We will postpone the discussion of these complications to Section 5, and assume for now that formula (3.6) applies, giving a chirp rate of $\gamma \propto qM^{-2}\alpha^{22}\tilde{a}^{11/3}$. This information is already enough to determine the scaling of three key quantities:

$$B \propto \frac{M_c}{M} q^{-3/2}\alpha^{-4}\tilde{a}^{-1/2}\,, \qquad \Delta t_{\rm float} \propto M_c q^{-2}\alpha^{-15}\tilde{a}^{-7/3}\,, \qquad D \propto \frac{M_c}{M} q^{-1}\alpha\tilde{a}^{1/3}\,. \tag{4.1}$$

The scaling of the Landau-Zener parameter Z depends instead on the overlap coefficient $\eta^{(g)}$. Given the hierarchy of length scales, $R_0 \gg r_c$, the "inner" term in (2.5) dominates the radial integral I_r. At fixed $\ell_* \neq 1$, we thus have

$$\begin{aligned} \eta^{(g)} &\propto q\alpha\, d^{(\ell_*)}_{\Delta m,g}(\beta)\, I_r = q\alpha\, d^{(\ell_*)}_{\Delta m,g}(\beta) \int_0^\infty \frac{r^{\ell_*}}{R_0^{\ell_*+1}} R_{n\ell}(r)^2 r^2\, \mathrm{d}r \\ &\propto M^{-1} q\alpha^{2\ell_*+5}\tilde{a}^{2(\ell_*+1)/3} d^{(\ell_*)}_{\Delta m,g}(\beta)\,, \end{aligned} \tag{4.2}$$

and so

$$Z \propto q\alpha^{4\ell_*-12}\tilde{a}^{(4\ell_*-7)/3}\big(d^{(\ell_*)}_{\Delta m,g}(\beta)\big)^2\,. \tag{4.3}$$

The dipole $\ell_* = 1$ is an exception for two reasons: (a) its "inner" term in (2.5) vanishes, (b) its "outer" term is not simply $r^{\ell_*}/R_*^{\ell_*+1}$. However, hyperfine resonances connect states with same ℓ: from the selection rule (2.8), only even values of ℓ_* contribute. We can thus safely ignore the dipole. The rest of the multipole expansion can be seen as a power series in the small parameter r_c/R_0, the smallest ℓ_* giving the strongest contribution. Because selection rules require $\ell_* \geq |g| = -g$,[4] a resonance with a given value of g will be be dominated by $\ell_* = -g$. The only two cases we will encounter in Section 5 are

$$g = -2 \qquad Z \propto q\alpha^{-4}\tilde{a}^{1/3}\big(d^{(2)}_{\Delta m,g}(\beta)\big)^2\,, \tag{4.4}$$

$$g = -4 \qquad Z \propto q\alpha^{4}\tilde{a}^{3}\big(d^{(4)}_{\Delta m,g}(\beta)\big)^2\,. \tag{4.5}$$

Furthermore, the assumption $\ell_* = -g$ allows us to write the explicit expression for the angular dependence of Z as

$$d^{(-g)}_{\Delta m,g}(\beta) \propto \sin^{\Delta m-g}(\beta/2)\cos^{-\Delta m-g}(\beta/2)\,. \tag{4.6}$$

[4] Strictly speaking, this constraint only applies on circular orbits. In general, the same inequality applies to g_β instead.

4.2 Fine resonances

Most of the assumptions made for hyperfine resonances work in the fine case too. The resonant frequency now scales as $\Omega_0 \propto M^{-1}\alpha^5$ and, similar to before, we arrive to

$$B \propto \frac{M_c}{M} q^{-3/2}\alpha^{-7/2}\,, \qquad \Delta t_{\rm float} \propto M_c q^{-2}\alpha^{-38/3}\,, \qquad D \propto \frac{M_c}{M} q^{-1}\alpha^{2/3}\,. \tag{4.7}$$

The scaling of the overlap coefficient reads $\eta^{(g)} \propto qM^{-1}\alpha^{(4\ell_*+13)/3}$ and we get

$$Z \propto q\alpha^{(8\ell_*-29)/3}\left(d^{(\ell_*)}_{\Delta m,g}(\beta)\right)^2\,. \tag{4.8}$$

The main difference with the previous case resides in the possible values of ℓ_*. Fine resonances connect states with different values of ℓ, and most of the cases we will study in Section 5 will have odd values of ℓ_*. For $g=-3$, all the previous arguments apply and the octupole $\ell_*=3$ is the dominant contribution. For $g=-1$, the extreme weakness of the dipole at large distances again leaves the octupole as the most important term; because now $\ell_* \neq -g$, however, the angular dependence will have a form different from (4.6), which we will describe on a case-by-case basis in Section 5. There is one further exception to this: if $\ell_a+\ell_b=1$, the selection rule (2.9) forbids all $\ell_* \geq 2$. Only in this case (corresponding to the $|211\rangle \to |200\rangle$ resonance) the dipole is entirely responsible for the coupling between the two states. Its anomalous expression (2.5) endows $\eta^{(g)}$ (and thus Z) with a non-power-law dependence on α: given the peculiarity of this case, we will treat it explicitly in Appendix D.

4.3 Bohr resonances

Bohr resonances are a different story. States with different principal quantum number n have different energies to leading order, meaning that the resonant orbits are placed at distances comparable to the cloud's size. There is no parametric separation between the two, as now $R_0 \propto M\alpha^{-2} \propto r_c$. At these orbital distances, the cloud's ionization is generally a more effective mechanism for energy loss than GWs. We prove this point in Figure 9, where the position of several Bohr resonances is shown on top of the ionization-to-GWs power ratio. This latter quantity scales as

$$\left.\frac{P_{\rm ion}}{P_{\rm GW}}\right|_{R_*=R_0} \propto \frac{M_c}{M}\alpha^{-5}\,. \tag{4.9}$$

With the possible exception of transitions to $|100\rangle$, as they happen extremely late in the inspiral, Bohr resonances and ionization thus happen *at the same time*. This observation raises two points.

1. Formula (3.6) for the chirp rate γ is no longer accurate, as ionization must now be included.
2. The derivation of the expression for $P_{\rm ion}$ laid down in [34] assumes that the system is away from bound-to-bound state resonances.

In Appendix C we extend the framework of [34] to describe the ionization of a system actively in resonance. Although this requires the addition of new terms, their effect is generally negligible for realistic parameters. It is thus a good approximation to simply adjust the value of γ by a factor $1+P_{\rm ion}/P_{\rm GW} \approx P_{\rm ion}/P_{\rm GW}$, where $P_{\rm ion}$ is computed as in [34–36]. The last approximation

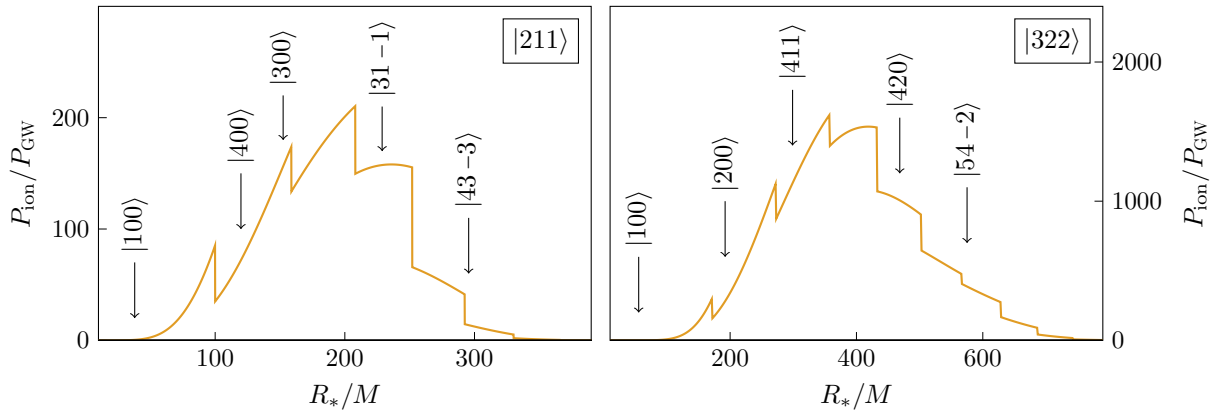


Figure 9: Position of a few selected Bohr resonances, compared to $P_{\rm ion}/P_{\rm GW}$, i.e., the ratio of the ionization power to the power emitted in GWs, shown here for a counter-rotating orbit and for a cloud in the $|211\rangle$ (*left panel*) or $|322\rangle$ (*right panel*) state. We assumed $M_{\rm c}/M = 0.01$ and $\alpha = 0.2$, but the relative position of the resonances and the shape of the curve do not depend on the parameters.

holds whenever $P_{\rm ion} \gg P_{\rm GW}$ and is always satisfied, unless the resonance involves $|100\rangle$ or the value of α is exceptionally large.

Under these assumptions, we arrive to

$$B \propto \sqrt{\frac{M_{\rm c}}{M}} q^{-3/2}\,, \qquad \Delta t_{\rm float} \propto M q^{-2} \alpha^{-3}\,, \qquad D \propto \frac{M_{\rm c}}{M} q^{-1}\,. \tag{4.10}$$

These quantities now also have a β-dependence, due to $P_{\rm ion}$ having different values for different inclinations. However, we will see in Section 5 that this detail is not relevant, so we neglect it here. As for the overlap $\eta^{(g)}$, there is now no clear hierarchy of multipoles. Luckily, R_0 has the same α-scaling as the argument of the hydrogenic wavefunctions $R_{n\ell}$: with an appropriate change of variable, we can show that

$$\eta^{(g)} \propto M^{-1} q \alpha^3 d^{(\ell_*)}_{\Delta m, g}(\beta)\,. \tag{4.11}$$

The β-dependence in (4.11) can be written in terms of a Wigner small d-matrix only when there is a single value of ℓ_* that contributes. As this is the case for many of the Bohr resonances we will encounter in Section 5, we keep that factor explicit here. Finally, the Landau-Zener parameter scales as

$$Z \propto \frac{M}{M_{\rm c}} q \left(d^{(\ell_*)}_{\Delta m, g}(\beta)\right)^2\,. \tag{4.12}$$

One particularly interesting aspect of Bohr resonances is the disappearance of any α-dependence from the Landau-Zener parameter Z and from the backreaction B. This is in contrast with the steep power-laws found for hyperfine and fine resonances, and it means that the character of Bohr resonances is much more *universal*.

5 Resonant history of the cloud

In this section we draw a consistent picture of the co-evolution of the cloud and the binary, using the tools developed in Sections 3 and 4. The results we derive here are needed to understand the state of the system by the time it becomes observable: for example, when it enters the LISA band. First, we discuss the generic behavior of the different types of resonances in Section 5.1; then, in Section 5.2 and 5.3, we study explicitly the history for a cloud initialized in the state $|211\rangle$ or $|322\rangle$.

5.1 General behavior

The initial state $|a\rangle = |n_a \ell_a m_a\rangle$ of the cloud, populated by superradiance, generally has $m_a = \ell_a = n_a - 1$. Within the multiplet of states $|n_a \ell_a m\rangle$ with $m \leq m_a$, this is the one with highest energy, as can be readily seen from (2.3). Hyperfine resonances, which occur the earliest in the inspiral, thus necessarily have $\Delta\epsilon < 0$ and are of the floating type. To understand their behavior, it is important to keep in mind a few key points.

Adiabaticity. The first question to answer is whether a given hyperfine resonance is adiabatic or not. We can apply the results of Section 3.4.1. If $2\pi ZB > f(\varepsilon)^{3/2}$ the resonance is adiabatic: the binary starts evolving as described in Section 3.4.2 until the transition completes after a time $\Delta t_{\rm float}$, or the resonance breaks due to any of the conditions derived in Section 3.4.3. Almost all hyperfine resonances turn out to be adiabatic in the entire parameter space, except in a narrow interval of almost counter-rotating inclinations, say $\pi - \delta_1 < \beta \leq \pi$, where δ_1 is the size of the interval. This is because, on floating orbits, the resonance condition $\Omega_0^{(g)} = \Delta\epsilon/g$ forces g to be negative; on the other hand, $\Delta m = m - m_a < 0$, and from (4.6) we see that for $\beta \to \pi$ the parameter Z goes to zero as a (high) power of $\cos(\beta/2)$. The explicit determination of the angle δ_1 as function of the parameters will be performed in Sections 5.2 and 5.3.

Cloud's decay and Γ-breaking. After saturation of the dominant superradiant mode $|n_a \ell_a m_a\rangle$, all states of the multiplet $|n_a \ell_a m\rangle$ with $m \neq m_a$ have $\mathrm{Im}(\omega) < 0$, meaning that they decay back in the BH with an e-folding time $t_{\rm decay} \equiv |2\,\mathrm{Im}(\omega_{n_a \ell_a m})|^{-1}$. It is thus necessary to compare $\Delta t_{\rm float}$ and $t_{\rm decay}$. One of the most important results of this work is the following: for intermediate or extreme-mass ratios, and typical values of $M_{\rm c}$ and α, the decay timescale $t_{\rm decay}$ is many orders of magnitude smaller than floating timescale, $\Delta t_{\rm float}$. It is not easy to prove this statement in full generality, due to the complicated dependence of $t_{\rm decay}$ on the parameters. Nevertheless, for small α and $\tilde{a}$, using the Detweiler approximation [54] and the results from Section 4.1, we have

$$\frac{t_{\rm decay}}{\Delta t_{\rm float}} \propto \frac{M}{M_{\rm c}} q^2 \alpha^{10-4\ell_a} \tilde{a}^{4/3}\,, \tag{5.1}$$

where $\tilde{a} \propto \alpha$ at the superradiant threshold. For $\alpha \to 0$ and small enough values of ℓ_a, this ratio becomes very small. In fact, for small q, any possible value of α results in $t_{\rm decay} \ll \Delta t_{\rm float}$. A more detailed comparison is given in Figure 10, where the numerical

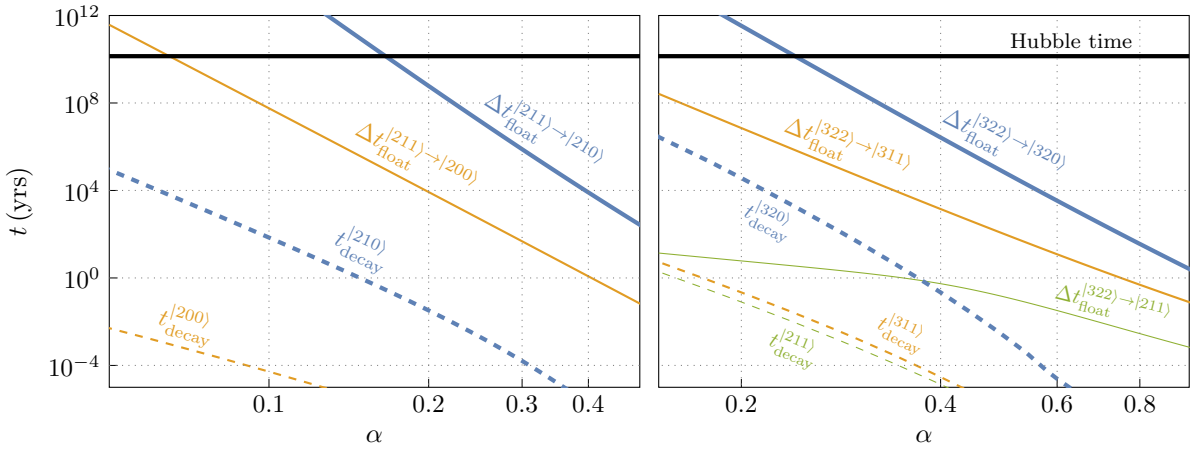


Figure 10: Floating timescale $\Delta t_{\rm float}$ (solid lines), compared to the decay timescale $t_{\rm decay}$ (dashed lines) of the final state, for some selected resonances. We use benchmark parameters and determine the decay rate independently through Leaver's continued fraction method [55–58] and the Chebyshev method in [48]. Two resonances for a $|211\rangle$ initial state are shown (*left panel*), namely $|211\rangle \to |210\rangle$ [blue] and $|211\rangle \to |200\rangle$ [orange]. Similarly, three resonances for a $|322\rangle$ initial state are shown (*right panel*), namely $|322\rangle \to |320\rangle$ [blue], $|322\rangle \to |311\rangle$ [orange] and $|322\rangle \to |211\rangle$ [green]. The thick, normal and thin lines indicate hyperfine, fine or Bohr resonances respectively. Note the Bohr resonance falling outside of the ionization regime for large α, changing the scaling of $\Delta t_{\rm float}$ from α^{-3} to α^{-8}, as predicted by (4.10) and (4.9).

coefficients are properly taken into account and the spin $\tilde{a}$ is set to correspond to the boundary of the BH superradiant region.

This result has a dramatic consequence: hyperfine transitions are never able to change the state of the cloud. Instead, the portion that is transferred to state $|b\rangle$ decays immediately back into the BH.[5] The analysis of Section 3.4.3 then applies, and the resonance Γ-breaks when the fraction of the cloud remaining in state $|a\rangle$ falls below the threshold determined in (3.45). In a relatively large portion of parameter space, generally around counter-rotating orbits, that formula returns $|c_a|^2 > 1$, meaning that the resonance Γ-breaks immediately. The outcome is effectively similar to a non-adiabatic resonance, that never even starts the floating phase. Similar to before, we will define an angular interval $\pi - \chi_1 < \beta \leq \pi$, within which the resonance is not effective. The ε-breaking and Z-breaking are instead less relevant for realistic parameters.

The strongest resonance. As shown in Section 3.2, on eccentric and inclined orbits a resonance between two given states is excited at many different orbital frequencies, depending on the value[6] of $|g| = 1, 2, 3, \ldots$ The strength of the coupling also depends on ε and β. Keeping track of so many different resonances would be very complicated. However, the hierarchy $t_{\rm decay} \ll \Delta t_{\rm float}$ implies that as soon as an adiabatic floating resonance is encoun-

[5] As a consequence, the mass and spin of the BH change. Our framework is not able to capture this effect, which we accordingly ignore in this work.

[6] As briefly mentioned in Section 3.2, two separate indices, say g_ε and g_β are necessary when both eccentricity and inclination are not zero. However, this technicality is not crucial in understanding the history of the system.

tered (and does not break early), the cloud is destroyed. This means that studying the "strongest" resonance (the one that destroys the cloud in the largest portion of parameter space) actually suffices to determine the fate of the cloud.

Up to moderate values of the eccentricity, the coupling $\eta^{(g)}$ that remains nonzero in the limit of circular orbit is much larger than all the others. We can then approximate the "strongest resonance" by ignoring eccentricity altogether. Regarding inclined orbits instead, we observe that higher values of g require contributions from higher values of the multipole index ℓ_*: at the separations of hyperfine resonances, the lowest value of ℓ_* (typically the quadrupole $\ell_* = 2$) produces the strongest coupling. Given two states, we will then study the resonance with the smallest value of $|g|$.

Applying the previous considerations to each possible hyperfine resonance, we are able to determine whether the cloud is destroyed in the process or survives to later stages of the inspiral. However, the binary might be able to "skip" hyperfine resonances for other reasons. This is because some of them are placed at extremely large binary separations: typically $R_*/M \gtrsim \mathcal{O}(10^3)$ for a $|211\rangle$ initial state, and $R_*/M \gtrsim \mathcal{O}(10^4 - 10^5)$ for $|322\rangle$. These distances are large enough that not only other kinds of astrophysical interactions may play a role, but their presence is in some cases necessary, in order to bring the binary close enough for the merger to happen within a Hubble time. Quantitatively, for a quasi-circular inspiral, the initial separation as function of the time-to-merger t_0 is given by

$$\frac{R_*}{M} = 2.3 \times 10^4 \left(\frac{t_0}{10^{10}\,\mathrm{yrs}}\right)^{1/4} \left(\frac{M}{10^4 M_\odot}\right)^{-1/4} \left(\frac{q}{10^{-3}}\right)^{1/4}. \tag{5.2}$$

In other words: if we want the binary to merge within a Hubble time, we might be forced to assume that it "starts" its evolution too close for hyperfine resonances to be encoutered, especially for a cloud initialized in the $|322\rangle$ state. This can be achieved by a variety of formation mechanisms, including dynamical capture [59, 60] and *in-situ* formation [60–64].

If the system is able to skip through hyperfine resonances, because they are either all non-adiabatic, or they Γ-break early, or the binary is formed at small enough separations, the cloud can be present when fine resonances are encountered. Their phenomenology is largely similar to hyperfine ones, as they too are all of the floating type. We defer the discussion of some state-dependent aspects to Sections 5.2 and 5.3. For the purpose of the present general discussion, it suffices to say that, once again, the cloud can survive this stage if $\pi - \delta_2 < \beta \leq \pi$ (for some angle δ_2 to be determined), if the resonance Γ-breaks early in an interval $\pi - \chi_2 < \beta \leq \pi$, or if the binary is formed *in situ* at very small radii.

Finally, if the cloud makes it to this point, it becomes potentially observable: the "Bohr region" can be in the LISA band and is rich of signatures of the cloud. These come in the form of ionization and Bohr resonances, the vast majority of which are sinking and non-adiabatic. State-dependent details will be discussed in Sections 5.2 and 5.3 and a summary of the observational signatures will be given in Section 6. A diagrammatic representation of the three stages of the resonant history is shown in Figure 1.

As a concluding remark, we note that the results derived here and in Section 3 are specific to resonances involving 2 states only. We have explicitly checked that this is the case for the

resonances discussed in the next sections, so we apply the results of Section 3 without further modification.

5.2 Evolution from a $|211\rangle$ initial state

The $|211\rangle$ state is the fastest-growing superradiant mode, and represents therefore a natural assumption for the initial state of the cloud. The requirements that the superradiant amplification takes place, and does so on timescales no longer than a Gyr, set a constraint on α:

$$0.02\left(\frac{M}{10^4 M_\odot}\right)^{1/9} \lesssim \alpha < 0.5\,. \tag{5.3}$$

Once grown, the cloud will decay in GWs with a rate roughly proportional to $M_c^2\alpha^{14}$, assuming the scalar field is real. The resulting decay of M_c is polynomial, rather than exponential in time; as such, we will not impose a further sharp bound on α, and treat M_c/M as an additional free parameter.

There are two possible hyperfine resonances, with the states $|210\rangle$ and $|21\,{-1}\rangle$. Following the line of reasoning laid down in Section 5.1, we ignore the fact that the same resonances can be triggered at multiple points if the orbit is eccentric. Both resonances are then mediated by $g=-2$ and they are positioned at

$$|211\rangle \xrightarrow{g=-2} |210\rangle \qquad \frac{R_0}{M} = 8.3\times 10^3 \left(\frac{\alpha}{0.2}\right)^{-4}\left(\frac{\tilde{a}}{0.5}\right)^{-2/3}, \tag{5.4}$$

$$|211\rangle \xrightarrow{g=-2} |21\,{-1}\rangle \qquad \frac{R_0}{M} = 5.2\times 10^3 \left(\frac{\alpha}{0.2}\right)^{-4}\left(\frac{\tilde{a}}{0.5}\right)^{-2/3}, \tag{5.5}$$

where the value of the spin should be set equal to the threshold of superradiant instability of $|211\rangle$, that is, $\tilde{a}\approx 4\alpha/(1+4\alpha^2)$. Both resonances become non-adiabatic in an interval $\pi-\delta_1<\beta\leq\pi$, with the strongest constraint on δ_1 given by $|211\rangle\to|210\rangle$. The value of δ_1 is determined from (3.26): this means setting $2\pi ZB = f(\varepsilon_0)^{3/2}$, where ε_0 is the eccentricity at the onset of the resonance, and solving for β as function of the parameters. Making use of the relations (4.1), (4.4) and (4.6), and evaluating numerically the overlap $\eta^{(2)}$ between the two states, we find

$$\delta_1 = 7.5^\circ \left(\frac{M_c/M}{10^{-2}}\right)^{-1/6}\left(\frac{q}{10^{-3}}\right)^{1/12}\left(\frac{\alpha}{0.2}\right)^{4/3}\left(\frac{\tilde{a}}{0.5}\right)^{1/36} f(\varepsilon_0)^{1/4}\,. \tag{5.6}$$

Although $|211\rangle\to|210\rangle$ is also non-adiabatic in a neighbourhood of $\beta=0$, such a co-rotating binary would still encounter the adiabatic floating resonance $|211\rangle\to|21\,{-1}\rangle$ later, so that the only "safe" inclinations are in the neighbourhood of counter-rotating determined in (5.6).

Having determined when hyperfine resonances can be adiabatic, we now calculate where they break, using the results of Section 3.4.3. As anticipated in Section 5.1, the Γ-breaking is the most relevant mechanism of resonance breaking. To assess its impact, we observe that, because $B\propto M_c$, equation (3.45) can be written as a relation for the final mass of the cloud at resonance breaking, $M_c^{\rm br} = M_c|c_a|^2$, which can be computed as function of α and β. If $M_c^{\rm br}>M_c$ is found, then the resonance breaks immediately as it starts, as if it was non-adiabatic. We show the result

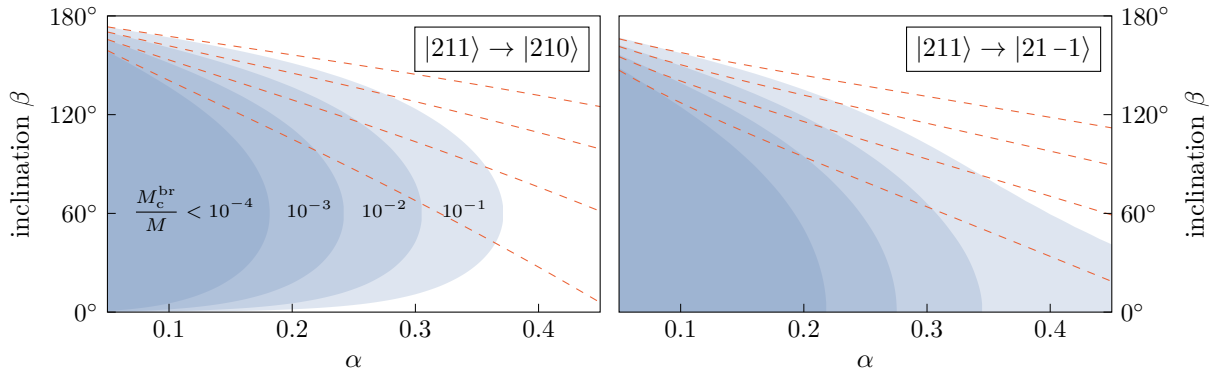


Figure 11: Mass of the cloud M_c^{br} at resonance Γ-breaking, as function of α and β, for the two hyperfine resonances from the initial state $|211\rangle$. The mass of the cloud decreases during the resonance from its initial value M_c, and the resonance breaks when the value M_c^{br} is reached. Values $M_c^{br} > M_c$ indicate that the resonance breaks immediately as it starts. The contours [blue] are calculated on circular orbits, as this gives a good approximation for the strongest constraint on M_c^{br} even when overtones due to orbital eccentricity (i.e., higher values of $|g|$ for the resonance between two given states) are taken into account. Due to the inaccuracy of the analytical approximations for the decay width $(\omega_{211})_I$, especially at large α, we have determined the contours with Leaver's [55–58] and Chebyshev [48] methods. The dashed lines [red] are analytical approximations to the blue contours in the proximity of $\beta = \pi$, based on (5.7).

in Figure 11. Note that in principle the resonance always Γ-breaks before the cloud is completely destroyed, but its observational impact becomes negligible when M_c^{br} is too small.

The combined constraints due to the Γ-breaking of $|211\rangle \to |210\rangle$ and $|211\rangle \to |21\,{-1}\rangle$ imply that the cloud survives in a neighborhood of $\beta = \pi$, say $\pi - \chi_1 < \beta < \pi$, similar to what we found for the adiabaticity of the resonances. An analytical approximation of χ_1 for $|211\rangle \to |210\rangle$ based on Detweiler's formula [54] is

$$\chi_1 \approx 38^\circ \left(\frac{M_c^{br}/M}{10^{-2}}\right)^{-1/6} \left(\frac{\alpha}{0.2}\right)^{7/6} \left(\frac{\tilde{a}}{0.5}\right)^{-5/18}, \tag{5.7}$$

which significantly underestimates the result for large α, as shown in Figure 11. Because $\chi_1 > \delta_1$, this angular interval overwrites (5.6) as the portion of parameter space where the cloud survives hyperfine resonances.

Finally, we check whether hyperfine resonances can ε-break or Z-break. Both ε and Z can vary significantly during the float, so we use the relation (3.39) as an order-of-magnitude estimate. For generic values of the inclination, both hyperfine resonances have

$$\sqrt{Z}B \sim 10^6 \left(\frac{M_c/M}{10^{-2}}\right) \left(\frac{q}{10^{-3}}\right)^{-1} \left(\frac{\alpha}{0.2}\right)^{-6} \left(\frac{\tilde{a}}{0.5}\right)^{-1/3}. \tag{5.8}$$

The resonances ε-breaks if $f(\varepsilon) = \sqrt{Z}B$, which is only satisfied at very high eccentricities, not smaller than 0.95 for typical parameters. Such extreme eccentricities are only reachable if the initial inclination is very close to $\beta = \pi$, as can be seen from Figure 6. But, as proved in (5.6) and (5.7), near-counter-rotating binaries do not undergo floating orbits at all, due to the

resonances being either non-adiabatic or Γ-breaking immediately. As for the Z-breaking, one can conservatively ignore the term Z/Z_0 in (3.41), falling back to the same relation as (3.39).

We conclude that the survival of the cloud to later stages of the inspiral is exclusively determined by the Γ-breaking. If the binary is outside the regions colored in Figure 11, and computed in (5.7), it encounters the only possible fine resonance:

$$|211\rangle \xrightarrow{g=-1} |200\rangle \qquad \frac{R_0}{M} = 3.4 \times 10^2 \left(\frac{\alpha}{0.2}\right)^{-10/3}, \tag{5.9}$$

whose angular dependence is determined through (4.6) as usual. This resonance, however, has anomalous behavior for two reasons:

1. it is entirely mediated by the dipole $\ell_* = 1$;
2. depending on the value of α, it may fall inside the ionization regime ($P_{\rm ion} \gtrsim P_{\rm GW}$) despite not being a Bohr resonance.

As a consequence, its Landau-Zener parameter Z does not scale as a pure power-law in α (nor $M_{\rm c}$), and must be computed numerically. The explicit result is reported in Appendix D. Similar to hyperfine resonances, we can compute angular intervals δ_2 and χ_2 where the resonance is non-adiabatic and Γ-breaks, respectively. The extremely large decay width of $|200\rangle$ (as all states with $\ell = 0$), however, makes χ_2 as large as to correspond with the whole possible range of inclinations, from 0° to 180°. Fine resonances are thus effectively never excited for a cloud in a $|211\rangle$ state.

Finally, if the binary arrives to the Bohr region with the cloud still intact, it encounters the Bohr resonances, all of which are of the sinking type and fall inside the ionization regime (with the exception of $|211\rangle \to |100\rangle$). No extra circularization is provided by the hyperfine resonances, if they do not significantly destroy the cloud. Nevertheless, by the time the binary arrives to the Bohr regime, not only has it presumably evolved for a long time under the circularizing effect of GW radiation, but it also starts ionize the cloud, further suppressing the eccentricity [36]. We will therefore assume that quasi-circular orbits are a good approximation by this point. The final population after each sinking resonance can be found using the approximation (3.46), which, together with the scaling relations (4.10) and (4.12), implies

$$|c_b|^2 \approx 3.7 \left(\frac{Z}{B^2}\right)^{1/3} \propto \frac{M}{M_{\rm c}} q^{4/3}. \tag{5.10}$$

For the benchmark parameters, the values of $|c_b|^2$ for the strongest sinking resonances (which are typically with states of the form $|n00\rangle$) are summarized in Figure 12, where we have assumed for simplicity a perfectly counter-rotating configuration ($\beta = \pi$). This is generally a good approximation, due to the relative smallness of the angle χ_1. We see that all resonances are very non-adiabatic, in total transferring less than 1% of the cloud to other states. Hence, ionization of $|211\rangle$ happens with minimal disturbance from Bohr resonances.

The only floating Bohr resonance is $|211\rangle \to |100\rangle$. It is worth noting that this is also the only Bohr resonance falling outside the ionization regime (see Figure 9), and that recent numerical studies [37] have shown that it has a resonance width much larger than all other resonances.

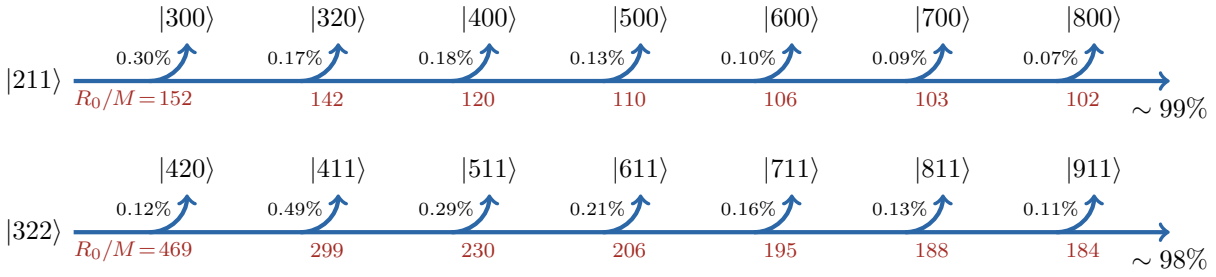


Figure 12: Strongest sinking Bohr resonances on a counter-rotating orbit for a clound in the $|211\rangle$ or $|322\rangle$ state. The percentages next to each resonance are the values of $|c_b|^2$ for benchmark parameters, and they scale with M_c and q according to (5.10), while the red numbers below are the resonant orbital separations R_0, in units of M.

This last observation means that the resonance might partially evade the analysis of the present paper, due to the nonlinear dependence of $P_{\rm GW}$ on R_* playing an important role. In any case, we expect the extremely large decay width of $|100\rangle$ to Γ-break the resonance in most or all realistic cases, preventing the float from happening.

5.3 Evolution from a $|322\rangle$ initial state

The second-fastest growing mode is $|322\rangle$. In this case, the constraint on α—imposing that the superradiance timescale is shorter than a Gyr—is

$$0.09\left(\frac{M}{10^4 M_\odot}\right)^{1/13} \lesssim \alpha < 1\,, \tag{5.11}$$

while the rate of cloud decay in GWs is proportional to $M_c\alpha^{18}$.

Compared to Section 5.2, a larger number of hyperfine resonances are possible, with any state of the form $|32m_b\rangle$, with $-2 \leq m_b \leq 1$. All of these can happen with $g = -4$, in which case the hexadecapole $\ell_* = 4$ is entirely responsible for the mixing of the states. However, the cases $m_b = 0$ and $m_b = 1$ can also resonate, at different separations, with $g = -2$: these are dominated by the quadrupole $\ell_* = 2$ instead, which makes these resonances much stronger than the others. Their positions are

$$|322\rangle \xrightarrow{g=-2} |321\rangle \qquad \frac{R_0}{M} = 5.4\times 10^4 \left(\frac{\alpha}{0.2}\right)^{-4}\left(\frac{\tilde{a}}{0.5}\right)^{-2/3}, \tag{5.12}$$

$$|322\rangle \xrightarrow{g=-2} |320\rangle \qquad \frac{R_0}{M} = 3.4\times 10^4 \left(\frac{\alpha}{0.2}\right)^{-4}\left(\frac{\tilde{a}}{0.5}\right)^{-2/3}, \tag{5.13}$$

which should be evaluated at $\tilde{a} \approx 2\alpha/(1+\alpha^2)$. The most stringent constraint on δ_1 is given by $|322\rangle \to |321\rangle$ and equals

$$\delta_1 = 5.4^\circ \left(\frac{M_c/M}{10^{-2}}\right)^{-1/6}\left(\frac{q}{10^{-3}}\right)^{1/12}\left(\frac{\alpha}{0.2}\right)^{4/3}\left(\frac{\tilde{a}}{0.5}\right)^{1/36}. \tag{5.14}$$

The angle χ_1 within which the same resonance Γ-breaks is instead

$$\chi_1 \approx 4.8^\circ \left(\frac{M_c^{\rm br}/M}{10^{-2}}\right)^{-1/6}\left(\frac{\alpha}{0.2}\right)^{11/6}\left(\frac{\tilde{a}}{0.5}\right)^{-5/18}, \tag{5.15}$$

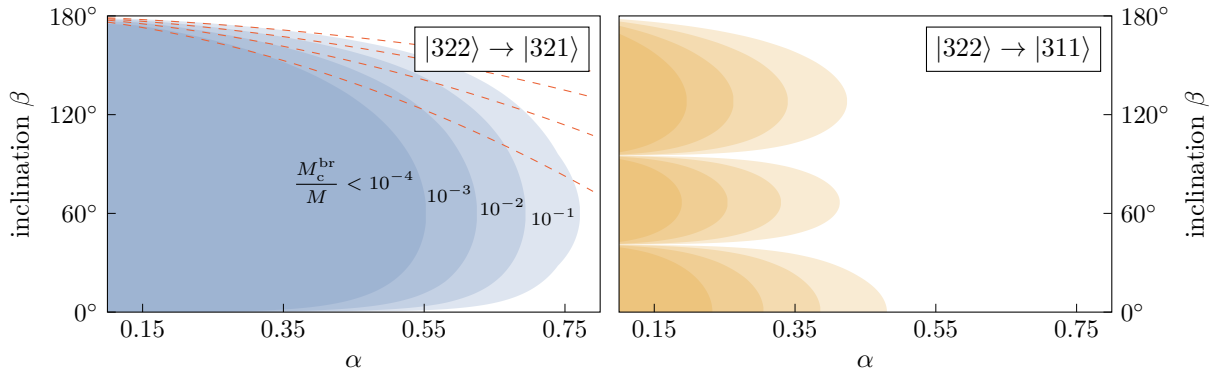


Figure 13: Same as Figure 11, for the strongest hyperfine (*left panel*) and fine (*right panel*) resonances from a $|322\rangle$ state. The analytical approximations of the contours are not shown in the latter case, as they quickly become inaccurate for moderate values of α.

also more accurately numerically computed and shown in Figure 13 (*left panel*). Similar to the resonant history of $|211\rangle$, some resonances (such as $|322\rangle \to |321\rangle$) become weak around $\beta = 0$, yet other resonances (such as $|322\rangle \to |320\rangle$) do not, thereby eliminating any possible "safe interval" around a co-rotating configuration.

Differently from Section 5.2, there is no clear hierarchy between δ_1 and χ_1. Which one is largest depends not only on α, but also on the chosen value of $M_c^{\rm br}$. The angular interval that leads to the survival of the cloud in appreciable amounts is however generally dominated by the Γ-breaking, as even very light clouds, say $M_c^{\rm br}/M < 10^{-4}$, are able to give clear signatures in the Bohr region [34].

As in the $|211\rangle$ case, the ε-breaking and Z-breaking prove to not be relevant for the resonant history: the value

$$\sqrt{Z}B \sim 10^7 \left(\frac{M_c/M}{10^{-2}}\right)\left(\frac{q}{10^{-3}}\right)^{-1}\left(\frac{\alpha}{0.2}\right)^{-6}\left(\frac{\tilde{a}}{0.5}\right)^{-1/3}. \tag{5.16}$$

requires extremely high eccentricities ($\varepsilon \gtrsim 0.98$), to give rise to a resonance breaking. The corresponding initial inclinations are extremely close to $\beta = \pi$ and would fall in the interval (5.14), where the resonance is not adiabatic.

A cloud in the $|322\rangle$ state can experience fine resonances with states with $\ell \neq 0$. Their decay width is smaller than those of the states with $\ell = 0$: as a consequence, fine resonances can destroy a significant portion of the cloud before they Γ-break. The fine resonance that gives the most stringent constraints on δ_2 and χ_2 is

$$|322\rangle \overset{g=-1}{\longrightarrow} |311\rangle \qquad \frac{R_0}{M} = 2.3 \times 10^3 \left(\frac{\alpha}{0.2}\right)^{-10/3}. \tag{5.17}$$

Analytical approximations for $\beta \approx \pi$ give[7]

$$\delta_2 = 3.2^\circ \left(\frac{M_c/M}{10^{-2}}\right)^{-1/4} \left(\frac{q}{10^{-3}}\right)^{1/8} \left(\frac{\alpha}{0.2}\right)^{31/24} \tag{5.18}$$

and

$$\chi_2 \approx 9^\circ \left(\frac{M_c^{\rm br}/M}{10^{-2}}\right)^{-1/4} \left(\frac{\alpha}{0.2}\right)^{3/2}, \tag{5.19}$$

while a more accurate numerical determination of the mass of the cloud at resonance breaking is given in Figure 13 (*right panel*). It is worth noting that the strength of the $|322\rangle \to |311\rangle$ resonance has a complicated β dependence, due to the octupole $\ell_* = 3 \neq -g$ being the dominant term. Consequently, this resonance becomes weak not only around $\beta = 180^\circ$, but also around $\beta = 41^\circ$ and 95° (as visible from Figure 13). However, other fine resonances remain strong at these intermediate inclinations and so, once again, the cloud can only reach the Bohr region if the inclination is in a narrow interval around the counter-rotating configuration.

In the Bohr region, the system encounters several sinking resonances, the strongest of which are with states of the form $|n11\rangle$. The final populations $|c_b|^2$ are displayed in Figure 12. For benchmark parameters, about 2% of the cloud is lost in the process. None of the floating resonances, with $n = 1$ or $n = 2$ states, becomes adiabatic within the interval of inclinations discussed above.

Finally, in case the binary is formed at radii small enough to avoid constraints on the inclination coming from fine resonances, an interesting scenario opens up. The strongest floating Bohr resonance is $|322\rangle \xrightarrow{g=-1} |211\rangle$, which becomes adiabatic, for benchmark parameters, for $\beta < 155^\circ$.[8] Among all possible scenarios we considered in Sections 5.2 and 5.3, this is the only case where the binary's evolution in the Bohr region features a new phenomenon, beyond ionization and non-adiabatic sinking resonances: namely, an adiabatic floating resonance. The companion's motion continues to ionize the cloud while this resonance takes place, potentially changing M_c significantly before its end. This is also the only floating resonance with the actual potential to partially move the cloud to a different state, rather than merely destroying it: as can be seen in Figure 10 (*right panel*), the hierarchy $\Delta t_{\rm float} \gg t_{\rm decay}$ is not valid in the entire parameter space. Hence, depending on the parameters, when the resonance ends, the inspiral can either continue without the cloud, or with a cloud in a (decaying) $|211\rangle$ state and a reduced value of M_c. In the latter case, the discussion in Section 5.2 applies from this point onwards.

[7] For $\alpha \gtrsim 0.5$, this resonance may marginally fall inside the ionization regime. However, the value of $P_{\rm ion}$ never becomes much larger than $P_{\rm GW}$. We therefore ignore this detail, which only slightly increases the value of δ_2 compared to the one presented in (5.18).

[8] Due to the weakness of the resonance compared to most the (hyper)fine ones, it is not possible to expand around $\beta = \pi$ and get a simple formula for the upper limit on the angle as function of the parameters. Nevertheless, a good approximation is given by the following cubic equation: $(\pi - \beta)^4 + 2.8(\pi - \beta)^6 > 0.056 \times (10^5 M_c q/M)^{1/2}$.

6 Observational signatures

The dynamics of the cloud-binary system are intricate and depend on the parameters. In Section 5 we determined when the cloud is entirely destroyed in the early inspiral, when it loses some of its mass upon resonance breaking, and when it remains intact until the binary enters the Bohr region. There are thus two main ways the cloud can leave an imprint on the GW waveform: (1) modifications of the waveform due to interaction with the cloud, in case it is still present in the late stages of the inspiral (Section 6.1); (2) permanent consequences on the binary parameters left by a cloud destroyed early in the inspiral (Section 6.2). A partially destroyed cloud, left by a broken resonance, may be able to combine both kinds of signatures.

6.1 Direct signatures of the cloud

As discussed extensively in Section 5, the requirement that the cloud survives the hyperfine and fine resonances forces either the inclination angle to be within $\mathcal{O}(10^\circ)$ of a counter-rotating configuration, or the binary to form at radii too small to ever excite those resonances. Then, most phenomena producing direct observational evidence of the cloud happen when the binary reaches the Bohr region. Here, ionization takes over GW radiation as the primary mechanism of orbital energy loss. When $P_{\rm ion} \gg P_{\rm GW}$, the evolution of the GW frequency $f_{\rm GW}$ approximately follows a universal shape [35],

$$f_{\rm GW}(t) = \frac{\alpha^3}{M} f\left(\frac{M_c q \alpha^3}{M^2} t\right), \tag{6.1}$$

where the function f can be explicitly determined from the shape of $P_{\rm ion}$. This universal behavior of $f_{\rm GW}(t)$ constitutes a direct evidence of the presence of the cloud.

On top of this, sinking resonances can cause non-negligible upward "jumps" of $f_{\rm GW}$ due to their backreaction, even if they are strongly non-adiabatic. For a Bohr resonance $|n_a \ell_a m_a\rangle \to |n_b \ell_b m_b\rangle$, they are located at

$$f_{\rm GW}^{\rm res} = \frac{26\,{\rm mHz}}{g}\left(\frac{10^4 M_\odot}{M}\right)\left(\frac{\alpha}{0.2}\right)^3\left(\frac{1}{n_a^2} - \frac{1}{n_b^2}\right), \tag{6.2}$$

where $g = m_b - m_a$, and thus fall inside the LISA band for benchmark parameters.[9]

The amplitude of the jump can be computed explicitly from (3.20) (assuming quasi-circular orbits):

$$\Delta f_{\rm GW} = \frac{0.61\,{\rm mHz}}{\Delta m^{1/3}}\left(\frac{10^4 M_\odot}{M}\right)\left(\frac{M_c/M}{0.01}\right)\left(\frac{q}{10^{-3}}\right)^{-1}\left(\frac{\alpha}{0.2}\right)^3\left(\frac{1}{n_a^2} - \frac{1}{n_b^2}\right)^{4/3}\left(\frac{|c_b|^2}{10^{-3}}\right), \tag{6.3}$$

where the values of $|c_b|^2$ and their dependence on the parameters are given in Figure 12 and equation (5.10). The increase in frequency comes with smaller, long-lived oscillations of the frequency, and with a slight increase of the eccentricity; both these effects have been shown in the right panels of Figure 4 for example parameters. The dephasing introduced by a single sinking resonance on top of the one coming from ionization is $\Delta\Phi_{\rm GW} \approx \pi f_{\rm GW}^{\rm res} \Delta f_{\rm GW}/\gamma$. This is of the order of thousands of radiants, although the exact number can vary by a few orders of

[9] Formula (6.2), with $n_b \to \infty$, also describes the position of the g-th "kink" of the function f appearing in (6.1), corresponding to the g-th discontinuity of $P_{\rm ion}$ (see Figure 9).

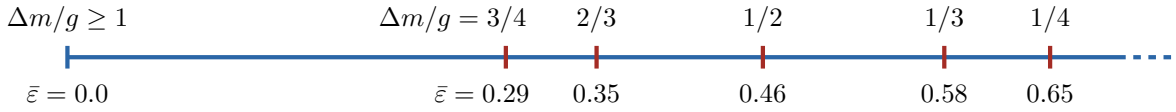


Figure 14: Example values of the fixed point $\bar{\varepsilon}$ depending on $\Delta m/g$. Numbers can be found by solving equations (3.21) and (3.22) on a floating orbit.

magnitude in different regions of the parameter space. Not only is this well above the expected LISA precision of $\Delta\Phi_{\rm GW} \sim 2\pi$, but such a dephasing would happen in a very narrow frequency range, in contrast to most other environmental effects, including ionization. This unique behavior would aid parameter estimation by directly linking the cloud's parameters with $\Delta\Phi_{\rm GW}$ via (6.2) and (6.3), especially if multiple jumps are observed within one signal.

As discussed in Sections 5.2 and 5.3, the only cases where a floating resonance can be observed in the Bohr region require a binary formation at very small radii, so that all early resonances are skipped without a strict requirement on the inclination angle. Resonances of the type $|n_a\ell_a m_a\rangle \to |100\rangle$ happen very late in the inspiral (see Figure 9), where relativistic corrections are expected to be more important [37]. The only other floating Bohr resonance encountered in Section 5 is $|322\rangle \to |211\rangle$. This is an interesting case, because it may not entirely destroy the cloud. The expected GW signal is a constant frequency $f_{\rm GW}$ given by equation (6.2), for a total floating time of[10]

$$\Delta t_{\rm float} = 5.8\,{\rm yrs}\left(\frac{M}{10^4 M_\odot}\right)\left(\frac{q}{10^{-3}}\right)^{-2}\left(\frac{\alpha}{0.2}\right)^{-3}. \tag{6.4}$$

Although the cloud's mass is continuously reduced by ionization while the resonance takes place, the value given in (6.4) remains independent of $M_{\rm c}$ as long as it is large enough to guarantee $P_{\rm ion} \gg P_{\rm GW}$.

6.2 Indirect signatures: impact on binary parameters

For sufficiently small orbital inclinations, as seen in Figures 1, 11 and 13, the cloud can be destroyed during one of the floating resonances in the early inspiral, to a level where it no longer affects the binary dynamics in an observable way. Then, by the time the system enters in band, its evolution is expected to follow the rules of vacuum general relativity. Nevertheless, the binary still carries the marks of the previously existing boson cloud, and of the resonance that destroyed it. These are due to the backreaction on the orbit from that floating resonance, and come in the form of a change in the eccentricity and tilt of the inclination angle.

While in Section 5 we could simplify the analysis by studying only the "strongest resonance", the impact on the orbital parameters strongly depends on which overtone (that is, which value of g) mediated the last adiabatic resonance encountered by the system.[11] As shown in Figure 6, the orbital parameters follow specific sets of trajectories on the (ε, β) plane, until the resonance

[10] This value assumes a quasi-circular co-rotating orbit. Moderate nonzero values of eccentricity or inclination introduce $\mathcal{O}(1)$ variations in $\Delta t_{\rm float}$.

[11] If the system undergoes multiple floats, for example because broken resonances leave a cloud massive enough to excite other adiabatic resonances, the evolution of the eccentricity follows several nontrivial steps. Here, however, we focus on the last of those as it has the most direct observational consequences.

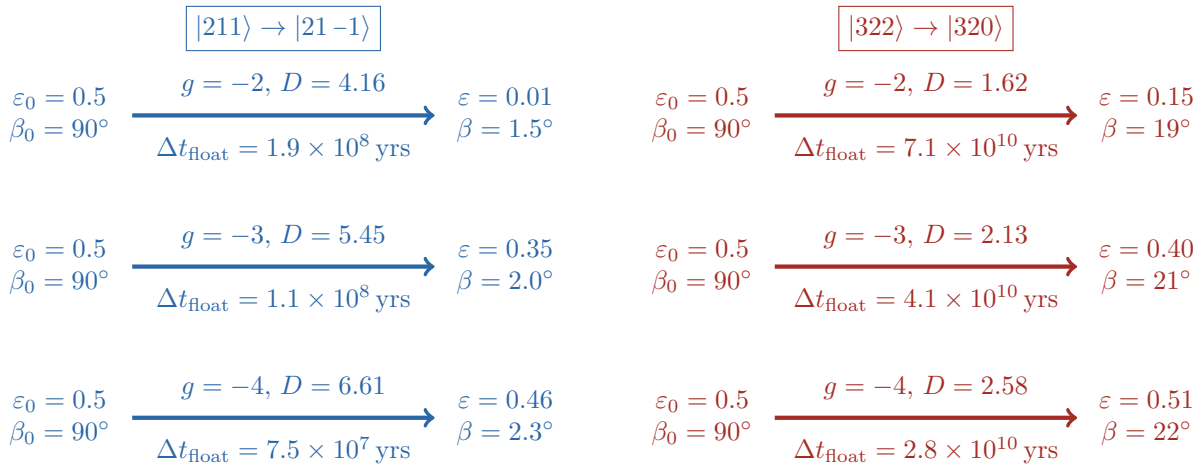


Figure 15: Examples of backreaction on the eccentricity ε and inclination β during floating orbits that destroy the cloud entirely. We show the "strongest resonance" ($\Delta m/g = 1$) and two overtones in each scenario, using the benchmark parameters $\alpha = 0.2$, $q = 10^{-3}$, $M_{\rm c} = 0.01M$ and $M = 10^4 M_\odot$. Each case is initialized with $\varepsilon_0 = 0.5$ and $\beta_0 = 90°$ for illustrative purposes, but we observed that the final values of ε and β are very robust against the choice of different initial conditions. The final values of ε and β, as well as $\Delta t_{\rm float}$, are computed integrating numerically equations (3.7), (3.20), (3.21) and (3.22). For benchmark parameters, the floating time of resonances from $|322\rangle$ exceeds the Hubble time; however, it strongly depends on the parameters, as derived in (4.1).

breaks or completes. While floating orbits *always* tilt the inclination angle towards a co-rotating configuration, the eccentricity is forced towards a fixed point, whose value depends on $\Delta m/g$. Some examples of the value of this fixed point are shown in Figure 14 for different values of $\Delta m/g$.

Assuming that the resonance does not break prematurely, the distance travelled by the binary in the (ε, β) plane depends on the parameter D alone, introduced in (3.32). Very roughly, the system gets e^D times closer to the eccentricity fixed point than it was before the resonance started. For our benchmark parameters, we find that most hyperfine and fine resonances have values of D between 1 and 10, meaning that the fixed point is approached significantly. The value of D, however, strongly varies with the parameters, as we found in Section 4. In particular, it is inversely proportional to q, implying that only intermediate or extreme mass ratio binaries change significantly their orbital parameters during a floating resonance. Example of variations of the parameters during a floating orbit are reported in Figure 15 for the resonances $|211\rangle \to |21\,{-1}\rangle$ and $|322\rangle \to |320\rangle$.

The eccentricity attractor points shown in Figure 14 and Figure 15 are a unique signature of the cloud-binary dynamics. Together with the suppression of the orbital inclination, this opens up the possibility of performing a statistical test of the parameters of a large number of binary inspirals, and compare them with the ones predicted from a suitable model of their formation channels. This task is likely to be complicated by the existence of other astrophysical mechanisms or formation processes that can affect eccentricity and inclination, but diving into these details is beyond the scope of the present work. It should also be kept in mind that, after the completion of

the resonance, GW emission will start circularizing the orbit once again, so that a "backtracking" of the eccentricity would be needed to test the existence of the eccentricity attractor points. For a recent analysis exploring binary eccentricity as signature of boson clouds see [65], which was completed at the same time as the present work.

Lastly, we note that the extremely long floating time associated with some hyperfine or fine resonances can stop many binaries from getting in band at all, consequently reducing the merger rate. For example, for our choice of benchmark parameters, the hyperfine resonances from the $|322\rangle$ state, shown in Figure 15, float for longer than the Hubble time.

7 Conclusions

In the context of gravitational-wave astronomy, binary black hole environments have long been proposed as a laboratory for fundamental physics. One such example are gravitational atoms, or clouds of ultralight bosons produced by superradiance around spinning black holes. Compared to other kinds of environment, the phenomenology of gravitational atoms is extremely rich. The two most striking types of interaction between the binary and the cloud are resonant phenomena [30, 31, 33] and friction effects [32, 34–36], both of which leave very distinct signatures on the emitted gravitational waveform. This complexity is a blessing for the potential detection and identification [10] of such systems. However, it is a curse for the achievement of a complete characterization of their evolution.

Previous studies have described the effects on the waveform as function of the state of the cloud and of the binary configuration at the time of observation. These are, however, the final products of a complex series of cloud-binary interactions that characterize former phases of the inspiral. Despite a number of relevant studies [30, 39–43, 66, 67], the combinations of cloud states and binary configurations compatible with this kind of evolution had not yet been determined.

In this work, we finalize such a program by systematically studying the chronological sequence of resonances encountered during the binary inspiral. We do so in the most general possible set of assumptions: we allow for any value of the initial eccentricity, inclination and separation of the binary; at the same time, we keep the scaling with the cloud's parameters explicit, so to apply our results to the entire parameter space. Furthermore, we take into account the backreaction of the resonances on the orbit, and study how this impacts the behavior of the resonances themselves. This aspect, as well as the impact of inclination and eccentricity on resonances (and viceversa), had never been studied before, and each of these novel results turns out to play a crucial role in our analysis. Finally, we perform explicitly the exercise of "following" the the evolution of the system from the initial states most likely to be populated by superradiance, $|211\rangle$ and $|322\rangle$, until the merger, and then summarize the gravitational wave signatures compatible with the scenarios studied.

In principle, one might have expected the evolution of the system to be extremely complicated. The S-matrix approach developed in [33] suggests a tree of populated states branching more and more, every time a new resonance is encountered. In practice, however, we find that the hierarchy

between the floating and decay timescales simplifies the picture dramatically.[12] During every hyperfine or fine adiabatic resonance, the cloud loses mass until the resonance breaks, often to the point where it is no longer directly observable. The conclusion is then remarkably simple, and similar among the two cases studied explicitly. Only binaries close enough to a counter-rotating configuration, where these early resonances are very weak, are able to carry the cloud up to the point where it becomes observable through the effects of ionization and a large number of weak resonances. Our detailed study of the nonlinear behavior of resonances allows us to precisely quantify the angular interval of inclinations where this scenario is realized, see equations (5.7), (5.15) and (5.19), as well as Figures 11 and 13.

The early disappearance of the cloud for generic orbital configurations may seem to suggest that the chances of detecting ultralight bosons using binary systems might be slim after all. It is certainly true that our work puts strict conditions for the direct observation of the cloud-binary interaction. To avoid all early resonances, either the initial separation must be small enough, or the orbital angular momentum must be approximately anti-aligned (within a tolerance interval whose size depends on the parameters) with the central BH's spin. The likelihood of either scenario depends on the astrophysical processes governing the formation of the binary system, and is subject to large uncertainties—though see [60, 64, 68, 69] and [70, 71] for the two cases respectively. We note, however, that the event leading to the cloud destruction—an adiabatic floating resonance—necessarily exerts a strong backreaction on the binary's inclination and eccentricity, generally reducing both quantities significantly. This fact raises the possibility to reverse-engineer the existence of a cloud from a statistical analysis of a large number of inspirals with well-measured orbital parameters.

As anticipated in [36], the present work answers the main remaining open questions left on the phenomenology of gravitational atoms in binaries, within a certain set of assumptions. We neglected a number of sub-leading effects. Some of them, like the accretion onto the secondary [34] and the cloud's self gravity [72, 73] can be straightforwardly included in the binary's evolution, and do not change qualitatively the picture drawn here. Others, like the backreaction of the cloud's decay in GWs [74], the non-resonant overlap between growing and decaying states [66, 67], and the change in the BH's mass and spin due to the absorption of the cloud during a resonance (see footnote 5), can potentially introduce new relevant features, at large, small and any separations, respectively. But perhaps most importantly, we stuck to a non-relativistic analysis; steps forward towards a fully relativistic description have recently been taken in [37, 75]. Future directions of studies in this field will likely focus on one or more of the above points.

Acknowledgements We thank Enrico Cannizzaro for help with the numerical computation of the decay timescales. During the final stages of this work, we learnt of the related work [65]: we are grateful to Rafael Porto for sharing their draft and coordinating the submission with us. TS is supported by the VILLUM Foundation (grant no. VIL37766), the Danish Research Foundation (grant no. DNRF162), and the European Union's H2020 ERC Advanced Grant "Black holes: gravitational engines of discovery" grant agreement no. Gravitas–101052587.

[12] As shown in Figure 10 and equation (5.1), the separation of timescales is larger for smaller mass ratios. For equal-mass ratios $q \sim 1$, the timescales could become comparable.

A Hyperfine resonances and angular momentum

A nonzero black hole spin is responsible for the existence of the hyperfine energy splitting, as it breaks the spherical symmetry of the background spacetime. At the same time, we study the backreaction of resonances (hyperfine or not) on the orbit in the Newtonian approximation, assuming the conservation of the total angular momentum, which leads to equations (3.20), (3.21) and (3.22). This methodology might appear as fundamentally inconsistent, so let us inspect it more closely.

The weak-field approximation of the Kerr metric, which is valid at large distances, reads

$$ds^2 = -\left(1-\frac{2M}{r}\right)\mathrm{d}t^2 + \left(1+\frac{2M}{r}\right)\mathrm{d}r^2 + r^2(\mathrm{d}\theta^2+\sin^2\theta\,\mathrm{d}\phi^2) - \tilde{a}M\frac{4M}{r}\sin^2\theta\,\mathrm{d}t\,\mathrm{d}\phi\,. \tag{A.1}$$

The last term is known to give rise to the Lense-Thirring precession, as the equation of motion of a scalar particle can be put in the form

$$\frac{\mathrm{d}^2\mathbf{r}}{\mathrm{d}t^2} = -\frac{M}{r^3}\mathbf{r} + 4\frac{\mathrm{d}\mathbf{r}}{\mathrm{d}t}\times\mathbf{B}\,, \tag{A.2}$$

where the *gravitomagnetic field* $\mathbf{B}$ is related to the black hole spin as

$$\mathbf{B} = \boldsymbol{\nabla}\times\mathbf{A}\,, \qquad \mathbf{A} = -\frac{\mathbf{J}\times\mathbf{r}}{2r^3}, \qquad \mathbf{J} = \tilde{a}M^2\hat{z}\,. \tag{A.3}$$

The corresponding Hamiltonian is

$$H = \frac{(\mathbf{p}-4\mu\mathbf{A})^2}{2\mu} - \frac{\mu M}{r} \approx \frac{\mathbf{p}^2}{2\mu} - \frac{\alpha}{r} + \frac{2\tilde{a}M^2}{r^3}L_z\,, \tag{A.4}$$

where $\mu = \alpha/M$ is the mass of the particle. We can immediately check that the last term in (A.4) gives rise to the expected hyperfine splitting,

$$\langle n\ell m|H|n\ell m\rangle = 2\tilde{a}M^2 m\left\langle n\ell m\left|\frac{1}{r^3}\right|n\ell m\right\rangle = 2\tilde{a}M^2 m\,\frac{(\mu\alpha)^3}{n^3\ell(\ell+1/2)(\ell+1)}\,, \tag{A.5}$$

which perfectly matches the last term in (2.3).

The orbital angular momentum $\mathbf{L} = \mathbf{r}\times\mathbf{p}$ evolves as

$$\frac{\mathrm{d}\mathbf{L}}{\mathrm{d}t} = i[H,\mathbf{L}] = \frac{2}{r^3}\mathbf{J}\times\mathbf{L}, \tag{A.6}$$

which is the expected Lense-Thirring precession. Applying this equation to the cloud-binary system gives rise to two additional terms on the right-hand side of (3.16) and (3.17), corresponding to the Lense-Thirring precession of the cloud (which vanishes in most cases, as $\mathbf{S}_\mathrm{c} \parallel \mathbf{J}$ even during a transition, as we will see below) and of the binary. This precession is however *parametrically small*. None of the other terms in (3.16) and (3.17) depends on the BH spin $\tilde{a}$, even in the case of hyperfine resonances, where the energy splitting is proportional to $\tilde{a}$. Not only for realistic parameters is this precession extremely slow, but it also does not disrupt the approach in the main text, as (3.17) can be simply replaced by the analogous equation for the (precessing) equatorial projection of the angular momentum.

Having justified the use of the conservation of total angular momentum, there is another potentially worrying aspect of the breaking of spherical symmetry, that has to do with the spin of the cloud when it is in a mixed state, for example during a transition. As long as the Hamiltonian is spherically symmetric, $|n\ell m\rangle$ are guaranteed to be eigenstates of the scalar field's orbital angular momentum $\mathbf{L}$. Its matrix elements are given by $L_z\,|n\ell m\rangle = m\,|n\ell m\rangle$ and, in the Condon– Shortley convention, $L_\pm\,|n\ell m\rangle = \sqrt{\ell(\ell+1)-m(m\pm1)}\,|n\ell, m\pm1\rangle$, where $L_\pm = L_x \pm iL_y$. If the cloud is in a mixed state of the form $|\psi\rangle = c_a\,|n_a\ell_a m_a\rangle + c_b\,|n_b\ell_b m_b\rangle$, its z component of the angular momentum is then $m_a|c_a|^2 + m_b|c_b|^2$, while the equatorial components vanish unless $\ell_a = \ell_b$ and $|m_a - m_b| = 1$.

Remarkably, all the previous results still hold for the Hamiltonian (A.4). That is because the perturbation $\sim L_z/r^3$ is diagonal on the basis $|\ell m\rangle$, only mixing states with different n. Even though the spacetime is not spherically symmetric, the angular structure of the eigenstates is unchanged. The equations in the main text then do not need any modification, except for the case of hyperfine transitions with $|\Delta m| = 1$. For a hyperfine transition with $m_b = m_a - 1$, careful computation (in the Schrödinger, not dressed, frame) of the equatorial components of $\mathbf{S}_\mathrm{c}$ shows that equation (3.17) would need to be corrected with a term

$$\frac{\mathrm{d}S_{\mathrm{c},x}}{\mathrm{d}\tau} \sim \frac{B}{g}\sqrt{\ell(\ell+1)-m_a(m_a-1)}\sqrt{Z}(|c_b|^2-|c_a|^2)\sin(C\tau/3)\,. \tag{A.7}$$

This is a fast oscillating term that averages to zero on timescales much shorter than the evolution of the orbital parameters and the duration of the resonance. We thus ignore it in the main text.

B General resonance breaking

The phenomenon of resonance breaking was discussed in Section 3.4.3 in the simplified scenarios where only one of the following quantities is allowed to vary at a time: the eccentricity ε, Landau-Zener parameter Z and cloud's mass M_c. We derive here the result in the general case. Taking the time derivative of (3.42), we find

$$\begin{aligned}\frac{\mathrm{d}^2\omega}{\mathrm{d}\tau^2} &= \frac{\mathrm{d}f(\varepsilon)}{\mathrm{d}\tau} + B\frac{\mathrm{d}^2|c_a|^2}{\mathrm{d}\tau^2} = \frac{\mathrm{d}f(\varepsilon)}{\mathrm{d}\tau} + B\left(\frac{\mathrm{d}^2c_a^*}{\mathrm{d}\tau^2}c_a + 2\frac{\mathrm{d}c_a^*}{\mathrm{d}\tau}\frac{\mathrm{d}c_a}{\mathrm{d}\tau} + c_a^*\frac{\mathrm{d}^2c_a}{\mathrm{d}\tau^2}\right)\\ &= \frac{\mathrm{d}f(\varepsilon)}{\mathrm{d}\tau} - \frac{f(\varepsilon)}{2Z}\frac{\mathrm{d}Z}{\mathrm{d}\tau} + \Gamma - 2ZB(|c_a|^2-|c_b|^2) + \left(\frac{1}{2Z}\frac{\mathrm{d}Z}{\mathrm{d}\tau} - \Gamma\right)\frac{\mathrm{d}\omega}{\mathrm{d}\tau} + \omega\sqrt{Z}B(c_a^*c_b + c_ac_b^*)\,,\end{aligned} \tag{B.1}$$

where the second line is obtained by repeated use of the Schrödinger equation (3.33) together with (3.42). Under the assumption that all coefficients appearing above evolve slowly during a floating orbit, equation (B.1) has the structure of a damped harmonic oscillator, with solution

$$\omega = \frac{\frac{\mathrm{d}f(\varepsilon)}{\mathrm{d}\tau} - \frac{f(\varepsilon)}{2Z}\frac{\mathrm{d}Z}{\mathrm{d}\tau} + \Gamma - 2ZB(|c_a|^2-|c_b|^2)}{-(c_a^*c_b + c_ac_b^*)} + \text{damped oscillatory terms}\,. \tag{B.2}$$

The resonance breaks whenever $c_b^*c_a + c_a^*c_b = 0$. By direct application of the Schrödinger equation, we find

$$\sqrt{Z}\frac{\mathrm{d}}{\mathrm{d}\tau}(c_a^*c_b + c_ac_b^*) = -\omega\frac{\mathrm{d}|c_a|^2}{\mathrm{d}\tau} - \Gamma\sqrt{Z}(c_a^*c_b + c_b^*c_a)\,. \tag{B.3}$$

By plugging in (B.3) the non-oscillatory term of (B.2), we arrive to an equation for the sole unknown $c_a^* c_b + c_b^* c_a$:

$$\frac{ZB}{2}\left(\frac{\mathrm{d}}{\mathrm{d}\tau}+2\Gamma\right)(c_a^* c_b + c_b^* c_a)^2 = \left(\frac{\mathrm{d}f(\varepsilon)}{\mathrm{d}\tau} - \frac{f(\varepsilon)}{2Z}\frac{\mathrm{d}Z}{\mathrm{d}\tau} + \Gamma - 2ZB(|c_a|^2 - |c_b|^2)\right)\frac{\mathrm{d}|c_a|^2}{\mathrm{d}\tau}\,. \tag{B.4}$$

Remarkably, the evolution of the eccentricity, the variation of the Landau-Zener parameter and the decay of the cloud contribute additively to (B.4), each with its own term. In realistic cases, Γ is large enough to force the population of state $|b\rangle$ to reach a saturation value $|c_b|^2 = f(\varepsilon)/(2\Gamma B)$, which is usually small enough to be neglected in (B.4). The point of resonance breaking point then only involves the population left in the initial state, $|c_a|^2$.

C Ionization at resonance

The expressions for the ionization rate and power derived in [34] are valid under the assumption that the frequency Ω of the perturbation is away from any bound-to-bound state resonance. In this appendix, we relax this assumption by computing the new term contributing at resonance and showing that its effect is ultimately negligible. To allow for an easy match with the notations of [34], here we denote the state initially populated by $|b\rangle$ and any other bound state by $|a\rangle$.

Igoring couplings between different continuum states (as justified in Appendix A2 of [34]), the Hamiltonian of the gravitational atom reads

$$\mathcal{H} = \sum_b \epsilon_b\,|b\rangle\langle b| + \sum_{a\neq b}\eta_{ab}(t)\,|a\rangle\langle b| + \sum_K \epsilon_K\,|K\rangle\langle K| + \sum_{K,b}\left[\eta_{Kb}(t)\,|K\rangle\langle b| + \text{h.c.}\right]\,, \tag{C.1}$$

where $|K\rangle \equiv |k;\ell m\rangle$ is a continuum state multi-index, $\epsilon_K \approx k^2/(2\mu)$ and the couplings $\eta_{ab}(t)$ and $\eta_{Kb}(t)$ are the matrix elements of the perturbation (2.4). As in [34], by integrating out the continuum the Schrödinger equation can be recast in the following form,[13]

$$i\frac{\mathrm{d}c_b}{\mathrm{d}t} = \mathcal{E}_b c_b(t) + \sum_{a\neq b}\left[\eta_{ba}(t)e^{i(\epsilon_b-\epsilon_a)t} + \mathcal{E}_{ba}(t)\right]c_a(t)\,, \tag{C.2}$$

where we define the *induced couplings*

$$\mathcal{E}_{ba}(t) \equiv -i\int_{-\infty}^{t}\mathrm{d}t'\sum_K \eta^*_{Kb}(t)\eta_{Ka}(t')e^{-i(\epsilon_K-\epsilon_b)t+i(\epsilon_K-\epsilon_a)t'}\,. \tag{C.3}$$

and the *induced energies* $\mathcal{E}_b \equiv \mathcal{E}_{bb}$. The first term in (C.2) controls the ionization of state $|b\rangle$, while the first term in the parenthesis is responsible for the $|b\rangle \to |a\rangle$ resonance. The last term, which is the focus of this appendix, is a coupling between $|b\rangle$ and $|a\rangle$ induced via the interaction with the continuum. Because $\mathcal{E}_{ba}(t)$ oscillates very rapidly unless $(m_b - m_a)\dot{\varphi}_* = \epsilon_b - \epsilon_a$, the parenthesis in (C.2) can be neglected altogether whenever the system is not actively on resonance.

[13] All quantities here depend on time, either through fast oscillatory terms due to the evolving phase φ_*, or through the slow frequency chirp. For ease of notation, we will only explicitly write the time dependence of terms falling in the first class.

Let us study what happens when this is the case instead. The same saddle-point approximation done in [34] can be applied to the case $a \neq b$, arriving to

$$\mathcal{E}_{ba}(t) = e^{i(\epsilon_b-\epsilon_a)t - i(m_b-m_a)\varphi_*(t)} \sum_{\ell,m} \left[-\frac{i\mu\, \eta_{Kb}^{*(g_b)} \eta_{Ka}^{(g_a)}}{2k_*^{(g_a)}} \Theta\big((k_*^{(g_a)})^2\big) \right]. \tag{C.4}$$

Here, we defined $g_a = m - m_a$, evaluated $|K\rangle$ at $k_*^{(g_a)} = \sqrt{2\mu((m-m_a)\dot{\varphi}_* + \varepsilon_a)}$, and expanded the bound-continuum coupling in its Floquet components, $\eta_{Ka} = \eta_{Ka}^{(g_a)} e^{i(m-m_a)t}$ (and similarly for $a \leftrightarrow b$). To understand the effect of the induced coupling $\mathcal{E}_{ba}$, we can temporarily set $\eta_{ba} = 0$ and write (C.2) as

$$\frac{\mathrm{d}|c_b|^2}{\mathrm{d}t} = \sum_a \sum_{\ell,m} \frac{\mu}{k_*^{(g_a)}} \Theta\big((k_*^{(g_a)})^2\big)\, \mathrm{Re}\Big[e^{i(\epsilon_b-\epsilon_a)t - i(m_b-m_a)\varphi_*(t)} \eta_{Kb}^{*(g_b)} \eta_{Ka}^{(g_a)} c_b^*(t) c_a(t) \Big]. \tag{C.5}$$

Here, the term with $a = b$ reproduces the ionization term $\mathcal{E}_b c_b(t)$ in (C.2). Moreover, the evolution of state $|a\rangle$ is determined by the same formula, swapping $b \leftrightarrow a$. For $a \neq b$, however, this operation transforms the term in brackets into its complex conjugate, so its real part stays unchanged. We thus see that the induced coupling $\mathcal{E}_{ba}$ does *not* contribute to a $|b\rangle \to |a\rangle$ transition alongside η_{ba}, as one might have expected from (C.2) and as was speculated in [34]. Instead, both $|c_b|^2$ and $|c_a|^2$ experience an *identical* depletion (in addition to ionization) or recombination, depending on the sign of the real part appearing in (C.5); both cases are possible.

We have validated the previous results by comparing them to an explicit numerical integration of the Schrödinger equation, with the continuum states modelled as a large set of discrete states, quadratically spaced in energy. By tuning the parameters to make the impact of the induced coupling clearly visible, we found that (C.5) gives indeed a very accurate description of the evolution of the populations around the resonance. In the main text, in particular for Bohr resonances, we are mainly concerned with the correction from the induced coupling to a naive approach where the contributions of ionization and the resonance are simply summed up. To determine its importance, we assume for simplicity that $\eta_{ab} = 0$, $|c_b|^2 = 1$ and $|c_a|^2 = 0$ at $t = -\infty$, and employ a (further) saddle-point approximation in (C.2) around the time t_0 such that $\dot{\varphi}_* = \Omega_0 = (\epsilon_b - \epsilon_a)/(m_b - m_a)$. The population at $t = +\infty$ is then

$$|c_a|^2 = \frac{2\pi}{|m_b - m_a|\gamma} \left| \sum_{\ell,m} \frac{\mu\, \eta_{Kb}^{*(g_b)} \eta_{Ka}^{(g_a)}}{2k_*^{(g_b)}} \Theta\big((k_*^{(g_b)})^2\big) \right|^2, \tag{C.6}$$

where the couplings and $k_*^{(g_b)}$ have to be evaluated at $\Omega = \Omega_0$. Similar to an argument already developed in [34], this quantity $|c_a|^2$ is $\mathcal{O}(q^3\alpha^4)$ and it has to compete with the $\eta^2/\gamma \sim \mathcal{O}(q\alpha^2)$ contributions due to direct coupling $|\eta_{ba}|^2/\gamma$. Once again, we have validated (C.6) by comparing it to a direct numerical integration of the Schrödinger equation, and evaluated it for a typical Bohr resonance, finding a final population of $\mathcal{O}(10^{-11})$. We conclude that simply adding the steady deoccupation introduced by ionization on top of the resonant transition studied in the main text is a good approximation for our purposes.

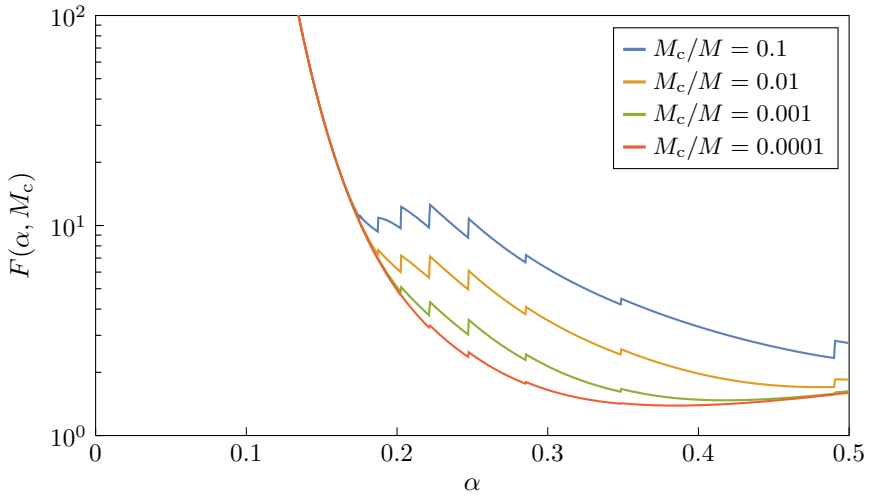


Figure 16: Function $F(\alpha, M_c)$ appearing in equation (D.1), which defines the angular interval δ_2 around a counter-rotating orbit where the resonance $|211\rangle \to |200\rangle$ is not adiabatic.

D $|211\rangle \to |200\rangle$ resonance

The strength of the fine resonance $|211\rangle \to |200\rangle$ has anomalous scaling with parameters, due to the dipole $\ell_* = 1$ being entirely responsible for the coupling and the binary separation falling partially inside the region where ionization dominates over GW emission. We therefore determine the angle δ_2, such that for $\pi - \delta_2 < \beta \leq \pi$ the resonance is non-adiabatic, as

$$\delta_2 = 6.7^\circ \left(\frac{M_c/M}{10^{-2}}\right)^{-1/4} \left(\frac{q}{10^{-3}}\right)^{1/8} \left(\frac{\alpha}{0.2}\right)^{7/8} F(\alpha, M_c)\,, \tag{D.1}$$

where the formula holds for small δ_2 and the function $F(\alpha, M_c)$ is calculated numerically and shown in Figure 16.

References

[1] E. Barausse, V. Cardoso, and P. Pani, "Can environmental effects spoil precision gravitational-wave astrophysics?", *Phys. Rev. D* **89** no. 10, (2014) 104059, arXiv:1404.7149 [gr-qc].

[2] G. Caneva Santoro, S. Roy, R. Vicente, M. Haney, O. J. Piccinni, W. Del Pozzo, and M. Martinez, "First constraints on compact binary environments from LIGO-Virgo data", arXiv:2309.05061 [gr-qc].

[3] **LISA** Collaboration, P. Amaro-Seoane *et al.*, "Laser Interferometer Space Antenna", arXiv:1702.00786 [astro-ph.IM].

[4] J. Baker *et al.*, "The Laser Interferometer Space Antenna: Unveiling the Millihertz Gravitational Wave Sky", arXiv:1907.06482 [astro-ph.IM].

[5] M. Maggiore *et al.*, "Science Case for the Einstein Telescope", *JCAP* **03** (2020) 050, arXiv:1912.02622 [astro-ph.CO].

[6] E. Barausse and L. Rezzolla, "The Influence of the hydrodynamic drag from an accretion torus on extreme mass-ratio inspirals", *Phys. Rev. D* **77** (2008) 104027, arXiv:0711.4558 [gr-qc].

[7] L. Speri, A. Antonelli, L. Sberna, S. Babak, E. Barausse, J. R. Gair, and M. L. Katz, "Probing Accretion Physics with Gravitational Waves", *Phys. Rev. X* **13** no. 2, (2023) 021035, arXiv:2207.10086 [gr-qc].

[8] K. Eda, Y. Itoh, S. Kuroyanagi, and J. Silk, "New Probe of Dark-Matter Properties: Gravitational Waves from an Intermediate-Mass Black Hole Embedded in a Dark-Matter Minispike", *Phys. Rev. Lett.* **110** no. 22, (2013) 221101, arXiv:1301.5971 [gr-qc].

[9] B. J. Kavanagh, D. A. Nichols, G. Bertone, and D. Gaggero, "Detecting dark matter around black holes with gravitational waves: Effects of dark-matter dynamics on the gravitational waveform", *Phys. Rev. D* **102** no. 8, (2020) 083006, arXiv:2002.12811 [gr-qc].

[10] P. S. Cole, G. Bertone, A. Coogan, D. Gaggero, T. Karydas, B. J. Kavanagh, T. F. M. Spieksma, and G. M. Tomaselli, "Distinguishing environmental effects on binary black hole gravitational waveforms", *Nature Astron.* **7** no. 8, (2023) 943–950, arXiv:2211.01362 [gr-qc].

[11] N. Becker and L. Sagunski, "Comparing accretion disks and dark matter spikes in intermediate mass ratio inspirals", *Phys. Rev. D* **107** no. 8, (2023) 083003, arXiv:2211.05145 [gr-qc].

[12] T. K. Karydas, B. J. Kavanagh, and G. Bertone, "Sharpening the dark matter signature in gravitational waveforms I: Accretion and eccentricity evolution", arXiv:2402.13053 [gr-qc].

[13] B. J. Kavanagh, T. K. Karydas, G. Bertone, P. Di Cintio, and M. Pasquato, "Sharpening the dark matter signature in gravitational waveforms II: Numerical simulations with the NbodyIMRI code", arXiv:2402.13762 [gr-qc].

[14] M. Garg, A. Derdzinski, S. Tiwari, J. Gair, and L. Mayer, "Measuring eccentricity and gas-induced perturbation from gravitational waves of LISA massive black hole binaries", arXiv:2402.14058 [astro-ph.GA].

[15] J. Bamber, J. C. Aurrekoetxea, K. Clough, and P. G. Ferreira, "Black hole merger simulations in wave dark matter environments", *Phys. Rev. D* **107** no. 2, (2023) 024035, arXiv:2210.09254 [gr-qc].

[16] J. C. Aurrekoetxea, K. Clough, J. Bamber, and P. G. Ferreira, "The effect of wave dark matter on equal mass black hole mergers", arXiv:2311.18156 [gr-qc].

[17] S. Weinberg, "A New Light Boson?", *Phys. Rev. Lett.* **40** (1978) 223–226.

[18] F. Wilczek, "Problem of Strong P and T Invariance in the Presence of Instantons", *Phys. Rev. Lett.* **40** (1978) 279–282.

[19] R. D. Peccei and H. R. Quinn, "CP Conservation in the Presence of Instantons", *Phys. Rev. Lett.* **38** (1977) 1440–1443.

[20] A. Arvanitaki, S. Dimopoulos, S. Dubovsky, N. Kaloper, and J. March-Russell, "String Axiverse", *Phys. Rev. D* **81** (2010) 123530, arXiv:0905.4720 [hep-th].

[21] P. Svrcek and E. Witten, "Axions In String Theory", *JHEP* **06** (2006) 051, arXiv:hep-th/0605206.

[22] L. Bergstrom, "Dark Matter Candidates", *New J. Phys.* **11** (2009) 105006, arXiv:0903.4849 [hep-ph].

[23] D. J. E. Marsh, "Axion Cosmology", *Phys. Rept.* **643** (2016) 1–79, arXiv:1510.07633 [astro-ph.CO].

[24] L. Hui, J. P. Ostriker, S. Tremaine, and E. Witten, "Ultralight scalars as cosmological dark matter", *Phys. Rev. D* **95** no. 4, (2017) 043541, arXiv:1610.08297 [astro-ph.CO].

[25] E. G. M. Ferreira, "Ultra-light dark matter", *Astron. Astrophys. Rev.* **29** no. 1, (2021) 7, arXiv:2005.03254 [astro-ph.CO].

[26] Y. B. Zel'Dovich, "Generation of Waves by a Rotating Body", *Soviet Journal of Experimental and Theoretical Physics Letters* **14** (1971) 180.

[27] Y. B. Zel'Dovich, "Amplification of Cylindrical Electromagnetic Waves Reflected from a Rotating Body", *Soviet Journal of Experimental and Theoretical Physics* **35** (1972) 1085.

[28] A. A. Starobinsky, "Amplification of waves reflected from a rotating "black hole" ", *Sov. Phys. JETP* **37** no. 1, (1973) 28–32.

[29] R. Brito, V. Cardoso, and P. Pani, "Superradiance: New Frontiers in Black Hole Physics", *Lect. Notes Phys.* **906** (2015) pp.1–237, arXiv:1501.06570 [gr-qc].

[30] J. Zhang and H. Yang, "Gravitational floating orbits around hairy black holes", *Phys. Rev. D* **99** no. 6, (2019) 064018, arXiv:1808.02905 [gr-qc].

[31] D. Baumann, H. S. Chia, and R. A. Porto, "Probing Ultralight Bosons with Binary Black Holes", *Phys. Rev. D* **99** no. 4, (2019) 044001, arXiv:1804.03208 [gr-qc].

[32] J. Zhang and H. Yang, "Dynamic Signatures of Black Hole Binaries with Superradiant Clouds", *Phys. Rev. D* **101** no. 4, (2020) 043020, arXiv:1907.13582 [gr-qc].

[33] D. Baumann, H. S. Chia, R. A. Porto, and J. Stout, "Gravitational Collider Physics", *Phys. Rev. D* **101** no. 8, (2020) 083019, arXiv:1912.04932 [gr-qc].

[34] D. Baumann, G. Bertone, J. Stout, and G. M. Tomaselli, "Ionization of gravitational atoms", *Phys. Rev. D* **105** no. 11, (2022) 115036, arXiv:2112.14777 [gr-qc].

[35] D. Baumann, G. Bertone, J. Stout, and G. M. Tomaselli, "Sharp Signals of Boson Clouds in Black Hole Binary Inspirals", *Phys. Rev. Lett.* **128** no. 22, (2022) 221102, arXiv:2206.01212 [gr-qc].

[36] G. M. Tomaselli, T. F. M. Spieksma, and G. Bertone, "Dynamical friction in gravitational atoms", *JCAP* **07** (2023) 070, arXiv:2305.15460 [gr-qc].

[37] R. Brito and S. Shah, "Extreme mass-ratio inspirals into black holes surrounded by scalar clouds", *Phys. Rev. D* **108** no. 8, (2023) 084019, arXiv:2307.16093 [gr-qc].

[38] F. Duque, C. F. B. Macedo, R. Vicente, and V. Cardoso, "Axion Weak Leaks: extreme mass-ratio inspirals in ultra-light dark matter", arXiv:2312.06767 [gr-qc].

[39] T. Takahashi and T. Tanaka, "Axion clouds may survive the perturbative tidal interaction over the early inspiral phase of black hole binaries", *JCAP* **10** (2021) 031, arXiv:2106.08836 [gr-qc].

[40] Q. Ding, X. Tong, and Y. Wang, "Gravitational Collider Physics via Pulsar-Black Hole Binaries", *Astrophys. J.* **908** no. 1, (2021) 78, arXiv:2009.11106 [astro-ph.HE].

[41] X. Tong, Y. Wang, and H.-Y. Zhu, "Gravitational Collider Physics via Pulsar–Black Hole Binaries II: Fine and Hyperfine Structures Are Favored", *Astrophys. J.* **924** no. 2, (2022) 99, arXiv:2106.13484 [astro-ph.HE].

[42] P. Du, D. Egana-Ugrinovic, R. Essig, G. Fragione, and R. Perna, "Searching for ultra-light bosons and constraining black hole spin distributions with stellar tidal disruption events", *Nature Commun.* **13** no. 1, (2022) 4626, arXiv:2202.01215 [hep-ph].

[43] T. Takahashi, H. Omiya, and T. Tanaka, "Evolution of binary systems accompanying axion clouds in extreme mass ratio inspirals", *Phys. Rev. D* **107** no. 10, (2023) 103020, arXiv:2301.13213 [gr-qc].

[44] E. Berti, R. Brito, C. F. B. Macedo, G. Raposo, and J. L. Rosa, "Ultralight boson cloud depletion in binary systems", *Phys. Rev. D* **99** no. 10, (2019) 104039, arXiv:1904.03131 [gr-qc].

[45] L. Hui, Y. T. A. Law, L. Santoni, G. Sun, G. M. Tomaselli, and E. Trincherini, "Black hole superradiance with dark matter accretion", *Phys. Rev. D* **107** no. 10, (2023) 104018, arXiv:2208.06408 [gr-qc].

[46] C. A. R. Herdeiro, E. Radu, and N. M. Santos, "A bound on energy extraction (and hairiness) from superradiance", *Phys. Lett. B* **824** (2022) 136835, arXiv:2111.03667 [gr-qc].

[47] W. E. East and F. Pretorius, "Superradiant Instability and Backreaction of Massive Vector Fields around Kerr Black Holes", *Phys. Rev. Lett.* **119** no. 4, (2017) 041101, arXiv:1704.04791 [gr-qc].

[48] D. Baumann, H. S. Chia, J. Stout, and L. ter Haar, "The Spectra of Gravitational Atoms", *JCAP* **12** (2019) 006, arXiv:1908.10370 [gr-qc].

[49] C. Zener, "Non-Adiabatic Crossing of Energy Levels", *Proceedings of the Royal Society of London* **137** no. 833, (1932) 696–702.

[50] L. Landau, "Zur Theorie der Energieübertragung", *Z. Sowjetunion* **2** (1932) 46–51.

[51] E. P. Wigner, *Group Theory and Its Application to the Quantum Mechanics of Atomic Spectra*. Academic Press, New York, 1959.

[52] P. C. Peters and J. Mathews, "Gravitational radiation from point masses in a Keplerian orbit", *Phys. Rev.* **131** (1963) 435–439.

[53] P. C. Peters, "Gravitational Radiation and the Motion of Two Point Masses", *Phys. Rev.* **136** (1964) B1224–B1232.

[54] S. Detweiler, "Klein-gordon equation and rotating black holes", *Phys. Rev. D* **22** (Nov, 1980) 2323–2326.

[55] E. W. Leaver, "An Analytic representation for the quasi normal modes of Kerr black holes", *Proc. Roy. Soc. Lond. A* **402** (1985) 285–298.

[56] V. Cardoso and S. Yoshida, "Superradiant instabilities of rotating black branes and strings", *JHEP* **07** (2005) 009, arXiv:hep-th/0502206.

[57] S. R. Dolan, "Instability of the massive Klein-Gordon field on the Kerr spacetime", *Phys. Rev. D* **76** (2007) 084001, arXiv:0705.2880 [gr-qc].

[58] E. Berti, V. Cardoso, and A. O. Starinets, "Quasinormal modes of black holes and black branes", *Class. Quant. Grav.* **26** (2009) 163001, arXiv:0905.2975 [gr-qc].

[59] P. Amaro-Seoane, "Relativistic dynamics and extreme mass ratio inspirals", *Living Rev. Rel.* **21** (2018) 4, arXiv:1205.5240 [astro-ph.CO].

[60] **LISA** Collaboration, P. A. Seoane *et al.*, "Astrophysics with the Laser Interferometer Space Antenna", *Living Rev. Rel.* **26** no. 1, (2023) 2, arXiv:2203.06016 [gr-qc].

[61] N. C. Stone, B. D. Metzger, and Z. Haiman, "Assisted inspirals of stellar mass black holes embedded in AGN discs: solving the 'final au problem'", *Mon. Not. Roy. Astron. Soc.* **464** no. 1, (2017) 946–954, arXiv:1602.04226 [astro-ph.GA].

[62] I. Bartos, B. Kocsis, Z. Haiman, and S. Márka, "Rapid and Bright Stellar-mass Binary Black Hole Mergers in Active Galactic Nuclei", *Astrophys. J.* **835** no. 2, (2017) 165, arXiv:1602.03831 [astro-ph.HE].

[63] B. McKernan, K. E. S. Ford, J. Bellovary, N. W. C. Leigh, Z. Haiman, B. Kocsis, W. Lyra, M.-M. M. Low, B. Metzger, M. O'Dowd, S. Endlich, and D. J. Rosen, "Constraining stellar-mass black hole mergers in agn disks detectable with ligo", *The Astrophysical Journal* **866** no. 1, (Oct, 2018) 66.

[64] Y. Levin, "Starbursts near supermassive black holes: young stars in the Galactic Center, and gravitational waves in LISA band", *Mon. Not. Roy. Astron. Soc.* **374** (2007) 515–524, arXiv:astro-ph/0603583.

[65] M. Boskovic, M. Koschnitzke, and R. A. Porto. *To appear.*

[66] X. Tong, Y. Wang, and H.-Y. Zhu, "Termination of superradiance from a binary companion", *Phys. Rev. D* **106** no. 4, (2022) 043002, arXiv:2205.10527 [gr-qc].

[67] K. Fan, X. Tong, Y. Wang, and H.-Y. Zhu, "Modulating binary dynamics via the termination of black hole superradiance", *Phys. Rev. D* **109** no. 2, (2024) 024059, arXiv:2311.17013 [gr-qc].

[68] J. Goodman and J. C. Tan, "Supermassive stars in quasar disks", *Astrophys. J.* **608** (2004) 108–118, arXiv:astro-ph/0307361.

[69] J. Goodman, "Selfgravity and QSO disks", *Mon. Not. Roy. Astron. Soc.* **339** (2003) 937, arXiv:astro-ph/0201001.

[70] S. Babak, J. Gair, A. Sesana, E. Barausse, C. F. Sopuerta, C. P. L. Berry, E. Berti, P. Amaro-Seoane, A. Petiteau, and A. Klein, "Science with the space-based interferometer LISA. V: Extreme mass-ratio inspirals", *Phys. Rev. D* **95** no. 10, (2017) 103012, arXiv:1703.09722 [gr-qc].

[71] P. Amaro-Seoane, C. F. Sopuerta, and M. D. Freitag, "The role of the supermassive black hole spin in the estimation of the EMRI event rate", *Mon. Not. Roy. Astron. Soc.* **429** no. 4, (2013) 3155–3165, arXiv:1205.4713 [astro-ph.CO].

[72] M. C. Ferreira, C. F. B. Macedo, and V. Cardoso, "Orbital fingerprints of ultralight scalar fields around black holes", *Phys. Rev. D* **96** no. 8, (2017) 083017, arXiv:1710.00830 [gr-qc].

[73] O. A. Hannuksela, K. W. K. Wong, R. Brito, E. Berti, and T. G. F. Li, "Probing the existence of ultralight bosons with a single gravitational-wave measurement", *Nature Astron.* **3** no. 5, (2019) 447–451, arXiv:1804.09659 [astro-ph.HE].

[74] Y. Cao and Y. Tang, "Signatures of ultralight bosons in compact binary inspiral and outspiral", *Phys. Rev. D* **108** no. 12, (2023) 123017, arXiv:2307.05181 [gr-qc].

[75] E. Cannizzaro, L. Sberna, S. R. Green, and S. Hollands, "Relativistic Perturbation Theory for Black-Hole Boson Clouds", *Phys. Rev. Lett.* **132** no. 5, (2024) 051401, arXiv:2309.10021 [gr-qc].

arXiv:2403.03106v1 [gr-qc] 5 Mar 2024

Understanding gravitationally induced decoherence parameters in neutrino oscillations using a microscopic quantum mechanical model

Alba Domi[1*†], Thomas Eberl[1*†], Max Joseph Fahn[1,2*†], Kristina Giesel[1,2*†], Lukas Hennig[1*†], Ulrich Katz[1*†], Roman Kemper[1,2*†] and Michael Kobler[1,2*†]

[1]Erlangen Centre for Astroparticle Physics, Friedrich-Alexander-Universität Erlangen-Nürnberg, Department of Physics, Nikolaus-Fiebiger-Straße 2, Erlangen, 91058, Germany.

[2]Friedrich-Alexander-Universität, Department of Physics, Theoretical Physics III, Institute for Quantum Gravity, Staudtstr. 7, Erlangen, 91058, Germany.

*Corresponding author(s). E-mail(s): alba.domi@fau.de; thomas.eberl@fau.de; max.j.fahn@fau.de; kristina.giesel@fau.de; lukas.hennig@fau.de; uli.katz@fau.de; roman.kemper@fau.de; michael.kobler@fau.de;

†These authors contributed equally to this work.

Abstract

In this work, a microscopic quantum mechanical model for gravitationally induced decoherence introduced by Blencowe and Xu is investigated in the context of neutrino oscillations. The focus is on the comparison with existing phenomenological models and the physical interpretation of the decoherence parameters in such models. The results show that for neutrino oscillations in vacuum gravitationally induced decoherence can be matched with phenomenological models with decoherence parameters of the form $\boldsymbol{\Gamma_{ij} \sim \Delta m_{ij}^4 E^{-2}}$. When matter effects are included, the decoherence parameters show a dependence on matter effects, which vary in the different layers of the Earth, that can be explained with the form of the coupling between neutrinos and the gravitational wave environment inspired by linearised gravity. Consequently, in the case of neutrino oscillations in matter, the microscopic model does not agree with many existing phenomenological models that assume constant decoherence parameters in matter, and their existing bounds cannot be used to further constrain the model considered here. The probabilities for neutrino oscillations with constant and varying decoherence parameters are compared and it is shown that the deviations can be up to 10%. On a theoretical level, these different models can be characterised by a different choice of Lindblad operators, with the model with decoherence parameters that do not include matter effects being less suitable from the point of view of linearised gravity.

Keywords: decoherence, neutrino oscillations, gravity, open quantum systems

1 Introduction

The search for quantum decoherence (QD) effects in connection with neutrino oscillations is a topic that has gained increasing interest in various research communities in recent years [1–32]. Neutrino experiments have searched for QD effects on current data via a phenomenological approach [21–25] and several works have analysed the sensitivity of future detectors [19, 33]. However, the connection between such phenomenological models and the underlying microscopic physics is not always immediate. It is interesting to understand, in terms of theoretical models in the framework of open quantum systems [34], how the phenomenological models used for neutrino oscillations can be derived from underlying microscopic physics.

Existing phenomenological models often start from the Lindblad equation and then parameterise the dissipator involved by selecting a finite number of parameters. In the most general, three-neutrino case, the number of free parameters is 45, but this number is usually reduced by requiring physically meaningful additional assumptions [13, 14, 18] such as unitarity or conservation of energy of the neutrino subsystem[1], see for instance [32] for a recent brief introduction to these models. These assumptions reduce the number of free parameters characterising the dissipator in the current phenomenological models to less than five, see for instance [23, 32].

From a theoretical perspective, the interest lies in the underlying microscopic model, from which the Lindblad equation can be derived under various assumptions about the open quantum system. A crucial choice in such microscopic models is the environment as well as the specific coupling of the environment and the system under consideration encoded in the interaction Hamiltonian. At the level of the Lindblad equation, the choice of coupling plays a role in two ways: firstly, the choice of coupling between the system and environment can be linked to some choice of Lindblad operators, see also [35] in the context of neutrino osicllations. Secondly, the environmental operators involved in the interaction Hamiltonian determine the specific form of the environmental correlation functions when the environmental degrees of freedom are traced out, which in turn determine the coefficients of the Lindblad operators involved in the dissipator.

In the framework of existing phenomenological models, which usually start at the level of the Lindblad equation, the dissipator for a three-neutrino scenario is often parameterised by the choice of eight dissipator operators, which is then transferred to the choice of a finite number of decoherence parameters, usually less than five. These decoherence parameters thus contain all the information about the choice of Lindblad operators and the form of the correlation functions of the environment. Starting from a microscopic model, the appropriate form and number of decoherence parameters can be calculated, and one has sufficient control over their physical interpretation and the assumptions that go into this calculation. However, linking a given set of decoherence parameters to an underlying microscopic model is more difficult, since the degrees of freedom of the environment have already been traced out and reconstructing the coupling between the system and the environment in this direction is less straightforward and unambiguous.

Moreover, a large class of phenomenological models assumes that the contribution in the dissipator, which is responsible for decoherence and usually leads to a damping of the probabilities for neutrino oscillations, depends on a positive or negative power of the neutrino energy [4, 10, 20–23, 29]. Different choices of the power define different models that generally yield other modifications of the oscillation probabilities.
From a quantum gravity perspective, the underlying microscopic models are of interest because they allow the formulation of models in which gravitationally induced decoherence can be investigated [3, 8, 9, 29–31], see also [36, 37] for reviews on gravitational decoherence. In the context of general relativity, a suitable starting point for the formulation of such microscopic models is linearised gravity coupled to a matter system, and in the framework of open quantum systems, the corresponding master equation can be derived in quantum field theory [12, 27, 38–40]. Since all these models contain an infinite number of degrees of freedom, the final master equations are rather complicated and difficult to handle for the case of neutrino oscillations. A possible solution is to consider the 1-particle sector of the field theory model and use this as the underlying microscopic model in a quantum mechanical setting in which the existing phenomenological models work, see for instance [41] for an analysis of the 1-particle sector of the quantum field theory model from [39] and also [27, 38]. In [41] the projection of the field-theoretical model with an infinite number of degrees of freedom onto its 1-particle sector is considered, which in turn can be formulated as a quantum mechanical model involving only finitely many degrees of freedom.

As a first step towards bridging the gap between the underlying microscopic models and the existing phenomenological ones, this work considers a quantum mechanical toy model for gravitationally induced decoherence introduced by Blencowe and Xu [42] and slightly generalised it in order to apply it in the context of neutrino oscillations. The model in [42] is inspired by the models in [12, 27, 38–40] as far as the choice of the environment and its coupling to a given matter system is concerned. To the authors knowledge, the model in [42], that was already briefly discussed in [40], has been investigated in the context of neutrino oscillations so far only in [43] where they conclude that this model leads to no decoherence effect. However, to our understanding, as it is discussed below, there is a non-vanishing decoherence effect.

In this work, the only free parameters that remain in the final Lindblad equation are the coupling parameter

[1] Conservation of energy in the overall system of neutrino and environment is of course always fulfilled

of the neutrino to the environment and a temperature parameter that characterises the environment of the thermal gravitational waves. In this way, it is possible to obtain a physical interpretation of the free parameters in the existing phenomenological models. Moreover, the gravitationally induced decoherence model presented in this work favours a certain power of the neutrino energy dependence in the dissipator. In the phenomenological model, this energy dependence is postulated, whereas, in this work it directly follows from the choice of the underlying microscopic model. In addition, as our results show, there is a clear physical interpretation of the decoherence parameters present in a subclass of phenomenological models. Interestingly, as we will explain in our results, the existing bounds for the decoherence parameters in the phenomenological models in [25, 32, 44] cannot be used to constrain the free parameters of the microscopic model considered in this work because they are based on assumptions that are not compatible with the model for gravitationally induced decoherence as formulated in this work.

In the most general case, and also in the model presented here, the Lindblad equation contains a so-called Lamb shift contribution, which is caused by the interaction with the gravitational environment. This contribution modifies the unitary evolution of the effective dynamics of the neutrinos and does neither lead to dissipation nor decoherence. However, it has the effect that the energy eigenvalues of the neutrinos are modified by a shift, which in the model considered here depends on a cutoff frequency. The latter is introduced as a regulator for some of the integrals involved in the calculation of the model's environmental correlation functions. As an energy shift depending on some regulator is rather inconvenient, we will show that along the lines of the Caldeira-Leggett model of quantum Brownian motion [45] the Lamb shift contribution can be eliminated by a suitable counter-term. Such a Lamb shift contribution is also present in the field theoretical models in [12, 27, 38–40] where a similar renormalisation procedure is applied. In many existing phenomenological models such a Lamb shift contribution is often just neglected and no counter term is considered. Our analysis show that such a strategy is justified for the model considered here, but in general requires a detailed investigation for each individual model considered, as in general the renormalisation of the Lamb shift term can provide additional contributions. Our results further show that the interpretation of the Lamb shift contribution discussed in [5] in the form of massless neutrino oscillations is, as we understand it, when carried over to the model here or the field theoretic models in [12, 27, 38–40], somewhat problematic.

The article is structured as follows: after the introduction in section 1 we briefly introduce in subsection 2.1 the model from [42] and its slight generalisation which is needed for the further analysis. Here we discuss the model for a generic choice of matter system with only very mild assumptions that are also consistent with those used in the existing phenomenological models. Here we skip details of the derivation that can partly be found in the appendix but discuss what kind of assumptions enter into the model and how these are motivated. The application of the model to a three neutrino-scenario is presented in section 2.2. It provides the solution of the effective neutrino dynamics under the influence of the gravitational environment that is taken as starting point in section 3 to compute the probabilities for neutrino oscillations that follow from the model considered in this work. The main focus in this section lies on the comparison of the model considered in this work and the existing phenomenological models. As will be shown they can be understood as two models with different couplings to the gravitational environment that agree for the special case of neutrino oscillations in vacuum. In the matter case, deviations in the oscillation probabilities appear, which are discussed and quantified. Finally, in section 4 the main results of this work are summarised and an outlook on possible future work in this direction is presented.

2 Decoherence model

The model investigated in this work is inspired from the field theory models for gravitationally induced decoherence [12, 27, 38–40] that all consider linearised gravity as the environment to which a given matter system is coupled. Because general relativity as well as generic matter systems involve gauge symmetries, some work is necessary in order to get the corresponding physical Hamiltonian of the total system that usually is the starting point of the decoherence model. This has been implemented in [12, 27, 38–40] either by gauge fixing [12, 27, 38, 40] or by the construction of gauge invariant observables [39] by means of choosing a suitable dynamical reference system. The classical total Hamiltonian H_{tot} in all these models has the form

$$H_{\text{tot}} = H_S + H_{\mathcal{E}} + H_{\text{int}},$$

where H_S encodes the dynamics of the system usually chosen to be some matter, $H_{\mathcal{E}}$ is the Hamiltonian for the environment, here linearised gravity, and H_{int} describes their interaction. Once a frame of reference has been chosen, the form of each Hamiltonian can be derived from the underlying action, and in particular

the form of the interaction Hamiltonian H_{int} is determined by the way matter and (linearised) gravity are coupled, namely via the energy-momentum tensor of matter and the metric. Thus, on the one hand it is an advantage to know the underlying field theory model because the microscopic Hamiltonian that enters any decoherence models can rather be derived than needing to be chosen, which results in decoherence models with less ambiguities. On the other hand as the results in [12, 27, 38–40] illustrate, the final form of the master equation which encodes the dynamics of the system's density matrix when the environmental degrees of freedom have been traced out, is very complicated and hence technically challenging. Therefore, as a first step in this work we will consider the quantum mechanical toy model for gravitationally induced decoherence introduced in the seminal work of Xu and Blencowe in [42]. This model is strongly inspired by the field theory models and hence mimics that usual gravitational coupling in the quantum mechanical toy model. To the knowledge of the authors although this model exists in the literature it has only been applied to investigate gravitationally induced decoherence in the context of neutrino oscillations in [43] where the authors however conclude that the model will lead to no decoherence effect. We will consider the slightly generalised model of [42] such that we can also apply it to neutrino oscillations and present the derivation of the corresponding master equation, which was not included in the presentation in [42] in detail to show that from our results non-vanishing decoherence effects are possible for this model.

2.1 Microscopic model for generic time independent system's Hamiltonian

In the work [42], a harmonic oscillator is considered as matter system and its dynamics are derived working with coherent states for the bath. Based on this, the decoherence on an initial superposition of coherent states is studied. Here, we want to consider the model in a more general context to be able to apply it later to neutrino oscillations. Therefore, we will leave the choice of the system's Hamiltonian generic in this section and only specify to neutrinos later. The only assumption we make for H_S is that it is time-independent. Likewise to the field theory case the total Hamiltonian splits into the individual contributions which are then quantised in a quantum mechanical context yielding

$$\hat{H} = \hat{H}_S + \hat{H}_{\mathcal{E}} + \hat{H}_{\text{int}} = \underbrace{\hat{H}_S^{(0)} + \hat{H}_S^{(C)}}_{\hat{H}_S} + \underbrace{\frac{1}{2}\sum_{i=1}^{N}\left[\hat{p}_i^2 + \omega_i^2 \hat{q}_i^2\right]}_{\hat{H}_{\mathcal{E}}} \underbrace{- \hat{H}_S \otimes \sum_{i=1}^{N} g_i \hat{q}_i}_{\hat{H}_{\text{int}}} , \tag{1}$$

where here the specific form of $\hat{H}_{\mathcal{E}}$ and $\hat{H}_{\text{int}}$ are inspired from the field theory model and $\hat{H}_S^{(C)}$ denotes a counter term of the form $\hat{H}_S^{(C)} = \sum_{i=1}^{N} \frac{\hbar g_i^2}{\omega_i^2}(\hat{H}_S^{(0)})^2$. This counter term is needed as it will later remove the unphysical contribution of the Lamb shift contribution. It is included analogously to the treatment of the Caldeira-Leggett model [45], see for instance [42] and can be understood as a tiny, due to g_i^2, frequency dependent correction to the unitary evolution of the non-renormalised and thus the bare system's Hamiltonian $\hat{H}_S^{(0)}$. The environment serves as a toy model for gravitational waves that interact with the system under consideration. In later applications in the section 2.2, the system is chosen as neutrinos. To resemble this, N independent harmonic oscillators with unit mass were chosen explaining the form of $\mathcal{H}_{\mathcal{E}}$. The lesson from the field theory models is that the interaction Hamiltonian, which includes the energy-momentum tensor and the metric, can be modeled by an interaction Hamiltonian operator, as shown in [42] that involves a coupling between the system's Hamiltonian $\hat{H}_S$ and the position operator of the environmental degrees of freedom $\hat{q}_i$. The coupling constant g_i, which has dimension of inverse length, can in principle be different for each oscillator.

Position and momentum operators of the oscillators in the environment fulfil the usual commutation relations:

$$[\hat{q}_i, \hat{p}_j] = i\hbar\delta_{ij} . \tag{2}$$

The entire Hilbert space is a tensor product of the system Hilbert space $\mathcal{H} = \mathcal{H}_S \otimes \mathcal{H}_{\mathcal{E}}$ where $\hat{H}_S$ and $\hat{H}_{\mathcal{E}}$ act trivially on $\mathcal{H}_{\mathcal{E}}$ and $\mathcal{H}_S$, respectively. Assuming that the interaction is small (i.e. g_i small) compared to the evolution in the absence of coupling with the environment, a time-convolutionless (TCL) master equation truncated to second order in the coupling g_i (see e.g. [34, 39]) provides a good approximation to the effective dynamics of the system, which is obtained after the degrees of freedom of the environment have been worked out. In the model discussed here, this master equation then assumes a simple form, since the interaction

Hamiltonian $H_{\rm int}$ contains a time-independent system Hamiltonian $\hat{H}_S$:

$$\begin{aligned}\frac{d}{dt}\hat{\rho}_S(t) &= -\frac{i}{\hbar}\left[\hat{H}_S,\hat{\rho}_S(t)\right] - \frac{1}{\hbar^2}\int_0^{t-t_0} d\tau\ \mathrm{Tr}_{\mathcal{E}}\left(\left[\hat{H}_{\rm int},\left[\hat{H}_{\rm int}(-\tau),\hat{\rho}_S(t)\otimes\hat{\rho}_{\mathcal{E}}\right]\right]\right) \qquad (3)\\ &= -\frac{i}{\hbar}\left[\hat{H}_S,\hat{\rho}_S(t)\right] + \frac{i\Lambda(t-t_0)}{\hbar^2}\left[(\hat{H}_S^{(0)})^2,\hat{\rho}_S(t)\right] + \frac{\Gamma(t-t_0)}{\hbar^2}\left(\hat{H}_S^{(0)}\hat{\rho}_S(t)\hat{H}_S^{(0)} - \frac{1}{2}\left\{(\hat{H}_S^{(0)})^2,\hat{\rho}_S(t)\right\}\right),\end{aligned}$$

where $[.,.]$ and $\{.,.\}$ denote a commutator and an anticommutator, respectively. $\mathrm{Tr}_{\mathcal{E}}(.)$ denotes the partial trace over the degrees of freedom of the environment that can be calculated once a state has been chosen for the environment, where we choose a Gibbs state i.e. $\hat{\rho}_{\mathcal{E}} = \frac{1}{Z}e^{-\beta\hat{H}_{\mathcal{E}}}$ with partition function $Z = \mathrm{Tr}_{\mathcal{E}}\left(e^{-\beta\hat{H}_{\mathcal{E}}}\right)$, where $\beta = \frac{1}{k_B T}$ with the Boltzmann constant k_B and similar to [38] we denote the involved 'temperature' parameter of the environment by T, which characterises the bath of the oscillators in the environment that mimic the thermal gravitational wave background in this toy model[2]. The density matrix of the matter system evaluated at temporal coordinate t is denoted by $\hat{\rho}_S(t)$ and $\hat{H}_{\rm int}(\tau)$ is the interaction Hamiltonian operator in the interaction picture evaluated at time $-\tau$, i.e. $\hat{H}_{\rm int}(\tau) := e^{\frac{i}{\hbar}(\hat{H}_S+\hat{H}_{\mathcal{E}})\tau}\hat{H}_{\rm int}e^{-\frac{i}{\hbar}(\hat{H}_S+\hat{H}_{\mathcal{E}})\tau}$. To derive the master equation in 3, we have assumed factorising initial conditions, i.e. $\hat{\rho}(t_0) = \hat{\rho}_S(t_0)\otimes\hat{\rho}_{\mathcal{E}}$. As the master equation is truncated after second order in the couplings g_i, all terms of $\hat{H}_S^{(C)}$ vanish in the second and third term. A detailed discussion of the derivation can be found, for example, in [39].

The first term of the master equation is the standard unitary evolution of the matter system itself. The second term, usually referred to as the Lamb shift contribution, leads to a renormalisation of the energy levels of the matter systems due to the presence of the environment, and the third term is the dissipator present in open quantum systems. An analogue contribution to the Lamb shift, which results here directly from the derivation of the master equation, is also present in the field-theoretical model. In addition in the field theory model a further gravitationally induced self-interaction term for the matter system is present, such a term is not involved in the quantum mechanically toy model because on the one hand it is strongly related to the gauge symmetries in general relativity and the construction of gauge invariant quantities, see for instance [39, 46] and on the other hand whether it is present in the 1-particle projection also depends on the normal ordering choosing in the field theory model, see the discussion in [39, 41]. In the field-theoretical case, a renormalisation must normally be carried out for this contribution. The dissipator resembles the effective interaction of the gravitational wave environment with the matter system. Both contributions would be absent if one treats the neutrinos as a closed quantum system. The latter two contributions involve two functions $\Lambda(t-t_0)$ and $\Gamma(t-t_0)$, respectively, both of which depend on a time interval $t-t_0$, where t is the time at which the master equation is evaluated and t_0 is the initial time. These two functions are explicitly given by

$$\Lambda(t-t_0) = 2\int_0^{t-t_0} d\tau \int_0^{\infty} d\omega\ \sin(\omega\tau)J(\omega) \qquad (4)$$

$$\Gamma(t-t_0) = 4\int_0^{t-t_0} d\tau \int_0^{\infty} d\omega\ \cos(\omega\tau)\coth\left(\frac{\hbar\omega}{2k_B T}\right)J(\omega)\,, \qquad (5)$$

where $J(\omega)$ is the spectral density that characterises the strength with which different frequencies in the environment contribute to the interaction with the matter system. From the model, it is given as

$$J(\omega) = \frac{1}{2}\sum_{i=1}^{N} g_i^2\frac{\hbar^2}{\omega_i}\delta(\omega-\omega_i)\,, \qquad (6)$$

where $\delta(.)$ denotes the Dirac delta function. Given that not all the oscillators in the environment are neither known in detail, nor of interest, one often approximates $J(\omega)$ by a smooth function in ω, see e.g. [34]. The usual requirements for this function are that it is linear in ω for small ω and that it tends to zero for large ω. Note that such a spectral density is also chosen, for example, in the Caldeira-Leggett model for quantum Brownian motion, and the linear dependence is crucial in this case to obtain the friction term present in that model after renormalisation. Such spectral density with such a linear behavior are usually called Ohmic spectral densities. Many models used in the existing literature [34, 42, 47] use an Ohmic spectral density and differ only by the chosen cutoff function, see for instance also [48] for an application of the Drude

[2] Note that this parameter is denoted as Θ in the models in [37–39].

regularisation. Note that a different than linear behaviour for small ω would for the model considered here lead to IR divergences for all ω^m with $m \leq 0$, $m \in \mathbb{Z}$ and partly also to a rather not physically reasonable scaling with the inverse temperature parameter T in the decoherence term. The latter corresponds to a strong decoherence effect when the temperature is low that becomes infinite for $T = 0$, that is when the Gibbs state corresponds to a vacuum state. For $m \geq 2$ with $m \in \mathbb{N}$ there exist no decoherence effects in the model considered in this work.

A comparison to the field theoretic model derived in [39], which motivates this toy model here, shows that linearity in ω for small ω is reasonable, while a cutoff for larger ω corresponds to the UV-divergencies in field theory that also have to be renormalised. In appendix A we discuss this comparison in more detail.

Since the choice of a particular spectral density is an assumption that goes into every model, we were interested in how the final result of the master equation depends on this choice. Therefore, we considered a few choices in this work that also include the most prominent ones used in the existing literature like the Lorentz-Drude and the exponential cutoff. These are shown below:

$$\text{Lorentz-Drude cutoff: } J(\omega) = \frac{2}{\pi}\eta^2\omega\frac{\Omega^2}{\Omega^2+\omega^2} \tag{7}$$

$$\text{Quartic cutoff: } J(\omega) = \frac{2}{\pi}\eta^2\omega\frac{(2\Omega)^4}{((2\Omega)^2+\omega^2)^2} \tag{8}$$

$$\text{Exponential cutoff: } J(\omega) = \frac{2}{\pi}\eta^2\omega e^{-\frac{2\omega}{\pi\Omega}} \tag{9}$$

$$\text{Gaussian cutoff: } J(\omega) = \frac{2}{\pi}\eta^2\omega e^{-\frac{\omega^2}{\pi\Omega^2}}\,. \tag{10}$$

In these functions, η^2 is a free parameter which we will discuss further below and Ω is a cutoff frequency used as regulator or the otherwise divergent integrals. Evaluating the $\int d\omega$ integral in (4) and (5) yields the integrands $I(\Lambda)$ and $I(\Gamma)$ defined as

$$\Lambda(t-t_0) = 2\int_0^{t-t_0} d\tau\; I(\Lambda) \tag{11}$$

$$\Gamma(t-t_0) = 4\int_0^{t-t_0} d\tau\; I(\Gamma)\,. \tag{12}$$

A plot of these functions is shown in figure 1.

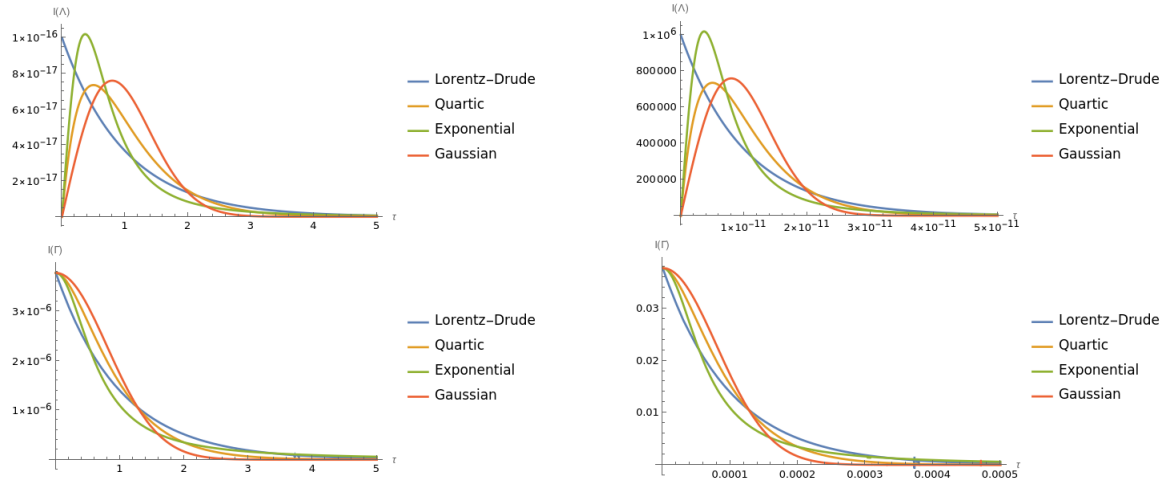


Fig. 1: Integrands $I(\Lambda)$ (first row) and $I(\Gamma)$ (second row) defined in (11) and (12) for the different cutoff functions and with parameter values $\eta = 10^{-8}$ s^2, $T = 0.9K$ and $\Omega = 1Hz$ (first column), $\Omega = 100GHz$ (second column, first row) and $\Omega = 10KHz$ (second column, second row).

As discussed below in section 3.2, for thermal gravitational waves a reasonable cutoff frequency is $\Omega = 100GHz$. Hence, in the case of $I(\Lambda)$, the integrand decays rapidly on timescales of $\tau = 10^{-10}s$ which is

much smaller than the timescale on which the core system varies, that is determined for the neutrinos investigated in this work by $\left(\frac{1}{\hbar}\frac{\Delta m^2}{2E}\right)^{-1}$, which[3] is around the order of magnitude of $1s$. Furthermore, the plots for $I(\Gamma)$ suggest that $\Gamma(t-t_0)$ is independent of Ω for $t-t_0$ sufficiently large enough, as the two axes scale inversely to each other with the same ratio. Already for $\Omega = 10KHz$, where $I(\Gamma)$ is numerically still well computable, the timescale on which $I(\Gamma)$ decays is much lower than the one on which the system state varies. This means that the environment rapidly "forgets" about the history of the system and thus the Markovian approximation for a memoryless process is justified. Therefore, in both cases the error committed when shifting the initial time $t_0 \to -\infty$ and hence the upper integration limit of the τ integration to $+\infty$ is negligible. Given that, we perform the so-called second Markov approximation for the further analysis, which then leads to time-independent results for Λ and Γ:

$$\Lambda := \Lambda(\infty) = 2\Omega\eta^2 \tag{13}$$

$$\Gamma := \Gamma(\infty) = \frac{8\eta^2 k_B T}{\hbar}\,. \tag{14}$$

As expected, Γ is independent of Ω. When introducing any of the above named spectral densities, the corresponding counter term is the same for all choices of the cutoff in the spectral density and given by:

$$\hat{H}_S^{(C)} = \frac{2}{\hbar}\int_0^\infty d\omega \frac{J(\omega)}{\omega}(\hat{H}_S^{(0)})^2 = \frac{2\Omega\eta^2}{\hbar}(\hat{H}_S^{(0)})^2\,, \tag{15}$$

which precisely cancels the Lamb-shift contribution in the second order TCL master equation in Markovian limit yielding:

$$\frac{d}{dt}\hat{\rho}_S(t) = -\frac{i}{\hbar}\left[\hat{H}_S^{(0)}, \hat{\rho}_S(t)\right] + \frac{8\eta^2}{\hbar^2}\frac{k_B T}{\hbar}\left(\hat{H}_S^{(0)}\hat{\rho}_S(t)\hat{H}_S^{(0)} - \frac{1}{2}\left\{(\hat{H}_S^{(0)})^2, \hat{\rho}_S(t)\right\}\right)\,. \tag{16}$$

This master equation includes still two free parameters, η which is related to the coupling parameter between the system and the environment and the environmental temperature parameter T that enters via $\beta = Tk_B$ in the Gibbs state, where k_B denotes the Boltzmann constant.

In order to compare the master equation (16) better to the existing phenomenological models later, we note that (16) can be written in Lindblad form

$$\frac{d}{dt}\hat{\rho}_S(t) = -\frac{i}{\hbar}\left[\hat{H}_S^{(0)}, \hat{\rho}_S(t)\right] + \frac{8\eta^2}{\hbar^2}\frac{Tk_B}{\hbar}\left(\hat{L}\hat{\rho}_S(t)\hat{L}^\dagger - \frac{1}{2}\left\{\hat{L}^\dagger\hat{L}, \hat{\rho}_S(t)\right\}\right)\,. \tag{17}$$

with the choice of the Lindblad operator $\hat{L} = \hat{H}_S^{(0)}$ using that $\hat{H}_S^{(0)}$ is self-adjoint, that is $\hat{L}^\dagger = \hat{L}$ and thus $\hat{L}^\dagger\hat{L} = \hat{L}^2$, see for instance [49] where also a Linblad operator proportional to the Hamiltonian of the system is chosen for a decoherence model inspired by discrete quantum gravity. In many phenomenological models, the Lindblad equation is taken as the starting point, often omitting the second term containing the contributions of the Lamb shift as well as a counter term. Then the model is characterised by a selection of Lindblad operators $\hat{L}_i$, of which there can generally be more than one, usually chosen to be either linear with the position and/or momentum operators of the matter system such that they can be written linearly in annihilation and creation operators see for instance [34] for the standard examples or [50] for a non-perturbative treatment of multi-time expectation values in open quantum systems for specific environments. The advantage of starting with a microscopic model as in (1) is that, for example, the functions $\Gamma(t-t_0)$ and $\Lambda(t_0)$ can be derived and calculated directly, resulting in a model with less ambiguities at the level of the Lindblad equation. Furthermore, the choice of the Lindblad operator, following the field-theoretical models [12, 27, 38–40], is directly linked to the property of how linearised gravity couples to matter, and therefore in this sense is also determined by the microscopic model. We discuss in the application to neutrino oscillations a comparison between the renormalised and non-renormalised model in section 3.2. Finally, it is worth noting that for the special case of zero temperature $T = 0$, in which the Gibbs state is only the vacuum state and thus the gravitational environment is assumed to be in a vacuum state, no decoherence effects are present, since in the model presented here the dissipator is linear in T. Note that this is a property

[3] As the dominant contribution to the neutrino evolution comes from the part $e^{\frac{i}{\hbar}\frac{\Delta m^2}{2E}t}$ and the matter effects have a similar order of magnitude.

of the gravtiational environment and independent of the chosen system under consideration and will thus also apply to the case of neutrinos in next section.

2.2 Application to neutrino oscillations

In this section, we evaluate and solve the master equation (16) for neutrinos with three different flavors as the matter system. To adapt the model to neutrinos choose the following system's Hamiltonian operator

$$\hat{H}_S^{(0)} = \hat{H}_{vac} + \hat{U}^\dagger \hat{H}_{mat} \hat{U}, \tag{18}$$

where the second term takes into account that the neutrinos propagates through the (different layers of the) Earth and the neutrino Hamiltonian in vacuum in the mass basis is given by

$$\hat{H}_{vac} = \begin{pmatrix} E_1 & 0 & 0 \\ 0 & E_2 & 0 \\ 0 & 0 & E_3 \end{pmatrix} = E\mathbb{1}_3 + \frac{c^4}{6E} \begin{pmatrix} -\Delta m_{21}^2 - \Delta m_{31}^2 & 0 & 0 \\ 0 & \Delta m_{21}^2 - \Delta m_{32}^2 & 0 \\ 0 & 0 & \Delta m_{31}^2 + \Delta m_{32}^2 \end{pmatrix}, \tag{19}$$

where we used that $E_i \approx E + \frac{m_i^2 c^4}{2E}$ and that we can modify the Hamiltonian by a constant matrix such that the difference $(E_i - E_j)$ is not modified because in the final equation only powers of the energy difference will contribute. Here the mass differences squared are denoted by $\Delta m_{ij}^2 = m_i^2 - m_j^2$, the mean neutrino energy by $E = \frac{1}{3}(E_1 + E_2 + E_3)$ and the PMNS matrix by $\hat{U}$. The matter contribution that takes into account the electron density of the Earth are given by

$$\hat{H}_{mat} = \pm\sqrt{2} G_f N_e \begin{pmatrix} 1 & 0 & 0 \\ 0 & 0 & 0 \\ 0 & 0 & 0 \end{pmatrix}, \tag{20}$$

where the sign depends on whether neutrinos $(+)$ or antineutrinos $(-)$ are involved, G_f is the Fermi coupling constant and N_e the electron density. In the literature, often different forms of $\hat{H}_{vac}$ are used that differ from the one presented here by the addition of a constant matrix in the mass basis and energy differences agree for all choices[4]. As shown in appendix B, this yields the same result as long as the final solution of the master equation only depends on energy differences $(E_i - E_j)$ or powers thereof because constant terms that agree for all i, j, e.g. E, are just canceled in the difference. While the equation (18) is formulated in terms of the vacuum mass basis, to solve the master equation it is advantageous to work in the effective mass basis in which $\hat{H}_S^{(0)}$ is diagonal[5]. This basis always changes when N_e changes, i.e. when we consider different layers of the Earth. We denote all quantities in the effective mass basis with a tilde and the transformation matrix with $\hat{\tilde{V}}$. If we define the diagonal matrix of the system in the effective mass basis $\hat{\tilde{H}}_S := \hat{\tilde{V}}^\dagger \hat{H}_S^{(0)} \hat{\tilde{V}}$, the master equation in terms of the effective mass basis can be written as

$$\frac{d}{dt}\hat{\tilde{\rho}}_S(t) = -\frac{i}{\hbar}\left[\hat{\tilde{H}}_S, \hat{\tilde{\rho}}_S(t)\right] + \frac{8\eta^2}{\hbar^2}\frac{T k_B}{\hbar}\left(\hat{\tilde{H}}_S \hat{\tilde{\rho}}_S(t) \hat{\tilde{H}}_S - \frac{1}{2}\left\{\hat{\tilde{H}}_S^2, \hat{\tilde{\rho}}_S(t)\right\}\right). \tag{22}$$

As we have already seen from (17), the dissipator involves second powers of the system's Hamiltonian, as well as is linear in temperature parameter T of the gravitational environment. A consequence of the second property is that there is no decoherence effect at a temperature of zero, e.g. when the environment is in a vacuum state. An implication of the first property is that such a form of the dissipator leads with respect to the effective mass basis to a decoherence term that is quadratic in the difference of the energy eigenvalues $(\tilde{H}_i - \tilde{H}_j)^2$. This can be also seen directly from the solution of the differential equation for $\widetilde{\rho}_S(t)$ in (22), which is discussed in the appendix C. In terms of the effective mass basis, this solution is given by

$$\widetilde{\rho}_{ij}(t) = \widetilde{\rho}_{ij}(0) \cdot e^{-\frac{i}{\hbar}\left(\tilde{H}_i - \tilde{H}_j\right)t - \frac{4\eta^2 k_B T}{\hbar^3}\left(\tilde{H}_i - \tilde{H}_j\right)^2 t}, \tag{23}$$

[4] See for instance [14–16] where this is used to work with a matrix in which one of the diagonal elements is zero:

$$\hat{H}_{vac} = \frac{c^4}{2E}\begin{pmatrix} 0 & 0 & 0 \\ 0 & \Delta m_{21}^2 & 0 \\ 0 & 0 & \Delta m_{31}^2 \end{pmatrix} \tag{21}$$

[5] See appendix B for an efficient way of computing the diagonalisation of the matrix in question

where $\widetilde{\rho}_{ij}(t)$ denotes the matrix elements of $\hat{\widetilde{\rho}}_S(t)$ and $\widetilde{H}_i$ denotes the elements of the diagonal matrix $\hat{\widetilde{H}}_S$. In relation to the effective mass basis, we explicitly obtain

$$\rho_{ij}(t) = \rho_{mn}(0)\widetilde{V}^{\dagger}_{km}\widetilde{V}_{nl}\widetilde{V}_{ik}\widetilde{V}^{\dagger}_{lj}e^{-\frac{i}{\hbar}(\widetilde{H}_k-\widetilde{H}_l)t-\frac{4\eta^2 k_B T}{\hbar^3}(\widetilde{H}_k-\widetilde{H}_l)^2 t} \tag{24}$$

where $\widetilde{V}_{ij}$ denote the matrix elements of $\hat{\widetilde{V}}$. The first term corresponds to the standard oscillation term which is non-vanishing for $\Delta m^2_{ij} \neq 0$. The second terms is the additional contribution due to coupling to the gravitational environment. Note, that as discussed above due to the counter term that we introduced in (15) the final solutions does not involve a Lamb shift contribution and is thus independent of the cutoff frequency. A model that also included a Lamb shift contribution is the one in [5] where due to such a contribution the model allows neutrino oscillations to be present even if the initial mass difference vanishes. Although it is not directly obvious from the parameter in which the authors in [5] encode the Lamb shift contribution (denoted as ω_3 in (3.1) in [5]), to our understanding the final value of this parameter depends on a choice of test function that needs to be introduced to regularise an otherwise infinite integral (see (A.14) in [5]). Although the derivation in [5] starts with a field theory setup, as far as we understand the derivation, carried over to the toy model presented here, such a test function would correspond to the cutoff frequency because the final value of ω_3 will in general depend on the chosen test function. Thus, it looks like they obtain a shift in the neutrino energy eigenvalues that still depends on some regulator and we would expect that similar to what happens here in the toy model and in the field theoretical models in [12, 27, 38–40] a suitable renormalisation procedure needs to be applied to obtain a cutoff independent effect. Such an effect might be potentially non-vanishing for the model in [5] in contrast to our case since they use a different coupling to the environment but this needs to be carefully checked. To demonstrate that working with a model where no renormalisation has been applied and the Lamb shift contribution is taken as a real physical contribution, we refer to figure 5 in section 3 where the toy model with and without a Lamb shift contribution are compared and thus is shown that if this non-physical effects are not removed, one might draw incorrect physical conclusions.

3 Results

Quantum decoherence in the neutrino sector has been investigated with long baseline neutrino detectors [32], such as MINOS+T2K [25], the future DUNE [19] and reactor experiments such as Daya Bay, RENO and the future JUNO [44], where the treatment of neutrino oscillations can be well approximated by vacuum, and neutrino telescopes such as IceCube [24, 51] and KM3NeT [23], where matter effects play a relevant role. All such analyses are based on a class of phenomenological quantum decoherence (PQD) models that can vary by the power with which the mean neutrino energy enters into the decoherence term as well as the number of non-vanishing decoherence parameters. In order to interpret the PQD model in terms of the microscopic gravitationally induced quantum decoherence model (GQD) presented in this work, and in order to see the differences among them, we investigate their behavior in different situations.

The model considered in this work has the property that only squared differences of neutrino energies enter into the contribution responsible for decoherence. It will be shown that, one of the consequences is that the model considered here is only compatible with a subclass of phenomenological model with an energy dependence E^{-2}, and this directly follows from the gravitationally induced decoherence that suggest a specific coupling between the neutrinos and the environment inspired by general relativity and linearised gravity respectively. That one does not obtain an energy dependence of E^n for $n > 0$ is caused by the fact that for this coupling only the squared energy differences are involved in the decoherence contribution and those scale with E^{-2} in the case of neutrinos. Furthermore, such corresponding decoherence parameters cannot be chosen independently from Δm^2_{ij}. The latter means that setting some of the decoherence parameters involved to zero and equal, respectively, as is done in some phenomenological models, leads to inconsistencies in the model if it is not assumed at the same time that these Δm^2_{ij} vanish and are identical, respectively.

Furthermore our results show that in the vacuum case, we can obtain an exact match between the aforementioned subclass of the $n = -2$ PQD models and the GQD model presented here if we choose the decoherence parameters involved in the PQD model appropriately. One might conclude that it should be possible to already set bounds to our free parameters η, which is related to the coupling constant in the interaction, and the temperature parameter T of the gravitational waves, based on current upper limits of the PQD γ_{ij} parameters. However, all the present analyses [25, 32, 44] make some assumptions while fitting the data, such as setting one of the $\gamma_{ij} = 0$ or two of them equal to each other, which are not compatible with the model considered here. It follows that it is not possible to directly constrain η and T from current bounds on γ_{ij}.

Interestingly, in the non-vacuum case such a match with the specific subclass of the PQD model cannot be achieved with those phenomenological models that assume constant decoherence parameters in each layer of the Earth as many models do, whereas in the model presented here they do vary. As a consequence, we obtain deviations in the oscillations probabilities in matter that can become large enough in the GeV energy regime to be resolved by neutrino telescopes, such as KM3NeT/ORCA [52]. There exist models that also take matter effect in the decoherence parameters into account see for instance [15, 33], however discussed below it is also not straight forward to match the model considered here with those. Being the difference in neutrino oscillations in matter an interesting scenario for testing the model considered here independently from the PQD model, all the oscillation probability plots presented in this section are evaluated for neutrinos propagating through the Earth, hence considering the non-negligible matter effects. Specifically, the oscillograms have been made with the public tool *OscProb* [53], where a new class modelling the GQD here presented has been developed by the authors, and for the Earth density profile, the PREM model, with 425 layers has been used [54].

3.1 Comparison to existing phenomenological models

In several works, such as in [1, 4, 21, 22, 55], a phenomenological model based on a Lindblad equation is used to model decoherence in neutrino oscillations with a solution of the form

$$\widetilde{\rho}_{ij}(t) = \widetilde{\rho}_{ij}(0) \cdot e^{-\frac{i}{\hbar}(\widetilde{H}_i - \widetilde{H}_j)t - \Gamma_{ij}t}\,, \tag{25}$$

where Γ_{ij} is usually parameterised as

$$\Gamma_{ij} = \gamma_{ij} E^n\,. \tag{26}$$

The model presented in this work can be related to the phenomenological model in the case of vacuum by identifying

$$\gamma_{ij} = \frac{\eta^2 c^8 k_B T}{\hbar^3}(\Delta m^2_{ij})^2 \quad \text{and} \quad n = -2, \tag{27}$$

where k_B denotes the Boltzmann constant. Hence, the toy model considered in this work has the property that the γ_{ij} are related to the square of the squared mass differences Δm^2_{ij}. The only two free parameters left in γ_{ij} are η, that encodes the strength of the coupling of the neutrinos to the gravitational environment, and T which is the temperature of the environment of thermal gravitational waves. If one considers cosmological models in which the usual inflationary epoch is preceded by a radiation-dominated era, a thermal gravitational wave background can be produced in the early universe. In these models, it is assumed that the thermal gravitons decouple at a temperature of the order of the Planck temperature and exhibit a black-body spectrum [56, 57]. As the universe expands, the black-body spectrum of the gravitons is maintained, but the temperature is strongly red-shifted. The estimates for the temperature of the thermal gravitational wave background in the present epoch are $T \simeq 0.9$ K [58], and thus below the temperature of the cosmic microwave background of $T_\gamma \simeq 2.72$ K. Furthermore, because the energy eigenvalues always involve the combination $\Delta m^2_{ij}/E$ this model suggests that the decoherence parameters depend inversely on the squared mean neutrino energy. This dependence stems from the form of the interaction Hamiltonian which was motivated by how gravity couples to matter according to general relativity. Compared to the phenomenological models, the approach presented here has the advantage that, if we assume that we obtain a value of the temperature parameter of thermal gravitational waves from other experiments, the Γ_{ij} only depend on one free parameter η. In order to constrain the free γ_{ij} parameters, in some phenomenological models, as for instance in [22, 32], additional requirements are included where some of the γ_{ij} are set to zero or equal to each other. These limits then result each in one single free parameter γ. However, from (27) it can be seen that such choices correspond to either setting some of the Δm^2_{ij} equal to zero or equal to each other, which stands in contradiction to experiments. Furthermore, the physical interpretation of this parameter is harder to access compared to the situation where the underlying microscopic model is known.

In matter, those phenomenological models that assume constant decoherence parameters γ_{ij} in matter cannot be matched by specific choices of parameters to the model used here. The reason for this is that while in the phenomenological models γ_{ij} is fixed at a certain value independently of the matter density present, in the model presented in this work, the decoherence parameter depends on $(\widetilde{H}_i - \widetilde{H}_j)$, which are the energy values of the neutrino which depend on the matter density and thus the different layers in the Earth. Hence, in the microscopic model matter effects are included directly via its coupling to the environment. This dependence is caused by the fact that in matter, the vacuum Hamiltonian is extended by the additional operator $\hat{H}_{mat}$ which depends on the electron density N_e in the considered matter layer, see (18), and thus

the final Hamiltonian and therefore also the decoherence parameter changes in each layer. Hence, the model presented here takes the effect of the different Earth layers into account in the coupling to the environment and can thus not be formulated with a single value for γ_{ij} as it is done for the phenomenological models (26). This is shown in Fig. 2, where a discrepancy between PQD and GQD appears when the neutrino travels through layers of increasing density within the Earth. The effect becomes relevant for neutrino trajectories passing within the Earth core. The decoherence effects considered in [15] also involve contributions from the matter Hamiltonian of the neutrinos. However, it is not so simple to match these models and the one considered here as the models in [15, 33] involve only the subleading contribution of decoherence effects in order to be able to still work with analytical expressions for the oscillations probabilities and this is used to perform an analysis for DUNE and T2HK in [33].

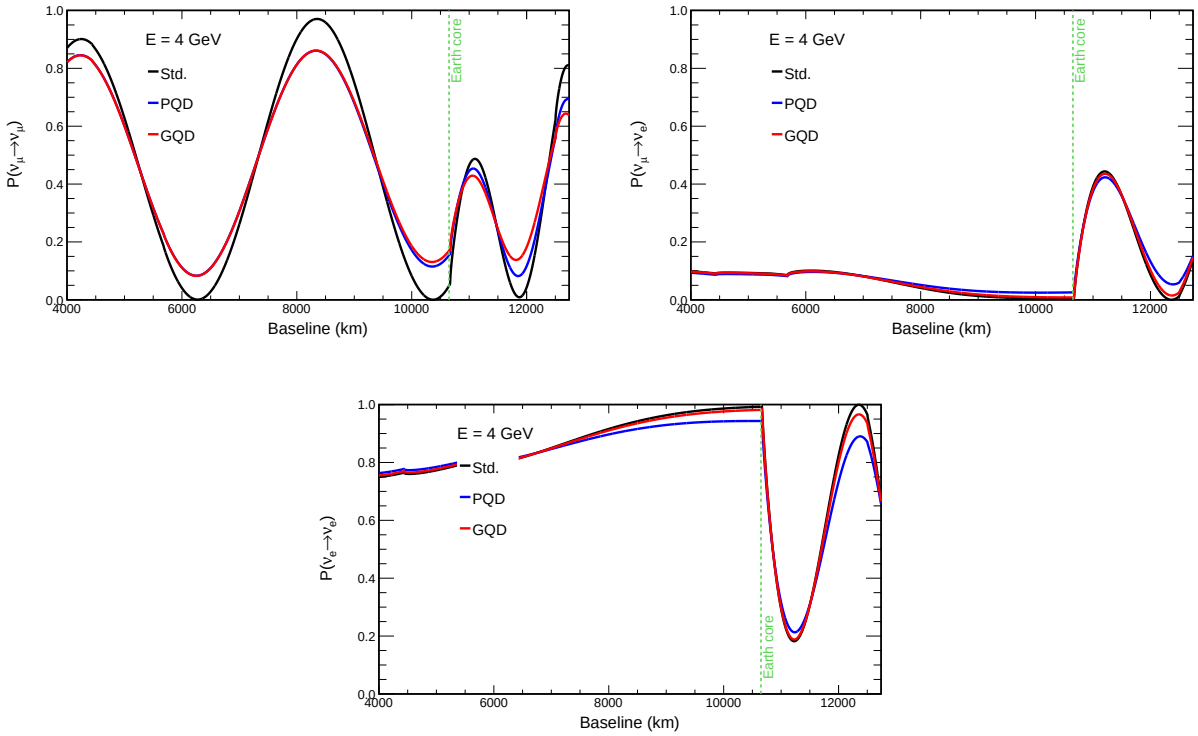


Fig. 2: Neutrino oscillation probabilities in matter for a 4 GeV neutrino as a function of the travelled baseline in Earth. The plot compares standard oscillations without decoherence (Std.) with the model in this work (GQD) and a phenomenological model with $n = -2$ (PQD). The GQD model parameters are set to $\eta = 10^{-8}$ s and $T = 0.9$K which implies for the PQD model in vacuum $\gamma_{21} = 1.00694 \cdot 10^{-25}, \gamma_{31} = 1.08067 \cdot 10^{-22}$ and $\gamma_{32} = 1.0157 \cdot 10^{-22}$. The Earth matter effects are accounted for via the PREM model [54]: the clear discontinuity for neutrino trajectories passing inside of the Earth core is due to the net change in density between mantle and core. The plot has been created using *OscProb*[53].

In the context of the Lindblad equation the phenomenological models with constant decoherence parameters γ_{ij} in matter can be identified with a model where the Lindblad operator is chosen to be the neutrino Hamiltonian in vacuum, whereas the model presented here chooses the full neutrino Hamiltonian as the Lindblad operator. If we restrict to the vacuum case both models obviously agree but deviate in the matter case. From the point of view of the gravitational environment it is not very obvious why the thermal gravitational background should only couple to the vacuum energy of the neutrino even if a non-vanishing matter density is present.

A further consequence of this is that bounds on decoherence effects of neutrino detectors that have been derived using the PQD models can only constrain η in the vacuum case. Although there are upper limits on the gamma parameters from neutrino experiments where matter effects are negligible, such as the results of the MINOS+T2K data [25], the baselines and neutrino energies of such experiments allow a vacuum treatment of neutrino oscillations. However, in [25], they fit the data assuming three scenarios which are not fully compatible with our choice of parameters. Therefore, we can not directly translate current upper limits on the gammas into upper limits on our parameters.

For the matter case a further sensitivity analysis is needed because the deviations in the oscillation probabilities predicted when using the PQD model with a decoherence parameter independent of the matter density or the one presented here (GQD) is a measurable effect as can be seen in figure 3, where the constant γ_{ij} were chosen to be equal to the decoherence parameters in the GQD model in vacuum such that the (PQD) and the (GQD) model perfectly match in the vacuum case. From the corresponding oscillograms in figure 4 it becomes visible that the probabilities can deviate by up to 10% for $\eta = 10^{-8}$ s and $T = 0.9K$.

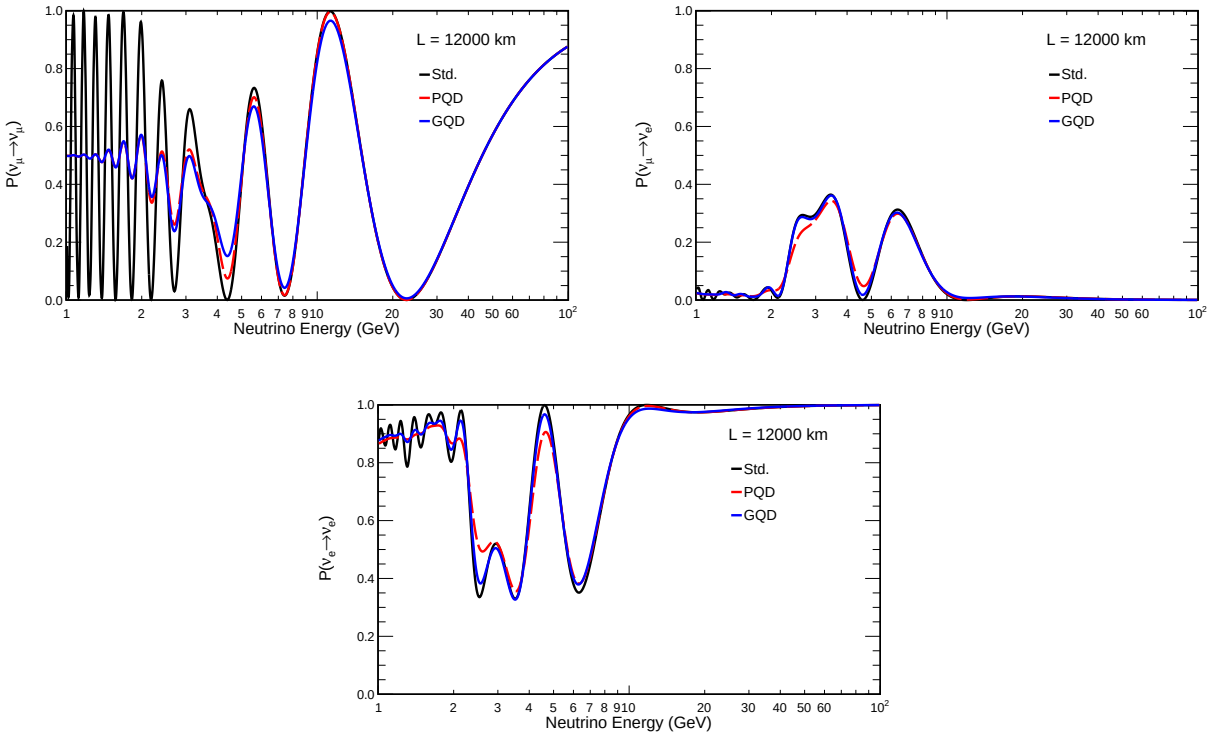


Fig. 3: Oscillation probabilities in matter for almost up-going neutrinos, passing through the Earth core (baseline of 12000 km, corresponding to $\cos\theta_{Zenith} = -0.94$, which is a trajectory passing through the Earth core). The plots compare standard oscillations without decoherence (Std.) with the model in this work (GQD) and a phenomenological model with $n = -2$ (PQD). For the GQD model $\eta = 10^{-8}$ s and $T = 0.9$K are assumed which implies for the PQD model in vacuum $\gamma_{21} = 1.00694 \cdot 10^{-25}, \gamma_{31} = 1.08067 \cdot 10^{-22}$, and $\gamma_{32} = 1.0157 \cdot 10^{-22}$. The Earth matter effects are accounted for via the PREM model [54]. The difference between constant decoherence parameters independent of the matter density (PQD) and a parameter depending on the matter density (GQD) is evident. The plots have been made with *OscProb* [53].

Figure 4 shows the difference in neutrino oscillation probabilities for the PGD and GQD models in Earth as a function of the neutrino energy and cosine zenith. Up-going events have $\cos\theta_Z = -1$. The choice of the η value matches the PQD γ_{ij} values in vacuum near to bounds. As it can be seen, differences up to 10% can be observed, highlighting the different energy behaviour of the two models which arise with matter effects. It follows that the model considered here can be independently constrained with respect to the PQD model by neutrino telescopes optimised for the GeV energy range, such as KM3NeT/ORCA [52].

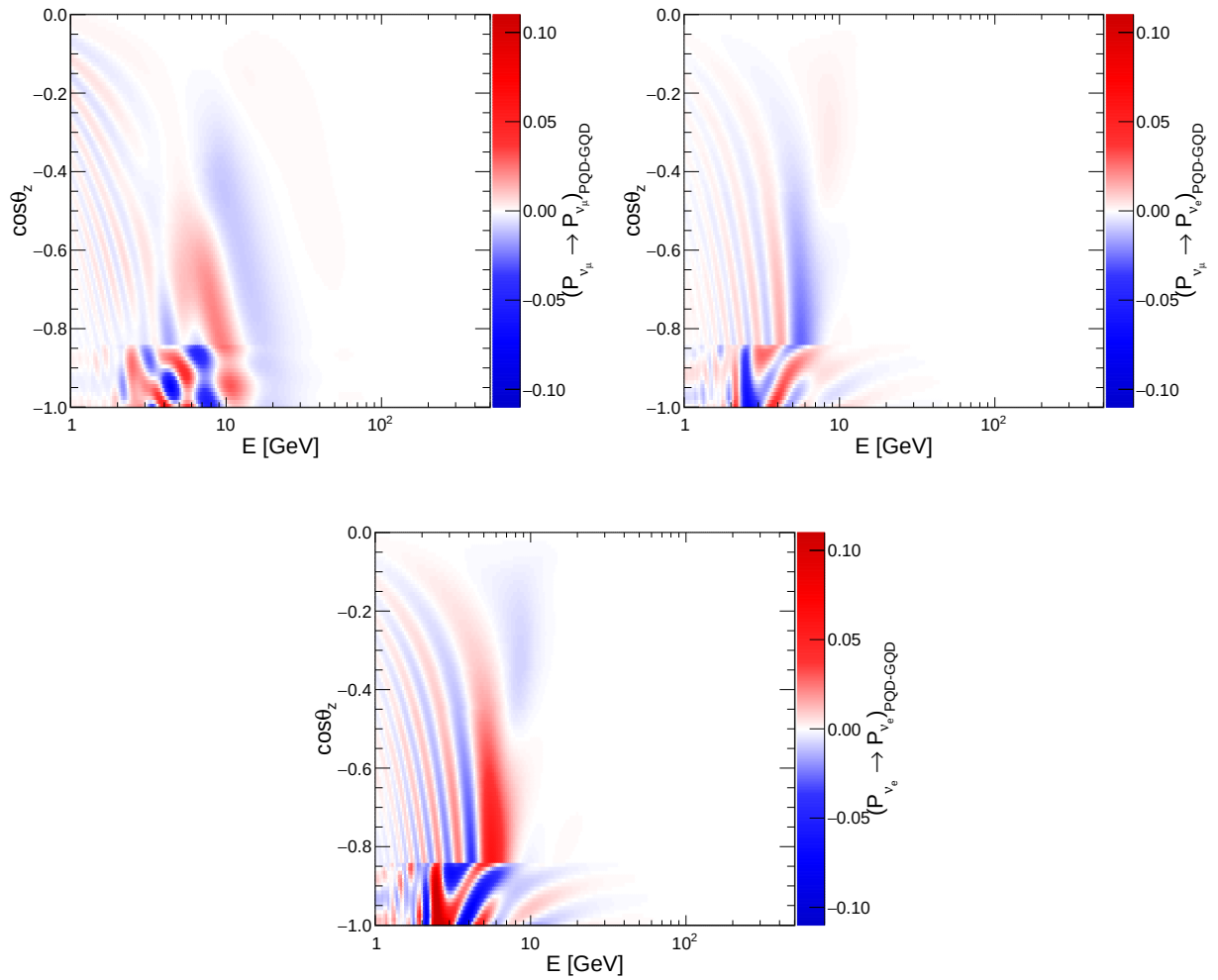


Fig. 4: Deviations for different oscillation behaviours in matter of the model in this work (GQD) and a phenomenological model for $n = -2$ (PQD). The plots were created using OscProb [53] and for the GQD model $\eta = 10^{-8}$ s and $T = 0.9K$ which implies for the PQD model in vacuum $\gamma_{21} = 1 \cdot 10^{-25}, \gamma_{31} = 1 \cdot 10^{-22}$ and $\gamma_{32} = 1 \cdot 10^{-22}$. The difference between constant decoherence parameters independent of the matter density (PQD) and a parameter depending on the matter density (GQD) is evident.

3.2 Effect of the renormalisation

In figure 5 a comparison of the model presented in this work (GQD) with and without renormalisation is presented. As expected in the GQD model the contribution of the Lamb shift in the non-renormalised Hamiltonian $H_S^{(0)}$ in (1) leads to an energy-dependent phase shift in the oscillations. However, as discussed in section 2.2, such a phase shift is non-physical because it still depends on the chosen cutoff frequency Ω and diverges in the limit $\Omega \to \infty$. After renormalising the neutrino Hamiltonian and considering the limit value $\Omega \to \infty$, the contribution of the Lamb shift is not present, as it is exactly cancelled by the counter term introduced in (15). Thus, these results show on the one hand that for the model considered in this work it is a justified procedure to do not consider the lamb-shift as well as the counter term at the level of the Lindblad equation, which is often done but needs in general a detailed analysis for each individual model separately. On the other hand, as already discussed in the context of massless neutrino oscillations discussed in [5], it further demonstrates that any physical interpretation of effects caused by the lamb shift term without a detailed analysis of the renormalised model can be problematic

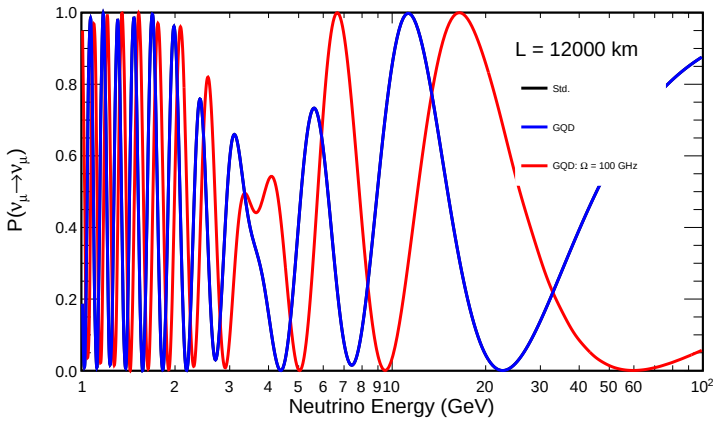


Fig. 5: Comparison of the model presented in this work (GQD) with and without renormalisation. In the latter case the cutoff-dependent Lamb shift contribution is still present in the unrenormalised Hamiltonian. The cutoff frequency has been chosen to be $\Omega = 100$GHz corresponding to the maximal frequency of thermal gravitational waves at temperature $T = 0.9$K, see for instance [58] and $\eta = 10^{-37}$ for which the oscillation with $\Omega = 100GHz$ do not get too fast. The value $\Omega = 100GHz$ was chosen because it corresponds approximately to the maximal frequency of the black-body spectrum for $T = 0.9$K. Considering the Lamb shift as a real physical effect is problematic because its contribution still depends on the cutoff frequency Ω and diverges when Ω is sent to infinity, which shows that a renormalisation procedure is required.

3.3 Coupling strength inspired from linearised gravity

In the model studied in this work, η is a free parameter which represents the coupling strength between the neutrinos and the gravitational environment. It cannot further be specified by the microscopic model in (1), as it depends on the g_i which are in turn not further specified. As discussed, the existing constraints from experimental data in [25, 32, 44] cannot be used to further constrain η because the assumptions used for the decoherence parameter in this analysis are not compatible with the model considered in this work. Hence, a further investigation on neutrino detectors sensitivities is needed to obtain such upper bounds.

From the theoretical point of view, the estimated value of η is determined by the way general relativity couples to matter. However, to the knowledge of the authors no full field-theoretic model for neutrinos has yet been derived, so there is yet no definite answer to the size of η. By comparison to full field-theoretic models like [27, 38, 39] it is nevertheless possible to attempt a first rather naive estimate for a suitable order of magnitude for the coupling parameter η. Using the model from [39], such an estimate can be found in appendix A. The resulting value $\eta \approx 10^{-42}$ s is rather tiny and corresponds to a γ_{ij} in the phenomenological models (for $n = -2$) of the order $\gamma_{ij} \approx 10^{-50} \frac{eV^2}{s}$. For such a tiny value of η modifications in the probability for the neutrino oscillations for similar values of the other involved parameters that have been used in section 3 one would not be able to detect modifications from the standard neutrino oscillations. This can also be seen from figure 6 where the modification in the probability for the neutrino oscillations are shown for three different values of η.

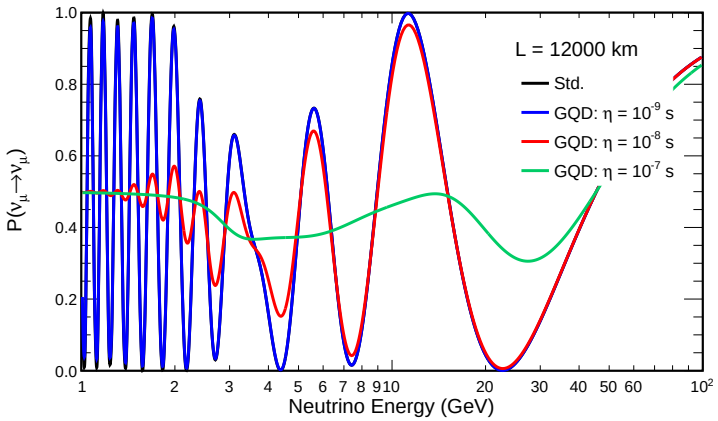
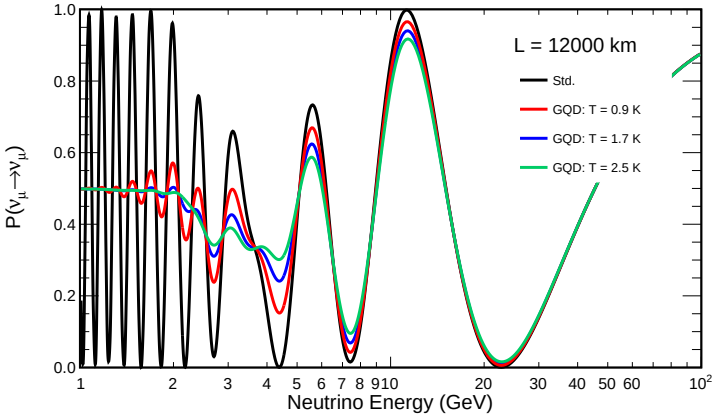


Fig. 6: Effect of the neutrino coupling to the gravitational environment, η, on the muon neutrino disappearance probability in Earth. Here, $T = 0.9$ K is assumed. The considered baseline assumes a neutrino propagation that passes through the Earth core. The plots were created using *OscProb* [53].

Specifically, for $\eta = 10^{-9}$ s, the GQD model is already almost not distinguishable from the standard scenario. For $\eta = 10^{-8}$ s the modifications start to become non-negligible and they become large already at $\eta = 10^{-7}$ s, which corresponds, in vacuum, to values for the γ_{ij} parameters of the PQD models of the order $\gamma_{ij} \approx 10^{-21} \frac{eV^2}{s}$.

Does this mean that, taking this estimate seriously, the effect of gravitationally induced decoherence will be too tiny? The answer to this question is not so simple and under debate in the current literature. For instance in [27, 38] it is discussed that the interpretation of the temperature parameter T as the temperature of the thermal gravitational waves is too restrictive. They also conclude that for $T = 0.9K$ the η that follows from the QFT model is too small to cause detectable decoherence effect. However, they argue that T should rather be interpreted as an effective parameter that for $T = 0$ includes gravitons in a vacuum state where no decoherence effects are present. For the choice of $T \simeq 0.9$K[6], this corresponds to cosmic thermal gravitational waves. For higher values of an effective T parameter they suggest that it can for instance be given if one chooses a quantum state for the environment that mimics a classical stochastic noise with an astrophysical origin such as a background caused by all rotating neutron stars in the galaxy. Another possibility they discuss is that, assuming that classical spacetimes arise from an underlying theory of quantum gravity at the thermodynamic level, a classical spacetime such as flat Minkowski spacetime is a macrostate and its emergence is therefore accompanied by classicalised thermodynamic fluctuations, which may be stronger than any quantum fluctuations in perturbative quantum gravity.

Fig. 7: Effect of the temperature of the gravitational environment T on the muon neutrino disappearance probability in Earth. Here, $\eta = 10^{-8}$ s is assumed. The plots were created using OscProb [53].



[6] In [27, 38] they choose $T = 2.7$K, the temperature of the cosmic microwave background. To the authors' knowledge, the temperature of thermal gravitational waves is expected to be somewhat lower, see e.g. [58].

Therefore, T, which is understood as an effective parameter in their discussion, cannot be determined by a QFT model based on linearised gravity. Further decoherence models with a similar parameter involved cam be found in [34, 59–61], where either parameter is not further specified or the value of the Planck temperature is discussed which is an obvious but not very restrictive upper bound for such an effective temperature parameter. To address this point figure 7 shows the effect of the temperature of the gravitational environment for neutrino oscillation probabilities in Earth as a function of the neutrino energy, for a fixed value of η. As it can be seen, a small variation in the temperature has visible effects in oscillation probabilities which could potentially be resolved by neutrino telescopes such as KM3NeT/ORCA.

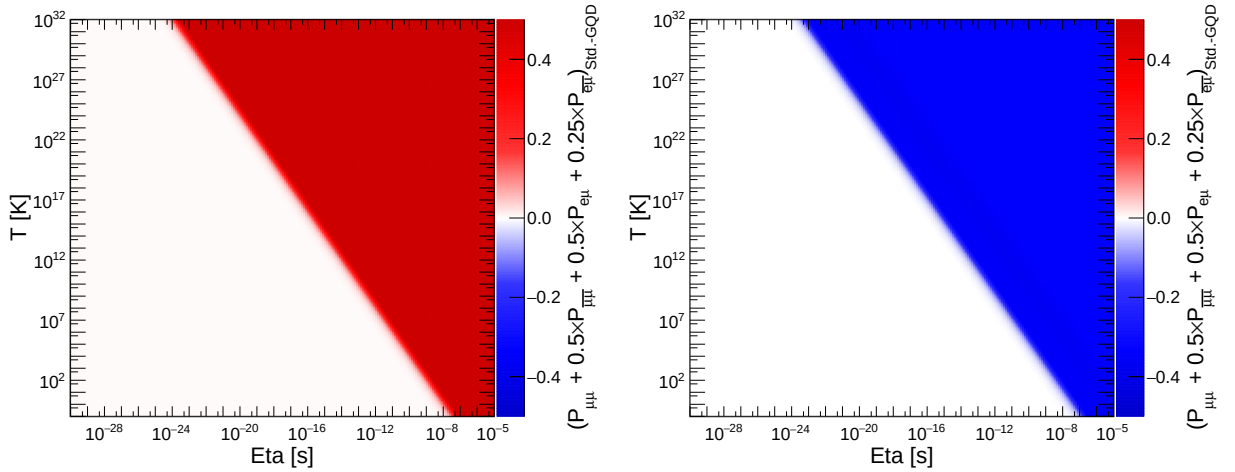


Fig. 8: Difference in atmospheric neutrino oscillation probabilities between the standard (Std.) scenario and GQD, as a function of η and T which starts at 0.1 K and goes up to the Planck temperature. Here, upgoing neutrinos ($\cos\theta_{zenith} = -0.1$) and with an energy of 6 GeV (left) and 18 GeV (right) are considered. The assumed ratio between neutrino flavours and neutrinos vs antineutrinos is a simplified approximation of the atmospheric neutrino flux. Matter effects are included via the PREM model [54]. The plots were created using *OscProb* [53].

In addition we show in figure 8 exemplary how the modifications of the probabilities for the oscillations vary with the temperature for atmospheric neutrinos. As expected and can be seen in figure 8 for higher temperatures also the parameter η can be smaller and still deviations in the oscillations probabilities are present. The comparison between the two plots in 8 show that for larger smaller energies the values of η from which one deviations to the standard oscillations are seen can be slightly smaller which is due to the fact that the mean neutrino energy enters with an inverse second power in the decoherence term. As for this plots atmospheric neutrinos with the maximum propagation length through the Earth were considered the analysis of the T, η range is in this sense restricted as we expect decoherence effects to become larger for larger propagation length.

A further aspect related to this that becomes relevant in the case of neutrino oscillations is that we can also enhance the decoherence effect if we consider longer propagation length of the neutrinos. In this case, where one wants to consider cosmic neutrinos, for example, a QFT model based on linearised gravity as in [27, 38–40] around a flat Minkowski spacetime might be too simple, and one would have to consider more complex models that involve gravitational waves in a FLRW spacetime as a more realistic setting, for which the estimate is also expected to change due to the presence of a non-trivial scale factor in cosmological spacetimes. From the point of view of quantum gravity, it therefore remains an exciting question whether decoherence effects in neutrino oscillations are actually measured and, if so, which theoretical models can then satisfactorily explain such measurements.

4 Conclusion

In this work, we have investigated gravitationally induced decoherence for neutrino oscillations based on the specific microscopic toy model in [42], which we have slightly generalised to apply it in the context

of neutrino oscillations. As any open quantum system, the model includes the choice of the system, here neutrinos, and its environment, which is modelled by a finite number of harmonic oscillators that mimic the thermal gravitational waves in the toy model in [42]. In addition, we specify the coupling between system and environment as strongly inspired by the way how gravity couples to matter in the toy model [42] and thus guided by the existing field theory models [12, 27, 38–40].

Our results give new insights on the physical properties of the underlying theoretical model and this allows us also to get a deeper understanding of the relation to the existing phenomenological models as well as the physical implications of the latter. Our analysis also allows us to take up some points that are debated in the literature and look at them from a different angle.

First of all, this concerns the work in [43] in which the model from [42] is also considered in a two neutrino-scenario, but the conclusion is drawn that no decoherence effects occur for this model. As the derivation of our master equation in section 2.2 shows this is not the case in our results. The final solution for the density matrix can be determined analytically and includes the standard neutrino oscillation term as well as an additional damping term leading to decoherence. To our understanding the difference to our analysis is that they obtain a decoherence term which only involves the squared difference of the mean energies of the neutrinos whereas in our derivation of the master equation the squared difference of the full energy eigenvalues of the neutrino contribute. Thus, in our case also the mean neutrino energy cancels but terms involving $(\Delta m_{ij}^2)^2/(2E)^2$ as well as additional contribution from matter effects yield a non-vanishing contribution. Our results are also supported by the former work in [62] where a similar contribution in the decoherence terms was obtained in the special case of vacuum oscillations.

Secondly, as discussed in section 2.2, it was necessary to perform a renormalisation of the neutrino Hamiltonian as otherwise we end up with a final decoherence model that still depends on a cutoff frequency of the thermal gravitational wave environment and, which is even more problematic, the non-renormalised model involves divergences if the cutoff goes to infinity. The introduction of the cutoff frequency was necessary to regularise an otherwise infinite integral over the spectral density in the derivation of the master equation. In the non-renormalised Hamiltonian, the cutoff frequency is included in the so-called Lamb shift contribution, which shifts the energy eigenvalues of the neutrinos in a way that depends on the cutoff frequency and the energy. After the renormalisation, this shift of the energy eigenvalues is no longer present, so that the Lamb shift makes no contribution and, in our understanding, can only be interpreted as an unphysical effect before renormalisation. This seems to be in contrast to the interpretation used in [5], where an analogous contribution of the Lamb shift, which in their case depends on a test function as a regulator, is used to explain massless neutrino oscillations. From our point of view, one would also have to apply a renormalisation procedure which we expect to lead to no contribution from the Lamb shift. However, there might be additional finite terms that survive after renormalisation, as their occurrence crucially depends on the coupling between system and environment, which is chosen differently in [2] than in our case, but such a conclusion requires further investigation.

In addition, even if we consider the non-renormalised version of the model presented in this work, no massless neutrino oscillations will be allowed by the model. The reason for this is that in the model considered here the Lamb shift contribution cannot be chosen independently of the differences of the squared neutrino masses Δm_{ij}^2 due to the fact that the neutrino energy couples to the environment, whereas in our understanding this is not the case in [2] demonstrating again that physical properties of the existing models crucially depend on the coupling to the environment. An interesting question is whether the final renormalised model in [2] still allows massless neutrino oscillations.

To also analyse to what extent the final model, and thus the counter term, depends on the choice of regulator, we considered four different choices, including the two most prominent ones, the Lorentz-Drude and the exponential cutoff of the Ohmic spectral density. As our results show, neither the explicit decoherence contribution nor the form of the counter term depend on this choice.

One of the insights we have gained by taking a microscopic model as a starting point is that the physical interpretation of the individual contributions in the damping term that causes decoherence becomes clearer. Firstly, the model considered here contains only two free parameters, namely the coupling strength to the environment and the temperature of the thermal gravitational waves. If we assume that the latter can be obtained from independent experiments, then we are only left with the coupling strength between the neutrinos and the environment that enters the interaction Hamiltonian. Furthermore, the underlying

gravitational coupling of matter to gravity that strongly inspired the toy model in [42] has the consequence, that exponential damping is determined by the difference of the neutrino energies squared. In a next step we used this insight to perform a comparison to existing phenomenological models where usually a finite number of decoherence parameters is considered for which upper bounds are determined.
As our results show, we obtain a physical interpretation of the decoherence parameters used in the phenomenological models which is related to the coupling between the neutrinos and the environment in the microscopic model. From a theoretical point of view, we therefore expect that the limits for such decoherence parameters can be interpreted with a better physical understanding of the underlying microscopic model. Our analysis shows that in the case of vacuum oscillations we can achieve exact agreement with a subclass of phenomenological models. These are those that involve three neutrino flavors and for which at least three of the decoherence parameters, usually denoted as γ_{ij} with $\Gamma_{ij} = \gamma_{ij} E^n$, with $n \in (-2, -1, 0, 1, 2)$, do not vanish, fulfil the relation to Δm^2_{ij} shown in (27) and the dependence of Γ_{ij} on the mean neutrino energy is given by E^{-2}, which corresponds to the phenomenological models $n = -2$. The fact that the power $n = -2$ is favored is a consequence of the coupling between the neutrinos and the gravitational wave environment. Hence, any other choice of power in the phenomenological models will be rather difficult to be linked to gravitationally induced decoherence from our perspective. This is in contrast to the decoherence models inspired by quantum gravity in [63–66], which suggest $n = 2$. The main difference to the model considered here is that in [63–66] the second power of the energy, but not the energy difference, is included in the decoherence term. Our results agree with the model presented in [49], in which the squared energy difference is also included in the decoherence damping term. This sounds somewhat contradictory at first, but is resolved if we consider the system as neutrinos. Then, due to the squared energy difference, the linear term in the neutrino energy is the same for all neutrinos and simply cancels out, and what remains is a term proportional to $\Delta m^4_{ij}/E^2$. This shows that the power n that is ultimately obtained depends crucially on both the choice of coupling to the environment and the choice of system, because for other than neutrinos the power will generally change, even with the same coupling to the environment is chosen, and the final form of the decoherence term depends on the resulting energy difference for the system under consideration.

Furthermore, from our investigation we found that we are not able to match that subclass of phenomenological models just mentioned with the model presented here if we consider neutrino oscillations in matter. The reason for this is that in many existing phenomenological models the decoherence parameters γ_{ij} do not depend on matter effects and thus are chosen to be constant for each layer of the Earth. In contrast, in the model presented here the neutrinos couple with their energy to the gravitational environment and the eigenvalues of the neutrino change if matter effects are present, thus the γ_{ij} cannot be chosen to be constant across the different Earth layers. From the figures and the discussion in section 3 it becomes clear that not taking such matter effects into account can lead to deviations in the probabilities for the neutrino oscillations of up to 10% for the energies investigated in this work, depending on the chosen parameters of the model. That the decoherence term in the oscillation probabilities should be different for vacuum and matter was also a conclusion drawn in [15]. However, to find an exact match with their models is not straight forward because they consider a perturbative expansion and consider only subleading decoherence terms.

At the level of the Lindblad equation, we can distinguish the two classes of models by a different choice of Lindblad operators. The subclass of phenomenological models is obtained by choosing the Lindblad operator as the vacuum Hamiltonian of the neutrino, while for the model presented here the Lindblad operator is the full Hamiltonian, which also contains matter contributions if they are present. Since we obtain these deviations in the probabilities for the neutrino oscillations, this is again an example of how different chosen couplings to the gravitational environment lead to different physical properties of the model. From this point of view, it is also clear why the models can match exactly in the case of neutrino oscillations in vacuum. From the standpoint of general relativity and linearised gravity respectively, a coupling with the vacuum Hamiltonian if matter is present seems not too obvious.

Another consequence of this is that for the model presented here, the already existing bounds on the decoherence parameters γ_{ij} could potentially be used to constrain the coupling strength with the gravitational environment (denoted as η in our work) in the case of neutrino oscillations in vacuum. However, this is not currently possible as present analyses either assume one of the $\gamma_{ij} = 0$ or two of them equal to each other.
This again shows that the information we obtain from the existence of such limits cannot be completely detached from the underlying microscopic model one would like to examine.
On the contrary, we can exploit matter effects to clearly distinguish between the phenomenological model and the model considered here in order to put direct bounds on our parameters. The effect appears to be

visible with atmospheric neutrinos in the GeV energy range, propagating through the Earth. This makes neutrino telescopes such as KM3NeT/ORCA very good candidates to perform such a study. In this respect, we suggest such an analysis in order to determine the bounds on η and T for the model considered here.

Since we have mentioned that we understand the analysis of the toy model of [42] in the context of neutrino oscillations as a first step to learn more about gravitationally induced decoherence, we would like to make some remarks on the limitations of our analysis and possible future steps. First, although the toy model is inspired by the field-theoretical models in [12, 27, 38–40], it is a quantum mechanical model. Starting with the field-theoretical model and then projecting onto its 1-particle sector is more complicated and could generally lead to a more complex model that might contain additional features that we lose if we start directly with a quantum mechanical model. Hence, a careful analysis of the 1-particle sector of the model from [39], as done in [41] or see also [27, 38], and a discussion of the results from [41] in the context of neutrino oscillations will therefore be part of our future work. Moreover, this will also allow to consider the renormalisation procedure in a broader context since it is quite simple in a quantum mechanical setup compared to field theory. Moreover, one can analyse in parallel the different assumptions one makes, such as the first and second Markov approximation, to end up with the final Lindblad equation and learn whether the application of renormalisation before or after gives the same final one-particle sector. Finally, in order to generalise the model considered in this work, we also plan to generalise the quantisation procedure of the toy model so that we can also cover loop quantum gravity inspired models, which we study in the context of neutrino oscillations and compare with existing analyses such as the one in [43, 67], where in [67] a minimum length model is analysed and [43] the decoherence effects are studied for different approaches in addition to [42], such as deformed symmetries [68], metric fluctuations [69] and fluctuating minimum lengths [70].

Acknowledgements

The authors would like to thank Theophile Cartraud and Renata Ferrero for their contributions to our discussions in the initial and final stages of the project, respectively. The authors would also like to thank Renata Ferrero for her useful and valuable comments and suggestions for improvement on an earlier version of the manuscript. The authors also thank Stefan Hofmann for fruitful discussions on thermal gravitational waves in the cosmological context. A. Domi would like to thank J. A. B. Coelho for useful discussions on quantum decoherence within neutrino oscillation context. This project has received funding from the European Union's Horizon 2021 research and innovation programme under the Marie Skłodowska-Curie grant agreement No. 101068013 (QGRANT), supporting A. Domi. M.J. Fahn and M. Kobler both thank the Heinrich-Böll foundation for financial support.

Appendix A Spectral Density from Field-theoretic model

To motivate the above choice of spectral density, in particular the linear dependence on ω for small ω, and obtain a possible choice for η, we compare our toy model with the field-theoretic one in [39], where for simplicity we drop all indices in the latter. In the field-theoretic case, the role of the configuration variable is taken over by the densitised triad $\widehat{\delta E}$ and the canonically conjugated momentum is $\widehat{\delta C}$, which is a combination of the connection and the densitised triad. Their quantisation is introduced in [39] in equations (3.6) and (3.7). To obtain the same commutation relations and environmental Hamiltonian as for the toy model discussed in this paper, we redefine $\widehat{\widetilde{\delta E}} := \sqrt{\kappa}\widehat{\delta E}$ and $\widehat{\widetilde{\delta C}} := \sqrt{\kappa}\widehat{\delta C}$, where $\kappa = \frac{8\pi G_N}{c^4}$ is the coupling constant in General relativity, containing Newton's gravitational constant G_N and the speed of light c. The reason for this redefinition is the fact that their original algebra (see [39] equation (3.3)) contains a factor κ^{-1}. In terms of these rescaled variables we obtain (see also [39] equations (3.3) and (3.2)):

$$\left[\widehat{\widetilde{\delta E}}, \widehat{\widetilde{\delta C}}\right] = i\hbar\delta \qquad\qquad \hat{H}_E = \frac{1}{2}\int d^3k \left[\widehat{\widetilde{\delta C}}(\vec{k})^2 + \Omega_k^2 \widehat{\widetilde{\delta E}}(\vec{k})^2\right], \tag{A1}$$

where the frequencies are defined as $\Omega_k := \sqrt{\vec{k}^2}$. In the interaction Hamiltonian (see [39] equation (2.39) and below), one then couples the energy momentum tensor to the metric, which corresponds to contractions of $\widehat{\widetilde{\delta E}}$, hence

$$\hat{H}_I \sim \int d^3k \frac{\sqrt{\kappa}}{2} \hat{T} \otimes \widehat{\widetilde{\delta E}}\,, \tag{A2}$$

where $\sim$ means "corresponds to". From this analogue one can deduce $g_i \sim \sqrt{\kappa}$. When computing correlation functions and hence Λ and Γ, the terms appearing are of the form (see [39] equations (4.38) and (3.6))

$$\int d^3k \frac{\kappa}{2\Omega_k} h(\vec{k}) \tag{A3}$$

compared to the expressions appearing here in (4) and (5) using (6):

$$\hbar^2 \sum_{i=1}^{N} \frac{g_i^2}{2\omega_i} h(\omega_i)\,. \tag{A4}$$

Assuming for simplicity that $h(\vec{k}) = h(\Omega_k)$, we can rewrite the integration in (A3) in spherical coordinates:

$$\int d^3k \frac{\kappa}{2\Omega_k} h(\Omega_k) = \int_0^\infty d\Omega\; 2\pi\kappa\Omega h(\Omega)\,. \tag{A5}$$

Motivated by this analogue, we take the following continuum limit for the toy model:

$$\hbar^2 \sum_{i=1}^{N} \frac{g_i^2}{2\omega_i} h(\omega_i) \longrightarrow \hbar^2 \int_0^\infty d\omega\; 2\pi\kappa\omega h(\omega)\,. \tag{A6}$$

This suggests to use as spectral density $J(\omega)$, which appears in integrals as $\int d\omega J(\omega) f(\omega)$, the following smooth function:

$$J(\omega) = \hbar^2 \sum_{i=1}^{N} \frac{g_i^2}{2\omega_i} \delta(\omega - \omega_i) \longrightarrow \frac{2\pi\kappa\hbar}{c}\omega\,, \tag{A7}$$

where we inserted additional inverse factors of $\hbar$ and c to obtain the correct dimensions, as the work in [39] is in natural units. To cure UV-divergence, we have to add a suitable cutoff, see the discussion in the main text. By comparison to the general form of the Ohmic spectral density in the main text, we find a possible choice for η motivated by the analogy to the field-theoretic case:

$$\eta^2 \sim \pi^2 \frac{\kappa\hbar}{c} = 8\pi^3 \frac{\ell_p^2}{c^2} \approx 10^{-84} s^2\,, \tag{A8}$$

where ℓ_p denotes the Planck length, thus

$$\frac{\eta^2}{\hbar^2} \approx 10^{-55} \frac{1}{eV^2} = 10^{-37} \frac{1}{GeV^2}\,. \tag{A9}$$

Appendix B A note on the diagonalisation

Due to the different orders of magnitude of E compared to $\frac{\Delta m_{ij}^2 c^4}{6E}$, working with $\hat{H}_{vac}$ as specified in (19) requires very high numerical precision and hence high computational effort. To simplify the computation, one can proceed in the following way: Splitting $\hat{H}_S^{(0)}$ into two parts in the following way:

$$\hat{H}_S^{(0)} = E\mathbb{1}_3 + \hat{H}_S^{(\Delta)}\,, \tag{B10}$$

the characteristic polynomial reads:

$$\det\left(\hat{H}_S^{(0)} - \lambda\mathbb{1}_3\right) = \det\left(\hat{H}_S^{(\Delta)} - \lambda^{(\Delta)}\mathbb{1}_3\right) = 0\,, \tag{B11}$$

where $\lambda^{(\Delta)} = \lambda - E$ are the eigenvalues of $\hat{H}_S^{(\Delta)}$. For the eigenvectors $v^{(\Delta)}$ of $\hat{H}_S^{(\Delta)}$ we find:

$$\hat{H}_S^{(\Delta)} v^{(\Delta)} = \lambda^{(\Delta)} v^{(\Delta)} \iff \hat{H}_S^{(0)} v^{(\Delta)} - E v^{(\Delta)} = \lambda v^{(\Delta)} - E v^{(\Delta)} \iff \hat{H}_S^{(0)} v^{(\Delta)} = \lambda v^{(\Delta)}\,, \tag{B12}$$

thus $\hat{H}_S^{(0)}$ and $\hat{H}_S^{(\Delta)}$ have the same eigenvectors. Hence, one can work with $\hat{H}_S^{(\Delta)}$ and its eigenvectors throughout the calculation and just has to use in the final results in for instance (23) that $\widetilde{H}_i = \lambda_{S,i}^{(\Delta)} + E$, where

$\lambda_{S,i}^{(\Delta)}$ are the eigenvalues of $\hat{H}_S^{(\Delta)}$. As the evolution of the neutrino in the end only depends on terms of the form $\left(\widetilde{H}_i - \widetilde{H}_j\right)$, the mean neutrino energy E will always cancel.

Appendix C Solution of the Master Equation

The master equation in effective mass basis (22) is

$$\frac{d}{dt}\rho(t) = -\frac{i}{\hbar}\left[H, \rho(t)\right] + l\left(H\rho(t)H - \frac{1}{2}\left\{H^2, \rho(t)\right\}\right) \tag{C13}$$

with the scalar prefactor $l = \frac{8\eta^2}{\hbar^2}\frac{k_B T}{\hbar}$. For better readability, we dropped all hats and tildes and indices, also for $H := \hat{\widetilde{H}}_S$. To solve this equation, we consider the three summands individually. As all operators that appear apart from the density matrix commute and are time-independent, we can solve the master equation for each summand individually and then combine the solutions.

- For the first summand we find:

$$\frac{d}{dt}\rho^{(1)}(t) = -\frac{i}{\hbar}\left[H, \rho^{(1)}(t)\right] \quad \Longrightarrow \quad \rho^{(1)}(t) = e^{-\frac{i}{\hbar}Ht}\rho^{(1)}(0)e^{\frac{i}{\hbar}Ht}\,. \tag{C14}$$

- The third summand yields:

$$\frac{d}{dt}\rho^{(2)}(t) = -\frac{l}{2}\left\{H^2, \rho^{(2)}(t)\right\} \quad \Longrightarrow \quad \rho^{(2)}(t) = e^{-\frac{l}{2}H^2 t}\rho^{(2)}(0)e^{-\frac{l}{2}H^2 t}\,. \tag{C15}$$

- For the second summand we obtain:

$$\frac{d}{dt}\rho^{(3)}(t) = l \cdot H\rho^{(3)}(t)H \quad \Longrightarrow \quad \rho^{(3)}(t) = \sum_{n=0}^{\infty}\frac{(lt)^n}{n!}H^n\rho^{(3)}(0)H^n \tag{C16}$$

Combining these in a suitable form, the total solution then reads:

$$\begin{aligned}\rho(t) &= \sum_{n=0}^{\infty}\frac{(lt)^n}{n!}H^n e^{-\frac{i}{\hbar}Ht - \frac{l}{2}H^2 t}\rho(0)e^{\frac{i}{\hbar}Ht - \frac{l}{2}H^2 t}H^n \\ &=: \sum_{n=0}^{\infty}\frac{(lt)^n}{n!}H^n F\rho(0)F^\dagger H^n\,,\end{aligned} \tag{C17}$$

where we defined $F := e^{-\frac{i}{\hbar}Ht - \frac{l}{2}H^2 t}$. Since F and H^n are diagonal in the effective mass basis, we can evaluate the matrix product directly and obtain:

$$\rho_{ij}(t) = \sum_{n=0}^{N}\frac{(lt)^n}{n!}\rho_{ij}(0)F_i F_j^* H_i^n H_j^n = \rho_{ij}(0)F_i F_j^* e^{lH_i H_j t}\,, \tag{C18}$$

where a star denotes complex conjugation and we refer to the components of the diagonal matrices as $F_i := F_{ii}$ and $H_i := H_{ii}$. Reinserting the original expressions, this yields the solution (23):

$$\widetilde{\rho}_{ij}(t) = \widetilde{\rho}_{ij}(0) \cdot e^{-\frac{i}{\hbar}\left(\widetilde{H}_i - \widetilde{H}_j\right)t - \frac{4\eta^2}{\hbar^2}\frac{k_B T}{\hbar}\left(\widetilde{H}_i - \widetilde{H}_j\right)^2 t}\,. \tag{C19}$$

References

[1] Gago, A.M., Santos, E.M., Teves, W.J.C., Zukanovich Funchal, R.: Quantum dissipative effects and neutrinos: Current constraints and future perspectives. Phys. Rev. D **63**, 073001 (2001) https://doi.org/10.1103/PhysRevD.63.073001 arXiv:hep-ph/0009222

[2] Benatti, F., Floreanini, R.: Open system approach to neutrino oscillations. JHEP **02**, 032 (2000) https://doi.org/10.1088/1126-6708/2000/02/032 arXiv:hep-ph/0002221

[3] Klapdor-Kleingrothaus, H.V., Pas, H., Sarkar, U.: Effects of quantum space-time foam in the neutrino sector. Eur. Phys. J. A **8**, 577–580 (2000) https://doi.org/10.1007/s100500070080 arXiv:hep-ph/0004123

[4] Lisi, E., Marrone, A., Montanino, D.: Probing possible decoherence effects in atmospheric neutrino oscillations. Phys. Rev. Lett. **85**, 1166–1169 (2000) https://doi.org/10.1103/PhysRevLett.85.1166 arXiv:hep-ph/0002053

[5] Benatti, F., Floreanini, R.: Massless neutrino oscillations. Phys. Rev. D **64**, 085015 (2001) https://doi.org/10.1103/PhysRevD.64.085015 arXiv:hep-ph/0105303

[6] Morgan, D., Winstanley, E., Brunner, J., Thompson, L.F.: Probing quantum decoherence in atmospheric neutrino oscillations with a neutrino telescope. Astropart. Phys. **25**, 311–327 (2006) https://doi.org/10.1016/j.astropartphys.2006.03.001 arXiv:astro-ph/0412618

[7] Anchordoqui, L.A., Goldberg, H., Gonzalez-Garcia, M.C., Halzen, F., Hooper, D., Sarkar, S., Weiler, T.J.: Probing Planck scale physics with IceCube. Phys. Rev. D **72**, 065019 (2005) https://doi.org/10.1103/PhysRevD.72.065019 arXiv:hep-ph/0506168

[8] Mavromatos, N.E., Sarkar, S.: Methods of approaching decoherence in the flavour sector due to space-time foam. Phys. Rev. D **74**, 036007 (2006) https://doi.org/10.1103/PhysRevD.74.036007 arXiv:hep-ph/0606048

[9] Mavromatos, N.E., Meregaglia, A., Rubbia, A., Sakharov, A., Sarkar, S.: Quantum-Gravity Decoherence Effects in Neutrino Oscillations: Expected Constraints From CNGS and J-PARC. Phys. Rev. D **77**, 053014 (2008) https://doi.org/10.1103/PhysRevD.77.053014 arXiv:0801.0872 [hep-ph]

[10] Fogli, G.L., Lisi, E., Marrone, A., Montanino, D., Palazzo, A.: Probing non-standard decoherence effects with solar and KamLAND neutrinos. Phys. Rev. D **76**, 033006 (2007) https://doi.org/10.1103/PhysRevD.76.033006 arXiv:0704.2568 [hep-ph]

[11] Farzan, Y., Schwetz, T., Smirnov, A.Y.: Reconciling results of LSND, MiniBooNE and other experiments with soft decoherence. JHEP **07**, 067 (2008) https://doi.org/10.1088/1126-6708/2008/07/067 arXiv:0805.2098 [hep-ph]

[12] Oniga, T., Wang, C.H.T.: Quantum gravitational decoherence of light and matter. Phys. Rev. D **93**(4), 044027 (2016) https://doi.org/10.1103/PhysRevD.93.044027 arXiv:1511.06678 [quant-ph]

[13] Balieiro Gomes, G., Guzzo, M.M., Holanda, P.C., Oliveira, R.L.N.: Parameter Limits for Neutrino Oscillation with Decoherence in KamLAND. Phys. Rev. D **95**(11), 113005 (2017) https://doi.org/10.1103/PhysRevD.95.113005 arXiv:1603.04126 [hep-ph]

[14] Oliveira, R.L.N.: Dissipative Effect in Long Baseline Neutrino Experiments. Eur. Phys. J. C **76**(7), 417 (2016) https://doi.org/10.1140/epjc/s10052-016-4253-z arXiv:1603.08065 [hep-ph]

[15] Carpio, J., Massoni, E., Gago, A.M.: Revisiting quantum decoherence for neutrino oscillations in matter with constant density. Phys. Rev. D **97**(11), 115017 (2018) https://doi.org/10.1103/PhysRevD.97.115017 arXiv:1711.03680 [hep-ph]

[16] Coelho, J.A.B., Mann, W.A.: Decoherence, matter effect, and neutrino hierarchy signature in long baseline experiments. Phys. Rev. D **96**(9), 093009 (2017) https://doi.org/10.1103/PhysRevD.96.093009 arXiv:1708.05495 [hep-ph]

[17] Coelho, J.A.B., Mann, W.A., Bashar, S.S.: Nonmaximal θ_{23} mixing at NOvA from neutrino decoherence. Phys. Rev. Lett. **118**(22), 221801 (2017) https://doi.org/10.1103/PhysRevLett.118.221801 arXiv:1702.04738 [hep-ph]

[18] Balieiro Gomes, G., Forero, D.V., Guzzo, M.M., De Holanda, P.C., Oliveira, R.L.N.: Quantum Decoherence Effects in Neutrino Oscillations at DUNE. Phys. Rev. D **100**(5), 055023 (2019) https://doi.org/10.1103/PhysRevD.100.055023 arXiv:1805.09818 [hep-ph]

[19] Carpio, J.A., Massoni, E., Gago, A.M.: Testing quantum decoherence at DUNE. Phys. Rev. D **100**(1), 015035 (2019) https://doi.org/10.1103/PhysRevD.100.015035 arXiv:1811.07923 [hep-ph]

[20] Carrasco, J.C., Díaz, F.N., Gago, A.M.: Probing CPT breaking induced by quantum decoherence at DUNE. Phys. Rev. D **99**(7), 075022 (2019) https://doi.org/10.1103/PhysRevD.99.075022 arXiv:1811.04982 [hep-ph]

[21] Coloma, P., Lopez-Pavon, J., Martinez-Soler, I., Nunokawa, H.: Decoherence in Neutrino Propagation Through Matter, and Bounds from IceCube/DeepCore. Eur. Phys. J. C **78**(8), 614 (2018) https://doi.org/10.1140/epjc/s10052-018-6092-6 arXiv:1803.04438 [hep-ph]

[22] Gomes, A.L.G., Gomes, R.A., Peres, O.L.G.: Quantum decoherence and relaxation in long-baseline neutrino data. JHEP **10**, 035 (2023) https://doi.org/10.1007/JHEP10(2023)035 arXiv:2001.09250 [hep-ph]

[23] KM3NeT Collaboration: Search for Quantum Decoherence in Neutrino Oscillations with KM3NeT/ORCA6. PoS **ICRC2023**, 1025 (2023) https://doi.org/10.22323/1.444.1025

[24] IceCube Collaboration: Searching for decoherence from quantum gravity at the IceCube south pole neutrino observatory. arXiv:2308.00105 (2023)

[25] Gomes, A.L.G., et al.: Quantum decoherence and relaxation in long-baseline neutrino data. Journal of High Energy Physics **2023**(35) (2023) https://doi.org/10.1007/JHEP10(2023)035

[26] Buoninfante, L., Capolupo, A., Giampaolo, S.M., Lambiase, G.: Revealing neutrino nature and CPT violation with decoherence effects. Eur. Phys. J. C **80**(11), 1009 (2020) https://doi.org/10.1140/epjc/s10052-020-08549-9 arXiv:2001.07580 [hep-ph]

[27] Lagouvardos, M., Anastopoulos, C.: Gravitational decoherence of photons. Class. Quant. Grav. **38**(11), 115012 (2021) https://doi.org/10.1088/1361-6382/abf2f3 arXiv:2011.08270 [gr-qc]

[28] Ohlsson, T., Zhou, S.: Density Matrix Formalism for PT-Symmetric Non-Hermitian Hamiltonians with the Lindblad Equation. Phys. Rev. A **103**(2), 022218 (2021) https://doi.org/10.1103/PhysRevA.103.022218 arXiv:2006.02445 [quant-ph]

[29] Stuttard, T., Jensen, M.: Neutrino decoherence from quantum gravitational stochastic perturbations. Phys. Rev. D **102**(11), 115003 (2020) https://doi.org/10.1103/PhysRevD.102.115003 arXiv:2007.00068 [hep-ph]

[30] Stuttard, T.: Neutrino signals of lightcone fluctuations resulting from fluctuating spacetime. Phys. Rev. D **104**(5), 056007 (2021) https://doi.org/10.1103/PhysRevD.104.056007 arXiv:2103.15313 [hep-ph]

[31] Banerjee, I.K., Dey, U.K.: Neutrino decoherence from generalised uncertainty. Eur. Phys. J. C **83**(5), 428 (2023) https://doi.org/10.1140/epjc/s10052-023-11565-0 arXiv:2208.12062 [hep-ph]

[32] De Romeri, V., Giunti, C., Stuttard, T., Ternes, C.A.: Neutrino oscillation bounds on quantum decoherence. JHEP **09**, 097 (2023) https://doi.org/10.1007/JHEP09(2023)097 arXiv:2306.14699 [hep-ph]

[33] Barenboim, G., Calatayud-Cadenillas, A., Gago, A.M., Ternes, C.A.: Quantum Decoherence effects on precision measurements at DUNE and T2HK (2024) arXiv:2402.16395 [hep-ph]

[34] Breuer, H.-P., Petruccione, F.: The Theory of Open Quantum Systems. Oxford University Press, USA (2007). https://doi.org/10.1093/acprof:oso/9780199213900.001.0001

[35] Xu, B.: Neutrino Decoherence in Simple Open Quantum Systems (2020) arXiv:2009.13471 [hep-ph]

[36] Bassi, A., Großardt, A., Ulbricht, H.: Gravitational Decoherence. Class. Quant. Grav. **34**(19), 193002 (2017) https://doi.org/10.1088/1361-6382/aa864f arXiv:1706.05677 [quant-ph]

[37] Anastopoulos, C., Hu, B.-L.: Gravitational decoherence: A thematic overview. AVS Quantum Sci. **4**(1), 015602 (2022) https://doi.org/10.1116/5.0077536 arXiv:2111.02462 [gr-qc]

[38] Anastopoulos, C., Hu, B.L.: A Master Equation for Gravitational Decoherence: Probing the Textures of Spacetime. Class. Quant. Grav. **30**, 165007 (2013) https://doi.org/10.1088/0264-9381/30/16/165007 arXiv:1305.5231 [gr-qc]

[39] Fahn, M.J., Giesel, K., Kobler, M.: A gravitationally induced decoherence model using Ashtekar variables. Class. Quant. Grav. **40**(9), 094002 (2023) https://doi.org/10.1088/1361-6382/acc5d5 arXiv:2206.06397 [gr-qc]

[40] Blencowe, M.P.: Effective Field Theory Approach to Gravitationally Induced Decoherence. Phys. Rev. Lett. **111**(2), 021302 (2013) https://doi.org/10.1103/PhysRevLett.111.021302 arXiv:1211.4751 [quant-ph]

[41] Fahn, M.J., Giesel, K.: Gravitationally induced decoherence of a scalar field: Investigating the one-particle sector and the interplay between renormalisation and Markov approximations, to appear soon (2024)

[42] Xu, Q., Blencowe, M.P.: Zero-dimensional models for gravitational and scalar QED decoherence. New J. Phys. **24**(11), 113048 (2022) https://doi.org/10.1088/1367-2630/aca427 arXiv:2005.02554 [quant-ph]

[43] D'Esposito, V., Gubitosi, G.: Constraints on quantum spacetime-induced decoherence from neutrino oscillations (2023) arXiv:2306.14778 [hep-ph]

[44] Gouvêa, A., De Romeri, V., Ternes, C.A.: Probing neutrino quantum decoherence at reactor experiments. Journal of High Energy Physics **2020**(18) (2020) https://doi.org/10.1007/JHEP08(2020)049

[45] Caldeira, A.O., Leggett, A.J.: Influence of dissipation on quantum tunneling in macroscopic systems. Phys. Rev. Lett. **46**, 211 (1981) https://doi.org/10.1103/PhysRevLett.46.211

[46] Fahn, M.J., Giesel, K., Kemper, R.: A gravitationally induced decoherence model for photons using Ashtekar variables, to appear soon (2024)

[47] Weiss, U.: Quantum Dissipative Systems. World Scientific, Singapore (2012)

[48] Grabert, H., Weiss, U., Talkner, P.: Quantum theory of the damped harmonic oscillator. Z. Physik B-Condensed Matter **55**, 87–94 (1984) https://doi.org/10.1007/BF01307505

[49] Gambini, R., Porto, R.A., Pullin, J.: Decoherence from discrete quantum gravity. Class. Quant. Grav. **21**, 51–57 (2004) https://doi.org/10.1088/0264-9381/21/8/L01 arXiv:gr-qc/0305098

[50] Smirne, A., Tamascelli, D., Lim, J., Plenio, M.B., Huelga, S.F.: Non-Perturbative Treatment of Open-System Multi-Time Expectation Values in Gaussian Bosonic Environments. Open Systems & Information Dynamics **29**(04), 2250019 (2022) https://doi.org/10.1142/S1230161222500196 arXiv:2209.00293 [quant-ph]

[51] Coloma, P., et al.: Decoherence in neutrino propagation through matter, and bounds from IceCube/DeepCore. European Phys. Journal C **78**(614) (2018) https://doi.org/0.1140/epjc/s10052-018-6092-6

[52] KM3NeT Collaboration: Letter of intent for KM3NeT 2.0. J. Phys. G: Nucl. Part. Phys. **43**, 084001 (2016) https://doi.org/10.1088/0954-3899/43/8/084001

[53] Coelho, J.A.B., *et al.*: OscProb. Zenodo (2024) https://doi.org/10.5281/zenodo.10666396

[54] Dziewonski, A.M., Anderson, D.L.: Preliminary reference earth model. Physics of the Earth and Planetary Interiors **25**(4), 297–356 (1981) https://doi.org/10.1016/0031-9201(81)90046-7

[55] Guzzo, M.M., Holanda, P.C., Oliveira, R.L.N.: Quantum Dissipation in a Neutrino System Propagating in Vacuum and in Matter. Nucl. Phys. B **908**, 408–422 (2016) https://doi.org/10.1016/j.nuclphysb.2016.04.030 arXiv:1408.0823 [hep-ph]

[56] Kolb, E.W., Turner, M.S.: The Early Universe vol. 69, (1990). https://doi.org/10.1201/9780429492860

[57] Gasperini, M., Giovannini, M., Veneziano, G.: Squeezed thermal vacuum and the maximum scale for inflation. Phys. Rev. D **48**, 439–443 (1993) https://doi.org/10.1103/PhysRevD.48.R439 arXiv:gr-qc/9306015

[58] Giovannini, M.: Primordial backgrounds of relic gravitons. Prog. Part. Nucl. Phys. **112**, 103774 (2020) https://doi.org/10.1016/j.ppnp.2020.103774 arXiv:1912.07065 [astro-ph.CO]

[59] Milburn, G.J.: Intrinsic decoherence in quantum mechanics. Phys. Rev. A **44**(9), 5401 (1991) https://doi.org/10.1103/PhysRevA.44.5401

[60] Milburn, G.J.: Lorentz invariant intrinsic decoherence. New J. Phys. **8**, 96 (2006) https://doi.org/10.1088/1367-2630/8/6/096 arXiv:gr-qc/0308021

[61] Diosi, L.: Intrinsic time-uncertainties and decoherence: Comparison of 4 models. Braz. J. Phys. **35**, 260–265 (2005) https://doi.org/10.1590/S0103-97332005000200009 arXiv:quant-ph/0412154

[62] Adler, S.L.: Comment on a proposed Super-Kamiokande test for quantum gravity induced decoherence effects. Phys. Rev. D **62**, 117901 (2000) https://doi.org/10.1103/PhysRevD.62.117901 arXiv:hep-ph/0005220

[63] Ellis, J.R., Lopez, J.L., Mavromatos, N.E., Nanopoulos, D.V.: Precision tests of CPT symmetry and quantum mechanics in the neutral kaon system. Phys. Rev. D **53**, 3846–3870 (1996) https://doi.org/10.1103/PhysRevD.53.3846 arXiv:hep-ph/9505340

[64] Ellis, J.R., Mavromatos, N.E., Nanopoulos, D.V., Winstanley, E.: Quantum decoherence in a four-dimensional black hole background. Mod. Phys. Lett. A **12**, 243–256 (1997) https://doi.org/10.1142/S0217732397000248 arXiv:gr-qc/9602011

[65] Ellis, J.R., Mavromatos, N.E., Nanopoulos, D.V.: Quantum decoherence in a D foam background. Mod. Phys. Lett. A **12**, 1759–1773 (1997) https://doi.org/10.1142/S0217732397001795 arXiv:hep-th/9704169

[66] Ellis, J.R., Mavromatos, N.E., Nanopoulos, D.V.: How large are dissipative effects in noncritical Liouville string theory? Phys. Rev. D **63**, 024024 (2001) https://doi.org/10.1103/PhysRevD.63.024024 arXiv:gr-qc/0007044

[67] Al-Nasrallah, E., Das, S., Illuminati, F., Petruzziello, L., Vagenas, E.C.: Discriminating quantum gravity models by gravitational decoherence. Nucl. Phys. B **992**, 116246 (2023) https://doi.org/10.1016/j.nuclphysb.2023.116246 arXiv:2110.10288 [gr-qc]

[68] Arzano, M., D'Esposito, V., Gubitosi, G.: Fundamental decoherence from quantum spacetime. Commun. Phys. **6**(1), 242 (2023) https://doi.org/10.1038/s42005-023-01159-3 arXiv:2208.14119 [gr-qc]

[69] Breuer, H.-P., Goklu, E., Lammerzahl, C.: Metric fluctuations and decoherence. Class. Quant. Grav. **26**, 105012 (2009) https://doi.org/10.1088/0264-9381/26/10/105012 arXiv:0812.0420 [gr-qc]

[70] Petruzziello, L., Illuminati, F.: Quantum gravitational decoherence from fluctuating minimal length and deformation parameter at the Planck scale. Nature Commun. **12**(1), 4449 (2021) https://doi.org/10.1038/s41467-021-24711-7 arXiv:2011.01255 [gr-qc]

arXiv:2403.03004v1 [astro-ph.CO] 5 Mar 2024

Ultralight vector dark matter search using data from the KAGRA O3GK run

A. G. Abac,[1] R. Abbott,[2] H. Abe,[3] I. Abouelfettouh,[4] F. Acernese,[5,6] K. Ackley,[7] C. Adamcewicz,[8] S. Adhicary,[9] N. Adhikari,[10] R. X. Adhikari,[2] V. K. Adkins,[11] V. B. Adya,[12] C. Affeldt,[13,14] D. Agarwal,[15] M. Agathos,[16] O. D. Aguiar,[17] I. Aguilar,[18] L. Aiello,[19] A. Ain,[20] P. Ajith,[21] T. Akutsu,[22,23] S. Albanesi,[24,25] R. A. Alfaidi,[26] A. Al-Jodah,[27] C. Alléné,[28] A. Allocca,[29,6] S. Al-Shammari,[19] P. A. Altin,[12] S. Alvarez-Lopez,[30] A. Amato,[31,32] L. Amez-Droz,[33] A. Amorosi,[33] C. Amra,[34] S. Anand,[2] A. Ananyeva,[2] S. B. Anderson,[2] W. G. Anderson,[2] M. Andia,[35] M. Ando,[36] T. Andrade,[37] N. Andres,[28] M. Andrés-Carcasona,[38] T. Andrić,[1,39] J. Anglin,[40] S. Ansoldi,[41,42] J. M. Antelis,[43] S. Antier,[44] M. Aoumi,[45] E. Z. Appavuravther,[46,47] S. Appert,[2] S. K. Apple,[48] K. Arai,[2] A. Araya,[49] M. C. Araya,[2] J. S. Areeda,[50] N. Aritomi,[4] F. Armato,[51] N. Arnaud,[35,52] M. Arogeti,[53] S. M. Aronson,[11] K. G. Arun,[54] G. Ashton,[55] Y. Aso,[22,56] M. Assiduo,[57,58] S. Assis de Souza Melo,[52] S. M. Aston,[59] P. Astone,[60] F. Aubin,[61] K. AultONeal,[43] G. Avallone,[62] S. Babak,[63] F. Badaracco,[51] C. Badger,[64] S. Bae,[65] S. Bagnasco,[25] E. Bagui,[66] Y. Bai,[2] J. G. Baier,[67] R. Bajpai,[22] T. Baka,[68] M. Ball,[69] G. Ballardin,[52] S. W. Ballmer,[70] S. Banagiri,[71] B. Banerjee,[39] D. Bankar,[15] P. Baral,[10] J. C. Barayoga,[2] B. C. Barish,[2] D. Barker,[4] P. Barneo,[37,72] F. Barone,[73,6] B. Barr,[26] L. Barsotti,[30] M. Barsuglia,[63] D. Barta,[74] S. D. Barthelmy,[75] M. A. Barton,[26] I. Bartos,[40] S. Basak,[21] A. Basalaev,[76] R. Bassiri,[18] A. Basti,[77,20] M. Bawaj,[78,46] P. Baxi,[79] J. C. Bayley,[26] A. C. Baylor,[10] M. Bazzan,[80,81] B. Bécsy,[82] V. M. Bedakihale,[83] F. Beirnaert,[84] M. Bejger,[85] D. Belardinelli,[86] A. S. Bell,[26] V. Benedetto,[87] D. Beniwal,[88] W. Benoit,[89] J. D. Bentley,[76] M. Ben Yaala,[90] S. Bera,[91] M. Berbel,[92] F. Bergamin,[13,14] B. K. Berger,[18] S. Bernuzzi,[93] M. Beroiz,[2] D. Bersanetti,[51] A. Bertolini,[32] J. Betzwieser,[59] D. Beveridge,[27] N. Bevins,[94] R. Bhandare,[95] U. Bhardwaj,[96,32] R. Bhatt,[2] D. Bhattacharjee,[67,97] S. Bhaumik,[40] S. Bhowmick,[98] A. Bianchi,[32,99] I. A. Bilenko,[100] G. Billingsley,[2] A. Binetti,[101] S. Bini,[102,103] O. Birnholtz,[104] S. Biscoveanu,[71,30] A. Bisht,[14] M. Bitossi,[52,20] M.-A. Bizouard,[44] J. K. Blackburn,[2] C. D. Blair,[27,59] D. G. Blair,[27] F. Bobba,[62,105] N. Bode,[13,14] G. Bogaert,[44] G. Boileau,[106,44] M. Boldrini,[107,60] G. N. Bolingbroke,[88] A. Bolliand,[108,34] L. D. Bonavena,[80] R. Bondarescu,[37] F. Bondu,[109] E. Bonilla,[18] M. S. Bonilla,[50] A. Bonino,[110] R. Bonnand,[28] P. Booker,[13,14] A. Borchers,[13,14] V. Boschi,[20] S. Bose,[15] V. Bossilkov,[59] V. Boudart,[111] A. Boumerdassi,[19] A. Bozzi,[52] C. Bradaschia,[20] P. R. Brady,[10] M. Braglia,[112] A. Branch,[59] M. Branchesi,[39,113] M. Breschi,[93] T. Briant,[114] A. Brillet,[44] M. Brinkmann,[13,14] P. Brockill,[10] E. Brockmueller,[13,14] A. F. Brooks,[2] D. D. Brown,[88] M. L. Brozzetti,[78,46] S. Brunett,[2] G. Bruno,[115] R. Bruntz,[116] J. Bryant,[110] F. Bucci,[58] J. Buchanan,[116] O. Bulashenko,[37,72] T. Bulik,[117] H. J. Bulten,[32] A. Buonanno,[118,1] K. Burtnyk,[4] R. Buscicchio,[119,120] D. Buskulic,[28] C. Buy,[121] R. L. Byer,[18] G. S. Cabourn Davies,[122] G. Cabras,[41,42] R. Cabrita,[115] L. Cadonati,[53] G. Cagnoli,[123] C. Cahillane,[70] J. Calderón Bustillo,[124] J. D. Callaghan,[26] T. A. Callister,[125] E. Calloni,[29,6] J. B. Camp,[75,51] G. Caneva Santoro,[38] M. Cannavacciuolo,[62] K. C. Cannon,[36] H. Cao,[126] Z. Cao,[127] L. A. Capistran,[128] E. Capocasa,[63] E. Capote,[70] G. Carapella,[62,105] F. Carbognani,[52] M. Carlassara,[13,14] J. B. Carlin,[129] M. Carpinelli,[119,130,52] G. Carrillo,[69] J. J. Carter,[13,14] G. Carullo,[131] J. Casanueva Diaz,[52] C. Casentini,[132,86] G. Castaldi,[133] S. Y. Castro-Lucas,[98] S. Caudill,[134,32,68] M. Cavaglià,[97] R. Cavalieri,[52] G. Cella,[20] P. Cerdá-Durán,[135,136] E. Cesarini,[86] W. Chaibi,[44] P. Chakraborty,[13,14] S. Chalathadka Subrahmanya,[76] C. Chan,[36] J. C. L. Chan,[125] K. H. M. Chan,[137] M. Chan,[138] W. L. Chan,[137] K. Chandra,[139] R.-J. Chang,[140] P. Chanial,[63] S. Chao,[141,142] C. Chapman-Bird,[26] E. L. Charlton,[116] P. Charlton,[143] E. Chassande-Mottin,[63] C. Chatterjee,[27] Debarati Chatterjee,[15] Deep Chatterjee,[30] M. Chaturvedi,[95] S. Chaty,[63] K. Chatziioannou,[2] A. Chen,[144] A. H.-Y. Chen,[145] D. Chen,[146] H. Chen,[141] H. Y. Chen,[147] K. H. Chen,[142] X. Chen,[27] Yi-Ru Chen,[141] Yanbei Chen,[148] Yitian Chen,[149] H. P. Cheng,[40] P. Chessa,[77,20] H. T. Cheung,[79] H. Y. Chia,[40] F. Chiadini,[150,105] C. Chiang,[142] G. Chiarini,[81] A. Chiba,[151] R. Chiba,[152] R. Chierici,[153] A. Chincarini,[51] M. L. Chiofalo,[77,20] A. Chiummo,[6,52] C. Chou,[145] S. Choudhary,[27] N. Christensen,[44] S. S. Y. Chua,[12] K. W. Chung,[64] G. Ciani,[80,81] P. Ciecielag,[85] M. Cieślar,[85] M. Cifaldi,[86] A. A. Ciobanu,[88] R. Ciolfi,[154,81] F. Clara,[4] J. A. Clark,[2,53] T. A. Clarke,[8] P. Clearwater,[155] S. Clesse,[66] F. Cleva,[44] E. Coccia,[39,113,38] E. Codazzo,[39] P.-F. Cohadon,[114] M. Colleoni,[91] C. G. Collette,[33] J. Collins,[59] S. Colloms,[26] A. Colombo,[119,120,156] M. Colpi,[119,120] C. M. Compton,[4] L. Conti,[81] S. J. Cooper,[110] T. R. Corbitt,[11] I. Cordero-Carrión,[157] S. Corezzi,[78,46] N. J. Cornish,[82] A. Corsi,[158] S. Cortese,[52] C. A. Costa,[17] R. Cottingham,[59] M. W. Coughlin,[89] A. Couineaux,[60] J.-P. Coulon,[44] S. T. Countryman,[159] J.-F. Coupechoux,[153] B. Cousins,[9] P. Couvares,[2,53] D. M. Coward,[27] M. J. Cowart,[59] D. C. Coyne,[2] R. Coyne,[160] K. Craig,[90] R. Creed,[19] J. D. E. Creighton,[10] T. D. Creighton,[161] P. Cremonese,[91]

A. W. Criswell,[89] J. C. G. Crockett-Gray,[11] M. Croquette,[114] R. Crouch,[4] S. G. Crowder,[162] J. R. Cudell,[111] T. J. Cullen,[2] A. Cumming,[26] E. Cuoco,[52,163,20] M. Cusinato,[135] P. Dabadie,[123] T. Dal Canton,[35] S. Dall'Osso,[60] G. Dálya,[84] B. D'Angelo,[51] S. Danilishin,[31,32] S. D'Antonio,[86] K. Danzmann,[14,13,14] K. E. Darroch,[116] L. P. Dartez,[4] A. Dasgupta,[83] S. Datta,[54] V. Dattilo,[52] A. Daumas,[63] N. Davari,[164,130] I. Dave,[95] A. Davenport,[98] M. Davier,[35] T. F. Davies,[27] D. Davis,[2] L. Davis,[27] M. C. Davis,[94] E. J. Daw,[165] M. Dax,[1] J. De Bolle,[84] M. Deenadayalan,[15] J. Degallaix,[166] M. De Laurentis,[29,6] S. Deléglise,[114] V. Del Favero,[75] F. De Lillo,[115] D. Dell'Aquila,[164,130] W. Del Pozzo,[77,20] F. De Marco,[60,107] F. De Matteis,[132,86] V. D'Emilio,[19] N. Demos,[30] T. Dent,[124] A. Depasse,[115] N. DePergola,[94] R. De Pietri,[167,168] R. De Rosa,[29,6] C. De Rossi,[52] R. De Simone,[150] A. Dhani,[1] S. Dhurandhar,[15] R. Diab,[40] M. C. Díaz,[161] M. Di Cesare,[29] G. Dideron,[169] N. A. Didio,[70] T. Dietrich,[1] L. Di Fiore,[6] C. Di Fronzo,[33] F. Di Giovanni,[135] M. Di Giovanni,[107,60] T. Di Girolamo,[29,6] D. Diksha,[32,31] A. Di Michele,[78] J. Ding,[63,170] S. Di Pace,[107,60] I. Di Palma,[107,60] F. Di Renzo,[153] Divyajyoti,[171] A. Dmitriev,[110] Z. Doctor,[71] E. Dohmen,[4] P. P. Doleva,[116] L. Donahue,[172] L. D'Onofrio,[60] F. Donovan,[30] K. L. Dooley,[19] T. Dooney,[68] S. Doravari,[15] O. Dorosh,[173] M. Drago,[107,60] J. C. Driggers,[4] Y. Drori,[2] J.-G. Ducoin,[174,63] L. Dunn,[129] U. Dupletsa,[39] D. D'Urso,[164,130] H. Duval,[175] P.-A. Duverne,[35] S. E. Dwyer,[4] C. Eassa,[4] M. Ebersold,[176,28] T. Eckhardt,[76] G. Eddolls,[26] B. Edelman,[69] T. B. Edo,[2] O. Edy,[122] A. Effler,[59] J. Eichholz,[12] H. Einsle,[44] M. Eisenmann,[22] R. A. Eisenstein,[30] A. Ejlli,[19] M. Emma,[55] E. Engelby,[50] A. J. Engl,[18] L. Errico,[29,6] R. C. Essick,[177] H. Estellés,[1] D. Estevez,[61] T. Etzel,[2] M. Evans,[30] T. Evstafyeva,[16] B. E. Ewing,[9] J. M. Ezquiaga,[125] F. Fabrizi,[57,58] F. Faedi,[58,57] V. Fafone,[132,86] S. Fairhurst,[19] P. C. Fan,[172] A. M. Farah,[125] B. Farr,[69] W. M. Farr,[178,179] G. Favaro,[80] M. Favata,[180] M. Fays,[111] M. Fazio,[90] J. Feicht,[2] M. M. Fejer,[18] E. Fenyvesi,[74,181] D. L. Ferguson,[147] I. Ferrante,[77,20] T. A. Ferreira,[11] F. Fidecaro,[77,20] A. Fiori,[20,77] I. Fiori,[52] M. Fishbach,[177] R. P. Fisher,[116] R. Fittipaldi,[182,105] V. Fiumara,[183,105] R. Flaminio,[28] S. M. Fleischer,[184] L. S. Fleming,[185] E. Floden,[89] E. M. Foley,[89] H. Fong,[138] J. A. Font,[135,136] B. Fornal,[186] P. W. F. Forsyth,[12] K. Franceschetti,[167] N. Franchini,[63] S. Frasca,[107,60] F. Frasconi,[20] A. Frattale Mascioli,[107,60] Z. Frei,[187] A. Freise,[32,99] O. Freitas,[188,135] R. Frey,[69] W. Frischhertz,[59] V. V. Frolov,[59] G. G. Fronzé,[25] M. Fuentes-Garcia,[2] S. Fujii,[152] I. Fukunaga,[189] P. Fulda,[40] M. Fyffe,[59] W. E. Gabella,[190] B. Gadre,[68] J. R. Gair,[1] S. Galaudage,[8,191] S. Gallardo,[192] B. Gallego,[192] R. Gamba,[93] A. Gamboa,[1] D. Ganapathy,[30] A. Ganguly,[15] S. G. Gaonkar,[15] B. Garaventa,[51,193] J. Garcia-Bellido,[112] C. García-Núñez,[185] C. García-Quirós,[176] J. W. Gardner,[12] K. A. Gardner,[138] J. Gargiulo,[52] A. Garron,[91] F. Garufi,[29,6] C. Gasbarra,[132,86] B. Gateley,[4] V. Gayathri,[10] G. Gemme,[51] A. Gennai,[20] J. George,[95] R. George,[147] O. Gerberding,[76] L. Gergely,[194] N. Ghadiri,[50] Archisman Ghosh,[84] Shaon Ghosh,[180] Shrobana Ghosh,[13,14] Suprovo Ghosh,[15] Tathagata Ghosh,[15] L. Giacoppo,[107,60] J. A. Giaime,[11,59] K. D. Giardina,[59] D. R. Gibson,[185] D. T. Gibson,[16] C. Gier,[90] P. Giri,[20,77] F. Gissi,[87] S. Gkaitatzis,[77,20] J. Glanzer,[11] A. E. Gleckl,[50] F. Glotin,[35] J. Godfrey,[69] P. Godwin,[2] N. L. Goebbels,[76] E. Goetz,[138] J. Golomb,[2] S. Gomez Lopez,[107,60] B. Goncharov,[39] G. González,[11] P. Goodarzi,[126] A. W. Goodwin-Jones,[27] M. Gosselin,[52] A. S. Göttel,[19] R. Gouaty,[28] D. W. Gould,[12] S. Goyal,[21] B. Grace,[12] A. Grado,[195,6] V. Graham,[26] A. E. Granados,[89] M. Granata,[166] V. Granata,[62] L. Granda Argianas,[94] S. Gras,[30] P. Grassia,[2] C. Gray,[4] R. Gray,[26] G. Greco,[46] A. C. Green,[32,99] S. M. Green,[122] S. R. Green,[1] A. M. Gretarsson,[43] E. M. Gretarsson,[43] D. Griffith,[2] W. L. Griffiths,[19] H. L. Griggs,[53] G. Grignani,[78,46] A. Grimaldi,[102,103] C. Grimaud,[28] H. Grote,[19] A. S. Gruson,[50] D. Guerra,[135] D. Guetta,[196,60] G. M. Guidi,[57,58] A. R. Guimaraes,[11] H. K. Gulati,[83] F. Gulminelli,[197,198] A. M. Gunny,[30] H. Guo,[186] W. Guo,[27] Y. Guo,[32,31] Anchal Gupta,[2] Anuradha Gupta,[199] Ish Gupta,[9] N. C. Gupta,[83] P. Gupta,[32,68] S. K. Gupta,[40] T. Gupta,[82] N. Gupte,[1] R. Gurav,[126] J. Gurs,[76] N. Gutierrez,[166] F. Guzman,[128] D. Haba,[3] M. Haberland,[1] L. Haegel,[63] G. Hain,[116] S. Haino,[200] E. D. Hall,[30] E. Z. Hamilton,[176] G. Hammond,[26] W.-B. Han,[201] M. Haney,[176,32] J. Hanks,[4] C. Hanna,[9] M. D. Hannam,[19] O. A. Hannuksela,[137] A. G. Hanselman,[125] H. Hansen,[4] J. Hanson,[59] R. Harada,[36] T. Harder,[44] K. Haris,[32,68] T. Harmark,[131] J. Harms,[39,113] G. M. Harry,[202] I. W. Harry,[122] B. Haskell,[85] C.-J. Haster,[203] J. S. Hathaway,[204] K. Haughian,[26] H. Hayakawa,[45] K. Hayama,[205] J. Healy,[204] A. Heffernan,[91] A. Heidmann,[114] M. C. Heintze,[59] J. Heinze,[110] J. Heinzel,[30] H. Heitmann,[44] F. Hellman,[206] P. Hello,[35] A. F. Helmling-Cornell,[69] G. Hemming,[52] M. Hendry,[26] I. S. Heng,[26] E. Hennes,[32] J.-S. Hennig,[31,32] M. Hennig,[31,32] C. Henshaw,[53] A. Hernandez,[180] T. Hertog,[101] M. Heurs,[13,14] A. L. Hewitt,[16,207] S. Higginbotham,[19] S. Hild,[31,32] P. Hill,[90] S. Hill,[26] Y. Himemoto,[208] A. S. Hines,[128] N. Hirata,[22] C. Hirose,[209] J. Ho,[142] S. Hoang,[35] S. Hochheim,[13,14] D. Hofman,[166] N. A. Holland,[32,99] K. Holley-Bockelmann,[190]

I. J. Hollows,[165] Z. J. Holmes,[88] D. E. Holz,[125] C. Hong,[18] J. Hornung,[69] S. Hoshino,[209] S. Hourihane,[2] E. J. Howell,[27] C. G. Hoy,[122] D. Hoyland,[110] C. A. Hrishikesh,[132] H.-F. Hsieh,[141] C. Hsiung,[210] H. C. Hsu,[142] S.-C. Hsu,[48,141] W.-F. Hsu,[101] P. Hu,[190] Q. Hu,[26] H. Y. Huang,[142] Y.-J. Huang,[9] Y. Huang,[30] Y. T. Huang,[48] A. D. Huddart,[211] B. Hughey,[43] D. C. Y. Hui,[212] V. Hui,[28] R. Hur,[69] S. Husa,[91] R. Huxford,[9] T. Huynh-Dinh,[59] A. Iakovlev,[213] G. A. Iandolo,[31] A. Iess,[163,20] K. Inayoshi,[214] Y. Inoue,[142] G. Iorio,[80] J. Irwin,[26] M. Isi,[178,179] M. A. Ismail,[142] Y. Itoh,[189,215] M. Iwaya,[152] B. R. Iyer,[21] V. JaberianHamedan,[27] P.-E. Jacquet,[114] S. J. Jadhav,[216] S. P. Jadhav,[155] T. Jain,[16] A. L. James,[19] P. A. James,[116] R. Jamshidi,[33] A. Z. Jan,[147] K. Jani,[190] L. Janiurek,[26] J. Janquart,[68,32] K. Janssens,[106,44] N. N. Janthalur,[216] S. Jaraba,[112] P. Jaranowski,[217] P. Jasal,[37] R. Jaume,[91] W. Javed,[19] A. Jennings,[4] W. Jia,[30] J. Jiang,[40] H.-B. Jin,[218,219] K. Johansmeyer,[180] G. R. Johns,[116] N. A. Johnson,[40] R. Johnston,[26] N. Johny,[13,14] D. H. Jones,[12] D. I. Jones,[220] R. Jones,[26] S. Jose,[171] P. Joshi,[9] L. Ju,[27] K. Jung,[221] J. Junker,[13,14] V. Juste,[61] T. Kajita,[222] C. Kalaghatgi,[68,32,223] V. Kalogera,[71] M. Kamiizumi,[45] N. Kanda,[215,189] S. Kandhasamy,[15] G. Kang,[224] J. B. Kanner,[2] S. J. Kapadia,[15] D. P. Kapasi,[12] S. Karat,[2] C. Karathanasis,[38] S. Karki,[97] R. Kashyap,[9] M. Kasprzack,[2] W. Kastaun,[13,14] J. Kato,[151] T. Kato,[152] S. Katsanevas,[52,*] E. Katsavounidis,[30] W. Katzman,[59] T. Kaur,[27] R. Kaushik,[95] K. Kawabe,[4] D. Keitel,[91] J. Kelley-Derzon,[40] J. Kennington,[9] R. Kesharwani,[15] J. S. Key,[225] S. Khadka,[18] F. Y. Khalili,[100] F. Khan,[13,14] I. Khan,[226,34] T. Khanam,[158] E. A. Khazanov,[213] M. Khursheed,[95] W. Kiendrebeogo,[44,227] N. Kijbunchoo,[88] C. Kim,[228] J. C. Kim,[229] K. Kim,[230] M. H. Kim,[231] S. Kim,[212] W. S. Kim,[232] Y.-M. Kim,[230] C. Kimball,[71] N. Kimura,[45] M. Kinley-Hanlon,[26] M. Kinnear,[19] J. S. Kissel,[4] T. Kiyota,[189] S. Klimenko,[40] T. Klinger,[19] A. M. Knee,[138] N. Knust,[13,14] P. Koch,[13,14] S. M. Koehlenbeck,[18] G. Koekoek,[32,31] K. Kohri,[233] K. Kokeyama,[19] S. Koley,[39] P. Kolitsidou,[110] M. Kolstein,[38] K. Komori,[36] A. K. H. Kong,[141] A. Kontos,[234] M. Korobko,[76] R. V. Kossak,[13,14] X. Kou,[89] A. Koushik,[106] N. Kouvatsos,[64] M. Kovalam,[27] N. Koyama,[209] D. B. Kozak,[2] S. L. Kranzhoff,[31,32] V. Kringel,[13,14] N. V. Krishnendu,[21] A. Królak,[235,173] G. Kuehn,[13,14] P. Kuijer,[32] S. Kulkarni,[199] A. Kulur Ramamohan,[12] A. Kumar,[216] Praveen Kumar,[124] Prayush Kumar,[21] Rahul Kumar,[4] Rakesh Kumar,[83] J. Kume,[80,81,36] K. Kuns,[30] S. Kuroyanagi,[112,236] S. Kuwahara,[36] K. Kwak,[221] K. Kwan,[12] G. Lacaille,[26] P. Lagabbe,[28] D. Laghi,[121] S. Lai,[145] A. H. Laity,[160] M. H. Lakkis,[33] E. Lalande,[237] M. Lalleman,[106] M. Landry,[4] B. B. Lane,[30] R. N. Lang,[30] J. Lange,[147] B. Lantz,[18] A. La Rana,[60] I. La Rosa,[91,107,28] A. Lartaux-Vollard,[35] P. D. Lasky,[8] J. Lawrence,[158] M. Laxen,[59] A. Lazzarini,[2] C. Lazzaro,[80,81] P. Leaci,[107,60] S. LeBohec,[186] Y. K. Lecoeuche,[138] H. M. Lee,[229] H. W. Lee,[238] K. Lee,[231] R.-K. Lee,[141] R. Lee,[30] S. Lee,[230] Y. Lee,[142] I. N. Legred,[2] J. Lehmann,[13,14] L. Lehner,[169] A. Lemaître,[239] M. Lenti,[58,240] M. Leonardi,[241,22] E. Leonova,[96] M. Lequime,[34] N. Leroy,[35] M. Lesovsky,[2] N. Letendre,[28] M. Lethuillier,[153] C. Levesque,[237] Y. Levin,[8] K. Leyde,[63] A. K. Y. Li,[2] K. L. Li,[140] T. G. F. Li,[137,101] X. Li,[148] Chien-Yu Lin,[142,141] Chun-Yu Lin,[242] E. T. Lin,[141] F. Lin,[142] H. Lin,[142] L. C.-C. Lin,[140] F. Linde,[223,32] S. D. Linker,[133,192] T. B. Littenberg,[243] A. Liu,[137] G. C. Liu,[210] Jian Liu,[27] F. Llamas,[161] J. Llobera-Querol,[91] R. K. L. Lo,[2] J.-P. Locquet,[101] L. London,[96] A. Longo,[57,58] D. Lopez,[176] M. Lopez Portilla,[68] M. Lorenzini,[132,86] V. Loriette,[35] M. Lormand,[59] G. Losurdo,[20] T. P. Lott IV,[53] J. D. Lough,[13,14] H. A. Loughlin,[30] C. O. Lousto,[204] M. J. Lowry,[116] H. Lück,[14,13,14] D. Lumaca,[86] A. P. Lundgren,[122] A. W. Lussier,[237] L.-T. Ma,[141] S. Ma,[148] M. Ma'arif,[142] R. Macas,[122] M. MacInnis,[30] R. R. Maciy,[13,14] D. M. Macleod,[19] I. A. O. MacMillan,[2] A. Macquet,[38] D. Macri,[30] K. Maeda,[151] S. Maenaut,[101] I. Magaña Hernandez,[10] S. S. Magare,[15] C. Magazzù,[20] R. M. Magee,[2] E. Maggio,[1] R. Maggiore,[32,99] M. Magnozzi,[51,193] M. Mahesh,[76] S. Mahesh,[244] M. Maini,[160] S. Majhi,[15] E. Majorana,[107,60] C. N. Makarem,[2] J. A. Malaquias-Reis,[17] S. Maliakal,[2] A. Malik,[95] N. Man,[44] V. Mandic,[89] V. Mangano,[60,107] B. Mannix,[69] G. L. Mansell,[70,30] M. Manske,[10] M. Mantovani,[52] M. Mapelli,[80,81] F. Marchesoni,[47,46,245] D. Marín Pina,[37,72,246] F. Marion,[28] S. Márka,[159] Z. Márka,[159] C. Markakis,[144] A. S. Markosyan,[18] A. Markowitz,[2] E. Maros,[2] A. Marquina,[157] S. Marsat,[121] F. Martelli,[57,58] I. W. Martin,[26] R. M. Martin,[180] B. B. Martinez,[128] M. Martinez,[38,247] V. Martinez,[123] A. Martini,[102] K. Martinovic,[64] J. C. Martins,[17] D. V. Martynov,[110] E. J. Marx,[30] L. Massaro,[31,32] A. Masserot,[28] M. Masso-Reid,[26] M. Mastrodicasa,[60] S. Mastrogiovanni,[60] M. Mateu-Lucena,[91] M. Matiushechkina,[13,14] M. Matsuyama,[189] N. Mavalvala,[30] N. Maxwell,[4] G. McCarrol,[59] R. McCarthy,[4] D. E. McClelland,[12] S. McCormick,[59] L. McCuller,[2] G. I. McGhee,[26] K. B. M. McGowan,[190] M. Mchedlidze,[180] C. McIsaac,[122] J. McIver,[138] K. McKinney,[162] A. McLeod,[27] T. McRae,[12] S. T. McWilliams,[244] D. Meacher,[10] A. K. Mehta,[1] Q. Meijer,[68] A. Melatos,[129] S. Mellaerts,[101] A. Menendez-Vazquez,[38] C. S. Menoni,[98] R. A. Mercer,[10] L. Mereni,[166] K. Merfeld,[69] E. L. Merilh,[59] J. R. Mérou,[91] J. D. Merritt,[69] M. Merzougui,[44]

C. Messenger,[26] C. Messick,[10] M. Meyer-Conde,[189] F. Meylahn,[13,14] A. Mhaske,[15] A. Miani,[102,103] H. Miao,[248] I. Michaloliakos,[40] C. Michel,[166] Y. Michimura,[2,36] H. Middleton,[110] A. L. Miller,[32] S. Miller,[2] M. Millhouse,[53] E. Milotti,[249,42] Y. Minenkov,[86] N. Mio,[250] Ll. M. Mir,[38] L. Mirasola,[251,60] M. Miravet-Tenés,[135] C.-A. Miritescu,[38] A. K. Mishra,[21] A. Mishra,[15] C. Mishra,[171] T. Mishra,[40] A. L. Mitchell,[32,99] J. G. Mitchell,[43] S. Mitra,[15] V. P. Mitrofanov,[100] G. Mitselmakher,[40] R. Mittleman,[30] O. Miyakawa,[45] S. Miyamoto,[152] S. Miyoki,[45] G. Mo,[30] L. Mobilia,[57,58] L. M. Modafferi,[91] S. R. P. Mohapatra,[2] S. R. Mohite,[10] M. Molina-Ruiz,[206] C. Mondal,[197] M. Mondin,[192] M. Montani,[57,58] C. J. Moore,[110] M. Morales,[50] D. Moraru,[4] F. Morawski,[85] A. More,[15] S. More,[15] C. Moreno,[43] G. Moreno,[4] S. Morisaki,[36,152] Y. Moriwaki,[151] G. Morras,[112] A. Moscatello,[80] P. Mourier,[91] B. Mours,[61] C. M. Mow-Lowry,[32,99] S. Mozzon,[122] F. Muciaccia,[107,60] D. Mukherjee,[243] Samanwaya Mukherjee,[15] Soma Mukherjee,[161] Subroto Mukherjee,[83] Suvodip Mukherjee,[252,169,96] N. Mukund,[30] A. Mullavey,[59] J. Munch,[88] C. L. Mungioli,[27] M. Munn,[4] W. R. Munn Oberg,[253] M. Murakoshi,[254] P. G. Murray,[26] S. Muusse,[12] S. L. Nadji,[13,14] A. Nagar,[25,255] N. Nagarajan,[26] K. N. Nagler,[43] K. Nakamura,[22] H. Nakano,[256] M. Nakano,[2] D. Nandi,[11] V. Napolano,[52] P. Narayan,[199] I. Nardecchia,[132,86] H. Narola,[68] L. Naticchioni,[60] R. K. Nayak,[257] B. F. Neil,[27] J. Neilson,[87,105] A. Nelson,[128] T. J. N. Nelson,[59] M. Nery,[13,14] A. Neunzert,[4] S. Ng,[50] C. Nguyen,[63] P. Nguyen,[69] L. Nguyen Quynh,[258] S. A. Nichols,[11] A. B. Nielsen,[259] G. Nieradka,[85] A. Niko,[142] Y. Nishino,[22,260] A. Nishizawa,[36] S. Nissanke,[96,32] E. Nitoglia,[153] W. Niu,[9] F. Nocera,[52] M. Norman,[19] C. North,[19] J. Novak,[108,261,262,263] J. F. Nuño Siles,[112] G. Nurbek,[161] L. K. Nuttall,[122] K. Obayashi,[254] J. Oberling,[4] J. O'Dell,[211] M. Oertel,[108,261,262,264,263] A. Offermans,[101] G. Oganesyan,[39,113] J. J. Oh,[232] K. Oh,[212] S. H. Oh,[232] T. O'Hanlon,[59] M. Ohashi,[45] M. Ohkawa,[209] F. Ohme,[13,14] H. Ohta,[36] A. S. Oliveira,[159] R. Oliveri,[108,261,262] V. Oloworaran,[27] B. O'Neal,[116] K. Oohara,[265,266] B. O'Reilly,[59] N. D. Ormsby,[116] M. Orselli,[46,78] R. O'Shaughnessy,[204] Y. Oshima,[267] S. Oshino,[45] S. Ossokine,[1] C. Osthelder,[2] D. J. Ottaway,[88] A. Ouzriat,[153] H. Overmier,[59] B. J. Owen,[158] A. E. Pace,[9] R. Pagano,[11] M. A. Page,[22] A. Pai,[139] S. A. Pai,[95] A. Pal,[268] S. Pal,[257] M. A. Palaia,[20,77] O. Palashov,[213] M. Pálfi,[187] P. P. Palma,[132,86] C. Palomba,[60] K. C. Pan,[141] P. K. Panda,[216] L. Panebianco,[57,58] P. T. H. Pang,[32,68] F. Pannarale,[107,60] B. C. Pant,[95] F. H. Panther,[27] C. D. Panzer,[89] F. Paoletti,[20] A. Paoli,[52] A. Paolone,[60,269] E. E. Papalexakis,[126] L. Papalini,[20,77] G. Papigkiotis,[270] A. Parisi,[32,96] J. Park,[230] W. Parker,[59] G. Pascale,[13,14] D. Pascucci,[84] A. Pasqualetti,[52] R. Passaquieti,[77,20] D. Passuello,[20] O. Patane,[4] M. Patel,[116] D. Pathak,[15] M. Pathak,[88] A. Patra,[19] B. Patricelli,[77,20] A. S. Patron,[11] S. Paul,[69] E. Payne,[2] T. Pearce,[19] M. Pedraza,[2] R. Pegna,[20] A. Pele,[2] F. E. Peña Arellano,[45] S. Penn,[253] M. D. Penuliar,[50] A. Perego,[102,103] A. Pereira,[123] J. J. Perez,[40] C. Périgois,[154,81,80] C. C. Perkins,[40] G. Perna,[80] A. Perreca,[102,103] J. Perret,[63] S. Perriès,[153] J. W. Perry,[32,99] D. Pesios,[270] C. Petrillo,[78] H. P. Pfeiffer,[1] H. Pham,[59] K. A. Pham,[89] K. S. Phukon,[110,32,223] H. Phurailatpam,[137] O. J. Piccinni,[38] M. Pichot,[44] M. Piendibene,[77,20] F. Piergiovanni,[57,58] L. Pierini,[60] G. Pierra,[153] V. Pierro,[87,105] M. Pietrzak,[85] M. Pillas,[35] F. Pilo,[20] L. Pinard,[166] C. Pineda-Bosque,[192] I. M. Pinto,[87,105,271,29] M. Pinto,[52] B. J. Piotrzkowski,[10] M. Pirello,[4] M. D. Pitkin,[16,207] A. Placidi,[46,78] E. Placidi,[107,60] M. L. Planas,[91] W. Plastino,[272,273] R. Poggiani,[77,20] E. Polini,[28] L. Pompili,[1] J. Poon,[137] E. Porcelli,[32] J. Portell,[37,72,246] E. K. Porter,[63] C. Posnansky,[9] R. Poulton,[52] J. Powell,[155] M. Pracchia,[28] B. K. Pradhan,[15] T. Pradier,[61] A. K. Prajapati,[83] K. Prasai,[18] R. Prasanna,[216] P. Prasia,[15] G. Pratten,[110] M. Principe,[133,87,271,105] G. A. Prodi,[274,103] L. Prokhorov,[110] P. Prosposito,[132,86] L. Prudenzi,[1] A. Puecher,[32,68] J. Pullin,[11] M. Punturo,[46] F. Puosi,[20,77] P. Puppo,[60] M. Pürrer,[160] H. Qi,[144] J. Qin,[12] G. Quéméner,[198,108,197] V. Quetschke,[161] C. Quigley,[19] P. J. Quinonez,[43] R. Quitzow-James,[97] F. J. Raab,[4] G. Raaijmakers,[96,32] N. Radulesco,[44] P. Raffai,[187] S. X. Rail,[237] S. Raja,[95] C. Rajan,[95] B. Rajbhandari,[204,158] D. S. Ramirez,[43] K. E. Ramirez,[59] F. A. Ramis Vidal,[91] A. Ramos-Buades,[1] D. Rana,[15] E. Randel,[98] S. Ranjan,[53] P. Rapagnani,[107,60] B. Ratto,[43] S. Rawat,[89] A. Ray,[10] V. Raymond,[19] M. Razzano,[77,20] J. Read,[50] M. Recaman Payo,[101] T. Regimbau,[28] L. Rei,[51] S. Reid,[90] S. W. Reid,[116] D. H. Reitze,[2] P. Relton,[19] A. Renzini,[2] P. Rettegno,[25] B. Revenu,[63,275] A. Reza,[32] M. Rezac,[50] A. S. Rezaei,[60,107] F. Ricci,[107,60] M. Ricci,[60] D. Richards,[211] C. J. Richardson,[43] J. W. Richardson,[126] A. Rijal,[43] K. Riles,[79] H. K. Riley,[19] S. Rinaldi,[77,20] J. Rittmeyer,[76] C. Robertson,[211] F. Robinet,[35] M. Robinson,[4] A. Rocchi,[86] L. Rolland,[28] J. G. Rollins,[2] M. Romanelli,[109] A. E. Romano,[276] R. Romano,[5,6] A. Romero,[175] I. M. Romero-Shaw,[16] J. H. Romie,[59] S. Ronchini,[39,113] T. J. Roocke,[88] L. Rosa,[6,29] T. J. Rosauer,[126] C. A. Rose,[10] D. Rosińska,[117] M. P. Ross,[48] M. Rossello,[91] S. Rowan,[26] S. K. Roy,[178,179] S. Roy,[68] D. Rozza,[164,130] P. Ruggi,[52] E. Ruiz Morales,[277,112] K. Ruiz-Rocha,[190] S. Sachdev,[53] T. Sadecki,[4] J. Sadiq,[124] P. Saffarieh,[32,99] M. R. Sah,[252] S. S. Saha,[141] T. Sainrat,[61]

S. Sajith Menon,[196,107,60] K. Sakai,[278] M. Sakellariadou,[64] T. Sako,[151] S. Sakon,[9] O. S. Salafia,[156,120,119] F. Salces-Carcoba,[2] L. Salconi,[52] M. Saleem,[89] F. Salemi,[107,60] M. Sallé,[32] S. Salvador,[198,197,108] A. Sanchez,[4] E. J. Sanchez,[2] J. H. Sanchez,[71] L. E. Sanchez,[2] N. Sanchis-Gual,[279,135] J. R. Sanders,[280] E. M. Sänger,[1] T. R. Saravanan,[15] N. Sarin,[8] A. Sasli,[270] P. Sassi,[46,78] B. Sassolas,[166] H. Satari,[27] R. Sato,[209] S. Sato,[151] Y. Sato,[151] O. Sauter,[40] R. L. Savage,[4] T. Sawada,[45] H. L. Sawant,[15] S. Sayah,[28] D. Schaetzl,[2] M. Scheel,[148] J. Scheuer,[71] M. G. Schiworski,[88] P. Schmidt,[110] S. Schmidt,[68] R. Schnabel,[76] M. Schneewind,[13,14] R. M. S. Schofield,[69] K. Schouteden,[101] H. Schuler,[9] B. W. Schulte,[13,14] B. F. Schutz,[19,13,14] E. Schwartz,[19] J. Scott,[26] S. M. Scott,[12] T. C. Seetharamu,[26] M. Seglar-Arroyo,[38] Y. Sekiguchi,[281] D. Sellers,[59] A. S. Sengupta,[282] D. Sentenac,[52] E. G. Seo,[26] J. W. Seo,[101] V. Sequino,[29,6] A. Sergeev,[213] M. Serra,[60] G. Servignat,[261] Y. Setyawati,[68] T. Shaffer,[4] U. S. Shah,[53] M. S. Shahriar,[71] M. A. Shaikh,[229] B. Shams,[186] L. Shao,[214] A. K. Sharma,[21] P. Sharma,[95] S. Sharma-Chaudhary,[97] P. Shawhan,[118] N. S. Shcheblanov,[283,239] B. Shen,[118] Y. Shikano,[284,285] M. Shikauchi,[36] K. Shimode,[45] H. Shinkai,[286] J. Shiota,[254] D. H. Shoemaker,[30] D. M. Shoemaker,[147] R. W. Short,[4] S. ShyamSundar,[95] A. Sider,[33] H. Siegel,[159,178,179] M. Sieniawska,[115] D. Sigg,[4] L. Silenzi,[46,47] M. Simmonds,[88] L. P. Singer,[75] A. Singh,[199] D. Singh,[9] M. K. Singh,[21] A. Singha,[31,32] A. M. Sintes,[91] V. Sipala,[164,130] V. Skliris,[19] B. J. J. Slagmolen,[12] T. J. Slaven-Blair,[27] J. Smetana,[110] J. R. Smith,[50] L. Smith,[26] R. J. E. Smith,[8] W. J. Smith,[190] J. Soldateschi,[240,287,58] S. N. Somala,[288] K. Somiya,[3] K. Soni,[15] S. Soni,[30] V. Sordini,[153] F. Sorrentino,[51] N. Sorrentino,[77,20] R. Soulard,[44] T. Souradeep,[15,289] A. Southgate,[19] E. Sowell,[158] V. Spagnuolo,[31,32] A. P. Spencer,[26] M. Spera,[80,81] P. Spinicelli,[52] A. K. Srivastava,[83] F. Stachurski,[26] D. A. Steer,[63] J. Steinlechner,[31,32] S. Steinlechner,[31,32] N. Stergioulas,[270] P. Stevens,[35] M. StPierre,[160] L. C. Strang,[129] G. Stratta,[290,291,60,292] M. D. Strong,[11] A. Strunk,[4] R. Sturani,[293] A. L. Stuver,[94] M. Suchenek,[85] S. Sudhagar,[15,85] N. Sueltmann,[76] A. G. Sullivan,[159] K. D. Sullivan,[11] L. Sun,[12] S. Sunil,[83] A. Sur,[85] J. Suresh,[36,115] P. J. Sutton,[19] Takamasa Suzuki,[209] Takanori Suzuki,[3] B. L. Swinkels,[32] A. Syx,[61] M. J. Szczepańczyk,[40] P. Szewczyk,[117] M. Tacca,[32] H. Tagoshi,[152] S. C. Tait,[26] H. Takahashi,[294] R. Takahashi,[22] A. Takamori,[49] K. Takatani,[189] H. Takeda,[295] M. Takeda,[189] C. J. Talbot,[90] C. Talbot,[30] M. Tamaki,[152] N. Tamanini,[121] D. Tanabe,[142] K. Tanaka,[296] S. J. Tanaka,[254] T. Tanaka,[295] A. J. Tanasijczuk,[115] D. Tang,[27] S. Tanioka,[70] D. B. Tanner,[40] L. Tao,[40] R. D. Tapia,[9] E. N. Tapia San Martín,[32] R. Tarafder,[2] C. Taranto,[132,86] A. Taruya,[297] J. D. Tasson,[172] M. Teloi,[33] R. Tenorio,[91] H. Themann,[192] A. Theodoropoulos,[135] M. P. Thirugnanasambandam,[15] L. M. Thomas,[110] M. Thomas,[59] P. Thomas,[4] J. E. Thompson,[148] S. R. Thondapu,[95] K. A. Thorne,[59] E. Thrane,[8] J. Tissino,[39] A. Tiwari,[15] Shubhanshu Tiwari,[176] Srishti Tiwari,[15] V. Tiwari,[110] M. R. Todd,[70] A. M. Toivonen,[89] K. Toland,[26] A. E. Tolley,[122] T. Tomaru,[22] K. Tomita,[189] T. Tomura,[45] C. Tong-Yu,[142] A. Toriyama,[254] N. Toropov,[110] A. Torres-Forné,[135,136] C. I. Torrie,[2] M. Toscani,[121] I. Tosta e Melo,[298] E. Tournefier,[28] A. A. Trani,[36] A. Trapananti,[47,46] F. Travasso,[47,46] G. Traylor,[59] J. Trenado,[37] M. Trevor,[118] M. C. Tringali,[52] A. Tripathee,[79] L. Troiano,[299,105] A. Trovato,[42,249] L. Trozzo,[6] R. J. Trudeau,[2] T. T. L. Tsang,[19] R. Tso,[148,†] S. Tsuchida,[300] L. Tsukada,[9] T. Tsutsui,[36] K. Turbang,[175,106] M. Turconi,[44] C. Turski,[84] H. Ubach,[37,72] A. S. Ubhi,[110] T. Uchiyama,[45] R. P. Udall,[2] T. Uehara,[301] K. Ueno,[36] C. S. Unnikrishnan,[252] T. Ushiba,[45] A. Utina,[31,32] M. Vacatello,[20,77] H. Vahlbruch,[13,14] N. Vaidya,[2] G. Vajente,[2] A. Vajpeyi,[8] G. Valdes,[128] J. Valencia,[91] M. Valentini,[99,32] S. A. Vallejo-Peña,[276] S. Vallero,[25] V. Valsan,[10] N. van Bakel,[32] M. van Beuzekom,[32] M. van Dael,[32,302] J. F. J. van den Brand,[31,99,32] C. Van Den Broeck,[68,32] D. C. Vander-Hyde,[70] M. van der Sluys,[32,68] A. Van de Walle,[35] J. van Dongen,[32,99] K. Vandra,[94] H. van Haevermaet,[106] J. V. van Heijningen,[115] J. Vanosky,[2] M. H. P. M. van Putten,[303] Z. van Ranst,[31,32] N. van Remortel,[106] M. Vardaro,[31,32] A. F. Vargas,[129] V. Varma,[1] M. Vasúth,[74] A. Vecchio,[110] G. Vedovato,[81] J. Veitch,[26] P. J. Veitch,[88] S. Venikoudis,[115] J. Venneberg,[13,14] P. Verdier,[153] D. Verkindt,[28] B. Verma,[134] P. Verma,[173] Y. Verma,[95] S. M. Vermeulen,[2] D. Veske,[159] F. Vetrano,[57] A. Veutro,[60] A. M. Vibhute,[4] A. Viceré,[57,58] S. Vidyant,[70] A. D. Viets,[304] A. Vijaykumar,[21] A. Vilkha,[204] V. Villa-Ortega,[124] E. T. Vincent,[53] J.-Y. Vinet,[44] S. Viret,[153] A. Virtuoso,[249,42] S. Vitale,[30] H. Vocca,[78,46] D. Voigt,[76] E. R. G. von Reis,[4] J. S. A. von Wrangel,[13,14] S. P. Vyatchanin,[100] L. E. Wade,[67] M. Wade,[67] K. J. Wagner,[204] R. C. Walet,[32] M. Walker,[116] G. S. Wallace,[90] L. Wallace,[2] H. Wang,[267] J. Z. Wang,[79] W. H. Wang,[161] Z. Wang,[142] G. Waratkar,[139] R. L. Ward,[12] J. Warner,[4] M. Was,[28] T. Washimi,[22] N. Y. Washington,[2] D. Watarai,[36] K. E. Wayt,[67] B. Weaver,[4] C. R. Weaving,[122] S. A. Webster,[26] M. Weinert,[13,14] A. J. Weinstein,[2] R. Weiss,[30] C. M. Weller,[48] R. A. Weller,[190] F. Wellmann,[13,14] L. Wen,[27] P. Weßels,[13,14] K. Wette,[12] J. T. Whelan,[204] D. D. White,[50] B. F. Whiting,[40] C. Whittle,[30] J. B. Wildberger,[1] O. S. Wilk,[67]

D. Wilken,[13,14,14] K. Willetts,[19] D. Williams,[26] M. J. Williams,[26] N. S. Williams,[110] J. L. Willis,[2] B. Willke,[14,13,14] M. Wils,[101] C. C. Wipf,[2] G. Woan,[26] J. Woehler,[31,32] J. K. Wofford,[204] N. E. Wolfe,[30] D. Wong,[138] H. T. Wong,[142] H. W. Y. Wong,[137] I. C. F. Wong,[137] J. L. Wright,[12] M. Wright,[26] C. Wu,[141] D. S. Wu,[13,14] H. Wu,[141] D. M. Wysocki,[10] L. Xiao,[2] V. A. Xu,[30] Y. Xu,[176] N. Yadav,[85] H. Yamamoto,[2] K. Yamamoto,[151] M. Yamamoto,[151] T. S. Yamamoto,[236] T. Yamamoto,[45] S. Yamamura,[152] R. Yamazaki,[254] S. Yan,[18] T. Yan,[110] F. W. Yang,[186] F. Yang,[159] K. Z. Yang,[89] L.-C. Yang,[145] Y. Yang,[145] Z. Yarbrough,[11] S.-W. Yeh,[141] A. B. Yelikar,[204] S. M. C. Yeung,[10] X. Yin,[30] J. Yokoyama,[36] T. Yokozawa,[45] J. Yoo,[149] H. Yu,[148] H. Yuzurihara,[45] A. Zadrożny,[173] A. J. Zannelli,[116] M. Zanolin,[43] M. Zeeshan,[204] T. Zelenova,[52] J.-P. Zendri,[81] M. Zeoli,[111,115] M. Zerrad,[34,226] M. Zevin,[71] A. C. Zhang,[159] J. Zhang,[12] L. Zhang,[2] R. Zhang,[40] T. Zhang,[110] Y. Zhang,[12] C. Zhao,[27] Yue Zhao,[186] Yuhang Zhao,[152,22,63] Y. Zheng,[97] H. Zhong,[89] S. Zhong,[27] R. Zhou,[206] Z.-H. Zhu,[127,305] M. E. Zucker,[30,2] and J. Zweizig[2]

(The LIGO Scientific Collaboration, the Virgo Collaboration, and the KAGRA Collaboration)

T. Fujimori,[189] H. Fujimoto,[267] T. Fujita,[306,36] Y. Manita,[295] I. Obata,[307] and H. Takidera[267]

[1] *Max Planck Institute for Gravitational Physics (Albert Einstein Institute), D-14476 Potsdam, Germany*
[2] *LIGO Laboratory, California Institute of Technology, Pasadena, CA 91125, USA*
[3] *Graduate School of Science, Tokyo Institute of Technology, 2-12-1 Ookayama, Meguro-ku, Tokyo 152-8551, Japan*
[4] *LIGO Hanford Observatory, Richland, WA 99352, USA*
[5] *Dipartimento di Farmacia, Università di Salerno, I-84084 Fisciano, Salerno, Italy*
[6] *INFN, Sezione di Napoli, I-80126 Napoli, Italy*
[7] *University of Warwick, Coventry CV4 7AL, United Kingdom*
[8] *OzGrav, School of Physics & Astronomy, Monash University, Clayton 3800, Victoria, Australia*
[9] *The Pennsylvania State University, University Park, PA 16802, USA*
[10] *University of Wisconsin-Milwaukee, Milwaukee, WI 53201, USA*
[11] *Louisiana State University, Baton Rouge, LA 70803, USA*
[12] *OzGrav, Australian National University, Canberra, Australian Capital Territory 0200, Australia*
[13] *Max Planck Institute for Gravitational Physics (Albert Einstein Institute), D-30167 Hannover, Germany*
[14] *Leibniz Universität Hannover, D-30167 Hannover, Germany*
[15] *Inter-University Centre for Astronomy and Astrophysics, Pune 411007, India*
[16] *University of Cambridge, Cambridge CB2 1TN, United Kingdom*
[17] *Instituto Nacional de Pesquisas Espaciais, 12227-010 São José dos Campos, São Paulo, Brazil*
[18] *Stanford University, Stanford, CA 94305, USA*
[19] *Cardiff University, Cardiff CF24 3AA, United Kingdom*
[20] *INFN, Sezione di Pisa, I-56127 Pisa, Italy*
[21] *International Centre for Theoretical Sciences, Tata Institute of Fundamental Research, Bengaluru 560089, India*
[22] *Gravitational Wave Science Project, National Astronomical Observatory of Japan, 2-21-1 Osawa, Mitaka City, Tokyo 181-8588, Japan*
[23] *Advanced Technology Center, National Astronomical Observatory of Japan, 2-21-1 Osawa, Mitaka City, Tokyo 181-8588, Japan*
[24] *Dipartimento di Fisica, Università degli Studi di Torino, I-10125 Torino, Italy*
[25] *INFN Sezione di Torino, I-10125 Torino, Italy*
[26] *SUPA, University of Glasgow, Glasgow G12 8QQ, United Kingdom*
[27] *OzGrav, University of Western Australia, Crawley, Western Australia 6009, Australia*
[28] *Univ. Savoie Mont Blanc, CNRS, Laboratoire d'Annecy de Physique des Particules - IN2P3, F-74000 Annecy, France*
[29] *Università di Napoli "Federico II", I-80126 Napoli, Italy*
[30] *LIGO Laboratory, Massachusetts Institute of Technology, Cambridge, MA 02139, USA*
[31] *Maastricht University, 6200 MD Maastricht, Netherlands*
[32] *Nikhef, 1098 XG Amsterdam, Netherlands*
[33] *Université Libre de Bruxelles, Brussels 1050, Belgium*
[34] *Institut Fresnel, Aix Marseille Université, CNRS, Centrale Marseille, F-13013 Marseille, France*
[35] *Université Paris-Saclay, CNRS/IN2P3, IJCLab, 91405 Orsay, France*
[36] *University of Tokyo, Tokyo, 113-0033, Japan.*
[37] *Institut de Ciències del Cosmos (ICCUB), Universitat de Barcelona (UB), c. Martí i Franquès, 1, 08028 Barcelona, Spain*
[38] *Institut de Física d'Altes Energies (IFAE), The Barcelona Institute of Science and Technology, Campus UAB, E-08193 Bellaterra (Barcelona), Spain*
[39] *Gran Sasso Science Institute (GSSI), I-67100 L'Aquila, Italy*
[40] *University of Florida, Gainesville, FL 32611, USA*
[41] *Dipartimento di Scienze Matematiche, Informatiche e Fisiche, Università di Udine, I-33100 Udine, Italy*
[42] *INFN, Sezione di Trieste, I-34127 Trieste, Italy*

[43] *Embry-Riddle Aeronautical University, Prescott, AZ 86301, USA*
[44] *Université Côte d'Azur, Observatoire de la Côte d'Azur, CNRS, Artemis, F-06304 Nice, France*
[45] *Institute for Cosmic Ray Research, KAGRA Observatory, The University of Tokyo, 238 Higashi-Mozumi, Kamioka-cho, Hida City, Gifu 506-1205, Japan*
[46] *INFN, Sezione di Perugia, I-06123 Perugia, Italy*
[47] *Università di Camerino, I-62032 Camerino, Italy*
[48] *University of Washington, Seattle, WA 98195, USA*
[49] *Earthquake Research Institute, The University of Tokyo, 1-1-1 Yayoi, Bunkyo-ku, Tokyo 113-0032, Japan*
[50] *California State University Fullerton, Fullerton, CA 92831, USA*
[51] *INFN, Sezione di Genova, I-16146 Genova, Italy*
[52] *European Gravitational Observatory (EGO), I-56021 Cascina, Pisa, Italy*
[53] *Georgia Institute of Technology, Atlanta, GA 30332, USA*
[54] *Chennai Mathematical Institute, Chennai 603103, India*
[55] *Royal Holloway, University of London, London TW20 0EX, United Kingdom*
[56] *The Graduate University for Advanced Studies (SOKENDAI), 2-21-1 Osawa, Mitaka City, Tokyo 181-8588, Japan*
[57] *Università degli Studi di Urbino "Carlo Bo", I-61029 Urbino, Italy*
[58] *INFN, Sezione di Firenze, I-50019 Sesto Fiorentino, Firenze, Italy*
[59] *LIGO Livingston Observatory, Livingston, LA 70754, USA*
[60] *INFN, Sezione di Roma, I-00185 Roma, Italy*
[61] *Université de Strasbourg, CNRS, IPHC UMR 7178, F-67000 Strasbourg, France*
[62] *Dipartimento di Fisica "E.R. Caianiello", Università di Salerno, I-84084 Fisciano, Salerno, Italy*
[63] *Université Paris Cité, CNRS, Astroparticule et Cosmologie, F-75013 Paris, France*
[64] *King's College London, University of London, London WC2R 2LS, United Kingdom*
[65] *Korea Institute of Science and Technology Information, Daejeon 34141, Republic of Korea*
[66] *Université libre de Bruxelles, 1050 Bruxelles, Belgium*
[67] *Kenyon College, Gambier, OH 43022, USA*
[68] *Institute for Gravitational and Subatomic Physics (GRASP), Utrecht University, 3584 CC Utrecht, Netherlands*
[69] *University of Oregon, Eugene, OR 97403, USA*
[70] *Syracuse University, Syracuse, NY 13244, USA*
[71] *Northwestern University, Evanston, IL 60208, USA*
[72] *Departament de Física Quàntica i Astrofísica (FQA), Universitat de Barcelona (UB), c. Martí i Franqués, 1, 08028 Barcelona, Spain*
[73] *Dipartimento di Medicina, Chirurgia e Odontoiatria "Scuola Medica Salernitana", Università di Salerno, I-84081 Baronissi, Salerno, Italy*
[74] *Wigner RCP, RMKI, H-1121 Budapest, Hungary*
[75] *NASA Goddard Space Flight Center, Greenbelt, MD 20771, USA*
[76] *Universität Hamburg, D-22761 Hamburg, Germany*
[77] *Università di Pisa, I-56127 Pisa, Italy*
[78] *Università di Perugia, I-06123 Perugia, Italy*
[79] *University of Michigan, Ann Arbor, MI 48109, USA*
[80] *Università di Padova, Dipartimento di Fisica e Astronomia, I-35131 Padova, Italy*
[81] *INFN, Sezione di Padova, I-35131 Padova, Italy*
[82] *Montana State University, Bozeman, MT 59717, USA*
[83] *Institute for Plasma Research, Bhat, Gandhinagar 382428, India*
[84] *Universiteit Gent, B-9000 Gent, Belgium*
[85] *Nicolaus Copernicus Astronomical Center, Polish Academy of Sciences, 00-716, Warsaw, Poland*
[86] *INFN, Sezione di Roma Tor Vergata, I-00133 Roma, Italy*
[87] *Dipartimento di Ingegneria, Università del Sannio, I-82100 Benevento, Italy*
[88] *OzGrav, University of Adelaide, Adelaide, South Australia 5005, Australia*
[89] *University of Minnesota, Minneapolis, MN 55455, USA*
[90] *SUPA, University of Strathclyde, Glasgow G1 1XQ, United Kingdom*
[91] *IAC3–IEEC, Universitat de les Illes Balears, E-07122 Palma de Mallorca, Spain*
[92] *Departamento de Matemáticas, Universitat Autònoma de Barcelona, 08193 Bellaterra (Barcelona), Spain*
[93] *Theoretisch-Physikalisches Institut, Friedrich-Schiller-Universität Jena, D-07743 Jena, Germany*
[94] *Villanova University, Villanova, PA 19085, USA*
[95] *RRCAT, Indore, Madhya Pradesh 452013, India*
[96] *GRAPPA, Anton Pannekoek Institute for Astronomy and Institute for High-Energy Physics, University of Amsterdam, 1098 XH Amsterdam, Netherlands*
[97] *Missouri University of Science and Technology, Rolla, MO 65409, USA*
[98] *Colorado State University, Fort Collins, CO 80523, USA*
[99] *Department of Physics and Astronomy, Vrije Universiteit Amsterdam, 1081 HV Amsterdam, Netherlands*

[100] *Lomonosov Moscow State University, Moscow 119991, Russia*
[101] *Katholieke Universiteit Leuven, Oude Markt 13, 3000 Leuven, Belgium*
[102] *Università di Trento, Dipartimento di Fisica, I-38123 Povo, Trento, Italy*
[103] *INFN, Trento Institute for Fundamental Physics and Applications, I-38123 Povo, Trento, Italy*
[104] *Bar-Ilan University, Ramat Gan, 5290002, Israel*
[105] *INFN, Sezione di Napoli, Gruppo Collegato di Salerno, I-80126 Napoli, Italy*
[106] *Universiteit Antwerpen, 2000 Antwerpen, Belgium*
[107] *Università di Roma "La Sapienza", I-00185 Roma, Italy*
[108] *Centre national de la recherche scientifique, 75016 Paris, France*
[109] *Univ Rennes, CNRS, Institut FOTON - UMR 6082, F-35000 Rennes, France*
[110] *University of Birmingham, Birmingham B15 2TT, United Kingdom*
[111] *Université de Liège, B-4000 Liège, Belgium*
[112] *Instituto de Fisica Teorica UAM-CSIC, Universidad Autonoma de Madrid, 28049 Madrid, Spain*
[113] *INFN, Laboratori Nazionali del Gran Sasso, I-67100 Assergi, Italy*
[114] *Laboratoire Kastler Brossel, Sorbonne Université, CNRS, ENS-Université PSL, Collège de France, F-75005 Paris, France*
[115] *Université catholique de Louvain, B-1348 Louvain-la-Neuve, Belgium*
[116] *Christopher Newport University, Newport News, VA 23606, USA*
[117] *Astronomical Observatory Warsaw University, 00-478 Warsaw, Poland*
[118] *University of Maryland, College Park, MD 20742, USA*
[119] *Università degli Studi di Milano-Bicocca, I-20126 Milano, Italy*
[120] *INFN, Sezione di Milano-Bicocca, I-20126 Milano, Italy*
[121] *L2IT, Laboratoire des 2 Infinis - Toulouse, Université de Toulouse, CNRS/IN2P3, UPS, F-31062 Toulouse Cedex 9, France*
[122] *University of Portsmouth, Portsmouth, PO1 3FX, United Kingdom*
[123] *Université de Lyon, Université Claude Bernard Lyon 1, CNRS, Institut Lumière Matière, F-69622 Villeurbanne, France*
[124] *IGFAE, Universidade de Santiago de Compostela, 15782 Spain*
[125] *University of Chicago, Chicago, IL 60637, USA*
[126] *University of California, Riverside, Riverside, CA 92521, USA*
[127] *Department of Astronomy, Beijing Normal University, Xinjiekouwai Street 19, Haidian District, Beijing 100875, China*
[128] *Texas A&M University, College Station, TX 77843, USA*
[129] *OzGrav, University of Melbourne, Parkville, Victoria 3010, Australia*
[130] *INFN, Laboratori Nazionali del Sud, I-95125 Catania, Italy*
[131] *Niels Bohr Institute, Copenhagen University, 2100 København, Denmark*
[132] *Università di Roma Tor Vergata, I-00133 Roma, Italy*
[133] *University of Sannio at Benevento, I-82100 Benevento, Italy and INFN, Sezione di Napoli, I-80100 Napoli, Italy*
[134] *University of Massachusetts Dartmouth, North Dartmouth, MA 02747, USA*
[135] *Departamento de Astronomía y Astrofísica, Universitat de València, E-46100 Burjassot, València, Spain*
[136] *Observatori Astronòmic, Universitat de València, E-46980 Paterna, València, Spain*
[137] *The Chinese University of Hong Kong, Shatin, NT, Hong Kong*
[138] *University of British Columbia, Vancouver, BC V6T 1Z4, Canada*
[139] *Indian Institute of Technology Bombay, Powai, Mumbai 400 076, India*
[140] *Department of Physics, National Cheng Kung University, No.1, University Road, Tainan City 701, Taiwan*
[141] *National Tsing Hua University, Hsinchu City 30013, Taiwan*
[142] *National Central University, Taoyuan City 320317, Taiwan*
[143] *OzGrav, Charles Sturt University, Wagga Wagga, New South Wales 2678, Australia*
[144] *Queen Mary University of London, London E1 4NS, United Kingdom*
[145] *Department of Electrophysics, National Yang Ming Chiao Tung University, 101 Univ. Street, Hsinchu, Taiwan*
[146] *Kamioka Branch, National Astronomical Observatory of Japan, 238 Higashi-Mozumi, Kamioka-cho, Hida City, Gifu 506-1205, Japan*
[147] *University of Texas, Austin, TX 78712, USA*
[148] *CaRT, California Institute of Technology, Pasadena, CA 91125, USA*
[149] *Cornell University, Ithaca, NY 14850, USA*
[150] *Dipartimento di Ingegneria Industriale (DIIN), Università di Salerno, I-84084 Fisciano, Salerno, Italy*
[151] *Faculty of Science, University of Toyama, 3190 Gofuku, Toyama City, Toyama 930-8555, Japan*
[152] *Institute for Cosmic Ray Research, KAGRA Observatory, The University of Tokyo, 5-1-5 Kashiwa-no-Ha, Kashiwa City, Chiba 277-8582, Japan*
[153] *Université Lyon, Université Claude Bernard Lyon 1, CNRS, IP2I Lyon / IN2P3, UMR 5822, F-69622 Villeurbanne, France*

[154] *INAF, Osservatorio Astronomico di Padova, I-35122 Padova, Italy*
[155] *OzGrav, Swinburne University of Technology, Hawthorn VIC 3122, Australia*
[156] *INAF, Osservatorio Astronomico di Brera sede di Merate, I-23807 Merate, Lecco, Italy*
[157] *Departamento de Matemáticas, Universitat de València, E-46100 Burjassot, València, Spain*
[158] *Texas Tech University, Lubbock, TX 79409, USA*
[159] *Columbia University, New York, NY 10027, USA*
[160] *University of Rhode Island, Kingston, RI 02881, USA*
[161] *The University of Texas Rio Grande Valley, Brownsville, TX 78520, USA*
[162] *Bellevue College, Bellevue, WA 98007, USA*
[163] *Scuola Normale Superiore, I-56126 Pisa, Italy*
[164] *Università degli Studi di Sassari, I-07100 Sassari, Italy*
[165] *The University of Sheffield, Sheffield S10 2TN, United Kingdom*
[166] *Université Lyon, Université Claude Bernard Lyon 1,*
CNRS, Laboratoire des Matériaux Avancés (LMA),
IP2I Lyon / IN2P3, UMR 5822, F-69622 Villeurbanne, France
[167] *Dipartimento di Scienze Matematiche, Fisiche e Informatiche, Università di Parma, I-43124 Parma, Italy*
[168] *INFN, Sezione di Milano Bicocca, Gruppo Collegato di Parma, I-43124 Parma, Italy*
[169] *Perimeter Institute, Waterloo, ON N2L 2Y5, Canada*
[170] *Corps des Mines, Mines Paris, Université PSL, 60 Bd Saint-Michel, 75272 Paris, France*
[171] *Indian Institute of Technology Madras, Chennai 600036, India*
[172] *Carleton College, Northfield, MN 55057, USA*
[173] *National Center for Nuclear Research, 05-400 Świerk-Otwock, Poland*
[174] *Institut d'Astrophysique de Paris, Sorbonne Université, CNRS, UMR 7095, 75014 Paris, France*
[175] *Vrije Universiteit Brussel, 1050 Brussel, Belgium*
[176] *University of Zurich, Winterthurerstrasse 190, 8057 Zurich, Switzerland*
[177] *Canadian Institute for Theoretical Astrophysics,*
University of Toronto, Toronto, ON M5S 3H8, Canada
[178] *Stony Brook University, Stony Brook, NY 11794, USA*
[179] *Center for Computational Astrophysics, Flatiron Institute, New York, NY 10010, USA*
[180] *Montclair State University, Montclair, NJ 07043, USA*
[181] *Institute for Nuclear Research, H-4026 Debrecen, Hungary*
[182] *CNR-SPIN, I-84084 Fisciano, Salerno, Italy*
[183] *Scuola di Ingegneria, Università della Basilicata, I-85100 Potenza, Italy*
[184] *Western Washington University, Bellingham, WA 98225, USA*
[185] *SUPA, University of the West of Scotland, Paisley PA1 2BE, United Kingdom*
[186] *The University of Utah, Salt Lake City, UT 84112, USA*
[187] *Eötvös University, Budapest 1117, Hungary*
[188] *Centro de Física das Universidades do Minho e do Porto,*
Universidade do Minho, PT-4710-057 Braga, Portugal
[189] *Department of Physics, Graduate School of Science,*
Osaka Metropolitan University, 3-3-138 Sugimoto-cho,
Sumiyoshi-ku, Osaka City, Osaka 558-8585, Japan
[190] *Vanderbilt University, Nashville, TN 37235, USA*
[191] *Université Côte d'Azur, Observatoire de la Côte d'Azur, CNRS, Lagrange, F-06304 Nice, France*
[192] *California State University, Los Angeles, Los Angeles, CA 90032, USA*
[193] *Dipartimento di Fisica, Università degli Studi di Genova, I-16146 Genova, Italy*
[194] *University of Szeged, Dóm tér 9, Szeged 6720, Hungary*
[195] *INAF, Osservatorio Astronomico di Capodimonte, I-80131 Napoli, Italy*
[196] *Ariel University, Ramat HaGolan St 65, Ari'el, Israel*
[197] *Université de Normandie, ENSICAEN, UNICAEN,*
CNRS/IN2P3, LPC Caen, F-14000 Caen, France
[198] *Laboratoire de Physique Corpusculaire Caen, 6 boulevard du maréchal Juin, F-14050 Caen, France*
[199] *The University of Mississippi, University, MS 38677, USA*
[200] *Institute of Physics, Academia Sinica, 128 Sec. 2, Academia Rd., Nankang, Taipei 11529, Taiwan*
[201] *Shanghai Astronomical Observatory, Chinese Academy of Sciences, 80 Nandan Road, Shanghai 200030, China*
[202] *American University, Washington, DC 20016, USA*
[203] *University of Nevada, Las Vegas, Las Vegas, NV 89154, USA*
[204] *Rochester Institute of Technology, Rochester, NY 14623, USA*
[205] *Department of Applied Physics, Fukuoka University,*
8-19-1 Nanakuma, Jonan, Fukuoka City, Fukuoka 814-0180, Japan
[206] *University of California, Berkeley, CA 94720, USA*
[207] *University of Lancaster, Lancaster LA1 4YW, United Kingdom*
[208] *College of Industrial Technology, Nihon University,*
1-2-1 Izumi, Narashino City, Chiba 275-8575, Japan

[209] *Faculty of Engineering, Niigata University, 8050 Ikarashi-2-no-cho, Nishi-ku, Niigata City, Niigata 950-2181, Japan*
[210] *Department of Physics, Tamkang University, No. 151, Yingzhuan Rd., Danshui Dist., New Taipei City 25137, Taiwan*
[211] *Rutherford Appleton Laboratory, Didcot OX11 0DE, United Kingdom*
[212] *Department of Astronomy and Space Science, Chungnam National University, 9 Daehak-ro, Yuseong-gu, Daejeon 34134, Republic of Korea*
[213] *Institute of Applied Physics, Nizhny Novgorod, 603950, Russia*
[214] *Kavli Institute for Astronomy and Astrophysics, Peking University, Yiheyuan Road 5, Haidian District, Beijing 100871, China*
[215] *Nambu Yoichiro Institute of Theoretical and Experimental Physics (NITEP), Osaka Metropolitan University, 3-3-138 Sugimoto-cho, Sumiyoshi-ku, Osaka City, Osaka 558-8585, Japan*
[216] *Directorate of Construction, Services & Estate Management, Mumbai 400094, India*
[217] *University of Białystok, 15-424 Białystok, Poland*
[218] *National Astronomical Observatories, Chinese Academic of Sciences, 20A Datun Road, Chaoyang District, Beijing, China*
[219] *School of Astronomy and Space Science, University of Chinese Academy of Sciences, 20A Datun Road, Chaoyang District, Beijing, China*
[220] *University of Southampton, Southampton SO17 1BJ, United Kingdom*
[221] *Department of Physics, Ulsan National Institute of Science and Technology (UNIST), 50 UNIST-gil, Ulju-gun, Ulsan 44919, Republic of Korea*
[222] *Institute for Cosmic Ray Research, The University of Tokyo, 5-1-5 Kashiwa-no-Ha, Kashiwa City, Chiba 277-8582, Japan*
[223] *Institute for High-Energy Physics, University of Amsterdam, 1098 XH Amsterdam, Netherlands*
[224] *Chung-Ang University, Seoul 06974, Republic of Korea*
[225] *University of Washington Bothell, Bothell, WA 98011, USA*
[226] *Aix Marseille Université, Jardin du Pharo, 58 Boulevard Charles Livon, 13007 Marseille, France*
[227] *Laboratoire de Physique et de Chimie de l'Environnement, Université Joseph KI-ZERBO, 9GH2+3V5, Ouagadougou, Burkina Faso*
[228] *Ewha Womans University, Seoul 03760, Republic of Korea*
[229] *Seoul National University, Seoul 08826, Republic of Korea*
[230] *Korea Astronomy and Space Science Institute, Daejeon 34055, Republic of Korea*
[231] *Sungkyunkwan University, Seoul 03063, Republic of Korea*
[232] *National Institute for Mathematical Sciences, Daejeon 34047, Republic of Korea*
[233] *Institute of Particle and Nuclear Studies (IPNS), High Energy Accelerator Research Organization (KEK), 1-1 Oho, Tsukuba City, Ibaraki 305-0801, Japan*
[234] *Bard College, Annandale-On-Hudson, NY 12504, USA*
[235] *Institute of Mathematics, Polish Academy of Sciences, 00656 Warsaw, Poland*
[236] *Department of Physics, Nagoya University, ES building, Furocho, Chikusa-ku, Nagoya, Aichi 464-8602, Japan*
[237] *Université de Montréal/Polytechnique, Montreal, Quebec H3T 1J4, Canada*
[238] *Inje University Gimhae, South Gyeongsang 50834, Republic of Korea*
[239] *NAVIER, École des Ponts, Univ Gustave Eiffel, CNRS, Marne-la-Vallée, France*
[240] *Università di Firenze, Sesto Fiorentino I-50019, Italy*
[241] *Department of Physics, University of Trento, via Sommarive 14, Povo, 38123 TN, Italy*
[242] *National Center for High-performance computing, National Applied Research Laboratories, No. 7, R&D 6th Rd., Hsinchu Science Park, Hsinchu City 30076, Taiwan*
[243] *NASA Marshall Space Flight Center, Huntsville, AL 35811, USA*
[244] *West Virginia University, Morgantown, WV 26506, USA*
[245] *School of Physics Science and Engineering, Tongji University, Shanghai 200092, China*
[246] *Institut d'Estudis Espacials de Catalunya, c. Gran Capità, 2-4, 08034 Barcelona, Spain*
[247] *Institucio Catalana de Recerca i Estudis Avançats (ICREA), Passeig de Lluís Companys, 23, 08010 Barcelona, Spain*
[248] *Tsinghua University, Beijing 100084, China*
[249] *Dipartimento di Fisica, Università di Trieste, I-34127 Trieste, Italy*
[250] *Institute for Photon Science and Technology, The University of Tokyo, 2-11-16 Yayoi, Bunkyo-ku, Tokyo 113-8656, Japan*
[251] *INFN Cagliari, Physics Department, Università degli Studi di Cagliari, Cagliari 09042, Italy*
[252] *Tata Institute of Fundamental Research, Mumbai 400005, India*
[253] *Hobart and William Smith Colleges, Geneva, NY 14456, USA*
[254] *Department of Physical Sciences, Aoyama Gakuin University, 5-10-1 Fuchinobe, Sagamihara City, Kanagawa 252-5258, Japan*

[255] *Institut des Hautes Etudes Scientifiques, F-91440 Bures-sur-Yvette, France*
[256] *Faculty of Law, Ryukoku University, 67 Fukakusa Tsukamoto-cho, Fushimi-ku, Kyoto City, Kyoto 612-8577, Japan*
[257] *Indian Institute of Science Education and Research, Kolkata, Mohanpur, West Bengal 741252, India*
[258] *Department of Physics and Astronomy, University of Notre Dame, 225 Nieuwland Science Hall, Notre Dame, IN 46556, USA*
[259] *University of Stavanger, 4021 Stavanger, Norway*
[260] *Department of Astronomy, The University of Tokyo, 7-3-1 Hongo, Bunkyo-ku, Tokyo 113-0033, Japan*
[261] *Laboratoire Univers et Théories, Observatoire de Paris, 92190 Meudon, France*
[262] *Observatoire de Paris, 75014 Paris, France*
[263] *Université PSL, 75006 Paris, France*
[264] *Université de Paris Cité, 75006 Paris, France*
[265] *Graduate School of Science and Technology, Niigata University, 8050 Ikarashi-2-no-cho, Nishi-ku, Niigata City, Niigata 950-2181, Japan*
[266] *Niigata Study Center, The Open University of Japan, 754 Ichibancho, Asahimachi-dori, Chuo-ku, Niigata City, Niigata 951-8122, Japan*
[267] *Department of Physics, The University of Tokyo, 7-3-1 Hongo, Bunkyo-ku, Tokyo 113-0033, Japan*
[268] *CSIR-Central Glass and Ceramic Research Institute, Kolkata, West Bengal 700032, India*
[269] *Consiglio Nazionale delle Ricerche - Istituto dei Sistemi Complessi, I-00185 Roma, Italy*
[270] *Department of Physics, Aristotle University of Thessaloniki, 54124 Thessaloniki, Greece*
[271] *Museo Storico della Fisica e Centro Studi e Ricerche "Enrico Fermi", I-00184 Roma, Italy*
[272] *Dipartimento di Ingegneria Industriale, Elettronica e Meccanica, Università degli Studi Roma Tre, I-00146 Roma, Italy*
[273] *INFN, Sezione di Roma Tre, I-00146 Roma, Italy*
[274] *Università di Trento, Dipartimento di Matematica, I-38123 Povo, Trento, Italy*
[275] *Subatech, CNRS/IN2P3 - IMT Atlantique - Nantes Université, 4 rue Alfred Kastler BP 20722 44307 Nantes CÉDEX 03, France*
[276] *Universidad de Antioquia, Medellín, Colombia*
[277] *Departamento de Física - ETSIDI, Universidad Politécnica de Madrid, 28012 Madrid, Spain*
[278] *Department of Electronic Control Engineering, National Institute of Technology, Nagaoka College, 888 Nishikatakai, Nagaoka City, Niigata 940-8532, Japan*
[279] *Departamento de Matemática da Universidade de Aveiro and Centre for Research and Development in Mathematics and Applications, 3810-183 Aveiro, Portugal*
[280] *Marquette University, Milwaukee, WI 53233, USA*
[281] *Faculty of Science, Toho University, 2-2-1 Miyama, Funabashi City, Chiba 274-8510, Japan*
[282] *Indian Institute of Technology, Palaj, Gandhinagar, Gujarat 382355, India*
[283] *Laboratoire MSME, Cité Descartes, 5 Boulevard Descartes, Champs-sur-Marne, 77454 Marne-la-Vallée Cedex 2, France*
[284] *Graduate School of Science and Technology, Gunma University, 4-2 Aramaki, Maebashi, Gunma 371-8510, Japan*
[285] *Institute for Quantum Studies, Chapman University, 1 University Dr., Orange, CA 92866, USA*
[286] *Faculty of Information Science and Technology, Osaka Institute of Technology, 1-79-1 Kitayama, Hirakata City, Osaka 573-0196, Japan*
[287] *INAF, Osservatorio Astrofisico di Arcetri, I-50125 Firenze, Italy*
[288] *Indian Institute of Technology Hyderabad, Sangareddy, Khandi, Telangana 502285, India*
[289] *Indian Institute of Science Education and Research, Pune, Maharashtra 411008, India*
[290] *Institut für Theoretische Physik, Johann Wolfgang Goethe-Universität, Max-von-Laue-Str. 1, 60438 Frankfurt am Main, Germany*
[291] *Istituto di Astrofisica e Planetologia Spaziali di Roma, 00133 Roma, Italy*
[292] *INAF, Osservatorio di Astrofisica e Scienza dello Spazio, I-40129 Bologna, Italy*
[293] *Universidade Estadual Paulista, 01140-070 Campinas, São Paulo, Brazil*
[294] *Research Center for Space Science, Advanced Research Laboratories, Tokyo City University, 8-15-1 Todoroki, Setagaya, Tokyo 158-0082, Japan*
[295] *Department of Physics, Kyoto University, Kita-Shirakawa Oiwake-cho, Sakyou-ku, Kyoto City, Kyoto 606-8502, Japan*
[296] *Institute for Cosmic Ray Research, Research Center for Cosmic Neutrinos, The University of Tokyo, 5-1-5 Kashiwa-no-Ha, Kashiwa City, Chiba 277-8582, Japan*
[297] *Yukawa Institute for Theoretical Physics (YITP), Kyoto University, Kita-Shirakawa Oiwake-cho, Sakyou-ku, Kyoto City, Kyoto 606-8502, Japan*
[298] *University of Catania, Department of Physics and Astronomy, Via S. Sofia, 64, 95123 Catania CT, Italy*

[299] *Dipartimento di Scienze Aziendali - Management and Innovation Systems (DISA-MIS), Università di Salerno, I-84084 Fisciano, Salerno, Italy*
[300] *National Institute of Technology, Fukui College, Geshi-cho, Sabae-shi, Fukui 916-8507, Japan*
[301] *Department of Communications Engineering, National Defense Academy of Japan, 1-10-20 Hashirimizu, Yokosuka City, Kanagawa 239-8686, Japan*
[302] *Eindhoven University of Technology, 5600 MB Eindhoven, Netherlands*
[303] *Department of Physics and Astronomy, Sejong University, 209 Neungdong-ro, Gwangjin-gu, Seoul 143-747, Republic of Korea*
[304] *Concordia University Wisconsin, Mequon, WI 53097, USA*
[305] *School of Physics and Technology, Wuhan University, Bayi Road 299, Wuchang District, Wuhan, Hubei, 430072, China*
[306] *Waseda Institute for Advanced Study, Waseda University, 1-6-1 Nishi-Waseda, Shinjuku, Tokyo 169-8050, Japan*
[307] *Kavli Institute for the Physics and Mathematics of the Universe, The University of Tokyo, 5-1-5 Kashiwa-no-Ha, Kashiwa City, Chiba 277-8583, Japan*

Among the various candidates for dark matter (DM), ultralight vector DM can be probed by laser interferometric gravitational wave detectors through the measurement of oscillating length changes in the arm cavities. In this context, KAGRA has a unique feature due to differing compositions of its mirrors, enhancing the signal of vector DM in the length change in the auxiliary channels. Here we present the result of a search for $U(1)_{B-L}$ gauge boson DM using the KAGRA data from auxiliary length channels during the first joint observation run together with GEO600. By applying our search pipeline, which takes into account the stochastic nature of ultralight DM, upper bounds on the coupling strength between the $U(1)_{B-L}$ gauge boson and ordinary matter are obtained for a range of DM masses. While our constraints are less stringent than those derived from previous experiments, this study demonstrates the applicability of our method to the lower-mass vector DM search, which is made difficult in this measurement by the short observation time compared to the auto-correlation time scale of DM.

I. INTRODUCTION

Recently, a number of novel dark matter (DM) searches using laser interferometric gravitational wave (GW) detectors have been proposed [1–6] and conducted [7–11]. Because of their extremely high sensitivity to the differential length changes of their arms in the frequency range $\mathcal{O}(10-10^3)$ Hz, they can probe the interaction between the detector and DMs, which have masses of $\mathcal{O}(10^{-14}-10^{-11})$ eV/c^2 and therefore oscillate coherently within this frequency band. Vector DM (or so-called dark photon DM) interacts with test masses of the interferometer, for example, via a coupling to the baryon (B) or baryon minus lepton ($B-L$) number current. Because of the non-relativistic dispersion (under the standard halo model [12, 13]), the vector DM field exerted on the test masses behave as an oscillating dark electric force, inducing a measurable change in the differential length of the arm cavity. Vector DMs of this type, which we refer to as $U(1)_B$ and $U(1)_{B-L}$ gauge boson, were previously searched in Ref. [9] by using the latest observational data from the Advanced LIGO [14–16] and Virgo [17, 18] detectors. Remarkably, the constraint on the coupling strength of vector DM to baryons from GW interferometers surpasses those from existing experiments such as the Eöt-Wash torsion balance [19, 20] and MICROSCOPE [21–23], by orders of magnitude for certain frequency bands. Similarly, dilatonic DM, whose interaction alters the apparent electron mass or the fine structure constant, was probed with data from the GEO600 interferometer [10, 24, 25]. These searches highlight the potential of GW detectors as direct probes of ultralight DM.

A Japanese laser interferometric GW detector, KAGRA [26–28], can also probe the vector DM interaction, but in a relatively unique way compared to the previous searches. For the Advanced LIGO and Virgo detectors, all the mirrors (including test masses) are made of the same material (fused silica), in other words, they have a common charge-to-mass ratio with respect to the dark electric field. Because the spatial variation scale (so-called coherence length) of the ultralight DM field is $\mathcal{O}(10^5-10^8)$km in our target mass range, all mirrors of each detector, which are separated only a few kilometers, respond to the vector field nearly identically. In contrast, KAGRA employs sapphire for cryogenic test masses and fused silica for room temperature auxiliary mirrors. Therefore, owing to the difference in the charge-to-mass ratios, those mirrors respond differently to the vector field, and the vector DM signal in the (differential) length change can be enhanced for auxiliary length monitors [3, 29]. Especially in the case of $U(1)_{B-L}$, where the difference in charge-mass ratio is relatively large, these channels are shown to have better sensitivity to vector DM than existing experiments in certain low frequency bands, when KAGRA reaches design sensitivity [3].

In this work, we conduct an ultralight vector DM search with KAGRA using the data of its auxiliary length

* Deceased, November 2022.
† Deceased, July 2023.

change monitors during the first joint observation run together with GEO600 (O3GK) [30]. Although the detector was in operation for two weeks during O3GK, the durations of the contiguous data segments were at most about 7 hours [31]. For our target mass range, this duration can be comparable to or smaller than the so-called coherence time, within which the amplitude and the phase of DM can be regarded as a constant. Since each such measurement is one realization of a random field, their stochasticity needs to be taken into account, especially when setting the upper bound on the coupling strength of the ultralight DM. Therefore, our pipeline is constructed based on a recent study [32], which thoroughly investigates the stochastic nature of the ultralight vector DM. Using the detection statistic discussed in Ref. [32], we numerically derive upper limits on the coupling strength incorporating the stochastic nature of the DM. On the other hand, various noise lines [31] result in a false detection as a DM signal. In order to distinguish outliers, we have implemented veto procedures making use of expected features of ultralight DM signals.

The rest of the paper is organized as follows. We first introduce our model of ultralight vector DM and discuss its stochastic nature in Sec. II. After describing our search method in Sec. III, the results of our analysis using O3GK data are presented in Sec. IV. Sec. V provides a discussion of these results and of the prospects for future searches.

II. DARK MATTER SEARCH WITH KAGRA

A. Vector Dark Matter Model

In this work, we consider a ultralight vector dark matter field $A_\mu(t,x)$, which is regarded as a gauge boson of $U(1)_D$ gauge symmetry with D being a label for a charge, such as B and $B-L$. We assume it interacts with ordinary matter through the coupling to the $U(1)_D$ current J^μ_D. The Lagrangian density $\mathcal{L}$ is then given as

$$\mathcal{L} = -\frac{\varepsilon_0 c^2}{4} F^{\mu\nu}F_{\mu\nu} + \frac{\varepsilon_0}{2}\left(\frac{m_A c^2}{\hbar}\right)^2 A^\mu A_\mu - \epsilon_D e J^\mu_D A_\mu, \tag{1}$$

where $F_{\mu\nu} = \partial_\mu A_\nu - \partial_\nu A_\mu$ is the field strength, c is the speed of light, $\hbar$ is the reduced Planck constant, m_A is the mass of the vector field, ε_0 is the permittivity of vacuum and ϵ_D is the gauge coupling constant normalized by the electromagnetic coupling constant. Since the temporal component of the vector field A_0 is negligibly small, we consider only its spatial components $\vec{A} = (A_x, A_y, A_z)$ in the following discussion.

Assuming the standard halo model, the local density of DM is $\rho_{\rm DM} \sim 0.4\,{\rm GeV/cm^3}$, and its virial velocity is $v_{\rm vir} \simeq 220$ km/sec around the solar system in our Galaxy [12, 13]. These profiles imply that DM would have an extremely large number density for the mass range $10^{-22}{\rm eV}/c^2 \lesssim m \lesssim 1{\rm eV}/c^2$ and behave as a classical wave oscillating at about the Compton frequency $f_c = m_A c^2/2\pi\hbar$. Then, one can describe it as the superposition of plane waves with different velocities $\vec{v}_{(i,n)}$ and phases $\theta_{(i,n)}$ as

$$A_i(t,\vec{x}) = \frac{A}{\sqrt{N}}\sum_{n=1}^{N}\cos\left(2\pi f_c\left(1+v^2_{(i,n)}/2c^2\right)t - \hbar^{-1}m_A\vec{v}_{(i,n)}\cdot\vec{x} + \theta_{(i,n)}\right), \tag{2}$$

where $\theta_{(i,n)}$ is a random variable following a uniform distribution over $[0,2\pi]$ and $A \equiv \sqrt{2\rho_{\rm DM}\hbar^2/\varepsilon_0 3m_A^2c^4}$. Note that, for simplicity, the absence of correlation between the direction of $\vec{A}$ and $\vec{v}$ is assumed. Here $\vec{v}_{(i,n)}$ follows the DM velocity distribution of the standard halo model [13]:

$$f_{\rm SHM}(\vec{v})\ {\rm d}^3\vec{v} = \frac{1}{(\pi v^2_{\rm vir})^{3/2}}\exp\left[-\frac{(\vec{v}+\vec{v}_\odot)^2}{v^2_{\rm vir}}\right]\ {\rm d}^3\vec{v}, \tag{3}$$

with the solar velocity $|\vec{v}_\odot| \simeq 232\,{\rm km/sec}$. This distribution results in the velocity dispersion of the DM as $\bar{v}^2 = v^2_\odot + (3/2)v^2_{\rm vir} \simeq \mathcal{O}(10^{-6}c^2)$. In such a non-relativistic regime, the time derivative of the field dominates over the spatial derivative. Hence, it can be regarded as a oscillating dark "electric" field, which induces displacements of the test masses in GW interferometers as $\delta\ddot{x}_i = \epsilon_D e(Q/M)\dot{A}_i$.

Another feature is that there appears a length scale, called "coherence length", which is evaluated as $L = 2\pi\hbar/m_A\sqrt{\bar{v}^2} \sim 10^7{\rm km}$ $(10^{-13}{\rm eV}\cdot c^{-2}/m_A)$. This scale characterizes the spatial variation of the ultralight DMs. As we will see below, the separation of test masses here is much shorter than L, we can take $\vec{x}=0$ in Eq. (2) without loss of generality and hereafter neglect the position dependence of the vector field.

B. Auxiliary length channels of KAGRA

From 2020 April 7 to 2020 April 21, KAGRA conducted its first joint observation run (O3GK) [30, 31], together with GEO600. The configuration of KAGRA interferometer during O3GK is shown in Fig. 1. Similarly to that of LIGO and Virgo, it is based on a Michelson interferometer with a Fabry-Pérot cavity in two perpendicular arms. Each arm cavity is formed by the input test mass (ITM) and the end test mass (ETM). The main channel to monitor the differential changes caused by GWs is called the differential arm length (DARM). The differential length between the beam splitter (BS) and two ITMs are controlled so that the Michelson fringe will be at the dark fringe at the anti-symmetric port, and the channel to monitor the differential Michelson interferometer length is called MICH. The power recycling mirror (PRM) and two ITMs form a power recycling cavity to effectively enhance the input power. The channel to monitor the power recycling cavity length is called PRCL.

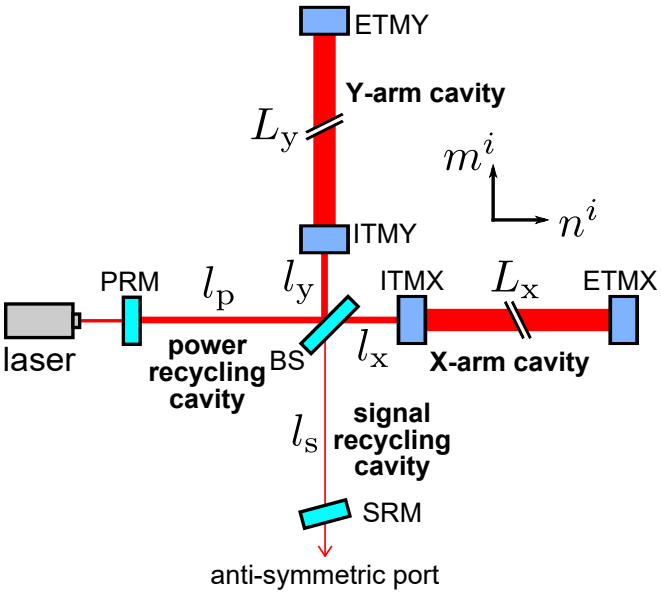


FIG. 1. The schematic of the KAGRA interferometer. ITM (ETM): input (end) test mass, BS: beam splitter, PRM: power recycling mirror, SRM: signal recycling mirror.

During O3GK, a signal recycling mirror (SRM) was tilted, and the signal recycling cavity was not formed [33]. Instead, this tilted SRM introduced an optical loss of 70%, which led to degraded shot noise for the DARM readout. Two auxiliary channels, MICH and PRCL were recorded using different interferometer sensing ports, and were not affected by this optical loss. Using the length symbols in Fig. 1, changes in DARM, MICH and PRCL can be written as

$$\delta L_{\rm DARM} = \delta(L_{\rm x} - L_{\rm y}), \tag{4}$$
$$\delta L_{\rm MICH} = \delta(l_{\rm x} - l_{\rm y}), \tag{5}$$
$$\delta L_{\rm PRCL} = \delta[(l_{\rm x} + l_{\rm y})/2 + l_{\rm p}], \tag{6}$$

respectively. Note that each length parameter is given as $L_x = L_y = 3000$m, $l_x = 26.7$m, $l_y = 23.3$m and $l_p = 41.6$m, all of which are much shorter than the coherence length of DM.

Previous vector DM searches using LIGO and Virgo focused on DARM channels with the highest displacement sensitivity. This sensitivity is equivalent to the sensitivity to vector DM interactions for both LIGO and Virgo employing room temperature fused silica mirrors for all the mirrors. This situation, however, drastically changes for KAGRA, which employs cryogenic sapphire mirrors for the test masses. As pointed out in Ref. [3], MICH and PRCL contain both the fused silica mirrors such as PRM and BS, and the sapphire test masses that respond differently to the vector DM due to the different charge-to-mass ratio. This results in the enhancement of the (differential) length change caused by vector DM in those channels. Since the difference becomes larger especially for the $U(1)_{B-L}$ gauge boson, hereafter we focus on the $D = B - L$ case.

C. Signal in the KAGRA's auxiliary length channels

Since the frequency of each plane wave is localized near the Compton frequency as $f_i = f_c\sqrt{1+v_i^2/c^2} \sim f_c(1+\mathcal{O}(10^{-6}))$, it is convenient to work in the Fourier space. Let us consider the Fourier transform of the signal in X channel with duration T and center time t_0:

$$\tilde{h}_X(f;t_0) \equiv \int_{t_0-T/2}^{t_0+T/2} dt\, h_X(t) {\rm e}^{-2\pi {\rm i} f(t-t_0+T/2)}. \tag{7}$$

To simplify the discussion, T is taken to be much shorter than the time scale of Earth's rotation. As discussed in [32], the oscillating length changes of an arm cavity can be decomposed into three contributions referred to as charge asymmetry, spatial difference and finite light traveling time [8]. For auxiliary length monitors of interest here, the dominant contribution is the one from charge asymmetry expressed as

$$\tilde{h}_X(f;t_0) = {\rm i}\frac{\epsilon_D e}{2\pi f}\Delta\left(\frac{Q_D}{M}\right) l_X^i(t_0)\tilde{A}_i(f;t_0), \tag{8}$$

where $\Delta(Q_D/M)$ is the difference of charge to mass ratio between two mirrors (BS and ITMX/Y) and in our case, it is $\Delta(Q_{B-L}/M) \sim 0.009/m_n$ with m_n being the neutron mass [3]. The vector $l_X^i(t_0)$ is given as

$$l_X^i(t) = \begin{cases} n^i(t) - m^i(t), & (X = \text{MICH}) \\ \dfrac{1}{2}\left(n^i(t) + m^i(t)\right), & (X = \text{PRCL}), \end{cases} \tag{9}$$

where n^i and m^i are unit vectors pointing along the orthogonal arm axes depicted in Fig. 1. Here $\tilde{A}_i(f;t_0)$ is the Fourier transform of the field amplitude. Since it is a superposition of a huge number of partial waves, the central limit theorem assures that $\tilde{A}_i(f;t_0)$ and consequently $\tilde{h}_X(f;t_0)$ follow a Gaussian distribution. Note that, when the DM density and the distance between the test masses are fixed, this type of contribution results in a larger field amplitude and hence in a larger signal for the lower frequencies [3, 32]. This is the reason why MICH and SRCL (not available in O3GK) has, under the design sensitivity, the capability of limiting the DM coupling beyond existing limits in the lower frequency band.

At this point, it is convenient to introduce the so-called coherence time

$$\tau \equiv 2\pi/m_A v_{\rm vir}^2 \sim 0.3 \text{ day } \left(\frac{10^{-13}\text{ eV}\cdot c^{-2}}{m_A}\right), \tag{10}$$

which quantifies the characteristic correlation lifetime of the DM field at different times $\langle\tilde{h}_X^*(f;t_0)\tilde{h}_X(f;t_1)\rangle$. Let T be the duration of a single chunk of data and $N_{\rm ch}$ be the number of equal-length chunks. For higher mass ranges, in general, the coherence time becomes shorter than the duration of each chunk as $\tau < T$. In this case,

the amplitude and phase of the DM randomly evolve within the chunks. While this decoherence reduces the growth of the signal-to-noise (SNR) ratio in amplitude as $\propto (N_{\rm ch}T)^{1/4}$ [32], each data chunk can be regarded as an independent measurement of DM, and in fact the statistical treatment can be simplified [32]. For a lower mass range ($\tau > T$), however, the correlation of the DM field between different data chunks cannot be neglected. This issue will be addressed in the following section describing the search pipeline.

Finally, let us give a concrete expression of the signal covariance $\langle \tilde{h}^*_X(f;t_0)\tilde{h}_X(f;t_1)\rangle$ used in our analysis. By combining Eqs. (2) and (3), it is derived as

$$\left\langle \tilde{h}^*_X(f;t_0)\tilde{h}_X(f;t_1)\right\rangle = \frac{\epsilon_D^2 e^2 A^2 T^2 v_{\rm vir}^3}{32\pi^{\frac{5}{2}} f^2 v_\odot^3}\left\{\Delta\left(\frac{Q_D}{M}\right)\right\}^2 \times l^i_X(t_0) l_{X,i}(t_1) {\rm e}^{-\frac{v_\odot^2}{v_{\rm vir}^2}+2\pi {\rm i} f_{\rm DM}(t_1-t_0)}\left(I(x_+)-I(x_-)\right). \tag{11}$$

Here $I(x)$ is a function of the DM frequency and the time

$$I(x) = \frac{X^2}{8}\left[\sqrt{\pi}X{\rm e}^{X^2/4}\left\{{\rm erf}\left(\frac{x}{X}-\frac{X}{2}\right) + {\rm erf}\left(\frac{x}{X}+\frac{X}{2}\right)\right\} - 4{\rm e}^{-x^2/X^2}\sinh(x)\right], \tag{12}$$

where we use the following parametrization,

$$x = \frac{2v_\odot}{v_{\rm vir}^2}v, \quad X = \frac{2v_\odot}{v_{\rm vir}\sqrt{1-{\rm i}\pi v_{\rm vir}^2 c^{-2} f_{\rm DM}(t_1-t_0)}}, \tag{13}$$

and

$$\frac{v_\pm}{c} \equiv \sqrt{2\left(\frac{f\pm 1/(2T)}{f_{\rm DM}}-1\right)}, \qquad x_\pm \equiv \frac{2v_\odot}{v_{\rm vir}^2}v_\pm. \tag{14}$$

For $t_0 = t_1$, our $I(x)$ coincides with the function $\Delta_s(f_n)$ in Ref. [32], which gives the deterministic part of the spectral shape.

III. SEARCH METHOD

A. Detection statistics

Here we introduce, and slightly extend, the detection statistic discussed in Ref. [32]. It is based on the existing methods of continuous GW searches [34–36] that also look for a narrow band signal similarly to our case. For comprehensive reviews of those method, see *e.g.* Refs. [37–39] The search method discussed in Ref. [32] is generally applicable to the ultralight DM searches using a single detector and interested readers could refer to Ref. [40] for the application of this detection statistic to the ultralight axion search.

As we discussed in Sec. II, the spectrum of the DM signal is localized within the narrow frequency band $f_c \le f \lesssim f_c(1+\kappa^2 v_{\rm vir}^2/c^2)$ where κ is $\mathcal{O}(1)$ constant and we set $\kappa = 3.17$ to guarantee that the fractional loss of signal power becomes less than 1%. For each single data chunk, we sum up the spectra over this frequency range:

$$\rho_i(f_c) \equiv \sum_{f_c \le f_n \le f_c(1+\kappa^2 v_{\rm vir}^2/c^2)} \frac{4|\tilde{d}(f_n;t_i)|^2}{TS(f_n;t_i)}, \tag{15}$$

where T again is the duration of the data chunks, $\tilde{d}(f_n;t_i)$ represents the Fourier transform of the i-th data chunk and $S(f_n;t_i)$ is the one-sided noise power spectral density (PSD) around $t = t_i$. Note that in order to neglect the effect of Earth's rotation as in Sec. II, T should be small enough and hereafter we take $T = 30$ min.

In our pipeline, $S(f_n;t_i)$ is estimated from $\tilde{d}(f_n;t_i)$ by applying the running median and then converting it to the mean value by multiplying a correction factor (see App.A of Ref. [41]). In the median estimation, 180 neighboring frequency bins corresponding to 0.1Hz band width are involved so that the effect of DM signal with narrow bandwidth can be smeared out. The number of bins involved in $\rho_i(f_c)$ is given as

$$N_{\rm bin} = \left\lceil \frac{\kappa \bar{v}^2 f_c}{\Delta f}\right\rceil = \left\lceil \kappa \frac{T}{\tau}\right\rceil, \tag{16}$$

where $\lceil x \rceil$ represents the minimum integer larger than x. By performing the summation over all chunks, we can define the detection statistics ρ as

$$\rho(f_c) \equiv \sum_i^{N_{\rm ch}} \rho_i(f_c), \tag{17}$$

where $N_{\rm ch}$ represents the number of chunks. Under the assumption of the stationarity and Gaussian distribution of noise, ρ follows a χ^2 distribution with $2N_{\rm bin}N_{\rm ch}$ degrees of freedom in the absence of signal. We chose the threshold to be the 95% percentile of this distribution.

B. Upper limit estimation

In this study, we derive upper limits based on the frequentist's method where β % confidence level upper limit is derived through the integration of the likelihood function $\mathcal{L}(\rho(f_c);\epsilon_D^{\beta\%})$ as

$$1-\frac{\beta}{100} = \int_0^{\rho_{obs}} d\rho \mathcal{L}(\rho(f_c);\epsilon_D^{\beta\%}). \tag{18}$$

One might expect the central limit theorem to be applicable to $\rho(f_c)$ since the number of chunks is relatively large. There is, however, a non-vanishing cross-correlation between different segments $\langle \rho_i \rho_j\rangle|_{i\neq j} \neq 0$ for $|t_i - t_j| < \tau$. This correlation prevents the convergence to a Gaussian distribution especially for lower-mass DM and makes the analytical expression of $\mathcal{L}(\rho(f_c);\epsilon_D)$ complicated [32]. In fact, this analytical expression suffers from numerical instability for intermediate regimes where the coherence

time and the duration of chunks are comparable. In our pipeline, therefore, the 95% upper limit on the coupling constant was numerically derived as follows.

Assuming that only Gaussian noise $\tilde{n}(f_n;t_i)$ and ultralight DM signals are present in the data, it can be expressed as $\tilde{d}(f_n;t_i)=\tilde{n}(f_n;t_i)+\tilde{h}_X(f_n;t_i)$. Therefore, dependence of ρ on the coupling constant can be decomposed as

$$\begin{aligned}\rho(f_c;\epsilon_D) &= \sum_{t_i,f_n}\frac{4}{TS}\left(|\tilde{n}|^2+2\mathrm{Re}\left[\tilde{n}^*\tilde{h}_X\right]+|\tilde{h}_X|^2\right) \\ &= \mathcal{N}^2+\epsilon_D\mathcal{N}\cdot\mathcal{S}+\epsilon_D^2\mathcal{S}^2.\end{aligned} \tag{19}$$

Here $\mathcal{N}^2$ represents contributions from $2N_{\rm bin}N_{\rm ch}$ unit Gaussian variables since the noise component in ρ is normalized by the PSD. On the other hand, $\mathcal{S}^2$ represents contributions solely from the Gaussian signal $\tilde{h}_X(f_n;t_i)$ (also normalized by noise PSD) whose correlation function is given as Eq. (11) under the standard halo model assumption. $\mathcal{N}\cdot\mathcal{S}$ is the contribution from the cross term of the unit Gaussian and the normalized signal. For a fixed DM mass (or f_c), we simulated 10^5 realizations of $\mathcal{N}^2$, $\mathcal{S}^2$, $\mathcal{N}\cdot\mathcal{S}$ from the covariance of the DM signal (11) and the estimated noise PSD $S_n(f_n;t_i)$. Then we can obtain a histogram of ρ that approximates the likelihood $\mathcal{L}(\rho(f_c);\epsilon_D)$ and depends on the value of ϵ_D. Then the value of ϵ_D, for which the observed value of the detection statistics $\rho_{\rm obs}(f_c)$ coincides with the 5% percentile of this realization, is identified as the 95% upper limit. We would like to emphasize that our method does not suffer from the numerical instability mentioned above and that it is applicable to arbitrary masses of DM.

IV. ANALYSIS

A. Data

We analyzed the O3GK data collected from the KAGRA detector in the observation mode, and the data from GEO600 is not used. During the O3GK run, the KAGRA detector had duty factors, the fraction of time the detector is in the observing mode to the total time, of $\sim 53\%$. The length channels considered in this study are the differential Michelson interferometer length (MICH) and the power recycling cavity length (PRCL). For both the MICH and PRCL channels, calibrations of data were performed offline for this study, whose parameters and information will be summarized in Ref. [42]. For the frequency band we used for the analysis, calibration uncertainty in MICH and PRCL channels are 20-30% in amplitude.

The amplitude spectral densities (ASDs), derived from $S(f_n;t_i)$, of these channels during O3GK are plotted in Fig 2. We should note that, for the last few days of O3GK, alignments of mirrors were dithered at significantly large amplitude for the beam position control [31]. These injected lines were accompanied by a large number of sidebands. Since our pipeline simply searches power excesses within narrow bandwidth, it is not straightforward to distinguish those noise lines from the DM signals. Hence the segments from the last three days of the O3GK, where the efficiency of the DM search was spoiled, were not included in our analysis. Consequently, the number of 30 minute chunks subject to our pipeline was 217.

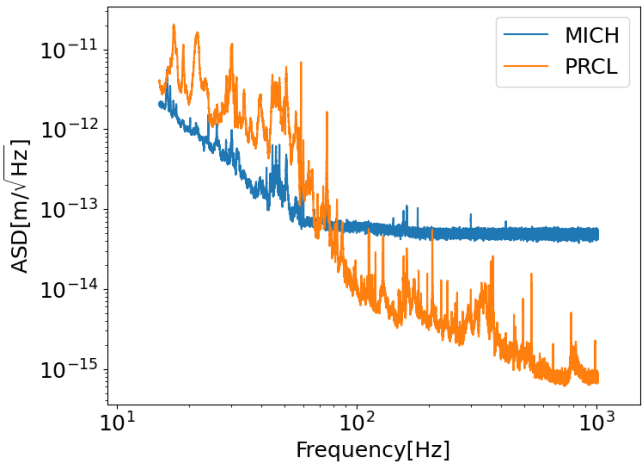


FIG. 2. ASDs of the MICH and PRCL estimated from the first 30 min chunk during O3GK.

Another limitation is that the vibration isolation systems for mirrors in MICH and PRCL were simplified compared to those in the full-design [31]. Consequently, there are many noise peaks in the lower frequency range, where the KAGRA's auxiliary degrees of freedom become more and more sensitive. Although our pipeline can be used in the lower frequency range $\lesssim$ 10Hz, the analysis was performed over the frequency range from 15 Hz to 1015 Hz for this demonstration analysis.

B. Candidates and veto procedure

In Fig. 3, the detection statistics $\rho(f_c)$ computed in our pipeline are shown respectively for MICH and PRCL. As expected from the many lines in ASDs shown in Fig. 2, more non-Gaussian power excess within an expected signal bandwidth is observed in the PRCL data. Under the 5% False-Alarm-Probability derived from χ^2 distribution for Gaussian noise, 1944 and 4133 lines are identified as candidates for MICH and PRCL, respectively. These candidates are then subject to the veto analysis as follows. First, according to the expected narrow band feature of DM signal, the peak of $\rho(f_c)$ should also have a comparable width if it has DM origin. As illustrated in the top panel of Fig. 4, candidates with a width more than two times broader than the expected DM signal width were vetoed. We also vetoed lines that were less than the peak width away from the vetoed peaks of ρ, as

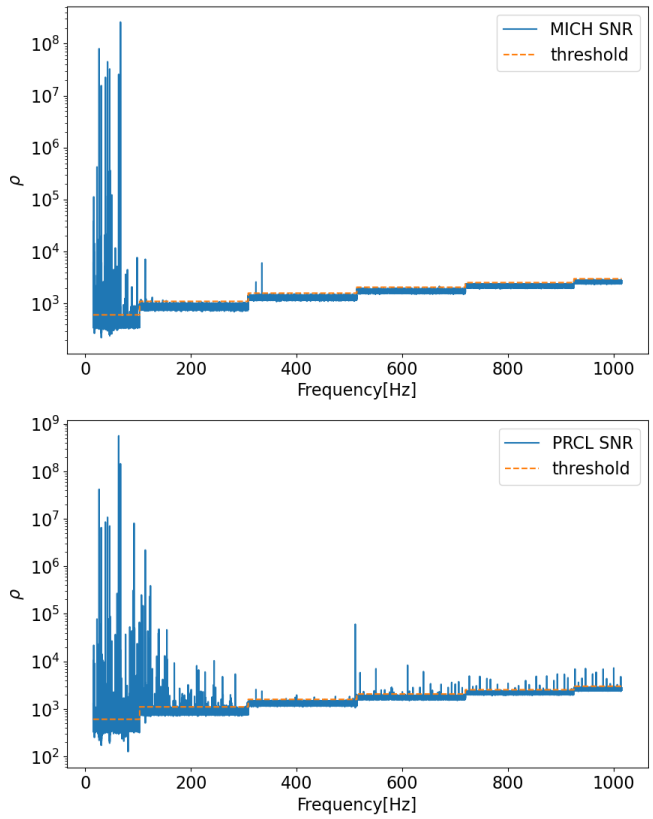


FIG. 3. The detection statistics ρ computed from 217 half-hour chunks during O3GK with MICH (*top panel*) and PRCL (*bottom panel*) channel. A step appears about every 200 Hz because of the increase in $N_{\rm bin}$, which varies from 1 to 6. The step height depends on the number of chunks.

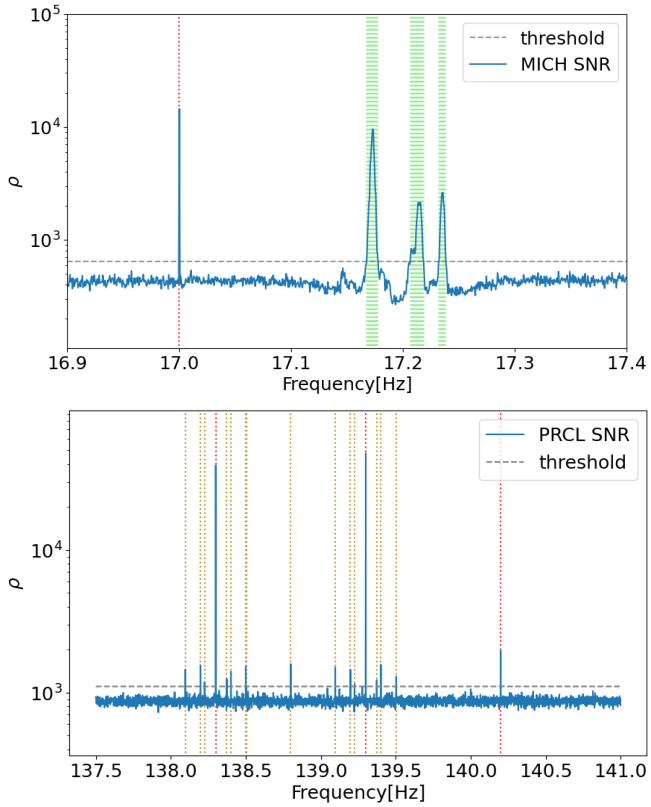


FIG. 4. A schematic picture of the veto procedure. For both cases, the vertical red lines denote surviving candidates after two veto procedure. (*Top panel*) Green vertical bands indicate the broad peak structures vetoed by the bandwidth criterion. (*Bottom panel*) The yellow vertical lines represent candidates with power excess that fails coincidence requirements.

there is a possibility that they originated from the same source as those broad peaks.

Second, in contrast to transient noise, expected to produce outliers in the O3GK data, DM signals should be more persistent on average, albeit with random statistical fluctuations. In the analysis, we chronologically divide the whole data chunks into two subsets and perform the same analyses within the first half 108 chunks and the second half 108 chunks. Then we take a coincidence between the candidates found in those two subsets to exclude transients that only appear during a limited duration. However, it must be noted that this procedure inevitably vetoes weaker DM signals with which $\rho(f_c)$ exceeds the detection threshold only after summing over all the chunks. Furthermore, unless the signal coherence time is sufficiently shorter than the data length of the subset, the field amplitude (and therefore the value of $\rho(f_c)$) can be significantly different for each subset. By examining the spectrum, we found that in the case of present data, such lines with the values of ρ close to the threshold are mostly sidebands of more intense lines, but this issue must be considered in future studies. For possible improvements to this veto procedure, see the discussion below.

After applying these two veto procedures, 77 lines remain as candidates in the MICH data while 202 lines remain in the PRCL data. Many of them are in the low frequency range below 100 Hz, where there are many lines due to injected signals and the suspension noise. By referring to, for example, the Appendix A. of Ref [31] discussing the noise lines of DARM during O3GK, we found that 57 out of 77 lines in the MICH data and 54 out of 202 lines in the PRCL data come from known lines. Note that there were few dedicated studies of the line identification for MICH and PRCL channels during O3GK, and lines of unknown origin still remain. Therefore, for our future reference, the candidate lines identified in this study are listed in Ref. [43].

C. Upper limit

There are several lines that have passed our pipeline detection criteria, but they cannot be claimed as DM signals given the current level of displacement sensitivity shown in Fig. 2 and the much shorter total observation time, compared to those assumed in Ref. [3]. With the

scaling of SNR $\propto (N_{\rm ch}T)^{1/4}$, their prediction on upper limits derived by setting SNR = 1 can be scaled to give an order of magnitude estimate of the upper limits we can derive from ρ. By comparing the design sensitivity (Fig. 2 in Ref. [3]) with our Fig. 2 and considering another suppression factor of $(N_{\rm ch}\cdot 30{\rm min}/1{\rm yr})^{1/4} \sim 0.01^{1/4}$ that comes from the difference between the real and assumed observation time, we expect that the upper limit on ϵ_{B-L} from O3GK data will be at best $\mathcal{O}(10^{-20})$. This is much weaker than those derived from the Eöt-Wash torsion balance [19, 20] and MICROSCOPE [21–23], predicting 10^{-24} to 10^{-23} in the frequency band of our interest.

Therefore, the upper limit estimation here should be considered as a demonstration of our pipeline, which can accurately analyze low-frequency regions and high-frequency regions as well. As such a demonstration, upper limits on the coupling constant are derived over the whole frequency range analyzed in this study. Note that in principle, upper limits can be derived even for $\rho(f_c)$ that exceed the detection threshold.

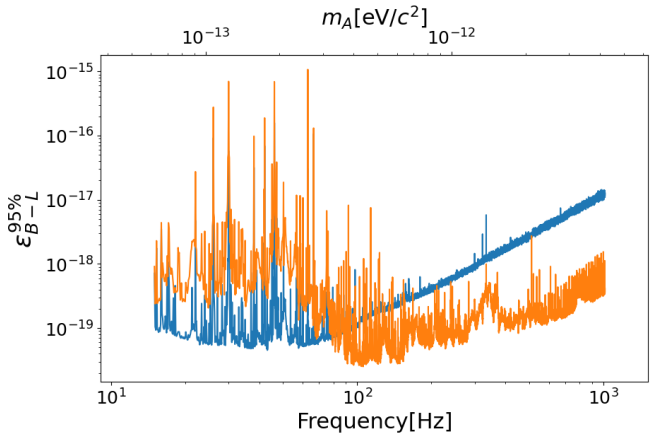


FIG. 5. 95% upper limit on the $B-L$ gauge coupling constant derived from MICH data (blue line) and PRCL data (orange line). Many narrow peaks observed in lower mass range are due to unknown line artifacts in the lower frequency range.

In Fig. 5, 95% upper limits on the coupling constant ϵ_{B-L} are shown. Here the constraint is smoothed by collecting the maximum value of $\rho(f_c)$ within a 0.1Hz bandwidth. For clarity, uncertainty of the calibration is not displayed. Let us stress that the stochastic nature of DM is properly taken into account in deriving this bound, by using the covariance of DM signal (11) for simulating the realization of $\rho(f_c)$. As demonstrated in Ref. [32], for example, incorrect deterministic treatment predicts a non-central χ^2 distribution of $\rho(f_c)$ and overestimates the upper bound by up to a factor of 3 in low mass (or long coherence time) regions. We also found that our result is consistent with the above rough estimate on the upper limit based on the SNR scaling, which is also a consequence of the stochastic nature of ultralight DMs [3, 32].

As expected, these upper limits derived from the KAGRA O3GK data are weaker than previous published limits by several orders of magnitude. Again, this is owing to both the current noise level of the KAGRA detector and the limited duration of the measurement time. In order to reach the unexplored parameter space, reduction of the dominant low-frequency noise and longer stable detector operation are indispensable.

V. DISCUSSION

In this work, an ultralight vector DM search with KAGRA was conducted for the first time by using the KAGRA data from the O3GK run. Our pipeline design is guided by a recent study on the stochastic nature of the ultralight vector DM [32]. Consequently, the KAGRA O3GK data, which has a relatively short measurement time compared to the DM coherence time for low DM masses, can be analyzed.

We found that our pipeline can discriminate candidates for vector DM signal from the broad peaks and transient lines, which are expected to have an instrumental origin. Nonetheless, there are several lines with unspecified origin meeting our criteria, especially for the lower frequency range. We expect that the number of such lines will decrease in upcoming observations because of, for example, an updated system for the suspension control and an improved understanding of the noise. Although the upper limits derived in this analysis are weaker than previous ones, they are found to be consistent with the prediction given in prior studies [3, 32]. Achieving the designed sensitivity and future upgrades of the KAGRA detector [44] will allow us to fully appreciate its unique feature as a vector DM detector exploiting the mirrors made of different materials to yield new constraints.

There are several directions for improving our DM search pipeline. First, as outlined in Sec. II, our analysis is performed assuming the equilibration of vector polarization. Depending on the production mechanism, however, only a specific polarization mode might be produced. Therefore, the formalism beyond this assumption may allow us to probe the cosmological origin of vector DM. Second, while the bandwidth criterion for the veto analysis is quite robust, the appropriateness of taking coincidence between subsets of whole data should depend on the strength and coherence time of the signal being searched for. Since the covariance of the vector DM signal is known, it is possible to implement a test to check whether the candidates follow a distribution consistent with the given covariance. This could provide a more robust way to distinguish a DM signal from the noise lines. Finally, our pipeline can be extended to include the analysis of the DARM channel data, which has been used in DM searches in other GW detectors.

ACKNOWLEDGEMENTS

This material is based upon work supported by NSF's LIGO Laboratory which is a major facility fully funded by the National Science Foundation. The authors also gratefully acknowledge the support of the Science and Technology Facilities Council (STFC) of the United Kingdom, the Max-Planck-Society (MPS), and the State of Niedersachsen/Germany for support of the construction of Advanced LIGO and construction and operation of the GEO 600 detector. Additional support for Advanced LIGO was provided by the Australian Research Council. The authors gratefully acknowledge the Italian Istituto Nazionale di Fisica Nucleare (INFN), the French Centre National de la Recherche Scientifique (CNRS) and the Netherlands Organization for Scientific Research (NWO), for the construction and operation of the Virgo detector and the creation and support of the EGO consortium. The authors also gratefully acknowledge research support from these agencies as well as by the Council of Scientific and Industrial Research of India, the Department of Science and Technology, India, the Science & Engineering Research Board (SERB), India, the Ministry of Human Resource Development, India, the Spanish Agencia Estatal de Investigación (AEI), the Spanish Ministerio de Ciencia e Innovación and Ministerio de Universidades, the Conselleria de Fons Europeus, Universitat i Cultura and the Direcció General de Política Universitaria i Recerca del Govern de les Illes Balears, the Conselleria d'Innovació, Universitats, Ciència i Societat Digital de la Generalitat Valenciana and the CERCA Programme Generalitat de Catalunya, Spain, the National Science Centre of Poland and the European Union – European Regional Development Fund; Foundation for Polish Science (FNP), the Swiss National Science Foundation (SNSF), the Russian Foundation for Basic Research, the Russian Science Foundation, the European Commission, the European Social Funds (ESF), the European Regional Development Funds (ERDF), the Royal Society, the Scottish Funding Council, the Scottish Universities Physics Alliance, the Hungarian Scientific Research Fund (OTKA), the French Lyon Institute of Origins (LIO), the Belgian Fonds de la Recherche Scientifique (FRS-FNRS), Actions de Recherche Concertées (ARC) and Fonds Wetenschappelijk Onderzoek – Vlaanderen (FWO), Belgium, the Paris Île-de-France Region, the National Research, Development and Innovation Office Hungary (NKFIH), the National Research Foundation of Korea, the Natural Science and Engineering Research Council Canada, Canadian Foundation for Innovation (CFI), the Brazilian Ministry of Science, Technology, and Innovations, the International Center for Theoretical Physics South American Institute for Fundamental Research (ICTP-SAIFR), the Research Grants Council of Hong Kong, the National Natural Science Foundation of China (NSFC), the Leverhulme Trust, the Research Corporation, the National Science and Technology Council (NSTC), Taiwan, the United States Department of Energy, and the Kavli Foundation. The authors gratefully acknowledge the support of the NSF, STFC, INFN and CNRS for provision of computational resources.

This work was supported by MEXT, JSPS Leading-edge Research Infrastructure Program, JSPS Grant-in-Aid for Specially Promoted Research 26000005, JSPS Grant-inAid for Scientific Research on Innovative Areas 2905: JP17H06358, JP17H06361 and JP17H06364, JSPS Core-to-Core Program A. Advanced Research Networks, JSPS Grantin-Aid for Scientific Research (S) 17H06133 and 20H05639 , JSPS Grant-in-Aid for Transformative Research Areas (A) 20A203: JP20H05854, the joint research program of the Institute for Cosmic Ray Research, University of Tokyo, National Research Foundation (NRF), Computing Infrastructure Project of Global Science experimental Data hub Center (GSDC) at KISTI, Korea Astronomy and Space Science Institute (KASI), and Ministry of Science and ICT (MSIT) in Korea, Academia Sinica (AS), AS Grid Center (ASGC) and the National Science and Technology Council (NSTC) in Taiwan under grants including the Rising Star Program and Science Vanguard Research Program, Advanced Technology Center (ATC) of NAOJ, and Mechanical Engineering Center of KEK.

Additional acknowledgements for support of individual authors may be found in the following document: `https://dcc.ligo.org/LIGO-M2300033/public`. For the purpose of open access, the authors have applied a Creative Commons Attribution (CC BY) license to any Author Accepted Manuscript version arising. We request that citations to this article use 'A.G. Abac *et al.* (LIGO-Virgo-KAGRA Collaboration), ...' or similar phrasing, depending on journal convention.

[1] A. Pierce, K. Riles, and Y. Zhao, Phys. Rev. Lett. **121**, 061102 (2018), arXiv:1801.10161 [hep-ph].

[2] K. Nagano, T. Fujita, Y. Michimura, and I. Obata, Phys. Rev. Lett. **123**, 111301 (2019), arXiv:1903.02017 [hep-ph].

[3] Y. Michimura, T. Fujita, S. Morisaki, H. Nakatsuka, and I. Obata, Phys. Rev. D **102**, 102001 (2020), arXiv:2008.02482 [hep-ph].

[4] A. L. Miller et al., Phys. Rev. D **103**, 103002 (2021), arXiv:2010.01925 [astro-ph.IM].

[5] K. Nagano, H. Nakatsuka, S. Morisaki, T. Fujita, Y. Michimura, and I. Obata, Phys. Rev. D **104**, 062008 (2021), arXiv:2106.06800 [hep-ph].

[6] A. L. Miller, F. Badaracco, and C. Palomba (LIGO Scientific, Virgo, KAGRA), Phys. Rev. D **105**, 103035 (2022), arXiv:2204.03814 [astro-ph.IM].

[7] H.-K. Guo, K. Riles, F.-W. Yang, and Y. Zhao, Commun. Phys. **2**, 155 (2019), arXiv:1905.04316 [hep-ph].

[8] S. Morisaki, T. Fujita, Y. Michimura, H. Nakatsuka, and I. Obata, Phys. Rev. D **103**, L051702 (2021), arXiv:2011.03589 [hep-ph].

[9] R. Abbott et al. (LIGO Scientific, KAGRA, Virgo), Phys. Rev. D **105**, 063030 (2022), arXiv:2105.13085 [astro-ph.CO].

[10] S. M. Vermeulen, P. Relton, H. Grote, V. Raymond, C. Affeldt, F. Bergamin, A. Bisht, M. Brinkmann, K. Danzmann, S. Doravari, V. Kringel, J. Lough, H. Lück, M. Mehmet, N. Mukund, S. Nadji, E. Schreiber, B. Sorazu, K. A. Strain, H. Vahlbruch, M. Weinert, B. Willke, and H. Wittel, Nature **600**, 424 (2021).

[11] A. L. Miller and L. Mendes, Phys. Rev. D **107**, 063015 (2023), arXiv:2301.08736 [gr-qc].

[12] G. Bertone, D. Hooper, and J. Silk, Phys. Rept. **405**, 279 (2005), arXiv:hep-ph/0404175.

[13] N. W. Evans, C. A. J. O'Hare, and C. McCabe, Phys. Rev. D **99**, 023012 (2019), arXiv:1810.11468 [astro-ph.GA].

[14] J. Aasi et al. (LIGO Scientific), Class. Quant. Grav. **32**, 074001 (2015), arXiv:1411.4547 [gr-qc].

[15] M. Tse et al., Phys. Rev. Lett. **123**, 231107 (2019).

[16] A. Buikema et al. (aLIGO), Phys. Rev. D **102**, 062003 (2020), arXiv:2008.01301 [astro-ph.IM].

[17] F. Acernese et al. (VIRGO), Class. Quant. Grav. **32**, 024001 (2015), arXiv:1408.3978 [gr-qc].

[18] F. Acernese et al. (Virgo), Phys. Rev. Lett. **123**, 231108 (2019).

[19] S. Schlamminger, K. Y. Choi, T. A. Wagner, J. H. Gundlach, and E. G. Adelberger, Phys. Rev. Lett. **100**, 041101 (2008), arXiv:0712.0607 [gr-qc].

[20] T. A. Wagner, S. Schlamminger, J. H. Gundlach, and E. G. Adelberger, Class. Quant. Grav. **29**, 184002 (2012), arXiv:1207.2442 [gr-qc].

[21] P. Touboul et al., Phys. Rev. Lett. **119**, 231101 (2017), arXiv:1712.01176 [astro-ph.IM].

[22] J. Bergé, P. Brax, G. Métris, M. Pernot-Borràs, P. Touboul, and J.-P. Uzan, Phys. Rev. Lett. **120**, 141101 (2018), arXiv:1712.00483 [gr-qc].

[23] P. Fayet, Phys. Rev. D **97**, 055039 (2018), arXiv:1712.00856 [hep-ph].

[24] H. Luck et al., J. Phys. Conf. Ser. **228**, 012012 (2010), arXiv:1004.0339 [gr-qc].

[25] K. L. Dooley et al., Class. Quant. Grav. **33**, 075009 (2016), arXiv:1510.00317 [physics.ins-det].

[26] K. Somiya (KAGRA), Class. Quant. Grav. **29**, 124007 (2012), arXiv:1111.7185 [gr-qc].

[27] Y. Aso, Y. Michimura, K. Somiya, M. Ando, O. Miyakawa, T. Sekiguchi, D. Tatsumi, and H. Yamamoto (The KAGRA Collaboration), Phys. Rev. D **88**, 043007 (2013).

[28] T. Akutsu et al. (KAGRA), PTEP **2021**, 05A101 (2021), arXiv:2005.05574 [physics.ins-det].

[29] Y. Michimura, T. Fujita, J. Kume, S. Morisaki, K. Nagano, H. Nakatsuka, A. Nishizawa, and I. Obata, J. Phys. Conf. Ser. **2156**, 012071 (2021), arXiv:2111.00420 [hep-ph].

[30] R. Abbott et al. (KAGRA, VIRGO, LIGO Scientific), PTEP **2022**, 063F01 (2022), arXiv:2203.01270 [gr-qc].

[31] H. Abe et al. (KAGRA), Prog. Theor. Exp. Phys. (2022), 10.1093/ptep/ptac093, arXiv:2203.07011 [astro-ph.IM].

[32] H. Nakatsuka, S. Morisaki, T. Fujita, J. Kume, Y. Michimura, K. Nagano, and I. Obata, Phys. Rev. D **108**, 092010 (2023), arXiv:2205.02960 [astro-ph.CO].

[33] T. Akutsu et al. (KAGRA collaboration), Progress of Theoretical and Experimental Physics **2021**, 05A101 (2020), https://academic.oup.com/ptep/article-pdf/2021/5/05A101/37974994/ptaa125.pdf.

[34] P. R. Brady, T. Creighton, C. Cutler, and B. F. Schutz, Phys. Rev. D **57**, 2101 (1998).

[35] P. Jaranowski, A. Królak, and B. F. Schutz, Phys. Rev. D **58**, 063001 (1998).

[36] P. R. Brady and T. Creighton, Phys. Rev. D **61**, 082001 (2000).

[37] R. Tenorio, D. Keitel, and A. M. Sintes, Universe **7**, 474 (2021), arXiv:2111.12575 [gr-qc].

[38] K. Riles, Living Rev. Rel. **26**, 3 (2023), arXiv:2206.06447 [astro-ph.HE].

[39] K. Wette, Astropart. Phys. **153**, 102880 (2023), arXiv:2305.07106 [gr-qc].

[40] Y. Oshima, H. Fujimoto, J. Kume, S. Morisaki, K. Nagano, T. Fujita, I. Obata, A. Nishizawa, Y. Michimura, and M. Ando, Phys. Rev. D **108**, 072005 (2023), arXiv:2303.03594 [hep-ex].

[41] B. Abbott et al. (LIGO Scientific), Phys. Rev. D **72**, 102004 (2005), arXiv:gr-qc/0508065.

[42] LVK, "O3GK KAGRA auxiliary length data release," https://gwosc.org/data/ (in preparation).

[43] J. Kume et al., "Unknown lines in MICH/PRCL data of KAGRA O3GK," LIGO-L2300092 (2023), https://dcc.ligo.org/L2300092/public.

[44] Y. Michimura, K. Komori, Y. Enomoto, K. Nagano, A. Nishizawa, E. Hirose, M. Leonardi, E. Capocasa, N. Aritomi, Y. Zhao, R. Flaminio, T. Ushiba, T. Yamada, L.-W. Wei, H. Takeda, S. Tanioka, M. Ando, K. Yamamoto, K. Hayama, S. Haino, and K. Somiya, Phys. Rev. D **102**, 022008 (2020).

Fermionic Fixed-Point Structure of Asymptotically Safe QED with a Pauli Term

Holger Gies[1, 2, 3] and Kevin K. K. Tam[1]

[1] *Theoretisch-Physikalisches Institut, Abbe Center of Photonics, Friedrich-Schiller-Universität Jena, Max-Wien-Platz 1, 07743 Jena, Germany*
[2] *Helmholtz-Institut Jena, Fröbelstieg 3, 07743 Jena, Germany*
[3] *GSI Helmholtzzentrum für Schwerionenforschung, Planckstr. 1, 64291 Darmstadt, Germany*

(Dated: March 6, 2024)

We test the physical viability of a recent proposal for an asymptotically safe modification of quantum electrodynamics (QED), whose ultraviolet physics is dominated by a non-perturbative Pauli spin-field coupling. We focus in particular on its compatibility with the absence of dynamical generation of fermion mass in QED. Studying the renormalization group flow of chiral four-fermion operators and their fixed points, we discover a distinct class of behavior compared to the standard picture of fixed-point annihilation at large gauge couplings and the ensuing formation of chiral condensates. Instead, transcritical bifurcations, where the fixed points merely exchange infrared stability, are observed. Provided that non-chiral operators remain irrelevant, our theory accommodates a universality class of light fermions for $N_{\rm f} > 1$ irreducible Dirac flavors. On the contrary, in the special case of $N_{\rm f} = 1$ flavor, this comes only at the expense of introducing one additional relevant parameter.

arXiv:2403.02980v1 [hep-th] 5 Mar 2024

I. INTRODUCTION

Quantum electrodynamics (QED) is an extremely well-tested theory, exhibiting remarkable agreement with precision experiments at low energies [1–5]. Of course, high-energy tests are also passed by the theory though at lower precision [6, 7] and ultimately require the embedding of QED into the electroweak sector of the standard model. Still, the high-energy behavior of pure QED remains of interest in its own right, as it has constituted a puzzle since the early days of quantum field theory: perturbation theory predicts a divergence of the minimal gauge coupling at a finite Landau pole [8, 9]. While this may simply signal the expected breakdown of perturbation theory in the strong-coupling regime, the conclusion of the existence of a finite scale of maximum ultraviolet (UV) extension is supported by lattice simulations [10–12] and functional methods [13].

The picture obtained from such nonperturbative methods is, however, decisively different from simple perturbation theory: a strong coupling phase of QED – even if it existed – can generically not be connected by a line of constant physics to physical QED because of chiral symmetry breaking. Strong gauge interactions induce fermion mass generation with masses on the order of the high scale being incompatible with the observed existence of a light electron. In continuum computations, the symmetry breaking can be traced back to fermionic self-interactions turning into relevant operators at strong coupling and triggering condensate formation [13–15]. The corresponding long-range limit of such a theory would then be a free photon theory.

As a resolution, a recent proposal has been based on the observation that the Pauli spin-field coupling term $\bar\psi\sigma_{\mu\nu}F^{\mu\nu}\psi$ has the potential to screen the Landau pole – and thus the strong-coupling regime – within an effective field theory [16]. In fact, a self-consistent analysis of pure QED with a Pauli term has provided evidence for the existence of interacting fixed-points potentially rendering QED asymptotically safe [17, 18] and thus high-energy complete. As a dimension-5 operator with only a single derivative with respect to the photon, the Pauli term represents the unique next-to-leading-order contribution in a combined derivative and power-counting operator expansion of the effective action.

By the techniques of functional renormalization, the extended theory space has been shown to include two non-trivial fixed points $\mathcal{B}$ and $\mathcal{C}$ at vanishing gauge coupling [17], each of which provides an ultraviolet (UV) completion of QED as an asymptotic safety scenario. Specifically, the fixed point $\mathcal{C}$ occurring at a finite Pauli coupling κ is compatible with a renormalization group (RG) trajectory reproducing the long-range values of phenomenological QED. As it features three relevant directions, the long-range physics is fully predictive, once three parameters have been fixed by experiment (e.g., the electron mass, the fine structure constant, and the anomalous magnetic moment of the electron). (By contrast, fixed point $\mathcal{B}$ predicts unphysically large values of the anomalous magnetic moment in the infrared (IR); while being potentially consistent and UV complete, this universality class is observationally not viable.)

In view of the impossibility to connect conventional strong-coupling QED with the observed existence of light electrons, an obvious question needs to be answered: does an asymptotically safe UV completion based on the Pauli term preserve chiral symmetry along its RG trajectories towards the infrared (IR)? This is not at all evident, since fixed point $\mathcal{C}$ – though featuring a vanishing mass – occurs at a deeply nonperturbative value of the Pauli coupling $\kappa^* = 3.82$, independently of fermion flavor number [18].

To further scrutinize the physical relevance of this continuum theory, we go beyond the Pauli term in the truncation of the effective action. Operators of particular interest are given by dimension-6 four-fermion channels of the Nambu-Jona-Lasinio (NJL) type, which appear in an

effective theory of spontaneous chiral symmetry breaking in quantum chromodynamics [19, 20]. Just as the formation of chiral condensates is responsible for the constituent quark masses, the focus of this work is to investigate whether the strong coupling regime at fixed point $\mathcal{C}$ dynamically generates mass at a UV scale, for example at the Planck scale, which would be in contradiction to the observation of light fermions of the Standard Model. Similar problems are known to impede non-trivial formulations of pure QED [10, 13–15].

In QED, chiral symmetry is broken explicitly by the mass term. In the same manner, the Pauli spin-field coupling is also a source of explicit breaking, both of which we consider as small in agreement with observation. While such small breakings allow for the appearance of many further four-fermion interactions, we concentrate here on an otherwise Fierz-complete basis of NJL-type channels, assuming that they play a dominant role in the case of interaction-induced dynamical chiral symmetry breaking. This assumption is similar to low-energy effective theories for QCD where explicit chiral breaking terms can be treated as a small perturbation.

In this setting, we discover that the distinct coupling of the two NJL-type channels by the Pauli term qualitatively alters the bifurcation behavior known from strong QED or QCD: instead of annihilation upon collision, the NJL fixed points merely exchange stability such that an IR attractor persists at arbitrarily strong Pauli coupling for more than $N_\mathrm{f} = 1$ fermion flavor. In such cases, there exists a universality class where the RG flow remains bounded and mass generation can be avoided without further fine-tuning. A similar conclusion can be drawn from our initial analysis for fixed point $\mathcal{B}$, despite the different role played by the aforementioned bifurcation.

The structure of this paper is as follows: In Sect. II, we introduce the abelian gauged NJL model with a Pauli term. Sect. III then presents the corresponding RG flow equation. Sect. IV is allocated to analyzing the fixed point structure in the four-fermion sector of our theory, drawing comparisons to previous results in relation to the pure NJL model (IV A) and the introduction of a gauge field (IV B).

II. GAUGED NJL MODEL WITH PAULI TERM

We consider the massless limit of an abelian gauged NJL model with a Pauli term. Satisfying Osterwalder-Schrader reflection positivity in Euclidean spacetime, the effective action reads

$$\Gamma_k = \int d^4x \Big\{ \bar\psi^a \left(i Z_\psi \partial\!\!\!/ + \bar e A\!\!\!/ + i\bar\kappa \sigma_{\mu\nu} F^{\mu\nu} \right) \psi^a + \frac{Z_A}{4} F_{\mu\nu}F^{\mu\nu} + \frac{Z_A}{2\xi} (\partial_\mu A^\mu)^2 + \frac{1}{2}\bar\lambda_+ (\mathrm{V}+\mathrm{A}) + \frac{1}{2}\bar\lambda_- (\mathrm{V}-\mathrm{A}) \Big\}. \quad (1)$$

Here $a = 1, \ldots, N_\mathrm{f}$ labels the Dirac flavors ψ^a interacting with a U(1) gauge field A_μ. The couplings $\bar e$, $\bar\kappa$ and $\bar\lambda_\pm$, as well as the wave function renormalizations $Z_{\psi,A}$, are dependent on the RG scale k. We further work in the Landau gauge $\xi = 0$ as a fixed point of the RG flow [21, 22]. For our purposes, it suffices to consider the point-like approximation where the four-fermion couplings $\bar\lambda(p_1, p_2, p_3) \to \bar\lambda(0,0,0)$ are approximated by their low-momentum limit [23]. Neglecting the explicit breaking of a chiral $\mathrm{SU}(N_\mathrm{f})_\mathrm{L} \otimes \mathrm{SU}(N_\mathrm{f})_\mathrm{R}$ symmetry by the Pauli term, the four-fermion channels

$$(\mathrm{V} \pm \mathrm{A}) \equiv \left(\bar\psi^a \gamma_\mu \psi^a\right)^2 \pm \left(\bar\psi^a i\gamma_\mu\gamma_5 \psi^a\right)^2, \quad (2)$$

would form a Fierz-complete basis under the RG flow. The $(\mathrm{V}+\mathrm{A})$ channel is Fierz equivalent to the conventional NJL channel. In the limit of vanishing $\bar\kappa, \bar\lambda_\pm$ (and upon inclusion of an explicit fermion mass term), the present model is identical to QED. If RG trajectories exist that match the QED long-range behavior, then a high-energy complete trajectory in the present model can be viewed as a UV-complete version of QED. In the search for scale-invariant fixed points facilitating UV-complete trajectories, it is convenient to define further dimensionless renormalized couplings

$$\lambda_\pm = \frac{k^2 \bar\lambda_\pm}{Z_\psi^2}, \quad e = \frac{\bar e}{Z_\psi \sqrt{Z_A}}, \quad \kappa = \frac{k\bar\kappa}{Z_\psi \sqrt{Z_A}}. \quad (3)$$

For the present study, we use the functional RG based on the effective average action Γ_k which interpolates between the classical bare action $\Gamma_{k\to\Lambda} = S$ and the full quantum effective action $\Gamma_{k\to 0} = \Gamma$ [23–28]. Defining the RG time as $t = \ln k$, the flow through theory space is governed by the Wetterich equation [29–32]

$$\partial_t \Gamma_k = \frac{1}{2} \mathrm{STr} \left[\partial_t R_k \left(\Gamma_k^{(2)}[\phi] + R_k \right)^{-1} \right], \quad (4)$$

where $R_k(p^2)$ acts as a momentum-dependent regulator, screening the contribution of IR modes with momenta below the cutoff k.

III. FLOW EQUATIONS

With the effective action Γ_k expressed in terms of the operators in (1), the Wetterich equation (4) can be projected onto the four-fermion sector to yield the beta functions

$$\partial_t \lambda_+ = (2 + 2\eta_\psi)\, \lambda_+ + 4 v_4\, l_4^{(\mathrm{F})}(0,0) \left[6\lambda_+^2 + (d_\gamma N_f + 4)\, \lambda_+ \lambda_- \right] \quad (5)$$

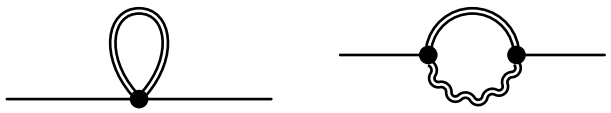
$$
\begin{aligned}
&- 24v_4\, l_4^{(\mathrm{B},\,\mathrm{F})}(0,0)\, e^2\lambda_+ - 48v_4\, l_4^{(1,\,\mathrm{B},\,\mathrm{F})}(0,0)\, \kappa^2\lambda_- \\
&+ 6v_4\, l_4^{(\mathrm{B}^2,\,\mathrm{F})}(0,0)\, e^4 - 48v_4\, l_4^{(1,\,\mathrm{B}^2,\,\mathrm{F})}(0,0)\, e^2\kappa^2 + 96v_4\, l_4^{(2,\,\mathrm{B}^2,\,\mathrm{F})}(0,0)\, \kappa^4,
\end{aligned}
$$

$$
\begin{aligned}
\partial_t\lambda_- = {}& (2+2\eta_\psi)\lambda_- + 2v_4\, l_4^{(\mathrm{F})}(0,0)\left[(d_\gamma N_f - 4)\,\lambda_-^2 + d_\gamma N_f \lambda_+^2\right] \\
&+ 24v_4\, l_4^{(\mathrm{B},\,\mathrm{F})}(0,0)\, e^2\lambda_- - 48v_4\, l_4^{(1,\,\mathrm{B},\,\mathrm{F})}(0,0)\, \kappa^2\lambda_+ \\
&- 6v_4\, l_4^{(\mathrm{B}^2,\,\mathrm{F})}(0,0)\, e^4 + 48v_4\, l_4^{(1,\,\mathrm{B}^2,\,\mathrm{F})}(0,0)\, e^2\kappa^2 - 96v_4\, l_4^{(2,\,\mathrm{B}^2,\,\mathrm{F})}(0,0)\, \kappa^4.
\end{aligned} \tag{6}
$$

Here we have adopted the notation for threshold functions introduced in [17]. The anomalous dimension

$$\eta_\psi = -\partial_t \ln Z_\psi \tag{7}$$

implements an RG improvement by resummation of 1PI diagrams contributing to the propagator, as depicted in Figure 1. In the point-like limit, four-fermion corrections to η_ψ must vanish, as momentum conservation in the tadpole diagram of Figure 1a ensures the independence of the loop momentum from external momentum. As such, the fermionic anomalous dimension at fixed point $\mathcal{C}$ remains at the value of $\eta_\psi^* = -1$ due to Pauli contributions (Figure 1b). This precisely renders the dimension-5 Pauli operator marginally relevant in $d = 4$, even before considering higher-order diagrams.



(a) (b)

FIG. 1: 1PI Feynman diagrams contributing to the fermionic anomalous dimension η_ψ. a) The tadpole diagrams vanish in the point-like limit where the momentum dependence of the NJL couplings $\lambda_\pm$ is neglected. b) The self-energy diagrams result in the value of $\eta_\psi = -1$ at fixed point $\mathcal{C}$, which renders both Pauli coupling κ and NJL coupling $\lambda_\pm$ perturbatively marginal in the absence of higher-order terms.

Likewise, the scaling terms in Eqs. (5)-(6) vanish, and thus the relevance of the NJL channels is decided entirely by the higher-order terms of the beta functions, as represented by Figure 2.

IV. FIXED POINT ANALYSIS

A. Pure NJL Model

Before we examine the fate of the NJL channels in the presence of the Pauli term, we first review the RG flow of the pure NJL model ($e = \kappa = \eta_\psi = 0$) [23, 33, 34], shown in Figure 3 for the case of $N_\mathrm{f} > 1$ irreducible flavors, for which the Dirac representation has dimension $d_\gamma = 4$. As the beta functions (5)-(6) form a pair of quadratic functions of the NJL couplings $\lambda_\pm$, there exist in general four fixed points $\mathcal{F}_i = \left(\lambda_+^{*i}, \lambda_-^{*i}\right)$, $i = 1, \ldots, 4$. We quantify the fixed-point properties in terms of their critical exponents θ which are related to the eigenvalues of the stability matrix $B_{ij} := \partial(\partial_t\lambda_i)/\partial\lambda_j|_{\lambda^*}$: $\theta = -\mathrm{eig}(B)$. Positive values of θ denote RG relevant directions that correspond to physical parameters to be fixed. Negative exponents, in turn, characterize RG irrelevant directions that do not exert an influence on the long-range IR physics.

As expected from power counting, the Gaussian fixed point $\mathcal{F}_1$ is purely IR attractive with critical exponents both being $\theta = -2$. The interacting fixed points $\mathcal{F}_2$ and $\mathcal{F}_3$ each has one relevant direction, while the fourth fixed point $\mathcal{F}_4$ is purely IR repulsive, i.e. relevant. Each of the fixed points $\mathcal{F}_{2,3,4}$ has one relevant eigendirection ($\theta = 2$) pointing along the line that connects the fixed point $\mathcal{F}_{i\geq 2}$ with the Gaussian fixed point $\mathcal{F}_1$. This is in line with general theorems [33, 35]. It is straightforward to also compute the remaining critical exponents analytically.

We observe that the purely IR-repulsive $\mathcal{F}_4$ moves towards infinity for $N_\mathrm{f} \to 1$ flavor. This is because the beta function (6) becomes linear in λ_-, with the vanishing fermionic loop contribution $\sim \lambda_-^2$ of Figure 2a.

The universality class defined by the Gaussian fixed point $\mathcal{F}_1$ corresponds to a chirally symmetric phase (regions II & IV) with massless fermions, as the NJL couplings $\lambda_\pm$ remain finite under the RG flow and approach zero in the long-range limit. Meanwhile, initial conditions within regions I & III lead to divergence at a finite RG scale k_{SB}, signaling the formation of a condensate which dresses the fermions with a mass $m_\psi \sim k_{SB}$. This phase of the model is used in low-energy QCD effective models.

In the simplest incarnation of the NJL model, the coupling λ_- is set to zero, and the coupling λ_+ corresponds to (-2) times the more familiar scalar-pseudoscalar chan-

nel (S−P). The fixed-point $\mathcal{F}_2$ (projected on the λ_+ axis) then defines the NJL critical coupling that separates the chirally symmetric weak-coupling phase from the chirally broken phase at strong coupling.

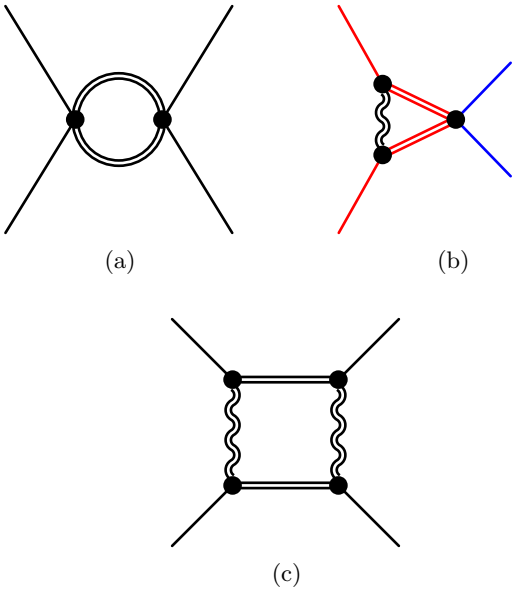


FIG. 2: 1PI Feynman diagrams contributing to the flow of the four-fermion vertex. a) The fermionic loops carry flavor number dependence such that the λ_-^2 contribution vanishes for a single irreducible flavor. b) The triangular diagrams only contribute to the RG flow in the chirally invariant NJL subspace when the photon is exchanged between fermions of identical flavor. Moreover, the flows of $\lambda_\pm$ are maximally coupled by these diagrams, unlike their gauge coupling counterparts. c) The box diagrams can induce a finite NJL coupling $\lambda_\pm$ purely through photonic fluctuations.

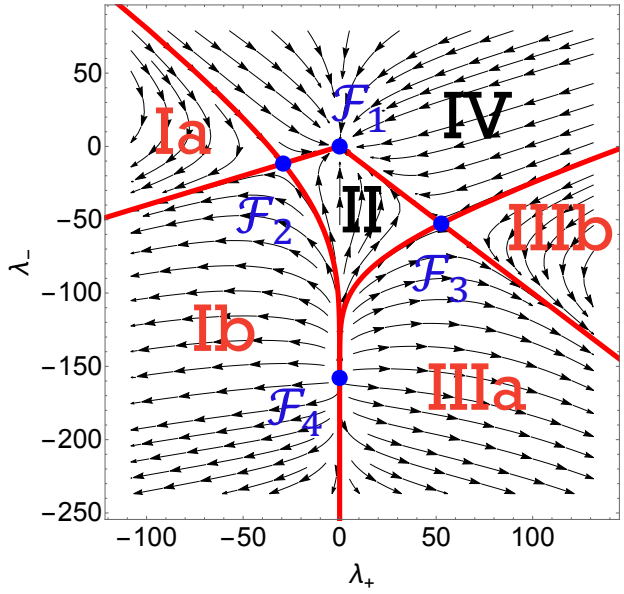


FIG. 3: Phase diagram of the NJL theory subspace spanned by the (V ± A) channels for $N_\mathrm{f} = 2$ irreducible Dirac flavors. Arrows indicate flow towards the infrared. Separatrices (red curves) flowing between fixed points $\mathcal{F}_i$ (blue points) delineate a universality class of light fermions (regions II & IV; black) as observed in nature. On the contrary, the RG flow in regions I & III diverge, heralding the onset of dynamical mass generation. For $N_\mathrm{f} = 1$, $\mathcal{F}_4$ lies at infinity.

B. Finite Gauge Coupling

With a nonzero gauge coupling e, the beta functions (5)-(6) reproduce the known result where the Gaussian fixed point $\mathcal{F}_1$ is annihilated by collision with $\mathcal{F}_2$ at a critical value e_crit. This – in a nutshell – illustrates the relevant mechanism that screens the perturbative Landau pole and inhibits a UV completion of long-range QED: even if QED were UV complete in the strong coupling region, it would exhibit high-scale chiral symmetry breaking and mass generation in contradiction to the observed light mass of the electron [11–14]. In analogous nonabelian settings, the similar mechanism involving the strong gauge coupling triggers the dynamical mass generation in the IR limit of quantum chromodynamics [23, 36–44].

Such an effect is already captured by the Fierz-incomplete single-channel approximation $\lambda_- \equiv 0$. The remaining beta function, now represented by a parabola, is shifted vertically by the finite gauge coupling until the fixed points undergo a saddle-node bifurcation into the complex plane.

C. Finite Pauli Coupling

In contrast to the theory space spanned by minimally coupled QED, the inclusion of the Pauli coupling has provided evidence for the existence of a new universality class governed by a non-Gaussian fixed point, called fixed point $\mathcal{C}$ in [17]. This fixed point occurs at $e^* = 0$, $\kappa^* \simeq 3.82$ and $\eta_\psi = -1$ with the Pauli coupling and the minimal coupling corresponding to relevant directions (in addition to the massive perturbation).

With regard to Eqs. (5) and (6), we note that the only qualitative difference lies in the terms $\partial_t \lambda_\pm \sim \kappa^2 \lambda_\mp$ corresponding to the exchange of a single photon (Figure 2b). Unlike their gauge coupling counterparts, these terms are non-diagonal in the $\lambda_\pm$ basis. Ultimately, this is due to the anticommutativity of all Dirac matrices with the γ_5 from the axial vector channel in Eq. (2).

For $N_\mathrm{f} > 1$ we again observe a collision between fixed points $\mathcal{F}_1$ and $\mathcal{F}_2$ at a critical value κ_crit, but instead of annihilation, they merely exchange stability such that both fixed points continue to exist in the real coupling

plane and $\mathcal{F}_2$ is now purely IR attractive. The result of this transcritical bifurcation is shown in Figure 4. The persistence of this attractor in the strong coupling regime maintains a universality class where mass generation is avoided (region II). This effect is not captured in the single-channel approximation $\lambda_- \equiv 0$.

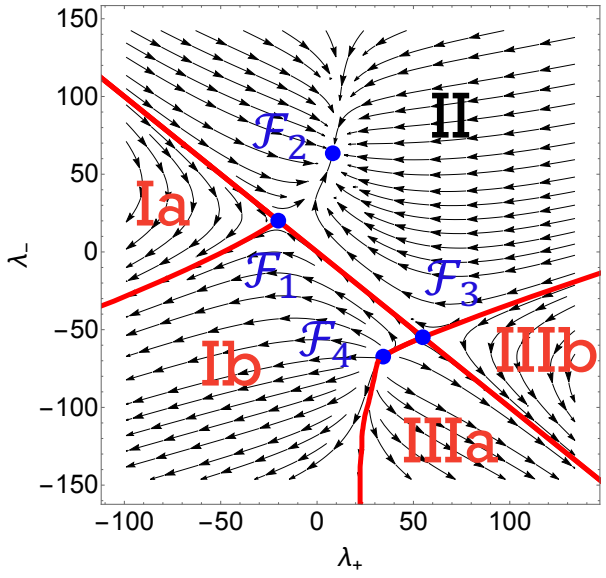


FIG. 4: Phase diagram of the four-fermion subspace spanned by the NJL-type (V ± A) channels at the Pauli-induced fixed point $\mathcal{C}$ ($\kappa^* = 3.82, \eta_\psi = -1$) for $N_\mathrm{f} = 2$ irreducible Dirac flavors. Arrows indicate flow towards the infrared. Compared to Figure 3, $\mathcal{F}_1$ and $\mathcal{F}_2$ have undergone a transcritical bifurcation and exchanged their stability. There remains a universality class of light fermions (region II).

For an interpretation of the fixed-points as possible routes to UV completion or as critical couplings defining universality classes, we summarize their critical exponents in Tab. I. With the gauge system being at fixed point $\mathcal{C}$ with a non-Gaussian Pauli coupling where $\eta_\psi = -1$, the naive non-Gaussian scaling of the four-fermion couplings suggests that the largest critical exponent should be close to zero. We therefore use large deviations from this expectation as an indication for sizable truncation artefacts. This reasoning is analogous to that applied to four-fermion models beyond 2 dimensions [23, 33, 35, 45, 46] .

From this perspective, $\mathcal{F}_3$ and $\mathcal{F}_4$ represent fixed points with large deviations from the expected scaling that are likely to be dominated by truncation artefacts. While we do not expect them to persist in larger truncations and they should thus not be used for a construction of UV complete trajectories, they and their separatrices may still be used as a qualitative estimate of the boundaries of the chirally symmetric phase II.

By contrast, $\mathcal{F}_1$ and $\mathcal{F}_2$ exhibit small leading exponents

	$\mathcal{F}_1$	$\mathcal{F}_2$	$\mathcal{F}_3$	$\mathcal{F}_4$
$N_\mathrm{f} = 2$:	$(0.102, -4.41)$	$(-0.101, -4.44)$	$(4.41, -5.78)$	$(10.0, 2.75)$
$N_\mathrm{f} = 1$:	$(3.14, -2.36)$	–	$(2.36, -6.30)$	–

TABLE I: Critical exponents θ of the fixed points in the plane of four-fermion interactions with the gauge system being at the fixed point $\mathcal{C}$ with a non-Gaussian Pauli coupling.

close to zero. Fixed point $\mathcal{F}_2$ with two negative exponents is fully IR attractive and thus should be viewed as a *shifted Gaussian fixed point* [34, 47], playing the role of the Gaussian fixed point with a location at finite coupling due to the residual non-Gaussian interactions induced by the Pauli coupling. On the other hand, $\mathcal{F}_1$ also exhibits small deviations from the expected scaling with a relevant direction that points approximately along the NJL channel. Whether or not $\mathcal{F}_1$ could be used to define UV complete trajectories should be checked in future investigations. For the present work, we focus on the existence of $\mathcal{F}_2$ as a completely attractive fixed point. This establishes that we find a qualitatively identical phase diagram to Figure 4 for more than one fermion flavor even for the case that the Pauli coupling κ^* is near fixed point $\mathcal{C}$. This statement holds independently of flavor number N_f [18] with the minor difference that the magnitude of κ^* is insufficient to induce the collision between $\mathcal{F}_1$ and $\mathcal{F}_2$ for larger flavor numbers > 5.25; in such cases, $\mathcal{F}_1$ simply remains the shifted Gaussian fixed point. A strong Pauli coupling phase of QED could thus allow for the construction of UV complete trajectories without being endangered by chiral symmetry breaking in contradistinction to a strong minimal coupling phase. Incidentally, a further transcritical bifurcation occurs for $N_\mathrm{f} \gtrsim 4.94$ between $\mathcal{F}_3$ and $\mathcal{F}_4$. This, however, leaves our conclusions about UV completion in the symmetric phase unaffected.

In the special case of $N_\mathrm{f} = 1$, as with the pure NJL model of Subsection IV A, the quadratic term in λ_- in equation (6) vanishes. Combined with the vanishing scaling term due to $\eta_\psi = -1$, all dependences on λ_- drop out from the beta function. A transcritical bifurcation between $\mathcal{F}_1$ and $\mathcal{F}_2$ is still observed, but the purely attractive $\mathcal{F}_2$ then lies at infinity along with the purely repulsive $\mathcal{F}_4$. While this offers, in principle, a construction of a similar UV complete scenario as in the $N_\mathrm{f} > 1$ case, the inherently large coupling values make it difficult to control the expansion scheme. The remaining two fixed points at finite coupling values $\mathcal{F}_1$ and $\mathcal{F}_3$ show large leading exponents with large deviations from the expected scaling, cf. Tab. I. Our present study therefore does not allow us to draw any definite conclusions about the existence of UV complete trajectories controlled by the Pauli coupling for the special case of $N_\mathrm{f} = 1$.

We should note however, that the explicit violation of chiral symmetry by the Pauli term generates further four-fermion channels, e.g., an additional Gross-Neveu channel outside the NJL subspace. This occurs through

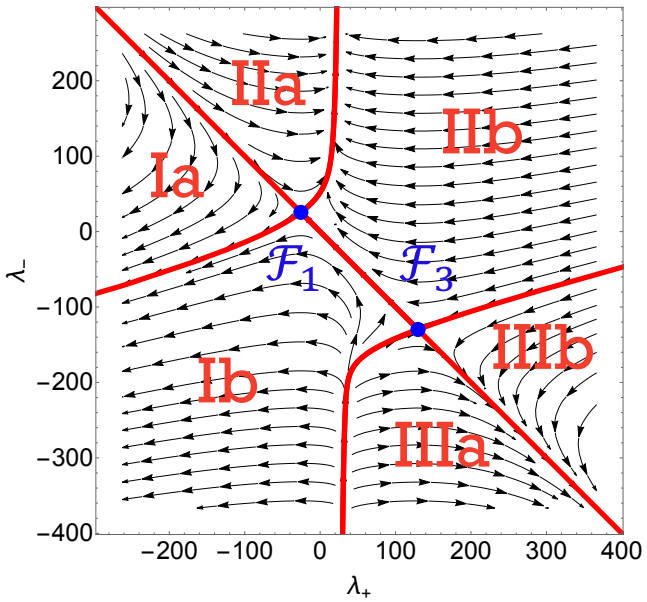


FIG. 5: Phase diagram of the NJL theory subspace spanned by the (V ± A) channels at the Pauli-induced fixed point $\mathcal{C}$ ($\kappa^* = 3.82, \eta_\psi = -1$) for $N_\mathrm{f} = 1$ irreducible Dirac flavor. Arrows indicate flow towards the infrared. Compared to Figure 4, $\mathcal{F}_2$ and $\mathcal{F}_4$ lie at infinity. This is because the beta function (6) no longer depends on λ_-, with the simultaneous vanishing of the scaling term and fermionic loop contribution $\sim \lambda_-^2$.

the exchange of a Pauli-coupled photon between different flavors (in contrast to Figure 2b). In Eqs. (5)-(6), we have discarded such contributions for simplicity. A Fierz-complete analysis of the RG relevance of such channels is beyond the scope of this work. Nevertheless, the structure of the resulting Fierz-complete equations remains similar to the chirally invariant subspace studied here: the inclusion of n four-fermion channels can potentially entail 2^n fixed points in the corresponding coupling space λ_i. As long as one of these fixed points features properties of a shifted Gaussian fixed point similar to $\mathcal{F}_2$ for $N_\mathrm{f} > 1$ in the present case, our main conclusions remain unaffected.

For completeness, let us mention that we have applied the same analysis to the compatibility of fixed point $\mathcal{B}$ discovered in [17] with light fermions. As an approximation, we neglect additional terms in the beta functions due to the finite fermion mass m and take into account such threshold effects only through the regulators in Eqs. (5)-(6). The most significant difference lies in the larger fermionic anomalous dimensions $\eta_\psi^* < -1$, which tends to reflect fixed points across the origin and reverse the direction of the RG flow. Once again, we observe a transcritical bifurcation between the now purely IR repulsive would-be Gaussian $\mathcal{F}_1$ and $\mathcal{F}_2$, but the latter is no longer responsible for avoiding heavy fermions. Instead, this role is taken up by the IR-stable $\mathcal{F}_4$, which lies at finite coupling values for $N_\mathrm{f} > 1$.

V. CONCLUSION

We have studied the renormalization flow of chirally invariant four-fermion operators when subject to a strong-coupling regime as provided by a recently discovered fixed point in QED including a non-Gaussion Pauli spin-field coupling. The flow of these fermionic operators is a crucial litmus test for the viability of an asymptotic safety scenario based on the non-Gaussian fixed point $\mathcal{C}$ as discussed in [17, 18]. This is because strong-coupling has the potential to drive chiral symmetry breaking in QED and generate a heavy electron mass incompatible with observation.

In fact, Pauli-induced asymptotic safety at fixed point $\mathcal{C}$ demands that the fermionic anomalous dimension $\eta_\psi = -1$ renders four-fermion couplings perturbatively marginal, at least at the present level of truncation. At first glance, this appears precarious as any propsective fixed points are then maximally susceptible to removal by the Pauli coupling term $\sim \kappa^4$ of the beta function.

However, the flow in the full chirally invariant plane spanned by the pointlike four-fermion interactions known from NJL-type models captures the effects of single-photon exchange (Figure 2b). The resulting coupled flow of the NJL-type couplings $\lambda_\pm$ exhibits transcritical bifurcations where the fixed points merely exchange stability, in stark contrast to the annihilation observed at strong minimal gauge coupling. As such, for $N_\mathrm{f} > 1$ irreducible Dirac flavors, there remains an infrared attractor at arbitrarily strong Pauli coupling, which prevents dynamical mass generation at a UV scale. This attractor is reminiscent of a shifted Gaussian fixed point. RG trajectories emanating from this fixed point are UV complete and do not introduce further physical parameters. We observe that this scenario is not visible in a Fierz-incomplete chiral truncation based on a single NJL coupling.

On the other hand, for $N_\mathrm{f} = 1$, the simultaneous vanishing of the scaling term and fermionic loop contribution $\sim \lambda_-^2$ conspire to prevent the existence of a fully attractive fixed point at finite coupling. While we do observe two fixed points, they do not satisfy all of our validity criteria and would come with further relevant directions, i.e., require a further physical parameter.

Our work may be further extended to include a Fierz-complete basis including also the non-chiral four-fermion interactions. This would accommodate the Gross-Neveu channel generated by single-photon exchange between different flavors, resumming all ladder and crossed-ladder diagrams. The inclusion of further channels generically leads to an increase in the number of fixed points [33, 35]. Our current scenario remains viable, if one of these fixed points remains fully IR attractive similar to a shifted Gaussian fixed point. While perfectly plausible, this remains to be confirmed.

We have not fully considered the feedback of the four-

fermion sector on the running of the gauge/Pauli couplings. While such a feedback on the minimal gauge coupling vanishes at the fermionic fixed points by virtue of the Ward-Takahashi identities [33], a similar mechanism is not expected for the feedback on the flow of the Pauli coupling. But symmetry arguments ensure that such contributions be proportional to the mass m, which vanishes at fixed point $\mathcal{C}$ and can only affect the flow towards the IR.

In summary, our findings provide further evidence for a scenario of an asymptotically safe UV completion of pure QED based on a non-Gaussian Pauli spin-field coupling. We identify a fixed-point collision with a subsequent exchange of stability properties as a crucial mechanism to avoid chiral symmtry breaking in the strong-coupling regime. This mechanism is, however, operative only for $N_\mathrm{f} > 1$.

ACKNOWLEDGMENTS

We thank Jobst Ziebell for valuable discussions. This work has been funded by the Deutsche Forschungsgemeinschaft (DFG) under Grant Nos. 398579334 (Gi328/9-1) and 406116891 within the Research Training Group RTG 2522/1, as well as under Grant Nos. 392856280, 416607684, and 416611371 within the Research Unit FOR2783/2.

[1] X. Fan, T. G. Myers, B. A. D. Sukra, and G. Gabrielse, Phys. Rev. Lett. **130**, 071801 (2023).
[2] A. Ali and P. Soding, eds., *HIGH-ENERGY ELECTRON POSITRON PHYSICS* (WSP, Singapore, 1988).
[3] R. P. FEYNMAN, *QED: The Strange Theory of Light and Matter*, rev - revised ed. (Princeton University Press, 1985).
[4] G. Gabrielse, Adv. Ser. Direct. High Energy Phys. **20**, 195 (2009).
[5] X. Fan, T. G. Myers, B. A. D. Sukra, and G. Gabrielse, Phys. Rev. Lett. **130**, 071801 (2023), arXiv:2209.13084 [physics.atom-ph].
[6] M. Aaboud *et al.* (ATLAS), Nature Phys. **13**, 852 (2017), arXiv:1702.01625 [hep-ex].
[7] A. M. Sirunyan *et al.* (CMS), Phys. Lett. B **797**, 134826 (2019), arXiv:1810.04602 [hep-ex].
[8] L. D. Landau, A. A. Abrikosov, and I. M. Khalatnikov, Doklady Akad. Nauk S.S.S.R. **95** (1954).
[9] L. Landau, *in Niels Bohr and the Development of Physics, ed. W. Pauli, Pergamon Press, London*, (1955).
[10] S. Kim, J. B. Kogut, and M.-P. Lombardo, Physics Letters B **502**, 345 (2001).
[11] S. Kim, J. B. Kogut, and M.-P. Lombardo, Phys. Rev. D **65**, 054015 (2002).
[12] M. Göckeler, R. Horsley, V. Linke, P. Rakow, G. Schierholz, and H. Stüben, Phys. Rev. Lett. **80**, 4119 (1998).
[13] H. Gies and J. Jaeckel, Phys. Rev. Lett. **93**, 110405 (2004).
[14] V. A. Miransky, Il Nuovo Cimento A (1965-1970) **90**, 149 (1985).
[15] K.-I. Aoki, K. Morikawa, J.-I. Sumi, H. Terao, and M. Tomoyose, Progress of Theoretical Physics **97**, 479 (1997).
[16] D. Djukanovic, J. Gegelia, and U.-G. Meißner, Commun. Theor. Phys. **69**, 263 (2018), arXiv:1706.10039 [hep-th].
[17] H. Gies and J. Ziebell, The European Physical Journal C **80** (2020), 10.1140/epjc/s10052-020-8171-8.
[18] H. Gies, K. K. K. Tam, and J. Ziebell, "Pauli-term-induced fixed points in d-dimensional qed," (2022).
[19] Y. Nambu and G. Jona-Lasinio, Phys. Rev. **122**, 345 (1961).
[20] Y. Nambu and G. Jona-Lasinio, Phys. Rev. **124**, 246 (1961).
[21] D. F. Litim and J. M. Pawlowski, Physics Letters B **435**, 181 (1998).
[22] U. Ellwanger, M. Hirsch, and A. Weber, (1995), 10.48550/ARXIV.HEP-TH/9506019.
[23] J. Braun, Journal of Physics G: Nuclear and Particle Physics **39**, 033001 (2012).
[24] J. Berges, N. Tetradis, and C. Wetterich, Physics Reports **363**, 223 (2002), renormalization group theory in the new millennium. IV.
[25] H. Gies, in *Renormalization Group and Effective Field Theory Approaches to Many-Body Systems* (Springer Berlin Heidelberg, 2012) pp. 287–348.
[26] S. Nagy, Annals of Physics **350**, 310 (2014).
[27] B. Delamotte, in *Renormalization Group and Effective Field Theory Approaches to Many-Body Systems* (Springer Berlin Heidelberg, 2012) pp. 49–132.
[28] J. M. Pawlowski, Annals of Physics **322**, 2831 (2007).
[29] C. Wetterich, Phys. Lett. **B301**, 90 (1993).
[30] M. Bonini, M. D'Attanasio, and G. Marchesini, Nucl. Phys. **B409**, 441 (1993), arXiv:hep-th/9301114 [hep-th].
[31] U. Ellwanger, *Proceedings, Workshop on Quantum field theoretical aspects of high energy physics: Bad Frankenhausen, Germany, September 20-24, 1993*, Z. Phys. **C62**, 503 (1994), [,206(1993)], arXiv:hep-ph/9308260 [hep-ph].
[32] T. R. Morris, Int. J. Mod. Phys. **A9**, 2411 (1994), arXiv:hep-ph/9308265 [hep-ph].
[33] H. Gies, J. Jaeckel, and C. Wetterich, Phys. Rev. **D69**, 105008 (2004), arXiv:hep-ph/0312034 [hep-ph].
[34] A. Eichhorn and H. Gies, New Journal of Physics **13**, 125012 (2011).
[35] F. Gehring, H. Gies, and L. Janssen, Phys. Rev. D **92**, 085046 (2015), arXiv:1506.07570 [hep-th].
[36] J. Braun and H. Gies, Physics Letters B **645**, 53 (2007).
[37] J. Braun and H. Gies, Journal of High Energy Physics **2006**, 024 (2006).
[38] J. Braun and H. Gies, Journal of High Energy Physics **2010**, 60 (2010).
[39] H. Gies and J. Jaeckel, The European Physical Journal C **46**, 433 (2006).
[40] M. Mitter, J. M. Pawlowski, and N. Strodthoff, Phys. Rev. D **91**, 054035 (2015), arXiv:1411.7978 [hep-ph].
[41] J. Braun, L. Fister, J. M. Pawlowski, and F. Rennecke, Phys. Rev. D **94**, 034016 (2016), arXiv:1412.1045 [hep-ph].

[42] G. Eichmann, H. Sanchis-Alepuz, R. Williams, R. Alkofer, and C. S. Fischer, Prog. Part. Nucl. Phys. **91**, 1 (2016), arXiv:1606.09602 [hep-ph].
[43] D. Binosi, L. Chang, J. Papavassiliou, S.-X. Qin, and C. D. Roberts, Phys. Rev. D **95**, 031501 (2017), arXiv:1609.02568 [nucl-th].
[44] A. K. Cyrol, M. Mitter, J. M. Pawlowski, and N. Strodthoff, Phys. Rev. D **97**, 054006 (2018), arXiv:1706.06326 [hep-ph].
[45] H. Gies and L. Janssen, Phys. Rev. D **82**, 085018 (2010), arXiv:1006.3747 [hep-th].
[46] L. Janssen and H. Gies, Phys. Rev. D **86**, 105007 (2012), arXiv:1208.3327 [hep-th].
[47] A. Eichhorn, Phys. Rev. D **86**, 105021 (2012), arXiv:1204.0965 [gr-qc].

arXiv:2403.02907v1 [astro-ph.CO] 5 Mar 2024

The Future of Primordial Black Holes: Open Questions and Roadmap

Antonio Riotto[1,2] **and Joe Silk**[3,4,5]

[1]Département de Physique Théorique, Université de Genève, , 24 quai Ansermet, CH-1211 Genève 4, Switzerland
[2]Gravitational Wave Science Center (GWSC), Université de Genève,, CH-1211 Geneva, Switzerland
[3]Institut d'Astrophysique, UMR 7095 CNRS, Sorbonne Université, , 98bis Bd Arago, 75014 Paris, France
[4]Department of Physics and Astronomy, The Johns Hopkins University,, Baltimore MD 21218, USA
[5]Beecroft Institute of Particle Astrophysics and Cosmology, Department of Physics, University of Oxford, Oxford OX1 3RH, UK

March 6, 2024

Abstract

We discuss some of the the open questions and the roadmap in the physics of primordial black holes. Black holes are the only dark matter candidate that is known to actually exit. Their conjectured primordial role is admittedly based on hypothesis rather than fact, most straightforwardly as a simple extension to the standard models of inflation, or even, in homage to quantum physics, more controversially via a slowing-down of Hawking evaporation. Regardless of one's stance on the theoretical basis for their existence, the possibility of primordial black holes playing a novel role in dark matter physics and gravitational wave astronomy opens up a rich astrophysical phenomenology that we lay out in this brief overview.

1 Introduction

Primordial black holes (PBHs) provide an attractive way to resolve the dark matter problem. Unlike essentially all other dark matter particle candidates, BHs actually exist, and there are several robust prospects for determining whether there is a primordial component over a broad mass range. Theoretically PBHs may populate the universe in a humongous range of masses from $10^{-20}\,M_\odot$ to $10^{20}\,M_\odot$. They could be the dark matter for masses around $10^{-12}\,M_\odot$. Moreover even if PBHs are dark matter-subdominant, , they could be responsible for some of the currently observed mergers of BHs in the solar mass range or they may play key roles as rare IMBH (Intermediate Mass BHs in the range $(10^3 - 10^6)M_\odot$ that may seed both SMBH (Supermassive Black Holes observed in the mass range $(10^6 - 10^{10})M_\odot$ and massive galaxies in the early universe.

PBHs formed very early and hence may be ubiquitous at the highest redshifts accessible by direct imaging, that is $z \lesssim 100$, when there was little astrophysical competition. This provides us with the possibility of finding truly unique high redshift signatures of PBHs, for example via gravity wave interferometers such as Einstein Telescope and Cosmic Explorer that will probe $z \lesssim 20$, for potential sources of EMRI signals.

Well before these telescopes are in action, there will be 21cm dark ages telescopes destined for the lunar far side, such as LUSEE-Night and DSL to probe PBH accretion imprints on diffuse hydrogen absorption against the CMB to $z \lesssim 100$, both scheduled for deployment in 2026. And on a similar time-scale we anticipate LIGO-class gravity wave telescopes to make significant inroads on the possible existence of solar mass black holes as well as black holes populating the "forbidden" region in the pair

instability gap, at masses $\gtrsim 50\,M_\odot$. Such observations would provide further evidence for the existence of PBHs.

We review some of these arguments in this chapter, with particular attention to the open questions, challenges and future opportunities.

2 Some open questions

How well do we know the PBH abundance? And over what mass range? How well can we ascertain the PBH clustering properties and therefore the GW signal from binary mergers via LIGO and future terrestrial GW interferometers? And can we use the vicinities of SMBH amd IMBH, most likely rich in dark matter and where PBH abundances are in consequence likely to be enhanced, as potential sources of EMRI signals for experiments such as LISA? We briefly discuss such open theoretical and observational questions below.

2.1 What is the abundance of PBHs?

The formation of a PBH in the early universe is a rare event and knowing the precise formation probability represents, even nowadays, a challenge. This issue is of fundamental importance as the formation probability is one of the key ingredients to calculate the current PBH abundance and mass function which not only enter in many observables, such as the merger rate of BH binaries, but which are also routinely used to express current constraints from various observations.

To illustrate the difficulty in assessing the precise abundance of PBHs, let us consider the most standard scenario in the literature where the PBHs are formed by the collapse of large inhomogeneities generated during the inflationary stage. The latter delivers a stochastic quantity, the curvature perturbation ζ on superhorizon scales, whose properties are known statistically. As we mentioned, PBHs are rare events which require a given observable, e.g. the density contrast δ or the compaction function C, to be above a typically large critical value. This implies that the calculation of the PBH abundance requires going beyond linear perturbation theory and the knowledge of the tail of the probability where the latter is typically far from being a simple Gaussian distribution. Nonlinearities enter into the game even when the initial curvature perturbation is Gaussian (which is typically not) because of the nonlinear relation between the overdensity/compaction function an the curvature perturbation itself. The logic chain is (in radiation)

$$\text{non-Gaussian}\,\zeta(r)\;\rightarrow\text{non-Gaussian compaction function}\,C(r)=C_1(r)-\frac{3}{8}C_1^2(r),\;\;C_1=-\frac{4}{3}r\zeta'(r). \tag{1}$$

The presence of nonlinearities at the various stages of the calculation makes the calculation cumbersome. One more complication comes from the fact that the critical threshold C_c to form a PBH depends on the shape of the initial perturbation, specifically on the curvature around the maximum r_m of the compaction function

$$C_c=C_c(q),\quad q=-\frac{r_m^2C''(r_m)}{4C(r_m)}, \tag{2}$$

where primes indicate derivatives with respect to the radius and we are assuming spherical symmetry. The formation probability therefore needs the knowledge of the exact probability $P[C(r_m),C''(r_m)]$. Given an initial profile of the curvature perturbation, one neeeds therefore to compute the corresponding critical profile for the compaction function. The latter determines the position of the maximum r_m in units of the typical momentum scale $k_\star$ of the power spectrum of the curvature perturbation and the correlators derived from the compaction function, which in turn determine its non-Gaussian statistics. Even though the dependence on the profile may be accounted for integrating over all possible values of the curvature of the compaction function at its maximum in real space or realizing that in some cases the broadest profiles count [1], the position of the maximum r_m is typically calculated only for the average profile of the curvature perturbation and this automatically introduces some intrinsic and unavoidable uncertainties due to the statistical nature of the observables. A possible, albeit incomplete, way to proceed might be to find an observable whose critical value does not depend on its profile, e.g. the volume average of the compaction function, as suggested in Ref. [2]

$$\overline{C}(r_m) = \frac{3}{R_m^3} \int_0^{R_m} \mathrm{d}x\, x^2\, C(x), \quad R_m = r_m\, e^{\zeta(r_m)}, \tag{3}$$

but no calculation exists in the literature so far and no understanding of why the volume average of the compaction function has a critical threshold which does not depend on the profile. Even without the need of mentioning other possible problems, e.g. dealing with the nonlinearities entering in the radiation transfer function when perturbations re-enter the horizon [3] or the need to deal with the phenomenon of operator mixing [4], we believe the calculation of the PBH abundance in the standard scenario is still an open issue which deserves further study. The same is true in alternative mechanisms to generate the PBHs, e.g. in supercooled first-order phase transitions [5] where the threshold criterion does not suffice.

2.2 What is the effect of PBH clustering?

Another open issue worth mentioning is the clustering of PBHs. It may significantly affect the merger rates of coalescing binaries and, consequently, the gravitational wave signal measured by the LIGO/Virgo collaboration and by future experiments. Indeed, even if isolated PBH binaries are not significantly affected by encounters with a third PBH, PBH binaries residing in PBH clusters might suffer such interactions, thus modifying the expected merger rate. If PBHs cluster or not is therefore an important question to address. A significant PBH clustering might also modify constraints arising from microlensing observations and from the cosmic microwave background. Clustering might also be relevant in determining PBH spins. While the gravitational collapse of a spherical overdensity during radiation domination generates nearly spinless PBHs [6], they may acquire a large spin in the presence of accretion [7]. Indeed, if PBHs cluster they can more easily merge to form binaries at late times, so that the resulting PBH coming from such merger will have a non-zero value even when no accretion is present.

Even though PBHs in the standard scenario formed through the collapse of large overdensities are initially not clustered [8, 9], PBH clusters form not long after matter-radiation equality [10] if $f_{\rm PBH}$ is large. Current N-body simulations are limited to large redshifts $z \sim 10^2$ and a chief challenge is how to extrapolate to lower redshifts relevant for some observational constraints. Analytical insight is certainly called for in understanding the complex evolution of the PBH population.

PBHs, even if rare, are potentially important for seeding galaxy and even quasar formation at very high redshift [11]. These would be intermediate mass PBHs that enhanced local growth by gravitational instability of cold dark matter. in such a scenario, both massive galaxies and SMBH would form at epochs much earlier than in the standard model of structure formation. Moreover SMBH formation would precede or be contemporaneous with massive galaxy formation, as actually favored by recent JWST observations [12].

2.3 What fraction of the currently observed GW events can be ascribed to PBHs?

Thanks to the many binary BH events detected so far with many more expected in the next few years, gravitational-wave astronomy is about to become a population study. Currently hierarchical Bayesian analysis combining astrophysical formation models and PBHs may only constrain the fraction of a putative subpopulation of PBHs in the data (see for instance Ref. [13]). The exciting possibility that PBHs are contributing to current observations will be verified only by further reducing uncertainties in astrophysical and primordial formation models. This is another fundamental open issue.

2.4 Are PBHs the Dark Matter?

The idea that PBH can comprise most of the dark matter is one of the main motivations for studying PBH. Unfortunately, observational constraints eliminate this possibility for most of the range of possible PBH masses, with a notable exception around asteroid mass PBH, spanning several decades in mass around $\sim 10^{-12}\,\mathrm{M}_\odot$ down to the limit $\sim 10^{-16}\,\mathrm{M}_\odot$, obtained from the isotropic x-ray and soft gamma ray background observational limits on fluxes produced by PBHs currently undergoing Hawking evaporation [14].

In the standard formation scenario of PBH, it is unavoidable that gravitational waves are generated with a frequency which today is in the mHz range, exactly where the LISA mission has maximum sensitivity [15]. The scenario of PBH as dark matter can be therefore tested in the future by LISA by measuring the GW two-point correlator. The fact that the asteroid mass range is still unconstrained is due to the fact that the microlensing constraints are ineffective around the value $10^{-11}\,M_\odot$ under which the geometric optics approximation is no longer valid and the constraints from the presence of neutron stars in globular clusters is based on extreme assumptions about the dark matter density. It is of tantamount importance to come out with possible ideas for constraining or identifying PBH in the asteroid mass range.

One promising approach is that PBH capture leads to neutron star conversion to BH. This could occur in dense star clusters that contain DM, as may be the case for nuclear star clusters, and NS conversion would occur in the case of capture of such "endoparasitic" PBHs for PBH masses larger than $\sim 10^{-11}\,M_\odot$ [16]. Such a phenomenon may produce a deficit of pulsars in our GC as possibly observed [17]. Another interesting avenue is to observe the number of massive main-sequence stars in ultra-faint dwarfs which should be suppressed if the dark matter is made of asteroid-mass PBHs [18], making measured the mass distribution of stars depleted in the high-mass range.

Furthermore, near-extremal PBHs provide an intriguing means of making evaporating PBHs stable on cosmological scales. Formation is simplest for low mass five-dimensional PBHs that initially act like four-dimensional PBHs, Hawking radiating down to the radius of the extra dimension where their effective temperature is effectively zero, to attain a stable mass [19]. These are generated in higher dimensional scenarios and Hawking radiation is generically found to be slowed down [20]. Other scenarios for producing near-extremal PBH include formation of maximally rotating or charged PBH at very early epochs [21], as well as via the quantum gravity phenomenon of so-called memory burden suppression [22]. Detectability is feasible down to scales as small as a few Planck masses for charged PBH relics via terrestrial detectors [23] or equally for high energy particle emission from occasional binary merger events [24].

3 The PBH Roadmap

Future experiments abound, ranging from approved projects to imminently enter the detailed design phase, to provide significantly enhanced constraints on PBH scenarios, including terrestrial laser interferometers (Einstein Telescope, Cosmic Explorer)[25], and space laser interferometers (LISA, DECIGO [26], TianQin and Taiji [27]), to atomic interferometers on the ground with demonstrators under construction and extensions planned to km scales (AION MAGIS, MAGIA, MIGA, ELGA, ZAIGA), as well as in space (AEDGE) [28], and designs for lunar interferometer/seismometer arrays (LGWA, GLOC)[29].

The science goals focus on bridging frequency gaps in the LIGO/VIRGO/KAGRA frequency range that has so far led to hundreds of detections of BH mergers in the $(10-100)M_\odot$ range by going both to higher and lower frequencies. The new science that can be explored ranges from the masses and equation of state of neutron stars as well as multimessenger signals from core collapse supernovae to kpc distances (kHz to Hz range) to SMBH and IMBH detections and BH inspiralling (Hz to mHz, and eventually μHz). One would ultimately approach the pulsar timing array sensitivities (NANOGrav, SKA) at nanohertz frequencies to enable exploration of first order very early universe phase transitions, and presence of loop decays in a network of cosmic strings [30].

We next address various "smoking-gun" signatures that may identify PBHs, notably including high redshift mergers and sub-solar mass PBHs.

3.1 High redshift mergers

The PBH model predicts a binary merger rate density which grows monotonically with redshift [31, 32, 33]. Focusing those binaries generated at early epochs, one has a well-defined time evolution with redshift

$$R^{\rm EB}(z) \propto \left(\frac{t(z)}{t(z=0)}\right)^{-34/37}, \tag{4}$$

extending up to redshifts $z \gtrsim \mathcal{O}(10^3)$. Since mergers from BHs of astrophysical origin switch off at redshifts $z \gtrsim (20-30)$ [34, 35, 36, 37, 38, 39, 40, 41, 42, 43], detecting merger redshifts at $z \gtrsim 30$ will

represent smoking guns for primordial binaries [44, 45, 46]. Of course, large measurement uncertainties on the inferred luminosity distance due to the low SNR at 3G detectors [46, 47, 48, 49] may bring relatively large errors, but recent studies show that identifying merger rate evolution at redshift larger than $\mathcal{O}(10)$ will allow to constrain PBH populations up to abundances as low as $f_{\rm PBH} \approx 10^{-5}$ [50] in the solar mass range, even accounting for the contamination of Pop III binaries, see Fig. 1.

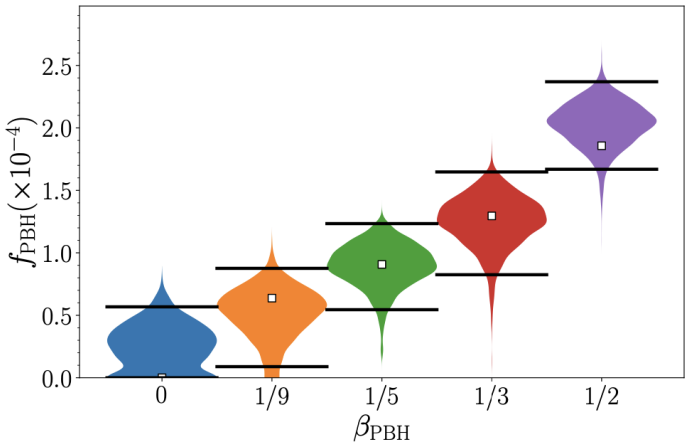


Figure 1: Posteriors of $f_{\rm PBH}$ given a lognormal PBH mass function centered at $M_c = 30\,M_\odot$ and variance equal to 0.3 at $\beta_{\rm PBH} = 0, 1/9, 1/5, 1/3$, and $1/2$, being $\beta_{\rm PBH}$ the fraction of the PBH merger rate to the total merger rate. The solid black lines indicate the 95% CIs. From Ref. [50].

3.2 Sub-solar PBHs

The detection of sub-solar BHs in a compact binary merger is regarded as one of the smoking gun signatures of PBHs. Indeed, BHs of astrophysical origin are not expected. The sub-solar mass range may be however populated by other compact objects like neutron stars, white dwarfs, or exotic compact objects [51] (e.g. boson stars [52]).

GW signatures of any population of PBH below the astrophysical production provide a powerful statistical constraint on any solar or subsolar component, as evidenced by the sharp decline observed in 03 events. There could of course be rare events generated by solar or subsolar PBHs that might contribute to DM at the $\mathcal{O}(10\%)$ level. One key ingredient is therefore to distinguish PBHs from other compact objects, e.g. through the measurements of the tidal disruption and tidal deformability Λ. A recent analysis has shown that for subsolar neutron-star binaries, the O4 and O5 projected sensitivities would allow measuring the effect of tidal disruption on the waveform in a large portion of the parameter space, also constraining the tidal deformability at $\mathcal{O}(10\%)$ level, thus excluding a primordial origin of the binary. Viceversa, for subsolar PBH binaries, model-agnostic upper bounds on the tidal deformability can rule out neutron stars or more exotic competitors. Assuming events similar to the sub-threshold candidate SSM200308 reported in LVK O3b data are PBH binaries, O4 projected sensitivity would allow ruling out the presence of neutron-star tidal effects at $\approx 3\sigma$ C.L., thus strengthening the PBH hypothesis. Future experiments would lead to even stronger ($> 5\sigma$) conclusions on potential discoveries of this kind, see Fig. 2.

PBHs of lunar mass, a regime where hints of unaccounted-for microlensing events have been reported by the OGLE survey of the galactic bulge [53], could be sufficiently numerous that nearby binaries might be detectable with future generation detectors [54].

3.3 Plugging the pair instability gap with PBH?

An equally powerful mass challenge for PBH arises from the pair instability gap. This is generated by the catastrophic core collapse of massive stars that results from pair-instability SNe, and predicts a deficit of astrophysical BH between $\sim 50\,M_\odot$ and $\sim 120\,M_\odot$. The full LIGO-Virgo O3 data set reveals

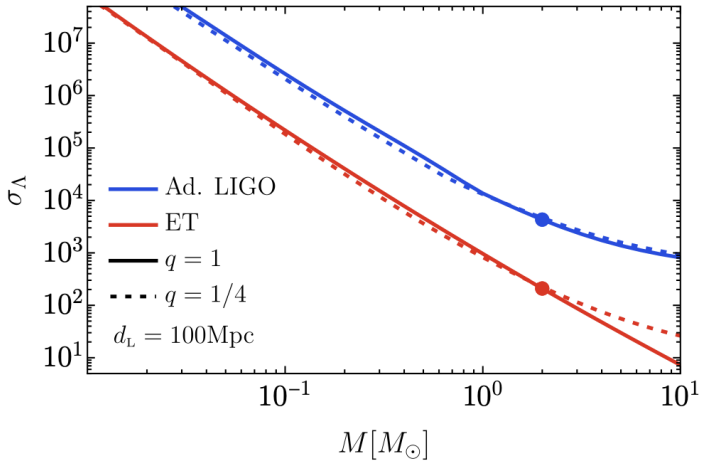


Figure 2: Precision of the deformability parameter Λ at both Ad. LIGO and ET. The binary is assumed to have spinless components and negligible eccentricity and deformability, as predicted by the PBH scenario. The solid (dashed) line indicates the result for mass ratios 1 (1/4). From Ref. [47].

a definitive decline in merger rates above $\sim 40\,M_\odot$ [55] but with several candidates filling this gap at high credibility [56].

Could PBH populate the pair instability gap? A smoking gun signature would be a feature in the BH mass spectrum, most likely indicative of a new formation mechanism.

3.4 PBH eccentricity

Even though PBH binaries are formed with large eccentricity at high redshift, they have enough time to circularize before the GW signal can enter the observation band of current and future detectors. This implies that an observation of a non-zero eccentricity e would rule out the interpretation as a primordial binary formed in the early Universe, while it may still be compatible with a PBH binary formed in the late-time universe [57, 58].

3.5 PBH spin

The PBHs form in the early universe through the standard scenario of the collapse of large overdensities inherit a characteristic mass-spin correlations induced by accretion effects [7]. Using this criterion for determining the possible primordial nature of individual GW events would require reducing uncertainties on the accretion model and studied at the population level [59].

Fig. 3 presents a flowchart from Ref. [47] one might follow to assess the primordial nature of a binary merger based on measurements of the redshift z, eccentricity e, tidal deformability Λ, component masses m, and dimensionless spins χ.

3.6 Future gamma-ray telescopes

PBHs have a range of potentially interesting direct gamma ray signals associated with Hawking evaporation. These include the 511 keV gamma-ray line, produced by electron-positron pair-annihilation, where positrons originate from black hole evaporation. The INTEGRAL detection of the Large Magellanic Cloud provides one of the strongest bounds attainable with present observations, and should be greatly improved upon by future MeV gamma-ray telescopes such as GECCO [60], as well as AMEGO [61] and ASTROGRAM [62], among others [63].

Exploding PBHs, the late-time limit of Hawking evaporation for small PBHs, provide intriguing candidates for future very high energy gamma ray telescopes that may address transient phenomena, that pertain especially to the new frontier of PBHs of ultralralow masses.

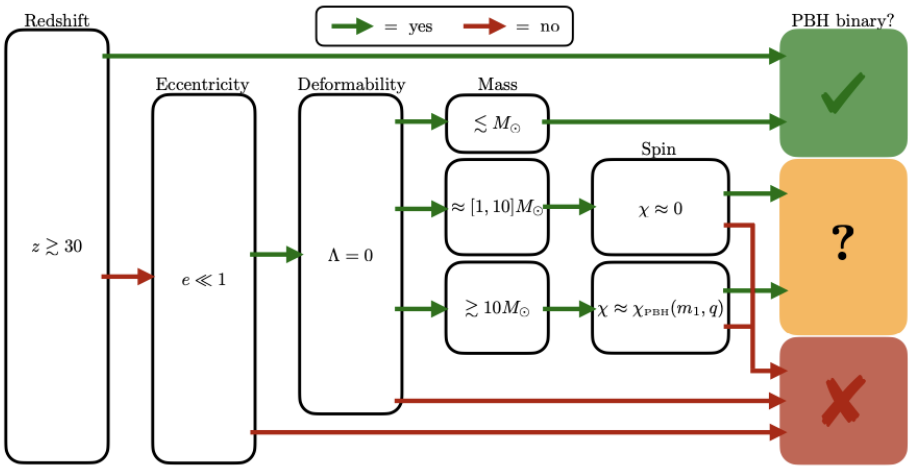


Figure 3: Flowchart from Ref. [47] to assess the primordial nature of a binary merger based on measurements of the redshift z, eccentricity e, tidal deformability Λ, component masses m, and dimensionless spins χ. Each arrow indicates if the condition in the box is met (green) or violated (red).

The Hawking temperature characterizes the effective temperature as inversely proportional to PBH mass and is constrained as discussed previously by soft gamma ray constraints at the $\sim 10^{17}$gm PBH mass scale, incorporating appropriate spectral corrections due to nonthermal aspects of the complex emission processes [64]. Once the allowable PBH mass range is extended to much lower masses due to slowing or suppression of Hawking radiation, as proposed in recent discussions of near-extremal and higher dimensional PBHs, intriguing prospects arise for high energy gamma ray experiments [21, 20, 65, 22]. As previously noted, new observational terrain opens up for exploring near-extremal PBH detection both directly via terrestrial experiments [23] and indirectly via binary merger events [24], where constraints at much higher gamma ray or even neutrino energies could become important.

Such gamma ray experiments include HAWC (100 GeV -50 TeV) and CTA (20 GeV-300 TeV) [66] at TeV scales, and at PeV-scale photon energies LHAASO [67] and SWGO [68]. Such searches will be closely coordinated with multimessenger projects spanning next generation underground gravitational wave telescopes (EINSTEIN (ET), COSMIC EXPLORER (CE)) and FRB observatories (CHORD) [69].

4 Conclusions

Support for the existence of PBHs hypothesis comes from a range of arguments spanning dark matter physics, inflationary models, astrophysics, gravitational microlensing and quantum cosmology. None are yet conclusive but the cumulative support for the existence of PBHs seems reasonably compelling. More to the point however is that there is a rich astrophysical agenda of open questions that contribute to a future road map for a plethora of research projects.

Two of the most fundamental PBH probes that distinguish them from astrophysical counterparts are their redshift and mass distributions.This combination provides an armoury of smoking guns that will inevitably enrich the next generation of gravitational wave and gravitational microlensing experiments. Confirmation will require improved statistics as single events may not be conclusive. it is only too easy to come up with rare events that can masquerade as PBH candidates, for example by appealing to higher order generations of merging events or to non-Gaussianity. We have laid out a possible future road map for definitively assessing whether PBHs can present a viable candidate for dark matter, or possibly contribute to other astrophysical or even quantum cosmology anomalies.

References

[1] A. Ianniccari, A. J. Iovino, A. Kehagias, D. Perrone, and A. Riotto. The Primordial Black Hole Abundance: The Broader, the Better. 2 2024.

[2] Albert Escrivà, Cristiano Germani, and Ravi K. Sheth. Universal threshold for primordial black hole formation. *Phys. Rev. D*, 101(4):044022, 2020.

[3] Valerio De Luca, Alex Kehagias, and Antonio Riotto. How well do we know the primordial black hole abundance: The crucial role of nonlinearities when approaching the horizon. *Phys. Rev. D*, 108(6):063531, 2023.

[4] Gabriele Franciolini, Andrea Ianniccari, Alex Kehagias, Davide Perrone, and Antonio Riotto. Renormalized Primordial Black Holes. 11 2023.

[5] Marcos M. Flores, Alexander Kusenko, and Misao Sasaki. Revisiting formation of primordial black holes in a supercooled first-order phase transition. 2 2024.

[6] V. De Luca, V. Desjacques, G. Franciolini, A. Malhotra, and A. Riotto. The initial spin probability distribution of primordial black holes. *JCAP*, 05:018, 2019.

[7] V. De Luca, G. Franciolini, P. Pani, and A. Riotto. Constraints on Primordial Black Holes: the Importance of Accretion. *Phys. Rev. D*, 102(4):043505, 2020.

[8] Yacine Ali-Haïmoud. Correlation function of high-threshold regions and application to the initial small-scale clustering of primordial black holes. *Physical Review Letters*, 121(8), aug 2018.

[9] Vincent Desjacques and Antonio Riotto. Spatial clustering of primordial black holes. *Phys. Rev. D*, 98(12):123533, 2018.

[10] Derek Inman and Yacine Ali-Haïmoud. Early structure formation in primordial black hole cosmologies. *Phys. Rev. D*, 100(8):083528, 2019.

[11] Bernard Carr and Joseph Silk. Primordial black holes as generators of cosmic structures. *Monthly Notices of the Royal Astronomical Society*, 478(3):3756–3775, May 2018.

[12] Joseph Silk, Mitchell Begelman, Colin Norman, Adi Nusser, and Rosemary Wyse. Which came first: supermassive black holes or galaxies? insights from jwst, 2024.

[13] Gabriele Franciolini, Vishal Baibhav, Valerio De Luca, Ken K. Y. Ng, Kaze W. K. Wong, Emanuele Berti, Paolo Pani, Antonio Riotto, and Salvatore Vitale. Searching for a subpopulation of primordial black holes in LIGO-Virgo gravitational-wave data. *Phys. Rev. D*, 105(8):083526, 2022.

[14] J. Iguaz, P.D. Serpico, and T. Siegert. Isotropic x-ray bound on primordial black hole dark matter. *Physical Review D*, 103(10), May 2021.

[15] N. Bartolo, V. De Luca, G. Franciolini, M. Peloso, D. Racco, and A. Riotto. Testing primordial black holes as dark matter with LISA. *Phys. Rev. D*, 99(10):103521, 2019.

[16] Chloe B. Richards, Thomas W. Baumgarte, and Stuart L. Shapiro. Accretion onto a small black hole at the center of a neutron star. *Physical Review D*, 103(10), May 2021.

[17] Jason Dexter and Ryan M. O'Leary. The peculiar pulsar population of the central parsec. *The Astrophysical Journal*, 783(1):L7, February 2014.

[18] Nicolas Esser, Sven De Rijcke, and Peter Tinyakov. The impact of primordial black holes on the stellar mass function of ultra-faint dwarf galaxies. 11 2023.

[19] Jose A. de Freitas Pacheco, Elias Kiritsis, Matteo Lucca, and Joseph Silk. Quasiextremal primordial black holes are a viable dark matter candidate. *Physical Review D*, 107(12), June 2023.

[20] Luis A. Anchordoqui, Ignatios Antoniadis, and Dieter Lüst. Dark dimension, the swampland, and the dark matter fraction composed of primordial black holes. *Phys. Rev. D*, 106(8):086001, October 2022.

[21] J. A. de Freitas Pacheco and Joseph Silk. Primordial Rotating Black Holes. *Phys. Rev. D*, 101(8):083022, 2020.

[22] Ana Alexandre, Gia Dvali, and Emmanouil Koutsangelas. New Mass Window for Primordial Black Holes as Dark Matter from Memory Burden Effect. 2 2024.

[23] Benjamin V. Lehmann, Christian Johnson, Stefano Profumo, and Thomas Schwemberger. Direct detection of primordial black hole relics as dark matter. *Journal of Cosmology and Astroparticle Physics*, 2019(10):046–046, October 2019.

[24] Yang Bai and Nicholas Orlofsky. Primordial extremal black holes as dark matter. *Physical Review D*, 101(5), March 2020.

[25] Guillem Domènech and Misao Sasaki. Probing primordial black hole scenarios with terrestrial gravitational wave detectors, 2024.

[26] Seiji Kawamura et al. Current status of space gravitational wave antenna DECIGO and B-DECIGO. *PTEP*, 2021(5):05A105, 2021.

[27] Yungui Gong, Jun Luo, and Bin Wang. Concepts and status of chinese space gravitational wave detection projects. *Nature Astronomy*, 5(9):881–889, September 2021.

[28] John Ellis, Malcolm Fairbairn, Juan Urrutia, and Ville Vaskonen. Probing supermassive black hole seed scenarios with gravitational wave measurements, 2023.

[29] Joris van Heijningen et al. The payload of the Lunar Gravitational-wave Antenna. *J. Appl. Phys.*, 133(24):244501, 2023.

[30] John Ellis, Malcolm Fairbairn, Gabriele Franciolini, Gert Hütsi, Antonio Iovino Jr. au2, Marek Lewicki, Martti Raidal, Juan Urrutia, Ville Vaskonen, and Hardi Veermäe. What is the source of the pta gw signal?, 2023.

[31] Yacine Ali-Haïmoud, Ely D. Kovetz, and Marc Kamionkowski. Merger rate of primordial black-hole binaries. *Phys. Rev. D*, 96(12):123523, 2017.

[32] Martti Raidal, Christian Spethmann, Ville Vaskonen, and Hardi Veermäe. Formation and Evolution of Primordial Black Hole Binaries in the Early Universe. *JCAP*, 02:018, 2019.

[33] V. De Luca, G. Franciolini, P. Pani, and A. Riotto. Primordial Black Holes Confront LIGO/Virgo data: Current situation. *JCAP*, 06:044, 2020.

[34] Tomoya Kinugawa, Kohei Inayoshi, Kenta Hotokezaka, Daisuke Nakauchi, and Takashi Nakamura. Possible Indirect Confirmation of the Existence of Pop III Massive Stars by Gravitational Wave. *Mon. Not. Roy. Astron. Soc.*, 442(4):2963–2992, 2014.

[35] Tomoya Kinugawa, Akinobu Miyamoto, Nobuyuki Kanda, and Takashi Nakamura. The detection rate of inspiral and quasi-normal modes of Population III binary black holes which can confirm or refute the general relativity in the strong gravity region. *Mon. Not. Roy. Astron. Soc.*, 456(1):1093–1114, 2016.

[36] Tilman Hartwig, Marta Volonteri, Volker Bromm, Ralf S. Klessen, Enrico Barausse, Mattis Magg, and Athena Stacy. Gravitational Waves from the Remnants of the First Stars. *Mon. Not. Roy. Astron. Soc.*, 460(1):L74–L78, 2016.

[37] K. Belczynski, T. Ryu, R. Perna, E. Berti, T. L. Tanaka, and T. Bulik. On the likelihood of detecting gravitational waves from Population III compact object binaries. *Mon. Not. Roy. Astron. Soc.*, 471(4):4702–4721, 2017.

[38] Kohei Inayoshi, Ryosuke Hirai, Tomoya Kinugawa, and Kenta Hotokezaka. Formation pathway of Population III coalescing binary black holes through stable mass transfer. *Mon. Not. Roy. Astron. Soc.*, 468(4):5020–5032, 2017.

[39] Boyuan Liu and Volker Bromm. The Population III origin of GW190521. *Astrophys. J. Lett.*, 903(2):L40, 2020.

[40] Boyuan Liu and Volker Bromm. Gravitational waves from Population III binary black holes formed by dynamical capture. *Mon. Not. Roy. Astron. Soc.*, 495(2):2475–2495, 2020.

[41] Tomoya Kinugawa, Takashi Nakamura, and Hiroyuki Nakano. Chirp Mass and Spin of Binary Black Holes from First Star Remnants. *Mon. Not. Roy. Astron. Soc.*, 498(3):3946–3963, 2020.

[42] Ataru Tanikawa, Hajime Susa, Takashi Yoshida, Alessandro A. Trani, and Tomoya Kinugawa. Merger rate density of Population III binary black holes below, above, and in the pair-instability mass gap. *Astrophys. J.*, 910(1):30, 2021.

[43] Neha Singh, Tomasz Bulik, Krzysztof Belczynski, and Abbas Askar. Exploring compact binary populations with the Einstein Telescope. *Astron. Astrophys.*, 667:A2, 2022.

[44] Savvas M. Koushiappas and Abraham Loeb. Maximum redshift of gravitational wave merger events. *Phys. Rev. Lett.*, 119(22):221104, 2017.

[45] V. De Luca, G. Franciolini, P. Pani, and A. Riotto. Bayesian Evidence for Both Astrophysical and Primordial Black Holes: Mapping the GWTC-2 Catalog to Third-Generation Detectors. *JCAP*, 05:003, 2021.

[46] Ken K. Y. Ng, Shiqi Chen, Boris Goncharov, Ulyana Dupletsa, Ssohrab Borhanian, Marica Branchesi, Jan Harms, Michele Maggiore, B. S. Sathyaprakash, and Salvatore Vitale. On the Single-event-based Identification of Primordial Black Hole Mergers at Cosmological Distances. *Astrophys. J. Lett.*, 931(1):L12, 2022.

[47] Gabriele Franciolini, Roberto Cotesta, Nicholas Loutrel, Emanuele Berti, Paolo Pani, and Antonio Riotto. How to assess the primordial origin of single gravitational-wave events with mass, spin, eccentricity, and deformability measurements. *Phys. Rev. D*, 105(6):063510, 2022.

[48] Matteo Martinelli, Francesca Scarcella, Natalie B. Hogg, Bradley J. Kavanagh, Daniele Gaggero, and Pierre Fleury. Dancing in the dark: detecting a population of distant primordial black holes. *JCAP*, 08(08):006, 2022.

[49] Ken K. Y. Ng et al. Measuring properties of primordial black hole mergers at cosmological distances: Effect of higher order modes in gravitational waves. *Phys. Rev. D*, 107(2):024041, 2023.

[50] Ken K. Y. Ng, Gabriele Franciolini, Emanuele Berti, Paolo Pani, Antonio Riotto, and Salvatore Vitale. Constraining High-redshift Stellar-mass Primordial Black Holes with Next-generation Ground-based Gravitational-wave Detectors. *Astrophys. J. Lett.*, 933(2):L41, 2022.

[51] Vitor Cardoso and Paolo Pani. Testing the nature of dark compact objects: a status report. *Living Rev. Rel.*, 22(1):4, 2019.

[52] Huai-Ke Guo, Kuver Sinha, and Chen Sun. Probing Boson Stars with Extreme Mass Ratio Inspirals. *JCAP*, 09:032, 2019.

[53] Hiroko Niikura, Masahiro Takada, Shuichiro Yokoyama, Takahiro Sumi, and Shogo Masaki. Constraints on earth-mass primordial black holes from ogle 5-year microlensing events. *Physical Review D*, 99(8), April 2019.

[54] Kaiki Taro Inoue and Takahiro Tanaka. Gravitational waves from sub-lunar-mass primordial black-hole binaries: A new probe of extradimensions. *Physical Review Letters*, 91(2), July 2003.

[55] The LIGO Scientific Collaboration, the Virgo Collaboration, the KAGRA Collaboration, and R. Abbott et al. The population of merging compact binaries inferred using gravitational waves through gwtc-3, 2022.

[56] Digvijay Wadekar, Javier Roulet, Tejaswi Venumadhav, Ajit Kumar Mehta, Barak Zackay, Jonathan Mushkin, Seth Olsen, and Matias Zaldarriaga. New black hole mergers in the ligo-virgo o3 data from a gravitational wave search including higher-order harmonics, 2023.

[57] Ilias Cholis, Ely D. Kovetz, Yacine Ali-Haïmoud, Simeon Bird, Marc Kamionkowski, Julian B. Muñoz, and Alvise Raccanelli. Orbital eccentricities in primordial black hole binaries. *Phys. Rev. D*, 94(8):084013, 2016.

[58] Yi-Fan Wang and Alexander H. Nitz. Prospects for detecting gravitational waves from eccentric subsolar mass compact binaries. *Astrophys. J.*, 912(1):53, 2021.

[59] Gabriele Franciolini and Paolo Pani. Searching for mass-spin correlations in the population of gravitational-wave events: The GWTC-3 case study. *Phys. Rev. D*, 105(12):123024, 2022.

[60] Mrunal Korwar and Stefano Profumo. Updated constraints on primordial black hole evaporation. *Journal of Cosmology and Astroparticle Physics*, 2023(05):054, May 2023.

[61] Henrike Fleischhack. Amego-x: Mev gamma-ray astronomy in the multimessenger era, 2021.

[62] Manuela Mallamaci, A. De Angelis, V. Tatischeff, R. Rando, M. Tavani, U. Oberlack, R. Walter, G. Ambrosi, A. Argan, P. von Balmoos, D. Bastieri, E. Bernardini, S. Brandt, A. Bulgarelli, A. Bykov, V. Fioretti, I.A. Grenier, L. Hanlon, D. Hartmann, M. Hernanz, G. Kanbach, I. Kuvvetli, P. Laurent, M. Mariotti, M.N. Mazziotta, J. Mc Enery, S. Mereghetti, A. Morselli, K. Nakazawa, M. Pearce, E. Prandini, J. Rico, R. Curado da Silva, X. Wu, Andrzej Zdziarski, and A. Zoglauer. All-Sky-ASTROGAM: a MeV Companion for Multimessenger Astrophysics. *PoS*, ICRC2019:579, 2019.

[63] Simeon Bird, Andrea Albert, Will Dawson, Yacine Ali-Haïmoud, Adam Coogan, Alex Drlica-Wagner, Qi Feng, Derek Inman, Keisuke Inomata, Ely Kovetz, Alexander Kusenko, Benjamin V. Lehmann, Julian B. Muñoz, Rajeev Singh, Volodymyr Takhistov, and Yu-Dai Tsai. Snowmass2021 cosmic frontier white paper: Primordial black hole dark matter. *Physics of the Dark Universe*, 41:101231, August 2023.

[64] Jérémy Auffinger. Primordial black hole constraints with hawking radiation—a review. *Progress in Particle and Nuclear Physics*, 131:104040, July 2023.

[65] F. Hoyle and R. A. Lyttleton. On the accretion of interstellar matter by stars. *Proceedings of the Cambridge Philosophical Society*, 36(3):325, January 1940.

[66] Xavier Boluna, Stefano Profumo, Juliette Blé, and Dana Hennings. Searching for exploding black holes, 2024.

[67] Zhen Cao et al. Ultrahigh-energy photons up to 1.4 petaelectronvolts from 12 γ-ray Galactic sources. *Nature*, 594(7861):33–36, 2021.

[68] J. Hinton and SWGO Collaboration. The Southern Wide-field Gamma-ray Observatory: Status and Prospects. In *37th International Cosmic Ray Conference*, page 23, March 2022.

[69] Keith Vanderlinde, Adrian Liu, Bryan Gaensler, Dick Bond, Gary Hinshaw, Cherry Ng, Cynthia Chiang, Ingrid Stairs, Jo-Anne Brown, Jonathan Sievers, Juan Mena, Kendrick Smith, Kevin Bandura, Kiyoshi Masui, Kristine Spekkens, Leo Belostotski, Matt Dobbs, Neil Turok, Patrick Boyle, Michael Rupen, Tom Landecker, Ue-Li Pen, and Victoria Kaspi. The canadian hydrogen observatory and radio-transient detector (chord). 2019.

What Can We Learn from Directed Flow at STAR-FTX Energies?

Yu. B. Ivanov[1, 2, *] and M. Kozhevnikova[3, †]

[1] *Bogoliubov Laboratory of Theoretical Physics, JINR Dubna, 141980 Dubna, Russia*
[2] *National Research Center "Kurchatov Institute", 123182 Moscow, Russia*
[3] *Veksler and Baldin Laboratory of High Energy Physics, JINR Dubna, 141980 Dubna, Russia*

We present results of simulations of directed flow of various hadrons in Au+Au collisions at collision energies of $\sqrt{s_{NN}} = 3$ and 4.5 GeV. Simulations are performed within the model three-fluid dynamics (3FD) and the event simulator based on it (THESEUS). The results are compared with recent STAR data. The directed flows of various particles provide information on dynamics in various parts and at various stages of the colliding system depending on the particle. However, the information on the equation of state is not always directly accessible because of strong influence of the afterburner stage or insufficient equilibration of the matter. It is found that the crossover scenario gives the best overall description of the data. This crossover EoS is soft in the hadronic phase. The transition into QGP in Au+Au collisions occurs at collision energies between 3 and 4.5 GeV, at baryon densities $n_B \gtrsim 4n_0$ and temperatures ≈ 150 MeV. In-medium effects in the directed flow of (anti)kaons are discussed.

arXiv:2403.02787v1 [nucl-th] 5 Mar 2024

I. INTRODUCTION

The directed flow is one of the most sensitive quantities to the dynamics of nucleus-nucleus collisions and properties of the matter produced in these collisions. It provides information about the stopping power of the nuclear matter, its equation of state (EoS), transition to quark-gluon phase (QGP) and more. All these issues were addressed in the analysis of the STAR data [1] obtained within Beam Energy Scan (BES) program at the Relativistic Heavy-Ion Collider (RHIC). The analysis was performed within various approaches [2–14], which include both hydrodynamic and kinetic models. An important conclusion of these studies is that the transition to the quark-gluon phase is most probably of the crossover or weak-first-order type and it stars at collision energies of $\sqrt{s_{NN}} < 8$ GeV in Au+Au collisions. A promising recent development is prediction of correlation between the directed flow and the angular momentum accumulated in the participant region of colliding nuclei [8, 15–19], which allows a deeper insight into collision dynamics.

The STAR-FXT (fixed-target) data on the directed flow of identified particles at energies $\sqrt{s_{NN}} = 3$ and 4.5 GeV were recently published in Refs. [20, 21]. These data were also analyzed within various, mostly kinetic models [11, 14, 22–33] in relation to various problems: the hyperon production [14, 26, 33], the production of light (hyper)nuclei [30, 31], etc. The EoS of the matter produced in the nucleus-nucleus collisions was the prime topic of the above theoretical considerations. It was discussed mostly in terms of softness and stiffness of the EoS [11, 22–24, 26, 29]. These studies were performed within different transport models: The relativistic version of the quantum molecular dynamics implemented into the transport code JAM [11], the hadronic transport code SMASH [22, 29], the Ultrarelativistic Quantum Molecular Dynamics (UrQMD) [23, 24], and a multiphase transport model [26].

All the aforementioned papers [11, 22–24, 26, 29] reported that stiff (to a different extent) EoS's are preferable for the reproduction of the directed flow (v_1) at $\sqrt{s_{NN}} = 3$ GeV, while the v_1 data at 4.5 GeV require a softer EoS. The latter was interpreted as indication of onset of the phase transition into QGP. This conclusion about preference of the stiff EoS at the energy of 3 GeV appears to contradict the earlier findings. The analysis of KaoS [34] and FOPI [35] data at collision energies $E_{lab} \leq 2A$ GeV ($\sqrt{s_{NN}} \leq 2.7$ GeV) within the Isospin Quantum Molecular Dynamics model led to the conclusion that the soft EoS with the incompressibility $K = 210$ MeV is strongly preferable [35–38]. Although, this energy range is somewhat below of the STAR-FXT one.

The energy range of the BNL Alternating Gradient Synchrontron (AGS), $E_{lab} = 2 - 10.7$ A·GeV ($\sqrt{s_{NN}} =$ 2.7-4.9 GeV), practically coincide with the currently explored STAR-FXT range. The results of the analysis of the AGS data [39, 40] are more controversial. Strong preference of the soft EoS was reported in Refs. [3, 4, 41–43]. In Refs. [3, 4], the EoS additionally softens at $\sqrt{s_{NN}} > 4$ GeV because of onset of the deconfinement transition. However, in Ref. [44] it was found that the best description of the data on the transverse flow is provided by a rather stiff EoS at 2A·GeV (NL3) while at higher bombarding energies (4–8 A·GeV) a medium EoS ($K = 300$ MeV) leads to better agreement with the data, while the differences in the soft-EoS and stiff-EoS transverse flows become of minor significance at 4–8 A·GeV. In Ref. [45], the proton flow was found to be also independent of stiffness of the EoS, however provided the momentum dependence in the nuclear mean fields is taken into account.

As recent studies [11, 22–26, 29, 32] of the STAR-FXT v_1 data deduced comparatively stiff EoS's at $\sqrt{s_{NN}} = 3$ GeV, some of them predicted comparatively low baryon densities (n_B) for onset of the denfinement transition.

*e-mail: yivanov@theor.jinr.ru
†e-mail: kozhevnikova@jinr.ru

This transition was associated with the softening of the EoS required for v_1 reproduction at the energy of 4.5 GeV. In terms of the normal nuclear density n_0, the deduced transition densities are 3-4n_0 [22], 4n_0 [24], 2.5n_0 [25], 3-5n_0 [26], $n_B >$ 2-3n_0 [29], and 5n_0 [32]. The model of three-fluid dynamics (3FD) [46, 47] predicts that the denfinement transition starts at approximately $n_B >$ 4-5n_0 at temperatures 100–150 MeV for the crossover EoS. However, the STAR-FXT data on the directed flow of identified particles at energies $\sqrt{s_{NN}} = 3$ and 4.5 GeV have not yet been fully considered within the 3FD model, with the exception of the proton and Λ-hyperon data at 3 GeV, which were analyzed with respect to the light (hyper)nuclei production [30, 31].

In view of the above reviewed developments, the debate about the EoS stiffness and onset of the QGP transition is far from being completed. A more extended discussion of the EoS constraints deduced from the directed-flow analysis can be found in recent review [48].

In the present paper, we present results of calculations of the directed flow of various hadrons at energies $\sqrt{s_{NN}} = 3$ and 4.5 GeV and compare them with recent STAR-FXT data [20, 21]. The calculations are performed within the 3FD model [46, 47] and also within the Three-fluid Hydrodynamics-based Event Simulator Extended by UrQMD final State interactions (THESEUS) [49–51]. The THESEUS simulations are intended to study the effect of the UrQMD afterburner stage on the directed flow. We present some conclusions that can be drawn from agreement or disagreement of the calculated results with the data.

II. 3FD MODEL AND THESEUS GENERATOR

The 3FD model [46, 47] simulates nonequilibrium at the early stage of nuclear collisions by means of two counterstreaming baryon-rich fluids. The third (fireball) fluid accumulates newly produced particles, dominantly populating the midrapidity region. These fluids are governed by conventional hydrodynamic equations coupled by friction terms in the right-hand sides of the Euler equations. The friction terms describe the energy–momentum exchange between the fluids. The hydrodynamic evolution ends with the freeze-out procedure described in Refs. [52, 53]. The 3FD model does not include any kinetic afterburner stage.

The THESEUS event generator [49–51] does include the afterburner stage that is described by the UrQMD model. The THESEUS generator transforms the 3FD output, which is recorded in terms of local flow velocities and thermodynamic quantities on the freeze-out hypersurface, into a set of observed particles, i.e. performs a particlization. The particlization is followed by the afterburner stage.

The afterburner stage is of prime importance for collisions at lower energies, where there is no clear rapidity separation between participant and spectator nucleons at the freeze-out. When the time for the nuclei to pass each other becomes long relative to the characteristic time scale for the participant evolution, the interaction between participants and spectators (so-called shadowing) becomes important [54–56]. In particular, the squeeze-out effect [57–59], is the consequence of this shadowing, i.e. results from blocking of the expanding central blob by the spectator matter. This shadowing only partially is taken into account within the 3FD evolution because the central fireball remains to be shadowed even after the freeze-out while particles escape from this fireball without interacting with spectators in the 3FD model.

The afterburner stage should, in principle, correct this deficiency. However, it does not do it completely. The reason is that the THESEUS assigns *the same time instant* to all produced particles during the particlization procedure, while different parts of the system are frozen-out at *different time instants* in 3FD. A time-extended transition from hydrodynamic evolution to afterburner dynamics would need treatment of the interaction of the kinetic afterburner phase with still hydrodynamically evolved matter. This is a difficult task both technically and conceptually. The lack of this interaction is the prime reason of shortcoming of the THESEUS particlization. At lower collision energies, participants are frozen out earlier than spectators. The spectators evolve slower because of the lower excitation energy and hence require longer time before the freeze-out. If the particlization is isochronous like in THESEUS, the evolution of the frozen-out participants stops untill the spectators also become frozen-out. Therefore, we skip the stage of shadowing the afterburner expansion of the central fireball by spectators still being in the hydrodynamic phase. The afterburner evolution is switched on only when the spectators also become frozen out, when they have already partially passed the expanding central fireball. Thus, the shadowing by spectators turns out to be reduced compared to what it would be if the entire collision process were kinetically treated, like in UrQMD or JAM.

The 3FD model has been extensively used to simulations of Au+Au collisions at AGS energies, which almost coincide with the STAR-FXT ones. Quantities, which are low sensitive to the afterburner stage, were well reproduced by the 3FD simulations. These are various bulk observables [47, 60, 61], proton directed [3, 4] and elliptic (at higher AGS energies) [59] flow, bulk properties and directed flow of light (hyper)nuclei at $\sqrt{s_{NN}} = 3$ GeV [30, 31]. Problems with reproduction of the elliptic flow of protons and light nuclei at $\sqrt{s_{NN}} = 3$ GeV in Ref. [30] are related to the aforementioned deficiency of the isochronous particlization in THESEUS. Precisely the same parameters of the 3FD model as those in Refs. [3, 4, 30, 31, 47, 60, 61] are used in the present simulations.

III. EQUATIONS OF STATE

The 3FD model is designed to work with different EoS's. Three different EoS's are traditionally used in the 3FD simulations: a purely hadronic EoS [62] and two EoS's with deconfinement transitions [63], i.e. an EoS with a first-order phase transition (1PT EoS) and one with a smooth crossover transition. While the hadronic EoS is quite flexible, i.e., it allows for changes of incompressibility, the EoS's with deconfinement transitions are strictly tabulated. These EoS's are illustrated in Fig. 1. As seen, all three EoS's are similar in the hadronic

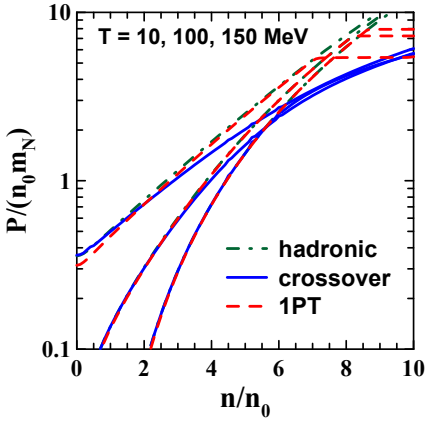


FIG. 1: Pressure (scaled by product of the normal nuclear density, $n_0 = 0.15$ 1/fm^3, and the nucleon mass, m_N) at three temperatures, $T = 10$, 100 and 150 MeV (from bottom upwards for corresponding curves), as function of the net baryon density (scaled by n_0) for the hadronic, crossover and 1PT EoS's.

phase. Note that the displayed version of the hadronic EoS is characterized by incompressibility $K = 190$ MeV. The simulations below are performed with this version of the hadronic EoS. The crossover pressure starts to deviate from the hadronic one at $n_B >$ 4-5n_0 at temperatures 100–150 MeV that are typical for the collisions at STAR-FXT energies, see Fig. 2.

Dynamical trajectories of the matter in the central cell of the colliding Au+Au nuclei in semicentral collisions ($b = 6$ fm) at energies $\sqrt{s_{NN}} = 3$ and 4.5 GeV are presented in Fig. 2 in terms of the baryon density and temperature. Evolution starts from the normal nuclear density and zero temperature and then follows an almost universal trajectory for some time. Shortly before reaching the turning point, at which density and temperature are maximal, the matter in this central cell becomes equilibrated, as it was demonstrated in Ref. [64], and therefore the temperature takes its conventional meaning. The turning points at the energy of 3 GeV only touches the QGP region according to the crossover EoS, see Fig. 1. The the same time the 4.5-GeV trajectories fall well into the crossover QGP region and even enter the the 1PT mixed phase. The trajectories for different EoS's move away from each other at higher densities and

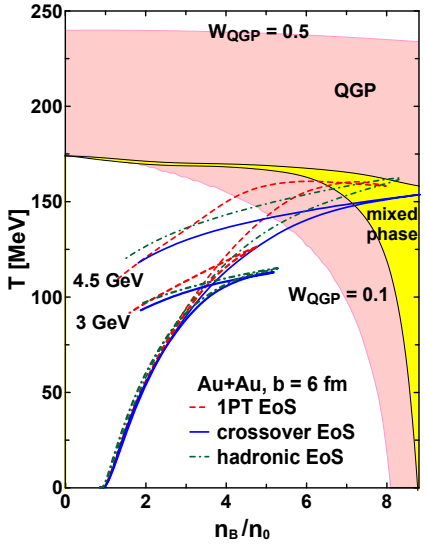


FIG. 2: Dynamical trajectories of the matter in the central cell of the colliding Au+Au nuclei in semicentral collisions (impact parameter is $b = 6$ fm) at energies $\sqrt{s_{NN}} = 3$ and 4.5 GeV. The trajectories are plotted in terms of the baryon density (n_B, scaled by the normal nuclear density n_0) and temperature T. The trajectories are presented for the three EoS's. The mixed phase of the 1PT EoS is displayed by the shadowed region marked as "mixed phase". The wide shadowed area displays the region of the crossover EoS between the QGP fractions $W_{QGP} = 0.1$ and 0.5.

temperatures. In particular, it demonstrates that the hadronic EoS and the 1PT one are not identical in the whole hadronic phase.

The crossover and 1PT phase diagrams require some comments. The QCD lattice calculations demonstrated that the transition into QGP at zero baryon chemical potential is a smooth crossover [65]. Due to that, the transition temperature is ambiguous because different definitions can lead to different values for it. Observables related to chiral symmetry result in the transition temperature around 155–160 MeV [66]. As seen from Fig. 2, the transition regions at zero baryon density (i.e. chemical potential) in EoS's of Ref. [63] are located at noticeably higher temperatures than 155–160 MeV. This happens because the EoS's of Ref. [63] were fitted to the old, still imperfect lattice data [67–69]. Moreover, the crossover transition constructed in Ref. [63] is very smooth. The hadronic fraction survives up to very high temperatures. In particular, this is seen from Fig. 2: the fraction of the quark-gluon phase (W_{QGP}) reaches value of 0.5 only at very high temperatures. Such a smooth crossover is also used in the PHSD model (Parton-Hadron-String Dynamics) [70]. However, this version of the crossover [63] certainly contradicts results of the lattice QCD calculations at zero chemical potential, where a fast crossover was found [65]. However, the aforementioned shortcomings are not severe for the present simulations at relatively low collision energies, because the system evolution

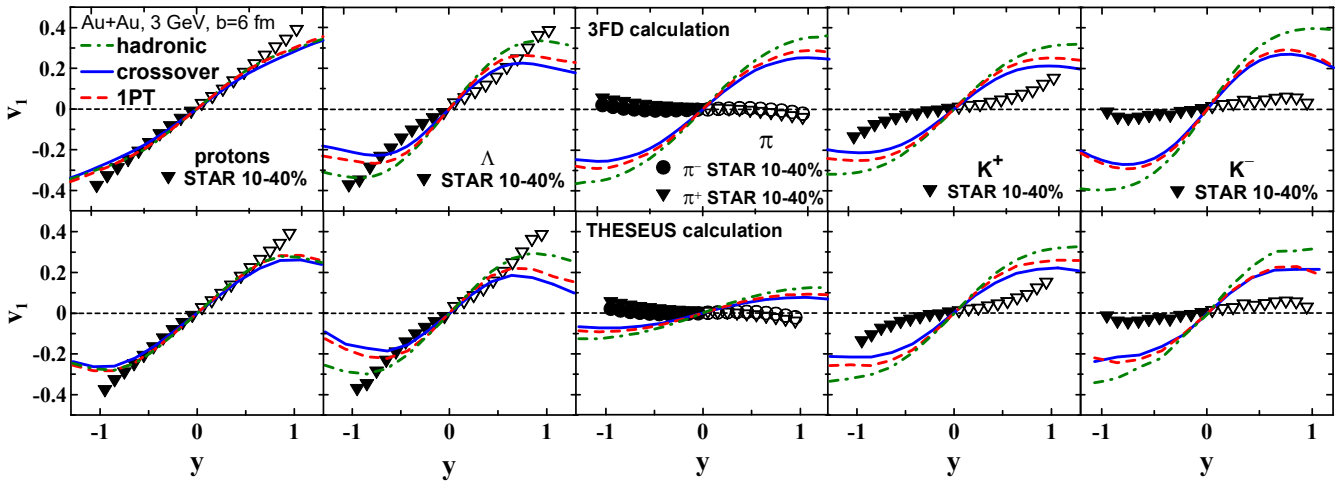


FIG. 3: Directed flow of protons, pions, Λ hyperons, and kaons as function of rapidity in semicentral (b = 6 fm) Au+Au collisions at collision energy of $\sqrt{s_{NN}}$ = 3 GeV. Results are calculated within the 3FD model (upper raw of panels) and the THESEUS (lower raw of panels) with hadronic, 1PT, and crossover EoS's. STAR data are from Ref. [21].

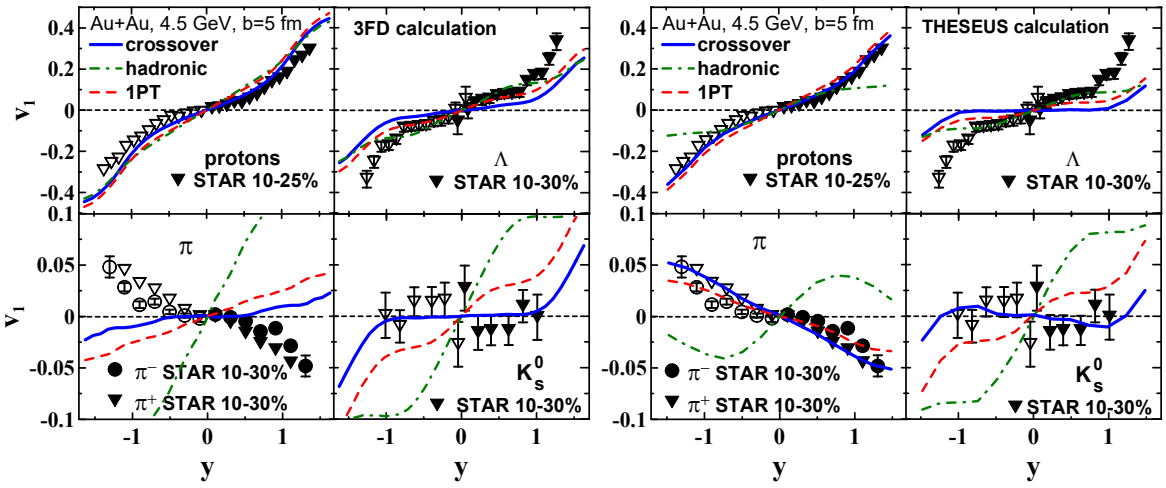


FIG. 4: Directed flow of protons, pions, Λ hyperons, and kaons (K^0 short) as function of rapidity in semicentral (b = 5 fm) Au+Au collisions at collision energy of $\sqrt{s_{NN}}$ = 4.5 GeV. Results are calculated within the 3FD model (left block of panels) and the THESEUS (right block of panels) with hadronic, 1PT, and crossover EoS's. STAR data are from Ref. [20].

takes place in the region of high baryon densities, where the EoS is not known from the first principles.

IV. DIRECTED FLOW

The calculated directed flow of protons, pions, Λ hyperons, and (anti)kaons as function of rapidity in semicentral Au+Au collisions at collision energies of $\sqrt{s_{NN}}$ = 3 and 4.5 GeV are presented in Figs. 3 and 4, respectively. These calculations were performed in the 3FD model without any afterburner and within THESEUS (i.e. with the UrQMD afterburner). The results are compared with STAR data [20, 21].

As seen, the proton v_1 flow is well reproduced with and without afterburner. The afterburner slightly improves the description at 4.5 GeV, while worsens it at forward/backward rapidities at 3 GeV without changing the midrapidity slope. The midrapidity proton flow turns out to be almost independent of the used EoS even at 4.5 GeV, where the QGP transition already takes place, see Fig. 2. This is because the proton flow is formed at the early stage of the collision [71–73]. At considered collision energies, this stage is developed in the hadronic phase for all considered EoS's, see Fig. 2, where all considered EoS's are very similar, see Fig. 1. Moreover, the stopping power of the matter, i.e. friction forces of the 3FD model [47], are identical in the hadronic phase for all considered scenarios. Consequently, the flow appears to be quite independent of the used EoS even at

4.5 GeV. Note that the proton directed flow does depend on the EoS at the BES RHIC energies [2–4], where the transition to QGP occurs already the early stage of the collision.

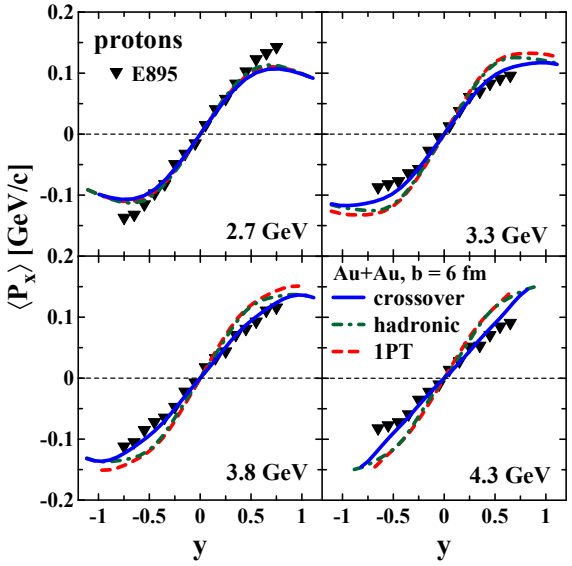


FIG. 5: Transverse flow of protons as function of rapidity in semicentral ($b = 6$ fm) Au+Au collisions at collision energies of $\sqrt{s_{NN}} = 2.7$–4.3 GeV ($E_{\rm lab} = 2A$, $4A$, $6A$, and $8A$ GeV). Results are calculated within the 3FD model with hadronic, 1PT, and crossover EoS's. E895 data are from Ref. [39].

Figure 5 illustrates the description of the old E895 data [39] in the same collision energy range. These data are presented in terms of transverse flow defined as [74]

$$\langle P_x \rangle(y) = \frac{\int d^2p_T \; p_x \; E \; dN/d^3p}{\int d^2p_T \; E \; dN/d^3p}, \qquad (1)$$

where p_x is the transverse momentum of the proton in the reaction plane, $E\; dN/d^3p$ is the invariant momentum distribution of protons with E being the proton energy, and integration runs over the transverse momentum p_T. This is done because the E895 data in terms of $v_1(y)$ raised many questions, as it was discussed in Ref. [3] in detail. In addition, they contradict the new STAR-FTX data. As seen from Fig. 5, the crossover EoS gives almost perfect description of the proton transverse flow in the midrapidity regions. This gives hope that the future STAR-FTX proton data at the energies between 3 and 4.5 GeV will be also well reproduced with the crossover scenario. The dependence on the EoS is quite moderate, similar to that at 3 and 4.5 GeV in Figs. 3 and 4.

The Λ flow turns out to be more sensitive to the EoS, see Figs. 3 and 4, because Λ's are produced in highly excited but still baryon-rich regions of the colliding system. These regions are formed later, when the temperature reaches high values, see Fig. 2. The afterburner stronger affects evolution in these regions. It reduces the midrapidity slope of the Λ flow, making the crossover EoS definitely preferable at 3 GeV, while the hadronic EoS turns out to be preferable at 4.5 GeV. In view of this sensitivity to the afterburner, definite conclusions on the EoS relevance can hardly be made based on the Λ flow.

The meson flow probes dynamics in highly excited baryon-rich and baryon-depleted regions of the system. The highly excited baryon-depleted regions are formed even later than the excited baryon-rich regions, when the transverse expansion already dominates. Nevertheless, the mesonic flow is very similar to the baryon one after the 3FD stage at 3 GeV, see Fig. 3, while substantially differ from the baryon flow at 4.5 GeV, see Fig. 4. Note that this difference at 4.5 GeV concerns only the EoS's involving the transition to the QGP, whereas the hadronic EoS results in the mesonic flow being similar to the baryon one. The reason is that the EoS becomes softer in the QGP and hence the pressure causing the directed flow is reduced. Therefore, the mesonic flow may indicate the transition to the QGP. However, there are other circumstances that may prevent us from drawing definite conclusions from the mesonic flow. One of them is the afterburner.

The pion flow is strongly affected by the afterburner. If the 3FD-calculated pion flow hardly resembles the corresponding data, after the afterburner stage, it almost perfectly describes these data at 4.5 GeV within the crossover and 1PT scenarios. The hadronic scenario evidently fails to reproduce the pion flow at 4.5 GeV. The afterburner even changes the sign of the midrapidity slope of the crossover and 1PT flows at 4.5 GeV. Note that the 3FD model and hence THESEUS do not distinguish positive, neutral, and negative pions. Therefore, the calculated pion flow refers to the flow of all pions. This strong dependence on the afterburner is a consequence of the shadowing discussed in Sec. II. At 3 GeV, the afterburner shifts the 3FD-calculated flow closer to the data but still not enough to reproduce them. This insufficient effect of the afterburner is a result of the shortcoming of the THESEUS particlization discussed in Sec. II: The afterburner skips the stage of shadowing the afterburner expansion of the central fireball by spectators still being in the hydrodynamic phase. At 4.5 GeV, this skipped stage is already of miner importance because the time for the nuclei to pass each other becomes shorter relative to the time scale of the participant evolution.

The K^+ directed flow is not changed by the afterburner stage because of small cross sections of their interactions with other hadrons. Indeed, the kaon-nucleon cross section is about 10 mb, while the nucleon-nucleon one is about 40 mb [38, 75, 76]. Indeed, at somewhat lower energies ($2A$ GeV) it was concluded that after their production the K-mesons suffer not more than one rescattering before escaping [77, 78]. At the energy of 3 GeV ($\approx 3A$ GeV), higher densities are achieved in the collisions and therefore rescatterings become more frequent, however

not frequent enough to thermalize the kaon. This explains why the calculated flow (on the assumption of the kaon thermalization) is so different from the data, see Fig. 3.

At slightly higher collision energy of 3.85 GeV (6A GeV), the rescatterings of the kaons with the nucleons in the dense matter already cause them to flow in the direction of the nucleons, as it was reported in Ref. [41]. Thus, the transition from rare-collisional to collisional regime occurs in the considered energy range. At the energy of 4.5 GeV, the kaons can be considered well thermalized at the late stage of nuclear collision, however the afterburner still does not affect the flow, as seen from Fig. 4.

At the same time, the K^- directed flow at 3 GeV is reduced by the afterburner because the NK^- cross section is of the order of 40 mb or even higher at low realative NK^- energies [38, 75, 76]. However, the calculated K^- flow is still essentially stronger than the experimental one. Apparently, this is a result of the aforementioned shortcoming of the THESEUS particlization, i.e. a lack of shadowing of the central fireball by still hydrodynamically evolving spectators.

Within the 3FD model, we calculate $v_1(y)$ for K^0_s mesons in terms of those for K^0 and $\bar{K}^0$ as follows

$$v_1^{K0s}(y) = \left(v_1^{K0}(y)\frac{dN^{K0}}{dy} + v_1^{\overline{K}0}(y)\frac{dN^{\overline{K}0}}{dy} \right) / \left(\frac{dN^{K0}}{dy} + \frac{dN^{\overline{K}0}}{dy} \right), \quad (2)$$

where dN^{K0}/dy and $dN^{\overline{K}0}/dy$ are rapidity distributions of the K^0 and $\bar{K}^0$ mesons. Eq. (2) does not imply that K^0_s consists of K^0 and $\bar{K}^0$ in this proportion. It only means that K^0_s mesons originate from K^0 and $\bar{K}^0$ mesons that are emitted from the interaction region. These K^0 and $\bar{K}^0$ mesons keep their momenta and thus their flow pattern after escaping from the interaction region. Therefore, the corresponding fractions of produced K^0_s mesons carry these K^0 and $\bar{K}^0$ flow patterns. The $\bar{K}^0$ number is about 20% of that of K^0 at 4.5 GeV.

The directed flow of K^0_s mesons at 4.5 GeV strongly depends on the EoS and moderately depends on the afterburner. This moderate dependence on the afterburner is a consequence of the large fraction of K^0 mesons in produced K^0_s. The K^0 mesons are practically unaffected by the afterburner. Therefore, the K^0_s directed flow is a good probe of the hot and dense stage of the collision. As seen from Fig. 4, the crossover EoS is certainly preferable for reproduction of the data.

Thus, the directed flows of various particles provide information on dynamics in various parts and at various stages of the colliding system depending on the particle. However, the information on the EoS is not always directly accessible because of strong influence of the afterburner stage or insufficient thermalization of kaons. The crossover scenario gives the best overall description of the data, of course, with all reservations regarding the above-mentioned difficulties in applying the model.

V. DIRECTED FLOW OF KAONS

The kaons deserve a separate discussion. As has been mentioned above, the afterburner does not affect the flow of kaons because of small cross sections of their interactions with other hadrons but noticeably changes the antikaon flow at 3 GeV, see Fig. 3. It is instructive to consider the kaon and antikaon flows at 4.5 GeV, in spite of absence of the corresponding data.

The directed flow of kaons, antikaons and K^0_s mesons as function of rapidity in semicentral ($b = 5$ fm) Au+Au collisions at collision energy of $\sqrt{s_{NN}} = 4.5$ GeV is presented in Fig. 6. The flows of kaons and antikaons are marked as (K^0, K^+) and $(\bar{K}^0, K^-)$, respectively, because the 3FD model does not distinguish the corresponding mesons. The kaon flow again turns out to be insensitive to the afterburner.

The flow of antikaons is enhanced by the afterburner, contrary to the reduction of the antikaon flow at 3 GeV. Notably, midrapidity slopes of the kaon and antikaon flow are of the opposite sign for the crossover and 1PT EoS's while they are both non-negative within the hadronic scenario. Apparently, the antiflow of the antikaons is again related to the aforementioned shadowing of the decay of central blob by the spectator matter. This shadowing is present already in the 3FD stage of the evolution, as seen from the upper raw of panels in Fig. 6. The afterburner additionally enhances this shadowing and hence the antiflow, see the middle raw of panels in Fig. 6. These opposite signs of the midrapidity slopes of the kaon and antikaon flows can be considered as a prediction for the flow at 4.5 GeV.

In-medium modifications of kaons are discussed in connection with chiral symmetry restoration and neutron star properties, see review [79]. In Refs. [38, 41, 76, 80], it was found that in-medium modifications of kaons are very important for description of the kaon observables, in particular, the kaon directed flow. It was reported that these in-medium effects can even change the midrapidity slope of the kaon flow at the energy of 3.85 GeV (6A GeV) [41], i.e. in the energy range we consider here.

In the relativistic mean-field approximation for the baryon degrees of freedom [81, 82], the in-medium (anti)kaon energy reads

$$E(\mathbf{p}) = \left[m_K^2 + \mathbf{p}^2 - \frac{\Sigma_{KN}}{f_K^2}\rho + \left(\frac{3}{8}\frac{n}{f_K^2}\right)^2 \right]^{1/2} \pm \frac{3}{8}\frac{n}{f_K^2}, \quad (3)$$

where $\mathbf{p}$ is the three-momentum of the (anti)kaon, the upper(lower) sign refers to $K(\bar{K})$.

$$n = \sum_B \langle \bar{B}\gamma^0 B \rangle,$$

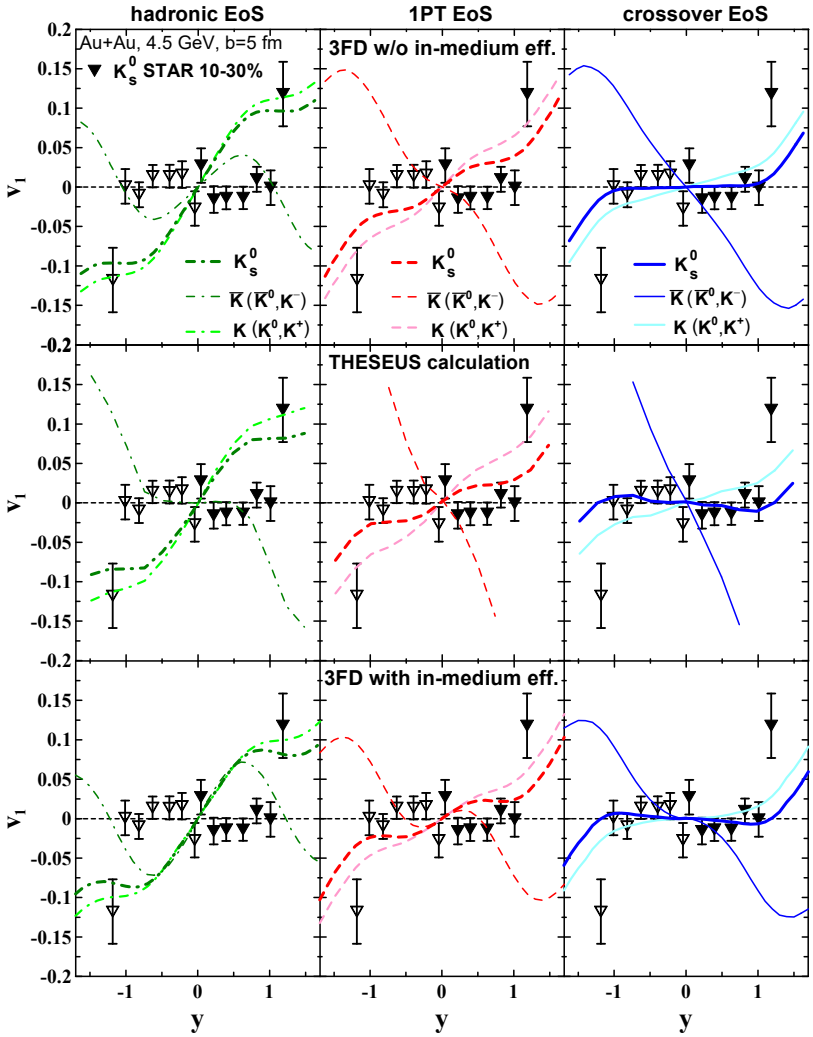


FIG. 6: Directed flow of kaons, antikaons and K_s^0 mesons as function of rapidity in semicentral ($b = 5$ fm) Au+Au collisions at collision energy of $\sqrt{s_{NN}} = 4.5$ GeV. Results are calculated within THESEUS (the middle raw of panels) and also within the 3FD model with (the lower raw of panels) and without (the upper raw of panels) in-medium modifications of (anti)kaons. STAR data are from Ref. [20].

$$\rho = \sum_B \langle \bar{B} B \rangle$$

are the proper baryon density and scalar baryon density, respectively, which are sums over various baryons B. Numerical values of the kaon decay constant, $f_K = 106$ MeV, and the kaon-nucleon sigma term, $\Sigma_{KN} = 350$ MeV, are taken from Ref. [38]. The term proportional to Σ_{KN} results from the attractive scalar interaction due to explicit chiral symmetry breaking.

The above expression was derived for the so-called s-wave interaction. Importance of p-wave kaon-baryon interactions was indicated in Refs. [83, 84]. The treatment of the kaon-baryon interaction beyond the mean-field approximation, i.e. with the G-matrix approach [76, 79], also turned out to be important. Therefore, Eq. (3) can only serve as a basis for the estimation of the in-medium effects in (anti)kaon production. Below we use Eq. (3) for this purpose. The same form of the in-medium kaon energy was used in Ref. [41].

The version of the UrQMD that is implemented in THESEUS is not suitable for treatment of the medium modified kaons. Therefore, we study the in-medium effects within the 3FD model. Results of the 3FD calculation of the directed flow taking into account the in-medium kaon modification at collision energy of $\sqrt{s_{NN}} = 4.5$ GeV is shown in the lower raw of panels of Fig. 6. As seen, the effect of this in-medium modification is quite moderate. However, it slightly improves the agreement with the K_s^0 data within the 1PT EoS and especially the crossover scenario. This improvement is practically the same as that resulted from the afterburner. It is remarkable that the change of the antikaon flow due to the in-medium effects is opposite to that caused by the afterburner.

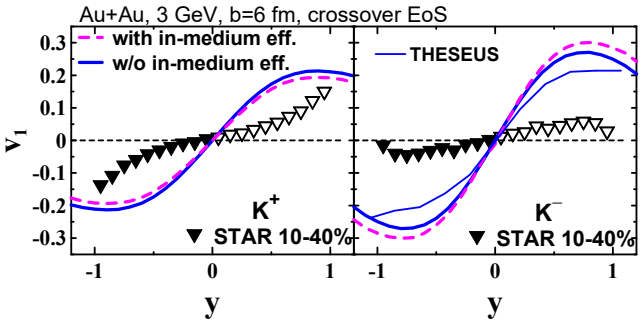


FIG. 7: Directed flow of kaons (left panel) and antikaons (right panel) as function of rapidity in semicentral (b = 6 fm) Au+Au collisions at collision energy of $\sqrt{s_{NN}}$ = 3 GeV. Results are calculated with and without in-medium modifications of (anti)kaons for the crossover EoS's. STAR data are from Ref. [20].

As seen from Fig. 7, the effect of the in-medium modifications of (anti)kaons is also small contrary to that found in Refs. [38, 41, 76, 80]. Apparently, this is because the kaons were incompletely equilibrated in the matter in kinetic simulations of Refs. [38, 41, 76, 80] and hence the in-medium effect was accumulated throughout the evolution of the system. In the 3FD simulations they are completely equilibrated and the in-medium modifications appear only at the freeze-out, leaving them insufficient time to manifest themselves. Again the in-medium modifications and the afterburner result in opposite changes in the antikaon directed flow. Only the afterburner decreases and the in-medium modification increases the flow, contrary to that at 4.5 GeV. This is because there is the normal flow at 3 GeV instead of antiflow at 4.5 GeV.

We can conclude that the directed flow of kaons or K^0_s is a promising probe of the EoS at hot and dense stage of the collision at 4.5 GeV because it is not affected by the afterburner stage. At 3 GeV, the kaons do not appear to be fully equilibrated in matter and therefore do not reflect the EoS of the matter. The antikaon flow is also a good EoS probe, which is however strongly modified during the afterburner evolution.

VI. SUMMARY

The directed flow of various hadrons at energies $\sqrt{s_{NN}}$ = 3 and 4.5 GeV were calculated and compared with recent STAR-FXT data [20, 21]. The calculations were performed within the 3FD model [46, 47] and also within the THESEUS generator [49–51] in order to to study the effect of the UrQMD afterburner stage on the directed flow. Three different EoS's are used in the simulations: a purely hadronic EoS [62] and two EoS's with deconfinement transitions [63], i.e. an EoS with a strong first-order phase transition and one with a smooth crossover transition.

At these collision energies, the time for the nuclei to pass each other is long relative to the time scale of the participant evolution and therefore the interaction between participants and spectators (shadowing) is important. In particular, the squeeze-out effect is a consequence of this shadowing. This shadowing only partially is taken into account within the 3FD evolution because the central fireball remains to be shadowed even after the freeze-out. Therefore, the afterburner stage becomes of prime importance.

The afterburner shifts the 3FD-calculated flow closer to the data but still not enough to reproduce the pion and antikaon flow at 3 GeV. This insufficient effect of the afterburner results from shortcoming of the THESEUS isochronous particlization: The afterburner skips the stage of shadowing of the post-freeze-out expansion of the central fireball by spectators still hydrodynamically evolving.

The directed flows of various particles provide information on dynamics in various parts and at various stages of the colliding system depending on the particle. However, the information on the EoS is not always directly accessible because of strong influence of the afterburner stage or insufficient equilibration, as it happens with kaons at 3 GeV. Based on these simulations, the following conclusions were drawn:

- The proton flow is formed at the early stage of the collision, where the matter is not yet equilibrated. Therefore, it probes the properties of this nonequilibrium matter rather than its EoS that implies the equilibrated matter. The proton flow is well reproduced within all three considered scenarios and is practically independent of the afterburner.

- The Λ flow turns out to be more sensitive to the EoS because Λ's are produced in highly excited but still baryon-rich regions of the colliding system. These regions are formed later, when the temperature reaches high values. The afterburner stronger affects evolution in these regions.

- The meson flow probes dynamics of highly excited baryon-rich and baryon-depleted regions of the system. The highly excited baryon-depleted regions are formed even later than the excited baryon-rich regions, when the transverse expansion already dominates.

- The pion flow is strongly affected by the afterburner. This strong dependence on the afterburner is a consequence of the shadowing.

- The directed flow of kaons or K^0_s is a promising probe of the EoS at hot and dense stage of the collision at 4.5 GeV because it is not affected by the afterburner stage. At 3 GeV, the kaons do not appear to be fully equilibrated in matter and therefore do not reflect the EoS of the matter. The antikaon flow is also a good EoS probe, which is however strongly modified during the afterburner evolution.

In conclusion, the crossover scenario gives the best overall description of the data, of course, with all reservations regarding the above-mentioned difficulties in applying the model. This crossover EoS is soft in the hadronic phase. This result agrees with that in Refs. [3, 4, 41, 42] but is in contrast to Refs. [11, 22–24, 26, 29], where stiff EoS's were found being preferable for the reproduction of the directed flow at 3 GeV. The conclusion about the preference of the stiff EoS [11, 22–24, 26, 29], was mostly based on the proton flow, which is formed at the early nonequilibrium stage of the collision. Therefore, the proton flow is a combined result of the EoS and the stopping power of the matter. Different combinations of the EoS and the stopping power can properly describe the proton flow. Directed flows of different hadrons, as well as other bulk observables should be considered together to decouple effects of the EoS and the stopping power.

Within the preferred crossover scenario, the transition into QGP in Au+Au collisions occurs at collision energies between 3 and 4.5 GeV, at baryon densities $n_B \gtrsim 4n_0$ and temperatures ≈ 150 MeV. This implies that the EoS additionally softens at 4.5 GeV. This softening and hence transition into QGP at 4.5 GeV well agrees with conclusions made in Refs. [11, 22–24, 26, 29].

Acknowledgments

Fruitful discussions with D.N. Voskresensky are gratefully acknowledged. This work was carried out using computing resources of the federal collective usage center "Complex for simulation and data processing for mega-science facilities" at NRC "Kurchatov Institute" [85]. and computing resources of the supercomputer "Govorun" at JINR [86].

[1] L. Adamczyk *et al.* [STAR], Beam-Energy Dependence of the Directed Flow of Protons, Antiprotons, and Pions in Au+Au Collisions, Phys. Rev. Lett. **112**, no.16, 162301 (2014) [arXiv:1401.3043 [nucl-ex]].

[2] V. P. Konchakovski, W. Cassing, Y. B. Ivanov and V. D. Toneev, Examination of the directed flow puzzle in heavy-ion collisions, Phys. Rev. C **90**, no.1, 014903 (2014) [arXiv:1404.2765 [nucl-th]].

[3] Y. B. Ivanov and A. A. Soldatov, Directed flow indicates a cross-over deconfinement transition in relativistic nuclear collisions, Phys. Rev. C **91**, no.2, 024915 (2015) [arXiv:1412.1669 [nucl-th]].

[4] Y. B. Ivanov and A. A. Soldatov, What can we learn from the directed flow in heavy-ion collisions at BES RHIC energies?, Eur. Phys. J. A **52**, no.1, 10 (2016) [arXiv:1601.03902 [nucl-th]].

[5] J. Steinheimer, J. Auvinen, H. Petersen, M. Bleicher and H. Stöcker, Examination of directed flow as a signal for a phase transition in relativistic nuclear collisions, Phys. Rev. C **89**, no.5, 054913 (2014) [arXiv:1402.7236 [nucl-th]].

[6] Y. Nara, H. Niemi, A. Ohnishi and H. Stöcker, Examination of directed flow as a signature of the softest point of the equation of state in QCD matter, Phys. Rev. C **94**, no.3, 034906 (2016) [arXiv:1601.07692 [hep-ph]].

[7] C. Shen and S. Alzhrani, Collision-geometry-based 3D initial condition for relativistic heavy-ion collisions, Phys. Rev. C **102**, no.1, 014909 (2020) [arXiv:2003.05852 [nucl-th]].

[8] S. Ryu, V. Jupic and C. Shen, Probing early-time longitudinal dynamics with the Λ hyperon's spin polarization in relativistic heavy-ion collisions, Phys. Rev. C **104**, no.5, 054908 (2021) [arXiv:2106.08125 [nucl-th]].

[9] L. Du, C. Shen, S. Jeon and C. Gale, Probing initial baryon stopping and equation of state with rapidity-dependent directed flow of identified particles, Phys. Rev. C **108**, no.4, 4 (2023) [arXiv:2211.16408 [nucl-th]].

[10] Y. Nara, H. Niemi, J. Steinheimer and H. Stöcker, Equation of state dependence of directed flow in a microscopic transport model, Phys. Lett. B **769**, 543-548 (2017) [arXiv:1611.08023 [nucl-th]].

[11] Y. Nara, T. Maruyama and H. Stoecker, Momentum-dependent potential and collective flows within the relativistic quantum molecular dynamics approach based on relativistic mean-field theory, Phys. Rev. C **102**, no.2, 024913 (2020) [arXiv:2004.05550 [nucl-th]].

[12] Y. Nara and H. Stoecker, Sensitivity of the excitation functions of collective flow to relativistic scalar and vector meson interactions in the relativistic quantum molecular dynamics model RQMD.RMF, Phys. Rev. C **100**, no.5, 054902 (2019) [arXiv:1906.03537 [nucl-th]].

[13] Y. Nara and A. Ohnishi, Mean-field update in the JAM microscopic transport model: Mean-field effects on collective flow in high-energy heavy-ion collisions at sNN=2–20 GeV energies, Phys. Rev. C **105**, no.1, 014911 (2022) [arXiv:2109.07594 [nucl-th]].

[14] Y. Nara, A. Jinno, K. Murase and A. Ohnishi, Directed flow of Λ in high-energy heavy-ion collisions and Λ potential in dense nuclear matter, Phys. Rev. C **106**, no.4, 044902 (2022) [arXiv:2208.01297 [nucl-th]].

[15] Y. B. Ivanov and A. A. Soldatov, Correlation between global polarization, angular momentum, and flow in heavy-ion collisions, Phys. Rev. C **102**, no.2, 024916 (2020) [arXiv:2004.05166 [nucl-th]].

[16] N. S. Tsegelnik, E. E. Kolomeitsev and V. Voronyuk, Helicity and vorticity in heavy-ion collisions at energies available at the JINR Nuclotron-based Ion Collider facility, Phys. Rev. C **107**, no.3, 034906 (2023) [arXiv:2211.09219 [nucl-th]].

[17] Z. F. Jiang, X. Y. Wu, S. Cao and B. W. Zhang, Directed flow and global polarization in Au+Au collisions across energies covered by the beam energy scan at RHIC, Phys. Rev. C **107**, no.3, 034904 (2023) [arXiv:2301.02960 [nucl-th]].

[18] Z. F. Jiang, X. Y. Wu, S. Cao and B. W. Zhang, Hyperon polarization and its relation with directed flow in high-energy nuclear collisions, Phys. Rev. C **108**, no.6, 6 (2023) [arXiv:2307.04257 [nucl-th]].

[19] I. Karpenko and J. Cimerman, Directed flow and hyperon polarization at RHIC BES from multi-fluid dynamics,

[arXiv:2312.11325 [nucl-th]].
[20] J. Adam *et al.* [STAR], Flow and interferometry results from Au+Au collisions at $\sqrt{s_{NN}} = 4.5$ GeV, Phys. Rev. C **103**, no.3, 034908 (2021) [arXiv:2007.14005 [nucl-ex]].
[21] M. S. Abdallah *et al.* [STAR], Disappearance of partonic collectivity in sNN=3GeV Au+Au collisions at RHIC, Phys. Lett. B **827**, 137003 (2022) [arXiv:2108.00908 [nucl-ex]].
[22] D. Oliinychenko, A. Sorensen, V. Koch and L. McLerran, Sensitivity of Au+Au collisions to the symmetric nuclear matter equation of state at 2–5 nuclear saturation densities, Phys. Rev. C **108**, no.3, 034908 (2023) [arXiv:2208.11996 [nucl-th]].
[23] J. Steinheimer, A. Motornenko, A. Sorensen, Y. Nara, V. Koch and M. Bleicher, The high-density equation of state in heavy-ion collisions: constraints from proton flow, Eur. Phys. J. C **82**, no.10, 911 (2022) [arXiv:2208.12091 [nucl-th]].
[24] M. Omana Kuttan, J. Steinheimer, K. Zhou and H. Stoecker, QCD Equation of State of Dense Nuclear Matter from a Bayesian Analysis of Heavy-Ion Collision Data, Phys. Rev. Lett. **131**, no.20, 202303 (2023) [arXiv:2211.11670 [hep-ph]].
[25] A. Li, G. C. Yong and Y. X. Zhang, Testing the phase transition parameters inside neutron stars with the production of protons and lambdas in relativistic heavy-ion collisions, Phys. Rev. D **107**, no.4, 043005 (2023) [arXiv:2211.04978 [nucl-th]].
[26] Z. M. Wu and G. C. Yong, Probing the incompressibility of dense hadronic matter near the QCD phase transition in relativistic heavy-ion collisions, Phys. Rev. C **107**, no.3, 034902 (2023) [arXiv:2302.11065 [nucl-th]].
[27] P. Parfenov, Model Study of the Energy Dependence of Anisotropic Flow in Heavy-Ion Collisions at $\sqrt{s_{NN}}$ = 2–4.5 GeV, Particles **5**, no.4, 561-579 (2022)
[28] M. Mamaev and A. Taranenko, Toward the System Size Dependence of Anisotropic Flow in Heavy-Ion Collisions at $\sqrt{s_{NN}}$= 2–5 GeV, Particles **6**, no.2, 622-637 (2023)
[29] N. Yao, A. Sorensen, V. Dexheimer and J. Noronha-Hostler, Structure in the speed of sound: from neutron stars to heavy-ion collisions, [arXiv:2311.18819 [nucl-th]].
[30] M. Kozhevnikova and Y. B. Ivanov, Light-nuclei production in Au+Au collisions at sNN=3 GeV within a thermodynamical approach: Bulk properties and collective flow, Phys. Rev. C **109**, no.1, 014913 (2024) [arXiv:2311.08092 [nucl-th]].
[31] M. Kozhevnikova and Y. B. Ivanov, Light Hypernuclei Production in Au+Au Collisions at $\sqrt{s_{NN}} = 3$ GeV within Thermodynamic Approach, Phys. Rev. C **109**, no.3, 034901 (2024) [arXiv:2401.04991 [nucl-th]].
[32] G. C. Yong, Phase diagram determination at fivefold nuclear compression, Phys. Lett. B **848**, 138327 (2024) [arXiv:2306.16005 [nucl-th]].
[33] S. N. Wei, W. Z. Jiang and Z. Q. Feng, The influence of hyperon potential on neutron star matter and heavy-ion collisions, [arXiv:2401.07653 [nucl-th]].
[34] C. T. Sturm *et al.* [KAOS], Evidence for a soft nuclear equation of state from kaon production in heavy ion collisions, Phys. Rev. Lett. **86**, 39-42 (2001) [arXiv:nucl-ex/0011001 [nucl-ex]].
[35] W. Reisdorf *et al.* [FOPI], Systematics of azimuthal asymmetries in heavy ion collisions in the 1 A GeV regime, Nucl. Phys. A **876**, 1-60 (2012) [arXiv:1112.3180 [nucl-ex]].
[36] C. Fuchs, A. Faessler, E. Zabrodin and Y. M. Zheng, Probing the nuclear equation of state by K+ production in heavy ion collisions, Phys. Rev. Lett. **86**, 1974-1977 (2001) [arXiv:nucl-th/0011102 [nucl-th]].
[37] C. Hartnack, H. Oeschler and J. Aichelin, Hadronic matter is soft, Phys. Rev. Lett. **96**, 012302 (2006) [arXiv:nucl-th/0506087 [nucl-th]].
[38] C. Hartnack, H. Oeschler, Y. Leifels, E. L. Bratkovskaya and J. Aichelin, Strangeness Production close to Threshold in Proton-Nucleus and Heavy-Ion Collisions, Phys. Rept. **510**, 119-200 (2012) [arXiv:1106.2083 [nucl-th]].
[39] H. Liu *et al.* [E895], Sideward flow in Au + Au collisions between 2-A-GeV and 8-A-GeV, Phys. Rev. Lett. **84**, 5488-5492 (2000) [arXiv:nucl-ex/0005005 [nucl-ex]].
[40] P. Chung *et al.* [E895], Antiflow of K0(s) mesons in 6-A-GeV Au + Au collisions, Phys. Rev. Lett. **85**, 940-943 (2000) [arXiv:nucl-ex/0101003 [nucl-ex]].
[41] S. Pal, C. M. Ko, Z. w. Lin and B. Zhang, Antiflow of kaons in relativistic heavy ion collisions, Phys. Rev. C **62**, 061903 (2000) [arXiv:nucl-th/0009018 [nucl-th]].
[42] P. Danielewicz, R. Lacey and W. G. Lynch, Determination of the equation of state of dense matter, Science **298**, 1592-1596 (2002) [arXiv:nucl-th/0208016 [nucl-th]].
[43] V. N. Russkikh and Y. B. Ivanov, Collective flow in heavy-ion collisions from AGS to SPS, Phys. Rev. C **74**, 034904 (2006) [arXiv:nucl-th/0606007 [nucl-th]].
[44] P. K. Sahu and W. Cassing, Differential flow of protons in Au+Au collisions at AGS energies, Nucl. Phys. A **712**, 357-369 (2002) [arXiv:nucl-th/0208002 [nucl-th]].
[45] M. Isse, A. Ohnishi, N. Otuka, P. K. Sahu and Y. Nara, Mean-field effects on collective flows in high-energy heavy-ion collisions from AGS to SPS energies, Phys. Rev. C **72**, 064908 (2005) [arXiv:nucl-th/0502058 [nucl-th]].
[46] Y. B. Ivanov, V. N. Russkikh and V. D. Toneev, Relativistic heavy-ion collisions within 3-fluid hydrodynamics: Hadronic scenario, Phys. Rev. C **73**, 044904 (2006) [nucl-th/0503088].
[47] Y. B. Ivanov, Alternative Scenarios of Relativistic Heavy-Ion Collisions: I. Baryon Stopping, Phys. Rev. C **87**, no.6, 064904 (2013) [arXiv:1302.5766 [nucl-th]].
[48] A. Sorensen, K. Agarwal, K. W. Brown, Z. Chajecki, P. Danielewicz, C. Drischler, S. Gandolfi, J. W. Holt, M. Kaminski and C. M. Ko, *et al.* Dense nuclear matter equation of state from heavy-ion collisions, Prog. Part. Nucl. Phys. **134**, 104080 (2024) [arXiv:2301.13253 [nucl-th]].
[49] P. Batyuk *et al.*, Event simulation based on three-fluid hydrodynamics for collisions at energies available at the Dubna Nuclotron-based Ion Collider Facility and at the Facility for Antiproton and Ion Research in Darmstadt, Phys. Rev. C **94**, 044917 (2016) [arXiv:1608.00965 [nucl-th]].
[50] P. Batyuk, D. Blaschke, M. Bleicher, Y. B. Ivanov, I. Karpenko, L. Malinina, S. Merts, M. Nahrgang, H. Petersen and O. Rogachevsky, Three-fluid Hydrodynamics-based Event Simulator Extended by UrQMD final State interactions (THESEUS) for FAIR-NICA-SPSBES/RHIC energies, EPJ Web Conf. **182**, 02056 (2018) [arXiv:1711.07959 [nucl-th]].
[51] M. Kozhevnikova, Y. B. Ivanov, I. Karpenko, D. Blaschke and O. Rogachevsky, Update of the Three-fluid Hydrodynamics-based Event Simulator: light-nuclei production in heavy-ion collisions, Phys. Rev. C **103**, no.4,

044905 (2021) [arXiv:2012.11438 [nucl-th]].
[52] V. N. Russkikh and Yu. B. Ivanov, Dynamical freeze-out in 3-fluid hydrodynamics, Phys. Rev. C **76**, 054907 (2007) [nucl-th/0611094].
[53] Yu. B. Ivanov and V. N. Russkikh, On freeze-out problem in relativistic hydrodynamics, Phys. Atom. Nucl. **72**, 1238 (2009) [arXiv:0810.2262 [nucl-th]].
[54] S. A. Bass, C. Hartnack, H. Stoecker and W. Greiner, Out-of-plane pion emission in relativistic heavy ion collisions: Spectroscopy of Delta resonance matter, Phys. Rev. Lett. **71**, 1144-1147 (1993)
[55] H. Heiselberg and A. M. Levy, Elliptic flow and HBT in noncentral nuclear collisions, Phys. Rev. C **59**, 2716-2727 (1999) [arXiv:nucl-th/9812034 [nucl-th]].
[56] H. Liu, S. Panitkin and N. Xu, Event anisotropy in high-energy nucleus-nucleus collisions, Phys. Rev. C **59**, 348-353 (1999) [arXiv:nucl-th/9807021 [nucl-th]].
[57] H. Sorge, Elliptical flow: A Signature for early pressure in ultrarelativistic nucleus-nucleus collisions, Phys. Rev. Lett. **78**, 2309-2312 (1997) [arXiv:nucl-th/9610026 [nucl-th]].
[58] P. Danielewicz, R. A. Lacey, P. B. Gossiaux, C. Pinkenburg, P. Chung, J. M. Alexander and R. L. McGrath, Disappearance of elliptic flow: a new probe for the nuclear equation of state, Phys. Rev. Lett. **81**, 2438-2441 (1998) [arXiv:nucl-th/9803047 [nucl-th]].
[59] Y. B. Ivanov and A. A. Soldatov, Elliptic Flow in Heavy-Ion Collisions at Energies $\sqrt{s_{NN}}$ = 2.7-39 GeV, Phys. Rev. C **91**, no.2, 024914 (2015) [arXiv:1401.2265 [nucl-th]].
[60] Y. B. Ivanov, Alternative Scenarios of Relativistic Heavy-Ion Collisions: II. Particle Production, Phys. Rev. C **87**, no.6, 064905 (2013) [arXiv:1304.1638 [nucl-th]].
[61] Y. B. Ivanov, Alternative Scenarios of Relativistic Heavy-Ion Collisions: III. Transverse Momentum Spectra, Phys. Rev. C **89**, no.2, 024903 (2014) [arXiv:1311.0109 [nucl-th]].
[62] I. N. Mishustin, V. N. Russkikh and L. M. Satarov, Fluid dynamical model of relativistic heavy ion collision, Sov. J. Nucl. Phys. **54**, 260-314 (1991).
[63] A. S. Khvorostukin, V. V. Skokov, V. D. Toneev and K. Redlich, Lattice QCD constraints on the nuclear equation of state, Eur. Phys. J. C **48**, 531 (2006) [nucl-th/0605069].
[64] Y. B. Ivanov and A. A. Soldatov, Equilibration and baryon densities attainable in relativistic heavy-ion collisions, Phys. Rev. C **101**, no.2, 024915 (2020) [arXiv:1911.10872 [nucl-th]].
[65] Y. Aoki, G. Endrodi, Z. Fodor, S. D. Katz and K. K. Szabo, The Order of the quantum chromodynamics transition predicted by the standard model of particle physics, Nature **443**, 675-678 (2006) [arXiv:hep-lat/0611014 [hep-lat]].
[66] S. Borsanyi, Z. Fodor, J. N. Guenther, R. Kara, S. D. Katz, P. Parotto, A. Pasztor, C. Ratti and K. K. Szabo, QCD Crossover at Finite Chemical Potential from Lattice Simulations, Phys. Rev. Lett. **125**, no.5, 052001 (2020) [arXiv:2002.02821 [hep-lat]].
[67] Z. Fodor, Lattice QCD results at finite temperature and density, Nucl. Phys. A **715**, 319-328 (2003) [arXiv:hep-lat/0209101 [hep-lat]].
[68] F. Csikor, G. I. Egri, Z. Fodor, S. D. Katz, K. K. Szabo and A. I. Toth, Equation of state at finite temperature and chemical potential, lattice QCD results, JHEP **05**, 046 (2004) [arXiv:hep-lat/0401016 [hep-lat]].
[69] F. Karsch, E. Laermann and A. Peikert, Quark mass and flavor dependence of the QCD phase transition, Nucl. Phys. B **605**, 579-599 (2001) [arXiv:hep-lat/0012023 [hep-lat]].
[70] W. Cassing and E. L. Bratkovskaya, Parton-Hadron-String Dynamics: an off-shell transport approach for relativistic energies, Nucl. Phys. A **831**, 215-242 (2009) [arXiv:0907.5331 [nucl-th]].
[71] H. G. Baumgardt, J. U. Schott, Y. Sakamoto, E. Schopper, H. Stoecker, J. Hofmann, W. Scheid and W. Greiner, Shock Waves and MACH Cones in Fast Nucleus-Nucleus Collisions, Z. Phys. A **273**, 359-371 (1975)
[72] H. Stoecker, Collective flow signals the quark gluon plasma, Nucl. Phys. A **750**, 121-147 (2005) [arXiv:nucl-th/0406018 [nucl-th]].
[73] A. M. Poskanzer and S. A. Voloshin, Methods for analyzing anisotropic flow in relativistic nuclear collisions, Phys. Rev. C **58**, 1671-1678 (1998) [arXiv:nucl-ex/9805001 [nucl-ex]].
[74] P. Danielewicz and G. Odyniec, Transverse Momentum Analysis of Collective Motion in Relativistic Nuclear Collisions, Phys. Lett. B **157**, 146-150 (1985) [arXiv:2109.05308 [nucl-th]].
[75] M. Bleicher, E. Zabrodin, C. Spieles, S. A. Bass, C. Ernst, S. Soff, L. Bravina, M. Belkacem, H. Weber and H. Stoecker, *et al.* Relativistic hadron hadron collisions in the ultrarelativistic quantum molecular dynamics model, J. Phys. G **25**, 1859-1896 (1999) [arXiv:hep-ph/9909407 [hep-ph]].
[76] T. Song, L. Tolos, J. Wirth, J. Aichelin and E. Bratkovskaya, In-medium effects in strangeness production in heavy-ion collisions at (sub)threshold energies, Phys. Rev. C **103**, no.4, 044901 (2021) [arXiv:2012.05589 [nucl-th]].
[77] W. Zwermann and B. Schurmann, THE INCLUSIVE PRODUCTION OF KAONS IN RELATIVISTIC NUCLEUS NUCLEUS COLLISIONS BASED ON TRANSPORT THEORY, Nucl. Phys. A **423**, 525-553 (1984)
[78] V. N. Russkikh and Y. B. Ivanov, Kaon production in intermediate-energy nuclear collisions, Nucl. Phys. A **543**, 751-766 (1992)
[79] L. Tolos and L. Fabbietti, Strangeness in Nuclei and Neutron Stars, Prog. Part. Nucl. Phys. **112**, 103770 (2020) [arXiv:2002.09223 [nucl-ex]].
[80] W. Cassing, V. P. Konchakovski, A. Palmese, V. D. Toneev and E. L. Bratkovskaya, Parton/hadron dynamics in heavy-ion collisions at FAIR energies, EPJ Web Conf. **95**, 01004 (2015) [arXiv:1408.4313 [nucl-th]].
[81] G. Q. Li, C. M. Ko and X. S. Fang, Subthreshold antikaon production in nucleus-nucleus collisions, Phys. Lett. B **329**, 149-156 (1994)
[82] J. Schaffner, A. Gal, I. N. Mishustin, H. Stoecker and W. Greiner, Kaon effective mass and energy in dense nuclear matter, Phys. Lett. B **334**, 268-274 (1994)
[83] E. E. Kolomeitsev, B. Kampfer and D. N. Voskresensky, Kaon polarization in nuclear matter, Nucl. Phys. A **588**, 889-917 (1995)
[84] E. E. Kolomeitsev and D. N. Voskresensky, Negative kaons in dense baryonic matter, Phys. Rev. C **68**, 015803 (2003) [arXiv:nucl-th/0211052 [nucl-th]].
[85] `http://ckp.nrcki.ru/`
[86] `http://hlit.jinr.ru/supercomputer_govorun/`

Kinetic temperature and radial flow velocity estimation using identified hadrons and light (anti-)nuclei produced in relativistic heavy-ion collisions at RHIC and LHC

Junaid Tariq*
Department of Physics, Quaid-i-Azam University, Islamabad 44000, Pakistan

M. U. Ashraf†
Centre for Cosmology, Particle Physics and Phenomenology (CP3), Université Catholique de Louvain, B-1348 Louvain-la-Neuve, Belgium

Grigory Nigmatkulov‡
Physics Department, University of Illinois at Chicago, Chicago, Illinois 60607, USA

(Dated: March 6, 2024)

We report the investigation of the kinetic freeze-out properties of identified hadrons ($\pi^{\pm}$, $K^{\pm}$ and $p(\bar{p})$) along with light (anti-)nuclei $d(\bar{d})$, $t(\bar{t})$ and ^3He in relativistic heavy-ion collisions at RHIC and LHC energies. A simultaneous fit is performed with the Blast-Wave (BW) model to the transverse momentum ($p_{\rm T}$) spectra of identified hadrons together with light (anti-)nuclei produced in Au+Au collisions at $\sqrt{s_{\rm NN}}$ = 7.7 – 200 GeV at the RHIC and in Pb+Pb collisions at $\sqrt{s_{\rm NN}}$ = 2.76 at the LHC. The energy and centrality dependence of freeze-out parameters, i.e., kinetic freeze-out temperature (T_{kin}) and collective flow velocity $\langle\beta\rangle$ has been studied. It is observed that light (anti-)nuclei also participate in the collective expansion of the medium created in the collision when included in a common fit with the light hadrons. We observe a marginal rise in the T_{kin} and a slight decrease in $\langle\beta\rangle$ when compared to the values obtained from the fit to light hadrons, indicating that heavier particles decouple earlier in time from the fireball compared to the light hadrons due to higher masses and are more sensitive to the effects of the radial flow. A similar $\langle\beta\rangle$ and significant larger T_{kin} is observed when fit is performed to only protons and light (anti-)nuclei. Additionally, we also observe that the T_{kin} increases from central to peripheral collisions, which is consistent with the argument of short-lived fireball in peripheral collisions. Whereas the $\langle\beta\rangle$ shows a decreasing trend from central to peripheral collisions indicating a more rapid expansion in the central collisions. Both, T_{kin} and $\langle\beta\rangle$ show a weak dependence on the collision energy at most energies. We also observe a strong anti-correlation between T_{kin} and $\langle\beta\rangle$.

PACS numbers: 25.75.-q, 25.75.Ld, 25.75.Nq

arXiv:2403.02759v1 [nucl-th] 5 Mar 2024

I. INTRODUCTION

The investigation of the properties of nuclear matter under extreme conditions is one of the main goals of the heavy-ion program at the Relativistic Heavy Ion Collider (RHIC) and the Large Hadron Collider (LHC) experiments. The ultrarelativistic heavy-ion collisions create a condition suitable for light (anti-)nuclei production, where a significantly high energy density is achieved over a large volume. These conditions produce a very hot and dense matter for a very short interval of time ($\approx 10^{-22}$ seconds) containing approximately equal number of quarks and anti-quarks. This deconfined matter of quarks and gluons, the Quark-Gluon plasma (QGP), is formed during the initial state of collisions. Afterwards, the system experiences a rapid expansion with drop in its temperature and finally undergoes a phase transition towards hadron gas.

In recent years, there has been a significant emphasis on studying the production of light nuclei in heavy-ion collisions at the Bevalac [1], SIS [2, 3], AGS [4–8], SPS [9–13], RHIC [14–21], and LHC [22–27]. The centrality and energy dependence of the production of light (anti-)nuclei has been a topic of significant interest and suggested a relevancy between the critical point and light (anti-)nuclei production [28–32]. However, the precise mechanisms and temporal aspects of light nuclei production in relativistic heavy-ion collisions continue to be subjects of debate due to relatively small binding energies ($\approx$ few MeV) and finite sizes of these nuclei.

It is of significant importance to study the production of light (anti-)nuclei for multiple reasons. First of all, it is not well understood how a cluster is formed in the interior of the fireball during the collision of heavy nuclei, which requires further quantitative investigation. It is probable that a substantial fraction of few-nucleon bound states observed near midrapidity are produced during the latter phases of the reaction, when the hadronic matter experiences dilution and most of the newly formed hydrogen and helium isotopes decouple from the source having no subsequent rescatterings. In this scenario, light (anti-)nuclei may be helpful to probe the dynamics of the fireball at the time of freeze-out.

The evolution of the system produced in relativistic heavy-ion collisions is mainly described by chemical and

* junaid.tariqhep@gmail.com
† usman.ashraf@cern.ch
‡ gnigmat@uic.edu

kinetic freeze-out scenarios. The chemical freeze-out represents the stage when the inelastic collisions among hadrons stop and there is no further composition of new bound states after this stage leads to fixed yield of produced particles at this stage. At the kinetic freeze-out, the ongoing elastic interactions between produced particles results a change in the momenta of particles. The chemical and kinetic freeze-outs are assumed to happen simultaneously at the boundary between hadronic and QGP phases and the system is at chemical and kinetic equilibrium with sudden freeze-out [33]. At the other end, one might also consider another scenario, where chemical and kinetic freeze-outs take place at significantly distinct time frames. The resonances produced at the chemical freeze-out stage would decay more rapidly and the system tend to evolve with elastic collisions between hadrons. In this case, the system stays at local thermal equilibrium until the kinetic freeze-out [34].

The formation of (anti-)nuclei is very sensitive to conditions such as chemical freeze-out conditions, the dynamics of the emitting source and final state effects. Numerous scenarios to study the production mechanisms of (anti-)nuclei have been proposed and are typically discussed within three approaches. The first is thermal-statistical model that is very successful in describing the integrated yield of not only hadrons but also for composite nuclei [35–39]. The production of light (anti-)nuclei can also be studied by the coalescence model, in which protons and neutrons with similar velocities and positions on the kinetic freeze-out surface coalesce to form nuclei [40–49]. The third approach is kinetic theory, which is based on the assumption that when light (anti-)nuclei are thermally produced at the chemical freeze-out, they might break and formed again by the final state coalescence during the evolution of the collision system [50–53]. Surprisingly, it appears that both, the thermal-statistical and coalescence approaches give very consistent predictions [54].

Additionally, the blast-wave (BW) [55] parametrization is extensively utilized to describe the $p_{\rm T}$ spectra of light (anti-)nuclei [19, 21]. The conceptual basis for the BW model is derived from its similarity to the freeze-out configuration within the hydrodynamic model [34]. The BW parametrization provides a remarkably good fit to the $p_{\rm T}$ spectra of light (anti-)nuclei produced in Au+Au collisions at $\sqrt{s_{\rm NN}}$ = 7.7 – 200 GeV at RHIC [19] and Pb+Pb collisions at $\sqrt{s_{\rm NN}}$ = 2.76 TeV at LHC [21]. The only difference between the two different types of collision systems is the exponent n in the velocity profile ($\beta = \beta_s(\frac{r}{R})^n$), which was set to 1 at RHIC, while it was treated as a free parameter at LHC.

Many studies have been performed to investigate the energy and centrality dependence of kinetic freeze-out temperature (T_{kin}) and the radial flow velocity (β_T) parameters by simultaneously fitting the $p_{\rm T}$ spectra of individual light hadrons (($\pi^{\pm}$, $K^{\pm}$ and $p(\bar{p})$)) [56, 57] produced in heavy ion collisions as well as combined with strange hadrons (K^0_S and Λ) [58, 59], and with $d, {}^3He$ with the BW model [21]. During the expansion phase of the strongly interacting system, the pressure gradient gives a rise to the collective flow. This results in a characteristic dependence of the shape of the $p_{\rm T}$ distribution on the particle mass and can be described with a common T_{kin} and β_T [55]. By a thorough analysis on the simultaneous fit to the $p_{\rm T}$ spectra of light hadrons ($\pi^{\pm}$, $K^{\pm}$ and $p(\bar{p})$) along with light (anti-)nuclei ($d(\bar{d})$ and $t(\bar{t})$) we attempt to investigate the freeze-out parameters (T_{kin} and β_T) extracted from the experimental data available for RHIC energies. In this work, we performed a systematic study of energy and centrality dependence of T_{kin} and β_T extracted from fitting the $p_{\rm T}$ spectra of light hadrons along with light (anti-)nuclei with the BW model from Au+Au collisions at $\sqrt{s_{\rm NN}}$ = 7.7 – 200 GeV and Pb+Pb collisions at 2.76 TeV.

This paper is organized as follows. In Section II, we describe the analysis method. Results and Discussion are presented in Section III. The conclusion is summarized in Section IV.

II. ANALYSIS METHOD

Blast-Wave (BW) [55] is a phenomenological model commonly used to fit the hadron as well as light (anti-)nuclei spectra by experimental collaborations [19, 21]. The model is based on the assumption that particles are emitted thermally for an expanding source with global variables: temperature (T) and velocity profile (β [55, 60]). The functional form can be written as:

$$\frac{d^2N}{p_T dp_T} \propto \int_0^R r dr m_T I_0\left(\frac{p_T \sinh\rho(r)}{T_{kin}}\right) \times K_1\left(\frac{m_T \cosh\rho(r)}{T_{kin}}\right), \tag{1}$$

where $m_T = \sqrt{p_T^2 + m^2}$ is the transverse mass of the hadron species. The I_0 and K_1 are the modified Bessel functions. The temperature of the localized thermal sources, from which particles radiate, is denoted by T_{kin}. While assuming the longitudinal expansion of the system to be boost invariant, the velocity profile of the thermal source can be parameterized as:

$$\rho = tanh^{-1}\beta(r) = tanh^{-1}(\beta_S(\frac{r}{R})^n). \tag{2}$$

The radial distance from the center of the fireball in the transverse plane is represented by r, the radius of the fireball is R, the transverse expansion velocity is $\beta(r)$ at radius $0 \leq r \leq R$. The β_S is the transverse expansion velocity at the surface and exponent of the velocity profile is n. The average radial flow velocity can be expressed as $\langle\beta\rangle = \beta_S \ . \ 2/(2+n)$ [61]. In order to study the light (anti-)nuclei distribution in different colliding systems, n was treated differently. In Au+Au collisions at $\sqrt{s_{\rm NN}}$ = 7.7 – 200 GeV at RHIC [19], n was fixed to 1, while treated as a free parameter in Pb+Pb collisions at $\sqrt{s_{\rm NN}}$ = 2.76 TeV at LHC [21] for better fit. This different

treatment of n to study the light (anti-)nuclei $p_{\rm T}$ distribution at RHIC and LHC reflects the different dynamical evolution of the fireball formed in heavy ion collisions. In the current work, to check the universality of the BW parametrization we use $n = 1$ for Au+Au and Pb+Pb collisions. Therefore, the free parameters are only T, β and the normalization factor. Generally, the important parameters to determine the shape of each spectrum are the T, n, β and the mass of the particle specie, but with the common T and β, the mass of particle specie is an important parameter which determine the shape of the spectrum in BW model [62].

III. RESULTS AND DISCUSSION

The results of our analysis are presented in this section.

A. Transverse Momentum ($p_{\rm T}$) Spectra

It is crucial to observe that blast-wave (BW) fits represent a simplified method that imitates the hydrodynamics involved in radial expansion and comes with specific constraints. For instance, it is acknowledged that the temperature is notably influenced by the chosen fit range and the particle species. Particularly, the quality of the BW fits using the FastReso package [63] is relatively good using a single temperature of ≈ 150 MeV for chemical and kinetic freeze-out and it has been reported in Ref. [64] that the temperature from these fits exhibits a weak dependence on centrality and collision system. This is possible in the FastReco approach through its explicit consideration of the feed-down effect from resonance decays. Furthermore, alternative methods utilize an extended BW model approach with additional parameters employed to LHC data for a better description [**?**]. The conventional (Boltzmann-Gibbs) blast-wave parameterization provides a straightforward and robust method for comparing the spectra of hadrons and light (anti-)nuclei, which is the objective of the current study.

The measured $p_{\rm T}$ spectra of light hadrons ($\pi^{\pm}$, $K^{\pm}$ and $p(\bar{p})$) and light (anti-)nuclei ($d(\bar{d})$ and $t(\bar{t})$) in Au+Au collisions at $\sqrt{s_{\rm NN}}$ = 7.7 – 200 GeV from RHIC [19, 56, 65] and Pb+Pb collisions at $\sqrt{s_{\rm NN}}$ = 2.76 TeV from LHC [21, 57] at available centrality classes are analyzed for this purpose. No data available for $\bar{t}$ in Au+Au collisions at $\sqrt{s_{\rm NN}}$ = 7.7 – 200 GeV and Pb+Pb collisions at $\sqrt{s_{\rm NN}}$ = 2.76 TeV. Therefore, we use ^3He along with $\pi^{\pm}$, $K^{\pm}$ and $p(\bar{p})$ in Pb+Pb collisions at $\sqrt{s_{\rm NN}}$ = 2.76 TeV for our analysis. Details of the data sets of light hadrons and light (anti-)nuclei under investigation are summarized in Table I. The simultaneous BW fits to the $p_{\rm T}$ spectra of particle species under investigation are performed by minimizing the value of χ^2/N_{DOF}, where N_{DOF} is the number of degrees of freedom and is defined as the number of data points minus the number of fitting parameters. The minimization procedure in the current analysis is done by using the MINUIT [66] package available within the ROOT framework [67].

For light hadrons, we repeated the analysis presented in Ref. [56] for a simultaneous fit to the $p_{\rm T}$ spectra with BW model. The obtained parameters from the BW fit are consistent with the previously reported results [56]. The low $p_{\rm T}$ part of the pion spectra is significantly influenced by resonance decays therefore, $p_{\rm T} < 0.5$ GeV/c is excluded from the fit. Conversely, at higher $p_{\rm T}$, eventual hard contributions may become significant, which are not anticipated to be effectively described by the BW model [68]. Therefore, the sensitivity of the BW model parameters especially T_{kin} is contingent upon the choice of $p_{\rm T}$ ranges used for fitting [57]. The fit range for light hadrons have been limited according to Ref. [56] (0.5 – 1.3 GeV/c, 0.25 – 1.4 GeV/c, 0.4 – 1.3 GeV/c for $\pi^{\pm}, K^{\pm}$ and $p(\bar{p})$ respectively). However, for light (anti-)nuclei the spectrum is fitted up to the maximum available $p_{\rm T}$ range. Figures 1 and 2 show the simultaneous BW fit using Eq. 1 to the $p_{\rm T}$ spectra of light hadrons and light (anti-)nuclei in Au+Au collisions at $\sqrt{s_{\rm NN}}$ = 39 GeV in 0–10%, 10–20% and 40–80% centrality classes and Pb+Pb collisions at $\sqrt{s_{\rm NN}}$ = 2.76 TeV in 0–20% and 20–80% centrality intervals respectively as an example. The spectra of light (anti-)nuclei are evidently well described by the common BW fit within uncertainties indicating that relatively heavy particles, like $d(\bar{d}), t(\bar{t})$ and ^3He, also participate in a collective flow field. The extracted fit parameters and χ^2/N_{DOF} are summarized in Table III and Table IV.

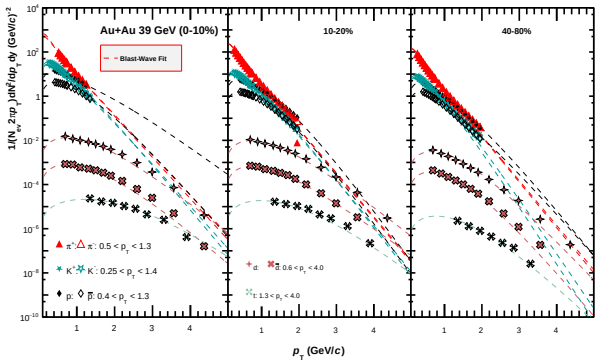


FIG. 1. (Color online) Blast-Wave model simultaneous fit to the $p_{\rm T}$ spectra of $\pi^{\pm}$, $K^{\pm}$, $p(\bar{p}), d(\bar{d})$ and $t(\bar{t})$ in Au+Au collisions at $\sqrt{s_{\rm NN}}$ = 39 GeV in 0–10%, 10–20% and 40–80% centrality classes. Statistical and systematic errors are added in quadrature.

B. Kinetic Freeze-out Parameters

The extracted freeze-out parameters from the BW fit have been presented in this section. It is important to point out that the whole measured $p_{\rm T}$ range for all particle species is very well described by the BW function

TABLE I. References for data

System	$\sqrt{S_{NN}}$ (GeV)	Particle	Collaboration	Reference
Au-Au	7.7, 11.5, 19.6, 27, 39	$\pi^{\pm}$, $K^{\pm}$, p, $\bar{p}$	STAR	[57]
Au-Au	14.5	$\pi^{\pm}$, $K^{\pm}$, p, $\bar{p}$	STAR	[69]
Au-Au	62.4	$\pi^{\pm}$,p, $\bar{p}$	STAR	[70]
Au-Au	62.4	$K^{\pm}$	STAR	[71]
Au-Au	200	$\pi^{\pm}$,p, $\bar{p}$	STAR	[70]
Au-Au	200	$K^{\pm}$	PHENIX	[72]
Au-Au	7.7, 11.5, 14.5, 19.6, 27, 39, 200	d, $\bar{d}$	STAR	[19]
Au-Au	7.7, 11.5, 14.5, 19.6, 27, 39, 200	t	STAR	[65]
Pb-Pb	2760	$\pi^{\pm}$,$K^{\pm}p$, $\bar{p}$	ALICE	[57]
Pb-Pb	2760	d, ^3He	ALICE	[21]
Pb-Pb	5020	$\pi^{\pm}$,$K^{\pm}p$, $\bar{p}$	ALICE	[73]
Pb-Pb	5020	d,$\bar{d}$, ^3He	ALICE	[74]

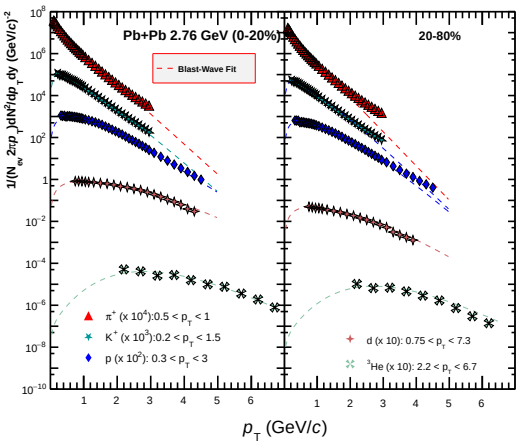


FIG. 2. (Color online) Blast-Wave model simultaneous fit to the $p_{\rm T}$ spectra of $\pi^{\pm}$, $K^{\pm}$, $p(\bar{p}), d(\bar{d})$ and $t(\bar{t})$ in Au+Au collisions at $\sqrt{s_{\rm NN}}$ = 2.76 TeV in 0–20% and 20–80% centrality classes. Statistical and systematic errors are added in quadrature.

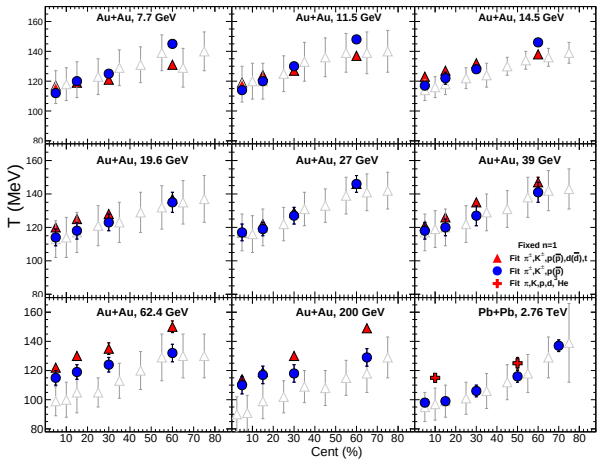


FIG. 3. (Color online) Centrality dependence of kinetic freeze-out temperature (T_{kin}) of light hadrons and light (anti-)nuclei in Au+Au collisions at $\sqrt{s_{\rm NN}}$ = 7.7 – 200 GeV and Pb+Pb collisions at $\sqrt{s_{\rm NN}}$ = 2.76 TeV.

(individual fit only), however, no physics meaning is attached to the parameters. A combined BW fits to different particle species can be useful to provide valuable insights into the freeze-out conditions and allow to compare quantitatively between different systems colliding at different $\sqrt{s_{\rm NN}}$ in terms of hydrodynamic interpretation. In principle different particle species can decouple at different times leading to different values of $\langle\beta\rangle$ and T_{kin} from the hadronic medium due to different hadronic cross sections. The interpretation of this statement becomes more arguable by forcing all the particle species to decouple assuming same set of parameters.

Figures 3 and 4 show the centrality dependence of temperature (T_{kin}) and radial flow velocity ($\langle\beta\rangle$), respectively. The parameters are extracted by simultaneous fits to the $p_{\rm T}$ spectra of light hadrons along with light (anti-)nuclei in Au+Au collisions at $\sqrt{s_{\rm NN}}$ = 7.7 – 200 GeV from RHIC and Pb+Pb collisions at $\sqrt{s_{\rm NN}}$ = 2.76 TeV from LHC. For simplicity, the centrality classes of $\pi^{\pm}$, $K^{\pm}$, $p(\bar{p})$ are merged and refitted to make it consistent with those used for $d(\bar{d})$ and $t(\bar{t})$ measurements, i.e. 0–10%, 10–20%, 20–40% and 40–80%. Due to unavailability of the triton $p_{\rm T}$ spectra from Pb+Pb collisions at $\sqrt{s_{\rm NN}}$ = 2.76 TeV, we included ^3He in the fits instead. Grey markers represent the published results for $\pi^{\pm}$, $K^{\pm}$, and $p(\bar{p})$ from Ref. [56]. Blue markers depict $\pi^{\pm}$, $K^{\pm}$, and $p(\bar{p})$ data with combined centrality classes. Red markers correspond to T_{kin} of $\pi^{\pm}$, $K^{\pm}$, $p(\bar{p})$, and $d(\bar{d})$. It is evident from Fig. 3 that T_{kin} exhibits an increasing trend as a function of centrality for all collision energies. Furthermore, the inclusion of heavier particle species, such as light (anti-)nuclei, results in slightly higher temperatures compared to those of light hadrons. This effect is more prominent at energies $\sqrt{s_{\rm NN}}$ $\geq$ 62.4 GeV. Fig. 4 shows that fitting both light hadrons with light (anti-)nuclei together leads to a smaller values of $\langle\beta\rangle$ as compared to those when only light hadrons are considered in the fits. To study the influence of light (anti-)nuclei data on the global characteristics, we repeat the fit by excluding $d(\bar{d})$ and t simultaneously exhibiting similar trend with slight smaller value of T_{kin} and

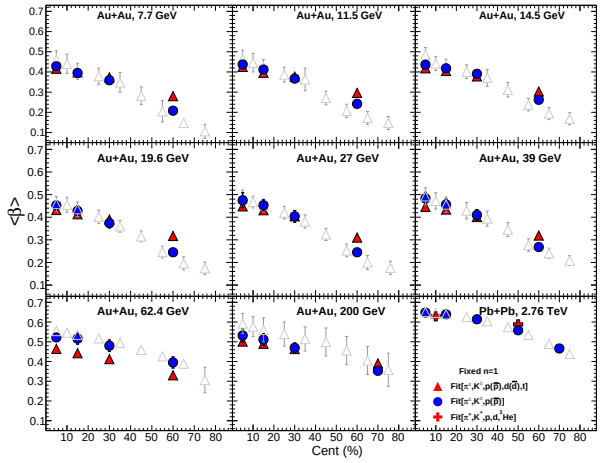


FIG. 4. (Color online) Centrality dependence of radial flow velocity ($\langle\beta\rangle$) of light hadrons and light (anti-)nuclei in Au+Au collisions at $\sqrt{s_{\rm NN}}$ = 7.7 – 200 GeV and Pb+Pb collisions at $\sqrt{s_{\rm NN}}$ = 2.76 TeV.

sightly larger values of $\langle\beta\rangle$. This suggest that heavier particles decouple earlier in time from the fireball compared to the light hadrons due to higher masses and are more sensitive to the effects of the radial flow. Moreover, the T_{kin} in mid-central 20–40% and peripheral collisions 40–80% at energies $\sqrt{s_{\rm NN}} \leq 19.6$ GeV is relatively lower as compared to central collisions and start to increase at energies at energies $\sqrt{s_{\rm NN}} \geq 27$ GeV. On the other hand, $\langle\beta\rangle$ is slightly larger at the same centrality classes and energies. This may be related to the change in the collision geometry and different production mechanisms of light (anti-)nuclei at lower energies specifically in peripheral collisions where spectators plays an important role. Thus, a clear hierarchical structure seems to be seen in kinetic freeze-out suggesting more massive particles leave the medium earlier in time compared to those of light particles. It is important to note that the published data from the STAR experiment at RHIC on Au+Au collisions at $\sqrt{s_{\rm NN}}$ = 62.4 GeV and 200 GeV [70–72] used a slightly different configuration of the detector setup as compared to $\sqrt{s_{\rm NN}}$ = 7.7 – 39 GeV data sets. This can be seen as a slight difference between our estimations and the published results. The foreseen analysis of identified hadrons with recent detector upgrades will be helpful to understand this slight difference. We have also repeated the analysis by treating n as a free parameter. It is shown that the best fit values of the extracted parameters T_{kin} and $\langle\beta\rangle$ are found to be nearly unaltered when letting the parameter n free for all energies.

In the coalescence model nuclei are assumed to be formed at a later stage of the collisions precisely at or after the kinetic freeze-out. Under this condition, one can anticipate that the $p_{\rm T}$ spectra of both protons and (anti-)nuclei reflect a common temperature and velocity field of the source at or later stage of the nuclear cluster formation. To provide a more detailed explanation, we have categorized various particle species into distinct sets and performed the BW fit. Set A includes $\pi^{\pm}$, $K^{\pm}$, $p(\bar{p})$, $d(\bar{d})$ and t; Set B comprises $p(\bar{p})$, $d(\bar{d})$ and t; Set C consists of $d(\bar{d})$ and t; and Set D contains only $\pi^{\pm}$, $K^{\pm}$, $p(\bar{p})$. Note that we use ^3He instead of t where no data for triton is available at LHC energies. The extracted parameters from different set of combinations in (0–10%) central Au+Au collisions at $\sqrt{s_{\rm NN}}$ = 27 GeV are listed in Table II as an example. The similar trend is observed for the rest of energies. It is evident from the Table II that including $p(\bar{p})$ in the fit with light (anti-)nuclei exhibits a similar velocity profile as observed when $\pi^{\pm}$, $K^{\pm}$, $p(\bar{p})$ are considered in the fit (Set A). However, there is a notable difference in the kinetic freeze-out temperature (T_{kin}) and is found to be significantly larger (129 ± 9) MeV which is unexpected in the context of final-state coalescence and requires further investigation. However, the observed results aligns with the hypothesis of statistical hadronization in which light (anti-)nuclei are formed close to the phase boundary without undergoing significant interactions at later stages of the system evolution. The observed scenario might be explained by considering prehadronic multiquark states and has been discussed in detail in Ref. [36, 75]. We repeat the exercise for Pb+Pb collisions at $\sqrt{s_{\rm NN}}$ = 2.76 TeV and observed similar findings. The corresponding extracted parameters are listed in Table II. The velocity profile of Set B, when including $p(\bar{p})$ in the fit along with light (anti-)nuclei, appears to be relatively lower compared to Set A. However, the T_{kin} is significantly larger (149 ± 7) MeV. To understand this, we introduced another set, denoted as Set B′, in which we keep the same velocity profile as that of Set A. As a result, the T_{kin} is noticeably reduced to (132 ± 5) MeV and is consistent with ALICE experimental results from Pb+Pb collisions at $\sqrt{s_{\rm NN}}$ = 5.02 TeV [75].

For further investigation, a simultaneous BW fit is performed to the $p_{\rm T}$ spectra of only light (anti-)nuclei in Au+Au collisions at $\sqrt{s_{\rm NN}}$ = 27 GeV (Set C). The extracted T_{kin} is 121 ± 10 MeV is in good agreement within uncertainties with the results of Set A, where all particles are included in the fit and are listed in Table II. This finding appears to be more consistent with the expectations of the coalescence model. It suggests that protons freeze-out earlier at a higher temperature as indicated by Set B. Subsequently, these protons and neutrons coalesce to form nuclei at a later stage through the coalescence process. When examining Set D, which considers only 0–10% central $\pi^{\pm}$, $K^{\pm}$, $p(\bar{p})$ $p_{\rm T}$ spectra in Au+Au collisions at $\sqrt{s_{\rm NN}}$ = 27 GeV in the fit the resulting T_{kin} is 116 ± 3 MeV. On the other hand, in Pb+Pb collisions at $\sqrt{s_{\rm NN}}$ = 2.76 TeV the value of T_{kin} from Set D relatively lower than that obtained from Set A, suggesting that the inclusion of the lightest particles contributes to the observation of lower kinetic freeze-out temperatures. It is observed that T_{kin} in 0–10% central Au+Au collisions at $\sqrt{s_{\rm NN}}$ = 27 GeV is considerably higher than those in 0–10% central Pb+Pb collisions reported at LHC energies, as documented in Ref. [57]. It is important to empha-

TABLE II. Combined parameters extracted from the blast-wave fit to the $p_{\rm T}$ spectra of different set of particle species (light hadrons and light (anti-)nuclei) in central (0–10%) Au+Au collisions at $\sqrt{s_{\rm NN}}$ = 27 GeV and Pb+Pb collisions at 2.76 TeV.

$\sqrt{s_{\rm NN}}$	Sets	Particle	$< \beta >$	T (MeV)	n	χ^2/ dof
27GeV	Set A	$\pi^{\pm}$, $K^{\pm}$, p, $\bar{p}$, $d(\bar{d}), t$	0.465 ± 0.003	116 ± 3	0.857 ± 0.040	0.53
	Set B	$p(\bar{p})$, $d(\bar{d}), t$	0.464 ± 0.017	129 ± 9	0.723 ± 0.104	0.72
	Set C	$d(\bar{d}), t$	0.460 ± 0.017	121 ± 10	0.840 ± 0.132	1.25
	Set D	$\pi^{\pm}$, $K^{\pm}$, p, $\bar{p}$	0.475 ± 0.033	116 ± 3	0.672 ± 0.198	0.28
2.76 TeV	Set A	$\pi^{\pm}$, $K^{\pm}$, p, $\bar{p}$, d,^{3}He	0.673 ± 0.003	115 ± 3	0.698 ± 0.015	0.75
	Set B	$p(\bar{p})$, $d(\bar{d})$,^{3}He	0.633 ± 0.08	149 ± 7	0.556 ± 0.031	0.41
	Set B′	$p(\bar{p})$, $d(\bar{d})$,^{3}He	0.673 ± 0.003	132 ± 5	0.688 ± 0.025	2.3
	Set C	d,^{3}He	0.622 ± 0.007	80 ± 17	0.779 ± 0.043	0.18
	Set D	$\pi^{\pm}$, $K^{\pm}$, p, $\bar{p}$	0.640 ± 0.018	98 ± 5	0.701 ± 0.120	0.25

size that lighter particles are more likely to be influenced by contributions originating from resonance decays and hard scatterings across a broader $p_{\rm T}$ range as compared to those of heavier particles. It is important to mention that the BW model is only a simplified hydrodynamic approach to understand the collective motion and freeze-out of particles and has certain limitations; therefore, one should be cautious when making any strong conclusions.

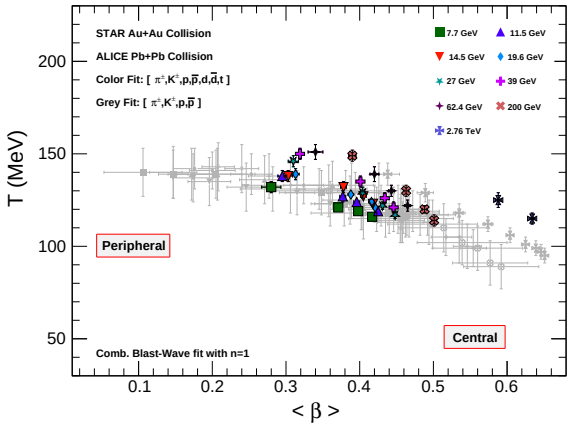


FIG. 5. (Color online) Variation of kinetic freeze-out temperature (T_{kin}) with radial flow velocity ($\langle\beta\rangle$) in Au+Au collisions at $\sqrt{s_{\rm NN}}$ = 7.7 – 200 GeV and Pb+Pb collisions at $\sqrt{s_{\rm NN}}$ = 2.76 TeV for different centrality classes. The centrality increases from left to right for a given energy.

Figure 5 shows the variation of extracted T_{kin} with $\langle\beta\rangle$ for different centrality classes and energies. The grey markers are the simultaneous fit to $\pi^{\pm}, K^{\pm}$ and $p(\bar{p})$ $p_{\rm T}$ spectra only and are taken from Ref. [56]. The colored markers are our combined BW fit to the $p_{\rm T}$ spectra of $\pi^{\pm}, K^{\pm}, p(\bar{p}), d(\bar{d}), t$ and ^3He. We observe that including light (anti-)nuclei in the analysis leads to a slight increase in T_{kin} and slight decrease in $\langle\beta\rangle$. This might be an indication of earlier freeze-out of the system by adding more heavier particle to the fit and might be more sensitive to the effects of radial flow. Moreover, the extracted parameters show strong two dimensional anti-correlation, i.e. higher values of T_{kin} corresponds to lower values of $\langle\beta\rangle$ and vice-versa.

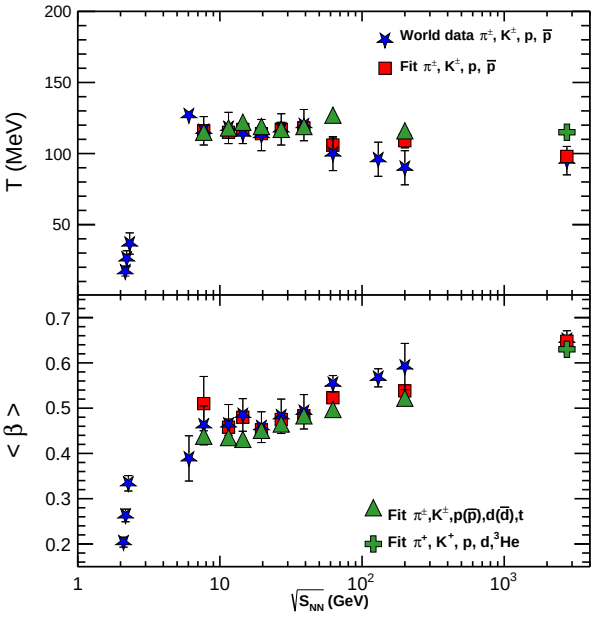


FIG. 6. (Color online) Energy dependence of kinetic freeze-out temperature (T_{kin}) (top) and radial flow velocity ($\langle\beta\rangle$) (bottom) for central heavy-ion collisions.

Energy dependence of kinetic freeze-out temperature (T_{kin}) and radial flow velocity ($\langle\beta\rangle$) extracted from the fit to $p_{\rm T}$ spectra of light hadrons along with light (anti-)nuclei is shown in Fig. 6. The red markers represent our fit to the $p_{\rm T}$ spectra of $\pi^{\pm}, K^{\pm}, p(\bar{p})$ in central (0–10%) Au+Au collisions at $\sqrt{s_{\rm NN}}$ = 7.7 – 200 GeV and Pb+Pb collisions at $\sqrt{s_{\rm NN}}$ = 2.76 TeV. The blue markers are the world published data for identified particles. Green markers correspond to the BW fit to the $p_{\rm T}$ spectra of light hadrons together with light (anti-)nuclei. It is observed that T_{kin} is relatively higher and $\langle\beta\rangle$ is lower when we include light (anti-)nuclei in the fit. Overall, they follow the trend of the world data. T_{kin} remains almost constant from energies $\sqrt{s_{\rm NN}}$ = 7.7 – 39 GeV and starts decreasing towards LHC energies. On the other hand, the transverse flow velocity $\langle\beta\rangle$ increases over the entire energy range.

IV. CONCLUSIONS

The analysis of transverse momentum $p_{\rm T}$ spectra of produced particles provide insights into the particle production mechanisms as well as the freeze-out conditions of the system. We reported the comprehensive investigation of the kinetic freeze-out properties of identified hadrons ($\pi^{\pm}$, $K^{\pm}$ and $p(\bar{p})$) along with light (anti-)nuclei $d(\bar{d})$, $t(\bar{t})$ and ^3He in relativistic heavy-ion collisions at RHIC and LHC energies. The $p_{\rm T}$ distribution of identified hadrons including light (anti-)nuclei is fitted simultaneously with the Blast-Wave model. This detailed study suggests that relatively heavier particles like light (anti-)nuclei participate in a common flow field resulting in a slight increase in T_{kin} and slight decrease in $\langle\beta\rangle$ in comparison to those when only identified hadrons are included in the fit. This indicates that heavier particles decouple earlier in time from the fireball compared to the light hadrons due to their higher masses and are more sensitive to the effects of radial flow. The strong anti-correlation between T_{kin} and $\langle\beta\rangle$, i.e. the value of T_{kin} increases from central to peripheral collisions indicating shorter-lived fireball in peripheral collisions, The value of $\langle\beta\rangle$ decrease from central to peripheral collisions is consistent with the picture of more rapid expansion of the system in central collisions at both, RHIC and LHC energies. The extracted T_{kin} show weak energy dependence at RHIC energies while decreases at the LHC energies and $\langle\beta\rangle$ shows increasing trend from RHIC to LHC energies. The T_{kin} obtained from the BW fit to only protons and light (anti-)nuclei is remarkably close to the chemical freeze-out temperature derived from statistical hadronization models. The certain limitations in the BW fit should be considered before make strong conclusion.

V. ACKNOWLEDGEMENT

The authors would like to acknowledge M. Aamir Shahzad, A. M. Khan for useful discussions.

A. References

[1] S. Nagamiya, M. C. Lemaire, E. Moller, S. Schnetzer, G. Shapiro, H. Steiner, and I. Tanihata. Production of Pions and Light Fragments at Large Angles in High-Energy Nuclear Collisions. *Phys. Rev. C*, 24:971–1009, 1981.

[2] W. Reisdorf et al. Systematics of central heavy ion collisions in the 1A GeV regime. *Nucl. Phys. A*, 848:366–427, 2010.

[3] J. Adamczewski-Musch et al. Directed, Elliptic, and Higher Order Flow Harmonics of Protons, Deuterons, and Tritons in Au + Au Collisions at $\sqrt{s_{NN}} = 2.4$ GeV. *Phys. Rev. Lett.*, 125:262301, 2020.

[4] N. Saito et al. Composite particle production in relativistic Au + Pt, Si + Pt, and p + Pt collisions. *Phys. Rev. C*, 49:3211–3218, 1994.

[5] S. Albergo et al. Light nuclei production in heavy ion collisions at relativistic energies. *Phys. Rev. C*, 65:034907, 2002.

[6] T. A. Armstrong et al. Measurements of light nuclei production in 11.5-A-GeV/c Au + Pb heavy ion collisions. *Phys. Rev. C*, 61:064908, 2000.

[7] T. A. Armstrong et al. Anti-deuteron yield at the AGS and coalescence implications. *Phys. Rev. Lett.*, 85:2685–2688, 2000.

[8] M. J. Bennett et al. Light nuclei production in relativistic Au + nucleus collisions. *Phys. Rev. C*, 58:1155–1164, 1998.

[9] Jehanne Simon-Gillo et al. Deuteron and anti-deuteron production in CERN experiment NA44. *Nucl. Phys. A*, 590:483C–486C, 1995.

[10] S. V. Afanasiev et al. Deuteron production in central Pb + Pb collisions at 158-A-GeV. *Phys. Lett. B*, 486:22–28, 2000.

[11] R. Arsenescu et al. An Investigation of the anti-nuclei and nuclei production mechanism in Pb + Pb collisions at 158-A-GeV. *New J. Phys.*, 5:150, 2003.

[12] T. Anticic et al. Energy and centrality dependence of deuteron and proton production in Pb + Pb collisions at relativistic energies. *Phys. Rev. C*, 69:024902, 2004.

[13] T. Anticic et al. Production of deuterium, tritium, and He3 in central Pb + Pb collisions at 20A,30A,40A,80A , and 158A GeV at the CERN Super Proton Synchrotron. *Phys. Rev. C*, 94(4):044906, 2016.

[14] C. Adler et al. Anti-deuteron and anti-He-3 production in s(NN)**(1/2) = 130-GeV Au+Au collisions. *Phys. Rev. Lett.*, 87:262301, 2001. [Erratum: Phys.Rev.Lett. 87, 279902 (2001)].

[15] S. S. Adler et al. Deuteron and antideuteron production in Au + Au collisions at s(NN)**(1/2) = 200-GeV. *Phys. Rev. Lett.*, 94:122302, 2005.

[16] S. Afanasiev et al. Elliptic flow for phi mesons and (anti)deuterons in Au + Au collisions at s(NN)**(1/2) = 200-GeV. *Phys. Rev. Lett.*, 99:052301, 2007.

[17] B. I. Abelev et al. Yields and elliptic flow of d(anti-d) and He-3(anti-He-3) in Au + Au collisions at s(NN)**(1/2) = 200- GeV. 9 2009.

[18] H. Agakishiev et al. Observation of the antimatter helium-4 nucleus. *Nature*, 473:353, 2011. [Erratum: Nature 475, 412 (2011)].

[19] Jaroslav Adam et al. Beam energy dependence of (anti-)deuteron production in Au + Au collisions at the BNL Relativistic Heavy Ion Collider. *Phys. Rev. C*, 99(6):064905, 2019.

[20] Jaroslav Adam et al. Precision measurement of the mass difference between light nuclei and anti-nuclei with the ALICE experiment at the LHC. *Nature Phys.*, 11(10):811–814, 2015.

[21] Jaroslav Adam et al. Production of light nuclei and anti-nuclei in pp and Pb-Pb collisions at energies available at the CERN Large Hadron Collider. *Phys. Rev. C*, 93(2):024917, 2016.

[22] Jaroslav Adam et al. ${}^{3}_{\Lambda}\mathrm{H}$ and ${}^{3}_{\Lambda}\overline{\mathrm{H}}$ production in Pb-Pb collisions at $\sqrt{s_{\rm NN}} = 2.76$ TeV. *Phys. Lett. B*, 754:360–372, 2016.

[23] Shreyasi Acharya et al. Measurement of deuteron spectra and elliptic flow in Pb–Pb collisions at $\sqrt{s_{\rm NN}} = 2.76$ TeV at the LHC. *Eur. Phys. J. C*, 77(10):658, 2017.

[24] Shreyasi Acharya et al. Production of deuterons, tritons, ^{3}He nuclei and their antinuclei in pp collisions at $\sqrt{s} =$

0.9, 2.76 and 7 TeV. *Phys. Rev. C*, 97(2):024615, 2018.

[25] J. Adam et al. Beam-energy dependence of the directed flow of deuterons in Au+Au collisions. *Phys. Rev. C*, 102(4):044906, 2020.

[26] M. S. Abdallah et al. Light nuclei collectivity from $\sqrt{s_{NN}}$ = 3 GeV Au+Au collisions at RHIC. *Phys. Lett. B*, 827:136941, 2022.

[27] Shreyasi Acharya et al. Measurement of anti-^{3}He nuclei absorption in matter and impact on their propagation in the Galaxy. *Nature Phys.*, 19(1):61–71, 2023.

[28] Xiaofeng Luo and Nu Xu. Search for the QCD Critical Point with Fluctuations of Conserved Quantities in Relativistic Heavy-Ion Collisions at RHIC : An Overview. *Nucl. Sci. Tech.*, 28(8):112, 2017.

[29] Kai-Jia Sun, Lie-Wen Chen, Che Ming Ko, and Zhangbu Xu. Probing QCD critical fluctuations from light nuclei production in relativistic heavy-ion collisions. *Phys. Lett. B*, 774:103–107, 2017.

[30] Edward Shuryak and Juan M. Torres-Rincon. Light-nuclei production and search for the QCD critical point. *Eur. Phys. J. A*, 56(9):241, 2020.

[31] Kai-Jia Sun, Lie-Wen Chen, Che Ming Ko, Jie Pu, and Zhangbu Xu. Light nuclei production as a probe of the QCD phase diagram. *Phys. Lett. B*, 781:499–504, 2018.

[32] Junaid Tariq, Sumaira Ikram, and M. U. Ashraf. Study of strange quark density fluctuations in Au + Au Collisions at $\sqrt{s_{\rm NN}}$ = 7.7–200 GeV from AMPT Model. *Eur. Phys. J. A*, 59(4):73, 2023.

[33] Wojciech Broniowski and Wojciech Florkowski. Explanation of the RHIC p(T) spectra in a thermal model with expansion. *Phys. Rev. Lett.*, 87:272302, 2001.

[34] Fabrice Retiere and Michael Annan Lisa. Observable implications of geometrical and dynamical aspects of freeze out in heavy ion collisions. *Phys. Rev. C*, 70:044907, 2004.

[35] A. Andronic, P. Braun-Munzinger, J. Stachel, and H. Stocker. Production of light nuclei, hypernuclei and their antiparticles in relativistic nuclear collisions. *Phys. Lett. B*, 697:203–207, 2011.

[36] Anton Andronic, Peter Braun-Munzinger, Krzysztof Redlich, and Johanna Stachel. Decoding the phase structure of QCD via particle production at high energy. *Nature*, 561(7723):321–330, 2018.

[37] Volodymyr Vovchenko, Kai Gallmeister, Jürgen Schaffner-Bielich, and Carsten Greiner. Nucleosynthesis in heavy-ion collisions at the LHC via the Saha equation. *Phys. Lett. B*, 800:135131, 2020.

[38] J. Cleymans, S. Kabana, I. Kraus, H. Oeschler, K. Redlich, and N. Sharma. Antimatter production in proton-proton and heavy-ion collisions at ultrarelativistic energies. *Phys. Rev. C*, 84:054916, 2011.

[39] A. Andronic, P. Braun-Munzinger, K. Redlich, and J. Stachel. The thermal model on the verge of the ultimate test: particle production in Pb-Pb collisions at the LHC. *J. Phys. G*, 38:124081, 2011.

[40] S. T. Butler and C. A. Pearson. Deuterons from High-Energy Proton Bombardment of Matter. *Phys. Rev.*, 129:836–842, 1963.

[41] Joseph I. Kapusta. Mechanisms for deuteron production in relativistic nuclear collisions. *Phys. Rev. C*, 21:1301–1310, 1980.

[42] Kai-Jia Sun and Lie-Wen Chen. Production of antimatter ^{5,6}Li nuclei in central Au+Au collisions at $\sqrt{s_{NN}} = 200$ GeV. *Phys. Lett. B*, 751:272–277, 2015.

[43] Lilin Zhu, Che Ming Ko, and Xuejiao Yin. Light (anti-)nuclei production and flow in relativistic heavy-ion collisions. *Phys. Rev. C*, 92(6):064911, 2015.

[44] Wenbin Zhao, Lilin Zhu, Hua Zheng, Che Ming Ko, and Huichao Song. Spectra and flow of light nuclei in relativistic heavy ion collisions at energies available at the BNL Relativistic Heavy Ion Collider and at the CERN Large Hadron Collider. *Phys. Rev. C*, 98(5):054905, 2018.

[45] Lilin Zhu, Hua Zheng, Che Ming Ko, and Yifeng Sun. Light nuclei production in Pb+Pb collisions at $\sqrt{s_{NN}}$ = 2.76 TeV. *Eur. Phys. J. A*, 54(10):175, 2018.

[46] Rui-Qin Wang, Feng-Lan Shao, and Jun Song. Momentum dependence of light nuclei production in $p-p$, $p-Pb$, and Pb-Pb collisions at energies available at the CERN Large Hadron Collider. *Phys. Rev. C*, 103(6):064908, 2021.

[47] Zi-Jian Dong, Gang Chen, Quan-Yu Wang, Zhi-Lei She, Yu-Liang Yan, Feng-Xian Liu, Dai-Mei Zhou, and Ben-Hao Sa. Energy dependence of light (anti)nuclei and (anti)hypertriton production in the Au-Au collision from $\sqrt{s_{NN}}$ = 11.5 to 5020 GeV. *Eur. Phys. J. A*, 54(9):144, 2018.

[48] Hui Liu, Dingwei Zhang, Shu He, Kai-jia Sun, Ning Yu, and Xiaofeng Luo. Light nuclei production in Au+Au collisions at sNN = 5–200 GeV from JAM model. *Phys. Lett. B*, 805:135452, 2020. [Erratum: Phys.Lett.B 829, 137132 (2022)].

[49] X. G. Deng and Y. G. Ma. Light nuclei production in Au + Au collisions at $\sqrt{s_{NN}}$ = 7.7-80 GeV from UrQMD model. *Phys. Lett. B*, 808:135668, 2020.

[50] Rudiger Scheibl and Ulrich W. Heinz. Coalescence and flow in ultrarelativistic heavy ion collisions. *Phys. Rev. C*, 59:1585–1602, 1999.

[51] Kai-Jia Sun, Rui Wang, Che Ming Ko, Yu-Gang Ma, and Chun Shen. Relativistic kinetic approach to light nuclei production in high-energy nuclear collisions. 6 2021.

[52] Dmytro Oliinychenko, Long-Gang Pang, Hannah Elfner, and Volker Koch. Microscopic study of deuteron production in PbPb collisions at $\sqrt{s} = 2.76TeV$ via hydrodynamics and a hadronic afterburner. *Phys. Rev. C*, 99(4):044907, 2019.

[53] Jan Staudenmaier, Dmytro Oliinychenko, Juan M. Torres-Rincon, and Hannah Elfner. Deuteron production in relativistic heavy ion collisions via stochastic multiparticle reactions. *Phys. Rev. C*, 104(3):034908, 2021.

[54] J. Steinheimer, K. Gudima, A. Botvina, I. Mishustin, M. Bleicher, and H. Stocker. Hypernuclei, dibaryon and antinuclei production in high energy heavy ion collisions: Thermal production versus Coalescence. *Phys. Lett. B*, 714:85–91, 2012.

[55] Ekkard Schnedermann, Josef Sollfrank, and Ulrich W. Heinz. Thermal phenomenology of hadrons from 200-A/GeV S+S collisions. *Phys. Rev. C*, 48:2462–2475, 1993.

[56] L. Adamczyk et al. Bulk Properties of the Medium Produced in Relativistic Heavy-Ion Collisions from the Beam Energy Scan Program. *Phys. Rev. C*, 96(4):044904, 2017.

[57] Betty Abelev et al. Centrality dependence of π, K, p production in Pb-Pb collisions at $\sqrt{s_{NN}}$ = 2.76 TeV. *Phys. Rev. C*, 88:044910, 2013.

[58] Vardan Khachatryan et al. Multiplicity and rapidity dependence of strange hadron production in pp, pPb, and PbPb collisions at the LHC. *Phys. Lett. B*, 768:103–129, 2017.

[59] Betty Bezverkhny Abelev et al. Multiplicity Dependence of Pion, Kaon, Proton and Lambda Production in p-Pb Collisions at $\sqrt{s_{NN}} = 5.02$ TeV. *Phys. Lett. B*, 728:25–38, 2014.

[60] Ekkard Schnedermann and Ulrich W. Heinz. A Hydrodynamical assessment of 200-A/GeV collisions. *Phys. Rev. C*, 50:1675–1683, 1994.

[61] O. Ristea, A. Jipa, C. Ristea, T. Esanu, M. Calin, A. Barzu, A. Scurtu, and I. Abu-Quoad. Study of the freeze-out process in heavy ion collisions at relativistic energies. *J. Phys. Conf. Ser.*, 420:012041, 2013.

[62] Jia Chen, Jian Deng, Zebo Tang, Zhangbu Xu, and Li Yi. Nonequilibrium kinetic freeze-out properties in relativistic heavy ion collisions from energies employed at the RHIC beam energy scan to those available at the LHC. *Phys. Rev. C*, 104(3):034901, 2021.

[63] Aleksas Mazeliauskas, Stefan Floerchinger, Eduardo Grossi, and Derek Teaney. Fast resonance decays in nuclear collisions. *Eur. Phys. J. C*, 79(3):284, 2019.

[64] Aleksas Mazeliauskas and Vytautas Vislavicius. Temperature and fluid velocity on the freeze-out surface from π, K, p spectra in pp, p-Pb and Pb-Pb collisions. *Phys. Rev. C*, 101(1):014910, 2020.

[65] Muhammad Abdulhamid et al. Beam Energy Dependence of Triton Production and Yield Ratio ($N_t \times N_p/N_d^2$) in Au+Au Collisions at RHIC. *Phys. Rev. Lett.*, 130:202301, 2023.

[66] F. James and M. Roos. Minuit: A System for Function Minimization and Analysis of the Parameter Errors and Correlations. *Comput. Phys. Commun.*, 10:343–367, 1975.

[67] Cern, root, version v.6.28/08, 2023. http://root.cern.ch.

[68] Smbat Grigoryan. A three component model for hadron p_T-spectra in pp and Pb–Pb collisions at the LHC. *Eur. Phys. J. A*, 57(12):328, 2021.

[69] Jaroslav Adam et al. Bulk properties of the system formed in $Au + Au$ collisions at $\sqrt{s_{NN}}$ =14.5 GeV at the BNL STAR detector. *Phys. Rev. C*, 101(2):024905, 2020.

[70] B. I. Abelev et al. Energy dependence of pi+-, p and anti-p transverse momentum spectra for Au+Au collisions at s(NN)**(1/2) = 62.4 and 200-GeV. *Phys. Lett. B*, 655:104–113, 2007.

[71] B. I. Abelev et al. Systematic Measurements of Identified Particle Spectra in pp, d^+ Au and Au+Au Collisions from STAR. *Phys. Rev. C*, 79:034909, 2009.

[72] A. Adare et al. Spectra and ratios of identified particles in Au+Au and d+Au collisions at $\sqrt{s_{NN}} = 200$ GeV. *Phys. Rev. C*, 88(2):024906, 2013.

[73] Shreyasi Acharya et al. Production of charged pions, kaons, and (anti-)protons in Pb-Pb and inelastic pp collisions at $\sqrt{s_{NN}} = 5.02$ TeV. *Phys. Rev. C*, 101(4):044907, 2020.

[74] Shreyasi Acharya et al. Light (anti)nuclei production in Pb-Pb collisions at sNN=5.02 TeV. *Phys. Rev. C*, 107(6):064904, 2023.

[75] Shreyasi Acharya et al. Measurement of (anti)alpha production in central Pb-Pb collisions at $\sqrt{s_{NN}} = 5.02$ TeV. 11 2023.

TABLE III. Extracted kinetic freeze-out parameters in Au+Au collisions at $\sqrt{s_{NN}}$ = 7.7 - 39 GeV from RHIC and Pb+Pb collisions at $\sqrt{s_{NN}}$ = 2.76 TeV with fixed $n = 1$ quoted with errors.

Collision	Centrality	$< \beta >$	T (MeV)	χ^2/ dof
Au-Au 7.7 GeV	$0 - 10\%$	0.416 ± 0.004	117 ± 2	2.40
	$10 - 20\%$	0.398 ± 0.004	119 ± 2	0.77
	$20 - 40\%$	0.373 ± 0.004	121 ± 2	1.30
	$40 - 80\%$	0.280 ± 0.013	131 ± 3	3.20
Au-Au 11.5 GeV	$0 - 10\%$	0.425 ± 0.003	119 ± 2	0.61
	$10 - 20\%$	0.396 ± 0.004	124 ± 2	3.10
	$20 - 40\%$	0.377 ± 0.004	127 ± 2	0.80
	$40 - 80\%$	0.435 ± 0.04	118 ± 2	2.11
Au-Au 14.5 GeV	$0 - 10\%$	0.418 ± 0.001	123 ± 2	0.44
	$10 - 20\%$	0.405 ± 0.004	127 ± 2	0.30
	$20 - 40\%$	0.378 ± 0.004	132 ± 2	0.33
	$40 - 80\%$	0.303 ± 0.006	138 ± 2	1.84
Au-Au 19.6 GeV	$0 - -10\%$	0.432 ± 0.004	125 ± 2	0.69
	$10 - 20\%$	0.413 ± 0.004	125 ± 2	0.34
	$20 - 40\%$	0.390 ± 0.004	128 ± 2	0.55
	$40 - 80\%$	0.317 ± 0.006	137 ± 2	0.60
Au-Au 27 GeV	$0 - 10\%$	0.448 ± 0.003	117 ± 3	0.64
	$10 - 20\%$	0.431 ± 0.003	122 ± 3	0.43
	$20 - 40\%$	0.404 ± 0.004	129 ± 3	0.31
	$40 - 80\%$	0.310 ± 0.007	146 ± 3	0.60
Au-Au 39 GeV	$0 - 10\%$	0.446 ± 0.003	121 ± 3	1.29
	$10 - 20\%$	0.434 ± 0.003	126 ± 3	0.45
	$20 - 40\%$	0.401 ± 0.004	135 ± 3	0.39
	$40 - 80\%$	0.319 ± 0.005	150 ± 3	0.72
Au-Au 62.4 GeV	$0 - 10\%$	0.464 ± 0.004	122 ± 3	1.43
	$10 - 20\%$	0.442 ± 0.004	130 ± 3	1.32
	$20 - 40\%$	0.412 ± 0.006	139 ± 4	1.01
	$40 - 80\%$	0.317 ± 0.010	150 ± 4	0.85
Au-Au 200 GeV	$0 - 10\%$	0.501 ± 0.003	114 ± 3	1.01
	$10 - 20\%$	0.488 ± 0.003	120 ± 3	0.86
	$20 - 40\%$	0.463 ± 0.003	130 ± 4	0.58
	$40 - 80\%$	0.390 ± 0.005	149 ± 4	1.90
Pb-Pb 2760 GeV	$0 - 20\%$	0.630 ± 0.004	123 ± 4	2.90
	$20 - 80\%$	0.585 ± 0.004	125 ± 5	1.66

TABLE IV. Extracted kinetic freeze-out parameters in Au+Au collisions at $\sqrt{s_{NN}}$ = 7.7 - 39 GeV from RHIC and Pb+Pb collisions at $\sqrt{s_{NN}}$ = 2.76 TeV with free n quoted with errors.

Collision	Centrality	$< \beta >$	T (MeV)	n	χ^2/ dof
Au-Au 7.7 GeV	$0-10\%$	0.438 ± 0.004	115 ± 2	0.786	2.10
	$10-20\%$	0.409 ± 0.005	118 ± 2	0.906	0.76
	$20-40\%$	0.374 ± 0.005	119 ± 2	1.07	0.78
	$40-80\%$	$---$	$---$	$---$	$---$
Au-Au 11.5 GeV	$0-10\%$	0.435 ± 0.004	118 ± 2	0.899	0.37
	$10-20\%$	0.418 ± 0.004	120 ± 2	0.927	0.35
	$20-40\%$	0.364 ± 0.004	129 ± 2	1.161	0.58
	$40-80\%$	0.240 ± 0.04	140 ± 2	2.270	1.30
Au-Au 14.5 GeV	$0-10\%$	0.431 ± 0.004	122 ± 2	0.891	0.39
	$10-20\%$	0.407 ± 0.005	127 ± 2	0.982	0.28
	$20-40\%$	0.377 ± 0.005	132 ± 2	1.010	0.40
	$40-80\%$	0.234 ± 0.005	143 ± 2	2.488	1.46
Au-Au 19.6 GeV	$0--10\%$	0.451 ± 0.005	119 ± 2	0.819	0.58
	$10-20\%$	0.415 ± 0.005	125 ± 2	0.979	0.35
	$20-40\%$	0.374 ± 0.005	129 ± 2	1.196	0.39
	$40-80\%$	0.268 ± 0.006	141 ± 3	1.905	0.35
Au-Au 27 GeV	$0-10\%$	0.465 ± 0.003	116 ± 3	0.857	0.54
	$10-20\%$	0.438 ± 0.003	122 ± 3	0.933	0.42
	$20-40\%$	0.393 ± 0.004	130 ± 3	1.120	0.27
	$40-80\%$	0.262 ± 0.007	149 ± 3	2.018	0.40
Au-Au 39 GeV	$0-10\%$	0.483 ± 0.004	119 ± 3	0.695	0.81
	$10-20\%$	0.451 ± 0.004	125 ± 3	0.850	0.35
	$20-40\%$	0.397 ± 0.005	136 ± 3	1.032	0.37
	$40-80\%$	0.289 ± 0.006	153 ± 3	0.449	0.55
Au-Au 62.4 GeV	$0-10\%$	0.497 ± 0.007	127 ± 4	0.671	0.86
	$10-20\%$	0.476 ± 0.007	133 ± 4	0.670	0.85
	$20-40\%$	0.433 ± 0.010	144 ± 4	0.711	0.80
	$40-80\%$	0.340 ± 0.018	157 ± 4	0.627	0.78
Au-Au 200 GeV	$0-10\%$	0.522 ± 0.003	116 ± 3	0.840	0.78
	$10-20\%$	0.504 ± 0.004	122 ± 3	0.867	0.61
	$20-40\%$	0.455 ± 0.004	129 ± 4	1.078	0.54
	$40-80\%$	0.345 ± 0.005	147 ± 4	1.619	1.33
Pb-Pb 2760 GeV	$0-20\%$	0.637 ± 0.004	115 ± 4	0.698	0.75
	$20-80\%$	0.588 ± 0.004	125 ± 5	0.863	1.15

Nuclear medium effects on the properties of $\Lambda(1405)$

J. Y. Süngü

Department of Physics, Kocaeli University, 41001, İzmit, Türkiye

N. Er

Department of Physics, Bolu Abant İzzet Baysal University, Gölköy Kampüsü, 14030, Bolu, Türkiye

E-mail: jyilmazkaya@kocaeli.edu.tr, nuray@ibu.edu.tr

Abstract. We study the $\Lambda(1405)$ resonance with $I(J^P) = 0(1/2^-)$ in the context of the pentaquark hypothesis in nuclear medium. For the investigation of the influence of the nuclear medium on the physical parameters of $\Lambda(1405)$, we propose a molecular-type structure involving K^-p and $\bar{K}^0n$ admixtures, correlated with the nuclear matter density. Our analysis reveals a substantial shift in both mass and residue, approximately 20% and 38%, respectively. These findings have significant implications for experimental researchers aimed at identifying in-medium characteristics of hyperon resonances.

1. Introduction

Exploring the nature of the $\Lambda(1405)$ resonance remains a persistent and complex topic of research initiated since its discovery in 1961 [1]. Three-quark models generally coincide well with experimental outcomes for numerous hadronic states. Nonetheless, the $\Lambda(1405)$ poses a challenge to the conventional framework. Because, even though it contains strange quark in its composition, it has lighter mass than its non-strange counterpart, $N(1535)$. Additionally, the observed mass difference from the $\Lambda(1520)$ state, assuming the spin-orbit partner of $\Lambda(1405)$, stands out as significantly larger compared to the nucleon sector. The mass distribution deviates from a Breit-Wigner pattern. While the Breit–Wigner widths of $\Lambda(1520)$ and $\Lambda(1405)$ are 16 and 50 MeV, the corresponding states $N(1520)$ and $N(1535)$ exhibit widths of 110 and 150 MeV, respectively. Furthermore, investigation into N_c scaling reveals that the existence of the three-quark configuration in the $\Lambda(1405)$ structure is unlikely. Remarkably, the electromagnetic size of $\Lambda(1405)$ is measured to be larger than that of typical three-quark hadrons. The difficulties of the three-quark picture led Dalitz and Tuan [2] to predict it as a quasi-bound state of $\bar{K}p$ encapsulated in the $\Sigma\pi$ continuum. Analysing the observed mass spectrum of $\pi^-\Sigma^+$, Hemingway reported a resonance mass of (1406.5 ± 4.0) MeV and a width of (50 ± 2) MeV for $\Lambda(1405)$. This assessment was conducted using $\bar{K}N$ scattering theory, as detailed in the studies by Dalitz and Tuan [3,4]. The Particle Data Group (PDG) [5] presents average mass and width values of $\Lambda(1405)$ resonance as:

$$\begin{aligned} M_\Lambda &= 1405.1^{+1.3}_{-0.9}\ \text{MeV}, \\ \Gamma_\Lambda &= 50.5 \pm 2.0\ \text{MeV}. \end{aligned} \tag{1}$$

Furthermore, an alternative framework proposing a double-pole structure for $\Lambda(1405)$ has emerged based on chiral $SU(3)$ dynamics. In this model, two poles for $\Lambda(1405)$ are suggested, positioned between 1420 and 1390 MeV/c^2, intricately linked with the $\bar{K}N$ and $\Sigma\pi$ channels, respectively [6–8]. The $\Lambda(1405)$ should be a mixture of these two states because all possible states with the same quantum number can combine via the strong force. To understand the inner structure of the $\Lambda(1405)$ resonance and gain insights into $\bar{K}N$ dynamics, it is essential to determine the dominant component, as discussed in [9]. Recently there have been some theoretical studies for $\Lambda(1405)$ assuming a molecule-like structure of $\bar{K}N$ [10–14]. It is probably the first exotic state to have a meson-baryon or pentaquark structure. The latest Particle Data Group review [5] cautiously acknowledges the potential presence of an additional resonance pole for $\Lambda(1380)$ with limited confidence. While recent studies suggest the $\Lambda(1405)$ particle might have two "poles" within its energy existence, and a narrow resonance seems evident just under the interaction threshold of kaons and nucleons, the properties and exact location of a potential second resonance remain unclear. The double-pole structure of $\Lambda(1405)$ makes this state particularly attractive, while we know now that such a structure is common to many other states in the hadron spectrum.

The interesting presence of the $\Lambda(1405)$ state below the $\bar{K}N$ threshold adds

a distinctive aspect to the $\bar{K}N$ interaction potential in the nuclear medium. Phenomenological potential models treat the $\Lambda(1405)$ as a $\bar{K}N$ bound state with a binding energy of 27 MeV [15, 16]. Lattice QCD calculations give more support for the molecule-like structure against to ordinary three-quark state [17, 18]. Ref. [19] used a chiral unitarity model, where the resonance is generated dynamically from $\bar{K}N$ interactions with other channels produced from the octets of baryons and mesons, shows that the line shape would rely on the decay mode. The assessments indicate variations in the line shape for different decay modes, and the measurements for charged decays deviate from the predictions. Moreover, in the work conducted by Ref. [20], a comprehensive analysis of the $\bar{K}N$ two-body scattering amplitude in the $I = 0$ channel near the $\bar{K}N$ mass threshold reveals the extraction of a resonance pole at $1417.7^{+6.0}_{-7.4}(fit)^{+1.1}_{1.0}(syst.)\mathrm{MeV/c^2}$. While a thorough analysis presented in Ref. [21] leans towards a single resonance, it does not conclusively dismiss the possibility of a two-pole scenario.

The strangeness sector of hadrons consists of some unusual resonances that indicate unexpected properties. Among them, only a few other states have such a long history as the mysterious $\Lambda(1405)$ [22]. Many experimental data on resonance $\Lambda(1405)$ have been announced [23–28]. This state manifests itself in the meson-baryon scattering amplitude with a spin-parity of $J^P = (\frac{1}{2})^-$, strangeness $S = -1$, and isospin $I = 0$. In 2011, the adoption of novel triggerable X-ray detectors developed within the SIDDHARTA project facilitated the most precise measurement of kaonic hydrogen K-series X-rays, leading to a significantly improved settling of the $\bar{K}p$ scattering length [23]. The spin-parity of the $\Lambda(1405)$ is determined with $J^P = 1/2^-$ using photoproduction data in the decay channel $\Lambda(1405) \to \Sigma^+ + \pi^-$ from the CLAS detector at Jefferson Lab [26]. The $\bar{K}N$ interaction's coupled-channel nature was verified through the exploration of $\bar{K}p$ correlations in proton-proton collisions at the LHC, as measured by ALICE [29]. Although the ALICE [27] and BGOOD data [28] confirm two-pole assumption, J-PARC [20] claim a single pole, closer to the $\bar{K}N$ mass threshold than the value given by the PDG. Recently, Anisovich et al. presented a single-pole representation for the $\Lambda(1405)$ contribution, fitting the data from Ref. [28] in γ and K^- induced reactions on protons and the kaonic hydrogen atom. They reported a pole position of (1422 ± 3) MeV/c^2 [30].

Research in the strangeness of nuclear physics traces back to the detection of the first hyperon, the Λ, in cosmic rays. The behavior of a Λ within a nuclear medium is primarily influenced by hadronic interactions among baryons and presents a complex many-body problem. This makes the Λ a valuable probe for understanding nuclear features that are not easily elucidated through other techniques. So, the Λ is a prominent baryon within the nucleus [31]. Describing the $\Lambda(1405)$ as a K^-p bound state, Koch et al. obtain that the mass of the $\Lambda(1405)$ is relocated upwards in energy above the K^-p threshold due to the Pauli blocking of intermediate states [32]. The $\Lambda(1405)$ resonance experiences very strong variations in the nuclear medium at densities nearly $(0.1-0.2)\rho_0$ dissolving chiefly through Pauli blocking of the intermediate proton states [33–35]. At

nuclear saturation density, it is predicted attractive mass shifts for the $\Lambda(1405)$ nearly 60 MeV [36].

Moreover, as indicated in Ref. [37], the $\Lambda(1405)$ emerges as the dominant exotic particle within stars, exhibiting prominence at different entropies for both neutrino-free and neutrino-trapped stellar matter. This observation stems from a relativistic model employed within a mean-field approximation. The microscopic composition of compact objects, such as Neutron Stars (NSs), remains an open problem. The NSs core is predominantly composed of strongly interacting protons and neutrons at low temperatures and high baryon density. However, as we delve deeper into the inner core, the natural processes during the formation of NSs may give rise to the production of pentaquarks. The existence of light pentaquarks in the heart of NSs has the potential to reduce the maximum mass. This exotic form of matter, known as strange matter, is thought to be abundant in the core of NSs, rendering them among the densest and most exotic objects in the universe. To acquire insights into hyperon-nucleon interactions within the nuclear medium and to figure out the inner structure of NSs, scientists are actively investigating the collective flow of hyper-nuclei in high-energy heavy-ion collisions [38]. The introduction of new particles, such as hyperons, during the star's evolution leads to a temperature drop below nucleon-only stellar matter. The Λ^0 baryons dominate the heavy baryon composition at all stages of stellar evolution, comprising over 18% of the overall matter content [37]. Noteworthy contributions to hyperon spectroscopy are anticipated from experiments like COMPASS, J-PARC, and the upcoming PANDA experiment [39].

In this context, this work aims to quantitatively investigate, how the nuclear medium modifies the physical properties of the $\Lambda(1405)$ resonance considering the in-medium dynamics of the $\Lambda(1405)$. This work operates under the assumption that the $\Lambda(1405)$ is a pentaquark state rather than a three-quark baryon state. This paper aims to achieve the following objectives: In the next section, we provide a brief overview of the Quantum Chromodynamics Sum Rules (QCDSRs) technique, which is utilized in our computations. Additionally, we discuss the alterations to the properties of $\Lambda(1405)$ induced by the nuclear medium. Section 3 presents a comprehensive analysis of our results, while Section 4 encapsulates the derived conclusions from these findings.

2. The Model

QCDSRs [40–42] stands out as one of the most potent and pragmatic tools utilized to extract the masses and decay constants of hadrons both in a vacuum, nuclear medium and hot medium [43–63]. The QCD vacuum is distinguished by a variety of condensates, including the gluon condensate $\langle G^2_{\mu\nu}\rangle$, the quark condensate $\langle q\bar{q}\rangle$, the mixed condensate $\langle \bar{q}\sigma Gq\rangle$, and additional ones. It is imperative to incorporate modified condensates when dealing with the nuclear medium.

This study is dedicated to formulating QCDSRs for the $\Lambda(1405)$ resonance within the framework of the nuclear medium. Our starting point is the covariant time-ordered

current-current correlator:

$$\Pi(q) = i \int d^4x e^{iq\cdot x} \langle \Omega_0 | \mathbf{T}[\mathbf{J}_\Lambda(x) \bar{\mathbf{J}}_\Lambda(0)] | \Omega_0 \rangle. \tag{2}$$

Here, q denotes the external four-momentum of the $\Lambda(1405)$ state in nuclear matter, $|\Omega_0\rangle$ represents the ground state in the nuclear medium, $\mathbf{T}$ is the time-ordered evolution operator, and $\mathbf{J}_\Lambda(x)$ signifies the hadronic current associated with the $\Lambda(1405)$. Considering the quantum characteristics of spin-1/2 light baryons, we prefer a pentaquark representation composed of $K^- p$ and $\bar{K}^0 n$ for the current associated with the $\Lambda(1405)$ state:

$$\mathbf{J}_\Lambda = \frac{1}{\sqrt{2}} (\mathbf{J}_{K^-} \mathbf{J}_p - \mathbf{J}_{\bar{K}^0} \mathbf{J}_n), \tag{3}$$

here

$$\mathbf{J}_{K^-} = \bar{u}_l \gamma_5 s_l; \qquad \mathbf{J}_p = \sum_{m=1}^{2} 2\epsilon^{ijk} (u_i^T C A_1^m d_j) A_2^m u_k, \tag{4}$$

$$\mathbf{J}_{\bar{K}^0} = \bar{d}_l \gamma_5 s_l; \qquad \mathbf{J}_n = \sum_{m=1}^{2} 2\epsilon^{ijk} (d_i^T C A_1^m u_j) A_2^m d_k, \tag{5}$$

where, i, j, k and l denote the color indices corresponding to the quark fields of u, d, and s quarks, respectively. C denotes the charge conjugation operator, while T symbolizes a transpose in Dirac space. The current is defined with respect to A_1^m and A_2^m as $A_1^1 = I$, $A_1^2 = A_2^1 = \gamma_5$, and $A_2^2 = \beta$. Here, β serves as an arbitrary mixing parameter.

The computation of the correlation function in Eq. (2) involves two distinct approaches: the phenomenological (or physical) side, which relies on hadronic characteristics, and the QCD (or theoretical) side, incorporating QCD parameters such as quark masses, in-medium quark, gluon, and quark-gluon mixed condensates. QCDSRs for different physical observables can be derived by equating coefficients of specific structures from both sides. The calculations begin in x-space and are subsequently transformed into momentum space. Applying the Borel transformation to both sides of the equation serves to suppress contributions from higher states and the continuum. In the final step of the computation, a continuum subtraction procedure is employed, accompanied by the assumption of quark-hadron duality.

• **Phenomenological approach**: In this perspective, the correlator encapsulates a comprehensive set of in-medium hadronic states, sharing quantum numbers with the corresponding interpolating current. Upon integration over four$-x$, the derived expression is as follows:

$$\Pi^{Phen.}(q) = -\frac{\langle \Omega_0 | \mathbf{J}_\Lambda(x) | \Lambda(q^*, s) \rangle \langle \Lambda(q^*, s) | \bar{\mathbf{J}}_\Lambda(0) | \Omega_0 \rangle}{q^{*2} - m^{*2}} + \cdots. \tag{6}$$

The notation $|\Lambda(q^*, s)\rangle$ denotes the pentaquark with in-medium four-momentum q^* and spin s. The symbol m^* shows the mass in the dense medium. The dots indicate

contributions from higher states and the continuum. To carry on, we present the subsequent matrix elements:

$$\begin{aligned}\langle\Omega_0|\mathbf{J}_\Lambda(x)|\Lambda(q^*,s)\rangle &= \lambda^* u(q,s),\\ \langle\Lambda(q^*,s)|\bar{\mathbf{J}}_\Lambda(0)|\Omega_0\rangle &= \bar{\lambda}^*\bar{u}(q,s).\end{aligned} \tag{7}$$

Here, λ^* denotes the in-medium residue of the $\Lambda(1405)$ resonance, while $u(q,s)$ represents the in-medium Dirac spinor. By substituting Eq. (7) into Eq. (6) and summing over spins, the resulting form of the correlation function's phenomenological side is as follows:

$$\begin{aligned}\Pi^{Phen.}(q) &= -\frac{\lambda^{*2}(\not{q}^* + m^*)}{q^{*2}-m^{*2}} + \cdots\\ &= -\frac{\lambda^{*2}}{\not{q}^* - m^*} + \cdots\\ &= -\frac{\lambda^{*2}}{(q_\mu - \Sigma_{v\mu})\gamma^\mu - m^*} + \cdots .\end{aligned} \tag{8}$$

The in-medium momentum, denoted as $q^*_\mu = q_\mu - \Sigma_{v\mu}$, and the in-medium mass, $m^*_\Lambda = m_\Lambda + \Sigma^S$, are defined, where $\Sigma_{v\mu}$ and Σ^S characterize the in-medium vector and scalar self-energy of the $\Lambda(1405)$ resonance, respectively. These physical quantities can be computed through QCDSRs in the nuclear medium. The contributions of the two independent vectors—particle four-momentum q_μ and medium four-velocity u_μ—to the vector self-energy are as follows:

$$\Sigma_{v\mu} = \Sigma_v u_\mu + \Sigma_v^{'} q_\mu. \tag{9}$$

In the given framework, u_μ signifies the four-velocity of the nuclear medium. It is noteworthy that the term $\Sigma_v^{'}$ is neglected owing to its negligible magnitude [62]. Our analysis is performed in the rest frame of the medium, characterized by $u_\mu = (1,0,0,0)$. The correlation function can be decomposed into individual structures, as depicted below:

$$\Pi^{Phen.}(q) = \Pi^{Phen.}_{\not{q}}(q^2,q_0)\not{q} + \Pi^{Phen.}_{\not{u}}(q^2,q_0)\not{u} + \Pi^{Phen.}_{U}(q^2,q_0)U + \cdots . \tag{10}$$

Here, U symbolizes the unit matrix, and q_0 represents the energy of the quasi-particle. The coefficients corresponding to different structures, namely the isoscalar invariant amplitudes $\Pi_i^{Phen.}(q^2,q_0)$, with $i = \not{q}$, $\not{u}$, and U in the aforementioned relation, are derived as:

$$\begin{aligned}\Pi^{Phen.}_{\not{q}}(q^2,q_0) &= -\lambda^{*2}\frac{1}{q^2-\mu^2},\\ \Pi^{Phen.}_{\not{u}}(q^2,q_0) &= +\lambda^{2}\frac{\Sigma_v}{q^2-\mu^2},\\ \Pi^{Phen.}_{U}(q^2,q_0) &= -\lambda^{*2}\frac{m^*}{q^2-\mu^2},\end{aligned} \tag{11}$$

where reduced mass can be written as $\mu = \sqrt{m^{*2} - \Sigma_v^2 + 2q_0\Sigma_v}$. Following the

application of the Borel transformation concerning q^2, the result is then given by:

$$\begin{aligned}
\mathcal{B}\Pi_{\not p}^{Phen.}(q^2,q_0) &= \lambda^{*2} e^{-\mu^2/M^2},\\
\mathcal{B}\Pi_{\not q}^{Phen.}(q^2,q_0) &= -\lambda^{*2}\Sigma_v e^{-\mu^2/M^2},\\
\mathcal{B}\Pi_{U}^{Phen.}(q^2,q_0) &= \lambda^{*2} m^* e^{-\mu^2/M^2},
\end{aligned} \tag{12}$$

here the parameter M^2 serves as the Borel mass, and its value will be determined in subsequent stages of the analysis.

• **QCD approach**: We inserted the interpolating currents in the correlator and utilized the Wick theorem to contract the quark fields. This process yields the following expression which is the same as the Ref. [13] in connection with the in-medium light quark propagator (D_q^{ij}):

$$\begin{aligned}
\Pi^{\rm QCD}(q) = 4i\epsilon_{abc}\epsilon_{a'b'c'}\int d^4x e^{iq\cdot x}\frac{1}{2}\Big\{ &{\rm Tr}[D_u^{d'd}(-x)\gamma_5 D_s{}^{dd'}(x)\gamma_5]\\
\times\Big\{ &-{\rm Tr}[D_d^{bb'}(x)\widetilde{D}_u^{aa'}(x)]\gamma_5 D_u^{cc'}(x)\gamma_5 + \gamma_5 D_u^{ca'}(x)\widetilde{D}_d^{bb'}(x)D_u^{ac'}(x)\gamma_5\\
&-\beta{\rm Tr}[D_d^{bb'}(x)\gamma_5\widetilde{D}_u^{aa'}(x)]\gamma_5 D_u^{cc'}(x) + \beta\gamma_5 D_u^{ca'}(x)\gamma_5\widetilde{D}_d^{bb'}(x)D_u^{ac'}(x)\\
&-\beta{\rm Tr}[D_d^{bb'}(x)\widetilde{D}_u^{aa'}(x)\gamma_5]D_u^{cc'}(x)\gamma_5 + \beta D_u^{ca'}(x)\widetilde{D}_d^{bb'}(x)\gamma_5 D_u^{ac'}(x)\gamma_5\\
&-\beta^2{\rm Tr}[D_d^{bb'}(x)\gamma_5\widetilde{D}_u^{aa'}(x)\gamma_5]D_u^{cc'}(x) + \beta^2 D_u^{ca'}(x)\gamma_5\widetilde{D}_d^{bb'}(x)\gamma_5 D_u^{ac'}(x)\Big\}\\
&+{\rm Tr}[D_d^{d'd}(-x)\gamma_5 D_s^{dd'}(x)\gamma_5]\Big\{ -{\rm Tr}[D_u^{bb'}(x)\widetilde{D}_d^{aa'}(x)]\gamma_5 D_d^{cc'}(x)\gamma_5\\
&+\gamma_5 D_d^{ca'}(x)\widetilde{D}_u^{bb'}(x)D_d^{ac'}(x)\gamma_5 - \beta{\rm Tr}[D_u^{bb'}(x)\gamma_5\widetilde{D}_d^{aa'}(x)]\gamma_5 D_d^{cc'}(x)\\
&+\beta\gamma_5 D_d^{ca'}(x)\gamma_5\widetilde{D}_u^{bb'}(x)D_d^{ac'}(x) - \beta{\rm Tr}[D_u^{bb'}(x)\widetilde{D}_d^{aa'}(x)\gamma_5]D_d^{cc'}(x)\gamma_5\\
&+\beta D_d^{ca'}(x)\widetilde{D}_u^{bb'}(x)\gamma_5 D_d^{ac'}(x)\gamma_5 - \beta^2{\rm Tr}[D_u^{bb'}(x)\gamma_5\widetilde{D}_d^{aa'}(x)\gamma_5]D_d^{cc'}(x)\\
&+\beta^2 D_d^{ca'}(x)\gamma_5\widetilde{D}_u^{bb'}(x)\gamma_5 D_d^{ac'}(x)\Big\}\Big\}.
\end{aligned} \tag{13}$$

Here, we use the shorthand $\widetilde{D}_q^{ij}(x) = CD_q^{Tij}(x)C$, where $D_q(x)$ stands for the propagators of u or d quarks, i and j denote color indices. We present detailed formulations for the quark propagators within the medium, encompassing crucial elements like in-medium quark, gluon, and mixed condensates. Throughout our calculations, the fixed-point gauge is utilized for the light quark propagator:

$$\begin{aligned}
D_q^{ij}(x) = &\frac{i}{2\pi^2}\delta^{ij}\frac{1}{(x^2)^2}\not{x} - \frac{m_q}{4\pi^2}\delta^{ij}\frac{1}{x^2} + \psi_q^i(x)\bar{\psi}_q^j(0)\\
&-\frac{ig_s}{32\pi^2}\mathcal{F}_{\mu\nu}^A(0)t^{ij,A}\frac{1}{x^2}[\not{x}\sigma^{\mu\nu} + \sigma^{\mu\nu}\not{x}] + \cdots .
\end{aligned} \tag{14}$$

In the given expression, ψ_q^i and $\bar{\psi}_q^j$ represent Grassmann background quark fields, $\mathcal{F}_{\mu\nu}^A$ signifies classical background gluon fields, and $t^{ij,A} = \frac{\lambda^{ij,A}}{2}$ where $\lambda^{ij,A}$ stands for the standard Gell-Mann matrices. By substituting the light quark propagator from Eq. (14) into the correlation function presented in Eq. (13), then incorporating Grassmann background quark fields and classical background gluon fields, we use terms representing

the ground-state matrix elements of related quark and gluon operators from Refs. [56,63]. We don't give the explicit forms of these expressions for the sake of brevity. On the QCD side, the invariant amplitudes $\Pi_i^{QCD}(q^{*2}, q_0)$ in relation to different structures in Eq. (10) is through the below dispersion integral:

$$\Pi_i^{QCD}(q^2, q_0) = \int_{(3m_u+m_d+m_s)^2}^{s_0^*} \frac{\rho^{QCD}(s, q_0)}{s - q^{*2}} ds. \tag{15}$$

In the above expression, $\rho^{QCD}(s, q_0)$ represents the two-point spectral densities derived from the imaginary parts of the correlation function and s_0^* is the in-medium continuum threshold.

The primary objective on the QCD side is to compute spectral densities using the explicit forms of the in-medium light quark propagator. The calculation involves standard procedures, and although explicit expressions of the spectral functions are not provided here due to their extensive nature, the methodology follows established techniques. As for the QCD side we can write the correlator in terms of separated structures as:

$$\Pi^{QCD}(q) = \boldsymbol{\xi}_{\not{q}}^{QCD}(q^2, q_0)\not{q} + \boldsymbol{\xi}_{\not{v}}^{QCD}(q^2, q_0)\not{v} + \boldsymbol{\xi}_{U}^{QCD}(q^2, q_0)U + \cdots . \tag{16}$$

After rigorous computational analysis, wherein we equate the phenomenological and QCD findings for each structural component, the resulting QCDSRs reveal the mass and residue of the $\Lambda(1405)$ state as follows:

$$\lambda^{*2} e^{-\mu^2/M^2} = \boldsymbol{\xi}_{\not{q}}^{QCD}(M^2, s_0^*), \tag{17}$$

$$-\lambda^{*2}\Sigma_v e^{-\mu^2/M^2} = \boldsymbol{\xi}_{\not{v}}^{QCD}(M^2, s_0^*), \tag{18}$$

$$\lambda^{*2} m^* e^{-\mu^2/M^2} = \boldsymbol{\xi}_{U}^{QCD}(M^2, s_0^*), \tag{19}$$

where $\xi_{\not{q},\not{v},U}^{QCD}(M^2, s_0^*)$ are the Borel-transformed invariant functions. The derivation of mass QCDSRs for the $\Lambda(1405)$ state takes various paths from the aforementioned equations. By applying a derivative with respect to $(-1/M^2)$ to both sides of Eq. (17) and eliminating λ^{*2} through division, a transformed equation emerges, offering insights into the following:

$$\mu_\Lambda^2 = \frac{d\xi_{\not{q}}^{QCD}(M^2, s_0^*)/d\Big(-\frac{1}{M^2}\Big)}{\xi_{\not{q}}^{QCD}(M^2, s_0^*)}. \tag{20}$$

Here, the in-medium mass of the Λ state is determined as:

$$m_\Lambda^{*2} = \mu_\Lambda^2 - 2\Sigma_v q_0 + \Sigma_v^2. \tag{21}$$

To determine the in-medium residue, denoted as λ^*, various possibilities can be used. Using Eq. (17), we can derive the following expression for the residue QCDSRs of the Λ state:

$$\lambda^{*2} = \xi_{\not{q}}^{QCD}(M^2, s_0^*) e^{\mu^2/M^2}. \tag{22}$$

We employ these extracted QCDSRs to compute the numerical values of both vacuum as the limit $\rho \to 0$ and for the in-medium physical quantities associated with the Λ resonance.

3. Numerical Results

Here, we undertake a numerical analysis of the obtained QCDSRs previously derived in Eqs. (20-22) to estimate mass and residue of the light spin-1/2 isoscalar $\Lambda(1405)$ state. To accomplish this, we rely on numerical values for various input parameters, including quark masses, as well as in-medium and vacuum condensates. These condensates include quark, gluon, and mixed condensates of different dimensions, and the specific values are detailed in Table (1). To determine the reliable range of the auxiliary parameter

Parameter	Numeric	Unit
m_u	$2.16^{+0.49}_{-0.26}$	MeV
m_d	$4.67^{+0.48}_{-0.17}$	MeV
m_s	$93.4^{+8.6}_{-3.4}$	MeV
m_Λ	$1405^{+1.3}_{-0.9}$	MeV
m_q	0.0034	GeV
σ_N	0.045	GeV
σ_{N_0}	0.035	GeV
m_0^2	0.8	GeV^2
ρ^{sat}	$(0.11)^3$	GeV^3
$\langle q^\dagger q\rangle_\rho$	$\frac{3}{2}\rho$	GeV^3
$\langle s^\dagger s\rangle_\rho$	0	GeV^3
$\langle \bar{q}q\rangle_0$	$(-0.241)^3$	GeV^3
$\langle \bar{s}s\rangle_0$	$0.8\langle \bar{q}q\rangle_0$	GeV^3
$\langle \bar{q}q\rangle_\rho$	$\langle \bar{q}q\rangle_0 + \frac{\sigma_N}{2m_q}\rho$	GeV^3
y	$1 - \frac{\sigma_{N_0}}{\sigma_N}$	–
$\langle \bar{s}s\rangle_\rho$	$\langle \bar{s}s\rangle_0 + y\frac{\sigma_N}{2m_q}\rho$	GeV^3
$\langle q^\dagger iD_0 q\rangle_\rho$	0.18ρ	GeV^4
$\langle s^\dagger iD_0 s\rangle_\rho$	$\frac{m_s\langle \bar{s}s\rangle_\rho}{4} + 0.02\ \text{GeV}\rho$	GeV^4
$\left\langle \frac{\alpha_s}{\pi}G^2\right\rangle_0$	$(0.33 \pm 0.04)^4$	GeV^4
$\left\langle \frac{\alpha_s}{\pi}G^2\right\rangle_\rho$	$\left\langle \frac{\alpha_s}{\pi}G^2\right\rangle_0 - 0.65\ \text{GeV}\rho$	GeV^4
$\langle \bar{q}g_s\sigma Gq\rangle_0$	$m_0^2\langle \bar{q}q\rangle_0$	GeV^5
$\langle \bar{q}g_s\sigma Gq\rangle_\rho$	$\langle \bar{q}g_s\sigma Gq\rangle_0 + 3\text{GeV}^2\rho$	GeV^5
$\langle \bar{s}g_s\sigma Gs\rangle_0$	$m_0^2\langle \bar{s}s\rangle_0$	GeV^5
$\langle \bar{s}g_s\sigma Gs\rangle_\rho$	$\langle \bar{s}g_s\sigma Gs\rangle_0 + 3y\rho$	GeV^5
$\langle q^\dagger iD_0 iD_0 q\rangle_\rho$	$0.031\ \text{GeV}^4\rho - \frac{1}{12}\langle \bar{q}g_s\sigma Gq\rangle_\rho$	GeV^5
$\langle s^\dagger iD_0 iD_0 s\rangle_\rho$	$0.031y\ \text{GeV}^2\rho - \frac{1}{12}\langle \bar{s}g_s\sigma Gs\rangle_\rho$	GeV^5

Table 1. Parameters employed as inputs in the calculations [5, 63–68].

β, we plot the QCD side of the result obtained from the $\not{q}$ structure for the $\Lambda(1405)$ state. As a parameter, we utilize $x = \cos\theta$, where $\theta = \arctan\beta$ and $\beta = -0.82$. Remarkably, the medium significantly expands the reliable ranges of β, marking a key

outcome of this study. The QCDSRs for the physical quantities outlined in Eq. (20-22) consist three auxiliary parameters: the Borel mass parameter M^2, the in-medium continuum threshold s_0^*, and the mixing parameter β that influences the symmetric and anti-symmetric spin-1/2 currents. We aim to identify their operational ranges in line with established methodological guidelines, ensuring that the physical quantities exhibit weak dependence on these parameters within these ranges.

For this purpose, we adhere to standard prescriptions of the method, demanding both pole dominance and the convergence of operator product expansion series. In technical terms, determining the upper limit of the Borel mass parameter involves ensuring that the pole contribution exceeds the contributions from higher states and the continuum. The lower boundary of M^2 is determined by requiring that the perturbative component surpasses the non-perturbative contributions and ensures convergence of the series containing non-perturbative operators. In this context, we set the Borel mass to guarantee that the pole contribution consistently constitutes a range between 80% and 50% of the total contribution. The choice of the continuum threshold is not arbitrary but is contingent on the energies of the first excited states in the relevant channels.

The considered resonance, when subjected to these criteria, meets all the necessary conditions. The mass and residue in the limit as $\rho \to 0$, denoted as $m_\Lambda, \lambda_\Lambda$ exhibits notable stability, as depicted in Fig. (1), and illustrates that the mass and residue variations concerning the continuum threshold are minimal within the selected window. The ranges of Borel mass parameter M^2 and the in-medium continuum threshold s_0^* satisfy all the procedural requirements as:

$$M^2 \in [1.5 - 2.0]\ \text{GeV}^2, \qquad s_0^* \in [2.3 - 2.9]\ \text{GeV}^2. \tag{23}$$

We also illustrate the ratio of the in-medium mass to the vacuum mass m_Λ^*/m_Λ and

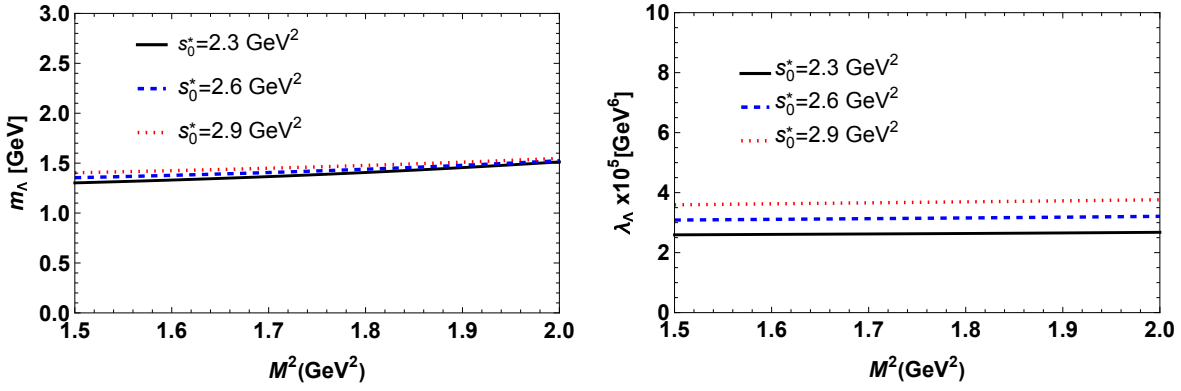


Figure 1. (**a**) Change of the $\Lambda(1405)$ vacuum mass in terms of M^2 Borel mass parameter. (**b**) The same graph for the residue.

$\lambda_\Lambda^*/\lambda_\Lambda$ in Fig. (2) below with respect to M^2 for the fully light Λ state at different values of the continuum threshold and the saturation nuclear matter density. The depicted figure demonstrates the strong stability of m_Λ^*/m_Λ across the chosen M^2 windows for all constituents. Notably, the $\Lambda(1405)$ experiences a considerable effect from the medium,

decreasing to approximately 80% and 62% of its vacuum value at saturation nuclear matter density for both the mass and residue, respectively. It is crucial to emphasize that the vacuum masses are extrapolated from in-medium calculations in the limit as ρ tends to zero.

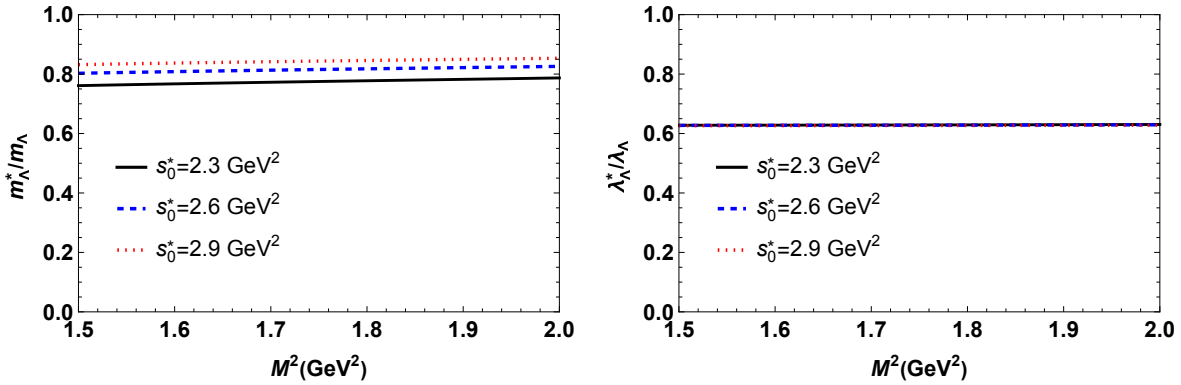


Figure 2. (**a**) The ratio of the in-medium mass to the vacuum mass for the $\Lambda(1405)$ as a function of M^2 Borel mass parameter at different values of the continuum threshold and saturation density. (**b**) The same plot for residue.

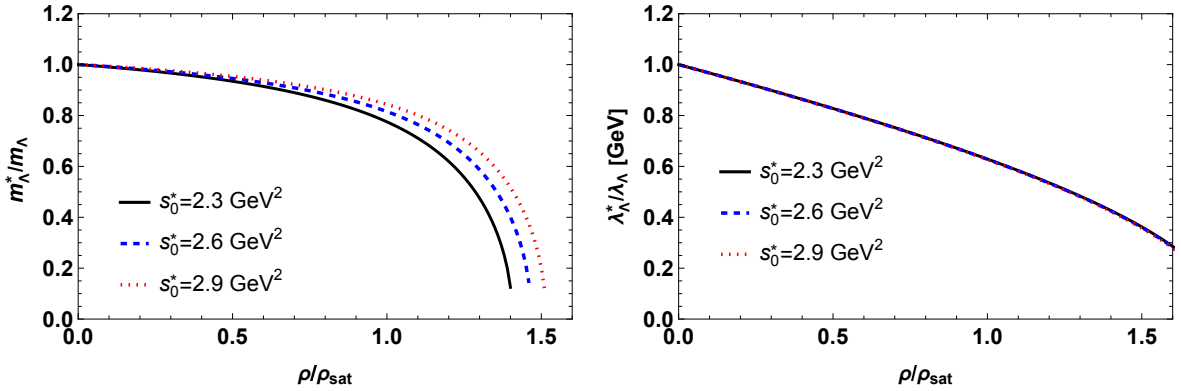


Figure 3. (**a**) The ratio of the in-medium mass to the vacuum mass for the $\Lambda(1405)$ as a function of ρ/ρ_{sat} at different values of the continuum threshold and the mean value of Borel mass parameter. (**b**) In-medium residue variation depicted in the accompanying graph.

The main objective of this study is to examine how the mass and residue of the states under consideration behaves with the density of the medium. In Fig. (3), we illustrate the ratio of nuclear medium mass to vacuum mass m^*_Λ/m_Λ and $\lambda^*_\Lambda/\lambda_\Lambda$versus ρ/ρ_{sat} for $\Lambda(1405)$ at different values of the continuum threshold, mean value of Borel mass parameter, and within the reliable regions of the mixing parameter β. Meanwhile we explore the mass and residue behavior within the range $\rho \in [0, 1.6]\rho_{sat}$ as it is seen in Fig. (3).

The pentaquark configuration of the $\Lambda(1405)$ resonance, containing one strange, three up, and one down quark, experiences a substantial mass reduction, reaching nearly

10% of its vacuum value at $\rho/\rho_{sat} = 1.5$. As illustrated in Fig. (3), at $\rho/\rho_{sat} = 1$, the in-medium mass to vacuum mass ratio stands at roughly 0.80 for this resonance. For the residue, these values correspond to $\sim 36\%$ and ~ 0.62.

The saturation nuclear matter density holds particular significance in our study. In Table (2), we present numerical values for the modified masses of the $\Lambda(1405)$ state at $\rho = \rho_{sat}$, alongside the vacuum masses of the fully light pentaquark candidate $\Lambda(1405)$ in the limit as $\rho \to 0$. The numerical results exhibit uncertainties attributed to errors in input parameters and uncertainties in determining the optimal working windows for auxiliary parameters.

Upon comparing vacuum mass with mass at the saturation point, it becomes evident that the $\Lambda(1405)$ state responds to its environment in a dense medium. In summary, we

State	$m(\rho = 0)$	$m^*(\rho = \rho_{sat})$
$\Lambda(1405)$	$1.408^{-0.126}_{+0.094}$	$1.141^{-0.122}_{+0.120}$

Table 2. The mass values of $\Lambda(1405)$ at vacuum and the mean modified mass at the saturation nuclear matter density in GeV.

State	$\lambda(\rho = 0)$	$\lambda^*(\rho = \rho_{sat})$
$\Lambda(1405)$	$3.152^{-0.559}_{+0.610} \times 10^{-5}$	$1.982^{-0.312}_{+0.364} \times 10^{-5}$

Table 3. The residue characteristic of $\Lambda(1405)$ under vacuum condition, alongside the mean modified residue at saturation nuclear matter density in unit of GeV^6.

compare the mass values of the fully light $\Lambda(1405)$ state with spin $-1/2$ using QCDSRs in the $\rho \to 0$ limit. Table (2) and (3) serve as the focal point for this comparison, encompassing theoretical predictions and existing experimental data within the $\Lambda(1405)$ channel. A careful examination of the table shows that results obtained through various methods [13, 17] are generally consistent, falling within mutually acceptable margins of error.

Our estimate for the mass of $\Lambda(1405)$, determined to be 1408^{-126}_{+94} MeV, harmoniously agrees with the PDG's mean value of $1405.1^{+1.3}_{-1.0}$ MeV. This congruence in predictions, not only for the $\Lambda(1405)$ but also for other related members, coupled with insights from various theoretical models, holds promise in illuminating future experiments. These experiments are poised to delve into the realm of fully light pentaquarks, offering the prospect of measuring their properties meticulously.

4. Conclusion

In recent years, there has been a profound exploration into the properties of hadrons, specifically mesons with strangeness, within dense matter. This investigation is closely

intertwined with the examination of exotic particles and the analysis of heavy-ion collisions. Particularly, the elusive nature of strange matter is believed to be abundant in the cores of neutron stars, marking them as among the densest and most exotic entities in the universe. While the notion of physically journeying to neutron stars for the study of this exotic matter remains firmly in the realm of science fiction, valuable insights into these celestial bodies can be gleaned through particle collisions conducted in heavy-ion collisions. This line of inquiry holds the potential not only to constrain existing theories but also to offer variable inputs for calculations, providing valuable information about the phase transition, structure, and composition of compact stars. The pursuit of understanding less-known resonances and confirming their existence plays a crucial role in establishing the multiple structures of hadrons.

Addressing the nature of $\Lambda(1405)$ within conventional three-quark models poses challenges. Our investigation focuses on the mass and residue of $\Lambda(1405)$ with the assumption of a pentaquark state in a cold nuclear medium. Employing in-medium QCDSRs up to dimension six, our study specifically explores the properties of $\Lambda(1405)$ considering it as a molecule and nucleon in a dense medium. The nuclear medium effect emerges as a significant factor, substantially influencing the in-medium characteristics of $\Lambda(1405)$, notably its mass and residue. According to our results we find the mass $1.141^{-0.122}_{+0.120}$ GeV and residue $1.982^{-0.312}_{+0.364} \times 10^{-5}$ GeV^6 at saturation density and $1.408^{-0.126}_{+0.094}$ GeV, $3.152^{-0.559}_{+0.610} \times 10^{-5}$ GeV^6 at vacuum. In the presence of nuclear matter, there is an approximately 20% change in the mass value of $\Lambda(1405)$, along with a 38% alteration in the residue value. Our results, in the limit as $\rho_{\rm sat} \to 0$, are consistent with experimental data [5] and support the meson-baryon molecular structure proposed for $\Lambda(1405)$ in Ref. [13]. The combined findings from experiments, lattice QCD simulations, and theoretical studies on the $\Lambda(1405)$ resonance are set to transform our understanding of hadron and nuclear physics.

5. Acknowledgement

We are grateful to K. Azizi for his valuable discussions.

References

[1] M. H. Alston and et al., Phys. Rev. Lett. **6**, 698-702 (1961)
[2] R. H. Dalitz and S. F. Tuan, Phys.Rev. Lett. **2**, 425-428 (1959)
[3] R. J. Hemingway, Nucl. Phys. B **253**, 742-752 (1985)
[4] R. H. Dalitz and A. Deloff, J. Phys. G **17**, 289-302 (1991)
[5] R. L. Workman *et al.* [Particle Data Group], PTEP **2022**, 083C01 (2022) and 2023 update
[6] V. K. Magas, E. Oset and A. Ramos, Phys. Rev. Lett. **95**, 052301 (2005)
[7] M. Hassanvand, S. Z. Kalantari, Y. Akaishi and T. Yamazaki, Phys. Rev. C **87**, no.5, 055202 (2013)
[8] D. Jido, J. A. Oller, E. Oset, A. Ramos and U. G. Meissner, Nucl. Phys. A **725**, 181-200 (2003)
[9] T. Hyodo and D. Jido, Prog. Part. Nucl. Phys. **67**, 55-98 (2012)
[10] A. Zhang, Y. R. Liu, P. Z. Huang, W. Z. Deng, X. L. Chen and S. L. Zhu, HEPNP **29**, 250 (2005)

[11] R. Molina and M. Döring, Phys. Rev. D **94**, no.5, 056010 (2016)
[12] L. Roca, J. Nieves and E. Oset, Phys. Rev. D **92**, no.9, 094003 (2015)
[13] K. Azizi, Y. Sarac and H. Sundu, [arXiv:2306.07393 [hep-ph]]
[14] F. K. Guo, C. Hanhart, U. G. Meißner, Q. Wang, Q. Zhao and B. S. Zou, Rev. Mod. Phys. **90**, no.1, 015004 (2018) [erratum: Rev. Mod. Phys. **94**, no.2, 029901 (2022)]
[15] U. G. Meißner, Symmetry **12**, no.6, 981 (2020)
[16] R. Del Grande, M. Bazzi, A. M. Bragadireanu, D. Bosnar, M. Cargnelli, A. Clozza, C. Curceanu, L. De Paolis, L. Fabbietti and F. Ghio, *et al.* J. Phys. Conf. Ser. **1643**, no.1, 012081 (2020)
[17] J. M. M. Hall, W. Kamleh, D. B. Leinweber, B. J. Menadue, B. J. Owen, A. W. Thomas and R. D. Young, Phys. Rev. Lett. **114**, no.13, 132002 (2015)
[18] J. Bulava *et al.* [Baryon Scattering (BaSc)], [arXiv:2307.10413 [hep-lat]].
[19] J. C. Nacher, E. Oset, H. Toki and A. Ramos, Phys. Lett. B **455**, 55-61 (1999)
[20] S. Aikawa *et al.* [J-PARC E31], Phys. Lett. B **837**, 137637 (2023)
[21] A. V. Anisovich, A. V. Sarantsev, V. A. Nikonov, V. Burkert, R. A. Schumacher, U. Thoma and E. Klempt, Eur. Phys. J. A **56**, no.5, 139 (2020)
[22] T. Hyodo and M. Niiyama, Prog. Part. Nucl. Phys. **120**, 103868 (2021)
[23] M. Bazzi *et al.* [SIDDHARTA], Phys. Lett. B **704**, 113-117 (2011)
[24] G. Agakishiev *et al.* [HADES], Phys.Rev. C **87**, 025201 (2013)
[25] H. Y. Lu *et al.* [CLAS], Phys.Rev. C **88**, 045202 (2013)
[26] K. Moriya *et al.* [CLAS], Phys. Rev. Lett. **112**, no.8, 082004 (2014)
[27] S. Acharya *et al.* [ALICE], Eur. Phys. J. C **83**, no.4, 340 (2023)
[28] G. Scheluchin *et al.* [BGOOD], Phys. Lett. B **833**, 137375 (2022)
[29] S. Acharya et al. [ALICE], Phys. Rev. Lett. **124**, 9, 092301 (2020)
[30] A. V. Anisovich *et al.* [arXiv:1905.05456 [nucl-ex]].
[31] A. Gal, E. V. Hungerford and D. J. Millener, Rev. Mod. Phys. **88**, no.3, 035004 (2016)
[32] V. Koch, Phys. Lett. B **337**, 7-13 (1994)
[33] T. Waas, N. Kaiser and W. Weise, Phys. Lett. B **379**, 34-38 (1996)
[34] T. Waas, N. Kaiser and W. Weise, Phys. Lett. B **365**, 12-16 (1996)
[35] V. Metag, M. Nanova and E. Y. Paryev, Prog. Part. Nucl. Phys. **97**, 199-260 (2017)
[36] M. F. M. Lutz and C. L. Korpa, Nucl. Phys. A **700**, 309-329 (2002)
[37] A. Issifu, K. D. Marquez, M. R. Pelicer and D. P. Menezes, Mon. Not. Roy. Astron. Soc. **522**, no.3, 3263-3270 (2023)
[38] L. Tolos and L. Fabbietti, Prog. Part. Nucl. Phys. **112**, 103770 (2020)
[39] S. N. Nakamura, EPJ Web Conf. **271**, 11003 (2022)
[40] M. A. Shifman, A. I. Vainshtein and V. I. Zakharov, Nucl. Phys. B **147** (1979), 385-447.
[41] M. A. Shifman, A. I. Vainshtein and V. I. Zakharov, Nucl. Phys. B **147** (1979), 448-518.
[42] B. L. Ioffe, Nucl. Phys. B **188** (1981), 317-341 [erratum: Nucl. Phys. B **191** (1981), 591-592].
[43] T. M. Aliev, K. Azizi and M. Savci, Phys. Rev. D **81**, 056006 (2010)
[44] T. M. Aliev, K. Azizi and A. Ozpineci, Phys. Rev. D **79**, 056005 (2009)
[45] T. M. Aliev, K. Azizi and M. Savci, Nucl. Phys. A **895**, 59-70 (2012)
[46] S. S. Agaev, K. Azizi and H. Sundu, Phys. Rev. D **93**, no.7, 074002 (2016)
[47] K. Azizi, Y. Sarac and H. Sundu, Phys. Rev. D **95**, no.9, 094016 (2017)
[48] N. Er and K. Azizi, Eur. Phys. J. C **82**, no.5, 397 (2022)
[49] K. Azizi and N. Er, Eur. Phys. J. C **81**, no.1, 61 (2021)
[50] K. Azizi and N. Er, Phys. Lett. B **811**, 135979 (2020)
[51] K. Azizi and N. Er, Phys. Rev. D **101**, no.7, 074037 (2020)
[52] K. Azizi and N. Er, Phys. Rev. D **100**, no.7, 074004 (2019)
[53] K. Azizi and N. Er, Nucl. Phys. B **936**, 151-168 (2018)
[54] K. Azizi, N. Er and H. Sundu, Phys. Rev. D **94**, no.11, 114002 (2016)
[55] K. Azizi, N. Er and H. Sundu, Phys. Rev. D **92**, no.5, 054026 (2015)
[56] K. Azizi and N. Er, Eur. Phys. J. C **74**, 2904 (2014)

[57] E. Güngör, H. Sundu, J. Y. Süngü and E. V. Veliev, Few Body Syst. **64**, no.3, 53 (2023)
[58] A. Türkan, J. Y. Süngü, E. Güngör, H. Reisoğlu and E. V. Veliev, Int. J. Theor. Phys. **61**, no.9, 238 (2022)
[59] A. Türkan, J. Y. Süngü and E. V. Veliev, Acta Phys. Polon. B **53**, no.1, 1 (2022)
[60] J. Y. Süngü, A. Türkan, H. Sundu and E. V. Veliev, Eur. Phys. J. C **82**, no.5, 453 (2022)
[61] J. Y. Süngü, A. Türkan, E. Sertbakan and E. V. Veliev, Eur. Phys. J. C **80**, no.10, 943 (2020)
[62] T. D. Cohen, R. J. Furnstahl and D. K. Griegel, Phys. Rev. C **45**, 1881-1893 (1992)
[63] T. D. Cohen, R. J. Furnstahl, D. K. Griegel and X. M. Jin, Prog. Part. Nucl. Phys. **35**, 221-298 (1995)
[64] V. M. Belyaev and B. L. Ioffe, Sov. Phys. JETP **57** (1983), 716-721 ITEP-132-1982.
[65] B. L. Ioffe, Prog. Part. Nucl. Phys. **56**, 232-277 (2006)
[66] A. W. Thomas, P. E. Shanahan and R. D. Young, Nuovo Cim. C **035N04**, 3-10 (2012)
[67] S. Dinter, V. Drach and K. Jansen, Int. J. Mod. Phys. E **20**, 110-117 (2011)
[68] J. M. Alarcon, J. Martin Camalich and J. A. Oller, Phys. Rev. D **85**, 051503 (2012)

Impact of (magneto-)thermoelectric effect on diffusion of conserved charges in hot and dense hadronic matter

He-Xia Zhang,[1,2,*] Ke-Ming Shen,[3,†] Yu-Xin Xiao,[4] and Ben-Wei Zhang[4,‡]

[1] *Guangdong Provincial Key Laboratory of Nuclear Science, Institute of Quantum Matter, South China Normal University, Guangzhou 510006, China*
[2] *Guangdong-Hong Kong Joint Laboratory of Quantum Matter, Southern Nuclear Science Computing Center, South China Normal University, Guangzhou 510006, China*
[3] *School of Science, East China University of Technology, Nanchang 330013, China*
[4] *Key Laboratory of Quark & Lepton Physics (MOE) and Institute of Particle Physics, Central China Normal University, Wuhan 430079, China*

We investigate the thermoelectric effect, which describes the 5generation of an electric field induced by temperature and conserved charge chemical potential gradients, in the hot and dense hadronic matter created in heavy-ion collisions. Utilizing the Boltzmann kinetic theory within the repulsive mean-field hadron resonance gas model, we evaluate both the diffusion thermopower matrix and diffusion coefficient matrix for the baryon number (B), electric charge (Q), and strangeness (S).The Landau-Lifshitz frame is enforced in the derivation. We find that the thermoelectric effect hinders the diffusion processes of multiple conserved charges, particularly reducing the coupling between electric charge and baryon number (strangeness) in baryon (strangeness) diffusion. Based on the fact that the repulsive mean-field interactions between hadrons have a significant effect on the diffusion thermopower matrix and diffusion coefficient matrix in the baryon-rich region, we extend the investigation to include the impact of the magnetic field, analyzing the magneto-thermoelectric effect on both the diffusion coefficient matrix and the Hall-like diffusion coefficient matrix. The sensitivity of the magnetic field-dependent diffusion thermopower matrix and magneto-thermoelectric modified diffusion coefficient matrix to the choices of various transverse conditions is also studied.

arXiv:2403.02705v1 [nucl-th] 5 Mar 2024

I. INTRODUCTION

Relativistic heavy-ion collision experiments open up a unique portal for understanding the properties of strongly interacting matter under extreme temperatures. A lot of experimental evidence in the relativistic heavy-ion collider (RHIC) [1–4] at Brookhaven National Laboratory (BNL) and in the large hadron collider (LHC) [5–10] at the European Organization for Nuclear Research (CERN) have indicated that a new deconfined state of matter – quark-gluon plasma (QGP) can be created. On the other hand, quantum chromodynamics (QCD) is the fundamental theory of the strong interaction and the lattice QCD calculation has predicted a smooth crossover for QCD matter from a hadronic phase to a QGP phase can be realized with increasing temperature (T) at the small or vanishing baryon chemical potential (μ_B) [11–13]. At large μ_B, the calculations in the low energy QCD effective models, viz., the (Polyakov-loop-) Nambu-Jona-Lasinio model [14–16], the (Polyakov-loop-) quark-meson model [17–20] have indicated that the QCD phase transition becomes a first-order phase transition and terminates at the critical endpoint (CEP) of second-order, which has sparked long-sought debate without conclusive experimental evidence yet [21]. Besides, the Beam Energy Scan (BES) program at RHIC [22, 23] and ongoing experimental programs at Facility for Antiproton and Ion Research (FAIR) [24, 25] and Nuclotron-based Ion Collider fAcility (NICA) [26, 27] also endeavor to shed light on the properties of dense nuclear matter and search the potential signature of the CEP in the QCD phase diagram.

Besides the equilibrium QCD thermodynamic properties, the medium response to perturbation around equilibrium, characterized by transport coefficients, plays an important role in describing the dynamics of bulk matter created in relativistic heavy-ion collisions. The ratio of shear viscosity to entropy density (η/s) has been shown to give a good description of flow data [28–30]. The bulk viscosity to entropy density (ζ/s) exhibits a novel behavior at some characteristic temperatures [31, 32]. During recent research [33, 34], electric conductivity has also been used as an input in magneto-hydrodynamic simulations of heavy-ion collisions. On the other hand, the diffusion coefficient, which describes the medium response to inhomogeneities in the number density and almost is ignored at top RHIC and LHC energies, becomes significant in low-energy heavy-ion collisions. Typically the diffusion coefficient matrix, measuring the coupling among diffusion currents of different conserved charges of the system, is required to give a proper dynamical description of low-energy heavy-ion collisions. This results from the fact that QCD matter constituents (hadrons and quarks) carry multiple quantum conserved numbers, e.g., baryon number (B), electric charge (Q), strangeness (S), etc. The complete diffusion coefficient matrix in both the QGP and hadron gas has been calculated within the Boltzmann kinetic theory [35–37] and the results reveal that the off-diagonal matrix elements in magnitude share

* hxzhang@m.scnu.edu.cn
† shen_keming@ecut.edu.cn
‡ bwzhang@mail.ccnu.edu.cn

the same order with diagonal ones and cannot be neglected in the hydrodynamic simulation of low-energy nuclear collisions. Recently, A. Das *et. al.* have explicitly imposed the Landau-Lifshitz frame into the previous derivation in [35, 36] and provide a unique expression in the hadron resonance gas model with and without excluded volume corrections [38]. In this work, we explore the effect of repulsive interactions on the diffusion properties of hadronic matter in the repulsive mean-field hadron resonance gas (RMFHRG) model, where the repulsive interactions between hadrons are considered through a density-dependent mean-field potential, and subsequently modify the diffusion coefficient.

The thermoelectric effect, a phenomenon involving the direct conversion of temperature differences to electric voltage and vice versa, has been extensively explored across various disciplines such as material science, solid-state physics, and chemistry. A well-known thermoelectric effect is the Seebeck effect, which refers to the generation of electric voltage caused by a temperature gradient in a semiconductor or conductor. Heavy-ion collisions allow us to study the Seebeck effect of QCD matter due to the temperature difference between the central region and peripheral region of the fireball. The Seebeck coefficient, defined as the ratio of the induced electric field and the collinear temperature gradient ($S = \boldsymbol{E}/\boldsymbol{\nabla} T$) in the absence of electric current, has been estimated in both the partonic and hadron phase of QCD matter [39–47]. Differing from the condensed matter studies, the non-vanishing net conserved number is required for the estimation of the Seebeck coefficient in QCD matter. To our best knowledge, all estimations are performed when only net baryon density is nonzero, without taking into account the contribution of other conserved charges to the thermoelectric effect. Actually, the gradients of multiple conserved charge chemical thermal potentials $\boldsymbol{\nabla}(\mu_q/T)$ with $q \in \{Q, B, S\}$ also is a source to generate an internal electric field, which is quantified by diffusion thermopower matrix $M^{qQ} = \boldsymbol{E}/(T\boldsymbol{\nabla}(\mu_q/T))$ in the limit of zero electric current. Such thermoelectric effect involving multiple conserved charges might further affect the recently proposed thermally spin Hall effect (TSHE) in the heavy-ion collisions at BES energies [48, 49]. As the thermoelectric effect is highly related to the gradient of conserved charge chemical potential, and it can affect the diffusion coefficient matrix in principle, to the best of our knowledge, there are no associated studies yet, which is the main motivation for our research.

Considering that a partial magnetic field created in the off-central heavy-ion collisions can survive to the hadronic phase due to the electric conductivity of medium [50–52], the motions of charged hadron driven by $\boldsymbol{\nabla}(T(\mu_q/T))$ can be deflected. This results in the generation of a transverse or Hall-like electric field, viz, $\boldsymbol{E} \sim \boldsymbol{\nabla}(T(\mu_q/T))\times\boldsymbol{H}$ in the magnetic field, known as the magneto-thermoelectric effect, which is measure by Hall-like diffusion thermopower. Similarly, the extra Hall-type diffusion currents of conserved charges also appear in the magnetic field and are quantified by the Hall-like diffusion coefficient matrix. The magneto-thermoelectric effect can affect both the diffusion coefficient matrix and the Hall-like diffusion coefficient matrix. Importantly, the expression of the magneto-thermoelectric modified diffusion coefficient matrix depends on the choices of transverse conditions: (1) all transverse gradients in temperature and chemical potential of conserved charge vanishes; (2) other transverse specific conserved charge diffusion current disappears apart from vanishing transverse electric current.

This paper is organized as follows. In Sec. II, we give a brief overview of the ideal hadron resonance gas (IHRG) model and repulsive mean-field hadron resonance gas (RMFHRG) model. The general expression for the diffusion thermopower and diffusion coefficient of conserved charges will be derived in Sec. III by solving the Boltzmann equation under relaxation time approximation in the framework of the RMFHRG model with and without magnetic field. We for the first time present the formulas of magneto-thermoelectric modified diffusion coefficient matrix under different transverse conditions. Sec. IV will discuss the influences of RMF correction, baryon chemical potential, magnetic field, and (magneto-)thermoelectric effect on the (Hall-like-) diffusion coefficient matrix. Finally comes our summary of this work in Sec. V.

Throughout this paper we adopt natural units $c = \hbar = k_B = 1$, and work in flat Minkowski space-time with metric tensor $g^{\mu\nu} = \mathrm{diag}(1, -1, -1, -1)$ thus the fluid velocity satisfies $u^\mu u_\mu = 1$. $\Delta^{\mu\nu} = g^{\mu\nu} - u^\mu u^\nu$ is the projection operator onto the three-dimensional subspace orthogonal to u^μ, $\Delta^\mu u_\nu = u_\mu \Delta^{\mu\nu} = 0$. The projection of any four-vector A^μ onto the three-dimensional subspace orthogonal to u^μ as $A^{\langle\mu\rangle} \equiv \Delta^\mu_\nu A^\nu$. The four-derivative can be decomposed as $\partial_\mu \equiv \partial/\partial^\mu \equiv \nabla_\mu + u_\mu D$, $D = u^\mu \partial_\mu$ and $\nabla_\nu = \Delta^\alpha_\nu \partial_\alpha$ denote the time derivative and spatial gradient operator in the local rest frame, respectively. In the local rest frame $\nabla^\mu \equiv (0, -\boldsymbol{\nabla})$, $u^\mu = (1, \boldsymbol{0})$.

II. MODEL DESCRIPTION

Hadron resonance gas (HRG) model [53, 54] is a simplistic thermal statistical model that successfully describes the low-temperature hadronic phase of QCD at chemical freeze-out. In the IHRG model, the attractive interactions between hadrons are implicitly considered by including all the resonances with zero width, while the repulsive interactions among hadrons, which are already known from nucleon-nucleon scattering experiments, are missing in the IHRG model. Accordingly, the extended versions of the IHRG model e.g., excluded volume HRG model [55–57], van der Waals HRG model [58, 59] and repulsive mean-field HRG model [60–63], are proposed to give a better fitting to various thermodynamic observables obtained from lattice QCD. In this work, the repulsive interactions between the hadrons are incorpo-

rated via a mean-field approach, and this extended version of the IHRG model is the so-called repulsive mean-field hadron resonance gas (RMFHRG) model.

A. Ideal hadron resonance gas (IHRG) model

In the IHRG model, the partition function containing all relevant degrees of freedom of the confined QCD phase is the starting point for obtaining the thermodynamics. The logarithm of the total partition function in the grand canonical ensemble is given as

$$\ln Z^{id} = \sum_a \ln Z_a^{id}(T, \mu_a, m_a), \tag{1}$$

where the partition function of hadron species a is

$$\ln Z_a^{id} = \pm VT \sum_a \int d\Gamma_a \ln[1 \pm e^{-\beta(\epsilon_a^0 - \mu_a)}]. \tag{2}$$

Here, the superscript id presents to the ideal gas and V is the system volume, we use the notation $d\Gamma_a = d_a d^3p_a/(2\pi)^3$, d_a is the spin degeneracy of hadron species a. $\beta = 1/T$ is the inverse temperature of the system. The front upper (lower) sign corresponds to fermions (bosons). $\epsilon_a^0 = \sqrt{\boldsymbol{p}_a^2 + m_a^2}$ is the single particle energy with mass m_a. $\mu_a(\{\mu_q\}) = B_a\mu_B + Q_a\mu_Q + S_a\mu_S$ is the chemical potential of species a, where $\{\mu_q\} \equiv \{\mu_B, \mu_Q, \mu_S\}$, with μ_B, μ_Q, μ_S being baryon, electric and strangeness chemical potential, respectively, B_a, Q_a and S_a are the baryon number, electric charge, and strangeness of the respective particle species a. Accordingly, the ideal thermodynamics such as total pressure (P^{id}), total energy density ($\mathcal{E}^{id}$), and total number density (ρ^{id}) in the IHRG model can be obtained as:

$$P^{id} = \sum_a P_a^{id} = \frac{\partial \ln Z^{id}}{\beta \partial V} = \sum_a \int d\Gamma_a \frac{\boldsymbol{p}_a^2}{3\epsilon_a^0} f_a^{id}, \tag{3}$$

$$\mathcal{E}^{id} = \sum_a \mathcal{E}_a^{id} = -\frac{1}{V}\frac{\partial \ln Z^{id}}{\partial \beta} = \sum_a \int d\Gamma_a \epsilon_a^0 f_a^{id}, \tag{4}$$

$$\rho^{id} = \sum_a \rho_a^{id} = \frac{T}{V}\frac{\partial \ln Z^{id}}{\partial \mu_a} = \sum_a \int d\Gamma_a f_a^{id}. \tag{5}$$

Here, f_a^{id} is the thermal equilibrium distribution function of particle species a in the IHRG model, which is given as

$$f_a^{id}(T, \mu_a) = [\exp[(\epsilon_a^0 - \mu_a)/\beta] \pm 1]^{-1}, \tag{6}$$

where the $\pm$ refers to the Fermi-Dirac and Bose-Einstein distribution functions, respectively.

B. Repulsive mean-field hadron resonance gas (RMFHRG) model

The RMFHRG model is a minimal extension of the IHRG model by including short-range repulsive interactions between hadrons via a mean-field approach, where the single-particle energy gets modified as [64]

$$\widetilde{\epsilon}_a = \epsilon_a^0 + U_a, \tag{7}$$

where U_a is the potential describing the repulsive interactions between hadrons and also behaves as the effective chemical potential. In this model, only the repulsive interactions among meson-meson pairs, baryon-baryon pairs, and antibaryon-antibaryon pairs are accounted [62]. Then the mean-field potentials for (anti-)baryons and mesons are given as [62, 64]

$$U_{a\in\{B,\bar{B}\}}(\rho_{B,\bar{B}}) = K_B\rho_{B,\bar{B}}, \; U_{a\in\{M\}}(\rho_M) = K_M\rho_M, \tag{8}$$

where the subscripts B, $\bar{B}$, M denote baryons, antibaryons, and mesons, respectively, $\rho_{B,\bar{B},M}$ are the associated total baryon, antibaryon, and meson number densities, respectively. Two phenomenological parameters K_M and K_B are introduced to scale the repulsive interaction strength among the mesons and (anti-)baryons, respectively. Accordingly, the logarithm of total partition function in the RMFHRG model is written as

$$\begin{aligned}\ln Z_{\rm RMF} &= \pm VT \sum_a \int d\Gamma_a \ln[1 \pm e^{-\beta(\epsilon_a^0 - \mu_a^*)}] \\ &\quad -\chi_{a\in\{M,B,\bar{B}\}}(\rho_{M,B,\bar{B}})\end{aligned} \tag{9}$$

where the effective chemical potential is $\mu_a^* = \sum_q q_a\mu_q - K_{B,\bar{B}}\rho_{B,\bar{B}}$ for (anti-)baryons, and $\mu_a^* = \sum_q q_a\mu_q - -K_M\rho_M$ for mesons. In the RMFHRG model, $\rho_{B,\bar{B},M}$ have following form:

$$\rho_{B,\bar{B},M} = \sum_{a\in\{B,\bar{B},M\}} \int d\Gamma_a \bar{f}_a^0. \tag{10}$$

Here, $\bar{f}_a^0$ is the thermal equilibrium distribution function of particle species a in the RMFHRG model, which reads as

$$\bar{f}_a^0(T, \mu_a) = f_a^{id}(T, \mu_a^*) = [\exp([\epsilon_a^0 - \mu_a^*]\beta) \pm 1]^{-1}. \tag{11}$$

In Eq. (9), χ_a is an additional correction factor to avoid the double counting of the mean-field potential and renders the correct number density per particle $\rho_a = \frac{\partial \ln Z_{\rm RMF}}{\partial \mu_a}$ (or the correct energy density per particle $\mathcal{E}_a = \partial\mathcal{E}/\partial\rho_a$), assuming hadron species a is a baryon or antibaryon, we can get

$$\rho_a = \rho_a - \rho_a\left(\frac{\partial U_a}{\partial \rho_{B,\bar{B}}}\frac{\partial \rho_{B,\bar{B}}}{\partial \mu_a}\right) - \frac{\partial \chi_a}{\partial \rho_{B,\bar{B}}}\frac{\partial \rho_{B,\bar{B}}}{\partial \mu_a}. \tag{12}$$

Hence, we can get the following form of χ_a:

$$\chi_{a\in\{B,\bar{B}\}}(\rho_{B,\bar{B}}) = -\frac{1}{2}K_B\rho_{B,\bar{B}}^2. \tag{13}$$

If hadron species a is a meson, $\chi_{a\in\{M\}}(\rho_M) = -\frac{1}{2}K_M\rho_M^2$. Using Eqs. (3-4) as well as Eq. (9), we can get the pressure and energy density for baryons, antibaryons,

and mesons in the RMFHRG model, which are expressed respectively as

$$P_{B,\bar{B},M} = \sum_{a\in\{B,\bar{B},M\}} P_a^{id}(T,\mu_a^*) - \chi_{B,\bar{B},M}(\rho_{B,\bar{B},M}) \quad (14)$$

$$\mathcal{E}_{B,\bar{B},M} = \sum_{a\in\{B,\bar{B},M\}} \mathcal{E}_a^{id}(T,\mu_a^*) + \chi_{B,\bar{B},M}(\rho_{B,\bar{B},M}) \quad (15)$$

The total pressure and total energy density in the RMFHRG model are $P = P_B + P_{\bar{B}} + P_M$ and $\mathcal{E} = \mathcal{E}_B + \mathcal{E}_{\bar{B}} + \mathcal{E}_M$, respectively. It's seen that the RMFHRG model gives an additional term in pressure and energy density compared to the IHRG model, the thermodynamic relation is still consistently satisfied. In the present RMFHRG model, all different (anti-)baryons or mesons have the same repulsive interaction strength, $K_B = 0.45\ \mathrm{GeV}\cdot\mathrm{fm}^3$ and $K_M = 0.05\ \mathrm{GeV}\cdot\mathrm{fm}^3$ are used to improve the agreement with the thermodynamic quantities obtained from the lattice QCD simulations at zero and finite baryon density [62, 63].

III. THERMOELECTRIC COEFFICIENTS AND DIFFUSION COEFFICIENTS OF CONSERVED CHARGES IN BOLTZMANN KINETIC THEORY

A. formalism

It is effective to calculate the transport coefficients of hadronic matter within the framework of the kinetic theory. The evolution of the single-particle phase-space distribution function $f_a(x,p_a)$ can be described by the Boltzmann equation within the covariant formalism [65],

$$p_a^\mu \partial_\mu f_a(x,p_a) + m_a K^\mu \partial_\mu^{(p)} f_a(x,p_a) = \mathcal{C}_a[f_a], \quad (16)$$

where $p_a^\mu = (\epsilon_a^0, \boldsymbol{p}_a)$ is the four-momentum of the particle species a, K^μ is the four-force experienced by individual particle, as well as $\mathcal{C}_a[f_a]$ represents the collision term. When the particle is affected by electromagnetic field force, then $K_a^\mu = -\epsilon_a^0 \partial^\mu U_a(x)/m_a + \frac{Q_a}{m_a} p_{a,\nu} F^{\mu\nu}$, with U_a being the repulsive mean-field potential among hadrons; $F^{\mu\nu}$ is the electromagnetic field-strength tensor, $F^{\mu\nu} \equiv E^\mu u^\nu - E^\nu u^\mu + \frac{1}{2}\epsilon^{\mu\nu\alpha\beta}(u_\alpha H_\beta - u_\beta H_\alpha)$, with $\epsilon^{\mu\nu\alpha\beta}$ being the totally anti-symmetric Levi-Civita tensor. The four-vectors $E^\mu \equiv F^{\mu\nu}u_\nu$ and $H^\mu = \epsilon^{\mu\nu\alpha\beta}F_{\nu\alpha}u_\beta/2$ are nothing but the electric and magnetic fields measured in the frame where the fluid moves with a velocity u^μ. E^μ and H^μ are all space like, $E^\mu u_\mu = 0, H^\mu u_\mu = 0$, and can be normalized as $E^\mu E_\mu = -E^2$, $H^\mu H_\mu = -H^2$, where $E \equiv |\boldsymbol{E}|$ and $H \equiv |\boldsymbol{H}|$. Note that in this work the electric field is induced by gradients of conserved charge density rather than an external field.

Considering that the system is slightly deviated from the local equilibrium, then the phase space distribution function of species a has the following form:

$$f_a = \bar{f}_a^0(1+\phi_a), \quad (17)$$

where the deviation function is $|\phi_a| \ll 1$. $\bar{f}_a^0$ is the local equilibrium distribution function in the RMFHRG model,

$$\bar{f}_a^0 = [\exp((p_a^\mu u_\mu + U_a)\beta - \sum_q q_a\alpha_q) + 1]^{-1}. \quad (18)$$

Here, $\alpha_q \equiv \mu_q\beta$ is defined as the chemical thermal potential of conserved charge q.

To get the solution to Eq. (16), the deviation function ϕ_a must have the following linear combination form:

$$\phi_a \approx -\sum_q \mathcal{B}_a^q p_a^\mu \nabla_\mu \alpha_q - \mathcal{G}_a p_a^\mu \beta E_\mu + \ldots, \quad (19)$$

where $\mathcal{B}_a^q$ and $\mathcal{G}_a$ are unknown functions with momentum p_a. Considering the $a+b \to c+d$ scattering process only for the sake of simplicity, the collision term in Eq. (16) is given as [66, 67]

$$\mathcal{C}_a = \gamma_{ab}\int d\Gamma_b d\Gamma_c d\Gamma_d W(a,b|c,d)\big[f_c f_d(1\pm f_a) \times(1\pm f_b) - f_a f_b(1\pm f_c)(1\pm f_d)\big], \quad (20)$$

where $\pm$ for bosons and fermions, respectively. $W(a,b|c,d)$ is the collisional transition rate. The factor $\gamma_{ab} = \frac{1}{1+\delta_{ab}}$ takes into account the possibility that the incoming particles are identical. Using the detailed balance condition $\bar{f}_c^0\bar{f}_d^0(1\pm\bar{f}_a^0)(1\pm\bar{f}_b^0) = \bar{f}_a^0\bar{f}_b^0(1\pm\bar{f}_c^0)(1\pm\bar{f}_d^0)$, the collision term can be rewritten as

$$\begin{aligned}\mathcal{C}_a &= \sum_{b,c,d}\gamma_{ab}\int d\Gamma_b d\Gamma_c d\Gamma_d W(a,b|c,d)\big\{\bar{f}_a^0\bar{f}_b^0[(1\pm\bar{f}_d^0)\phi_c \\ &\quad +(1\pm\bar{f}_c^0)\phi_d] - \bar{f}_c^0\bar{f}_d^0[(1\pm\bar{f}_b^0)\phi_a + (1\pm\bar{f}_a^0)\phi_b]\big\} \\ &= -\sum_{b,c,d}\gamma_{ab}\int d\Gamma_b d\Gamma_c d\Gamma_d W(a,b|c,d)\frac{\bar{f}_a^0\bar{f}_b^0(1\pm\bar{f}_c^0)}{(1\pm\bar{f}_a^0)} \\ &\quad \times(1\pm\bar{f}_d^0)\phi_a. \end{aligned} \quad (21)$$

Here, we have assumed particle species a is out of equilibrium ($\phi_a \neq 0$), while all other particles are in equilibrium ($\phi_b = \phi_c = \phi_d = 0$). On the other hand, we shall consider the collision term of Eq. (16) in a simple and popular approximation called the relaxation time approximation (RTA) [68], then the collision term can be simplified as:

$$-\frac{\epsilon_a^0\bar{f}_a^0\phi_a}{\tau_a} = \mathcal{C}_a = -\frac{\epsilon_a^0\delta f_a}{\tau_a}. \quad (22)$$

Here, τ_a is the relaxation time of species a which describes how fast the system reaches the equilibrium again. $\delta f_a = f_a - \bar{f}_a^0$ is perturbation term. Then, the energy-momentum tensor $T^{\mu\nu}$ and the net conserved charge four-current N_q^μ can be expressed in terms of the phase space distribution function as follows:

$$T^{\mu\nu} = \sum_a \int d\Gamma_a \frac{p_a^{*\mu}p_a^\nu}{\epsilon_a^0} f_a + g^{\mu\nu}\chi_a, \quad (23)$$

$$N_q^\mu = \sum_a q_a \int d\Gamma_a \frac{p_a^\mu}{\epsilon_a^0} f_a, \quad (24)$$

with $p_a^{*\mu} = p_a^\mu + U_a^\mu$. In the non-equilibrium system, the energy-momentum diffusion four-current and the conserved charge diffusion four-current are $W^\mu \equiv \Delta^\mu_\nu T^{\alpha\nu} u_\alpha$ and $V_q^\mu \equiv \Delta^\mu_\nu N_q^\nu$, respectively [69, 70], which also can be written as

$$W^\mu = \sum_a \int d\Gamma_a \frac{\Delta^\mu_\nu p_a^\nu (\epsilon_a^0 + U_a)}{\epsilon_a^0} \bar{f}_a^0 \phi_a, \tag{25}$$

$$V_q^\mu = \sum_a q_a \int d\Gamma_a \frac{\Delta^\mu_\nu p_a^\nu}{\epsilon_a^0} \bar{f}_a^0 \phi_a. \tag{26}$$

Unlike the ideal hydrodynamics in which the fluid four-velocity is determined because the energy and conserved charge number current flowing parallel to each other, and then the local rest frame of fluid is defined via the requirement that these currents vanish identically, the energy flow and charge number flow in the dissipative hydrodynamics are separate, then the definition of fluid four-velocity is not uniquely defined [71]. There are two simple and natural choices to fix the local rest frame of fluid, i.e., Eckart (or conserved charge) frame and Landau-Lifshitz (or energy) frame. In the Eckart frame, the fluid velocity is parallel to one of the conserved charge currents, and the overall diffusion of one of the conserved net charges vanishes in the local rest frame. However, in low-energy heavy-ion collisions, there are multiple conserved charges, which are not necessarily non-vanishing in all regions of space-time, the definition of the rest frame according to Eckart is less suitable [69]. In the Landau-Lifshitz frame, the fluid velocity is parallel to the energy flow, and the energy diffusion current in the local rest frame is required to vanish. In the present study, the Landau-Lifshitz matching condition in the local rest frame is imposed during the derivation of transport coefficients.

Replacing the right-hand side of Eq. (16) with Eq. (22), the perturbation term δf_a for the first-order gradient expansion is computed as

$$\begin{aligned}
\delta f_a &= \frac{\tau_a}{\epsilon_a^0} \bar{f}_a^0 (1 - \bar{f}_a^0) \Big[p_a^\mu p_a^\nu \beta (u_\mu D u_\nu + \nabla_\mu u_\nu) \\
&\quad + p_a^\mu (p_a \cdot u + U_a)(u_\mu D\beta + \nabla_\mu \beta) \\
&\quad - p_a^\mu \sum_q q_a (u_\mu D\alpha_q + \nabla_\mu \alpha_q) \\
&\quad + p_a^\mu \beta (u_\mu D U_a + \nabla_\mu U_a) - p_a^\mu \beta (u_\mu D U_a + \nabla_\mu U_a) \\
&\quad + Q_a \beta p_{a,\nu} \left(E^\nu - \frac{p_{a,\mu}}{\epsilon_a^0} \frac{1}{2} (H^{\mu\nu} - H^{\nu\mu}) \right) \Big],
\end{aligned} \tag{27}$$

where $p_{a,\nu} E^\nu = p_{a,\langle\nu\rangle} E^\nu$, the rank-two tensor $X^{\mu\nu} \equiv \epsilon^{\mu\nu\alpha\beta} X_\alpha u_\beta$, leading to $u_\mu X^{\mu\nu} = 0$. In the ideal hydrodynamics, taking the projection of $\partial_\mu T^{\mu\nu} = 0$ in the direction orthogonal to u_ν, one gets $u_\nu \partial_\mu T^{\mu\nu} = u_\nu [D\mathcal{E} u^\nu + (\mathcal{E} + P)\theta u^\nu + (\mathcal{E} + P) D u^\nu - \nabla^\nu P] = 0$, where the θ is expansion rate. Since $u_\nu u^\nu = 1$, we have $u_\nu \partial_\mu u^\nu = 0$, then we can get $D u_\mu = \frac{1}{\omega} \nabla_\mu P$ with ω being enthalpy density. Recalling the Gibbs-Duhem relation: $dP = sdT + \sum_q n_q d\mu_q$, one obtains $\nabla_\mu P = -\beta^{-1} \omega \nabla_\mu \beta + \beta^{-1} \sum_q n_q \nabla_\mu \alpha_q$ with n_q being conserved net charge density. Using momentum conservation $\nabla_\mu P = 0$, we can get $\nabla_\mu \beta = \sum_q \frac{n_q}{\omega} \nabla_\mu \alpha_q$.

B. for vanishing magnetic field

In Eq. (27), we first only consider spatial-dependent gradient terms, and don't consider magnetic field effect, then δf_a can be reduced as

$$\begin{aligned}
\delta f_a &= \frac{\tau_a}{\epsilon_a^0} \bar{f}_a^0 (1 - \bar{f}_a^0) \Big[p_a^\mu p_a^\nu \beta \nabla_\mu u_\nu + Q_a \beta p_{a,\nu} E^\nu \\
&\quad + p_a^\mu \sum_q \left((p_a \cdot u + U_a) \frac{n_q}{\omega} - q_a \right) \nabla_\mu \alpha_q \Big].
\end{aligned} \tag{28}$$

Only keep the terms related to the conserved charge diffusion current, above equation is again reduced as

$$\delta f_a \simeq \tau_a \frac{p_a^\mu}{\epsilon_a^0} F_a Q_a E_\mu + \sum_q \tau_a \frac{p_a^\mu}{\epsilon_a^0} H_a^q \nabla_\mu \alpha_q. \tag{29}$$

The functions of F_a and H_a^q in Eq. (29) are given as

$$F_a = \beta \bar{f}_a^0 (1 \pm \bar{f}_a^0), \tag{30}$$

$$H_a^q = \left(\frac{n_q}{\omega} (\epsilon_a^0 + U_a) - q_a \right) \bar{f}_a^0 (1 \pm \bar{f}_a^0). \tag{31}$$

In the Landau-Lishift matching condition, the energy flow is required to vanish in the local rest frame of fluid, i.e., $W^i = 0$, then inserting Eq. (19) into Eq. (25), one gets

$$\sum_a \int d\Gamma_a \widetilde{\epsilon}_a \frac{p_a^i p_a^j}{\epsilon_a^0} \left[\sum_q \mathcal{B}_a^q \nabla_j \alpha_q + \mathcal{G}_a \beta E_j \right] \bar{f}_a^0 = 0. \tag{32}$$

Considering that we have the particular solutions $\mathcal{B}^q_{a,\mathrm{part}}$, $\mathcal{G}_{a,\mathrm{part}}$, another solutions can be written as $\mathcal{B}_a^q = \mathcal{B}^q_{a,\mathrm{part}} - b^q$ and $\mathcal{G}_a = \mathcal{G}_{a,\mathrm{part}} - g$, respectively, where b^q and g are the constant independent of particle species a. Then inserting these into Eq. (32) to resolve the freedom of solutions, we can get

$$\begin{aligned}
&\sum_a \int d\Gamma_a \widetilde{\epsilon}_a \frac{p_a^i p_a^j}{\epsilon_a^0} \left[\sum_q \mathcal{B}^q_{a,\mathrm{part}} \nabla_j \alpha_q + \mathcal{G}_{a,\mathrm{part}} \beta E_j \right] \bar{f}_a^0 \\
&= \sum_a \int d\Gamma_a \widetilde{\epsilon}_a \frac{p_a^i p_a^j}{\epsilon_a^0} \left[\sum_q b^q \nabla_j \alpha_q + g \beta E_j \right] \bar{f}_a^0.
\end{aligned} \tag{33}$$

Using the identity $3T\omega = \sum_a \int d\Gamma_a (\epsilon_a^0 + U_a) \frac{\boldsymbol{p}_a^2}{\epsilon_a^0} \bar{f}_a^0$, and comparing the coefficients of $\nabla_j \alpha_q$ and βE_j, we can get

$$b^q = \frac{1}{3T\omega} \sum_a \int d\Gamma_a (\epsilon_a^0 + U_a) \frac{\boldsymbol{p}_a^2}{\epsilon_a^0} \mathcal{B}^q_{a,\mathrm{part}} \bar{f}_a^0, \tag{34}$$

$$g = \frac{1}{3T\omega} \sum_a \int d\Gamma_a (\epsilon_a^0 + U_a) \frac{\boldsymbol{p}_a^2}{\epsilon_a^0} \mathcal{G}_{a,\mathrm{part}} \bar{f}_a^0. \tag{35}$$

Inserting Eq. (19) into Eq. (26), and using Eqs. (34-35) as well as the identity $\sum_a \int q'_a d\Gamma_a \frac{\boldsymbol{p}_a^2}{3\epsilon_a^0} \bar{f}_a^0 = n_{q'} T$, the diffusion current of conserved charge q' can be written as

$$\begin{aligned} V^\mu_{q'} &= \sum_a q'_a \int d\Gamma_a \frac{p_a^{\langle\mu\rangle} p_a^{\langle\nu\rangle}}{\epsilon_a^0} \Big\{ -\sum_q (\mathcal{B}^q_{a,\mathrm{part}} - b^q) \nabla_\nu \alpha_q \\ &\quad -(\mathcal{G}_{a,\mathrm{part}} - g)\beta E_\nu \Big\} \bar{f}_a^0, \\ &= \sum_a \int d\Gamma_a \frac{p_a^{\langle\mu\rangle} p_a^{\langle\nu\rangle}}{\epsilon_a^0} \left[\frac{n_{q'}(\epsilon_a^0 + U_a)}{\omega} - q'_a \right] \\ &\quad \times \left[\sum_q \mathcal{B}^q_{a,\mathrm{part}} \nabla_\nu \alpha_q + \beta \mathcal{G}_{a,\mathrm{part}} E_\nu \right] \bar{f}_a^0. \end{aligned} \tag{36}$$

We replace the right-hand side of Eq. (22) using Eq. (29), and substitute ϕ_a with Eq. (19) into the left-hand side of Eq. (22), then equate δf_a and $\bar{f}_a^0 \phi_a$ by matching tensor structure, the particular solutions for the functions $\mathcal{B}_a^q$ and $\mathcal{G}_a$ from ϕ_a finally are computed as:

$$\mathcal{B}^q_{a,\mathrm{part}} = \frac{\tau_a}{\epsilon_a^0} \left[q_a - \frac{n_q}{\omega}(\epsilon_a^0 + U_a) \right] (1 \pm \bar{f}_a^0), \tag{37}$$

$$\mathcal{G}_{a,\mathrm{part}} = -Q_a \frac{\tau_a}{\epsilon_a^0} (1 \pm \bar{f}_a^0). \tag{38}$$

According to the linear response theory, Eq. (36) can be presented as the following matrix form:

$$\begin{bmatrix} V_B^\mu \\ V_Q^\mu \\ V_S^\mu \end{bmatrix} = \begin{bmatrix} \eta^{BQ} \\ \eta^{QQ} \\ \eta^{SQ} \end{bmatrix} E^\mu + \begin{bmatrix} \kappa^{BB} & \kappa^{QB} & \kappa^{SB} \\ \kappa^{BQ} & \kappa^{QQ} & \kappa^{SQ} \\ \kappa^{BS} & \kappa^{QS} & \kappa^{SS} \end{bmatrix} \begin{bmatrix} \nabla^\mu \alpha_B \\ \nabla^\mu \alpha_Q \\ \nabla^\mu \alpha_S \end{bmatrix}. \tag{39}$$

Here, the diffusion coefficient matrix $\kappa^{qq'}$ ($q, q' \in \{B, Q, S\}$), which quantifies the coupling between the diffusion of different conserved charges, reads as

$$\begin{aligned} \kappa^{qq'} &= \sum_a \frac{d_a}{3} \int \frac{d^3 p_a}{(2\pi)^3} \tau_a \frac{\boldsymbol{p}_a^2}{(\epsilon_a^0)^2} \left[q'_a - (\epsilon_a^0 + U_a) \frac{n'_q}{\omega} \right] \\ &\quad \times \left[q_a - (\epsilon_a^0 + U_a) \frac{n_q}{\omega} \right] \bar{f}_a^0 (1 \pm \bar{f}_a^0), \end{aligned} \tag{40}$$

which is equivalent to the expression derived from Ref. [38], if ignoring the effect of quantum statistics and the repulsive mean-field interactions between hadrons. In Eq. (39), the thermoelectric transport coefficient matrix $\eta^{qq'}$ is given as

$$\begin{aligned} \eta^{qq'} &= \sum_a \frac{d_a \beta}{3} \int \frac{d^3 p_a}{(2\pi)^3} \tau_a \frac{\boldsymbol{p}_a^2}{(\epsilon_a^0)^2} q'_a \\ &\quad \times \left[q_a - (\epsilon_a^0 + U_a) \frac{n_q}{\omega} \right] \bar{f}_a^0 (1 \pm \bar{f}_a^0). \end{aligned} \tag{41}$$

Take $q'_a = Q_a$, the η^{qQ} is redefined as thermoelectric conductivity of conserved charge q. When net electric diffusion current vanishes, i.e., $V_Q^i = \boldsymbol{V}_Q = 0$, we can get the induced internal electric field:

$$\boldsymbol{E} = \sum_q M^{qQ} T \boldsymbol{\nabla} \alpha_q. \tag{42}$$

Here, M^{qQ} is defined as diffusion thermopower of conserved charge q, which quantifies the ability of hadronic matter to convert the gradients of conserved charge chemical thermal potential to an electric field, and it reads as

$$M^{qQ} = \beta \kappa^{qQ} / \eta^{QQ}. \tag{43}$$

Inserting Eq. (42) into Eq. (39), then the matrix form of Eq. (36) can be rewritten as

$$\begin{bmatrix} V_B^\mu \\ V_Q^\mu \\ V_S^\mu \end{bmatrix} = \begin{bmatrix} \widetilde{\kappa}^{BB} & \widetilde{\kappa}^{QB} & \widetilde{\kappa}^{SB} \\ \widetilde{\kappa}^{BQ} & \widetilde{\kappa}^{QQ} & \widetilde{\kappa}^{SQ} \\ \widetilde{\kappa}^{BS} & \widetilde{\kappa}^{QS} & \widetilde{\kappa}^{SS} \end{bmatrix} \begin{bmatrix} \nabla^\mu \alpha_B \\ \nabla^\mu \alpha_Q \\ \nabla^\mu \alpha_S \end{bmatrix}. \tag{44}$$

Here, the thermoelectric modified diffusion coefficients in the electric current sector vanish, i.e., $\widetilde{\kappa}^{BQ} = \widetilde{\kappa}^{SQ} = \widetilde{\kappa}^{QQ} = 0$. The thermoelectric modified diffusion coefficient matrix elements in baryon and strangeness sectors have the following form:

$$\widetilde{\kappa}^{qq''} = \kappa^{qq''} - T M^{qQ} \eta^{q''Q}. \tag{45}$$

with $q'' \in \{B, S\}$.

C. for finite magnetic field

Next, we investigate the influence of the magnetic field on the thermoelectric effect and diffusion processes of multiple conserved charges in the hadronic medium. In the presence of a weak magnetic field, the magnetic field is not the dominant energy scale and its impact can be manifested at the classical level with the so-called cyclotron motion of charged particles. We reasonably propose that the scattering mechanism of constituents and the thermodynamic quantities are unaffected by the magnetic field. In the uniform electric field $\boldsymbol{E}$ and external magnetic field $\boldsymbol{H}$ ($\boldsymbol{E} \perp \boldsymbol{H} \perp \boldsymbol{\nabla}\alpha_q$), considering a time-independent phase space distribution function, Eq. (16) can be reformulated as

$$\boldsymbol{v}_a \cdot \boldsymbol{\nabla} f_a + [Q_a(\boldsymbol{E} + \boldsymbol{v}_a \times \boldsymbol{H}) - \boldsymbol{\nabla} U_a] \cdot \frac{\partial f_a}{\partial \boldsymbol{p}_a} = -\frac{\delta f_a}{\tau_a}. \tag{46}$$

where the RTA has been utilized, and $\boldsymbol{v}_a \equiv \frac{d\epsilon_a^0}{d\boldsymbol{p}_a} = \boldsymbol{p}_a / \epsilon_a^0$ is the three-velocity of particle species a. Neglecting any term that is second order in δf_a, Eq. (46) can be rewritten as

$$\begin{aligned} \frac{f_a}{\tau_a} + Q_a \boldsymbol{v}_a \times \boldsymbol{H} \cdot \frac{\partial f_a}{\partial \boldsymbol{p}_a} &= -Q_a \boldsymbol{E} \cdot \frac{\partial \bar{f}_a^0}{\partial \boldsymbol{p}_a} - (\boldsymbol{v}_a \cdot \boldsymbol{\nabla} \bar{f}_a^0) \\ &\quad + \frac{\bar{f}_a^0}{\tau_a} + \boldsymbol{\nabla} U_a \cdot \frac{\partial \bar{f}_a^0}{\partial \boldsymbol{p}_a}. \end{aligned} \tag{47}$$

We further assume the solution of Eq. (47) satisfies the following linear form,

$$\begin{aligned} f_a &= \bar{f}_a^0 - \tau_a Q_a \boldsymbol{E} \cdot \frac{\partial \bar{f}_a^0}{\partial \boldsymbol{p}_a} - \boldsymbol{\Xi} \cdot \frac{\partial \bar{f}_a^0}{\partial \boldsymbol{p}_a} - \tau_a \boldsymbol{v}_a \cdot \boldsymbol{\nabla} \bar{f}_a^0 \\ &\quad + \tau_a \boldsymbol{\nabla} U_a \cdot \frac{\partial \bar{f}_a^0}{\partial \boldsymbol{p}_a}, \end{aligned} \tag{48}$$

with $\boldsymbol{\Xi}$ being an unknown quantity related to the magnetic field. Inserting Eq. (48) into Eq. (47) we obtain

$$\begin{aligned} 0 &= \frac{F_a}{\tau_a}\boldsymbol{\Xi}\cdot\boldsymbol{v}_a + \frac{Q_a}{\epsilon_a^0}F_a\boldsymbol{v}_a\times\boldsymbol{H}\cdot\boldsymbol{\Xi} + \frac{Q_a^2}{\epsilon_a^0}\tau_a F_a\boldsymbol{v}_a\times\boldsymbol{H}\cdot\boldsymbol{E} \\ &\quad + \frac{Q_a\tau_a}{\epsilon_a^0}\boldsymbol{v}_a\times\boldsymbol{H}\cdot\sum_q H_a^q\boldsymbol{\nabla}\alpha_q. \end{aligned} \tag{49}$$

After some tedious calculations, we can get the form $\boldsymbol{\Xi}$ as follows:

$$\begin{aligned} \boldsymbol{\Xi} &= \frac{\tau_a}{(\omega_{c,a}\tau_a)^2+1}[-\omega_{c,a}^2 Q_a\boldsymbol{E} + \frac{\omega_{c,a}}{\tau_a}Q_a(\boldsymbol{E}\times\boldsymbol{h}) \\ &\quad + \frac{\omega_{c,a}H_a^q}{\tau_a F_a}(\boldsymbol{\nabla}\alpha_q\times\boldsymbol{h}) - \frac{\omega_{c,a}^2 H_a^q}{F_a}\boldsymbol{\nabla}\alpha_q], \end{aligned} \tag{50}$$

where $\boldsymbol{h}=\boldsymbol{H}/H$, all the information of magnetic field is encoded in cyclotron frequency of species a, i.e., $\omega_{c,a}=Q_aH/\epsilon_a^0$. Inserting Eq. (50) into Eq. (48), we finally obtain the magnetic field-dependent perturbation term of the distribution function,

$$\begin{aligned} \delta f_a &= \frac{\tau_a^2}{(\omega_{c,a}\tau_a)^2+1}\big[\omega_{c,a}F_aQ_a(\boldsymbol{E}\times\boldsymbol{h})\cdot\boldsymbol{v}_a \\ &\quad + \frac{1}{\tau_a}F_aQ_a\boldsymbol{E}\cdot\boldsymbol{v}_a + \sum_q\omega_{c,a}H_a^q(\boldsymbol{\nabla}\alpha_q\times\boldsymbol{h})\cdot\boldsymbol{v}_a \\ &\quad + \sum_q\frac{1}{\tau_a}H_a^q\boldsymbol{v}_a\cdot\boldsymbol{\nabla}\alpha_q\big]. \end{aligned} \tag{51}$$

Repeating some procedures in the previous subsection (Eqs. (17)-(26), Eqs. (32)-(38)), the particular solutions for the functions $\mathcal{B}_a^q$ and $\mathcal{G}_a$ from ϕ_a in the magnetic field are computed as

$$\begin{aligned} \mathcal{B}_{a,\mathrm{part}}^{q,H\neq0} &= \frac{\tau_a}{\epsilon_a^0}\left[q_a - \frac{n_q}{\omega}(\epsilon_a^0+U_a)\right](1\pm\bar{f}_a^0) \\ &\quad\times\frac{[\omega_{c,a}\tau_a(\boldsymbol{h}\times\boldsymbol{v}_a)+1]}{(\omega_{c,a}\tau_a)^2+1}, \end{aligned} \tag{52}$$

$$\mathcal{G}_{a,\mathrm{part}}^{H\neq0} = -\frac{Q_a\tau_a}{\epsilon_a^0}(1\pm\bar{f}_a^0)\frac{[1+\omega_{c,a}\tau_a(\boldsymbol{h}\times\boldsymbol{v}_a)]}{(\omega_{c,a}\tau_a)^2+1}. \tag{53}$$

Therefore, the diffusion current of conserved charge q' in the magnetic field is computed as:

$$\begin{aligned} \boldsymbol{V}^{q'} &= -\sum_{a,q}\int d\Gamma_a\frac{\boldsymbol{p}_a}{(\epsilon_a^0)^2}\frac{\tau_a\boldsymbol{p}_a\cdot[\omega_{c,a}\tau_a(\boldsymbol{\nabla}\alpha_q\times\boldsymbol{h})+\boldsymbol{\nabla}\alpha_q]}{(\omega_{c,a}\tau_a)^2+1} \\ &\quad\times\left[q_a-(\epsilon_a^0+U_a)\frac{n_q}{\omega}\right]\left[q_a'-(\epsilon_a^0+U_a)\frac{n_{q'}}{\omega}\right] \\ &\quad\times\bar{f}_a^0(1\pm\bar{f}_a^0) \\ &\quad+\sum_a q_a'\int d\Gamma_a\frac{\boldsymbol{p}_a}{(\epsilon_a^0)^2}\frac{Q_a}{T}\frac{\tau_a\boldsymbol{p}_a\cdot[\omega_{c,a}\tau_a(\boldsymbol{E}\times\boldsymbol{h})+\boldsymbol{E}]}{(\omega_{c,a}\tau_a)^2+1} \\ &\quad\times\left[q_a'-\frac{n_{q'}}{\omega}(\epsilon_a^0+U_a)\right]\bar{f}_a^0(1\pm\bar{f}_a^0). \end{aligned} \tag{54}$$

Take the magnetic field along the z-axis and decompose the above equation into x- and y-directions, the following matrix form can be obtained:

$$\begin{bmatrix} V_x^{q'} \\ V_y^{q'} \end{bmatrix} = \begin{bmatrix} \eta_{xx}^{Qq'Q} & \eta_{xy}^{Qq'Q} \\ \eta_{yx}^{Qq'Q} & \eta_{yy}^{Qq'Q} \end{bmatrix}\begin{bmatrix} E_x \\ E_y \end{bmatrix} + \sum_q \begin{bmatrix} \kappa_{xx}^{Qqq'} & \kappa_{xy}^{Qqq'} \\ \kappa_{yx}^{Qqq'} & \kappa_{yy}^{Qqq'} \end{bmatrix}\begin{bmatrix} -\nabla_x\alpha_q \\ -\nabla_y\alpha_q \end{bmatrix}. \tag{55}$$

Here, the thermoelectric conductivity tensors ($\eta^{Qq'Q}$) and diffusion coefficient tensors ($\kappa^{Qqq'}$) in a magnetic field satisfy the Onsager's reciprocity relation [72, 73]: $\kappa_{xx}^{Qqq'}(\eta_{xx}^{Qq'Q}) = \kappa_{yy}^{Qqq'}(\eta_{yy}^{Qq'Q})$ and $\kappa_{xy}^{Qqq'}(\eta_{xy}^{Qq'Q}) = -\kappa_{yx}^{Qqq'}(-\eta_{yx}^{Qq'Q})$. Accordingly, the magnetic field-dependent thermoelectric conductivity matrix element ($\eta_{xx}^{Qq'Q}$) and the Hall-like or transverse thermoelectric conductivity matrix element ($\eta_{yx}^{Qq'Q}$) can be expressed as

$$\begin{aligned} \begin{bmatrix} \eta_{xx}^{Qq'Q} \\ \eta_{yx}^{Qq'Q} \end{bmatrix} &= \sum_a\frac{d_aQ_a}{3T}\int\frac{d^3p_a}{(2\pi)^3}\frac{\boldsymbol{p}_a^2}{(\epsilon_a^0)^2}\frac{\left(q_a'-(\epsilon_a^0+U_a)\frac{n_{q'}}{\omega}\right)}{(\omega_{c,a}\tau_a)^2+1} \\ &\quad\times\begin{bmatrix}\tau_a \\ -\omega_{c,a}\tau_a^2\end{bmatrix}\bar{f}_a^0(1\pm\bar{f}_a^0). \end{aligned} \tag{56}$$

The magnetic field-dependent diffusion coefficient matrix element ($\kappa_{xx}^{Qqq'}$) and the Hall-like diffusion coefficient matrix element ($\kappa_{yx}^{Qqq'}$) can be given as

$$\begin{aligned} \begin{bmatrix} \kappa_{xx}^{Qqq'} \\ \kappa_{yx}^{Qqq'} \end{bmatrix} &= \sum_a\frac{d_a}{3}\int\frac{d^3p_a}{(2\pi)^3}\frac{\boldsymbol{p}_a^2}{(\epsilon_a^0)^2}\frac{\left(q_a-(\epsilon_a^0+U_a)\frac{n_q}{\omega}\right)}{(\omega_{c,a}\tau_a)^2+1} \\ &\quad\times\left(q_a'-(\epsilon_a^0+U_a)\frac{n_{q'}}{\omega}\right)\begin{bmatrix}\tau_a \\ -\omega_{c,a}\tau_a^2\end{bmatrix} \\ &\quad\times\bar{f}_a^0(1\pm\bar{f}_a^0). \end{aligned} \tag{57}$$

To better distinguish the expressions of transport coefficients in different transverse restriction conditions later, we convert Eq. (55) into the following matrix form:

$$\begin{bmatrix} E_x \\ E_y \\ V_x^{q''} \\ V_y^{q''} \end{bmatrix} = \begin{bmatrix} \rho_{xx}^{QQ} & \rho_{xy}^{QQ} & \sum_q -TM_{xx}^{QqQ} & \sum_q -TM_{xy}^{QqQ} \\ \rho_{yx}^{QQ} & \rho_{yy}^{QQ} & \sum_q -TM_{yx}^{QqQ} & \sum_q -TM_{yy}^{QqQ} \\ \Pi_{xx}^{Qq''Q} & \Pi_{xy}^{Qq''Q} & \sum_q \widetilde{\kappa}_{xx}^{Qqq''} & \sum_q \widetilde{\kappa}_{xy}^{Qqq''} \\ \Pi_{yx}^{Qq''Q} & \Pi_{yy}^{Qq''Q} & \sum_q \widetilde{\kappa}_{yx}^{Qqq''} & \sum_q \widetilde{\kappa}_{yy}^{Qqq''} \end{bmatrix} \begin{bmatrix} V_x^Q \\ V_y^Q \\ -\nabla_x\alpha_q \\ -\nabla_y\alpha_q \end{bmatrix}, \quad q \in \{B,Q,S\},\ q'' \in \{B,S\}. \tag{58}$$

Solving the set of coupled matrix equations (58) under the condition of vanishing gradients of transverse conserved charge chemical thermal potential ($\nabla_y\alpha_q = 0$) with $\nabla_x\alpha_q = 0 = V_y^Q = 0$, then the electric resistance tensors (ρ^{QQ}) can be obtained as

$$\rho_{xx}^{QQ} = \rho_{yy}^{QQ} = \frac{E_x}{V_x^Q}\bigg|_{\nabla_y\alpha_q=0} = \frac{\eta_{xx}^{QQQ}}{(\eta_{xx}^{QQQ})^2 + (\eta_{xy}^{QQQ})^2} \tag{59}$$

$$\rho_{yx}^{QQ} = -\rho_{xy}^{QQ} = \frac{E_y}{V_x^Q}\bigg|_{\nabla_y\alpha_q=0} = \frac{\eta_{xy}^{QQQ}}{(\eta_{xx}^{QQQ})^2 + (\eta_{xy}^{QQQ})^2} \tag{60}$$

Similarly, a Hall-like diffusion thermopower of conserved charge q (M_{yx}^{QqQ}) can appear in the magnetic field. Under the condition of $\nabla_y\alpha_q = 0$ with $V_x^Q = V_y^Q = 0$, the magnetic field-dependent diffusion thermopower and Hall-like diffusion thermopower of conserved charge q can respectively be obtained as

$$M_{xx}^{QqQ} = \frac{E_x}{T\nabla_x\alpha_q}\bigg|_{\nabla_y\alpha_q=0} = \beta\rho_{xx}^{QQ}\kappa_{xx}^{QqQ} - \beta\rho_{xy}^{QQ}\kappa_{xy}^{QqQ}, \tag{61}$$

$$M_{yx}^{QqQ} = \frac{E_y}{T\nabla_x\alpha_q}\bigg|_{\nabla_y\alpha_q=0} = -\beta\rho_{xx}^{QQ}\kappa_{xy}^{QqQ} - \beta\rho_{xy}^{QQ}\kappa_{xx}^{QqQ}. \tag{62}$$

Taking vanishing magnetic field, $M_{xx}^{QqQ} = M^{Qq}$. Using the set of coupled equations (58), the magneto-thermoelectric modified diffusion coefficient ($\widetilde{\kappa}_{xx}^{Qqq''}$) and Hall-like magneto-thermoelectric modified diffusion coefficient ($\widetilde{\kappa}_{yx}^{Qqq''}$) under the condition of $\nabla_y\alpha_q = 0$ with $V_x^Q = V_y^Q = 0$, can respectively be computed as

$$\begin{aligned} \widetilde{\kappa}_{xx}^{Qqq''} &= \frac{V_x^{q''}}{-\nabla_x\alpha_q}\bigg|_{\nabla_y\alpha_q=0} \\ &= \kappa_{xx}^{Qqq''} - \eta_{xx}^{Qq''Q}TM_{xx}^{QqQ} + \eta_{yx}^{Qq''Q}TM_{yx}^{QqQ} \end{aligned} \tag{63}$$

$$\begin{aligned} \widetilde{\kappa}_{yx}^{Qqq''} &= \frac{V_y^{q''}}{-\nabla_x\alpha_q}\bigg|_{\nabla_y\alpha_q=0} \\ &= \kappa_{yx}^{Qqq''} - \eta_{yx}^{Qq''Q}TM_{xx}^{QqQ} - \eta_{xx}^{Qq''Q}TM_{yx}^{QqQ} \end{aligned} \tag{64}$$

In condensed matter physics, a transverse temperature gradient ($\nabla_y T$) can be developed by the longitudinal temperature gradient ($\nabla_x T$) under a static magnetic field (H_z), which is called the Righi-Leduc effect or thermal Hall effect. The associated Righi-Leduc coefficient is calculated in the transverse adiabatic condition i.e., $I_y = 0$, with I_y being transverse heat current. In the hadronic matter with multiple conserved charges, similar to the Righi-Leduc effect, a transverse or Hall-like conserved charge density gradient ($\nabla_y\alpha_q$) perpendicular to both the $\nabla_x\alpha_q$ and H_z can be generated. The corresponding coefficient is obtained under the condition of vanishing transverse diffusion current i.e., $V_y^{q''} = 0$. Hence, using the matrix Eq. (58), and imposing the conditions of $V_y^{q''} = V_x^Q = V_y^Q = 0$, the Righi-Leduc-type relation in the hadronic medium reads as

$$\begin{aligned} 0 &= \sum_q \widetilde{\kappa}_{yx}^{Qqq''}\nabla_x\alpha_q + \sum_q \widetilde{\kappa}_{xx}^{Qqq''}\nabla_y\alpha_q \\ &\to \mathcal{L}^q_{V_y^{q''}=0} = \frac{\nabla_y\alpha_q}{\nabla_x\alpha_q}\bigg|_{V_y^{q''}=0} = \frac{\widetilde{\kappa}_{xy}^{Qqq''}}{\widetilde{\kappa}_{xx}^{Qqq''}}, \end{aligned} \tag{65}$$

with $\mathcal{L}^q_{V_y^{q''}=0}$ being Righi-Leduc-like coefficient. Accordingly, the magnetic field-dependent diffusion thermopower under the condition of $V_y^{q''} = 0$ with $V_x^Q = V_y^Q = 0$ is computed as

$$M^{QqQ}_{xx,V_y^{q''}=0} = M_{xx}^{QqQ} + M_{xy}^{QqQ}\mathcal{L}^q_{V_y^{q''}=0}. \tag{66}$$

When the magnetic field is turned off, the expressions of transport coefficients in the transverse condition of $\nabla_y\alpha_q = 0$ equal to those in the transverse condition of $V_y^{q''} = 0$. Similarly, the magneto-thermoelectric modified diffusion coefficient under the condition of $V_y^{q''} = 0$ with $V_x^Q = V_y^Q = 0$, is computed as

$$\widetilde{\kappa}^{Qqq''}_{xx,V_y^{q''}=0} = \widetilde{\kappa}_{xx}^{Qqq''} + \widetilde{\kappa}_{xy}^{Qqq''}\mathcal{L}^q_{V_y^{q''}=0}. \tag{67}$$

D. Thermal averaged relaxation time

Comparing Eq. (21) and Eq. (22), all the scattering information of hadrons is encoded in the relaxation time, τ_a, and its inverse is given as

$$\begin{aligned} \tau_a^{-1} &= \sum_{b,c,d}\gamma_{ab}\int d\Gamma_b d\Gamma_c d\Gamma_d W(a,b|c,d)\bar{f}_b^0(1\pm\bar{f}_c^0) \\ &\quad\times\frac{(1\pm\bar{f}_d^0)}{1\pm\bar{f}_a^0}. \end{aligned} \tag{68}$$

The collisional transition rate is given as

$$W(a,b|c,d) = \frac{(2\pi)^4\delta^4(p_a+p_b-p_c-p_d)}{16\epsilon_a^0\epsilon_b^0\epsilon_c^0\epsilon_d^0}|\bar{\mathcal{M}}_{ab\to cd}|^2, \tag{69}$$

where $|\bar{\mathcal{M}}|$ is the dimensionless transition amplitude averaged over the spin degeneracy factor in both initial and final states. To simplify the estimation of relaxation time, $(1 \pm \bar{f}_c^0)\frac{(1\pm\bar{f}_d^0)}{1\pm\bar{f}_a^0} \simeq 1$, and we use the formula of scattering cross section [74]

$$\sigma_{ab} = \frac{\int d\Gamma_c d\Gamma_d (2\pi)^4 \delta^4(p_a + p_b - p_c - p_d)|\bar{\mathcal{M}}|^2}{16\epsilon_c^0\epsilon_d^0\sqrt{(p_a\cdot p_b)^2 - m_a^2 m_b^2}}, \quad (70)$$

then we can rewrite τ_a^{-1} as

$$\tau_a^{-1} \equiv \sum_b \gamma_{ab}\rho_b\sigma_{ab}v_{ab}, \quad (71)$$

where $\rho_b = \int d\Gamma_b \bar{f}_b^0$ is the number density of species b. It's worth noting the RMF interactions between hadrons can enter the scattering process by modifying the number density of hadron species b, hence the number density of hadron species b needs to be distinguished in the IHRG model and RMFHRG models. In Eq. (71), the relative velocity v_{ab} is defined as

$$v_{ab} = \frac{\sqrt{(\epsilon_a^0\epsilon_b^0 - \boldsymbol{p}_a\cdot\boldsymbol{p}_b)^2 - m_a^2 m_b^2}}{\epsilon_a^0\epsilon_b^0}. \quad (72)$$

In this work, we shall consider the momentum-independent relaxation time, then thermal averaged cross section $\langle\sigma_{ab}v_{ab}\rangle$ can be given as

$$\langle\sigma_{ab}v_{ab}\rangle = \frac{\int d^3p_a d^3p_b \bar{f}_a^0\bar{f}_b^0\sigma_{ab}v_{ab}}{\int d^3p_a d^3p_b \bar{f}_a^0\bar{f}_b^0}. \quad (73)$$

We only consider elastic scattering for the 2-to-2 process and all hadrons are regarded as hard spheres with the same radius r_h and σ_{ab} is a constant with $\sigma_{ab} = 4\pi r_h^2 =$ 30 mb.

IV. NUMERICAL RESULTS AND DISCUSSIONS

A. Results for vanishing magnetic field

All our calculations are performed in the condition of $n_S = 0 = \mu_Q = 0$ [36, 38], which is expected in the initial stages of heavy-ion collision [75, 76]. This results in a nonzero strangeness chemical potential, which is a function of T and μ_B. In the HRG models, we take all available hadrons up to a mass cutoff $\Lambda = 3.0$ GeV from available `Thermal-FIST` package [77]. The BES program at RHIC covers beam energy from $\sqrt{s_{NN}} = 3$ GeV to 200 GeV, with the baryon chemical potential ranging from $\mu_B \simeq 0.75$ GeV to 0.02 GeV [78–80], we take $\mu_B \leq 0.6$ GeV in this investigation. To better understand the behaviors of the diffusion coefficient matrix later, we first detailedly discuss the T and μ_B dependence of the scaled conductivity matrix $\sigma^{qq'}$, which is given as

$$\sigma^{qq'} = \sum_a \frac{d_a\beta}{3}\int\frac{d^3p_a}{(2\pi)^3}\tau_a\frac{\boldsymbol{p}_a^2}{(\epsilon_a^0)^2}q_a'q_a\bar{f}_a^0(1\pm\bar{f}_a^0). \quad (74)$$

It is highly related to diffusion coefficient matrix and $\sigma^{qq'}/T$ is equal to $\kappa^{qq'}/T^2$ at $\mu_B = 0$. Actually, the variation of $\sigma^{qq'}/T$ with T and μ_B is determined by the interplay between charge number density (or distribution function) and scattering rate (or the relaxation time $\tau_a \sim 1/\Gamma_{\rm scatt}$). In Fig. 1, we see that for $\mu_B = 0$, the σ^{QQ}/T (σ^{qB}/T) in magnitude decreases (increases) monotonically as T increases, whereas both σ^{QS}/T and σ^{SS}/T first increase with T and then decrease, which is qualitatively consistent with the SMASH simulation results (symbol lines) [81] The sign of σ^{SB}/T is negative due to the associated dominant carriers, viz hyperons carrying a positive baryon number with a negative strangeness. As shown in Fig. 1, all scaled conductivities in the SMASH simulation with Green-Kubo formalism are larger than our results. We can also see that the effect of RMF interaction on the conductivity matrix for $\mu_B = 0$ is minimal. This is because the RMF correction for $\mu_B = 0$ only has a small suppression on charge number density and a small enhancement on relaxation time, the mutual compensation makes the RMF correction on the conductivities ignorable.

The thermal behaviors of all scaled conductivities for $\mu_B = 0.3$ GeV are almost unchanged compared to the case of $\mu_B = 0$, and from Fig. 1 we note that σ^{qB}/T in magnitude has an obvious enhancement because the dependence of σ^{qB}/T on μ_B is mainly governed by the baryon density, which is an increasing function of μ_B. We also observe that σ^{QS}/T and σ^{SS}/T at $\mu_B = 0.3$ GeV have a nominal reduction compared to those at $\mu_B = 0$. The reason behind this is that the dominant carriers for both σ^{QS}/T and σ^{SS}/T are kaons (K), the number density of kaons has a small enhancement due to the presence of nonzero μ_S, whereas such enhancement can be canceled out by the increase of the scattering rates of kaons due to colliding with more baryons. The σ^{QQ}/T also has an invisible variation at $\mu_B = 0.3$ GeV compared at $\mu_B = 0$, which is the competition result between meson contribution (mostly pions) to σ^{QQ} and baryon contribution (mostly nucleons) to σ^{QQ}. At $\mu_B = 0.3$ GeV, the decrease of pion contribution to σ^{QQ} with μ_B is almost compensated by the increase of nucleon contribution to σ^{QQ} with μ_B. As μ_B increases further, the baryon density becomes more and more significant, and all conductivities at $\mu_B = 0.6$ GeV have a significant variation. We note that the temperature dependence of both σ^{QB}/T and σ^{BB}/T even can overturn at $\mu_B = 0.6$ GeV. This is because the decreasing behavior of the relaxation time of predominant nucleons with T dominates over the increasing behavior of the distribution function with T. We also observe that all conductivities except σ^{QQ}/T have a significant variation due to the RMF correction at $\mu_B = 0.6$ GeV compared to those at $\mu_B = 0$ or 0.3 GeV. The σ^{BQ}/T, σ^{BB}/T, and $-\sigma^{BS}/T$ has an obvious suppression because the including of the RMF correction significantly decreases the baryon density of the system at $\mu_B = 0.6$ GeV. While the RMF correction leads a significant enhancement on σ^{QS}/T and σ^{SS}/T at

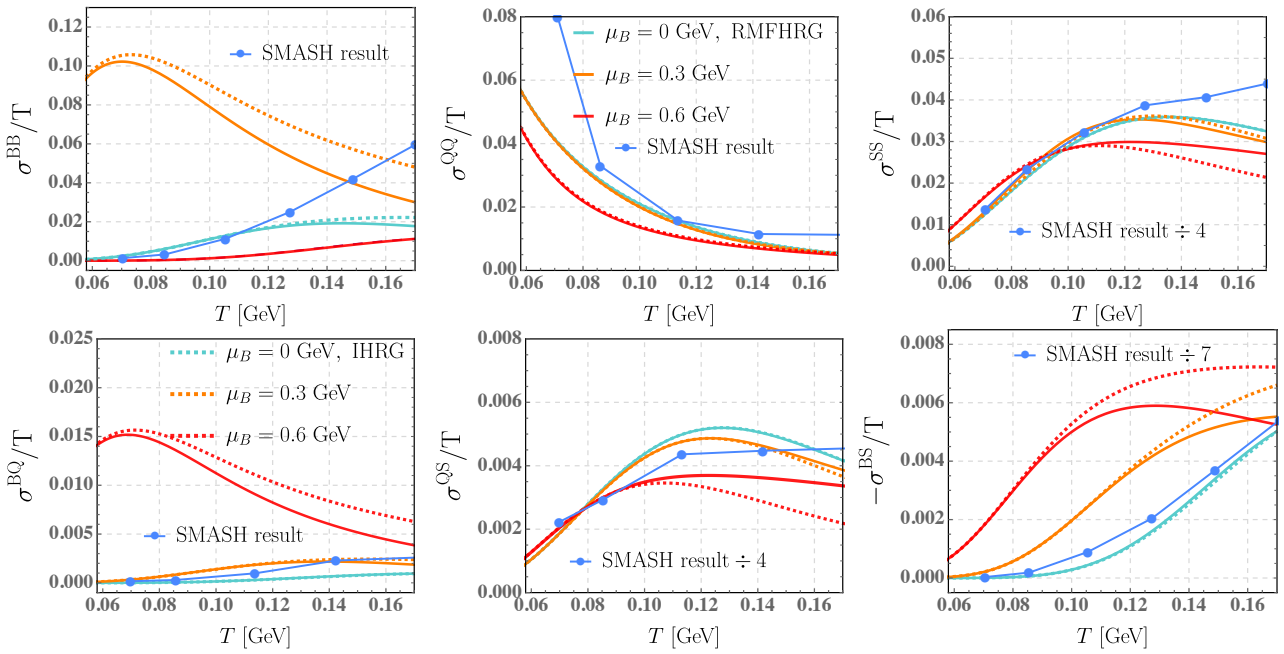


FIG. 1: The temperature dependence of complete scaled conductivity matrix $\sigma^{qq'}/T$ for different baryon chemical potentials, i.e, $\mu_B = 0$ (blue), 0.3 GeV (orange) and 0.6 GeV (red) in the IHRG model (dotted lines) and RMFHRG model (solid lines). The symbol lines are the estimations in the full SMASH simulation using Green-Kubo formalism at zero μ_B [81].

$\mu_B = 0.6$ GeV compared that at $\mu_B = 0.3$ GeV. This is because at $\mu_B = 0.3$ GeV the associated predominant carriers to both the σ^{QS}/T and σ^{SS}/T are still kaons, the kaon density only is affected by the RMF interaction between meson and meson, while the relaxation time of kaons can be influenced by the RMF interaction among various hadron-hadron pairs due to colliding with different hadrons, which are canceled out at $\mu_B = 0.3$ GeV. As μ_B increases further, the increase in kaon relaxation time caused by the RMF correction significantly overtakes the decrease in the kaon density, leading to a visible enhancement on both σ^{QS}/T and σ^{SS}/T at $\mu_B = 0.6$ GeV. For purely electric conductivity σ^{QQ}/T, it nearly cannot be changed by the RMF correction even at high μ_B. The reason behind this just is the exact cancellation between the RMF correction on the σ^{QQ}/T contributed by mesons and the RMF correction on the σ^{QQ}/T contributed by baryons. The μ_B and T dependence of all conductivities can not be altered by adding the RMF interactions.

With the knowledge provided above, we can easily comprehend the results of the diffusion coefficient matrix. In Fig. 2, we display the T and μ_B dependence of complete scaled diffusion coefficient matrix $\kappa^{qq'}/T^2$ in both the IHRG and RMFHRG models. Similar to the conductivity matrix, the $\kappa^{qq'}$ and $\kappa^{q'q}$ are symmetric. The diffusion coefficient matrix element is decomposed as $\sum_a [q_a q'_a + \widetilde{\epsilon}_a^2 \frac{n_q n'_q}{\omega^2} + q'_a \widetilde{\epsilon}_a \frac{n_q}{\omega} + q_a \widetilde{\epsilon}_a \frac{n'_q}{\omega}] \bar{f}_a^0 (1 \pm \bar{f}_a^0)$ in the integrand of Eq. (40). In our considered T and μ_B region, the dominant region of $\widetilde{\epsilon}_a$ in Eq. (40) is lower than ω/n_q (though ϵ_a^0 can be infinite due to momentum), thus the qualitative behavior of the scaled diffusion coefficient matrix is similar to the associated scaled conductivity matrix. From Fig. 2 we can see that the off-diagonal elements can reach a similar magnitude as the diagonal terms. Our results in the IHRG model are quantitatively and qualitatively close to the results from A. Das et al [38] (for a more detailed discussion see the appendix). We note that the values of κ^{BB}/T^2 and κ^{QB}/T^2 for high T at $\mu_B = 0.4$ GeV is larger than at $\mu_B = 0.6$ GeV in the IHRG model. When T is high enough the value of κ^{QB}/T^2 at $\mu_B = 0.2$ GeV can overtake that at $\mu_B = 0.4$ GeV, such decreasing dependence of κ^{BB} and κ^{QB} on μ_B in high T regions is consistent with the results in the QGP within dynamical quasi-particle model [37] and holographic model [82, 83]. Strikingly different with the σ^{BB}/T, the κ^{BB}/T^2 nearly is unaffected by the RMF interactions at $\mu_B = 0.6$ GeV as in Fig. 2. This is because that the decrease in $\sigma^{BB/T}$ and increase in the integral of $\sum_a \widetilde{\epsilon}_a^2 n_B^2/(\omega^2 T^2) \bar{f}_a^0 (1 \pm \bar{f}_a^0)$ caused by the RMF correction in Eq. (40) are nearly cancelled out. In Fig. 2, we also note that the RMF correction can increase $-\kappa^{BS}/T^2$ at $\mu_B = 0.6$ GeV, which is opposite to the behavior of $-\sigma^{BS}/T^2$ at $\mu_B = 0.6$ GeV shown in Fig. 1. This can also be well understood from Eq. (40), in which the integral term related to $-\sum_a S_a \widetilde{\epsilon}_a n_B/(\omega T^2) \bar{f}_a^0 (1 \pm \bar{f}_a^0)$ is enhanced by the inclusion of RMF correction, and this increase can overwhelm the reduction in $-\sigma^{BS}$ caused by the RMF correction, resulting in an enhancement on $-\kappa^{BS}/T^2$. Here, we comment that although in the state-

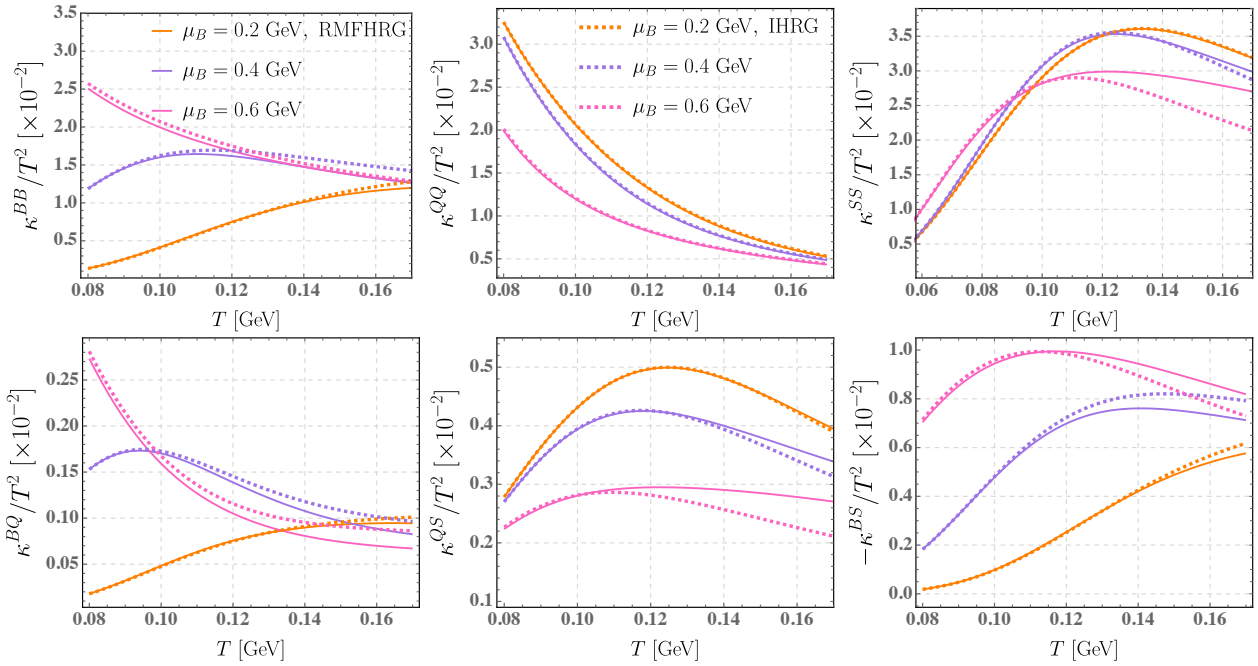


FIG. 2: The temperature dependence of complete scaled diffusion coefficient matrix $\kappa^{qq'}/T^2$ at $\mu_B = 0.2$ GeV (orange), 0.4 GeV (purple), 0.6 GeV (magenta) in the IHRG model (dotted lines) and RMFHRG model (solid lines).

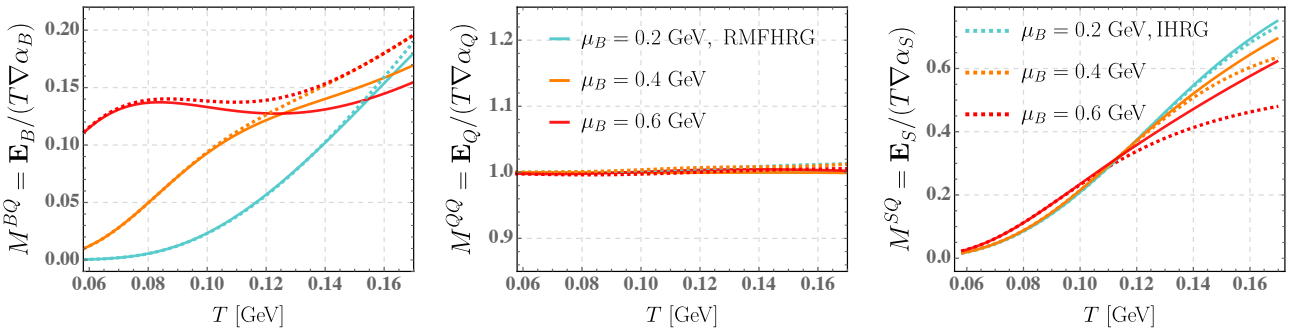


FIG. 3: The temperature dependence of conserved charge diffusion thermopower matrix M^{qQ} at $\mu_B = 0.2$ GeV (green), 0.4 GeV (orange), 0.6 GeV (red) in the IHRG model (dashed lines) and RMFHRG model (solid lines). The total induced electric field is presented as $\boldsymbol{E} = \boldsymbol{E}_B + \boldsymbol{E}_Q + \boldsymbol{E}_S$ with $\boldsymbol{E}_q$ being the induced electric field by the gradients in conserved charge chemical potential μ_q.

ment of Refs. [35–37], the matching condition in the local rest frame is imposed during the derivation of diffusion coefficient matrix, the obtained expression is similar to the $\eta^{qq'}T$ without the quantum statistic effect and repulsive mean-field effect in Eq. (41) (for detailed discussion see the appendix).

Until now, we have discussed the case that the gradients of conserved charge densities are completely directly converted to the diffusion currents. As mentioned in the introduction, the gradients of conserved charge densities can also produce an electric field, which in turn affects the diffusion currents of conserved charges. To exhibit the response of the electric field to conserved charge chemical thermal potential gradients, we display the variation of diffusion thermopower matrix M^{qQ} with T and μ_B in both the IHRG and RMFHRG models. As shown in Fig. 3, we observe that both M^{BQ} and M^{SQ} are increasing functions with T, whereas the M^{QQ} almost remains unchanged and approaches 1. This behavior of M^{QQ} can well be understood from Eq. (43), where κ^{QQ}/T^2 is almost in magnitude equal to η^{QQ}/T. We note M^{BQ} is the smallest, meaning the hadron gas (mainly protons) has a weak ability to convert the gradient of baryon chemical thermal potential into an electric field. With increasing μ_B, we see that M^{BQ} visibly increases, while at high T, M^{BQ} for different μ_B gradually converge. The decrease

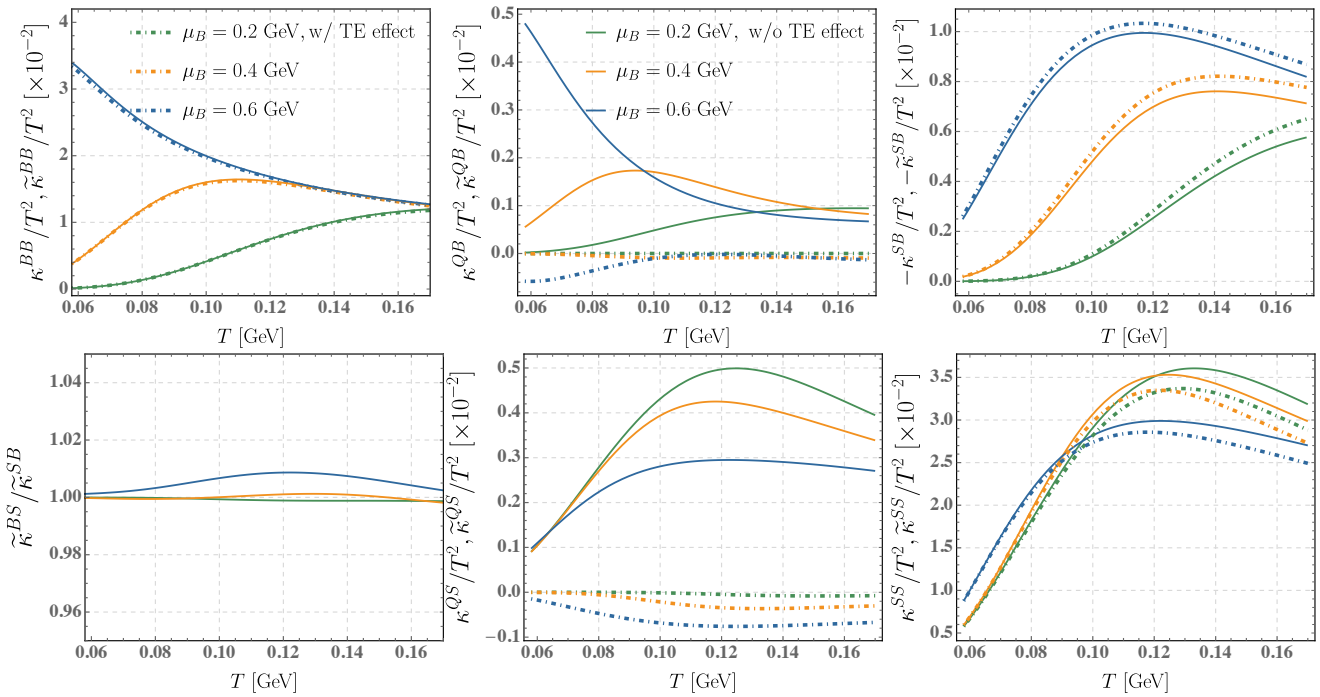


FIG. 4: The comparison between diffusion coefficients matrix $\kappa^{qq''}/T^2$ (solid lines) and thermoelectric modified diffusion coefficient matrix $\widetilde{\kappa}^{qq''}/T^2$ (dot-dashed lines) in the RMFHRG model at $\mu_B = 0.2$ GeV (green), 0.4 GeV (orange), 0.6 GeV (blue) is shown. The below left panel represents the degree of asymmetry between $\widetilde{\kappa}^{BS}$ and $\widetilde{\kappa}^{SB}$.

of M^{SQ} with μ_B in high T region due to that the strong dependence of κ^{SQ}/T^2 on μ_B dominates over the decreasing nature of T/η^{QQ} with μ_B. In Fig. 3, we also observe that the RMF correction can give a significant enhancement on M^{SQ} and reduction on M^{BQ} at high μ_B, such responses mainly stem from κ^{SQ} and κ^{BQ}, respectively.

To intuitively exhibit the impact of the thermoelectric effect on the diffusion coefficient matrix, in Fig. 4 we give a comparison between $\kappa^{qq'}/T^2$ and $\widetilde{\kappa}^{qq'}/T^2$ in the RMFHRG model. Once the thermoelectric effect is considered, diffusion coefficients in the electric charge sector vanish, only diffusion coefficients in the baryon and strangeness sectors exist. We first discuss the diffusion coefficients in the baryon sector. In the upper panel of Fig. 4 we see that the κ^{BB} is nearly unaffected by the thermoelectric effect, which can be well understood from Eq. (45) that the product of M^{BQ} and η^{BQ} is so nominal in magnitude compared to κ^{BB}. The thermoelectric effect can enhance $-\kappa^{SB}/T^2$, which further reduces the net baryon current. It's worth noting that the thermoelectric effect can significantly suppress κ^{QB}/T^2 (κ^{QS}/T^2), making $\widetilde{\kappa}^{QB}$ ($\widetilde{\kappa}^{QS}$) much smaller than κ^{BQ} (κ^{SQ}) and even changing the sign. This means that the thermoelectric effect significantly decouples the correlation between electric current and baryon (strangeness) current, making the gradient of electric chemical potential insignificant for baryon (strangeness) diffusion. Hence, the baryon diffusion current can be reduced by the thermoelectric effect, and $V_B \approx \widetilde{\kappa}^{BB}\nabla\alpha_B + \widetilde{\kappa}^{BS}\nabla\alpha_S$ if gradients have comparable magnitude. As shown in the lower left panel of Fig. 4, the inclusion of thermoelectric effect does not explicitly break the symmetry between $\widetilde{\kappa}^{SB}$ and $\widetilde{\kappa}^{BS}$. Different from κ^{BB}/T^2, we observe that the inclusion of the thermoelectric effect can obviously decrease κ^{SS}/T^2, as a result, the strangeness diffusion current has a significant reduction. We remark that the T and μ_B dependence of $\widetilde{\kappa}^{qq''}/T^2$ is still consistent with that of $\kappa^{qq''}/T^2$.

B. Results for finite magnetic field

We also study the magneto-thermoelectric effect of hadronic matter and examine its impact on both the magnetic field-dependent diffusion coefficient matrix and the Hall-like diffusion coefficient matrix. So far, the realistic time evolution of initial magnetic field is unclear, according to the naive parametrization $eH(\sqrt{s_{NN}}) = 0.021\sqrt{s_{NN}}m_\pi^2$ (m_π is the pion mass) for Au+Au collisions with fixed collision parameter $b = 10$ fm [84], using $eH = eH_0(\tau_0/\tau)^a$ with $a = 1$, $eH \sim 4m_\pi^2$ for the thermalization timescale $\tau_0 \sim 1$ fm, we can get $eH \sim 0.008$ GeV^2 for the hadronization time scale $\tau \sim 10$ fm. In this work, the magnetic field region is taken $eH \in [0 \sim 0.005]$ GeV^2, as done in Ref. [46]. All the estimations at finite magnetic fields are performed in the RMFHRG model with a fixed baryon chemical potential $\mu_B = 0.3$ GeV. As shown in the upper panel of Fig. 5, the temperature dependence of scaled magnetic field-dependent thermoelectric

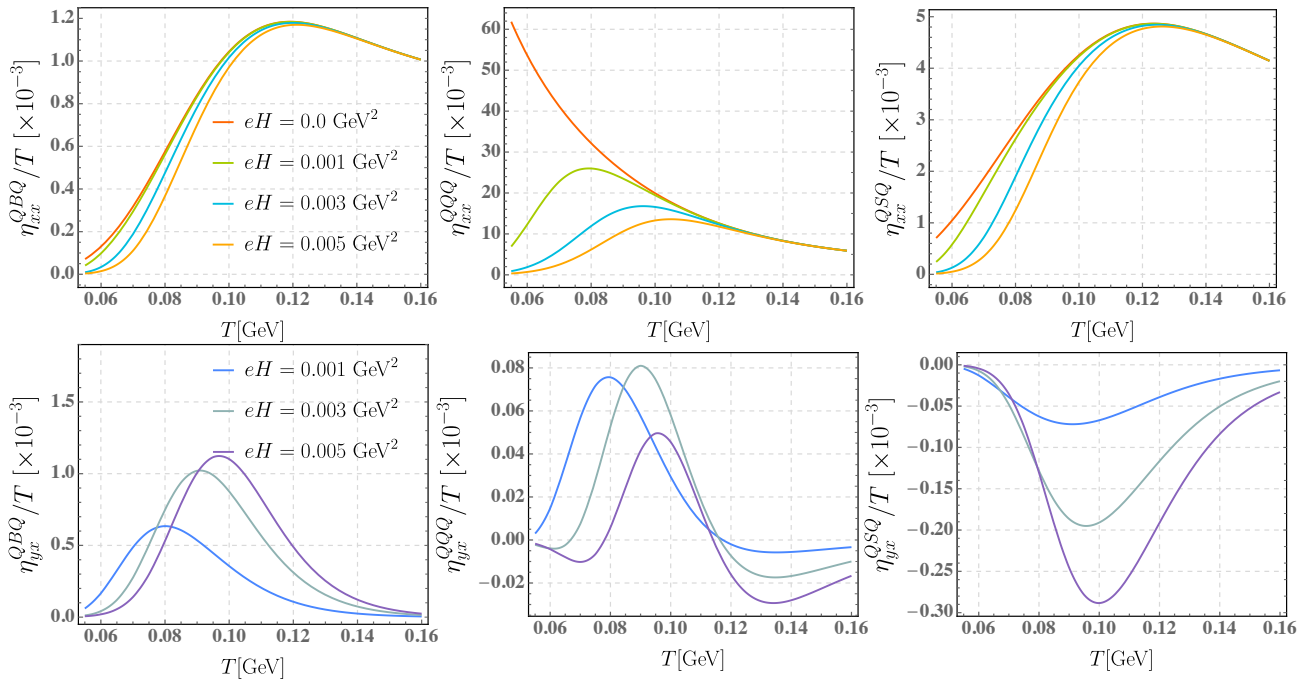


FIG. 5: (Upper panel) The scaled magnetic field-dependent thermoelectric conductivity matrix η^{QqQ}_{xx}/T as a function of temperature in the RMFHRG model for different values of magnetic field, $eH = 0.0$ GeV^2 (warm red), $eH = 0.001$ GeV^2 (warm green), $eH = 0.003$ GeV^2 (warm blue), $eH = 0.005$ GeV^2 (warm orange) at $\mu_B = 0.3$ GeV. (Lower panel) The scaled Hall-like thermoelectric conductivity matrix η^{QqQ}_{yx}/T as a function of temperature in thhe RMFHRG model for $eH = 0.001$ GeV^2 (cool blue), $eH = 0.003$ GeV^2 (cool green), $eH = 0.005$ GeV^2 (cool purple) at $\mu_B = 0.3$ GeV.

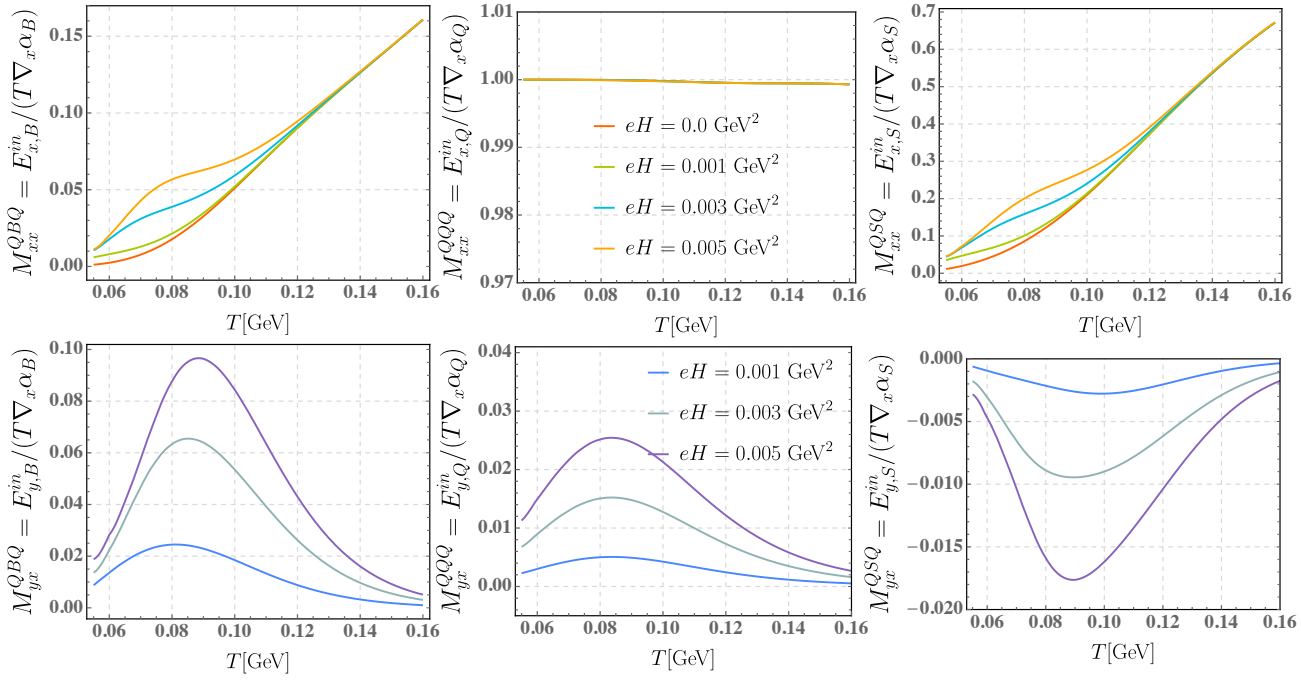


FIG. 6: Same as Fig. 5 for magnetic field-dependent diffusion thermopower matrix M^{QqQ}_{xx} and Hall-like diffusion thermopower matrix M^{QqQ}_{yx}.

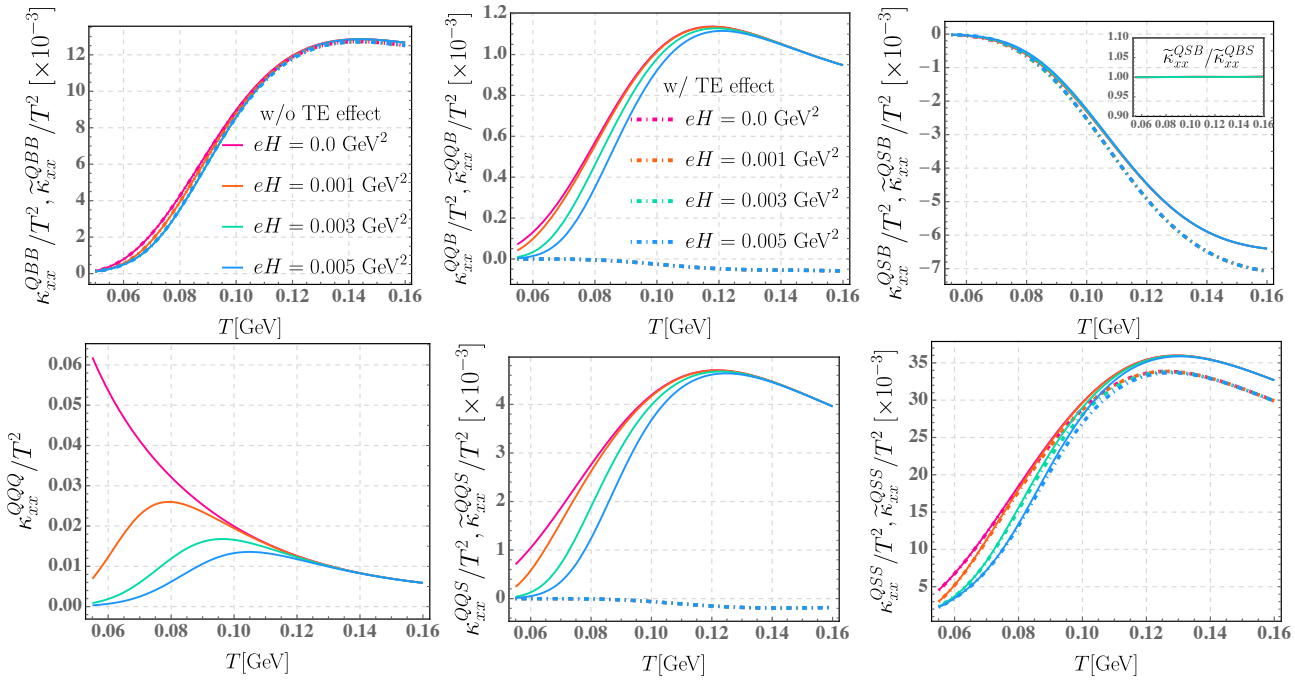


FIG. 7: Both complete scaled magnetic field-dependent diffusion coefficient matrix $\kappa_{xx}^{Qqq'}/T^2$(solid lines) and complete scaled magneto-thermoelectric modified diffusion coefficient matrix $\widetilde{\kappa}_{xx}^{Qqq''}/T^2$ (dot-dashed lines) for $eH = 0.0$ GeV^2 (magenta), 0.001 GeV^2 (red), 0.003 GeV^2 (green), 0.005 GeV^2 (blue) at $\mu_B = 0.3$ GeV in the RMFHRG model. The illustration in the below right panel quantifies the degree of asymmetry between $\widetilde{\kappa}_{xx}^{QBS}$ and $\widetilde{\kappa}_{xx}^{QSB}$.

conductivities η_{xx}^{QqQ}/T at the finite magnetic field is unchanged compared with that at zero magnetic field. It is observed that η_{xx}^{QQQ}/T at the finite magnetic field first increases with temperature and finally decreases. Such non-monotonic behavior of η_{xx}^{QQQ}/T with T mainly is the convoluted result between magnetic field effect and relaxation time in the integrand of Eq. (56), which can be well understood in analogy with the detailed discussion about magnetic field-dependent electric conductivity in Refs. [39, 85]. The dominant carries of η_{xx}^{QQQ}/T are charged pions, the scattering rate of pions at low T is smaller than ω_c, leading $\frac{\tau_a}{(\omega_{c,a}\tau_a)^2+1} \sim 1/(\omega_{c,a}^2\tau_a)$, the pion scattering rate at high T is much larger than ω_c, making $\frac{\tau_a}{(\omega_{c,a}\tau_a)^2+1} \sim \tau_a$. As a result, all the scaled magnetic field-dependent thermoelectric conductivities first decrease as the magnetic field increases and finally converge at high T. From the lower panel of Fig. 5 we also note that all the scaled Hall-like thermoelectric conductivities η_{yx}^{QqQ}/T exhibit a non-monotonic temperature dependence, which is due to the convolution between multiple factors, e.g. the relaxation time, the cyclotron frequency, as well as the factor n_q/ω. In the hadron gas, the predominant protons (p) and Sigma baryons (Σ^+) contribute to η_{yx}^{QqQ}/T. We observe that η_{yx}^{QSQ}/T is negative, this can be analyzed from Eq. (56), in which the dominant integrand term $\sim \sum_a S_a Q_a \widetilde{\epsilon}_a n_Q/\omega \bar{f}_a^0(1+\bar{f}_a^0)$ makes the sign of η_{yx}^{QSQ}/T determined by the strangeness of Sigma baryons. The dependence of η_{yx}^{QBQ}/T on the magnetic field is non-monotonic just because the proton scattering rate in low T region is much smaller than the associated ω_c, leading $\frac{\omega_{c,a}\tau_a^2}{(\omega_{c,a}^2\tau_a)^2+1} \sim 1/\omega_{c,a}$, while in high T region, the proton scattering rate plays a dominant role, $\omega_{c,a}\tau_a \ll 1$, and then $\frac{\omega_{c,a}\tau_a^2}{(\omega_{c,a}\tau_a)^2+1} \sim \omega_{c,a}$. For the η_{yx}^{QSQ}/T, its dependence on the magnetic field almost is monotonic just because the scattering rate of predominant Sigma baryons is always larger than $\omega_{c,a}$ in the entire considered T region. We also note the magnetic field dependence of η_{yx}^{QQQ}/T is similar to that of η_{yx}^{QBQ}/T, but its sign is different at low and high T. This is because the behaviors of η_{yx}^{QQQ}/T at low (high) T are determined by the contribution from protons (Sigma baryons).

Next, we discuss the qualitative behaviors of both magnetic field-dependent diffusion thermopower matrix M_{xx}^{QqQ} and Hall-like diffusion thermopower matrix M_{yx}^{QqQ} with temperature and magnetic field, respectively. As shown in the upper panel of Fig. 6, the magnetic field effect gives an enhancement on both M_{xx}^{QBQ} and M_{xx}^{QSQ} in low T region, which means the ability of hadron gas to convert baryon and strangeness chemical potential gradients to the electric field is strengthened by adding magnetic field, whereas the M_{xx}^{QQQ} seems almost magnetic field-independent. All M_{yx}^{QqQ} show a strong dependence on the magnetic field in the studied temperature region.

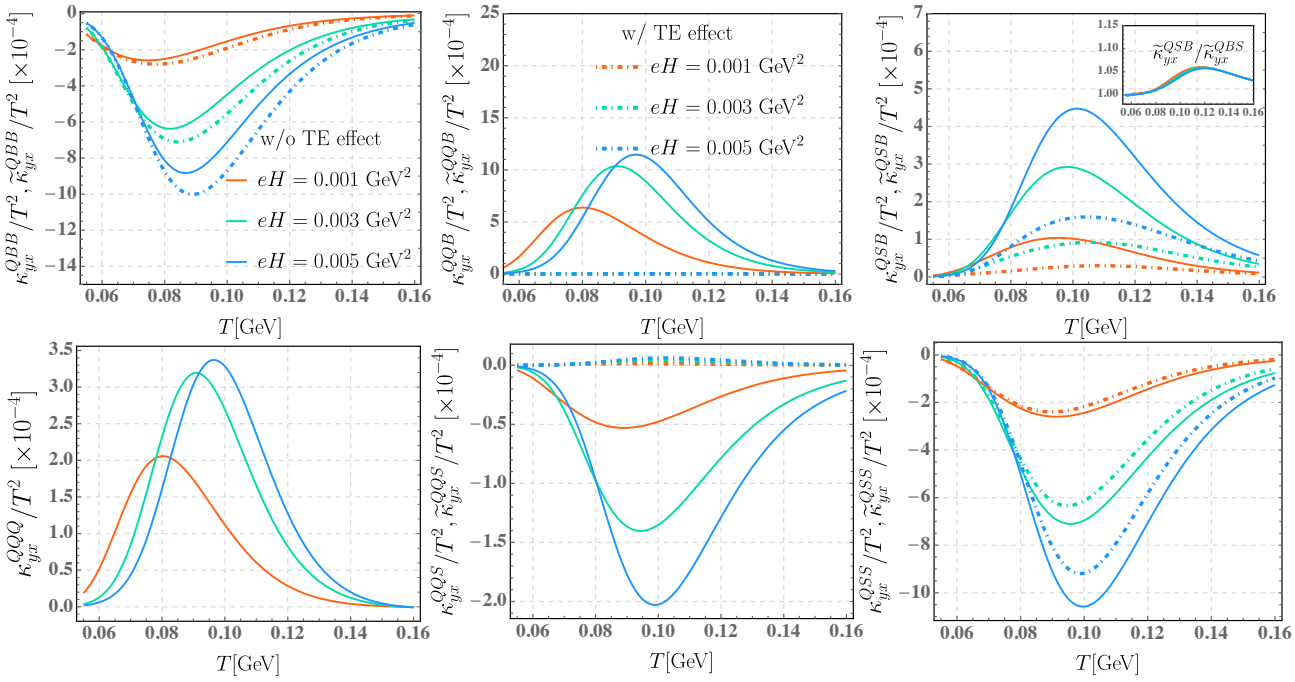


FIG. 8: Same as Fig. 7 for both complete scaled Hall-like diffusion coefficient matrix $\kappa_{yx}^{Qqq'}/T^2$ and complete scaled magneto-thermoelectric modified Hall-like diffusion coefficient matrix $\widetilde{\kappa}_{yx}^{Qqq''}/T^2$.

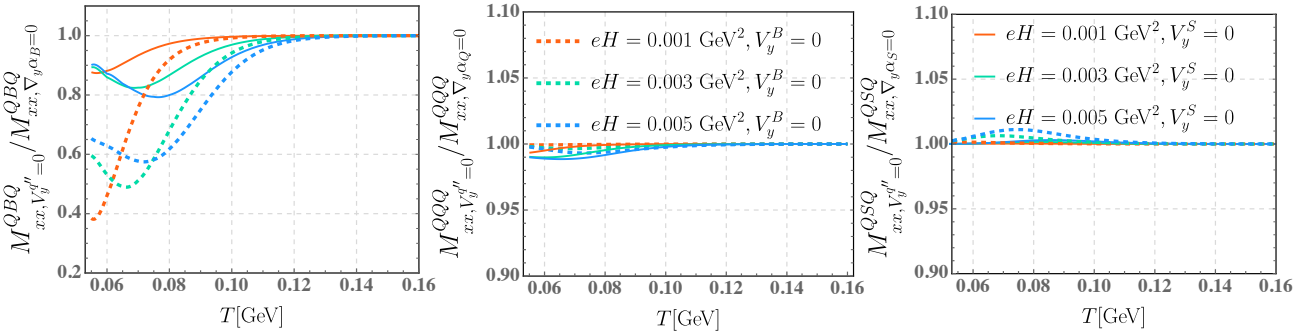


FIG. 9: The ratio of magnetic field-dependent diffusion thermopower matrix under the condition of $V_y^{q''} = 0$ to magnetic field-dependent diffusion thermopower matrix under the condition of $\nabla_y \alpha_q = 0$ as a function of temperature at $eH = 0.001$ GeV^2 (red), 0.003 GeV^2 (green), 0.005 GeV^2 (blue). The dashed lines and solid lines correspond to the results in the condition of $V_y^B = 0$ and the condition of $V_y^S = 0$, respectively. All calculations are performed at $\mu_B = 0.3$ GeV in the RMFHRG model.

As in the lower panel of Fig. 6, all M_{yx}^{QqQ} in magnitude shows a similar peak structure in the entire T region and increases as eH increases. We also note that M_{yx}^{QBQ} is comparable in magnitude with the M_{xx}^{QBQ} at low T.

As in the case of the vanishing magnetic field, we also compare the magnetic field-dependent diffusion coefficient matrix before and after incorporating the magneto-thermoelectric effect in Fig. 7. We note that all $\kappa_{xx}^{Qqq'}/T^2$ except κ_{xx}^{QQQ}/T^2 can not change their shape in the presence of magnetic field, the associated explanation of κ_{xx}^{QQQ}/T^2 is similar to that of η_{xx}^{QQQ}/T. As shown in Fig. 7, κ_{xx}^{QBB} and κ_{xx}^{QSB} in the baryon sector seem insensitive to magnetic field, while the remaining terms have significant reductions in the low T region due to the inclusion of magnetic field. Thus, the presence of a magnetic field can significantly hinder the baryon and electric diffusion if gradients have similar magnitudes. The qualitative behavior of the magneto-thermoelectric modified diffusion coefficient matrix ($\widetilde{\kappa}_{xx}^{Qqq''}$) is consistent with the non-modified one ($\kappa_{xx}^{Qqq''}$). The symmetry between $\widetilde{\kappa}_{xx}^{QSB}$ and $\widetilde{\kappa}_{xx}^{QBS}$ still is satisfied as shown in the illustration of the upper right panel of Fig. 7.

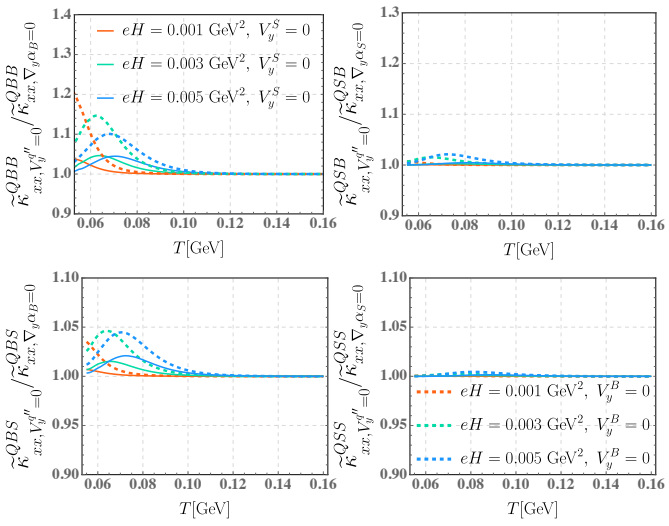


FIG. 10: The ratio of magneto-thermoelectric modified diffusion coefficient matrix under the condition of $V_y^{q''} = 0$ to that under the condition of $\nabla_y \alpha_q = 0$ as a function of temperature at $eH = 0.001$ GeV^2 (red), 0.003 GeV^2 (green), 0.005 GeV^2 (blue). The dashed lines and solid lines correspond to the results in the condition of $V_y^B = 0$ and the condition of $V_y^S = 0$, respectively. All calculations are performed at $\mu_B = 0.3$ GeV in the RMFHRG model.

Compared with $\kappa_{xx}^{Qqq'}/T^2$, all Hall-like diffusion coefficient matrix elements $\kappa_{yx}^{Qqq'}/T^2$ as in Fig. 8 exhibit a strong dependence on the magnetic field and show a peak structure in magnitude. The associated explanation of κ_{yx}^{QQq}/T^2 with T and eH is similar to that of η_{yx}^{QqQ}/T^2. We also note that $\kappa_{yx}^{Qqq''}/T^2$ have obvious responses to the magneto-thermoelectric effect. Similar to $\widetilde{\kappa}_{xx}^{QQB}$ ($\widetilde{\kappa}_{xx}^{QQS}$), the magneto-thermoelectric effect can significantly suppress the magnitude of $\widetilde{\kappa}_{yx}^{QQB}$ ($\widetilde{\kappa}_{yx}^{QQS}$), making the transverse coupling between electric charge and baryon (strangeness) charge nonsignificant in Hall-like baryon (strangeness) current. Strikingly different from κ_{xx}^{QBB}, we find that the magneto-thermoelectric effect can give an obvious enhancement on the magnitude of κ_{yx}^{QBB}. The eH and T dependence of $\widetilde{\kappa}_{yx}^{Qqq''}$ still similar to that of $\kappa_{yx}^{Qqq''}$. One key finding is that the presence of magneto-thermoelectric effect causes a significant asymmetry between $\widetilde{\kappa}_{yx}^{QSB}$ and $\widetilde{\kappa}_{yx}^{QBS}$, as shown in the illustration of the upper right panel of Fig. 8. With the increase of μ_B, the degree of asymmetry can be strengthened further.

The above calculations in terms of magnetic field-dependent diffusion thermopower matrix and magneto-thermoelectric modified diffusion coefficient matrix in the magnetic field background are carried out under the assumption that the conserved charge chemical thermal potential gradients are only limited to the longitudinal direction, i.e., $\nabla_x \alpha_q \neq 0$, $\nabla_y \alpha_q = 0$. As mentioned in Sec. III, under the condition of vanishing transverse diffusion current of conserved charge, i.e., $V_y^{q''} = 0$ with $q'' \in \{B, S\}$, a transverse gradient $\nabla_y \alpha_q$ can be generated by $\nabla_x \alpha_q$, subsequently induces a transverse electric field. In such conditions, the magnitude of the magneto-thermoelectric modified diffusion coefficient matrix may be different from the counterpart under the condition of $\nabla_y \alpha_q = 0$. In Fig. 9, we present the ratio of magnetic field-dependent diffusion thermopower under the conditions of $V_y^B = 0$ and $V_y^S = 0$ to the magnetic field-dependent diffusion thermopower in the condition of $\nabla_y \alpha_q = 0$ to intuitively quantify the difference due to the choice of transverse conditions. We find that choosing the condition of $V_y^{q''} = 0$ can lead to an obvious reduction on M_{xx}^{QBQ} in low T region, whereas both M_{xx}^{QQQ} and M_{xx}^{QSQ} show almost insensitive with varying transverse conditions. This result is unsurprising since, under the condition of $\nabla_y \alpha_q = 0$, the M_{yx}^{QQQ} (M_{yx}^{QSQ}) is much smaller than M_{xx}^{QQQ} (M_{xx}^{QSQ}) as illustrated in Fig. 6, and the $\mathcal{L}^q_{V_y^{q''}=0}$ is always less than 1 due to $|\widetilde{\kappa}_{yx}^{Qqq''}| < |\widetilde{\kappa}_{xx}^{Qqq''}|$, as a result, the product of M_{yx}^{QQQ} (M_{yx}^{QSQ}) and $\mathcal{L}^Q_{V_y^{q''}=0}$ in Eq. (66) is nominal compared to M_{xx}^{QQQ} (M_{xx}^{QSQ}).

Finally, we show the sensitivity of magneto-thermoelectric modified diffusion coefficient matrix $\widetilde{\kappa}_{xx}^{Qqq''}$ to the various choices of transverse conditions in Fig. 10. We don't present the results for $\widetilde{\kappa}_{xx}^{QQB}$ and $\widetilde{\kappa}_{xx}^{QQS}$ because they are of a small order of magnitude compared to the other terms. We observe that taking the magneto-thermoelectric modified diffusion coefficient matrix in the condition of $\nabla_y \alpha_q = 0$ as a baseline, the variation of $\widetilde{\kappa}_{xx}^{Qqq''}$ due to the change in transverse conditions is small, except that $\widetilde{\kappa}_{xx}^{QBB}$ can have a significant reduction in the condition of $V_y^B = 0$ at low T.

V. SUMMARY

We studied the thermoelectric effect and diffusion process of multiple conserved charges in hot and dense hadronic matter. Their corresponding diffusion thermopower matrix M^{qQ} and diffusion coefficient matrix $\kappa^{qq'}$ with $q, q' \in \{B, Q, S\}$ were evaluated in both the IHRG and RMFHRG models by solving the relativistic Boltzmann equation in relaxation time approximation, where the Landau-Lifshitz energy frame was imposed. In the RMFHRG model, the repulsive interaction between hadrons was treated as a density-dependent mean-field potential, leading to a shift in the single-particle energy. In the magnetic field, the additional Hall-like diffusion thermopower matrix M_{yx}^{QqQ} and Hall-like diffusion coefficient matrix $\kappa_{yx}^{Qqq'}$ can emerge. We further explored the impact of magneto-thermoelectric effect on $\kappa_{xx}^{Qqq'}$ and $\kappa_{yx}^{Qqq'}$. The sensitivity of magnetic field-dependent diffusion thermopower matrix M_{xx}^{QqQ} and magneto-thermoelectric modified diffusion coefficient matrix $\widetilde{\kappa}_{xx}^{Qqq'}$ ($q'' \in \{B, S\}$) to different transverse restrictions has also been studied. Here are our main results.

- All diffusion coefficients except κ^{QQ} are sensitive to the RMF interaction in the baryon-rich region, which means the repulsive interaction between hadrons is vital in the diffusion properties of QCD matter created in the lower collision energies.

- Both M^{BQ} and M^{SQ} exhibit a strong dependence on T and μ_B, whereas, the M^{QQ} almost remains unchanged with varying T and μ_B, and nearly equal to 1. The RMF correction can significantly enhance (reduce) M^{SQ} (M^{BQ}) at large μ_B.

- The thermoelectric effect generally prevents the baryon (strangeness) diffusion, and in particular, significantly decouples the correlation between electric charge and baryon number (strangeness).

- In the magnetic field, both M^{QBQ}_{xx} and M^{QSQ}_{xx} increase with the magnetic field at low T, whereas the M^{QQQ}_{xx} is almost magnetic field independent. The magnitude of the complete Hall-like diffusion thermopower matrix is strongly affected by eH and exhibits a peak structure in the considered T region. Compared to M^{QQQ}_{xx} and M^{QSQ}_{xx}, the magnitude of M^{QBQ}_{xx} at low T is sensitive to the choices of various transverse restriction conditions.

- Apart from κ^{QBB}_{xx} and κ^{QSB}_{xx}, remaining diffusion coefficients are sensitive to eH, and decrease with eH at low T. This means that the magnetic field can prevent electric charge and strangeness diffusion. The quantitative and qualitative characteristics of magneto-thermoelectric modified diffusion coefficients remain relatively stable under varying transverse restriction conditions.

- The full Hall-like diffusion coefficients in magnitude have a similar peak structure in the considered T region and exhibit strong magnetic field dependence. It's noted that the symmetry between the strangeness-baryon diffusion coefficient and baryon-strangeness diffusion coefficient could be broken after including the magneto-thermoelectric effect, i.e., $\widetilde{\kappa}^{QSB}_{yx} \neq \widetilde{\kappa}^{QBS}_{yx}$.

These findings could offer valuable insights into the dynamics of distinct conserved charges and contribute to the development of dissipative (magneto-)hydrodynamics that explicitly account for multiple conserved charges.

ACKNOWLEDGMENTS

This work was supported by Guangdong Major Project of Basic and Applied Basic Research (2020B0301030008), the Natural Science Foundation of China (12247132), and the China Postdoctoral Science Foundation (2023M731159).

APPENDIX

In Fig. 11, we present a comparison between the diffusion coefficient matrix result in this investigation and the diffusion coefficient matrix result from A. Das et al [38] within the IHRG model. In Ref. [38], the diffusion coefficient matrix $\kappa^{qq'}$ is obtained as

$$\kappa^{qq'} = \sum_a \frac{d_a}{3}\int \frac{d^3p_a}{(2\pi)^3}\tau_a \frac{\boldsymbol{p}_a^2}{(\epsilon_a^0)^2}\left[q'_a - \epsilon_a^0\frac{n'_q}{\omega}\right] \times \left[q_a - \epsilon_a^0\frac{n_q}{\omega}\right] f_a^{(0)}, \tag{75}$$

with $f_a^{(0)}$ being the equilibrium distribution function in the classical limit, i.e., the Boltzmann distribution function. As shown in Fig. 11, it's clear that our full diffusion coefficient results are close to the results of A. Das et al. The small numerical discrepancy mainly comes from the different choices in degrees of freedom and the lack of quantum statistic effect in [38].

Alternatively, we note that the expression of $\kappa^{qq'}$, which has been derived in Refs [35–37] is different from ours. In Refs. [35–37], it is given as

$$\kappa^{qq'} = \frac{\tau}{3}\sum_a \frac{d^3p_a}{(2\pi)^3}\frac{\boldsymbol{p_a^2}}{(\epsilon_a^0)^2}(q'_a - \frac{\epsilon_a^0 n'_q}{\omega})q_a f_a^{(0)} \tag{76}$$

$$= \frac{\tau}{3}\sum_a \frac{d^3p_a}{(2\pi)^3}\frac{\boldsymbol{p_a^2}}{(\epsilon_a^0)^2}q'_a q_a f_a^{(0)} - \tau\frac{T n_{q'} n_q}{\omega}. \tag{77}$$

In Ref. [36], a constant relaxation time τ for all the hadron species is used. Comparing with the thermoelectric transport coefficient $\eta^{qq'}$ in Eq. (41), the $\eta^{qq'}/T$ is formally similar to the $\kappa^{qq'}/T^2$ obtained in Refs. [35–37] by ignoring the quantum statistic effect and repulsive mean-field effect. As shown in Fig. 12, our results are smaller than the results in Ref. [36], and the qualitative behaviors of $\kappa^{qq'}/T^2$ in the baryon current are also slightly different to the results in Ref. [36]. It is clear that η^{BS}/T in Fig. 12 is not equivalent to η^{SB}/T at $\mu_B = 0.6$ GeV. This means that the symmetry of the off-diagonal diffusion coefficients ($\kappa^{qq'} = \kappa^{q'q}$) illustrated in Refs. [35, 36] is not strictly valid once the quantum statistic effect is considered. Comparing Fig. 2 and Fig. 12, we also observe that the quantitative and qualitative discrepancy between $\kappa^{qq'}/T^2$ and $\eta^{qq'}/T$ is minimal, thus the numerical discrepancy between the diffusion coefficient matrix in this investigation and in Ref. [36] mainly stems from the numbers of degrees of freedom and relaxation time.

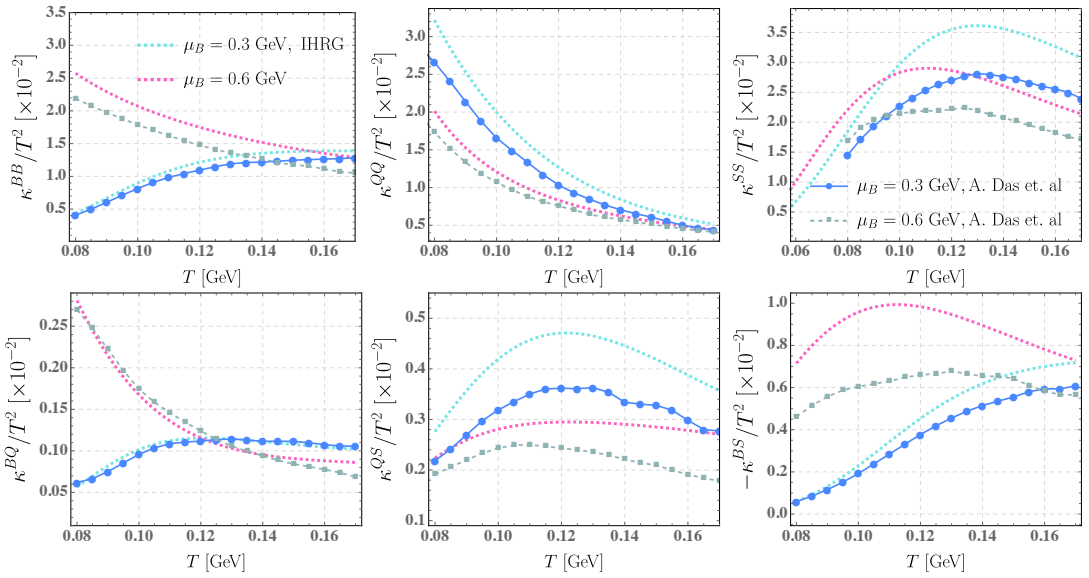


FIG. 11: The diffusion coefficient matrix result from A. Das et al [38] compared with our result in the IHRG model with the same setting ($n_S = 0,\ \mu_Q = 0$). The symbol lines are the results from A. Das et al in the IHRG model at $\mu_B = 0.3$ GeV (circles) and $\mu_B = 0.6$ GeV(squares), respectively.

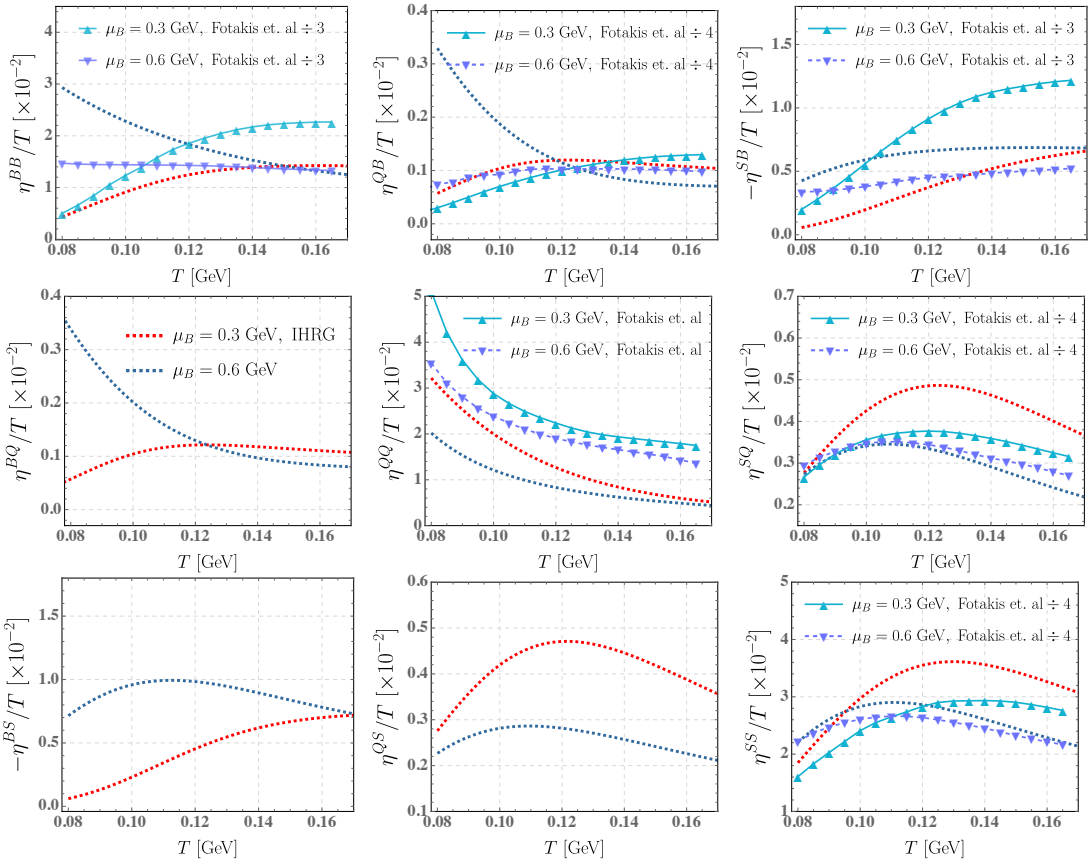


FIG. 12: The temperature dependence of scaled thermoelectric transport coefficient matrix $\eta^{qq'}/T$ in baryon (top row), electric (middle row), strangeness sectors (bottom row) at $\mu_B = 0.3$ GeV (red), 0.6 GeV (blue) within the IHRG model (dashed lines). These results are compared with the diffusion coefficient matrix result by Fotakis et al at $\mu_B = 0.3$ GeV (upper triangles) and 0.6 GeV (lower triangles) with the same setting ($n_S = 0,\ \mu_Q = 0$). [36].

[1] I. Arsene *et al.* [BRAHMS], Nucl. Phys. A **757**, 1-27 (2005)
[2] B. B. Back *et al.* [PHOBOS], Nucl. Phys. A **757**, 28-101 (2005).
[3] K. Adcox *et al.* [PHENIX], Nucl. Phys. A **757**, 184-283 (2005).
[4] J. Adams *et al.* [STAR], Nucl. Phys. A **757**, 102-183 (2005).
[5] K. Aamodt *et al.* [ALICE], Phys. Rev. Lett. **105**, 252301 (2010).
[6] S. Chatrchyan *et al.* [CMS], JHEP **08**, 141 (2011).
[7] G. Aad *et al.* [ATLAS], Phys. Lett. B **707**, 330-348 (2012).
[8] S. Chatrchyan *et al.* [CMS], Eur. Phys. J. C **72**, 2012 (2012).
[9] S. Chatrchyan *et al.* [CMS], Phys. Rev. C **84**, 024906 (2011).
[10] K. Aamodt *et al.* [ALICE], Phys. Lett. B **696**, 30-39 (2011).
[11] Y. Aoki, G. Endrodi, Z. Fodor, S. D. Katz and K. K. Szabo, Nature **443**, 675-678 (2006).
[12] M. Cheng, N. H. Christ, S. Datta, J. van der Heide, C. Jung, F. Karsch, O. Kaczmarek, E. Laermann, R. D. Mawhinney and C. Miao, *et al.* Phys. Rev. D **74**, 054507 (2006).
[13] O. Philipsen, Prog. Part. Nucl. Phys. **70**, 55-107 (2013).
[14] Y. Nambu and G. Jona-Lasinio, Phys. Rev. **122**, 345-358 (1961).
[15] T. Hatsuda and T. Kunihiro, Phys. Rept. **247**, 221-367 (1994).
[16] K. Fukushima, Phys. Rev. D **77**, 114028 (2008) [erratum: Phys. Rev. D **78**, 039902 (2008)].
[17] B. J. Schaefer and J. Wambach, Phys. Rev. D **75**, 085015 (2007).
[18] B. J. Schaefer and M. Wagner, Phys. Rev. D **79**, 014018 (2009).
[19] B. J. Schaefer, J. M. Pawlowski and J. Wambach, Phys. Rev. D **76**, 074023 (2007).
[20] B. J. Schaefer and M. Wagner, Phys. Rev. D **85**, 034027 (2012).
[21] R. A. Lacey, Phys. Rev. Lett. **114**, no.14, 142301 (2015).
[22] M. M. Aggarwal *et al.* [STAR], [arXiv:1007.2613 [nucl-ex]].
[23] B. Mohanty [STAR], J. Phys. G **38**, 124023 (2011).
[24] N. A. Tahir, C. Deutsch, V. E. Fortov, V. Gryaznov, D. H. H. Hoffmann, M. Kulish, I. V. Lomonosov, V. Mintsev, P. Ni and D. Nikolaev, *et al.* Phys. Rev. Lett. **95**, 035001 (2005).
[25] T. Ablyazimov *et al.* [CBM], Eur. Phys. J. A **53**, no.3, 60 (2017).
[26] B. Friman, C. Hohne, J. Knoll, S. Leupold, J. Randrup, R. Rapp, and P. Senger, *The CBM Physics Book: Compressed Baryonic Matter in Laboratory Experiments* (Springer, New York, 2011).
[27] V. Kekelidze, R. Lednicky, V. Matveev, I. Meshkov, A. Sorin and G. Trubnikov, Phys. Part. Nucl. Lett. **9**, 313-316 (2012).
[28] P. Romatschke and U. Romatschke, Phys. Rev. Lett. **99**, 172301 (2007).
[29] P. Kovtun, D. T. Son and A. O. Starinets, Phys. Rev. Lett. **94**, 111601 (2005).
[30] U. Heinz and R. Snellings, Ann. Rev. Nucl. Part. Sci. **63**, 123-151 (2013).
[31] C. Sasaki and K. Redlich, Phys. Rev. C **79**, 055207 (2009).
[32] F. Karsch, D. Kharzeev and K. Tuchin, Phys. Lett. B **663**, 217-221 (2008).
[33] V. Roy, S. Pu, L. Rezzolla and D. Rischke, Phys. Lett. B **750**, 45-52 (2015).
[34] V. Roy, S. Pu, L. Rezzolla and D. H. Rischke, Phys. Rev. C **96**, no.5, 054909 (2017).
[35] M. Greif, J. A. Fotakis, G. S. Denicol and C. Greiner, Phys. Rev. Lett. **120**, no.24, 242301 (2018).
[36] J. A. Fotakis, M. Greif, C. Greiner, G. S. Denicol and H. Niemi, Phys. Rev. D **101**, no.7, 076007 (2020).
[37] J. A. Fotakis, O. Soloveva, C. Greiner, O. Kaczmarek and E. Bratkovskaya, Phys. Rev. D **104**, no.3, 034014 (2021).
[38] A. Das, H. Mishra and R. K. Mohapatra, Phys. Rev. D **106**, no.1, 014013 (2022).
[39] H. X. Zhang, J. W. Kang and B. W. Zhang, Eur. Phys. J. C **81**, no.7, 623 (2021).
[40] A. Das and H. Mishra, Eur. Phys. J. ST **230**, no.3, 607-634 (2021).
[41] H. X. Zhang, Y. X. Xiao, J. W. Kang and B. W. Zhang, Nucl. Sci. Tech. **33**, no.11, 150 (2022).
[42] M. Kurian, Phys. Rev. D **103**, no.5, 054024 (2021).
[43] D. Dey and B. K. Patra, Phys. Rev. D **102**, no.9, 096011 (2020).
[44] D. Dey and B. K. Patra, Phys. Rev. D **104**, 076021 (2021).
[45] S. A. Khan and B. K. Patra, Phys. Rev. D **107**, no.7, 074034 (2023).
[46] A. Das, H. Mishra and R. K. Mohapatra, Phys. Rev. D **102**, no.1, 014030 (2020).
[47] J. R. Bhatt, A. Das and H. Mishra, Phys. Rev. D **99**, no.1, 014015 (2019).
[48] S. Y. F. Liu and Y. Yin, Phys. Rev. D **104**, no.5, 054043 (2021).
[49] B. Fu, L. Pang, H. Song and Y. Yin, [arXiv:2201.12970 [hep-ph]].
[50] V. Voronyuk, V. D. Toneev, W. Cassing, E. L. Bratkovskaya, V. P. Konchakovski and S. A. Voloshin, Phys. Rev. C **83**, 054911 (2011).
[51] K. Tuchin, Phys. Rev. C **83**, 017901 (2011).
[52] L. McLerran and V. Skokov, Nucl. Phys. A **929**, 184-190 (2014).
[53] J. Cleymans and K. Redlich, Phys. Rev. C **60**, 054908 (1999).
[54] F. Becattini, J. Cleymans, A. Keranen, E. Suhonen and K. Redlich, Phys. Rev. C **64**, 024901 (2001).
[55] D. H. Rischke, M. I. Gorenstein, H. Stoecker and W. Greiner, Z. Phys. C **51**, 485-490 (1991).
[56] A. Andronic, P. Braun-Munzinger, J. Stachel and M. Winn, Phys. Lett. B **718**, 80-85 (2012).
[57] G. P. Kadam and H. Mishra, Phys. Rev. C **92**, no.3, 035203 (2015).
[58] V. Vovchenko, M. I. Gorenstein and H. Stoecker, Phys. Rev. Lett. **118**, no.18, 182301 (2017).
[59] V. Vovchenko, A. Motornenko, P. Alba, M. I. Gorenstein, L. M. Satarov and H. Stoecker, Phys. Rev. C **96**, no.4, 045202 (2017).

[60] P. Huovinen and P. Petreczky, Phys. Lett. B **777**, 125-130 (2018).

[61] S. Pal, G. Kadam and A. Bhattacharyya, [arXiv:2305.13212 [hep-ph]].

[62] G. Kadam and H. Mishra, Phys. Rev. D **100**, no.7, 074015 (2019).

[63] S. Pal, G. Kadam, H. Mishra and A. Bhattacharyya, Phys. Rev. D **103**, no.5, 054015 (2021).

[64] K. A. Olive, Nucl. Phys. B **190**, 483-503 (1981).

[65] J. Weil *et al.* [SMASH], Phys. Rev. C **94**, no.5, 054905 (2016).

[66] P. Chakraborty and J. I. Kapusta, Phys. Rev. C **83**, 014906 (2011).

[67] M. Albright and J. I. Kapusta, Phys. Rev. C **93**, no.1, 014903 (2016).

[68] J. L. Anderson and H. R. Witting, Physica 74, 466 (1974).

[69] J. A. Fotakis, E. Molnár, H. Niemi, C. Greiner and D. H. Rischke, Phys. Rev. D **106**, no.3, 036009 (2022).

[70] E. Molnar, H. Niemi and D. H. Rischke, Phys. Rev. D **93**, no.11, 114025 (2016).

[71] R. Derradi de Souza, T. Koide and T. Kodama, Prog. Part. Nucl. Phys. **86**, 35-85 (2016).

[72] Callen, H. B. (1948). *The Application of Onsager's Reciprocal Relations to Thermoelectric, Thermomagnetic, and Galvanomagnetic Effects.* Physical Review, 73(11), 1349–1358.

[73] Redin, R. D., *Thermomagnetic and galvanomagnetic effects* (1957). Ames Laboratory ISC Technical Reports. 176.

[74] M. E. Peskin and D. V. Schroeder, *An Introduction to quantum field theory*, Addison-Wesley, 1995, ISBN 978-0-201-50397-5.

[75] C. Greiner, P. Koch and H. Stoecker, Phys. Rev. Lett. **58**, 1825-1828 (1987).

[76] J. Cleymans and H. Satz, Z. Phys. C **57**, 135-148 (1993).

[77] V. Vovchenko and H. Stoecker, Comput. Phys. Commun. **244**, 295-310 (2019).

[78] J. Cleymans, H. Oeschler, K. Redlich and S. Wheaton, Phys. Rev. C **73**, 034905 (2006).

[79] G. Odyniec, J. Phys. Conf. Ser. **455**, 012037 (2013).

[80] B. Aboona *et al.* [STAR], Phys. Rev. Lett. **130**, no.8, 082301 (2023).

[81] J. Hammelmann, J. Staudenmaier and H. Elfner, [arXiv:2307.15606 [nucl-th]].

[82] J. Grefa, M. Hippert, J. Noronha, J. Noronha-Hostler, I. Portillo, C. Ratti and R. Rougemont, Phys. Rev. D **106**, no.3, 034024 (2022)

[83] R. Rougemont, J. Noronha and J. Noronha-Hostler, Phys. Rev. Lett. **115**, no.20, 202301 (2015).

[84] W. T. Deng and X. G. Huang, Phys. Rev. C **85**, 044907 (2012).

[85] A. Das, H. Mishra and R. K. Mohapatra, Phys. Rev. D **99**, no.9, 094031 (2019), Phys. Rev. D **101**, no.3, 034027 (2020).

The Mass Gap of the Space-time and its Shape

Ahmed Farag Ali[△▽*]

[△]*Essex County College, 303 University Ave,*

Newark, NJ 07102, United States. and

[▽]*Department of Physics, Faculty of Science,*

Benha University, Benha, 13518, Egypt.

arXiv:2403.02655v1 [hep-th] 5 Mar 2024

Abstract

Snyder's quantum space-time which is Lorentz invariant is investigated. It is found that the quanta of space-time have a positive mass that is interpreted as a positive real mass gap of space-time. This mass gap is related to the minimal length of measurement which is provided by Snyder's algebra. Several reasons to consider the space-time quanta as a 24-cell are discussed. Geometric reasons include its self-duality property and its 24 vertices that may represent the standard model of elementary particles. The 24-cell symmetry group is the Weyl/Coxeter group of the F_4 group which was found recently to generate the gauge group of the standard model. It is found that 24-cell may provide a geometric interpretation of the mass generation, Avogadro number, color confinement, and the flatness of the observable universe. The phenomenology and consistency with measurements is discussed.

"The knowledge at which geometry aims is knowledge of the eternal"— Plato.

*Electronic address: aali29@essex.edu

Contents

I. Introduction 2

II. space-time quanta and Bekensetin universal bound 3

III. Shape of space-time quanta 4

IV. Symmetry of space-time quanta 7

V. space-time quanta and Spectral mass gap 8

VI. Phenomenological implications 9

VII. conclusion 10

Acknowledgments 11

References 11

I. INTRODUCTION

In 1947, Snyder established a remarkable step that reconciles the minimal length of measurement with Lorentz symmetry by constructing quantum Lorentzian space-time [1]. The price was introducing non-commutative geometry and the generalized uncertainty principle (GUP) in Snyder's algebra. For Non-commutative geometry part, it is found to emerge naturally at limits of M/string theory [2] as higher dimensional corrections of ordinary Yang-Mills theory [3]. Several implications of non-commutative geometry were investigated in quantum field theory and condensed matter systems [4, 5]. For the GUP part, it emerged in several approaches to quantum gravity such as string theory, loop quantum gravity, and quantum geometry [6–12]. Phenomenological and experimental implications of the GUP have been investigated in low and high-energy systems [13–25]. Useful reviews on quantum space-time and GUP can be found in [26–28]. Snyder's algebra is generated by three main generators which are position x_μ, momentum p_μ and Lorentz generators $J_{\mu\nu} = x_\mu p_\nu - x_\nu p_\mu$. They satisfy the Poincaré commutation relations and suggest new commutation relations

that provide a quantum/minimal length as follows:

$$[x_\mu, x_\nu] = i\hbar\ (\frac{\kappa\ \ell_{Pl}}{\hbar c})^2\ J_{\mu\nu}, \tag{1}$$

$$[x_\mu, p_\nu] = i\hbar\ (\eta_{\mu\nu} + (\frac{\kappa\ \ell_{Pl}}{\hbar c})^2\ p_\mu p_\nu), \text{with} \qquad \mu, \nu = 0, 1, 2, 3 \tag{2}$$

where ℓ_{Pl} is a Planck length, κ is a dimensionless parameter that identifies the minimal measurable length, and $\eta_{\mu\nu} = (-1, 1, 1, 1)$. Eq. (1) introduces the non-commutative geometry and Eq. (2) introduces a GUP. Both equations are invariant under Lorentz symmetry [1].

II. SPACE-TIME QUANTA AND BEKENSETIN UNIVERSAL BOUND

In this section, we investigate the physical properties of space-time quanta implied by Snyder's algebra. It is clear that Eq. (1) only vanishes if there is no fundamental minimal/quantum length (i.e $\kappa\ell_{Pl} = 0$). This means non-commutative geometry would vanish if there is no minimal/quantum length. On the contrary, we find that the GUP commutation relation in Eq. (2) vanishes. The time-energy commutation relation of Eq. (2) vanishes when:

$$E\ =\ E_\kappa = \pm\ \frac{\hbar\ c}{\kappa\ \ell_{\rm Pl}}, \tag{3}$$

where $E = p_0$ and E_κ represents the maximum bound on energy. The position-momentum commutation relation Eq. (2) vanishes when:

$$p\ =\ p_\kappa = \pm\ i\ \sqrt{3}\ \frac{\hbar}{\kappa\ \ell_{\rm Pl}} \tag{4}$$

where $p = \sqrt{p_x^2 + p_y^2 + p_z^2}$, and p_κ represents momentum bound that are implied by minimal length ($\kappa\ \ell_{\rm Pl}$). This implies "real" solutions for energy and "imaginary" solution for momentum. To put it another way, time and energy can be known with certainty, implying a complete/perfect description of the space-time quanta in terms of time and energy that is invariant under Lorentz transformation which is satisfied by Snyder algebra. The quanta of space-time in that sense behave like perfect classical physics at the minimum measurable length scale in terms of energy and time. This may be consistent with the asymptotic freedom property of Yang–Mills theory in which quantum fields behave at a short distance in a very similar way to classical fields [29, 30]. Vanishing time-energy uncertainty may shed light on the nature of the wavefunction collapse to form the quanta of space-time. Particle

mass has been interpreted as a result of wavefunction collapse [31]. We found recently that vanishing uncertainty could resolve the EPR paradox [32] and explain the radii values of Hydrogen atom/nuclei [33, 34].

On another side, Bekenstein found a universal bound [35–37] that defines the maximal amount of information that is necessary to *perfectly* and completely describes a physical object up to the quantum level. Bekenstein universal bound is given by:

$$H \leq \frac{2\pi\ R\ E}{\hbar\ c} \tag{5}$$

where H is related to thermodynamic entropy as $S = k_B H$, where k_B is the Boltzmann constant. H gives the number of bits contained in the quantum states in the sphere with radius R that encloses the physical system, and E is the energy of the physical system. According to Snyder's algebra in Eq. (1) and Eq. (2), the sphere that encloses the space-time quanta is identified by a radius $R = \kappa\ \ell_{\rm Pl}$. Since the space-time quanta implies bound on energy given by Eq. (3), the inequality in Eq. (5) turns to be equality for space-time quanta that relates the maximum amount of information H_κ to the maximum measurable energy E_κ:

$$E_\kappa = \frac{\hbar\ c}{\kappa\ \ell_{\rm Pl}}\ \frac{H_\kappa}{2\pi} \tag{6}$$

When we compare Eq. (3) with Eq. (6), we get:

$$H_\kappa = 2\ \pi \tag{7}$$

that completely describes the quanta of space-time. Notice here that H_κ depends only on π and is independent of κ and nature constants.

III. SHAPE OF SPACE-TIME QUANTA

A natural question arises, what is the geometric shape of the space-time quanta? To answer this question, we need first to apply the energy-momentum relation that is satisfied by Snyder's algebra [38]:

$$E^2 - p^2c^2 = m^2c^4 \tag{8}$$

where m is the mass of the physical object. Substituting Eq. (3) and Eq. (4) into Eq. (8), we get:

$$m_\kappa = \frac{2}{\kappa\ \ell_{\rm Pl}}\frac{\hbar}{c} \tag{9}$$

This means that the mass of the space-time quanta is completely determined by its unique length and it is strictly a "positive real value". It is worth mentioning that generalized forms of Snyder algebra with de Sitter background imply modification of dispersion relation [39] that may introduce corrections to the mass of space-time quanta obtained in Eq.(9). The flatness of quantum Lorentzian space-time suggests that the space-time quanta be described by 4-polytope geometry [40]. We use elementary particle physics as a guide to building the quanta of space-time. The standard model of particle physics has 25 fundamental particles that include 12 fermions (quarks and leptons), 4 gauge bosons that carry electromagnetic force and weak nuclear force, 8 gluons that carry strong nuclear force, and 1 Higgs scalar field. The quanta of space-time must carry a signature of information from all these fundamental particles that constitute the fundamental structure of nature. The space-time quanta must be "self-dual" as well to preserve its uniqueness. Therefore, we look for a highly symmetric 4-dimensional geometric object that is self-dual and identified by only unique length which could represent the fundamental particles of nature on its vertices. This could be a uniform 4-polytope which is a 4-dimensional object with flat sides/faces and is vertex-transitive symmetric which means an isometric map of any vertex onto any other. A regular 4-polytope has the highest degree of symmetry as its faces/cells are regular polytopes and transitive on the symmetries of the polytope. More symmetries are found in regular 4-polytopes that define the convex region as a subset that intersects every line into a single line segment. There are two self-dual convex regular polytopes that are 5-cell, which has 5 vertices, and 24-cell which has 24 vertices. We choose the 24-cell because it has enough vertices to assign with elementary particles. A representation in a plane of a regular 24-cell is given in Fig. (1):

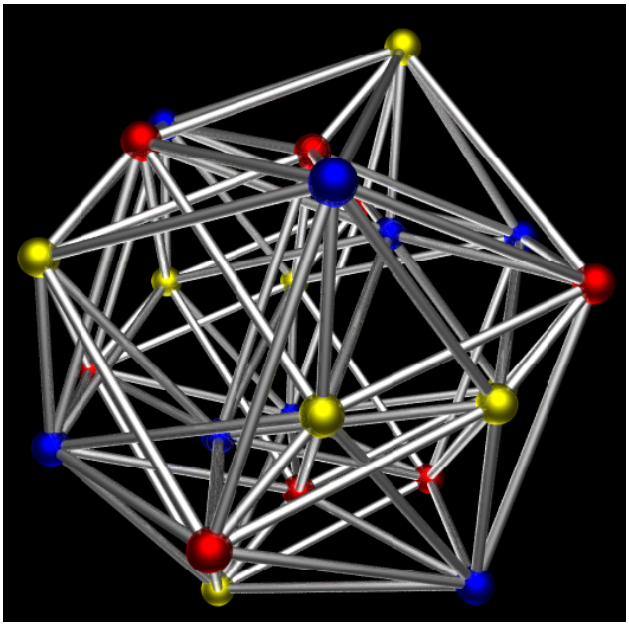


FIG. 1:

24-cell diagram: The vertices of 24-cell are divided into three subsets of three colors, each is a regular 16-cell. Image copied from this link with CC-BY-SA-4.0 license

The 24-cell geometric properties can be summarized as follows:

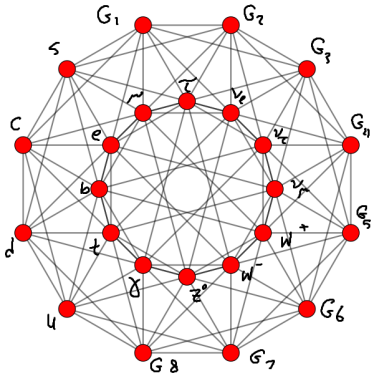
- Its boundary in 3-dimensions forms 24 octahedral cells with six meeting at each vertex, and three at each edge
- It has 96 triangular faces, 96 edges, and 24 vertices. The vertex figure is a cube
- self-dual [41]
- identified by one length where edge length equals the distance between the center and vertex (radius)

The 24-cell exists in 4- dimensional Euclidean geometry, but Minkowski space-time is 4-dimensional "pseudo-Euclidean". This can be simply resolved if time is represented as an imaginary spatial dimension which is well-established in quantum field theory [42] and in Euclidean quantum gravity [43]. To put it another way, the space-time quanta is represented by a 24-cell with considering time as an imaginary spatial dimension. The covariance principle requires that the space-time quanta should represent the elementary particles of the standard model [44]. In the next section, we show how to do this representation.

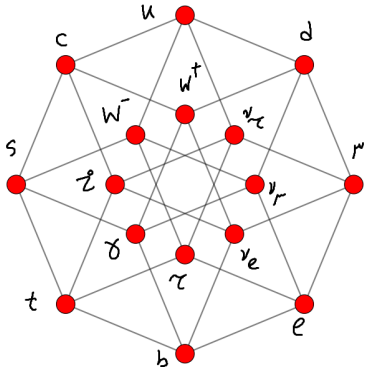
IV. SYMMETRY OF SPACE-TIME QUANTA

The symmetry group of 24-cell is the Weyl/Coxeter group of F_4 group [40]. The 48 root vectors of F_4 represent the vertices of the 24-cell in two dual configurations. F_4 group is one of five exceptional simple Lie groups that are non-abelian and do not have nontrivial connected normal subgroups. The remarkable importance of the F_4 group has been realized recently in [45] to explain the gauge symmetry of the standard model of particle physics. It is proved that F_4 has two stabilizer groups that are $H_1 = (SU(3) \times SU(3))/\mathbb{Z}_3$ and $H_2 = Spin(9)$ that their intersection $H_1 \cap H_2$ generates the standard model gauge symmetry $(SU(3) \times SU(2) \times U(1))/\mathbb{Z}_6$. Further details and implications can be found in [46–58]. This supports our postulate of identifying the space-time quanta as the 24-cell. In addition, a geometric connection between 24-cell and Calabi-Yau Threefolds with Hodge Numbers (1,1) is realized in [59] that was useful in determining the mass spectrum of type-IIB flux vacua [60]. It is worth mentioning that 24-cell was crystallized to represent the spinfoam topology by trivalent spin network [61].

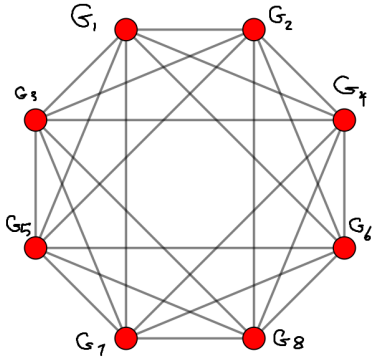
Let us now have a close look at Fig. (1) which shows a representation in a plane of 24-cell, where the vertices are divided into three subsets of three colors, each being a regular 16-cell. 24-cell vertices can be grouped into three different sets of eight vertices each one defining 16-cells with the rest defining the dual tesseract that has sixteen vertices [40]. These three different sets could be used to represent the three colors in quantum chromodynamics. Each set of eight vertices is represented by a 16-cell which is a regular convex 4-polytope that has eight vertices that can represent the eight gluons in the 24-cell. The other sixteen vertices of tesseract could be used to represent the twelve fermions and four gauge bosons. The tesseract is the four-dimensional analog of the cube. In that sense, the 24-cell can be formed by the 16-cell which could be assigned with eight gluons, and the tesseract which could be assigned with twelve fermions and four gauge bosons. Since the Higgs field couples only with the twelve fermions and four gauge bosons, therefore the tesseract as a whole could represent the shape of the Higgs particle. In addition, this property of 24-cell may explain the geometric meaning of preserving the gluons symmetry which may explain the color confinement. Besides, it explains why gluons could have three colors by grouping 24-cell vertices into three different sets of 16-cell as shown in Fig. (1). It also explains the flatness of the observable universe which is composed of 16 observable particles by the tesseract



(a) 24-cell Coxeter plane that represents elementary particles of the standard model



(b) Tesseract Coxeter plane- that act like Higgs particle with 16 vertices assigned to 12 fermions and 4 gauge bosons



(c) 16-cell Coxeter plane that acts like eight gluons that may explain strong force confinement

FIG. 2: representation of fundamental particles on vertices of 24-cell, 16-cell and Tesseract

that has sixteen vertices and which is flat. We can represent the particles by orthogonal projections of 24-cell, 16-cell, and tesseract in the Coxeter plane in two dimensions as in Fig. (2).

V. SPACE-TIME QUANTA AND SPECTRAL MASS GAP

The solution of the mass gap problem as described in [62] requires proving that Yang-Mills theory exists and that the mass of all particles predicted by the theory is strictly positive. Both conditions are satisfied by the space-time quanta. According to Eq. (9), we find that the mass of space-time quanta is a real positive value. The space-time quanta is quatified by the parameter κ in Snyder algebra that was found to generate both non-commutative geometry and GUP at the same time. For Non-commutative geometry part, it is found to emerge naturally at limits of M/string theory [2] as higher dimensional corrections of ordinary Yang-Mills theory [3]. Since the space-time is locally flat, the space-time quanta must be described by a 4-polytope. We introduce a geometric and symmetric reason to consider the 24-cell as the space-time quanta. The most important reason is that 24-cell is the Weyl/Coxeter group of F_4 group that can generate the standard model gauge symmetry

as shown in recent studies [45]. Therefore, Yang-Mill's theory exists as a F_4 group and is explained by the space-time quanta from the first geometric principles as 24-cell. The gluon masses should be related to the 16-cell which is related to the 24-cell we explained in previous sections. We conclude that the space-time quanta introduces a geometric origin of the spectral mass gap [62]. The spectral mass gap is entirely determined by the length/radius of 24-cell according to Eq. (9). Recently, it was shown that spectral gaps exist in Hamiltonian with quasicrystalline order [63]. Quasicrystal considerations in Holography, the basic structure of nature, and cosmology are discussed in [64–71]. We think the quantum space-time may be a quasicrystal with a fundamental structure of a 24-cell. Experimental observations of quantum time quasicrystal are reported in [72]. This quasicrystal order is expected to follow from simulating Snyder's algebra with considering 24-cell as its fundamental structure. This needs further investigation.

VI. PHENOMENOLOGICAL IMPLICATIONS

Phenomenological studies expect to prop information about dark matter at ILC [73]. We intuit that the fundamental structure of dark matter/energy is the space-time quanta. Previous studies suggested that a minimal length of measurements forms a dark matter candidate [74]. There is an interesting observation about the 24-cell. All permutations of vertices in 24-cell are given by factorial $24! = 6.2044 \times 10^{23}$ which is quite close to the Avogadro number (6.0221×10^{23}) which determines the "approximate" number of nucleons per gram of matter based on thermodynamical and statistical computations. The relative error between the two values is around 2.9%. This may shed light on the geometric meaning of the mole unit. The number of observable stars in the universe is between 10^{22} to 10^{23}! [75, 76] which is again close to the number predicted by 24-cell. According to the interpretation of creating a mass of space-time quanta by vanishing uncertainty, the minimal length is expected to correspond to the electroweak length scale at which masses are created. Therefore, the minimal length is determined from the measured Higgs mass ($\approx 125.35\ GeV/c^2$) [76] and substituting it in Eq. (9) that implies a minimal length as follows:

$$\kappa\ \ell_{\rm Pl} \approx 10^{-18}\ \ \text{m} \tag{10}$$

This would give the length scale at which uncertainty vanishes to form a mass of space-time quanta. In that sense, we reinterpret the Higgs mechanism as a state in which the uncertainty vanishes to form the mass of space-time quanta. The electroweak length scale determines the unique length of the 24-cell. The effective minimal length has been interpreted recently as a charge radius of scattering for every physical particle [77]. Recent studies show that the minimum measurable charge radius measured so far is around 10^{-18} for the neutrinos, Higgs, W-bosons, and Z-boson, [76, 78, 79] which is consistent with our interpretations.
One notice that the permutations of the 16-cell that forms the gluons part of the 24-cell are equal to factorial 8! and the permutation of tesseract that represents Higgs, photon, W, Z, quarks, and leptons is given by factorial 16!. Based on our model, the 16-cell represents the Planck scale and the tesseract represents the electroweak scale. The multiplications of their permutations ($8!16! = 8.4360689 \times 10^{17}$) may explain the scale ratio between the Planck scale and the electroweak scale. The measured scale ratio between the Planck scale and the electroweak scale is approximately 10^{17}. This may imply a quantum computational explanation of the hierarchy in nature.

VII. CONCLUSION

We found that the GUP implied by Snyder's algebra vanishes at a specific energy scale. We define this energy scale as the scale of space-time quanta at which wavefunction collapses to form a mass. The mass of space-time quanta forms a mass gap of space-time. The covariance principle requires the space-time quanta to be a 4-dimensional object and to represent the elementary particles. Based on the geometric and symmetric analysis, we propose that the space-time quanta be represented by the 24-cell. First, it is highly-symmetric convex regular 4-polytope and self-dual. Second, The symmetry group of 24-cell is the Weyl/Coxeter group of F_4 group that generates the gauge group of the standard model by the intersection of its two stabilizer groups. In addition, the 24-cell has a beautiful geometric property in which its vertices can be grouped into 3 different sets of eight vertices, each defining 16-cell with the rest defining the dual tesseract with 16 vertices. Therefore, we represent 8 vertices of 16-cell with the 8 gluons that may give a geometric interpretation of the color confinement. We represent 16 vertices of tesseract with the 12 fermions and 4 gauge bosons which may explain the flatness of the observable universe. The Higgs particle is represented as the tesseract

which explains why Higgs only couple with 12 fermions and 4 gauge bosons and does not couple with 8 gluons. Vanishing uncertainty implies the creation of a mass of space-time quanta, so the length of 24-cell is identified by the electroweak length scale 10^{-18} m of mass creation and which is consistent with experimental measurements of the smallest measured value of charge radius of scattering for neutrinos, Higgs, Z-boson, and W boson. We think that a 24-cell symmetry group which is a solvable group of order "1152" could be useful in quantum computing. We hope to report on this application in the future.

Acknowledgments

I thank the Editor and referee for their meticulous review of this manuscript and express gratitude towards Klee Irwin, Raymond Aschheim, Fang Fang, Richard Clawson, and Dugan Hammock for their enlightening discussions on Polytopes and Quasicrystals. Special thanks to Ahmed Almheiri for his engaging lecture on the Path integral for chords.

This manuscript is a tribute to my father, Farag Mohamed Ali, whose legacy illuminates my journey, and in memory of Mustafa Shalaby, whose teachings have profoundly inspired my exploration of physics' core principles.

---

[1] H. S. Snyder, Phys. Rev. **71**, 38 (1947).

[2] A. Connes, M. R. Douglas, and A. S. Schwarz, JHEP **02**, 003 (1998), arXiv:hep-th/9711162 .

[3] N. Seiberg and E. Witten, JHEP **09**, 032 (1999), arXiv:hep-th/9908142 .

[4] M. R. Douglas and N. A. Nekrasov, Rev. Mod. Phys. **73**, 977 (2001), arXiv:hep-th/0106048 .

[5] R. J. Szabo, Phys. Rept. **378**, 207 (2003), arXiv:hep-th/0109162 .

[6] D. Amati, M. Ciafaloni, and G. Veneziano, Phys. Lett. B **216**, 41 (1989).

[7] L. J. Garay, Int. J. Mod. Phys. A **10**, 145 (1995), arXiv:gr-qc/9403008 .

[8] F. Scardigli, Phys. Lett. B **452**, 39 (1999), arXiv:hep-th/9904025 .

[9] K. Konishi, G. Paffuti, and P. Provero, Phys. Lett. B **234**, 276 (1990).

[10] A. Kempf *et al.*, Phys. Rev. D **52**, 1108 (1995), arXiv:hep-th/9412167 .

[11] M. Maggiore, Phys. Lett. B **304**, 65 (1993), arXiv:hep-th/9301067 .

[12] S. Capozziello *et al.*, Int. J. Theor. Phys. **39**, 15 (2000), arXiv:gr-qc/9910017 .

[13] S. Das and E. C. Vagenas, Phys. Rev. Lett. **101**, 221301 (2008), arXiv:0810.5333 [hep-th] .

[14] I. Pikovski *et al.*, Nature Phys. **8**, 393 (2012), arXiv:1111.1979 [quant-ph] .

[15] F. Marin *et al.*, Nature Phys. **9**, 71 (2013).

[16] L. Petruzziello *et al.*, Nature Commun. **12**, 4449 (2021), arXiv:2011.01255 [gr-qc] .

[17] S. P. Kumar *et al.*, Nature Commun. **11**, 3900 (2020), arXiv:1908.11164 [quant-ph] .

[18] H. Moradpour *et al.*, Mon. Not. Roy. Astron. Soc. **488**, L69 (2019), arXiv:1907.12940 [gr-qc] .

[19] D. Gao and M. Zhan, Physical Review A **94**, 013607 (2016).

[20] M. Bawaj *et al.*, Nature Commun. **6**, 7503 (2015), arXiv:1411.6410 [gr-qc] .

[21] P. Girdhar *et al.*, New J. Phys. **22**, 093073 (2020), arXiv:2005.08984 [quant-ph] .

[22] A. Ashoorioon *et al.*, Phys. Rev. D **71**, 023503 (2005), arXiv:astro-ph/0410139 .

[23] R. Easther *et al.*, Phys. Rev. D **67**, 063508 (2003), arXiv:hep-th/0110226 .

[24] M. P. Dabrowski and F. Wagner, The European Physical Journal C **79**, 1 (2019).

[25] R. Easther *et al.*, Phys. Rev. D **64**, 103502 (2001), arXiv:hep-th/0104102 .

[26] A. Addazi *et al.*, (2021), arXiv:2111.05659 [hep-ph] .

[27] S. Hossenfelder, Living Rev. Rel. **16**, 2 (2013), arXiv:1203.6191 [gr-qc] .

[28] S. Mignemi, Ukr. J. Phys. **64**, 991 (2019), arXiv:1911.06127 [hep-th] .

[29] D. J. Gross and F. Wilczek, Phys. Rev. Lett. **30**, 1343 (1973).

[30] H. D. Politzer, Phys. Rev. Lett. **30**, 1346 (1973).

[31] J. R. Ellis, S. Mohanty, and D. V. Nanopoulos, Phys. Lett. B **221**, 113 (1989).

[32] A. Einstein, B. Podolsky, and N. Rosen, Phys. Rev. **47**, 777 (1935).

[33] A. F. Ali, (2022), arXiv:2210.13974 [quant-ph] .

[34] A. F. Ali, (2022), 10.2139/ssrn.4292472.

[35] J. D. Bekenstein, Phys. Rev. D **23**, 287 (1981).

[36] J. D. Bekenstein, Found. Phys. **35**, 1805 (2005), arXiv:quant-ph/0404042 .

[37] J. D. Bekenstein, Phys. Lett. B **481**, 339 (2000), arXiv:hep-th/0003058 .

[38] L. Lu and A. Stern, Nucl. Phys. B **860**, 186 (2012), arXiv:1110.4112 [hep-th] .

[39] R. Banerjee, K. Kumar, and D. Roychowdhury, JHEP **03**, 060 (2011), arXiv:1101.2021 [hep-th] .

[40] H. S. M. Coxeter, *Regular polytopes* (Courier Corporation, 1973).

[41] M. J. Wenninger, *Dual models* (Cambridge University Press, 2003).

[42] G. C. Wick, Phys. Rev. **96**, 1124 (1954).

[43] G. W. Gibbons and S. W. Hawking, *Euclidean quantum gravity* (World Scientific, 1993).

[44] S. Weinberg, Phys. Rev. Lett. **19**, 1264 (1967).

[45] I. Todorov and M. Dubois-Violette, Int. J. Mod. Phys. A **33**, 1850118 (2018), arXiv:1806.09450 [hep-th] .

[46] F. Bernardoni, S. L. Cacciatori, B. L. Cerchiai, and A. Scotti, Adv. Theor. Math. Phys. **12**, 889 (2008), arXiv:0705.3978 [math-ph] .

[47] J. C. Baez, The n-Category Cafe **27** (2018).

[48] L. Boyle, (2020), arXiv:2006.16265 [hep-th] .

[49] M. Dubois-Violette, Nucl. Phys. B **912**, 426 (2016), arXiv:1604.01247 [math.QA] .

[50] L. Boyle and S. Farnsworth, New J. Phys. **22**, 073023 (2020), arXiv:1910.11888 [hep-th] .

[51] I. Todorov, Springer Proc. Math. Stat. **335**, 29 (2019), arXiv:1911.13124 [hep-th] .

[52] V. Bhatt, R. Mondal, V. Vaibhav, and T. P. Singh, J. Phys. G **49**, 045007 (2022), arXiv:2108.05787 [hep-ph] .

[53] V. Vaibhav and T. P. Singh, (2021), arXiv:2108.01858 [hep-ph] .

[54] I. Todorov and S. Drenska, Adv. Appl. Clifford Algebras **28**, 82 (2018), arXiv:1805.06739 [hep-th] .

[55] N. Furey and M. J. Hughes, Phys. Lett. B **831**, 137186 (2022), arXiv:2210.10126 [hep-ph] .

[56] K. Krasnov, J. Math. Phys. **62**, 021703 (2021), arXiv:1912.11282 [hep-th] .

[57] M. Dubois-Violette and I. Todorov, Nucl. Phys. B **938**, 751 (2019), arXiv:1808.08110 [hep-th] .

[58] N. Furey, Phys. Lett. B **785**, 84 (2018), arXiv:1910.08395 [hep-th] .

[59] V. Braun, JHEP **05**, 101 (2012), arXiv:1102.4880 [hep-th] .

[60] J. J. Blanco-Pillado, K. Sousa, M. A. Urkiola, and J. M. Wachter, JHEP **04**, 149 (2021), arXiv:2007.10381 [hep-th] .

[61] R. Aschheim, in *Loops 11: International Conference on Quantum Gravity* (2012) arXiv:1212.5473 [cs.IT] .

[62] A. Jaffe and E. Witten, The millennium prize problems **1**, 129 (2006).

[63] P. Hege, M. Moscolari, and S. Teufel, Phys. Rev. B **106**, 155140 (2022), arXiv:2205.10622 [quant-ph] .

[64] L. Boyle, M. Dickens, and F. Flicker, Phys. Rev. X **10**, 011009 (2020), arXiv:1805.02665

[hep-th] .

[65] R. Aschheim, L. Bubuianu, F. Fang, K. Irwin, V. Ruchin, and S. I. Vacaru, Annals of Physics **394**, 120 (2018).

[66] K. Irwin, Activitas Nervosa Superior **62**, 48 (2020).

[67] F. Fang, S. Paduroiu, D. Hammock, and K. Irwin, Crystals **8**, 416 (2018).

[68] M. Amaral, D. Chester, F. Fang, and K. Irwin, Symmetry **14**, 1780 (2022).

[69] F. Fang, S. Paduroiu, D. Hammock, and K. Irwin, in *Electron Crystallography* (IntechOpen, 2019) p. 27.

[70] K. Irwin, M. Amaral, R. Aschleim, and F. Fang, in *Proceedings of the Fourth International Conference on the Nature and Ontology of Spacetime, Varna, Bulgaria*, Vol. 30 (2016) pp. 117–160.

[71] K. Irwin, "Simple programs - qc cycle clocks," (2020).

[72] S. Autti, V. B. Eltsov, and G. E. Volovik, Phys. Rev. Lett. **120**, 215301 (2018), arXiv:1712.06877 [cond-mat.other] .

[73] K. Fujii *et al.*, (2017), arXiv:1710.07621 [hep-ex] .

[74] R. J. Adler, P. Chen, and D. I. Santiago, Gen. Rel. Grav. **33**, 2101 (2001), arXiv:gr-qc/0106080 .

[75] G. Rudnick, H.-W. Rix, M. Franx, I. Labbé, M. Blanton, E. Daddi, N. M. F. Schreiber, A. Moorwood, H. Röttgering, I. Trujillo, *et al.*, The Astrophysical Journal **599**, 847 (2003).

[76] P. A. Zyla *et al.* (Particle Data Group), PTEP **2020**, 083C01 (2020).

[77] A. F. Ali, I. Elmashad, and J. Mureika, Phys. Lett. B **831**, 137182 (2022), arXiv:2205.14009 [physics.gen-ph] .

[78] P. T. P. Hutauruk, A. Sulaksono, and K. Tsushima, Nucl. Phys. A **1017**, 122356 (2022), arXiv:2009.08781 [hep-ph] .

[79] B. Lehnert, Progress in Physics **10**, 5 (2014).

PROCEEDINGS OF SCIENCE

Double Deeply Virtual Compton Scattering at Jefferson Lab Hall A

Marie Boër[a,*] **and Debaditya Biswas**[a]

[a] *Virginia Tech,*
Blacksburg, VA, USA.

E-mail: mboer@jlab.org

This paper presents our project and perspectives to measure for the first time beam spin asymmetries from Double Deeply Virtual Compton Scattering in the $eP \to e'P'\mu^+\mu^-$ reaction at Jefferson Lab. Our goal is to constrain the so-called Generalized Parton Distribution (GPDs) in a kinematic region that isn't accessible from other reactions, such as Deeply Virtual Compton Scattering, to allow for their extrapolation to "zero skewness", i.e. at a specific kinematic point enabling for tomographic interpretations of the nucleon's partonic structure. We are discussing DDVCS phenomenology and our approach, as well as our experimental project aimed at complementing the SoLID experiment at JLab Hall A with a new muon detector.

25th International Spin Physics Symposium (SPIN 2023)
24-29 September 2023
Durham, NC, USA

*Speaker

© Copyright owned by the author(s) under the terms of the Creative Commons Attribution-NonCommercial-NoDerivatives 4.0 International License (CC BY-NC-ND 4.0).

arXiv:2403.02605v1 [nucl-ex] 5 Mar 2024

1. Introduction

The so-called Generalized Parton Distribution (GPDs) [1, 2] are matrix elements parametrizing the soft structure of the nucleon in "Hard Exclusive" reactions [3, 4]. GPDs contain information on the longitudinal momentum versus transverse position of the partons (quarks and gluons) [5, 6]. We have been studying GPDs for the last ~30 years as we are looking to move towards multidimensional images of the nucleon structure. One of the interesting interpretations of GPDs is the possibility to access tomographic views of the nucleon, where we can relate the transverse position of the partons to the quark and gluon densities [7]. This kind of interpretation relies on extrapolations of GPDs to certain kinematics that can't be accessed experimentally, and on models, referred to as "zero skewness" [8], i.e. reactions where all the momentum transferred to the nucleon is purely transverse. Our goal is to study Double Deeply Virtual Compton Scattering to constrain the GPDs at this limit.

"Hard Exclusive" reactions refers to: a "hard scale" of at least 1 GeV^2, allowing for factorization between a soft part parametrized by the GPDs, and a hard part, calculable [9]; "exclusivity" refers to all products of the reaction being known, enabling measurement of the total momentum transfer to the nucleon (we use Mandelstam variable "t", the squared momentum transfer). Fig.1 is the general Compton-like process, where a photon is scattered off a quark in the nucleon. We display the factorization lane, the bottom part representing the GPDs. The incoming and scattered photons have to be of different virtuality to allow for a non-zero momentum exchange to the nucleon. We can distinguish between 3 particular cases of "Compton Scattering": Deeply Virtual Compton Scattering (DVCS), where the incoming photon is virtual (spacelike) and the outgoing one is real; Timelike Compton Scattering (TCS), where the incoming photon is real and the outgoing one is virtual, subsequently decaying into a lepton pair; and Double Deeply Virtual Compton Scattering (DDVCS), where both photons are virtual. DVCS has been measured at multiple facilities [10–25], TCS has recently been measured for the first time at JLab [26], DDVCS has never been measured.

There are several GPDs, for quarks and gluons, and to account for relative helicity states of the quark-nucleon system. At leading order and leading twist (lowest order in photon's virtuality related to extra-gluon exchanges), for a spin 1/2 nucleon, we have 4 (x2 for quarks and gluons) chiral-even GPDs, and 4 (x2) chiral-odd GPDs (with quark helicity flip), i.e. 16 total (see for instance [5, 27]). These GPDs depend on 3 variables: t, x (nucleon's longitudinal momentum fraction carried by the parton), ξ ("skewness", related to the longitudinal momentum transfer to the quark in light cone frame). We will neglect here their evolution with the photons' virtuality (namely Q^2=-q^2 and/or Q'^2=q'^2 for incoming and outgoing photons, respectively, defined from their squared 4-momenta). GPDs can't be measured directly: we measure Compton Form Factors (CFFs), functions of the GPDs, accessible from fits of cross sections and asymmetries of the various reactions. Most models are currently constrained by measurements of DVCS only, where GPDs can only be accessed at specific kinematic points, for x=$\pm\xi$. TCS being the "time-reversal" equivalent of DVCS at leading order and leading twist [28], it accesses GPDs at the same kinematics. On the other hand, we can vary the relative virtualities of the two photons in DDVCS to access different kinematics, such as $|x| < \xi$ [5, 29, 30]. It is essential to deconvolute these 2 variables and extrapolate the GPDs to ξ=0 [8], which is needed for tomographic interpretations.

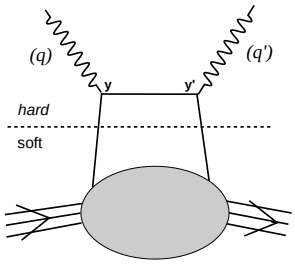


Figure 1: General Compton-like reaction diagram at leading twist, leading order. Dash lane indicates the factorization between a soft part, parameterized by the GPDs and a hard calculable part.

Indeed, one can't directly access the GPDs with DVCS, TCS or DDVCS: we are measuring functions of them, the Compton Form Factors (CFFs), which can be extracted from fitting experimental observables (cross sections, spin or charge asymmetries...). For instance, the CFF $\mathcal{H}$ associated with the GPD H and accessible in DVCS or TCS experiments writes

$$\mathcal{H}(\xi,t) = \sum_q e_q^2 \left\{ \mathcal{P} \int_{-1}^{1} dx\, H^q(x,\xi,t) \left[\frac{1}{\xi - x} - \frac{1}{\xi + x} \right] + i\pi \left[H^q(\xi,\xi,t) - H^q(-\xi,\xi,t) \right] \right\} \quad (1)$$

where the sum runs over all parton flavors with elementary electrical charge e_q, and $\mathcal{P}$ indicates the Cauchy principal value of the integral. The imaginary part of the CFF accesses the GDP values at $x = \pm\xi$ and the real part comes in an integral over x. It involves the convolution of parton propagators and the GPD values out-of the diagonals $x = \pm\xi$ (Fig. 2). Thanks to the virtuality of the final state photon (see section2), DDVCS provides a way to circumvent this limitation [29, 30], allowing to vary independently x and ξ. Considering the same GPD H, the corresponding CFF for the DDVCS process writes

$$\mathcal{H}(\xi',\xi,t) = \sum_q e_q^2 \left\{ \mathcal{P} \int_{-1}^{1} dx\, H^q(x,\xi,t) \left[\frac{1}{\xi' - x} - \frac{1}{\xi' + x} \right] + i\pi \left[H^q(\xi',\xi,t) - H^q(-\xi',\xi,t) \right] \right\} \quad (2)$$

involving an additional scaling variable ξ representing here the GPD skewness. We can therefore explore the GPDs out of the "diagonal" $x = \pm\xi$ (Fig .2).

2. Phenomenology of DDVCS

DDVCS is measured in the reaction $eN \to e'N'L^+L^-$, where N is a nucleon, e is a lepton (beam), L^+L^- is a lepton pair coming from the decay an outgoing virtual photon. At the quark level, the process which occur for DDVCS is: $\gamma_1 N \to \gamma_2 N'$ (as in Fig.1). In fact, DDVCS interfers with two Bethe-Heitler like processes ("BH" = BH1 and BH2), where the lepton pair comes from (1) a radiative virtual photon emission from the lepton beam ("BH1") and (2) a lepton pair produced by the exchanged photons ("BH2"). We are representing the different subprocesses Fig.3: the DDVCS process is displayed at the top, we took the case of an electron beam and a final muon pair; we are displaying the two cases of Bethe-Heitler at the bottom ("BH1" on the left, "BH2" on the right).

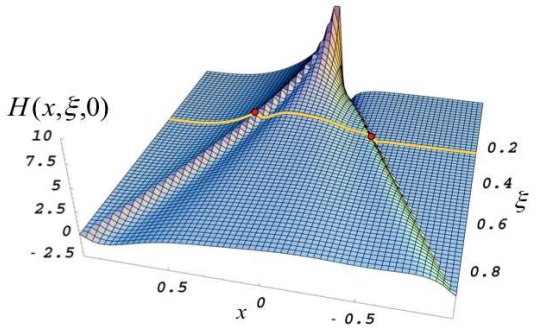


Figure 2: Graphical representation of the DVCS Compton form factor (CFF) showing a typical model for the GPD H at t=0; the red points indicates the GPD values involved in the CFF imaginary part, and the yellow line underlines the integral path of the CFF real part.

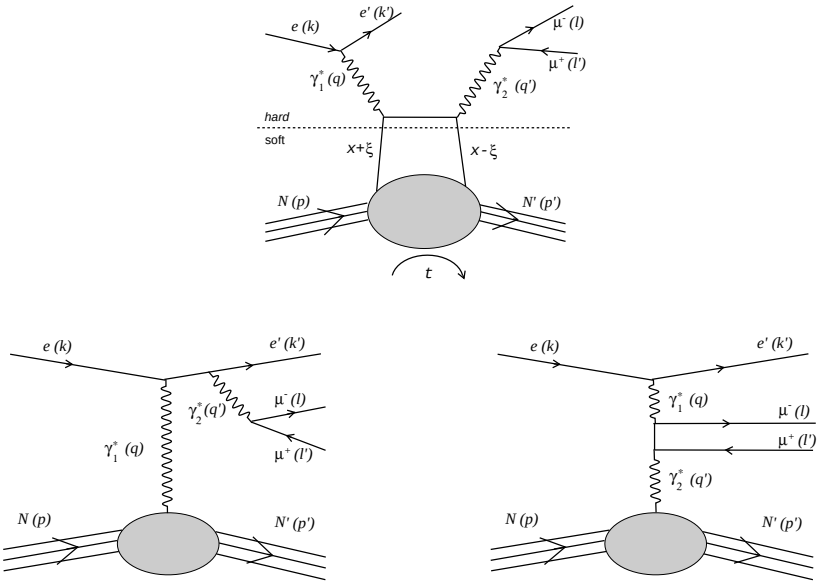


Figure 3: Electroproduction of a muon pair off a quark in a nucleon, at leading order and leading twist (CC not represented). Top: DDVCS process. Bottom left: Bethe-Heitler like process from a radiative virtual photon emission (referred to in this paper as "BH1". Bottom right: Bethe-Heitler process from exchanged virtual photon conversion (referred to here as "BH2"). We indicated some kinematic variables and 4-momenta as indicated in the text.

Note that crossed diagrams aren't represented. At leading twist and leading order, 6 diagrams interfer in the reaction of electroproduction of a muon pair off a nucleon. We are choosing to study DDCCS+BH in the di-muon channel to avoid concerns in having two electron in the final state (antisymmetrization for the interpretation, particle identification and kinematic reconstruction at the experimental level...), since our available beam at Jefferson Lab (JLab) is an electron beam.

As indicated in Fig.3, we are using here the following notation for the 4-vectors of the different particles involved:

$$e(k) - e'(k') + p(p_1) \equiv \gamma^\star(q_1) + p(p_1) \rightarrow p'(p_2) + \gamma^\star(q_2) \rightarrow p'(p_2) + \mu^+(l^+) + \mu^-(l^-). \quad (3)$$

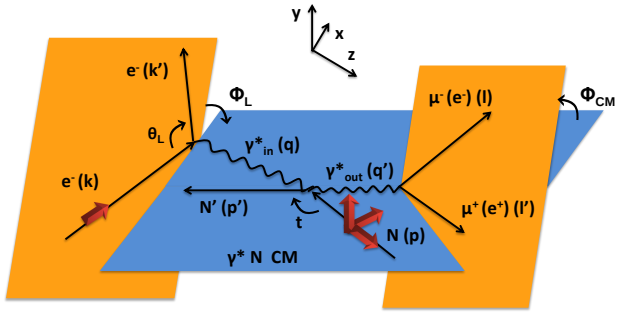


Figure 4: Reference frame, kinematics, angles, for the DDVCS reaction, using notations defined in [29] and our angle's notation.

For our kinematics, we are using the notations defined in [29], expressed in the reference frame represented Fig. 4. The photon virtualities (incoming and outgoing, respectively) are defined as

$$Q^2 = -q^2; \quad Q'^2 = q'^2. \tag{4}$$

We define the symmetrical momentum variables p and q as

$$q = \frac{1}{2}(q + q'); \qquad p = p + p', \tag{5}$$

and the four-momentum transfer to the nucleon $\Delta = p - p' = q - q'$ with $t = \Delta^2$. The DDVCS scaling variables write

$$x_B = -\frac{1}{2}\frac{q_1 \cdot q_1}{p_1 \cdot q_1}; \qquad \xi' = -\frac{q \cdot q}{p \cdot q}; \qquad \xi = \frac{\Delta \cdot q}{p \cdot q}. \tag{6}$$

The symmetrical momentum q can be decomposed as

$$q^2 = -\frac{1}{2}\left(Q^2 - Q'^2 + \frac{\Delta^2}{2}\right). \tag{7}$$

We can decompose the skewness variables in terms of virtualities and Δ:

$$\xi = \frac{Q^2 - Q'^2 + (\Delta^2/2)}{2(Q^2/x_B) - Q^2 - Q'^2 + \Delta^2}, \qquad \xi' = -\frac{Q^2 + Q'^2}{2(Q^2/x_B) - Q^2 - Q'^2 + \Delta^2}, \tag{8}$$

which expresses GPDs variables of interest (ξ, ξ', t) in terms of experimentally measured quantities. Note that the different Q'^2-dependence in the numerators of ξ and ξ' expresses the ability to access out-of diagonals phase space ($x \neq \xi$) from the "lever arm" in Q^2 versus Q'^2; and that for DVCS or TCS, $\xi = \xi'$ (at the asymptotic limit).

We made projections for realistic kinematics accessible at Jefferson Lab, using an 11 GeV electron beam, cuts at Q^2=1 GeV^2, Q'^2=4 GeV^2, $Q^2 - Q'^2$=1 GeV^2, $W^2 > 2$GeV^2, $-t < 0.55$GeV^2, among other kinematic considerations. Neglecting the acceptance effects, we obtained Fig.5, showing how much "off-diagonal" phase space we would be able to cover in an experiment. Red boxes on this figure indicate one proposed binning in t, ξ and ξ'. We decided to exclude the central region ($Q^2 \sim Q'^2$) as it can't be interpreted with our current knowledge (factorization may not hold).

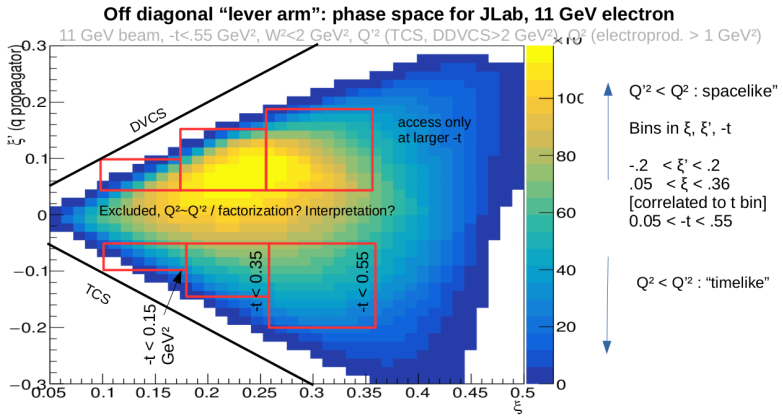


Figure 5: Accessible "off-diagonal" phase-space for DDVCS+BH for experiments at Jefferson Lab. Cuts are indicated on the figure and the main text. Note that the figure (blue/yellow area) integrates our statistics over t: red boxes represent bins in t, where the maximal limits are indicated in the boxes.

3. DDVCS+BH observables and projections

We define as "experimental observables" unpolarized, beam and/or target polarized cross sections and spin asymmetries (normalized difference of 2 relative spin states). At JLab, we would like to measure unpolarized and beam polarized cross sections. CFFs can be extracted from fitting these cross sections. The differential cross section for the electroproduction of muon pair off the nucleon can be written [31]

$$\frac{d^7\sigma}{dx_B\, dy\, dt\, d\phi\, dQ'^2\, d\Omega_\mu} = \frac{1}{(2\pi)^3}\,\frac{\alpha^4}{16}\,\frac{x_B y}{Q^2\sqrt{1+\varepsilon^2}}\,\sqrt{1-\frac{4m_\mu^2}{Q'^2}}\;|\mathcal{T}|^2, \tag{9}$$

where the reaction amplitude can generically be expressed as

$$|\mathcal{T}|^2 = |\mathcal{T}_{VCS}|^2 + \mathcal{I}_1 + \mathcal{I}_2 + |\mathcal{T}_{BH_1}|^2 + |\mathcal{T}_{BH_2}|^2 + \mathcal{T}_{BH_{12}}, \tag{10}$$

with the pure DDVCS amplitude $|\mathcal{T}_{VCS}|^2$, the interference amplitudes $\mathcal{I}_1$ and $\mathcal{I}_2$ between the DDVCS and two Bethe-Heitler sub-processes, and the pure BH amplitude built itself from the two elementary BH subprocesses. We refer to [31] for more details on the harmonic structure of these amplitudes.

The interference amplitude bewteen the BH and DDVCS processes is an observable of interest since it involves linear combinations of Compton form factors. The imaginary part of the amplidudes can be accessed directly via beam spin asymmetries. Not only beam spin asymmetries are easier to measure than cross sections, but "pure" Bethe-Heitler terms in the amplitude cancel in beam spin asymmetries (at the numerator), leading to a better sensitivity to the CFFs and GPDs. Considering the harmonic dependence of the cross section, it was shown [31] that the same basic information about GPDs can be obtained from the appropriate moments in ϕ or φ_μ, a feature of particular interest for experimental consistency. Taking advantage of the symmetry properties of the BH propagators to minimize the BH contribution, the first ϕ-moment and φ_μ-moment of the beam spin asymmetry

can be written [31]

$$\left\{ \begin{array}{c} A_{\rm LU}^{\sin\phi} \\ A_{\rm LU}^{\sin\varphi_\mu} \end{array} \right\} = \frac{1}{\mathcal{N}} \int_{\pi/4}^{3\pi/4} d\theta_\mu \int_0^{2\pi} d\varphi_\mu \int_0^{2\pi} d\phi \left\{ \begin{array}{c} 2\sin\phi \\ 2\sin\varphi_\mu \end{array} \right\} \frac{d^7\overrightarrow{\sigma} - d^7\overleftarrow{\sigma}}{dx_B\, dy\, dt\, d\phi\, dQ'^2\, d\Omega_\mu}$$
$$\propto \Im\mathrm{m}\left\{ F_1\mathcal{H} - \frac{t}{4M_N^2} F_2\mathcal{E} + \xi'(F_1+F_2)\widetilde{\mathcal{H}} \right\}, \tag{11}$$

where F_1 and F_2 are the proton's form factors, $\mathcal{H}, \tilde{\mathcal{H}}, \mathcal{E}$ are the CFFs depending on GPDs H, $\tilde{H}$, E, respectively, and with the normalization factor given by

$$\mathcal{N} = \int_{\pi/4}^{3\pi/4} d\theta_\mu \int_0^{2\pi} d\varphi_\mu \int_0^{2\pi} d\phi \frac{d^7\overrightarrow{\sigma} + d^7\overleftarrow{\sigma}}{dx_B\, dy\, dt\, d\phi\, dQ'^2\, d\Omega_\mu}, \tag{12}$$

and where we omit for clarity the (ξ', ξ, t)-dependence of the CFFs. In the case of a proton target the measurement gives access to the "out-of diagonal" kinematic dependencies of GPD H (dominant term).

We display in this section some of our projections made for JLab kinematics. Calculations are made from VGG model for GPDs [32], based on the DDVCS calculations from [29], with modifications. Our kinematic studies are performed with our event generator. Fig. 6 displays the differential cross section and the beam spin asymmetry A_{LU} for two relevant kinematics for the determination of GPDs that we aim at measuring at JLab, in Hall A. These experimental observables are been obtained using the prescription of Eq. 11 for the integration over the angular phase space of the di-muon pair. Sizeable asymmetries are predicted together with, as expected, a strong sensitivity of the cross section to kinematic conditions. Since the azimuthal and polar angle of the final muon pair are strongly correlated to each other and to the rate of BH (especially "BH2") in the full DDVCS+BH reaction, we calculated the unpolarized cross section (Fig. 7, left) and beam spin asymmetry (right) at different θ_μ. The "actual" observables that will be used for the extraction of the CFFs are unpolarized cross sections and beam spin asymmetries, differential in the initial and final azimuthal angles, integrated over the final polar angle. Extremes values in θ are cut out from this integral ($40 \leq \theta_\mu \leq 140^0$), due to the large BH dominance in this regions coming from the peaks induced by the "BH2" diagrams.

4. Measuring DDVCS with the SoLID spectrometer at JLab Hall A

Different projects exist at JLab to measure DDVCS in Halls A, B, C. The project presented in this paper is based on our letter of intent [33], submitted in 2023, and aiming at measuring the DDVCS+BH beam spin asymmetries with a slightly modified version of the SoLID (future) spectrometer. The projections presented in this section are based on this LOI. Our idea is to supplement the SoLID spectrometer [34], as in it's setup approved for the J/Ψ experiment [35], with a dedicated muon detector, also serving as trigger. We are displaying our full setup, from GEANT4 simulations, Fig. 8 (left). The additional muon detector is shown Fig. 8 (right), and made of an alternance of 3 layers of iron (for shielding), 3 layers of straw tubes (for tracking), then 2 layers of plastic scintillators at the back-end to trigger on the muon pair. The iron plates will be coming from CLEO-II.

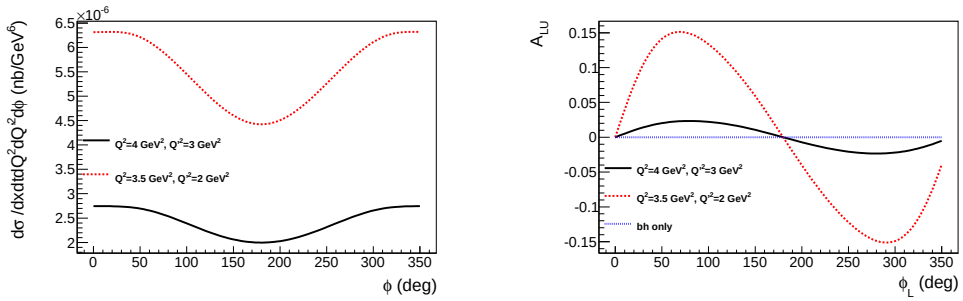


Figure 6: Out-of-plane angular dependence of the differential cross section (left) and the beam spin asymmetry (right) for the $eP \rightarrow e'p\mu^+\mu^-$ process at E=11 GeV, x_B=0.25, t=-0.4 GeV^2, and different virtual photon masses.

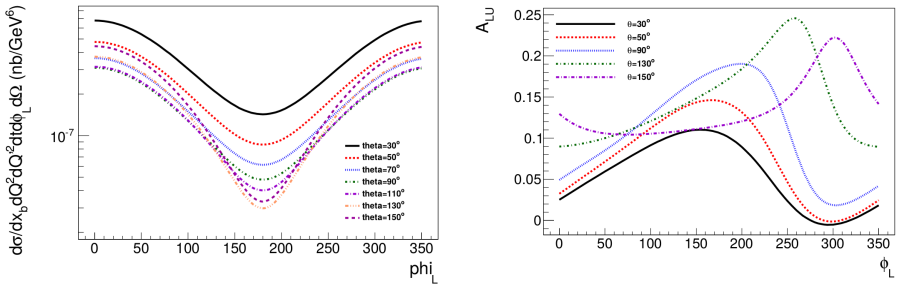


Figure 7: Out-of-plane angular dependence of the differential cross section for various polar angles of the muon (left) and for the differential beam spin asymmetry (right)

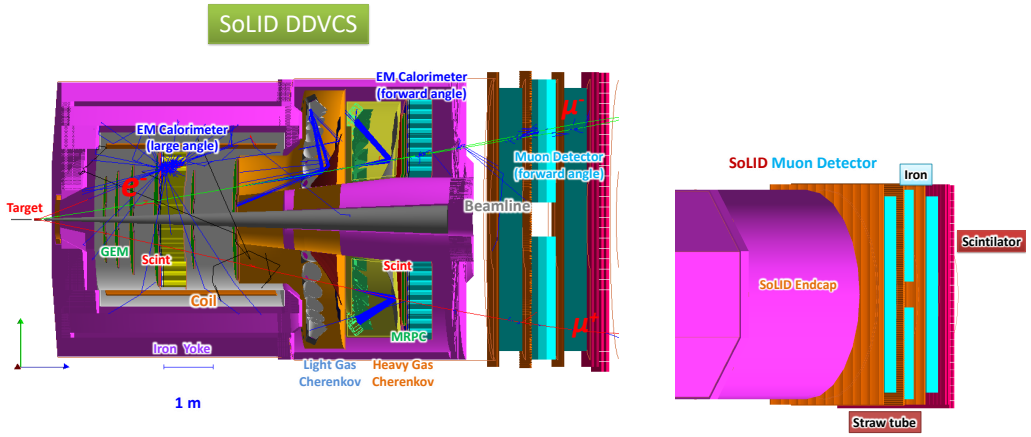


Figure 8: Left: SoLID DDVCS with the forward angle muon detector added to the $J\psi$ setup [35]. Right: Preliminary design of SoLID muon detector at forward angle in Geant4 simulation.

SoLID is designed to use a solenoid field and allows to carry out experiments with high energy $\sim$ 11 GeV electron beams on unpolarized and polarized targets at luminosities of up to $L = 10^{37}$ cm^{-2} sec^{-1} in an open geometry. The solenoid field, reaching about 1.4T is provided by re-using the CLEO-II magnet. Part of the CLEO-II iron flux return will be modified and reused, and two new iron endcaps will be added at the front and back of the solenoid. Forward angle detectors cover polar angles from 8.5° to 16°, and consist of planes of Gas Electron Multipliers (GEM) for tracking, a light-gas Cherenkov (LGCC) for e/π separation, a heavy gas Cherenkov (HGCC) for π/K separation, a Multi-gap Resistive Plate Chamber (MRPC) for time-of-flight, and an Electromagnetic Calorimeter (FAEC). Large-angle detectors cover polar angle from 17° to 24.5° and consist of several planes of GEM for tracking, and an Electromagnetic Calorimeter (LAEC).

5. Summary

We presented the motivations and our proposed setup for an experiment aiming at measuring DDVCS+BH with the SoLID spectrometer at JLab Hall A, supplemented by new muon detectors. The DDVCS+BH azymuthal dependencies of the beam spin asymmetries are sensitive to the imaginary part of the amplitudes and to the interference between DDVCS and BH. DDVCS has never been measured, and accessing CFFs from its observables will enable, for the first time, to deconvolute the proton's and quark's momenta, which is essential for tomographic interpretations of the GPDs.

Acknowledgements: The authors would like to thank, in alphabetic order, for their inputs or contributions, S. Alavarado, A. Camsonne, R. Gilman, M. Guidal, E. Voutier, S. Zhao, Z. Zhao. We also would like to thank all the members of the SoLID collaboration. This work is supported by the Virginia Tech Physics Department.

References

[1] D. Müller, D. Robaschick, B. Geyer, F.M. Dittes, J. Hořejši, Fortschr. Phys. **42**, 101 (1994).

[2] X. -D. Ji, Phys. Rev. D **55**, 7114 (1997)

[3] X. Ji, Phys. Rev. Lett. **78**, 610 (1997).

[4] A.V. Radyushkin, Phys. Rev. **D 56**, 5524 (1997).

[5] M. Diehl, Phys. Rep. **388**, 41 (2003).

[6] A. V. Belitsky, A. V. Radyushkin, Phys. Rept. **418**, 1 (2005).

[7] M. Burkardt, Phys.Rev.D 66 (2002) 114005

[8] Y. Guo, X. Ji, G. Santiago, G. Shiells, J. Yangl, JHEP 05 (2023) 150

[9] J. C. Collins and A. Freund, Phys. Rev. D 59 (1999) 074009.

[10] (H1 Collaboration) C. Adloff *et al.*, Phys. Lett. B **517**, 47 (2001).

[11] (HERMES Collaboration) A. Airapetian *et al.*, Phys. Rev. Lett. **87**, 182001 (2001).

[12] (CLAS Collaboration) S. Stepanyan *et al.*, Phys. Rev. Lett. **87**, 182002 (2001).

[13] (ZEUS Collaboration) S. Chekanov *et al.*, Phys. Lett. B **573**, 46 (2003).

[14] (CLAS Collaboration) S. Chen *et al.*, Phys. Rev. Lett. **97**, 072002 (2006).

[15] (Hall A DVCS Collaboration) C. Muñoz Camacho *et al.*, Phys. Rev. Lett. **97**, 262002 (2006).

[16] (HERMES Collaboration) A. Airapetian *et al.*, Phys. Rev. D **75**, 011103 (2007).

[17] (HERMES Collaboration) A. Airapetian *et al.*, JHEP **06**, 066 (2008).

[18] (CLAS Collaboration) F.X. Girod *et al.*, Phys. Rev. Lett. **100**, 162002 (2008).

[19] (HERMES Collaboration) A. Airapetian *et al.*, JHEP **06**, 019 (2010).

[20] (HERMES Collaboration) A. Airapetian *et al.*, Phys. Lett. B **704**, 15 (2011).

[21] (CLAS Collaboration) H.S. Jo *et al.*, Phys. Rev. Lett. 115, 212003 (2015).

[22] (Hall A DVCS) M. Defurne *et al.*, (Jefferson Lab Hall A), Phys. Rev. C 92 (2015) no.5

[23] N. Hirlinger Saylor et al. (CLAS Collaboration), Phys. Rev. C 98, 045203 (2018).

[24] R. Akhunzyanov et al., (COMPASS coll), Phys. Lett. B 793 (2019) 188. (Erratum: Phys.Lett.B 800, 135129 (2020)).

[25] F. Georges et al. (Jefferson Lab Hall A Collaboration) Phys. Rev. Lett. 128, 252002

[26] P. Chatagnon et al. (CLAS Collaboration) Phys. Rev. Lett. 127, 262501 (2022)

[27] M. Guidal, H. Moutarde and M. Vanderhaeghen, Rept. Prog. Phys. **76**, 066202 (2013)

[28] E. R. Berger, M. Diehl and B. Pire, EPJC 23 (2002) 675-689

[29] M. Guidal, M. Vanderhaeghen, Phys. Rev. Lett. **90**, 012001 (2003).

[30] A. V. Belitsky, D. Müller, Phys. Rev. Lett. **90**, 022001 (2003).

[31] A. V. Belitsky, D. Müller, Phys. Rev. D **68**, 116005 (2003).

[32] M. Vanderhaeghen, P.A.M. Guichon, M. Guidal, Phys. Rev. D **60**, 094017 (1999).

[33] A. Camsonne (contact), M. Boër, E. Voutier, Z. Zhao, LOI PAC 51, DDVCS in SoLID (2023)

[34] SoLID Pre-Conceptual Design Report (2019)

[35] Z. Meziani et al, J/Ψ SoLID experiment E12-12-006.

arXiv:2403.02602v1 [nucl-th] 5 Mar 2024

Macroscopic neutrinoless double beta decay: long range quantum coherence

Gordon Baym and Jen-Chieh Peng
Illinois Center for Advanced Studies of the Universe
and Department of Physics, University of Illinois, 1110 W. Green Street, Urbana, IL 61801

(Dated: March 6, 2024)

We introduce the concept of "macroscopic neutrinoless double beta decay" (MDBD) for Majorana neutrinos. In this process an antineutrino produced by a nucleus undergoing beta decay, $X \to Y + e^- + \bar{\nu}_e$, is absorbed as a neutrino by another identical X nucleus via the inverse beta decay reaction, $\nu_e + X \to e^- + Y$. The distinct signature of MDBD is that the total kinetic energy of the two electrons equals twice the endpoint energy of single beta decay. The amplitude for MDBD, a coherent sum over the contribution of different mass states of the intermediate neutrinos, reflects quantum coherence over macroscopic distances, and is a new macroscopic quantum effect. We evaluate the rate of MDBD for a macroscopic sample of "X" material, e.g., tritium, acting both as the source and the target. The accidental background for MDBD originating from two separate single beta decays, which contains two final state neutrinos, can be readily rejected by measuring the energy of the detected two electrons. We discuss the similarities and differences between the MDBD and conventional neutrinoless double beta decay.

PACS numbers:

I. INTRODUCTION

The neutrino, if a Majorana rather than a Dirac fermion, would be its own antiparticle. A key experimental signature distinguishing Majorana neutrinos from Dirac neutrinos is nuclear neutrinoless double beta decay (0νDBD),

$$(A, Z) \to (A, Z+2) + e^- + e^-. \tag{1}$$

Despite the importance of determining whether neutrinos are Majorana or Dirac, and despite a major experimental effort, only upper limits for 0νDBD have so far been obtained [1–3]. Ongoing and future experiments with multi-ton detectors will further improve the sensitivity in these searches [4].

The existence of a Majorana neutrino implies lepton-number non-conservation, hence physics beyond the Standard Model. Majorana neutrinos have only two spin states: when massless the left-handed state is a neutrino and the right-handed an antineutrino. The "sea-saw" mechanism for Majorana neutrinos can then provide a natural explanation for the very light neutrino masses inferred from tritium beta decay (TBD) and neutrino oscillation experiments [5].

The standard picture of neutrinoless double beta decay is that the *antineutrino* emitted from a neutron in a nucleus is absorbed as a *neutrino* on a neutron in the same nucleus. But there is in general no requirement in neutrinoless double beta decay that the second neutron be in the same nucleus (or indeed that the second nucleus be the same nuclide as the first, or even that the two down quarks undergoing weak interactions be in different neutrons). In this paper, we introduce the concept of "macroscopic neutrinoless double beta decay" (MDBD), in which a Majorana neutrino emitted from one nucleus is absorbed in a second nucleus. For example, in the single beta decay (XBD) from parent nucleus $X = (A, Z)$ to daughter nucleus $Y = (A, Z+1)$,

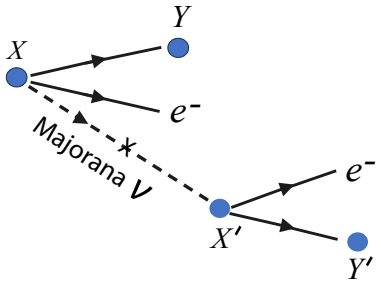


FIG. 1: Illustration of macroscopic neutrinoless double beta decay, with time running to the right. The first nucleus, X undergoes a beta decay emitting an electron and a Majorana antineutrino, which is absorbed as a neutrino by a second nucleus X' in an inverse beta decay. The sum of the energies of the two electron emitted is just the sum of the individual endpoint energies in the beta decays of X and X'.

$$X \to Y + e^- + \bar{\nu}_e, \tag{2}$$

the antineutrino produced is, for Dirac type neutrinos, distinct from ν_e and cannot participate in the inverse beta decay (IXBD) reaction

$$\nu_e + X \to e^- + Y; \tag{3}$$

the nucleus X can only absorb an electron neutrino, ν_e, to reach the final state $e^- + Y$. If neutrinos are Majorana however, then the neutrino and antineutrino are not distinct particles, and the antineutrino in the XBD can then participate in the IXBD. The combination of these

two sequential reactions, (2) and (3), is the macroscopic neutrinoless double beta decay, illustrated in Fig. 1,

$$X + X' \to Y + Y' + e^- + e^-, \tag{4}$$

where we add a prime to indicate the freedom of the two nuclei being different nuclides. This process is the macroscopic analog of the conventional neutrinoless double beta decay, 0νDBD. Both decays effectively turn two neutrons into two protons plus two electrons. Both decays violate lepton number conservation and require the neutrino to be Majorana.

Detection of neutrinoless double beta decay, whether in a single nucleus or via MDBD exchange of a non-zero mass Majorana neutrino between different nuclei would violate lepton number conservation and would establish that neutrinos are Majorana and not Dirac. In neutrinoless double beta decay the initial and final nuclei (or quarks more precisely) exchange a Majorana neutrino in various mass states. An important aspect of this exchange is the possibility of quantum interference between neutrino exchange in different mass states. This interference is implicitly included in calculation of microscopic 0νDBD [1]. Macroscopic beta decay, however, opens new quantum interference effects over the macroscopic distance scales of the separation between source and target nuclei.

The two processes have notable differences. All β-unstable nuclei are potential candidates for MDBD, while only a limited number of nuclei are candidates for 0νDBD. The uncertainties in the rate of MDBD are considerably smaller than in 0νDBD. In 0νDBD within a single nucleus, the uncertainty in the matrix elements [6, 7] owes both to the many processes within the standard model that can contribute to the decay, e.g., $n \to \Delta^{++} + 2e$, where the Δ^{++} lives virtually, as well as exchanges of virtual particles beyond the standard model in addition to Majorana neutrino exchange. Beyond-the-standard-model physics that could lead to 0νDBD include right-handed weak currents, exchange of heavy neutrinos or supersymmetric particles, etc.[1] By contrast, MDBD must come only from light massive Majorana neutrinos. Moreover, the matrix elements for sequential beta and inverse beta decay reactions in MDBD are precisely known.

Not only does the antineutrino source in neutrinoless MDBD not need to be the same nucleus as the target, the antineutrino emitted, as we detail later, does not need even to be an electron type. For example in $\pi^- \to \mu^- + \bar{\nu}_\mu$, the muon antineutrino, if Majorana, can be absorbed as an electron neutrino in an inverse beta decay.

In addition, while the 0νDBD rate is insensitive to the geometry of the source and is linearly proportional to the source mass, the rate for MDBD rate, as we spell out below, depends sensitively on the geometry of the source and is proportional to the source mass to the 4/3 power.

We emphasize that we do not introduce MDBD as a replacement for traditional 0νDBD experiments. While we calculate yields for several model MDBD systems, realistic experiments with radioactive nuclei are not feasible at the moment. Nonetheless the new concept of MDBD should stimulate new ways of looking at neutrinoless weak interactions.

In the next Section, II, we first review the calculation of the rate of single beta decay, and the cross section for inverse beta decay. In Sec. III we derive the rate of MDBD as a coherent quantum process between the initial single beta decay and the inverse beta decay, and derive the dependence of the MDBD rate on the geometry of the source. Then in Sec. IV we discuss how the MDBD signal is readily differentiated from the experimental two electron backgrounds. We conclude in Sec. V.

II. BETA AND INVERSE BETA DECAY WITH MASSIVE NEUTRINOS

In this section we first review the role of chirality and helicity for massive neutrinos in beta and inverse beta decay. We then briefly review the rates for emission of an antineutrino of given helicity in beta decay and the absorption of a neutrino of given helicity in inverse beta decay.

A. Chirality and helicity

Eigenstates of γ_5 have definite chirality; we denote the γ_5 eigenvalue in these states as *positive* ($\gamma_5 = 1$) or *negative* ($\gamma_5 = -1$). While chirality and helicity (the eigenvalue h of the projection of the spin direction along the direction of motion, $\hat{\Sigma}\cdot\hat{p}$) coincide for massless neutrinos, where a positive chirality state always has positive helicity, h=1, and a negative chirality state always has negative helicity h=-1, they are not the same for finite mass neutrinos. We denote positive helicity as *right handed*, and negative helicity as *left handed*.

In beta decay, antineutrinos are emitted with positive chirality, $\gamma_5 = 1$, while neutrinos can be absorbed in the inverse reaction only if they have negative chirality. Neutrinos are preferentially absorbed with helicity opposite to that of the antineutrino in beta decay. Since chirality is conserved for massless neutrinos, a massless Majorana antineutrino emitted in beta decay has the wrong chirality ever to be absorbed as a neutrino; both MDBD and 0νDBD are forbidden.

Independent of the neutrino mass, however, neutrinos and antineutrinos, in the absence of external forces, e.g., gravitational [10] or magnetic [11], propagate in states of definite helicity. When neutrinos have finite mass, chirality is no longer a constant of the motion,

[1] Nonetheless, even if such processes were to underlie 0νDBD, the observation of such double beta decays would establish that the neutrino is Majorana [8, 9].

since γ_5 does not commute with the mass term in the Hamiltonian. In detail, as reviewed in the Appendix, an antineutrino emitted with positive chirality has amplitude $\alpha^{\pm} = \sqrt{(1 \pm \beta_\nu)/2}$ to be right or left handed, where $\beta_\nu = v_\nu/c$, with v_ν the neutrino velocity. Similarly, a right or left handed neutrino has amplitude $\sqrt{(1 \mp \beta_\nu)/2} = \alpha^{\mp}$ to have the negative chirality needed to be absorbed in an inverse beta decay. Thus a Majorana neutrino effectively has a total amplitude for emission with positive chirality and absorption with negative chirality, summed over both intermediate helicities, $\alpha^+\alpha^- + \alpha^-\alpha^+ = \sqrt{1-\beta_\nu^2} = m_\nu/E_\nu$, where m_ν and E_ν are the neutrino mass and energy. States of definite helicity have amplitudes to be of either chirality, thus allowing neutrinoless double beta decay for finite mass Majorana neutrinos.

B. Single beta decay

We now discuss the amplitude, $\mathcal{A}^{ih}_{BD}$, and then the rate of beta decay, (2), with emission of a $\bar\nu_e$ in mass state i and helicity h, neglecting nuclear recoil (a better and better approximation the heavier the parent nucleus). The amplitude is

$$\mathcal{A}^{ih}_{BD} = \mathcal{M}_i \alpha^{ih}_{\bar\nu}. \tag{5}$$

where $\mathcal{M}_i \propto G_F V_{ud} U_{ei}$, with G_F the Fermi weak coupling constant, $V_{ud} = 0.97425$ the Cabbibo-Kobayashi-Maskawa (CKM) up-down quark matrix element, and U_{ei} the Pontecorvo-Maki-Nakagawa-Sakata (PMNS) neutrino mixing matrix element. For right and left antineutrino helicities, $\alpha^{i,h=\pm1}_{\bar\nu} = \alpha^{\pm}$. For given neutrino energy, β_i depends on the neutrino mass, m_i; since for $m_i \ll E_{\nu i}$, $\beta_i \simeq 1 - m_i^2/2E_{\nu i}^2$,

$$\alpha^{iR}_{\bar\nu} \simeq 1, \quad \alpha^{iL}_{\bar\nu} \simeq \frac{m_i}{2E_{\nu i}}. \tag{6}$$

The dependence on the neutrino mass state is through the factors U_{ei} and $\alpha^{ih}_{\bar\nu}$, and the helicity dependence resides in $\alpha^{ih}_{\bar\nu}$.

The full squared matrix element has the form

$$|\mathcal{M}_i|^2 = 2\pi W(E_e)|U_{ei}|^2, \tag{7}$$

where for tritium for example [12, 13],

$$W(E_e) = \frac{G_F^2}{2\pi}|V_{ud}|^2 F(Z,E_e)(m_{^3\mathrm{He}}/m_{^3\mathrm{H}})|M_f|^2, \tag{8}$$

with $F(Z,E_e)$ the Fermi Coulomb factor for the electron-^{3}He system, and $|M_f|^2$ the sum of the nuclear form factors for Fermi and Gamow-Teller transitions.[2] In further calculation we symbolically write the matrix element as $\mathcal{M}_i = \sqrt{2\pi W} U_{ei}$.

The rate of beta decay with emission of a neutrino of given helicity is then

$$d\Gamma^h_{XBD} = \sum_i \frac{d^3p_\nu}{(2\pi)^3}\frac{d^3p_e}{(2\pi)^3} 2\pi |\mathcal{M}_i|^2 (\alpha^{ih}_{\bar\nu})^2 \delta(\Delta M - E_e - E_{\nu i}), \tag{9}$$

where $\Delta M = m_X - m_Y$ is the total energy released in the beta decay.

Integrating over all electron states, and writing $d^3p_\nu = 4\pi p_\nu E_\nu dE_\nu$, we have

$$\frac{d\Gamma^h_{XBD}}{dE_\nu} = \frac{\bar\sigma(E_e)}{2\pi^2}\sum_i |U_{ei}|^2 (1 + h\beta_i) E_\nu \sqrt{E_\nu^2 - m_i^2}, \tag{10}$$

where $E_e = \Delta M - E_\nu$ and

$$\bar\sigma(E_e) \equiv p_e E_e W(E_e). \tag{11}$$

The differential rate of beta decay, for $m_i \ll E_\nu$, summed over h and using $\sum_i |U_{ei}|^2 = 1$, is

$$\frac{d\Gamma_{XBD}}{dE_\nu} \simeq \frac{\bar\sigma(E_e)}{\pi^2} E_\nu^2. \tag{12}$$

For tritium, in the limit of a zero energy neutrino [12], $\bar\sigma \simeq 3.834 \times 10^{-45}$ cm^2. The inverse of the mean lifetime, τ, of the nucleus X against beta decay (17.8 yr for tritium) is then $\int dE_\nu (d\Gamma_{XBD}/dE_\nu)$.

C. Inverse beta decay

While the rate of beta decay is an incoherent sum over the mass states in the emitted antineutrino, the rate of inverse beta decay depends strongly on the nature of the neutrino impinging on the target nucleus. For example, neutrinos from the Big Bang arrive at Earth in definite mass eigenstates, a result of the spatial separation of the mass components of a neutrino wavepacket caused by the dependence of the neutrino velocity on the mass state. By contrast, neutrinos from nuclear weak interactions, in ^{51}Cr for example [14], are emitted in pure electron neutrino flavor states. These neutrinos can initiate inverse beta decay whether the neutrino is Dirac or Majorana. On the other hand, antineutrinos can participate in inverse beta decay (with electron emission) only if the neutrino is Majorana. These antineutrinos can be either in mass eigenstates, e.g., if they come from the Big Bang, or in flavor eigenstates, e.g., from tritium beta decay or a nuclear power plant. If the incident neutrino was emitted as a Majorana antineutrino, the amplitude for inverse beta decay is a coherent sum over the mass eigenstates in the neutrino.

[2] For tritium, $|M_f|^2 = 1 + 2.788(g_A/g_V)^2$, with $(g_A/g_V)^2 = 1.6116$, while for the neutron, $|M_f|^2 = 1 + 3(g_A/g_V)^2$.

Common to all these processes is the inverse beta decay amplitude for a neutrino in a given mass state. Specifically, the amplitude, $\mathcal{A}^{ih}_{IXBD}$, for inverse beta decay induced by a neutrino with velocity β_i, mass m_i and helicity h incident on a target nucleus, is

$$\mathcal{A}^{ih}_{IXBD} = \mathcal{M}_i \alpha^{ih}_\nu, \tag{13}$$

where $\alpha^{ih}_\nu = \sqrt{(1-h\beta_i)/2}$, with $\mathcal{M}_i$ the same as before.

The cross section for inverse beta decay for an incident neutrino in a given mass state i and helicity h is similarly (cf. Eq. (9)),

$$\begin{aligned}\frac{d\sigma^{ih}_{IXBD}}{d\Omega_e} &= \\ &\int \frac{p_e^2 dp_e}{(2\pi)^2} |\mathcal{M}_i|^2 (\alpha^{ih}_\nu)^2 \delta(m_X + E_\nu - m_Y - E_e) \\ &= \frac{p_e E_e}{(2\pi)^2} |\mathcal{M}_i|^2 (\alpha^{ih}_\nu)^2 = \frac{\bar\sigma(E_e)}{4\pi} |U_{ei}|^2 (1-h\beta_i),\end{aligned} \tag{14}$$

and the total IXBD cross section σ^{ih}_{IXBD} equals $\bar\sigma |U_{ei}|^2 (1-h\beta_i)$. As in beta decay, the helicity dependence is in the factor α^{ih}_ν. The scale of both the lifetime of a nucleus under beta decay, and the IXBD cross section is set by $\bar\sigma(E_e)$.

If the initial neutrino is fully relativistic in mass state i ($\beta_\nu \to 1$), then only the left handed helicity component can lead to emission of an electron, and the cross section for an incident mass state i is $2\bar\sigma |U_{ei}|^2$. (Were the initial neutrino in an incoherent sum over mass states i, the cross section would bcome $2\bar\sigma$.) But for slowly moving relic neutrinos ($\beta_\nu \to 0$), $\alpha^{ih}_\nu \to 1/\sqrt{2}$ and the IXBD amplitude becomes independent of the neutrino helicity. More generally, if the initial neutrino state is a coherent sum of mass states, the rate of IXBD reflects interference between the states, a problem we focus on in calculating the rate of MDBD below.

III. MACROSCOPIC DOUBLE BETA DECAY

We turn now to calculating the rate of macroscopic double beta decay in terms of the known physics of the single beta decay, XBD, and inverse beta decay, IXBD. The rate of MDBD within a sample of atoms of nucleus X, with the sample acting both as the source of beta decays as well as the target for inverse beta decays, depends on both the microscopics of XBD and IXBD as well as the geometry of the ensemble of X atoms present. For spacing between the atoms large compared with the characteristic intermediate neutrino wavelength, the neutrinos can be taken to be on-shell, in contrast to neutrinoless double beta decay within a single nucleus. The MDBD process can take place for either helicity of the intermediate neutrino.

Since the Majorana neutrino in MDBD exists only as an intermediary between the initial electron and final electron emission processes, the contributions of the different neutrino mass states are coherent, and give rise to quantum interference. To see this effect it is necessary to evaluate the MDBD rate in terms of the total amplitude for the process.

While neutrino oscillations become important in processes over astrophysical distances, e.g., in the sun and in neutron stars, they are insignificant in MDBD over laboratory distances, except for very small neutrino energies. The characteristic length (in meters) in neutrino oscillations for a neutrino of energy E_ν (in MeV) is $L(\mathrm{m})_{osc} \simeq E_\nu(\mathrm{MeV})/\Delta m^2_{31}(\mathrm{eV}^2)$, where $\Delta m^2_{31} = m_3^2 - m_1^2 \simeq 2.5\times10^{-3}\mathrm{eV}^2$ corresponds to the difference of the squares of the masses of the heaviest and lightest neutrinos. Thus $L_{osc} \sim E_\nu(\mathrm{MeV})$ km. Neutrinos of sub-keV energy could undergo neutrino oscillations in MDBD in large samples, but their effect would be hard to observe.

We assume the initial beta decay to take place at point $\vec r$ and the inverse beta decay at $\vec r\,'$. The total amplitude for the process $X + X \to Y + Y + e^- + e^-{}'$ is

$$\begin{aligned}&\mathcal{A}_{MDBD}(\vec r - \vec r\,') = \\ &\sum_{ih} \int \frac{d^3 p_\nu}{(2\pi)^3} \frac{\left(\mathcal{A}^{ih}_{XBD} e^{i(\vec p_\nu + \vec p_e)\cdot\vec r}\right)\left(\mathcal{A}^{ih}_{IXBD} e^{i(\vec p\,'_e - \vec p_\nu)\cdot\vec r\,'}\right)}{\Delta M - E_e - E_\nu + i\eta},\end{aligned} \tag{15}$$

where $\eta \to 0^+$. Then using the amplitudes (5) and (13), doing the sum over helicities,

$$\sum_h \alpha^{ih}_{\bar\nu} \alpha^{ih}_\nu = \sqrt{1-\beta_i^2} = m_{\nu i}/E_\nu, \tag{16}$$

and the angular integration over the directions of the intermediate neutrino, we have

$$\begin{aligned}\mathcal{A}_{MDBD} &= e^{i(\vec p_e\cdot\vec r + \vec p\,'_e\cdot\vec r\,')} \frac{\sqrt{W(E_e)W(E'_e)}}{\pi|\vec r - \vec r\,'|} \sum_i U^2_{ei} m_{\nu i} \\ &\times \int \frac{E_\nu dE_\nu \sin(p_\nu|\vec r - \vec r\,'|)}{\Delta M - E_e - E_\nu + i\eta}.\end{aligned} \tag{17}$$

For large $|\vec r - \vec r\,'|$ compared with characteristic $1/p_\nu$, only the on-shell contribution of the neutrino (from the imaginary part $-i\pi\delta(X)$ of the denominator term, $1/(X + i\eta)$) is significant. In this macroscopic limit the integral in the lower line of Eq. (17) becomes $-i\pi E_\nu \sin(p_\nu|\vec r - \vec r\,'|)$, where now $E_\nu = \Delta M - E_e$. We drop the overall phase factors, which do not enter the MDBD rate, and finally arrive at the MDBD amplitude,

$$\mathcal{A}_{MDBD} = \sqrt{W(E_e)W(E'_e)} \frac{\sin(p_\nu|\vec r - \vec r\,'|)}{|\vec r - \vec r\,'|} \sum_i U^2_{ei} m_{\nu i}. \tag{18}$$

The total rate of MDBD with one emitter and one

absorber is then

$$\Gamma_{MDBD} = \int \frac{d^3p_e}{(2\pi)^3}\frac{d^3p'_e}{(2\pi)^3}|\mathcal{A}_{MDBD}|^2 2\pi\delta(2\Delta M - E_e - E'_e). \quad (19)$$

For $p_\nu|\vec{r}-\vec{r}\,'| \gg 1$ the $\sin^2$ factor, slightly cross-grained in $\vec{r}\,'$, becomes 1/2, and thus

$$\Gamma_{MDBD} = \frac{\mathcal{K}}{4\pi|\vec{r}-\vec{r}\,'|^2}, \quad (20)$$

where the microscopic rate factor, after doing the E'_e integral, becomes

$$\mathcal{K} = \bar{m}^2 \int \frac{\bar{\sigma}(E_e)\bar{\sigma}(E'_e)}{\pi^2} dE_e. \quad (21)$$

Here $E'_e = 2\Delta M - E_e$, and

$$\bar{m} \equiv |\sum_i U_{ei}^2 m_{\nu i}| \quad (22)$$

is the average neutrino mass entering neutrinoless double beta decay.

We can understand the remaining structure of the MDBD rate by considering simply the single mass state contribution, denoted as Γ^i_{MDBD}. The beta decay of an X nucleus at point $\vec{r}$ produces a flux, per unit neutrino energy, of neutrinos in helicity state h of energy E_ν at point $\vec{r}\,'$,

$$\frac{dF^{ih}(\vec{r}\,')}{dE_{\nu i}} = \frac{1}{4\pi|\vec{r}-\vec{r}\,'|^2}\frac{d\Gamma^{ih}_{XBD}}{dE_{\nu i}}. \quad (23)$$

Thus the full rate for neutrinos emitted at point $\vec{r}$ in mass state i to be absorbed at point $\vec{r}\,'$ is

$$\Gamma^i_{MDBD} = \sum_h \int \frac{dF^{ih}(\vec{r}\,')}{dE_{\nu i}} dE_{\nu i}\sigma^{ih}_{IXBD} = \frac{\mathcal{K}_i}{4\pi|\vec{r}-\vec{r}\,'|^2}, \quad (24)$$

where

$$\mathcal{K}_i = \int dE_{\nu i}\sum_h \frac{d\Gamma^{ih}_{XBD}}{dE_{\nu i}}\sigma^{ih}_{IXBD} = |U_{ei}|^4 m^2_{\nu i}\int dE_{\nu i}\frac{\bar{\sigma}(E_e)\bar{\sigma}(E'_e)}{\pi^2}; \quad (25)$$

this result is precisely the single neutrino mass state (i) contribution to $\mathcal{K}$, Eq. (21), with the identifications $E_e = \Delta M - E_{\nu i}$ and $E'_e = \Delta M + E_{\nu i} = 2\Delta M - E_e$.

The integral in $\mathcal{K}$ depends very weakly on the neutrino masses since $m_\nu \ll m_e$, and we neglect them in the integral. Furthermore the $\bar{\sigma}$ do not vary greatly over the range of neutrino energies, and we write them as $\bar{\sigma}$ evaluated at the end point energy times a correction. Neglecting the energy dependence in the Fermi Coulomb term, F in $\bar{\sigma}$ we have

$$\mathcal{K} = \frac{1}{\pi^2}\bar{m}^2\bar{\sigma}^2_{end}K_{end}\mathcal{J}, \quad (26)$$

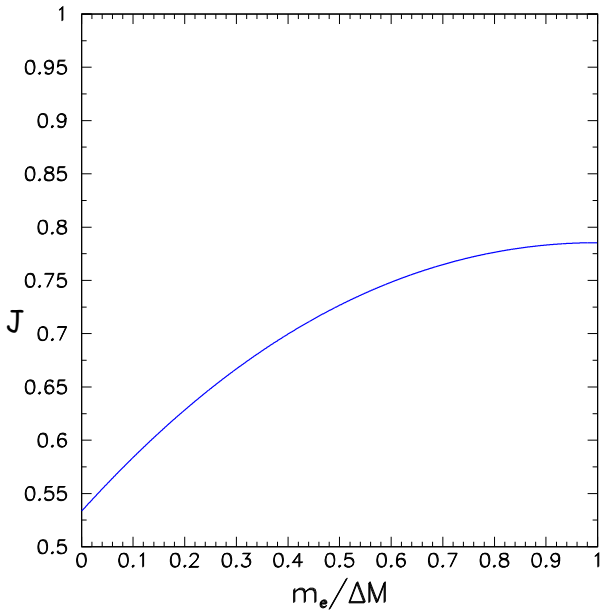


FIG. 2: The dimensionless integral $\mathcal{J}$ entering the MDBD rate, as a function of $m_e/\Delta M$.

where $K_{end} = \Delta M - m_e$ is the endpoint kinetic energy of the XBD, $\bar{\sigma}_{end} \equiv \bar{\sigma}(E_e = \Delta M)$, and the dimensionless factor $\mathcal{J}$ is given by

$$\mathcal{J}(m_e/\Delta M) = \int_0^{K_{end}} \frac{dE_\nu}{K_{end}}\frac{p_e E_e p'_e E'_e}{(K^2_{end} - m_e^2)K^2_{end}}. \quad (27)$$

Figure 2 shows $\mathcal{J}$ as a function of $m_e/\Delta M$. In the limit that the Q value in the XBD is small compared with the electron mass, or $\Delta M - m_e << m_e$, as in tritium, then $\mathcal{J} \to \pi/4$ (this factor arises from the averaging of the momenta of the electrons), and

$$\mathcal{K} \to \frac{\bar{m}^2\bar{\sigma}^2_{end}}{4\pi}K_{end}. \quad (28)$$

In the opposite limit, $\Delta M \gg m_e$, the correction factor $\mathcal{J}$ becomes 8/15, and $\mathcal{K} \to (8\bar{m}^2\bar{\sigma}^2_{end}/15\pi^2)K_{end}$.

A. Quantum interference and coherence

The rate of MDBD is proportional to the square of the weighted neutrino mass $|\sum_i U^2_{ei}m_{\nu i}|^2$. This term includes both the direct ($i = j$) MDBD process, with a sum of the rates for single mass eigenstates, $\sum_i |U_{ei}|^4 m^2_{\nu i}$, as well as the interference between different mass eigenstates ($i \neq j$). By contrast, if the incident neutrino is an incoherent sum of mass states, then the rate is proportional to the $i = j$ term alone, i.e.,

$$\sum_i |U_{ei}|^4 m^2_{\nu i} \equiv m^2_{incoh}, \quad (29)$$

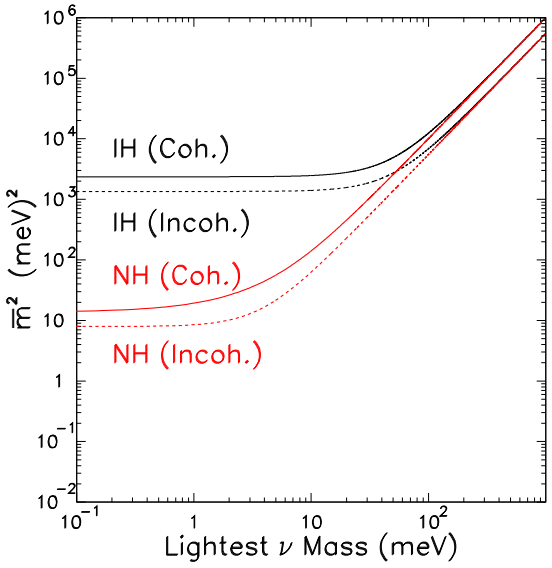


FIG. 3: The calculated $\bar{m}^2$ for the normal (NH) and inverted (IH) neutrino mass hierarchies with and without interference between the mass eigenstates. The curves labelled "coherent" assume zero Majorana phases (with respect to the CP phase), while the curves labelled "incoherent" neglect the off-diagonal interference between different mass eigenstates. In this case coherence increases $\bar{m}^2$ and the rate of MDBD.

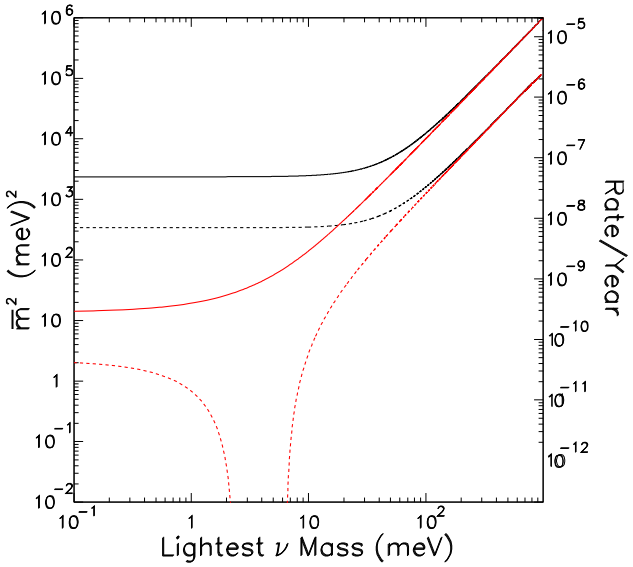


FIG. 4: Full range of $\bar{m}^2$ for the normal and inverted hierarchies. The solid curves show the same curves labelled "coherent" in Fig. 3, while the dashed curves show the maximal destructive interference from possible Majorana phases. The scale on the right shows the corresponding MDBD rate expected in a 100 g tritium target. The rate is proportional to the mass of the target to the 4/3 power.

a very different weighting of the neutrino masses.

The dependence of $\bar{m}$ on possible phases of the U_{ei} is a consequence of quantum interference between different mass states i in macroscopic double beta decay. Explicitly, $\bar{m}$ can be written in terms of the CP phase δ and Majorana phases λ_a and λ_b, as,

$$\bar{m} = \left||U_{e1}|^2 e^{2i\lambda_a} m_1 + |U_{e2}|^2 e^{2i\lambda_b} m_2 + |U_{e3}|^2 e^{-2i\delta} m_3\right|. \tag{30}$$

Figure 3 shows $\bar{m}^2$ as a function of lightest neutrino mass for the normal and inverted mass hierarchies, using the neutrino oscillation parameters tabulated in [17]. The curves labelled "incoherent" neglect the interference terms in $\bar{m}^2$, and include only the diagonal sum over mass eigenstates, i.e., with $\bar{m}^2$ replaced by m^2_{incoh}. In the curves labelled "coherent," we assume that the Majorana CP phases equal $-\delta$, so that all the phases drop out of $\bar{m}$, and $\bar{m}^2 - m^2_{incoh} = \sum_{i\neq j} |U_{ei}|^2 |U_{ej}|^2 m_{\nu i} m_{\nu j} > 0$. In this case, coherence increases the MDBD rate. For given neutrino mass splittings, the curves are in fact simply quadratic functions of the lightest neutrino mass.

On the other hand, if the Majorana CP phases differ from $-\delta$, coherence can, as illustrated in Fig. 4, decrease the rate, exactly as in 0νDBD [1]. Figure 4 also shows, on the right hand scale, the MDBD rate for a spherical source of 100 g of tritium, calculated from Eq. (33) below.

Macroscopic double beta decay remains coherent as long as the neutrino wavepacket travelling from source to target stays together. However, the different mass components of the wavepacket physically separate and destroy coherence at large distances owing to the mass dependence of their velocities, $\delta v/c \sim \frac{1}{2}\Delta m^2_\nu / E^2_\nu$ [11]. If the initial neutrino wavepacket is of length ℓ, then decoherence takes place over distances $L_{dec} \sim \ell E^2_\nu / \Delta m^2_\nu \sim \ell E_\nu L_{osc}$, where L_{osc}, discussed above, is the length over which neutrino oscillations become significant. The estimate $\ell E_\nu \sim 1$ nm-MeV [15] implies that L_{dec} is $\sim 10^4 L_{osc}$, or $L_{dec} \sim 10^4 E_\nu(\mathrm{MeV})/\Delta m^2_\nu(\mathrm{eV}^2)$ m. A detailed discussion of decoherence over astrophysical distances must thus take flavor oscillations of the neutrino wave packets into account.

B. Dependence of the MDBD rate on geometry

We next consider the rate of MDBD in a macroscopic sample of N atoms of X with uniform density n. For an ensemble of beta emitters, Eq. (24) implies the total rate of MDBD,

$$\mathcal{R}_{MDBD} = \int d^3r d^3r' \frac{n^2 \mathcal{K}}{4\pi|\vec{r}-\vec{r}\,'|^2} = \frac{N^2\mathcal{K}}{4\pi}\left\langle \frac{1}{(\vec{r}-\vec{r}\,')^2}\right\rangle. \tag{31}$$

For isotropic scaling at fixed density, the rate scales as the fourth power of the linear size of the system, or $N^{4/3}$. On the other hand, the rate of 0νDBD scales with N.

The detailed evaluation of the integral depends on the geometry of the target. It is readily evaluated for a spherical target of radius R by writing,

$$\int \frac{d^3r d^3r'}{(\vec{r}-\vec{r}')^2} = \int \frac{d^3k}{4\pi k} \left| \int d^3r e^{i\vec{k}\cdot\vec{r}} \right|^2 = 4\pi^2 R^4, \quad (32)$$

where we use $\int d^3r e^{i\vec{k}\cdot\vec{r}} = (4\pi/k^3)(\sin kR - kR\cos kR)$.

The total double beta decay rate for a spherical source[3] is then

$$\mathcal{R}_{MDBD} = \frac{9}{16\pi}\frac{N^2}{R^2}\mathcal{K}, \quad (33)$$

which shows explicitly the scaling with the size of the sample (at fixed density) as $N^{4/3}$.

C. Estimate of R_{MDBD}

We estimate R_{MDBD} from Eq. (33) with (28). For tritium,

$$\mathcal{R}_{MDBD} = \frac{9}{64\pi^2}\frac{N_T^2}{R^2}\bar{m}^2\bar{\sigma}_T^2 K_{end}\,; \quad (34)$$

with a 100 g sphere of tritium ($N_T \simeq 2\times10^{25}$ nuclei), $\mathcal{R}_{MDBD} \simeq 2.32\times10^{-5}(\bar{m}/1\,\mathrm{eV})^2$/year. It is instructive to compare this rate with the conventional neutrinoless double beta decay rates for various nuclei. No 0νDBD events have been positively identified [4], and the most sensitive recent results include those on ^{76}Ge [18, 19], ^{136}Xe [20–22], ^{130}Te [23], ^{82}Se [24, 25], and ^{100}Mo [26]. Table I lists the expected 0νDBD rates for these nuclei with an exposure of 100 g-yr, assuming $\bar{m} = 0.1$ eV. As we see in the Table, the tritium MDBD rate is four to five orders of magnitude lower than those expected for 0νDBD. This difference reflects the much smaller Q=16.8 keV value in tritium beta decay than in 0νDBD, e.g., Q = 2.04 MeV for ^{76}Ge and Q=2.46 MeV for ^{136}Xe 0νDBD.

To illustrate the importance of a large Q value, we compare MDBD for neutrons (where $n \to p + e^- + \bar{\nu}_e$ followed by $\nu_e + n \to p + e^-$) with tritium. In this double beta decay Q= 2 ×0.782 MeV = 1.564 MeV. Furthermore $\bar{\sigma}_n$ is a factor $\sim$ 20 larger than in tritium, which has comparable matrix elements. In a sample of 100 g of neutrons occupying the spherical volume as would 100 g of tritium, the MDBD rate is a factor $\sim 10^5$ larger than in a comparable sample of tritium. In fact, the MDBD rate for such a neutron sample is comparable to that in an equivalent sample of nuclei in 0νDBD. Clearly though, it would be impossible to do such an experiment in a cloud of laboratory neutrons.[4]

A somewhat more realistic candidate nucleus to consider in searching for MDBD is ^{11}C, which undergoes a β^+ decay with a half life of 22.3 min. with a Q value of 1.98 MeV. We estimate that a 100 g spherical sample of ^{11}C. which has a density 2.2 g/cm^3, and contains 3/11 of the number of atoms in a 100 g sample of tritium, would have a MDBD rate of 5.14×10^{-5} per year for $\bar{m} = 0.1$ eV, as shown in Table I. This rate is significantly larger than the MDBD rate for tritium, but still lower than the rate for the 0νDBD sources listed in Table I. As mentioned, the MDBD rate contains no uncertainties arising from the nuclear matrix elements, distinctly different from in 0νDBD.

IV. MDBD SIGNAL VS. BACKGROUND

A. Electron distribution in MDBD

The characteristic feature of MDBD is that the sum of the two electron energies is just twice the total energy released in a single beta decay. The distribution of the electron pairs has the structure, in the limit of small neutrino mass,

$$\begin{aligned} d^2N(E_e,E_e') &\propto p_eE_eF(E_e)dE_e p_e'E_e'F(E_e')dE_e' \\ &\times \int dE_\nu \delta(\Delta M - E_\nu - E_e)\delta(\Delta M + E_\nu - E_e') \\ &= p_eE_eF(E_e)F(E_e')dE_e p_e'E_e'dE_e' \\ &\times\delta(2\Delta M - E_e - E_e'). \end{aligned} \quad (35)$$

The E_ν^2 from the neutrino phase space is canceled by neutrino helicity factor $1-\beta^2 = (m_\nu/E_\nu)^2$. Then the single electron distribution in MDBD has the form,

$$\frac{dN_e}{dK_e} \propto p_eE_eF(E_e)F(E_e')p_e'E_e', \quad (36)$$

where here $E_e' = 2\Delta M - E_e$.

This distribution, shown in Fig. 5 in terms of the electron kinetic energy K_e for tritium MDBD, is clearly symmetric about the single beta decay endpoint, $K_e = K_{end}$.

[3] We give the result for a spherical source only for illustration, ignoring the complication that electrons produced within a sufficiently large spherical sample rapidly lose energy traversing the source and cannot readily be detected. For such a reason, the PTOLEMY experiment [16] is aiming for two dimensional targets, using tritiated graphene. A realistic MDBD experimental design would similarly require a more planar geometry, at the cost of reducing the probability of a given antineutrino from the initial beta decay finding a target for inverse decay.

[4] On the other hand, a neutron star contains beneath its crust a stable liquid of order 10^{57} neutrons in a ∼10 km sphere, which implies a geometric enhancement over MDBD in 100 g of tritium by a factor $\sim 10^{53}$. The rate of MDBD is, however, significantly suppressed by Pauli exclusion in both URCA and modified URCA processes, as well as by BCS pairing. Unfortunately there is no way apparent to distinguish such MDBD processes in neutron stars, even in their cooling.

Nucleus	$T_{1/2}$ for $\bar{m} = 0.1$ eV	Yield per 100 g-yr
^{3}H (MDBD)	–	2.3×10^{-7}
n (MDBD)	–	3.4×10^{-2}
^{11}C (MDBD)	–	5.1×10^{-5}
^{76}Ge (0νDBD) [18, 19]	$3.7 \times 10^{25} < T_{1/2} < 2.0 \times 10^{26}$ yr	$2.7 \times 10^{-3} < Y < 1.5 \times 10^{-2}$
^{136}Xe (0νDBD) [20–22]	$0.1 \times 10^{26} < T_{1/2} < 1.8 \times 10^{26}$ yr	$1.7 \times 10^{-3} < Y < 3.0 \times 10^{-2}$
^{130}Te (0νDBD) [23]	$5.9 \times 10^{24} < T_{1/2} < 6.7 \times 10^{25}$ yr	$4.7 \times 10^{-3} < Y < 5.4 \times 10^{-2}$
^{82}Se (0νDBD) [24, 25]	$1.0 \times 10^{25} < T_{1/2} < 7.5 \times 10^{25}$ yr	$6.8 \times 10^{-3} < Y < 4.8 \times 10^{-2}$
^{100}Mo (0νDBD) [26]	$4.7 \times 10^{24} < T_{1/2} < 1.4 \times 10^{25}$ yr	$2.9 \times 10^{-2} < Y < 8.8 \times 10^{-2}$

TABLE I: Expected yields, Y, for MDBD and 0νDBD for a 100 g-yr exposure using various nuclei. We assume the Majorana neutrino effective mass $\bar{m} = 0.1$ eV. The uncertainties in the predicted $T_{1/2}$ and yield for 0νDBD reflect the range of uncertainties of the nuclear matrix elements adopted by Ref. [4] to relate the current experimental limits on $T_{1/2}$ to values of $\bar{m}$. For MDBD we assume 100 g spherical sources of tritium (and neutrons, for illustration) with density 1 g/cm^3 and ^{11}C with density 2.2 g/cm^3.

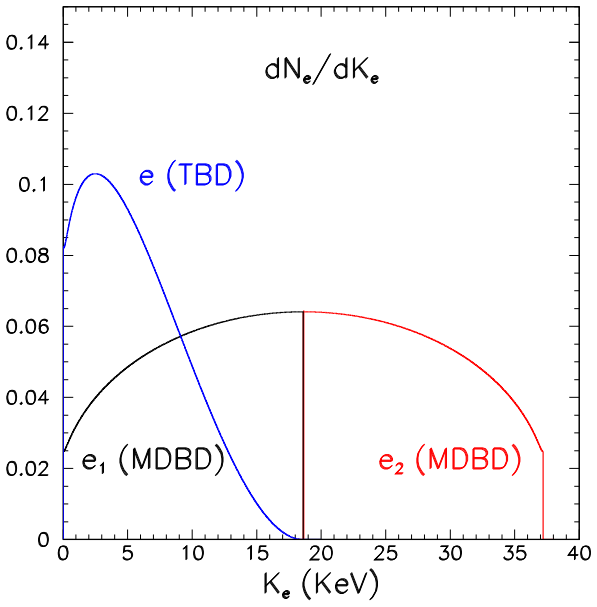


FIG. 5: The electron distributions in single tritium beta decay and in tritium MDBD, where e_1 is the lower energy and e_2 the higher energy electron. Here e_1 is the electron produced in the initial beta day, and e_2 the electron emitted in the final inverse beta decay. The detailed structure of the single electron energy distributions at K_{end}, shown as a single vertical line, is in fact two curves separated essentially by $2m_\nu$, too fine to be seen in the figure.

The figure shows for comparison the electron distribution from single beta decay, which vanishes near K_{end}, as we see from Eq. (12), essentially as

$$\frac{dN_e}{dK_e} \propto \frac{d\Gamma}{dE_e} = \frac{\bar{\sigma}(E_e)}{2\pi^2}(\Delta M - m_e - K_e)^2; \qquad (37)$$

the distribution is dominated by electrons emitted with a right handed neutrino. In this figure, we normalize the individual distributions to unity, and take the Fermi Coulomb correction to be $2\pi\eta/(1 - e^{-2\pi\eta})$ with $\eta = Ze^2/v_e$. The non-zero neutrino mass leads to a falloff of the e_1 distribution at $K_{end} - m_\nu$ and a rise of the e_2 distribution at $K_{end} + m_\nu$, too fine a structure to see in the figure.

B. Background

Although the signal for a macroscopic neutrinoless double beta decay is that the sum of the energies of the two electrons in the event is precisely $2K_{end}$, it would seem, given the high rates of single beta decay, that the challenge of separating the signal from the background is insurmountable. The 2×10^{25} tritons in 100 g of tritium, with a half-life of 12.3 years, would produce $\sim 2.5 \times 10^{16}$ decays per second. However, only a tiny fraction of the decays give electrons with energy near the beta decay endpoint. An analogous challenge to separate the signal from the background is encountered in the proposed detection of relic neutrinos using the ITBD reaction [16, 27], where the signals are separated from the endpoint by twice the neutrino mass. Long et al. [12] show that an energy resolution better than 0.7 m_ν is sufficient to reach a signal to background ratio better than 1.

The signal to noise ratios for MDBD should be much better than in relic neutrino detection, and do not require superb energy resolution. As shown in Fig. 5, one of the two electrons from MDBD has an energy greater the endpoint energy of TBD, and up to twice the endpoint energy. By requiring that the more energetic electron from the MDBD candidate event has an energy sufficiently higher than the endpoint energy, the background can be rejected at only a small cost to the MDBD detection efficiency.

The favorable background rejection capability of MDBD is further illustrated in Fig. 6a, where the axes are the individual electron kinetic energies. An MDBD event would appear as a point on the diagonal line

$K_1+K_2 = \Delta M - 2m_e$ in this figure. The MDBD accidental background from two electrons emitted in two independent single beta decays would lie in the red box in the figure, and except at the single point where the red square touches the straight line, the background is separated from the two electron MDBD event. The background from the upper-right corner of the square in Fig. 6a can be readily rejected by requiring that the MDBD candidate events are well separated from this corner.

By contrast, the background in the 0νDBD reaction is from the 2νDBD reaction. The two electron kinetic energies from the 2νDBD background can reach the diagonal signal line in 0νDBD everywhere, as shown by the red triangle in Fig. 6b. These 2νDBD background events cannot be rejected without a significant loss of detection efficiency for the 0νDBD signals, unless superb energy resolution is achieved.

The time separation between the two electrons can also be used to reject accidental background in MDBD. The two electrons from an MDBD event occur in a narrow time window, the travel time from source to target, $\delta t \sim R/c$, which can be of order tens of picoseconds, while the electrons from single beta decays are uncorrelated in time. In contrast the 2νDBD background in 0νDBD cannot be rejected on the basis of time separation.

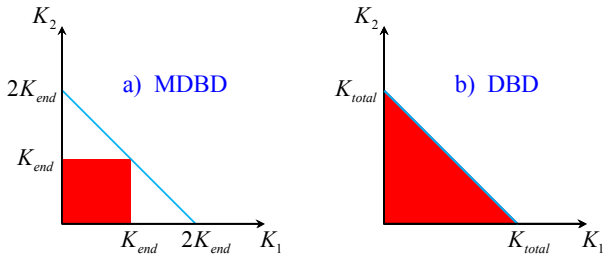


FIG. 6: The energy spectrum of two-electron events, with background in red, in a) MDBD and b) 0νDBD. The axes are the kinetic energies of the individual electrons. The kinetic energies of the two electrons in both neutrinoless double beta decays lie along the (blue) diagonal line extending from the first electron having K_{total} (with $K_{total} = 2K_{end}$ in MDBD) and the second with 0, to the reverse. The energies of two electrons produced in single beta decays, the background in MDBD, lie in the red box in a), reaching the diagonal line only at a single point. In contrast, in 0νDBD experiments the background from double beta decay with neutrinos lies in the red triangle in b), coming up to the diagonal line everywhere.

V. CONCLUSION

While neutrinoless double beta decay of single nuclei is the most promising experimental tool for testing the fundamental question of the Dirac or Majorana nature of neutrinos, the new process of macroscopic neutrinoless double beta decay we have introduced here is another manifestation of Majorana neutrinos with non-zero mass. The MDBD process shares features in common with single nucleus neutrinoless double beta decay; both depend on neutrinos being massive and Majorana, and both are affected by quantum intererence between different neutrino mass states. The two processes have significant differences, however, including the absence of nuclear matrix element uncertainties for the MDBD rate and the different nature of the experimental backgrounds in these two processes. In addition MDBD exhibits the new phenomenon of quantum coherence over macroscopic distances, related, but not equivalent to neutrino oscillations.

Macroscopic double beta decay combines the processes of beta decay – as is being studied for tritium in the KATRIN [28] experiment for measuring the neutrino mass – and capture of neutrinos, as in the PTOLEMY experiment [16] to detect primordial neutrinos from the Big Bang. The MDBD process combining these two processes, could in principle be accessible in either of these two experiments. Our detailed analysis of various characteristics of MDBD, including expected rates, makes it clear that, given the quantities of tritium present, MDBD events are too rare to be detectable in the two experiments.

Nor is MDBD a viable alternative, at this point, to the well established neutrinoless double beta decay experiments to test the Majorana nature of neutrinos. We do not present MDBD as a currently feasible experiment. Nevertheless, the similarities and distinct differences between these two processes provide useful perspectives on the underlying mechanisms for these two processes, and indicate new directions in which the concept of MDBD can be explored.

An example, as mentioned earlier, is the analog of MDBD that can occur with emission of a Majorana antineutrino with a flavor α other than electron, e.g., in $\pi^- \to \mu^- + \bar{\nu}_\mu$. The amplitude for capture of the emitted antineutrino on a nucleus as an electron neutrino would be proportional to $\sum_i U_{\alpha i} U_{ei} m_{\nu i}$, which is non-zero even if no phases enter the $U_{\alpha i}$. Such conversion of a Majorana $\bar{\nu}_\mu$ into a ν_e cannot occur in neutrinoless double beta decay within a single nucleus, simply by energy conservation, but can occur macroscopically.

Acknowledgments

This research was supported in part by the NSF Grant No. PHY-1812377 and by the Japan Science and Technology Agency (JST) as part of the Adopting Sustainable Partnerships for Innovative Research Ecosystem (ASPIRE), Grant Number JPMJAP2318, and was carried out in part at the Aspen Center for Physics, which is supported by National Science Foundation grant PHY-2210452, and at the National Central University in Taiwan under the Yushan Fellow Program.

[1] M. J. Dolinski, A. W. P. Poon, and W. Rodejohann, Neutrinoless double-beta decay: status and prospects, Annu. Rev. Nucl. Part Sci. **69**, 219 (2019).

[2] S. R. Elliott and P. Vogel, Double beta decay, Annu. Rev. Nucl. Part. Sci. 52, 115 (2002).

[3] M. Agostini, G. Benato, J. A. Detwiler, J. Menéndez, and F. Vissani, Toward the discovery of matter creation with neutrinoless $\beta\beta$ decay, Rev. Mod. Phys. 95, 025002 (2023).

[4] A. Barabash, Future beta decay experiments: recent achievements and future prospects, Universe **9**, 290 (2023).

[5] A. Balantekin and B. Kayser, On the properties of neutrinos, Annu. Rev. Nucl. Part Sci. **68**, 313 (2018).

[6] W. C. Haxton and G. J. Stephenson, Double Beta Decay, Prog. Part. Nucl. Phys. 12, 409 (1984).

[7] J. Engel and J. Menéndez, Status and Future of Nuclear Matrix Elements for Neutrinoless Double-Beta Decay: A Review, Rep. Prog. Phys. 80, 046301 (2017).

[8] J. Schechter and J. F. Valle, Neutrinoless double-β decay in SU(2)×U(1) theories, Phys. Rev. D 25, 2951 (1982).

[9] M. Duerr, M, Lindner, and A. Merle, On the Quantitative Impact of the Schechter-Valle Theorem, JHEP 1106:091 (2011).

[10] G. Baym and J. C. Peng, Evolution of Primordial Neutrino Helicities in Cosmic Gravitational Inhomogeneities, Phys. Rev. D 103, 123019 (2021).

[11] G. Baym and J. C. Peng, Evolution of Primordial Neutrino Helicities in Astrophysical Magnetic Fields and Implications for their Detection, Phys. Rev. Lett. 126, 191803 (2021).

[12] A. J. Long, C. Lunardini, and E. Sabancilar, Detecting non-relativistic cosmic neutrinos by capture on tritium: phenomenology and physics potential, J. Cosm. and Astropart. Phys. JCAP 1408, 038 (2014).

[13] R. G. H. Robertson and D. A. Knapp, Direct Measurements of Neutrino Mass, Annu. Rev. Nucl. Part. Sci. 38, 185 (1988).

[14] J. C. Peng and G. Baym, Inverse tritium beta decay with relic neutrinos, solar neutrinos, and a ^{51}Cr source, Phys. Rev. D 106, 063018 (2022).

[15] B. J. P. Jones, E. Marzec, and J. Spitz, Width of a beta-decay-induced antineutrino wave packet, Phys. Rev. D 107, 013008 (2023).

[16] E. Baracchini et al., PTOLEMY: A Proposal for Thermal Relic Detection of Massive Neutrinos and Directional Detection of MeV Dark Matter; arXiv:1808.01892; M. G. Betti et al. (PTOLEMY Collaboration), Neutrino physics with the PTOLEMY project: active neutrino properties and the light sterile case, JCAP 07, 047 (2019), arXiv:1902.05508 [astro-ph.CO].

[17] X. Qian and J. C. Peng, Physics with Reactor Neutrinos, Rep. Prog. Phys. 82, 036201 (2019).

[18] I. J. Arnquist et al. (Majorana Collaboration), Final Result of the Majorana Demonstrator's Search for Neutrinoless Double-β Decay in ^{76}Ge, Phys. Rev. Letters 130, 062501 (2023).

[19] M. Agostini et al. (GERDA Collaboration), Final Results of GERDA on the Search for Neutrinoless Double-β Decay, Phys. Rev. Letters 125, 252502 (2020)

[20] S. Abe et al. (KamLAND-Zen Collaboration), Search for the Majorana Nature of Neutrinos in the Inverted Mass Ordering Region with KamLAND-Zen,, Phys. Rev. Letters 130, 051801 (2023).

[21] E. Aprile et al. (XENON Collaboration), Double-weak decays of ^{124}Xe and ^{136}Xe in the XENON1T and XENONnT experiments, Phys. Rev. C 106, 024328 (2022).

[22] G. Anton et al. (EXO-200 Collaboration), Search for Neutrinoless Double-β Decay with the Complete EXO-200 Dataset, Phys. Rev. Letters 123, 161802 (2019).

[23] D. Q. Adams et al. (CUORE Collaboration), Search for Majorana neutrinos exploiting millikelvin cryogenics with CUORE, Nature 604, 53 (2022).

[24] G. Anton et al. (CUPID Collaboration), Final result on the neutrinoless double beta decay of ^{82}Se with CUPID-0, Phys. Rev. Letters 129, 111801 (2022).

[25] R. Arnold et al. (NEMO Collaboration), Final results on ^{82}Se double beta decay to the ground state of ^{82}Kr from the NEMO-3 experiment, Eur. Phys. J. C 78, 821 (2018).

[26] C. Augier et al. (CUPID Collaboration), Final results on the $0\nu\beta\beta$ decay half-life limit of ^{100}Mo from the CUPID-Mo experiment, Eur. Phys. J. C 82, 1033 (2022).

[27] S. Weinberg, Universal Neutrino Degeneracy, Phys. Rev., 1457 (1962).

[28] M. Aker et al., New Constraint on the Local Relic Neutrino Background Overdensity with the First KATRIN Data Runs, Phys. Rev. Lett. 129, 011806 (2022).

Appendix A: Helicity and chirality eigenstates eigenstates

Finite mass neutrinos can have positive in addition to negative helicity. Here we derive the decomposition of helicity eigenstates into chiral eigenstates.

The Dirac state of a left handed (negative helicity) neutrino of energy E and mass m, propagating in the +z direction say, is

$$\begin{aligned} u_{\nu L} &= \sqrt{\frac{E+m}{2E}}\left(0,1,0,-\frac{p}{E+m},0\right)^T \\ &\equiv (0,W_+,0,-W_-)^T, \end{aligned} \tag{A1}$$

where T denotes the transpose, and $W_\pm \equiv \sqrt{(E\pm m)/2E}$. From $W_+^2+W_-^2=1$ and $W_+W_-=\beta_\nu/2$, we have $(W_+\pm W_-)^2 = 1\pm\beta_\nu$, and

$$W_\pm = \frac{1}{2}\left(\sqrt{1+\beta}\pm\sqrt{1-\beta}\right). \tag{A2}$$

Similarly, the state of a right handed (positive helicity) neutrino is

$$u_{\nu R} = \sqrt{\frac{E+m}{2E}}\left(1,0,\frac{p}{E+m},0\right)^T \equiv (W_+,0,W_-,0)^T. \tag{A3}$$

On the other hand, the γ_5 eigenstates for spin up or

down (denoted by arrows) along the z-direction are

$$u_{\pm\uparrow} = \frac{(1,0,\pm 1,0)^T}{\sqrt{2}}, \quad u_{\pm\downarrow} = \frac{(0,1,0,\pm 1)^T}{\sqrt{2}}. \quad \text{(A4)}$$

The helicity eigenstates can thus be written as

$$u_{\nu R} = \sqrt{\frac{1+\beta_\nu}{2}} u_{+\uparrow} + \sqrt{\frac{1-\beta\nu}{2}} u_{-\uparrow}, \quad \text{(A5)}$$

and

$$u_{\nu L} = \sqrt{\frac{1-\beta_\nu}{2}} u_{+\downarrow} + \sqrt{\frac{1+\beta_\nu}{2}} u_{-\downarrow}. \quad \text{(A6)}$$

The amplitude for a $\gamma_5 = \pm 1$ eigenstate to have right handed helicity is $\sqrt{(1 \pm \beta_\nu)/2}$ and to have left handed helicity is $\sqrt{(1 \mp \beta_\nu)/2}$. The expectation value of the neutrino helicity $\langle h \rangle$ in a $\gamma_5 = \pm 1$ state is simply $\pm\beta_\nu$.

EUROPEAN ORGANISATION FOR NUCLEAR RESEARCH (CERN)





Submitted to: Physics Reports

CERN-EP-2024-056
6th March 2024

arXiv:2403.02455v1 [hep-ex] 4 Mar 2024

The quest to discover supersymmetry at the ATLAS experiment

The ATLAS Collaboration

The search for supersymmetry with the ATLAS experiment at the CERN Large Hadron Collider intensified after the discovery of the Higgs boson in 2012. The search programme expanded in both breadth and depth, profiting from the increased integrated luminosity and higher centre-of-mass energy of Run 2, and gaining new sensitivity to unexplored areas of supersymmetry parameter space through the use of new experimental signatures and innovative analysis techniques. This report summarises the supersymmetry searches at ATLAS using up to 140 fb^{-1} of pp collisions at $\sqrt{s} = 13$ TeV, including the limits set on the production of gluinos, squarks, and electroweakinos for scenarios either with or without R-parity conservation, and including models where some of the supersymmetric particles are long-lived.

© 2024 CERN for the benefit of the ATLAS Collaboration.
Reproduction of this article or parts of it is allowed as specified in the CC-BY-4.0 license.

Contents

1 Introduction **2**

2 Supersymmetric models **4**

3 The ATLAS detector **8**

4 Analysis strategy **8**

5 Strongly produced supersymmetric particles **10**
5.1 Gluino pair production 11
5.2 Squark pair production 14

6 Weakly produced supersymmetric particles **18**
6.1 Slepton pair production 18
6.2 Electroweakino pair production 20

7 R-parity-violating decays **23**

8 Long-lived supersymmetric particles **26**

9 Beyond simplified models **29**

10 Discussion and conclusions **31**

1 Introduction

One of the most significant contributions of the CERN Large Hadron Collider (LHC) [1] to high-energy physics comes through the particles that the ATLAS [2] and CMS [3] collaborations have *not* found. Both collaborations have pursued an unprecedented programme of searches for phenomena not predicted by the Standard Model (SM). The wide variety of signatures explored, and the richness of the models considered, has had a powerful influence on community's paradigms of physics beyond the Standard Model.

Among these paradigms, supersymmetry (SUSY) [4–9] is one of the most closely examined. The approach of imposing symmetries on Lagrangians led to the construction of electroweak theory, the unification of the weak and electromagnetic interaction and, eventually, the development of the Standard Model. The phenomenology of SUSY stems from requiring the Lagrangian to be invariant under an operator that maps fermionic fields into bosonic ones, and vice versa. It was found that only additional space-time symmetry could be added to the Poincaré group [5]. To impose this symmetry, one needs to add many new *superpartners* of the Standard Model particles. The much richer particle content, and some of the free parameters that one needs to add to make SUSY a broken symmetry (for example, it is known that there is no superpartner of the electron with mass $m = 0.511\,\text{MeV}$), makes SUSY an ideal framework to accommodate many of the shortcomings of the Standard Model. The quantum corrections to the Higgs boson mass coming from the fermions are counterbalanced by those coming from their superpartners, stabilising the mass to a value near the electroweak scale in a natural way. On top of that, the modified particle content changes the evolution of the running gauge couplings of the SM, potentially allowing

them to converge to a common value, a necessary condition for unification of the electroweak and strong interactions. The additional particles come with new mixing parameters, potentially allowing additional sources of CP violation and thus paving the way for an explanation of the cosmological matter–antimatter asymmetry. SUSY even offers the attractive possibility of generating electroweak symmetry breaking dynamically. Finally, there may be room for one or more dark-matter candidates among the particles introduced in the model.

Because of its elegance and flexibility, SUSY has received significant theoretical and experimental attention in the past decades. The generic prediction of the existence of SUSY particles at the TeV scale created widespread expectations for experimental results from the LHC collaborations in the early 2000s. The ATLAS Collaboration rose to these expectations by developing a thorough, robust and extensive experimental effort to search for SUSY in data from Run 1, at $\sqrt{s} = 7$ and 8 TeV, and Run 2, at $\sqrt{s} = 13$ TeV. The aim of this paper is to review and summarise this monumental effort at the end of the Run 2. Section 2 gives a quick overview of the main theoretical and phenomenological aspects of supersymmetry, introducing the approach ATLAS used to explore the vast SUSY parameter space. Section 3 provides a brief description of the ATLAS dectector before Section 4 discusses generic aspects related to the design of SUSY searches, the background estimation, and the statistical approach used to interpret the search results and set limits on sparticle masses, couplings, and production cross-sections.

These searches covered a large variety of experimental signatures arising from models featuring a stable weakly interacting particle (the R-parity-conserving, or RPC, models) and from models without such a potential dark-matter candidate (R-parity-violating, or RPV, models). Both types of models are described in Section 2. Sections 5 and 6 review the analyses targeting the production of SUSY particles via strong or electroweak interactions, respectively, when using RPC SUSY models: generically speaking, the common feature of these searches is the presence of missing transverse momentum $\mathbf{p}_{\mathrm{T}}^{\mathrm{miss}}$ (with magnitude $E_{\mathrm{T}}^{\mathrm{miss}}$) in signal events, arising from the presence of a dark-matter candidate, which goes undetected. Section 7 discusses RPV SUSY searches, where an $E_{\mathrm{T}}^{\mathrm{miss}}$ signature is typically absent. Experimental signatures involving long-lived particles arise quite naturally in some regions of the parameter space: Section 8 focuses on the effort to target such signatures with unconventional experimental techniques.

Each of the searches discussed in these sections makes use of simplified models (discussed in Section 2) to optimise the analysis and interpret the results. While the simplified-model approach gives a direct connection to the signal topologies, it has the drawback of yielding mass limits that rarely generalise to more complex/complete SUSY models. Section 9 focuses on reinterpreting the analyses designed using simplified models in the more general phenomenological Minimal Supersymmetric Standard Model, with the aim of giving an overall picture of the actual impact of ATLAS on the supersymmetric landscape.

This paper has multiple purposes. The authors hope that it will serve as a useful introduction to the field for those wanting to take an active role in research activities connected to SUSY. At the same time, it may be a handy collection of information and references for the HEP community, either for easy access to ATLAS research on the subject or simply as an overview of the searches performed.

2 Supersymmetric models

To make the SM supersymmetric,[1] one has first to postulate the existence of an extended Higgs field sector: two complex doublets provide the minimum number of fields that can give mass to the up-type and down-type particles without spoiling gauge invariance. The next step is to introduce the supersymmetric partners of each SM field: for each fermion f (characterised by a left-handed and a right-handed component, f_{L} and f_{R}, respectively), one introduces two supersymmetric scalar fields $\tilde{f}_{\mathrm{L}}$ and $\tilde{f}_{\mathrm{R}}$. Although the subscripts L and R have nothing to do with chirality at this point, one often refers to these scalar fields as the *left-* and *right-chiral sfermions*.[2] These two fields mix to yield the mass eigenstates $\tilde{f}_1$ and $\tilde{f}_2$, with $m(\tilde{f}_1) < m(\tilde{f}_2)$ by convention. For the electroweak boson fields, one starts from 16 spin degrees of freedom before electroweak symmetry breaking (two each for the B and $\mathbf{W}$ massless spin-1 fields, eight corresponding to the two complex Higgs doublets). This requires the introduction of eight supersymmetric fermionic partners: one *bino*, three *winos* and four *higgsinos*. The electroweak symmetry breaking results in the usual three massive vector bosons $W^{\pm}$ and Z, and the massless γ (11 degrees of freedom), plus five spin-0 bosons (h, H, A, $H^{\pm}$; it is often assumed that the 125 GeV scalar particle is the h). The bino, winos and higgsinos mix, yielding eight fermionic mass eigenstates (the neutralinos $\tilde{\chi}_1^0 \ldots \tilde{\chi}_4^0$ and the charginos $\tilde{\chi}_1^{\pm}$ and $\tilde{\chi}_2^{\pm}$, with the subscript increasing with increasing mass), corresponding to 16 degrees of freedom. Finally, the fermionic *gluino*, $\tilde{g}$, is introduced as a superpartner of the gluon, and in models where SUSY is broken by supergravity, the gravitino, $\tilde{G}$, is the fermionic superpartner of the hypothetical graviton.

The particle content of the SM is therefore more than doubled by its supersymmetrisation. Supersymmetry requires that the couplings of the SUSY partners are identical to the corresponding ones in the SM (after accounting for the extended Higgs sector). If supersymmetry were an exact symmetry of nature, then the SUSY particle masses would be equal to those of the corresponding SM partners. The absence, so far, of any observed SUSY particle implies that SUSY must be a broken symmetry. The SUSY breaking mechanism, although unknown, can modify the phenomenology and mass spectrum of the SUSY sector. For example, conventional theories of gravity-mediated SUSY breaking, 'supergravity' (SUGRA) theories, include massive gravitinos due to a modified Higgs mechanism. Gauge-mediated SUSY breaking (GMSB) theories usually have a nearly massless gravitino as the lightest supersymmetric particle (LSP), while anomaly-mediated SUSY breaking (AMSB) models usually feature long-lived $\tilde{\chi}_1^{\pm}$ decays to pure-wino $\tilde{\chi}_1^0$ LSPs. The scale at which SUSY is broken is inherently tied to the breaking mechanism, and also impacts naturalness arguments that favour light top squarks, higgsinos, and moderately light gluinos to avoid excessive tuning of the Higgs boson mass corrections. The complexity of defining the mechanism and scale of SUSY breaking is usually avoided by incorporating effective *soft-SUSY-breaking* terms in the model. They include many parameters: 105, including supersymmetric particle masses and field phases that cannot be absorbed by a redefinition of the fields. The model sketched so far is called the Minimal Supersymmetric Standard Model (MSSM).

Vast regions of the MSSM parameter space are not consistent with the observed particle physics phenomenology. Further assumptions motivated by experimental results are often made. To prevent the proton from decaying too quickly [10], conservation of a multiplicative quantum number called R-parity is often assumed. The R-parity of a particle is a function of its baryon number B, the lepton number L, and

[1] Non-minimal extensions of the SM can be obtained by first extending the SM and then completing it by introducing the supersymmetric partners of the SM fields, or by considering multiple versions of the SUSY operators applied to the SM fields.

[2] The supersymmetric scalars (partners of SM fermions) take the name of the SM partner with an 's' prepended. For example, the electron has two partner *selectrons*. The supersymmetric fermions (partners of SM bosons) take the name of their SM partner with an 'ino' suffix. For example, the supersymmetric partner of the gluon is the *gluino*.

the spin S, and is defined as

$$R = (-1)^{3(B-L)+2S},$$

giving a value of -1 for SUSY particles and $+1$ for SM particles. Its conservation has important phenomenological consequences because an even number of SUSY particles must always appear at a Feynman vertex. This implies that SUSY particles must be produced in pairs, and that the LSP is stable. A necessary condition for the LSP to be a good dark-matter candidate is that it interacts with ordinary matter only through weak interactions, which implies that LSPs produced (either directly or from the decay of a SUSY particle) in pp collisions do not interact with the detector, and missing transverse momentum becomes a characteristic event signature.

While R-parity conservation gives rise to a compelling phenomenology, it is not dictated by any fundamental principle. R-parity-violating (RPV) couplings are allowed, as long as their magnitude is not incompatible with existing observations. Because of this constraint, RPV couplings are typically small enough to be neglected in the production of SUSY particles, but they can have important consequences for SUSY particle decays: in particular, the LSP can decay into SM particles. This eliminates, in general, the possibility of retaining a good dark-matter candidate, and opens many options for the identity of the LSP, which can essentially be any SUSY particle. Since the LSP can decay, there is no expectation of having missing transverse momentum in the final state. RPV SUSY delivers very different event topologies than RPC SUSY.

Other assumptions can be made in order to reduce the volume of parameter space to be explored in the MSSM. Relatively general and well-motivated assumptions [11–13] about the flavour and mass structures of the MSSM allow the number of free parameters to be reduced to 19 or 20 (depending on the nature of the LSP): this so-called phenomenological MSSM (pMSSM) was investigated extensively during Run 1 of the LHC by both ATLAS [14] and CMS [15].

The strategy chosen by ATLAS to map its search programme to such a vast parameter space was to make use of simplified models [16–18]. In a simplified model, one assumes that only a handful of SUSY particles are relevant for the phenomenology of pp collisions. It is often assumed that a single type of SUSY particle is produced, with its decay involving only a few SUSY particles, or only the LSP. Designing an analysis for a specific simplified model means targeting a specific event topology. The limits obtained for simplified models hold whenever the assumed particle mass hierarchy and decays are realised in a fully developed SUSY model (either the MSSM or some more complex model). The main drawback of this approach is that it is often difficult to generalise a mass exclusion limit obtained for a SUSY particle. In a general SUSY model, many production processes and decay chains often compete with each other, and sometimes interference structures need to be taken into account when computing cross-sections. In short, the complexity of the actual model clashes with the clean and simple assumptions of the simplified models, so the simplified-model limits should always be presented along with caveats due to the assumptions made in designing the models, namely the (typically single) production process and decay mode.

The production cross-sections for strongly interacting SUSY particles hardly depend on any SUSY model parameter beside the sparticle masses. This is a consequence of the SU(3) gauge interaction driving the process. The Feynman diagrams involved in strong production are the equivalent of those for production of gluons and quarks in the SM. At the next-to-leading order in the strong coupling constant α_s and beyond, interference between diagrams containing squarks and gluinos makes the production cross-section for each of the relevant processes ($\tilde{g}\tilde{g}$, $\tilde{g}\tilde{q}$, $\tilde{q}\tilde{q}$) dependent on the specific mass spectrum of the model. For example, destructive interference between t-channel exchange of $\tilde{g}$ and $\tilde{q}$ makes the $\tilde{g}\tilde{g}$ production cross-section

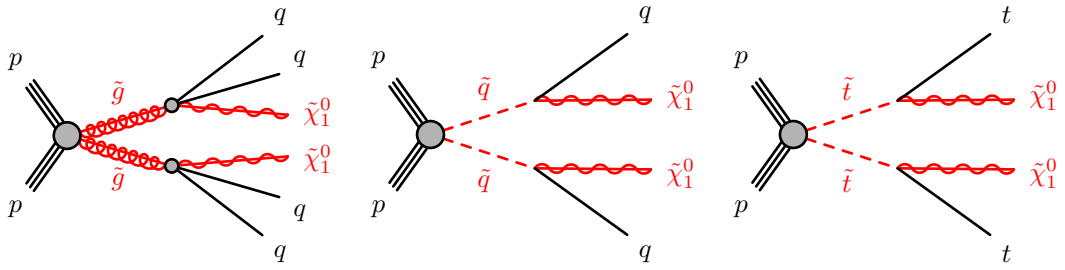


Figure 1: Simplified models of (a) gluino pair production followed by $\tilde{g} \rightarrow q\bar{q}\tilde{\chi}_1^0$; (b) squark pair production followed by $\tilde{q} \rightarrow q\tilde{\chi}_1^0$; and (c) top squark (stop) pair production followed by $\tilde{t} \rightarrow t^{(*)}\tilde{\chi}_1^0$. No distinction between particle and antiparticle is done in these diagrams.

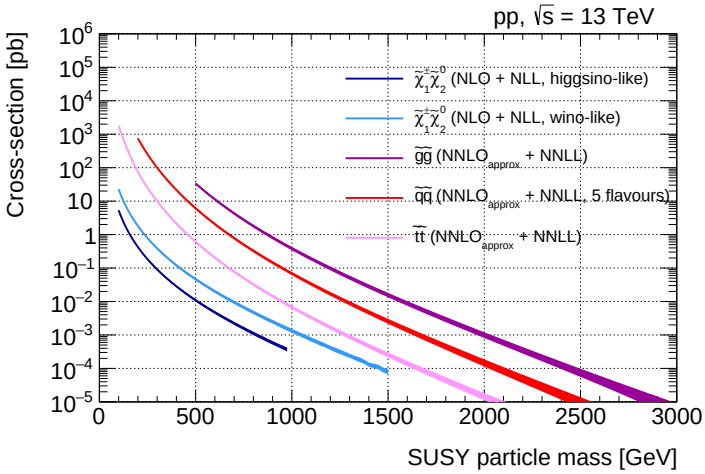


Figure 2: Direct pair-production cross-sections for a few processes mediated by the strong or electroweak processes. The width of the line represents the theoretical uncertainty. The values of the cross-sections and uncertainties are those agreed upon by the LHC SUSY Cross Section Working Group [19].

dependent on the $\tilde{q}$ masses. However, if the other SUSY particles are assumed not to take part (not even virtually) in the production process, then the production cross-sections depend only on the sparticle mass. These are the assumptions typically made in simplified models of gluino or squark pair production, shown in Figures 1(a) and 1(b) respectively, and in Figure 1(c) if the squark is a top squark (or 'stop').

The production cross-sections for squarks and gluinos with simplified-model assumptions are shown in Figure 2. The cross-section shown for squark production assumes that the 10 squarks corresponding to the u, d, c, s, and b flavours (and two chirality states) are all degenerate in mass. The cross-section scales linearly with the number of squark types that can be produced.

For example, the production cross-section for a pair of gluinos with $m(\tilde{g}) = 2$ TeV is about 1 fb, assuming that the mass of all other SUSY particles is large enough for them to be irrelevant in the cross-section evaluation. Consequently, between 100 and 200 gluinos with $m_{\tilde{g}} = 2$ TeV would have been produced at the ATLAS interaction point during Run 2. The production of SUSY particles with such a large mass

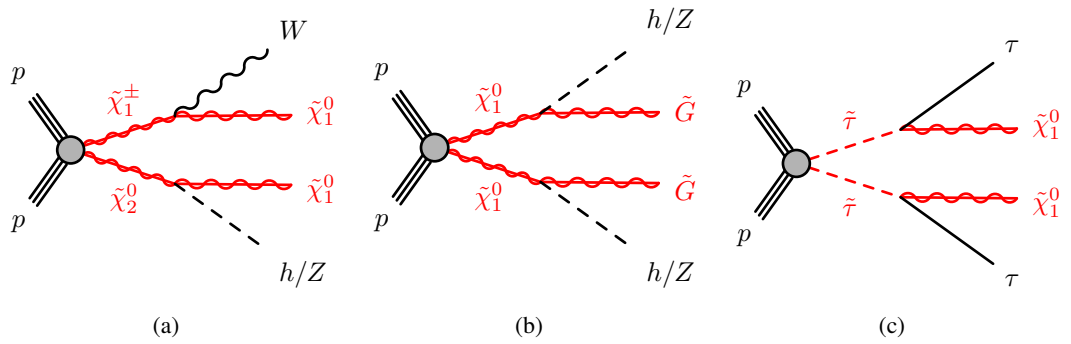


Figure 3: Simplified models of (a) $\tilde{\chi}_1^{\pm}\tilde{\chi}_2^0$ production followed by $\tilde{\chi}_1^{\pm} \to W^{\pm}\tilde{\chi}_1^0, \tilde{\chi}_2^0 \to h/Z\tilde{\chi}_1^0$; (b) $\tilde{\chi}_1^0\tilde{\chi}_1^0$ production followed by $\tilde{\chi}_1^0 \to h/Z\tilde{G}$; and (c) direct $\tilde{\tau}$ pair production followed by $\tilde{\tau} \to \tau\tilde{\chi}_1^0$. No distinction between particle and antiparticle is done in these diagrams.

typically results in a quite distinctive event topology, so that the event selection can achieve sufficient background rejection while retaining relatively large signal acceptance and efficiency. It is therefore not surprising that ATLAS is typically sensitive to gluinos in the mass range up to $m_{\tilde{g}} = 2$ TeV or somewhat higher, unless specific mass hierarchies are realised such that event selections with very small acceptance and/or efficiency need to be deployed. Following the same logic, one sees that the sensitivity of ATLAS to tenfold-degenerate squark pair production reaches masses approximately 0.5 TeV lower than those corresponding to gluino pair production.

The electroweak interaction couples SUSY particles to the SM quarks in the protons with a strength that depends specifically on the model parameters affecting the electroweak sector. Therefore, the production cross-section for electroweakinos (Figures 3(a) and 3(b)), for example, depends on the mixing in terms of wino, higgsino and (for neutralinos) bino states. Thus the production cross-section for a $\tilde{\chi}_1^{\pm}\tilde{\chi}_2^0$ pair is larger if each is a pure wino state, and smaller if each is a pure higgsino state, as shown in Figure 2. Likewise, the production cross-section for a $\tilde{\chi}_1^0\tilde{\chi}_1^0$ pair vanishes if the $\tilde{\chi}_1^0$ is a pure higgsino. Similarly, the production cross-section for slepton pairs (Figure 3(c)) depends on the weak-isospin structure of the sleptons, i.e. on the mixing of the slepton in terms of right- and left-handed chirality.

Because of the number of mass eigenstates available and the variety of possible electroweak parameter-space configurations, families of simplified models of electroweakino production have been defined. They stem from specific electroweakino mass hierarchies that arise in limit cases of the electroweak-sector mass parameters. In the MSSM, the soft SUSY-breaking mass term for the bino, winos and higgsinos are indicated with M_1, M_2 and μ, respectively. The structure of the electroweakino mass matrices is such that a well-defined hierarchy of these parameters translates into a clear mass-eigenstate structure. If, for example, $M_1 < M_2 \ll \mu$, one has a bino-like $\tilde{\chi}_1^0$ LSP with $m(\tilde{\chi}_1^0) \sim M_1$, and nearly degenerate $\tilde{\chi}_2^0$ and $\tilde{\chi}_1^{\pm}$ with masses of the order of M_2. If $\mu \ll M_1, M_2$, then the first four electroweakinos ($\tilde{\chi}_1^0$, $\tilde{\chi}_2^0$ and two charginos $\tilde{\chi}_1^{\pm}$, $\tilde{\chi}_2^{\pm}$) will all have almost degenerate masses of the order of μ, leading to a very compressed scenario. Such a higgsino LSP case will yield event topologies with soft decay products emitted in transitions between the electroweakino states. Similarly, $M_2 \ll \mu, M_1$ (wino LSP) yields $m(\tilde{\chi}_1^0) \sim m(\tilde{\chi}_1^{\pm}) \sim M_2$. Most of the SUSY scenarios that inspire the models described in Sections 6 and 8 refer to one of these paradigms.

3 The ATLAS detector

The ATLAS experiment [2] is a multipurpose particle detector with a forward–backward symmetric cylindrical geometry and nearly 4π coverage in solid angle.[3] It is designed to identify a wide variety of particles and measure their momenta and energies. These particles include electrons, muons, τ-leptons and photons, as well as gluons and quarks, which produce collimated jets of particles in the detector. It consists of an inner tracking detector surrounded by a thin superconducting solenoid providing a 2 T axial magnetic field to measure charged-particle trajectories and momenta, followed by electromagnetic (EM) and hadron calorimeters that are used in the identification of particles and in the measurement of their energies, and a muon spectrometer (MS) for measuring the trajectories and momenta of muons. A two-level trigger system is used to select events [20]. The first-level trigger is implemented in hardware and uses a subset of the detector information to accept events at a rate below 100 kHz from the LHC's 40 MHz proton bunch crossings. This is followed by a software-based trigger that reduces the accepted event rate to 1 kHz on average depending on the data-taking conditions. An extensive software suite [21] is used in data simulation, in the reconstruction and analysis of real and simulated data, in detector operations, and in the trigger and data acquisition systems of the experiment.

4 Analysis strategy

The analyses that produced the SUSY mass exclusion limits discussed in Sections 5 to 8 were designed to be complementary, and target many different event topologies that can arise from the production and decay of SUSY particles. They employ a variety of tools and techniques, which makes each of them largely unique in terms of analysis strategy and, of course, sensitivity to the SUSY parameter space. However, all the analyses discussed apply similar strategies for background estimation, and they all share a common statistical approach in testing, first of all, for compatibility with the SM background prediction (and, therefore, whether the analysis observed a SUSY signal or not), and, in absence of a signal, in setting limits on SUSY production cross-sections, and eventually on sparticle masses.

The design of the analysis starts from the definition of one or more selections determining the signal region(s) (SR). Typically, the SR are designed by maximising the significance of the targeted signal process relative to the SM background as predicted by a Monte Carlo (MC) simulation. Actual collision data is not used in selection regions with a large expected signal contribution, to avoid any bias while defining the selection. This first phase identifies the set of variables to be used for the selection. They are typically employed in a multivariate selection, using either a boosted decision tree (BDT) or a neural network (NN), or varied to identify a set of selection criteria to be applied to each of them, sometimes referred to as a 'cut-and-count' approach. In all cases, the final selection criteria (for the BDT or NN discriminant, or for the individual variables) are set after the final background estimation is in place.

The preliminary SR definition allows the identification of the relevant SM background processes for the analysis. *Reducible* background processes pass the signal region selection despite not having the signal characteristics at particle level. Reducible backgrounds are relevant when some events from a

[3] ATLAS uses a right-handed coordinate system with its origin at the nominal interaction point (IP) in the center of the detector and the z-axis along the beam pipe. The x-axis points from the IP to the center of the LHC ring, and the y-axis points upwards. Cylindrical coordinates (r, ϕ) are used in the transverse plane, ϕ being the azimuthal angle around the z-axis. The pseudorapidity is defined in terms of the polar angle θ as $\eta = -\ln\tan(\theta/2)$. Angular distance is measured in units of $\Delta R \equiv \sqrt{(\Delta\eta)^2 + (\Delta\phi)^2}$.

high-cross-section SM process (e.g. multijet, W+jets, or Z+jets production) 'fake' one or several of the SR criteria. The faking probabilities are typically small, but the high cross-section may make the process relevant. Reducible backgrounds are often estimated by using techniques that strongly rely on the use of data from real collisions, since the faking mechanisms are not always reproduced reliably by the detector simulation. Some of the most common contexts where estimation of reducible background is relevant are as follows:

- In analyses where signal events have many leptons, or lepton pairs of the same charge ('same-sign', or SS leptons), backgrounds contributions from jets faking leptons, 'fake' leptons from photon conversions, and non-prompt leptons from hadron decays, can become relevant. Contributions from fake and non-prompt (FNP) leptons are typically estimated using a loose-to-tight method [22]: the FNP contribution to the 'tight' leptons used in the selection is estimated from 'loose' leptons by using scale factors estimated in a dedicated FNP-lepton-dominated selection. Similar techniques are employed to estimate fake-τ-lepton contributions to SR selecting events containing hadronic τ-lepton decays [23].
- Analyses using SS leptons may suffer from contributions from processes involving leptons with opposite charges ('opposite-sign', or OS leptons), where one of the two lepton charges is misidentified. The charge-flip probability is estimated by comparing yields in OS and SS regions where a $Z \to \ell\ell$ peak is clearly visible. Obviously, $Z \to \ell^{\pm}\ell^{\pm}$ arises from $Z \to \ell^{\pm}\ell^{\mp}$ with a charge-flip. Charge-flip probabilities are typically negligible for muons.
- The background affecting analyses looking for signals from long-lived particles is almost always reducible. For example, one of the main backgrounds when looking for displaced secondary vertices due to decays of long-lived particles arises from random crossings of tracks that the detector is not able to resolve. The probability to have a random crossing is assumed to be independent of the tracks forming the vertex and is determined from a control region and then applied to lower track-multiplicity vertices to estimate the background contribution.

Irreducible backgrounds are those that have the same event topology as the signal. They are typically estimated by relying on MC predictions for their kinematic distributions. Sometimes the overall normalisation of the process is determined in a fit with the help of dedicated control regions (CR), i.e. selection regions where event rates are dominated by the process whose normalisation needs to be estimated. In additional, validation regions (VR) can be defined, with a topology as similar as possible to the SR, but with only a small expected signal contamination: they are used to verify that the background prediction agrees with the data before looking at the yields in the SR. Validation regions are not used in the statistical interpretation of the results. A sketch of a possible generic analysis set-up for an analysis using two variables (for example, two output nodes of a multiclass NN classifier) as the final discriminant, highlighting generic expectations for the signal and background yields, relative background (statistical and systematic) uncertainty, and signal significance, is shown in Figure 4.

In the following, the background estimation strategy of some of the analyses considered is sketched as an example of the approaches above, or in case it is particularly relevant to the discussion.

A likelihood function is built as the product of Poisson probability functions $P\left(n_i^{\text{obs}}, n_i^{\text{exp}}\right)$, describing the probability of observing n_i^{obs} events in region i (where i is any CR or SR) when n_i^{exp} are expected. Here n_i^{exp} depends on free-floating normalisation parameters for the signal μ_{s} and for the relevant irreducible background processes $\boldsymbol{\mu}_{\text{b}}$. These free-floating parameters are defined so that the yield corresponding to the nominal cross-section is obtained for $\mu = 1$. Systematic uncertainties are treated as nuisance parameters

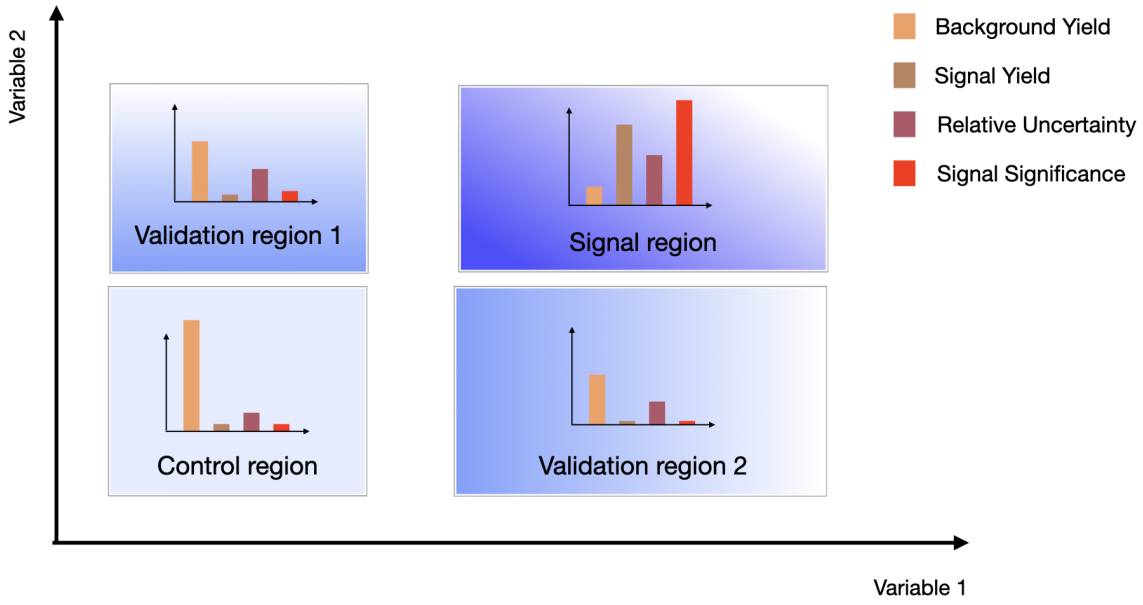


Figure 4: Illustrative set-up for an analysis using two variables as the final discriminant. The definition of mutually exclusive signal, control and validation regions is sketched, and indicative values for the signal and background yields, relative uncertainty and signal significance in each region are shown (on an arbitrary scale).

and are constrained with normal distributions $G\left(\theta_j^0 - \theta_j\right)$, where θ_j^0 is the expected value of the nuisance parameter corresponding to the j^{th} systematic uncertainty. The parameters μ_{s}, $\boldsymbol{\mu}_{\text{b}}$ and $\boldsymbol{\theta}$ are determined by maximum-likelihood fits. The resulting likelihood is:

$$\mathcal{L}\left(\mathbf{n}^{\text{obs}}, \boldsymbol{\theta}^0 | \mu_{\text{s}}, \boldsymbol{\mu}_{\text{b}}, \boldsymbol{\theta}\right) = \prod_{i \in \text{ SR,CR}} P\left(n_i^{\text{obs}}, n_i^{\text{exp}}\left(\mu_{\text{s}}, \boldsymbol{\mu}_{\text{b}}, \boldsymbol{\theta}^0, \boldsymbol{\theta}\right)\right) \times \prod_{j \in \text{ syst. unc.}} G\left(\theta_j^0 - \theta_j\right).$$

The test statistic used to test whether new physics is observed or to determine exclusion limits is the profile likelihood ratio [24]. No significant excess above the SM expectation has been observed at the LHC, so this paper concentrates on the resulting exclusion limits. A quantity $\hat{\mu}_{\text{s}}$ is defined as the μ_{s} value corresponding to a CL_{s} [25] of 0.05 for the profile-likelihood-ratio test statistic obtained under the signal-plus-background hypothesis. Models for which $\hat{\mu}_{\text{s}} \leq 1$ are said to be excluded at 95% confidence level (CL). All limits described in this paper are at 95% CL.

5 Strongly produced supersymmetric particles

Squarks and gluinos are produced with couplings that are proportional to the strong coupling constant α_{s}. Therefore, their production cross-sections are significantly larger than for sleptons and electroweakinos of the same mass. This also implies that squark and gluino production were the first sparticle production processes to which ATLAS achieved sensitivity: the sensitivity to gluinos, for example, was already well into the TeV range by the end of LHC Run 1.

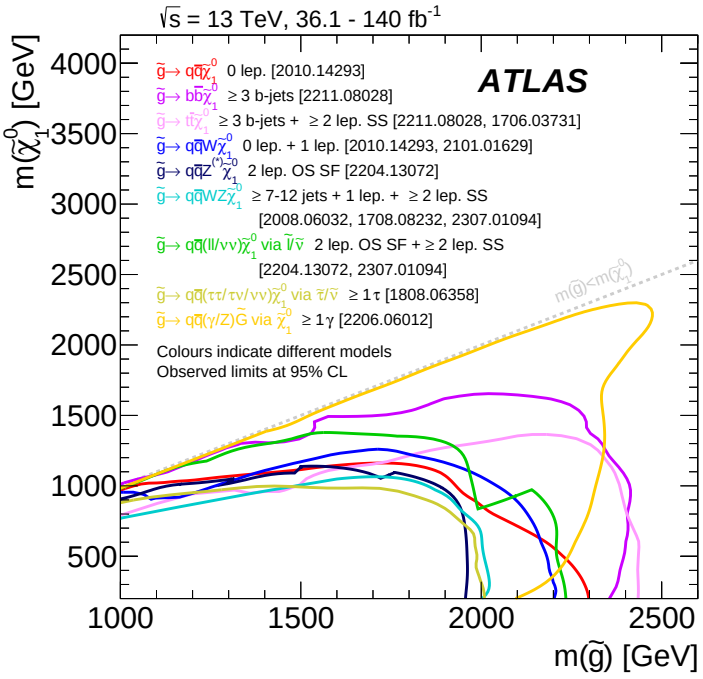


Figure 5: Exclusion limits from 13 TeV data in the $m(\tilde{g})$–$m(\tilde{\chi}_1^0)$ plane for different simplified models featuring the decay of the gluino to the lightest supersymmetric particle (lightest neutralino or gravitino) either directly or through a cascade chain featuring other SUSY particles with intermediate masses. For each line, the gluino decay mode is reported in the legend and it is assumed to proceed with 100% branching fraction. Some limits depend on additional assumptions about the masses of intermediate states, as described in the references cited in the plot.

5.1 Gluino pair production

The sensitivity of ATLAS to gluino pair production followed by RPC decays of the $\tilde{g}$ is shown in Figure 5. All the limits shown were obtained by assuming a simplified signal model and the cross-sections shown in Figure 2: in particular, the production cross-section is a function of the gluino mass only, and it therefore decreases strongly at increasing values along the $m(\tilde{g})$-axis. In all cases, the limits are presented as a function of the gluino mass and lightest neutralino mass. Different curves represent either different assumptions about the gluino decay chain, or different analysis results.

Focusing on the limit intercepts with the $m(\tilde{g})$-axis, i.e. those for $m(\tilde{\chi}_1^0) = 0$ GeV, the first observation is that the 2 TeV range predicted from simple cross-section considerations in Section 2 is indeed realised. The second observation is that the limits on the gluino mass depend significantly on the line considered (i.e. the assumed gluino decay), and on $m(\tilde{\chi}_1^0)$. This is readily understood as a consequence of the total energy available in the decay being determined by the mass difference $m(\tilde{g}) - m(\tilde{\chi}_1^0)$. A small value of this quantity corresponds to smaller values of the momenta of the final-state objects, and, therefore, to signal topologies that are more difficult to separate from the SM background.

The different models in Figure 5 correspond to scenarios that assume different RPC gluino decays. Together, they give a very good overview of the extent of the effort made in the search for this sparticle.

The simplest RPC Feynman vertex that can be considered is one where the gluino couples to a squark

and a quark. The flavour of the squark, and the way it couples to the electroweak sector determines the complexity of the final state. In one of the simplest simplified models, the squarks and all electroweakino states but one ($\tilde{\chi}_1^0$) have a very large mass. The first case considered is one where the squark is not the stop. The gluino decay chain is $\tilde{g} \to \tilde{q}^* q \to qq\tilde{\chi}_1^0$. The case where the virtuality of the $\tilde{q}^*$ is such that the $\tilde{g}$ becomes long-lived is phenomenologically compelling and theoretically very interesting (arising from models of split-SUSY [26, 27]), and it is discussed in Section 8. Here the discussion is limited to the case where the $\tilde{g}$ decay is prompt. The analysis that drives the sensitivity [28] targets both direct gluino and direct squark pair production by requiring no leptons in the final state and significant $E_{\mathrm{T}}^{\mathrm{miss}}$, which is also exploited for triggering purposes: the corresponding limit is indicated by the red line in Figure 5. The analysis selection is based on the jet multiplicity in the event (N_{jet}), the significance of the missing transverse momentum $E_{\mathrm{T}}^{\mathrm{miss}}/H_{\mathrm{T}}$, and $m_{\mathrm{eff}} = H_{\mathrm{T}} + E_{\mathrm{T}}^{\mathrm{miss}}$. Here H_{T} denotes the scalar sum of the transverse momentum (p_{T}) of the jets in the event. The dominant background process in the considered signal regions is $Z(\to \nu\bar{\nu})+\mathrm{jets}$. This is estimated using simulated events corrected with auxiliary measurements of the $\gamma+\mathrm{jets}$ and $Z(\to \ell^{\pm}\ell^{\mp})+\mathrm{jets}$ processes in a similar phase-space region. Other relevant background processes are $W+\mathrm{jets}$ and $t\bar{t}$ production, with a $W \to \ell\nu$ decay to satisfy the $E_{\mathrm{T}}^{\mathrm{miss}}$ requirement. For the latter class of processes, the lepton either fails the identification requirements or is a hadronically decaying τ-lepton. A small contribution from multijet production is estimated with the jet smearing method, where the background prediction is seeded from simulated events corrected to account for the detector's response to jets as measured in data [29].

Gluino masses up to about 2.2 TeV are excluded for massless $\tilde{\chi}_1^0$. For gluinos decaying to $\tilde{\chi}_1^0$ LSPs, there is no sensitivity to gluinos with masses above about 1.3 TeV if the masses of the gluino and $\tilde{\chi}_1^0$ are similar. It is important to always bear in mind that the obtained limits assume a branching fraction of 100% for the particular decay. Also, the assumption that squarks do not affect the gluino production cross-sections can be quite a strong one, requiring squarks with masses of tens of TeV. Further interpretations in Ref. [28] address some of these points, providing limits in models where the gluino and squark masses are similar.

If the assumptions about the electroweak sector are modified, and a richer spectrum of relatively light electroweakino states is allowed, then the phenomenology becomes more complex, with different squark decays potentially competing with each other. ATLAS has considered various benchmark gluino decays, especially focusing on models involving longer gluino decay chains. In some cases, the gluino decay chain may lead to the production of vector bosons, which opens up possibilities for final states containing leptons, possibly with same-sign charges. Additionally, longer gluino decay chains with hadronic vector-boson decays can result in final states with a higher jet multiplicity or involve hadronic resonances. Figure 5 shows some of the limits obtained in these scenarios in different shades of blue. In one scenario (light blue line in Figure 5, also shown in Figure 6), the squark is assumed to decay as $\tilde{q}^* \to q\tilde{\chi}_1^{\pm} \to qW\tilde{\chi}_1^0$, leading to $\tilde{g} \to q\bar{q}'W\tilde{\chi}_1^0$. This scenario is targeted both by Ref. [28], already discussed, and by an analysis requiring the presence of one lepton from the W decay [30]. The latter applies a selection that rejects background processes containing one W boson decaying leptonically by requiring large values of the transverse mass m_{T} of the lepton and $\mathbf{p}_{\mathrm{T}}^{\mathrm{miss}}$, based on the jet multiplicity. The rest of the selection exploits the topology of the expected final state by using variables such as $E_{\mathrm{T}}^{\mathrm{miss}}$, N_{jet}, and m_{eff} (including the lepton p_{T} in the scalar sum of transverse momenta). The two analyses selecting events with either no or one lepton in the final state have dedicated selections for models where the $\tilde{g}$ and $\tilde{\chi}_1^0$ masses are similar, resulting in improved exclusion limits for such compressed mass-difference scenarios. The resulting exclusion limits from the two analyses in this simplified model are similar, with each excluding a range up to $m(\tilde{g}) = 2.2$ TeV for $m(\tilde{\chi}_1^0) = 0$. The limit is reduced by about 1 TeV in the compressed scenario.

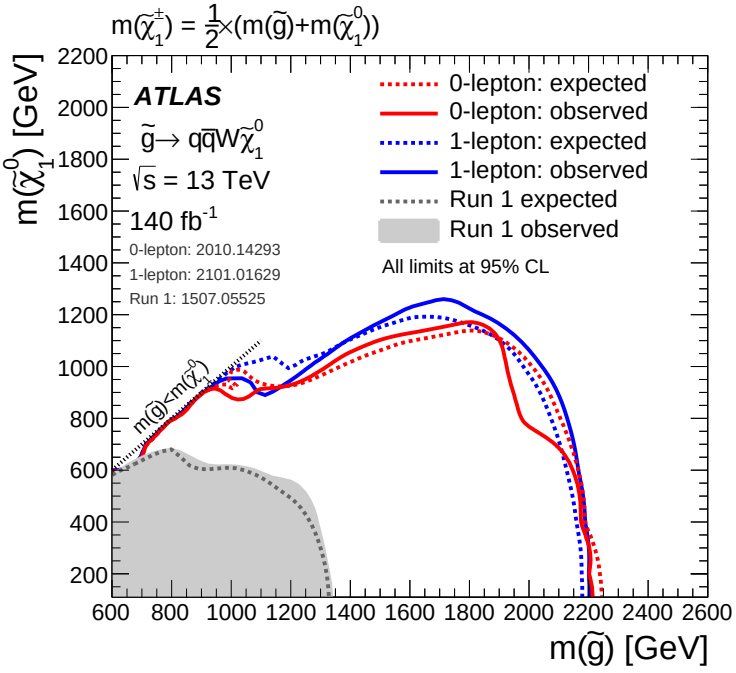


Figure 6: Exclusion limits from 13 TeV data in the $m(\tilde{g})$–$m(\tilde{\chi}_1^0)$ plane for the simplified model where a pair of gluinos are produced, and each decays promptly via an on-shell chargino into a pair of quarks, a W boson, and the lightest neutralino. The chargino mass is assumed to be midway between the gluino and neutralino masses. Theoretical signal cross-section uncertainties are not included in the limits shown.

Other cases considered explicitly in Figure 5 are those with $\tilde{q}^* \to q\tilde{\chi}_2^0 \to qZ\tilde{\chi}_1^0$, targeted by an analysis requiring an opposite-sign same-flavour (OS SF) lepton pair compatible with a Z boson in association with $E_{\mathrm{T}}^{\mathrm{miss}}$ and jets [31], and those arising from a longer decay chain such as $\tilde{q}^* \to q\tilde{\chi}_2^0 \to q\tilde{\chi}^\pm \to qW\tilde{\chi}_2^0 \to qWZ\tilde{\chi}_1^0$, targeted by multiple analyses requiring either large jet multiplicities [32] or SS leptons in addition to jets [33]. Scenarios involving intermediate electroweakino decays via sleptons have also been considered.

The yellow line in Figure 5 displays a behaviour completely different from the others. It applies to scenarios inspired by General Gauge Mediation (GGM) [34], where the LSP is often a light gravitino with a mass around 1 GeV or less. The phenomenology in these scenarios is determined by the nature of the next-to-lightest supersymmetric particle (NLSP). The case shown here is one where the NLSP is a neutralino that decays to the LSP with photon or Z boson emissions, and the resulting topology includes photons in the final state, yielding a distinctive $\gamma + E_{\mathrm{T}}^{\mathrm{miss}}$ + jets final-state signature. The amount of $E_{\mathrm{T}}^{\mathrm{miss}}$ in the event largely determines the analysis acceptance: in this case it is proportional to $m(\tilde{\chi}_1^0) - m(\tilde{G})$, so the maximum acceptance is obtained for large neutralino masses. Overall, the limits on the gluino mass are in line with those of the other analyses.

The cases where the virtual squark produced in the gluino decay is a third-generation squark are singled out in pink and purple in Figure 5. The physics reason to single them out is connected with naturalness considerations and is discussed in Section 5.2. The topological reason to single them out comes from the presence of b-quarks in the final state, yielding a powerful experimental handle with the application

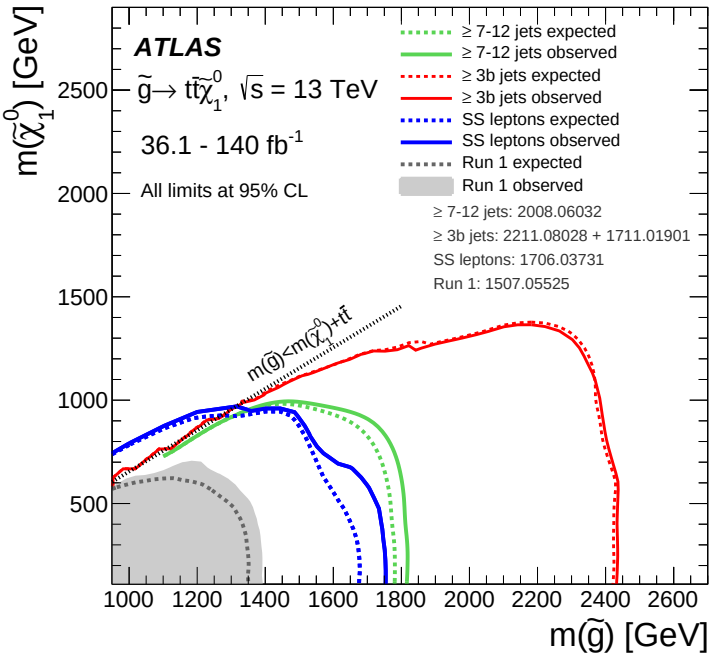


Figure 7: Exclusion limits from 13 TeV data in the $m(\tilde{g})$–$m(\tilde{\chi}_1^0)$ plane for a simplified model where a pair of gluinos decay promptly via off-shell top squarks into four top quarks and two lightest neutralinos. The SS lepton analysis sensitivity covers $m(\tilde{g}) < m(\tilde{\chi}_1^0) + 2m(t)$ due to the off-shell top quark contribution. Theoretical signal cross-section uncertainties are not included in the limits shown.

of b-tagging techniques [35] to identify b-jets. Neglecting potential flavour-violating decays of the stop or sbottom, the decay of a gluino pair via a third-generation squark with a branching fraction of 100% yields four b-jets in the final state. An analysis selecting events with three or more b-jets [36] dominates the sensitivity to these scenarios. The selection is based on a neural network that uses the kinematic variables of the jets, b-jets, leptons and $\mathbf{p}_{\mathrm{T}}^{\mathrm{miss}}$ as input. The network was trained to separate the $\tilde{g} \to t\bar{t}\tilde{\chi}_1^0$ and $\tilde{g} \to b\bar{b}\tilde{\chi}_1^0$ decays from the SM background, dominated by $t\bar{t}$, single top and Z + jets production. A different selection, which did not make use of multivariate techniques, was optimised to target mixed final states such as those arising from scenarios where both the stop and the sbottom take part in gluino decay, leading to final states with variable numbers of b- and t-quarks.

Summary limits on the model of gluino pair production yielding four top quarks and $E_{\mathrm{T}}^{\mathrm{miss}}$ are shown in Figure 7. The richness of the topology of the final state makes it a target of many analyses. In particular, SS analyses achieve sensitivity to regions of the parameter space where the top quarks emitted in the decay are virtual.

5.2 Squark pair production

The search for pair production of squarks is closely connected with that of gluinos. A summary of the mass exclusion limits is shown in Figure 8, assuming an eightfold mass degeneracy for the squarks (two chirality states for each of the four lightest SM flavours). Depending on the structure and mass hierarchy

of the electroweak sector, the squarks will have decay chains that resemble those already discussed for gluino pair production. If the only electroweak state that couples to the quark is a neutralino LSP, then the squark decay chain is $\tilde{q} \to q\tilde{\chi}_1^0$. The final state will contain jets and missing transverse momentum, and the analysis discussed in Ref. [28] has good sensitivity for most values of the mass difference $\Delta m(\tilde{q}, \tilde{\chi}_1^0) = m(\tilde{q}) - m(\tilde{\chi}_1^0)$. For small $\Delta m(\tilde{q}, \tilde{\chi}_1^0)$, the final state contains very small $E_{\mathrm{T}}^{\mathrm{miss}}$, unless one focuses on the production of squarks recoiling against substantial QCD initial-state radiation (ISR). This case is explicitly targeted in Ref. [37]: the analysis searches for an excess of events with large $E_{\mathrm{T}}^{\mathrm{miss}}$ recoiling against substantial hadronic activity. After a number of selections aimed at making sure that the events under investigation do not arise from jet energy mismeasurement or beam backgrounds, the dominant background processes are $W(\to \ell\nu)$ + jets (where the ℓ is lost or is a τ-lepton) and $Z(\to \nu\bar{\nu})$ + jets production. A sophisticated background estimation procedure exploits the similarity of these processes with $Z(\to \ell^{\pm}\ell^{\mp})$ + jets and γ + jets. As in the gluino case, a richer electroweak spectrum leads to longer decay chains, producing one-step $\tilde{q} \to qW\tilde{\chi}_1^0$ [28, 30] or $\tilde{q} \to qZ^{(*)}\tilde{\chi}_1^0$ [31] decays, or two-step $\tilde{q} \to qWZ\tilde{\chi}_1^0$ [33] decays. Similarly to the gluino case, scenarios involving sleptons in the electroweak-state decays, or GGM-like scenarios with a gravitino LSP, were also considered and targeted by specific analyses.

Overall, mass exclusion limits for eightfold-degenerate squarks range from 1.3 TeV to 1.8–1.9 TeV for $m(\tilde{\chi}_1^0) = 0$ GeV, and worsen with decreasing values of $\Delta m(\tilde{q}, \tilde{\chi}_1^0)$. For $\Delta m(\tilde{q}, \tilde{\chi}_1^0)$ of the order of a few GeV, the exclusion limit is about 900 GeV. These limits were obtained assuming simplified models.

The production cross-section for squarks scales linearly with the assumed degeneracy. For example, the limit in Ref. [28] for $m(\tilde{\chi}_1^0) = 0$ GeV decreases from about 1.85 TeV to about 1.2 TeV if production of a single $\tilde{q}$ chirality state is assumed.

Third-generation squarks ($\tilde{b}$ and $\tilde{t}$), and to some extent the $\tilde{c}$, have been targeted by dedicated analyses. The presence of b-jets (or c-jets) in the final state offers an additional experimental handle for improving the background rejection. The third-generation squarks are also constrained to be at the TeV scale by naturalness considerations: because of the large Yukawa coupling, stop loops are the main contribution to the first-order corrections to the lightest Higgs boson's mass in the MSSM [38]. Naturalness requirements place constraints on the stop masses and mixing between $\tilde{t}_{\mathrm{L}}$ and $\tilde{t}_{\mathrm{R}}$. They also constrain the $\tilde{b}_{\mathrm{L}}$ because it belongs to the same weak-isospin doublet as the $\tilde{t}_{\mathrm{L}}$ and therefore shares the same SUSY mass parameter.

A summary of the $\tilde{b}$ mass exclusion limits is shown in Figure 9. The limit in blue corresponds to the simplest decay chain, involving only a $\tilde{\chi}_1^0$ LSP. The analysis targeting this final state [39] requires the presence of b-jets and $E_{\mathrm{T}}^{\mathrm{miss}}$, and exploits the presence of kinematical endpoints in contransverse mass [40] for the dominant $t\bar{t}$ production background. Compressed scenarios are targeted by an analysis exploiting ISR hadronic activity and using dedicated techniques for tagging low-p_{T} b-jets [41]. Longer $\tilde{b}$ decay chains are targeted by analyses explicitly looking for the presence of a Higgs boson in the $\tilde{\chi}_2^0 \to h\tilde{\chi}_1^0$ decay [42, 43].

Dedicated training of neural networks using input variables sensitive to the displaced decays of b-hadrons can produce relatively efficient c-jet tagging algorithms, which can be used effectively in the search for $\tilde{c} \to c\tilde{\chi}_1^0$. The analysis [44] was performed with a fraction of the available Run 2 integrated luminosity and follows a logic similar to that in Ref. [39].

Stop pair production was the target of an extensive search campaign as early as Run 1 [45], and Run 2 saw further development of the search strategy, with a variety of new final states being targeted. The popularity of stop searches is due to the stop's connection with the naturalness problem. From an

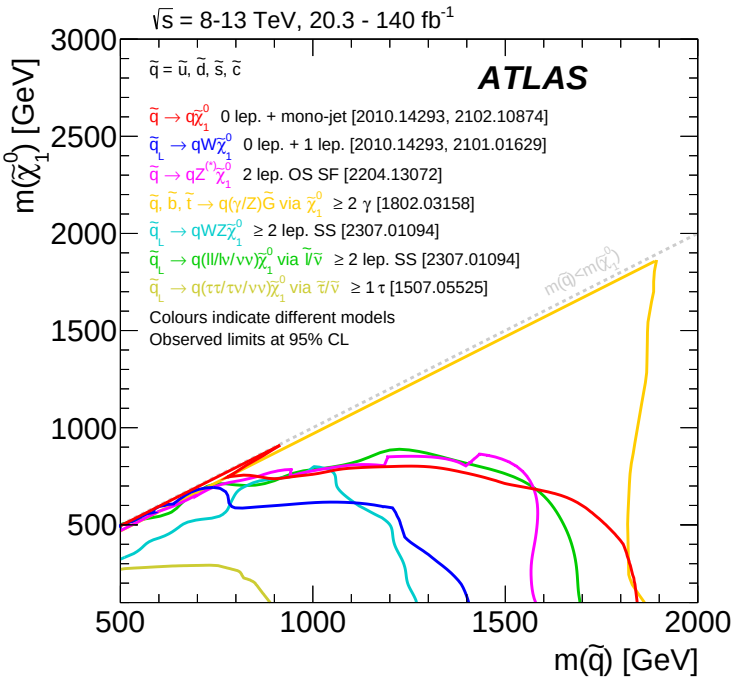


Figure 8: Exclusion limits from 8 TeV and 13 TeV data in the $m(\tilde{q})$–$m(\tilde{\chi}_1^0)$ plane for different simplified models featuring the decay of squarks to the lightest supersymmetric particle (lightest neutralino or gravitino) either directly or through a cascade chain featuring other SUSY particles with intermediate masses. For each line, the squark decay mode is reported in the legend and it is assumed to proceed with 100% branching fraction. The limits on $\tilde{q}_{\mathrm{L}} \to qW\tilde{\chi}_1^0$ assume the chargino mass to be midway between the squark and neutralino masses. The other $\tilde{q}_{\mathrm{L}}$ interpretations assume the first intermediate particle to be midway between the squark and neutralino masses, and the second intermediate particle to be midway between the first intermediate particle and neutralino masses. The additional assumptions about the masses of the intermediate states are described in the references cited in the plot.

experimental point of view, the phenomenology of stop decay is very rich because of the large top quark mass: assuming the simplest electroweak-sector configuration (a $\tilde{\chi}_1^0$ LSP), the kinematics of the decay is determined not only by the $\tilde{t}_1$ and $\tilde{\chi}_1^0$ masses, but also by how their difference $\Delta m(\tilde{t}_1, \tilde{\chi}_1^0)$ compares to the top quark and W boson masses. If $\Delta m(\tilde{t}_1, \tilde{\chi}_1^0) > m(t)$, then the $\tilde{t}_1$ will experience a two-body decay $\tilde{t}_1 \to t\tilde{\chi}_1^0$, followed by an on-shell decay of the top quark into an on-shell W boson and a b-quark. If $m(W) + m(b) < \Delta m(\tilde{t}_1, \tilde{\chi}_1^0) < m(t)$, the stop will decay into three bodies, $\tilde{t}_1 \to bW\tilde{\chi}_1^0$, via an off-shell top. Finally, if $m(b) < \Delta m(\tilde{t}_1, \tilde{\chi}_1^0) < m(W) + m(b)$, the decay will be into four bodies, $\tilde{t}_1 \to bff'\tilde{\chi}_1^0$, with f representing a generic fermion. These different regions are clearly displayed in Figure 10. The parameter space is targeted with a suite of analyses looking for different lepton (electron and muon) multiplicities. Depending on the decay of the $W^{(*)}$, the final state can contain zero [46], one [47] or two [48] leptons.

The zero-lepton analysis defines a series of different signal regions based on the number of top quark and W boson decays that can be tagged by making use of large-radius jets to collect all the decay products. Depending on the region, the selection is completed by using additional variables such as $E_{\mathrm{T}}^{\mathrm{miss}}$ and the transverse mass of the $E_{\mathrm{T}}^{\mathrm{miss}}$ and b-jets to reject the dominant background from $t\bar{t}$ and Z + jets production. As in Ref. [39], the compressed region is targeted with dedicated tools to tag low-p_{T} b-jets.

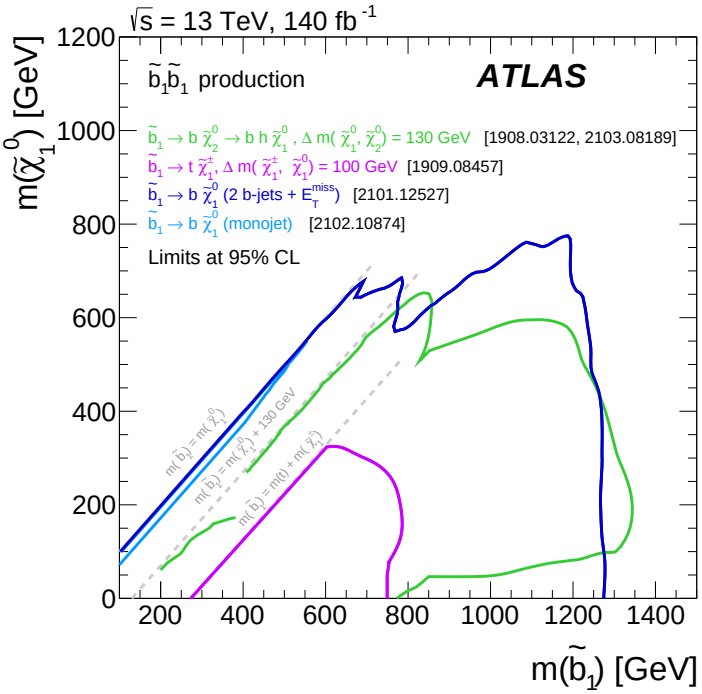


Figure 9: Exclusion limits in the $m(\tilde{b}_1)$–$m(\tilde{\chi}_1^0)$ plane for direct sbottom production. The lightest neutralino ($\tilde{\chi}_1^0$) is assumed to be the LSP. Several different decay scenarios are shown, along with different parameterisations of the intermediate particles in the models.

The one-lepton analysis also utilises a set of signal regions targeting the two-, three- and four-body decays separately. A challenging background process is $t\bar{t}$ production where both top quarks decay leptonically, and one lepton is lost or is a hadronically decaying τ-lepton. This background process is targeted by making use of a variable called *topness*, which yields an estimate of how much a given event with one lepton in the final state resembles a dileptonic $t\bar{t}$ decay, based on expected detector resolutions and mass constraints present in such events. An updated result (shown in red in Figure 10) is obtained by separating events into mutually exclusive categories based on the number of reconstructed large-radius jets, and the number of those compatible with arising from the decay of a top quark: for each category, dedicated neural networks are trained to disentangle the signal from the background. This improves the sensitivity, especially at intermediate stop masses and large neutralino masses.

A challenging mass hierarchy is the one where $\Delta m(\tilde{t}_1, \tilde{\chi}_1^0) \approx m(t)$: the final state and kinematics of $\tilde{t}_1\tilde{t}_1 \rightarrow t\bar{t}\tilde{\chi}_1^0\tilde{\chi}_1^0$ closely resemble those from $t\bar{t}$ production, especially if $m(\tilde{\chi}_1^0) \approx 0$. In this case, precision measurements of SM $t\bar{t}$ production can come to the rescue, as indicated in the inset plot of Figure 10: a precise measurement of spin correlations in $t\bar{t}$ events [49] allows constraints to be placed on the additional production of a pair of scalar particles.

Figure 10 shows that stop pair production is excluded (for the decays considered) up to stop masses of about 1.3 TeV for $m(\tilde{\chi}_1^0) = 0$. The limit drops to about $m(\tilde{t}_1) \sim 600$ GeV in the compressed region.

If a more complex electroweak sector is considered, for example one allowing $\tilde{t}_1 \rightarrow b\tilde{\chi}_1^+$ and $\tilde{t}_1 \rightarrow t\tilde{\chi}_2^0$, then additional kinematic configurations and particles become possible. Typically, the analyses discussed have good sensitivity to these scenarios. Additional analyses explicitly looking for the presence of a Higgs

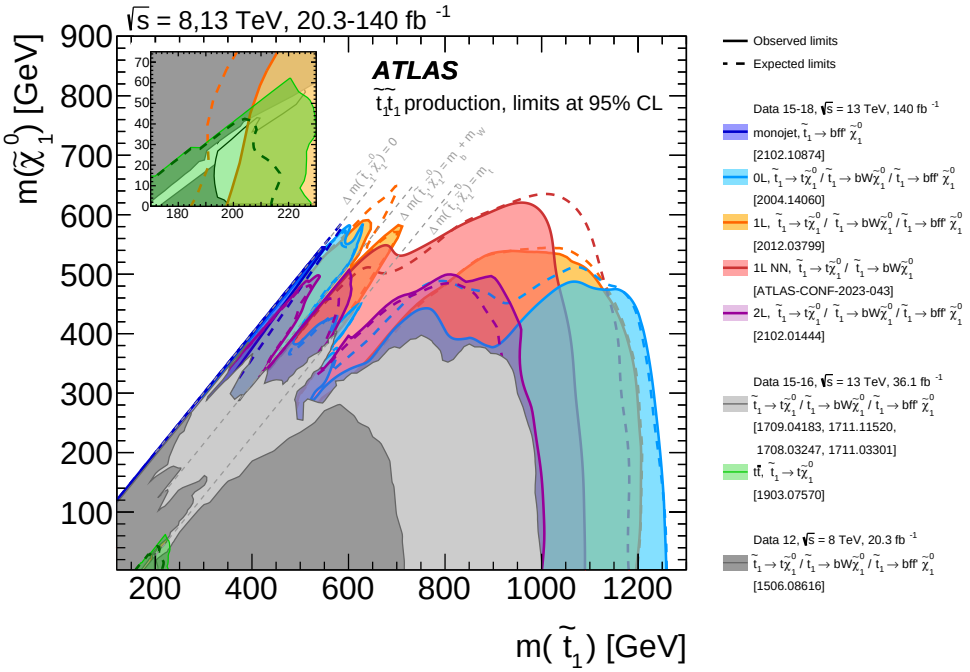


Figure 10: Summary of the dedicated ATLAS searches for top squark (stop) pair production based on pp collision data taken at $\sqrt{s} = 13$ TeV. Exclusion limits are shown in the $m(\tilde{t}_1)$–$m(\tilde{\chi}_1^0)$ plane. The dashed and solid lines show the expected and observed limits, respectively, including all uncertainties except the theoretical signal cross-section uncertainty (PDF and scale). Three decay modes are considered separately with 100% branching fraction: $\tilde{t}_1 \to t + \tilde{\chi}_1^0$ (where the $\tilde{t}_1$ is mostly $\tilde{t}_R$), $\tilde{t}_1 \to Wb\tilde{\chi}_1^0$ (three-body decay for $m(\tilde{t}_1) < m(t) + m(\tilde{\chi}_1^0)$), and $\tilde{t}_1 \to ff'b\tilde{\chi}_1^0$ (four-body decay).

or Z boson in the final state have also been developed [50], achieving interesting sensitivities. The case of a stop decay explicitly involving a $\tilde{\tau}$ has also been explored [51]. Finally, the flavour-changing decay of a stop into a charm quark and a neutralino LSP was targeted in Ref. [52]

6 Weakly produced supersymmetric particles

The electroweak production of SUSY particles includes some of the smallest cross-section processes at the LHC, with final-state signatures that are difficult to separate from SM processes. The ATLAS search programme aims to exploit all channels – from the clean, but rare, leptonic final states to the higher branching-fraction hadronic decays – in the quest to discover SUSY.

6.1 Slepton pair production

First- and second-generation slepton production, with decays into a charged lepton and a $\tilde{\chi}_1^0$ LSP ($\tilde{\ell}\tilde{\ell}$, with $\tilde{\ell} \to \ell\tilde{\chi}_1^0$) with 100% branching fraction, results in a clean final state of two OS SF leptons (e^+e^- or $\mu^+\mu^-$) and $E_{\mathrm{T}}^{\mathrm{miss}}$. A Run 2 search [53] considering general slepton production scenarios had the simple goal of

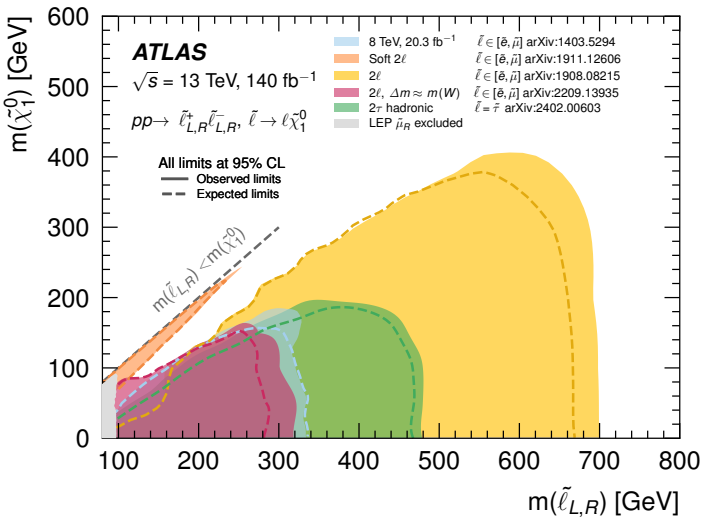


Figure 11: Exclusion limits in the $m(\tilde{\ell})$–$m(\tilde{\chi}^0_1)$ plane for different analyses probing the direct production of sleptons with decays into a lepton and neutralino. The types of sleptons (flavour and coupling) included in each search is specified in the legend.

achieving better sensitivity to higher slepton and neutralino masses than in the Run 1 search. A more recent search was more targeted and focused on the more compressed slepton production scenarios with $m(\tilde{\ell}) - m(\tilde{\chi}^0_1) < 100\,\text{GeV}$ [54], dividing the search between signatures with or without an ISR jet to exploit the boosted topology of $\tilde{\ell}\tilde{\ell}$ production with ISR. Both approaches use multiple bins in stransverse mass, m_{T2} [55], which are optimised for mass exclusion potential in $\tilde{\ell}\tilde{\ell}$ production. SM backgrounds containing Z boson or low-mass resonances are suppressed by discarding OS SF lepton pairs with compatible invariant mass, while $t\bar{t}$ production is suppressed by discarding events containing b-tagged jets. At least moderate $E_{\text{T}}^{\text{miss}}$ significance is required in order to suppress backgrounds with misreconstructed $E_{\text{T}}^{\text{miss}}$.

The most compressed slepton scenarios are targeted using a bespoke analysis requiring two low-p_{T} leptons, an ISR jet, and high $E_{\text{T}}^{\text{miss}}$ [56]. Low m_{T2} is used for signal–background discrimination, along with R_{ISR}, the ratio of the $E_{\text{T}}^{\text{miss}}$ to the p_{T} of the ISR system. A novel muon identification working point is used to recover some of the efficiency otherwise lost as $3\,\text{GeV} < p_{\text{T}} < 6\,\text{GeV}$ muons traverse the calorimeters.

The three searches see no significant excesses in the data compared to the SM background expectation, allowing limits to be set in simplified SUSY models, as shown in Figure 11. For mass-degenerate left- and right-handed slepton pair production, $\tilde{\ell}$ masses up to 700 GeV are excluded for massless $\tilde{\chi}^0_1$. For the very compressed scenarios with $m(\tilde{\ell}) - m(\tilde{\chi}^0_1) \sim 10\,\text{GeV}$, sleptons are excluded up to masses of 251 GeV. The so-called 'slepton-gap' between the LEP and LHC limits is now closed with the results from the latest slepton search, excluding sleptons up to 150 GeV for $m(\tilde{\ell}) - m(\tilde{\chi}^0_1) \sim 50\,\text{GeV}$. This still leaves an interesting parameter-space region to explore between the sensitivities in Ref. [56] and Refs. [53, 54].

Searches for third-generations sleptons, the staus, use final states with two hadronically decaying τ-leptons and high $E_{\text{T}}^{\text{miss}}$. The analysis in Ref. [57] uses a cut-and-count approach with two signal regions. The more recent analysis in Ref. [58] improves upon this by using four overlapping BDTs targeting different $\tilde{\tau}$–$\tilde{\chi}^0_1$ mass regimes. All four BDT signal regions show a 0.7σ–1.3σ deficit – a common deficit since the signal regions partially overlap. The exclusion limits for mass-degenerate left- and right-handed staus are shown

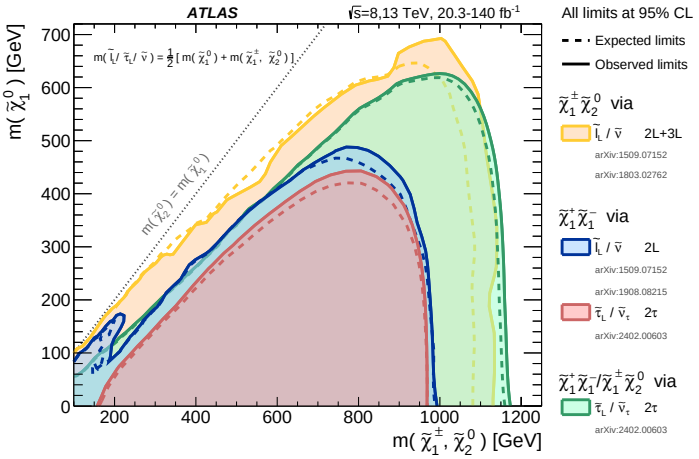


Figure 12: The exclusion limits on $\tilde{\chi}_1^+\tilde{\chi}_1^-$ and $\tilde{\chi}_1^\pm\tilde{\chi}_2^0$ production with $\tilde{\ell}$-mediated decays, as a function of the $\tilde{\chi}_1^\pm$, $\tilde{\chi}_2^0$ and $\tilde{\chi}_1^0$ masses. The production cross-section is for pure-wino $\tilde{\chi}_1^+\tilde{\chi}_1^-$ and $\tilde{\chi}_1^\pm\tilde{\chi}_2^0$. Each individual exclusion contour represents a union of the excluded regions from one or more analyses.

in Figure 11, where stau masses up to 500 GeV are excluded. When considering the production of purely right-handed staus, which has a lower cross-section, staus masses up to 350 GeV are excluded. There is little sensitivity to the more compressed $\tilde{\tau}$–$\tilde{\chi}_1^0$ mass scenarios, because the searches rely on high-p_{T} hadronically decaying τ-leptons to trigger the event.

6.2 Electroweakino pair production

Sleptons may also feature as intermediate states in chargino and neutralino decay chains. The production of chargino pairs or chargino–neutralino pairs decaying via sleptons results in two-lepton or three-lepton final states, respectively, along with $E_{\mathrm{T}}^{\mathrm{miss}}$. The exclusion limits in these models set by these searches [53, 58, 59] are shown in Figure 12, where chargino production is excluded for chargino masses up to 1 TeV and chargino–neutralino production is excluded for masses up to 1.15 TeV.

Charginos and neutralinos will decay via SM W, Z or h bosons if decays via sleptons are not kinematically allowed. The decays from the SM bosons include a rich array of hadronic and leptonic final states, allowing searches to be made using jets only, or one, two or three leptons in the final state. The same two-lepton search described above for slepton production is also used to search for production of low-mass chargino pairs decaying via W bosons [53], with further searches improving sensitivity to the $\Delta m\left(\tilde{\chi}_1^\pm, \tilde{\chi}_1^0\right) \sim m(W)$ scenarios [54]. The all-hadronic final state [60] makes use of the large hadronic branching fraction of SM boson decays to target very high-mass chargino production with large $\Delta m\left(\tilde{\chi}_1^\pm, \tilde{\chi}_1^0\right)$. The large mass splittings lead to boosted topologies, motivating the use of large-radius jets and boson-tagging algorithms to identify potential signal from boosted SM boson decays. Finally, a one-lepton, two-jet final state targets the intermediate chargino mass scenarios [61], which are not covered by the all-hadronic and two-lepton searches. No significant excesses were observed in the searches for chargino pair production, and a statistical combination of the three channels is performed in Ref. [62] and shown in Figure 13 for pure-wino charginos. Chargino masses up to 780 GeV are excluded for massless $\tilde{\chi}_1^0$, and $\tilde{\chi}_1^0$ masses up to 170 GeV are excluded for $\tilde{\chi}_1^\pm$ masses of ~400–600 GeV.

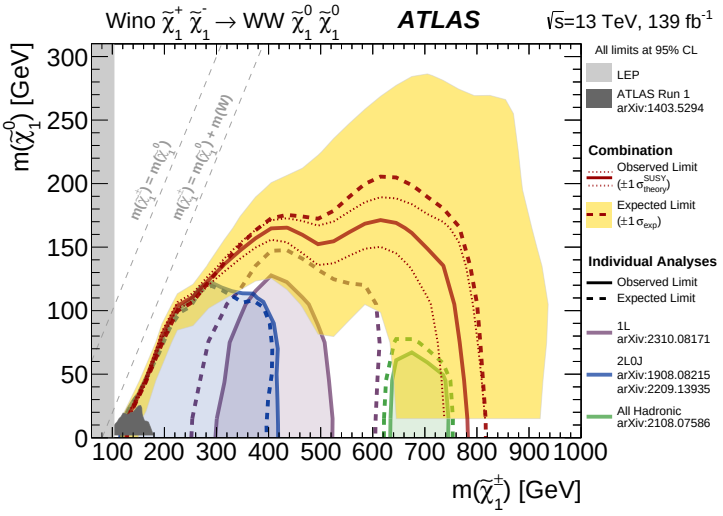
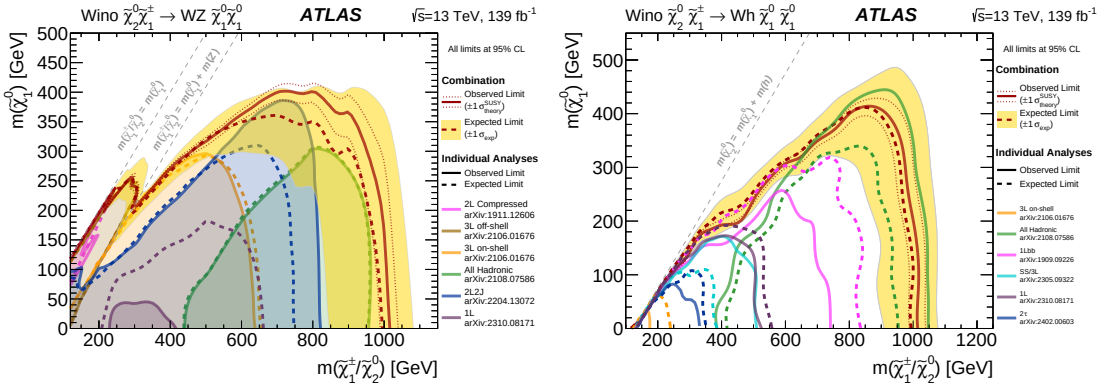


Figure 13: The exclusion limits on $\tilde{\chi}_1^+\tilde{\chi}_1^-$ production with W-boson-mediated decays, as a function of the $\tilde{\chi}_1^\pm$ and $\tilde{\chi}_1^0$ masses. The production cross-section is for pure-wino $\tilde{\chi}_1^+\tilde{\chi}_1^-$.

The all-hadronic channel is also powerful in the search for chargino–neutralino production and dominates the sensitivity to high-mass, large-$\Delta m\left(\tilde{\chi}_1^\pm/\tilde{\chi}_2^0, \tilde{\chi}_1^0\right)$ scenarios with decays via SM bosons, as seen in Figures 14(a) and 14(b). A two-lepton, two-jet search [31] selecting $Z \rightarrow \ell\ell$ and $W \rightarrow qq$ events with large $E_{\mathrm{T}}^{\mathrm{miss}}$ is sensitive to moderately high mass $\tilde{\chi}_1^\pm\tilde{\chi}_2^0$ scenarios with decays via W and Z bosons. A few of the two-lepton, two-jet signal regions with closely spaced jets observed 2σ deficits, resulting in a stronger observed limit than expected. The sensitivity to moderately low mass $\tilde{\chi}_1^\pm\tilde{\chi}_2^0 \rightarrow WZ\tilde{\chi}_1^0\tilde{\chi}_1^0$ scenarios is dominated by the three-lepton channel [63], which selects for decays of on- and off-shell W/Z bosons, with signal regions binned in OS SF lepton invariant mass, $E_{\mathrm{T}}^{\mathrm{miss}}$, m_{T}, and hadronic activity. Finally, the two-lepton compressed analysis described above is sensitive to $\tilde{\chi}_1^\pm\tilde{\chi}_2^0$ WZ scenarios with the smallest mass splittings.

When the $\tilde{\chi}_2^0$ decays via a Higgs boson, the one-lepton plus two-b-jet channel [64] is almost as powerful as the all-hadronic channel, and has unique sensitivity to moderate-mass scenarios. Here, pairs of b-tagged jets consistent with a $h \rightarrow b\bar{b}$ decay, as well as high $E_{\mathrm{T}}^{\mathrm{miss}}$, m_{T} and m_{CT}, are used to suppress SM processes. Leptonic final states are also used to search for these scenarios, but the sensitivity is limited to low masses due to the low branching fraction of the Higgs boson decay to leptons (possibly via SM bosons) [58, 63, 65]. A statistical combination of all the channels targeting chargino–neutralino production is performed in Ref. [62] and shown in Figures 14 and 14(b). Pure-wino chargino–neutralino production is excluded up to $\tilde{\chi}_1^\pm/\tilde{\chi}_2^0$ masses of ~1000 GeV for massless $\tilde{\chi}_1^0$, and up to $\tilde{\chi}_1^0$ masses of ~400 GeV for $\tilde{\chi}_1^\pm/\tilde{\chi}_2^0$ masses of ~800 GeV – whether the $\tilde{\chi}_2^0$ decays via a Z or Higgs boson. For decays solely through W and Z bosons, $\tilde{\chi}_1^\pm/\tilde{\chi}_2^0$ masses up to 300 GeV are excluded for $\Delta m(\tilde{\chi}_1^\pm/\tilde{\chi}_2^0, \tilde{\chi}_1^0) \sim m(Z)$, decreasing to 240 GeV for $\Delta m(\tilde{\chi}_1^\pm/\tilde{\chi}_2^0, \tilde{\chi}_1^0) = 10$ GeV.

The higgsino mass parameter μ enters into the MSSM expression for the light Higgs boson's mass at tree level [38]. Therefore, a relatively low μ (of the order of a few hundred GeV at most) is one of the firm predictions of naturalness arguments applied to SUSY [66]. The search for pure-higgsino chargino–neutralino production is driven by the two-lepton compressed [56] and three-lepton analyses [63]



(a) (b)

Figure 14: The exclusion limits on $\tilde{\chi}_1^\pm\tilde{\chi}_2^0$ production with $\tilde{\chi}_1^\pm \to \tilde{\chi}_1^0 W^\pm$ and (a) $\tilde{\chi}_2^0 \to \tilde{\chi}_1^0 Z$ or (b) $\tilde{\chi}_2^0 \to \tilde{\chi}_1^0 h$, as a function of the $\tilde{\chi}_1^\pm$, $\tilde{\chi}_2^0$ and $\tilde{\chi}_1^0$ masses. The production cross-section is for pure-wino $\tilde{\chi}_1^\pm$ and $\tilde{\chi}_2^0$.

described above, as well as the disappearing-track analysis [67] (see Section 8). The off-shell regions of the three-lepton analysis provide sensitivity to the larger mass splittings between the produced higgsinos and the LSP, $\Delta m(\tilde{\chi}_1^\pm, \tilde{\chi}_1^0) > 15$ GeV, while the more compressed analysis covers the smaller mass splittings down to about 1 GeV. A statistical combination of the two-lepton compressed analysis and three-lepton analysis is performed in Ref. [63], excluding pure-higgsino production of charginos with masses up to 180 GeV (190 GeV) for $\Delta m(\tilde{\chi}_1^\pm, \tilde{\chi}_1^0) \sim 30$ GeV (5 GeV). This decreases to 135 GeV for the intermediate mass splittings, where the combination has the most impact compared to the individual analyses. For $\Delta m(\tilde{\chi}_1^\pm, \tilde{\chi}_1^0) < 1$ GeV, the pair produced higgsinos start to have a flight path of a fraction of a mm, and their decay products are mildly displaced with respect to the primary vertex. An innovative analysis, exploiting the presence of a low-p_{T} isolated, good-quality track with only loose requirements on its impact parameter targets the prompt decay of the produced charginos and neutralinos into $\tilde{\chi}_1^0$, achieving sensitivity up to chargino masses of about 170 GeV for mass splittings 0.3 GeV $< \Delta m(\tilde{\chi}_1^\pm, \tilde{\chi}_1^0) <$ 0.9 GeV [68]. For the smallest mass splittings, the chargino is long-lived and is targeted by the disappearing-track analysis, where chargino masses below 210 GeV are excluded for $\Delta m(\tilde{\chi}_1^\pm, \tilde{\chi}_1^0) \lesssim 0.3$ GeV. All these results are summarised in Figure 15.

Higgsino GGM scenarios are targeted by numerous ATLAS SUSY analyses selecting for either the leptonic or hadronic decays of the Z boson, or Higgs boson decays to b-quarks. A statistical combination of the channels targeting higgsino GGM models is performed in Ref. [62] and shown in Figure 16. For high $\tilde{\chi}_1^0 \to Z\tilde{G}$ branching fractions, the four-lepton search [70] and all-hadronic search [60] both select for two Z candidates and high $E_{\mathrm{T}}^{\mathrm{miss}}$, and dominate the sensitivity to low and high higgsino masses, respectively. The two-lepton two-jet channel [31] spans the intermediate higgsino mass range and extends to the lowest $\tilde{\chi}_1^0 \to Z\tilde{G}$ branching fraction in the searches involving a Z boson. The multi-b-jet search [71] and two-γ two-b-jet search [72] target GGM scenarios with high $\tilde{\chi}_1^0 \to h\tilde{G}$ branching fractions. The multi-b-jet channel makes use of the common Higgs boson decay into $b\bar{b}$, with signal regions binned in $E_{\mathrm{T}}^{\mathrm{miss}}$ and m_{eff} for low-mass scenarios, or selecting on a BDT parameterized in higgsino mass for high-mass scenarios. The $\tilde{\chi}_1^0$ branching fraction into either $Z\tilde{G}$ or $h\tilde{G}$ is fully covered by the individual searches, with higgsino masses up to 960 GeV excluded for the two extreme branching fraction scenarios. The sensitivity drops

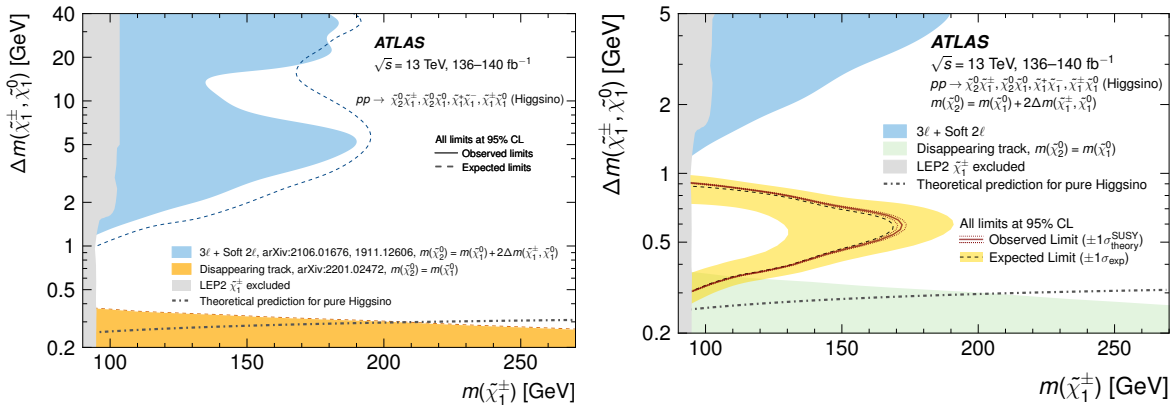


Figure 15: Exclusion limits for higgsino pair production $\tilde{\chi}_1^+\tilde{\chi}_1^-$, $\tilde{\chi}_1^\pm\tilde{\chi}_1^0$, $\tilde{\chi}_1^\pm\tilde{\chi}_2^0$, and $\tilde{\chi}_1^0\tilde{\chi}_2^0$ with off-shell SM-boson-mediated decays to the lightest neutralino, $\tilde{\chi}_1^0$, as a function of the $\tilde{\chi}_1^\pm$ and $\tilde{\chi}_1^0$ masses. The production cross-section is for pure higgsinos. The LEP2 $\tilde{\chi}_1^\pm$ exclusion is taken from Ref. [69]

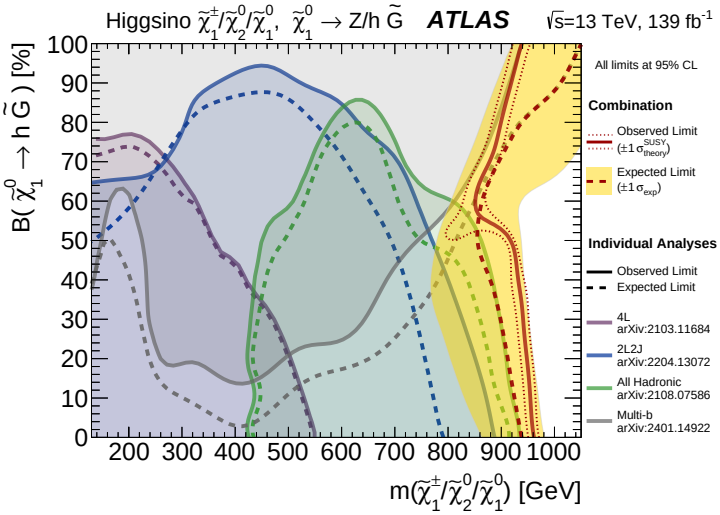


Figure 16: Exclusion limits in a General Gauge Mediation model from 13 TeV data. The model assumes a pure-higgsino NLSP that promptly decays into either a Z boson and gravitino or a Higgs boson and gravitino. The limits are displayed as a function of the mass of the nearly mass-degenerate higgsino multiplet and the branching fraction of the ightest higgsino into a Higgs boson and gravitino.

to masses of 850 GeV for the mixed branching fraction scenarios, where the combination has the most impact.

7 R-parity-violating decays

The MSSM potential includes terms that violate the conservation of baryon number and lepton number,

$$\frac{1}{2}\lambda_{ijk}L_iL_j\bar{E}_k + \lambda'_{ijk}L_iQ_j\bar{D}_k + \frac{1}{2}\lambda''_{ijk}\bar{U}_i\bar{D}_j\bar{D}_k + \kappa_iL_iH_2,$$

where L_i and Q_i are the lepton and quark SU(2)-doublet superfields, respectively, and $\bar{E}_i$, $\bar{U}_i$ and $\bar{D}_i$ are the corresponding singlet superfields. The fermion generations are denoted by the indices i, j and k, while the Higgs field that couples to up-type quarks is represented by the Higgs SU(2)-doublet superfield H_2. The λ_{ijk}, λ'_{ijk} and λ''_{ijk} parameters are three sets of new Yukawa couplings, while the κ_i parameters have dimensions of mass. In this section, RPV couplings are assumed to be large enough to allow decays to be prompt. In the case of very small RPV couplings, SUSY particles could be long-lived, leading to rather different experimental signatures which are discussed in Section 8.

The nine λ_{ijk} couplings violate lepton number conservation via interactions between the three generations of leptons and sleptons, allowing a $\tilde{\chi}_1^0$ LSP to decay via virtual sleptons into $\ell_k^{\pm}\ell_{i/j}^{\mp}\nu_{j/i}$. Pair production of a promptly decaying NLSP is assumed, potentially producing four or more charged leptons from the two $\tilde{\chi}_1^0$ decays in the event. These scenarios were explored with the four-lepton final state in Ref. [70], selecting electrons, muons and hadronically decaying τ-leptons for sensitivity to the λ_{12k} and λ_{i33} couplings, where $i, k \in 1, 2$. Since the electron and muon reconstruction efficiencies at the ATLAS experiment are similarly high, the sensitivities to λ_{121} and λ_{122} scenarios are nearly identical [73] and can be considered simply as λ_{12k} (and similarly for λ_{i33}). The $\lambda_{12k} \neq 0$ couplings are targeted using electrons and muons only, while sensitivity to the $\lambda_{i33} \neq 0$ couplings is increased by including up to two hadronically decaying τ-leptons among the four leptons. For each coupling scenario, three different NLSP production processes are considered: wino pair production ($\tilde{\chi}_1^{\pm}/\tilde{\chi}_2^0/\tilde{\chi}_1^+\tilde{\chi}_1^-$), slepton pair production ($\tilde{\ell}\tilde{\ell}/\tilde{\nu}\tilde{\nu}/\tilde{\ell}\tilde{\nu}$), or gluino pair production ($\tilde{g}\tilde{g}$). The strongest limits are set on $\tilde{g}\tilde{g}$ production with $\lambda_{12k} \neq 0$ as shown in Figure 17, where gluino masses up to 2.5 TeV are excluded. This mass limit decreases to 1.9 TeV for $\lambda_{i33} \neq 0$ scenarios, due to the lower reconstruction efficiency for hadronic τ-lepton decays. Lower mass exclusion limits of 1.6 TeV and 1.2 TeV (1.1 TeV and 0.9 TeV) are set on $\lambda_{12k} \neq 0$ ($\lambda_{i33} \neq 0$) scenarios of wino pair production and slepton pair production, respectively, due to the lower cross-sections. The sensitivity for other λ_{ijk} scenarios is expected to fall between the two extremes of the λ_{12k} and λ_{i33} scenarios studied.

The 27 λ'_{ijk} couplings violate lepton and baryon number conservation with interactions between leptons, quarks, and squarks, allowing a $\tilde{\chi}_1^0$ LSP to now decay via virtual squarks into $\ell_k^{\pm}q_i\bar{q}_j/\nu_k q_i q_j$, where q_i and $\bar{q}_j$ may be up-type or down-type quarks as needed to conserve charge. The lepton from one or each $\tilde{\chi}_1^0$ decay, along with several jets, is used to probe models of gluino pair production. The one-lepton analysis [74] divides the search regions according to the number of jets and number of b-tagged jets, as well as the charge of the lepton. Increasing thresholds are set on the p_{T} of the counted jets to obtain sensitivity to a wide range of scenarios. A second search selects two leptons with same-sign charges [33], multiple jets and high m_{eff}, benefiting from a lower SM background than in the one-lepton search. Figure 17 shows that the two searches set similar mass limits in the gluino production models, excluding gluinos with masses below ~2.2 TeV. The two-lepton search has less reliance on reconstructing the jet from the gluino decay ($\tilde{g} \rightarrow qq\tilde{\chi}_1^0$) and has a slight advantage if $m(\tilde{g}) - m(\tilde{\chi}_1^0)$ is small.

Finally, the nine λ''_{ijk} couplings violate baryon number conservation with interactions between quarks and squarks, allowing a $\tilde{\chi}_1^0$ LSP to now decay via virtual squarks into $q_k q_i q_j$, where q_k is an up-type quark and $q_{i/j}$ are down-type quarks. The one-lepton analysis already mentioned [74] also sets (for the first time) limits on higgsino pair production followed by their decay via λ'' couplings into third-generation quarks. The multijet search [75] selects events with a large number of high-p_{T} jets, allowing the presence of b-tagged jets to increase the sensitivity to b-quarks from the RPV $\tilde{\chi}_1^0$ decay. Again, gluinos with masses below ~2.2 TeV are excluded in Figure 17, but the sensitivity drops off rapidly for high and low $\tilde{\chi}_1^0$ masses where the jets are either too low in momentum or too collimated to be reconstructed. The analysis uses an

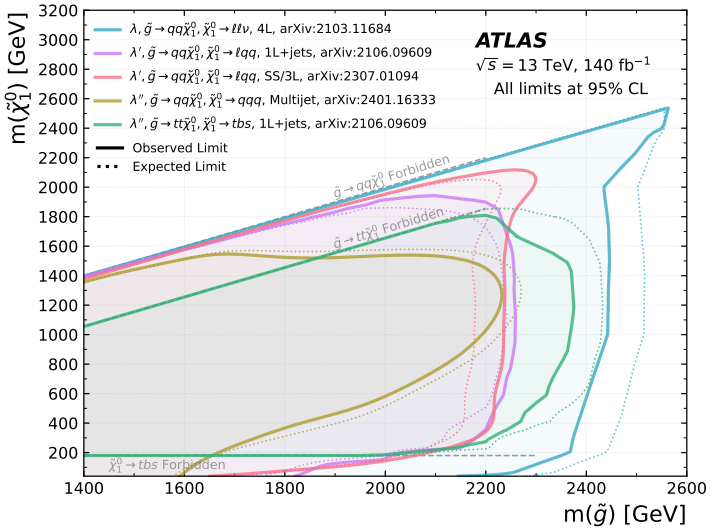


Figure 17: Exclusion limits at 95% CL based on 13 TeV data in the (gluino, lightest neutralino) mass plane for different simplified models featuring the decay of the gluino to the lightest supersymmetric particle (lightest neutralino) which in turn decays via R-parity-violating couplings to Standard Model particles. For each line, the gluino decay mode is reported in the legend and it is assumed to proceed with 100% branching fraction. Some limits depend on additional assumptions, as described in the references cited in the plot.

approach similar to that of the one-lepton search described above [74], which itself is also sensitive to the $\lambda''_{ijk} \neq 0$ scenarios when leptons are produced in top quark decays. The one-lepton signal regions with many b-tagged jets have good sensitivity to the $\tilde{g} \to tt\tilde{\chi}_1^0$, $\tilde{\chi}_1^0 \to tbs$ scenarios, excluding gluinos with masses below ~2.35 TeV as shown in Figure 17. A second approach in the multijet analysis uses a neural network with an architecture based on transformers to group jets together in order to help deal with the large combinatorial problem caused by the large number of jets in the final state, and search for a mass resonance from the two gluinos decaying directly via the λ''_{ijk} coupling, $\tilde{g} \to qqq$. In this case, gluinos with masses below ~1.8 TeV are excluded.

Less simple RPV SUSY scenarios have also been explored by the ATLAS Collaboration. For example, an MSSM scenario explored in Ref. [76] adds $B - L$ symmetry breaking with right-handed sneutrinos that is small enough to satisfy proton decay constraints, and also adds L symmetry breaking at tree level. The latter gives rise to charginos and neutralinos that decay into a SM boson and a lepton, e.g. $\tilde{\chi}_1^\pm \to Z\ell$, where a fully leptonic decay of the Z boson allows the chargino mass resonance to be fully reconstructed. The invariant mass of the three leptons is binned to achieve good sensitivity to a wide range of these $B - L$ SUSY scenarios, and the presence of additional leptons can be used to identify the presence of SM boson decays from the second produced sparticle. With no significant excess seen in the data, chargino masses up to 1.1 TeV are excluded for $\mathcal{B}(\tilde{\chi}_1^\pm \to Z\mu) = 100\%$, with lower mass exclusion limits obtained with different assumptions.

No direct limits have yet been placed on the size of the RPV couplings. However, if the coupling is not particularly small, it allows prompt sparticle decay and its effect is included in the limits set here. When the RPV coupling becomes very small, the sparticle becomes long-lived and experimental signatures are rather different – these are the topic of Section 8.

8 Long-lived supersymmetric particles

As is the case for SM particles, SUSY particles produced at the LHC may be long-lived and travel a significant distance before decaying. Longer lifetimes may be due to weak couplings to their decay products, decays through heavy mediator particles, or small mass differences between the particle and the decay products. The experimental signatures of long-lived new particles can be unconventional and depend on where and how the SUSY particle decays. A long-lived SUSY particle could travel from the ATLAS interaction point, through the inner-detector tracking system and then the calorimeters, and even through the muon spectrometer (or decay at any point along the way), leaving different signatures along its path depending on its properties. A charged particle decaying in the inner detector to a nearly degenerate stable neutral particle will manifest itself as a disappearing (or kinked) track, while a neutral particle's decay in the inner detector to charged and neutral particles would appear as tracks pointing back to a displaced vertex. The calorimeters may also be used for long-lived particle signatures, with photons that do not point back to the original interaction point ('non-pointing' photons), or strongly interacting long-lived particles that are stopped in the calorimeters by ionisation energy loss and nuclear scattering. Finally, if a SUSY particle is charged and very long-lived, the experimental signature would be similar to that of a muon, albeit with high mass. A neutral, weakly interacting long-lived new particle traversing the ATLAS detector would not be detected and would appear as missing transverse momentum.

A long-lived charged SUSY particle, such as a slepton or chargino, may be produced directly in pp collisions, or from prompt decays of other SUSY particles, such as a gluino. If its lifetime is $\sim 0.1-10$ ns because it is nearly degenerate with the invisible LSP, the charged SUSY particle would leave a track in the inner detector until the point of decay, where that track then disappears (the emitted charged decay products typically have momenta which are too low for their tracks to be reconstructed efficiently by the standard algorithm, although there is enough activity to reconstruct the additional decay products with a dedicated technique [77]). The backgrounds to such a signature include badly measured tracks, leptons undergoing large bremsstrahlung or scattering, and high-momentum charged hadrons interacting with material in the inner detector, and all are estimated directly from data using smeared tracks in control regions. Additional objects in the events, such as large $E_{\mathrm{T}}^{\mathrm{miss}}$, are usually selected to improve sensitivity to particular SUSY scenarios. The disappearing-track analysis [67] excludes pure-wino charginos with masses up to ~850 GeV for lifetimes of about 1 ns, as shown in Figure 18. The mass sensitivity for lower lifetimes is limited by the requirement of a minimum number of hits on the different layers of the inner detector, while the veto on track extensions imposed to satisfy the 'disappearing track' criterion limits the sensitivity at longer lifetimes.

If a charged particle has a longer lifetime, it may propagate beyond the inner detector before decaying. The track it leaves would be rather distinctive, with high ionisation energy loss since the expected high mass of the SUSY particle dictates it must be moving slowly, with $\beta = v/c \ll 1$. An analysis selecting tracks with large ionisation energy loss ($\mathrm{d}E/\mathrm{d}x$) in the pixel detector, instead of disappearing tracks, is used to search for longer-lived charged SUSY particles [78]. Careful corrections to the measured $\mathrm{d}E/\mathrm{d}x$ and reconstructed mass are made to account for the tracker's decreasing charge collection efficiency due to radiation damage as the integrated luminosity increases. The sensitivity offered by the large-$\mathrm{d}E/\mathrm{d}x$ analysis is complementary to that of the disappearing-track analysis, covering the longer-lifetime scenarios. Wino-like charginos with masses up to ~1050 GeV are excluded for lifetimes longer than 10 ns, as shown in Figure 18. The observed limits are weaker than the expected ones because the number of observed events exceeds the background prediction, quantified by a global Z significance of 3.3. This excess was investigated in a more recent

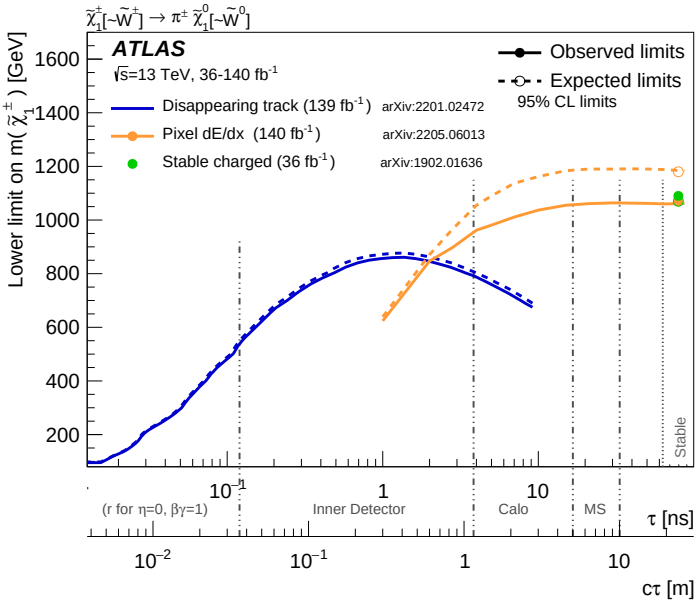


Figure 18: Constraints in the chargino mass-vs-lifetime plane for an AMSB model with $\tan\beta = 5$ and $\mu > 0$. The wino-like chargino is pair-produced and decays into a wino-like neutralino and a very soft charged pion. The solid lines indicate the observed limits, while the dashed lines indicate the expected limits. The area below the curves is excluded. "Calo" and "MS" refer to the ATLAS calorimeter and muon spectrometer systems, respectively. The analyses also have sensitivity at lifetimes other than those shown, but only the limits at tested lifetimes are shown. The three dots at large lifetime represent results for which the particle is assumed to be stable. In this context, stable means escaping the detector. The exclusion contours from the pixel $\mathrm{d}E/\mathrm{d}x$ search are each extrapolated to the stable regime with a straight line.

analysis [79] which considered measurements of time-of-flight to the calorimeter as well as $\mathrm{d}E/\mathrm{d}x$ in the pixel detector, and found compatibility with the background prediction.

An alternative approach, sensitive to neutral long-lived SUSY particles leaving no tell-tale track in the inner detector, is to reconstruct the long-lived particle's decay products. Charged decay products leave tracks that can be traced back to a common displaced vertex, with those from SUSY decays easily distinguishable from SM decays by their large invariant mass. A specialised track reconstruction algorithm optimised for tracks with large impact parameters was used to improve the efficiency of displaced-vertex reconstruction [80]. Random track combinations and merged vertices mimicking a high-mass displaced vertex typically dominate the backgrounds. A smaller component comes from hadronic interactions with detector material that are usually concentrated in regions with high matter density and are vetoed. However, those occurring in less dense regions can also appear as a high-mass displaced vertex. The searches for long-lived SUSY particles using displaced vertices [81] have excluded gluino masses up to 2400 GeV for lifetimes of ~0.1 ns, as shown in Figure 19. Prompt-decay SUSY analyses are typically more sensitive to gluino lifetimes below 0.01 ns, while the large-$\mathrm{d}E/\mathrm{d}x$ and stopped-gluino searches cover the longer lifetimes above ~5 ns.

A long-lived gluino may form an R-hadron with a SM vacuum quark, travel part way through the detector, and then stop in the calorimeter due to energy losses via ionisation and nuclear scattering. It may decay at a much later time, from about 100 ns to one year later, so a search for hadronic activity in the absence of collisions, while empty LHC beam bunches pass through ATLAS, is used [82]. The efficiency of R-hadron

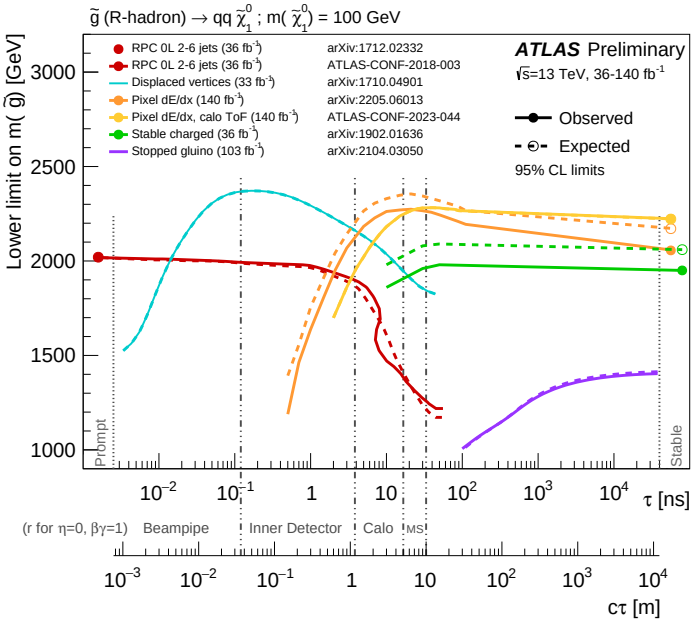


Figure 19: Constraints in the gluino mass-vs-lifetime plane for a split-supersymmetry model with the gluino R-hadron decaying into a gluon or light quarks and a neutralino with a mass of 100 GeV. The solid lines indicate the observed limits, while the dashed lines indicate the expected limits. The regions below the curves are excluded. "Calo" and "MS" refer to the ATLAS calorimeter and muon spectrometer systems, respectively.

detection depends on the fraction that stop in the detector, the probability of R-hadron decay during empty bunches, and the efficiency of hadronic-activity reconstruction [83]. The cosmic-ray muon background is taken from low-luminosity run periods, while the beam-halo background is estimated from unpaired crossings. Long-lived gluinos with masses up to 1400 GeV are excluded for lifetimes of 10^4–10^{12} ns, as shown in Figure 19.

Reconstructed objects, such as electrons, muons, and photons, can also be used to search for long-lived SUSY particles. In these cases, the leptons and photons should point back to the decay vertex of the SUSY particle rather than the interaction point, i.e. their tracks should be displaced. The specialised tracking procedure in Ref. [80] reconstructs electrons and muons with large transverse impact parameters, 10 mm $< |d_0| <$ 300 mm. The signature is very simple, requiring two large impact parameter ($|d_0| >$ 3 mm) leptons as expected from the decay of a pair of sleptons [84]. With no significant excess observed in the data, long-lived selectrons and smuons with masses up to about 700 GeV are excluded for lifetimes of about 0.1 ns (or, equivalently, co-NSLP slectron/smuon masses up to 820 GeV), while long-lived staus with masses up to about 340 GeV are excluded for the same lifetime. Another analysis, in Ref. [85], covers shorter-lifetime slepton scenarios, in an attempt to cover any sensitivity gap between long-lived and promptly decaying sleptons: in this case, the analysis uses standard tracking algorithms to select 'micro-displaced' leptons with 0.1 mm $< |d_0| <$ 3 mm forming high-mass pairs. With this approach, smuon masses up to 520 GeV are excluded for lifetimes of about 10^{-2} ns.

Despite the lack of tracking information, the flight path of a photon can be traced back to a location other than the collision vertex by using the spatial measurement and timing capabilities of the ATLAS detector's liquid-argon EM calorimeter. A photon from a long-lived particle decay will have delayed timing compared to promptly produced photons, and the longitudinal shape of the shower will point back to a displaced

vertex instead of the collision vertex. Two such non-pointing photons forming a high-mass displaced vertex are selected (assumed to be from the same decay) in Ref. [86], and these non-pointing photons may also be interpreted as displaced electrons since only EM calorimeter information is used. The background is estimated from data by exploiting the non-correlation in timing and pointing for photons from SM processes. Long-lived neutralinos that decay into a Z boson and gravitino and have lifetimes of 0.2 ns and masses below about 700 GeV are excluded.

In summary, an array of unconventional signatures in the ATLAS detector have been used to search for long-lived SUSY particles. From the implementation of specialised tracking algorithms, to searching for activity in the absence of collisions, the effort extends beyond the boundaries of typical SUSY searches at ATLAS and sets stringent limits on the masses of SUSY particles with lifetimes spanning many orders of magnitude.

9 Beyond simplified models

Having summarised and discussed in Sections 5 to 8 the main exclusion limits obtained from ATLAS Run 2 data when using simplified models, the obvious question is: how do these limits change when more realistic SUSY models are considered?

At the end of Run 1, ATLAS produced two papers trying to answer this question using slightly different methodologies. Reference [14] used a general 19-parameter pMSSM [12, 87] and sampled the parameter space while assuming a flat prior within the chosen parameter range. The models were checked to see if they were excluded by any of the ATLAS analyses available at the time. Results were quoted in terms of the fraction of models excluded at a given sparticle mass. A further study was performed [88] by varying only the pMSSM parameters affecting the electroweak sector ($\tan\beta$, M_1, M_2, μ, and M_A) and evaluating a global likelihood for models relevant for an explanation of the dark-matter relic density.

A similar study was repeated at the end of Run 2 [89]. The emphasis was again on the electroweak sector, with the gluino, squarks, and sleptons having very high masses. The five parameters mentioned above were varied (along with other parameters to satisfy constraints connected with the Higgs sector). Two samplings were performed: the 'EWKino' sample started from 20 000 models randomly sampled with uniform priors, while the 'Bino-DM' sample started with 437 500 models with a bino-like LSP that satisfy a requirement on the observed dark-matter relic density as an upper limit. The ability of several ATLAS Run 2 analyses targeting electroweak production to exclude each of the models considered was assessed. The impact of additional constraints from electroweak precision measurements, flavour observables and dark-matter direct detection experiments was also considered. The technical aspects of processing the large number of models are a testament to the evolution of the reinterpretation and recasting tools that the ATLAS Collaboration produced during Run 2 [90–92], but their discussion is beyond the scope of this paper.

Figure 20 shows, as a function of the electroweakino mass, the fraction of models in the EWKino sample that pass all external constraints but are excluded by ATLAS. In general, the excluded fraction decreases with increasing sparticle mass. About 50% of the models featuring a neutralino LSP with a mass of 500 GeV are excluded by ATLAS. This fraction increases to about 80% for masses of 200 GeV. Heavier electroweakinos with large masses are excluded in a significant fraction of the models: this is often the effect of correlations with the lighter states. For example, in models with a long-lived wino-like lightest chargino, its lifetime is determined by the mass of $\tilde{\chi}_2^0$.

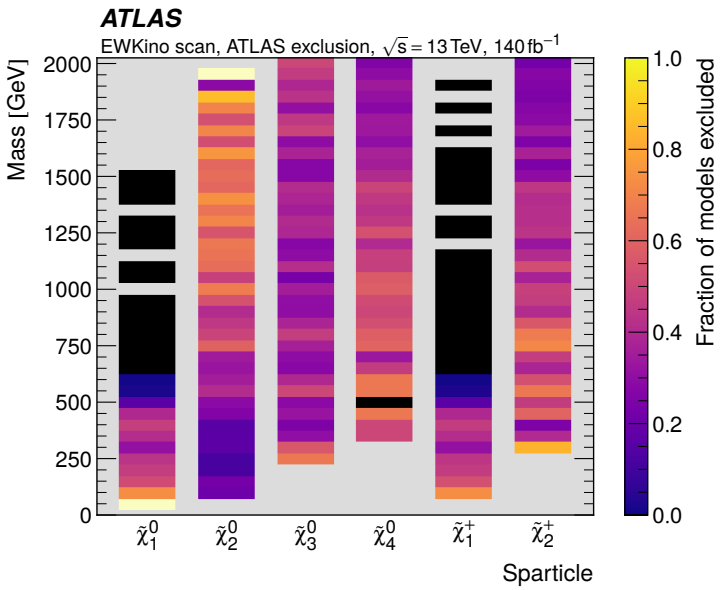


Figure 20: Fraction of models passing external constraints but excluded by ATLAS, depending on the mass of the electroweakinos for the EWKino samples.

A complementary view is given in Figure 21: here the Bino-DM sample is considered, and the fraction of models excluded is given in the format usually used by experiments doing direct searches for dark matter, i.e. in the plane of the WIMP–nucleon spin-independent scattering cross-section versus the mass of the WIMP. ATLAS excludes a very large fraction of the Z/H funnel, where the WIMP mass is close to half the mass of one of the bosons, so that the WIMP self-interaction is regulated by an enhanced cross-section for annihilation via boson exchange. A large fraction of the models are generally excluded for WIMP masses up to about 150 GeV, while the exclusion is progressively more limited above this WIMP mass.

A very useful by-product of studies like the one in Ref. [89] is the identification of classes of models that are not excluded by ATLAS, despite the masses of the involved sparticles being well within the exclusion limits provided by the simplified models. This information was used at the end of Run 1 to design some of the simplified models for Run 2, and will be used again to guide the evolution of the research programme in Run 3 and beyond.

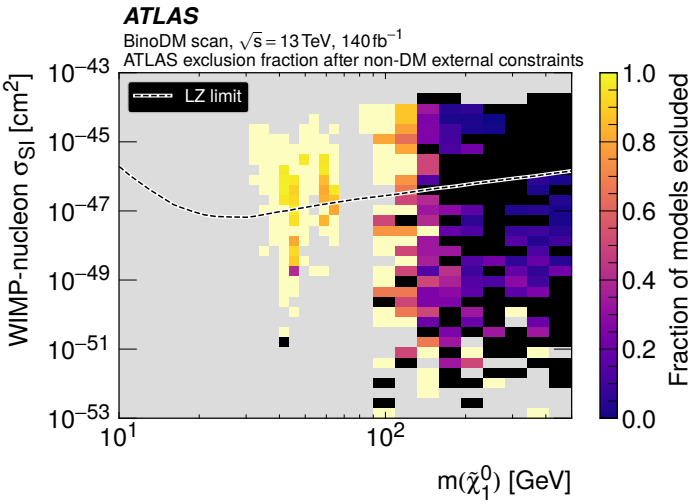


Figure 21: Fraction of models passing all non-DM external constraints but excluded by ATLAS in the WIMP–nucleon spin-independent scattering cross-section vs $m(\tilde{\chi}_1^0)$ plane.

10 Discussion and conclusions

The main results of searches for direct production of supersymmetric particles by the ATLAS Collaboration using the Run 2 dataset are summarised in this paper. The authors hope that the material will provide a useful overview for the casual reader, and a handy collection of references for those actively interested in the subject.

The achievements of the ATLAS Collaboration (and of its counterpart, CMS) are remarkable, and exclude important regions of the parameter space. The question that anyone reading this paper is likely to have in mind at this point is: where does this monumental experimental effort leave the community in terms of the existence of SUSY in nature?

In this form, the question is simply too wide to be answered in a convincing way. Since it is probably impossible to prove that the mass of the photon is exactly zero, it is experimentally impossible to prove that the superpartners of the SM particles do not exist, not even at some very large mass scale. However, the community has concluded that the mass of the photon is small enough to not have any phenomenological consequences for a large variety of phenomena at a cosmological scale. Likewise, one can try to provide answers to specific questions once they are asked in the framework of a supersymmetric theory.

The pre-LHC SUSY landscape was dominated by a relatively small number of frameworks arising from specific top-down approaches to the way SUSY was broken. Models that belong to this family are the constrained MSSM (cMSSM, or mSUGRA), anomaly-mediated SUSY breaking (AMSB), and gauge-mediated SUSY breaking (GMSB). In their minimal forms, the predictions of these models were already under very severe pressure by the end of Run 1. The limits on the masses of the gluinos and squarks (already in the TeV regime at the time) excluded a vast amount of the parameter space for the cMSSM [93]. The limits on pure-wino dark matter imposed by the disappearing-track results severely constrained the existence of long-lived charginos, and the difficulty in accommodating a Higgs boson with a mass of 125 GeV strongly excluded AMSB as a viable framework [94]. Similarly, minimal GMSB needs

top squarks with very high mass to obtain a Higgs boson mass compatible with that observed [95]. Beyond the need to connect searches to specific topologies, the rise of simplified models in Run 2 is also partly due to the heavy pressure of the Run 1 searches and Higgs boson results on mainstream SUSY-breaking models. In short, the Run 1 results changed the theoretical thinking and opened up the parameter space.

The Run 2 research programme was driven by a more agnostic approach – the big questions (such as: Is SUSY the way nature has chosen to stabilise the Higgs boson mass at the electroweak scale? Is SUSY the reason for the existence of dark matter?) were still used as a guideline, but the approach was much closer to 'turn every stone' than in the past. The classical paradigm of SUSY as a solution to the hierarchy problem requires higgsinos with masses of at most a few hundred GeV, top squarks at the TeV scale, and gluinos not too far above that. The current limits, well into the few-TeV region for gluinos and a TeV for top squarks, exceed the expectations for classical naturalness definitions, although more modern reanalysis of the arguments relaxes the constraints [96]. For the first time, hadron collider experiments started to surpass the LEP limits on higgsinos – and further investigations into the existence of higgsinos will be a highlight of Run 3 and beyond. As discussed in Section 9, many scenarios that include viable dark-matter candidates have been severely constrained by the LHC results, most notably the Z/h funnels for bino dark matter (those models where the self-annihilation cross-section for binos is enhanced by the proximity of the neutralino mass to half that of the Z or h boson). First sensitivity to the existence of a light stau was achieved during Run 2, although the interesting region for probing the stau funnel as a dark-matter regulation mechanism is still beyond experimental reach.

These results have led to a culture shock in the community: from being the prime candidate as a framework for physics beyond the SM, SUSY at the EW scale seems now to be perceived as a somewhat disfavoured candidate mechanism to extend the SM. Regardless of the community's perception, the pMSSM scans clearly show that SUSY still has a lot to offer, both as a source of viable models of new physics and as a spectacular tool for generating new signatures, and is thus a source of new ideas for searches. Hopefully, one of the benefits of reviews like this one is to help the average high-energy physicist to put the experimental effort in the right context: despite its main incarnations having been severely impacted by data from the LHC, the framework of EW-scale SUSY still offers viable extensions of the SM.

Together with those from the CMS Collaboration, the results summarised in this paper represent the state of the art (at the time of writing) in the worldwide experimental search for SUSY. No large increase in the centre-of-mass energy of the collisions is foreseen (in the ongoing Run 3, protons are collided at $\sqrt{s} = 13.6$ TeV). While it will take a long time for the size of the available dataset to increase substantially, the authors are confident that the creativity and skill of the experimentalists will improve the sensitivity of ATLAS to SUSY particles at a rate well beyond simple integrated luminosity scaling, as has happened so many times in the past. Therefore, while the results discussed in this paper are based on much of the overall capability of the LHC to probe unexplored territory in the SUSY parameter space, experimental breakthroughs will open new sensitivity windows, and, hopefully, start to shed some light on the questions that still today, more than ever, call for an extension of the Standard Model of particle physics.

Acknowledgements

We thank CERN for the very successful operation of the LHC and its injectors, as well as the support staff at CERN and at our institutions worldwide without whom ATLAS could not be operated efficiently.

The crucial computing support from all WLCG partners is acknowledged gratefully, in particular from CERN, the ATLAS Tier-1 facilities at TRIUMF/SFU (Canada), NDGF (Denmark, Norway, Sweden), CC-IN2P3 (France), KIT/GridKA (Germany), INFN-CNAF (Italy), NL-T1 (Netherlands), PIC (Spain), RAL (UK) and BNL (USA), the Tier-2 facilities worldwide and large non-WLCG resource providers. Major contributors of computing resources are listed in Ref. [97].

We gratefully acknowledge the support of ANPCyT, Argentina; YerPhI, Armenia; ARC, Australia; BMWFW and FWF, Austria; ANAS, Azerbaijan; CNPq and FAPESP, Brazil; NSERC, NRC and CFI, Canada; CERN; ANID, Chile; CAS, MOST and NSFC, China; Minciencias, Colombia; MEYS CR, Czech Republic; DNRF and DNSRC, Denmark; IN2P3-CNRS and CEA-DRF/IRFU, France; SRNSFG, Georgia; BMBF, HGF and MPG, Germany; GSRI, Greece; RGC and Hong Kong SAR, China; ISF and Benoziyo Center, Israel; INFN, Italy; MEXT and JSPS, Japan; CNRST, Morocco; NWO, Netherlands; RCN, Norway; MEiN, Poland; FCT, Portugal; MNE/IFA, Romania; MESTD, Serbia; MSSR, Slovakia; ARRS and MIZŠ, Slovenia; DSI/NRF, South Africa; MICINN, Spain; SRC and Wallenberg Foundation, Sweden; SERI, SNSF and Cantons of Bern and Geneva, Switzerland; MOST, Taipei; TENMAK, Türkiye; STFC, United Kingdom; DOE and NSF, United States of America.

Individual groups and members have received support from BCKDF, CANARIE, CRC and DRAC, Canada; PRIMUS 21/SCI/017 and UNCE SCI/013, Czech Republic; COST, ERC, ERDF, Horizon 2020, ICSC-NextGenerationEU and Marie Skłodowska-Curie Actions, European Union; Investissements d'Avenir Labex, Investissements d'Avenir Idex and ANR, France; DFG and AvH Foundation, Germany; Herakleitos, Thales and Aristeia programmes co-financed by EU-ESF and the Greek NSRF, Greece; BSF-NSF and MINERVA, Israel; Norwegian Financial Mechanism 2014-2021, Norway; NCN and NAWA, Poland; La Caixa Banking Foundation, CERCA Programme Generalitat de Catalunya and PROMETEO and GenT Programmes Generalitat Valenciana, Spain; Göran Gustafssons Stiftelse, Sweden; The Royal Society and Leverhulme Trust, United Kingdom.

In addition, individual members wish to acknowledge support from CERN: European Organization for Nuclear Research (CERN PJAS); Chile: Agencia Nacional de Investigación y Desarrollo (FONDECYT 1190886, FONDECYT 1210400, FONDECYT 1230987); China: National Natural Science Foundation of China (NSFC - 12175119, NSFC 12275265); European Union: European Research Council (ERC - 948254, ERC 101089007), Horizon 2020 Framework Programme (MUCCA - CHIST-ERA-19-XAI-00), Italian Center for High Performance Computing, Big Data and Quantum Computing (ICSC, NextGenerationEU); France: Agence Nationale de la Recherche (ANR-20-CE31-0013, ANR-21-CE31-0022), Investissements d'Avenir Labex (ANR-11-LABX-0012); Germany: Baden-Württemberg Stiftung (BW Stiftung-Postdoc Eliteprogramme), Deutsche Forschungsgemeinschaft (DFG - 469666862, DFG - CR 312/5-2); Italy: Istituto Nazionale di Fisica Nucleare (ICSC, NextGenerationEU); Japan: Japan Society for the Promotion of Science (JSPS KAKENHI 22H01227, JSPS KAKENHI 22KK0227, JSPS KAKENHI JP21H05085, JSPS KAKENHI JP22H04944); Netherlands: Netherlands Organisation for Scientific Research (NWO Veni 2020 - VI.Veni.202.179); Norway: Research Council of Norway (RCN-314472); Poland: Polish National Agency for Academic Exchange (PPN/PPO/2020/1/00002/U/00001), Polish National Science Centre (NCN 2021/42/E/ST2/00350, NCN OPUS nr 2022/47/B/ST2/03059, NCN UMO-2019/34/E/ST2/00393, UMO-2020/37/B/ST2/01043, UMO-2022/47/O/ST2/00148); Slovenia: Slovenian Research Agency (ARIS grant J1-3010); Spain: BBVA Foundation (LEO22-1-603), Generalitat Valenciana (Artemisa, FEDER, IDIFEDER/2018/048), La Caixa Banking Foundation (LCF/BQ/PI20/11760025), Ministry of Science and Innovation (RYC2019-028510-I, RYC2020-030254-I), PROMETEO and GenT Programmes Generalitat Valenciana (CIDEGENT/2019/023, CIDEGENT/2019/027); Sweden: Swedish Research Council (VR 2022-03845), Knut and Alice Wallenberg Foundation (KAW 2022.0358); Switzerland: Swiss National

Science Foundation (SNSF - PCEFP2_194658); United Kingdom: Leverhulme Trust (Leverhulme Trust RPG-2020-004); United States of America: Neubauer Family Foundation.

References

[1] L. Evans and P. Bryant, *LHC Machine*, JINST **3** (2008) S08001.

[2] ATLAS Collaboration, *The ATLAS Experiment at the CERN Large Hadron Collider*, JINST **3** (2008) S08003.

[3] CMS Collaboration, *The CMS Experiment at the CERN LHC*, JINST **3** (2008) S08004.

[4] Y. Golfand and E. Likhtman, *Extension of the Algebra of Poincare Group Generators and Violation of P Invariance*, JETP Lett. **13** (1971) 323, [Pisma Zh. Eksp. Teor. Fiz. **13** (1971) 452].

[5] D. Volkov and V. Akulov, *Is the neutrino a goldstone particle?*, Phys. Lett. B **46** (1973) 109.

[6] J. Wess and B. Zumino, *Supergauge transformations in four dimensions*, Nucl. Phys. B **70** (1974) 39.

[7] J. Wess and B. Zumino, *Supergauge invariant extension of quantum electrodynamics*, Nucl. Phys. B **78** (1974) 1.

[8] S. Ferrara and B. Zumino, *Supergauge invariant Yang-Mills theories*, Nucl. Phys. B **79** (1974) 413.

[9] A. Salam and J. Strathdee, *Super-symmetry and non-Abelian gauges*, Phys. Lett. B **51** (1974) 353.

[10] G. R. Farrar and P. Fayet, *Phenomenology of the production, decay, and detection of new hadronic states associated with supersymmetry*, Phys. Lett. B **76** (1978) 575.

[11] A. Djouadi, J.-L. Kneur and G. Moultaka, *SuSpect: A Fortran code for the supersymmetric and Higgs particle spectrum in the MSSM*, Comput. Phys. Commun. **176** (2007) 426, arXiv: hep-ph/0211331.

[12] C. F. Berger, J. S. Gainer, J. L. Hewett and T. G. Rizzo, *Supersymmetry Without Prejudice*, JHEP **02** (2009) 023, arXiv: 0812.0980 [hep-ph].

[13] A. Djouadi et al., 'The Minimal supersymmetric standard model: Group summary report', *GDR (Groupement De Recherche) - Supersymetrie*, 1999, arXiv: hep-ph/9901246.

[14] ATLAS Collaboration, *Summary of the ATLAS experiment's sensitivity to supersymmetry after LHC Run 1 — interpreted in the phenomenological MSSM*, JHEP **10** (2015) 134, arXiv: 1508.06608 [hep-ex].

[15] CMS Collaboration, *Phenomenological MSSM interpretation of CMS searches in pp collisions at $\sqrt{s} = 7$ and 8 TeV*, JHEP **10** (2016) 129, arXiv: 1606.03577 [hep-ex].

[16] J. Alwall, M.-P. Le, M. Lisanti and J. G. Wacker, *Searching for directly decaying gluinos at the Tevatron*, Phys. Lett. B **666** (2008) 34, arXiv: 0803.0019 [hep-ph].

[17] J. Alwall, P. Schuster and N. Toro, *Simplified models for a first characterization of new physics at the LHC*, Phys. Rev. D **79** (2009) 075020, arXiv: 0810.3921 [hep-ph].

[18] D. Alves et al., *Simplified models for LHC new physics searches*, J. Phys. G **39** (2012) 105005, arXiv: 1105.2838 [hep-ph].

[19] https://twiki.cern.ch/twiki/bin/view/LHCPhysics/SUSYCrossSections.

[20] ATLAS Collaboration, *Performance of the ATLAS trigger system in 2015*, Eur. Phys. J. C **77** (2017) 317, arXiv: 1611.09661 [hep-ex].

[21] ATLAS Collaboration, *The ATLAS Collaboration Software and Firmware*, ATL-SOFT-PUB-2021-001, 2021, URL: https://cds.cern.ch/record/2767187.

[22] ATLAS Collaboration, *Tools for estimating fake/non-prompt lepton backgrounds with the ATLAS detector at the LHC*, JINST **18** (2023) T11004, arXiv: 2211.16178 [hep-ex].

[23] ATLAS Collaboration, *Improved description of the di-tau final state in events with associated production of a W boson and jets in the ATLAS detector using the tau-promotion method*, ATL-PHYS-PUB-2019-039, 2019, URL: https://cds.cern.ch/record/2692073.

[24] G. Cowan, K. Cranmer, E. Gross and O. Vitells, *Asymptotic formulae for likelihood-based tests of new physics*, Eur. Phys. J. C **71** (2011) 1554, arXiv: 1007.1727 [physics.data-an], Erratum: Eur. Phys. J. C **73** (2013) 2501.

[25] A. L. Read, *Presentation of search results: the CL_S technique*, J. Phys. G **28** (2002) 2693.

[26] G. Giudice and A. Romanino, *Split supersymmetry*, Nucl. Phys. B **699** (2004) 65, arXiv: hep-ph/0406088, Erratum: Nucl. Phys. B **706** (2005) 65.

[27] N. Arkani-Hamed and S. Dimopoulos, *Supersymmetric unification without low energy supersymmetry and signatures for fine-tuning at the LHC*, JHEP **06** (2005) 073, arXiv: hep-th/0405159.

[28] ATLAS Collaboration, *Search for squarks and gluinos in final states with jets and missing transverse momentum using* 139 fb^{-1} *of* $\sqrt{s}$ = 13 *TeV pp collision data with the ATLAS detector*, JHEP **02** (2021) 143, arXiv: 2010.14293 [hep-ex].

[29] ATLAS Collaboration, *Search for squarks and gluinos with the ATLAS detector in final states with jets and missing transverse momentum using* 4.7 fb^{-1} *of* $\sqrt{s}$ = 7 *TeV proton–proton collision data*, Phys. Rev. D **87** (2013) 012008, arXiv: 1208.0949 [hep-ex].

[30] ATLAS Collaboration, *Search for squarks and gluinos in final states with one isolated lepton, jets, and missing transverse momentum at* $\sqrt{s}$ = 13 *TeV with the ATLAS detector*, Eur. Phys. J. C **81** (2021) 600, arXiv: 2101.01629 [hep-ex], Erratum: Eur. Phys. J. C **81** (2021) 956.

[31] ATLAS Collaboration, *Searches for new phenomena in events with two leptons, jets, and missing transverse momentum in* 139 fb^{-1} *of* $\sqrt{s}$ = 13 *TeV pp collisions with the ATLAS detector*, Eur. Phys. J. C **83** (2023) 515, arXiv: 2204.13072 [hep-ex].

[32] ATLAS Collaboration, *Search for new phenomena in final states with large jet multiplicities and missing transverse momentum using* $\sqrt{s}$ = 13 *TeV proton–proton collisions recorded by ATLAS in Run 2 of the LHC*, JHEP **10** (2020) 062, arXiv: 2008.06032 [hep-ex].

[33] ATLAS Collaboration, *Search for pair production of squarks or gluinos decaying via sleptons or weak bosons in final states with two same-sign or three leptons with the ATLAS detector*, JHEP **02** (2024) 107, arXiv: 2307.01094 [hep-ex].

[34] P. Meade, N. Seiberg and D. Shih, *General Gauge Mediation*, Prog. Theor. Phys. Suppl. **177** (2009) 143, arXiv: 0801.3278 [hep-ph].

[35] ATLAS Collaboration, *ATLAS flavour-tagging algorithms for the LHC Run 2 pp collision dataset*, Eur. Phys. J. C **83** (2023) 681, arXiv: 2211.16345 [physics.data-an].

[36] ATLAS Collaboration, *Search for supersymmetry in final states with missing transverse momentum and three or more b-jets in* $139\,fb^{-1}$ *of proton–proton collisions at* $\sqrt{s} = 13$ *TeV with the ATLAS detector*, Eur. Phys. J. C **83** (2023) 561, arXiv: 2211.08028 [hep-ex].

[37] ATLAS Collaboration, *Search for new phenomena in events with an energetic jet and missing transverse momentum in pp collisions at* $\sqrt{s} = 13$ *TeV with the ATLAS detector*, Phys. Rev. D **103** (2021) 112006, arXiv: 2102.10874 [hep-ex].

[38] S. Heinemeyer, *MSSM Higgs physics at higher orders*, Int. J. Mod. Phys. A **21** (2006) 2659, arXiv: hep-ph/0407244.

[39] ATLAS Collaboration, *Search for new phenomena in final states with b-jets and missing transverse momentum in* $\sqrt{s} = 13$ *TeV pp collisions with the ATLAS detector*, JHEP **05** (2021) 093, arXiv: 2101.12527 [hep-ex].

[40] D. R. Tovey, *On measuring the masses of pair-produced semi-invisibly decaying particles at hadron colliders*, JHEP **04** (2008) 034, arXiv: 0802.2879 [hep-ph].

[41] ATLAS Collaboration, *Soft b-hadron tagging for compressed SUSY scenarios*, ATLAS-CONF-2019-027, 2019, URL: https://cds.cern.ch/record/2682131.

[42] ATLAS Collaboration, *Search for bottom-squark pair production with the ATLAS detector in final states containing Higgs bosons, b-jets and missing transverse momentum*, JHEP **12** (2019) 060, arXiv: 1908.03122 [hep-ex].

[43] ATLAS Collaboration, *Search for bottom-squark pair production in pp collision events at* $\sqrt{s} = 13$ *TeV with hadronically decaying τ-leptons, b-jets and missing transverse momentum using the ATLAS detector*, Phys. Rev. D **104** (2021) 032014, arXiv: 2103.08189 [hep-ex].

[44] ATLAS Collaboration, *Search for supersymmetry in final states with charm jets and missing transverse momentum in* 13 *TeV pp collisions with the ATLAS detector*, JHEP **09** (2018) 050, arXiv: 1805.01649 [hep-ex].

[45] ATLAS Collaboration, *ATLAS Run 1 searches for direct pair production of third-generation squarks at the Large Hadron Collider*, Eur. Phys. J. C **75** (2015) 510, arXiv: 1506.08616 [hep-ex].

[46] ATLAS Collaboration, *Search for a scalar partner of the top quark in the all-hadronic $t\bar{t}$ plus missing transverse momentum final state at* $\sqrt{s} = 13$ *TeV with the ATLAS detector*, Eur. Phys. J. C **80** (2020) 737, arXiv: 2004.14060 [hep-ex].

[47] ATLAS Collaboration, *Search for new phenomena with top quark pairs in final states with one lepton, jets, and missing transverse momentum in pp collisions at* $\sqrt{s} = 13$ *TeV with the ATLAS detector*, JHEP **04** (2021) 174, arXiv: 2012.03799 [hep-ex].

[48] ATLAS Collaboration, *Search for new phenomena in events with two opposite-charge leptons, jets and missing transverse momentum in pp collisions at $\sqrt{s} = 13$ TeV with the ATLAS detector*, JHEP **04** (2021) 165, arXiv: 2102.01444 [hep-ex].

[49] ATLAS Collaboration, *Measurements of top-quark pair spin correlations in the $e\mu$ channel at $\sqrt{s} = 13$ TeV using pp collisions in the ATLAS detector*, Eur. Phys. J. C **80** (2020) 754, arXiv: 1903.07570 [hep-ex].

[50] ATLAS Collaboration, *Search for top squarks in events with a Higgs or Z boson using $139\,fb^{-1}$ of pp collision data at $\sqrt{s} = 13$ TeV with the ATLAS detector*, Eur. Phys. J. C **80** (2020) 1080, arXiv: 2006.05880 [hep-ex].

[51] ATLAS Collaboration, *Search for new phenomena in pp collisions in final states with tau leptons, b-jets, and missing transverse momentum with the ATLAS detector*, Phys. Rev. D **104** (2021) 112005, arXiv: 2108.07665 [hep-ex].

[52] ATLAS Collaboration, *A search for top-squark pair production, in final states containing a top quark, a charm quark and missing transverse momentum, using the 139 fb^{-1} of pp collision data collected by the ATLAS detector*, (2024), arXiv: 2402.12137 [hep-ex].

[53] ATLAS Collaboration, *Search for electroweak production of charginos and sleptons decaying into final states with two leptons and missing transverse momentum in $\sqrt{s} = 13$ TeV pp collisions using the ATLAS detector*, Eur. Phys. J. C **80** (2020) 123, arXiv: 1908.08215 [hep-ex].

[54] ATLAS Collaboration, *Search for direct pair production of sleptons and charginos decaying to two leptons and neutralinos with mass splittings near the W-boson mass in $\sqrt{s} = 13$ TeV pp collisions with the ATLAS detector*, JHEP **06** (2023) 031, arXiv: 2209.13935 [hep-ex].

[55] C. G. Lester and D. J. Summers, *Measuring masses of semi-invisibly decaying particle pairs produced at hadron colliders*, Phys. Lett. B **463** (1999) 99, arXiv: hep-ph/9906349.

[56] ATLAS Collaboration, *Searches for electroweak production of supersymmetric particles with compressed mass spectra in $\sqrt{s} = 13$ TeV pp collisions with the ATLAS detector*, Phys. Rev. D **101** (2020) 052005, arXiv: 1911.12606 [hep-ex].

[57] ATLAS Collaboration, *Search for direct stau production in events with two hadronic τ-leptons in $\sqrt{s} = 13$ TeV pp collisions with the ATLAS detector*, Phys. Rev. D **101** (2020) 032009, arXiv: 1911.06660 [hep-ex].

[58] ATLAS Collaboration, *Search for electroweak production of supersymmetric particles in final states with two τ-leptons in $\sqrt{s} = 13$ TeV pp collisions with the ATLAS detector*, (2024), arXiv: 2402.00603 [hep-ex].

[59] ATLAS Collaboration, *Search for electroweak production of supersymmetric particles in final states with two or three leptons at $\sqrt{s} = 13$ TeV with the ATLAS detector*, Eur. Phys. J. C **78** (2018) 995, arXiv: 1803.02762 [hep-ex].

[60] ATLAS Collaboration, *Search for charginos and neutralinos in final states with two boosted hadronically decaying bosons and missing transverse momentum in pp collisions at $\sqrt{s} = 13$ TeV with the ATLAS detector*, Phys. Rev. D **104** (2021) 112010, arXiv: 2108.07586 [hep-ex].

[61] ATLAS Collaboration,
Search for direct production of electroweakinos in final states with one lepton, jets and missing transverse momentum in pp collisions at $\sqrt{s}$ = 13 TeV with the ATLAS detector, (2023), arXiv: 2310.08171 [hep-ex].

[62] ATLAS Collaboration,
A statistical combination of ATLAS Run 2 searches for charginos and neutralinos at the LHC, (2024), arXiv: 2402.08347 [hep-ex].

[63] ATLAS Collaboration, *Search for chargino–neutralino pair production in final states with three leptons and missing transverse momentum in $\sqrt{s}$ = 13 TeV pp collisions with the ATLAS detector*, Eur. Phys. J. C **81** (2021) 1118, arXiv: 2106.01676 [hep-ex].

[64] ATLAS Collaboration, *Search for direct production of electroweakinos in final states with one lepton, missing transverse momentum and a Higgs boson decaying into two b-jets in pp collisions at $\sqrt{s}$ = 13 TeV with the ATLAS detector*, Eur. Phys. J. C **80** (2020) 691, arXiv: 1909.09226 [hep-ex].

[65] ATLAS Collaboration, *Search for direct production of winos and higgsinos in events with two same-charge leptons or three leptons in pp collision data at $\sqrt{s}$ = 13 TeV with the ATLAS detector*, JHEP **11** (2023) 150, arXiv: 2305.09322 [hep-ex].

[66] H. Baer, V. Barger, P. Huang and X. Tata,
Natural Supersymmetry: LHC, dark matter and ILC searches, JHEP **05** (2012) 109, arXiv: 1203.5539 [hep-ph].

[67] ATLAS Collaboration, *Search for long-lived charginos based on a disappearing-track signature using 136 fb^{-1} of pp collisions at $\sqrt{s}$ = 13 TeV with the ATLAS detector*, Eur. Phys. J. C **82** (2022) 606, arXiv: 2201.02472 [hep-ex].

[68] ATLAS Collaboration, *Search for nearly mass-degenerate higgsinos using low-momentum mildly-displaced tracks in pp collisions at $\sqrt{s}$ = 13 TeV with the ATLAS detector*, (2024), arXiv: 2401.14046 [hep-ex].

[69] The LEP SUSY Working Group and the ALEPH, DELPHI, L3 and OPAL experiments, note LEPSUSYWG/02-04.1, http://lepsusy.web.cern.ch/lepsusy/Welcome.html.

[70] ATLAS Collaboration, *Search for supersymmetry in events with four or more charged leptons in 139 fb^{-1} of $\sqrt{s}$ = 13 TeV pp collisions with the ATLAS detector*, JHEP **07** (2021) 167, arXiv: 2103.11684 [hep-ex].

[71] ATLAS Collaboration, *Search for pair production of higgsinos in events with two Higgs bosons and missing transverse momentum in $\sqrt{s}$=13 TeV pp collisions at the ATLAS experiment*, (2024), arXiv: 2401.14922 [hep-ex].

[72] ATLAS Collaboration, *Search for pair-produced Higgsinos decaying via Higgs or Z bosons to final states containing a pair of photons and a pair of b-jets with the ATLAS detector*, ATLAS-CONF-2023-009, 2023, URL: https://cds.cern.ch/record/2854839.

[73] ATLAS Collaboration, *Search for supersymmetry in events with four or more leptons in $\sqrt{s}$ = 8 TeV pp collisions with the ATLAS detector*, Phys. Rev. D **90** (2014) 052001, arXiv: 1405.5086 [hep-ex].

[74] ATLAS Collaboration, *Search for R-parity-violating supersymmetry in a final state containing leptons and many jets with the ATLAS experiment using $\sqrt{s}$ = 13 TeV proton–proton collision data*, Eur. Phys. J. C **81** (2021) 1023, arXiv: 2106.09609 [hep-ex].

[75] ATLAS Collaboration, *A search for R-parity-violating supersymmetry in final states containing many jets in pp collisions at $\sqrt{s}$ = 13 TeV with the ATLAS detector*, 2024, arXiv: 2401.16333 [hep-ex].

[76] ATLAS Collaboration, *Search for trilepton resonances from chargino and neutralino pair production in $\sqrt{s}$ = 13 TeV pp collisions with the ATLAS detector*, Phys. Rev. D **103** (2021) 112003, arXiv: 2011.10543 [hep-ex].

[77] ATLAS Collaboration, *Performance of tracking and vertexing techniques for a disappearing track plus soft track signature with the ATLAS detector*, ATL-PHYS-PUB-2019-011, 2019, URL: https://cds.cern.ch/record/2669015.

[78] ATLAS Collaboration, *Search for heavy, long-lived, charged particles with large ionisation energy loss in pp collisions at $\sqrt{s}$ = 13TeV using the ATLAS experiment and the full Run 2 dataset*, JHEP **06** (2023) 158, arXiv: 2205.06013 [hep-ex].

[79] ATLAS Collaboration, *Search for heavy,long-lived charged particles with large specific ionisation and low-beta in 140 fb^{-1} of pp collisions at $\sqrt{s}$ = 13 TeV using the ATLAS experiment*, ATLAS-CONF-2023-044, 2023, URL: https://cds.cern.ch/record/2870112.

[80] ATLAS Collaboration, *Performance of the reconstruction of large impact parameter tracks in the inner detector of ATLAS*, ATL-PHYS-PUB-2017-014, 2017, URL: https://cds.cern.ch/record/2275635.

[81] ATLAS Collaboration, *Search for long-lived, massive particles in events with displaced vertices and multiple jets in pp collisions at $\sqrt{s}$ = 13 TeV with the ATLAS detector*, JHEP **06** (2023) 200, arXiv: 2301.13866 [hep-ex].

[82] ATLAS Collaboration, *A search for the decays of stopped long-lived particles at $\sqrt{s}$ = 13 TeV with the ATLAS detector*, JHEP **07** (2021) 173, arXiv: 2104.03050 [hep-ex].

[83] ATLAS Collaboration, *Generation and Simulation of R-Hadrons in the ATLAS Experiment*, ATL-PHYS-PUB-2019-019, 2019, URL: https://cds.cern.ch/record/2676309.

[84] ATLAS Collaboration, *Search for displaced leptons in $\sqrt{s}$ = 13 TeV pp collisions with the ATLAS detector*, Phys. Rev. Lett. **127** (2021) 051802, arXiv: 2011.07812 [hep-ex].

[85] ATLAS Collaboration, *Search for pairs of muons with small displacements in pp collisions at $\sqrt{s}$ = 13 TeV with the ATLAS detector*, Phys. Lett. B **846** (2023) 138172, arXiv: 2305.02005 [hep-ex].

[86] ATLAS Collaboration, *Search in diphoton and dielectron final states for displaced production of Higgs or Z bosons with the ATLAS detector in $\sqrt{s}$ = 13 TeV pp collisions*, Phys. Rev. D **108** (2023) 012012, arXiv: 2304.12885 [hep-ex].

[87] M. W. Cahill-Rowley, J. L. Hewett, S. Hoeche, A. Ismail and T. G. Rizzo, *The New Look pMSSM with Neutralino and Gravitino LSPs*, Eur. Phys. J. C **72** (2012) 2156, arXiv: 1206.4321 [hep-ph].

[88] ATLAS Collaboration, *Dark matter interpretations of ATLAS searches for the electroweak production of supersymmetric particles in $\sqrt{s}$ = 8 TeV proton–proton collisions*, JHEP **09** (2016) 175, arXiv: 1608.00872 [hep-ex].

[89] ATLAS Collaboration, *ATLAS Run 2 searches for electroweak production of supersymmetric particles interpreted within the pMSSM*, (2024), arXiv: 2402.01392 [hep-ex].

[90] ATLAS Collaboration, *SimpleAnalysis: Truth-level Analysis Framework*, ATL-PHYS-PUB-2022-017, 2022, URL: https://cds.cern.ch/record/2805991.

[91] ATLAS Collaboration, *Implementation of simplified likelihoods in HistFactory for searches for supersymmetry*, ATL-PHYS-PUB-2021-038, 2021, URL: https://cds.cern.ch/record/2782654.

[92] ATLAS Collaboration, *Reproducing searches for new physics with the ATLAS experiment through publication of full statistical likelihoods*, ATL-PHYS-PUB-2019-029, 2019, URL: https://cds.cern.ch/record/2684863.

[93] O. Buchmueller et al., *The CMSSM and NUHM1 after LHC Run 1*, Eur. Phys. J. C **74** (2014) 2922, arXiv: 1312.5250 [hep-ph].

[94] H. Baer, V. Barger and D. Sengupta, *Anomaly-mediated SUSY breaking model retrofitted for naturalness*, Phys. Rev. D **98** (2018) 015039, arXiv: 1801.09730 [hep-ph].

[95] A. Delgado, M. Garcia-Pepin and M. Quiros, *GMSB with Light Stops*, JHEP **08** (2015) 159, arXiv: 1505.07469 [hep-ph].

[96] H. Baer et al., *What hadron collider is required to discover or falsify natural supersymmetry?*, Phys. Lett. B **774** (2017) 451, arXiv: 1702.06588 [hep-ph].

[97] ATLAS Collaboration, *ATLAS Computing Acknowledgements*, ATL-SOFT-PUB-2023-001, 2023, URL: https://cds.cern.ch/record/2869272.

The ATLAS Collaboration

G. Aad [103], E. Aakvaag [16], B. Abbott [121], K. Abeling [55], N.J. Abicht [49], S.H. Abidi [29], M. Aboelela [44], A. Aboulhorma [35e], H. Abramowicz [152], H. Abreu [151], Y. Abulaiti [118], B.S. Acharya [69a,69b,l], A. Ackermann [63a], C. Adam Bourdarios [4], L. Adamczyk [86a], S.V. Addepalli [26], M.J. Addison [102], J. Adelman [116], A. Adiguzel [21c], T. Adye [135], A.A. Affolder [137], Y. Afik [39], M.N. Agaras [13], J. Agarwala [73a,73b], A. Aggarwal [101], C. Agheorghiesei [27c], A. Ahmad [36], F. Ahmadov [38,y], W.S. Ahmed [105], S. Ahuja [96], X. Ai [62e], G. Aielli [76a,76b], A. Aikot [164], M. Ait Tamlihat [35e], B. Aitbenchikh [35a], I. Aizenberg [170], M. Akbiyik [101], T.P.A. Åkesson [99], A.V. Akimov [37], D. Akiyama [169], N.N. Akolkar [24], S. Aktas [21a], K. Al Khoury [41], G.L. Alberghi [23b], J. Albert [166], P. Albicocco [53], G.L. Albouy [60], S. Alderweireldt [52], Z.L. Alegria [122], M. Aleksa [36], I.N. Aleksandrov [38], C. Alexa [27b], T. Alexopoulos [10], F. Alfonsi [23b], M. Algren [56], M. Alhroob [142], B. Ali [133], H.M.J. Ali [92], S. Ali [149], S.W. Alibocus [93], M. Aliev [33c], G. Alimonti [71a], W. Alkakhi [55], C. Allaire [66], B.M.M. Allbrooke [147], J.F. Allen [52], C.A. Allendes Flores [138f], P.P. Allport [20], A. Aloisio [72a,72b], F. Alonso [91], C. Alpigiani [139], M. Alvarez Estevez [100], A. Alvarez Fernandez [101], M. Alves Cardoso [56], M.G. Alviggi [72a,72b], M. Aly [102], Y. Amaral Coutinho [83b], A. Ambler [105], C. Amelung [36], M. Amerl [102], C.G. Ames [110], D. Amidei [107], K.J. Amirie [156], S.P. Amor Dos Santos [131a], K.R. Amos [164], S. An [84], V. Ananiev [126], C. Anastopoulos [140], T. Andeen [11], J.K. Anders [36], S.Y. Andrean [47a,47b], A. Andreazza [71a,71b], S. Angelidakis [9], A. Angerami [41,aa], A.V. Anisenkov [37], A. Annovi [74a], C. Antel [56], M.T. Anthony [140], E. Antipov [146], M. Antonelli [53], F. Anulli [75a], M. Aoki [84], T. Aoki [154], J.A. Aparisi Pozo [164], M.A. Aparo [147], L. Aperio Bella [48], C. Appelt [18], A. Apyan [26], S.J. Arbiol Val [87], C. Arcangeletti [53], A.T.H. Arce [51], E. Arena [93], J-F. Arguin [109], S. Argyropoulos [54], J.-H. Arling [48], O. Arnaez [4], H. Arnold [115], G. Artoni [75a,75b], H. Asada [112], K. Asai [119], S. Asai [154], N.A. Asbah [36], K. Assamagan [29], R. Astalos [28a], K.S.V. Astrand [99], S. Atashi [160], R.J. Atkin [33a], M. Atkinson [163], H. Atmani [35f], P.A. Atmasiddha [129], K. Augsten [133], S. Auricchio [72a,72b], A.D. Auriol [20], V.A. Austrup [102], G. Avolio [36], K. Axiotis [56], G. Azuelos [109,ae], D. Babal [28b], H. Bachacou [136], K. Bachas [153,p], A. Bachiu [34], F. Backman [47a,47b], A. Badea [39], T.M. Baer [107], P. Bagnaia [75a,75b], M. Bahmani [18], D. Bahner [54], K. Bai [124], A.J. Bailey [164], J.T. Baines [135], L. Baines [95], O.K. Baker [173], E. Bakos [15], D. Bakshi Gupta [8], V. Balakrishnan [121], R. Balasubramanian [115], E.M. Baldin [37], P. Balek [86a], E. Ballabene [23b,23a], F. Balli [136], L.M. Baltes [63a], W.K. Balunas [32], J. Balz [101], E. Banas [87], M. Bandieramonte [130], A. Bandyopadhyay [24], S. Bansal [24], L. Barak [152], M. Barakat [48], E.L. Barberio [106], D. Barberis [57b,57a], M. Barbero [103], M.Z. Barel [115], K.N. Barends [33a], T. Barillari [111], M-S. Barisits [36], T. Barklow [144], P. Baron [123], D.A. Baron Moreno [102], A. Baroncelli [62a], G. Barone [29], A.J. Barr [127], J.D. Barr [97], F. Barreiro [100], J. Barreiro Guimarães da Costa [14a], U. Barron [152], M.G. Barros Teixeira [131a], S. Barsov [37], F. Bartels [63a], R. Bartoldus [144], A.E. Barton [92], P. Bartos [28a], A. Basan [101], M. Baselga [49], A. Bassalat [66,b], M.J. Basso [157a], R.L. Bates [59], S. Batlamous [35e], B. Batool [142], M. Battaglia [137], D. Battulga [18], M. Bauce [75a,75b], M. Bauer [36], P. Bauer [24], L.T. Bazzano Hurrell [30], J.B. Beacham [51], T. Beau [128], J.Y. Beaucamp [91], P.H. Beauchemin [159], P. Bechtle [24], H.P. Beck [19,o], K. Becker [168], A.J. Beddall [82], V.A. Bednyakov [38], C.P. Bee [146], L.J. Beemster [15], T.A. Beermann [36], M. Begalli [83d], M. Begel [29], A. Behera [146], J.K. Behr [48], J.F. Beirer [36], F. Beisiegel [24], M. Belfkir [117b], G. Bella [152], L. Bellagamba [23b], A. Bellerive [34], P. Bellos [20], K. Beloborodov [37], D. Benchekroun [35a], F. Bendebba [35a], Y. Benhammou [152],

K.C. Benkendorfer[61], L. Beresford[48], M. Beretta[53], E. Bergeaas Kuutmann[162], N. Berger[4], B. Bergmann[133], J. Beringer[17a], G. Bernardi[5], C. Bernius[144], F.U. Bernlochner[24], F. Bernon[36,103], A. Berrocal Guardia[13], T. Berry[96], P. Berta[134], A. Berthold[50], S. Bethke[111], A. Betti[75a,75b], A.J. Bevan[95], N.K. Bhalla[54], M. Bhamjee[33c], S. Bhatta[146], D.S. Bhattacharya[167], P. Bhattarai[144], K.D. Bhide[54], V.S. Bhopatkar[122], R.M. Bianchi[130], G. Bianco[23b,23a], O. Biebel[110], R. Bielski[124], M. Biglietti[77a], C.S. Billingsley[44], M. Bindi[55], A. Bingul[21b], C. Bini[75a,75b], A. Biondini[93], C.J. Birch-sykes[102], G.A. Bird[32], M. Birman[170], M. Biros[134], S. Biryukov[147], T. Bisanz[49], E. Bisceglie[43b,43a], J.P. Biswal[135], D. Biswas[142], K. Bjørke[126], I. Bloch[48], A. Blue[59], U. Blumenschein[95], J. Blumenthal[101], V.S. Bobrovnikov[37], M. Boehler[54], B. Boehm[167], D. Bogavac[36], A.G. Bogdanchikov[37], C. Bohm[47a], V. Boisvert[96], P. Bokan[36], T. Bold[86a], M. Bomben[5], M. Bona[95], M. Boonekamp[136], C.D. Booth[96], A.G. Borbély[59], I.S. Bordulev[37], H.M. Borecka-Bielska[109], G. Borissov[92], D. Bortoletto[127], D. Boscherini[23b], M. Bosman[13], J.D. Bossio Sola[36], K. Bouaouda[35a], N. Bouchhar[164], J. Boudreau[130], E.V. Bouhova-Thacker[92], D. Boumediene[40], R. Bouquet[57b,57a], A. Boveia[120], J. Boyd[36], D. Boye[29], I.R. Boyko[38], J. Bracinik[20], N. Brahimi[4], G. Brandt[172], O. Brandt[32], F. Braren[48], B. Brau[104], J.E. Brau[124], R. Brener[170], L. Brenner[115], R. Brenner[162], S. Bressler[170], D. Britton[59], D. Britzger[111], I. Brock[24], G. Brooijmans[41], E. Brost[29], L.M. Brown[166], L.E. Bruce[61], T.L. Bruckler[127], P.A. Bruckman de Renstrom[87], B. Brüers[48], A. Bruni[23b], G. Bruni[23b], M. Bruschi[23b], N. Bruscino[75a,75b], T. Buanes[16], Q. Buat[139], D. Buchin[111], A.G. Buckley[59], O. Bulekov[37], B.A. Bullard[144], S. Burdin[93], C.D. Burgard[49], A.M. Burger[36], B. Burghgrave[8], O. Burlayenko[54], J.T.P. Burr[32], C.D. Burton[11], J.C. Burzynski[143], E.L. Busch[41], V. Büscher[101], P.J. Bussey[59], J.M. Butler[25], C.M. Buttar[59], J.M. Butterworth[97], W. Buttinger[135], C.J. Buxo Vazquez[108], A.R. Buzykaev[37], S. Cabrera Urbán[164], L. Cadamuro[66], D. Caforio[58], H. Cai[130], Y. Cai[14a,14e], Y. Cai[14c], V.M.M. Cairo[36], O. Cakir[3a], N. Calace[36], P. Calafiura[17a], G. Calderini[128], P. Calfayan[68], G. Callea[59], L.P. Caloba[83b], D. Calvet[40], S. Calvet[40], M. Calvetti[74a,74b], R. Camacho Toro[128], S. Camarda[36], D. Camarero Munoz[26], P. Camarri[76a,76b], M.T. Camerlingo[72a,72b], D. Cameron[36], C. Camincher[166], M. Campanelli[97], A. Camplani[42], V. Canale[72a,72b], A.C. Canbay[3a], E. Canonero[96], J. Cantero[164], Y. Cao[163], F. Capocasa[26], M. Capua[43b,43a], A. Carbone[71a,71b], R. Cardarelli[76a], J.C.J. Cardenas[8], F. Cardillo[164], G. Carducci[43b,43a], T. Carli[36], G. Carlino[72a], J.I. Carlotto[13], B.T. Carlson[130,q], E.M. Carlson[166,157a], L. Carminati[71a,71b], A. Carnelli[136], M. Carnesale[75a,75b], S. Caron[114], E. Carquin[138f], S. Carrá[71a], G. Carratta[23b,23a], A.M. Carroll[124], T.M. Carter[52], M.P. Casado[13,i], M. Caspar[48], F.L. Castillo[4], L. Castillo Garcia[13], V. Castillo Gimenez[164], N.F. Castro[131a,131e], A. Catinaccio[36], J.R. Catmore[126], T. Cavaliere[4], V. Cavaliere[29], N. Cavalli[23b,23a], Y.C. Cekmecelioglu[48], E. Celebi[21a], S. Cella[36], F. Celli[127], M.S. Centonze[70a,70b], V. Cepaitis[56], K. Cerny[123], A.S. Cerqueira[83a], A. Cerri[147], L. Cerrito[76a,76b], F. Cerutti[17a], B. Cervato[142], A. Cervelli[23b], G. Cesarini[53], S.A. Cetin[82], D. Chakraborty[116], J. Chan[171], W.Y. Chan[154], J.D. Chapman[32], E. Chapon[136], B. Chargeishvili[150b], D.G. Charlton[20], M. Chatterjee[19], C. Chauhan[134], Y. Che[14c], S. Chekanov[6], S.V. Chekulaev[157a], G.A. Chelkov[38,a], A. Chen[107], B. Chen[152], B. Chen[166], H. Chen[14c], H. Chen[29], J. Chen[62c], J. Chen[143], M. Chen[127], S. Chen[154], S.J. Chen[14c], X. Chen[62c,136], X. Chen[14b,ad], Y. Chen[62a], C.L. Cheng[171], H.C. Cheng[64a], S. Cheong[144], A. Cheplakov[38], E. Cheremushkina[48], E. Cherepanova[115], R. Cherkaoui El Moursli[35e], E. Cheu[7], K. Cheung[65], L. Chevalier[136], V. Chiarella[53], G. Chiarelli[74a], N. Chiedde[103], G. Chiodini[70a], A.S. Chisholm[20], A. Chitan[27b], M. Chitishvili[164], M.V. Chizhov[38], K. Choi[11], Y. Chou[139],

E.Y.S. Chow [114], K.L. Chu [170], M.C. Chu [64a], X. Chu [14a,14e], J. Chudoba [132], J.J. Chwastowski [87], D. Cieri [111], K.M. Ciesla [86a], V. Cindro [94], A. Ciocio [17a], F. Cirotto [72a,72b], Z.H. Citron [170], M. Citterio [71a], D.A. Ciubotaru [27b], A. Clark [56], P.J. Clark [52], C. Clarry [156], J.M. Clavijo Columbie [48], S.E. Clawson [48], C. Clement [47a,47b], J. Clercx [48], Y. Coadou [103], M. Cobal [69a,69c], A. Coccaro [57b], R.F. Coelho Barrue [131a], R. Coelho Lopes De Sa [104], S. Coelli [71a], B. Cole [41], J. Collot [60], P. Conde Muiño [131a,131g], M.P. Connell [33c], S.H. Connell [33c], E.I. Conroy [127], F. Conventi [72a,af], H.G. Cooke [20], A.M. Cooper-Sarkar [127], A. Cordeiro Oudot Choi [128], L.D. Corpe [40], M. Corradi [75a,75b], F. Corriveau [105,w], A. Cortes-Gonzalez [18], M.J. Costa [164], F. Costanza [4], D. Costanzo [140], B.M. Cote [120], G. Cowan [96], K. Cranmer [171], D. Cremonini [23b,23a], S. Crépé-Renaudin [60], F. Crescioli [128], M. Cristinziani [142], M. Cristoforetti [78a,78b], V. Croft [115], J.E. Crosby [122], G. Crosetti [43b,43a], A. Cueto [100], H. Cui [14a,14e], Z. Cui [7], W.R. Cunningham [59], F. Curcio [164], J.R. Curran [52], P. Czodrowski [36], M.M. Czurylo [36], M.J. Da Cunha Sargedas De Sousa [57b,57a], J.V. Da Fonseca Pinto [83b], C. Da Via [102], W. Dabrowski [86a], T. Dado [49], S. Dahbi [149], T. Dai [107], D. Dal Santo [19], C. Dallapiccola [104], M. Dam [42], G. D'amen [29], V. D'Amico [110], J. Damp [101], J.R. Dandoy [34], M. Danninger [143], V. Dao [36], G. Darbo [57b], S.J. Das [29,ag], F. Dattola [48], S. D'Auria [71a,71b], A. D'avanzo [72a,72b], C. David [33a], T. Davidek [134], B. Davis-Purcell [34], I. Dawson [95], H.A. Day-hall [133], K. De [8], R. De Asmundis [72a], N. De Biase [48], S. De Castro [23b,23a], N. De Groot [114], P. de Jong [115], H. De la Torre [116], A. De Maria [14c], A. De Salvo [75a], U. De Sanctis [76a,76b], F. De Santis [70a,70b], A. De Santo [147], J.B. De Vivie De Regie [60], D.V. Dedovich [38], J. Degens [93], A.M. Deiana [44], F. Del Corso [23b,23a], J. Del Peso [100], F. Del Rio [63a], L. Delagrange [128], F. Deliot [136], C.M. Delitzsch [49], M. Della Pietra [72a,72b], D. Della Volpe [56], A. Dell'Acqua [36], L. Dell'Asta [71a,71b], M. Delmastro [4], P.A. Delsart [60], S. Demers [173], M. Demichev [38], S.P. Denisov [37], L. D'Eramo [40], D. Derendarz [87], F. Derue [128], P. Dervan [93], K. Desch [24], C. Deutsch [24], F.A. Di Bello [57b,57a], A. Di Ciaccio [76a,76b], L. Di Ciaccio [4], A. Di Domenico [75a,75b], C. Di Donato [72a,72b], A. Di Girolamo [36], G. Di Gregorio [36], A. Di Luca [78a,78b], B. Di Micco [77a,77b], R. Di Nardo [77a,77b], M. Diamantopoulou [34], F.A. Dias [115], T. Dias Do Vale [143], M.A. Diaz [138a,138b], F.G. Diaz Capriles [24], M. Didenko [164], E.B. Diehl [107], S. Díez Cornell [48], C. Diez Pardos [142], C. Dimitriadi [162,24], A. Dimitrievska [17a], J. Dingfelder [24], I-M. Dinu [27b], S.J. Dittmeier [63b], F. Dittus [36], M. Divisek [134], F. Djama [103], T. Djobava [150b], C. Doglioni [102,99], A. Dohnalova [28a], J. Dolejsi [134], Z. Dolezal [134], K.M. Dona [39], M. Donadelli [83c], B. Dong [108], J. Donini [40], A. D'Onofrio [72a,72b], M. D'Onofrio [93], J. Dopke [135], A. Doria [72a], N. Dos Santos Fernandes [131a], P. Dougan [102], M.T. Dova [91], A.T. Doyle [59], M.A. Draguet [127], E. Dreyer [170], I. Drivas-koulouris [10], M. Drnevich [118], M. Drozdova [56], D. Du [62a], T.A. du Pree [115], F. Dubinin [37], M. Dubovsky [28a], E. Duchovni [170], G. Duckeck [110], O.A. Ducu [27b], D. Duda [52], A. Dudarev [36], E.R. Duden [26], M. D'uffizi [102], L. Duflot [66], M. Dührssen [36], I. Duminica [27g], A.E. Dumitriu [27b], M. Dunford [63a], S. Dungs [49], K. Dunne [47a,47b], A. Duperrin [103], H. Duran Yildiz [3a], M. Düren [58], A. Durglishvili [150b], B.L. Dwyer [116], G.I. Dyckes [17a], M. Dyndal [86a], B.S. Dziedzic [87], Z.O. Earnshaw [147], G.H. Eberwein [127], B. Eckerova [28a], S. Eggebrecht [55], E. Egidio Purcino De Souza [128], L.F. Ehrke [56], G. Eigen [16], K. Einsweiler [17a], T. Ekelof [162], P.A. Ekman [99], S. El Farkh [35b], Y. El Ghazali [35b], H. El Jarrari [36], A. El Moussaouy [109], V. Ellajosyula [162], M. Ellert [162], F. Ellinghaus [172], N. Ellis [36], J. Elmsheuser [29], M. Elsawy [117a], M. Elsing [36], D. Emeliyanov [135], Y. Enari [154], I. Ene [17a], S. Epari [13], P.A. Erland [87], M. Errenst [172], M. Escalier [66], C. Escobar [164], E. Etzion [152], G. Evans [131a], H. Evans [68], L.S. Evans [96], A. Ezhilov [37], S. Ezzarqtouni [35a], F. Fabbri [23b,23a], L. Fabbri [23b,23a], G. Facini [97], V. Fadeyev [137], R.M. Fakhrutdinov [37], D. Fakoudis [101],

S. Falciano[75a], L.F. Falda Ulhoa Coelho[36], P.J. Falke[24], J. Faltova[134], C. Fan[163], Y. Fan[14a], Y. Fang[14a,14e], M. Fanti[71a,71b], M. Faraj[69a,69b], Z. Farazpay[98], A. Farbin[8], A. Farilla[77a], T. Farooque[108], S.M. Farrington[52], F. Fassi[35e], D. Fassouliotis[9], M. Faucci Giannelli[76a,76b], W.J. Fawcett[32], L. Fayard[66], P. Federic[134], P. Federicova[132], O.L. Fedin[37,a], M. Feickert[171], L. Feligioni[103], D.E. Fellers[124], C. Feng[62b], M. Feng[14b], Z. Feng[115], M.J. Fenton[160], L. Ferencz[48], R.A.M. Ferguson[92], S.I. Fernandez Luengo[138f], P. Fernandez Martinez[13], M.J.V. Fernoux[103], J. Ferrando[92], A. Ferrari[162], P. Ferrari[115,114], R. Ferrari[73a], D. Ferrere[56], C. Ferretti[107], F. Fiedler[101], P. Fiedler[133], A. Filipčič[94], E.K. Filmer[1], F. Filthaut[114], M.C.N. Fiolhais[131a,131c,c], L. Fiorini[164], W.C. Fisher[108], T. Fitschen[102], P.M. Fitzhugh[136], I. Fleck[142], P. Fleischmann[107], T. Flick[172], M. Flores[33d,ab], L.R. Flores Castillo[64a], L. Flores Sanz De Acedo[36], F.M. Follega[78a,78b], N. Fomin[16], J.H. Foo[156], A. Formica[136], A.C. Forti[102], E. Fortin[36], A.W. Fortman[17a], M.G. Foti[17a], L. Fountas[9,j], D. Fournier[66], H. Fox[92], P. Francavilla[74a,74b], S. Francescato[61], S. Franchellucci[56], M. Franchini[23b,23a], S. Franchino[63a], D. Francis[36], L. Franco[114], V. Franco Lima[36], L. Franconi[48], M. Franklin[61], G. Frattari[26], W.S. Freund[83b], Y.Y. Frid[152], J. Friend[59], N. Fritzsche[50], A. Froch[54], D. Froidevaux[36], J.A. Frost[127], Y. Fu[62a], S. Fuenzalida Garrido[138f], M. Fujimoto[103], K.Y. Fung[64a], E. Furtado De Simas Filho[83e], M. Furukawa[154], J. Fuster[164], A. Gabrielli[23b,23a], A. Gabrielli[156], P. Gadow[36], G. Gagliardi[57b,57a], L.G. Gagnon[17a], S. Galantzan[152], E.J. Gallas[127], B.J. Gallop[135], K.K. Gan[120], S. Ganguly[154], Y. Gao[52], F.M. Garay Walls[138a,138b], B. Garcia[29], C. García[164], A. Garcia Alonso[115], A.G. Garcia Caffaro[173], J.E. García Navarro[164], M. Garcia-Sciveres[17a], G.L. Gardner[129], R.W. Gardner[39], N. Garelli[159], D. Garg[80], R.B. Garg[144,m], J.M. Gargan[52], C.A. Garner[156], C.M. Garvey[33a], P. Gaspar[83b], V.K. Gassmann[159], G. Gaudio[73a], V. Gautam[13], P. Gauzzi[75a,75b], I.L. Gavrilenko[37], A. Gavrilyuk[37], C. Gay[165], G. Gaycken[48], E.N. Gazis[10], A.A. Geanta[27b], C.M. Gee[137], A. Gekow[120], C. Gemme[57b], M.H. Genest[60], A.D. Gentry[113], S. George[96], W.F. George[20], T. Geralis[46], P. Gessinger-Befurt[36], M.E. Geyik[172], M. Ghani[168], K. Ghorbanian[95], A. Ghosal[142], A. Ghosh[160], A. Ghosh[7], B. Giacobbe[23b], S. Giagu[75a,75b], T. Giani[115], P. Giannetti[74a], A. Giannini[62a], S.M. Gibson[96], M. Gignac[137], D.T. Gil[86b], A.K. Gilbert[86a], B.J. Gilbert[41], D. Gillberg[34], G. Gilles[115], L. Ginabat[128], D.M. Gingrich[2,ae], M.P. Giordani[69a,69c], P.F. Giraud[136], G. Giugliarelli[69a,69c], D. Giugni[71a], F. Giuli[36], I. Gkialas[9,j], L.K. Gladilin[37], C. Glasman[100], G.R. Gledhill[124], G. Glemža[48], M. Glisic[124], I. Gnesi[43b,f], Y. Go[29], M. Goblirsch-Kolb[36], B. Gocke[49], D. Godin[109], B. Gokturk[21a], S. Goldfarb[106], T. Golling[56], M.G.D. Gololo[33g], D. Golubkov[37], J.P. Gombas[108], A. Gomes[131a,131b], G. Gomes Da Silva[142], A.J. Gomez Delegido[164], R. Gonçalo[131a,131c], L. Gonella[20], A. Gongadze[150c], F. Gonnella[20], J.L. Gonski[144], R.Y. González Andana[52], S. González de la Hoz[164], R. Gonzalez Lopez[93], C. Gonzalez Renteria[17a], M.V. Gonzalez Rodrigues[48], R. Gonzalez Suarez[162], S. Gonzalez-Sevilla[56], L. Goossens[36], B. Gorini[36], E. Gorini[70a,70b], A. Gorišek[94], T.C. Gosart[129], A.T. Goshaw[51], M.I. Gostkin[38], S. Goswami[122], C.A. Gottardo[36], S.A. Gotz[110], M. Gouighri[35b], V. Goumarre[48], A.G. Goussiou[139], N. Govender[33c], I. Grabowska-Bold[86a], K. Graham[34], E. Gramstad[126], S. Grancagnolo[70a,70b], C.M. Grant[1,136], P.M. Gravila[27f], F.G. Gravili[70a,70b], H.M. Gray[17a], M. Greco[70a,70b], C. Grefe[24], I.M. Gregor[48], K.T. Greif[160], P. Grenier[144], S.G. Grewe[111], A.A. Grillo[137], K. Grimm[31], S. Grinstein[13,s], J.-F. Grivaz[66], E. Gross[170], J. Grosse-Knetter[55], J.C. Grundy[127], L. Guan[107], C. Gubbels[165], J.G.R. Guerrero Rojas[164], G. Guerrieri[69a,69c], F. Guescini[111], R. Gugel[101], J.A.M. Guhit[107], A. Guida[18], E. Guilloton[168], S. Guindon[36], F. Guo[14a,14e], J. Guo[62c], L. Guo[48], Y. Guo[107], R. Gupta[48], R. Gupta[130], S. Gurbuz[24], S.S. Gurdasani[54],

G. Gustavino [36], M. Guth [56], P. Gutierrez [121], L.F. Gutierrez Zagazeta [129], M. Gutsche [50], C. Gutschow [97], C. Gwenlan [127], C.B. Gwilliam [93], E.S. Haaland [126], A. Haas [118], M. Habedank [48], C. Haber [17a], H.K. Hadavand [8], A. Hadef [50], S. Hadzic [111], A.I. Hagan [92], J.J. Hahn [142], E.H. Haines [97], M. Haleem [167], J. Haley [122], J.J. Hall [140], G.D. Hallewell [103], L. Halser [19], K. Hamano [166], M. Hamer [24], G.N. Hamity [52], E.J. Hampshire [96], J. Han [62b], K. Han [62a], L. Han [14c], L. Han [62a], S. Han [17a], Y.F. Han [156], K. Hanagaki [84], M. Hance [137], D.A. Hangal [41], H. Hanif [143], M.D. Hank [129], J.B. Hansen [42], P.H. Hansen [42], K. Hara [158], D. Harada [56], T. Harenberg [172], S. Harkusha [37], M.L. Harris [104], Y.T. Harris [127], J. Harrison [13], N.M. Harrison [120], P.F. Harrison[168], N.M. Hartman [111], N.M. Hartmann [110], Y. Hasegawa [141], S. Hassan [16], R. Hauser [108], C.M. Hawkes [20], R.J. Hawkings [36], Y. Hayashi [154], S. Hayashida [112], D. Hayden [108], C. Hayes [107], R.L. Hayes [115], C.P. Hays [127], J.M. Hays [95], H.S. Hayward [93], F. He [62a], M. He [14a,14e], Y. He [155], Y. He [48], Y. He [97], N.B. Heatley [95], V. Hedberg [99], A.L. Heggelund [126], N.D. Hehir [95,*], C. Heidegger [54], K.K. Heidegger [54], W.D. Heidorn [81], J. Heilman [34], S. Heim [48], T. Heim [17a], J.G. Heinlein [129], J.J. Heinrich [124], L. Heinrich [111,ac], J. Hejbal [132], A. Held [171], S. Hellesund [16], C.M. Helling [165], S. Hellman [47a,47b], R.C.W. Henderson[92], L. Henkelmann [32], A.M. Henriques Correia[36], H. Herde [99], Y. Hernández Jiménez [146], L.M. Herrmann [24], T. Herrmann [50], G. Herten [54], R. Hertenberger [110], L. Hervas [36], M.E. Hesping [101], N.P. Hessey [157a], E. Hill [156], S.J. Hillier [20], J.R. Hinds [108], F. Hinterkeuser [24], M. Hirose [125], S. Hirose [158], D. Hirschbuehl [172], T.G. Hitchings [102], B. Hiti [94], J. Hobbs [146], R. Hobincu [27e], N. Hod [170], M.C. Hodgkinson [140], B.H. Hodkinson [127], A. Hoecker [36], D.D. Hofer [107], J. Hofer [48], T. Holm [24], M. Holzbock [111], L.B.A.H. Hommels [32], B.P. Honan [102], J. Hong [62c], T.M. Hong [130], B.H. Hooberman [163], W.H. Hopkins [6], Y. Horii [112], S. Hou [149], A.S. Howard [94], J. Howarth [59], J. Hoya [6], M. Hrabovsky [123], A. Hrynevich [48], T. Hryn'ova [4], P.J. Hsu [65], S.-C. Hsu [139], M. Hu [17a], Q. Hu [62a], S. Huang [64b], X. Huang [14a,14e], Y. Huang [140], Y. Huang [14a], Z. Huang [102], Z. Hubacek [133], M. Huebner [24], F. Huegging [24], T.B. Huffman [127], C.A. Hugli [48], M. Huhtinen [36], S.K. Huiberts [16], R. Hulsken [105], N. Huseynov [12], J. Huston [108], J. Huth [61], R. Hyneman [144], G. Iacobucci [56], G. Iakovidis [29], I. Ibragimov [142], L. Iconomidou-Fayard [66], J.P. Iddon [36], P. Iengo [72a,72b], R. Iguchi [154], T. Iizawa [127], Y. Ikegami [84], N. Ilic [156], H. Imam [35a], M. Ince Lezki [56], T. Ingebretsen Carlson [47a,47b], G. Introzzi [73a,73b], M. Iodice [77a], V. Ippolito [75a,75b], R.K. Irwin [93], M. Ishino [154], W. Islam [171], C. Issever [18,48], S. Istin [21a,ai], H. Ito [169], R. Iuppa [78a,78b], A. Ivina [170], J.M. Izen [45], V. Izzo [72a], P. Jacka [132,133], P. Jackson [1], B.P. Jaeger [143], C.S. Jagfeld [110], G. Jain [157a], P. Jain [54], K. Jakobs [54], T. Jakoubek [170], J. Jamieson [59], K.W. Janas [86a], M. Javurkova [104], L. Jeanty [124], J. Jejelava [150a,z], P. Jenni [54,g], C.E. Jessiman [34], C. Jia[62b], J. Jia [146], X. Jia [61], X. Jia [14a,14e], Z. Jia [14c], S. Jiggins [48], J. Jimenez Pena [13], S. Jin [14c], A. Jinaru [27b], O. Jinnouchi [155], P. Johansson [140], K.A. Johns [7], J.W. Johnson [137], D.M. Jones [147], E. Jones [48], P. Jones [32], R.W.L. Jones [92], T.J. Jones [93], H.L. Joos [55,36], R. Joshi [120], J. Jovicevic [15], X. Ju [17a], J.J. Junggeburth [104], T. Junkermann [63a], A. Juste Rozas [13,s], M.K. Juzek [87], S. Kabana [138e], A. Kaczmarska [87], M. Kado [111], H. Kagan [120], M. Kagan [144], A. Kahn[41], A. Kahn [129], C. Kahra [101], T. Kaji [154], E. Kajomovitz [151], N. Kakati [170], I. Kalaitzidou [54], C.W. Kalderon [29], N.J. Kang [137], D. Kar [33g], K. Karava [127], M.J. Kareem [157b], E. Karentzos [54], I. Karkanias [153], O. Karkout [115], S.N. Karpov [38], Z.M. Karpova [38], V. Kartvelishvili [92], A.N. Karyukhin [37], E. Kasimi [153], J. Katzy [48], S. Kaur [34], K. Kawade [141], M.P. Kawale [121], C. Kawamoto [88], T. Kawamoto [62a], E.F. Kay [36], F.I. Kaya [159], S. Kazakos [108], V.F. Kazanin [37], Y. Ke [146], J.M. Keaveney [33a], R. Keeler [166], G.V. Kehris [61], J.S. Keller [34], A.S. Kelly[97], J.J. Kempster [147], P.D. Kennedy [101], O. Kepka [132], B.P. Kerridge [135], S. Kersten [172], B.P. Kerševan [94], L. Keszeghova [28a],

S. Ketabchi Haghighat[156], R.A. Khan[130], A. Khanov[122], A.G. Kharlamov[37], T. Kharlamova[37], E.E. Khoda[139], M. Kholodenko[37], T.J. Khoo[18], G. Khoriauli[167], J. Khubua[150b], Y.A.R. Khwaira[66], B. Kibirige[33g], A. Kilgallon[124], D.W. Kim[47a,47b], Y.K. Kim[39], N. Kimura[97], M.K. Kingston[55], A. Kirchhoff[55], C. Kirfel[24], F. Kirfel[24], J. Kirk[135], A.E. Kiryunin[111], C. Kitsaki[10], O. Kivernyk[24], M. Klassen[63a], C. Klein[34], L. Klein[167], M.H. Klein[44], S.B. Klein[56], U. Klein[93], P. Klimek[36], A. Klimentov[29], T. Klioutchnikova[36], P. Kluit[115], S. Kluth[111], E. Kneringer[79], T.M. Knight[156], A. Knue[49], R. Kobayashi[88], D. Kobylianskii[170], S.F. Koch[127], M. Kocian[144], P. Kodyš[134], D.M. Koeck[124], P.T. Koenig[24], T. Koffas[34], O. Kolay[50], I. Koletsou[4], T. Komarek[123], K. Köneke[54], A.X.Y. Kong[1], T. Kono[119], N. Konstantinidis[97], P. Kontaxakis[56], B. Konya[99], R. Kopeliansky[41], S. Koperny[86a], K. Korcyl[87], K. Kordas[153,e], A. Korn[97], S. Korn[55], I. Korolkov[13], N. Korotkova[37], B. Kortman[115], O. Kortner[111], S. Kortner[111], W.H. Kostecka[116], V.V. Kostyukhin[142], A. Kotsokechagia[136], A. Kotwal[51], A. Koulouris[36], A. Kourkoumeli-Charalampidi[73a,73b], C. Kourkoumelis[9], E. Kourlitis[111,ac], O. Kovanda[124], R. Kowalewski[166], W. Kozanecki[136], A.S. Kozhin[37], V.A. Kramarenko[37], G. Kramberger[94], P. Kramer[101], M.W. Krasny[128], A. Krasznahorkay[36], J.W. Kraus[172], J.A. Kremer[48], T. Kresse[50], J. Kretzschmar[93], K. Kreul[18], P. Krieger[156], S. Krishnamurthy[104], M. Krivos[134], K. Krizka[20], K. Kroeninger[49], H. Kroha[111], J. Kroll[132], J. Kroll[129], K.S. Krowpman[108], U. Kruchonak[38], H. Krüger[24], N. Krumnack[81], M.C. Kruse[51], O. Kuchinskaia[37], S. Kuday[3a], S. Kuehn[36], R. Kuesters[54], T. Kuhl[48], V. Kukhtin[38], Y. Kulchitsky[37,a], S. Kuleshov[138d,138b], M. Kumar[33g], N. Kumari[48], P. Kumari[157b], A. Kupco[132], T. Kupfer[49], A. Kupich[37], O. Kuprash[54], H. Kurashige[85], L.L. Kurchaninov[157a], O. Kurdysh[66], Y.A. Kurochkin[37], A. Kurova[37], M. Kuze[155], A.K. Kvam[104], J. Kvita[123], T. Kwan[105], N.G. Kyriacou[107], L.A.O. Laatu[103], C. Lacasta[164], F. Lacava[75a,75b], H. Lacker[18], D. Lacour[128], N.N. Lad[97], E. Ladygin[38], A. Lafarge[40], B. Laforge[128], T. Lagouri[173], F.Z. Lahbabi[35a], S. Lai[55], I.K. Lakomiec[86a], N. Lalloue[60], J.E. Lambert[166], S. Lammers[68], W. Lampl[7], C. Lampoudis[153,e], G. Lamprinoudis[101], A.N. Lancaster[116], E. Lançon[29], U. Landgraf[54], M.P.J. Landon[95], V.S. Lang[54], O.K.B. Langrekken[126], A.J. Lankford[160], F. Lanni[36], K. Lantzsch[24], A. Lanza[73a], A. Lapertosa[57b,57a], J.F. Laporte[136], T. Lari[71a], F. Lasagni Manghi[23b], M. Lassnig[36], V. Latonova[132], A. Laudrain[101], A. Laurier[151], S.D. Lawlor[140], Z. Lawrence[102], R. Lazaridou[168], M. Lazzaroni[71a,71b], B. Le[102], E.M. Le Boulicaut[51], L.T. Le Pottier[17a], B. Leban[23b,23a], A. Lebedev[81], M. LeBlanc[102], F. Ledroit-Guillon[60], A.C.A. Lee[97], S.C. Lee[149], S. Lee[47a,47b], T.F. Lee[93], L.L. Leeuw[33c], H.P. Lefebvre[96], M. Lefebvre[166], C. Leggett[17a], G. Lehmann Miotto[36], M. Leigh[56], W.A. Leight[104], W. Leinonen[114], A. Leisos[153,r], M.A.L. Leite[83c], C.E. Leitgeb[18], R. Leitner[134], K.J.C. Leney[44], T. Lenz[24], S. Leone[74a], C. Leonidopoulos[52], A. Leopold[145], C. Leroy[109], R. Les[108], C.G. Lester[32], M. Levchenko[37], J. Levêque[4], L.J. Levinson[170], G. Levrini[23b,23a], M.P. Lewicki[87], D.J. Lewis[4], A. Li[5], B. Li[62b], C. Li[62a], C-Q. Li[111], H. Li[62a], H. Li[62b], H. Li[14c], H. Li[14b], H. Li[62b], J. Li[62c], K. Li[139], L. Li[62c], M. Li[14a,14e], Q.Y. Li[62a], S. Li[14a,14e], S. Li[62d,62c,d], T. Li[5], X. Li[105], Z. Li[127], Z. Li[105], Z. Li[14a,14e], S. Liang[14a,14e], Z. Liang[14a], M. Liberatore[136], B. Liberti[76a], K. Lie[64c], J. Lieber Marin[83b], H. Lien[68], K. Lin[108], R.E. Lindley[7], J.H. Lindon[2], E. Lipeles[129], A. Lipniacka[16], A. Lister[165], J.D. Little[4], B. Liu[14a], B.X. Liu[143], D. Liu[62d,62c], E.H.L. Liu[20], J.B. Liu[62a], J.K.K. Liu[32], K. Liu[62d], K. Liu[62d,62c], M. Liu[62a], M.Y. Liu[62a], P. Liu[14a], Q. Liu[62d,139,62c], X. Liu[62a], X. Liu[62b], Y. Liu[14d,14e], Y.L. Liu[62b], Y.W. Liu[62a], J. Llorente Merino[143], S.L. Lloyd[95], E.M. Lobodzinska[48], P. Loch[7], T. Lohse[18], K. Lohwasser[140], E. Loiacono[48],

M. Lokajicek[132,*], J.D. Lomas[20], J.D. Long[163], I. Longarini[160], L. Longo[70a,70b], R. Longo[163], I. Lopez Paz[67], A. Lopez Solis[48], N. Lorenzo Martinez[4], A.M. Lory[110], G. Löschcke Centeno[147], O. Loseva[37], X. Lou[47a,47b], X. Lou[14a,14e], A. Lounis[66], P.A. Love[92], G. Lu[14a,14e], M. Lu[66], S. Lu[129], Y.J. Lu[65], H.J. Lubatti[139], C. Luci[75a,75b], F.L. Lucio Alves[14c], F. Luehring[68], I. Luise[146], O. Lukianchuk[66], O. Lundberg[145], B. Lund-Jensen[145], N.A. Luongo[6], M.S. Lutz[36], A.B. Lux[25], D. Lynn[29], R. Lysak[132], E. Lytken[99], V. Lyubushkin[38], T. Lyubushkina[38], M.M. Lyukova[146], H. Ma[29], K. Ma[62a], L.L. Ma[62b], W. Ma[62a], Y. Ma[122], D.M. Mac Donell[166], G. Maccarrone[53], J.C. MacDonald[101], P.C. Machado De Abreu Farias[83e], R. Madar[40], T. Madula[97], J. Maeda[85], T. Maeno[29], H. Maguire[140], V. Maiboroda[136], A. Maio[131a,131b,131d], K. Maj[86a], O. Majersky[48], S. Majewski[124], N. Makovec[66], V. Maksimovic[15], B. Malaescu[128], Pa. Malecki[87], V.P. Maleev[37], F. Malek[60,n], M. Mali[94], D. Malito[96], U. Mallik[80], S. Maltezos[10], S. Malyukov[38], J. Mamuzic[13], G. Mancini[53], M.N. Mancini[26], G. Manco[73a,73b], J.P. Mandalia[95], I. Mandić[94], L. Manhaes de Andrade Filho[83a], I.M. Maniatis[170], J. Manjarres Ramos[90], D.C. Mankad[170], A. Mann[110], S. Manzoni[36], L. Mao[62c], X. Mapekula[33c], A. Marantis[153,r], G. Marchiori[5], M. Marcisovsky[132], C. Marcon[71a], M. Marinescu[20], S. Marium[48], M. Marjanovic[121], M. Markovitch[66], E.J. Marshall[92], Z. Marshall[17a], S. Marti-Garcia[164], T.A. Martin[168], V.J. Martin[52], B. Martin dit Latour[16], L. Martinelli[75a,75b], M. Martinez[13,s], P. Martinez Agullo[164], V.I. Martinez Outschoorn[104], P. Martinez Suarez[13], S. Martin-Haugh[135], G. Martinovicova[134], V.S. Martoiu[27b], A.C. Martyniuk[97], A. Marzin[36], D. Mascione[78a,78b], L. Masetti[101], T. Mashimo[154], J. Masik[102], A.L. Maslennikov[37], P. Massarotti[72a,72b], P. Mastrandrea[74a,74b], A. Mastroberardino[43b,43a], T. Masubuchi[154], T. Mathisen[162], J. Matousek[134], N. Matsuzawa[154], J. Maurer[27b], A.J. Maury[66], B. Maček[94], D.A. Maximov[37], R. Mazini[149], I. Maznas[116], M. Mazza[108], S.M. Mazza[137], E. Mazzeo[71a,71b], C. Mc Ginn[29], J.P. Mc Gowan[166], S.P. Mc Kee[107], C.C. McCracken[165], E.F. McDonald[106], A.E. McDougall[115], J.A. Mcfayden[147], R.P. McGovern[129], G. Mchedlidze[150b], R.P. Mckenzie[33g], T.C. Mclachlan[48], D.J. Mclaughlin[97], S.J. McMahon[135], C.M. Mcpartland[93], R.A. McPherson[166,w], S. Mehlhase[110], A. Mehta[93], D. Melini[164], B.R. Mellado Garcia[33g], A.H. Melo[55], F. Meloni[48], A.M. Mendes Jacques Da Costa[102], H.Y. Meng[156], L. Meng[92], S. Menke[111], M. Mentink[36], E. Meoni[43b,43a], G. Mercado[116], C. Merlassino[69a,69c], L. Merola[72a,72b], C. Meroni[71a,71b], J. Metcalfe[6], A.S. Mete[6], C. Meyer[68], J-P. Meyer[136], R.P. Middleton[135], L. Mijović[52], G. Mikenberg[170], M. Mikestikova[132], M. Mikuž[94], H. Mildner[101], A. Milic[36], D.W. Miller[39], E.H. Miller[144], L.S. Miller[34], A. Milov[170], D.A. Milstead[47a,47b], T. Min[14c], A.A. Minaenko[37], I.A. Minashvili[150b], L. Mince[59], A.I. Mincer[118], B. Mindur[86a], M. Mineev[38], Y. Mino[88], L.M. Mir[13], M. Miralles Lopez[59], M. Mironova[17a], A. Mishima[154], M.C. Missio[114], A. Mitra[168], V.A. Mitsou[164], Y. Mitsumori[112], O. Miu[156], P.S. Miyagawa[95], T. Mkrtchyan[63a], M. Mlinarevic[97], T. Mlinarevic[97], M. Mlynarikova[36], S. Mobius[19], P. Mogg[110], M.H. Mohamed Farook[113], A.F. Mohammed[14a,14e], S. Mohapatra[41], G. Mokgatitswane[33g], L. Moleri[170], B. Mondal[142], S. Mondal[133], K. Mönig[48], E. Monnier[103], L. Monsonis Romero[164], J. Montejo Berlingen[13], M. Montella[120], F. Montereali[77a,77b], F. Monticelli[91], S. Monzani[69a,69c], N. Morange[66], A.L. Moreira De Carvalho[131a], M. Moreno Llácer[164], C. Moreno Martinez[56], P. Morettini[57b], S. Morgenstern[36], M. Morii[61], M. Morinaga[154], F. Morodei[75a,75b], L. Morvaj[36], P. Moschovakos[36], B. Moser[36], M. Mosidze[150b], T. Moskalets[54], P. Moskvitina[114], J. Moss[31,k], A. Moussa[35d], E.J.W. Moyse[104], O. Mtintsilana[33g], S. Muanza[103], J. Mueller[130], D. Muenstermann[92], R. Müller[19], G.A. Mullier[162], A.J. Mullin[32], J.J. Mullin[129],

D.P. Mungo [156], D. Munoz Perez [164], F.J. Munoz Sanchez [102], M. Murin [102], W.J. Murray [168,135], M. Muškinja [94], C. Mwewa [29], A.G. Myagkov [37,a], A.J. Myers [8], G. Myers [107], M. Myska [133], B.P. Nachman [17a], O. Nackenhorst [49], K. Nagai [127], K. Nagano [84], J.L. Nagle [29,ag], E. Nagy [103], A.M. Nairz [36], Y. Nakahama [84], K. Nakamura [84], K. Nakkalil [5], H. Nanjo [125], R. Narayan [44], E.A. Narayanan [113], I. Naryshkin [37], M. Naseri [34], S. Nasri [117b], C. Nass [24], G. Navarro [22a], J. Navarro-Gonzalez [164], R. Nayak [152], A. Nayaz [18], P.Y. Nechaeva [37], F. Nechansky [48], L. Nedic [127], T.J. Neep [20], A. Negri [73a,73b], M. Negrini [23b], C. Nellist [115], C. Nelson [105], K. Nelson [107], S. Nemecek [132], M. Nessi [36,h], M.S. Neubauer [163], F. Neuhaus [101], J. Neundorf [48], R. Newhouse [165], P.R. Newman [20], C.W. Ng [130], Y.W.Y. Ng [48], B. Ngair [117a], H.D.N. Nguyen [109], R.B. Nickerson [127], R. Nicolaidou [136], J. Nielsen [137], M. Niemeyer [55], J. Niermann [55], N. Nikiforou [36], V. Nikolaenko [37,a], I. Nikolic-Audit [128], K. Nikolopoulos [20], P. Nilsson [29], I. Ninca [48], H.R. Nindhito [56], G. Ninio [152], A. Nisati [75a], N. Nishu [2], R. Nisius [111], J-E. Nitschke [50], E.K. Nkadimeng [33g], T. Nobe [154], D.L. Noel [32], T. Nommensen [148], M.B. Norfolk [140], R.R.B. Norisam [97], B.J. Norman [34], M. Noury [35a], J. Novak [94], T. Novak [48], L. Novotny [133], R. Novotny [113], L. Nozka [123], K. Ntekas [160], N.M.J. Nunes De Moura Junior [83b], J. Ocariz [128], A. Ochi [85], I. Ochoa [131a], S. Oerdek [48,t], J.T. Offermann [39], A. Ogrodnik [134], A. Oh [102], C.C. Ohm [145], H. Oide [84], R. Oishi [154], M.L. Ojeda [48], Y. Okumura [154], L.F. Oleiro Seabra [131a], S.A. Olivares Pino [138d], G. Oliveira Correa [13], D. Oliveira Damazio [29], D. Oliveira Goncalves [83a], J.L. Oliver [160], Ö.O. Öncel [54], A.P. O'Neill [19], A. Onofre [131a,131e], P.U.E. Onyisi [11], M.J. Oreglia [39], G.E. Orellana [91], D. Orestano [77a,77b], N. Orlando [13], R.S. Orr [156], V. O'Shea [59], L.M. Osojnak [129], R. Ospanov [62a], G. Otero y Garzon [30], H. Otono [89], P.S. Ott [63a], G.J. Ottino [17a], M. Ouchrif [35d], F. Ould-Saada [126], T. Ovsiannikova [139], M. Owen [59], R.E. Owen [135], K.Y. Oyulmaz [21a], V.E. Ozcan [21a], F. Ozturk [87], N. Ozturk [8], S. Ozturk [82], H.A. Pacey [127], A. Pacheco Pages [13], C. Padilla Aranda [13], G. Padovano [75a,75b], S. Pagan Griso [17a], G. Palacino [68], A. Palazzo [70a,70b], J. Pampel [24], J. Pan [173], T. Pan [64a], D.K. Panchal [11], C.E. Pandini [115], J.G. Panduro Vazquez [96], H.D. Pandya [1], H. Pang [14b], P. Pani [48], G. Panizzo [69a,69c], L. Panwar [128], L. Paolozzi [56], S. Parajuli [163], A. Paramonov [6], C. Paraskevopoulos [53], D. Paredes Hernandez [64b], A. Pareti [73a,73b], K.R. Park [41], T.H. Park [156], M.A. Parker [32], F. Parodi [57b,57a], E.W. Parrish [116], V.A. Parrish [52], J.A. Parsons [41], U. Parzefall [54], B. Pascual Dias [109], L. Pascual Dominguez [152], E. Pasqualucci [75a], S. Passaggio [57b], F. Pastore [96], P. Patel [87], U.M. Patel [51], J.R. Pater [102], T. Pauly [36], C.I. Pazos [159], J. Pearkes [144], M. Pedersen [126], R. Pedro [131a], S.V. Peleganchuk [37], O. Penc [36], E.A. Pender [52], G.D. Penn [173], K.E. Penski [110], M. Penzin [37], B.S. Peralva [83d], A.P. Pereira Peixoto [139], L. Pereira Sanchez [144], D.V. Perepelitsa [29,ag], E. Perez Codina [157a], M. Perganti [10], H. Pernegger [36], O. Perrin [40], K. Peters [48], R.F.Y. Peters [102], B.A. Petersen [36], T.C. Petersen [42], E. Petit [103], V. Petousis [133], C. Petridou [153,e], T. Petru [134], A. Petrukhin [142], M. Pettee [17a], N.E. Pettersson [36], A. Petukhov [37], K. Petukhova [134], R. Pezoa [138f], L. Pezzotti [36], G. Pezzullo [173], T.M. Pham [171], T. Pham [106], P.W. Phillips [135], G. Piacquadio [146], E. Pianori [17a], F. Piazza [124], R. Piegaia [30], D. Pietreanu [27b], A.D. Pilkington [102], M. Pinamonti [69a,69c], J.L. Pinfold [2], B.C. Pinheiro Pereira [131a], A.E. Pinto Pinoargote [101,136], L. Pintucci [69a,69c], K.M. Piper [147], A. Pirttikoski [56], D.A. Pizzi [34], L. Pizzimento [64b], A. Pizzini [115], M.-A. Pleier [29], V. Plesanovs [54], V. Pleskot [134], E. Plotnikova [38], G. Poddar [95], R. Poettgen [99], L. Poggioli [128], I. Pokharel [55], S. Polacek [134], G. Polesello [73a], A. Poley [143,157a], A. Polini [23b], C.S. Pollard [168], Z.B. Pollock [120], E. Pompa Pacchi [75a,75b], D. Ponomarenko [114], L. Pontecorvo [36], S. Popa [27a], G.A. Popeneciu [27d], A. Poreba [36], D.M. Portillo Quintero [157a], S. Pospisil [133], M.A. Postill [140], P. Postolache [27c], K. Potamianos [168], P.A. Potepa [86a],

I.N. Potrap[38], C.J. Potter[32], H. Potti[1], J. Poveda[164], M.E. Pozo Astigarraga[36], A. Prades Ibanez[164], J. Pretel[54], D. Price[102], M. Primavera[70a], M.A. Principe Martin[100], R. Privara[123], T. Procter[59], M.L. Proffitt[139], N. Proklova[129], K. Prokofiev[64c], G. Proto[111], J. Proudfoot[6], M. Przybycien[86a], W.W. Przygoda[86b], A. Psallidas[46], J.E. Puddefoot[140], D. Pudzha[37], D. Pyatiizbyantseva[37], J. Qian[107], D. Qichen[102], Y. Qin[13], T. Qiu[52], A. Quadt[55], M. Queitsch-Maitland[102], G. Quetant[56], R.P. Quinn[165], G. Rabanal Bolanos[61], D. Rafanoharana[54], F. Ragusa[71a,71b], J.L. Rainbolt[39], J.A. Raine[56], S. Rajagopalan[29], E. Ramakoti[37], I.A. Ramirez-Berend[34], K. Ran[48,14e], N.P. Rapheeha[33g], H. Rasheed[27b], V. Raskina[128], D.F. Rassloff[63a], A. Rastogi[17a], S. Rave[101], B. Ravina[55], I. Ravinovich[170], M. Raymond[36], A.L. Read[126], N.P. Readioff[140], D.M. Rebuzzi[73a,73b], G. Redlinger[29], A.S. Reed[111], K. Reeves[26], J.A. Reidelsturz[172], D. Reikher[152], A. Rej[49], C. Rembser[36], M. Renda[27b], M.B. Rendel[111], F. Renner[48], A.G. Rennie[160], A.L. Rescia[48], S. Resconi[71a], M. Ressegotti[57b,57a], S. Rettie[36], J.G. Reyes Rivera[108], E. Reynolds[17a], O.L. Rezanova[37], P. Reznicek[134], H. Riani[35d], N. Ribaric[92], E. Ricci[78a,78b], R. Richter[111], S. Richter[47a,47b], E. Richter-Was[86b], M. Ridel[128], S. Ridouani[35d], P. Rieck[118], P. Riedler[36], E.M. Riefel[47a,47b], J.O. Rieger[115], M. Rijssenbeek[146], M. Rimoldi[36], L. Rinaldi[23b,23a], T.T. Rinn[29], M.P. Rinnagel[110], G. Ripellino[162], I. Riu[13], J.C. Rivera Vergara[166], F. Rizatdinova[122], E. Rizvi[95], B.R. Roberts[17a], S.H. Robertson[105,w], D. Robinson[32], C.M. Robles Gajardo[138f], M. Robles Manzano[101], A. Robson[59], A. Rocchi[76a,76b], C. Roda[74a,74b], S. Rodriguez Bosca[36], Y. Rodriguez Garcia[22a], A. Rodriguez Rodriguez[54], A.M. Rodríguez Vera[116], S. Roe[36], J.T. Roemer[160], A.R. Roepe-Gier[137], J. Roggel[172], O. Røhne[126], R.A. Rojas[104], C.P.A. Roland[128], J. Roloff[29], A. Romaniouk[37], E. Romano[73a,73b], M. Romano[23b], A.C. Romero Hernandez[163], N. Rompotis[93], L. Roos[128], S. Rosati[75a], B.J. Rosser[39], E. Rossi[127], E. Rossi[72a,72b], L.P. Rossi[61], L. Rossini[54], R. Rosten[120], M. Rotaru[27b], B. Rottler[54], C. Rougier[90], D. Rousseau[66], D. Rousso[32], A. Roy[163], S. Roy-Garand[156], A. Rozanov[103], Z.M.A. Rozario[59], Y. Rozen[151], A. Rubio Jimenez[164], A.J. Ruby[93], V.H. Ruelas Rivera[18], T.A. Ruggeri[1], A. Ruggiero[127], A. Ruiz-Martinez[164], A. Rummler[36], Z. Rurikova[54], N.A. Rusakovich[38], H.L. Russell[166], G. Russo[75a,75b], J.P. Rutherfoord[7], S. Rutherford Colmenares[32], K. Rybacki[92], M. Rybar[134], E.B. Rye[126], A. Ryzhov[44], J.A. Sabater Iglesias[56], P. Sabatini[164], H.F-W. Sadrozinski[137], F. Safai Tehrani[75a], B. Safarzadeh Samani[135], S. Saha[1], M. Sahinsoy[111], A. Saibel[164], M. Saimpert[136], M. Saito[154], T. Saito[154], A. Sala[71a,71b], D. Salamani[36], A. Salnikov[144], J. Salt[164], A. Salvador Salas[152], D. Salvatore[43b,43a], F. Salvatore[147], A. Salzburger[36], D. Sammel[54], E. Sampson[92], D. Sampsonidis[153,e], D. Sampsonidou[124], J. Sánchez[164], V. Sanchez Sebastian[164], H. Sandaker[126], C.O. Sander[48], J.A. Sandesara[104], M. Sandhoff[172], C. Sandoval[22b], D.P.C. Sankey[135], T. Sano[88], A. Sansoni[53], L. Santi[75a,75b], C. Santoni[40], H. Santos[131a,131b], A. Santra[170], K.A. Saoucha[161], J.G. Saraiva[131a,131d], J. Sardain[7], O. Sasaki[84], K. Sato[158], C. Sauer[63b], F. Sauerburger[54], E. Sauvan[4], P. Savard[156,ae], R. Sawada[154], C. Sawyer[135], L. Sawyer[98], I. Sayago Galvan[164], C. Sbarra[23b], A. Sbrizzi[23b,23a], T. Scanlon[97], J. Schaarschmidt[139], U. Schäfer[101], A.C. Schaffer[66,44], D. Schaile[110], R.D. Schamberger[146], C. Scharf[18], M.M. Schefer[19], V.A. Schegelsky[37], D. Scheirich[134], F. Schenck[18], M. Schernau[160], C. Scheulen[55], C. Schiavi[57b,57a], M. Schioppa[43b,43a], B. Schlag[144,m], K.E. Schleicher[54], S. Schlenker[36], J. Schmeing[172], M.A. Schmidt[172], K. Schmieden[101], C. Schmitt[101], N. Schmitt[101], S. Schmitt[48], L. Schoeffel[136], A. Schoening[63b], P.G. Scholer[34], E. Schopf[127], M. Schott[101], J. Schovancova[36], S. Schramm[56], T. Schroer[56], H-C. Schultz-Coulon[63a], M. Schumacher[54], B.A. Schumm[137], Ph. Schune[136], A.J. Schuy[139], H.R. Schwartz[137], A. Schwartzman[144], T.A. Schwarz[107],

Ph. Schwemling [136], R. Schwienhorst [108], A. Sciandra [137], G. Sciolla [26], F. Scuri [74a], C.D. Sebastiani [93], K. Sedlaczek [116], P. Seema [18], S.C. Seidel [113], A. Seiden [137], B.D. Seidlitz [41], C. Seitz [48], J.M. Seixas [83b], G. Sekhniaidze [72a], L. Selem [60], N. Semprini-Cesari [23b,23a], D. Sengupta [56], V. Senthilkumar [164], L. Serin [66], L. Serkin [69a,69b], M. Sessa [76a,76b], H. Severini [121], F. Sforza [57b,57a], A. Sfyrla [56], Q. Sha [14a], E. Shabalina [55], A.H. Shah [32], R. Shaheen [145], J.D. Shahinian [129], D. Shaked Renous [170], L.Y. Shan [14a], M. Shapiro [17a], A. Sharma [36], A.S. Sharma [165], P. Sharma [80], P.B. Shatalov [37], K. Shaw [147], S.M. Shaw [102], A. Shcherbakova [37], Q. Shen [62c,5], D.J. Sheppard [143], P. Sherwood [97], L. Shi [97], X. Shi [14a], C.O. Shimmin [173], J.D. Shinner [96], I.P.J. Shipsey [127], S. Shirabe [89], M. Shiyakova [38,u], J. Shlomi [170], M.J. Shochet [39], J. Shojaii [106], D.R. Shope [126], B. Shrestha [121], S. Shrestha [120,ah], E.M. Shrif [33g], M.J. Shroff [166], P. Sicho [132], A.M. Sickles [163], E. Sideras Haddad [33g], A. Sidoti [23b], F. Siegert [50], Dj. Sijacki [15], F. Sili [91], J.M. Silva [52], M.V. Silva Oliveira [29], S.B. Silverstein [47a], S. Simion [66], R. Simoniello [36], E.L. Simpson [59], H. Simpson [147], L.R. Simpson [107], N.D. Simpson [99], S. Simsek [82], S. Sindhu [55], P. Sinervo [156], S. Singh [156], S. Sinha [48], S. Sinha [102], M. Sioli [23b,23a], I. Siral [36], E. Sitnikova [48], J. Sjölin [47a,47b], A. Skaf [55], E. Skorda [20], P. Skubic [121], M. Slawinska [87], V. Smakhtin [170], B.H. Smart [135], S.Yu. Smirnov [37], Y. Smirnov [37], L.N. Smirnova [37,a], O. Smirnova [99], A.C. Smith [41], E.A. Smith [39], H.A. Smith [127], J.L. Smith [102], R. Smith [144], M. Smizanska [92], K. Smolek [133], A.A. Snesarev [37], S.R. Snider [156], H.L. Snoek [115], S. Snyder [29], R. Sobie [166,w], A. Soffer [152], C.A. Solans Sanchez [36], E.Yu. Soldatov [37], U. Soldevila [164], A.A. Solodkov [37], S. Solomon [26], A. Soloshenko [38], K. Solovieva [54], O.V. Solovyanov [40], V. Solovyev [37], P. Sommer [36], A. Sonay [13], W.Y. Song [157b], A. Sopczak [133], A.L. Sopio [97], F. Sopkova [28b], J.D. Sorenson [113], I.R. Sotarriva Alvarez [155], V. Sothilingam [63a], O.J. Soto Sandoval [138c,138b], S. Sottocornola [68], R. Soualah [161], Z. Soumaimi [35e], D. South [48], N. Soybelman [170], S. Spagnolo [70a,70b], M. Spalla [111], D. Sperlich [54], G. Spigo [36], S. Spinali [92], D.P. Spiteri [59], M. Spousta [134], E.J. Staats [34], R. Stamen [63a], A. Stampekis [20], M. Standke [24], E. Stanecka [87], W. Stanek-Maslouska [48], M.V. Stange [50], B. Stanislaus [17a], M.M. Stanitzki [48], B. Stapf [48], E.A. Starchenko [37], G.H. Stark [137], J. Stark [90], P. Staroba [132], P. Starovoitov [63a], S. Stärz [105], R. Staszewski [87], G. Stavropoulos [46], J. Steentoft [162], P. Steinberg [29], B. Stelzer [143,157a], H.J. Stelzer [130], O. Stelzer-Chilton [157a], H. Stenzel [58], T.J. Stevenson [147], G.A. Stewart [36], J.R. Stewart [122], M.C. Stockton [36], G. Stoicea [27b], M. Stolarski [131a], S. Stonjek [111], A. Straessner [50], J. Strandberg [145], S. Strandberg [47a,47b], M. Stratmann [172], M. Strauss [121], T. Strebler [103], P. Strizenec [28b], R. Ströhmer [167], D.M. Strom [124], R. Stroynowski [44], A. Strubig [47a,47b], S.A. Stucci [29], B. Stugu [16], J. Stupak [121], N.A. Styles [48], D. Su [144], S. Su [62a], W. Su [62d], X. Su [62a], D. Suchy [28a], K. Sugizaki [154], V.V. Sulin [37], M.J. Sullivan [93], D.M.S. Sultan [127], L. Sultanaliyeva [37], S. Sultansoy [3b], T. Sumida [88], S. Sun [107], S. Sun [171], O. Sunneborn Gudnadottir [162], N. Sur [103], M.R. Sutton [147], H. Suzuki [158], M. Svatos [132], M. Swiatlowski [157a], T. Swirski [167], I. Sykora [28a], M. Sykora [134], T. Sykora [134], D. Ta [101], K. Tackmann [48,t], A. Taffard [160], R. Tafirout [157a], J.S. Tafoya Vargas [66], Y. Takubo [84], M. Talby [103], A.A. Talyshev [37], K.C. Tam [64b], N.M. Tamir [152], A. Tanaka [154], J. Tanaka [154], R. Tanaka [66], M. Tanasini [57b,57a], Z. Tao [165], S. Tapia Araya [138f], S. Tapprogge [101], A. Tarek Abouelfadl Mohamed [108], S. Tarem [151], K. Tariq [14a], G. Tarna [103,27b], G.F. Tartarelli [71a], P. Tas [134], M. Tasevsky [132], E. Tassi [43b,43a], A.C. Tate [163], G. Tateno [154], Y. Tayalati [35e,v], G.N. Taylor [106], W. Taylor [157b], A.S. Tee [171], R. Teixeira De Lima [144], P. Teixeira-Dias [96], J.J. Teoh [156], K. Terashi [154], J. Terron [100], S. Terzo [13], M. Testa [53], R.J. Teuscher [156,w], A. Thaler [79], O. Theiner [56], N. Themistokleous [52], T. Theveneaux-Pelzer [103], O. Thielmann [172], D.W. Thomas [96], J.P. Thomas [20], E.A. Thompson [17a], P.D. Thompson [20], E. Thomson [129],

R.E. Thornberry[44], Y. Tian[55], V. Tikhomirov[37,a], Yu.A. Tikhonov[37], S. Timoshenko[37], D. Timoshyn[134], E.X.L. Ting[1], P. Tipton[173], S.H. Tlou[33g], K. Todome[155], S. Todorova-Nova[134], S. Todt[50], M. Togawa[84], J. Tojo[89], S. Tokár[28a], K. Tokushuku[84], O. Toldaiev[68], R. Tombs[32], M. Tomoto[84,112], L. Tompkins[144,m], K.W. Topolnicki[86b], E. Torrence[124], H. Torres[90], E. Torró Pastor[164], M. Toscani[30], C. Tosciri[39], M. Tost[11], D.R. Tovey[140], A. Traeet[16], I.S. Trandafir[27b], T. Trefzger[167], A. Tricoli[29], I.M. Trigger[157a], S. Trincaz-Duvoid[128], D.A. Trischuk[26], B. Trocmé[60], L. Truong[33c], M. Trzebinski[87], A. Trzupek[87], F. Tsai[146], M. Tsai[107], A. Tsiamis[153,e], P.V. Tsiareshka[37], S. Tsigaridas[157a], A. Tsirigotis[153,r], V. Tsiskaridze[156], E.G. Tskhadadze[150a], M. Tsopoulou[153], Y. Tsujikawa[88], I.I. Tsukerman[37], V. Tsulaia[17a], S. Tsuno[84], K. Tsuri[119], D. Tsybychev[146], Y. Tu[64b], A. Tudorache[27b], V. Tudorache[27b], A.N. Tuna[61], S. Turchikhin[57b,57a], I. Turk Cakir[3a], R. Turra[71a], T. Turtuvshin[38,x], P.M. Tuts[41], S. Tzamarias[153,e], E. Tzovara[101], F. Ukegawa[158], P.A. Ulloa Poblete[138c,138b], E.N. Umaka[29], G. Unal[36], A. Undrus[29], G. Unel[160], J. Urban[28b], P. Urquijo[106], P. Urrejola[138a], G. Usai[8], R. Ushioda[155], M. Usman[109], Z. Uysal[82], V. Vacek[133], B. Vachon[105], K.O.H. Vadla[126], T. Vafeiadis[36], A. Vaitkus[97], C. Valderanis[110], E. Valdes Santurio[47a,47b], M. Valente[157a], S. Valentinetti[23b,23a], A. Valero[164], E. Valiente Moreno[164], A. Vallier[90], J.A. Valls Ferrer[164], D.R. Van Arneman[115], T.R. Van Daalen[139], A. Van Der Graaf[49], P. Van Gemmeren[6], M. Van Rijnbach[126], S. Van Stroud[97], I. Van Vulpen[115], P. Vana[134], M. Vanadia[76a,76b], W. Vandelli[36], E.R. Vandewall[122], D. Vannicola[152], L. Vannoli[53], R. Vari[75a], E.W. Varnes[7], C. Varni[17b], T. Varol[149], D. Varouchas[66], L. Varriale[164], K.E. Varvell[148], M.E. Vasile[27b], L. Vaslin[84], G.A. Vasquez[166], A. Vasyukov[38], R. Vavricka[101], F. Vazeille[40], T. Vazquez Schroeder[36], J. Veatch[31], V. Vecchio[102], M.J. Veen[104], I. Veliscek[29], L.M. Veloce[156], F. Veloso[131a,131c], S. Veneziano[75a], A. Ventura[70a,70b], S. Ventura Gonzalez[136], A. Verbytskyi[111], M. Verducci[74a,74b], C. Vergis[24], M. Verissimo De Araujo[83b], W. Verkerke[115], J.C. Vermeulen[115], C. Vernieri[144], M. Vessella[104], M.C. Vetterli[143,ae], A. Vgenopoulos[153,e], N. Viaux Maira[138f], T. Vickey[140], O.E. Vickey Boeriu[140], G.H.A. Viehhauser[127], L. Vigani[63b], M. Villa[23b,23a], M. Villaplana Perez[164], E.M. Villhauer[52], E. Vilucchi[53], M.G. Vincter[34], G.S. Virdee[20], A. Vishwakarma[52], A. Visibile[115], C. Vittori[36], I. Vivarelli[23b,23a], E. Voevodina[111], F. Vogel[110], J.C. Voigt[50], P. Vokac[133], Yu. Volkotrub[86b], J. Von Ahnen[48], E. Von Toerne[24], B. Vormwald[36], V. Vorobel[134], K. Vorobev[37], M. Vos[164], K. Voss[142], M. Vozak[115], L. Vozdecky[121], N. Vranjes[15], M. Vranjes Milosavljevic[15], M. Vreeswijk[115], N.K. Vu[62d,62c], R. Vuillermet[36], O. Vujinovic[101], I. Vukotic[39], S. Wada[158], C. Wagner[104], J.M. Wagner[17a], W. Wagner[172], S. Wahdan[172], H. Wahlberg[91], M. Wakida[112], J. Walder[135], R. Walker[110], W. Walkowiak[142], A. Wall[129], E.J. Wallin[99], T. Wamorkar[6], A.Z. Wang[137], C. Wang[101], C. Wang[11], H. Wang[17a], J. Wang[64c], R.-J. Wang[101], R. Wang[61], R. Wang[6], S.M. Wang[149], S. Wang[62b], T. Wang[62a], W.T. Wang[80], W. Wang[14a], X. Wang[14c], X. Wang[163], X. Wang[62c], Y. Wang[62d], Y. Wang[14c], Z. Wang[107], Z. Wang[62d,51,62c], Z. Wang[107], A. Warburton[105], R.J. Ward[20], N. Warrack[59], S. Waterhouse[96], A.T. Watson[20], H. Watson[59], M.F. Watson[20], E. Watton[59,135], G. Watts[139], B.M. Waugh[97], C. Weber[29], H.A. Weber[18], M.S. Weber[19], S.M. Weber[63a], C. Wei[62a], Y. Wei[127], A.R. Weidberg[127], E.J. Weik[118], J. Weingarten[49], M. Weirich[101], C. Weiser[54], C.J. Wells[48], T. Wenaus[29], B. Wendland[49], T. Wengler[36], N.S. Wenke[111], N. Wermes[24], M. Wessels[63a], A.M. Wharton[92], A.S. White[61], A. White[8], M.J. White[1], D. Whiteson[160], L. Wickremasinghe[125], W. Wiedenmann[171], M. Wielers[135], C. Wiglesworth[42], D.J. Wilbern[121], H.G. Wilkens[36], J.J.H. Wilkinson[32], D.M. Williams[41], H.H. Williams[129], S. Williams[32], S. Willocq[104], B.J. Wilson[102], P.J. Windischhofer[39], F.I. Winkel[30], F. Winklmeier[124], B.T. Winter[54],

J.K. Winter[102], M. Wittgen[144], M. Wobisch[98], Z. Wolffs[115], J. Wollrath[160], M.W. Wolter[87], H. Wolters[131a,131c], M.C. Wong[137], E.L. Woodward[41], S.D. Worm[48], B.K. Wosiek[87], K.W. Woźniak[87], S. Wozniewski[55], K. Wraight[59], C. Wu[20], M. Wu[14d], M. Wu[114], S.L. Wu[171], X. Wu[56], Y. Wu[62a], Z. Wu[4], J. Wuerzinger[111,ac], T.R. Wyatt[102], B.M. Wynne[52], S. Xella[42], L. Xia[14c], M. Xia[14b], J. Xiang[64c], M. Xie[62a], X. Xie[62a], S. Xin[14a,14e], A. Xiong[124], J. Xiong[17a], D. Xu[14a], H. Xu[62a], L. Xu[62a], R. Xu[129], T. Xu[107], Y. Xu[14b], Z. Xu[52], Z. Xu[14c], B. Yabsley[148], S. Yacoob[33a], Y. Yamaguchi[155], E. Yamashita[154], H. Yamauchi[158], T. Yamazaki[17a], Y. Yamazaki[85], J. Yan[62c], S. Yan[59], Z. Yan[104], H.J. Yang[62c,62d], H.T. Yang[62a], S. Yang[62a], T. Yang[64c], X. Yang[36], X. Yang[14a], Y. Yang[44], Y. Yang[62a], Z. Yang[62a], W-M. Yao[17a], H. Ye[14c], H. Ye[55], J. Ye[14a], S. Ye[29], X. Ye[62a], Y. Yeh[97], I. Yeletskikh[38], B.K. Yeo[17b], M.R. Yexley[97], P. Yin[41], K. Yorita[169], S. Younas[27b], C.J.S. Young[36], C. Young[144], C. Yu[14a,14e], Y. Yu[62a], M. Yuan[107], R. Yuan[62b], L. Yue[97], M. Zaazoua[62a], B. Zabinski[87], E. Zaid[52], Z.K. Zak[87], T. Zakareishvili[164], N. Zakharchuk[34], S. Zambito[56], J.A. Zamora Saa[138d,138b], J. Zang[154], D. Zanzi[54], O. Zaplatilek[133], C. Zeitnitz[172], H. Zeng[14a], J.C. Zeng[163], D.T. Zenger Jr[26], O. Zenin[37], T. Ženiš[28a], S. Zenz[95], S. Zerradi[35a], D. Zerwas[66], M. Zhai[14a,14e], D.F. Zhang[140], J. Zhang[62b], J. Zhang[6], K. Zhang[14a,14e], L. Zhang[14c], P. Zhang[14a,14e], R. Zhang[171], S. Zhang[107], S. Zhang[44], T. Zhang[154], X. Zhang[62c], X. Zhang[62b], Y. Zhang[62c,5], Y. Zhang[97], Y. Zhang[14c], Z. Zhang[17a], Z. Zhang[66], H. Zhao[139], T. Zhao[62b], Y. Zhao[137], Z. Zhao[62a], Z. Zhao[62a], A. Zhemchugov[38], J. Zheng[14c], K. Zheng[163], X. Zheng[62a], Z. Zheng[144], D. Zhong[163], B. Zhou[107], H. Zhou[7], N. Zhou[62c], Y. Zhou[14c], Y. Zhou[7], C.G. Zhu[62b], J. Zhu[107], Y. Zhu[62c], Y. Zhu[62a], X. Zhuang[14a], K. Zhukov[37], N.I. Zimine[38], J. Zinsser[63b], M. Ziolkowski[142], L. Živković[15], A. Zoccoli[23b,23a], K. Zoch[61], T.G. Zorbas[140], O. Zormpa[46], W. Zou[41], L. Zwalinski[36].

[1]Department of Physics, University of Adelaide, Adelaide; Australia.
[2]Department of Physics, University of Alberta, Edmonton AB; Canada.
[3(a)]Department of Physics, Ankara University, Ankara;[(b)]Division of Physics, TOBB University of Economics and Technology, Ankara; Türkiye.
[4]LAPP, Université Savoie Mont Blanc, CNRS/IN2P3, Annecy; France.
[5]APC, Université Paris Cité, CNRS/IN2P3, Paris; France.
[6]High Energy Physics Division, Argonne National Laboratory, Argonne IL; United States of America.
[7]Department of Physics, University of Arizona, Tucson AZ; United States of America.
[8]Department of Physics, University of Texas at Arlington, Arlington TX; United States of America.
[9]Physics Department, National and Kapodistrian University of Athens, Athens; Greece.
[10]Physics Department, National Technical University of Athens, Zografou; Greece.
[11]Department of Physics, University of Texas at Austin, Austin TX; United States of America.
[12]Institute of Physics, Azerbaijan Academy of Sciences, Baku; Azerbaijan.
[13]Institut de Física d'Altes Energies (IFAE), Barcelona Institute of Science and Technology, Barcelona; Spain.
[14(a)]Institute of High Energy Physics, Chinese Academy of Sciences, Beijing;[(b)]Physics Department, Tsinghua University, Beijing;[(c)]Department of Physics, Nanjing University, Nanjing;[(d)]School of Science, Shenzhen Campus of Sun Yat-sen University;[(e)]University of Chinese Academy of Science (UCAS), Beijing; China.
[15]Institute of Physics, University of Belgrade, Belgrade; Serbia.
[16]Department for Physics and Technology, University of Bergen, Bergen; Norway.
[17(a)]Physics Division, Lawrence Berkeley National Laboratory, Berkeley CA;[(b)]University of California,

Berkeley CA; United States of America.
[18]Institut für Physik, Humboldt Universität zu Berlin, Berlin; Germany.
[19]Albert Einstein Center for Fundamental Physics and Laboratory for High Energy Physics, University of Bern, Bern; Switzerland.
[20]School of Physics and Astronomy, University of Birmingham, Birmingham; United Kingdom.
[21(a)]Department of Physics, Bogazici University, Istanbul;[(b)]Department of Physics Engineering, Gaziantep University, Gaziantep;[(c)]Department of Physics, Istanbul University, Istanbul; Türkiye.
[22(a)]Facultad de Ciencias y Centro de Investigaciónes, Universidad Antonio Nariño, Bogotá;[(b)]Departamento de Física, Universidad Nacional de Colombia, Bogotá; Colombia.
[23(a)]Dipartimento di Fisica e Astronomia A. Righi, Università di Bologna, Bologna;[(b)]INFN Sezione di Bologna; Italy.
[24]Physikalisches Institut, Universität Bonn, Bonn; Germany.
[25]Department of Physics, Boston University, Boston MA; United States of America.
[26]Department of Physics, Brandeis University, Waltham MA; United States of America.
[27(a)]Transilvania University of Brasov, Brasov;[(b)]Horia Hulubei National Institute of Physics and Nuclear Engineering, Bucharest;[(c)]Department of Physics, Alexandru Ioan Cuza University of Iasi, Iasi;[(d)]National Institute for Research and Development of Isotopic and Molecular Technologies, Physics Department, Cluj-Napoca;[(e)]National University of Science and Technology Politechnica, Bucharest;[(f)]West University in Timisoara, Timisoara;[(g)]Faculty of Physics, University of Bucharest, Bucharest; Romania.
[28(a)]Faculty of Mathematics, Physics and Informatics, Comenius University, Bratislava;[(b)]Department of Subnuclear Physics, Institute of Experimental Physics of the Slovak Academy of Sciences, Kosice; Slovak Republic.
[29]Physics Department, Brookhaven National Laboratory, Upton NY; United States of America.
[30]Universidad de Buenos Aires, Facultad de Ciencias Exactas y Naturales, Departamento de Física, y CONICET, Instituto de Física de Buenos Aires (IFIBA), Buenos Aires; Argentina.
[31]California State University, CA; United States of America.
[32]Cavendish Laboratory, University of Cambridge, Cambridge; United Kingdom.
[33(a)]Department of Physics, University of Cape Town, Cape Town;[(b)]iThemba Labs, Western Cape;[(c)]Department of Mechanical Engineering Science, University of Johannesburg, Johannesburg;[(d)]National Institute of Physics, University of the Philippines Diliman (Philippines);[(e)]University of South Africa, Department of Physics, Pretoria;[(f)]University of Zululand, KwaDlangezwa;[(g)]School of Physics, University of the Witwatersrand, Johannesburg; South Africa.
[34]Department of Physics, Carleton University, Ottawa ON; Canada.
[35(a)]Faculté des Sciences Ain Chock, Réseau Universitaire de Physique des Hautes Energies - Université Hassan II, Casablanca;[(b)]Faculté des Sciences, Université Ibn-Tofail, Kénitra;[(c)]Faculté des Sciences Semlalia, Université Cadi Ayyad, LPHEA-Marrakech;[(d)]LPMR, Faculté des Sciences, Université Mohamed Premier, Oujda;[(e)]Faculté des sciences, Université Mohammed V, Rabat;[(f)]Institute of Applied Physics, Mohammed VI Polytechnic University, Ben Guerir; Morocco.
[36]CERN, Geneva; Switzerland.
[37]Affiliated with an institute covered by a cooperation agreement with CERN.
[38]Affiliated with an international laboratory covered by a cooperation agreement with CERN.
[39]Enrico Fermi Institute, University of Chicago, Chicago IL; United States of America.
[40]LPC, Université Clermont Auvergne, CNRS/IN2P3, Clermont-Ferrand; France.
[41]Nevis Laboratory, Columbia University, Irvington NY; United States of America.
[42]Niels Bohr Institute, University of Copenhagen, Copenhagen; Denmark.
[43(a)]Dipartimento di Fisica, Università della Calabria, Rende;[(b)]INFN Gruppo Collegato di Cosenza, Laboratori Nazionali di Frascati; Italy.

[44]Physics Department, Southern Methodist University, Dallas TX; United States of America.
[45]Physics Department, University of Texas at Dallas, Richardson TX; United States of America.
[46]National Centre for Scientific Research "Demokritos", Agia Paraskevi; Greece.
[47(a)]Department of Physics, Stockholm University;[(b)]Oskar Klein Centre, Stockholm; Sweden.
[48]Deutsches Elektronen-Synchrotron DESY, Hamburg and Zeuthen; Germany.
[49]Fakultät Physik , Technische Universität Dortmund, Dortmund; Germany.
[50]Institut für Kern- und Teilchenphysik, Technische Universität Dresden, Dresden; Germany.
[51]Department of Physics, Duke University, Durham NC; United States of America.
[52]SUPA - School of Physics and Astronomy, University of Edinburgh, Edinburgh; United Kingdom.
[53]INFN e Laboratori Nazionali di Frascati, Frascati; Italy.
[54]Physikalisches Institut, Albert-Ludwigs-Universität Freiburg, Freiburg; Germany.
[55]II. Physikalisches Institut, Georg-August-Universität Göttingen, Göttingen; Germany.
[56]Département de Physique Nucléaire et Corpusculaire, Université de Genève, Genève; Switzerland.
[57(a)]Dipartimento di Fisica, Università di Genova, Genova;[(b)]INFN Sezione di Genova; Italy.
[58]II. Physikalisches Institut, Justus-Liebig-Universität Giessen, Giessen; Germany.
[59]SUPA - School of Physics and Astronomy, University of Glasgow, Glasgow; United Kingdom.
[60]LPSC, Université Grenoble Alpes, CNRS/IN2P3, Grenoble INP, Grenoble; France.
[61]Laboratory for Particle Physics and Cosmology, Harvard University, Cambridge MA; United States of America.
[62(a)]Department of Modern Physics and State Key Laboratory of Particle Detection and Electronics, University of Science and Technology of China, Hefei;[(b)]Institute of Frontier and Interdisciplinary Science and Key Laboratory of Particle Physics and Particle Irradiation (MOE), Shandong University, Qingdao;[(c)]School of Physics and Astronomy, Shanghai Jiao Tong University, Key Laboratory for Particle Astrophysics and Cosmology (MOE), SKLPPC, Shanghai;[(d)]Tsung-Dao Lee Institute, Shanghai;[(e)]School of Physics and Microelectronics, Zhengzhou University; China.
[63(a)]Kirchhoff-Institut für Physik, Ruprecht-Karls-Universität Heidelberg, Heidelberg;[(b)]Physikalisches Institut, Ruprecht-Karls-Universität Heidelberg, Heidelberg; Germany.
[64(a)]Department of Physics, Chinese University of Hong Kong, Shatin, N.T., Hong Kong;[(b)]Department of Physics, University of Hong Kong, Hong Kong;[(c)]Department of Physics and Institute for Advanced Study, Hong Kong University of Science and Technology, Clear Water Bay, Kowloon, Hong Kong; China.
[65]Department of Physics, National Tsing Hua University, Hsinchu; Taiwan.
[66]IJCLab, Université Paris-Saclay, CNRS/IN2P3, 91405, Orsay; France.
[67]Centro Nacional de Microelectrónica (IMB-CNM-CSIC), Barcelona; Spain.
[68]Department of Physics, Indiana University, Bloomington IN; United States of America.
[69(a)]INFN Gruppo Collegato di Udine, Sezione di Trieste, Udine;[(b)]ICTP, Trieste;[(c)]Dipartimento Politecnico di Ingegneria e Architettura, Università di Udine, Udine; Italy.
[70(a)]INFN Sezione di Lecce;[(b)]Dipartimento di Matematica e Fisica, Università del Salento, Lecce; Italy.
[71(a)]INFN Sezione di Milano;[(b)]Dipartimento di Fisica, Università di Milano, Milano; Italy.
[72(a)]INFN Sezione di Napoli;[(b)]Dipartimento di Fisica, Università di Napoli, Napoli; Italy.
[73(a)]INFN Sezione di Pavia;[(b)]Dipartimento di Fisica, Università di Pavia, Pavia; Italy.
[74(a)]INFN Sezione di Pisa;[(b)]Dipartimento di Fisica E. Fermi, Università di Pisa, Pisa; Italy.
[75(a)]INFN Sezione di Roma;[(b)]Dipartimento di Fisica, Sapienza Università di Roma, Roma; Italy.
[76(a)]INFN Sezione di Roma Tor Vergata;[(b)]Dipartimento di Fisica, Università di Roma Tor Vergata, Roma; Italy.
[77(a)]INFN Sezione di Roma Tre;[(b)]Dipartimento di Matematica e Fisica, Università Roma Tre, Roma; Italy.
[78(a)]INFN-TIFPA;[(b)]Università degli Studi di Trento, Trento; Italy.

[79]Universität Innsbruck, Department of Astro and Particle Physics, Innsbruck; Austria.
[80]University of Iowa, Iowa City IA; United States of America.
[81]Department of Physics and Astronomy, Iowa State University, Ames IA; United States of America.
[82]Istinye University, Sariyer, Istanbul; Türkiye.
[83(a)]Departamento de Engenharia Elétrica, Universidade Federal de Juiz de Fora (UFJF), Juiz de Fora;[(b)]Universidade Federal do Rio De Janeiro COPPE/EE/IF, Rio de Janeiro;[(c)]Instituto de Física, Universidade de São Paulo, São Paulo;[(d)]Rio de Janeiro State University, Rio de Janeiro;[(e)]Federal University of Bahia, Bahia; Brazil.
[84]KEK, High Energy Accelerator Research Organization, Tsukuba; Japan.
[85]Graduate School of Science, Kobe University, Kobe; Japan.
[86(a)]AGH University of Krakow, Faculty of Physics and Applied Computer Science, Krakow;[(b)]Marian Smoluchowski Institute of Physics, Jagiellonian University, Krakow; Poland.
[87]Institute of Nuclear Physics Polish Academy of Sciences, Krakow; Poland.
[88]Faculty of Science, Kyoto University, Kyoto; Japan.
[89]Research Center for Advanced Particle Physics and Department of Physics, Kyushu University, Fukuoka ; Japan.
[90]L2IT, Université de Toulouse, CNRS/IN2P3, UPS, Toulouse; France.
[91]Instituto de Física La Plata, Universidad Nacional de La Plata and CONICET, La Plata; Argentina.
[92]Physics Department, Lancaster University, Lancaster; United Kingdom.
[93]Oliver Lodge Laboratory, University of Liverpool, Liverpool; United Kingdom.
[94]Department of Experimental Particle Physics, Jožef Stefan Institute and Department of Physics, University of Ljubljana, Ljubljana; Slovenia.
[95]School of Physics and Astronomy, Queen Mary University of London, London; United Kingdom.
[96]Department of Physics, Royal Holloway University of London, Egham; United Kingdom.
[97]Department of Physics and Astronomy, University College London, London; United Kingdom.
[98]Louisiana Tech University, Ruston LA; United States of America.
[99]Fysiska institutionen, Lunds universitet, Lund; Sweden.
[100]Departamento de Física Teorica C-15 and CIAFF, Universidad Autónoma de Madrid, Madrid; Spain.
[101]Institut für Physik, Universität Mainz, Mainz; Germany.
[102]School of Physics and Astronomy, University of Manchester, Manchester; United Kingdom.
[103]CPPM, Aix-Marseille Université, CNRS/IN2P3, Marseille; France.
[104]Department of Physics, University of Massachusetts, Amherst MA; United States of America.
[105]Department of Physics, McGill University, Montreal QC; Canada.
[106]School of Physics, University of Melbourne, Victoria; Australia.
[107]Department of Physics, University of Michigan, Ann Arbor MI; United States of America.
[108]Department of Physics and Astronomy, Michigan State University, East Lansing MI; United States of America.
[109]Group of Particle Physics, University of Montreal, Montreal QC; Canada.
[110]Fakultät für Physik, Ludwig-Maximilians-Universität München, München; Germany.
[111]Max-Planck-Institut für Physik (Werner-Heisenberg-Institut), München; Germany.
[112]Graduate School of Science and Kobayashi-Maskawa Institute, Nagoya University, Nagoya; Japan.
[113]Department of Physics and Astronomy, University of New Mexico, Albuquerque NM; United States of America.
[114]Institute for Mathematics, Astrophysics and Particle Physics, Radboud University/Nikhef, Nijmegen; Netherlands.
[115]Nikhef National Institute for Subatomic Physics and University of Amsterdam, Amsterdam; Netherlands.

[116]Department of Physics, Northern Illinois University, DeKalb IL; United States of America.
[117(a)]New York University Abu Dhabi, Abu Dhabi;[(b)]United Arab Emirates University, Al Ain; United Arab Emirates.
[118]Department of Physics, New York University, New York NY; United States of America.
[119]Ochanomizu University, Otsuka, Bunkyo-ku, Tokyo; Japan.
[120]Ohio State University, Columbus OH; United States of America.
[121]Homer L. Dodge Department of Physics and Astronomy, University of Oklahoma, Norman OK; United States of America.
[122]Department of Physics, Oklahoma State University, Stillwater OK; United States of America.
[123]Palacký University, Joint Laboratory of Optics, Olomouc; Czech Republic.
[124]Institute for Fundamental Science, University of Oregon, Eugene, OR; United States of America.
[125]Graduate School of Science, Osaka University, Osaka; Japan.
[126]Department of Physics, University of Oslo, Oslo; Norway.
[127]Department of Physics, Oxford University, Oxford; United Kingdom.
[128]LPNHE, Sorbonne Université, Université Paris Cité, CNRS/IN2P3, Paris; France.
[129]Department of Physics, University of Pennsylvania, Philadelphia PA; United States of America.
[130]Department of Physics and Astronomy, University of Pittsburgh, Pittsburgh PA; United States of America.
[131(a)]Laboratório de Instrumentação e Física Experimental de Partículas - LIP, Lisboa;[(b)]Departamento de Física, Faculdade de Ciências, Universidade de Lisboa, Lisboa;[(c)]Departamento de Física, Universidade de Coimbra, Coimbra;[(d)]Centro de Física Nuclear da Universidade de Lisboa, Lisboa;[(e)]Departamento de Física, Universidade do Minho, Braga;[(f)]Departamento de Física Teórica y del Cosmos, Universidad de Granada, Granada (Spain);[(g)]Departamento de Física, Instituto Superior Técnico, Universidade de Lisboa, Lisboa; Portugal.
[132]Institute of Physics of the Czech Academy of Sciences, Prague; Czech Republic.
[133]Czech Technical University in Prague, Prague; Czech Republic.
[134]Charles University, Faculty of Mathematics and Physics, Prague; Czech Republic.
[135]Particle Physics Department, Rutherford Appleton Laboratory, Didcot; United Kingdom.
[136]IRFU, CEA, Université Paris-Saclay, Gif-sur-Yvette; France.
[137]Santa Cruz Institute for Particle Physics, University of California Santa Cruz, Santa Cruz CA; United States of America.
[138(a)]Departamento de Física, Pontificia Universidad Católica de Chile, Santiago;[(b)]Millennium Institute for Subatomic physics at high energy frontier (SAPHIR), Santiago;[(c)]Instituto de Investigación Multidisciplinario en Ciencia y Tecnología, y Departamento de Física, Universidad de La Serena;[(d)]Universidad Andres Bello, Department of Physics, Santiago;[(e)]Instituto de Alta Investigación, Universidad de Tarapacá, Arica;[(f)]Departamento de Física, Universidad Técnica Federico Santa María, Valparaíso; Chile.
[139]Department of Physics, University of Washington, Seattle WA; United States of America.
[140]Department of Physics and Astronomy, University of Sheffield, Sheffield; United Kingdom.
[141]Department of Physics, Shinshu University, Nagano; Japan.
[142]Department Physik, Universität Siegen, Siegen; Germany.
[143]Department of Physics, Simon Fraser University, Burnaby BC; Canada.
[144]SLAC National Accelerator Laboratory, Stanford CA; United States of America.
[145]Department of Physics, Royal Institute of Technology, Stockholm; Sweden.
[146]Departments of Physics and Astronomy, Stony Brook University, Stony Brook NY; United States of America.
[147]Department of Physics and Astronomy, University of Sussex, Brighton; United Kingdom.

[148]School of Physics, University of Sydney, Sydney; Australia.
[149]Institute of Physics, Academia Sinica, Taipei; Taiwan.
[150(a)]E. Andronikashvili Institute of Physics, Iv. Javakhishvili Tbilisi State University, Tbilisi;[(b)]High Energy Physics Institute, Tbilisi State University, Tbilisi;[(c)]University of Georgia, Tbilisi; Georgia.
[151]Department of Physics, Technion, Israel Institute of Technology, Haifa; Israel.
[152]Raymond and Beverly Sackler School of Physics and Astronomy, Tel Aviv University, Tel Aviv; Israel.
[153]Department of Physics, Aristotle University of Thessaloniki, Thessaloniki; Greece.
[154]International Center for Elementary Particle Physics and Department of Physics, University of Tokyo, Tokyo; Japan.
[155]Department of Physics, Tokyo Institute of Technology, Tokyo; Japan.
[156]Department of Physics, University of Toronto, Toronto ON; Canada.
[157(a)]TRIUMF, Vancouver BC;[(b)]Department of Physics and Astronomy, York University, Toronto ON; Canada.
[158]Division of Physics and Tomonaga Center for the History of the Universe, Faculty of Pure and Applied Sciences, University of Tsukuba, Tsukuba; Japan.
[159]Department of Physics and Astronomy, Tufts University, Medford MA; United States of America.
[160]Department of Physics and Astronomy, University of California Irvine, Irvine CA; United States of America.
[161]University of Sharjah, Sharjah; United Arab Emirates.
[162]Department of Physics and Astronomy, University of Uppsala, Uppsala; Sweden.
[163]Department of Physics, University of Illinois, Urbana IL; United States of America.
[164]Instituto de Física Corpuscular (IFIC), Centro Mixto Universidad de Valencia - CSIC, Valencia; Spain.
[165]Department of Physics, University of British Columbia, Vancouver BC; Canada.
[166]Department of Physics and Astronomy, University of Victoria, Victoria BC; Canada.
[167]Fakultät für Physik und Astronomie, Julius-Maximilians-Universität Würzburg, Würzburg; Germany.
[168]Department of Physics, University of Warwick, Coventry; United Kingdom.
[169]Waseda University, Tokyo; Japan.
[170]Department of Particle Physics and Astrophysics, Weizmann Institute of Science, Rehovot; Israel.
[171]Department of Physics, University of Wisconsin, Madison WI; United States of America.
[172]Fakultät für Mathematik und Naturwissenschaften, Fachgruppe Physik, Bergische Universität Wuppertal, Wuppertal; Germany.
[173]Department of Physics, Yale University, New Haven CT; United States of America.
[a] Also Affiliated with an institute covered by a cooperation agreement with CERN.
[b] Also at An-Najah National University, Nablus; Palestine.
[c] Also at Borough of Manhattan Community College, City University of New York, New York NY; United States of America.
[d] Also at Center for High Energy Physics, Peking University; China.
[e] Also at Center for Interdisciplinary Research and Innovation (CIRI-AUTH), Thessaloniki; Greece.
[f] Also at Centro Studi e Ricerche Enrico Fermi; Italy.
[g] Also at CERN, Geneva; Switzerland.
[h] Also at Département de Physique Nucléaire et Corpusculaire, Université de Genève, Genève; Switzerland.
[i] Also at Departament de Fisica de la Universitat Autonoma de Barcelona, Barcelona; Spain.
[j] Also at Department of Financial and Management Engineering, University of the Aegean, Chios; Greece.
[k] Also at Department of Physics, California State University, Sacramento; United States of America.
[l] Also at Department of Physics, King's College London, London; United Kingdom.
[m] Also at Department of Physics, Stanford University, Stanford CA; United States of America.

[n] Also at Department of Physics, Stellenbosch University; South Africa.
[o] Also at Department of Physics, University of Fribourg, Fribourg; Switzerland.
[p] Also at Department of Physics, University of Thessaly; Greece.
[q] Also at Department of Physics, Westmont College, Santa Barbara; United States of America.
[r] Also at Hellenic Open University, Patras; Greece.
[s] Also at Institucio Catalana de Recerca i Estudis Avancats, ICREA, Barcelona; Spain.
[t] Also at Institut für Experimentalphysik, Universität Hamburg, Hamburg; Germany.
[u] Also at Institute for Nuclear Research and Nuclear Energy (INRNE) of the Bulgarian Academy of Sciences, Sofia; Bulgaria.
[v] Also at Institute of Applied Physics, Mohammed VI Polytechnic University, Ben Guerir; Morocco.
[w] Also at Institute of Particle Physics (IPP); Canada.
[x] Also at Institute of Physics and Technology, Mongolian Academy of Sciences, Ulaanbaatar; Mongolia.
[y] Also at Institute of Physics, Azerbaijan Academy of Sciences, Baku; Azerbaijan.
[z] Also at Institute of Theoretical Physics, Ilia State University, Tbilisi; Georgia.
[aa] Also at Lawrence Livermore National Laboratory, Livermore; United States of America.
[ab] Also at National Institute of Physics, University of the Philippines Diliman (Philippines); Philippines.
[ac] Also at Technical University of Munich, Munich; Germany.
[ad] Also at The Collaborative Innovation Center of Quantum Matter (CICQM), Beijing; China.
[ae] Also at TRIUMF, Vancouver BC; Canada.
[af] Also at Università di Napoli Parthenope, Napoli; Italy.
[ag] Also at University of Colorado Boulder, Department of Physics, Colorado; United States of America.
[ah] Also at Washington College, Chestertown, MD; United States of America.
[ai] Also at Yeditepe University, Physics Department, Istanbul; Türkiye.
[*] Deceased

ACE Science Workshop Report

Stefania Gori (ed.)[1], Nhan Tran (ed.)[2], Karri DiPetrillo[3], Bertrand Echenard[4], Jeffrey Eldred[2], Roni Harnik[2], Pedro Machado[2], Matthew Toups[2], I. P. Fernando[5], Robert Bernstein[2], Innes Bigaran[2,6], Cari Cesarotti[9], Bhaskar Dutta[7], Christian Herwig[2], Sergo Jindariani[2], Ryan Plestid[4], Vladimir Shiltsev[10], Matthew Solt[5], Alexandre Sousa[8], Diktys Stratakis[2], Zahra Tabrizi[6], Anil Thapa[5], Jacob Zettlemoyer[2], and Jure Zupan[8]

[1]University of California Santa Cruz, Santa Cruz, CA 95064, USA
[2]Fermi National Accelerator Laboratory, Batavia, IL 60510, USA
[3]University of Chicago, Chicago, IL 60637, USA
[4]California Institute of Technology, Pasadena, CA 91125, USA
[5]University of Virginia, Charlottesville, VA 22904, USA
[6]Northwestern University, Evanston, IL 60208, USA
[7]Mitchell Institute and Texas A&M University, College Station, TX 77843, USA
[8]University of Cincinnati, Cincinnati, OH 45221, USA
[9]Massachusetts Institute of Technology, Cambridge, MA 02139, USA
[10]Northern Illinois University, DeKalb, IL 60115, USA

arXiv:2403.02422v1 [hep-ex] 4 Mar 2024

ABSTRACT

We summarize the Fermilab Accelerator Complex Evolution (ACE) Science Workshop, held on June 14-15, 2023. The workshop presented the strategy for the ACE program in two phases: ACE Main Injector Ramp and Target (MIRT) upgrade and ACE Booster Replacement (BR) upgrade. Four plenary sessions covered the primary experimental physics thrusts: Muon Collider, Neutrinos, Charged Lepton Flavor Violation, and Dark Sectors. Additional physics and technology ideas were presented from the community that could expand or augment the ACE science program. Given the physics framing, a parallel session at the workshop was dedicated to discussing priorities for accelerator R&D. Finally, physics discussion sessions concluded the workshop where experts from the different experimental physics thrusts were brought together to begin understanding the synergies between the different physics drivers and technologies. In December of 2023, the P5 report was released setting the physics priorities for the field in the next decade and beyond, and identified ACE as an important component of the future US accelerator-based program. Given the presentations and discussions at the ACE Science Workshop and the findings of the P5 report, we lay out the topics for study to determine the physics priorities and design goals of the Fermilab ACE project in the near-term.

Contents

1 Executive Summary **3**

2 Fermilab Accelerator Complex Evolution (ACE) and physics thrusts **5**
2.1 Fermilab Accelerator Complex Evolution . . . 5
2.2 Physics drivers and experimental thrusts . . . 5
2.2.1 Muon Collider . . . 6
2.2.2 Neutrino physics . . . 7
2.2.3 Charged Lepton Flavor Violation . . . 7
2.2.4 Accelerator-based dark sectors . . . 7
2.3 Additional technology and physics directions . . . 8
2.3.1 Physics experiments . . . 8
2.3.2 Technology development . . . 9

3 Physics, detector, and accelerator complementarity **10**
3.1 CLFV - Dark Sectors . . . 10
3.2 CLFV - Muon Collider . . . 10
3.3 CLFV - Neutrinos . . . 11
3.4 Dark Sectors - Muon Colliders . . . 12
3.5 Dark Sectors - Neutrinos . . . 12
3.6 Muon Collider - Neutrinos . . . 13
3.7 Accelerator technology and R&D . . . 14

1 Executive Summary

The Fermilab Accelerator Complex Evolution (ACE) Science Workshop [1], held on June 14-15, 2023, brought together an international cohort of physicists with expertise in theory, experiment, and accelerator technologies to begin a coordinated discussion defining the Fermilab ACE physics program. The aim of this intensive workshop was to review the motivations and current state of the primary physics thrusts and their accelerator needs and to outline a strategic road map to understand the complementarity of their emerging scientific demands. A detailed description of the preliminary ACE approach is outlined in the Proton Intensity Upgrade - Central Design Group (PIU-CDG) report [2].

ACE consists of two primary phases:

1. **ACE-MIRT (Main Injector Ramp and Target) upgrade**: this aims to upgrade the Main Injector to reduce the ramp time and deliver more beam power to DUNE (max $\sim$ 2.1 MW) as soon as possible. This also requires target R&D to ensure that DUNE can handle up to 2.4 MW of beam power, the ultimate design goal.

2. **ACE-BR (Booster Replacement) upgrade**: the Booster replacement aims to replace the Booster synchrotron which accelerates protons from 800 MeV to 8 GeV to **deliver** the full >2.4 MW of beam power to DUNE, and to **enable** the development of the next generation of US accelerator-based particle physics experiments while modernizing the complex to provide **reliable** beam to all its users.

The scientific potential of the Fermilab ACE science program is very broad and includes a wide variety of physics topics discussed during the Snowmass 2021 process [3] across the energy, neutrino, rare processes and precision, theory, and cosmic frontiers. The primary experimental physics thrusts and related experiments presented at the workshop were:

- **Charged Lepton Flavor Violation (CLFV) experiments**: using high intensity beams of muons aim to significantly improve indirect searches for new physics up to scales of $\mathcal{O}(10^5$ TeV).
- **Dark sector experiments**: using high intensity beams of protons and muons aim to explore uncovered parameter space of thermal dark matter models, as well as models that address the strong CP problem (axion-like-particles), the origin of neutrino masses (sterile neutrinos), and the hierarchy problem (dark scalars).
- **Muon Collider** (MC): enables direct searches for new physics at the $\mathcal{O}$(10 TeV) scale with intense proton beams that can serve as technology demonstrators and a front-end proton driver facility. It also enables unique precision measurements of Standard Model (SM) particles, like the Higgs boson.
- **Neutrino experiments beyond DUNE**: enable exploration of the neutrino sector beyond DUNE via direct searches connected to anomalies and high precision Standard Model measurements.

While these focus areas comprise the primary experimental physics thrusts considered, other experimental proposals or ideas outside of these thrusts were presented in open sessions for remarks from the community, as well as in parallel discussion sessions. For example, rare meson decays, mono-energetic neutrino beams, or muon beams could be used to test dark sector physics. ACE can also be used for spin physics studies and energy research. The breadth of these ideas can be synergistic with the primary experimental physics thrusts or expand the overall physics potential of ACE.

The synergy between the several physics thrusts was also discussed during the workshop. Neutrino detectors and neutrino beam measurements can be used to test the physics of the dark sector. A muon collider could be used to test non-standard neutrino interactions and dark matter freeze-out models across a broad range of energies: high mass (>1 TeV) WIMPs could be produced at the main interaction point, and light muon-philic dark sectors could be produced in the muon dumps. Neutrinos are a probe of lepton flavor symmetries, and, therefore, CLFV and neutrino experiments provide complementary probes of new physics. Finally, CLFV experiments can explore the parameter space of new sub-GeV dark particles with flavor violating couplings.

Outcomes

The preliminary points for study and outcomes of the workshop are discussed below. We discuss the ACE project design constraints, technology R&D, and physics synergies:

ACE design parameters

- **ACE-MIRT (Main Injector Ramp and Targetry) era:**
  - The 8 GeV proton intensity and accelerator timeline economics during the ACE-MIRT era needs to be understood in more detail because the Main Injector (MI) cycle time reduction provides less beam power for the muon program, short baseline neutrino program, and MC R&D.

  - The ACE program should continue to provide a fraction of MI cycles to the 120 GeV beam slow extraction program to support test beam, dark sector physics, and spin physics.
  - An accumulator ring at 0.8 GeV for pulsed proton beam would greatly enhance the physics capabilities of the proton beam dump dark sector program and the CLFV program.
- **ACE-BR (Booster Replacement) – 2 GeV Linac:** A 2 GeV Linac is a part of all the current ACE-BR designs. The benefits and trade-offs of an earlier construction start need to be understood:
  - Due to increased muon production vs. proton energy, a 2 GeV beam would improve the physics reach of next generation CLFV experiments.
  - A 2 GeV CW beam could serve as good MC cooling demonstrator front-end. Its benefits versus the 8 GeV booster beam during the ACE-MIRT era require more study.
  - Design of an accumulator ring optimized for 2 GeV but that can operate at 0.8 GeV should be explored to enable flexible operations across the ACE-MIRT and ACE-BR eras.
  - Resource benefits by beginning the 2 GeV Linac construction soon after PIP-II completion needs to be understood.
- **ACE-BR (Booster Replacement) – 2→8 GeV:**
  - To deliver 2.4 MW to DUNE, each of the 6 ACE-BR configurations are sufficient.
  - To enable ACE to serve as a Muon Collider proton driver front-end, the ACE-BR configurations need to be re-optimized.
  - An H^- Linac option for ACE-BR is a more natural fit for MC than an RCS due to the requirement synergies with DUNE.
  - Further study is needed to understand if an 8 GeV accumulator ring used in a ACE-BR Linac scenario for DUNE would also be sufficient to serve as the MC proton driver accumulator ring and provide beam for other physics scenarios.

Technology R&D and Physics complementarity

- **Accelerator R&D:**
  - High Power Targetry is the highest priority accelerator R&D area because it is required during the ACE-MIRT era to achieve the DUNE physics goals. It is also identified as a key area of synergistic R&D for the MC and a future CLFV program.
  - Other high priority accelerator R&D topic areas include high power H^- stripping (including laser stripping), MC cooling demonstrator, and high current accumulator ring designs that can operate at 0.8-2 GeV.
- **Physics synergies to be studied:**
  - The physics case for a neutrino factory needs to be re-visited in a post-DUNE scenario. A number of important points were discussed, especially tau neutrino physics and precision neutrino measurements, but the physics cases need to be collated.
  - Better understanding of how neutrino mass benchmark models map onto CLFV physics reach would provide sharp targets for the CLFV program.

Outlook and next steps

Following the release of the P5 report [4], the particle physics community has been provided with a roadmap outlining the physics priorities for the upcoming decade and beyond. The P5 report specifically highlights ACE as an important component of this plan (Recommendation 4(g), Recommendation 6, Area Recommendation 12), due to the potential presented by the Muon Collider. A primary aim of ACE is to facilitate the development of a proton driver essential for the Muon Collider while being able to deliver a world-class experimental physics program that can address several of the P5 physics drivers: Elucidate the Mysteries of Neutrinos; Reveal the Secrets of the Higgs Boson; Search for Direct Evidence of New Particles; Pursue Quantum Imprints of New Phenomena; Determine the Nature of Dark Matter. Defining the exciting potential of the ACE experimental program and the design of the facility are important recommendations of the P5 report.

The immediate future involves holding a series of workshops to gather input from the community and build consensus with the initial focus on refining the accelerator design to align with new P5 priorities. It is also necessary to understand how the various proposed physics concepts can fit together within the ACE design, including research and development paths. After the workshop focused on accelerator design, another physics workshop will be convened. With a concrete ACE layout and design, it will set out to establish physics priorities and explore the possibilities that will lead to a conceptual design (CD-0) in the following years to be presented to a targeted panel that determines the path forward for the US accelerator-based physics program [4].

2 Fermilab Accelerator Complex Evolution (ACE) and physics thrusts

2.1 Fermilab Accelerator Complex Evolution

The Fermilab Accelerator Complex Evolution (ACE) consists of two primary phases, the Main Injector Ramp and Target (MIRT) upgrade and the Booster Replacement (BR) upgrade. ACE-MIRT aims to upgrade the Main Injector to reduce the ramp time and deliver more beam power to DUNE (max $\sim$ 2.1 MW) as soon as possible; this also requires target R&D to ensure that DUNE can handle up to 2.4 MW of beam power. ACE-BR aims to replace the Booster synchrotron which accelerates protons from 800 MeV to 8 GeV to enable full delivery of >2.4 MW of beam power to DUNE and **enable** the development of the next generation of US accelerator-based particle physics experiments, including multi-TeV collider research, while modernizing the complex to provide **reliable** beam to all its users.

The ACE-MIRT upgrade aims to significantly enhance the proton output directed towards the DUNE Phase I detector. By reducing the Main Injector (MI) cycle time from 1.2–1.4 seconds to 0.65 seconds, the initiative seeks to increase beam power and upgrade target systems to accommodate up to 2.1 MW. Achieving this shortened cycle requires a substantial increase in voltage and electrical power, necessitating enhancements to power supplies, transformers, feeders, the size of service buildings, the introduction of additional cooling, and more tunnel penetrations. Additionally, the RF accelerating system will undergo modifications, either by replacing existing cavities with a new design that offers more volts per cavity or by adding more cavities of the current design, alongside updates to regulation, control, and instrumentation systems.

Addressing challenges of beam dynamics, losses, and shielding is crucial for ACE-MIRT. Upgrades to the MI collimators and the abort line are essential to accommodate the changes. During the shortened 0.65-second cycle, before the implementation of a Booster Replacement, the Recycler Ring will not be available for Mu2e, and only one Booster batch will be available for the 8 GeV proton beam experiments. The target research and development (R&D) segment focuses on identifying suitable candidate materials, conducting high-energy proton irradiation and pulsed-beam experiments to simulate expected radiation damage and beam interaction conditions, followed by Post-Irradiation Examination (PIE) to assess material properties, microscopic structural changes, and high-cycle fatigue testing.

Following ACE-MIRT, **the ACE-BR upgrade** aims to construct a new Booster to serve as a reliable platform for the future of the Accelerator Complex. This upgrade will continue to ensure the delivery of high-intensity beams for DUNE while enhancing the Fermilab's capability to support next generation accelerator experiments from precision measurements to searches for new physics with beams ranging from 1-120 GeV. The project also intends to supply the high-intensity proton source necessary for future multi-TeV accelerator research, marking a significant leap forward in the complex's capabilities.

Exploring Booster replacement options, the project considers extending the Superconducting RF (SRF) Linac to higher energies or constructing a new Rapid-Cycling Synchrotron (RCS). Through the evaluation of three representative options for each approach, all requiring an extension of the SRF Linac to 2 GeV, the RCS option emerges as advantageous due to reduced space charge at the increased energy. Conversely, the high-energy linac option necessitates a beam with approximately 2 GeV to leverage high-frequency, $\beta = 1$, high-gradient cavities, which can be efficiently grouped and powered by a single, high-power klystron. The final selection and optimization of ACE-BR design will be based on outcomes of upcoming workshops and community design studies and physics prioritization.

Within this phased upgrade approach for the Fermilab accelerator complex, we can conceive **physics spigots** where additional experiments beyond DUNE would be feasible. We divide them into the ACE-MIRT and ACE-BR eras.

- ACE-MIRT era:
  - **S0A**: 800 MeV, PIP-II continuous wave
  - **S0B**: 800 MeV, PIP-II pulsed linac
  - **S0C**: 800 MeV, PIP-II pulsed with accumulator ring
  - **S0D**: 8 GeV, Booster pulsed
  - **S0E**: 8 GeV, Recycler Ring (RR) & Delivery Ring (RR) (muon campus)
  - **S0F**: 120 GeV, MI continuous wave via slow extraction
- ACE-BR era:
  - **S1A**: 2 GeV, continuous wave or pulsed linac
  - **S1B**: 2 GeV, pulsed with accumulator ring
  - **S1D**: 8 GeV, pulsed, muon campus (RR/DR)
  - **S1E**: 8 GeV, Recycler Ring (RR) & Delivery Ring (RR) (muon campus) [same as ACE-MIRT]
  - **S1F**: 120 GeV, MI continuous wave via slow extraction [same as ACE-MIRT]

2.2 Physics drivers and experimental thrusts

ACE physics aligns well with all three science themes presented in the P5 report: (1) Decipher the Quantum Realm; (2) Explore New Paradigms in Physics; (3) Illuminate the Hidden Universe. Within each theme P5 identified two physics drivers,

that represent the most promising avenues of investigation for the next 10 to 20 years. ACE will address five out of these six physics drivers: **(1.1)** Elucidate the Mysteries of Neutrinos; **(1.2)** Reveal the Secrets of the Higgs Boson; **(2.1)** Search for Direct Evidence of New Particles; **(2.2)** Pursue Quantum Imprints of New Phenomena; **(3.1)** Determine the Nature of Dark Matter. In the following, we briefly highlight the main role of ACE in pursuing these goals.

(1.1) Parameters of the PMNS matrix are much less known than the corresponding parameters of the CKM matrix. Several models predict relations between the two. Therefore, an important goal will be to reach a similar level of precision. Future post-DUNE neutrino experiments with neutrinos produced from muon and anti-muon decays will allow the measurement of new oscillation observables through $\nu_e \to \nu_\mu$ and $\nu_e \to \nu_\tau$ transitions. **(1.2)** A future high-energy muon collider will be able to achieve the most precise measurements of several Higgs properties including the $WWHH$ and HHH couplings. **(2.1)** Several open questions in particle physics could be addressed by heavy NP particles with a mass beyond the LHC reach or by light NP particles that are only very weakly coupled to the SM (the "dark sector"). A high-energy muon collider will be able to probe new particles with a mass above 10 TeV. Future neutrino experiments, low energy muon experiments, and proton fixed target experiments will be able to produce and detect a broad range of dark sector particles with a mass at or below the GeV scale. **(2.2)** Lepton flavor universality (LFU) and lepton flavor number are two approximate symmetries of the SM. Searches for charged lepton flavor universality breaking and for charged lepton flavor violation (CLFV) are therefore paramount. A well balanced program should include tests of $\mu \to e$, $\tau \to e$ and $\tau \to \mu$ transitions. Exciting prospects to test CLFV at Fermilab are expected. In particular, the Advanced Muon Facility will push the bound on the New Physics scale responsible for $\mu \to e$ transitions to $\sim 10^5$ TeV, a factor of several larger than what is obtainable at the Mu2e experiment, and help elucidate the nature of new physics in case of an observation. This is complementary to what can be done at (present and future) high-energy colliders searching for the Higgs decay $H \to \mu e$. **(3.1)** The progress in DM direct and indirect detection experiments, together with LHC searches, have put under tension vanilla models for Weakly-Interacting-Massive-particle (WIMP) DM. However, several WIMP scenarios, including the famous Higgsino DM scenario, remain unprobed. A high-energy muon collider will be able to probe these scenarios for heavy DM up to masses above 10 TeV. DM could belong to a light dark sector of particles only feebly interacting with the SM. To achieve the observed relic abundance for a DM particle with a mass below the few GeV scale, additional dark sector particles are generically necessary. Fermilab high-intensity beams offer a broad set of opportunities to test the dark sector paradigm, from DM searches in missing momentum signatures at muon fixed target experiments to visible dark sector particle (dark photons, axions, ...) searches at proton beam dump experiments to the production of dark sector particles from meson decays at neutrino experiments.

Inspired by the above P5 physics drivers, we map them onto four primary experimental physics thrusts which are well-suited to the Fermilab ACE and around which we organize a future experimental program. Four sessions at the ACE Science Workshop focused on these experimental thrusts and are summarized below.

2.2.1 Muon Collider

The Muon Collider physics case is broad and exciting, including studying properties of the Higgs boson (including detailed characterization of the Higgs potential); rigorously testing predictions of the Standard Model (SM); investigating WIMP (Weakly Interacting Massive Particles) dark matter; exploring previously uncharted territories of quantum field theories; and enhancing research in the neutrino sector. Furthermore, the Muon Collider offers the potential for auxiliary fixed target and beam dump experiments to maximize its physics potential.

The path to eventual realization of a Muon Collider lies through a vigorous R&D program aimed at demonstrating key accelerator and detector technologies. In the workshop, R&D challenges for both the Muon Collider detectors and accelerator development were presented and discussed. On the accelerator side, the R&D plan includes development of a proton source compatible with the ACE plan, simulation of the proton accumulation and compression stages, and conducting experiments at existing facilities to demonstrate that the required proton bunch structure is attainable. The R&D plan also involves studies of high-power target materials and designing a comprehensive target station that includes proton beam delivery, a production solenoid, cooling systems, a beam dump, and a particle selection chicane. Experimental R&D studies of the target system would strongly benefit from the ACE beam. Beyond the proton driver and the target, ACE can offer a basis for a Muon Cooling Demonstrator facility that will allow the testing of key technologies related to ionization cooling. Such facility will consist of a muon source, a sequence of cooling cells, the upstream and downstream beam diagnostics instrumentation, and the associated infrastructure. The scheme will benchmark a realistic cooling lattice to give us the input, knowledge, and experience to design a real, buildable cooling channel for a Muon Collider. Such a demonstrator will require operation with proton beam, which ACE can potentially provide.

On the detector side, efforts to mitigate Beam-Induced Background (BIB) have demonstrated promising results through the application of innovative detector designs, advanced technologies (e.g. 5D detectors), and modern reconstruction software. The path forward involves substantial R&D on the promising detector technologies (e.g. LGADs, MAPs, Dual Readout Calorimeters) and potential synergies within the high energy physics community in development of the next generation of advanced reconstruction algorithms.

A key outcome of the workshop was that an 8 GeV linac provides more flexible design over an RCS for the Muon Collider proton driver. Another important outcome is that of the 6 configurations considered for ACE currently, all would need to be re-optimized to satisfy the needs of the Muon Collider proton driver.

2.2.2 Neutrino physics

At neutrino factories, the precise knowledge of muon energy and charge allows for highly accurate neutrino energy spectra and exceptionally clean neutrino beams. Charge-identifying detectors can effectively eliminate beam-related background, enabling high-energy neutrino beams to facilitate measurements of electron neutrino to muon neutrino and electron neutrino to tau neutrino oscillations, thereby opening up new oscillation channels and the potential for additional observables. Precision neutrino oscillation measurements are crucial for probing new phenomena, and with current projects like DUNE and Hyper-K underway, muon storage rings emerge as a promising next step. As the Muon Collider garners renewed interest, the neutrino factory concept could serve as an interim step or a complementary program, contingent on a solid physics case and community support.

Fermilab is currently hosting a leading accelerator-based short-baseline neutrino program, focusing on neutrino-argon interaction measurements, neutrino flavor conversion, and dark sector physics. This effort is supported by the Booster Neutrino Beam facility, which has exceeded performance expectations and benefited from decades of data collection by various experiments (MiniBooNE, SciBooNE, ANNIE, MicroBooNE, and the SBN program), resulting in a well-characterized beam. Future upgrades to the Booster and extended running post-2027 could significantly enhance the scientific contributions of this program. The discovery of a new physics signal within the SBN program would be transformative, prompting further investigation either through additional neutrino or antineutrino running. Exploring the feasibility of such additional runs, especially in light of potential Booster upgrades and in conjunction with the forthcoming SBN results, along with possible detector enhancements, is highly valuable for the field.

2.2.3 Charged Lepton Flavor Violation

Charged Lepton Flavor Violating (CLFV) processes are critical in the search for new physics, offering both a high scale reach and the ability to diagnose models by identifying the source(s) of flavor breaking. The study of these processes is highly complementary to searches performed at colliders. If new physics is discovered at the LHC or other experiments, CLFV can provide exclusive insights into its symmetry structure. Conversely, if new physics remains elusive, CLFV stands as one of the best methods to investigate the mass scale of such undiscovered phenomena. Thanks to the availability of intense sources and their relatively long lifetime, muons offer a promising avenue to search for these reactions. A global experimental program is underway in the US, Europe, and Asia, with anticipated improvement in sensitivity of several orders of magnitude during this decade. In particular, the Mu2e experiment [5] at Fermilab is expected to probe muon-to-electron conversion with discovery potential at $\sim 10^{-16}$, a factor 10^4 better than current limits.

Beamline upgrades and a new facility at Fermilab could further extend the discovery potential by orders of magnitude, a tremendous opportunity for the muon program. The Mu2e-II project [6] is a near-term evolution of Mu2e, planning to increase its reach by an order of magnitude. The Advanced Muon Facility (AMF) [7] is a more ambitious proposal for a new high-intensity muon science complex to enable broad muon science - including CLFV searches in at least four muon modes - with unprecedented sensitivity. The AMF complex is based on a fixed-field alternating gradient synchrotron (FFA) to create a cold, intense muon beam with low momentum dispersion. The FFA requires intense proton pulses with a bunch length of the order of 10 ns. A compressor is needed to rebunch the PIP-II beam to obtain the desired structure; several options have been laid out in the context of the ACE upgrade. This facility would provide a unique opportunity to fully exploit the capabilities of PIP-II to produce a world-class physics program. Its development also has strong synergies with current R&D efforts on a muon collider or a future dark matter program at FNAL, two key science priorities.

2.2.4 Accelerator-based dark sectors

Accelerators are key tools for probing dark sectors in the laboratory, particularly within the thermal dark matter regime, and they represent a strategic direction for new physics research at intensity frontier experiments. There is a robust theoretical and experimental push to explore the most plausible models of dark sectors.

The Fermilab Accelerator Complex is slated for upgrades to transition into the PIP-II era by the end of the decade, offering opportunities for additional enhancements as part of the ACE plan, such as incorporating an accumulator ring with short-pulse structures. These upgrades will open up significant physics opportunities, especially at a PIP-II beam dump facility that can accommodate various detector types with different thresholds in a dedicated experimental hall (see also Ref. [8]). Furthermore, existing and planned neutrino facilities are capable of searching for various dark sectors, often in tandem with their primary neutrino research objectives, across different energy ranges (800 MeV, 8 GeV, 120 GeV) that complement each other. Finally, the 120 GeV proton fixed target experiments provide an additional opportunity to searches for dark sectors that are sensitive to a broad spectrum of models. The proposed DarkQuest upgrade [9] to the existing SpinQuest experiment is envisioned

as a catalyst for a sustained dark sector research program, leveraging existing infrastructure for new explorations in a short timeframe and with potential for further enhancements in detector and beam technology to increase sensitivity.

2.3 Additional technology and physics directions

The workshop included contributions from the community that spanned additional physics ideas, accelerator R&D, and detector concepts that should be considered in the design of ACE. These could be provide synergy with the initially identified physics thrusts or may provide additional important motivations or directions for the future facility.

2.3.1 Physics experiments

KPIPE [8 GeV] The KPIPE project aims to employ an extensive liquid scintillator detector to investigate the disappearance of ν_μ neutrinos over a considerable distance, focusing on 236 MeV kaon decay-at-rest (KDAR) ν_μ CC events. It relies on a pure and mono-energetic flux of muon neutrinos for its observations. The extended length of the detector is crucial for accurately measuring the oscillation wave. Notably, KPIPE demonstrates strong sensitivity, particularly effective in scenarios with high-δm^2 values. It serves as a valuable addition to the SBN program, offering complementary insights. Additionally, KPIPE is distinguished by its cost-effectiveness. The 8 GeV proton beam requirements for KPIPE are high power and low duty factor, typically around 10^{-5}.

FerMINI [120 GeV] The FerMINI at MINOS experiment focuses on the exploration of millicharged particles (mCP) through a fixed-target setup employing stacks of scintillators. It investigates triple or double coincident signatures as indicators of the presence of mCPs. There are several motivations behind the study of mCPs including the concept of charge quantization within the framework of Grand Unified Theories (GUTs) and string compactifications; a direct connection to models involving dark photons; and a connection to the 21 cm absorption spectrum, offering insights into fundamental aspects of cosmology and astrophysics.

LongQuest [120 GeV] LongQuest, operating within the current NM4 SpinQuest facility, is dedicated to the pursuit of long-lived particle searches. This initiative has several advantages and distinctive features. Firstly, it offers superior shielding, ensuring minimal interference with ongoing SpinQuest operations. Additionally, the facility could also serve as an alternative site for the FerMINI project. One of the key components of LongQuest is its dark photon decay fiducial volume. Positioned at a baseline distance ranging from 33 to 37 m, this volume is specifically designed for the measurement of di-electrons or di-photons. Equipped with additional EMCal (Electromagnetic Calorimeter) and pre-Shower Detectors, this setup is sensitive to a range of dark sector physics scenarios with an expected 10^{18}-10^{20} Protons on Target (POT).

REDTOP [$\leq$ 2 GeV] The REDTOP (Rare Eta Decays To Probe New Physics) experiment is being proposed, with the intent of collecting a data sample of order 10^{14} η (10^{12} η') mesons for studying very rare decays. Such statistics are sufficient for investigating several symmetry violations, and for searching for particles and fields beyond the Standard Model. Utilizing a high intensity proton beam of $\leq$ 2 GeV, REDTOP will have sensitivity to processes that couple the Standard Model to New Physics through all four of the so-called *portals*: the Vector, the Scalar, the Axion and the Heavy Lepton portal. The sensitivity of the experiment is also adequate for probing several conservation laws, in particular CP, T and Lepton Universality, and for the determination of the η form factors, which is crucial for the interpretation of the recent measurement of muon $g-2$.

Muon Beam Dumps [$\leq$ 2 GeV or 8 GeV] Muon-beam dump experiments serve as excellent platforms for the exploration of dark scalars and other light dark sector particles, primarily due to their focus on muon couplings and their sensitivity to displaced decays. These experiments also offer the advantage of seamless integration with other muon-related research endeavors. Notably, the investigation of muonic dark sectors presents a promising avenue for addressing anomalies associated with muons, such as the muon g-2 anomaly. FNALμ, a prominent example, can be feasibly implemented within the existing infrastructure of Fermilab with minor modifications or additions, further enhancing its appeal and potential for significant scientific discovery.

DAMSA [$\leq$ 2 GeV] DAMSA (Dump produced Aboriginal Matter Search at an Accelerator) [10] is a very short baseline beam-dump experiment aimed at uncovering Dark Sector Particles (DSPs) using high-intensity, low-energy proton beams. Developed for 600 MeV proton beams initially, DAMSA is now adaptable to the 800 MeV PIP-II and ACE beams, offering compatibility with Fermilab's infrastructure. With collaborative efforts from ten US institutions and eight South Korean institutions, DAMSA presents an exciting opportunity to transform Fermilab's accelerator facilities into world-leading DSP research hub.

Muonium and future muon physics [$\leq$ 2 GeV] Both the muonium–antimuonium (M-$\bar{\text{M}}$ (M is a bound μe atom) and Mu2e experiments are critical and complementary in rare and precision physics searches. While muonium–antimuonium spectroscopy's previous results are over 20 years old, indicating a ripe opportunity for new efforts, the exploration of muonium gravity (testing antigravity on the μ^+) has never been feasible until now, with the development of new techniques like SFHe

production. The Muon Test Area (MTA) presents a unique opportunity to kickstart a leading Fermilab muonium program, facilitating initial investigations into muonium–antimuonium oscillations, spectroscopy, and gravity, each offering unique insights into new physics phenomena. These experiments hold promise for shedding light on CLFV physics and providing a novel avenue for testing gravitational couplings in the second generation.

Muon fixed target missing momentum [120 GeV] The M^3 experiment utilizes the muon missing momentum technique to search for dark matter. Unlike LDMX, which employs electron beams, M^3 employs a muon fixed target experiment, necessitating adjustments to the detector, including a thicker target. The experiment requires a low current muon beam with individual muons having energies greater than or equal to 10 GeV. Additionally, the muons must be individually identifiable, with an expected range of 10^{10} to 10^{13} Muons on Target (MOT). Phase 1 (10^{10} MOT) focuses on achieving complete coverage of the g-2 region, enabling the detection of any invisibly-decaying particle lighter than the muon. Phase 2 (10^{13} MOT) allows for the exploration of large portions of the well-motivated dark matter parameter space with an increased MOT count.

Accelerator driven nuclear reactors [$\leq$ 2 GeV] Mu*STAR, short for Muons' Subcritical Technology Advanced Reactor, is an accelerator-driven subcritical reactor (ADSR) designed to burn spent nuclear fuel from other reactors to produce carbon-free nuclear energy. It offers a viable solution to nuclear waste disposal while meeting public and legal demands for responsible nuclear technology.

Exploration of TMDs at a SpinQuest upgrade together with the Dark sector Physics [120 GeV] The extension of the upcoming SpinQuest (E1039) experiment aims to extract gluon transversity distributions from the Deuteron target (ND3). The prospective advancements of the Fermilab's Accelerator Complex Evolution (ACE) plan, enable not only the extraction of gluon transversity distributions with greater statistical accuracy with a deuteron target but also with a range of tensor-polarized nuclear targets with spin ≥ 1 to explore the nuclear dependences. The high-intensity beam and optimized timing between proton spills facilitate the uniqueness of Fermilab's capability for precise polarized target asymmetry measurements in Drell-Yan scattering. Also, this approach opens up the opportunity to measure ten additional leading twist quark transverse-momentum-dependent distributions (TMDs) for tensor-polarized targets, which have not been previously investigated well. The investigation will primarily focus on studying these TMDs through the Drell-Yan process, providing valuable insights into the nuclear EMC effect, as well as the 3-dimensional structure of the nucleon, supported by lattice QCD insights into nucleon spin components, marks a significant advance in understanding strong force, color confinement, and partonic interactions, setting a new standard for spin physics research. Additionally, the investigations into the Dark sector physics [9] will also be conducted at the NM4 facility, concurrently on the 120 GeV Main Injector, representing the proposed SpinQuest-upgrade.

Dedicated Muon EDMs [$\leq$ 2 GeV] A potential EDM experiment could be conducted in the g-2 storage ring by modifying the quadrupole system to generate a radial electric dipole field pointing inward, with minimal changes to the current setup, except for altered orbit curvature and a higher potential difference across the inner/outer plates to create the electric field. The adaptation would allow for a significant reduction in the requirements for the existing magnetic dipole field, inflector, and kicker systems.This setup presents an excellent chance to explore the systematics for a future dedicated run, marking the first application of the frozen spin technique and potentially enabling physics EDM measurements within a limited timeframe. Such an experiment could serve as a valuable proof of concept for a future dedicated EDM physics experiment.

2.3.2 Technology development

Test Beams: FTBF [120 GeV] and ITA [800 MeV] The Fermilab Test Beam Facility (FTBF) plays a critical role in supporting a broad spectrum of research and detector development with its two main beamlines, MTest and MCenter, offering particles ranging from 120 GeV protons to secondaries of approximately 200 MeV. Additionally, the facility includes an Irradiation Test Area (ITA) that provides low energy, high rate protons (400 MeV at 2.2e15 protons/hr), with the beam available for about eight months a year, from November through June. MTest facilitates short-term projects with a proton beam of 120 GeV and secondary beams between 1-66 GeV, whereas MCenter caters to longer-term experiments with its secondary and tertiary beams down to 200 MeV.

Despite the extensive capabilities and heavy demand from significant projects like CMS, ATLAS upgrades, and various neutrino-related experiments, the FTBF faces challenges such as over-subscription by 10-20%, aging infrastructure in the switchyard line, and substantial downtime that impacts experiment schedules. The increasing need for clean, low energy secondary beams and the potential discontinuation of the ITA in the absence of LINAC operations in the PIP-II era underscore the pressing requirements for facility updates and expansions to accommodate evolving research needs, including a high-intensity 800 MeV irradiation area for comprehensive particle exposure studies.

High Powered Targetry This is discussed more as a part of Section 3.7.

Time Slicing of Neutrino Fluxes in Oscillation Experiments By utilizing a higher-frequency RF bunch structure for the primary proton beam on target and employing precision timing to select different energy and flavor spectra from a wide-band neutrino beam, based on the neutrinos' relative arrival times with respect to the RF bunch structure, we propose a 'stroboscopic' method. This approach is complementary to techniques that differentiate neutrino energy spectra based on their angle relative to the beam axis, allowing for the selection of varying energy spectra from the same on-axis detector and applying equally to both near and far detectors in an oscillation experiment. Discriminating energy and flavor of neutrinos produced by in-flight hadrons necessitates proton bunch lengths on the order of 100 ps and comparable time resolution in the detector. The correlation of neutrino events with the parent proton interaction is currently hampered by the nanosecond-scale width of the proton bunches targeting the beam. By employing a superconducting RF cavity to rebunch the existing 53.1 MHz RF bunch structure at a tenfold higher RF frequency, the requisite shorter bunch length can be achieved.

Fast tracking for triggering High-rate experiments at PIP-II / ACE could potentially enhance their physics capability significantly through the use of track triggers for signal identification, background rejection, and overcoming the challenges posed by sub-optimal beam timing structures. The success of this approach hinges on the deployment of sufficiently fast and granular tracking detectors. It's crucial to evaluate which experimental signatures, such as those from REDTOP and other experiments, would benefit the most from the incorporation of track triggers, thereby boosting the overall performance and outcome of these high-rate scientific endeavors.

3 Physics, detector, and accelerator complementarity

3.1 CLFV - Dark Sectors

Editors: Matt Solt, Jure Zupan

The advantage of accelerator-based dark sector experiments over direct detection experiments is their relative insensitivity to specific dark matter models due to semi-relativistic versus non-relativistic scattering. Moreover, accelerator-based experiments can perform many type of searches and probe a variety of dark sector models at pp collider, e^+e^- colliders, proton and electron fixed target experiments, and beam dump experiments. One can search for visible final states, either by searching for promptly decaying resonances or displaced vertices, or for invisible final states through various kinematic handles: missing mass, missing momentum, and missing energy. The CLFV decays into light new physics states, should such states be found, would have a parametrically enhanced reach to high effective mass scales. For example, classic CLFV observables (such as $\mu \to e$, $\mu \to e\gamma$ and $\mu \to 3e$) probe scales at the level of $\sim 10^6$ GeV, the decay $\mu \to ea$, where a is an axion, would probe a scale of 10^9 GeV.

A clear outcome of the session was that the physics cases for performing CLFV measurements and dark sector searches is very strong, with much of the discussion devoted to outline R&D direction to achieve the optimal physics program:

- **How do we maximize probing CLFV and dark sector searches with PIP-II and ACE capabilities?** Through discussions with accelerator experts, a strong case was made to build a compressor ring in stages, build it as soon as possible, and make sure that both the AMF and the beam dump programs are possible. The preferred option would be to build a 2 GeV ring, but operate it first at 0.8 GeV. Accelerator physics considerations showed this should be possible, but the optimal scenario to operate the ring should be refined.
- **What type of beam?** Different experiments prefer different beam operation parameters, and the beam structure depends on how the dark sector is being sourced. Short bunches are probably preferred if it is produced in primary collisions, while the duration of the pulses are less important if it is from muon decays (e.g. from stopped muons).
- **Exotic signatures.** The exotic signatures such as $\mu \to 5e$, $\mu \to ea$, ..., are interesting, but they are most motivated if they can be done already as part of an experiment aimed at some of the golden signatures (e.g., $\mu \to e\gamma$, $\mu \to e$ conversion, $\mu \to 3e$).
- **Muonium program.** There are other probes such as muonium-antimuonium oscillations, which are complementary to the rest of the program, since they probe different type of physics, though perhaps more exotic.

3.2 CLFV - Muon Collider

Editors: Bob Bernstein, Sergo Jindariani, Diktys Stratakis

Future Lepton Flavor Violation experiments (e.g. AMF and Mu2e-II) and the Muon Collider (MC) present a number of potential research and development (R&D) opportunities, particularly in accelerator, target, and magnet technologies, that could complement each other and that was the main subject of the discussion. The following components were discussed: the Production Solenoid, the Target, the Compressor Ring, and the Fixed Field Alternating (FFA) Gradient synchrotron. For each component, design parameters for Mu2e-II, AMF, and MC were laid out for commonalities and overlaps.

After the discussion, it became evident that the Production Solenoid has some clear areas of overlap between Mu2e-II, AMF, and the MC. The study of megawatt-class targets is important for all experiments in the 800 MeV to 8 GeV range as AMF and the MC have similar requirements for target beam power, while Mu2e-II has lower requirements. The protection of the superconducting solenoid will be important in all cases as well as the materials under consideration. As the designs of the production solenoids for each experiment evolve, it will be important to understand the synergies and potentially build a common team and test infrastructure for this R&D.

The proton Compressor Ring is another area of synergy although the requirements in energy and bunch length are about an order of magnitude different. Technologically, there are some synergies in the R&D but significant differences in requirements make it unlikely that the same ring can be used for both facilities. For the muon storage/accelerator FFA, because of the large difference in the required energies, the designs do not have a lot of overlap and this is the least likely area of complementarity.

In general, the exploration between the MC and AMF/Mu2e-II offered some interesting directions for a collaborative R&D program that could benefit both experimental thrusts. Shared tools and techniques such as simulation efforts can accelerate progress and cultivate joint expertise.

3.3 CLFV - Neutrinos

Editors: Innes Bigaran, Ryan Plestid, Anil Thapa

Neutrinos are a unique probe of lepton flavor symmetries. Within the standard model, lepton flavor symmetries L_e, L_μ and L_τ are accidentally conserved: their conservation is not built into the theory but is emergent. There is no reason why some more complete theory should continue to preserve these symmetries. Indeed, the measurement of neutrino flavor oscillations (which provides evidence of nonzero neutrino masses) indicates that some physics beyond the renormalisable standard model must break these flavor symmetries. Neutrino masses in some extended theory could be either Dirac or Majorana in nature, where the latter could imply a violation of total lepton number $L = L_e + L_\mu + L_\tau$. Moreover, charged leptons and neutrinos are linked by $SU(2)$ symmetry: as left-handed leptons, they are part of the same electroweak doublet, which leads to many neutrino mass models naturally giving rise to CLFV that can be searched for at experiments.

Our discussion focused on highlighting how CLFV and neutrino experiments could mutually enrich the understanding of fundamental physics, particularly in light of the ACE upgrade. We separated the discussion into three stages: a discussion of CLFV experiments, of neutrino experiments, and complementarity between the two. What emerged as a key take-away message from our discussion was the need for closer interactions (a) between experimentalists in both CLFV and neutrinos, and (b) coordination between theory and experiment, on how best to move forward with united efforts to further explore this interplay. Some topics which were discussed in detail are listed below.

- *Could we have neutrino-mass motivated targets for CLFV experiments?*
  CLFV processes involving the muon, i.e. $\mu \to e\gamma$, $\mu \to e$ conversion on nuclei, and muonium oscillation can be enhanced in various extensions to the SM that incorporate neutrino masses. Upgrades of experiments probing these processes are part of the ACE upgrade proposal, e.g. Mu2e-II, other CLFV muon decay probes. Models extended by right-handed neutrinos (e.g. type-I seesaw) can lead to large effects in CLFV if one explores the flavor structure of Dirac masses. Furthermore, extensions of the SM with exotic scalars (e.g. type-II seesaw) have a Yukawa coupling structure which correlates neutrino oscillation with CLFV decays.

- *Could the ACE upgrade make it viable for Fermilab to become a world-leader in the study of muon decays and muon conversion?*
  Developments of the advanced muon facility (AMF) mean that Fermilab will be a site where the sheer flux of muons produced will be beyond what has been seen elsewhere in the world. Given that this will be the case, then could we harness these muons to do all manners of study of their rare properties? There was broad consensus that provided the muon facility is designed to allow for efficient storage of both μ^+ and μ^- then Fermilab is well positioned to offer the best experiments in all three golden channels of CLFV.

- *Is there a strong physics case for a tau optimized flux?*
  Neutrino oscillation experts broadly agreed that such a case is complementary rather than foundational. Statistics will be limited in tau samples, and atmospherics offer an existing probe of the ν_τ sector with better statistical capabilities (and without the difficulties inherent to reconstructing $\tau^\pm$ leptons).

- *Could there be room for a neutrino factory-like concept at an AMF or a future muon collider?*
  An advantage of having neutrinos produced from muon decay rather than from meson decays is that they have a well-known energy and flavor spectrum. AMF with a muon storage ring could be extended to allow muons to decay and produce a focused beam of neutrinos, which would be essential for precision measurements of neutrino properties. Neutrino factories have historically been considered with a ~ 1 GeV muon storage ring; roughly commensurate with

the needs for a muon collider. CLFV experiments prefer a much lower energy, the AMF plan is for a $\sim 20-30$ MeV storage ring with an alternate technology (a fixed field alternating gradient synchrotron). From the perspective of neutrino oscillation physics, the absolute energy scale is not crucial but rather sets the necessary baseline. The tight momentum resolution of the AMF storage ring would allow for a nearly mono-energetic neutrino source. Drawbacks include a smaller boost factor and therefore wider opening angle for the neutrino beam. The broad consensus was that this was worth further investigations.

Although slightly beyond the scope of our discussion group, there was also interest expressed in a controlled neutrino source for hadronic physics studies,

- *Could there be scope for neutrino and/or muon deep-inelastic scattering (DIS) experiments in the ACE upgrade?* Muon DIS on polarized targets (an extension of Spin-Quest) could provide a fundamental understanding of the structure of nucleons. Polarized neutrino DIS experiments would open-up new opportunities to understand neutrino scattering cross sections, which are paramount for interpreting future results from experiments like DUNE. In general, these experiments can provide further information about the spin-structure of nucleons and allow for more precise measurements of neutrino properties. Moreover, deviations from SM predictions for neutrino-nucleon interactions could indicate the presence of new-physics effects.

3.4 Dark Sectors - Muon Colliders

Editors: Cari Cesarotti, Yonatan Kahn

The discussion on the complementarity between dark sector experiments and muon colliders proceeded in two stages:

How to leverage *current* muon beams for dark sector searches. We concluded that the requirements for muon beam cooling demonstrators are in some sense maximally orthogonal to the needs for dark sector experiments, which typically require high-intensity beams, a large integrated luminosity, and a regular bunch structure. However, we identified a promising possibility for a future experiment: using the discarded forward muons from Mu2e for a new beam dump experiment. The 8 GeV proton beam results in $\sim 10^{19}$ POT/year, integrating to about 10^{21} POT after PIP II in 2028–2029. Roughly 1% of these protons will result in muons with energy of ~ 3 GeV or above, of which Mu2e only uses a negligible fraction. The time structure of the beam is not amenable to a missing momentum search, but a search for long-lived muonphilic particles with mass below $2m_\mu$ which decay to electrons or photons seems possible if a detector could be placed $\mathcal{O}(10\text{ m})$ away. Investigating the feasibility of this setup would be an excellent synergistic use of the Fermilab accelerator facilities. While we are particularly interested in a muon beam for the ultimate muon collider, it is worth noting that the proton beam necessary for producing the muons could also be leveraged for auxiliary experiments as well.

How to leverage *future* muon colliders for dark sector searches. To date, muon collider physics studies have mostly focused on Higgs and electroweak precision phenomenology, as well as new particle with electroweak couplings. To our knowledge, a comprehensive study of weakly-coupled dark sectors (for example, the minimal dark photon, or a muon-specific dark force) at the collider itself has not yet been undertaken (though there have been studies of using the muon beam in a beam dump experiment). In addition, as was emphasized in Ian Low's talk, muon colliders may have access to yet another dark sector portal, the neutrino portal, due to the fact that neutrinos may be visible through their electroweak radiation in calorimeters. Investigating this unique feature of muon colliders may lead to new ideas for dark sector searches, for example those involving right-handed neutrinos, through a long-lived particle experiment analogous to FASER at the LHC.

3.5 Dark Sectors - Neutrinos

Editors: Bhaskar Dutta, Alex Sousa, Jacob Zettlemoyer

In the dark sector and neutrino discussion session, we considered a number of questions around the ACE plans and how the Fermilab neutrino and dark sector program may benefit from the ACE options. We note that complementarity exists within ACE to optimize the location and detection threshold of our detectors to probe a wide range of physics in the neutrino and dark sectors. There is obvious synergy between the detector technologies used for neutrino and dark sector physics. A constant theme of our discussion was the use of beam timing to increase the physics scope or neutrino and dark sector searches, either through coupling PIP-II to a proton accumulator ring, or using the nanosecond pulse structure of PIP-II operating in continuous wave (CW) mode.

We also explored potential options to extend the reach of dark sector search experiments to unexplored regions of parameter space. A PIP-II beam dump facility equipped with a high-Z target, and/or a higher beam energy, with judicious choices of detector location would offer excellent opportunities to probe new ranges of dark sector particle masses. Enhanced kaon production and detection would enable particularly sensitive searches.

We discussed the broad ideas for producing and detecting dark sector particles and possible gaps in what we were considering. Some examples include light dark matter, axion-like particles, heavy neutral leptons, and millicharged particles.

Gathering notable interest during the discussion, was the possibility of using resonant π^0 production at neutrino experiments for complementarity with the dark sector parameter search space using precision measurements of Dalitz decays or pion production.

We discussed how the options under ACE would benefit the DUNE experiment, the current flagship neutrino experiment located in the US. The discussion around the physics scope expansion focused on the ν_τ sector where an expansion of the beam power or energy beyond the baseline under ACE could enable significant inroads into improving our knowledge of this very difficult to measure sector. We noted that it may be possible under ACE to go beyond 2.4 MW, with the likely primary constraints being the target and absorber capabilities. Those constraints notwithstanding, reaching a beam power as high as 4 MW might be possible, with the limitation on the accelerator at that point becoming space charge effects. Additional discussion touched on the capability of the Main Injector to support such enhancements.

We discussed possible detector technologies that we could deploy at PIP-II under ACE for neutrino and dark sector searches. Some of these options are being explored in more detail and were discussed at a recent PIP-II Beam Dump Facility Workshop held at Fermilab in May 2023, with a white paper (Ref. [8]) summarizing the discussions in more detail. Interesting possibilities include water-based liquid scintillator (WbLS), granular detectors such as the LiquidO technology, fast tracking or fully pixelated detectors expanding upon the capabilities of liquid argon TPCs, optical liquid argon detectors with high photocathode coverage, enabling searches for keV-scale physics and expanding the range of dark sector models for which the detector is sensitive. Another possibility are CCD detectors performing powerful searches for millicharged particles. We considered possible synergies with the large tracking detectors used in collider experiments along with direct dark matter detection experiments in exploring how to improve detector development dedicated to searching for dark sector particles.

Further discussion centered on probes of new physics enabled by running the neutrino beam facilities in a beam dump mode, similar to how MiniBooNE operated previously, to pioneer proton beam dump based searches. The main advantage of running in this mode is the drastic reduction of the neutrino decay-in-flight and possible neutron backgrounds affecting new physics measurements by short-baseline detectors. We noted this is a possibility for the SBND detector once PIP-II comes online, making use of the BNB beamline in the PIP-II era, especially before the LBNF beam becomes operational. We note that a beam dump could be installed at the BNB to allow both on- and off-target running concurrently. This could provide a powerful tool for searching for light dark matter due to the detector distance from the target and the lower energy such that it covers complementary parameter space to other planned experiments.

We also discussed other beam dump possibilities that are enabled by the ACE plan. Some experiments such as PIP2-BD can take advantage of the powerful timing capabilities of an $\mathcal{O}(1)$-GeV accumulator ring coupled to the PIP-II Linac. The Switchyard beamline could offer another potential location for a new beam dump facility, though significant investment would likely be required.

There was an additional comment during the summary session about the increasing synergies of the neutrino and nuclear physics communities. Understanding neutrino-nucleus interactions is becoming essential to make precision measurements and predictions in the neutrino sector, while at the same time there is significant interest in studying nucleon and nuclear structure. One possible question in this direction is whether Fermilab under the ACE plan could provide something unique beyond the HEP community, with one example being nuclear physics measurements using neutrinos produced from a very intense GeV-scale muon beam. Such a beam, with high-precision knowledge of the muon flux, could enable detailed studies of neutrino-nucleus interactions.

3.6 Muon Collider - Neutrinos

Editors: Christian Herwig, Zahra Tabrizi

Projects such as the Deep Underground Neutrino Experiment (DUNE) and Hyper-Kamiokande (Hyper-K), now under construction, aim to achieve the statistical precision necessary to explore leptonic CP-invariance violation. These experiments, along with JUNO, are poised to conduct precision studies on various oscillation parameters, contributing to our understanding of neutrino physics and potentially shedding light on phenomena such as the MSW effect.

Neutrino factories, proposed around the time neutrino oscillations were discovered, offer a distinct approach to generating neutrino beams using muon decay and storage rings. Despite challenges in muon production and acceleration, these facilities present high luminosity and well-defined beam properties, making them ideal for studying neutrino oscillations. The synergy between neutrino factories and muon colliders is evident, as both face similar technological hurdles and stand to benefit from shared advancements.

Given the rich physics opportunities afforded by neutrino factories and the need to prepare for future neutrino physics programs beyond DUNE, detailed studies on their complex and detectors are timely. These efforts are crucial for advancing our understanding of fundamental physics and unlocking new discoveries in the realm of neutrino science.

The ACE upgrade presents various aspects potentially aligned with the needs of a muon collider, such as shared accumulator rings, though the extent of alignment depends on specific considerations. Discussions from other sessions, including S.

Nagaitsev's talk, provide further insights on these commonalities and may serve as a natural starting point to updated ACE-BR design proposals. However, any of the high-power proton-driven systems put forth as a part of the ACE-BR study can offer numerous opportunities for neutrino sources beyond decay-in-flight pions, including processes such as pion DAR, kaon decay, and muon decay.

Considering the post-DUNE/Hyper-K era, questions arise regarding the ideal experiment in light of anomalies persisting or dissipating. Should anomalies persist, a neutrino factory could offer valuable exploration avenues, while alternative scenarios prompt the consideration of other experimental avenues. In addition to this, a neutrino factory presents the compelling possibility to indirectly search for New Physics in a manner synergistic with high-energy probes through the effective field theory approach, by matching WEFT and SMEFT parameters across energy scales.

In addition to the neutrino factory concept, high-energy neutrinos produced in MC collisions allow the possibility to conduct new measurements and searches through novel processes such as $\nu\bar{\nu}$ fusion processes. Auxiliary MC detectors, akin to FASERNu, may facilitate investigations into additional new physics domains in addition to probing neutrino interactions at some of the highest energy scales. Furthermore, there is potential for novel measurements using high-energy neutrinos, with the physics case for such endeavors well-established since the inception of the neutrino factory concept. Exploration of topics such as Higgs-neutrino couplings and mapping the neutrino floor for dark matter detection are among the intriguing possibilities in this context.

3.7 Accelerator technology and R&D

Editors: Jeff Eldred, Vladimir Shiltsev

There were two talks at the Accelerator Parallel Session of the ACE Science Workshop providing technical overviews of the ACE Booster Replacement (ACE-BR) accelerator upgrade configurations. The first three ACE configurations involve a 2 GeV upgrade of the PIP-II Linac and a new 8 GeV RCS. The second three ACE configurations involve an 8-GeV upgrade of the PIP-II Linac and a new 8-GeV accumulator ring (AR). Overall the configurations concepts feature detailed technical design for many subsystems and have well-precedented projections of accelerator performance [11, 12].

Since the time of the workshop, P5 has called for the development of a new strategic 20-year plan for Fermilab accelerator (Area Recommendation 12) oriented towards a future collider program (Recommendation 6). The ACE-BR scenarios were a detailed look at the proton accelerator complex upgrades with a core mission focus on the DUNE neutrino program. Consequently the exercise was able to identify R&D items for accelerator development that are highly relevant to the P5 vision, but more work is needed to redevelop the specific upgrade scenarios towards incorporating future collider programs. More broadly, the critical need for advancements in accelerator R&D is called out in P5 Recommendations 8-10.

The speakers were asked to identify technical risks and corresponding R&D areas and raised a few topics. For both types of ACE-BR configurations, H^- foil-stripping injection was identified the greatest technical challenge and most constraining performance limit. H^- foil-injection requires managing particle loss scattering off the injection foil as well as mechanical degradation of the foil itself due to beam heating effects. Careful optimization of the H^- foil injection section should proceed in parallel with development of H^- laser-stripping technology (e.g. at Oak Ridge SNS [13]). Aside from injection, the ACE-BR configurations benefit from continuing innovations and improvements in SRF cavity and RF power technology, from Q-factors to accelerator gradients to achievable pulse length [12, 14]. Lastly, two "RCS" ACE-BR configurations require use of metallized ceramic beampipes which would benefit from early prototyping (following J-PARC's precedent [15] but with new parameters and vendors).

One talk at the Accelerator Parallel Session addressed targetry development for the next-generation Intensity Frontier programs. The ACE Main Injector Ramp and Targetry (ACE-MIRT) plan has DUNE/LBNF beam powers increasing to multi-MW much faster than originally projected (ideally 2 MW around the 2033 possible end of Mu2e run), and in parallel envisions staging a series of neutrino (i.e. low-Z) targets rated for increasingly greater beam powers. Although the instantaneous thermal shock on the LBNF targets are not impacted by the increased repetition rate, the target lifetime will be impacted by the more rapidly accumulating radiation dose on the target materials. P5 called out the ACE-MIRT program in broad terms as part of Recommendation 2a.

In fact, high-power operations requires all targetry materials to perform at a higher accumulated dose; consequently the study of the performance of a variety of irradiated materials is a critical R&D area. The Radiation Damage In Accelerator Target Environments (RaDIATE) collaboration has studied the performance of irradiated materials using the Brookhaven Linac Isotope Producer (BLIP) but there may be the opportunity to enhance Fermilab's proton irradiation capabilities using the PIP-II linac beam or the 8-GeV extracted beam [16, 17].

The ACE upgrade plan for the Fermilab proton complex envisions a diverse and growing science program at 2 GeV, 8 GeV, 120 GeV. Several of these programs may need targetry R&D program programs of their own. In particular a significant synergy has been identified in the needs of the the Muon CLFV and Muon Collider programs (see Section 3.2 on the complementarity session). The programs require narrow high-Z targets for pion production in a large acceptance solenoid and it should be noted

that Mu2e, Mu2e-II, AMF, and MuC proposals form a natural sequence of ever more ambitious targetry needs. To this end, the muon programs need not only the study of irradiated materials, but also the development and testing of target concepts.

One staging strategy for the AMF or MuC front-end could be to begin a target demonstrator facility at a lesser proton power as soon as possible, with a path to upgrade proton power, targetry, and physics capabilities as the facility matures. For AMF, this could involve the construction of a compact accumulator ring (also called proton compressor) to deliver 200-400 kW 20 ns proton pulses at 0.8 GeV. The program would serve a beam dump physics program [18] and a muon production target demonstrator initially, but compatible with 1+ MW beam power for AMF with a subsequent energy upgrade of the PIP-II linac. For the MuC front-end, this could involve a 8 GeV H^- linac operating at 5mA for 2ms every 10 Hz into an 8 GeV AR (i.e. an ACE-BR configuration) for a 800 kW target demonstrator. Subsequently, the 8 GeV linac current would be upgraded to 10-20mA (1.6-3.2 MW), and a 8 GeV compressor ring and combiner beamline would be constructed to shorten the pulses from the 8-GeV AR for the MuC proton driver front-end.

One talk at the Accelerator Parallel Session specifically addressed immediate Muon Collider R&D needs. P5 called for collider R&D in Recommendation 4. In addition to the targetry development program, R&D for high gradient RF in strong magnetic fields is needed for the cooling cell design. Within the next five years, the talk calls for a (1) conceptual design for a muon cooling demonstrator facility, (2) site identification and cost estimates for a muon cooling demonstrator facility, and (3) to begin fabrication of a prototype cooling cell for the facility. At Fermilab, the 8 GeV beamline and (ACE era) 2 GeV linac beamline are being investigated as locations to host the muon cooling demonstrator.

The final talk at the Accelerator Parallel Session discussed the PIP-II Accumulator Ring (PAR) proposal, a 0.8 GeV AR sited in between the PIP-II linac and the Fermilab Booster. The PAR ring would facilitate injection into the Fermilab Booster and provide a new PIP-II era experimental program. If the PAR ring could be constructed on a sufficiently aggressive timetable, it would provide excellent value in shortening the timetable for beam commissioning to LBNF. Regardless of timing, the PAR ring would concurrently be capable of a 100 kW low-duty factor proton program for beam dump physics [18]. However, the requirement of facilitating injection into the Booster (thereby benefiting the LBNF timeline) comes with tradeoffs for providing powerful beam to GeV-scale experiments. If the AR design had a more compact circumference (instead of matching Booster) it would deliver shorter pulses to experiments (improving the physics reach). Secondly, if the ring were not sited near the Booster, it could be compatible with a later energy upgrade when the PIP-II linac is extended (see staging discussion for AMF above). A conceptual design for an AR with this approach is under development.

Not directly discussed in the Accelerator Parallel Session were the requirements of optimizing the reliability of the Fermilab Booster. Later, P5 highlighted the need for the assessment of Booster reliability and the identification of pro-active measures to guarantee the longevity of Booster operations. On March 5th, 2024 a mini-workshop "AD Prep for DUNE PIP-II Era Workshop" will be held as a preliminary measure towards addressing this important topic. Whether any new upgrades for Booster reliability should be incorporated into ACE-MIRT or considered as standalone items is also a matter to be determined on a case-by-case basis.

Acknowledgments

We would like to thank all the speakers of the workshop for their time and expertise in preparing and giving their presentations. In particular, we thank Sergey Belomestnykh, David Sperka, Ishara Fernando, Evan Niner, Jaehoon Yu for their feedback on this report. We would also like to acknowledge all of the attendees of the workshop for their comments and contributions which provided valuable input and lively discussion.

References

1. ACE Science Workshop. https://indico.fnal.gov/e/aces2023 (2023).

2. Ainsworth, Robert et al. Report from the Fermilab Proton Intensity Upgrade Central Design Group. https://indico.fnal.gov/e/aces2023 (2023).

3. Butler, J. N. *et al.* Report of the 2021 U.S. Community Study on the Future of Particle Physics (Snowmass 2021) Summary Chapter. In *Snowmass 2021* (2023). 2301.06581.

4. Muryamama, H. *et al.* Exploring the Quantum Universe: Pathways to Innovation and Discovery in Particle Physics. https://www.usparticlephysics.org/2023-p5-report/ (2023).

5. Bartoszek, L. *et al.* Mu2e Technical Design Report (2015). 1501.05241.

6. Byrum, K. *et al.* Mu2e-II: Muon to electron conversion with PIP-II. In *2022 Snowmass Summer Study* (2022). 2203.07569.

7. Aoki, M. *et al.* A New Charged Lepton Flavor Violation Program at Fermilab. In *2022 Snowmass Summer Study* (2022). 2203.08278.

8. Aguilar-Arevalo, A. A. *et al.* Physics Opportunities at a Beam Dump Facility at PIP-II at Fermilab and Beyond (2023). 2311.09915.

9. Apyan, A. *et al.* DarkQuest: A dark sector upgrade to SpinQuest at the 120 GeV Fermilab Main Injector. In *2022 Snowmass Summer Study* (2022). 2203.08322.

10. Jang, W. *et al.* Search prospects for axionlike particles at rare nuclear isotope accelerator facilities. *Phys. Rev. D* **107**, L031901, DOI: 10.1103/PhysRevD.107.L031901 (2023).

11. Nagaitsev, S. & Lebedev, V. A cost-effective upgrade path for the fermilab accelerator complex (2022). 2111.06932.

12. Belomestnykh, S. *et al.* An 8 GeV linac as the booster replacement in the Fermilab power upgrade: a Snowmass 2021 white paper (2023). 2203.05052.

13. Cousineau, S. *et al.* High efficiency laser-assisted h^- charge exchange for microsecond duration beams. *Phys. Rev. Accel. Beams* **20**, 120402, DOI: 10.1103/PhysRevAccelBeams.20.120402 (2017).

14. Belomestnykh, S. *et al.* RF accelerator technology R&D: Report of AF7-rf topical group to Snowmass 2021 (2022). 2208.12368.

15. Kinsho, M., Ogiwara, N., Saito, Y. & Kabeya, Z. Alumina ceramics vacuum duct for the 3gev-rcs of the j-parc. vol. 2005, 2604 – 2606, DOI: 10.1109/PAC.2005.1591197 (2005).

16. Pellemoine, F. *et al.* Irradiation facilities and irradiation methods for high power target (2022). 2203.08239.

17. Ammigan, K. *et al.* Novel materials and concepts for next-generation high power target applications (2022). 2203.08357.

18. Toups, M. *et al.* PIP2-BD: GeV Proton Beam Dump at Fermilab's PIP-II Linac. In *2022 Snowmass Summer Study* (2022). 2203.08079.

Signatures of ultralight bosons in the orbital eccentricity of binary black holes

Mateja Bošković,[1] Matthias Koschnitzke,[1,2] and Rafael A. Porto[1]

[1] *Deutsches Elektronen-Synchrotron DESY, Notkestr. 85, 22607 Hamburg, Germany*
[2] *II. Institut für Theoretische Physik, Universität Hamburg, Luruper Chaussee 149, 22761 Hamburg, Germany*

We show that the existence of clouds of ultralight particles surrounding black holes during their cosmological history as members of a binary system can leave a measurable imprint on the distribution of masses and orbital eccentricities observable with future gravitational-wave detectors. Notably, we find that for nonprecessing binaries with chirp masses $\mathcal{M} \lesssim 10\,M_\odot$, formed exclusively in isolation, larger-than-expected values of the eccentricity, i.e. $e \gtrsim 10^{-2}$ at gravitational-wave frequencies $f_{\rm GW} \simeq 10^{-2}\,$Hz, would provide tantalizing evidence for a new particle of mass between $[0.5, 2.5] \times 10^{-12}\,$eV in nature. The predicted evolution of the eccentricity can also drastically affect the in-band phase evolution and peak frequency. These results constitute unique signatures of boson clouds of ultralight particles in the dynamics of binary black holes, which will be readily accessible with the Laser Interferometer Space Antenna, as well as future mid-band and Deci-hertz detectors.

arXiv:2403.02415v1 [gr-qc] 4 Mar 2024

Introduction. The birth of gravitational-wave (GW) science [1] heralds a new era of discoveries in astrophysics, cosmology, and particle physics [2]. Measuring the properties of GW signals with current and future observatories, such as the Laser Interferometer Space Antenna (LISA) [3], the Einstein Telescope (ET) [4] and Cosmic Explorer (CE) [5], as well as other Mid-band [6] and Deci-hertz detectors [7], not only will unravel the origins of binary black hole (BBH) mergers, it also opens the possibility to discover (very-weakly-coupled) ultralight particles that are ubiquitous in theories of the early universe [8–12]. Notably, the mass, spin alignment, and eccentricity are expected to be correlated with formation channels, *isolated* or *dynamical*, e.g. [13–31]; whereas boson clouds (or "gravitational atoms" [8, 9]), formed around black holes via superradiance instabilities [32–36], can produce a large backreaction on the orbital evolution. Following analogies with atomic physics [37], the cloud may encounter Landau-Zener (LZ) resonances [38], or ionization effects [39–41]. The presence of a cloud then leads to large finite-size effects [37, 42], floating/sinking orbits [38], as well as other sharp features [40], that become unique signatures of ultralight particles in the BBH dynamics.

For the most part, up until now backreaction effects have been studied under the simplified assumption of planar, quasi-circular orbits. The reason is twofold [37]. Firstly, several formation scenarios lead to spins that are parallel to the orbital angular momentum [18]. Secondly, the decay of eccentricity through GW emission in vacuum [43, 44] is expected to have circularized the orbit in the late stages of the BBH dynamics. We retain here the former but relax the latter assumption. As we shall see, adding eccentricity not only introduces a series of *overtones* [41, 45, 46], it can also have a dramatic influence in the orbital dynamics as the cloud transits a LZ-type transition. Although the strength of the new resonances is proportional to the eccentricity, depending on their position and nature (floating or sinking), a small departure from circularity can lead to transitions that not only would deplete the cloud, but also induce a rapid growth of eccentricity towards a large critical (fixed-point) value: $e_{\rm cr} \in [0.3, 0.6]$. As measurements of the eccentricity are correlated with formation channels, the predicted increase can impact the inferred binary's origins. Measurements of larger-than-expected eccentricities would then provide strong evidence for the existence of a new ultralight particle in nature. In particular, because of the critical fixed point, a fraction of the BBHs undergo a rapid growth of orbital eccentricity to a common value. As a result, the distribution of masses and eccentricities may feature a skewed correlation by the time they reach the detector's band. Furthermore, for chirp masses $\mathcal{M} < 10 M_\odot$ and spin(s) aligned with the orbital angular momentum—expected to exclusively form in the field—the presence of a boson cloud at earlier times can shift a fraction of the population towards values of $e \gtrsim 10^{-2}$ at 10^{-2}Hz, readily accessible to LISA [3]. Furthermore, the GW-evolved eccentricity may also be within reach of the planned mid-band [6] or Deci-hertz [7] observatories. For all such events, a new ultralight boson of mass $[0.5, 2.5] \times 10^{-12}$ eV forming a cloud and decaying through a LZ-type transition prior to detection, may be the ultimate culprit.

The more drastic evidence is given when the resonant transition occurs in band with measurable frequency evolution. Plethora of phenomena are discussed in [37, 38] for circular orbits. In addition to overtones, the increase in eccentricity would imply that higher harmonics become more relevant, which in turn affects the peak frequency of the GWs, even for floating orbits. We point out here some salient features and elaborate further on the details elsewhere [46].

The gravitational atom. Ultralight particles of mass μ can form a cloud around a rotating black hole of mass M, via superradiant instabilities [8, 9]. The typical mass of the (initial) cloud scales as $M_{\rm c,0}/M \simeq \alpha$, whereas its typical size is $r_c \simeq \frac{r_g}{\alpha^2}$, with $r_g \equiv \frac{GM}{c^2}$, and

$$\alpha = \frac{GM\mu}{\hbar c} \simeq 0.1 \left(\frac{M}{15 M_\odot}\right) \left(\frac{\mu}{10^{-12}\text{eV}}\right) . \qquad (1)$$

The (scalar) cloud evolves according to a Schrödinger-like equation [47, 48], with eigenstates $|a\rangle \equiv |n_a l_a m_a\rangle$, and (n, l, m) the principal, orbital and azimuthal angular momentum, "quantum numbers". (For vector clouds [38, 48, 49], we must include the total angular momentum.)

The energy eigenvalues of the cloud scale as $\epsilon_{nlm} = \mu\left(1 - \frac{\alpha^2}{2n^2} + f_{nl}\,\alpha^4 + h_{nl}\,\tilde{a}\,m\,\alpha^5\right)$, with $\tilde{a}$ the dimensionless spin of the black hole, see [48]. At saturation, we have $\tilde{a} \simeq \alpha$, whereas the combined system black hole plus cloud may still be rapidly rotating. One of the main difference w.r.t. ordinary atoms, however, is the presence of a decay/growing time, $\Gamma^{-1}_{nlm} \propto \mu\,\alpha^{4l+5}$, for a given eigenstate [9, 47, 48, 50]. The (scalar) cloud may be populated by the dominant *growing* mode, $|211\rangle$, or an *excited* state, $|322\rangle$. Depending on α, they may be robust to GW emission (from the cloud itself) on astrophysical scales [9, 51–55]. They can also deplete through resonant transitions in binaries [37, 38], as we discuss here. In what follows we work with $G = \hbar = c = 1$ units.

Gravitational collider goes eccentric. Following [37, 38] we consider a boson cloud around a black hole of mass M in a bound orbit with a companion object of mass $M_\star$, with $q \equiv M_\star/M$ the mass ratio. The coordinates are centered at the black hole plus cloud system, with $R_\star$ the radial distance to the perturber, and $\varphi_\star$ the azimuthal angle. We consider planar motion with the spin parallel to the orbital angular momentum, with the orbit described by the semi-major axis a and the eccentricity e, while $\varphi_\star$ corresponds to the true anomaly. We take the orbital frequency to be positive such that the two, co-rotating and the counter-rotating, orientations are identified by $\dot{\varphi}_\star = s|\dot{\varphi}_\star|$, with $s = \pm 1$.

The gravitational perturbations of the companion induce mixing of the atomic levels. For a perturber outside of the cloud $r \gg r_{\rm c}$ the off-diagonal matrix elements of the Hamiltonian, $\langle b|\,V_\star\,|a\rangle$, are given by a multipole expansion that can be written as an harmonic series [37, 38]

$$\langle b|\,V_\star\,|a\rangle_{l_\star} = \sum_{|m_\star|\leq l_\star} \eta^{(m_\star)}_{ab} {\rm e}^{-im_\star\varphi_\star}\,, \tag{2}$$

with $\eta^{(m_\star)}_{ab} \propto R_\star^{-(l_\star+1)}$. The matrix elements obey selection rules which determine possible transitions, which we refer as hyperfine (only $\Delta m \neq 0$), fine ($\Delta\ell \neq 0, \Delta n = 0$), and Bohr ($\Delta n \neq 0$), respectively [37, 38].

For illustrative purposes, we consider a two-level model. The Hamiltonian equation is given by

$$i\begin{pmatrix}\dot{c}_a\\ \dot{c}_b\end{pmatrix} = \begin{pmatrix} -\frac{\Delta\epsilon}{2} & \eta_0\left(\frac{R_\star}{R_0}\right)^{-(l_\star+1)}{\rm e}^{i\Delta m\varphi_\star}\\ {\rm c.c.} & \frac{\Delta\epsilon}{2} - i\Gamma_b\end{pmatrix}\begin{pmatrix}c_a\\ c_b\end{pmatrix}, \tag{3}$$

with $\Delta\epsilon \equiv \epsilon_b - \epsilon_a$ the energy split, Γ_b the width of the decaying mode, and η_0 the value of the perturbation at a reference point R_0. For the purpose of analytical understanding, we use a small-eccentricity approximation,

$$\varphi_\star \simeq \vartheta + 2e\sin\vartheta\,,\; R_* \simeq a(1 - e\cos\vartheta)\,, \tag{4}$$

$$\dot{\vartheta} \equiv s\Omega\,,\; \Omega = \sqrt{M(1+q)/a^3}\,, \tag{5}$$

in terms of ϑ, the mean anomaly [56], and apply the Jacobi-Anger expansion into Bessel functions. Hence, the Hamiltonian in (3) becomes

$$\mathcal{H} = \mathcal{D} + \sum_{k=-\infty}^{\infty}\begin{pmatrix} & \eta_k{\rm e}^{-i(k+\Delta m)\vartheta}\\ \eta_k{\rm e}^{i(k+\Delta m)\vartheta} & \end{pmatrix}, \tag{6}$$

$$\mathcal{D} = \begin{pmatrix} -\frac{\Delta\epsilon}{2} & \\ & \frac{\Delta\epsilon}{2} - i\Gamma_b\end{pmatrix},\; \eta_k \sim \eta_0 \mathfrak{f}^{\frac{2}{3}(l_\star+1)}\frac{e^{|k|}}{|k|!},\;\; \mathfrak{f} \equiv \frac{\Omega}{\Omega_0}\,,$$

where we traded distance for orbital frequency. The case $(e, \Gamma_b) = 0$ was studied in [38]. The slow GW-induced evolution of the orbital frequency, $\Omega(t) \simeq \Omega_0 + \gamma_0 t$ with $\gamma_0 = \frac{96}{5} q M^{5/3}\frac{\Omega_0^{11/3}}{(1+q)^{1/3}}$, leads to a LZ transition [57, 58] between the energy levels. The transition is triggered for

$$\Omega_0 = s\frac{\Delta\epsilon}{\Delta m} > 0\,. \tag{7}$$

This value, dictated by the spectrum of the cloud, will serve as our reference point in the evolution. Ignoring backreaction effects (see below), the LZ solution is controlled by $z_0 \equiv \eta_0^2/(\gamma_0|\Delta m|)$ and $v_0 \equiv \Gamma_b/\sqrt{\gamma_0|\Delta m|}$. Yet, somewhat surprisingly [59], starting asymptotically from the $|a\rangle$ state, and independently of the value of v_0, in the limit $2\pi z_0 \gg 1$ one then finds a complete population transfer into the (decaying) $|b\rangle$ mode.

For eccentric orbits, the evolution in (6) also features a transition at Ω_0 (for $k = 0$). However, it introduces a series of overtones

$$\Omega_k = \mathfrak{f}_k\,\Omega_0\,,\quad \mathfrak{f}_k = \frac{\Delta m}{\Delta m + k}\,,\quad k \in \mathbb{Z}\,. \tag{8}$$

Provided each k-resonance is sufficiently narrow, we can ignore the other ($k' \neq k$) terms in (6). As in [38], we can linearize the orbital evolution near the transition, $\Omega(t) = \Omega_k + f(e)\gamma_k t$, where $f(e) = \frac{1 + \frac{73e^2}{24} + \frac{37e^4}{96}}{(1-e^2)^{7/2}}$ and $\gamma_k \equiv \gamma_0\mathfrak{f}_k^{11/3}$, such that the LZ solution now depends on the modified $z_k \equiv \frac{\eta_k^2}{f(e)\gamma_k|\Delta m + k|}$ and $v_k \equiv \frac{\Gamma_b}{\sqrt{f(e)\gamma_k|\Delta m + k|}}$, respectively.

Orbital backreaction. Dissipative effects, such as GW emission, from the binary [38, 60] or the cloud itself [51–55], ionization [39–41, 60], and decay widths [59, 61, 62], strongly influence the LZ phenomenology, and vice versa. We focus here on the prevailing case of two-body GW emission, with the companion *outside* the cloud, thus focusing on (hyper)fine resonances, combined with a two-level LZ transition into a decaying mode.

The orbital dynamics is governed by flux-balance equations at infinity [38, 41, 44, 46, 62, 63], and at the black

hole's horizon [8, 64, 65]:

$$\dot{E}_{\rm o}+\dot{E}_{\rm c}+\dot{M} \;=\; \mathcal{F}_{\rm GW}\equiv -\frac{32 f(e)}{5}\frac{M^5 q^2(q+1)}{a^5}\,, \quad (9)$$

$$\dot{L}_{\rm o}+s(\dot{L}_{\rm c}+\dot{S}) \;=\; \mathcal{T}_{\rm GW}\equiv \frac{\mathcal{F}_{\rm GW}}{\Omega}\frac{g(e)}{f(e)}\,, \quad (10)$$

$$\dot{M}=2\Gamma_b E_{{\rm c}(b)} \quad , \quad \dot{S}=2\Gamma_b L_{{\rm c}(b)}\,, \quad (11)$$

with $g(e)=\frac{1+\frac{7e^2}{8}}{(1-e^2)^2}$, and $\dot{M}$, $\dot{S}$ the change of mass and spin due to the decay of the $|b\rangle$ state onto the black hole. The orbital energy and angular momentum are given by $E_{\rm o}=-\frac{M^2 q}{2a}$ and $L_{\rm o}^2=\frac{(M^5q^3)(1-e^2)}{2(q+1)|E_{\rm o}|}$, while for the cloud is a sum over the populated states, $E_{{\rm c}(i)}\equiv(M_{\rm c,0}/\mu)\epsilon_i|c_i|^2$, and similarly for $L_{{\rm c}(i)}$ with $\epsilon_i\to m_i$.

The above equations can then be rewritten as

$$\frac{d\Omega}{dt} \;=\; r\gamma_0 \mathfrak{f}^{11/3} f(e)\,, \quad (12)$$

$$r \;\equiv\; \frac{\dot{E}_{\rm o}}{\mathcal{F}_{\rm GW}}=1-b\frac{{\rm sgn}(s\Delta m)\mathfrak{f}^{-11/6}}{\sqrt{f(e)\gamma_0|\Delta m+k|}}\frac{d|c_a|^2}{dt}\,, \quad (13)$$

$$\frac{de^2}{dt} \;=\; \frac{2}{3}\mathfrak{f}^{8/3}\frac{\gamma_0}{\Omega_0}f(e)\sqrt{1-e^2}\times \left[r\left(\mathfrak{f}-\sqrt{1-e^2}\right)-\mathfrak{f}+\frac{g(e)}{f(e)}\right], \quad (14)$$

in terms of the orbital parameters, where

$$b\equiv\frac{3M_{\rm c,0}}{M}\frac{|\Delta m|\mathfrak{f}^{-3/2}}{|\Delta m+k|^{-1/2}}\frac{(1+q)^{1/3}}{\alpha q}\frac{(M\Omega_0)^{1/3}\,\Omega_0}{\sqrt{\gamma_0}}\,, \quad (15)$$

parameterises the backreaction effects on the orbit due to the cloud. As anticipated in [38], "effective" LZ parameters emerge: $\zeta_k(t)\equiv z_k/r(t)$ and $w_k(t)\equiv v_k/\sqrt{r(t)}$, making it a fully nonlinear system. We can nonetheless estimate the value of the energy-momentum transfer near the resonance by self-consistently solving the condition $\zeta_k=z_k/r_k(\zeta_k)$. For moderate-to-large population transfer ($\zeta_k\gtrsim 1$), we find the limiting results:

$$r_k\simeq\left(1-{\rm sgn}(s\Delta m)\frac{b_k}{4\sqrt{z_k}}\right)^{-1}, \qquad (w_k\ll\zeta_k) \quad (16)$$

$$r_k\simeq 2\left(1+\sqrt{1-{\rm sgn}(s\Delta m)\frac{b_k}{z_k v_k}}\right)^{-1}, \; (w_k\gg\zeta_k)\,.$$

As discussed in [38], the orbital evolution branches into either floating ($r\simeq 0$), for $s\Delta m<0$, or sinking orbits ($r\gtrsim 1$), for $s\Delta m>0$. However, except for the the trivial case when $\zeta_k\ll 1$, due to the nonlinear nature of the problem the transfer of energy and angular momentum from the cloud to the orbit does not simply reduce to the quest for adiabaticity of the LZ transition, not even for $w_k\ll\zeta_k$. For instance, for extreme cases, with $z_k\gg 1$, the (unperturbed) transition spreads over long time scales, $\Delta t_{\rm LZ}\simeq 4\sqrt{z_k/\gamma_k}$ [66], which in turn reduces the orbital impact, as we see in (16). As it turns out, in the large backreaction scenario, the sweet spot for floating orbits occurs when $b_k\gg\sqrt{z_k}$. Even though, due to the properties of the LZ solution, a strong decay width ($w_k\gg\zeta_k$) does not alter this picture, the impact on the orbit evolution as well as the population transfer becomes suppressed by $1/v_k$, as shown in (16). On the other hand, for the sinking case, the largest values of r_k are obtained for nonadiabatic transitions.

Eccentric fixed point. For the GW-dominated epochs, with $r\simeq 1$, the leading order term in (14) vanishes, and the first contribution is at $\mathcal{O}(e^2)$. Likewise for the $k=0$ (main) resonance, for which the first term is $\propto\left(\frac{r}{2}-\frac{11}{3}\right)e^2$. As a result, the eccentricity is damped unless the orbit gets a large kick ($r\gtrsim 7.3$). As the influence of the cloud increases, the RHS of (14) asymptotes (modulo a positive prefactor) to $(\mathfrak{f}_k-1)(r-1)$, in which case it enters at leading order. Moreover, the differences in the GW fluxes in (9) and (10) generate a distinction between the early and late resonances. In the floating case, with $r\simeq 0$, the eccentricity grows for the early resonances ($\mathfrak{f}_k<1$) and decays for the late ones ($\mathfrak{f}_k>1$). This can be understood by noticing that, when $\dot{E}_{\rm o}\simeq 0$, we have $\dot{L}_{\rm o}\propto\left(\frac{\Omega-\Omega_0}{\Omega\Omega_0}+\mathcal{O}(e^2)\right)$, and using $d(L_{\rm o}^2)\propto -d(e^2)$ the eccentricity grows for $\Omega_k<\Omega_0$ and decays whenever $\Omega_k\geq\Omega_0$. This trend is reversed in the sinking case.

Due to the changes in the time evolution of the eccentricity across different resonances, it is instructive to look at the opposite limit $e\to 1$. In that case, the RHS of (14) becomes $\propto\frac{r-1}{(1-e)^3}$. Let us consider the case of a floating orbit. Since the sign of $\frac{de}{dt}$ is positive for $\Omega_k<\Omega_0$, but turns negative when the eccentricity approaches $e\simeq 1$, this implies the existence of a critical "attractor" fixed point, $e_{\rm cr}$, given by the condition $g(e_{\rm cr})/f(e_{cr})=\mathfrak{f}_k$ [cf. (14)]. For instance,

$$e_{\rm cr}=\{0.46,0.35,0.29\}, \quad \text{for} \quad |\Delta m|=\{1,2,3\}\,, \quad (17)$$

with $k=-1$. Similarly, an unstable fixed point develops for the earlier and main sinking resonances.

For the case of floating orbits (with $s\Delta m<0$), if the backreaction is sufficiently effective to enforce $r_k\simeq 0$ while the eccentricity approaches the critical point, one can then estimate the floating time $\Delta t_{\rm FL}\simeq b_k/\sqrt{\gamma_k}$, left-over population $|c_a(\infty)|^2\lesssim r_k$, and notably the growth of the eccentricity upon exiting the resonant transition,

$$e_{\rm fin}\simeq e_{\rm cr}\sqrt{1-{\rm e}^{-{\rm C_k}}}\,, \quad \text{with } {\rm C_k}\sim\frac{\sqrt{\gamma_k}}{\Omega_k}b_k\,. \quad (18)$$

Although we have derived various analytic results under simplifying assumptions, we have demonstrated through numerical studies that the above behavior remains valid for generic (planar) orbits. See [46] and the supplemental material for details.

The cloud's eccentric fossil. As it was argued in the

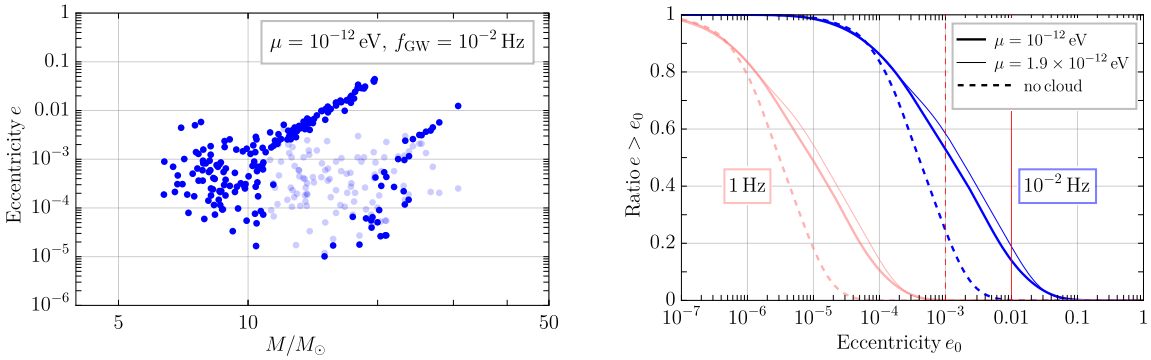


Figure 1. BBH eccentricities at $f_{\rm GW} = 10^{-2}$Hz (*left*), evolved with a uniformly distributed $q \in [0.1, 1]$ and the cloud on the heavier black hole. The pale blue dots account for the values without the cloud [15]. (BBHs with $e \lesssim 10^{-6}$ are not shown.) Cumulative values (*right*), with (solid) and without (dotted) the cloud, both at 10^{-2} Hz (blue) and 1 Hz (pink), respectively.

literature [15–17], the distribution of masses and eccentricities observed with LISA can in principle distinguish between formation channels. However, the contrast between vacuum evolution and the large eccentricities produced by the cloud's resonant transition can lead to dramatic changes in the expected evolution of the system. As a proof of concept, we take the stellar-mass BBH population studied in [15], with chirp masses $\mathcal{M} \lesssim 10 M_\odot$, expected to form exclusively in isolation. We consider clouds of ultralight bosons of mass between 10^{-13} and 10^{-11} eV, in a planar (co-rotating) orbit with the parent black hole's spin aligned with the orbital angular momentum. Superradiance may then excite the $|322\rangle$ state which, depending on black hole's mass and birth orbital frequency, will experience a series of (hyper)fine transitions.[1] To illustrate the distinct physical effects, and following [14, 15], we consider a birth orbital frequency (for the cloud+BBH system) at $\Omega_{\rm ini}/\pi \simeq 10^{-4}$Hz,[2] and evolve until $f_{\rm GW} = 10^{-2}$ and 1 Hz, with [68]

$$f_{\rm GW} \simeq \frac{\Omega}{\pi} \frac{(1+e)^{1.1954}}{(1-e^2)^{3/2}} \,, \tag{19}$$

the peak GW frequency. The final distribution is shown on the left panel of Fig. 1. While some of the BBHs experience an early overtone of the hyperfine transition, the majority are affected by transitions through the fine overtones instead. The BBH then float over a period of time while increasing the orbital eccentricity. Moreover, the cloud typically either terminates there or decays later at the $k = 0$ resonance. Depending on the parameters,

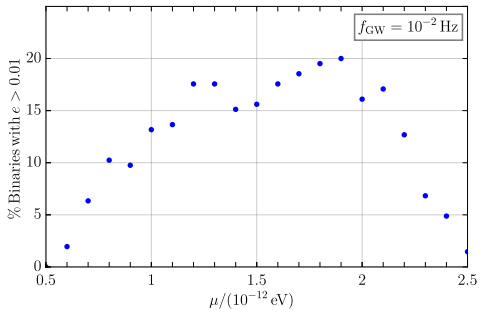


Figure 2. Percentage of binaries with eccentricities above 0.01 at $f_{\rm GW} = 10^{-2}$ Hz for different values of μ.

the ultimate decay may either decrease the eccentricity or have a small impact on the orbit. As a result, a *wedge-type* distribution emerges, with the heavier black holes (within each wedge) subject to the largest increase in eccentricities.

The cumulative effect (i.e. the ratio of binaries with e above a reference eccentricity e_0) is shown on the right panel of Fig. 1, where a significant fraction of the population (with different parent masses) is affected by the resonances, yielding values of the eccentricities at 1Hz that may be within reach of mid-band and Decihertz detectors. As the value of μ increases (decreases) the location of the wedge in the distribution moves towards lower (higher) masses. The dependence on the value of μ for this population of BBH (with $\mathcal{M} \lesssim 10 M_\odot$), reaching $e \gtrsim 10^{-2}$ at $f_{\rm GW} = 10^{-2}$ Hz, is shown in Fig. 2.

Eccentric in band. Due to the connection to formation channels, we discussed a sub-population of BBHs. However, similar conclusions apply to black holes with higher masses [46]. For instance, for a GW170809-type event [69] ($\mathcal{M} \simeq 24 M_\odot$), with a parent black hole $M \simeq 20 M_\odot$ and a (heavier) companion $M_\star \simeq 40 M_\odot$, we find $f_{\rm GW} \gtrsim 10^{-2}$ Hz at the $k = -1$ fine transition for $\mu \simeq 1.5 \times 10^{-12}$ eV. The BBH reaches the resonance

[1] For the BBH population and values of μ we consider here, the largest impact on the orbital evolution happens for $\alpha \gtrsim 0.1$. Hence, the overall effect from the earlier, but shorter-lived, $|211\rangle$ component of the cloud becomes subdominant.

[2] Moreover, even in cases where the birth orbital frequency of the binary system may be lower, stellar evolution [67] can also lead to *younger* (secondary) black holes carrying the cloud.

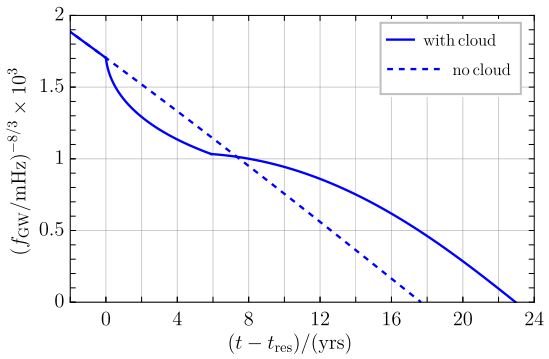


Figure 3. Evolution of the peak frequency through a resonant transition (at $t - t_{\rm res} = 0$) in the LISA band of a GW170809-like event, compared to the evolution without the cloud.

and floats, with approximately constant orbital frequency for about six years, while the eccentricity increases from $e \lesssim 10^{-2}$ to $e \simeq 0.1$, and likewise the peak GW frequency grows, while the cloud depletes. The resulting frequency evolution till merger, which is distinct from the growth of the eccentricity that may occur due to other astrophysical mechanisms [70, 71], is displayed in Fig. 3. In addition to the notable features, higher harmonics would also become more relevant as the eccentricity increases [72]. As for the case of large tidal Love numbers [37, 42],[3] new dedicated templates will be needed to search for these peculiar phenomena in the GW data.

Conclusions. We have shown that the presence of a boson cloud surrounding a black hole in a binary system can impact the distribution of masses and eccentricities observable with GW detectors. We have also found that a greater-than-expected value of the eccentricity, $e \gtrsim 10^{-2}$ at GW frequencies $f_{\rm GW} \simeq 10^{-2}$Hz, develops for a (sub-)population of isolated stellar-mass BBHs (with $\mathcal{M} \lesssim 10M_\odot$), right at the heart of the LISA band. Likewise, these BBHs will decay through GW emission to values of the eccentricities, i.e. $e \simeq 10^{-4} - 10^{-3}$, within experimental reach of mid-band [6] and Decihertz [7] detectors. The observation of such GW signals would then provide tantalizing evidence for the existence of an ultralight particle of mass between 5×10^{-13} and 2.5×10^{-12} eV in nature. Furthermore, we have also shown that in-band resonance transitions are possible, yielding dramatic changes in the GW frequency evolution, constituting yet another smoking-gun signature of the imprint of a boson cloud in the BBH dynamics.

There are several venues for further exploration. Firstly, we have concentrated here on (co-rotating) transitions that are outside of the cloud, thus ignoring Bohr resonances altogether, which are subject to dynamical friction [40, 41]. Preliminary studies suggest that a similar increase of eccentricity occurs for certain type of transitions at higher frequencies, which would put them within reach of the ET and CE detectors [46], but a more in-depth study is needed. Secondly, we have considered aligned-spin BBHs. This is justified for the isolated populations. However, to encompass also dynamically-formed systems, we must add inclination and new (off-plane) transitions [41]. While our results remain unchanged for quasi-planar motion, we also expect similar conclusions to apply for inclined orbits (see [73] for related work). Finally, identical results can be drawn also for neutron star/black hole binaries. For instance, for those formed in isolation, the parent black hole mass is expected to be near $M \simeq 7M_\odot$, and likewise in binaries with negligible eccentricity at $f_{\rm GW} \simeq 1$Hz [13, 25, 31]. The presence of a boson cloud would then also lead to larger-than-expected eccentricities, providing additional circumstantial evidence for a new ultralight particle in nature.

Acknowledgements. While this letter was in preparation we learned of the related work in [73]. We thank G.M. Tomaselli for informative discussions and the authors of [73] for sharing a draft and coordinating the release. The work of MB and MK is supported in part by the Deutsche Forschungsgemeinschaft (DFG, German Research Foundation) under Germany's Excellence Strategy – EXC 2121 "Quantum Universe" – 390833306. MB and RAP are supported in part by the ERC Consolidator Grant "Precision Gravity: From the LHC to LISA" provided by the European Research Council (ERC) under the European Union's H2020 research and innovation programme (grant No. 817791).

SUPPLEMENTAL MATERIAL

Appendix A: Gravitational atom

The range of ultralight masses that we probe yield a (very) high "axion decay constant" (f_a), generically suppressing self-interactions [74–77] and coupling to other species [78–82]. In addition, for the black hole masses we studied, with $5M_\odot \lesssim M \lesssim 50M_\odot$, we arrive at small-to-moderate values of $\alpha \lesssim 0.25$, keeping relativistic corrections to the hydrogenic states small [55, 60, 83, 84]. In this regime, the eigenvalues are given by [37, 48]

$$\epsilon_{nlm} = \mu\left(1 - \frac{\alpha^2}{2n^2} - \left[\frac{1}{8n} + \frac{6}{2l+1} - \frac{2}{n}\right]\frac{\alpha^4}{n^3} + \frac{16}{2l(2l+1)(2l+2)}\frac{\tilde{a}m\alpha^5}{n^3}\right). \quad \text{(A1)}$$

Furthermore, from Detweiler's approximation [47, 48],

$$\Gamma_{nlm} \simeq 2\tilde{r}_+ C_{nl} g_{lm}(\tilde{a}, \alpha, \omega)(m\Omega_H - \omega_{nlm})\alpha^{4l+5}, \quad \text{(A2)}$$

[3] Notice that a fraction of the cloud may still survive the resonant floating period(s), even for large decaying widths, which can also produce a measurable imprint in the waveforms through finite-size effects [37].

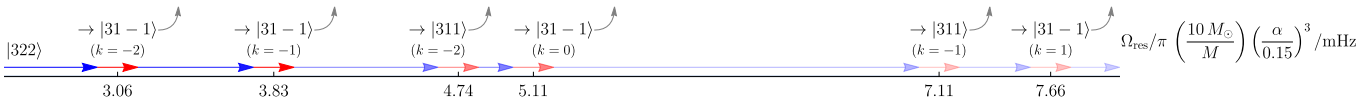


Figure 4. Orbital resonance frequencies of possible (fine) transitions for the $|322\rangle$-component of the cloud. The blue and red arrows represent vacuum and floating BBH evolution, respectively; whereas the grey arrows point to various (rapidly decaying) modes that ultimate deplete the cloud. The thinner the line the smaller the cloud gets.

with $C_{nl} \equiv \frac{2^{4l+1}(n+l)!}{n^{2l+4}(n-l-1)!}\left[\frac{l!}{(2l)!(2l+1)!}\right]^2$, $g_{lm}(\tilde{a},\alpha,\omega) \equiv \prod_{k=1}^{l}\left(k^2(1-\tilde{a}^2)+(\tilde{a}m-2r_+\omega)^2\right)$ and $\tilde{r}_+ \equiv 1+\sqrt{1-\tilde{a}^2}$, $\tilde{r}_+ \equiv r_+/M$, and $\Omega_H \equiv \tilde{a}/(2r_+)$; whereas for the cloud itself decaying into GWs, we use the (non-relativistic) approximation in [51].

Appendix B: Tidal interactions

For equatorial orbits and resonances triggered away from the cloud, the tidal interaction is given by [37, 38]

$$\langle b|\, V_\star\, |a\rangle \equiv \sum_{l_\star=2}^{\infty}\sum_{|m_\star|\le l_\star}\eta^{(\star)}_{ab}\,, \tag{B1}$$

$$\eta^{(\star)}_{ab} = -\frac{q\alpha}{r_c}\mathsf{R}_\star^{-(l_\star+1)}\frac{4\pi}{2l_\star+1}Y^*_{(\star)}\left(\frac{\pi}{2},\varphi_\star\right)I_r I_\Omega\,,$$

$$I_r \approx \int^{\infty} d\mathsf{r}\mathsf{r}^2\hat{\mathcal{R}}_b\hat{\mathcal{R}}_a\mathsf{r}^{l_\star} \tag{B2}$$

$$I_\Omega \equiv \int d\Omega Y_b^*(\theta,\phi)Y_{(\star)}(\theta,\phi)Y_a(\theta,\phi)\,, \tag{B3}$$

where $(\star)\equiv(l_\star,m_\star)$, $\mathsf{r}\equiv r/r_c$, $\hat{\mathcal{R}}_c = r_c^{3/2}\mathcal{R}_c$ is the (dimensionless) hydrogenic radial wavefunction, Y_{lm} is the spherical harmonic. We leave to [46] the discussion on resonances "inside the cloud", including dipole-mediated transitions [60, 84, 85].

The Jacobi-Anger expansion,

$$e^{\pm i\Delta m(\vartheta+2e\sin(\vartheta))} = \sum_{k=-\infty}^{\infty}(\pm1)^k J_k(2e\Delta m)e^{i(k\pm\Delta m)\vartheta}\,, \tag{B4}$$

can be applied to the off-diagonal terms of the Hamiltonian [cf. (3) in the main text]. Using the properties of the Bessel function [4], the tidal perturbation [cf. (6) of the main text] becomes

$$\eta^{(\star)}_{ab,k} = \eta_0\mathsf{f}^{\frac{2}{3}(l_\star+1)}\frac{(\Delta m e)^{|k|}}{|k!|}\left(1+\frac{(l_\star+1)k}{2\Delta m}\right)+\mathcal{O}(e^{|k|+1})\,,$$

$$\eta^{(\star)}_{ab,0} = \frac{q\alpha}{r_c}\mathsf{R}_0^{-(l_\star+1)}\frac{4\pi}{2l_\star+1}\left|Y^*_{(\star)}\left(\frac{\pi}{2},\varphi_\star\right)\right|I_r I_\Omega\,. \tag{B5}$$

This interaction is nonzero only if the selection rules are satisfied [37, 38]: $-m_b+m_\star+m_a=0$, $l_b+l_\star+l_a=2p$, $|l_a-l_b|\le l_\star\le l_a+l_b$. Furthermore, for equatorial orbits, for even (odd) $l_\star$ only the spherical harmonics even (odd) in $m_\star\neq0$ are nonzero.

Appendix C: Atomic resonances

As the populated state has a maximal azimuthal number $m_{\rm max}=n-1$, at the (hyper)fine resonances, it can only transition into states with lower m. Such transitions are only possible on co-rotating orbits, where they obey $s\Delta m<0$, yielding floating-type motion[5]. From the selection rules for the tidal interactions, the $|211\rangle$ state has only one hyperfine transition to $|21-1\rangle$, while the only possible fine transition, to $|200\rangle$, can only occur inside the cloud. Furthermore, for small values of α, we find that the floating time of this transition would take longer than a Hubble time, preventing them to reach the LISA band. At the same time, (barring a precise fine tuning of the birth frequency of the BBH+cloud) for large values of α we expect the $|211\rangle$ component of the cloud to decay through its own GW emission before reaching the resonant transition (see also [62, 86]). On the other hand, the (longer-lived) $|322\rangle$ state may experience various types of resonances. In contrast to early and late resonances with $k=\pm1$, all of the $k=0$ hyperfine transitions to $|32m\rangle$ happen at the same frequency (Δm drops out of the ratio). The dominant main (hyperfine) transition is the one to $|320\rangle$, with $l_\star=2$ [as the $|322\rangle\to|32-2\rangle$ resonance can only be mediated by the hexadecapole ($l_\star=4$), making it extremely weak and nonadiabatic]. Transitions to the $|32\pm1\rangle$ states are not possible for equatorial orbits.

[4] Parity $J_k(-x)=J_{-k}(x)=(-1)^kJ_k(x)$, recurrence formulas $x\left(J_{k+1}(x)+J_{k-1}(x)\right)=2kJ_k(x)$ and the asymptotic expansion $J_{|k|}(x)\sim(x/2)^{|k|}|k|!$, $x\ll1$.

[5] Notice that for the $k>|\Delta m|$ overtones, sinking transitions are possible on counter-rotating orbits ($s=-1$). The lowest one, at $k=2$, occurs for $\Delta m=-1$.

The fine resonances from the excited state are (octopolar) to the $|31-1\rangle$, $|311\rangle$ and (quadrupolar) $|300\rangle$ states, in that order in the frequency domain. We show a succession of transitions in Fig. 4. We ignored the (sinking) high-$l_\star$ Bohr resonances that can overlap with the range of frequencies that we consider here, since they do not significantly affect the dynamical evolution. We postpone the general analysis of Bohr transitions to [46].

Appendix D: Nonlinear Landau-Zener transition

Linear solution

The solution of the (linear) LZ transition with $\dot{\Omega}_k \simeq f(e)\gamma_k \simeq$ const, including a decaying width, is given by [59, 61, 62] (see also [38, 58])

$$|c_a|^2 = \exp\left(-v_k\tau - \frac{\pi}{2}z_k\right)\left|D_{iz_k}\left(e^{i\frac{3\pi}{4}}(\tau - iv_k)\right)\right|^2 \quad \text{(D1)}$$

$$|c_b|^2 = \exp\left(-v_k\tau - \frac{\pi}{2}z_k\right)z_k\left|D_{iz_k-1}\left(e^{i\frac{3\pi}{4}}(\tau - iv_k)\right)\right|^2 ,$$

where D are parabolic cylinder functions [58], and we introduced a dimensionless time

$$\tau \equiv t\sqrt{|\Delta m + k|f(e)\gamma_k}\,. \quad \text{(D2)}$$

Remarkably, the transition probability at infinity, $|c_a(\infty)|^2 = \mathrm{e}^{-2\pi z_k}$, is independent of v_k.[6]

In general, the presence of a decay width tends to smooth the LZ transition, by transferring a fraction of the initial state earlier than the case with $v_k = 0$, and also by damping late-time oscillations. Consequently, for large widths, $\frac{d}{d\tau}|c_a|^2$ peaks earlier than the $v_k = 0$ case. In the limit $v_k \gg z_k$, the LZ solution acquires a simple form [61, 62]

$$|c_a|^2 = \exp\left[-2z_k\left(\arctan\left(\frac{\tau}{v_k}\right) + \frac{\pi}{2}\right)\right], \quad \text{(D3)}$$

$$|c_b|^2 = |c_a|^2\frac{z_k}{\tau^2 + v_k^2}\,. \quad \text{(D4)}$$

In this regime, $\frac{d}{d\tau}|c_a|^2$ peaks at $\tau_{\rm max} \simeq -z_k v_k$, and the width of the transition roughly scales as

$$\frac{\Delta\Omega}{\sqrt{|\Delta m + k|f(e)\gamma}} \simeq 2v_k\sqrt{1 + 2z_k^2}\,. \quad \text{(D5)}$$

[6] However, this fails to be the case for generic $\dot{\Omega}_k \sim t^n$ [61], namely during late inspiral.

Balance equations

In the two-level system with a decaying mode, we can relate the total energy and the angular momentum of the $|a, b, \mathrm{BH}\rangle$ state as [cf. (9)-(11) in the main text]

$$(\dot{L}_{\rm c} + \dot{S}) = (\dot{E}_{\rm c} + \dot{M})\frac{\Delta m}{\Delta\epsilon} \times \frac{\rho_\epsilon(t)}{\rho_m(t)} \quad \text{(D6)}$$

$$\rho_x \equiv \frac{x_a}{\Delta x}\frac{d}{dt}|c_a|^2 - \Gamma_a|c_a|^2 - \sum\hat{\Gamma}_a|c_a|^2 + (a \to b)\,, \quad \text{(D7)}$$

where $x \equiv \{\epsilon, m\}$, and the $\hat{\Gamma}$ represents other sources of dissipation, such as GW emission from the cloud [9, 51–55] or ionization [39–41]. From the Schrödinger equation [cf. (3)], we find

$$\rho_x = \frac{d}{dt}|c_a|^2 + 2|c_a|^2\Gamma_a + 2\frac{x_b}{\Delta x}\sum\left(\hat{\Gamma}_a|c_a|^2 + \hat{\Gamma}_b|c_b|^2\right),$$

and a similar equation applies with $a \leftrightarrow b$. After superradiance saturates the growth of the cloud in the $|a\rangle$ state, we have $\Gamma_a \simeq 0$. Moreover, for the floating time of the resonances we consider here, we can ignore other sources of dissipation during the LZ transition (setting $\hat{\Gamma} \simeq 0$) [46]. Hence, $\rho_x = (d/dt)|c_a|^2$, which implies $\rho_\epsilon/\rho_m = 1$, yielding the expression in (12)-(14) of the main text.

Nonlinear backreaction effects

Because of the backreaction on the orbital frequency, which in turns controls the LZ transition, the problem becomes nonlinear, and it depends on the level-occupancy through the derivative of the parent state occupancy [cf. (13) in the main text]. We plot the this derivative for the linear LZ problem in Fig. 5. In the parts of the parameter space where it has compact support, the backreaction simply renormalizes the parameters $(z_k, v_k) \to (\zeta_k, w_k)$ [cf. (14) of the main text] near the maximum value, as

$$\zeta_k = \frac{\eta_k^2}{|\Delta m + k|\dot{\Omega}_k} = \frac{\eta_k^2}{|\Delta m + k|\gamma_k f(e) r} = \frac{z_k}{r_k(\zeta_k)}\,, \quad \text{(D8)}$$

and with the energy transfer itself depending on the level-occupancy of the cloud. The solution can, nonetheless, be found self-consistently in terms of the relevant parameters.

This mapping provides a useful indicator, even in the regime of strong backreaction, to evaluate whether, e.g., floating can occur, by indicating the breakdown of the linearization of the full problem. From the self-consistency condition (D8) the "true" time scale for the nonlinear problem follows $\mathrm{T} = \sqrt{r_k}\tau$. The LZ function derivatives

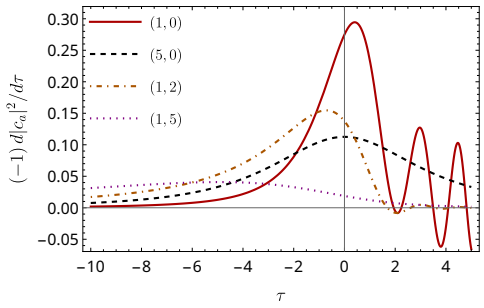


Figure 5. (Negative) derivative of the parent state occupancy, evaluated for a linear LZ transition. Brackets in the legend correspond to (z_k, v_k). Note the decrease, and shift to the left, of the amplitude, as well as the widening of the function and damping of the late-time oscillations, as the ratio v_k/z_k increases.

can now be expressed in terms these quantities,

$$\frac{d|c_i|^2}{d\tau} = \sqrt{\frac{z_k}{\zeta_k}}\frac{d|c_i|^2}{d\mathrm{T}}\,, \tag{D9}$$

leading to

$$-\frac{d|c_a|^2}{d\tau}\Big|_{\tau=-\zeta_k w_k} = \sqrt{\frac{z_k}{\zeta_k}}\psi_k(\zeta_k, w_k)\,, \tag{D10}$$

$$\psi_k \equiv \frac{1}{2}e^{-\frac{1}{2}(\pi\zeta_k)}\left[2w_k\left|\mathcal{C}H_{i\zeta}\left(\frac{\mathcal{C}w_k\Delta w_k}{2}\right)\right|^2 - \left(\mathcal{C}H_{1-i\zeta}\left(\frac{\mathcal{C}^*\Delta w_k^*}{2}\right)H_{i\zeta}\left(\frac{\mathcal{C}\Delta w_k}{2}\right) + \text{c.c.}\right)\right],$$

where $\mathcal{C} = 1+i$, $\Delta w_k = w_k(1-i\zeta_k)$ and H is the Hermite function. In what follows, for the sake of notation brevity, we take the small-eccentricity approximation, with $f(e) \simeq 1$. This is also justified by the fact that the eccentricity before the LZ transition is typically small across the parameter space, which we use to evaluate the type of transition the cloud will experience.

Negligible-decay regime

The ψ_k function simplifies in the asymptotic regime

$$\lim_{\zeta\to 0}\psi_k \sim \sqrt{\pi}\zeta\,, \quad \& \quad \lim_{\zeta\to\infty}\psi_k \sim \frac{1}{4\sqrt{\zeta}} \quad (w_k \ll \zeta_k)\,,$$

in which

$$\zeta_k \sim z_k\left(1 - \mathrm{sgn}(s\Delta m)\frac{b_k}{4\sqrt{z_k}}\right)\,, \tag{D11}$$

and the value of r_k given in (16) of the main text. As advertised, the energy transfer for the adiabatic floating ($s\Delta m < 0$), is extremised by large values of b_k with moderate z_k parameters. In contrast, sinking ($s\Delta m > 0$) is consistent with large adiabaticity only for moderate backreaction $b_k < 4\sqrt{z}_k$. Furthermore, the large backreaction limit ($b_k \gg 1$) of the weakly-adiabatic regime

$$\zeta_k \sim \mathrm{sgn}(s\Delta m)\left(\frac{z_k}{b_k^2\pi}\right)^{1/3}\,,\; r_k \sim \mathrm{sgn}(s\Delta m)(\pi b_k^2 z_k^2)^{1/3}\,,$$

is only possible for sinking orbits. In such scenarios, the strong backreaction then mostly leads to nonadiabatic sinking transitions, with a potentially significant impact on the orbit

Strong-decay regime

In general, the impact of the decay width depends on the dynamical timescale of the LZ transition and should be compared with the strength of the coupling. Moreover, for eccentric orbits, even if $z_0 > v_0$ at $\mathfrak{f}_0 = 1$, this hierarchy may be reversed for $\mathfrak{f}_k \neq 1$, due to the $e^{2|k|}$ suppression in z_k. Similarly to the case of negligible decay, we can also obtain approximate relations in the limit described by (D3), yielding

$$\psi_k \;\sim\; \frac{2\zeta_k \mathrm{e}^{-\zeta_k[\pi - 2\arctan(\zeta_k)]}}{w_k(\zeta_k^2+1)}\,, \tag{D12}$$

$$r_k \;\sim\; 1 \pm 2b_k z_k \frac{\mathrm{e}^{-\zeta_k[\pi-2\arctan(\zeta_k)]}}{v_k(\zeta_k^2+1)}\,. \tag{D13}$$

In general, this regime shares various qualitative behavior as in the $w_k \ll \zeta_k$ case, but with the adiabaticity gain/loss and orbital impact suppressed by the ratio b_k/v_k. In particular, large adiabaticity is consistent only for floating orbits, where we have

$$\zeta_k \simeq \frac{\sqrt{2}}{\mathrm{e}}\sqrt{\frac{b_k z_k}{v_k}}\,, \quad r_k = \frac{z_k}{\zeta_k} \to 0\,. \quad (b_k \gg 1)$$

In contrast, for sinking orbits, the strong backreaction requires a small population transfer, and we find

$$\zeta_k \simeq \frac{v_k}{2b_k}\,, \quad r_k \simeq \frac{2b_k z_k}{v_k} \gg 1\,. \quad (b_k \gg 1)$$

Notice that, somewhat counter-intuitively, a strong-decay width not only does not necessarily imply the total depletion of the cloud, instead it suppresses r_k, hence the ability of the system to float, resulting in a *lesser* amount of the cloud being transferred to the decaying mode (see (E9) below).

Appendix E: Floating

For values of the energy transfer $r_k \lesssim 0.2$, the growth of the orbital frequency is sufficiently suppressed to allow for the possibility of floating. In that case, the growth of (initially small) eccentricity is given, in units of the

dynamical time introduced in (D5), by

$$e(t) \simeq \sqrt{e_{\rm in}^2 + I_e \tau (1-\mathfrak{f}_k)}\,, \qquad (\mathfrak{f}_k \neq 1) \quad \text{(E1)}$$

$$e(t) \simeq e_{\rm in} \exp\left\{-\frac{11}{6} I_e \tau\right\}, \qquad (\mathfrak{f}_k = 1) \quad \text{(E2)}$$

$$I_e \equiv \frac{2}{3}\frac{\sqrt{\gamma_0}}{\Omega_0}\frac{\mathfrak{f}_k^{5/6}}{|\Delta m + k|^{1/2}}\,.$$

The critical points of the evolution of the eccentricity depend both on $|\Delta m|$ and $|k|$. For the first few values of $|k|$ they are described by the polynomial fit $e_{\rm cr} = g_0 + g_1 k + g_2 k^2$, where $g_0 = \{0.3, 0.2, 0.16\}$, $g_1 = \{0.18, 0.16, 0.14\}$, $g_2 = \{2, 1.6, 1.3\} \times 10^{-2}$, all for $|\Delta m| = \{1, 2, 3\}$ in respective order.

To calculate the evolution of the eccentricity towards the fixed point, we change the time variable in the evolution equations [cf. (14)], from t to $e^2(t)$, yielding

$$\int_{e_{\rm in}^2}^{e_{\rm fin}^2} \frac{d(e^2)}{\sqrt{1-e^2}\left[\frac{g(e)}{f(e)} - \mathfrak{f}_k\right]} = I_e b_k \left(1 - |c_a(\infty)|^2\right)\,, \quad \text{(E3)}$$

The result can then be approximated by (18) in the main text, where

$$\mathrm{C}_k = c_{\Delta m,k}\left[I_e b_k \left(1 - |c_a(\infty)|^2\right) + \frac{e_{\rm in}^2}{1-\mathfrak{f}_k}\right], \quad \text{(E4)}$$

and $c_{\Delta m,-1} = \{2.37, 2, 1.37\}$ for $\Delta m = \{-1, -2, -3\}$. From the value of $e_{\rm fin}^2$ in (E3), we can also estimate the duration of the floating period

$$\Delta\tau_{\rm Fl} = \frac{1}{I_e}\int_{e_{\rm in}^2}^{e_{\rm fin}^2} d(e^2) \frac{1}{\sqrt{f(e)}\sqrt{1-e^2}\left[\frac{g(e)}{f(e)} - \mathfrak{f}_k\right]}\,,$$

$$\simeq \frac{\mathrm{C}_k}{\tilde{c}_{\Delta m,k} I_e}\,, \quad \frac{c_{\Delta m,k}}{\tilde{c}_{\Delta m,k}} = \frac{1}{\sqrt{f(e_{\rm cr})}}\,. \quad \text{(E5)}$$

An exemplary parameter space of final eccentricity and floating time is shown in Fig. 6.

Strong floating provides a distinct phase of the nonlinear LZ transition, during which typically most of the population transfer occurs. From (12) of the main text, we have

$$\frac{d|c_a|^2}{d\tau} = \frac{r(\tau) - 1}{b_k}\,, \quad \text{(E6)}$$

yielding a linear-in-time decay of the population during floating, and a transfer of population given by

$$|c_a(\infty)|^2 \simeq |c_a(\tau < \mathrm{Fl})|^2 - (1 - r_k)\frac{\Delta\tau_{\rm Fl}}{b_k}\,. \quad \text{(E7)}$$

In the strong decay regime, the condition $r(t) \to 0$ at the resonance is necessary at each point in time, but not sufficient to guarantee a steady floating-type period. In addition, there must be enough of the cloud left to sustain a small $r(t)$. Following [62], one can estimate the sufficient condition by considering the minimum amount of cloud needed to "startjump" a floating period. Applying the linear LZ solution (D3) in (13) of the main text, we find

$$|c_a|^2_{\rm min} \simeq \frac{v_k\sqrt{f(e_{\rm in})}}{2 b_k z_k(e_{\rm in})}(1 - r_k)\,. \quad \text{(E8)}$$

The left hand side can be interpreted as the minimal amount of cloud needed to start floating at a particular resonance. In turn, if the right hand side is larger than one, floating cannot start. The same condition can also be used to estimate the amount of cloud left when floating stops, by matching into the linear LZ solution *backwards*, from the end of the floating time,

$$|c_a(\infty)|^2 \simeq \frac{v_k\sqrt{f(e_{\rm fin})}}{2 b_k z_k(e_{\rm fin})}(1 - r_k)\,, \quad \text{(E9)}$$

which then becomes the portion of the cloud surviving *after* floating stops. Strong decay and small z_k could in principle interrupt the floating period and leave a moderate amount of the cloud intact.[7]

However, at the overtones we have $z_k \sim e^{|2k|}$, which is increasing during floating. Hence, as the eccentricity approaches the critical point, for instance at the $k = -1$ overtone, the value of z_k increases by a factor $(e_{\rm cr}/e_{\rm in})^2 \simeq 10^2 - 10^3$, thus significantly extending the floating period, and reducing the amount of cloud left after the transition, in comparison with the naïve estimate in (E8).

In general, the equations in (E3), (E5) and (E9) must be solved self-consistently in order to determine the end state of floating. As an estimate, we may apply (E1) to (E9), and assuming $e_{\rm in} \ll 1$, we have

$$\frac{\Delta\tau_{\rm Fl}}{b_k/\sqrt{f(e_{\rm cr})}} \simeq \left(\frac{x-1}{2x} + \sqrt{\frac{(x+1)^2}{4x^2} - \frac{\lambda}{x}}\right) \quad \text{(E10)}$$

$$\lambda = \frac{v_k}{2 b_k z_k(e_{\rm in})}\,, \quad x = \frac{I_e b_k (1 - f_k)}{e_{\rm in}^2}\,.$$

Notice that for the $k = -1$ overtone, the dependence on $e_{\rm in}$ drops out from the ratio λ/x. In this case $\lambda \ll x$, and we find the longest periods of floating, $\Delta\tau_{\rm Fl} \simeq b_k/\sqrt{f(e_{\rm cr})}$, and largest depletion of the $|c_a(\infty)|^2 \lesssim r_k$. Depending on the resonances and the parameter space, such hierarchy may be also valid for higher overtones.

[7] This is consistent with the "resonance breaking" phenomena discussed in [73]. We thank the authors of [73] for bringing it to our attention.

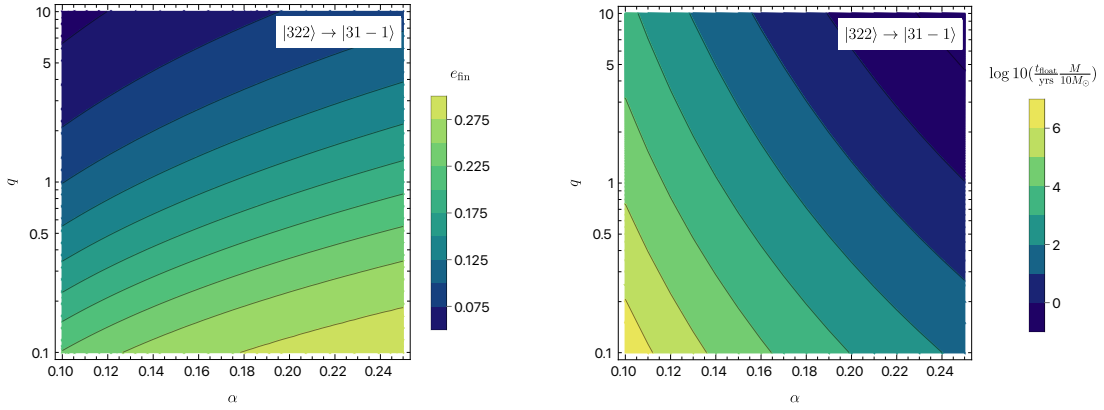


Figure 6. Final eccentricity (*left*) and floating time (*right*), for the $|322\rangle \to |31-1\rangle$ transition with $k=-1$, assuming initial conditions that lead to a (long-lasting) floating orbit ($r_{-1} \simeq 0$) and $e_{\rm in} \ll 1$.

Appendix F: Numerical validation

For generic orbits, the instantaneous position can be expressed as $R_\star = a(1-e\cos u)$, as a function of the eccentric anomaly u. The eccentric anomaly is then related to the mean anomaly via Kepler's equation $u - e\sin(u) = \vartheta$ (e.g. [56]). We have validated the analytic results obtained using the small-eccentricity approximation by numerically solving the Schrödinger equation for arbitrary (planar) orbits, coupled with the energy-momentum balance equations [cf. (3),(9)-(11) of the main text], for a number of representative examples. We use the NDSolve routine in Mathematica [87], monitoring the violation of unitarity in the $\Gamma_b = 0$ regime, residual for $\Gamma_b \geq 0$, as well as the state occupation numbers (D1). We have also checked the consistency of our results by comparing with the values in [48] for $(e, \Gamma_b) = 0$.

In general, the numerical results are broadly consistent with the analytical arguments. As expected, the largest discrepancy occurs for the estimates of $r(t)$ and $|c_a(\infty)|^2$. For the floating regime, the analytic results tend to overestimate their respective values by a factor of few to an order of magnitude. Hence, our conclusions based on the analytic approximations *err on the side of caution*. In Fig. 7 we present (left) the numerical eccentricity evolution of a two-level system with $\Delta m = 2$ for values $\{z_0 = 4, v_0 = 2, b_0 = 200, e_0 = 10^{-2}\}$, at the main resonance. For these parameters, we have $\{z_{-1} = 7\cdot 10^{-3}, v_{-1} = 3.4, b_{-1} = 450, I_e = 2\cdot 10^{-4}\}$ at the $k=-1$ overtone, for which one finds a strong-decay regime: $v_{-1}/z_{-1} = 512$. We start the numerical evaluation before the first overtone, following also the case $v_{-1} = 0$. Away from the resonance, the orbital evolution closely follows standard GW evolution in vacuum. The approximations from Sec. D then correctly predict the strong floating that occurs (in both setups) at the frequency given by (8). Notice that, modulo small deviations, both cases follow the $r_k \simeq 0$ prediction for the eccentricity growth in (E3). Furthermore, broadly consistent with our estimates, the left-over occupancy of the inital state is given by $|c_a(\infty)|^2 \simeq 10^{-4}$ and $|c_a(\infty)|^2 \simeq 10^{-3}$, with and without the decay, respectively. Finally, reducing the backreaction to $b_0 = 25$ (Fig. 7, right), the decaying case does not develop floating as $r_k \simeq 0.8$, although as expected, eccentricity will still grow slightly and the transfer of population is somewhat increased compared to the linear LZ transition. In contrast, the non-decaying case still exhibits a strong floating, follows the predicted growth of the eccentricity and transfers the parent state up to $|c_a(\infty)|^2 \simeq 5\times 10^{-3}$.

Appendix G: Eccentricity distribution

To evaluate the distribution of eccentricities in the population from [15], we order (in frequency) all possible hyperfine and fine resonances with the corresponding overtones, up to $|k| = 5$. (A subset is displayed in Fig. 1.) We then calculate the corresponding parameters (z_k, v_k, b_k) for every resonance the cloud may encounter. The condition that the initial state had enough time to reach the resonance is imposed, constrained by the lifetime imposed by its own GW emission. We evolve in vacuum via [43, 44] between transitions. At every resonance, we estimate r_k as explained in App. D, and from there the floating time, eccentricity growth, and left-over cloud, as explained in App. E. We use a cutoff at 10^{-3} of the initial $M_{c,0}/M$, to estimate when the cloud's influence on the orbital dynamics becomes negligible.

For the BBHs shown in Fig. 1, only a few percent experience a floating transition $|322\rangle \to |31-1\rangle$ with $k<-1$, while 25 % float at the $k=-1$ resonance, making it the dominant one. Approximately 15 % of the population float at the $k=0$ transition. Only a few experience resonances to $|311\rangle$ or $|300\rangle$ states. The black holes with the largest masses, hence largest values of α for fixed μ, can float at the $|320\rangle$ hyperfine transition, where of the order of 5 % (each), see the main or $k=1$ resonance and

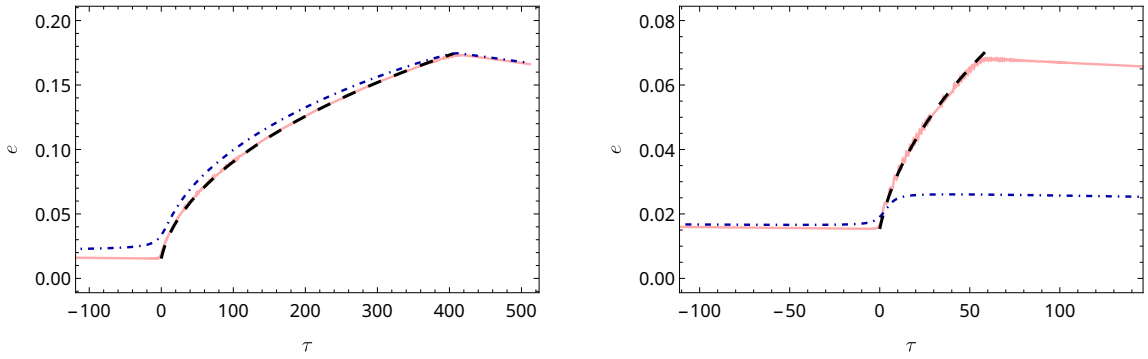


Figure 7. Full numerical evolution of the two examples described in App. F. The two figures correspond to the same z_k but different values for b_k (on the left is a few times larger than on the right). The curves show the evolution in the regime of vanishing (pink), and large decay $v_k \gg z_k$ (blue, dot-dashed), contrasted against the semi-analytic solution for the eccentricity evolution in the $r_k = 0$ limit (black, dashed) [cf. (14) in the main text].

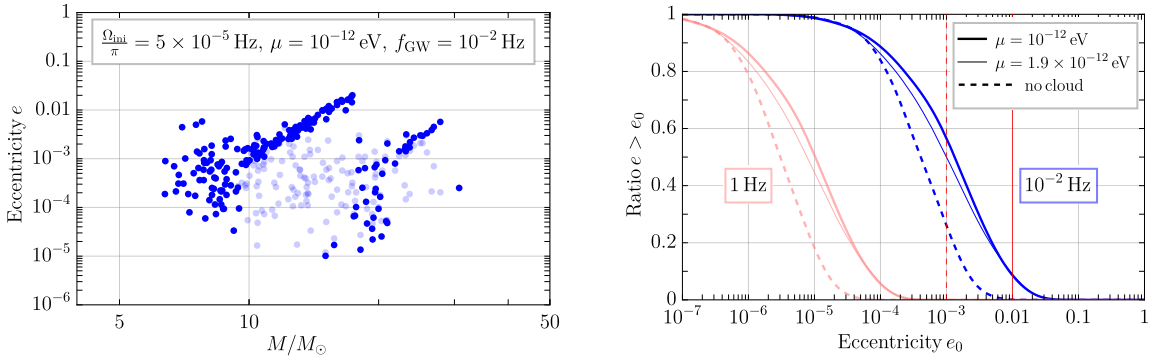


Figure 8. Same as Fig. 1, but with $\Omega_{\rm ini}/\pi = 5\times10^{-5}$ as the birth orbital frequency for the BBH+cloud system.

decrease eccentricity there; or see an earlier resonance, and increase eccentricity instead. In general, hyperfine transitions correspond to the weak-decay regime, while fine transitions are typically of the strong-decay type.

Birth frequency

Similar to Fig. 1, we show in Fig. 8 the eccentricity distribution at $f_{\rm GW} = 10^{-2}\,$Hz, but with a lower birth frequency for the BBH+cloud system, at $\Omega_{\rm ini}/\pi = 5\times10^{-5}\,$Hz. Although the number of larger-than-expected eccentricity points is somewhat lower, the plot illustrates the robustness of our predictions against changes in the initial conditions. In general, a large portion of BBHs that merge within a Hubble time will be born with orbital frequencies between $[0.5, 1]\times10^{-5}$Hz [14]. Moreover, BBHs that are formed through a common-envelope mechanism that can bring the binary closer, e.g. [67], at the same time may produce a (younger) secondary black hole that can ultimately carry the boson cloud, pushing the cloud's birth frequency towards higher values, thus avoiding altogether ($k = 0$) hyperfine transitions that can decrease the eccentricity. Overall, our findings demonstrate that a skewed-type distribution and larger-than-expected eccentricities are robust predictions of the presence of boson clouds in the BBH dynamics.

[1] R. Abbott *et al.* (KAGRA, VIRGO, LIGO Scientific), Open Data from the Third Observing Run of LIGO, Virgo, KAGRA, and GEO, Astrophys. J. Suppl. **267**, 29 (2023), arXiv:2302.03676 [gr-qc].

[2] R. Alves Batista *et al.*, EuCAPT White Paper: Opportunities and Challenges for Theoretical Astroparticle Physics in the Next Decade, (2021), arXiv:2110.10074 [astro-ph.HE].

[3] K. G. Arun *et al.* (LISA), New horizons for fundamental physics with LISA, Living Rev. Rel. **25**, 4 (2022), arXiv:2205.01597 [gr-qc].

[4] M. Maggiore *et al.*, Science Case for the Einstein Telescope, JCAP **03**, 050, arXiv:1912.02622 [astro-ph.CO].

[5] D. Reitze *et al.*, Cosmic Explorer: The U.S. Contribution to Gravitational-Wave Astronomy beyond LIGO, Bull. Am. Astron. Soc. **51**, 035 (2019), arXiv:1907.04833 [astro-ph.IM].

[6] S. Baum, Z. Bogorad, and P. W. Graham, Gravitational Wave Science in the Mid-Band with Atom Interferometers, (2023), arXiv:2309.07952 [gr-qc].

[7] S. Kawamura *et al.*, Current status of space gravitational wave antenna DECIGO and B-DECIGO, PTEP **2021**, 05A105 (2021), arXiv:2006.13545 [gr-qc].

[8] A. Arvanitaki, S. Dimopoulos, S. Dubovsky, N. Kaloper, and J. March-Russell, String Axiverse, Phys. Rev. D **81**, 123530 (2010), arXiv:0905.4720 [hep-th].

[9] A. Arvanitaki and S. Dubovsky, Exploring the String Axiverse with Precision Black Hole Physics, Phys. Rev. D **83**, 044026 (2011), arXiv:1004.3558 [hep-th].

[10] D. J. E. Marsh, Axion Cosmology, Phys. Rept. **643**, 1 (2016), arXiv:1510.07633 [astro-ph.CO].

[11] M. Demirtas, C. Long, L. McAllister, and M. Stillman, The Kreuzer-Skarke Axiverse, JHEP **04**, 138, arXiv:1808.01282 [hep-th].

[12] V. M. Mehta, M. Demirtas, C. Long, D. J. E. Marsh, L. McAllister, and M. J. Stott, Superradiance in string theory, JCAP **07**, 033, arXiv:2103.06812 [hep-th].

[13] K. Belczynski, V. Kalogera, and T. Bulik, A Comprehensive study of binary compact objects as gravitational wave sources: Evolutionary channels, rates, and physical properties, Astrophys. J. **572**, 407 (2001), arXiv:astro-ph/0111452.

[14] I. Kowalska, T. Bulik, K. Belczynski, M. Dominik, and D. Gondek-Rosinska, The eccentricity distribution of compact binaries, Astronomy & Astrophysics **527**, A70 (2011).

[15] K. Breivik, C. L. Rodriguez, S. L. Larson, V. Kalogera, and F. A. Rasio, Distinguishing Between Formation Channels for Binary Black Holes with LISA, Astrophys. J. Lett. **830**, L18 (2016), arXiv:1606.09558 [astro-ph.GA].

[16] A. Nishizawa, E. Berti, A. Klein, and A. Sesana, eLISA eccentricity measurements as tracers of binary black hole formation, Phys. Rev. D **94**, 064020 (2016), arXiv:1605.01341 [gr-qc].

[17] A. Nishizawa, A. Sesana, E. Berti, and A. Klein, Constraining stellar binary black hole formation scenarios with eLISA eccentricity measurements, Mon. Not. Roy. Astron. Soc. **465**, 4375 (2017), arXiv:1606.09295 [astro-ph.HE].

[18] C. L. Rodriguez, M. Zevin, C. Pankow, V. Kalogera, and F. A. Rasio, Illuminating Black Hole Binary Formation Channels with Spins in Advanced LIGO, Astrophys. J. Lett. **832**, L2 (2016), arXiv:1609.05916 [astro-ph.HE].

[19] C. L. Rodriguez, P. Amaro-Seoane, S. Chatterjee, and F. A. Rasio, Post-Newtonian Dynamics in Dense Star Clusters: Highly-Eccentric, Highly-Spinning, and Repeated Binary Black Hole Mergers, Phys. Rev. Lett. **120**, 151101 (2018), arXiv:1712.04937 [astro-ph.HE].

[20] C. L. Rodriguez, P. Amaro-Seoane, S. Chatterjee, K. Kremer, F. A. Rasio, J. Samsing, C. S. Ye, and M. Zevin, Post-Newtonian Dynamics in Dense Star Clusters: Formation, Masses, and Merger Rates of Highly-Eccentric Black Hole Binaries, Phys. Rev. D **98**, 123005 (2018), arXiv:1811.04926 [astro-ph.HE].

[21] M. E. Lower, E. Thrane, P. D. Lasky, and R. Smith, Measuring eccentricity in binary black hole inspirals with gravitational waves, Phys. Rev. D **98**, 083028 (2018), arXiv:1806.05350 [astro-ph.HE].

[22] L. Randall and Z.-Z. Xianyu, Eccentricity without Measuring Eccentricity: Discriminating among Stellar Mass Black Hole Binary Formation Channels, Astrophys. J. **914**, 75 (2021), arXiv:1907.02283 [astro-ph.HE].

[23] X. Fang, T. A. Thompson, and C. M. Hirata, The Population of Eccentric Binary Black Holes: Implications for mHz Gravitational Wave Experiments, Astrophys. J. **875**, 75 (2019), arXiv:1901.05092 [astro-ph.HE].

[24] I. M. Romero-Shaw, P. D. Lasky, E. Thrane, and J. C. Bustillo, GW190521: orbital eccentricity and signatures of dynamical formation in a binary black hole merger signal, Astrophys. J. Lett. **903**, L5 (2020), arXiv:2009.04771 [astro-ph.HE].

[25] M. A. Sedda, Dissecting the properties of neutron star - black hole mergers originating in dense star clusters, Commun. Phys. **3**, 43 (2020), arXiv:2003.02279 [astro-ph.GA].

[26] H. Glanz and H. B. Perets, Common envelope evolution of eccentric binaries, Monthly Notices of the Royal Astronomical Society **507**, 2659 (2021), arXiv:2105.02227 [astro-ph.SR].

[27] M. Zevin, I. M. Romero-Shaw, K. Kremer, E. Thrane, and P. D. Lasky, Implications of Eccentric Observations on Binary Black Hole Formation Channels, Astrophys. J. Lett. **921**, L43 (2021), arXiv:2106.09042 [astro-ph.HE].

[28] A. Gualandris, F. M. Khan, E. Bortolas, M. Bonetti, A. Sesana, P. Berczik, and K. Holley-Bockelmann, Eccentricity evolution of massive black hole binaries from formation to coalescence, Monthly Notices of the Royal Astronomical Society **511**, 4753–4765 (2022).

[29] M. Garg, S. Tiwari, A. Derdzinski, J. G. Baker, S. Marsat, and L. Mayer, The minimum measurable eccentricity from gravitational waves of LISA massive black hole binaries, (2023), arXiv:2307.13367 [astro-ph.GA].

[30] P. Saini, Resolving the eccentricity of stellar mass binary black holes with next generation ground-based gravitational wave detectors 10.1093/mnras/stae037 (2023), arXiv:2308.07565 [astro-ph.HE].

[31] R. Dhurkunde and A. H. Nitz, Search for eccentric NSBH and BNS mergers in the third observing run of Advanced LIGO and Virgo, (2023), arXiv:2311.00242 [astro-ph.HE].

[32] Y. B. Zel'Dovich, Generation of Waves by a Rotating Body, Soviet Journal of Experimental and Theoretical Physics Letters **14**, 180 (1971).

[33] Y. B. Zel'Dovich, Amplification of Cylindrical Electromagnetic Waves Reflected from a Rotating Body, Soviet Journal of Experimental and Theoretical Physics **35**, 1085 (1972).

[34] W. H. Press and S. A. Teukolsky, Floating Orbits, Superradiant Scattering and the Black-hole Bomb, Nature **238**, 211 (1972).

[35] W. E. East, Massive Boson Superradiant Instability of Black Holes: Nonlinear Growth, Saturation, and Gravitational Radiation, Phys. Rev. Lett. **121**, 131104 (2018), arXiv:1807.00043 [gr-qc].

[36] R. Brito, V. Cardoso, and P. Pani, Superradiance: New Frontiers in Black Hole Physics, Lect. Notes Phys. **906**, pp.1 (2015), arXiv:1501.06570 [gr-qc].

[37] D. Baumann, H. S. Chia, and R. A. Porto, Probing Ultralight Bosons with Binary Black Holes, Phys. Rev. D **99**, 044001 (2019), arXiv:1804.03208 [gr-qc].

[38] D. Baumann, H. S. Chia, R. A. Porto, and J. Stout, Gravitational Collider Physics, Phys. Rev. D **101**, 083019 (2020), arXiv:1912.04932 [gr-qc].

[39] D. Baumann, G. Bertone, J. Stout, and G. M. Tomaselli, Ionization of gravitational atoms, Phys. Rev. D **105**, 115036 (2022), arXiv:2112.14777 [gr-qc].

[40] D. Baumann, G. Bertone, J. Stout, and G. M. Tomaselli, Sharp Signals of Boson Clouds in Black Hole Binary Inspirals, Phys. Rev. Lett. **128**, 221102 (2022), arXiv:2206.01212 [gr-qc].

[41] G. M. Tomaselli, T. F. M. Spieksma, and G. Bertone, Dynamical friction in gravitational atoms, JCAP **07**, 070, arXiv:2305.15460 [gr-qc].

[42] H. S. Chia, T. D. P. Edwards, D. Wadekar, A. Zimmerman, S. Olsen, J. Roulet, T. Venumadhav, B. Zackay, and M. Zaldarriaga, In Pursuit of Love: First Templated Search for Compact Objects with Large Tidal Deformabilities in the LIGO-Virgo Data, (2023), arXiv:2306.00050 [gr-qc].

[43] P. C. Peters and J. Mathews, Gravitational radiation from point masses in a Keplerian orbit, Phys. Rev. **131**, 435 (1963).

[44] P. C. Peters, Gravitational Radiation and the Motion of Two Point Masses, Phys. Rev. **136**, B1224 (1964).

[45] E. Berti, R. Brito, C. F. B. Macedo, G. Raposo, and J. L. Rosa, Ultralight boson cloud depletion in binary systems, Phys. Rev. D **99**, 104039 (2019), arXiv:1904.03131 [gr-qc].

[46] M. Boskovic, M. Koschnitzke, and R. A. Porto, In preparation, .

[47] S. L. Detweiler, KLEIN-GORDON EQUATION AND ROTATING BLACK HOLES, Phys. Rev. D **22**, 2323 (1980).

[48] D. Baumann, H. S. Chia, J. Stout, and L. ter Haar, The Spectra of Gravitational Atoms, JCAP **12**, 006, arXiv:1908.10370 [gr-qc].

[49] W. E. East, Superradiant instability of massive vector fields around spinning black holes in the relativistic regime, Phys. Rev. D **96**, 024004 (2017), arXiv:1705.01544 [gr-qc].

[50] S. R. Dolan, Instability of the massive Klein-Gordon field on the Kerr spacetime, Phys. Rev. D **76**, 084001 (2007), arXiv:0705.2880 [gr-qc].

[51] H. Yoshino and H. Kodama, Gravitational radiation from an axion cloud around a black hole: Superradiant phase, PTEP **2014**, 043E02 (2014), arXiv:1312.2326 [gr-qc].

[52] R. Brito, V. Cardoso, and P. Pani, Black holes as particle detectors: evolution of superradiant instabilities, Class. Quant. Grav. **32**, 134001 (2015), arXiv:1411.0686 [gr-qc].

[53] A. Arvanitaki, M. Baryakhtar, and X. Huang, Discovering the QCD Axion with Black Holes and Gravitational Waves, Phys. Rev. D **91**, 084011 (2015), arXiv:1411.2263 [hep-ph].

[54] R. Brito, S. Ghosh, E. Barausse, E. Berti, V. Cardoso, I. Dvorkin, A. Klein, and P. Pani, Gravitational wave searches for ultralight bosons with LIGO and LISA, Phys. Rev. D **96**, 064050 (2017), arXiv:1706.06311 [gr-qc].

[55] N. Siemonsen, T. May, and W. E. East, Modeling the black hole superradiance gravitational waveform, Phys. Rev. D **107**, 104003 (2023), arXiv:2211.03845 [gr-qc].

[56] S. Tremaine, *Dynamics of Planetary Systems* (2023).

[57] L. Landau, Zur theorie der energieubertragung. ii (1932).

[58] C. Zener, Nonadiabatic crossing of energy levels, Proc. Roy. Soc. Lond. A **137**, 696 (1932).

[59] V. M. Akulin and W. P. Schleich, Landau-zener transition to a decaying level, Phys. Rev. A **46**, 4110 (1992).

[60] R. Brito and S. Shah, Extreme mass-ratio inspirals into black holes surrounded by scalar clouds, Phys. Rev. D **108**, 084019 (2023), arXiv:2307.16093 [gr-qc].

[61] N. V. Vitanov and S. Stenholm, Pulsed excitation of a transition to a decaying level, Phys. Rev. A **55**, 2982 (1997).

[62] T. Takahashi, H. Omiya, and T. Tanaka, Evolution of binary systems accompanying axion clouds in extreme mass ratio inspirals, Phys. Rev. D **107**, 103020 (2023), arXiv:2301.13213 [gr-qc].

[63] T. Takahashi, H. Omiya, and T. Tanaka, Axion cloud evaporation during inspiral of black hole binaries: The effects of backreaction and radiation, PTEP **2022**, 043E01 (2022), arXiv:2112.05774 [gr-qc].

[64] G. Ficarra, P. Pani, and H. Witek, Impact of multiple modes on the black-hole superradiant instability, Phys. Rev. D **99**, 104019 (2019), arXiv:1812.02758 [gr-qc].

[65] L. Hui, Y. T. A. Law, L. Santoni, G. Sun, G. M. Tomaselli, and E. Trincherini, Black hole superradiance with dark matter accretion, Phys. Rev. D **107**, 104018 (2023), arXiv:2208.06408 [gr-qc].

[66] N. V. Vitanov, Transition times in the Landau-Zener model, Phys. Rev. A **59**, 988 (1999), arXiv:quant-ph/9811066.

[67] K. Belczynski *et al.*, Evolutionary roads leading to low effective spins, high black hole masses, and O1/O2 rates for LIGO/Virgo binary black holes, Astron. Astrophys. **636**, A104 (2020), arXiv:1706.07053 [astro-ph.HE].

[68] L. Wen, On the eccentricity distribution of coalescing black hole binaries driven by the Kozai mechanism in globular clusters, Astrophys. J. **598**, 419 (2003), arXiv:astro-ph/0211492.

[69] B. P. Abbott *et al.* (LIGO Scientific, Virgo), GWTC-1: A Gravitational-Wave Transient Catalog of Compact Binary Mergers Observed by LIGO and Virgo during the First and Second Observing Runs, Phys. Rev. X **9**, 031040 (2019), arXiv:1811.12907 [astro-ph.HE].

[70] L. Randall and Z.-Z. Xianyu, An Analytical Portrait of Binary Mergers in Hierarchical Triple Systems, Astrophys. J. **864**, 134 (2018), arXiv:1802.05718 [gr-qc].

[71] L. Randall and Z.-Z. Xianyu, Observing Eccentricity Oscillations of Binary Black Holes in LISA, (2019), arXiv:1902.08604 [astro-ph.HE].
[72] D. Wadekar, J. Roulet, T. Venumadhav, A. K. Mehta, B. Zackay, J. Mushkin, S. Olsen, and M. Zaldarriaga, New black hole mergers in the LIGO-Virgo O3 data from a gravitational wave search including higher-order harmonics, (2023), arXiv:2312.06631 [gr-qc].
[73] G. M. Tomaselli, T. F. M. Spieksma, and G. Bertone, To appear, .
[74] H. Yoshino and H. Kodama, The bosenova and axiverse, Class. Quant. Grav. **32**, 214001 (2015), arXiv:1505.00714 [gr-qc].
[75] A. Gruzinov, Black Hole Spindown by Light Bosons, (2016), arXiv:1604.06422 [astro-ph.HE].
[76] M. Baryakhtar, M. Galanis, R. Lasenby, and O. Simon, Black hole superradiance of self-interacting scalar fields, Phys. Rev. D **103**, 095019 (2021), arXiv:2011.11646 [hep-ph].
[77] H. S. Chia, C. Doorman, A. Wernersson, T. Hinderer, and S. Nissanke, Self-interacting gravitational atoms in the strong-gravity regime, JCAP **04**, 018, arXiv:2212.11948 [gr-qc].
[78] J. a. G. Rosa and T. W. Kephart, Stimulated Axion Decay in Superradiant Clouds around Primordial Black Holes, Phys. Rev. Lett. **120**, 231102 (2018), arXiv:1709.06581 [gr-qc].
[79] M. Boskovic, R. Brito, V. Cardoso, T. Ikeda, and H. Witek, Axionic instabilities and new black hole solutions, Phys. Rev. D **99**, 035006 (2019), arXiv:1811.04945 [gr-qc].
[80] H. Fukuda and K. Nakayama, Aspects of Nonlinear Effect on Black Hole Superradiance, JHEP **01**, 128, arXiv:1910.06308 [hep-ph].
[81] T. F. M. Spieksma, E. Cannizzaro, T. Ikeda, V. Cardoso, and Y. Chen, Superradiance: Axionic couplings and plasma effects, Phys. Rev. D **108**, 063013 (2023), arXiv:2306.16447 [gr-qc].
[82] Y. Chen, X. Xue, and V. Cardoso, Black Holes as Neutrino Factories, (2023), arXiv:2308.00741 [hep-ph].
[83] E. Cannizzaro, L. Sberna, S. R. Green, and S. Hollands, Relativistic Perturbation Theory for Black-Hole Boson Clouds, Phys. Rev. Lett. **132**, 051401 (2024), arXiv:2309.10021 [gr-qc].
[84] F. Duque, C. F. B. Macedo, R. Vicente, and V. Cardoso, Axion Weak Leaks: extreme mass-ratio inspirals in ultralight dark matter, (2023), arXiv:2312.06767 [gr-qc].
[85] S. L. Detweiler and E. Poisson, Low multipole contributions to the gravitational selfforce, Phys. Rev. D **69**, 084019 (2004), arXiv:gr-qc/0312010.
[86] Y. Cao and Y. Tang, Signatures of ultralight bosons in compact binary inspiral and outspiral, Phys. Rev. D **108**, 123017 (2023), arXiv:2307.05181 [gr-qc].
[87] W. R. Inc., Mathematica, Version 13.2, champaign, IL, 2022.

Draft version March 6, 2024
Typeset using LaTeX **twocolumn** style in AASTeX63

arXiv:2403.02398v1 [astro-ph.GA] 4 Mar 2024

Microlensing optical depth and event rate toward the Large Magellanic Cloud based on 20 years of OGLE observations

Przemek Mróz,[1] Andrzej Udalski,[1] Michał K. Szymański,[1] Mateusz Kapusta,[1] Igor Soszyński,[1] Łukasz Wyrzykowski,[1] Paweł Pietrukowicz,[1] Szymon Kozłowski,[1] Radosław Poleski,[1] Jan Skowron,[1] Dorota Skowron,[1] Krzysztof Ulaczyk,[2,1] Mariusz Gromadzki,[1] Krzysztof Rybicki,[3,1] Patryk Iwanek,[1] Marcin Wrona,[1] and Milena Ratajczak[1]

[1] *Astronomical Observatory, University of Warsaw, Al. Ujazdowskie 4, 00-478 Warszawa, Poland*
[2] *Department of Physics, University of Warwick, Coventry CV4 7 AL, UK*
[3] *Department of Particle Physics and Astrophysics, Weizmann Institute of Science, Rehovot 76100, Israel*

(Received; Revised; Accepted)

ABSTRACT

Measurements of the microlensing optical depth and event rate toward the Large Magellanic Cloud (LMC) can be used to probe the distribution and mass function of compact objects in the direction toward that galaxy – in the Milky Way disk, Milky Way dark matter halo, and the LMC itself. The previous measurements, based on small statistical samples of events, found that the optical depth is an order of magnitude smaller than that expected from the entire dark matter halo in the form of compact objects. However, these previous studies were not sensitive to long-duration events with Einstein timescales longer than 2.5–3 years, which are expected from massive ($10 - 100\,M_\odot$) and intermediate-mass ($10^2 - 10^5\,M_\odot$) black holes. Such events would have been missed by the previous studies and would not have been taken into account in calculations of the optical depth. Here, we present the analysis of nearly 20-year-long photometric monitoring of 78.7 million stars in the LMC by the Optical Gravitational Lensing Experiment (OGLE) from 2001 through 2020. We describe the observing setup, the construction of the 20-year OGLE dataset, the methods used for searching for microlensing events in the light curve data, and the calculation of the event detection efficiency. In total, we find 16 microlensing events (thirteen using an automated pipeline and three with manual searches), all of which have timescales shorter than 1 yr. We use a sample of thirteen events to measure the microlensing optical depth toward the LMC $\tau = (0.121 \pm 0.037) \times 10^{-7}$ and the event rate $\Gamma = (0.74 \pm 0.25) \times 10^{-7}\,\mathrm{yr}^{-1}\,\mathrm{star}^{-1}$. These numbers are consistent with lensing by stars in the Milky Way disk and the LMC itself, and demonstrate that massive and intermediate-mass black holes cannot comprise a significant fraction of dark matter.

Keywords: Gravitational microlensing (672), Dark matter (353), Milky Way dark matter halo (1049), Large Magellanic Cloud (903), Primordial black holes (1292), Intermediate-mass black holes (816)

1. INTRODUCTION

The discoveries of gravitational waves produced during mergers of massive black holes in distant galaxies by LIGO and Virgo detectors (Abbott et al. 2016, 2019, 2021, 2023) raised questions if such black holes exist in the Milky Way and, if yes if they can be detected using other means than gravitational waves. Most black holes detected in the Milky Way using electromagnetic observations have typically masses below $15 - 20\,M_\odot$ (Corral-Santana et al. 2016), whereas those detected by gravitational-wave detectors are on average more massive. They can reach more than $100\,M_\odot$ (Abbott et al. 2020a,b).

The origin of black holes discovered by gravitational-wave detectors is a subject of vigorous debate (e.g., Costa et al. 2023 and references therein). Several authors (e.g., Bird et al. 2016; Sasaki et al. 2016;

Corresponding author: Przemek Mróz
pmroz@astrouw.edu.pl

Clesse & García-Bellido 2017) proposed that some of them may be primordial black holes (PBHs), which are thought to have been produced in the early universe (e.g., Zel'dovich & Novikov 1967; Hawking 1971; Carr & Hawking 1974; Chapline 1975). If such black holes existed in the Milky Way dark matter halo in large numbers, then they should cause long-timescale gravitational microlensing events that may be potentially detected.

Searches for massive compact objects in the Milky Way halo have been carried out since the early 1990s, following the idea put forward by Paczyński (1986), who proposed monitoring the brightness of millions of stars in the Magellanic Clouds on timescales from hours to years. If the whole dark matter was composed of compact objects, for example PBHs, then the microlensing optical depth toward the center of the Large Magellanic Cloud (LMC) should equal approximately 4.4×10^{-7} (e.g., Alcock et al. 2000; Mróz et al. 2024). The microlensing optical depth depends on the distribution of matter along the line of sight, and it can be interpreted as the probability of observing microlensing events toward a given position.

The subsequent studies of microlensing events toward the LMC found that the optical depth is substantially smaller than the value expected from the dark matter halo. Alcock et al. (2000) estimated $\tau = 1.2^{+0.4}_{-0.3} \times 10^{-7}$ after the analysis of 5.7 yr of time-series photometric data for 11.9 million stars observed by the MACHO project. A re-analysis of the MACHO data by Bennett (2005) found a slightly lower value of $\tau = (1.0 \pm 0.3) \times 10^{-7}$. However, independent studies by EROS (Tisserand et al. 2007) and the Optical Gravitational Lensing Experiment (OGLE; Wyrzykowski et al. 2009, 2011) did not confirm the MACHO findings and found that the optical depth toward the LMC is an order of magnitude lower. Moreover, it was realized that the measurements by EROS and OGLE are consistent with the self-lensing phenomenon (background stars are lensed by foreground objects in the LMC; Sahu 1994), leaving little room for compact objects in the Milky Way halo (e.g., Calchi Novati et al. 2009; Calchi Novati & Mancini 2011).

The EROS-2 survey used the MarLy 1-meter telescope at La Silla Observatory, Chile, and monitored the LMC between 1996 and 2003. Tisserand et al. (2007) detected only one microlensing event in a sample of 7 million stars observed by EROS for 6.7 yr and inferred an upper limit on $\tau < 0.36 \times 10^{-7}$.

The OGLE project uses a 1.3-m Warsaw Telescope located at Las Campanas Observatory, Chile. The observations of the LMC by OGLE started during the second phase of the survey (OGLE-II; Udalski et al. 1997) in the years 1996–2000. During that time, 21 fields were observed that covered a central part of the LMC (with a total area of 4.72 $\deg^2$). A 2048×2048 camera with a pixel size of 0.417 arcsec pixel^{-1} was operated in a drift-scan mode, allowing for observations of a field 2048×8192 pixels wide in one exposure. The OGLE-II data were analyzed by Wyrzykowski et al. (2009), who reported the detection of only two candidates for microlensing events and measured the microlensing optical depth of $(0.43 \pm 0.33) \times 10^{-7}$.

A larger area of 40 $\deg^2$ toward the LMC was observed during the third phase of the survey (OGLE-III; Udalski 2003) during the years 2001–2009. The project operated a mosaic camera comprising eight 2048×4096 CCD detectors, with a pixel scale of 0.26 arcsec pixel^{-1}. Wyrzykowski et al. (2011) found four candidate microlensing events in the OGLE-III data. They estimated the microlensing optical depth of $(0.16 \pm 0.12) \times 10^{-7}$ toward the LMC.

From the observational point of view, the microlensing optical depth can be estimated from

$$\tau = \frac{\pi}{2 N_\mathrm{s} \Delta T} \sum_i \frac{t_{\mathrm{E},i}}{\varepsilon(t_{\mathrm{E},i})}, \tag{1}$$

where $t_{\mathrm{E},i}$ is the Einstein timescale of the ith event, $\varepsilon(t_{\mathrm{E},i})$ is the detection efficiency of the event, ΔT is the duration of observations, and N_s is the number of source stars observed in the experiment. The summation is performed over all events detected.

Because of the limited duration of the MACHO, EROS, OGLE-II, and OGLE-III surveys (from five to nine years), these experiments were not sensitive to very long-duration microlensing events that are expected from massive ($10 - 100\,M_\odot$) and intermediate-mass ($10^2 - 10^5\,M_\odot$) black holes ($t_\mathrm{E} \approx 1.7\,\mathrm{yr}\sqrt{M/100\,M_\odot}$, where M is the mass of the lens). The inspection of detection efficiency curves published by Alcock et al. (2000), Tisserand et al. (2007), and Wyrzykowski et al. (2009, 2011) reveals zero efficiency at $t_\mathrm{E} \gtrsim 2.5 - 3\,\mathrm{yr}$. If black holes with masses in the range $10 - 1000\,M_\odot$ existed in a large number in the Milky Way halo, they would have been missed by these experiments and would not have been taken into account in calculations of the optical depth.

In this paper, we analyzed the data collected during the fourth phase of the OGLE project (OGLE-IV; Udalski et al. 2015) during the years 2010–2020. Because the OGLE-III and OGLE-IV surveys had a similar setup, we combined the two data sets to create homogeneous, nearly 20-year-long light curves for about 33 million objects. An additional 29 million objects were observed only during the OGLE-IV phase. We used the

combined OGLE-III/OGLE-IV data to search for microlensing events with timescales as long as ~ 10 years, filling the gap in the sensitivity of the previous surveys. Our main goal was to verify if long-timescale events can significantly contribute to the optical depth toward the LMC.

In Section 2, we describe the new combined OGLE-III/OGLE-IV data set used in the analysis. The selection of microlensing events and their properties are discussed in Sections 3 and 4. In Section 5, we estimate the number of source stars observed in our experiment. Section 6 describes the simulations used to measure the event detection efficiency. The measurements of the optical depth and event rate toward the LMC are presented and discussed in Sections 7 and 8. The calculation of the constraints on the frequency of PBHs in dark matter is presented in detail in a companion paper (Mróz et al. 2024).

2. DATA

2.1. *OGLE-IV Data*

The fourth phase of the OGLE project (OGLE-IV; Udalski et al. 2015) was commenced in March 2010. However, the regular observations started a few months later, in June 2010. We analyzed the data collected from June 29, 2010 (JD = 2455378) to March 15, 2020 (JD = 2458924), in total nearly ten years of the time-series data.

The observations were taken with a mosaic CCD camera containing thirty-two 2048×4102 detectors with a pixel scale of 0.26 arcsec pixel^{-1}, resulting in a total field of view of about 1.4 deg^2. A detailed description of this instrument was presented by Udalski et al. (2015).

We analyzed observations of 213 fields covering nearly 300 deg^2 around the LMC. The location of the fields in the sky is presented in Figure 1. Table 1 includes the basic information about the analyzed fields, including their equatorial coordinates.

The vast majority of observations were taken through the I-band filter, closely resembling that of the Cousins photometric system. The typical exposure time was 150 s, providing photometry in the range of $13 \lesssim I \lesssim 21.7$ mag. Each OGLE-IV field was observed in the I-band from 121 to 911 times (with a median number of 368 epochs), with a typical cadence of 3–10 days. Some additional observations (from 5 to 313 with a median of 16, depending on the field) were collected in the Johnson V-band filter to characterize the objects.

The photometry was performed using the Difference Image Analysis technique (DIA; Alard & Lupton 1998; Woźniak 2000). For each field observed by OGLE-IV, a reference image was created by stacking several (typically 3–8) high-quality, low-seeing frames. The reference image was then subtracted from the incoming frames, and the photometry was performed on the subtracted images. Variable sources that were detected on subtracted images were flagged. See Udalski et al. (2015) for a detailed description of the image reduction pipeline, photometric calibration, and astrometric transformations.

Reference images for the analyzed fields were constructed from the images taken between 2010 and 2012. Because the dispersion of proper motions of stars in the LMC is typically smaller than 0.05 mas yr^{-1} in one direction (Mróz et al. 2024), the positions of stars changed by less than 0.002 OGLE pixel, even after 10 years, enabling us to achieve high-quality photometric observations throughout the entire analyzed period. This may not be the case for foreground, high proper motion stars, whose light curves may exhibit systematic trends.

2.2. *Combined OGLE-III/OGLE-IV Data*

The observing setup of the OGLE-IV survey was similar to that of OGLE-III. Therefore, we explored a possibility of combining the two data sets to create homogeneous 20-year-long light curves. A naive approach would involve cross-matching stars detected on OGLE-III and OGLE-IV reference images and then combining their light curves. However, because the reference images differ, the OGLE-III and OGLE-IV light curves may be systematically shifted, especially in the most crowded fields. This situation may happen when two stars are resolved in OGLE-IV but may not be resolved in OGLE-III (or vice versa).

Instead, we reduced the OGLE-III images using the OGLE DIA pipeline (Woźniak 2000) using the OGLE-IV reference images. As discussed above, the dispersion of proper motions of stars in the LMC is small enough that decent subtractions were possible even for the earliest OGLE-III frames. A significant difficulty in performing the DIA photometry was connected to the fact that OGLE-III and OGLE-IV fields were different, so the images had to be split into smaller chunks, rotated, shifted, and resampled before performing the DIA photometry. In rare cases, when the overlap between OGLE-III and OGLE-IV images was small, the OGLE-III data may be missing for individual objects.

Table 1 presents a list of OGLE-IV fields together with the number of stars observed during both OGLE-III and OGLE-IV (that is, from 2001 to 2020) and during only OGLE-IV (from 2010 to 2020). The OGLE-III data were available for 33 million stars, and an additional 29 million objects were observed only during the OGLE-IV phase. Note that this is not equivalent to the num-

ber of microlensing source stars that enter the optical depth calculations (Eq. 1). OGLE-III fields were observed from 385 to 637 times in the I-band. However, some stars may be located in overlapping fields, and the available number of epochs may be larger. The number of epochs, separately for OGLE-III and OGLE-IV phases, is shown in the fourth and fifth columns of Table 1.

Although the observing setups of OGLE-III and OGLE-IV were very similar, different filters were used (Udalski 2003; Udalski et al. 1997, 2015). The transmission curves of I-band filters (both of which were very similar to that of the standard Cousins filter) were slightly different. We thus found a color-dependent shift between mean magnitudes in the new OGLE-III data set and the OGLE-IV light curves. This shift was independent of the field. The median shift for stars in the color range $-0.171 \leq V - I \leq 2.602$ is presented in Table 2.

We corrected all new OGLE-III photometric measurements for all analyzed stars by adding a constant magnitude shift that depends on the mean color of the star. The correction was found from the cubic spline interpolation of data presented in Table 2. If the star's color were outside the interpolation range, we estimated the correction using the linear extrapolation of the trend. Figure 2 presents the comparison between the final new OGLE-III and OGLE-IV mean magnitudes for one of the analyzed fields (LMC502.11) as a function of color (upper diagram) and mean magnitude (lower diagram). The mean difference between OGLE-III and OGLE-IV mean magnitudes is consistent with zero in the entire analyzed range.

Figure 3 shows the comparison between the rms scatter in the new OGLE-III and OGLE-IV light curves for one of the analyzed fields (LMC502.11). The black dashed and solid lines mark the lower envelope of the distributions for the new OGLE-III and OGLE-IV data sets, respectively. The new OGLE-III light curves are slightly more noisy than the OGLE-IV light curves; their mean scatter is larger by $\approx 12\%$.

About 5.5 million objects in the central LMC fields were observed in the second phase of the OGLE survey (OGLE-II) in 1996–2000. Although including the OGLE-II data would extend their light curves to 24 years, boosting the sensitivity to long-timescale microlensing events, we decided not to do that. The OGLE-II camera had a different pixel size than the OGLE-III and OGLE-IV cameras, making it nearly impossible to obtain homogeneous DIA photometry across all three survey phases. However, whenever the OGLE-II data were available, we used them to check the archival photometric behavior of the analyzed events.

2.3. *Correction of Error Bars*

The error bars that are returned by the DIA pipeline are known to be underestimated (e.g., Skowron et al. 2016). We therefore rescaled the error bars using the formula $\delta m_{\rm new} = \sqrt{(\gamma \delta m_{\rm old})^2 + \varepsilon^2}$, where γ and ε are coefficients depending on the field and filter. We closely followed the procedures outlined by Skowron et al. (2016) to measure the values of γ and ε. In short, we calculated the rms scatter of constant stars in a given field as a function of magnitude. We then found γ and ε for which the rescaled uncertainties follow the statistical behavior of nearby constant stars. Because the noise properties of the new OGLE-III and OGLE-IV light curves are slightly different (Figure 3), we calculated and applied the coefficients separately for OGLE-III and OGLE-IV light curves. The best-fit coefficients are reported in Table 3.

3. SEARCH FOR EVENTS

We searched for microlensing events using the database of 62 million light curves of objects detected on OGLE-IV reference images. The OGLE-III data were available for 33 million stars and were extracted using the procedure described in Section 2. The uncertainties reported by the photometric pipeline were corrected as described in Section 2.3, and then magnitudes were transformed into flux units.

Our search procedure was similar to that developed by Mróz et al. (2017), who analyzed OGLE-IV light curves of stars in high-cadence Galactic bulge fields. It consisted of three steps, which are summarized in Table 4. First, objects showing any brightening with respect to the flat part of the light curve were selected. We placed a window of length W on a light curve and calculated the mean flux ($F_{\rm base}$) and standard deviation ($\sigma_{\rm base}$) using data points outside the window (after removing 4σ outliers). We also calculated $\chi^2_{\rm out} = \sum_i (F_i - F_{\rm base})^2/\sigma_i^2$, where (F_i, σ_i) is the flux and its uncertainty of the ith data point outside the window. We then searched for at least $n_{\rm bump}$ consecutive data points brighter than $F_{\rm base} + 3\sigma_{\rm base}$ within the window (which we called a 'bump'). If the bump was identified, we calculated several quantities, including its amplitude Δm, duration Δt, and significance $\chi_{3+} = \sum_i (F_i - F_{\rm base})/\sigma_i$, where the summation was performed over all data points within the bump. We also counted the number of epochs $n_{\rm DIA}$ when the DIA pipeline detected the object on subtracted images. Subsequently, the window was shifted by S days, and the entire procedure was repeated until the end of the light curve was reached. A bump with the largest value of χ_{3+} was finally selected.

For objects with both OGLE-III and OGLE-IV data available, we ran the algorithm twice using $(W, S) = (6000, 500)$ and $(3000, 500)$ days. We also ran the algorithm separately on OGLE-III and OGLE-IV light curves with $(W, S) = (1500, 300)$ days. This procedure enabled us to select events lasting several years and those with timescales of several days. For the next step, we selected events fulfilling the following criteria: a) $n_{\rm bump} \geq 5$, b) $n_{\rm DIA} \geq 3$, c) $\chi_{3+} \geq 32$, d) $\Delta m \geq 0.1$ mag. If the duration of the bump was shorter than 1000 days, we also required $\chi^2_{\rm out}/{\rm dof} \leq 2$ (that is, no significant variability outside of the window). For bumps longer than 100 days, we required their amplitude to be at least 0.4 mag to minimize the contamination from stars varying on long timescales. This simple procedure allowed us to reduce the number of analyzed light curves from over 62 million to 56,000.

In the next step, we further reduced the number of candidate events by eliminating obvious non-microlensing light curves. The vast majority of removed objects were "blue bumper" stars, which are bright and blue main-sequence stars located in the optical color–magnitude diagrams in the region defined by $(V-I)_0 \leq 0.5$ and $I_0 \leq 19.5$. Outbursts of "blue bumper" stars are known to mimic light curves of gravitational microlensing events (e.g., Alcock et al. 1997). Since these outbursts may be repeating, many objects can be removed by requiring that there was only one brightening in the analyzed light curve. In addition to removing objects with multiple peaks, we removed all stars brighter than $I_0 \leq 19.5$ and bluer than $(V-I)_0 \leq 0.5$ from our sample. We de-reddened the observed colors and magnitudes using the reddening maps of Skowron et al. (2021). Finally, we removed variable objects in the vicinity (30′) of the supernova SN 1987A remnant. These are known to be artifacts caused by the moving light echo from the supernova (e.g., Tisserand et al. 2007; Wyrzykowski et al. 2011). Over 7000 objects were removed in this step.

Finally, a microlensing point-source point-lens model was fitted to the data, and several goodness-of-the-fit statistics were evaluated. The model is described by a formula

$$F_i = F_0 \left[1 + f_{\rm s} \left(A(t_i; t_0, t_{\rm E}, u_0) - 1\right)\right], \qquad (2)$$

where $f_{\rm s} = F_{\rm s}/(F_{\rm s} + F_{\rm b})$ is the dimensionless blending parameter and F_0 is the baseline flux. Here, $F_{\rm s}$ and $F_{\rm b}$ are the source star flux (which is magnified during the event), and the additional blend flux (which remains constant throughout the event, and may come from unrelated stars blended with the source and/or the lens itself), respectively. The magnification was evaluated using the Paczyński (1986) formula

$$A(t_i; t_0, t_{\rm E}, u_0) = \frac{u^2+2}{u\sqrt{u^2+4}}, \qquad (3)$$

where $u = \sqrt{\left((t_i - t_0)/t_{\rm E}\right)^2 + u_0^2}$, t_0 is the time of the smallest lens-source separation, u_0 is the minimal lens-source separation (in Einstein radius units), and $t_{\rm E}$ is the Einstein radius crossing timescale.

The best-fit parameters were found by minimizing the function

$$\chi^2 = \sum_{i=1}^{N} \left(\frac{F_i - F_0 \left[1 + f_{\rm s} \left(A(t_i; t_0, t_{\rm E}, u_0) - 1\right)\right]}{\sigma_i} \right)^2 \qquad (4)$$

using the Levenberg-Marquardt algorithm as implemented in the GNU Scientific Library[1], where N is the number of data points. The starting values were calculated based on the properties (time of the peak, duration, amplitude) of the bump. The algorithm yielded the best-fit parameters and their covariance matrix. We fitted two types of models: one with the blend flux set to zero ($F_{\rm b} = 0$) (a "four-parameter" model), and one with the blend flux allowed to vary (a "five-parameter" model). We used the five-parameter model as a default model. However, if the five-parameter fit did not converge or it yielded an unphysical value of the blending parameter ($f_{\rm s} - \sigma(f_{\rm s}) \geq 1$)), we used the four-parameter fit instead.

We calculated χ^2 of the best-fit model for the entire data set, as well as $\chi^2_{t_{\rm E}}$ and $\chi^2_{\rm bump}$ for the data points within $t_{\rm E}$ of the peak and within the bump, respectively. We required that the model described the data well, i.e., all three statistics $\chi^2/{\rm d.o.f.} \leq 2$. Additionally, we required the best-fit value $u_0 \leq 1$, the best-fit t_0 should be within the time range covered by the data, the source magnitude should be brighter than $I_{\rm s} = 22$ mag, and the Einstein timescale to be reasonably well measured, that is, $\sigma(t_{\rm E})/t_{\rm E} \leq 1$. Finally, we fitted a straight line to the data and calculated $\chi^2_{\rm line}$ of the best-fit model. We required that the microlensing model should describe the data better than the straight line, that is $\chi^2_{\rm line} - \chi^2 \geq 250\chi^2/{\rm d.o.f.}$

We did not take into account the microlensing parallax effect when performing the search for the events. The microlensing parallax induces a subtle deviation from the standard point-lens point-source model in the light curves of long-timescale events ($t_{\rm E} \gtrsim 60 - 100$ d) due to the orbital motion of the Earth. Blaineau & Moniez (2020) demonstrated that neglecting the parallax in the

[1] https://www.gnu.org/software/gsl/

fits affects marginally the selection of long-timescale microlensing events. Since the microlensing parallax $\pi_{\rm E}$ scales inversely proportional with the square root of the lens mass M (that is, $\pi_{\rm E} \propto M^{-1/2}$), we expect that the parallaxes of events due to high-mass lenses would be small. For the Milky Way and LMC dark matter halo models presented by Mróz et al. (2024), the mean microlensing parallaxes scale as $\pi_{\rm E} \approx 0.1/\sqrt{M/M_\odot}$ and $\pi_{\rm E} \approx 0.02/\sqrt{M/M_\odot}$, respectively. On the other hand, the microlensing parallax can be neglected for short-timescale events because the relative lens-source trajectory can be accurately approximated as a straight line.

Only thirteen objects passed all selection cuts, forming the final statistical sample of events analyzed in this and companion papers. All events are listed in Table 5, together with their equatorial coordinates, mean I-band magnitude, and $V-I$ color in the baseline. Events OGLE-LMC-04 and OGLE-LMC-05 were previously identified by Wyrzykowski et al. (2011) in the OGLE-III data. The remaining eleven events were new discoveries; we named them OGLE-LMC-NN, where NN runs from 07 through 17. The event OGLE-LMC-15 was announced in September 2018 by the Microlensing Observations in Astrophysics (Bond et al. 2001) survey as MOA-2018-LMC-003.

In addition to automated searches, we manually inspected the light curves of all 56,358 objects that passed the "cut 1" criteria. We identified three additional events. OGLE-LMC-06 was previously found by Wyrzykowski et al. (2011) as a binary-lens event. Because the standard point-source point-lens model poorly fits the data, this event was rejected by the "cut 3" criteria. The best-fit source magnitude of OGLE-LMC-18 placed it below our limit ($I_{\rm s} = 22\,{\rm mag}$), while OGLE-LMC-19 was located in the region occupied by "blue bumper" stars in the color–magnitude diagram. The light curve of the latter object is symmetric, has high amplitude, and can be well-fitted by a standard point-source point-lens microlensing model, so there is no reason to suspect this is a false positive. The three events identified in by-eye searches were not included in the following statistical analysis.

4. DETECTED EVENTS

Once we identified all microlensing events in our sample, we used the Markov chain Monte Carlo (MCMC) methods to refine the best-fit parameters and their uncertainties. We assumed flat (uniform) priors on all parameters except the prior on the blend flux:

$$\mathcal{L}_{\rm prior} = \begin{cases} 1 & \text{if } F_{\rm b} \geq 0, \\ \exp\left(-\frac{F_{\rm b}^2}{2\sigma_{\rm b}^2}\right) & \text{if } F_{\rm b} < 0, \end{cases} \tag{5}$$

where $\sigma_{\rm b}$ is the flux corresponding to a $I = 20.5$ star. This prior enabled us to avoid solutions with unphysically large values of negative blend flux. We ran the MCMC using the code Emcee by Foreman-Mackey et al. (2013), providing us with posterior distributions for model parameters for all events. The modeling results, including the median and the 68% confidence range of the marginalized posterior distributions, are summarized in Table 9. (Table 9 does not contain OGLE-LMC-06, because its light curve cannot be adequately described by a point-source point-lens model.) The best-fit models are plotted in Figure 4.

In addition to standard point-source point-lens models, we also fitted models incorporating the annual microlensing parallax effect. The modeling was performed in the geocentric frame (Gould 2004), with the two additional parameters $(\pi_{{\rm E},N}, \pi_{{\rm E},E})$ (North and East components of the microlensing parallax vector $\boldsymbol{\pi}_{\rm E}$) describing the light curve. The formula for magnification is identical to that in Eq. (3). However, the definition of the u parameter is different: $u = \sqrt{\tau^2 + \beta^2}$, where

$$\tau(t_i) = \frac{t_i - t_0}{t_{\rm E}} + \delta\tau, \quad \beta(t_i) = u_0 + \delta\beta, \tag{6}$$

and

$$(\delta\tau, \delta\beta) = (\boldsymbol{\pi}_{\rm E} \cdot \Delta\boldsymbol{s}, \boldsymbol{\pi}_{\rm E} \times \Delta\boldsymbol{s}), \tag{7}$$

where $\Delta\boldsymbol{s}$ is the projected position of the Sun in the adopted geocentric frame (Gould 2004). For four events from the sample, including the microlens parallax effects improved the fit significantly: OGLE-LMC-09 ($\Delta\chi^2 = 252.3$), OGLE-LMC-10 ($\Delta\chi^2 = 129.0$), OGLE-LMC-12 ($\Delta\chi^2 = 8.2$), and OGLE-LMC-15 ($\Delta\chi^2 = 11.7$). These objects are likely due to lenses located in the foreground Milky Way disk, as discussed by Mróz et al. (2024) in more detail.

For some events with the available V-band data taken during the magnified part of the light curve, we measured the color of the source using the model-independent regression. Source colors are reported in Table 6, and they are generally similar to the colors of events in the baseline, confirming that the majority of observed light originates from the source star. Figure 5 presents a de-reddened color–magnitude diagram of one of the observed fields (LMC516.14). Positions of detected events (in the baseline) are indicated by blue circles. Most of the events occurred on giants and subgiants, and a few events are located on the blue end of the main sequence, confirming that the source stars are located in the LMC.

The overall properties of all events (their positions in the sky, timescales, and microlensing parallaxes) are

consistent with lenses located in the LMC or in the foreground Milky Way disk. A comparison with predictions from the LMC and Milky Way models is discussed in detail in the companion paper (Mróz et al. 2024).

4.1. *Comparison with Previous Searches for Microlensing Events toward the LMC*

The analyzed dataset, by design, contained the vast majority of OGLE-III light curves previously investigated by Wyrzykowski et al. (2011), who discovered four events. We successfully recovered three of them (OGLE-LMC-04, OGLE-LMC-05, and OGLE-LMC-06). The only remaining event (OGLE-LMC-03) was not selected by our pipeline because a 2000–2009 portion of its light curve was missing in the new database. This event is one of a few examples in which the new OGLE-III image reductions failed (Section 2.2). On the other hand, we identified two events (OGLE-LMC-07 and OGLE-LMC-08) that occurred during the OGLE-III phase and were missed by Wyrzykowski et al. (2011).

With the extended OGLE-IV dataset, we also had an opportunity to verify the candidate microlensing events detected by previous searches. If objects underwent additional outbursts or exhibited some other variability, their microlensing interpretation is unlikely to be correct. Wyrzykowski et al. (2009) discovered two candidate events in the OGLE-II data from 1996–2000. The updated light curve of OGLE-LMC-01 showed no variability in data collected after 2001, but OGLE-LMC-02 exhibited three additional outbursts: in March 2010, December 2014, and February 2019. The latter object shares several similarities to known transient supersoft X-ray sources in the LMC and SMC (Maccarone et al. 2019; Mróz et al. 2023) and will be discussed in more detail elsewhere. Since OGLE-LMC-02 is not a microlensing event, the estimates of the optical depth and event rate from OGLE-II data by Wyrzykowski et al. (2009) need to be revised: $\tau = (0.28^{+0.70}_{-0.08}) \times 10^{-7}$ and $\Gamma = (1.1^{+2.8}_{-0.3}) \times 10^{-7}$ yr^{-1}.

One of the candidate events found by Tisserand et al. (2007) in the full sample of EROS stars (EROS2-SMC-2) underwent a low-amplitude outburst in November 2017. The EROS limits on the microlensing optical depth remain unchanged because Tisserand et al. (2007) did not use this event to determine the optical depth.

Among 17 candidate events announced by Alcock et al. (2000) using the MACHO data, two objects showed outbursts in the OGLE-III and OGLE-IV data: MACHO-LMC-7 (in March 2005, January 2007, February 2009, November 2010, January 2012, November 2015, September 2018) and MACHO-LMC-23 (in November 2001). The variability of MACHO-LMC-23 was already noticed by Tisserand et al. (2007) and Wyrzykowski et al. (2011). Wyrzykowski et al. (2011) flagged MACHO-LMC-7 as a variable object. Additionally, we found that three candidate events (MACHO-LMC-08, MACHO-LMC-18, and MACHO-LMC-27) show periodic variability in the baseline (with periods 2.310617 ± 0.000010, 7.02772 ± 0.00015, and 1.532534 ± 0.000025 day, respectively), indicating that outbursts detected by MACHO were likely of stellar origin. Although some microlensing events with periodic variability in the baseline are known toward the Galactic bulge (e.g., Wyrzykowski et al. 2006), they are two orders less common than microlensing events with a constant baseline. The probability of observing three variable-baseline events given the expected 0.2 events in a sample of 17 events is only 10^{-3}. All five objects are likely to be false positives, demonstrating a high contamination rate ($\approx 30\%$) of the MACHO sample. Removing these objects from the sample used to derive the microlensing optical depth by Alcock et al. (2000) lowers it by almost 40%, to 0.74×10^{-7}. We cannot rule out, however, that the contamination rate of the MACHO sample is even higher.

Six out of sixteen analyzed microlensing events (OGLE-LMC-07, OGLE-LMC-09, OGLE-LMC-10, OGLE-LMC-13, OGLE-LMC-14, OGLE-LMC-18) were observed in 1996–2000 by the OGLE-II survey. Light curves of all six events were flat. Finally, we retrieved the archival MACHO photometry for all sixteen microlensing events analyzed in this work. The MACHO data spanned the period from July 1992 to December 1999, so they are complementary to the OGLE-III and OGLE-IV data sets and extend the light curve coverage to nearly 28 years. We found no outbursts or brightenings in the archival MACHO light curves, consistent with the classification of all analyzed objects as microlensing events.

5. NUMBER OF SOURCE STARS

The number of stars detected on OGLE reference images is not equivalent to the number of microlensing source stars that enter the microlensing optical depth calculation (Eq. 1). First, in ground-based, seeing-limited images, two or more stars may be blended and cannot be resolved. Second, some stars observed by OGLE are in the foreground Milky Way disk, and the probability that they would be lensed by compact objects in the Milky Way halo is negligible. Therefore, they should not enter the optical depth calculation.

To quantify the effects of blending on star counts, we used the archive of high-quality stellar photometry from the *Hubble Space Telescope* (*HST*) by Holtzman et al.

(2006). The *HST* images were deeper and had a superb resolution compared to ground-based images, so the vast majority of stars were resolved. The *HST* images in the $F814W$ filter (closely matching the standard I band filter) were available for 64 fields, spanning over a factor of 20 in stellar surface density, from low-density regions in the outer part of the LMC, to the densest fields in the LMC bar.

We calculated the surface density of stars per arcmin^2 on the *HST* images Σ^{HST} and compared it to the surface density of stars per arcmin^2 detected on OGLE reference images $\Sigma^{\rm OGLE}$. Following Wyrzykowski et al. (2011), we called the ratio $\Sigma^{HST}/\Sigma^{\rm OGLE}$ a correction factor (CF), because it allowed us to convert the raw OGLE star counts to the actual number of stars that may be microlensed. We calculated stellar surface density separately for three magnitude ranges: for stars brighter than $I = 21$, $I = 21.5$, and $I = 22$ mag.

As an example, Figure 6 shows the correction factor as a function of the OGLE star density for stars brighter than $I = 21$ mag. We found that it was related to the observed surface density of stars by a formula:

$$\mathrm{CF} = \frac{\Sigma^{HST}}{\Sigma^{\rm OGLE}} = c + \exp\left(a(\log\Sigma^{\rm OGLE} - 2.5) + b\right), \quad (8)$$

where $a = 4.04 \pm 0.21$, $b = -2.246 \pm 0.072$, and $c = 1.00 \pm 0.02$ are the best-fit coefficients.

We derived similar fits for stars brighter than $I = 21.5$ mag: $a = 3.985 \pm 0.077$, $b = -1.527 \pm 0.027$, and $c = 1.03 \pm 0.02$; and for stars brighter than $I = 22$ mag: $a = 2.746 \pm 0.032$, $b = -0.489 \pm 0.010$, and $c = 1.05 \pm 0.01$. These relations allowed us to convert the raw star counts into the total number of possible microlensing source stars. By comparing the predicted number of stars with the actual *HST* observations, the accuracy of determination of star counts was estimated to be 3% (for stars brighter than $I = 21$), 7% (for stars brighter than $I = 21.5$), and 11% (for stars brighter than $I = 22$).

In the next step, we used the star counts in fields located in the outer parts of the LMC region, at RA $\gtrsim$ $6^{\rm h}30^{\rm m}$ or Decl. $\gtrsim -60°$, to estimate the Milky Way foreground. We found that the surface density of foreground stars depends on the Galactic latitude b as:

$$\log\Sigma^{\rm foreground} = \alpha + \beta(|b| - 30°), \quad (9)$$

where α and β are the best-fit coefficients. For stars brighter than $I = 21$ mag: $\alpha = 0.846 \pm 0.016$, $\beta = -0.0231 \pm 0.0019$; for stars brighter than $I = 21.5$ mag: $\alpha = 0.873 \pm 0.018$, $\beta = -0.0231 \pm 0.0022$; for stars brighter than $I = 22$ mag: $\alpha = 0.893 \pm 0.019$, $\beta = -0.0230 \pm 0.0023$.

The final number of source stars observed in a given field was calculated by multiplying the number of stars detected on OGLE reference images by the correction factor (depending on stellar density, Eq. 8), and subtracting the foreground stars (using Eq. 9). The results are presented in Table 7 in which we report $N_{\rm total}$ – the total number of stars (after correcting the raw star counts for blending), and $N_{\rm corr}$ – the number of possible microlensing source stars after removing foreground Milky Way sources. Figure 7 shows the surface density of source stars brighter than $I = 22$ mag.

6. DETECTION EFFICIENCY

We ran extensive simulations to measure the detection efficiency of microlensing events as a function of their Einstein timescale in our experiment. Our method was similar to that described by Mróz et al. (2019). We created synthetic light curves of microlensing events by injecting the simulated signal into light curves from the database. The simulated light curves, therefore, had the same noise properties, sampling, and outliers as the original light curves. We subsequently ran the event and detection modeling pipeline (Section 3) on the synthetic light curves and calculated the fraction of events that pass all selection criteria (Table 4).

The time of the peak t_0 was drawn from a uniform distribution from the range $2452000 \leq t_0 \leq 2459000$ (from April 2001 to May 2020) for fields observed during OGLE-III and OGLE-IV phases, and $2455000 \leq t_0 \leq 2459000$ (from June 2009 to May 2020) for fields observed during OGLE-IV only. The Einstein timescale $t_{\rm E}$ was drawn from a log-uniform distribution from the range 1 to 10^4 days, and the impact parameter u_0 was drawn from a uniform distribution from the range $0 \leq u_0 \leq 1$. The blending parameter $f_{\rm s}$, depending on the mean magnitude of the star, was drawn from the empirical distribution derived by cross-matching OGLE and *HST* stars (Section 5). To take into account binary-lens events, which our automated searches may miss, we lowered the detection efficiency by 10% (Wyrzykowski et al. 2011; Mróz et al. 2019).

We simulated 30,000 events per detector, almost 10^6 events per field, and calculated the detection efficiency in 25 identical bins in $\log t_{\rm E}$. The example detection efficiency curves (for field LMC501) are shown in Figure 8. For fields observed during OGLE-III and OGLE-IV phases, the sensitivity peaks at $t_{\rm E} = 2.5\,$yr and declines by 50% at $t_{\rm E} = 13.8\,$yr. For fields observed during OGLE-IV only, the sensitivity peak is at $t_{\rm E} = 1.2\,$yr, and the detection efficiency falls by 50% at $t_{\rm E} = 6.2\,$yr. We calculated detection efficiencies averaged for sources brighter than $I = 21$, $I = 21.5$, and $I = 22$ mag.

7. OPTICAL DEPTH

The microlensing optical depth τ and event rate Γ were evaluated using the formulae

$$\tau = \frac{\pi}{2N_{\rm s}} \sum_i \frac{1}{\Delta T_i} \frac{t_{{\rm E},i}}{\varepsilon(t_{{\rm E},i})}, \qquad \Gamma = \frac{1}{N_{\rm s}} \sum_i \frac{1}{\Delta T_i} \frac{1}{\varepsilon(t_{{\rm E},i})}, \tag{10}$$

where $\Delta T = 7000$ days or $\Delta T = 4000$ days if the event was observed during both OGLE-III and OGLE-IV phases or during OGLE-IV only, respectively. $N_{\rm s} = 78.7 \times 10^6$ is the number of source stars in the LMC monitored in our experiment (Table 7). To take into account uncertainties on the event timescale, we replaced the terms $t_{{\rm E},i}/\varepsilon(t_{{\rm E},i})$ and $1/\varepsilon(t_{{\rm E},i})$ by the mean over N_i samples from the posterior distribution of $t_{{\rm E},i}$:

$$\frac{t_{{\rm E},i}}{\varepsilon(t_{{\rm E},i})} \longrightarrow \frac{1}{N_i} \sum_{k=1}^{N_i} \frac{t_{{\rm E},ik}}{\varepsilon(t_{{\rm E},ik})}, \qquad \frac{1}{\varepsilon(t_{{\rm E},i})} \longrightarrow \frac{1}{N_i} \sum_{k=1}^{N_i} \frac{1}{\varepsilon(t_{{\rm E},ik})}. \tag{11}$$

We used only events passing our automated selection criteria to calculate the optical depth and event rate. Our sample includes thirteen such events. The total optical depth toward the OGLE-IV fields is estimated at $\tau = (0.121 \pm 0.037) \times 10^{-7}$ and the total event rate is $\Gamma = (0.74 \pm 0.25) \times 10^{-7}\,{\rm yr}^{-1}\,{\rm star}^{-1}$. There is an additional systematic error of 11% related to the accuracy of finding the number of source stars (Section 5). The contribution of each event to the total optical depth and event rate is reported in Table 8.

If we used the median value from the posterior distribution of $t_{\rm E}$ (and the detection efficiency evaluated at the median timescale), instead of using the full posterior, then the total optical depth was estimated at $\tau = (0.112 \pm 0.035) \times 10^{-7}$ and the event rate was $\Gamma = (0.69 \pm 0.23) \times 10^{-7}\,{\rm yr}^{-1}\,{\rm star}^{-1}$. These values are about 7% lower than those calculated using the full posterior distribution; we consider them as less accurate.

8. DISCUSSION

This work represents a significant improvement over the previous efforts to measure the optical depth and event rate toward the LMC. The previous determinations of these quantities by EROS (Tisserand et al. 2007), OGLE-II (Wyrzykowski et al. 2009), and OGLE-III surveys (Wyrzykowski et al. 2011) were based on a small number statistics (either one or two events). Combining the OGLE-III and OGLE-IV datasets enabled us to create homogeneous light curves covering nearly 20 years of photometric monitoring. The analysis of this vast dataset, containing the light curves of 62 million stars, led to the discovery of 16 microlensing events. Thirteen passed our strict selection criteria, allowing us to measure the microlensing optical depth and event rate toward the LMC with unprecedented precision.

Our measurements are in good agreement with the results reported by Wyrzykowski et al. (2011) from the OGLE-III survey, who found $\tau = (0.16 \pm 0.12) \times 10^{-7}$. Although they did not explicitly report the event rate measurement, the data presented by Wyrzykowski et al. (2011) enabled us to find $\Gamma = (1.14 \pm 0.88) \times 10^{-7}\,{\rm yr}^{-1}\,{\rm star}^{-1}$. These measurements are formally consistent within the reported error bars (which are large). However, the best estimates are 30–50% higher than reported here (Section 7). The difference in sky coverage betwen OGLE-III and OGLE-IV fields can explain this difference. The optical depth and event rate were slightly higher since the OGLE-III fields covered a smaller sky area than OGLE-IV, centered on the inner LMC. When we restricted our sample to events located within OGLE-III fields, then the optical depth and event rate were $\tau = (0.150 \pm 0.050) \times 10^{-7}$ and $\Gamma = (0.83 \pm 0.32) \times 10^{-7}\,{\rm yr}^{-1}\,{\rm star}^{-1}$, reaching a better agreement with the Wyrzykowski et al. (2011) findings.

The findings presented in this work also confirm the results from EROS, OGLE-II, and OGLE-III that the optical depth toward the LMC is about an order of magnitude smaller than that reported by the MACHO collaboration (Alcock et al. 2000; Bennett 2005). It was argued that this discrepancy results from different samples of stars analyzed in each experiment: EROS and OGLE-III were concentrated on bright stars ($R < 19.7$ for EROS, $I \leq 18.8$ for OGLE-III), whereas MACHO analyzed stars as faint as $V = 22$. In this work, we studied a sample of all stars observed by OGLE-IV and confirmed the low value of the optical depth. Moreover, we found that at least five candidate events reported by MACHO (30% of their sample) are likely due to stellar variability rather than microlensing. A detailed analysis of the MACHO events is beyond the scope of this work, but we cannot rule out that the contamination is even higher, partly explaining the discrepancy.

Our primary motivation for carrying out this work and combining the OGLE-III and OGLE-IV datasets was the fact that all previous microlensing experiments were not sensitive to events with timescales longer than $t_{\rm E} \gtrsim 2.5 - 3$ yr, raising the possibility that such long-timescale events were not accounted for in the calculation of the microlensing optical depth. We did not find any such long-timescale events in our data, confirming that the optical depth toward the LMC is significantly smaller than that expected from the dark matter halo in

the form of compact objects. Our conclusions about the abundance of compact objects in dark matter are presented in detail in a companion paper (Mróz et al. 2024). In short, we found that all detected events can be explained by lensing by stars in the foreground Milky Way or in the LMC itself, without the need to invoke dark matter in the form of compact objects. We found that compact objects in the mass range from $1.8 \times 10^{-4}\,M_{\odot}$ to $6.3\,M_{\odot}$ cannot compose more than 1% of dark matter, and objects in the mass range from $1.3 \times 10^{-5}\,M_{\odot}$ to $860\,M_{\odot}$ cannot make up more than 10% of dark matter.

An exact origin of lenses can be traced with follow-up observations. Revisiting the events with adaptive-optics observations may reveal the source and the lens separated in the sky. Combining the lens flux measurements with additional information, for example from the microlens parallax effects, should enable us to pinpoint the mass and distance to the lens.

The data presented in this paper are publicly available at https://www.astrouw.edu.pl/ogle/ogle4/LMC_OPTICAL_DEPTH

ACKNOWLEDGEMENTS

We thank all the OGLE observers for their contribution to the collection of the photometric data over the decades. This research was funded in part by National Science Centre, Poland, grant OPUS 2021/41/B/ST9/00252 awarded to P.M.

REFERENCES

Abbott, B. P., Abbott, R., Abbott, T. D., et al. 2019, Physical Review X, 9, 031040
Abbott, B. P., Abbott, R., Abbott, T. D., et al. 2016, PhRvL, 116, 061102
Abbott, R., Abbott, T. D., Abraham, S., et al. 2021, ApJL, 913, L7
Abbott, R., Abbott, T. D., Abraham, S., et al. 2020a, PhRvL, 125, 101102
Abbott, R., Abbott, T. D., Abraham, S., et al. 2020b, ApJL, 900, L13
Abbott, R., Abbott, T. D., Acernese, F., et al. 2023, Physical Review X, 13, 041039
Alard, C., & Lupton, R. H. 1998, ApJ, 503, 325
Alcock, C., Allsman, R. A., Alves, D., et al. 1997, ApJ, 486, 697
Alcock, C., Allsman, R. A., Alves, D. R., et al. 2000, ApJ, 542, 281
Bennett, D. P. 2005, ApJ, 633, 906
Bird, S., Cholis, I., Muñoz, J. B., et al. 2016, PhRvL, 116, 201301
Blaineau, T., & Moniez, M. 2020, A&A, 636, L9
Bond, I. A., Abe, F., Dodd, R. J., et al. 2001, MNRAS, 327, 868
Calchi Novati, S., & Mancini, L. 2011, MNRAS, 416, 1292
Calchi Novati, S., Mancini, L., Scarpetta, G., & Wyrzykowski, Ł. 2009, MNRAS, 400, 1625
Carr, B. J., & Hawking, S. W. 1974, MNRAS, 168, 399
Chapline, G. F. 1975, Nature, 253, 251
Clesse, S., & García-Bellido, J. 2017, Physics of the Dark Universe, 15, 142
Corral-Santana, J. M., Casares, J., Muñoz-Darias, T., et al. 2016, A&A, 587, A61
Costa, G., Chruślińska, M., Klencki, J., et al. 2023, arXiv e-prints, arXiv:2311.15778
Foreman-Mackey, D., Hogg, D. W., Lang, D., & Goodman, J. 2013, PASP, 125, 306
Gould, A. 2004, ApJ, 606, 319
Hawking, S. 1971, MNRAS, 152, 75
Holtzman, J. A., Afonso, C., & Dolphin, A. 2006, ApJS, 166, 534
Maccarone, T. J., Nelson, T. J., Brown, P. J., et al. 2019, Nature Astronomy, 3, 173
Mróz, P., Szegedi, H., Page, K. L., et al. 2023, The Astronomer's Telegram, 16373, 1
Mróz, P., Udalski, A., Skowron, J., et al. 2017, Nature, 548, 183
Mróz, P., Udalski, A., Skowron, J., et al. 2019, ApJS, 244, 29
Mróz, P., Udalski, A., Szymański, M. K., et al. 2024, submitted
Paczyński, B. 1986, ApJ, 304, 1
Sahu, K. C. 1994, Nature, 370, 275
Sasaki, M., Suyama, T., Tanaka, T., & Yokoyama, S. 2016, PhRvL, 117, 061101
Skowron, D. M., Skowron, J., Udalski, A., et al. 2021, ApJS, 252, 23
Skowron, J., Udalski, A., Kozłowski, S., et al. 2016, AcA, 66, 1
Tisserand, P., Le Guillou, L., Afonso, C., et al. 2007, A&A, 469, 387
Udalski, A. 2003, AcA, 53, 291
Udalski, A., Kubiak, M., & Szymański, M. 1997, AcA, 47, 319
Udalski, A., Szymański, M. K., & Szymański, G. 2015, AcA, 65, 1
Woźniak, P. R. 2000, AcA, 50, 421
Wyrzykowski, L., Udalski, A., Mao, S., et al. 2006, AcA, 56, 145

Wyrzykowski, Ł., Kozłowski, S., Skowron, J., et al. 2009, MNRAS, 397, 1228
Wyrzykowski, Ł., Kozłowski, S., Skowron, J., et al. 2011, MNRAS, 413, 493
Zel'dovich, Y. B., & Novikov, I. D. 1967, Soviet Ast., 10, 602

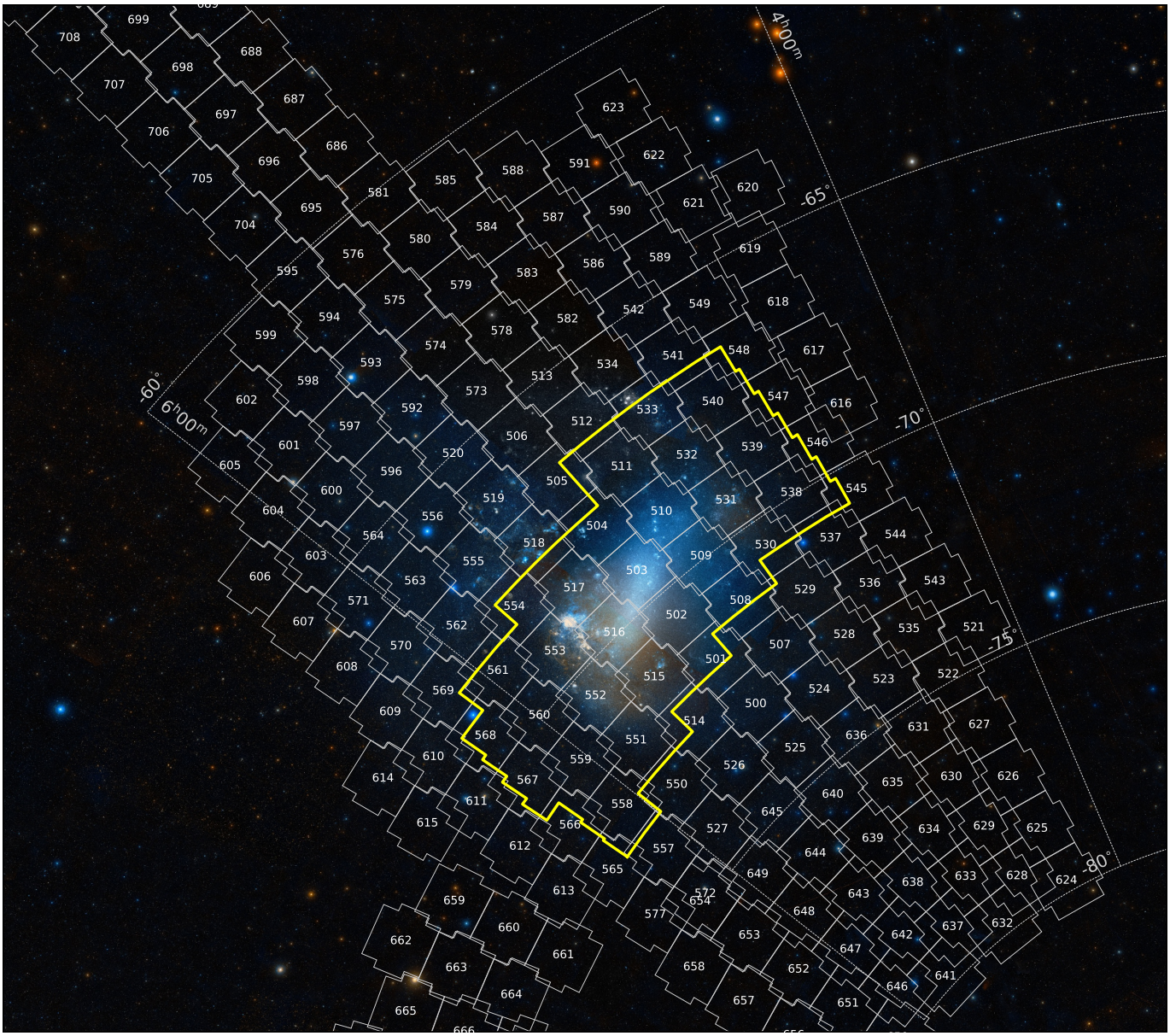


Figure 1. OGLE-IV fields toward the Large Magellanic Cloud (white polygons); numbers in the polygons indicate the field number. The yellow line marks a region observed during the OGLE-III phase. The background image is reproduced with permission from WikiSky.org.

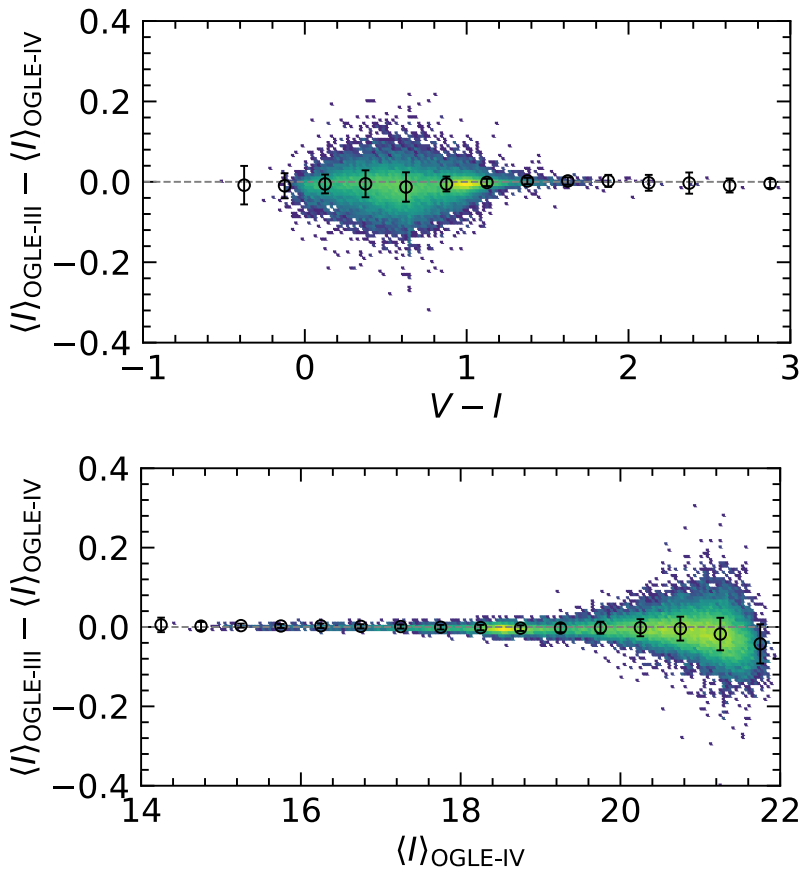


Figure 2. Comparison between the new OGLE-III and OGLE-IV mean magnitudes for one of the analyzed fields (LMC502.11), as a function of color (upper diagram) and mean magnitude (lower diagram). The black data points represent the median difference calculated in several color (magnitude) bins. The error bars are calculated as the median absolute deviation multiplied by 1.4826. The color scale is logarithmic.

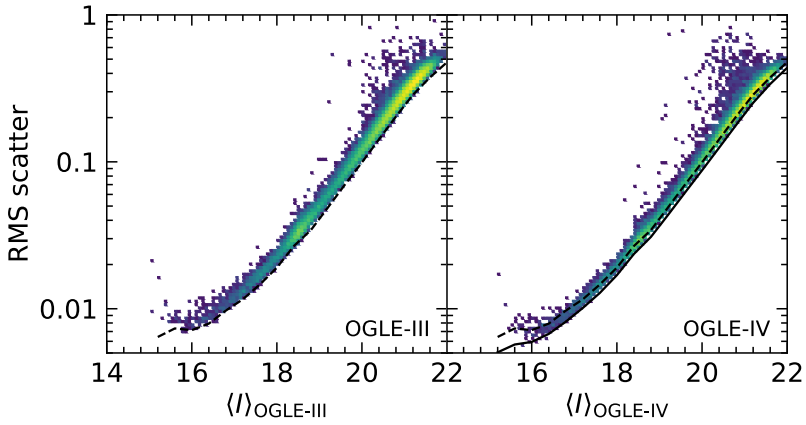


Figure 3. Rms scatter in the light curves as a function of mean magnitude (for stars in the field LMC502.11). Left: OGLE-III data (2001–2009), right: OGLE-IV data (2010–2020). The black dashed (solid) line marks the lower envelope of the distribution for OGLE-III (OGLE-IV) data. The color scale is logarithmic.

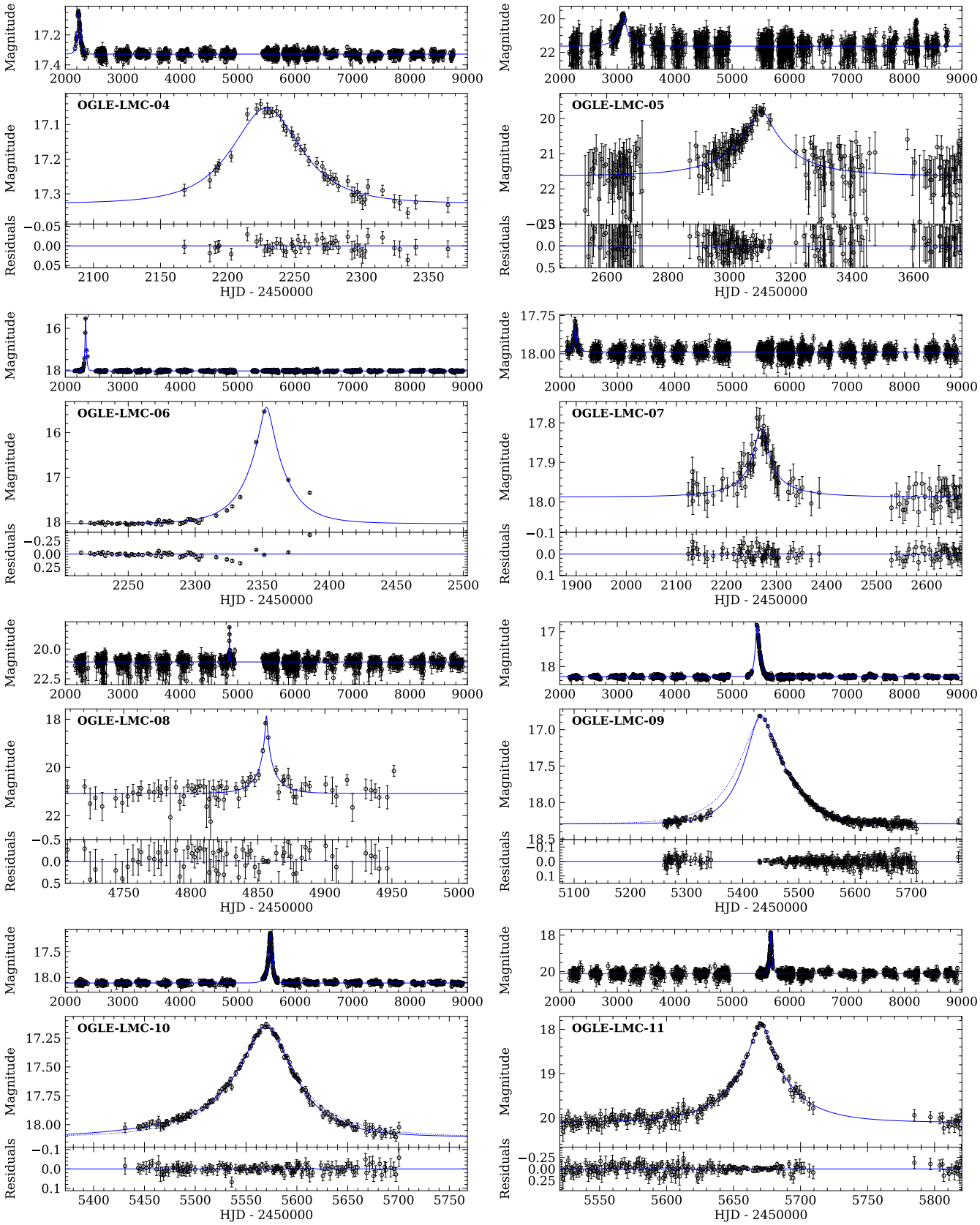


Figure 4. Light curves of detected events. The solid blue line shows the best-fit point-source point-lens model (with or without the parallax). For events with detected annual parallax effects, the dotted line shows the best-fit model without the parallax.

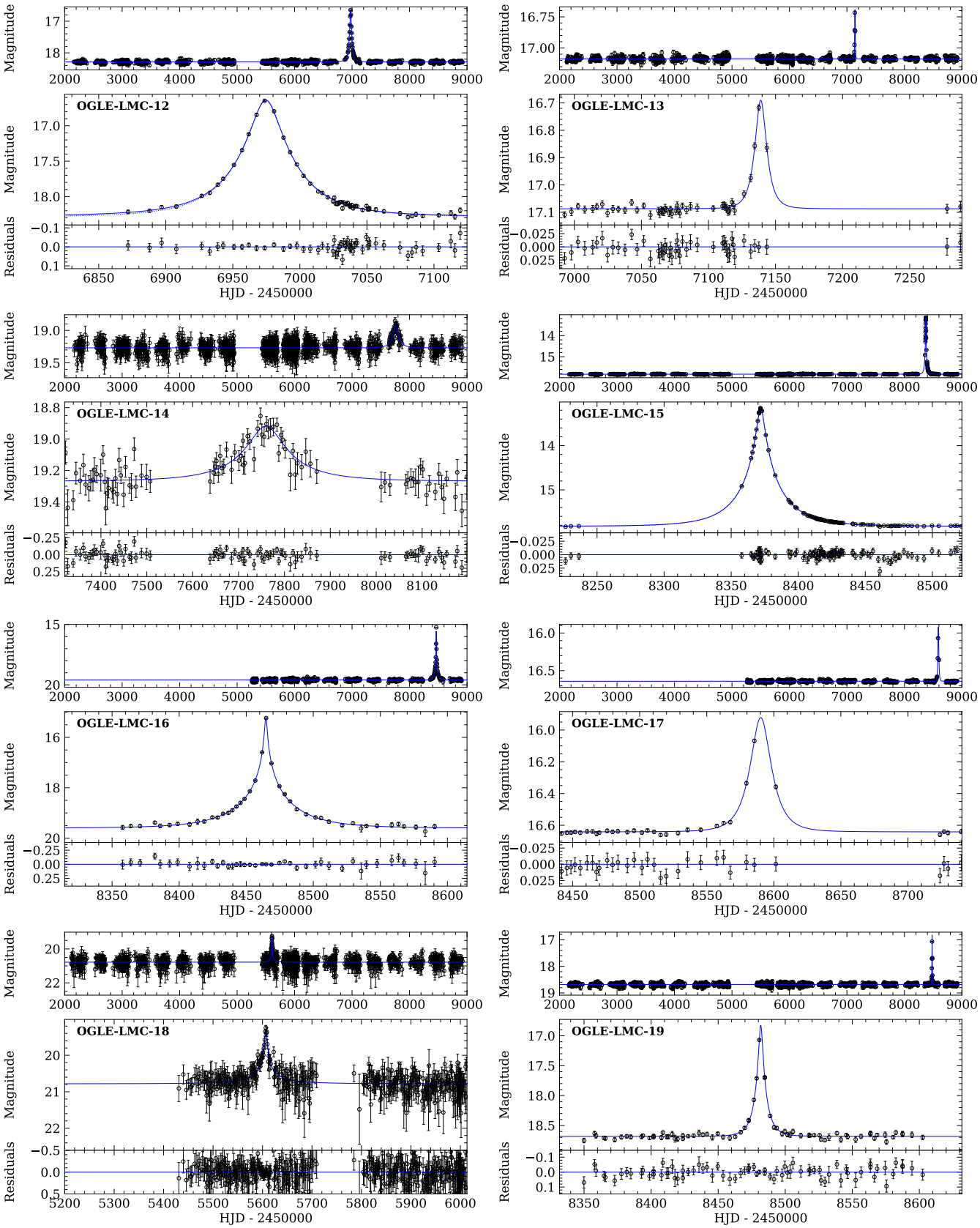


Figure 4. (continuation)

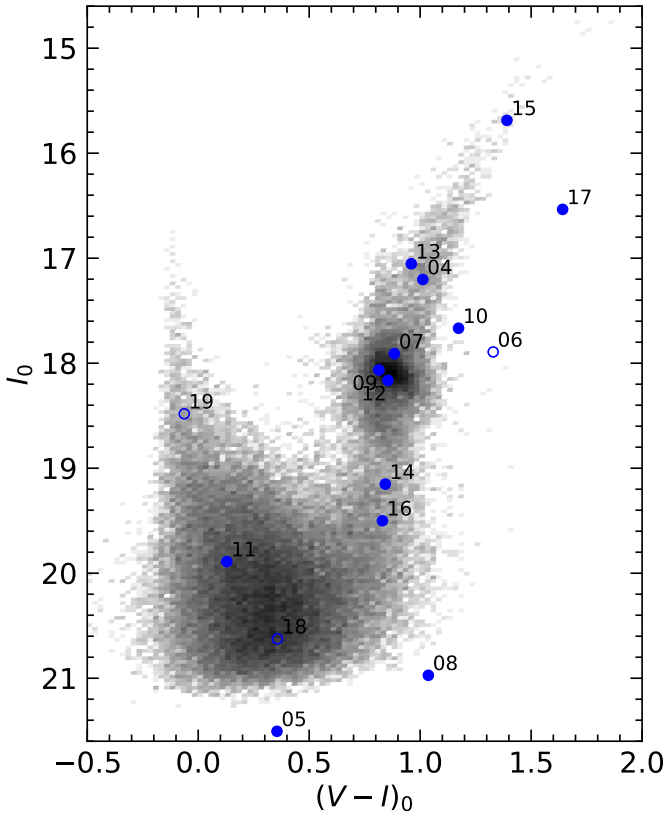


Figure 5. De-reddened color–magnitude diagram of the field LMC516.14. Blue circles mark the positions of the detected microlensing events in the baseline. Empty circles mark three events that do not enter the final statistical sample.

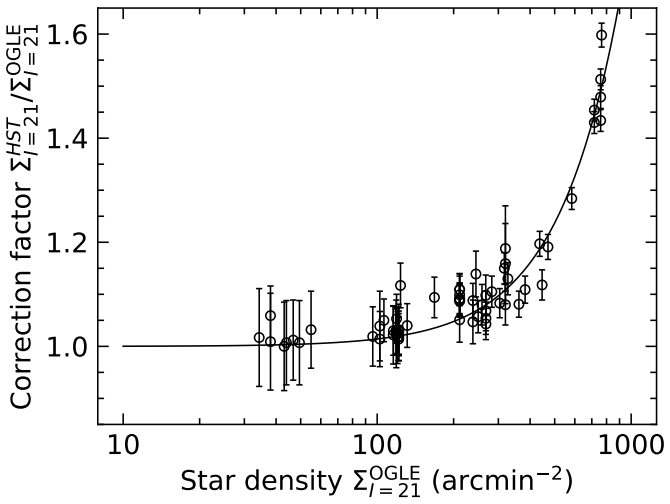


Figure 6. Ratio between the mean surface density of stars brighter than $I = 21$ detected in the *HST* and OGLE images (correction factor) as a function of density of stars observed by OGLE.

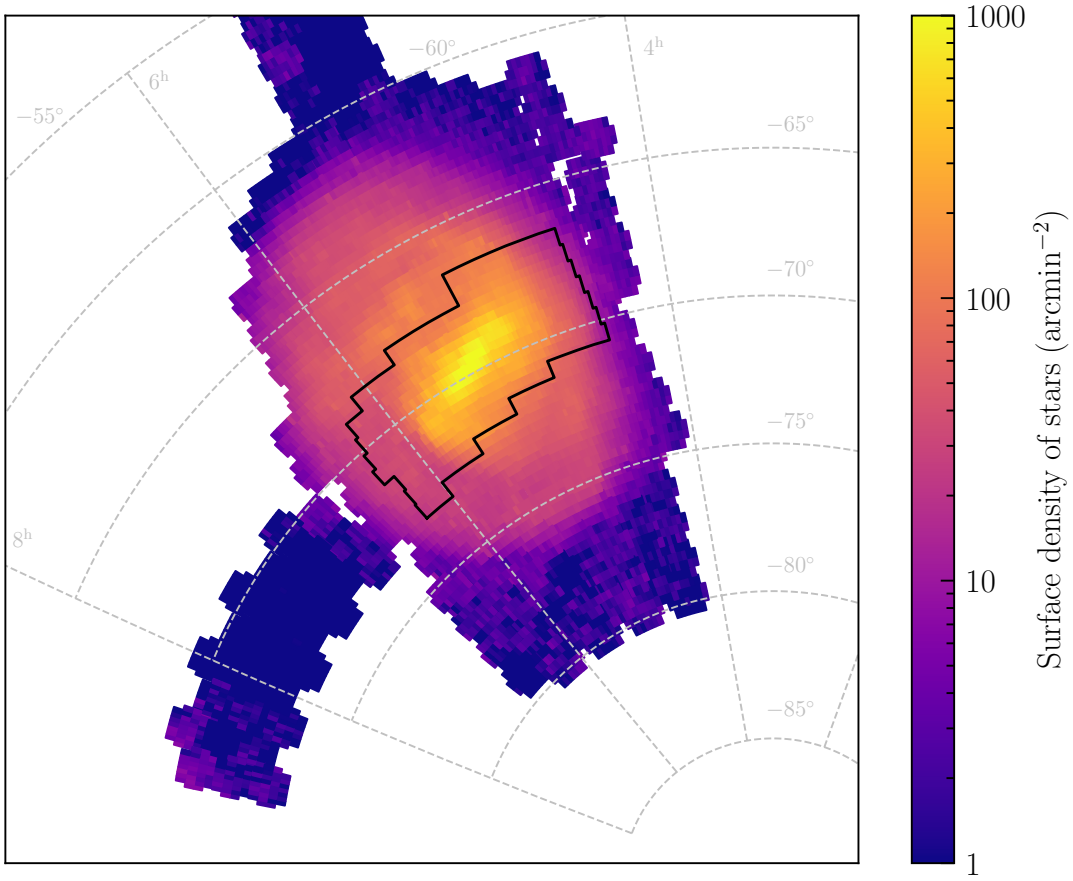


Figure 7. Surface density of source stars brighter than $I = 22$ in the analyzed OGLE-IV fields.

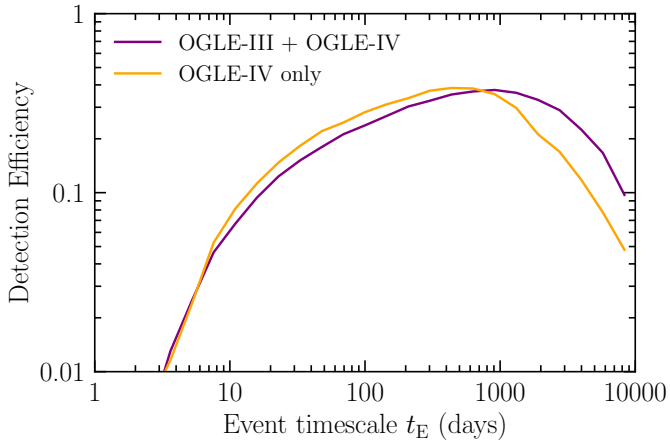


Figure 8. Detection efficiency to microlensing events as a function of the Einstein timescale for field LMC501 (averaged for sources brighter than $I = 22$ mag). The purple line marks the detection efficiency for stars observed during OGLE-III and OGLE-IV phases of the project, and the orange line – for stars observed during OGLE-IV only.

Table 1. OGLE-IV Fields Toward the Large Magellanic Cloud

Field	R.A. (J2000)	Decl. (J2000)	$N_{\rm Epochs}$ (2001–2009)	$N_{\rm Epochs}$ (2010–2020)	$N_{\rm Stars}/1000$ (2001–2020)	$N_{\rm Stars}/1000$ (2010–2020)	$N_{\rm Stars}/1000$ (Total)
LMC500	$05^{\rm h}19^{\rm m}00^{\rm s}$	$-73°00'00''$	0	571	0.0	407.5	407.5
LMC501	$05^{\rm h}19^{\rm m}00^{\rm s}$	$-71°46'10''$	0–1779	559	582.5	205.3	787.8
LMC502	$05^{\rm h}19^{\rm m}00^{\rm s}$	$-70°32'20''$	445–2110	881	1833.1	0.0	1833.1
LMC503	$05^{\rm h}19^{\rm m}00^{\rm s}$	$-69°18'30''$	460–2191	884	3364.6	0.0	3364.6
LMC504	$05^{\rm h}19^{\rm m}00^{\rm s}$	$-68°04'40''$	0–1228	833	1150.8	149.0	1299.8
LMC505	$05^{\rm h}19^{\rm m}00^{\rm s}$	$-66°50'50''$	0–500	552	215.0	604.0	818.9
LMC506	$05^{\rm h}19^{\rm m}00^{\rm s}$	$-65°37'00''$	0	554	0.0	589.9	589.9
LMC507	$05^{\rm h}03^{\rm m}20^{\rm s}$	$-72°23'05''$	0	568	0.0	520.9	520.9
LMC508	$05^{\rm h}04^{\rm m}17^{\rm s}$	$-71°09'15''$	0–1769	806	796.3	158.3	954.6
LMC509	$05^{\rm h}05^{\rm m}07^{\rm s}$	$-69°55'25''$	427–1946	796	2041.3	0.0	2041.3
...	...	...	...	...	...	...	...
Total	...	...	...	...	32969.9	29271.6	62241.5

Note—The coordinates are given for the epoch J2000. $N_{\rm Epochs}$ is the number of epochs, separately for the OGLE-III (2001–2009) and OGLE-IV (2010–2020) phases. $N_{\rm Stars}$ is the number of stars (in thousands) observed in a given field; this is not equivalent to the number of microlensing source stars that enter the calculations (see the text). We discriminate between stars observed during both OGLE-III and OGLE-IV phases (with the available photometric data spanning 2001–2020) and those observed during OGLE-IV only (2010–2020). (This table is available in its entirety in machine-readable form.)

Table 2. Median Difference Between the New OGLE-III and OGLE-IV Magnitudes

$V-I$	ΔI	$V-I$	ΔI	$V-I$	ΔI
−0.171	−0.068	0.876	−0.020	1.624	0.020
−0.123	−0.064	0.927	−0.016	1.674	0.022
−0.075	−0.061	0.976	−0.014	1.722	0.024
−0.027	−0.057	1.025	−0.011	1.772	0.027
0.023	−0.053	1.076	−0.008	1.823	0.029
0.095	−0.044	1.127	−0.005	1.873	0.031
0.196	−0.034	1.177	−0.002	1.939	0.034
0.298	−0.030	1.228	0.001	2.044	0.037
0.402	−0.028	1.277	0.004	2.145	0.040
0.500	−0.028	1.326	0.006	2.242	0.047
0.608	−0.029	1.375	0.008	2.350	0.053
0.680	−0.030	1.425	0.010	2.440	0.059
0.730	−0.028	1.474	0.013	2.602	0.072
0.776	−0.026	1.524	0.015		
0.825	−0.023	1.574	0.017		

Table 3. Error Bar Correction Coefficients for the I-band Data

Field	$\gamma_{\text{OGLE-III}}$	$\varepsilon_{\text{OGLE-III}}$	$\gamma_{\text{OGLE-IV}}$	$\varepsilon_{\text{OGLE-IV}}$
LMC501.01	...	...	1.115	0.0062
LMC501.02	...	...	1.069	0.0057
LMC501.03	...	...	1.155	0.0063
LMC501.04	...	...	1.178	0.0059
LMC501.05	...	...	1.182	0.0057
LMC501.06	...	...	1.157	0.0061
LMC501.07	...	...	1.156	0.0063
LMC501.08	1.189	0.0063	1.127	0.0043
LMC501.09	1.206	0.0062	1.087	0.0042
LMC501.10	1.191	0.0081	1.082	0.0053
...	...	...	...	...

NOTE—(This table is available in its entirety in machine-readable form.)

Table 4. Selection Cuts

Cut 0.	**All stars in the databases**	62,591,045
Cut 1.	**Stars with at least one significant brightening in the light curve**	
	At least five consecutive data points 3σ above the baseline flux ($n_{\rm bump} \geq 5$)	
	Object detected on at least three subtracted images ($n_{\rm DIA} \geq 3$)	
	The total "significance" of the bump ($\chi_{3+} = \sum_i (F_i - F_{\rm base})/\sigma_i \geq 32$)	
	Amplitude of the bump at least 0.1 mag ($\Delta m \geq 0.1$ mag)	
	Amplitude of the bump at least 0.4 mag if the bump is longer than 100 days	
	If a bump is shorter than 1000 days, no significant variability outside the window ($\chi^2_{\rm out}$/d.o.f. ≤ 2)	56,358
Cut 2.	**Removing false positives**	
	Stars with multiple bumps in the data	
	"Blue bumpers" ($(V-I)_0 \leq 0.5$, $I_0 \leq 19.5$)	
	Stars in the vicinity of SN 1987A	49,325
Cut 3.	**Microlensing model describes the light curve well**	
	Fit converged	
	χ^2/d.o.f. ≤ 2 (all data points)	
	$\chi^2_{t_{\rm E}}$/d.o.f. ≤ 2 (for $\lvert t - t_0 \rvert < t_{\rm E}$)	
	$\chi^2_{\rm bump}$/d.o.f. ≤ 2 (for data points within the bump)	
	t_0 within the time range covered by the data	
	Impact parameter is smaller than 1 ($u_0 \leq 1$)	
	Uncertainty on the Einstein timescale ($\sigma(t_{\rm E})/t_{\rm E} \leq 1$)	
	Source star brighter than 22 mag ($I_{\rm s} \leq 22$)	
	Microlensing model is significantly better than a straight line ($\chi^2_{\rm line} - \chi^2 \geq 250\chi^2$/d.o.f.)	13

Table 5. Detected Microlensing Events

Event	R.A. (J2000)	Decl. (J2000)	OGLE-IV ID	I (mag)	$V-I$ (mag)
OGLE-LMC-04	$05^{\rm h}25^{\rm m}39\overset{\rm s}{.}57$	$-70°19'49\overset{''}{.}6$	LMC502.17.57865	17.31	1.10
OGLE-LMC-05	$05^{\rm h}24^{\rm m}49\overset{\rm s}{.}10$	$-67°50'04\overset{''}{.}9$	LMC504.17.27728	21.67	0.49
OGLE-LMC-06	$05^{\rm h}19^{\rm m}47\overset{\rm s}{.}80$	$-70°46'26\overset{''}{.}6$	LMC502.12.400	18.04	1.45
OGLE-LMC-07	$05^{\rm h}21^{\rm m}07\overset{\rm s}{.}64$	$-69°34'45\overset{''}{.}1$	LMC503.11.3147	17.99	0.95
OGLE-LMC-08	$05^{\rm h}12^{\rm m}29\overset{\rm s}{.}58$	$-68°05'50\overset{''}{.}6$	LMC504.16.27046	21.11	1.15
OGLE-LMC-09	$05^{\rm h}00^{\rm m}23\overset{\rm s}{.}51$	$-69°30'49\overset{''}{.}9$	LMC509.32.3044	18.23	0.95
OGLE-LMC-10	$05^{\rm h}41^{\rm m}47\overset{\rm s}{.}97$	$-70°40'52\overset{''}{.}1$	LMC552.15.15750	17.98	1.43
OGLE-LMC-11	$05^{\rm h}14^{\rm m}10\overset{\rm s}{.}19$	$-67°49'14\overset{''}{.}0$	LMC504.24.15713	20.00	0.22
OGLE-LMC-12	$05^{\rm h}16^{\rm m}31\overset{\rm s}{.}35$	$-71°05'11\overset{''}{.}8$	LMC502.05.27026	18.28	0.95
OGLE-LMC-13	$05^{\rm h}22^{\rm m}11\overset{\rm s}{.}57$	$-69°33'29\overset{''}{.}5$	LMC503.10.65388	17.09	0.99
OGLE-LMC-14	$05^{\rm h}14^{\rm m}33\overset{\rm s}{.}55$	$-68°50'58\overset{''}{.}8$	LMC503.32.13953	19.27	0.94
OGLE-LMC-15	$05^{\rm h}33^{\rm m}05\overset{\rm s}{.}32$	$-69°30'31\overset{''}{.}2$	LMC516.29.8037	15.82	1.50
OGLE-LMC-16	$05^{\rm h}07^{\rm m}45\overset{\rm s}{.}58$	$-65°57'49\overset{''}{.}9$	LMC512.21.20190	19.61	0.92
OGLE-LMC-17	$06^{\rm h}07^{\rm m}25\overset{\rm s}{.}55$	$-67°19'41\overset{''}{.}1$	LMC570.03.200	16.63	1.72
OGLE-LMC-18	$05^{\rm h}21^{\rm m}25\overset{\rm s}{.}25$	$-69°12'54\overset{''}{.}7$	LMC503.20.21374	20.75	0.46
OGLE-LMC-19	$04^{\rm h}46^{\rm m}14\overset{\rm s}{.}25$	$-69°03'20\overset{''}{.}2$	LMC531.25.9430	18.68	0.10

NOTE—The table provides the mean I-band brightness and $V-I$ color in the baseline.

Table 6. Color of the Source Star from the Model-Independent Regression

Event	$(V-I)_{\rm s}$
OGLE-LMC-05	0.51 ± 0.22 [a]
OGLE-LMC-09	1.011 ± 0.020
OGLE-LMC-10	1.285 ± 0.047
OGLE-LMC-11	0.221 ± 0.020
OGLE-LMC-12	0.906 ± 0.036
OGLE-LMC-13	0.906 ± 0.048
OGLE-LMC-15	1.476 ± 0.004

[a] Wyrzykowski et al. (2011)

Table 7. Number of Microlensing Source Stars Observed in OGLE-IV Fields

Field	R.A. (deg)	Decl. (deg)	$N_{\rm total}^{21\,\rm mag}$	$N_{\rm corr}^{21\,\rm mag}$	$N_{\rm total}^{21.5\,\rm mag}$	$N_{\rm corr}^{21.5\,\rm mag}$	$N_{\rm total}^{22\,\rm mag}$	$N_{\rm corr}^{22\,\rm mag}$
LMC500.01	81.3326	–73.4710	8119	7106	11055	9977	12185	11055
LMC500.02	80.8051	–73.4710	8193	7187	10559	9489	11558	10437
LMC500.03	80.2775	–73.4710	7780	6780	9527	8463	10346	9232
LMC500.04	79.7500	–73.4710	7412	6420	9859	8803	10752	9645
LMC500.05	79.2225	–73.4710	7565	6579	10020	8970	10933	9834
LMC500.06	78.6949	–73.4710	7098	6118	9760	8718	10656	9564
LMC500.07	78.1674	–73.4710	7846	6873	10624	9588	11662	10576
LMC500.08	81.8602	–73.1496	9457	8437	13042	11958	14538	13401
LMC500.09	81.3326	–73.1496	9892	8880	12295	11218	13586	12457
LMC500.10	80.8051	–73.1496	10252	9246	13021	11952	14471	13350
...	...	...	...	...	...	...	...	...
Total (million)	...	...	47.126	39.763	67.992	60.175	86.861	78.682

Note—The coordinates are given for the epoch J2000. $N_{\rm total}$ is the number of possible microlensing source stars (after correcting the raw star counts for blending), and $N_{\rm corr}$ is the number of possible microlensing source stars after removing foreground Milky Way sources. (This table is available in its entirety in machine-readable form.)

Table 8. Microlensing Optical Depth and Event Rate Toward the LMC

Event	$\langle\varepsilon(t_{\rm E})\rangle$	$\langle 1/\varepsilon(t_{\rm E})\rangle$	$\langle t_{\rm E}/\varepsilon(t_{\rm E})\rangle$	ΔT	τ	Γ
			(days)	(days)	(10^{-7})	($10^{-7}\,{\rm yr}^{-1}$)
OGLE-LMC-04	0.1671	6.018	219.32	7000	0.0063	0.0399
OGLE-LMC-05	0.2692	3.770	688.01	7000	0.0196	0.0250
OGLE-LMC-07	0.1749	6.219	444.43	7000	0.0127	0.0412
OGLE-LMC-08	0.0826	13.338	175.12	7000	0.0050	0.0885
OGLE-LMC-09	0.2467	4.076	425.42	7000	0.0121	0.0270
OGLE-LMC-10	0.1911	5.240	340.83	7000	0.0097	0.0347
OGLE-LMC-11	0.1652	6.086	252.41	7000	0.0072	0.0404
OGLE-LMC-12	0.1872	5.343	241.59	7000	0.0069	0.0354
OGLE-LMC-13	0.0419	25.364	179.82	7000	0.0051	0.1682
OGLE-LMC-14	0.2090	4.886	483.57	7000	0.0138	0.0324
OGLE-LMC-15	0.1334	7.494	234.51	7000	0.0067	0.0497
OGLE-LMC-16	0.1960	5.114	213.74	4000	0.0107	0.0593
OGLE-LMC-17	0.1261	8.139	113.76	4000	0.0057	0.0945
Total:	...	...	...	...	$\mathbf{0.121 \pm 0.037}$	$\mathbf{0.74 \pm 0.25}$

Table 9. Best-fit Parameters of Detected Events

Event	t_0	$t_{\rm E}$ (d)	u_0	$\pi_{{\rm E},N}$	$\pi_{{\rm E},E}$	$I_{\rm s}$ (mag)	$f_{\rm s}$	χ^2	N
OGLE-LMC-04	2452229.045 ± 0.719	$35.165^{+8.302}_{-4.622}$	$0.825^{+0.199}_{-0.231}$	...	...	$17.929^{+0.626}_{-0.467}$	$0.575^{+0.309}_{-0.252}$	638.1	581
OGLE-LMC-05	$2453104.123^{+4.389}_{-3.857}$	$165.941^{+87.842}_{-49.125}$	$0.219^{+0.162}_{-0.099}$	...	...	21.428 ± 0.765	$1.196^{+1.202}_{-0.583}$	308.0	436
OGLE-LMC-07	2452269.233 ± 1.444	$52.127^{+72.009}_{-25.366}$	$0.362^{+0.622}_{-0.246}$	...	...	$20.646^{+1.480}_{-1.798}$	$0.086^{+0.366}_{-0.064}$	428.4	500
OGLE-LMC-08	$2454856.318^{+0.073}_{-0.081}$	$13.497^{+6.005}_{-3.924}$	$0.053^{+0.035}_{-0.024}$	...	...	21.093 ± 0.509	$0.990^{+0.579}_{-0.369}$	432.4	467
OGLE-LMC-09	2455432.621 ± 0.469	70.383 ± 1.736	0.387 ± 0.018	...	...	17.772 ± 0.068	1.623 ± 0.104	997.6	818
OGLE-LMC-09	2455432.025 ± 0.811	$102.756^{+23.386}_{-17.555}$	$0.181^{+0.057}_{-0.046}$	0.315 ± 0.018	$0.132^{+0.034}_{-0.028}$	18.785 ± 0.368	$0.636^{+0.252}_{-0.183}$	745.3	818
OGLE-LMC-10	2455568.724 ± 0.160	80.791 ± 4.204	0.247 ± 0.019	...	...	18.971 ± 0.096	$0.453^{+0.042}_{-0.038}$	620.6	587
OGLE-LMC-10	2455570.014 ± 0.201	$64.595^{+6.134}_{-5.008}$	0.340 ± 0.048	0.197 ± 0.039	-0.040 ± 0.075	18.520 ± 0.200	$0.686^{+0.134}_{-0.116}$	491.6	587
OGLE-LMC-11	2455670.398 ± 0.089	$41.474^{+3.122}_{-2.771}$	0.148 ± 0.015	...	...	19.932 ± 0.118	1.178 ± 0.130	828.0	824
OGLE-LMC-12	2456974.451 ± 0.099	45.923 ± 1.517	0.216 ± 0.011	...	...	18.329 ± 0.063	0.962 ± 0.057	874.1	877
OGLE-LMC-12	2456974.623 ± 0.124	$45.051^{+2.033}_{-1.716}$	0.227 ± 0.016	$-0.089^{+0.077}_{-0.069}$	$-0.306^{+0.144}_{-0.123}$	$18.264^{+0.093}_{-0.083}$	1.022 ± 0.084	865.9	877
OGLE-LMC-13	2457138.949 ± 0.192	$7.007^{+1.936}_{-1.059}$	0.638 ± 0.203	...	...	$17.730^{+0.636}_{-0.490}$	$0.553^{+0.315}_{-0.245}$	784.4	861
OGLE-LMC-14	2457759.472 ± 3.487	$88.188^{+59.008}_{-25.697}$	$0.581^{+0.399}_{-0.310}$	...	...	$20.285^{+1.156}_{-1.023}$	$0.392^{+0.614}_{-0.257}$	931.4	868
OGLE-LMC-15	2458372.030 ± 0.009	32.204 ± 0.185	0.081 ± 0.001	...	...	15.892 ± 0.010	0.941 ± 0.008	1047.7	899
OGLE-LMC-15	2458372.034 ± 0.010	31.278 ± 0.459	0.085 ± 0.002	-0.317 ± 0.135	0.047 ± 0.036	15.845 ± 0.021	0.983 ± 0.019	1036.0	899
OGLE-LMC-16	2458464.623 ± 0.024	41.800 ± 1.599	0.019 ± 0.001	...	...	19.497 ± 0.049	1.100 ± 0.050	497.5	591
OGLE-LMC-17	2458590.262 ± 0.225	$13.790^{+1.836}_{-1.046}$	$0.491^{+0.075}_{-0.106}$	...	...	$16.898^{+0.336}_{-0.219}$	$0.790^{+0.177}_{-0.210}$	521.2	657
OGLE-LMC-18	2455606.738 ± 0.240	$101.230^{+89.561}_{-38.668}$	$0.026^{+0.019}_{-0.013}$	...	...	$23.572^{+0.752}_{-0.611}$	$0.076^{+0.057}_{-0.038}$	903.8	868
OGLE-LMC-19	2458481.729 ± 0.038	$8.200^{+0.690}_{-0.599}$	0.168 ± 0.026	...	...	18.799 ± 0.146	0.898 ± 0.125	1261.8	1227

Physical running of couplings in quadratic gravity

Diego Buccio[1],* John F. Donoghue[2],† Gabriel Menezes[3] ‡,§ and Roberto Percacci[1]¶
[1] *International School for Advanced Studies, Via Bonomea 265, 34134 Trieste, Italy and INFN, Sezione di Trieste, Trieste, Italy*
[2] *Department of Physics, University of Massachusetts, Amherst, MA 01003, USA*
[3] *Instituto de Física Teórica, Universidade Estadual Paulista, Rua Dr. Bento Teobaldo Ferraz, 271 - Bloco II, 01140-070 São Paulo, São Paulo, Brazil*

We argue that the well-known beta functions of quadratic gravity do not correspond to the physical dependence of scattering amplitudes on external momenta, and derive the correct physical beta functions. Asymptotic freedom turns out to be compatible with the absence of tachyons.

arXiv:2403.02397v1 [hep-th] 4 Mar 2024

Quadratic gravity is an extension of Einstein's theory whose action contains terms quadratic in curvature. In signature $-+++$ it reads

$$S=\int d^4x\sqrt{|g|}\left[\frac{{m_P}^2}{2}(R-2\Lambda)-\frac{1}{2\lambda}C^2-\frac{1}{\xi}R^2\right]\ , \quad (1)$$

where $m_P=\sqrt{8\pi G}$ is the Planck mass, Λ is the cosmological constant, $C_{\mu\nu\rho\sigma}$ is the Weyl tensor. We will not consider the Euler (Gauss-Bonnet) term here. This theory is renormalizable [1]. In addition to the massless graviton it propagates a massive spin-2 particle that is a ghost and if $\lambda<0$ it is a tachyon[1]. It also has a massive spin-0 particle that is a tachyon for $\xi>0$. In spite of these apparent pathologies, it has attracted renewed interest recently [2–8]. In these studies, it is suggested that it may be possible that the ghost state is acceptable, although tachyonic states are considered fatal.

The first attempt to compute beta functions for this theory was made by Julve and Tonin in [9], but that work missed the contribution of the Nakanishi-Lautrup ghosts. This was corrected in [10] and then, with some further corrections, in [11]. The final result is

$$\beta_\lambda \ = \ -\frac{1}{(4\pi)^2}\frac{133}{10}\lambda^2\ , \quad (2)$$

$$\beta_\xi \ = \ -\frac{1}{(4\pi)^2}\frac{5(72\lambda^2-36\lambda\xi+\xi^2)}{36}\ , \quad (3)$$

Since then, these beta functions have been confirmed in several calculations using different techniques [12–16]. With these beta functions, full asymptotic freedom can only be obtained for the case of a tachyonic coupling $\xi>0$.

The beta functions (2,3) give the dependence of the renormalized λ and ξ on the renormalization scale μ. We call this the *μ-running*. However, what one is really interested in is the dependence of the running couplings on external momenta, that we call *physical running*. [2]

In problems characterized by a single momentum scale p, e.g. the total center of mass energy $p=\sqrt{s}$, the p-dependence is usually the same as the μ-dependence, because for dimensional reasons they occur as $\log(p/\mu)$. In the presence of a non-negligible mass scale m, the amplitude generally contains, in addition to terms of the form $\log(p/\mu)$, also terms of the form $\log(m/\mu)$ and in this way the p-dependence is no longer correctly reflected by the μ-dependence. One clear source of such spurious μ-dependence are tadpoles, Feynman diagrams that by construction do not depend on the external momenta. In such cases, the μ-running is not the same as physical running.

In most familiar quantum field theories such as the Standard Model this is not a problem as one can use mass independent renormalization schemes. However, we claim that it is not always correct in higher derivative theories. Two of us have indeed found that in higher derivative sigma models the scale dependent beta functions calculated with a ultraviolet cutoff [21] or those obtained from the dependence on an infrared cutoff [22] are indeed contaminated by tadpoles, and hence not physical [23]. In the present letter we claim that the same is true in quadratic gravity, and we compute the physical beta functions.

Calculations of the beta functions so far have been based on the background field method, expanding $g_{\mu\nu}=\bar{g}_{\mu\nu}+h_{\mu\nu}$ around a general background $\bar{g}$. In the following a bar always indicates a quantity calculated from

‡On leave of absence from Departamento de Física, Universidade Federal Rural do Rio de Janeiro.

[1] Ghosts are particles whose propagator is the negative of the usual one, while tachyons are particles with a pole at spacelike momenta.

[2] These and other definitions of running have been discussed in a simple model of a higher-derivative shift-invariant scalar theory, where the full form of the scattering amplitude is accessible [17], see also [18–20].

the background metric. Almost all calculations used the heat kernel, which is very convenient because it preserves manifest covariance at all stages. These are standard techniques and there are many textbooks and reviews approaching the subject, see for instance [24–29].

The first step is always the linearization of the action and the choice of a suitable gauge-fixing term, leading to an action

$$S^{(2)} = \int d^4x \sqrt{|\bar{g}|} h_{\alpha\beta} \mathcal{H}^{\alpha\beta,\gamma\delta} h_{\gamma\delta} \ . \tag{4}$$

One can choose the gauge such that the operator governing the propagation of gravitons has the form (suppressing the indices),

$$\mathcal{H} = \bar{\Box}^2 \mathbb{K} + \mathbb{J}^{\mu\nu} \bar{\nabla}_\mu \bar{\nabla}_\nu + \mathbb{L}^\mu \bar{\nabla}_\mu + \mathbb{W} \tag{5}$$

and $\mathbb{K}$, $\mathbb{J}$, $\mathbb{L}$, $\mathbb{W}$ are matrices in the space of symmetric tensors, depending on $\bar{R}$ and its covariant derivatives. In particular

$$\mathbb{K} = \frac{1}{4\lambda}\mathbb{P}_{\rm tl} + \frac{9}{4(3\xi - 2\lambda)}\mathbb{P}_{\rm tr} \tag{6}$$

where $\mathbb{P}_{\rm tr}^{\alpha\beta,\gamma\delta} = \frac{1}{4}\bar{g}^{\alpha\beta}\bar{g}^{\gamma\delta}$ is the projector on the trace part and $\mathbb{P}_{\rm tl} = \mathbb{I} - \mathbb{P}_{tr}$ the projector on the traceless part. In flat space, $\mathbb{K}$ can be viewed as a tensorial wave function renormalization constant that gives different weights to the spin-2 and spin-0 components of h. As usual it is convenient to canonically normalize the fields by redefining $h \to \sqrt{\mathbb{K}^{-1}} h$, so that the action can be rewritten as

$$S^{(2)} = \int d^4x \sqrt{|\bar{g}|} h_{\alpha\beta} \mathcal{O}^{\alpha\beta,\gamma\delta} h_{\gamma\delta} \ , \tag{7}$$

where, suppressing again the indices,

$$\mathcal{O} = \bar{\Box}^2 \mathbb{I} + \mathbb{V}^{\mu\nu} \bar{\nabla}_\mu \bar{\nabla}_\nu + \mathbb{N}^\mu \bar{\nabla}_\mu + \mathbb{U} \ , \tag{8}$$

and $\mathbb{V} = \sqrt{\mathbb{K}^{-1}} \mathbb{J} \sqrt{\mathbb{K}^{-1}}$ etc. Now $\mathbb{V}$ contains terms proportional to $\bar{R}$ and m_P^2, $\mathbb{N}$ contains terms proportional to $\bar{\nabla}\bar{R}$, whereas $\mathbb{U}$ contains terms proportional to $\bar{R}^2$, $\bar{\nabla}^2\bar{R}$, $m_P^2\bar{R}$ and $m_P^2\Lambda$. The logarithmic divergences, or equivalently the $1/\epsilon$ poles in dimensional regularization, are proportional to the heat kernel coefficient

$$\frac{1}{32\pi^2}\int d^4x \, {\rm tr}\Big[\frac{\mathbb{I}}{90}\left(\bar{R}^2_{\rho\lambda\sigma\tau} - \bar{R}^2_{\rho\lambda} + \frac{5}{2}\bar{R}^2\right) + \frac{1}{6}\mathbb{R}_{\rho\lambda}\mathbb{R}^{\rho\lambda} - \frac{\bar{R}_{\rho\lambda}\mathbb{V}^{\rho\lambda} - \frac{1}{2}\bar{R}\mathbb{V}^\rho{}_\rho}{6} + \frac{\mathbb{V}_{\rho\lambda}\mathbb{V}^{\rho\lambda} + \frac{1}{2}\mathbb{V}^\rho{}_\rho\mathbb{V}^\lambda{}_\lambda}{24} - \mathbb{U}\Big] \ , \tag{9}$$

where $\mathbb{R}_{\rho\lambda} = [\nabla_\rho, \nabla_\lambda]$ acting on symmetric tensors.

The operator (8) is of the same form as the one acting on the scalars in the higher derivative sigma models, and so are the divergences (9) (except for the terms ${\rm tr}\bar{R}\mathbb{V}$). We can then use the same arguments of [23]. The terms in the first line of (9) are the ones that we would get for $\mathcal{O} = \bar{\Box}^2$. Using the formula ${\rm Tr}\log\Box^2 = 2{\rm Tr}\log\Box$ one can conclude that none of those terms could be a tadpole, because with a standard p^2 propagator a diagram must have at least two propagators to be logarithmically divergent.

On the other hand consider ${\rm tr}\mathbb{U}$. This term comes from the functional trace ${\rm Tr}\mathbb{U}/\Box^2$. Clearly the most divergent part of this expression, that comes from the flat propagator, is a tadpole. Some more detailed arguments lead to the conclusion that also some of the ${\rm tr}\bar{R}\mathbb{V}$ divergences are due to tadpoles. This is enough to conclude that the standard beta functions (2,3) cannot be the physical ones.

We thus wish to evaluate the physical beta functions. In order to use flat space Feynman diagrams, we go back to the original Julve-Tonin approach and assume that the background is itself a small deformation of flat space $\bar{g}_{\mu\nu} = \eta_{\mu\nu} + f_{\mu\nu}$. Expanding around flat space, the action (7) gives rise to an operator of the form

$$\begin{aligned}\mathcal{O} \ &\equiv \ \boxdot^2 \mathbb{I} + \mathcal{D}^{\mu\nu\rho\sigma}\partial_\mu\partial_\nu\partial_\rho\partial_\sigma + \mathcal{C}^{\mu\nu\rho}\partial_\mu\partial_\nu\partial_\rho \\ &+ \ \mathcal{V}^{\mu\nu}\partial_\mu\partial_\nu + \mathcal{N}^\mu\partial_\mu + \mathcal{U} \ ,\end{aligned} \tag{10}$$

where $\boxdot$ is the flat Laplacian, $\mathcal{D}$ and $\mathcal{C}$ come from the expansion of $\sqrt{\bar{g}}\bar{\Box}^2$ and $\mathcal{V}$, $\mathcal{N}$ and $\mathcal{U}$ are equal to $\mathbb{V}$, $\mathbb{N}$ and $\mathbb{U}$ plus terms coming from the expansion of $\sqrt{\bar{g}}\bar{\Box}^2$. Each of these terms is an infinite series in f. Recall that the functional trace of the logarithm of an operator can be approximated by

$$\begin{aligned}{\rm tr}\log\mathcal{O} &= {\rm tr}\log\left(\boxdot^2 + A\right) \\ &\approx {\rm tr}\left[2\log\boxdot + A\frac{1}{\boxdot^2} - \frac{1}{2}A\frac{1}{\boxdot^2}A\frac{1}{\boxdot^2} + \cdots\right] .\end{aligned} \tag{11}$$

In the above expansion, A generically represents the remaining contributions to $\mathcal{O}$ appearing in Eq. (10), and again we are suppressing Lorentz indices for brevity. Furthermore, the first term in the perturbative expansion of Eq. (11) corresponds to tadpole integrals, while the second term can be evaluated as a bubble Feynman diagram. Our discussion here concerns how to compute terms proportional to $\log p^2$.

The physical running of λ and ξ comes from terms

$$b_\lambda \bar{C}^{\mu\nu\rho\sigma}\log\bar{\Box}\bar{C}_{\mu\nu\rho\sigma} + b_\xi \bar{R}\log\bar{\Box}\bar{R} \tag{12}$$

in the effective action, and the beta functions are

$$\beta_\lambda = -4b_\lambda\lambda^2 \ , \quad \beta_\xi = -2b_\xi\xi^2 \ .$$

In flat space contributions to the coefficients b_λ and b_ξ can be read from the two point function of the background fluctuation f, which is represented graphically by the diagrams in Figure 1.

The two h-h-f vertices in the bubble diagrams are obtained by expanding $\mathcal{D}$, $\mathcal{C}$, $\mathcal{V}$, $\mathcal{N}$ and $\mathcal{U}$ to first order, while for the tadpole one has to expand to second order. Being logarithmically divergent, the tadpole contributes

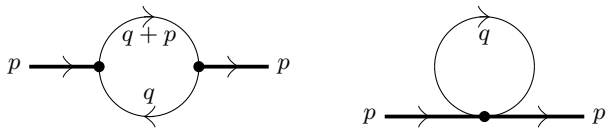


FIG. 1: Diagrams contributing to the two-point function: bubbles (left) and tadpoles (right). The thin line can be the h propagator or one of the ghosts, the thick line is the f propagator, with momentum p. The vertices can come from expanding any one among $\mathcal{D}$, $\mathcal{C}$, $\mathcal{V}$, $\mathcal{N}$, $\mathcal{U}$.

to the μ-running but not to the p-dependence that we are interested in. Thus the bulk of the calculation consists of working out the Feynman integrals for each of the 15 possible pairs of vertices in the bubble and then evaluating the result for the specific form of the operator (10).

The calculation is simplified by neglecting the terms proportional to m_P. This is justified in the UV limit, as seen explicitly in the case of the simple shift-invariant scalar model [17]. The calculation of the relevant Feynman integrals becomes straightforward and the results are given in the Appendix, where we also present all possible pairs of vertices appearing in the bubble integral.

In the calculation one sees in detail how it happens that the μ-running differs from the physical running. In dimensional regularization the $\log\mu$ terms always appear together with the $1/\epsilon$ pole, so the μ-running just traces the log divergences of the theory. We have checked that putting together all the bubble *and* tadpole diagrams one reconstructs the covariant expression (12) with the coefficients leading to the standard beta functions (2,3). If we just drop the tadpoles, the resulting function of f is not the linearization of a covariant expression. Thus, the physical running cannot be obtained from the μ-running by just dropping the tadpole contribution. Instead, there are other contributions.

As we have explained earlier, in the presence of a mass, the μ-dependence does not correctly describe the amplitude. In our theory the only mass is the Planck mass and one would expect that in the limit $p \gg m_P$, it becomes negligible. However, if we neglect m_P, the four-derivative propagator leads to infrared divergences. This is a new phenomenon that does not occur in standard two-derivative theories. There are then two ways to regulate the theory. One is to continue to use dimensional regularization to regulate also the IR divergences. In this case *all* the logs are again of the form $\log p^2/\mu^2$, but in addition to the UV logs there are now also IR logs, that change the beta function. As we explain more fully below, summing all the $\log p^2$ terms now gives again a covariant expression, but with a different coefficient. This is the physical beta function. On the other hand, one could alternatively reintroduce artificially a small mass m as an IR regulator [3]. The presence of the regulator mass leads to terms of the form $\log p^2/m^2$, and we are interested in the $\log p^2$ effects. We have checked that both procedures lead exactly to the same result. Notice that the small-time expansion of the heat kernel always gives only the UV divergences.

In our diagrams the IR divergences always appear with powers of the external momentum p in the denominator and therefore give rise to apparently nonlocal $1/\Box$ or $1/\Box^2$ terms. However, since the interactions always involve derivatives, they are offset by an equal number of powers of p in the numerator. Due to differential identities such as

$$\bar\nabla_\mu\bar\nabla_\nu\bar R^{\mu\nu\rho\sigma}\bar\nabla_\alpha\bar\nabla_\beta\bar R^{\alpha\beta}{}_{\rho\sigma} = \bar R_{\mu\nu}\bar\Box^2\bar R^{\mu\nu} - \frac{1}{4}\bar R\bar\Box^2\bar R + O(\bar R^3)\ , \tag{13}$$

or their linearized versions, these momenta always appear in the combination p^2 and cancel the inverse powers of p. In this way also the logs of infrared origin appear as coefficients of local operators. However, these operators are not by themselves the linearization of a covariant expression. It is only when one adds them to the UV logs that they give rise to a covariant expression as in (12). Both types of logs are physical and both are needed to maintain general covariance.

These points can be seen easily by considering the vertex $\mathbb{U}$. It enters the heat kernel calculation linearly, see (9), corresponding to a tadpole. It is only the part of $\mathbb{U}$ quadratic in curvature that contributes to the beta functions (2,3) describing μ running. By contrast in our calculation we need two powers of $\mathbb{U}$ and hence only the part proportional to $\bar\nabla\bar\nabla\bar R$ contributes at order f^2. These $\mathbb{U}$-$\mathbb{U}$ bubbles are UV finite but contain $\log p/m$ contributions coming from the IR region. These come with a factor p^4 in the denominator, from the propagators, but also p^4 in the numerator from the vertices. Thus they contribute to the terms (12).

Finally we observe that with our choice of gauge, the Faddeev-Popov ghost operators are of second order in derivatives and none of these exotic phenomena can happen. Thus their contribution can be taken from traditional heat kernel calculations.

Putting everything together, our final result is

$$\beta_\lambda = -\frac{1}{(4\pi)^2}\frac{(1617\lambda - 20\xi)\lambda}{90}\ , \tag{14}$$

$$\beta_\xi = -\frac{1}{(4\pi)^2}\frac{\xi^2 - 36\lambda\xi - 2520\lambda^2}{36}\ , \tag{15}$$

[3] This is actually easier than keeping the Hilbert term, because we can use the same m for all components of h, whereas the Hilbert term gives different contributions to the mass of the trace and tracefree parts, but it should have the same physical effect.

The flowlines around the free fixed point $\lambda = \xi = 0$ are shown in Figure 2.

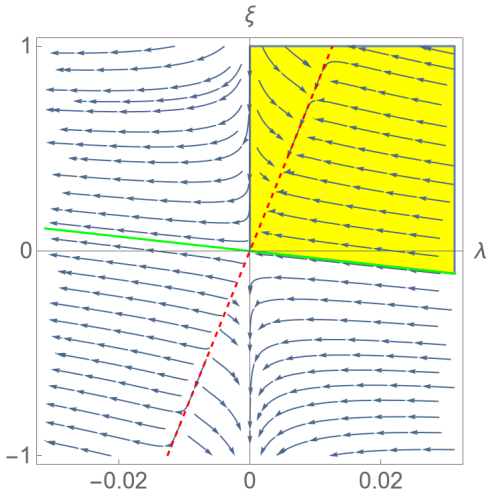


FIG. 2: Flowlines of the beta functions (14,15). The red dashed line corresponds to (16) and the green line to (17). Initial points in the shaded area are asymptotically free. In the two left quadrants the massive spin 2 state is a tachyon, in the two upper quadrants the massive spin 0 state is a tachyon.

There are three separatrices, along which the motion is purely radial. The line $\lambda = 0$ is UV repulsive for $\xi > 0$ and UV attractive for $\xi < 0$; the line s_1 is defined by

$$\xi = \frac{569 + \sqrt{386761}}{15}\lambda \approx 79.4\lambda \tag{16}$$

and is attractive for $\lambda > 0$ and repulsive for $\lambda < 0$, and the line s_2 is defined by

$$\xi = \frac{569 - \sqrt{386761}}{15}\lambda \approx -3.53\lambda \tag{17}$$

and is repulsive for $\lambda > 0$ and attractive for $\lambda < 0$. Thus the region that is attracted towards the free fixed point is the upper right quadrant, plus a triangular slice of the lower right quadrant that lies above the separatrix s_2.

Recall that absence of tachyons requires $\lambda > 0$ and $\xi < 0$. There is a unique trajectory that is asymptotically free and lies entirely in the tachyon-free area, and that is the separatrix s_2. This behavior is to be contrasted with the flow related to μ running in Eqns. (2,3), for which the analog of the separatrix s_2 is the only asymptotically free trajectory, but with a positive slope, with the result that it lies entirely in the tachyonic region. The physical running couplings allow asymptotic freedom without tachyons. Moreover there may be an additional possibility. One can have asymptotically free trajectories where the coupling ξ changes sign, as long as it is negative at the momenta where the pole in the propagator occurs, thus avoiding a tachyonic state. One can see these trajectories that lie above s_2 and thus have $\xi > 0$ in the far UV but eventually cross into $\xi < 0$ when one goes towards the IR. For these, it could be sufficient to demand that $\xi < 0$ at momenta corresponding to the poles of the propagators.

In summary, the physical running with the momenta is the appropriate running coupling to be used in amplitudes. We have noted the difference between this running and that which just follows $\log \mu$ when applied to theories with higher derivatives. In the case of quadratic gravity, we have calculated the beta functions for physical running. In contrast with previous work which followed cutoffs or $\log \mu$, this can lead to asymptotic freedom without tachyons.

Acknowledgements – JFD acknowledges partial support from the U.S. National Science Foundation under grant NSF-PHY-21-12800. GM acknowledges partial support from Conselho Nacional de Desenvolvimento Científico e Tecnológico - CNPq under grant 317548/2021-2, Fundação Carlos Chagas Filho de Amparo à Pesquisa do Estado de São Paulo - FAPESP under grant 2023/06508-8 and Fundação Carlos Chagas Filho de Amparo à Pesquisa do Estado do Rio de Janeiro - FAPERJ under grant E-26/201.142/2022.

Appendix – High energy limit of $\log(p^2)$ coefficients in bubble integrals

In this Appendix we review some basic notions of the background-field method. We also collect all the 15 possible pairs of vertices and all the associated $\log p^2$ terms emerging from relevant Feynman integrals discussed in the main text.

Let us begin our discussion by reviewing the one-loop effective action associated with a massless scalar field propagating in a curved background. In the background-field method, the action $S[\phi]$ is written in term of a classical background field $\bar{\phi}$ and a quantum fluctuation φ as $S[\bar{\phi}, \varphi]$, where $\phi = \bar{\phi} + \varphi$. In this representation, the effective action will be

$$e^{-\Gamma[\bar{\phi}]} = \int D\varphi\, e^{-S[\bar{\phi},\varphi]} \tag{18}$$

Near to a configuration of the classical field $\bar{\phi}_0$ which is a solution of equations of motion, and hence a minimum of

the classical action, the action can be approximated by the action computed in its minimum and a quantum part, quadratic in quantum fluctuations, equal to the Hessian of the action computed in the minimum:

$$S[\bar{\phi}_0, \varphi] \approx S[\bar{\phi}_0] + \frac{1}{2}\varphi \frac{\delta S[\phi]}{\delta\phi\delta\phi}|_{\phi=\bar{\phi}_0}\varphi \tag{19}$$

So the effective action is given by

$$e^{-\Gamma[\bar{\phi}]} = e^{-S[\bar{\phi}]}\int D\varphi e^{-\frac{1}{2}\varphi\mathcal{O}\varphi} \tag{20}$$

were we have defined

$$\mathcal{O} = \frac{\delta S[\phi]}{\delta\phi\delta\phi}|_{\bar{\phi}=\bar{\phi}_0}.$$

The functional integral is now just a Gaussian integral in φ and is equal to $(\det\mathcal{O})^{-\frac{1}{2}}$. We can write the one-loop corrected effective action as

$$\Gamma[\bar{\phi}] = S[\bar{\phi}] + \frac{1}{2}\log\det\mathcal{O} \tag{21}$$

Moreover, $\log\det\mathcal{O} = \mathrm{tr}\log\mathcal{O}$, so $\Delta_1\Gamma = \frac{1}{2}\mathrm{tr}\log\mathcal{O}$.

Let's consider a quadratic operator with structure

$$\mathcal{O} = \boxdot^2 + D^{\mu\nu\rho\sigma}\partial_\mu\partial_\nu\partial_\rho\partial_\sigma + C^{\mu\nu\rho}\partial_\mu\partial_\nu\partial_\rho + V^{\mu\nu}\partial_\mu\partial_\nu + N^\mu\partial_\mu + U \tag{22}$$

where all terms have mass dimension 4. After a Fourier transform, one can build 15 different bubble integrals with the interaction vertices D, C, V, N and U, which differ from each other only by the numerator in the momentum integral and can be computed using standard Feynman integrals. All bubbles are symmetric under the exchange of vertices, as can be easily verified using the variable redefinition $q \to -q - p$ and considering that U, V and D are invariant when moved from the left to the right of the diagram, while N and C go to $-N$ and $-C$, since the external momentum p is ingoing on the left and outgoing on the right.

The contribution from bubble diagrams to the one-loop effective action is

$$UU + NN + VV + CC + DD + 2(UV + UN + UC + UD + NV + NC + ND + VC + VD + CD). \tag{23}$$

If $\mathcal{O}$ is a self-adjoint operator, that means $\langle x|\mathcal{O}y\rangle = \langle\mathcal{O}x|y\rangle$. The symmetry of $\mathcal{O}$ permits us to take it as the inverse propagator and compute only the particular contraction between vertices dictated by the expansion of the functional trace of the logarithm of the operator $\mathcal{O}$

$$\begin{aligned}\mathrm{tr}\log\left(\mathcal{O}_{sym}\right) \approx \mathrm{tr}\log\left(\boxdot^2\right) + \mathrm{tr}\Bigg[(D_{\rho\lambda\alpha\beta}\partial^\rho\partial^\lambda\partial^\alpha\partial^\beta + \cdots)\frac{1}{\boxdot^2} - \\ \frac{1}{2}(D_{\rho\lambda\alpha\beta}\partial^\rho\partial^\lambda\partial^\alpha\partial^\beta + \cdots)\frac{1}{\boxdot^2}(D_{\rho\lambda\alpha\beta}\partial^\rho\partial^\lambda\partial^\alpha\partial^\beta + \cdots)\frac{1}{\boxdot^2} + \cdots\Bigg] + \cdots\end{aligned} \tag{24}$$

where the dots represent the remaining contributions not displayed in the above equation for clarity. In addition, we have indicated by $\mathcal{O}_{sym}$ the result of computing the contraction just mentioned. We report in table I the high energy limit of the part proportional to $\log(p^2)$ in all the possible bubble diagrams.

Now let us consider the graviton field. Given a quadratic operator acting on a rank 2 symmetric tensor field

$$\mathcal{O} = \boxdot^2\mathbb{I} + \mathcal{D}^{\mu\nu\rho\sigma}\partial_\mu\partial_\nu\partial_\rho\partial_\sigma + \mathcal{C}^{\mu\nu\rho}\partial_\mu\partial_\nu\partial_\rho + \mathcal{V}^{\mu\nu}\partial_\mu\partial_\nu + \mathcal{N}^\mu\partial_\mu + \mathcal{U}\ , \tag{25}$$

the contribution from bubble diagrams to the one-loop effective action reads

$$\mathcal{U}\mathcal{U} + \mathcal{N}\mathcal{N} + \mathcal{V}\mathcal{V} + \mathcal{C}\mathcal{C} + \mathcal{D}\mathcal{D} + 2(\mathcal{U}\mathcal{V} + \mathcal{U}\mathcal{N} + \mathcal{U}\mathcal{C} + \mathcal{U}\mathcal{D} + \mathcal{N}\mathcal{V} + \mathcal{N}\mathcal{C} + \mathcal{N}\mathcal{D} + \mathcal{V}\mathcal{C} + \mathcal{V}\mathcal{D} + \mathcal{C}\mathcal{D}), \tag{26}$$

where each term $\mathcal{A}\mathcal{B}$ in the sum corresponds to a bubble Feynman diagram composed by vertices $\mathcal{A}$ and $\mathcal{B}$ from (25). We introduce a generalized index notation for symmetric rank-2 tensors, $h_A := h_{\mu\nu}$ and $\hat{1} = \delta_{AB}$. The operator $\mathcal{O}$ and all its coefficients are matrices in the space of symmetric tensors, so they carry hidden indices A, B. By convention

vertices	numerator	$\log(p^2)$ term
UU	$-\frac{1}{2}UU$	$-\frac{UU}{16\pi^2 p^4}$
UN	$-\frac{i}{2}UN^\mu q_\mu$	$i\frac{UN^\mu p_\mu}{32\pi^2 p^4}$
UV	$\frac{1}{2}UV^{\mu\nu}q_\mu q_\nu$	$\frac{UV^{\mu\nu}p_\mu p_\nu}{32\pi^2 p^4}$
UC	$\frac{i}{2}UC^{\mu\nu\rho}q_\mu q_\nu q_\rho$	$-i\frac{UC^{\mu\nu\rho}p_\mu p_\nu p_\rho}{32\pi^2 p^4}$
UD	$-\frac{1}{2}UD^{\mu\nu\rho\sigma}q_\mu q_\nu q_\rho q_\sigma$	$-\frac{1}{32\pi^2}\left(\frac{1}{p^4}UD^{\mu\nu\rho\sigma}p_\mu p_\nu p_\rho p_\sigma - \frac{1}{8}UD^{\mu}{}_{\mu}{}^{\nu}{}_{\nu}\right)$
NN	$-\frac{1}{2}N^\mu N^\nu q_\mu (q+p)_\nu$	0
NV	$-\frac{i}{2}N^\mu V^{\nu\rho}(p+q)_\mu q_\nu q_\rho$	0
NC	$\frac{1}{2}N^\sigma C^{\mu\nu\rho}q_\mu q_\nu q_\rho (q+p)_\sigma$	$-\frac{N^\mu C_\mu{}^\nu{}_\nu}{256\pi^2}$
ND	$\frac{i}{4}N^\lambda D^{\mu\nu\rho\sigma}q_\mu q_\nu q_\rho q_\sigma((q+p)_\lambda - q_\lambda)$	$-\frac{i}{64\pi^2}\left(\frac{N^\lambda p_\lambda D^\mu{}_\mu{}^\nu{}_\nu}{8} - \frac{N^\lambda p_\lambda D^{\mu\nu\rho\sigma}p_\mu p_\nu p_\rho p_\sigma}{p^4}\right)$
VV	$-\frac{1}{2}V^{\mu\nu}V^{\rho\sigma}q_\mu q_\nu (q+p)_\rho (q+p)_\sigma$	$\frac{1}{384\pi^2}\left(V^{\mu\nu}V_{\mu\nu} + \frac{V^\mu_\mu V^\nu_\nu}{2}\right)$
VC	$-\frac{i}{2}V^{\sigma\lambda}C^{\mu\nu\rho}q_\mu q_\nu q_\rho (q+p)_\sigma (q+p)_\lambda$	$-\frac{i}{256\pi^2}\left(-p_\mu V^\mu_\nu C^{\nu\rho}{}_\rho + \frac{p_\mu V^\nu{}_\nu C^{\mu\rho}{}_\rho}{2} + p_\mu V_{\nu\rho}C^{\mu\nu\rho}\right)$
VD	$\frac{1}{4}V^{\lambda\delta}D^{\mu\nu\rho\sigma}q_\mu q_\nu q_\rho q_\sigma \times$ $((q+p)_\lambda (q+p)_\delta + q_\lambda q_\delta)$	$\frac{1}{64\pi^2}\Big(\frac{V^{\lambda\delta}p_\lambda p_\delta D^{\mu\nu\rho\sigma}p_\mu p_\nu p_\rho p_\sigma}{p^4} - \frac{3V^{\mu\nu}p_\mu p_\nu D^\rho{}_\rho{}^\sigma{}_\sigma}{40} -$ $\frac{p_\mu p_\nu V^\mu{}_\rho D^{\nu\rho\sigma}{}_\sigma}{10} - \frac{3p_\mu p_\nu V^\rho{}_\rho D^{\mu\nu\sigma}{}_\sigma}{20} -$ $\frac{3p_\mu p_\nu V_{\rho\sigma}D^{\mu\nu\rho\sigma}}{10} + \frac{p^2 V^\mu_\mu D^\nu{}_\nu{}^\rho{}_\rho}{40} +$ $\frac{p^2 V_{\mu\nu}D^{\mu\nu\rho}{}_\rho}{10}\Big)$
CC	$-\frac{1}{2}C^{\mu\nu\rho}C^{\sigma\lambda\delta}q_\mu q_\nu q_\rho \times$ $(q+p)_\sigma (q+p)_\lambda (q+p)_\delta$	$-\frac{1}{640\pi^2}\Big(\frac{C^{\mu\nu\rho}C_{\mu\nu\rho}p^2}{2} + \frac{3C^\mu{}_\nu{}^\nu C_\mu{}^\rho{}_\rho p^2}{4} +$ $3p_\mu p_\nu C^{\mu\rho\sigma}C^\nu{}_{\rho\sigma} + \frac{3p_\mu p_\nu C^{\mu\rho}{}_\rho C^{\nu\sigma}{}_\sigma}{2} - \frac{9p_\mu p_\rho C^{\mu\rho}{}_\nu C^{\nu\sigma}{}_\sigma}{2}\Big)$
CD	$-\frac{i}{2}C^{\lambda\delta\alpha}D^{\mu\nu\rho\sigma}q_\mu q_\nu q_\rho q_\sigma \times$ $(q+p)_\lambda (q+p)_\delta (q+p)_\alpha$	$-\frac{i}{320\pi^2}\Big(-\frac{3C^{\rho\sigma\delta}D^{\mu\nu}{}_{\sigma\delta}p_\mu p_\nu p_\rho}{2} - \frac{3C^{\rho\sigma}{}_\sigma D^{\mu\nu\delta}{}_\delta p_\mu p_\nu p_\rho}{4} +$ $C^\sigma{}_{\sigma\delta}D^{\mu\nu\rho\delta}p_\mu p_\nu p_\rho + \frac{3C^{\mu\nu}{}_\sigma D^{\rho\sigma\delta}{}_\delta p_\mu p_\nu p_\rho}{2} - \frac{C^{\mu\nu\rho}D^\sigma{}_\sigma{}^\delta{}_\delta p_\mu p_\nu p_\rho}{4} +$ $\frac{3p^2 p_\mu C^{\mu\nu\rho}D_{\nu\rho}{}^\delta{}_\delta}{4} + \frac{3p^2 p_\mu C^{\mu\nu}{}_\nu D^\rho{}_\rho{}^\sigma{}_\sigma}{16} - \frac{3p^2 p_\mu C^\nu{}_\nu{}^\rho D^\mu{}_\rho{}^\delta{}_\delta}{4} -$ $\frac{p^2 p_\mu C_{\nu\rho\sigma}D^{\mu\nu\rho\sigma}}{2}\Big)$
DD	$-\frac{1}{2}D^{\mu\nu\rho\sigma}D^{\lambda\delta\alpha\beta}q_\mu q_\nu q_\rho q_\sigma \times$ $(q+p)_\lambda (q+p)_\delta (q+p)_\alpha (q+p)_\beta$	$-\frac{1}{140\pi^2}\Big(-\frac{9D^{\mu\nu}{}_{\alpha\beta}D^{\rho\sigma\alpha\beta}p_\mu p_\nu p_\rho p_\sigma}{16} - \frac{9D^{\mu\nu\lambda}{}_\lambda D^{\rho\sigma\delta}{}_\delta p_\mu p_\nu p_\rho p_\sigma}{32} +$ $D^{\mu\nu\rho\delta}D^\sigma{}_\delta{}^\lambda{}_\lambda p_\mu p_\nu p_\rho p_\sigma - \frac{5D^{\mu\nu\rho\sigma}D^\lambda{}_\lambda{}^\delta{}_\delta p_\mu p_\nu p_\rho p_\sigma}{32} -$ $\frac{3p^2 p_\mu p_\nu D^{\mu\rho\sigma\lambda}D^\nu{}_{\rho\sigma\lambda}}{8} - \frac{9p^2 p_\mu p_\nu D^{\mu\rho}{}_\rho{}^\lambda D^\nu{}_\lambda{}^\sigma{}_\sigma}{16} +$ $\frac{3p^2 p_\mu p_\nu D^{\mu\nu\rho\sigma}D_{\rho\sigma}{}^\lambda{}_\lambda}{4} + \frac{3p^2 p_\mu p_\nu D^{\mu\nu\rho}{}_\rho D^\sigma{}_\sigma{}^\lambda{}_\lambda}{16} -$ $\frac{3p^4 D^{\mu\nu\rho\sigma}D_{\mu\nu\rho\sigma}}{128} - \frac{9p^4 D^\mu{}_\mu{}^{\rho\sigma}D_{\rho\sigma}{}^\nu{}_\nu}{128} - \frac{9p^4 D^\mu{}_\mu{}^\nu{}_\nu D^\rho{}_\rho{}^\sigma{}_\sigma}{1024}\Big)$

TABLE I: Scalar bubble loops.

such indices always come after the ones contracted with derivatives, e.g. $\mathcal{V}^{\mu\nu AB}$. Terms proportional to $\log p^2$ from each of these diagrams are reported in table II.

Taking as $\mathcal{O}$ the operator $\Box^2$ expanded at first order in f with respect to the perturbed metric, $g_{\mu\nu} = \eta_{\mu\nu} + f_{\mu\nu}$, one finds

$$-\frac{11}{48\pi^2}\bar{R}^{\mu\nu}\bar{R}_{\mu\nu} + \frac{7}{96\pi^2}\bar{R}^2 \ . \tag{27}$$

Since $\mathrm{tr}\log(\Box^2) = 2\mathrm{tr}\log\Box$, we would expect that the result must be equal to

$$2\frac{1}{16\pi^2}b_4(\Box) = -\frac{R^{\mu\nu}R_{\mu\nu}}{144\pi^2} - \frac{R^{\mu\nu\rho\sigma}R_{\mu\nu\rho\sigma}}{18\pi^2} + \frac{5R^2}{288\pi^2} \tag{28}$$

(where b_4 is the heat kernel coefficient). This expression is indeed equal to (27) if one takes $R^{\mu\nu\rho\sigma}R_{\mu\nu\rho\sigma} = 4R^{\mu\nu}R_{\mu\nu} - R^2$, which is equivalent to adding a total derivative term.

Taking instead $\mathcal{O}$ to be the full operator given by Eq. (8), expanded around flat space, leads to

$$\frac{1617\lambda - 20\xi}{1440\pi^2\lambda}\bar{R}^{\mu\nu}\bar{R}_{\mu\nu} - \frac{37800\lambda^3 + 540\lambda^2\xi + 3219\lambda\xi^2 - 40\xi^3}{8640\pi^2\lambda\xi^2}\bar{R}^2 \ , \tag{29}$$

vertices	numerator	$\log(p^2)$ term
$\mathcal{U}\mathcal{U}$	$-\frac{1}{2}\mathcal{U}_{AB}\mathcal{U}^{BA}$	$-\frac{\mathcal{U}^{AB}\mathcal{U}_{BA}}{16\pi^2 p^4}$
$\mathcal{U}\mathcal{N}$	$-\frac{i}{2}\mathcal{U}_{AB}\mathcal{N}^{\mu\,BA}q_\mu$	$i\frac{\mathcal{U}^{AB}\mathcal{N}^{\mu}_{BA}p_\mu}{32\pi^2 p^4}$
$\mathcal{U}\mathcal{V}$	$\frac{1}{2}\mathcal{U}_{AB}\mathcal{V}^{\mu\nu\,BA}q_\mu q_\nu$	$\frac{\mathcal{U}^{AB}\mathcal{V}^{\mu\nu}_{BA}p_\mu p_\nu}{32\pi^2 p^4}$
$\mathcal{U}\mathcal{C}$	$\frac{i}{2}\mathcal{U}_{AB}\mathcal{C}^{\mu\nu\rho\,BA}q_\mu q_\nu q_\rho$	$-i\frac{\mathcal{U}^{AB}\mathcal{C}^{\mu\nu\rho}_{BA}p_\mu p_\nu p_\rho}{32\pi^2 p^4}$
$\mathcal{U}\mathcal{D}$	$-\frac{1}{2}\mathcal{U}_{AB}\mathcal{D}^{\mu\nu\rho\sigma\,BA}q_\mu q_\nu q_\rho q_\sigma$	$-\frac{1}{32\pi^2}\left(\frac{\mathcal{U}^{AB}\mathcal{D}^{\mu\nu\rho\sigma}_{BA}p_\mu p_\nu p_\rho p_\sigma}{p^4}-\frac{\mathcal{U}^{AB}\mathcal{D}^{\mu\ \ \nu}_{\mu\ \ \nu\,BA}}{8}\right)$
$\mathcal{N}\mathcal{N}$	$-\frac{1}{2}\mathcal{N}^{\mu}_{AB}\mathcal{N}^{\nu\,BA}q_\mu(q+p)_\nu$	0
$\mathcal{N}\mathcal{V}$	$-\frac{i}{2}\mathcal{N}^{\mu}_{AB}\mathcal{V}^{\nu\rho\,BA}q_\nu q_\rho(p+q)_\mu$	0
$\mathcal{N}\mathcal{C}$	$\frac{1}{2}\mathcal{N}^{\sigma}_{AB}\mathcal{C}^{\mu\nu\rho\,BA}q_\mu q_\nu q_\rho(q+p)_\sigma$	$-\frac{\mathcal{N}^{\sigma\,AB}\mathcal{C}_{\sigma\ \ \mu\,BA}^{\ \ \mu}}{256\pi^2}$
$\mathcal{N}\mathcal{D}$	$\frac{i}{2}\mathcal{N}^{\lambda}_{AB}\mathcal{D}^{\mu\nu\rho\sigma\,BA}q_\mu q_\nu q_\rho q_\sigma(q+p)_\lambda$	$-\frac{i}{128\pi^2}\left(\frac{\mathcal{N}^{\lambda}_{AB}p_\lambda\mathcal{D}^{\mu\ \ \nu\,BA}_{\mu\ \ \nu}}{4}-\mathcal{N}^{\rho}_{AB}p_\mu\mathcal{D}^{\mu\ \ \nu\,BA}_{\rho\ \ \nu}\right)$
$\mathcal{V}\mathcal{V}$	$-\frac{1}{2}\mathcal{V}^{\mu\nu}_{AB}\mathcal{V}^{\rho\sigma\,BA}q_\mu q_\nu(q+p)_\rho(q+p)_\sigma$	$\frac{1}{384\pi^2}\left(\mathcal{V}^{\mu\nu}_{AB}\mathcal{V}_{\mu\nu}{}^{BA}+\frac{\mathcal{V}^{\mu}_{\ \mu AB}\mathcal{V}^{\nu\ \ BA}_{\ \ \nu}}{2}\right)$
$\mathcal{V}\mathcal{C}$	$-\frac{i}{2}\mathcal{V}^{\sigma\lambda}_{AB}\mathcal{C}^{\mu\nu\rho\,BA}q_\mu q_\nu q_\rho(q+p)_\sigma(q+p)_\lambda$	$-\frac{i}{256\pi^2}\Big(\frac{p_\mu\mathcal{V}^{\nu\ \ BA}_{\ \ \nu\,AB}\mathcal{C}^{\mu\rho\ \ BA}_{\ \ \rho}}{2}+p_\mu\mathcal{V}_{\nu\rho\,AB}\mathcal{C}^{\mu\nu\rho\,BA}$ $-p_\mu\mathcal{V}^{\mu\nu}_{AB}\mathcal{C}_{\nu\ \ \rho}^{\ \ \rho\ \ BA}\Big)$
$\mathcal{V}\mathcal{D}$	$\frac{1}{2}\mathcal{V}^{\lambda\delta}_{AB}\mathcal{D}^{\mu\nu\rho\sigma\,BA}q_\mu q_\nu q_\rho q_\sigma(q+p)_\lambda(q+p)_\delta$	$\frac{1}{160\pi^2}\Big(-\frac{3\mathcal{V}^{\mu\nu}_{AB}p_\mu p_\nu\mathcal{D}^{\rho\ \ \sigma\ \ BA}_{\rho\ \ \sigma}}{16}+p_\mu p_\nu\mathcal{V}^{\mu}_{\rho\,AB}\mathcal{D}^{\nu\rho\sigma\ \ BA}_{\ \ \ \ \sigma}-$ $\frac{3p_\mu p_\nu\mathcal{V}^{\rho}_{\ \rho\,AB}\mathcal{D}^{\mu\nu\sigma\ \ BA}_{\ \ \ \ \sigma}}{8}-\frac{3p_\mu p_\nu\mathcal{V}_{\rho\sigma\,AB}\mathcal{D}^{\mu\nu\rho\sigma\,BA}}{4}+$ $\frac{p^2\mathcal{V}^{\mu}_{\ \mu\,AB}\mathcal{D}^{\nu\ \ \rho\ \ BA}_{\ \ \nu\ \ \rho}}{16}+\frac{p^2\mathcal{V}_{\mu\nu\,AB}\mathcal{D}^{\mu\nu\rho\ \ BA}_{\ \ \ \ \rho}}{4}\Big)$
$\mathcal{C}\mathcal{C}$	$-\frac{1}{2}\mathcal{C}^{\mu\nu\rho}_{AB}\mathcal{C}^{\sigma\lambda\delta\,BA}q_\mu q_\nu q_\rho\times$ $(q+p)_\sigma(q+p)_\lambda(q+p)_\delta$	$\frac{1}{640\pi^2}\Big(-3p_\mu p_\nu\mathcal{C}^{\mu\rho\sigma}_{AB}\mathcal{C}^{\nu\ \ BA}_{\ \rho\sigma}-\frac{3p_\mu p_\nu\mathcal{C}^{\mu\rho}_{\ \ \rho\,AB}\mathcal{C}^{\nu\sigma\ \ BA}_{\ \ \sigma}}{2}-$ $\frac{p^2\mathcal{C}^{\mu\nu\rho}_{AB}\mathcal{C}_{\mu\nu\rho}{}^{BA}}{2}-\frac{3p^2\mathcal{C}^{\mu\ \ \nu}_{\mu\ \ \nu\,AB}\mathcal{C}_{\nu\ \ \rho}^{\ \ \rho\ \ BA}}{4}+\frac{9p_\mu p_\nu\mathcal{C}^{\mu\nu\sigma}_{AB}\mathcal{C}_{\sigma\ \ \rho}^{\ \ \rho\ \ BA}}{2}\Big)$
$\mathcal{C}\mathcal{D}$	$-\frac{i}{2}\mathcal{C}^{\lambda\delta\alpha}_{AB}\mathcal{D}^{\mu\nu\rho\sigma\,BA}q_\mu q_\nu q_\rho q_\sigma\times$ $(q+p)_\lambda(q+p)_\delta(q+p)_\alpha$	$\frac{i}{320\pi^2}\Big(\frac{3\mathcal{C}^{\rho\sigma\delta}_{AB}\mathcal{D}^{\mu\nu\ \ \ BA}_{\ \ \sigma\delta}p_\mu p_\nu p_\rho}{2}+\frac{3\mathcal{C}^{\rho\sigma}_{\ \ \sigma\,AB}\mathcal{D}^{\mu\nu\delta\ \ BA}_{\ \ \ \ \delta}p_\mu p_\nu p_\rho}{4}-$ $\frac{3\mathcal{C}^{\mu\nu}_{\ \ \sigma\,AB}\mathcal{D}^{\rho\sigma\delta\ \ BA}_{\ \ \ \ \delta}p_\mu p_\nu p_\rho}{2}+\frac{\mathcal{C}^{\mu\nu\rho}_{AB}\mathcal{D}^{\sigma\ \ \delta\ \ BA}_{\sigma\ \ \delta}p_\mu p_\nu p_\rho}{4}-$ $\mathcal{C}^{\sigma}_{\sigma\delta\,AB}\mathcal{D}^{\mu\nu\rho\delta\,BA}p_\mu p_\nu p_\rho-\frac{3p^2p_\mu\mathcal{C}^{\mu\nu\rho}_{AB}\mathcal{D}_{\nu\rho\ \ \delta}^{\ \ \delta\ \ BA}}{4}-$ $\frac{3p^2p_\mu\mathcal{C}^{\mu\nu\ \ \ }_{\nu\ \ \rho\,AB}\mathcal{D}^{\rho\ \ \sigma\ \ BA}_{\ \ \rho\ \ \sigma}}{16}+\frac{p^2p_\mu\mathcal{C}^{\nu\rho\sigma}_{AB}\mathcal{D}^{\mu\ \ \ BA}_{\ \ \nu\rho\sigma}}{2}+$ $\frac{3p^2p_\mu\mathcal{C}^{\nu\ \ \sigma}_{\ \ \nu\ \ AB}\mathcal{D}^{\mu\ \ \delta\ \ BA}_{\ \ \sigma\ \ \delta}}{4}\Big)$
$\mathcal{D}\mathcal{D}$	$-\frac{1}{2}\mathcal{D}^{\mu\nu\rho\sigma}_{AB}\mathcal{D}^{\lambda\delta\alpha\beta\,BA}q_\mu q_\nu q_\rho q_\sigma\times$ $(q+p)_\lambda(q+p)_\delta(q+p)_\alpha(q+p)_\beta$	$-\frac{1}{140\pi^2}\Big(-\frac{9\mathcal{D}^{\mu\nu}_{\ \ \alpha\beta\,AB}\mathcal{D}^{\rho\sigma\alpha\beta\,BA}p_\mu p_\nu p_\rho p_\sigma}{16}-$ $\frac{9\mathcal{D}^{\mu\nu\lambda\ \ \ \ }_{\ \ \lambda\,AB}\mathcal{D}^{\rho\sigma\delta\ \ BA}_{\ \ \ \ \delta}p_\mu p_\nu p_\rho p_\sigma}{32}+\mathcal{D}^{\mu\nu\rho\delta}_{AB}\mathcal{D}^{\sigma\ \ \lambda\ \ BA}_{\ \delta\ \ \lambda}p_\mu p_\nu p_\rho p_\sigma-$ $\frac{10\mathcal{D}^{\mu\nu\rho\sigma}_{AB}\mathcal{D}^{\lambda\ \ \delta\ \ BA}_{\ \lambda\ \ \delta}p_\mu p_\nu p_\rho p_\sigma}{64}-\frac{3p^2p_\mu p_\nu\mathcal{D}^{\mu\rho\sigma\lambda}_{AB}\mathcal{D}^{\nu\ \ \ BA}_{\ \ \rho\sigma\lambda}}{8}-$ $\frac{9p^2p_\mu p_\nu\mathcal{D}^{\mu\rho\ \ \lambda\ \ }_{\ \ \rho\,AB}\mathcal{D}^{\nu\ \ \sigma\ \ BA}_{\ \ \lambda\ \ \sigma}}{16}+\frac{3p^2p_\mu p_\nu\mathcal{D}^{\mu\nu\rho\sigma}_{AB}\mathcal{D}_{\rho\sigma\ \ \lambda}^{\ \ \lambda\ \ BA}}{4}+$ $\frac{3p^2p_\mu p_\nu\mathcal{D}^{\mu\nu\rho\ \ \ \ }_{\ \ \rho\,AB}\mathcal{D}^{\sigma\ \ \lambda\ \ BA}_{\ \ \sigma\ \ \lambda}}{16}-\frac{3p^4\mathcal{D}^{\mu\nu\rho\sigma}_{AB}\mathcal{D}_{\mu\nu\rho\sigma}{}^{BA}}{128}-$ $\frac{9p^4\mathcal{D}^{\mu\ \ \rho\sigma\ \ }_{\mu\ \ \rho\,AB}\mathcal{D}_{\rho\sigma\ \ \nu}^{\ \ \nu\ \ BA}}{128}-\frac{9p^4\mathcal{D}^{\mu\ \ \nu\ \ }_{\mu\ \ \nu\,AB}\mathcal{D}^{\rho\ \ \sigma\ \ BA}_{\rho\ \ \sigma}}{1024}\Big)$

TABLE II: Bubble loops for the graviton field.

that lead to our final result for the beta functions, Eqs. (14) and (15).

* Electronic address: dbuccio@sissa.it
† Electronic address: donoghue@physics.umass.edu
§ Electronic address: gabriel.menezes10@unesp.br
¶ Electronic address: percacci@sissa.it

[1] K. S. Stelle, "Renormalization of Higher Derivative Quantum Gravity," Phys. Rev. D **16** (1977) 953.
[2] A. Salvio and A. Strumia, "Agravity," JHEP **06** (2014), 080 [arXiv:1403.4226 [hep-ph]].
[3] L. Alvarez-Gaume, A. Kehagias, C. Kounnas, D. Lüst, A. Riotto, "Aspects of Quadratic Gravity," Fortsch. Phys. **64** (2016), 176-189 [arXiv:1505.07657 [hep-th]].
[4] B. Holdom and J. Ren, "QCD analogy for quantum gravity," Phys. Rev. D **93** (2016) no.12, 124030 [arXiv:1512.05305

[hep-th]].
[5] D. Anselmi and M. Piva, "The Ultraviolet Behavior of Quantum Gravity," JHEP **05** (2018), 027 [arXiv:1803.07777 [hep-th]].
[6] A. Salvio, "Quadratic Gravity," Front. in Phys. **6**, 77 (2018) [arXiv:1804.09944 [hep-th]].
[7] J. F. Donoghue and G. Menezes, "On quadratic gravity," Nuovo Cim. C **45**, no.2, 26 (2022) [arXiv:2112.01974 [hep-th]].
[8] L. Buoninfante, "Massless and partially massless limits in Quadratic Gravity," JHEP **12** (2023), 111 [arXiv:2308.11324 [hep-th]].
[9] J. Julve, M. Tonin, "Quantum Gravity with Higher Derivative Terms," Nuovo Cim. B **46** (1978) 137.
[10] E.S. Fradkin, A.A. Tseytlin, "Renormalizable Asymptotically Free Quantum Theory Of Gravity," Phys. Lett. B **104** (1981) 377; Nucl. Phys. B **201** (1982) 469.
[11] I. G. Avramidi and A. O. Barvinsky, "Asymptotic freedom in higher derivative quantum gravity," Phys. Lett. B **159** (1985), 269-274
[12] G. de Berredo-Peixoto and I. L. Shapiro, "Higher derivative quantum gravity with Gauss-Bonnet term," Phys. Rev. D **71** (2005) 064005 [hep-th/0412249].
[13] A. Codello and R. Percacci, "Fixed points of higher derivative gravity," Phys. Rev. Lett. **97** (2006) 221301 [hep-th/0607128].
[14] M. Niedermaier, "Gravitational Fixed Points from Perturbation Theory," Phys. Rev. Lett. **103** (2009) 101303; "Gravitational fixed points and asymptotic safety from perturbation theory," Nucl. Phys. B **833** (2010) 226.
[15] F. Saueressig, K. Groh, S. Rechenberger and O. Zanusso, "Higher derivative gravity from the universal renormalization group machine," PoS EPS-HEP 2011 124 (2011), arXiv:1111.1743 [hep-th]
[16] G. Narain and R. Anishetty, "Short Distance Freedom of Quantum Gravity," Phys. Lett. B **711** (2012), 128-131 [arXiv:1109.3981 [hep-th]].
[17] D. Buccio, J. F. Donoghue and R. Percacci, "Amplitudes and renormalization group techniques: A case study," Phys. Rev. D **109** (2024) no.4, 045008 [arXiv:2307.00055 [hep-th]].
[18] D. Buccio and R. Percacci, "Renormalization group flows between Gaussian fixed points," JHEP **10** (2022), 113 [arXiv:2207.10596 [hep-th]].
[19] A. A. Tseytlin, "Comments on a 4-derivative scalar theory in 4 dimensions," Theor. Math. Phys. **217** (2023) no.3, 1969-1986 [arXiv:2212.10599 [hep-th]].
[20] B. Holdom, "Running couplings and unitarity in a 4-derivative scalar field theory," Phys. Lett. B **843** (2023), 138023 [arXiv:2303.06723 [hep-th]].
[21] P. Hasenfratz, "Four-dimensional asymptotically free nonlinear sigma models," Nucl. Phys. B **321** (1989), 139-162
[22] R. Percacci and O. Zanusso, "One loop beta functions and fixed points in Higher Derivative Sigma Models," Phys. Rev. D **81** (2010), 065012 [arXiv:0910.0851 [hep-th]].
[23] J. F. Donoghue and G. Menezes, "Higher Derivative Sigma Models," [arXiv:2308.13704 [hep-th]].
[24] N. D. Birrell and P. C. W. Davies, "Quantum Fields in Curved Space," Cambridge Univ. Press, 1984.
[25] A. O. Barvinsky and G. A. Vilkovisky, "The Generalized Schwinger-Dewitt Technique in Gauge Theories and Quantum Gravity," Phys. Rept. **119**, 1-74 (1985).
[26] L. E. Parker and D. Toms, "Quantum Field Theory in Curved Spacetime: Quantized Field and Gravity," Cambridge University Press, 2009.
[27] I. L. Buchbinder, S. D. Odintsov and I. L. Shapiro, "Effective action in quantum gravity," Bristol, UK: IOP (1992).
[28] R. Percacci, "An Introduction to Covariant Quantum Gravity and Asymptotic Safety," World Scientific, 2017.
[29] J. F. Donoghue, E. Golowich and B. R. Holstein, "Dynamics of the Standard Model: Second edition," Cambridge University Press, 2022.

arXiv:2403.02386v1 [astro-ph.GA] 4 Mar 2024

No massive black holes in the Milky Way halo

Przemek Mróz[1*], Andrzej Udalski[1], Michał K. Szymański[1], Igor Soszyński[1], Łukasz Wyrzykowski[1], Paweł Pietrukowicz[1], Szymon Kozłowski[1], Radosław Poleski[1], Jan Skowron[1], Dorota Skowron[1], Krzysztof Ulaczyk[1,2], Mariusz Gromadzki[1], Krzysztof Rybicki[1,3], Patryk Iwanek[1], Marcin Wrona[1], Milena Ratajczak[1]

[1*]Astronomical Observatory, University of Warsaw, Al. Ujazdowskie 4, Warszawa, 00-478, Poland.
[2]Department of Physics, University of Warwick, Coventry CV4 7 AL, UK.
[3]Department of Particle Physics and Astrophysics, Weizmann Institute of Science, Rehovot 76100, Israel.

*Corresponding author(s). E-mail(s): pmroz@astrouw.edu.pl;

The gravitational wave detectors have unveiled a population of massive black holes that do not resemble those observed in the Milky Way [1–3]. They may have formed due to the evolution of massive low-metallicity stars [4], dynamical interactions in dense stellar environments [5, 6], or density fluctuations in the very early Universe (primordial black holes) [7–9]. If the latter hypothesis is correct, primordial black holes should comprise from several to 100% of dark matter to explain the black hole merger rates observed by gravitational wave detectors [10–12]. If such black holes existed in the Milky Way dark matter halo, they would cause long-timescale gravitational microlensing events lasting years. Here, we present the results of the search for the long-timescale microlensing events among the light curves of 78.7 million stars located in the Large Magellanic Cloud (LMC) that were monitored for 20 years (2001-2020) by the Optical Gravitational Lensing Experiment (OGLE) survey [13]. We did not find any events with timescales longer than one year. The properties of all thirteen microlensing events with timescales shorter than one year detected by OGLE toward the LMC can be explained by astrophysical objects located either in the LMC itself or in the Milky Way disk, without the need to invoke dark matter

in the form of compact objects. We find that compact objects in the mass range from $1.8 \times 10^{-4}\,M_\odot$ to $6.3\,M_\odot$ cannot compose more than 1% of dark matter, and compact objects in the mass range from $1.3 \times 10^{-5}\,M_\odot$ to $860\,M_\odot$ cannot make up more than 10% of dark matter. This conclusively rules out primordial black hole mergers as a dominant source of gravitational waves.

Gravitational microlensing was proposed by [14] as a promising tool for searching for dark matter in the Milky Way halo. This idea prompted extensive searches by the first-generation microlensing surveys [15–18]. Here, we analyze the longest digital photometric data set to search for extremely long-timescale microlensing events. The data were collected for nearly 20 years during the third (OGLE-III; 2001–2009; [19]) and fourth (OGLE-IV; 2010–2020; [13]) phases of the OGLE project. Since OGLE-III and OGLE-IV had similar observing setups, it was possible to merge the observations to create a 20-year-long photometric time-series dataset. We developed a new method of reductions of photometric observations, which enabled us to obtain homogeneous light curves. The design of the survey, extraction of photometry, and methods used to search for microlensing events and calculate the event detection efficiency are described in detail in a companion paper [20].

About 33 million objects are detected in the overlapping OGLE-III/OGLE-IV region, and an additional 29 million objects are observed by OGLE-IV only. The number of stars that may be microlensed is even higher because of blending, which occurs when two or more stars cannot be resolved in ground-based seeing-limited images. We used the archival high-resolution images from the Hubble Space Telescope [21] to correct the star counts for blending. After removing the contribution from foreground Milky Way stars, we found that the survey monitored for microlensing about 78.7 million source stars in the LMC brighter than $I = 22$ mag [20].

We searched for microlensing events using a variation of the method described by [22]. The algorithm tries to identify a flat portion of the light curve, and then searches for consecutive data points that are magnified with respect to the flat part. Then, a standard point-source point-lens microlensing model [14] is fitted to the light curve, and the goodness-of-the-fit statistics are evaluated. The events are selected on the basis of a series of selection cuts. This procedure enabled us to find thirteen events that fulfill all detection criteria. Additionally, three events were identified by a manual inspection of the light curves, although they did not meet all selection criteria. The sample of thirteen events is used for a later statistical analysis [20].

We also carried out extensive light curve simulations to measure the event detection efficiency as a function of the event timescale [20]. To this end, we created synthetic light curves of microlensing events by injecting the microlensing signal into the light curves of constant stars observed by the project. Then, we measured the fraction of simulated events that passed all selection criteria. This procedure enabled us to take into account the noise in the data, as well as the effects of irregular sampling, gaps in the data, outliers, etc.

The contribution of primordial black holes (PBHs) and other compact objects to dark matter is often parameterized by $f = \Omega_{\rm PBH}/\Omega_{\rm DM}$, where $\Omega_{\rm PBH}$ is the density of dark matter in the form of PBHs and $\Omega_{\rm DM}$ is the density of dark matter. Note that we expect to detect some gravitational microlensing events even if $f = 0$: they come

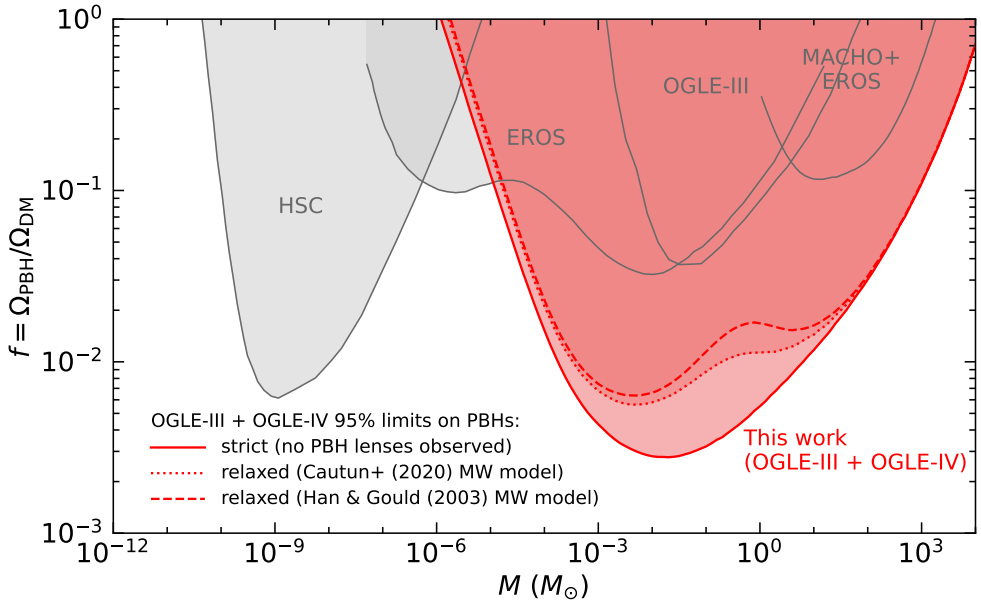


Fig. 1 95% upper limits on PBHs (and other compact objects) as constituents of dark matter. The solid red line marks the limits derived in this paper under the assumption that all gravitational microlensing events detected by OGLE in the direction of the LMC are due to objects in the LMC itself or the Milky Way disk. If this assumption is relaxed, the limits (dotted and dashed lines) depend on the choice of the Milky Way disk model ([23] or [24], respectively). The gray lines mark the limits determined by the following surveys: EROS [16], OGLE-III [17], Hyper Suprime-Cam (HSC) [25], and MACHO+EROS [18]. The new limits are publicly available online at https://www.astrouw.edu.pl/ogle/ogle4/LMC_OPTICAL_DEPTH/.

from lensing objects located in the Milky Way disk and the LMC itself. The latter phenomenon is also called self-lensing [e.g., 26].

We found that all thirteen microlensing events detected in our survey can be explained by brown dwarfs, stars, and stellar remnants located in the LMC and the foreground Milky Way disk (Methods). We adopted the LMC disk model from ref. [15] with some modifications, and considered two Milky Way disk models by [23] and [24] (Methods). We calculated the theoretical microlensing event rate and the event timescale distribution in each field analyzed by OGLE. Then, we estimated the expected number of events by multiplying the event rate by the duration of the observations, the number of source stars, and the average event detection efficiency. In total, we expected to find 12.7 or 20.4 events, depending on the Milky Way disk model, which can be compared to the total number of thirteen events in the final statistical sample. We also found that positions, timescales, and microlensing parallaxes of the detected events are consistent with the predictions of the adopted model (Methods).

To infer the constraints on the value of f, we calculated the expected number of events and their timescale distribution, assuming that the entire dark matter halo is composed of compact objects of the same mass M. We assumed the contracted

Milky Way halo model by [23] and the LMC halo model by [27] (Methods). Our experiment has the highest sensitivity to PBHs with masses of $0.01\,M_\odot$; we should have detected more than 1100 events if the entire dark matter were composed of such objects. However, thanks to the long duration of observations, OGLE has a high sensitivity for even more massive objects. For $M = 1\,M_\odot$, we should have detected 554 events; for $M = 10\,M_\odot$—258 events; for $M = 100\,M_\odot$—99 events; for $M = 1000\,M_\odot$—27 events. Additional information that can be used to further constrain the abundance of PBHs in the Milky Way and LMC haloes is included in the timescales of observed events (Methods).

Our 95% upper limits on PBHs (and other compact objects) as constituents of dark matter are presented in Figure 1. The solid red line marks the strict limits derived in this paper under the assumption that all gravitational microlensing events detected by OGLE in the direction of the LMC are due to known stellar populations in the LMC itself or the Milky Way disk. These limits are inversely proportional to the number of events expected if the entire dark matter was composed of compact objects of a given mass. As expected, the limits are strongest ($f = 2.8 \times 10^{-3}$) for $M \approx 0.01\,M_\odot$, for which the model predicts the largest number of expected events. The compact objects of mass $M = 1\,M_\odot$ may make up less than $f = 0.55\%$ of dark matter; $M = 10\,M_\odot$—$f = 1.2\%$; $M = 100\,M_\odot$—$f = 3.0\%$; $M = 1000\,M_\odot$—$f = 11\%$. The PBHs in the mass range $1.8 \times 10^{-4}\,M_\odot < M < 6.3\,M_\odot$ cannot compose more than 1% of dark matter, and the PBHs in the mass range $1.3 \times 10^{-5}\,M_\odot < M < 8.6 \times 10^{2}\,M_\odot$ cannot make up more than 10% of dark matter.

We also found that, thanks to the long duration of the survey and the large number of stars monitored, the derived limits weakly depend on the choice of the Milky Way halo model. In particular, we tested the dark matter halo model of [28] and found consistent results (as shown in Extended Data Figure 1). The latter model was based on recent measurements of the rotation curve in the outer regions of the Milky Way by the *Gaia* satellite.

The dotted and dashed lines in Figure 1 mark the relaxed limits, for the derivation of which we did not make any assumptions about the origin of events. These limits only slightly depend on the choice of the Milky Way disk model. Overall, the differences between different models are minimal for the least massive ($M \lesssim 10^{-4}\,M_\odot$) and the most massive ($M \gtrsim 10\,M_\odot$) PBHs, because we do not expect that known stellar objects would produce microlensing events with timescales that could be attributed to those by extremely low- or high-mass PBHs. In the intermediate mass range ($10^{-4}\,M_\odot \lesssim M \lesssim 10\,M_\odot$), microlensing events caused by PBHs may be mistaken with those caused by known stellar populations in the LMC or the Milky Way disk. Therefore, the relaxed limits are slightly weaker than the strict ones in this mass range.

Limits presented in Figure 1 are derived for a delta-function mass function of PBHs and, in principle, may become weaker if the underlying mass function is extended. Such extended mass functions of PBHs are frequently discussed in the context of binary black hole mergers discovered by gravitational wave detectors [10–12]. For example, the model presented by [10] predicts four peaks in the mass spectrum of PBHs at 10^{-6}, 1, 30, and $10^{6}\,M_\odot$. These peaks would be associated with different phase transitions in the quark–gluon plasma filling the early universe ($W^{\pm}/Z^{0}$ decoupling,

the quark–hadron transitions, and e^+e^- annihilation), which are thought to enhance the formation of PBHs.

Several studies argue that such a multi-peak mass function of PBHs can naturally explain the observed merger rates of black hole binaries observed by gravitational wave detectors and a significant fraction (from several to 100%) of dark matter [e.g., 10–12]. This hypothesis has one important prediction: PBHs in the Milky Way dark matter halo should cause long-timescale gravitational microlensing events that last years. For example, if the entire dark matter was composed of PBHs with the mass spectrum described by the model of [10] (with the spectral index $\tilde{n}_s = 0.96$), we should have detected over 600 microlensing events. The non-detection gives us a 95% upper limit on the fraction of dark matter in the form of PBHs of $f = 1.2\%$ (assuming a Milky Way disk model by [24]). Similar limits of the order of 1% can be obtained for other multi-peak mass functions proposed in the literature. Our observations, therefore, conclusively rule out PBH mergers as a dominant source of gravitational waves.

Acknowledgements. We thank all the OGLE observers for their contribution to the collection of the photometric data over the decades. We thank T. Bulik for insightful comments on the manuscript. This research was funded in part by National Science Centre, Poland, grant OPUS 2021/41/B/ST9/00252 awarded to P.M.

Author contributions. P.M. led the analysis and interpretation of the data and wrote the manuscript. A.U. is the PI of the OGLE project, and was responsible for the data reduction. All authors collected the OGLE photometric observations, and reviewed, discussed, and commented on the presented results and on the manuscript.

Competing interests. The authors declare no competing interests.

Materials & Correspondence. Correspondence and requests for materials should be addressed to Przemek Mróz (pmroz@astrouw.edu.pl).

Methods

Model

Let us suppose that we have a sample of $N_{\rm obs}$ events and let $t_{{\rm E},i}$ be the Einstein timescale of the ith event. We use that information to measure f (or derive upper limits on f) by maximizing the likelihood function defined as

$$\mathcal{L}(f,M) = e^{-N_{\rm exp}(f,M)} \prod_{i=1}^{N_{\rm obs}} \left[N_{\rm s} \Delta t \frac{d\Gamma}{dt_{\rm E}} (t_{{\rm E},i}, f, M)\, \varepsilon(t_{{\rm E},i}) \right], \tag{1}$$

where $N_{\rm s}$ is the number of microlensing sources observed in the experiment, Δt is the duration of observations, and $\varepsilon(t_{\rm E})$ is the event detection efficiency in the experiment (as a function of the Einstein timescale). Here $d\Gamma/dt_{\rm E}$ is the differential event rate, which contains contributions from lenses in the Milky Way disk, LMC, and Milky Way and LMC dark matter haloes:

$$\begin{aligned} \frac{d\Gamma}{dt_{\rm E}} = & f \frac{d\Gamma_{\rm MW\ halo}}{dt_{\rm E}} (t_{\rm E}, M) + f \frac{d\Gamma_{\rm LMC\ halo}}{dt_{\rm E}} (t_{\rm E}, M) \\ & + \frac{d\Gamma_{\rm MW\ disk}}{dt_{\rm E}} (t_{\rm E}) + \frac{d\Gamma_{\rm LMC}}{dt_{\rm E}} (t_{\rm E}) \,, \end{aligned} \tag{2}$$

and

$$N_{\rm exp}(f,M) = N_{\rm s} \Delta t \int \frac{d\Gamma}{dt_{\rm E}} (t'_{\rm E}, f, M)\, \varepsilon(t'_{\rm E}) dt'_{\rm E} \tag{3}$$

is the expected number of events. Eq. (1) can be derived by dividing the observed event timescale distribution into infinitesimally small bins that contain either one or zero events, and assuming that the number of events detected in each bin follows the Poisson distribution. The microlensing event rate and the event timescale distribution are calculated following the standard approach [e.g., 29]. We describe the components of the model in the following subsections.

Milky Way halo

Our model is based on the contracted halo model of [23], which was inferred by fitting physically motivated models to the *Gaia* DR2 Galactic rotation curve and other data [30]. The model includes the effect of the contraction of the dark matter halo in the presence of baryons, which was observed in large galaxy formation simulations [e.g., 31–33]. The model predicts the total mass of the dark matter Milky Way halo of $0.97 \times 10^{12}\, M_\odot$ within 200 kpc.

We use the best-fitting model of [23] to predict the rotation curve of the Milky Way $V_0(R)$ (which, by design, matches the *Gaia* data very well), where R is the Galactocentric radius. We assume that the distribution of velocities of halo particles (in the rest frame of the Galaxy) can be considered as Maxwellian [34] with the standard deviation of velocities in one direction equal to $V_0(R)/\sqrt{2}$. (There is some evidence that (at least some) black holes may attain a large recoil velocity after a binary black hole merger [e.g., 35]. If all PBHs had such additional velocity, the derived limits would be

modified, such that they would be moved toward more massive PBHs.) Assuming that the Milky Way halo is composed of objects of identical mass M, the mean Einstein timescale of events predicted by the model is equal to $t_{\rm E} = 62\,{\rm d}\sqrt{M/M_\odot}$, which is in good agreement with the predictions of models by [15] or [18].

LMC halo

The *Gaia* observations indicate that stars in the Orphan stream have velocity vectors that are significantly misaligned with the stream track [36]. Ref. [27] demonstrated that this effect can be explained by gravitational perturbations from the LMC, and inferred the total mass of the LMC of $1.49 \times 10^{11}\,M_\odot$ (in the model with the spherical Milky Way, which can move in response to the LMC; ref. [27] also considered models with an oblate or a prolate Milky Way halo, which result in the LMC mass that is $5-8\%$ smaller). The total mass of the Milky Way in the [27] model (enclosed within a radius of 50 kpc) is $4.04 \times 10^{11}\,M_\odot$, which is in excellent agreement with that inferred from the [23] model of the Milky Way halo ($4.1 \times 10^{11}\,M_\odot$).

Following [27], we assume that the LMC halo can be modeled by a Hernquist profile with the total mass of $1.49 \times 10^{11}\,M_\odot$. The scale length is 17.1 kpc, and is taken so that the mass enclosed within 8.7 kpc matches the measured value of $1.7 \times 10^{10}\,M_\odot$ from [37].

Milky Way disk

For consistency with the Milky Way halo model presented above, we adopt the best-fitting thin and thick disk models from [23]. The stellar density is described by the double exponential profile with a scale height of 0.3 kpc (thin disk) or 0.9 kpc (thick disk) and a radial scale length of 2.63 kpc (thin disk) or 3.80 kpc (thick disk). The total masses of the thin and thick disks are $3.18 \times 10^{10}\,M_\odot$ and $0.92 \times 10^{10}\,M_\odot$, respectively. As an alternative, we also consider the thin and thick Milky Way disk models of [24]. The scale heights in the model are 0.156 kpc (thin disk) and 0.439 kpc (thick disk), the scale length is 2.75 kpc for both think and thick disk. The total masses of the thin and thick disks are $0.98 \times 10^{10}\,M_\odot$ and $0.60 \times 10^{10}\,M_\odot$, respectively. We assume that stars in the Milky Way disk follow the circular velocity curve derived above with a dispersion of $30\,{\rm km\,s^{-1}}$ in each direction. We adopt the mass function of [38].

LMC

To take into account the effects of self-lensing by stars located within the LMC itself, we adopt the LMC disk model of [39] and [15] with some slight modifications. The disk is modeled as a double exponential profile with the scale length of 1.8 kpc and the scale height of 0.3 kpc [39], the total stellar mass of $2.7 \times 10^9\,M_\odot$ [40], the inclination and position angle of 25° and 132°, respectively [41]. We adopt the LMC distance of 49.59 kpc [41]. We assume that the stellar mass function is identical to that of the Milky Way. We use an empirical model of the kinematics of stars in the LMC, which is based on *Gaia* EDR3 data (see below). Following [15], we do not consider a separate LMC bar component.

Limits on the PBH abundance

Limits under the hypothesis that all microlensing events detected by OGLE can be explained by known stellar populations

We start by deriving upper limits on the PBH abundance by assuming that all detected events can be explained by astrophysical objects located in the Milky Way disk or the LMC itself. In other words, we assume that we did not see any events due to dark matter in the form of compact objects. In this case, the likelihood function (Eq. (1)) simplifies to:

$$\mathcal{L}(f, M) = e^{-N_{\rm exp}(f,M)}, \tag{4}$$

where $N_{\rm exp}(f, M)$ is the expected number of microlensing events, defined in Eq. (3).

Extended Data Figure 2 shows the number of gravitational microlensing events expected to be detected by OGLE if the entire dark matter were composed of compact objects of a given mass. The blue and red lines in Figure 2 mark the expected number of events that originate from lenses in the Milky Way and LMC haloes, respectively. For PBHs more massive than $0.1\,M_\odot$, Milky Way halo lenses contribute to $\approx 70\%$ of the expected events. For lower masses, LMC halo lenses start to dominate, because the LMC events generally have longer timescales than those by Milky Way halo objects and so are easier to detect. The thin solid lines in Figure 2 show the contribution from fields observed during both the OGLE-III and OGLE-IV phases (from 2001 to 2020), while dashed lines—fields observed during OGLE-IV only (from 2010 to 2020). The latter contribute less than 10% of the sensitivity of the experiment, because they are located on the outskirts of the LMC (and therefore contain fewer source stars) and were observed for a shorter period of time.

Given the likelihood function $\mathcal{L}(f, M)$ (Eqs. (1) and (4)) and our model (Section 3), we employ the Bayes' theorem to derive the posterior distribution for PBH abundance $P(f|M)$:

$$P(f|M) \propto \mathcal{L}(f, M) P_0(f), \tag{5}$$

where $P_0(f)$ is a flat (uniform) prior on $f \in [0, 10]$. We use the Markov chain Monte Carlo (MCMC) sampler of [42] to sample from the posterior and derive 95% upper limits on f as a function of the PBH mass M. To speed up the calculations, we first evaluate $\ln \mathcal{L}(f, M)$ on a grid of 101 logarithmically spaced masses ranging from $10^{-6}\,M_\odot$ to $10^4\,M_\odot$ and 101 logarithmically spaced values of f from 10^{-4} to 10, and use the linear interpolation to calculate the likelihood between the grid points.

Can all microlensing events detected by OGLE be explained by non-dark-matter objects?

In this section, we would like to verify our assumption that all gravitational microlensing events detected by OGLE in the direction of the LMC can be explained by known astrophysical sources. We show that the presented simple models of the LMC (Section 3) and the Milky Way disk (Section 3) are capable of explaining the number and properties (positions, timescales, parallaxes) of virtually all gravitational microlensing events detected in our experiment. We emphasize that we did not attempt to construct a perfect Milky Way/LMC model nor we did not fit the components

of that model to match the data ideally, which would be beyond the scope of this work. Our main goal is to measure the contribution of compact objects to dark matter and study how the choice of an astrophysical model affects our limits on the PBH abundance.

First, we use our fiducial model of the Milky Way disk (Section 3) and the LMC (Section 3) to calculate the theoretical microlensing event rate and the event timescale distribution in each field analyzed by OGLE. Then, we estimate the expected number of events in each field by multiplying the event rate by the duration of the observations, the number of source stars, and the average event detection efficiency (Eq. (3)). The results are summarized in Extended Data Table 1, separately for fields observed during both the OGLE-III and OGLE-IV phases (2001–2020) and observed by OGLE-IV only (2010–2020).

We expect to detect 5.7 microlensing events due to self-lensing by stars in the LMC itself and 7.0 or 14.7 events due to stars in the Milky Way disk (assuming disk models by [24] or [23], respectively). The total mass of the Milky Way disk in the latter model is 2.6 times larger than in the former, which explains why the model predicts twice as many microlensing events. In total, we expect 12.7 or 20.4 events, depending on the Milky Way disk model, which can be compared to the total number of thirteen events in the final statistical sample of [20]. The Milky Way disk model of [24] is clearly favored, although the model of [23] is still allowed, because the Poisson probability of observing 13 or less events given the expected 20.4 events is 5.6%.

Extended Data Figure 3 shows the number of events expected to be detected in each OGLE field. Most events are expected to be found in the central regions of the LMC, where the self-lensing event rate is highest and the number of source stars is largest. Approximately 80% of the events are expected to be located within 3 deg from the LMC center (defined by [43]) in both the [24] and [23] models. There are two events in the [20] sample that are located more than 3 deg of the LMC center, OGLE-LMC-16 (3.2 deg) and OGLE-LMC-17 (4.9 deg), in excellent agreement with the predictions of the [24] model (2.5 events). The cumulative distribution of the angular distances of the detected events from the LMC center matches that expected from both models, with p-values of 0.29 and 0.16 for the [24] and [23] models, respectively.

The distribution of Einstein timescales of events that are expected to be detected by OGLE (taking into account the detection efficiencies in a given field) is presented in Extended Data Figure 4. 80% of the expected events should have timescales between 26 and 417 d in the [24] model (between 25 and 316 d in the [23] model). Events with lenses located in the LMC are expected to have generally longer timescales than those originating from the Milky Way disk lenses, because the relative lens-source proper motions are smaller.

The timescales of the detected events generally match those expected from the model (Extended Data Figure 4). However, three events in the sample have timescales shorter than 25 d (OGLE-LMC-08: $t_{\rm E} = 13.5^{+6.0}_{-4.0}$ d, OGLE-LMC-13: $t_{\rm E} = 7.0^{+2.0}_{-1.1}$ d, OGLE-LMC-17: $t_{\rm E} = 13.8^{+1.9}_{-1.1}$ d), whereas the model predicts that about 10% of all events (that is, 1.3) should fall in this range. It is possible that this is due to a statistical fluctuation, the Poisson probability of observing three events given the expected 1.3 events is about 10%. The model may also underpredict the number of

low-mass lenses or the number of high-proper motion objects, both of which contribute to the population of short-timescale microlensing events.

Extended Data Figure 5 shows the distribution of the microlensing parallaxes of events expected to be detected in our experiment, assuming the Milky Way disk model by [24]. (The distribution of microlensing parallaxes is very similar in the [23] model, except that the second peak has a larger amplitude.) The distribution is clearly bimodal: the two peaks correspond to two distinct populations of lenses, those in the Milky Way disk, and those in the LMC. The Milky Way disk lenses are located nearby, and so their microlens parallaxes are relatively large; they peak at $\pi_{\rm E} \approx 0.5$. The second population of lenses that reside in the LMC is characterized by small parallaxes (typically $\pi_{\rm E} \approx 0.01$). The different values of the parallaxes are consistent with our expectations. For the same lens mass, the microlens parallax scales as $\pi_{\rm E} \propto \sqrt{\pi_{\rm rel}}$, where $\pi_{\rm rel}$ is the relative lens–source parallax. For events with Milky Way disk lenses, $\pi_{\rm rel} \approx 1/D_{\rm l} \approx 1\,{\rm mas}$. For the LMC lenses, $\pi_{\rm rel} \approx \Delta D/D_{\rm s}^2 \approx 1/2500\,{\rm mas}$, where $\Delta D \approx 1\,{\rm kpc}$ is the thickness of the LMC disk, so the LMC self-lensing events should have microlensing parallaxes that are about 50 times smaller than the Milky Way disk events, which is consistent with the simulations presented in Extended Data Figure 5.

The statistical sample of [20] contains four events with reliably measured microlensing parallaxes. This does not mean that the remaining events have parallaxes close to zero; rather, these events are too short or too faint to robustly measure the microlens parallax. However, whenever the parallax is clearly detected in the light curve and its value is larger than $\pi_{\rm E} \approx 0.1$, the lensing object is very likely to be located in the Milky Way disk.

Full limits on PBHs

The Einstein timescales of detected events carry information that can be used to further constrain the abundance of PBHs in the Milky Way and LMC haloes. According to Extended Data Figure 2, if the entire dark matter was composed of black holes of $2200\,M_\odot$, we ought to detect thirteen microlensing events. However, the typical Einstein timescales of these events should be on the order of 9 yr, in stark contrast to the observed values.

To take into account the information included in the timescales of the detected events, we evaluate the full likelihood function defined in Eq. (1). We follow the same procedure as above. We calculate $\ln \mathcal{L}(f, M)$ on a grid of 101 logarithmically spaced masses ranging from $10^{-6}\,M_\odot$ to $10^4\,M_\odot$ and 101 logarithmically spaced values of f from 10^{-4} to 10.

Although most of the detected events have precisely measured timescales, the fractional error bar on $t_{\rm E}$ may be larger than 20% for some events. Thus, we replace the term $\varepsilon(t_{{\rm E},i}) d\Gamma/dt_{\rm E}\,(t_{{\rm E},i}, f, M)$ in the definition of $\mathcal{L}(f, M)$ by the mean over N_i samples from the posterior distribution of $t_{{\rm E},i}$:

$$\frac{1}{N_i} \sum_{k=1}^{N_i} \left[\varepsilon(t_{{\rm E},ik}) \frac{d\Gamma}{dt_{\rm E}}\,(t_{{\rm E},ik}, f, M) \right], \tag{6}$$

where the index i denotes the ith event and the index k runs from 1 through $N_i = 2 \times 10^5$.

Extended Data Figure 6 shows the contours of the log-likelihood function, separately for the [24] and [23] models. Regardless of the model chosen, it is clear there is no evidence that PBHs in the mass range $10^{-6}\,M_\odot < M_{\rm PBH} < 10^4\,M_\odot$ comprise a measurable fraction of the dark matter mass. For the [24] model, the likelihood is highest for $(\log M, \log f) = (-1.5, -2.55)$. However, the model with $\log f = -4$ is disfavored by only $\Delta\chi^2 \equiv 2(\ln \mathcal{L}_{\rm max} - \ln \mathcal{L}) \approx 3.7$. Similarly, for the second model, the likelihood is highest for $(\log M, \log f) = (-1.8, -2.85)$, and the model with $\log f = -4$ is disfavored only by $\Delta\chi^2 \approx 1.5$.

We found that the highest-likelihood grid point has $\log f > -4$ mostly due to one event, OGLE-LMC-13, which has the shortest timescale in the sample of only $t_{\rm E} = 7.0^{+2.0}_{-1.1}$ d. Indeed, such a short-timescale event seems to be very rare in our simulations (Extended Data Figure 4). If the event is removed from the sample, models with $\log f = -4$ are disfavored by less than $\Delta\chi^2 \approx 1.5$.

We calculate the posterior distribution for the PBH abundance $P(f|M)$ using the MCMC approach. Our 95% upper limits on the PBH abundance in dark matter are presented in Figure 1 by dashed ([24] model) and dotted ([23] model) lines, and they can be compared to those derived above (solid red line in Figure 1). Overall, the differences are very small for the least massive ($M_{\rm PBH} \lesssim 10^{-4}\,M_\odot$) and the most massive ($M_{\rm PBH} \gtrsim 10\,M_\odot$) PBHs, because we do not expect that ordinary astrophysical lenses would produce microlensing events with timescales that could be attributed to those by extremely low- or high-mass PBHs.

In the intermediate mass range ($10^{-4}\,M_\odot \lesssim M_{\rm PBH} \lesssim 10\,M_\odot$), microlensing events caused by PBHs may be mistaken with those caused by known astrophysical objects in the LMC or the Milky Way disk. Therefore, the derived limits are slightly weaker. The difference between the 95% upper limits on PBHs calculated assuming the [24] Milky Way disk model and those calculated above is the largest for $\log M = -0.6$ and amounts to $\Delta \log f = 0.59$ dex (that is, the limits are about a factor of 3.9 weaker). The choice of the Milky Way model may also slightly affect the derived limits. The difference between the 95% upper limits on PBHs calculated assuming the [24] and the [23] models is greatest for $\log M = -0.1$ and equals to $\Delta \log f = 0.18$ dex at that mass.

Discussion

The limits on the PBH abundance that are presented in the previous section (and in Figure 1) are calculated based on a full statistical sample of thirteen microlensing events detected over 20 years of the OGLE observations of the LMC [20]. As discussed in a companion paper [20], the sample includes all microlensing events with source stars brigher than $I = 22$ mag. Likewise, the detection efficiencies $\varepsilon(t_{\rm E})$ and the number of source stars $N_{\rm s}$ used in the calculations include only sources brighter than $I = 22$ mag. However, the event detection efficiency rapidly drops with the brightness of source stars; the fainter the source, the lower the chances of detecting the microlensing event. Faint source stars are additionally more difficult to count because of the increased amount of blending from unrelated stars [20]. As a result, although the final sample

of events is larger, there is a risk of introducing unknown systematic errors in the analysis.

Events with brighter source stars should be less prone to such systematic effects. Therefore, we check how our results depend on the adopted limiting magnitude. We re-calculate the detection efficiency for all fields and the number of source stars for limiting magnitudes of $I = 21$ and $I = 21.5$ mag. Then, we follow the methods described above to infer the 95% upper limits on the PBH abundance. The results of the calculations are presented in Extended Data Figure 7. Red and blue lines in Extended Data Figure 7 mark the limits for the limiting magnitudes of 21 and 21.5 mag, respectively, whereas black lines indicate the original limits calculated for the limiting magnitude of 22 mag.

As expected, the differences between the inferred limits are relatively small. The limits for the limiting magnitudes of 21.5 and 22 mag differ by at most $\Delta \log f = -0.10$ dex, for the limiting magnitudes of 21 and 22 mag—by at most $\Delta \log f = -0.20$ dex. This demonstrates that possible systematic effects related to the inclusion of faint source stars are very small and do not influence our conclusions.

The recent studies of the Galactic rotation curve by [28] and [44] seem to indicate that the mass of the dark matter Milky Way halo may be smaller than in the adopted model. If we use the "B2" halo model of [28] (with the Einasto profile of index 0.43), then the optical depth toward the center of the LMC is approximately 4.2×10^{-7}, and our limits on PBHs as dark matter are very similar to those calculated with the fiducial model (Extended Data Figure 1).

LMC proper motion and rotation

We use the *Gaia* EDR3 data to measure the mean LMC proper motion and to devise a simple model of the LMC rotation. The proper motion and rotation of the LMC (and other nearby dwarf galaxies) were extensively studied by [45] based on *Gaia* DR2 data and here we closely follow their approach. We select stars brighter than $G = 19$ that are located within 8 deg of the dynamical center of the HI LMC disk ($\alpha_0 = 78.77°$, $\delta_0 = -69.01°$) [37, 45], have a reliable astrometric solution (with RUWE ≤ 1.4), and have parallaxes consistent with that of the LMC ($\varpi \leq 1$ mas and $\varpi/\sigma_\varpi \leq 10$), in total about 4.8 million sources. We then calculate the positions x, y and proper motions μ_x, μ_y of all stars in an ortographic projection centered at (α_0, δ_0) using equations:

$$\begin{aligned} x =& \cos\delta \sin(\alpha - \alpha_0), \\ y =& \sin\delta \cos\delta_0 - \cos\delta \sin\delta_0 \cos(\alpha - \alpha_0), \\ \mu_x =& \mu_\alpha \cos(\alpha - \alpha_0) - \mu_\delta \sin\delta \sin(\alpha - \alpha_0), \\ \mu_y =& \mu_\alpha \sin\delta_0 \sin(\alpha - \alpha_0) \\ &+ \mu_\delta(\cos\delta \cos\delta_0 + \sin\delta \sin\delta_0 \cos(\alpha - \alpha_0)). \end{aligned} \tag{7}$$

The median proper motions of the selected stars are presented in Extended Data Figure 8.

The median proper motion of the LMC (which is determined using stars located within 5° of the dynamical center) is $\mu_x = 1.851 \pm 0.340$ mas yr^{-1} and $\mu_y = 0.277 \pm$

$0.382\,\mathrm{mas\,yr^{-1}}$, in good agreement with the results of [45]. Here the uncertainties denote the dispersion of proper motions in a given direction. This corresponds to $\mu_l = -0.662 \pm 0.381\,\mathrm{mas\,yr^{-1}}$ and $\mu_b = 1.751 \pm 0.342\,\mathrm{mas\,yr^{-1}}$ in the Galactic coordinates.

The proper motion pattern seen in the middle and bottom panels of Extended Data Figure 8 reflects the rotation of the LMC and, in the first order, can be approximated by the central value and two gradients. Additional striping pattern of lower amplitude is indicative of small-scale systematics in *Gaia* EDR3 [46]. To minimize their influence, we calculate the median proper motion (and its dispersion) in 100×100 bins in the range $|x| \leq 0.15\,\mathrm{rad}$ and $|y| \leq 0.15\,\mathrm{rad}$ and fit the following linear model to the binned data:

$$\begin{aligned} \mu_x &= \mu_{x,0} + \frac{\partial \mu_x}{\partial x} x + \frac{\partial \mu_x}{\partial y} y, \\ \mu_y &= \mu_{y,0} + \frac{\partial \mu_y}{\partial x} x + \frac{\partial \mu_y}{\partial y} y. \end{aligned} \tag{8}$$

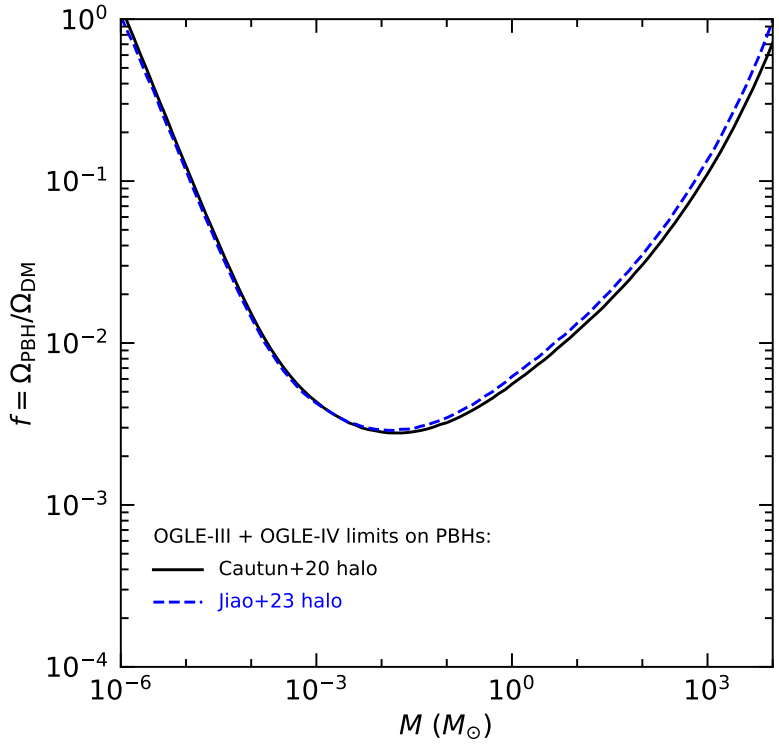
The six fit coefficients are determined using the least squares approach using bins with at least 10 stars. The model is fit in 7 annuli with a width of 1 deg. The best-fit parameters are presented in Extended Data Table 2.

Data availability

The data used to perform the analysis (event detection efficiencies, source star counts, posterior distributions of event parameters) are publicly available at https://www.astrouw.edu.pl/ogle/ogle4/LMC_OPTICAL_DEPTH/.

Code availability

The custom codes for the simulation of microlensing events toward the LMC and the calculation of limits on PBHs as dark matter are available upon request from the corresponding author.



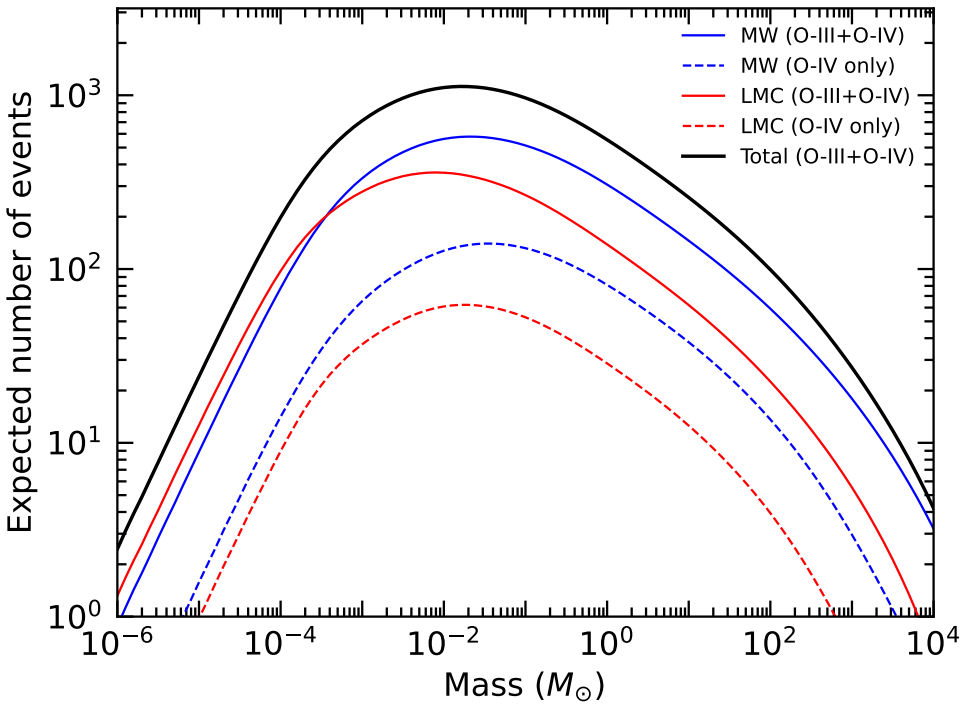
Extended Data Figure 1 95% upper limits on the PBH abundance for Cautun et al. (2020) [23] and Jiao et al. (2023) [28] dark matter halo models.

	OGLE-III & OGLE-IV	OGLE-IV Only	Total
Milky Way disk [24]	5.5	1.5	7.0
Milky Way disk [23]	11.5	3.2	14.7
LMC	5.3	0.4	5.7
Total (disk model [24])	10.8	1.9	12.7
Total (disk model [23])	16.8	3.6	20.4

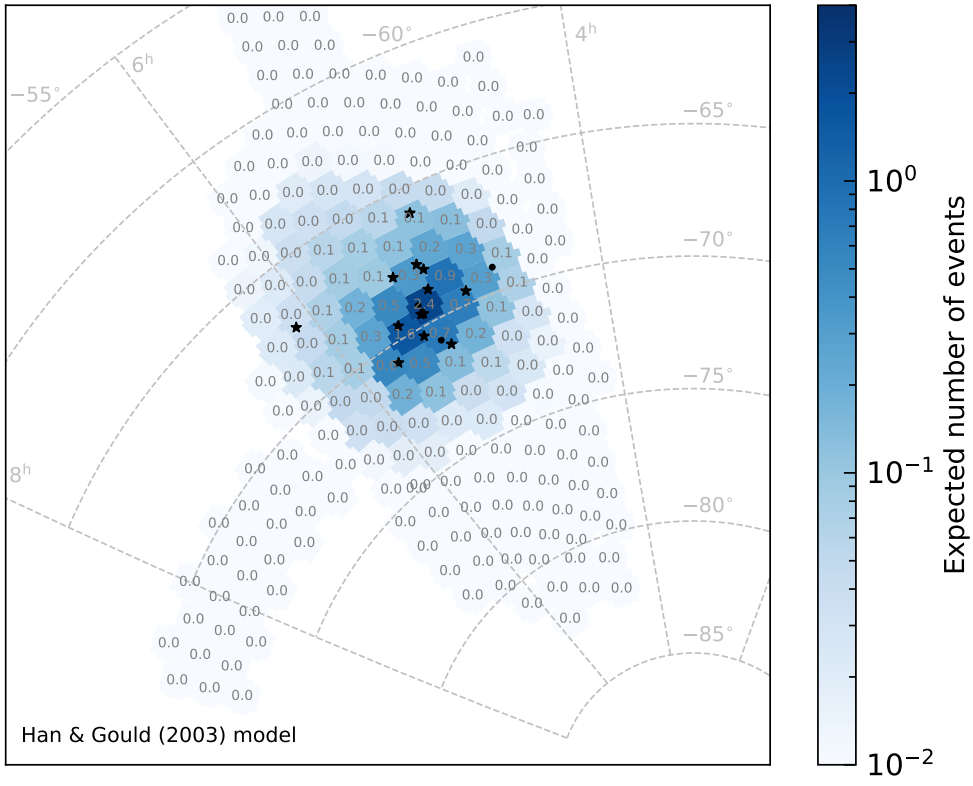
Extended Data Table 1 The expected number of microlensing events caused by astrophysical objects located in the Milky Way disk and the LMC.

ρ (deg)	$\partial\mu_x/\partial x$	$\partial\mu_x/\partial y$	$\mu_{x,0}$	$\partial\mu_y/\partial x$	$\partial\mu_y/\partial y$	$\mu_{y,0}$	rms(μ_x)	rms(μ_y)
$0 < \rho < 1$	-3.6832	-6.7018	1.8535	5.6324	-1.5691	0.2348	0.029	0.023
$1 < \rho < 2$	-2.3530	-5.6825	1.8565	5.7179	-0.7549	0.2135	0.041	0.027
$2 < \rho < 3$	-1.2292	-4.5601	1.8471	5.3498	-0.3510	0.2178	0.037	0.028
$3 < \rho < 4$	-1.0871	-3.5981	1.8355	4.5304	-0.5892	0.2357	0.035	0.036
$4 < \rho < 5$	-0.9070	-2.7004	1.8348	3.7424	-0.5745	0.2659	0.042	0.057
$5 < \rho < 6$	-0.7520	-2.1700	1.8430	3.2343	-0.4711	0.2770	0.049	0.058
$6 < \rho < 7$	-0.7497	-1.7328	1.8510	2.8296	-0.4742	0.2655	0.048	0.050

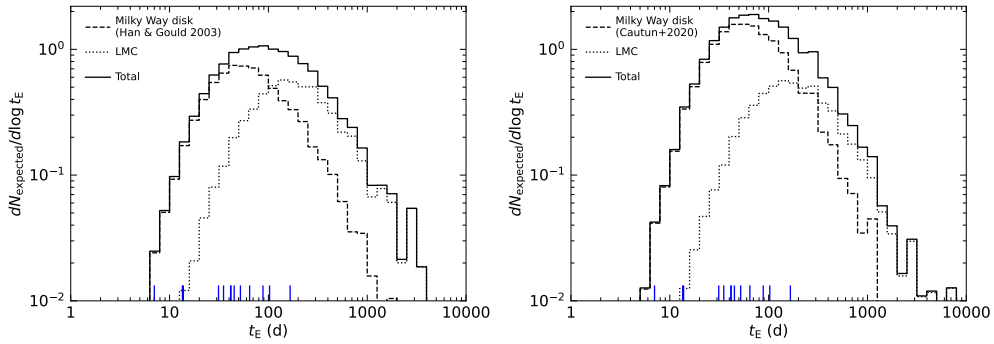
Extended Data Table 2 Parameters of the LMC proper motion model. Units of $\partial\mu_x/\partial x$, $\partial\mu_x/\partial y$, $\partial\mu_y/\partial x$, and $\partial\mu_y/\partial y$ are mas yr^{-1} rad^{-1}, whereas $\mu_{x,0}$, $\mu_{y,0}$, rms(μ_x), and rms(μ_y) are given in mas yr^{-1}.



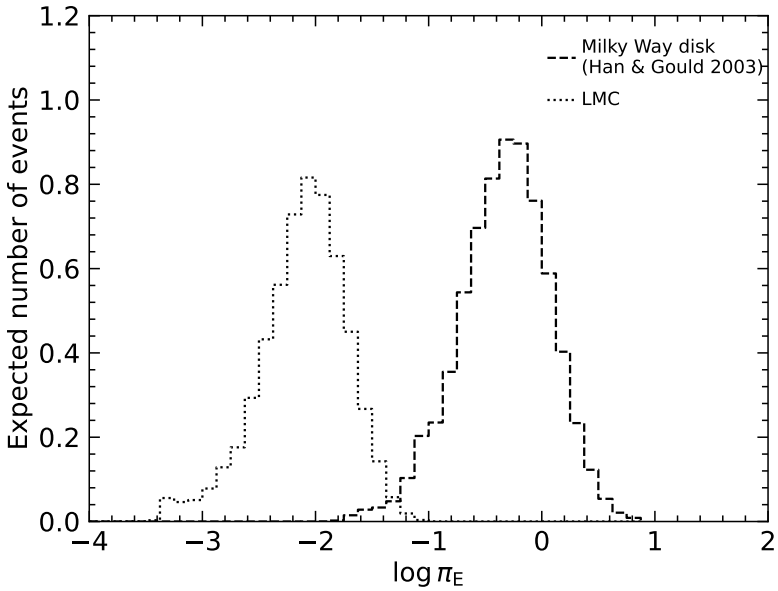
Extended Data Figure 2 Number of gravitational microlensing events expected to be detected by OGLE if entire dark matter were composed of compact objects of a given mass $N_{\rm exp}(f = 1, M)$. Thin solid lines correspond to fields observed during OGLE-III and OGLE-IV phases (from 2001 to 2020), dashed lines – fields observed during OGLE-IV only (from 2010 to 2020). Blue lines mark the contribution from the Milky Way dark matter halo, red lines – the LMC dark matter halo.



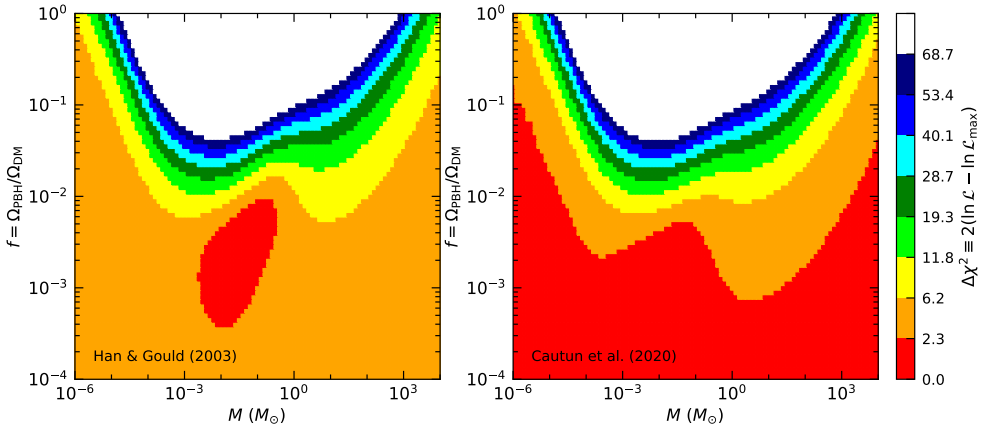
Extended Data Figure 3 Number of gravitational microlensing events from known stellar populations (Milky Way disk and LMC) expected to be detected by OGLE (assuming the [24] Milky Way disk model) in the analyzed fields. Black asterisks mark events that are a part of the statistical sample of [20], black dots mark other events.



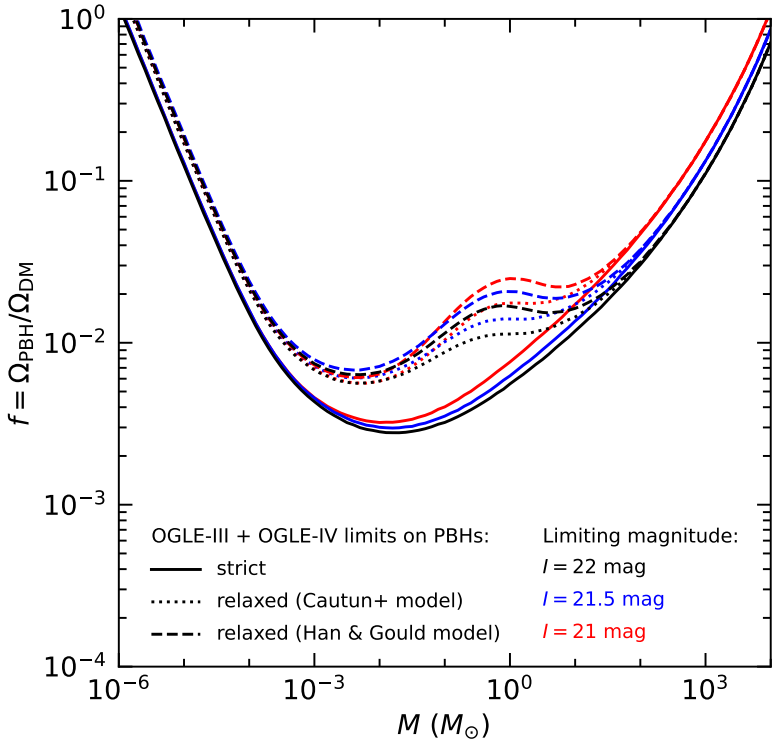
Extended Data Figure 4 Distribution of Einstein timescales of microlensing events that are expected to be detected in our experiment, for the [24] Milky Way disk model (left panel) and the [23] model (right). Vertical blue lines mark the detected events.



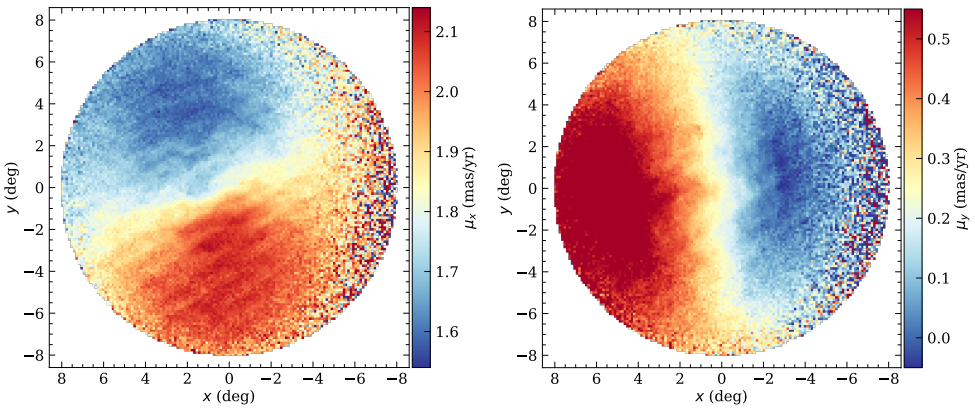
Extended Data Figure 5 Distribution of microlens parallaxes of events that are expected to be detected in our experiment (assuming the Milky Way disk model of [24]).



Extended Data Figure 6 The contours of the likelihood function (Eq. 1) for the [24] (left panel) and [23] Milky Way disk model (right panel). The color codes the difference $\Delta\chi^2 \equiv 2(\ln\mathcal{L}_{\rm max} - \ln\mathcal{L})$.



Extended Data Figure 7 95% upper limits on the PBH abundance as a function of the limiting magnitude.



Extended Data Figure 8 *Gaia* EDR3 proper motions of LMC stars.

References

[1] Abbott, B. P. *et al.* Observation of Gravitational Waves from a Binary Black Hole Merger. *Phys. Rev. Lett.* **116**, 061102 (2016).

[2] Abbott, B. P. *et al.* GWTC-1: A Gravitational-Wave Transient Catalog of Compact Binary Mergers Observed by LIGO and Virgo during the First and Second Observing Runs. *Phys. Rev. X* **9**, 031040 (2019).

[3] Abbott, R. *et al.* Population Properties of Compact Objects from the Second LIGO-Virgo Gravitational-Wave Transient Catalog. *Astrophys. J. Lett.* **913**, L7 (2021).

[4] Belczynski, K., Holz, D. E., Bulik, T. & O'Shaughnessy, R. The first gravitational-wave source from the isolated evolution of two stars in the 40-100 solar mass range. *Nature* **534**, 512–515 (2016).

[5] Askar, A., Szkudlarek, M., Gondek-Rosińska, D., Giersz, M. & Bulik, T. MOCCA-SURVEY Database - I. Coalescing binary black holes originating from globular clusters. *Mon. Not. R. Astron. Soc.* **464**, L36–L40 (2017).

[6] Rodriguez, C. L., Amaro-Seoane, P., Chatterjee, S. & Rasio, F. A. Post-Newtonian Dynamics in Dense Star Clusters: Highly Eccentric, Highly Spinning, and Repeated Binary Black Hole Mergers. *Phys. Rev. Lett.* **120**, 151101 (2018).

[7] Bird, S. *et al.* Did LIGO Detect Dark Matter? *Phys. Rev. Lett.* **116**, 201301 (2016).

[8] Sasaki, M., Suyama, T., Tanaka, T. & Yokoyama, S. Primordial Black Hole Scenario for the Gravitational-Wave Event GW150914. *Phys. Rev. Lett.* **117**, 061101 (2016).

[9] Clesse, S. & García-Bellido, J. The clustering of massive Primordial Black Holes as Dark Matter: Measuring their mass distribution with advanced LIGO. *Phys. Dark Universe* **15**, 142–147 (2017).

[10] Carr, B., Clesse, S., García-Bellido, J. & Kühnel, F. Cosmic conundra explained by thermal history and primordial black holes. *Phys. Dark Universe* **31**, 100755 (2021).

[11] Jedamzik, K. Consistency of Primordial Black Hole Dark Matter with LIGO/Virgo Merger Rates. *Phys. Rev. Lett.* **126**, 051302 (2021).

[12] Escrivà, A., Bagui, E. & Clesse, S. Simulations of PBH formation at the QCD epoch and comparison with the GWTC-3 catalog. *J. Cosmol. Astropart. P.* **2023**, 004 (2023).

[13] Udalski, A., Szymański, M. K. & Szymański, G. OGLE-IV: Fourth Phase of the

Optical Gravitational Lensing Experiment. *Acta Astronom.* **65**, 1–38 (2015).

[14] Paczyński, B. Gravitational microlensing by the galactic halo. *Astrophys. J.* **304**, 1–5 (1986).

[15] Alcock, C. *et al.* The MACHO Project: Microlensing Results from 5.7 Years of Large Magellanic Cloud Observations. *Astrophys. J.* **542**, 281–307 (2000).

[16] Tisserand, P. *et al.* Limits on the Macho content of the Galactic Halo from the EROS-2 Survey of the Magellanic Clouds. *Astron. Astrophys.* **469**, 387–404 (2007).

[17] Wyrzykowski, L. *et al.* The OGLE view of microlensing towards the Magellanic Clouds - IV. OGLE-III SMC data and final conclusions on MACHOs. *Mon. Not. R. Astron. Soc.* **416**, 2949–2961 (2011).

[18] Blaineau, T. *et al.* New limits from microlensing on Galactic black holes in the mass range 10 $M_\odot$ ¡ M ¡ 1000 $M_\odot$. *Astron. Astrophys.* **664**, A106 (2022).

[19] Udalski, A. The Optical Gravitational Lensing Experiment. Real Time Data Analysis Systems in the OGLE-III Survey. *Acta Astronom.* **53**, 291–305 (2003).

[20] Mróz, P. *et al.* Microlensing optical depth and event rate toward the Large Magellanic Cloud based on 20 years of OGLE observations. *submitted* (2024).

[21] Holtzman, J. A., Afonso, C. & Dolphin, A. The Local Group Stellar Populations Archive from the Hubble Space Telescope WFPC2. *Astrophys. J. Suppl. S.* **166**, 534–548 (2006).

[22] Mróz, P. *et al.* No large population of unbound or wide-orbit Jupiter-mass planets. *Nature* **548**, 183–186 (2017).

[23] Cautun, M. *et al.* The milky way total mass profile as inferred from Gaia DR2. *Mon. Not. R. Astron. Soc.* **494**, 4291–4313 (2020).

[24] Han, C. & Gould, A. Stellar Contribution to the Galactic Bulge Microlensing Optical Depth. *Astrophys. J.* **592**, 172–175 (2003).

[25] Niikura, H. *et al.* Microlensing constraints on primordial black holes with Subaru/HSC Andromeda observations. *Nature Astronomy* **3**, 524–534 (2019).

[26] Sahu, K. C. Stars within the Large Magellanic Cloud as potential lenses for observed microlensing events. *Nature* **370**, 275–276 (1994).

[27] Erkal, D. *et al.* The total mass of the Large Magellanic Cloud from its perturbation on the Orphan stream. *Mon. Not. R. Astron. Soc.* **487**, 2685–2700 (2019).

[28] Jiao, Y. *et al.* Detection of the Keplerian decline in the Milky Way rotation curve. *Astron. Astrophys.* **678**, A208 (2023).

[29] Clanton, C. & Gaudi, B. S. Synthesizing Exoplanet Demographics from Radial Velocity and Microlensing Surveys. I. Methodology. *Astrophys. J.* **791**, 90 (2014).

[30] Eilers, A.-C., Hogg, D. W., Rix, H.-W. & Ness, M. K. The Circular Velocity Curve of the Milky Way from 5 to 25 kpc. *Astrophys. J.* **871**, 120 (2019).

[31] Schaye, J. *et al.* The EAGLE project: simulating the evolution and assembly of galaxies and their environments. *Mon. Not. R. Astron. Soc.* **446**, 521–554 (2015).

[32] Fattahi, A. *et al.* The APOSTLE project: Local Group kinematic mass constraints and simulation candidate selection. *Mon. Not. R. Astron. Soc.* **457**, 844–856 (2016).

[33] Grand, R. J. J. *et al.* The Auriga Project: the properties and formation mechanisms of disc galaxies across cosmic time. *Mon. Not. R. Astron. Soc.* **467**, 179–207 (2017).

[34] Griest, K. *et al.* Gravitational microlensing as a method of detecting disk dark matter and faint disk stars. *Astrophys. J. Lett.* **372**, L79–L82 (1991).

[35] Varma, V. *et al.* Evidence of Large Recoil Velocity from a Black Hole Merger Signal. *Phys. Rev. Lett.* **128**, 191102 (2022).

[36] Koposov, S. E. *et al.* Piercing the Milky Way: an all-sky view of the Orphan Stream. *Mon. Not. R. Astron. Soc.* **485**, 4726–4742 (2019).

[37] van der Marel, R. P. & Kallivayalil, N. Third-epoch Magellanic Cloud Proper Motions. II. The Large Magellanic Cloud Rotation Field in Three Dimensions. *Astrophys. J.* **781**, 121 (2014).

[38] Kroupa, P. On the variation of the initial mass function. *Mon. Not. R. Astron. Soc.* **322**, 231–246 (2001).

[39] Gyuk, G., Dalal, N. & Griest, K. Self-lensing Models of the Large Magellanic Cloud. *Astrophys. J.* **535**, 90–103 (2000).

[40] van der Marel, R. P., Alves, D. R., Hardy, E. & Suntzeff, N. B. New Understanding of Large Magellanic Cloud Structure, Dynamics, and Orbit from Carbon Star Kinematics. *Astron. J.* **124**, 2639–2663 (2002).

[41] Pietrzyński, G. *et al.* A distance to the Large Magellanic Cloud that is precise to one per cent. *Nature* **567**, 200–203 (2019).

[42] Foreman-Mackey, D., Hogg, D. W., Lang, D. & Goodman, J. emcee: The MCMC Hammer. *Publ. Astron. Soc. Pac.* **125**, 306 (2013).

[43] Kim, S. *et al.* An H I Aperture Synthesis Mosaic of the Large Magellanic Cloud. *Astrophys. J.* **503**, 674–688 (1998).

[44] Ou, X., Eilers, A.-C., Necib, L. & Frebel, A. The dark matter profile of the Milky Way inferred from its circular velocity curve. *Mon. Not. R. Astron. Soc.* **528**, 693–710 (2024).

[45] Gaia Collaboration *et al.* Gaia Data Release 2. Kinematics of globular clusters and dwarf galaxies around the Milky Way. *Astron. Astrophys.* **616**, A12 (2018).

[46] Lindegren, L. *et al.* Gaia Early Data Release 3. The astrometric solution. *Astron. Astrophys.* **649**, A2 (2021).

arXiv:2403.02000v1 [astro-ph.CO] 4 Mar 2024

Observational Constraints on the Dark Energy with a Quadratic Equation of State

Hossein Moshafi[a,*], Alireza Talebian[a], Ebrahim Yusofi[a,b], Eleonora Di Valentino[c]

[a]School of Astronomy, Institute for Research in Fundamental Sciences (IPM), P. O. Box 19395-5531, Tehran, Iran
[b]Innovation and Management Research Center, Ayatollah Amoli Branch, Islamic Azad University, Amol, Mazandaran, Iran
[c]School of Mathematics and Statistics, University of Sheffield, Hounsfield Road, Sheffield S3 7RH, United Kingdom

Abstract

In this study, we introduce a novel late-time effective dark energy model characterized by a quadratic equation of state (EoS) and rigorously examine its observational constraints. Initially, we delve into the background dynamics of this model, tracing the evolution of fluctuations in linear order. Our approach involves substituting the conventional cosmological constant with a dynamically effective dark energy fluid. Leveraging a diverse array of observational datasets encompassing the Planck 2018 Cosmic Microwave Background (CMB), Type Ia Supernovae (SNe), Baryon Acoustic Oscillations (BAO), and a prior on the Hubble constant H_0 (R21), we constrain the model parameters. We establish the model's consistency by comparing the Hubble parameter as a function of redshift against observational Hubble data (OHD), benchmarking its performance against the Standard ΛCDM model. Additionally, our investigation delves into studies of the model's dynamical behavior by computing cosmological parameters such as the deceleration parameter, relative Hubble parameter, and the evolution of the Hubble rate. Furthermore, employing Bayesian analysis, we determine the Bayesian Evidence for our proposed model compared to the reference ΛCDM model. While our analysis unveils the favorable behavior of the model in various observational tests, the well-known cosmological tensions persist when the full dataset combination is explored.

Keywords: Dark Energy, Quadratic Equation of State, Cosmic Voids, Hubble Tension
PACS:

Contents

1 Introduction **2**

2 The Model with a Quadratic EoS **2**

3 Observational data **4**

4 Statistical methods and Analysis **4**
4.1 Bayesian inference 5

5 Testing $\mathbb{W}$CDM model with Cosmological Data **6**

6 Summary and Discussions **8**

*Corresponding author
Email addresses: moshafi86@gmail.com;moshafi@ipm.ir (Hossein Moshafi), talebian@ipm.ir (Alireza Talebian), eyusofi@ipm.ir (Ebrahim Yusofi), e.divalentino@sheffield.ac.uk (Eleonora Di Valentino)

1. Introduction

One of the most groundbreaking discoveries in recent cosmology is the observation of cosmological acceleration in our Universe. Despite this revelation, the true nature of this acceleration remains elusive and is referred to as dark energy (DE). According to the widely accepted standard model of cosmology, called ΛCDM (which aligns remarkably well with current cosmological observations), DE is a cosmological constant and accounts for $\sim 70\%$ of the energy budget of the Universe. For a more comprehensive understanding of DE, various cosmological models have been introduced. Constructing a cosmological model requires two essential elements: a gravitational theory defining the Universe's geometry and a comprehensive picture of its matter content. In this context, DE can be conceptualized either as an altered form of matter (such as quintessence, k-essence, phantom, $\cdots$) or as a modification within gravitational theories (like $f(R)$ gravity, Gauss–Bonnet, $\cdots$) [10].

The models based on modified matter can be achieved through the introduction of an exotic matter source exhibiting negative pressure. The most straightforward instances include fluids characterized by a linear equation of state (EoS) [36, 52, 60, 61, 62, 85], denoted as $p = w\rho$, where p represents pressure and ρ signifies energy density.

In diverse cosmological models, including those rooted in extra dimensions (such as String theory, Brane-worlds, etc.), and within intricate and more realistic systems, the relationship between pressure and density may not adhere to a linear correlation [84, 39, 23, 25]. If we assume $p = p(\rho)$ for any barotropic fluid to be an analytic function, we can consider a more general form of the equation of state of the form $p = p_0 + A_1\rho + A_2\rho^2 + O(\rho^3)$. In the Brane-world [76, 19, 48] scenario, the assumption of the extra dimensions produces a quadratic term in the energy density. In addition, it has been shown that Loop Quantum Gravity (LQG) corrections result in a modified Friedmann equation with the modification appearing as a negative term which is quadratic in the energy density [81, 15, 16, 70, 73].

In this paper, we study an effective dark energy fluid with a quadratic EoS [13]. The non-linear term in EoS can be originated from the merger process of clusters/voids and may act as a possible source for cosmic acceleration [88, 55]. The model can explain the evolution of voids [74, 80] in an under-dense environment within a void-dominated universe [66]. Also, it is shown that this fluid has a possible balancing effect on the cosmological expansion [55]. In this work, we substitute a new energy density component $\rho_{\rm v}$, instead of the cosmological constant ρ_Λ in ΛCDM, and we call it $\mathbb{W}$CDM model. We consider the observational data (including the deceleration parameter, relative Hubble parameter, and the evolution of the Hubble rate) in the framework of the proposed model.

For comprehensive evaluation against other cosmological models, examining how the $\mathbb{W}$CDM model performs with respect to the cosmological tensions, including the Hubble constant H_0 tension [83, 67, 27], proves to be particularly insightful. There was another well-studied problem called S_8 tension [14, 12, 1, 5, 53, 24, 28] which seems to be alleviated by the recent study by [2]. Several models have been proposed for alleviating these problems in the literature [47, 40, 29, 3, 42, 30, 79, 82, 44, 60, 59, 46, 4]. Roughly speaking, two primary categories of DE models aimed at addressing the H_0 tension by introducing novel physics: early-time and late-time DE models. These categories depend on the modifications to the expansion history, whether they occur before or after the recombination epoch, respectively. Within this framework, the proposed $\mathbb{W}$CDM model in our study aligns with the latter category.

The paper is organized as follows: in Section 2 we explain the dynamics of the model and derive the equation of motion of linear perturbations. For testing the model, we introduce the observational data sets and the statistical methods used in this work in Sections 3 and 4, respectively. Our results for this model in the light of the combination of different datasets are summarized in Section 5. Finally, we discuss the results in Section 6.

2. The Model with a Quadratic EoS

We consider a model consisting of a new variable energy density $\rho_{\rm v}$ instead of the constant dark energy density in the standard ΛCDM model. The new source is a cosmological barotropic fluid with a non-linear EoS. In this work, we are focusing on the quadratic case [13, 45, 55],

$$p_{\rm v} = w_{\rm v}\,\rho_{\rm v} + \beta\,\rho_{\rm v}^2 \tag{1}$$

in which $P_{\rm v}$ and $w_{\rm v}$ are the pressure and the equation of state parameter, respectively. The new parameter β comes from the non-linearity effect in the over-dense regime that can originate from the merger of clusters/voids in this area

and sets the characteristic energy scale ρ_c of the quadratic term

$$\beta \equiv \frac{b}{\rho_c} \tag{2}$$

where b is a constant non-zero parameter that must be determined with the observational data.

As an example of application, the equation of state of (1) can describe a cosmic fluid with two different regimes: under-dense regime (linear term $\propto \rho_v$) and over-dense regime (non-linear term $\propto \rho_v^2$). Our model requires the existence of some phenomenological interactions as the possibility of merging and collapsing of these two regimes. More precisely, starting with the linear EoS for the fluid, the merging (collapsing) of two under-dense (over-dense) regimes leads to the final pressure of the fluid being modified by the non-linear term in (1) [45]. In the general case, the rate of merging and collapsing could be a function of space and time, and two under-dense and over-dense regions can coexist at the same time [75].

This picture is consistent with the findings on the evolution and merging of the vast cosmic voids [74, 80, 66] if voids are considered as the under-dense regime of our fluid while the density of the fluid on the boundary of voids where the dark matter halos are located is high and non-linear. More specifically, in the evolution of voids, two processes are reported: *merging* of two voids into larger voids in large-scale under-dense regions and their *collapsing* and disappearance in local over-dense regions [74]. For instance, two small voids merge and form a giant cosmic void. When the adjacent sub-voids meet up and merge, the matter between them is squeezed into thin walls and filaments [80]. In such a merging cosmic fluid, our universe consists of under-dense and over-dense regions in the form of a cosmic web, in which under-density regions are located inside the voids, and over-dense regions including strings, clusters, and shells are located at the boundary of the voids [66].

In our model, we assume the characteristic energy scale ρ_c be the critical energy density of the Universe, i.e. $\rho_c \sim \rho_0$. This assumption is based on the previous studies [87, 88] in which the non-linear term in the total pressure can be related to the surface tension of the voids.

Using the *continuity equation*, the energy density of the fluids ρ_v as a function of the scale factor a for the cases $w_v \neq -1$ is given by [45, 55]

$$\rho_v(a) = \frac{\rho_{v_0} a^{-3(1+w_v)}}{1 + \frac{\beta\rho_{v_0}}{1+w_v}[1 - a^{-3(1+w_v)}]}, \tag{3}$$

and for the special case ($w_v = -1$) is given by

$$\rho_v(a) = \frac{\rho_{v_0}}{1 + 3\beta\rho_{v_0} \ln a}, \tag{4}$$

where ρ_{v_0} is the energy density of the fluid at present $a = 1$. In the limit $\beta \to 0$, the model (3) covers the phantom ($w_v < -1$) [21] and quintessence ($w_v \geqslant -1$) models [63] while the model (4) meets the well-known ΛCDM model.

As seen, the model is a dynamical dark energy in which the cosmological constant is replaced by a quadratic barotropic fluid. The cosmic background evolution is described through the Friedmann equation,

$$H^2(z) = \frac{8\pi G}{3} \sum_i \rho_i(z) \tag{5}$$

in which G is the gravitational constant and H is Hubble parameter and the total energy density consists of

$$\sum_i \rho_i(z) = \rho_r(z) + \rho_b(z) + \rho_{cdm}(z) + \rho_v(z) \tag{6}$$

where ρ_r, ρ_b and ρ_{cdm} are the energy density of radiation, baryon, and cold dark matter, respectively, while ρ_v is given by (3) or (4) depending on w_v. In the following, we study some important cosmological parameters in the framework of the $\mathbb{W}$CDM model, by careful examination of the background evolution and first-order perturbations in the light of observational data.

To investigate the linear growth of density perturbations of both the pressureless dark matter and dark energy fluid in our model, we use perturbed Einstein's equation in the conformal-Newtonian gauge. In this formalism, the linear

density contrast of non-relativistic DM, $\delta_{\rm m}$, and DE, $\delta_{\rm v}$, satisfy the following equations in Fourier space [11]

$$k^2\Phi + 3\mathcal{H}\left(\Phi' - \mathcal{H}\Psi\right) = 4\pi G a^2\left[\rho_{\rm m}\delta_{\rm m} + \rho_{\rm v}\delta_{\rm v} + \rho_{\rm r}\delta_{\rm r}\right], \tag{7}$$

$$k^2\left(\Phi' - \mathcal{H}\Psi\right) = -4\pi G a^2\left[(1+w_{\rm m})\rho_{\rm m}\theta_{\rm m} + (1+w_{\rm v}+\beta\rho_{\rm v})\rho_{\rm v}\theta_{\rm v} + (1+w_{\rm r})\rho_{\rm r}\theta_{\rm r}\right], \tag{8}$$

$$\Psi = -\Phi, \tag{9}$$

$$\Phi'' + 2\mathcal{H}\Phi' - \mathcal{H}\Psi' - \left(\mathcal{H}^2 + 2\mathcal{H}'\right)\Psi = -4\pi G a^2\left[c^2_{\rm s,m}\rho_{\rm m}\delta_{\rm m} + (w_{\rm v}+2\beta\rho_{\rm v})\rho_{\rm v}\delta_{\rm v} + c^2_{\rm s,r}\rho_{\rm r}\delta_{\rm r}\right], \tag{10}$$

$$\delta_{\rm v}' + 3\mathcal{H}\beta\rho_{\rm v}\delta_{\rm v} = -\left(1+w_{\rm v}+\beta\rho_{\rm v}\right)\left(\theta_{\rm v} + 3\Phi'\right), \tag{11}$$

$$\theta_{\rm v}' + \theta_{\rm v}\left[(1-3w_{\rm v})\mathcal{H} - 6\beta\rho_{\rm v}\right] = k^2\left(\frac{w_{\rm v}+2\beta\rho_{\rm v}}{1+w_{\rm v}+\beta\rho_{\rm v}}\delta_{\rm v} + \Psi\right) \tag{12}$$

where η is the conformal time and the prime denotes the derivative to the conformal time. Ψ & Φ are Bardeen potentials and $\mathcal{H}$ is conformal Hubble parameter. $c^2_{\rm s,r}$ and $c^2_{\rm s,m}$ are the sound speeds and $\theta_{\rm v}, \theta_{\rm m}$ and $\theta_{\rm r}$ are divergence of velocities of corresponding components. Finally $\rho_{\rm m} = \rho_{\rm b} + \rho_{\rm cdm}$ and $\rho_{\rm r} = \rho_\gamma + \rho_\nu$ are the density matter and density radiation, respectively. The power spectrum of matter perturbations $P(k)$ is defined as

$$\langle\delta_{\rm m}(\vec{k})\,\delta_{\rm m}(\vec{k'})\rangle = (2\pi)^3\,\delta_D\left(\vec{k}+\vec{k'}\right)P(k) \tag{13}$$

where δ_D is a Dirac delta function and $\delta_{\rm m}$ is Fourier transformed density field. The variance of the mass distribution smoothed on $R = 8h^{-1}$Mpc scales is defined

$$\sigma_8^2 = \frac{1}{2\pi^2}\int P(k)\left[\frac{3j_1(kR)}{kR}\right]^2 k^2 dk \tag{14}$$

where $j_1(kR)$ is a spherical Bessel function.

We've implemented the background and the perturbation equations with correct modifications into the `CAMB` code [51] and calculated matter, and temperature and polarization power spectra.

3. Observational data

In this section, we describe the cosmological data sets used in this work in brief. The description of the data catalogs is as follows:

1. **CMB**: We use the most precise full-sky measurements of Cosmic Microwave Background (CMB) radiation performed by *Planck* satellite. We use both high-ℓ temperature and polarization angular power spectra from the final release of "*Planck 2018*" baseline `PLIK-LITE TTTEEE` along with *Planck* `low-`ℓ and `low-E (SimAll)` ($\ell \leq 30$) [5, 6, 7]. We mention all of *Planck* data (including temperature and polarization) by "CMB".
2. **R21**: To test the ability of this model to reconcile the H_0 tension, we additionally include a Gaussian prior of the form $H_0 = 73.04 \pm 1.04$ km/s Mpc, as reported by the SH0ES Collaboration [68]. We refer to this prior as "R21".
3. **BAO**: We also consider the various measurements of the Baryon Acoustic Oscillations (BAO) from different galaxy surveys as the *Planck* collaboration in their 2018 analysis [5], i.e. 6dFGS [17], SDSS-MGS [69], and BOSS DR12 [9]. We mention all these data points by "BAO".
4. **SN**: We include the measurements of the 1048 Supernovae Type Ia luminosity distance in the red-shift interval $z \in [0.01, 2.3]$, from the Pantheon sample [72]. We show this catalog of SuperNovae by "SN".

In some analysis, we use a combination of "CMB+BAO+SN" data which we refer to this combination as "CBS".

4. Statistical methods and Analysis

Here, we briefly introduce the statistical methods used in our analysis. The cosmological analysis we carry out in this work is based on Bayesian inference. To analyze the data and extract the constraints on the cosmological

Parameter	Priors
$w_{\rm v}$	$[-1.5, +1.5]$
b	$[0.0, 1.0]$
$\Omega_b h^2$	$[0.005, 0.1]$
$\Omega_c h^2$	$[0.001, 0.99]$
$\tau_{\rm re}$	$[0.01, 0.8]$
$100\Theta_{\rm MC}$	$[0.5, 10]$
$\log\left[10^{10} A_s\right]$	$[1.6, 3.91]$
n_s	$[0.8, 1.2]$

Table 1: Flat priors used on various free parameters of $\mathbb{W}$CDM model, during statistical analysis.

parameters for $\mathbb{W}$CDM model, we have modified carefully the widely used cosmological Markov Chain Monte Carlo package `CosmoMC` [50, 49], which is publicly available.[1] This package is equipped with a convergence diagnostic based on the Gelman and Rubin statistic [35], assuming $|R-1| < 0.01$ for all parameters, and implements an efficient sampling of the posterior distribution using the fast/slow parameter decorrelations [49].

One measure to check the consistency of our model with observational data in comparison to the standard model is the "Akaike Information Criterium" (AIC) which is a tool to measure the improvement of the fit. We compute the AIC of the extended model $\mathbb{W}$CDM relative to that of ΛCDM, defined as

$$\Delta\mathrm{AIC} = \chi^2_{\mathrm{min},\mathbb{W}\mathrm{CDM}} - \chi^2_{\mathrm{min},\Lambda\mathrm{CDM}} + 2(N_{\mathbb{W}\mathrm{CDM}} - N_{\Lambda\mathrm{CDM}}) \,, \tag{15}$$

where $N_{\mathbb{W}\mathrm{CDM}}$ and $N_{\Lambda\mathrm{CDM}}$ stand for the number of free parameters of $\mathbb{W}$CDM model and ΛCDM model [8], respectively.

To put the model to the test for Hubble tension we use the "rule of thumb difference in mean" or Gaussian Tension (GT) [65], defined as

$$\frac{\bar{x}_{\mathcal{D}} - \bar{x}_{\mathrm{SH0ES}}}{(\sigma^2_{\mathcal{D}} + \sigma^2_{\mathrm{SH0ES}})^{1/2}} \,, \tag{16}$$

where $\bar{x}_{\mathcal{D}}$ and $\sigma_{\mathcal{D}}$ are the mean and standard deviation of the H_0 for model based on observational data $\mathcal{D}$, and $\bar{x}_{\mathrm{SH0ES}}$ and σ_{SH0ES} correspond to $H_0 = 73.04 \pm 1.04$ km/s Mpc [68].

We do a Maximum Likelihood Analysis by using `CosmoMC` as a cosmological MCMC code. To find the best fit of parameters of $\mathbb{W}$CDM model, we assume a parameter space as:

$$\mathcal{P}_0 \equiv \left\{w_{\rm v}, b, \Omega_b h^2, \Omega_c h^2, 100\theta_{\rm MC}, \tau, n_s, \ln[10^{10} A_s]\right\} , \tag{17}$$

where b is the void merging parameter, $w_{\rm v}$ represents the equation of state parameter, $\tau_{\rm re}$ is the reionization optical depth, n_s is the scalar spectral index, A_s is the amplitude of the scalar primordial power spectrum, and $\Theta_{\rm MC}$ is an approximation of θ_*, which represents the angular scale of the sound horizon at decoupling. We always consider a flat Universe ($\Omega_{\rm K} = 0$). The priors assumed for parameters are summarized in Table1.

4.1. Bayesian inference

A natural question that arises is how the model is efficient compared to the standard ΛCDM cosmology. For this purpose, we need a statistical measure for comparison between models where the base model will be fixed as ΛCDM. This statistical comparison comes through the Bayesian Evidence. Here, we use publicly available code `MCEvidence` [37, 38] to compute the Bayesian evidence of the models.

According to Bayes' theorem, the probability of a model M with a set of parameters Θ, in light of the observed data D, is given by the *Posterior* $\mathcal{P}$:

$$\mathcal{P}(\Theta \mid D, M) = \frac{\mathcal{L}(D \mid \Theta, M)\Pi(\Theta \mid M)}{\mathcal{E}(D \mid M)}, \tag{18}$$

[1] http://cosmologist.info/cosmomc

where $\mathcal{L}$ is the Likelihood function, Π represents the set of Priors, containing the *a priori* information about the parameters of the model. $\mathcal{E}$ is the so-called Evidence, to which we pay particular attention.

For a given model M, the Bayesian evidence $\mathcal{E}$ is the normalizing constant in the right-hand side of Eq. (18). It normalizes the area under the posterior $\mathcal{P}$ to unity and is given by

$$\mathcal{E}(D \mid M) = \int d\Theta \mathcal{L}(D|\Theta, M)\Pi(\Theta|M)\,. \tag{19}$$

The evidence can be neglected in model fitting, but it becomes important in model comparison. When comparing two different models M_1 and M_2 using Bayes' theorem (18), the ratio of posterior probabilities of the two models $\mathcal{P}_1$ and $\mathcal{P}_2$ will be proportional to the ratio of their evidence, this is

$$\frac{\mathcal{P}_1(\Theta_1 \mid D, M_1)}{\mathcal{P}_2(\Theta_2 \mid D, M_2)} = \frac{\Pi_1(\Theta_1|M_1)}{\Pi_2(\Theta_2|M_2)} \frac{\mathcal{E}_1(D \mid M_1)}{\mathcal{E}_2(D \mid M_2)}\,. \tag{20}$$

This ratio between posteriors leads to the definition of the *Bayes Factor* B_{12}, which in logarithmic scale is written as

$$\ln \mathcal{B}_{12} \equiv \log\left[\frac{\mathcal{E}_1(D \mid M_1)}{\mathcal{E}_2(D \mid M_2)}\right] = \ln\left[\mathcal{E}_1(D \mid M_1)\right] - \ln\left[\mathcal{E}_2(D \mid M_2)\right]\,. \tag{21}$$

If $\ln \mathcal{B}_{12}$ is larger (smaller) than unity, the data favors model M_1 (M_2). To assess the strength of the evidence contained in the data, we use the empirical revised Jeffreys [41] scale, see Table 2.

$\lvert \ln \mathcal{B}_{12} \rvert$	Evidence for model M_1
$\lvert \ln \mathcal{B}_{12} \rvert < 1$	Inconclusive
$1 \leq \lvert \ln \mathcal{B}_{12} \rvert < 2.5$	Significant
$2.5 \leq \lvert \ln \mathcal{B}_{12} \rvert < 5$	Strong
$\lvert \ln \mathcal{B}_{12} \rvert \geq 5$	Decisive

Table 2: Revised Jeffreys scale quantifying the observational viability of cosmological model M_1 compared to some reference model M_2 [43].

5. Testing $\mathbb{W}$CDM model with Cosmological Data

In this section, we aim to find observational constraints on the cosmological parameters of the $\mathbb{W}$CDM model by considering the priors assumed in Table 1. We have summarized the observational constraints on parameters of the $\mathbb{W}$CDM model in Table 3 where we report mean values and 68% confidence intervals of the parameters from "CMB", "CMB+R21", "CMB+SN", "CMB+SN+R21" and "CMB+BAO+SN (CBS)" datasets. It is worth mentioning that by using only "CMB" data, our model formally reduces the tension in the H_0 parameter, but this is due to a volume effect from the increase of the error bars for a larger number of degrees of freedom, and the mean value is actually shifting in the wrong direction.

In Fig. 1, we have presented relative 1D posteriors of H_0 from different combinations of datasets. The shaded area shows the measurement of H_0 done by the SH0ES team [68]. Moreover, in Fig. 2 we see a two-dimensional contour plot of H_0 vs. Ω_m for different combinations of data. As we see considering the R21 prior for the H_0 parameter leads to higher values for the Hubble constant but the combination of CMB, BAO, and SN data increases the tension again. Finally, different contour plots at 1σ and 2σ confidence levels showing the correlation between H_0 and Ω_m vs. different parameters of the model are shown in Fig. 3.

In the last row of Table 3 we have shown the values of Bayes Factor in the logarithmic scale $\ln \mathcal{B}_{12}$ computed for $\mathbb{W}$CDM model against the ΛCDM one considering all the datasets. We find that the values of $\ln \mathcal{B}_{12}$ for "CMB+SN" and a combination of "CMB+BAO+SN" are negative indicating that ΛCDM is preferred in these datasets significantly and strongly, respectively. However, in the combination of CMB data with a prior on H_0 (R21) we find a positive value for $\ln \mathcal{B}_{12}$ that indicates very strong evidence for $\mathbb{W}$CDM model over the reference model ΛCDM. This

Parameter	CMB	CMB+R21	CMB+SN	CMB+SN+R21	CBS
$w_{\rm v}$	-0.43 ± 0.30	$-0.84^{+0.21}_{-0.25}$	$-0.71^{+0.18}_{-0.27}$	$-0.79^{+0.14}_{-0.29}$	$-0.69^{+0.17}_{-0.28}$
b	unconstrained	unconstrained	unconstrained	< 0.554	unconstrained
Ω_m	$0.409^{+0.068}_{-0.10}$	0.2684 ± 0.0085	0.314 ± 0.012	0.2836 ± 0.0079	0.3080 ± 0.0079
H_0	$60.3^{+5.7}_{-7.0}$	72.9 ± 1.0	67.6 ± 1.0	70.59 ± 0.75	67.91 ± 0.82
S_8	0.898 ± 0.060	0.792 ± 0.019	0.833 ± 0.021	0.795 ± 0.019	0.820 ± 0.014
$10^9 A_s$	2.092 ± 0.034	2.092 ± 0.034	2.091 ± 0.033	2.091 ± 0.035	2.091 ± 0.034
n_s	0.9618 ± 0.0057	0.9649 ± 0.0056	0.9630 ± 0.0055	0.9684 ± 0.0055	0.9660 ± 0.0046
τ	0.0518 ± 0.0080	0.0532 ± 0.0081	0.0520 ± 0.0079	0.0544 ± 0.0082	0.0535 ± 0.0080
$\chi^2_{\rm R21}$	$--$	1.1	$--$	7.3	$--$
$\chi^2_{\rm BAO}$	$--$	$--$	$--$	$--$	6.3
$\chi^2_{\rm SN}$	$--$	$--$	1035.8	1040.7	1035.6
$\chi^2_{\rm CMB}$	630.2	633.4	630.8	632.8	630.7
ΔAIC	+3.9	-13.1	+4.69	-2.06	+5.07
$\ln \mathcal{B}_{12}$	-0.26	+6.08	-2.39	+0.20	-2.86

Table 3: 68 % CL constraints on free and derived parameters of the $\mathbb{W}$CDM model from *Planck* CMB power spectra in combination with BAO and Type Ia SuperNovae data plus a Gaussian prior on the Hubble constant H_0 as measured by SH0ES team.

is because for the $\mathbb{W}$CDM model the Hubble tension is reduced because of a volume effect, so it is easier to accommodate a higher H_0 value than in the standard ΛCDM scenario. Finally, for the "CMB" and "CMB+SN+R21" cases, we find a value of $|\ln \mathcal{B}_{12}|$ that is < 1 indicating that the $\mathbb{W}$CDM model is as favored as ΛCDM from the data point of view.

For more insight we have plotted three-dimensional contours (see Fig. 4) for Hubble constant H_0 vs. Ω_m, in one case with the merging rate of cosmic voids b, as the third dimensions in color, and in the other case with the equation of state parameter $w_{\rm v}$. Fig. 4 shows that while there is no clear correspondence between larger values of the Hubble expansion rate and b, on the contrary, they occur with $w_{\rm v}$ closer to -1.

We calculated the power spectrum of the CMB temperature anisotropies for the $\mathbb{W}$CDM model for the best fit obtained with the "CMB" dataset. The result is shown in Fig. 5 which demonstrates a very good consistency with observational data. The shaded area in Fig. 5 denotes the cosmic variance of the power spectrum. According to this figure for higher multipoles (ℓ) the prediction of $\mathbb{W}$CDM and ΛCDM are very similar. However, for the plateau part of the power spectrum ($\ell < 30$) the tail of the $\mathbb{W}$CDM model is lower than the standard model, helping in recovering the low quadruple. It shows our model has a weaker Integrated Sachs-Wolfe effect (ISW) which can be due to the effect of large over-densities in the cosmic super-clusters. This feature is expected because of the large value of S_8 parameter (according to Table 3) which means we have more clusters in $\mathbb{W}$CDM model than ΛCDM.

In Fig. 6 we see the evolution of the Hubble parameter for the $\mathbb{W}$CDM model based on the best-fit of the different dataset combinations in comparison with ΛCDM model. The data points include the current Observational Hubble Data (OHD) in the ranges $0 \leq z \leq 2.36$ (see Table 4), which were obtained by using the "cosmic chronometric approach (CCA)" [32, 31, 57, 77]. As we can see in Fig. 6 the $\mathbb{W}$CDM model at low redshift shows good consistency with observational data. However, at higher redshifts, the Hubble rate based on best-fit parameters from the analysis of only "CMB" and also "CMB+BAO+SN (CBS)" data show deviation from some observational data points. Moreover, for investigating the accelerating behavior of $\mathbb{W}$CDM model, we have represented the evolution of the deceleration parameter $q(z)$ in Fig. 7.

The relative difference in Hubble parameter of the $\mathbb{W}$CDM model with ΛCDM model is defined as follows:

$$\Delta\mathcal{H}(z) = 100 \times \left[\frac{\mathcal{H}_{\mathbb{W}\rm CDM}(z)}{\mathcal{H}_{\Lambda\rm CDM}(z)} - 1\right]. \tag{22}$$

The above quantity is illustrated in Fig. 8 as a function of redshift.

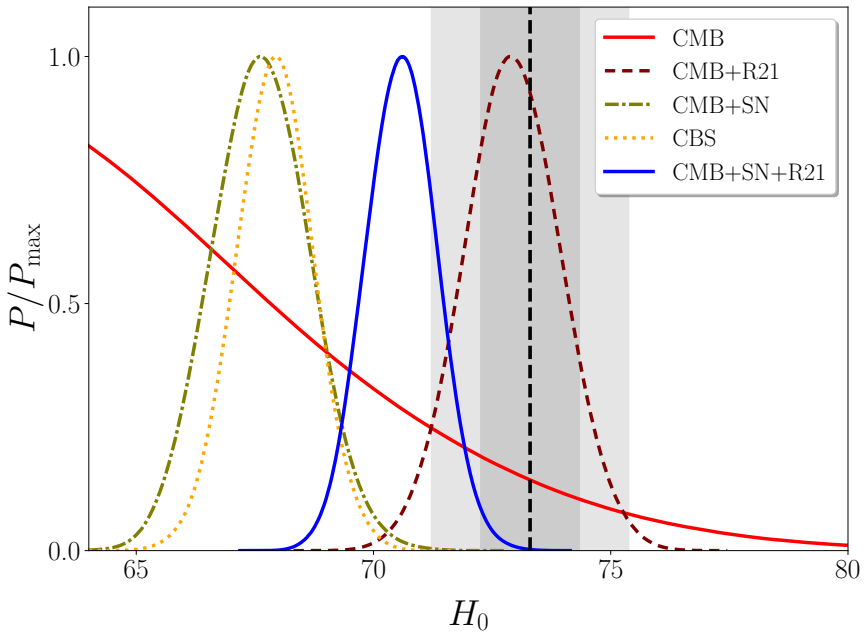


Figure 1: 1D posteriors of H_0 are shown for the different dataset combinations. The shaded area shows the measurement of H_0 done by the SH0ES team and its 1σ and 2σ errors [68].

6. Summary and Discussions

In this paper, we have investigated the observational predictions of a homogeneous and isotropic cosmological fluid with a non-linear EoS given by Eq. (1) for DE. The model introduces two additional free parameters beyond the ΛCDM model. In the standard cosmological model, the dark fluid is attributed to the accelerating expansion of the Universe, characterized by $w_{\rm v} \simeq -1$ and $\Omega_{\rm v} \simeq 0.7$.

We examined an effective fluid with a non-linear quadratic EoS that drives the accelerating expansion. Such non-linear terms in the EoS may arise from the merger process of clusters/voids. The outcome of such mergers could be the observed accelerating expansion at cosmic scales.

In this study, we considered Einstein's field equation at the background level in the presence of the dark fluid to investigate the Hubble parameter tension. Additionally, we calculated the amplitude of matter density fluctuations at the perturbation level. We assessed the model's consistency with observational data by examining it with various combinations of cosmological data. Testing the model solely with "CMB" observational data (Planck 2018), we obtained a constraint for the Hubble constant that reads $H_0 = 60.3^{+5.7}_{-7.0}$ km/sMpc. This result suggests a reduction in the Hubble tension to approximately a 2σ level. However, due to significant large error bars in the H_0 parameter caused by a volume effect, the Hubble parameter lacks precise constraints.

Furthermore, we demonstrated the consistency of the Hubble rate as a function of redshift in our model compared to OHD from Table 4, contrasting it with the Standard ΛCDM model in Fig. 6. Additionally, we explored the dynamical behavior of the model by calculating other observational functions, such as the deceleration parameter (Fig. 7), and relative Hubble parameter (Fig. 8).
We calculated the Bayesian Evidence for our model in comparison with the reference model ΛCDM (last row of Table 3). Our findings indicate a strong preference for the $\mathbb{W}$CDM model over the ΛCDM model when utilizing CMB (*Planck*) data along with a prior on H_0 (R21). However, this preference is attributed to a reduced Hubble constant tension in this specific scenario and diminishes when R21 is not taken into account.

It is important to note that our study focused on a specific case of a non-linear EoS. While our analysis reveals favorable behavior in various observational tests, it is noteworthy that the well-known cosmological tensions persist when the full dataset combination is explored. Future work will be directed towards considering more general non-

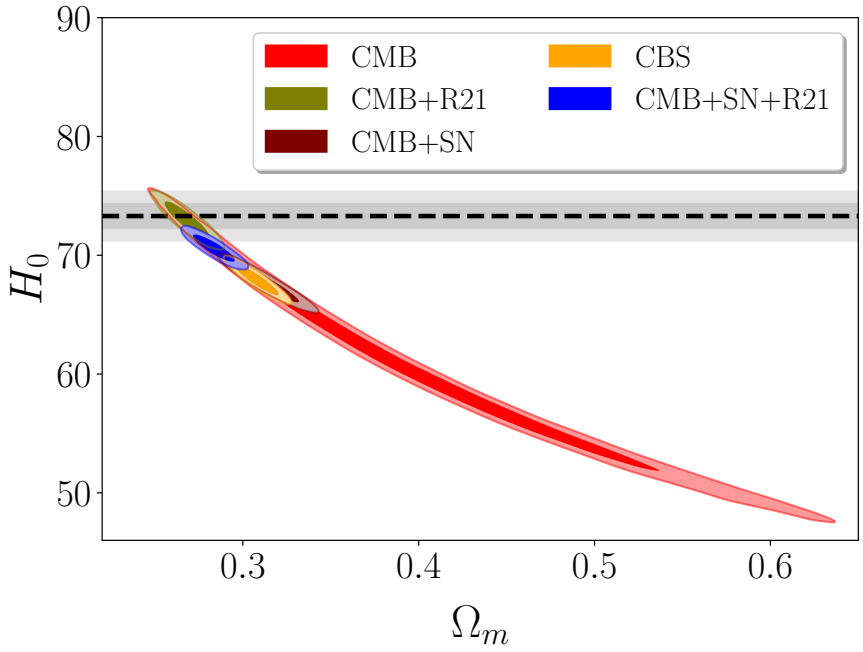


Figure 2: 2D contour plots at 1σ and 2σ confidence levels for H_0 vs. Ω_m for the $\mathbb{W}$CDM model for different combination of data. The dashed line marker is a central value of the H_0 measurement reported by the SH0ES team (R21) and the shaded area shows the 1σ and 2σ confidence levels of this measurement.

linear EoS for dark energy. In subsequent studies, we plan to explore these cases for the dark energy model and also investigate the non-linear structure formation of such models to derive statistics for dark matter halos and cosmic voids.

Acknowledgments

The authors are grateful to Hassan Firouzjahi for his valuable remarks and comments. Also, we thank Sunny Vagnozzi for his helpful comments. We acknowledge Haidar Sheikhahmadi for his revision and fruitful comments. A. T. would like to thank the Yukawa Institute for Theoretical Physics at Kyoto University, ICTP, University of Rwanda, and ICTP-EAIFR for their kind hospitalities when some parts of the project were carried out. E.D.V. is supported by a Royal Society Dorothy Hodgkin Research Fellowship. E.Y. is supported by the Islamic Azad University, Ayatollah Amoli branch, Amol, Iran. This article is based upon work from COST Action CA21136, Addressing observational tensions in cosmology with systematics and fundamental physics (CosmoVerse) supported by COST (European Cooperation in Science and Technology).

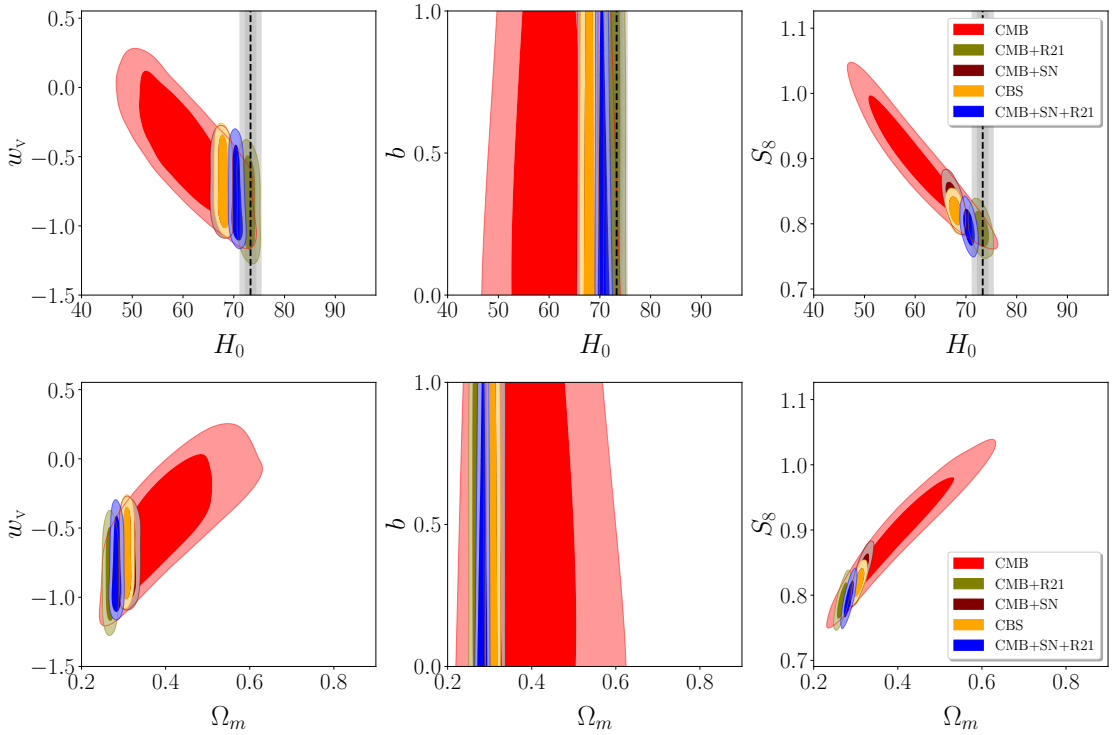


Figure 3: 2D contour plots of H_0 and Ω_m vs. the parameters w_v , b, and S_8 for the $\mathbb{W}$CDM model for different combination of data. The vertical dashed line in the upper panel indicates the measurement of the Hubble parameter made by [68] and the shaded area depicts the 1σ and 2σ error bars.

References

[1] T. M. C. Abbott *et al.* [DES], Phys. Rev. D **107**, no.8, 083504 (2023) doi:10.1103/PhysRevD.107.083504 [arXiv:2207.05766 [astro-ph.CO]].
[2] Abbott, T. M. C., *et al.*, Open J. Astrophys. **6**, 2305.17173 (2023) doi:10.21105/astro.2305.17173
[3] E. Abdalla, G. Franco Abellán, A. Aboubrahim, A. Agnello, O. Akarsu, Y. Akrami, G. Alestas, D. Aloni, L. Amendola and L. A. Anchordoqui, *et al.* JHEAp **34**, 49-211 (2022) doi:10.1016/j.jheap.2022.04.002 [arXiv:2203.06142 [astro-ph.CO]].
[4] Banihashemi, A., Khosravi, N. and Shafieloo, A. JCAP **06**, 003 (2021) doi:10.1088/1475-7516/2021/06/003
[5] N. Aghanim *et al.* [Planck], Astron. Astrophys. **641**, A6 (2020) [erratum: Astron. Astrophys. **652**, C4 (2021)] doi:10.1051/0004-6361/201833910 [arXiv:1807.06209 [astro-ph.CO]].
[6] N. Aghanim *et al.* [Planck], Astron. Astrophys. **641**, A8 (2020) doi:10.1051/0004-6361/201833886 [arXiv:1807.06210 [astro-ph.CO]].
[7] N. Aghanim *et al.* [Planck], Astron. Astrophys. **641**, A5 (2020) doi:10.1051/0004-6361/201936386 [arXiv:1907.12875 [astro-ph.CO]].
[8] Akaike, H. 1974, IEEE Transactions on Automatic Control, 19, 716 doi:10.1109/TAC.1974.1100705
[9] S. Alam *et al.* [BOSS], Mon. Not. Roy. Astron. Soc. **470**, no.3, 2617-2652 (2017) doi:10.1093/mnras/stx721 [arXiv:1607.03155 [astro-ph.CO]].
[10] Amendola, L., & Tsujikawa, S. 2010, Dark Energy: Theory and Observations (Cambridge University Press). https://books.google.co.uk/books?id=XgeOhg_AIIYC
[11] —. 2015, Dark Energy: Theory and Observations (Cambridge University Press)
[12] A. Amon *et al.* [DES], Phys. Rev. D **105**, no.2, 023514 (2022) doi:10.1103/PhysRevD.105.023514 [arXiv:2105.13543 [astro-ph.CO]].
[13] K. N. Ananda and M. Bruni, Phys. Rev. D **74**, 023523 (2006) doi:10.1103/PhysRevD.74.023523 [arXiv:astro-ph/0512224 [astro-ph]].
[14] M. Asgari *et al.* [KiDS], Astron. Astrophys. **645**, A104 (2021) doi:10.1051/0004-6361/202039070 [arXiv:2007.15633 [astro-ph.CO]].
[15] A. Ashtekar, T. Pawlowski and P. Singh, Phys. Rev. D **73**, 124038 (2006) doi:10.1103/PhysRevD.73.124038 [arXiv:gr-qc/0604013 [gr-qc]].
[16] A. Ashtekar, T. Pawlowski and P. Singh, Phys. Rev. D **74**, 084003 (2006) doi:10.1103/PhysRevD.74.084003 [arXiv:gr-qc/0607039 [gr-qc]].
[17] F. Beutler, C. Blake, M. Colless, D. H. Jones, L. Staveley-Smith, L. Campbell, Q. Parker, W. Saunders and F. Watson, Mon. Not. Roy. Astron. Soc. **416**, 3017-3032 (2011) doi:10.1111/j.1365-2966.2011.19250.x [arXiv:1106.3366 [astro-ph.CO]].
[18] Blake, C., Brough, S., Colless, M., et al. 2012, Mon. Not. Roy. Astron. Soc. **405** doi:10.1111/j.1365-2966.2012.21473.x
[19] H. A. Bridgman, K. A. Malik and D. Wands, Phys. Rev. D **65**, 043502 (2002) doi:10.1103/PhysRevD.65.043502 [arXiv:astro-ph/0107245 [astro-ph]].
[20] Busca, D., et al. 2013, A & A, 552, A96, doi:10.1051/0004-6361/201220724
[21] R. R. Caldwell, Phys. Lett. B **545**, 23-29 (2002) doi:10.1016/S0370-2693(02)02589-3 [arXiv:astro-ph/9908168 [astro-ph]].
[22] Chuang, C.-H., & Wang, Y. 2013, Mon. Not. Roy. Astron. Soc., 435, 255

z	$H(z)$	Ref.	z	$H(z)$	Ref.
0.0	67.77 ± 1.3	[54]	0.07	69.0 ± 19.6	[78]
0.09	69.0 ± 12.0	[77]	0.01	69.0 ± 12.0	[78]
0.12	68.6 ± 26.2	[78]	0.17	83.0 ± 8.0	[78]
0.179	75.0 ± 4.0	[57]	0.1993	75.0 ± 5.0	[57]
0.2	72.9 ± 29.6	[78]	0.24	79.7 ± 2.7	[34]
0.27	77.0 ± 14.0	[78]	0.28	88.8 ± 36.6	[78]
0.35	82.7 ± 8.4	[9]	0.352	83.0 ± 14.0	[57]
0.38	81.5 ± 1.9	[22]	0.3802	83.0 ± 13.5	[9]
0.4	95.0 ± 17	[77]	0.4004	77.0 ± 10.2	[58]
0.4247	87.1 ± 11.2	[58]	0.43	86.5 ± 3.7	[34]
0.44	82.6 ± 7.8	[18]	0.44497	92.8 ± 12.9	[58]
0.47	89 ± 49.6	[64]	0.4783	80.9 ± 9.0	[58]
0.48	97.0 ± 60.0	[78]	0.51	90.4 ± 1.9	[22]
0.57	96.8 ± 3.4	[71]	0.593	104 ± 13	[57]
0.60	87.9 ± 6.1	[18]	0.61	97.3 ± 2.1	[22]
0.68	92.0 ± 8.0	[57]	0.73	97.3 ± 7.0	[18]
0.781	105 ± 12.0	[57]	0.875	125 ± 17.0	[57]
0.88	90 ± 40.0	[78]	0.9	117 ± 23.0	[78]
1.037	154 ± 20.0	[34]	1.3	168 ± 17	[78]
1.363	160 ± 33.6	[56]	1.43	177 ± 18	[78]
1.53	140 ± 14	[78]	1.75	202 ± 40	[56]
1.965	186.5 ± 50.4	[34]	2.3	224 ± 8.0	[20]
2.34	222 ± 7.0	[26]	2.36	226 ± 8	[33]

Table 4: The currently available OHD measurements.

[23] M. Cicoli, J. P. Conlon, A. Maharana, S. Parameswaran, F. Quevedo and I. Zavala, Phys. Rept. **1059**, 1-155 (2024) doi:10.1016/j.physrep.2024.01.002 [arXiv:2303.04819 [hep-th]].

[24] R. Dalal, X. Li, A. Nicola, J. Zuntz, M. A. Strauss, S. Sugiyama, T. Zhang, M. M. Rau, R. Mandelbaum and M. Takada, *et al.* Phys. Rev. D **108**, no.12, 123519 (2023) doi:10.1103/PhysRevD.108.123519 [arXiv:2304.00701 [astro-ph.CO]].

[25] U. Danielsson, O. Henriksson and D. Panizo, Phys. Rev. D **107**, no.2, 026020 (2023) doi:10.1103/PhysRevD.107.026020 [arXiv:2211.10191 [hep-th]].

[26] T. Delubac *et al.* [BOSS], Astron. Astrophys. **574**, A59 (2015) doi:10.1051/0004-6361/201423969 [arXiv:1404.1801 [astro-ph.CO]].

[27] E. Di Valentino, L. A. Anchordoqui, O. Akarsu, Y. Ali-Haimoud, L. Amendola, N. Arendse, M. Asgari, M. Ballardini, S. Basilakos and E. Battistelli, *et al.* Astropart. Phys. **131**, 102605 (2021) doi:10.1016/j.astropartphys.2021.102605 [arXiv:2008.11284 [astro-ph.CO]].

[28] E. Di Valentino, L. A. Anchordoqui, Ö. Akarsu, Y. Ali-Haimoud, L. Amendola, N. Arendse, M. Asgari, M. Ballardini, S. Basilakos and E. Battistelli, *et al.* Astropart. Phys. **131**, 102604 (2021) doi:10.1016/j.astropartphys.2021.102604 [arXiv:2008.11285 [astro-ph.CO]].

[29] E. Di Valentino, O. Mena, S. Pan, L. Visinelli, W. Yang, A. Melchiorri, D. F. Mota, A. G. Riess and J. Silk, Class. Quant. Grav. **38**, no.15, 153001 (2021) doi:10.1088/1361-6382/ac086d [arXiv:2103.01183 [astro-ph.CO]].

[30] H. G. Escudero, J. L. Kuo, R. E. Keeley and K. N. Abazajian, Phys. Rev. D **106**, no.10, 103517 (2022) doi:10.1103/PhysRevD.106.103517 [arXiv:2208.14435 [astro-ph.CO]].

[31] M. O. Farooq, [arXiv:1309.3710 [astro-ph.CO]].

[32] O. Farooq, F. R. Madiyar, S. Crandall and B. Ratra, Astrophys. J. **835**, no.1, 26 (2017) doi:10.3847/1538-4357/835/1/26 [arXiv:1607.03537 [astro-ph.CO]].

[33] A. Font-Ribera *et al.* [BOSS], JCAP **05**, 027 (2014) doi:10.1088/1475-7516/2014/05/027 [arXiv:1311.1767 [astro-ph.CO]].

[34] E. Gaztanaga, A. Cabre and L. Hui, Mon. Not. Roy. Astron. Soc. **399**, 1663-1680 (2009) doi:10.1111/j.1365-2966.2009.15405.x [arXiv:0807.3551 [astro-ph]].

[35] A. Gelman and D. B. Rubin, Statist. Sci. **7**, 457-472 (1992) doi:10.1214/ss/1177011136

[36] Harko, T., Asadi, K.,Moshafi, H., and Sheikhahmadi, H. Phys. Dark Univ. **38**, 101131 (2022) doi:10.1016/j.dark.2022.101131

[37] A. Heavens, Y. Fantaye, A. Mootoovaloo, H. Eggers, Z. Hosenie, S. Kroon and E. Sellentin, [arXiv:1704.03472 [stat.CO]].

[38] A. Heavens, Y. Fantaye, E. Sellentin, H. Eggers, Z. Hosenie, S. Kroon and A. Mootoovaloo, Phys. Rev. Lett. **119**, no.10, 101301 (2017) doi:10.1103/PhysRevLett.119.101301 [arXiv:1704.03467 [astro-ph.CO]].

[39] R. Jalalzadeh, S. Jalalzadeh and B. Malekolkalami, Phys. Dark Univ. **41**, 101235 (2023) doi:10.1016/j.dark.2023.101235 [arXiv:2304.07229 [gr-qc]].

[40] K. Jedamzik, L. Pogosian and G. B. Zhao, Commun. in Phys. **4**, 123 (2021) doi:10.1038/s42005-021-00628-x [arXiv:2010.04158 [astro-ph.CO]].

[41] Jeffreys, H. 1961, Theory of probability (Oxford: Clarendon Press)
[42] M. Kamionkowski and A. G. Riess, Ann. Rev. Nucl. Part. Sci. **73**, 153-180 (2023) [arXiv:2211.04492 [astro-ph.CO]].
[43] R. E. Kass and A. E. Raftery, J. Am. Statist. Assoc. **90**, no.430, 773-795 (1995) doi:10.1080/01621459.1995.10476572
[44] A. R. Khalife, M. B. Zanjani, S. Galli, S. Günther, J. Lesgourgues and K. Benabed, [arXiv:2312.09814 [astro-ph.CO]].
[45] M. Khanpour, E. Yusofi and B. Khanpour, [arXiv:1709.08612 [astro-ph.CO]].
[46] N. Khosravi, S. Baghram, N. Afshordi and N. Altamirano, Phys. Rev. D **99**, no.10, 103526 (2019) doi:10.1103/PhysRevD.99.103526 [arXiv:1710.09366 [astro-ph.CO]].
[47] L. Knox and M. Millea, Phys. Rev. D **101**, no.4, 043533 (2020) doi:10.1103/PhysRevD.101.043533 [arXiv:1908.03663 [astro-ph.CO]].
[48] D. Langlois, Astrophys. Space Sci. **283**, 469-479 (2003) doi:10.1023/A:1022552617831 [arXiv:astro-ph/0301022 [astro-ph]].
[49] A. Lewis, Phys. Rev. D **87**, no.10, 103529 (2013) doi:10.1103/PhysRevD.87.103529 [arXiv:1304.4473 [astro-ph.CO]].
[50] A. Lewis and S. Bridle, Phys. Rev. D **66**, 103511 (2002) doi:10.1103/PhysRevD.66.103511 [arXiv:astro-ph/0205436 [astro-ph]].
[51] A. Lewis, A. Challinor and A. Lasenby, Astrophys. J. **538**, 473-476 (2000) doi:10.1086/309179 [arXiv:astro-ph/9911177 [astro-ph]].
[52] X. Li and A. Shafieloo, Astrophys. J. Lett. **883**, no.1, L3 (2019) doi:10.3847/2041-8213/ab3e09 [arXiv:1906.08275 [astro-ph.CO]].
[53] X. Li, T. Zhang, S. Sugiyama, R. Dalal, R. Terasawa, M. M. Rau, R. Mandelbaum, M. Takada, S. More and M. A. Strauss, *et al.* Phys. Rev. D **108**, no.12, 123518 (2023) doi:10.1103/PhysRevD.108.123518 [arXiv:2304.00702 [astro-ph.CO]].
[54] E. Macaulay *et al.* [DES], Mon. Not. Roy. Astron. Soc. **486**, no.2, 2184-2196 (2019) doi:10.1093/mnras/stz978 [arXiv:1811.02376 [astro-ph.CO]].
[55] S. Mohammadi, E. Yusofi, M. Mohsenzadeh and M. K. Salem, Mon. Not. Roy. Astron. Soc. **525**, no.3, 3274-3280 (2023) doi:10.1093/mnras/stad2514 [arXiv:2309.07826 [astro-ph.CO]].
[56] M. Moresco, Mon. Not. Roy. Astron. Soc. **450**, no.1, L16-L20 (2015) doi:10.1093/mnrasl/slv037 [arXiv:1503.01116 [astro-ph.CO]].
[57] M. Moresco, A. Cimatti, R. Jimenez, L. Pozzetti, G. Zamorani, M. Bolzonella, J. Dunlop, F. Lamareille, M. Mignoli and H. Pearce, *et al.* JCAP **08**, 006 (2012) doi:10.1088/1475-7516/2012/08/006 [arXiv:1201.3609 [astro-ph.CO]].
[58] M. Moresco, L. Pozzetti, A. Cimatti, R. Jimenez, C. Maraston, L. Verde, D. Thomas, A. Citro, R. Tojeiro and D. Wilkinson, JCAP **05**, 014 (2016) doi:10.1088/1475-7516/2016/05/014 [arXiv:1601.01701 [astro-ph.CO]].
[59] Moshafi, H., Baghram, S. and Khosravi, N. Phys. Rev. D **104**, no.6, 063506 (2021) doi:10.1103/PhysRevD.104.063506 [arXiv:2012.14377 [astro-ph.CO]].
[60] Moshafi, H., Firouzjahi, H. and Talebian, A. Astrophys. J. **940**, no.2, 121 (2022) doi:10.3847/1538-4357/ac9c58
[61] B. Mostaghel, H. Moshafi and S. M. S. Movahed, Eur. Phys. J. C **77**, no.8, 541 (2017) doi:10.1140/epjc/s10052-017-5085-1 [arXiv:1611.08196 [astro-ph.CO]].
[62] Mostaghel, B., Moshafi, H., and Movahed,S. M. S Mon. Not. Roy. Astron. Soc. **481**, no.2, 1799-1808 (2018) doi:10.1093/mnras/sty2384
[63] Papantonopoulos, E. 2005, The Physics of the Early Universe, Lecture Notes in Physics (Springer Berlin Heidelberg). https://books.google.co.jp/books?id=2fkFPh2jNIkC
[64] A. L. Ratsimbazafy, S. I. Loubser, S. M. Crawford, C. M. Cress, B. A. Bassett, R. C. Nichol and P. Väisänen, Mon. Not. Roy. Astron. Soc. **467**, no.3, 3239-3254 (2017) doi:10.1093/mnras/stx301 [arXiv:1702.00418 [astro-ph.CO]].
[65] M. Raveri and W. Hu, Phys. Rev. D **99**, no.4, 043506 (2019) doi:10.1103/PhysRevD.99.043506 [arXiv:1806.04649 [astro-ph.CO]].
[66] Redmount, I. H. 1988, Monthly Notices of the Royal Astronomical Society, 235, 1301, doi:10.1093/mnras/235.4.1301
[67] A. G. Riess, Nature Rev. Phys. **2**, no.1, 10-12 (2019) doi:10.1038/s42254-019-0137-0 [arXiv:2001.03624 [astro-ph.CO]].
[68] A. G. Riess, W. Yuan, L. M. Macri, D. Scolnic, D. Brout, S. Casertano, D. O. Jones, Y. Murakami, L. Breuval and T. G. Brink, *et al.* Astrophys. J. Lett. **934**, no.1, L7 (2022) doi:10.3847/2041-8213/ac5c5b [arXiv:2112.04510 [astro-ph.CO]].
[69] A. J. Ross, L. Samushia, C. Howlett, W. J. Percival, A. Burden and M. Manera, Mon. Not. Roy. Astron. Soc. **449**, no.1, 835-847 (2015) doi:10.1093/mnras/stv154 [arXiv:1409.3242 [astro-ph.CO]].
[70] K. Saaidi, H. Sheikhahmadi and A. H. Mohammadi, Astrophys. Space Sci. **338**, 355-361 (2012) doi:10.1007/s10509-011-0944-y [arXiv:1201.0275 [gr-qc]].
[71] P. Sarmah and U. D. Goswami, Mod. Phys. Lett. A **37**, no.21, 2250134 (2022) doi:10.1142/S0217732322501346 [arXiv:2203.00385 [gr-qc]].
[72] D. M. Scolnic *et al.* [Pan-STARRS1], Astrophys. J. **859**, no.2, 101 (2018) doi:10.3847/1538-4357/aab9bb [arXiv:1710.00845 [astro-ph.CO]].
[73] R. Sengupta, B. C. Paul, M. Kalam, P. Paul and A. Aich, Eur. Phys. J. Plus **138**, no.10, 929 (2023) doi:10.1140/epjp/s13360-023-04541-w [arXiv:2302.09062 [gr-qc]].
[74] Sheth, R. K., & Van De Weygaert, R. 2004, Monthly Notices of the Royal Astronomical Society, 350, 517, doi:10.1111/j.1365-2966.2004.07661.x
[75] J. Shim, C. Park, J. Kim and H. S. Hwang, Astrophys. J. **908**, no.2, 211 (2021) doi:10.3847/1538-4357/abd0f6 [arXiv:2012.03511 [astro-ph.CO]].
[76] T. Shiromizu, K. i. Maeda and M. Sasaki, Phys. Rev. D **62**, 024012 (2000) doi:10.1103/PhysRevD.62.024012 [arXiv:gr-qc/9910076 [gr-qc]].
[77] J. Simon, L. Verde and R. Jimenez, Phys. Rev. D **71**, 123001 (2005) doi:10.1103/PhysRevD.71.123001 [arXiv:astro-ph/0412269 [astro-ph]].
[78] D. Stern, R. Jimenez, L. Verde, M. Kamionkowski and S. A. Stanford, JCAP **02**, 008 (2010) doi:10.1088/1475-7516/2010/02/008 [arXiv:0907.3149 [astro-ph.CO]].
[79] S. Vagnozzi, Universe **9**, no.9, 393 (2023) doi:10.3390/universe9090393 [arXiv:2308.16628 [astro-ph.CO]].
[80] Van De Weygaert, R., & Platen, E. 2011, International Journal of Modern Physics: Conference Series, 01, 41–66, doi:10.1142/s2010194511000092
[81] K. Vandersloot, Phys. Rev. D **71**, 103506 (2005) doi:10.1103/PhysRevD.71.103506 [arXiv:gr-qc/0502082 [gr-qc]].
[82] L. Verde, N. Schöneberg and H. Gil-Marín, [arXiv:2311.13305 [astro-ph.CO]].
[83] L. Verde, T. Treu and A. G. Riess, Nature Astron. **3**, 891 doi:10.1038/s41550-019-0902-0 [arXiv:1907.10625 [astro-ph.CO]].
[84] K. Wood, P. M. Saffin and A. Avgoustidis, JCAP **07**, 062 (2023) doi:10.1088/1475-7516/2023/07/062 [arXiv:2304.09205 [hep-th]].
[85] W. Yang, E. Di Valentino, S. Pan, S. Basilakos and A. Paliathanasis, Phys. Rev. D **102**, no.6, 063503 (2020) doi:10.1103/PhysRevD.102.063503 [arXiv:2001.04307 [astro-ph.CO]].
[86] E. Yusofi, M. Khanpour, B. Khanpour, M. A. Ramzanpour and M. Mohsenzadeh, Mon. Not. Roy. Astron. Soc. **511**, no.1, L82-L86 (2022)

doi:10.1093/mnrasl/slac006 [arXiv:1907.12418 [astro-ph.CO]].
[87] E. Yusofi and M. A. Ramzanpour, [arXiv:2204.12180 [astro-ph.CO]].
[88] E. Yusofi, M. Khanpour, B. Khanpour, M. A. Ramzanpour and M. Mohsenzadeh, Mon. Not. Roy. Astron. Soc. **511**, no.1, L82-L86 (2022) doi:10.1093/mnrasl/slac006 [arXiv:1907.12418 [astro-ph.CO]].

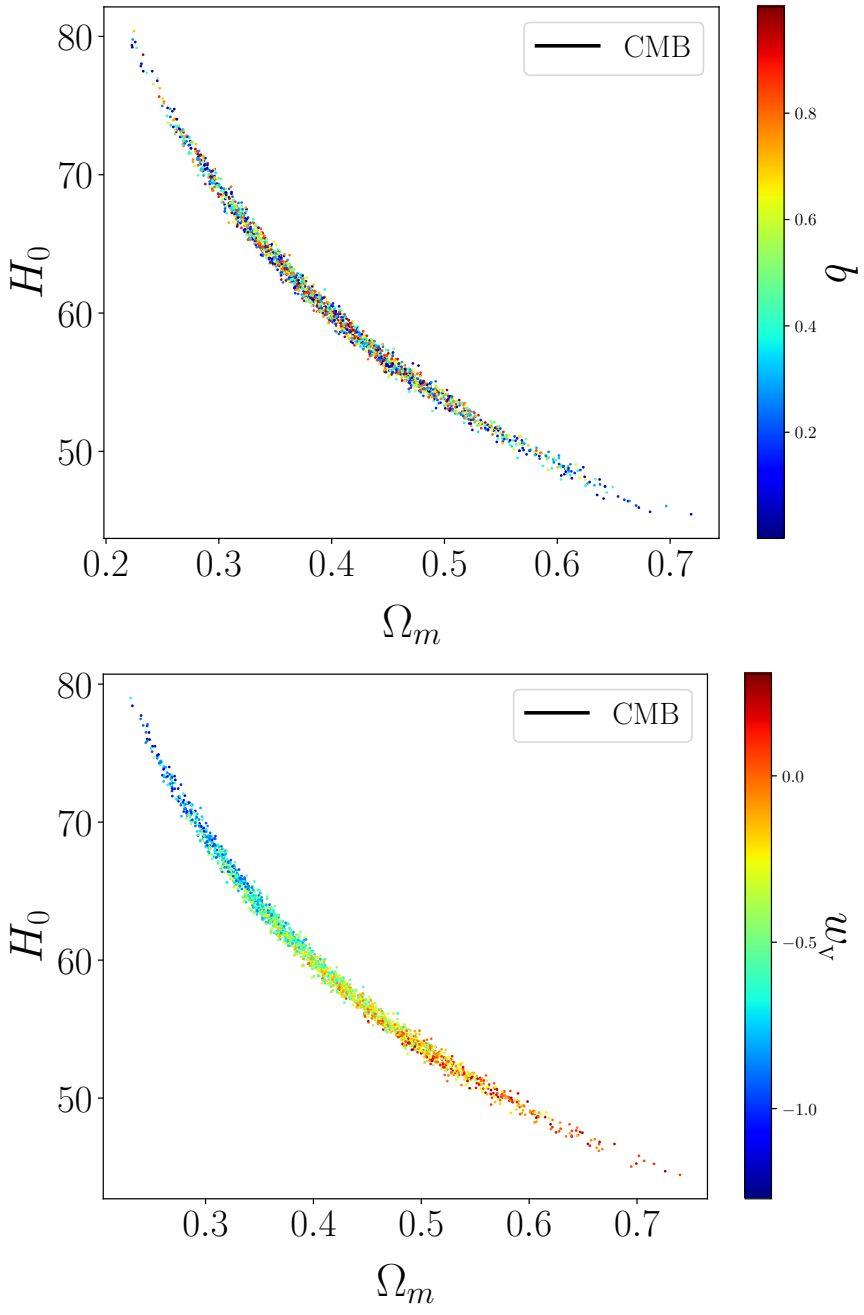


Figure 4: *Upper:* Three-dimensional contour of H_0 vs. Ω_m, where the b parameter is shown as a third dimension by variation of its color. *Lower:* Similar plot as in the upper panel where the effect of w_ν parameter is shown as the third dimension.

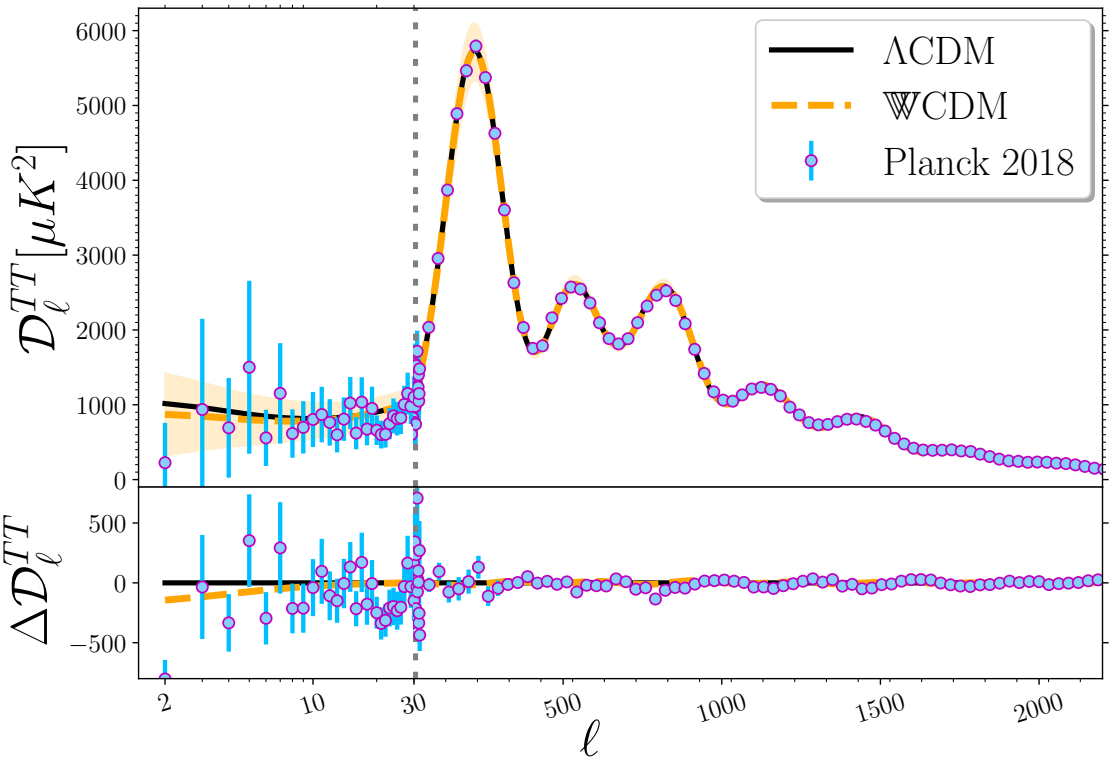


Figure 5: Power spectrum of the temperature anisotropies for the 𝕎CDM model with a dashed orange line obtained with the best-fit of the parameters for the "CMB". The theoretical prediction of the ΛCDM model is shown with a solid black line. Blue points show observational data of *Planck* 2018 release. The shaded area represents the cosmic variance of the power spectrum. The lower panel shows the residual of the two models to observational data.

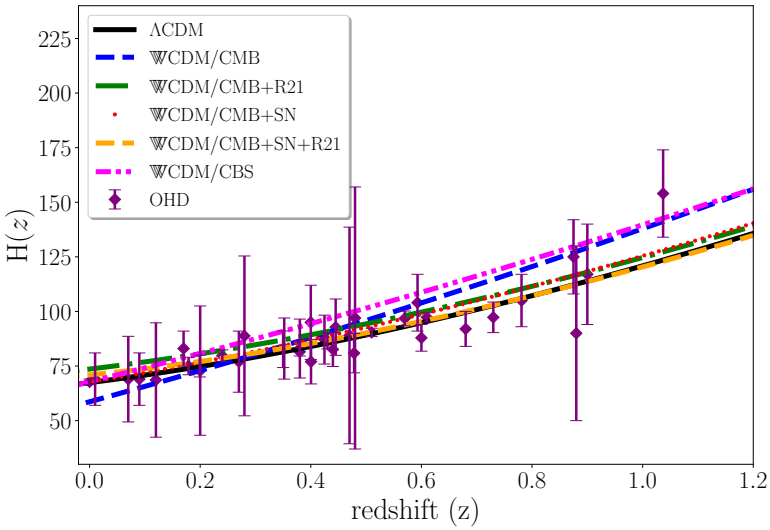


Figure 6: Evolution of Hubble parameter for the 𝕎CDM model, using best-fit values of cosmological parameters for "CMB" (dashed blue), "CMB+R21" (dash-dotted green), "CMB+SN" (dotted red), "CMB+SN+R21" (dashed orange), and "CBS" (dotted magenta). The $H(z)$ of ΛCDM model is shown with a solid black line. OHD points in Table 4 are shown in purple.

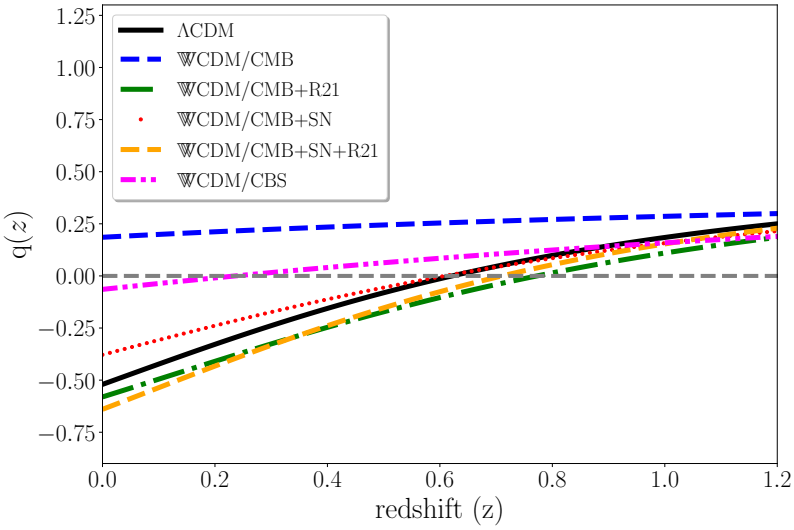


Figure 7: Evolution of deceleration parameter $q(z)$ for the 𝕎CDM model, using best-fit cosmological parameters from Table 3 for "CMB" (dashed blue), "CMB+R21" (dash-dotted green), "CMB+SN" (dotted red), "CMB+SN+R21" (dashed orange), and "CBS" (dotted magenta). For comparison, the standard ΛCDM prediction is also shown in a solid black line.

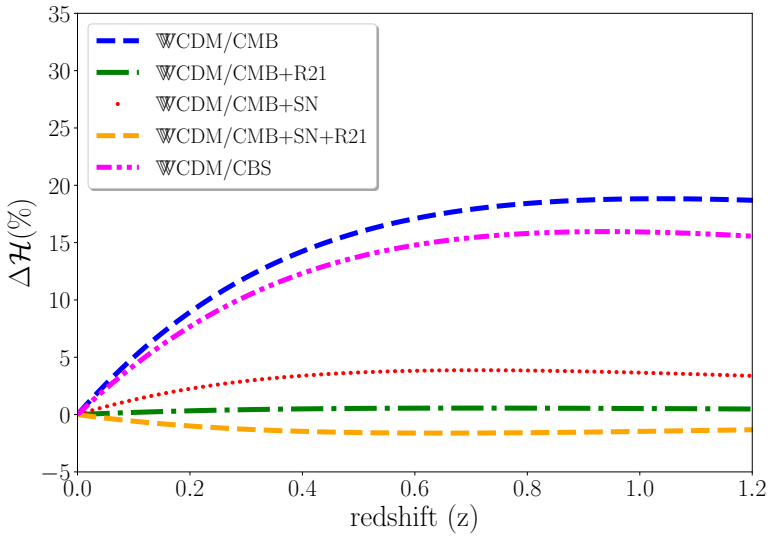


Figure 8: Relative difference of the Hubble parameter as a function of the redshift for the 𝕎CDM model, using best-fit cosmological parameters from Table 3 for "CMB" (dashed blue), "CMB+R21" (dash-dotted green), "CMB+SN" (dotted red), "CMB+SN+R21" (dashed orange), and "CBS" (dotted magenta).

The Density of Relic Neutrinos Near the Surface of Earth

Andrei Gruzinov[1,*] and Mehrdad Mirbabayi[2]
[1] *Weizmann Institute of Science, Rehovot, Israel*
[2] *International Centre for Theoretical Physics, Trieste, Italy*
(Dated: March 6, 2024)

It has been claimed that matter effects cause an asymmetry in the density of relic neutrinos versus antineutrinos near the surface of Earth, of order $\mathcal{O}(G_F^{1/2}) \sim 10^{-4}$, with the vertical extent $\sim$ 10m. We argue that the effect is of order $\mathcal{O}(G_F) \sim 10^{-8}$, with the vertical extent $\sim$ 1mm.

arXiv:2403.03152v1 [hep-ph] 5 Mar 2024

I. INTRODUCTION

Direct detection of relic neutrinos (cosmic neutrino background) must be just a matter of time – one day it will be achieved and the neutrino density near the surface of Earth will be measured.

An unexpectedly large effect of Earth on the relic Dirac neutrinos was found in [1]. It has been claimed that relic electron neutrinos and μ and τ antineutrinos have an overdensity near the surface of Earth

$$\frac{\delta\rho}{\rho} \sim \frac{\sqrt{m_\nu V}}{T}, \tag{1}$$

where $m_\nu \sim 0.1$eV is the neutrino mass, $T = 1.68 \times 10^{-4}$eV is the temperature that appears in the Fermi-Dirac distribution of cosmic neutrinos $f(k) = 1/(1 + e^{k/T})$, and

$$V \sim G_F \frac{\rho_E}{m_p} \tag{2}$$

is the neutrino potential inside Earth; ρ_E is the mass density near the surface of Earth. According to [1] this $O(G_F^{1/2}) \sim 10^{-4}$ overdensity has the vertical extent of $\sim$ 10m.

We will show that in fact there is an *underdensity*, of order $O(G_F) \sim 10^{-8}$, with the vertical extent $\sim$ 1mm, if one follows [1] and treats different neutrino flavors as independent non-relativistic particles.

A more realistic approach would be to work with a 3×3 non-diagonal potential in the neutrino mass basis. But since this does not change the qualitative conclusion, we stick to a simple toy model with only electron neutrinos, within which the precise value of density contrast is derived in §III: at the surface of a large sphere, with uniform density ρ_E and constant atomic and mass numbers Z,A inside,

$$\frac{\delta\rho}{\rho} = \mp\frac{\ln 2}{3\zeta(3)}\frac{m_\nu V_0}{T^2}, \tag{3}$$

where upper (lower) sign refers to neutrinos (antineutrinos), and [2]

$$V_0 = \frac{3\frac{Z}{A} - 1}{2\sqrt{2}} G_F \frac{\rho_E}{m_p} \tag{4}$$

giving

$$\frac{\delta\rho}{\rho}|_{\rm water} = \mp\frac{\sqrt{2}\ln 2}{18\zeta(3)}\frac{m_\nu}{m_p}\frac{G_F\rho_{\rm water}}{T^2} = \mp 8.5\times 10^{-9}\times\frac{m_\nu}{0.1{\rm eV}}. \tag{5}$$

The paper is organized as follows:

- In §II we prove a "Density Theorem" for Maxwell-Boltzmann particles, showing that for a potential barrier there is an $\mathcal{O}(G_F)$ underdensity. We then prove that for Fermi-Dirac, there is also an *underdensity*.
- In §III we apply the thermal method of §II to the Earth potential to calculate the neutrino and antineutrino density at order $\mathcal{O}(G_F)$, obtaining Eq.(3).
- In §IV we show that the first-order perturbation theory agrees with the thermal method.
- In §V we discuss the flat-Earth approximation. It, too, agrees with the thermal method.
- In §VI we list the sources of discrepancy between [1] and our conclusion.

II. THE "DENSITY THEOREM"

In thermal equilibrium, the density of a non-relativistic classical gas in a potential $V(\mathbf{r})$ is given by $n(\mathbf{r}) = n_0 \exp(-V(\mathbf{r})/T)$ assuming the potential vanishes at infinity, where the gas density is n_0. For a *collisionless* gas with Maxwell-Boltzmann distribution at infinity, we still have $n(\mathbf{r}) = n_0 \exp(-V(\mathbf{r})/T)$, as long as the potential energy is positive and has no local minima. This is because in such potentials all trajectories come from infinity and the equilibrium distribution function depends only on the particle energy [3].

By the same argument collisionless, non-degenerate quantum particles with Maxwell-Boltzmann distribution

* Permanently at Center for Cosmology and Particle Physics, Physics Department, NYU.

at infinity and $V(\mathbf{r}) \geq 0$ will be in thermal equilibrium everywhere. However, unlike the classical case the density at a point $\mathbf{r}$ depends not just on $V(\mathbf{r})$ but also on the behavior of the potential in its vicinity. In an arbitrary potential, one can compute the thermal particle density from the density matrix equation [4]:

$$n(\mathbf{r}) = n_0 (2\pi\beta)^{3/2} \rho(\beta; \mathbf{r}, \mathbf{r}), \tag{6}$$

$$\left(\partial_\tau - \frac{1}{2}\nabla^2_{\mathbf{r}} + V(\mathbf{r})\right) \rho(\tau; \mathbf{r}, \mathbf{r}_1) = 0, \tag{7}$$

$$\rho(0; \mathbf{r}, \mathbf{r}_1) = \delta(\mathbf{r} - \mathbf{r}_1); \tag{8}$$

$\beta = 1/T$ is the inverse temperature, the particle mass $m = 1$.

Eq.(7) describes diffusion with multiplication. To compute the density $n(\mathbf{r}_0)$ one can do an integral over all paths $\mathbf{r}(\tau)$ which start and end at $\mathbf{r}_0$:

$$\mathbf{r}(0) = \mathbf{r}(\beta) = \mathbf{r}_0. \tag{9}$$

Going along each path, initially equal weights w are destroyed at a rate V:

$$\frac{dw}{d\tau} = -V(\mathbf{r}(\tau))w. \tag{10}$$

The weight w cannot be destroyed faster than at a rate $V_{\max}$, the weight w cannot be destroyed slower that at a rate $V_{\min}$, and the diffusion with multiplication interpretation immediately leads to the following "Density Theorem" :

$$e^{-\frac{V_{\max}}{T}} < \frac{n(\mathbf{r})}{n_0} < e^{-\frac{V_{\min}}{T}}, \tag{11}$$

a result that is manifest from the path integral representation of thermal density

$$n(\mathbf{r}_0) = \int_{\mathbf{r}(0)=\mathbf{r}_0}^{\mathbf{r}(\beta)=\mathbf{r}_0} D\mathbf{r}(\tau)\ e^{-\int_0^\beta d\tau \left[\frac{1}{2}|\dot{\mathbf{r}}|^2 + V(\mathbf{r})\right]}, \tag{12}$$

If neutrinos were Maxwellian at infinity, then, rigorously

$$e^{-\frac{V_{\max}}{T}} - 1 < \frac{n - n_0}{n_0} < 0, \tag{13}$$

which is an underdensity not greater than $\mathcal{O}(G_F)$.

The Fermi-Dirac distribution, can be represented as a superposition of Maxwell-Boltzmann distributions of different temperatures:

$$\frac{1}{e^{\frac{k}{T}} + 1} = \int_0^\infty d\alpha\ F(\alpha)\ e^{-\frac{k^2}{2\alpha T^2}}, \tag{14}$$

where the weight function

$$F(\alpha) = (2\pi\alpha)^{-1/2} \sum_{n=1}^{\infty} (-1)^{n+1}\ n\ e^{-\frac{1}{2}n^2\alpha} \tag{15}$$

is positive at all α. Since there is an underdensity in a potential barrier for a Maxwell-Boltzmann of any temperature, it follows that a potential barrier creates an *underdensity* for the Fermi-Dirac distribution too.

III. DENSITY NEAR EARTH

When $|V(\mathbf{r})| \ll T$, the density equation (7) can be solved perturbatively. In a spherical potential $V(\mathbf{r}) = V_0\theta(r_E - r)$, with r_E the Earth radius, the density contrast on the surface is given by

$$\frac{\delta\rho}{\rho} = -\frac{V_0}{2T}, \tag{16}$$

as long as $r_E \gg \sqrt{1/T}$: on average, the path-integral trajectory spends half the "time" inside Earth. More generally, particle density is affected by the potential within a diffusion length $\sqrt{1/T}$.

Neutrinos have a Fermi-Dirac distribution with $T \gg 1/r_E$ and $\sqrt{V_0}$. In their case, Eq.(14) helps express $\delta\rho$ and ρ as integrals over Maxwell-Boltzmann results with temperature αT^2. The integral is dominated by $\alpha \sim 1$. Therefore, we can substitute $\rho_\alpha \propto \alpha^{3/2}$ and $\delta\rho_\alpha$ from (16), to find

$$\frac{\delta\rho}{\rho} = -\frac{V_0}{2T^2}\frac{\int_0^\infty d\alpha\ \alpha^{1/2}F(\alpha)}{\int_0^\infty d\alpha\ \alpha^{3/2}F(\alpha)} = -\frac{\ln 2}{3\zeta(3)}\frac{V_0}{T^2}, \tag{17}$$

with veritical extent $\sim 1/T \sim 1$mm.

So far, the discussion of collisionless particles was restricted to those with non-negative potential because it guarantees the absence of bound states. In the collisionless limit, the distribution of bound states is not fixed by the condition at infinity, but it depends on the formation history of the potential well.

In addition, the expansion (14) includes arbitrarily low Maxwell-Boltzmann temperatures, αT^2. When $\alpha T^2 < V_0$, our thermal method, which is valid for a *non-degenerate* quantum gas, is inapplicable because it predicts exponentially large occupation for the bound states. So in full generality, we cannot prove a density theorem for antineutrinos.

Nevertheless, we claim the result for antineutrino overdensity is the same as (17) up to a sign. First, because the density of antineutrino bound states in Earth is $\mathcal{O}(V_0^{3/2})$, and any assumption about their occupation number (which is ≤ 1) has no effect at $\mathcal{O}(V_0)$. Hence, for Maxwellian distribution of unbound states, we can safely apply the thermal method if $T > V_0$ and get (16) up to a sign.

In the Fermi-Dirac case, exponentially large occupations would be avoided if we cut off the integral (14) at some $\alpha_{\min} \sim V_0/T^2$. This would introduce an error of $\mathcal{O}(V_0^2)$ in ρ, which is again subdominant.

Below, we will see that perturbation theory and flat-Earth approximation both reproduce the same result.

IV. PERTURBATION THEORY

For small enough V_0, one can compute $\delta\rho$ by a straightforward application of first-order perturbation theory. To

be absolutely sure, we have also confirmed it by a brute-force numerical simulation, for a sphere, with and without bound states.

We first compute energy eigenstates, $E = \frac{1}{2}k^2$, in a potential $V(\mathbf{r})$,

$$-\frac{1}{2}\nabla^2\psi + V\psi = \frac{k^2}{2}\psi. \tag{18}$$

The unperturbed state is

$$\psi_0 = e^{i\mathbf{k}\cdot\mathbf{r}}, \tag{19}$$

and the perturbation, to first order, satisfies

$$(\nabla^2 + k^2)\delta\psi = 2V\psi_0, \tag{20}$$

giving

$$\delta\psi(\mathbf{r}) = -\frac{1}{2\pi}\int d^3r' \ \frac{e^{ikR}}{R}\ V(\mathbf{r}')\psi_0(\mathbf{r}'), \tag{21}$$

$$\mathbf{R} \equiv \mathbf{r} - \mathbf{r}'. \tag{22}$$

The density perturbation, to first order,

$$\begin{aligned}\delta|\psi(\mathbf{r})|^2 &= \psi_0^*(\mathbf{r})\delta\psi(\mathbf{r}) + \psi_0(\mathbf{r})\delta\psi^*(\mathbf{r}) \\ &= -\frac{1}{2\pi}\int d^3R \ \frac{e^{ikR - i\mathbf{k}\cdot\mathbf{R}}}{R}\ V(\mathbf{r}-\mathbf{R}) + \text{c.c.}\end{aligned} \tag{23}$$

For an arbitrary isotropic distribution over momenta $f(k)$, the overdensity is

$$\frac{\delta\rho(\mathbf{r})}{\rho} = -\int d^3R\ G(R)\ V(\mathbf{r}-\mathbf{R}), \tag{24}$$

$$G(R) = \frac{1}{2\pi R^2}\frac{\int dk\ kf(k)\ \sin(2kR)}{\int dk\ k^2 f(k)}. \tag{25}$$

For Maxwell-Boltzmann $f(k) \propto e^{-\frac{k^2}{2T}}$,

$$G_{\rm MB}(R) = \frac{1}{\pi R}\ e^{-2TR^2}. \tag{26}$$

Taking $V = V_0\theta(r_E - r)$, with $Tr_E^2 \gg 1$, the density perturbation exactly at the surface of Earth is

$$\frac{\delta\rho}{\rho} = -\frac{V_0}{2}\int d^3R\ G_{\rm MB}(R) = -\frac{V_0}{2T}. \tag{27}$$

We have confirmed this result numerically, for a large sphere. This, of course, also follows from an approximate density matrix calculation: on average, the path-integral trajectory spends half the "time" inside Earth.

For Fermi-Dirac,

$$G_{\rm FD}(R) = \frac{1}{\pi R}\ \frac{\sum(-1)^{n+1}\frac{n}{(n^2+4T^2R^2)^2}}{\sum(-1)^{n+1}\frac{1}{n^3}}, \tag{28}$$

$$\int d^3R\ G_{\rm FD}(R) = \frac{2\ln 2}{3\zeta(3)}\frac{1}{T^2}, \tag{29}$$

which gives (17) for the density exactly at the surface of Earth. The perturbation theory answer for antineutrinos is the same up to a sign. We have confirmed this result numerically, for a large sphere.

In our numerical simulations we computed all energy eigenstates inside a sphere of radius 2, with a square potential barrier or well of radius 1, for a particle of mass 1. The eigenstates were computed by separation of angular variables (up to $l = 500$). Then the radial coordinate was discretized (up to 1000 zones) and the resulting tridiagonal matrix was numerically diagonalized. In the Maxwell-Boltzmann case, we put $T \gg |V_0| \gg 1$. In the Fermi-Dirac case, we put $T^2 \gg |V_0| \gg 1$. For the well, the bound states were empty, or had occupation numbers equal to 1 (for Fermi-Dirac), or had occupation numbers given by the Maxwell-Boltzmann factor.

V. THE FLAT EARTH APPROXIMATION

It often helps to reduce a $3d$ problem to a $1d$ problem; it turns out to be a complication when computing the relic neutrino density around the Earth. The Earth radius r_E is indeed very large as compared with the characteristic momentum of neutrinos T and the critical momentum

$$k_* \equiv \sqrt{2V_0} \tag{30}$$

at which waves experience $\mathcal{O}(1)$ scattering. This motivates replacing the Earth with a wide $1d$ potential barrier/well of height V_0.

Below we will confirm that under such a reduction, the density contrast would still be $\mathcal{O}(V_0)$ but as the result of a delicate cancellation of $\mathcal{O}(\sqrt{V_0})$ contributions. In $1d$, the phase space of modes that are significantly scattered by a wide potential is $\mathcal{O}(\sqrt{V_0})$ and so is the naive expectation for $\delta\rho$.

Starting from a spherically symmetric $3d$ problem, one arrives at a $1d$ problem by first expanding the exact energy levels in terms of spherical harmonics. The radial wavefunctions satisfy

$$(rA_l(r))'' + \left[k^2 - 2V(r) - \frac{l(l+1)}{r^2}\right] rA_l(r) = 0. \tag{31}$$

See figure 1 for a sketch of the effective potential experienced by $\psi_l = rA_l$. The solutions for A_l are given in terms of different combinations of spherical Bessel functions inside and outside Earth. For a given distribution of momenta at infinity

$$\rho(r) = \sum_l (2l+1)\int dk k^2 f(k)|A_l(r)|^2, \tag{32}$$

and an exact formula for $\delta\rho$ can be written in terms of the Bessel functions [5]. However, an enormous number

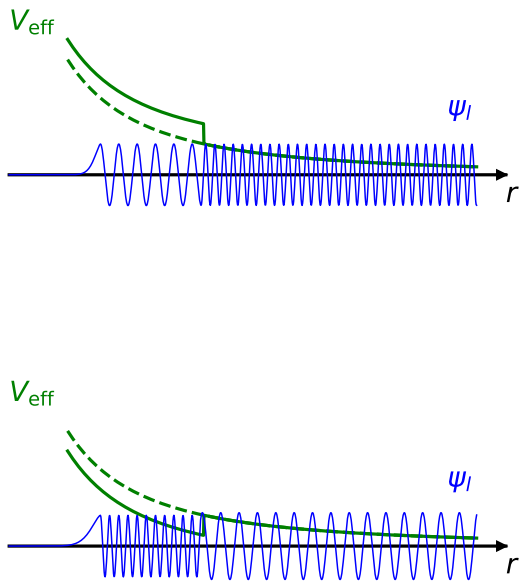


FIG. 1. The effective potential for the radial wavefunctions consists of a step/dip on top of the centrifugal barrier.

of terms, of order $Tr_E \sim 10^9$, have to be included for the sum over l to converge.

One can try to use this large hierarchy to simplify the computation. The first simplification is achieved by switching to $x = r - r_E$, and working at leading order in x/r_E to obtain

$$\psi_l''(x) + \left[k^2 - \frac{l(l+1)}{r_E^2} - 2V(x) + 2\frac{l(l+1)}{r_E^3}x\right]\psi_l(x) = 0, \tag{33}$$

where $V(x) = \pm V_0\theta(-x)$. The solutions are combinations of Airy functions. They are significantly modified with respect to unperturbed solutions when

$$k_\perp \equiv \sqrt{k^2 - \frac{l(l+1)}{r_E^2}} \sim k_*. \tag{34}$$

In the quasi-classical picture, these are (anti)neutrinos that hit the surface of Earth with a small inclination angle $\theta \sim k_*/T$. They might appear to be the main contributors to $\delta\rho$.

So far we have approximated the centrifugal barrier by a linear potential near the Earth surface. Next, suppose particles with $k_\perp \sim k_*$ gain a large WKB exponent between $x = 0$ and the turning point due to the centrifugal barrier, i.e.

$$k_* r_E \gg (l(l+1))^{1/3} \sim (Tr_E)^{2/3}. \tag{35}$$

Then we can make the further *flat Earth approximation*, namely, to replace the effective potential by a wide barrier/well of constant height $\pm V_0$. The centrifugal barrier ensures that all waves are eventually fully reflected, and hence ψ_l can be chosen real, but the exact way this reflection happens does not affect $\rho(x = 0)$.

The condition (35) is not met for the actual values of r_E, T, k_*, which give $k_*(r_E/T^2)^{1/3} \sim 1/10$. Geometrically, the inclination angle $\theta \sim k_*/T$ is so small that such particles rapidly exit the Earth [5].

Nevertheless, we proceed by considering fictitious parameters for which the condition holds because it is instructive to see how $\delta\rho = \mathcal{O}(V_0)$ comes about. First, we perform a fully $1d$ calculation

$$\delta\rho(0) = \int_0^\infty dk f(k)\left(|\psi_k(0)|^2 - |\psi_k^{(0)}(0)|^2\right), \tag{36}$$

where $\psi_k(x)$ and $\psi_k^{(0)}(x)$ are, respectively, the perturbed and unperturbed wavefunctions with energy $k^2/2$. It is easy to embed this calculation in $3d$ by sending $k \to k_\perp$, $f(k) \to (2l+1)f\left(\sqrt{{k_\perp}^2 + l(l+1)/r_E^2}\right)$ and summing over l.

In the quasi-classical approximation, the unperturbed wavefunctions rapidly oscillate (as a function of k at fixed x) and $|\psi_k^{(0)}(0)|^2$ can be replaced by $1/2$. The perturbed wavefunctions for neutrinos $[V(x) = V_0\theta(-x)]$ can be written as

$$\psi_k(x) = \begin{cases} A(k)\sin\phi_L(k,x), & x < 0, \\ \sin\phi_R(k,x), & x > 0, \end{cases} \tag{37}$$

for $k > k_*$, and

$$\psi_k(x) = \begin{cases} A(k)\exp(\phi_L(k,x)), & x < 0, \\ \sin\phi_R(k,x), & x > 0, \end{cases} \tag{38}$$

for $k < k_*$, where

$$\partial_x\phi_L(k,0) = |\kappa|, \qquad \partial_x\phi_R(k,0) = k, \qquad \kappa^2 \equiv k^2 - k_*^2. \tag{39}$$

The wavefunctions and their derivative are continuous at $x = 0$. It follows

$$|\psi_k(0)|^2 = \begin{cases} \frac{k^2\sin^2\phi_L(k,0)}{k^2\sin^2\phi_L(k,0) + \kappa^2\cos^2\phi_L(k,0)}, & k > k_*, \\ \frac{k^2}{k^2-\kappa^2}, & k < k_*. \end{cases} \tag{40}$$

Substituting in (36), we have the sum of the following two integrals

$$I_< = \int_0^{k_*} dk f(k)\frac{2k^2 - k_*^2}{2k_*^2}, \tag{41}$$

and

$$I_> = \frac{1}{2}\int_{k_*}^\infty dk f(k)\frac{k^2\sin^2\phi_L - \kappa^2\cos^2\phi_L}{k^2\sin^2\phi_L + \kappa^2\cos^2\phi_L}, \tag{42}$$

where for brevity we dropped the argument of $\phi_L(k,0)$. For Maxwellian distribution $f(k) = e^{-\frac{k^2}{2T}}$ with $k_* \ll \sqrt{T}$, we find

$$I_< = -\frac{k_*}{6} - \frac{k_*^3}{60T} + \cdots \tag{43}$$

Evaluating $I_>$ is trickier because of the rapid oscillations of the integrand. For a wide barrier $k|\partial\phi_L/dk| \gg 1$, so within each oscillation k and κ are approximately constant. To use this fact, we change the integration variable to ϕ_L, split it as

$$I_> = \frac{1}{2}\sum_n \int_{n\pi}^{(n+1)\pi} d\phi_L \frac{dk}{d\phi_L} f(k) \frac{k^2\sin^2\phi_L - \kappa^2\cos^2\phi_L}{k^2\sin^2\phi_L + \kappa^2\cos^2\phi_L}, \tag{44}$$

and neglect the variation of $k, \kappa, dk/d\phi_l$, and $f(k)$ inside the integral to find

$$\begin{aligned} I_> \approx & \frac{1}{2}\sum_n \frac{dk}{d\phi_L} f(k)\pi\frac{(k-\kappa)^2}{k_*^2} \\ \approx & \frac{1}{2}\int_{k_*}^{\infty} dk f(k)\frac{(k-\kappa)^2}{k_*^2}. \end{aligned} \tag{45}$$

For the same Maxwellian distribution,

$$I_> = -I_< - \frac{\sqrt{\pi}k_*^2}{4\sqrt{2T}} + \mathcal{O}(k_*/\sqrt{T})^4, \tag{46}$$

while the unperturbed density is $\sqrt{\pi T/2}$. Hence, to leading order in V_0

$$\frac{\delta\rho(0)}{\rho} = -\frac{V_0}{2T}. \tag{47}$$

The result for antineutrinos is the same up to a sign. For them, however, the effective $1d$ potential is a well rather than a barrier, which has $\mathcal{O}(\sqrt{V_0})$ bound states. The occupation numbers of these bound states are seemingly independent of the conditions imposed at infinity, and obviously, the $\mathcal{O}(\sqrt{V_0})$ contributions will not cancel for an arbitrary distribution over these bound states.

Indeed, for an actually $1d$ collisionless gas this distribution depends on the formation history of the potential well. If it is formed adiabatically, then the occupation number of bound states would be the same as the ones in the continuum right above the well and $\delta\rho = \mathcal{O}(V_0)$ [3].

Our $1d$ model is instead just an approximation to the $3d$ problem, where the phase space of bound states is $\mathcal{O}(V_0^{3/2})$. When $\sqrt{{k_\perp}^2 + l(l+1)/r_E^2} > k_*$, the potential well below the Earth surface is a metastable vacuum (see figure 1). The bound states found in the flat Earth limit are approximations to a subset of the unbound states with large amplitude inside the well and, at equilibrium, their occupation is unambiguously fixed by the distribution at infinity. We will call them quasi-bound states.

To demonstrate the cancellation of $\mathcal{O}(\sqrt{V_0})$ effects, a similar computation as above can be repeated. The unbound wavefunctions are given by

$$\psi_k(x) = \begin{cases} A(k)\sin\phi_L(k,x), & x<0 \\ \sin\phi_R(k,x), & x>0, \end{cases} \tag{48}$$

with $k>0$ and

$$\partial_x\phi_L(k,0) = \sqrt{k^2+k_*^2}, \qquad \partial_x\phi_R(k,0) = k. \tag{49}$$

The quasi-bound states, for a wide potential well can be approximated by a continuum

$$\psi_\kappa(x) = \begin{cases} \sin\Phi_L(\kappa,x), & x<0 \\ A(\kappa)\exp(-\Phi_R(\kappa,x)), & x>0, \end{cases} \tag{50}$$

where $0<\kappa<k_*$, and

$$\partial_x\Phi_L(\kappa,0) = \kappa, \qquad \partial_x\Phi_R(\kappa,0) = \sqrt{k_*^2-\kappa^2}. \tag{51}$$

Junction conditions at $x=0$ give

$$|\psi_k(0)|^2 = \begin{cases} \frac{k^2\sin^2\phi_L(k,0)}{k^2\sin^2\phi_L(k,0)+\kappa^2\cos^2\phi_L(k,0)}, & \text{unbound,} \\ \frac{\kappa^2}{k_*^2}, & \text{quasi-bound.} \end{cases} \tag{52}$$

The variation of $\rho(0)$ differs from (36) by the extra contribution of the quasi-bound states with the associated distribution $f_B(\kappa)$

$$\delta\rho(0) = \int_0^\infty dk f(k)\left(|\psi_k(0)|^2 - \frac{1}{2}\right) + \int_0^{k_*} d\kappa f_B(\kappa)\frac{\kappa^2}{k_*^2}. \tag{53}$$

The first integral is similar to $I_>$. For $f(k) = e^{-\frac{k^2}{2T}}$ with $k_* \ll \sqrt{T}$,

$$\delta\rho(0)_{\text{unbound}} = -\frac{k_*}{3} + \frac{k_*^2}{8}\sqrt{\frac{\pi}{2T}} - \frac{k_*^3}{15T} + \cdots \tag{54}$$

whereas assuming the same distribution of the quasi-bound states, namely $f_B(\kappa) = e^{-\frac{\kappa^2-k_*^2}{2T}}$,

$$\delta\rho(0)_{\text{quasi-bound}} = \frac{k_*}{3} + \frac{k_*^3}{15T} + \cdots \tag{55}$$

giving in total $\delta\rho(0)/\rho = V_0/2T$.

Finally, the answer in $3d$ follows from the substitutions described below (36) and using the expansion (14) of Fermi-Dirac distribution in terms of Maxwell-Boltzmann distributions. For every Maxwell-Boltzmann temperature, the distributions of $k_\perp$ and l factorize, the dependence on $k_\perp$ being $\exp(-{k_\perp}^2/2\alpha T^2)$. Hence, for any α, and regardless of l, the neutrino/antineutrino density perturbation is

$$\delta\rho_\alpha = \mp\frac{V_0}{2\alpha T^2}\rho_\alpha. \tag{56}$$

Using $\rho_\alpha \propto \alpha^{3/2}$ and integrating over α gives (3).

VI. CONCLUSION

The "Density Theorem" (§II), the "thermal calculus" (§III), the perturbation theory (§IV), the brute-force numerical calculation (§IV), the approximate treatment of Bessel functions (§V)—all these point to the conclusion that the density perturbation of relic neutrinos and antineutrinos from the interaction with Earth is small, $\mathcal{O}(G_F) \sim 10^{-8}$.

Amusingly, perturbation theory and flat Earth approximation have non-overlapping ranges of validity, the former requiring $\epsilon_1 \equiv m_\nu V_0 r_E/T \ll 1$ while the latter $\epsilon_2 \equiv T^2(m_\nu V_0)^{-3/2}/r_E \ll 1$, and neither is satisfied for the actual values of parameters, which give $\epsilon_1 \sim 10^2, \epsilon_2 \sim 10^3$. Nevertheless, when applicable, they both give the same answer. It is enough to have $Tr_E \gg 1$ and $T^2 \gg m_\nu V_0$, the conditions upon which the thermal computation relied.

This is just an example showing how efficient thermal methods are in addressing statistical physics questions. Another, more dramatic example is to consider giving up the assumption of spherical symmetry of Earth, which makes finding the perturbed energy levels cumbersome or utterly impossible while for the thermal method all that matters is the behavior of the potential in a neighborhood of size $1/T$.

A necessary condition to apply the thermal method to neutrinos, which form an effectively collisionless gas, is that unbound energy levels are occupied as dictated by the distribution at infinity. As we have seen in §V, if $\epsilon_2 \ll 1$, the potential develops exponentially long-lived quasi-bound states. Hence, the assumption of equilibrium would be invalid if the lifetime of these becomes longer than the age of universe. In reality, however, $\epsilon_2 \sim 10^3$.

What led [1] to a different conclusion? The authors first study the flat Earth limit. They consider a semi-infinite potential, say $V(x < 0) = \pm V_0$, and obtain an asymptotic value $\rho(x \to \infty)$ that is different from the unperturbed ρ. There is nothing wrong with studying this potential per se, but as a model for Earth it would be more realistic to consider either a finite-size potential barrier/well, or a particle on a half-line (appropriate for the radial wavefunctions for perfectly spherical Earth). Either way the asymptotic density would remain unchanged. Still, they would have obtained an asymmetry of $O(\sqrt{V_0})$ near the surface because they do not include the bound states of antineutrinos in the computation. As discussed in §V, as a model for the $3d$ problem these are quasi-bound states that have to be included and only then $\delta\rho/\rho = \mathcal{O}(V_0)$.

Next, the authors consider the spherical Earth limit. In this case, only a geometric optics argument is given based on the fact that neutrinos (but not antineutrinos) with very small inclination angles are reflected by the Earth surface. This is argued to result in an overdensity of neutrinos very close to the surface. Here the error is to forget that any fully reflected neutrino is replacing a neutrino that in the absence of Earth would have directly arrived at the same location but now is being deflected. More generally, by the Liouville theorem there is no effect in the geometric optics approximation. We think this point has been explained in section 3.1 of [5].

The expression (15) that [5] gives for $\delta\rho$ in the $3d$ case is correct. But as acknowledged there, adding $\mathcal{O}(10^9)$ terms (necessary for the sum to converge) is challenging. The paper does not discuss whether the effect is $\mathcal{O}(V_0)$ or $\mathcal{O}(\sqrt{V_0})$, but the numerical answer given there for the sum is too large.

ACKNOWLEDGMENTS

We thank Mina Arvanitaki, Savas Dimapolus, Ken Van Tilburg and Giovanni Villadoro for useful discussions.

[1] A. Arvanitaki and S. Dimopoulos, Phys. Rev. D **108**, 043517 (2023).
[2] P. Langacker, J. P. Leveille, and J. Sheiman, On the Detection of Cosmological Neutrinos by Coherent Scattering, Phys. Rev. D **27**, 1228 (1983).
[3] L. D. Landau and E. M. Lifshitz, *Physical Kinetics, §36* (Pergamon Press, 1981).
[4] R. Feynman, *Statistical Mechanics, §3.1* (CRC Press, 1998).
[5] G.-y. Huang, Neutrino-antineutrino Asymmetry of CνB on the Surface of the Round Earth, (2024), arXiv:2401.07347 [hep-ph].

Probing Recoil Signatures of Inelastic Dark Matter

Hong-Jian He,[a,b*] Yu-Chen Wang,[a†] Jiaming Zheng,[a‡]

[a] T. D. Lee Institute & School of Physics and Astronomy,
Key Laboratory for Particle Astrophysics and Cosmology,
Shanghai Key Laboratory for Particle Physics and Cosmology,
Shanghai Jiao Tong University, Shanghai, China.

[b] Physics Department and Institute of Modern Physics, Tsinghua University, Beijing, China;
Center for High Energy Physics, Peking University, Beijing, China.

arXiv:2403.03128v1 [hep-ph] 5 Mar 2024

Abstract

Different dark matter (DM) candidates could have different types of DM-lepton and/or DM-quark interactions. For direct detection experiments, this leads to diversity in the recoil spectra, where both DM-electron and DM-nucleus scatterings may contribute. Furthermore, kinematic effects such as those of the inelastic scattering can also play an important role in shaping the recoil spectra. In this work, we systematically study signatures of the light exothermic inelastic DM from the recoil spectra including both the DM-electron scattering and Migdal effect. Such inelastic DM has mass around (sub-)GeV scale and the DM mass-splitting ranges from 1keV to 30keV. We analyze the direct detection sensitivities to such light inelastic DM. For different inelastic DM masses and mass-splittings, we find that the DM-electron recoil and Migdal effect can contribute significantly and differently to the direct detection signatures. Hence, it is important to perform combined analysis to include both the DM-electron recoil and Migdal effect. We further demonstrate that this analysis has strong impacts on the cosmological and laboratory bounds for the inelastic DM.

*Email: hjhe@sjtu.edu.cn
†Email: wangyc21@sjtu.edu.cn
‡Email: zhengjm3@sjtu.edu.cn

Contents

1. Introduction **2**

2. Inelastic Dark Matter Interactions for Exothermic Scattering **4**

3. Electron Recoil Signals from Exothermic Inelastic Dark Matter **6**

3.1. Inelastic DM-Electron Scattering 6

3.2. Inelastic DM-Nucleus Scattering 7

4. Limits from Direct Detection Experiments **9**

4.1. Constraints by XENONnT Electron Recoil Data 9

4.2. Constraints by S2-Only Data of XENON1T 13

5. Probing Inelastic DM with Dark Photon Mediator **16**

5.1. Model Realization: Inelastic DM with Dark Photon Mediator 17

5.2. Cosmological and Laboratory Constraints on Inelastic DM 20

6. Conclusions **24**

References **25**

1. Introduction

The origin and nature of dark matter (DM) have remained largely unknown so far after decades of dedicated efforts through the direct, indirect and collider searches. Such detection methods depend on how the DM interacts with the standard model (SM) particles. The DM models have provided various DM-SM interactions and are under close inspection via distinct direct search strategies. The searches for nuclear recoil (NR) have set stringent limits on the DM-nucleon scattering cross sections [1–5] on the GeV-TeV scale DM. For lighter dark matter, the nuclear recoil energy falls below the detection threshold. In contrast, an electron acquires much more recoil energy from its direct scattering with light DM particles [6–9]. The electron recoil (ER) signal is thus an important target for searching the (sub-)GeV DM candidates [10]. The electron recoil signal can also probe DM-nucleon interaction through Migdal effect [11][12]. When the DM scatters with an atomic nucleus, the nucleus gains a velocity relative to the electron cloud and may induce atomic ionization and excitation. For sub-GeV DM, this process can generate keV-scale electron recoil signals that are detectable in the direct detection experiments [13–18].

Conventionally, the DM-nucleon and DM-electron interactions are constrained independently. For DM-nucleon spin-independent (SI) interactions, constraints are usually derived by assuming identical

contributions from neutron and proton. This enhances the DM-nucleus scattering cross section by a coherence factor of A^2, where A is the number of nucleons. However, these assumptions may be violated in various DM models. First, the DM particle in general may interact with both nucleons and electrons. Second, the DM-neutron and DM-proton interactions may not be identical or coherent within the nucleus, so they may induce a coherence factor other than A^2, which will change not only the overall DM-nucleon event rates, but also the relative strength between DM-electron and DM-nucleon interactions. These may significantly change the constraints on different DM models.

Potential kinematic effects, such as those induced by exothermic inelastic dark matter [19–23], may further complicate the direct detection signals. In such a scenario, the DM particles consist of more than one mass eigenstates. The heavier eigenstate could be cosmologically stable when the mass-splitting between it and the lightest state is O(keV) for GeV-scale DM. When a heavier DM state scatters with a target atom, it converts to the lighter state and deposits energy from the mass-splitting into the kinetic energy of final states. For GeV-scale DM much heavier than the electron, such inelastic DM-electron scattering results in a peak-like ER spectrum. If the DM couples to both the electron and nucleons, this signal can be comparable to the electron recoil signal from the Migdal effect by DM-nucleus scatterings. Hence a joint analysis including both effects is important. The recent direct detection experiments already published the electron recoil data with low threshold and high sensitivity [6–8]. It is ideal to use these datasets and analyze such kinematic effects in DM interactions.

In this work, we study direct detection signatures of the light exothermic inelastic DM with keV-scale mass-splitting. Since electrons, neutrons, and protons may couple differently to the dark sector, we consider various combinations of typical couplings in the present analysis. For each case, we compute the inelastic DM-electron and DM-nucleus scattering rates, including the induced Migdal effect. We demonstrate that the DM-electron scattering spectrum is highly dependent on the mass-splitting, whereas the Migdal effect induced by DM-nucleus scattering is enhanced by the energy injection from the de-excitation of the heavier DM state. We further derive the bounds for each case by confronting the XENONnT ER data [7] and XENON1T S2-only data [9] with the joint effects of DM-electron and DM-nucleon interactions. These results are then applied to concrete DM models.

This paper is organized as follows. In Section 2, we present a generic effective theory formulation of the light exothermic inelastic DM interactions. We consider both the DM-electron scattering and DM-nucleus scattering with Migdal effect. For this we will present the benchmark scenarios of the dark charge assignments. In Section 3, we study the electron recoil signatures from both the direct DM-electron scattering and the Migdal effect (induced by DM-nucleus scattering). In Section 4, we demonstrate how direct detection experiments (such as XENON1T and XENONnT) can constrain the parameter space of the light inelastic DM. We present an explicit minimal model realization of the light inelastic DM in Section 5, and analyze constraints from both the cosmological and laboratory measurements. Finally, we conclude in Section 6.

2. Inelastic Dark Matter Interactions for Exothermic Scattering

In this section, we present a generic effective theory formulation of the light inelastic DM interactions. With this, we will study the interplay between the DM-nucleon and DM-electron interactions.

We consider a two-component dark matter with a mass-splitting Δm. We denote the lighter (heavier) component X (X') for scalar dark matter and χ (χ') for fermionic dark matter. Here X and X' are real scalar fields and form a complex scalar $\hat{X} \equiv (X + \mathtt{i}X')/\sqrt{2}$ in the limit $\Delta m \to 0$. Similarly, χ and χ' are Weyl spinors and can form a pseudo-Dirac spinor $\hat{\chi} \equiv (\chi_1, \chi_2^\dagger)^T$, where $\chi_{1,2} \equiv (\chi \mp \chi')/\sqrt{2}$. When the situation is not sensitive to the spin-statistics of the DM, we will only use the notation (X, X') for both the scalar and fermionic DM. Consider that the DM particles interact with the visible sector through a vector mediator whose effect can be described by the generic dimension-6 effective operators at low energy,

$$\mathcal{O} = \frac{c}{M^2} J_{X\mu} J^\mu_{\rm vis}\,, \tag{2.1}$$

where the mediator mass M serves as the cutoff scale and the operator $\mathcal{O}$ is invariant under the SM gauge group. In the above, we denote the dark current $J_{X\mu}$ for scalar DM (X, X'), and this notation is replaced by $J_{\chi\mu}$ for the fermionic DM (χ, χ'). The two dark currents J^μ_X and J^μ_χ take the following forms:

$$J^\mu_X = \mathtt{i}(\hat{X}^*\partial^\mu\hat{X} - \hat{X}\partial^\mu\hat{X}^*) = (X'\partial^\mu X - X'\partial^\mu X)\,, \tag{2.2a}$$

$$J^\mu_\chi = \overline{\hat{\chi}}\gamma_\mu\hat{\chi} = \mathtt{i}(\chi'^\dagger\bar{\sigma}_\mu\chi - \chi^\dagger\bar{\sigma}_\mu\chi')\,. \tag{2.2b}$$

The mass-splitting between the dark components can be induced by the spontaneous symmetry-breaking mechanism that generates the mass of the vector mediator. This will be shown by a concrete UV completion model in Sec. 5. The current for the visible sector can be separated into leptonic and hadronic parts, $J^\mu_{\rm vis} = J^\mu_\ell + J^\mu_q$, and takes the general form:

$$J^\mu_\ell = c_L\bar{L}\gamma^\mu L + c_e\bar{e}_R\gamma^\mu e_R\,, \tag{2.3a}$$

$$J^\mu_q = c_Q\bar{Q}\gamma^\mu Q + c_u\bar{u}_R\gamma^\mu u_R + c_d\bar{d}_R\gamma^\mu d_R\,, \tag{2.3b}$$

where (c_L, c_e) and (c_Q, c_u, c_d) denote respectively the lepton and quark couplings to the vector mediator. For the direct detection analysis, we express the general currents (2.3) for electron and (u, d)-quarks as follows:

$$J^\mu_e = c^V_e\bar{e}\gamma^\mu e + c^A_e\bar{e}\gamma^\mu\gamma^5 e\,, \tag{2.4a}$$

$$J^\mu_q = c^V_q\bar{q}\gamma^\mu q + c^A_q\bar{q}\gamma^\mu\gamma^5 q\,, \tag{2.4b}$$

where the quark field $q = u, d$. Hereafter, we will only consider the vector current of quarks in the DM-nucleon scattering for the following reasons. The nuclear expectation value of the quark axial current is proportional to the spin fractions in the target nucleus [24] and is much smaller than the nuclear expectation value of the quark vector current in general cases because the latter is enhanced by the number of nucleons. Besides, the DM current in the effective operator is chosen to be a vector

current, and its couplings with quark (electron) axial currents only contribute to the DM-nucleus (electron) scattering amplitudes with terms suppressed by the small DM-velocity. Hence, we will work at the leading order of the small momentum transfer and neglect the quark or electron axial current in the direct detection analysis. The DM-quark interaction matches to the spin-independent DM-nucleon interactions [25]:

$$\frac{c}{M^2} J_{X\mu}(q_p \bar{p}\gamma^\mu p + q_n \bar{n}\gamma^\mu n)\,, \tag{2.5}$$

where the coupling coefficients (dark charges) for protons and neutrons are $q_p = 2c_u^V + c_d^V$ and $q_n = c_u^V + 2c_d^V$. In the limit of $\Delta m \to 0$, the DM-nucleon scattering cross section for $X' + (n,p) \to X + (n,p)$ can be expressed as

$$\sigma_{n,p} \simeq \frac{|c|^2 q_{n,p}^2 \mu_{n,p}^2}{\pi M^4} = \frac{4\alpha q_{n,p}^2 \mu_{n,p}^2}{\Lambda^4}\,, \tag{2.6}$$

where $\mu_{n,p} = m_{n,p} m_X/(m_{n,p}+m_X)$ is the reduced mass. In the second step of Eq.(2.6), we have defined an effective cutoff scale $\Lambda \equiv M\,(e/|c|)^{\frac{1}{2}}$, where $\alpha = e^2/4\pi$ denotes the fine structure constant and e is the unit of electric charge. Then, the DM-nucleus (N) spin-independent scattering cross section takes the form:

$$\sigma_N \simeq \frac{4\alpha q_N^2 \mu_N^2}{\Lambda^4}\,, \tag{2.7}$$

where the DM-nucleus effective coupling $q_N(A,Z) = Z q_p + (A-Z) q_n$ [25][26][27], and the reduced mass $\mu_N = m_N m_X/(m_N+m_X)$. The quantities A and Z denote the nucleon number and the electric charge of the nucleus, whereas m_N denotes the nucleus mass. We can ignore the nuclear form factor because for the parameter space considered in the present study, the momentum transfer in a DM-nucleus scattering is always small as compared to the inverse of the nuclear radius. We can also ignore the nuclear excitations as the energy transfer is relatively small. In parallel, the DM-electron scattering cross section is given by

$$\sigma_e \simeq \frac{4\alpha q_e^2 \mu_e^2}{\Lambda^4}\,, \tag{2.8}$$

where the dark charge of electron is $q_e = c_e^V$. For the case $m_X \gg m_e$, the reduced mass is $\mu_e \simeq m_e$. Taking the ratio of cross sections of Eqs.(2.7)-(2.8), we have

$$\frac{\sigma_e}{\sigma_N} \simeq \left(\frac{q_e \mu_e}{q_N \mu_N}\right)^2. \tag{2.9}$$

Eq.(2.9) shows that the interplay between DM-electron scattering and (spin-independent) DM-nucleus scattering can be encoded into the charge ratio between q_e and $q_{n,p}$. Although this work is motivated by studying a dark sector with a vector mediator, the parameterization of the signal cross sections $(\sigma_e, \sigma_n, \sigma_p)$ applies to general spin-independent interactions. Hence, the analysis of the electron recoil spectrum in the following sections can be applied to other models with modified matching conditions between quark-level and nucleon-level interactions. In the following, we will consider several benchmark combinations of $q_{e,n,p} = 0, \pm 1$ as shown in Table 1. Note that the sign of q_e does not affect the signals. In the same table, we also indicate the corresponding colored curve for each scenario as to be shown in the figures presenting the electron recoil spectra of Section 4. The

Benchmark Scenarios					
(a).	$(q_e, q_n, q_p) = (0, 0, 1)$,	(green dashed)	(e).	$(q_e, q_n, q_p) = (1, 0, 0)$,	(black solid)
(b).	$(q_e, q_n, q_p) = (0, 1, 0)$,	(blue dashed)	(f).	$(q_e, q_n, q_p) = (1, 0, 1)$,	(green solid)
(c).	$(q_e, q_n, q_p) = (0, 1, 1)$,	(red dashed)	(g).	$(q_e, q_n, q_p) = (1, 1, 0)$,	(blue solid)
(d).	$(q_e, q_n, q_p) = (0, 1, -1)$,	(purple dashed)	(h).	$(q_e, q_n, q_p) = (1, 1, 1)$,	(red solid)
			(i).	$(q_e, q_n, q_p) = (1, 1, -1)$,	(purple solid)

Table 1: Benchmark scenarios with different dark charge assignments of (q_e, q_n, q_p) as discussed in text, which correspond to the colored curves (indicated in this Table) as shown the relevant figures. The charges are expressed as $(q_e, q_n, q_p) = (c_e^V\,,\, 2c_u^V + c_d^V\,,\, c_u^V + 2c_d^V)$.

benchmark scenarios (a)-(d) have $q_e = 0$, so the electron recoil signal arises only from the Migdal effect of DM-nucleus scattering. The benchmark (e) has $q_{n,p} = 0$ and its signal comes exclusively from the DM-electron scattering. For benchmarks (f)-(j), the signals arise from both DM-nucleus and DM-electron scattering.

3. Electron Recoil Signals from Exothermic Inelastic Dark Matter

In this section, we proceed to discuss the electron recoil signals of exothermic inelastic DM scattering, in which a heavier DM component X' de-excites to a lighter component X, and deposits the energy from the mass-splitting into the kinetic energy of the final states. The electron recoil signatures may arise from direct DM-electron scattering or from the Migdal effect following the DM-nucleon scattering.

3.1. Inelastic DM-Electron Scattering

For the present study of the inelastic DM-electron scattering, we have $m_X \gg m_e$ and $p_X \gg p_e$. Thus, the range of momentum transfer lies in the range, $q_- \leqslant q \leqslant q_+$, with

$$\frac{q_\pm}{m_X} = \left| v_{\rm DM} \pm \sqrt{v_{\rm DM}^2 - 2\left(\frac{E_R - \Delta m}{m_X}\right)} \right|, \tag{3.1}$$

where $v_{\rm DM}$ stands for the DM velocity [20]. As shown in [22][28][29], the atomic form factors are peaked at $q \sim O(10{\rm keV})$. Thus, most of the observed events satisfy $q_- < O(10{\rm keV})$, which constrain the width of the electron recoil signal:

$$|E_R - \Delta m| < v_{\rm DM} \times O(10{\rm keV}) \sim 0.01{\rm keV}. \tag{3.2}$$

This means that the electron recoil spectrum is sharply peaked at $E_R = \Delta m$.

The differential event rate of the DM-electron scattering with respect to the recoil energy E_R is given by [10][22]:

$$\frac{{\rm d}R_{\rm ER}}{{\rm d}E_R} = \frac{\rho_{\rm DM}}{m_X} \frac{\sigma_e}{8m_e^2} \int {\rm d}^3 v \frac{f(\vec{v} + \vec{v}_e)}{v} \sum_{n,\ell} \frac{1}{E_R - E_{n\ell}} \int {\rm d}q\, q |f_{n\ell}(E_R, q)|^2, \tag{3.3}$$

where $\rho_{\rm DM}\simeq 0.3\,{\rm GeV/cm^3}$ is the local DM density, $f(\vec{v})$ the local DM velocity distribution function in the galactic frame, $\vec{v}_e$ the velocity of Earth, $E_{n\ell}$ the energy level of atomic electron, and $|f_{n\ell}(E_R,q)|^2$ the atomic form factor. Here for simplicity we assume that the local DM consists of only the heavier DM component.

With the approximation that the out-going electron behaves like free plane wave [10][22], the atomic form factor can be estimated as

$$|f_{n\ell}|^2 = \frac{2\ell+1}{2\pi^3}\frac{m_e(E_R-E_{n\ell})}{q}\int_{k_-}^{k_+}{\rm d}k\,k|\chi_{n\ell}(k)|^2\,, \tag{3.4}$$

where the momenta $k_\pm = |\sqrt{2m_e(E_R-E_{n\ell})}\pm q|$ and $\chi_{n\ell}$ denotes the radial wave function. In this work, we adopt the numerical results for the radial wave functions given in [30]. Beyond the plane wave approximation, the wave function of the ionized electron is affected by the attractive potential near the nucleus. This induces an additional enhancement to the above plane wave approximation, similar to the Sommerfeld enhancement. Following [10], we multiply $|f_{n\ell}|^2$ by a Fermi factor which takes the following form in the non-relativistic limit,

$$F_{\rm Fermi} = \frac{2\pi\eta}{1-e^{-2\pi\eta}}\,, \tag{3.5}$$

where $\eta = Z_{\rm eff}\alpha m_e/\sqrt{2m_e(E_R-E_{n\ell})}$ with $Z_{\rm eff}=1$.

The DM velocity is assumed to follow a Maxwell-Boltzmann distribution in the galactic frame and truncated at the galactic escape velocity, $v_{\rm esc}\simeq 0.00181$ [31],

$$f(v)\propto\begin{cases}\exp(-v^2/v_0^2)-\exp(-v_{\rm esc}^2/v_0^2), & v\leqslant v_{\rm esc}\,,\\ 0, & v>v_{\rm esc}\,,\end{cases} \tag{3.6}$$

where $v_0\simeq v_e\simeq 0.00073$ is the circular speed of the solar system around the galactic center. The minimum DM velocity for a scattering event to occur with electron recoil energy E_R and momentum transfer q is given by $v_{\rm min}=|q^2+2m_X(E_R-\Delta m)|/(2qm_X)$. Since the integral

$$\xi(E_R,q)\equiv\int_{v_{\rm min}}^{\infty}{\rm d}^3v\frac{f(\vec{v}+\vec{v}_e)}{v} \tag{3.7}$$

has an analytic form [31, 32] as a function of the recoil energy E_R and momentum transfer q, it is practically more convenient to evaluate the following integral for the recoil spectrum,

$$\frac{{\rm d}R_{\rm ER}}{{\rm d}E_R} = \frac{\rho_{\rm DM}}{m_X}\frac{\sigma_e}{8m_e^2}\sum_{n,\ell}\frac{1}{E_R-E_{n\ell}}\int{\rm d}q\,q\,\xi(E_R,q)|f_{n\ell}(E_R,q)|^2\,. \tag{3.8}$$

3.2. Inelastic DM-Nucleus Scattering

For the inelastic DM-nucleus scattering with $m_X\ll m_N$, we can approximate $q\sim m_X v_{\rm DM}$ and

$$E_{\rm NR}\sim\frac{q^2}{m_N}+\frac{m_X}{m_N}\Delta m\,. \tag{3.9}$$

Its contribution to the electron recoil is further suppressed by a quenching factor $\mathcal{L}$,

$$E_{\rm NR\to ER} \;=\; \mathcal{L}\, E_{\rm NR}\,. \tag{3.10}$$

As will be discussed in Section 4, for the present study we focus on the case with DM mass range $(0.1\text{–}10)\,\mathrm{GeV}$, thus the $E_{\rm NR\to ER}$ contributions are always below the detection threshold, whereas the direct nuclear recoil signals are significant only when m_X is large.

In a DM-nucleus scattering event, the recoiled nucleus acquires a small velocity relative to its surrounding electron cloud; this may lead to ionization of electrons in the outer orbits, as described by the Migdal effect [11][12]. Exothermic scattering may enhance the Migdal effect [21][33][34] by releasing the extra energy Δm into the ionized atomic electrons,

$$\frac{1}{2}\mu_N v_{\rm DM}^2 + \Delta m \;=\; \frac{1}{2}\mu_N v'^2 + E_{\rm ER}\,, \tag{3.11}$$

where $v_{\rm DM}$ is the DM velocity in the laboratory frame, v' the relative velocity after scattering, and $E_{\rm ER} = E_{n\ell} + E_e$ the total electronic energy release, including the atomic ionization energy $E_{n\ell}$ and the kinetic energy of the ionized electron E_e. The kinematics determines the nuclear recoil energy,

$$E_{\rm NR} \;=\; \frac{\mu_N^2 v_{\rm DM}^2}{m_N}\left[1+\frac{\Delta m - E_{\rm ER}}{\mu_N v_{\rm DM}^2} - \sqrt{1+\frac{2(\Delta m - E_{\rm ER})}{\mu_N v_{\rm DM}^2}}\,\cos\theta\right], \tag{3.12}$$

where θ is the scattering angle in the center-of-mass frame. For a given $E_{\rm ER} > \Delta m$, there is a minimal DM velocity imposed by kinematics,

$$v_{\rm DM}^{\rm min} \;=\; \sqrt{\frac{2(E_{\rm ER}-\Delta m)}{\mu_N}}. \tag{3.13}$$

We see that the minimal DM velocity is reduced due to the energy release Δm. The inelastic scattering is always kinematically allowed so long as $E_{\rm ER} \leqslant \Delta m$ since this condition removes the lower bound (3.13) on $v_{\rm DM}$.

The differential electron recoil rate of the Migdal effect per unit target mass with respect to $E_{\rm ER}$ is related to the nuclear recoil rate,

$$\frac{\mathrm{d}R_{\rm MIGD}}{\mathrm{d}E_{\rm ER}} \;\simeq\; \int \mathrm{d}E_{\rm NR}\mathrm{d}v \left[\frac{\mathrm{d}R_{\rm NR}}{\mathrm{d}E_{\rm NR}\mathrm{d}v}\sum_{n,\ell}\frac{1}{2\pi}\frac{\mathrm{d}P_{q_e}^c(n,\ell\to E_e)}{\mathrm{d}E_{\rm ER}}\right], \tag{3.14}$$

where $P_{q_e}^c(n,\ell\to E_e)$ is the probability of exciting an electron of level-(n,ℓ) to a free electron with kinetic energy E_e [12]. The momentum transfer to the excited Migdal electron is $q_e = 2m_e^2 E_{\rm NR}/m_N$. Note that here $1/q_e$ is much larger than the typical orbital radius of the atomic electron, and thus $P_{q_e}^c \propto q_e^2$ [12]. Hence, the enhanced q_e due to the exothermic scattering with DM enhances the excitation probability. The differential nuclear recoil rate per unit target mass is given by

$$\frac{\mathrm{d}R_{\rm NR}}{\mathrm{d}E_{\rm NR}\mathrm{d}v} \;\simeq\; \frac{\rho_{\rm DM}}{m_X}\frac{\sigma_{\rm Xe}}{2\mu_N^2}\frac{f(v+v_e)}{v}\,. \tag{3.15}$$

The nuclear recoil also contributes to the detected electronic energy $E_{\rm det} = \mathcal{L} E_{\rm NR} + E_{\rm ER}$, where $\mathcal{L} \approx 0.15$ is the quenching factor parametrizing the transfer of nuclear recoil energy to the measurable electronic excitations. For the sub-GeV DM and an electron recoil detection threshold around 0.1 keV, the contribution from the quenching of nuclear recoil would be negligible. Nevertheless, we include this effect in our numerical analysis.

4. Limits from Direct Detection Experiments

In this section, using published data from the DM direct detection experiments, we analyze the electron recoil spectrum described in Section 3 and derive constraints on the inelastic DM. We consider the light inelastic DM in the mass range $(0.1-10)$ GeV with a mass-splitting around $(1-30)$ keV in the following analysis.

4.1. Constraints by XENONnT Electron Recoil Data

The XENONnT experiment recently published the low-energy electron recoil data from its first science run [7]. The data can be used to set bounds on the scale Λ for the inelastic interaction introduced in Section 2. We extract the electron recoil data, background model B_0, and detection efficiency $f_{\rm eff}(E)$ from Ref. [7]. The detector smearing of the electron recoil spectrum is approximated by a skew-Gaussian distribution [35],

$$f(E_{\rm d}, E) = \frac{1}{\sqrt{2\pi}\, w} e^{-\frac{(E_{\rm d}-\xi)^2}{2w^2}} \left[1 + \mathrm{erf}\left(\alpha \frac{E_{\rm d}-\xi}{\sqrt{2}\, w}\right)\right], \tag{4.1}$$

where E is the physical energy, E_d the detected energy, and

$$\alpha(E) = 2.41 E^{-0.30}, \tag{4.2a}$$

$$w(E) = 0.374\sqrt{E} + 0.005E\,, \tag{4.2b}$$

$$\xi(E) = E - \sqrt{\frac{2}{\pi}} \frac{\alpha w}{\sqrt{1+\alpha^2}}\,. \tag{4.2c}$$

The function $\alpha(E)$ should not be confused with the fine structure constant $\alpha = e^2/4\pi$ used in this paper. Thus, the event number detected per keV per ton-year is given by

$$\frac{{\rm d}N}{{\rm d}E_{\rm d}} = N_T \int \frac{{\rm d}R}{{\rm d}E_R} f(E_{\rm d}, E_R) f_{\rm eff}(E_R) {\rm d}E_R\,, \tag{4.3}$$

where N_T is the number of target xenon atoms per ton, E_R the (physical) recoil energy and E the detected energy. The physical rate ${\rm d}R/dE_R$ for DM-electron scattering and the Migdal effect are given in Eqs.(3.8) and (3.14), respectively. Given that the DM mass $m_X \leqslant 10\,$GeV, the mass-splitting $\Delta m \leqslant 30\,$keV, and the quenching factor $\mathcal{L} = 0.15$ [cf. Eq.(3.10)], the nuclear recoil contribution to the electron recoil data [as shown in Eq.(3.10)] is below the detection threshold and thus can be neglected.

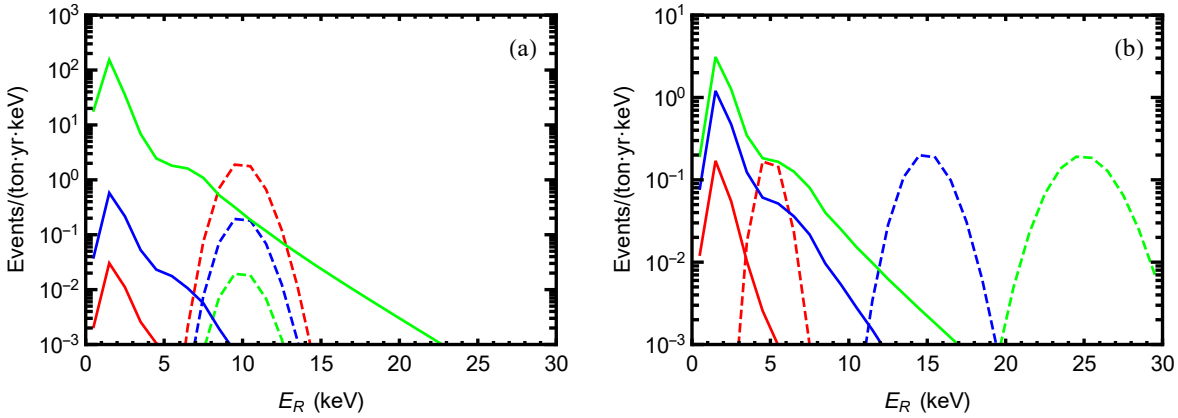


Figure 1: Electron recoil signals for XENONnT detection as induced by the inelastic DM scattering. The solid curves arise from the Migdal effect, and the dashed curves are contributed by the DM-electron scattering. We set the cutoff scale $\Lambda = 500\,\text{GeV}$, and choose the dark charges $(q_e, q_n, q_p) = (1, 1, -1)$. Plot-(a): The input mass-splitting is set as $\Delta m = 10\,\text{keV}$. The (red, blue, green) curves present results for the DM mass $m_X = (0.1, 1, 10)\,\text{GeV}$, respectively. Plot-(b): The input DM mass is set as $m_X = 1\,\text{GeV}$. The (red, blue, green) curves present results for $\Delta m = (5, 15, 25)\,\text{keV}$, respectively.

In Fig. 1, we present the predicted electron recoil spectra for XENONnT detector. (The color of each curve in this figure is not related to those for the benchmark scenarios defined in Table 1 of Section 2.) We see that the shape and position of the spectrum generated by the Migdal effect are almost fixed, whereas the overall normalization depends on the DM mass m_X and mass-splitting Δm. As for the signals from the DM-electron scattering, their heights are proportional to $1/m_X$ due to the local DM number density, and their shapes are always a sharp peak around Δm. This shows that for larger DM mass, the Migdal effect gives the leading contribution to the electron recoil events, while for smaller DM mass, the DM-electron scattering becomes dominant.

Throughout this analysis, we do not fluctuate the background, because its normalization is fixed by the electron recoil data at $E_R = (0-140)\,\text{keV}$, far beyond the range affected by DM scattering. We calculate the χ^2 value for the background model B_0 [7] with $E_R \leqslant 30\,\text{keV}$ and obtain $\chi^2_{\text{bkg}} = 19.84$. Thus, at the 95% C.L., we set $\chi^2 \leqslant 19.84 + 3.84$, which corresponds to one degree of freedom (the free parameter Λ). We plot the resulting limits in Fig. 2. The (top, middle, bottom) rows correspond to the DM mass $m_X = (10,\ 1,\ 0.1)\,\text{GeV}$, respectively. For each selected m_X, we present the limits on the cross sections of the DM-electron (DM-nucleon) scattering in the left (right) panels, and the corresponding limits on the cutoff scale Λ. The color of each curve matches the corresponding benchmark scenario as defined in Table 1 of Section 2.

The different impacts from the DM-electron scattering and from the Migdal effect can be seen by comparing the black curve (with $q_n = q_p = 0$) to the colored curves (with $q_n \neq 0$ and/or $q_p \neq 0$) in the left panels of Fig. 2. We note that some exclusion contours are smooth curves whereas others are twisty curves. The smoother ones correspond to the scenarios with the Migdal effect dominating the signal, i.e., when the DM mass is large (in the top panels except the black curve) and/or $q_e = 0$ (the dashed curves). This is because in such cases the shape of the total electron recoil spectrum is almost

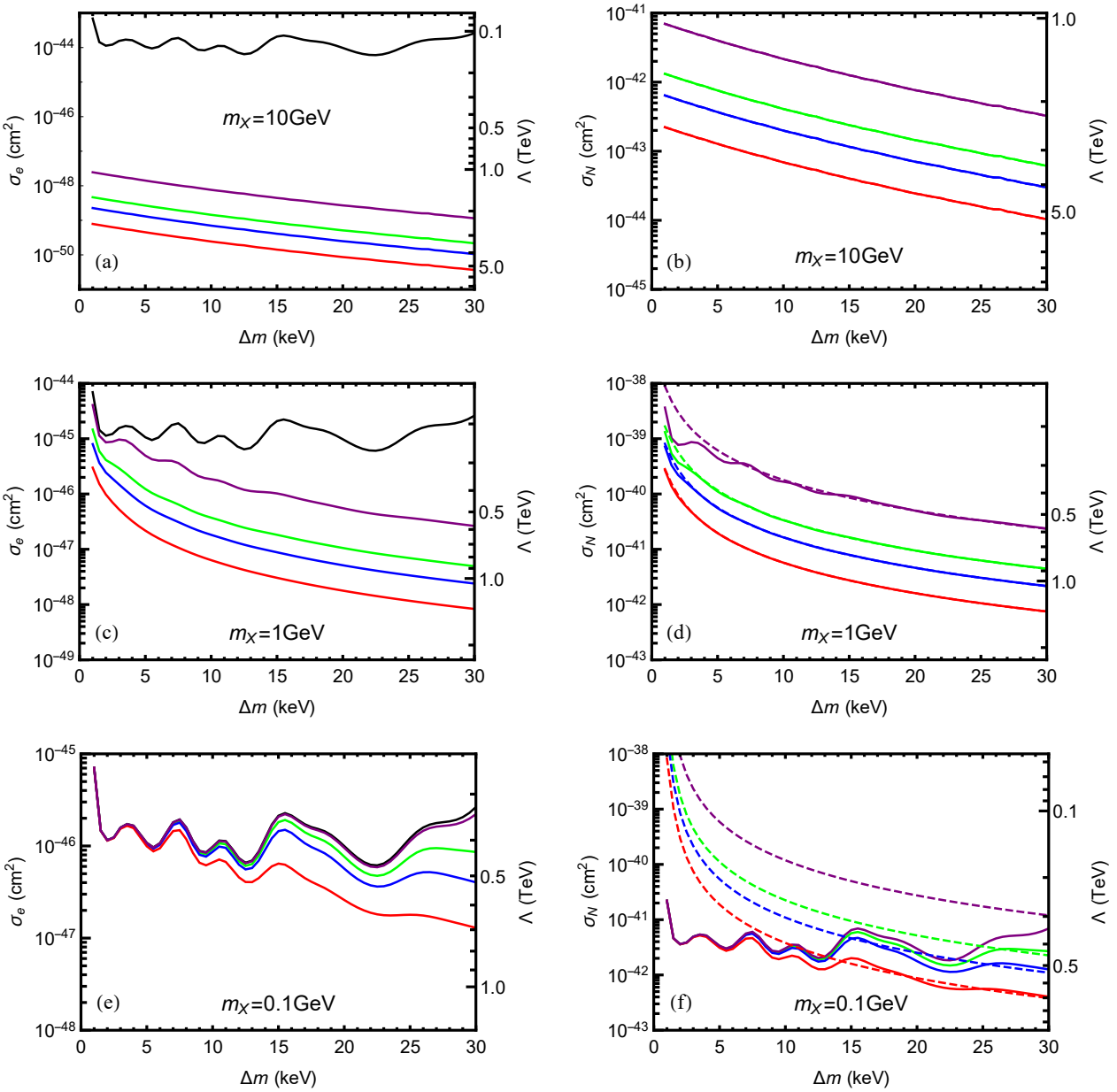


Figure 2: Limits on the DM-electron and DM-nucleon scattering cross sections from the XENONnT ER data, presented in the left and right panels respectively. The panels from top to bottom correspond to the DM masses $m_X = (10,\, 1,\, 0.1)\,\mathrm{GeV}$. The color of each curve matches the corresponding benchmark scenario (as indicated) in Table 1 (Section 2), i.e., dashed curves for $q_e = 0$ and solid curves for $q_e = 1$, whereas green curves for $(q_n, q_p) = (0, 1)$, blue curves for $(q_n, q_p) = (1, 0)$, red curves for $(q_n, q_p) = (1, 1)$, purple curves for $(q_n, q_p) = (1, -1)$, and black curves for $(q_n, q_p) = (0, 0)$. The region above each curve is exceluded.

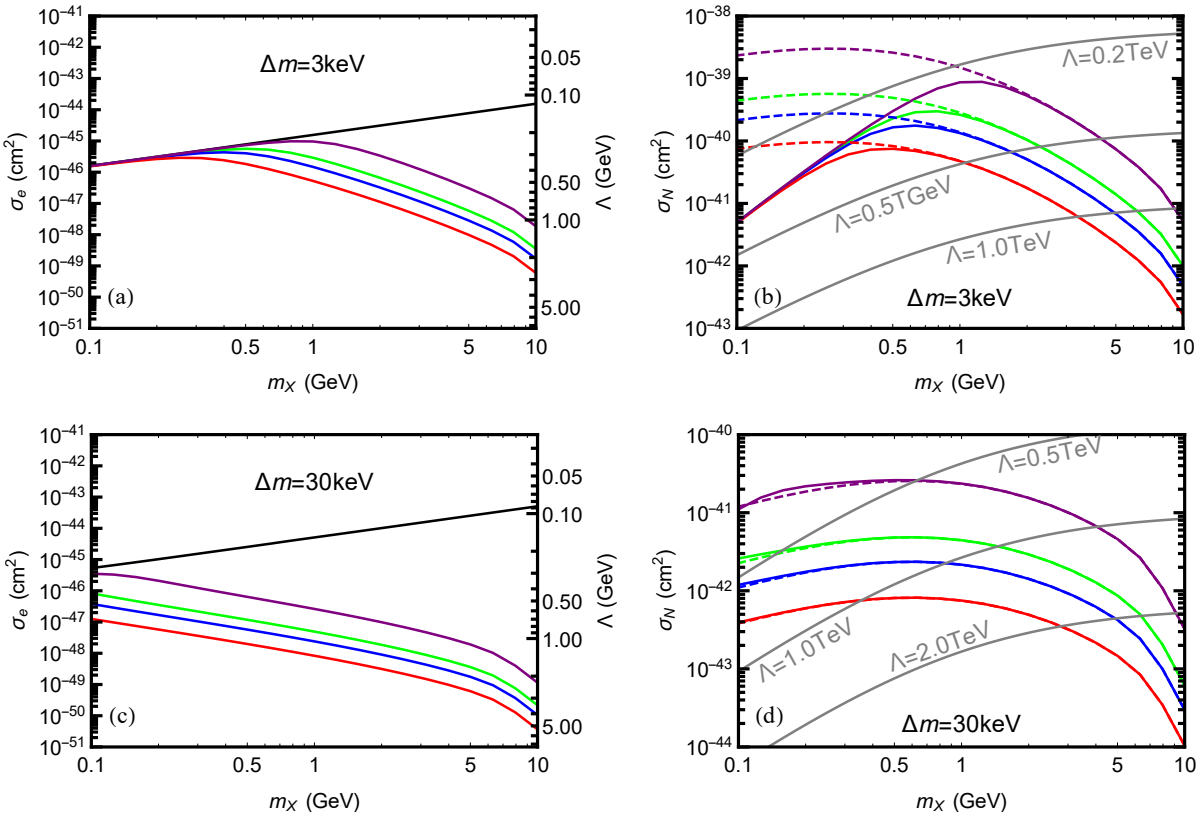


Figure 3: Limits on the DM-electron and DM-nucleon scattering cross sections from the XENONnT ER data, presented in the left and right panels respectively. The upper (lower) panels correspond to $\Delta m = 3\,\text{keV}$ (30 keV). The color of each curve matches the corresponding benchmark scenario (as indicated) in Table 1 (Section 2), i.e., dashed curves for $q_e = 0$ and solid curves for $q_e = 1$, whereas green curves for $(q_n, q_p) = (0, 1)$, blue curves for $(q_n, q_p) = (1, 0)$, red curves for $(q_n, q_p) = (1, 1)$, purple curves for $(q_n, q_p) = (1, -1)$, and black curves for $(q_n, q_p) = (0, 0)$. In plots (b) and (d), the gray curves from top to bottom correspond to $\Lambda = (0.2, 0.5, 1.0)\,\text{TeV}$, respectively. In all plots the region above each curve is excluded.

fixed, and the height of the peak is a smooth function of Δm. Since most Migdal events are in the region of $E_R < 3\,\text{keV}$, a low detection threshold for electron recoil is crucial to its detection. On the other hand, when DM-electron scattering is dominant (the solid curves in the bottom panels or the black curves), the total electron recoil spectrum has peak-like structure whose peak positions depend on Δm. Thus, the fluctuations among the data bins make each contour curve exhibit a distinctive twisty shape. A sufficiently high resolution in the electron recoil detection is required to determine the mass-spiltting Δm.

We see that the Migdal effect generally dominates the recoil signals for $m_X \gtrsim 1\,\text{GeV}$ (top and middle panels of Fig. 2) if the DM couples to nucleons. Even for smaller m_X, the Migdal effect can still be significant if the mass-splitting Δm is large and increases the electron ionization probability through the enhanced energy release to electrons. This feature is evident in Fig. 3. For large mass-splitting such as $\Delta m = 30\,\text{keV}$ in Fig. 3(c)-(d), the DM-electron scattering contribution is always subleading, so that the colored curves ($q_n \neq 0$ and/or $q_p \neq 0$) always give much stronger constraints than the black curve ($q_n = q_p = 0$) in Fig. 3(c), and the differences between dashed curves ($q_e = 0$) and solid curves ($q_e = 1$) in Fig. 3(d) is negligible. In Fig. 3(a)-(b) with $\Delta m = 3\,\text{keV}$, the DM-electron scattering becomes dominant for $m_X \lesssim 1\,\text{GeV}$. This makes the colored curves coincide with the black one in the region $m_X \lesssim 1\,\text{GeV}$ of Fig. 3(a), whereas large differences between the dashed and solid curves appear in the region $m_X \lesssim 1\,\text{GeV}$ of Fig. 3(b). Such observation signifies the necessity of analyzing the contributions of both DM-electron and DM-nucleus scattering simultaneously because it is nontrivial to determine the relative impacts of the two contributions.

4.2. Constraints by S2-Only Data of XENON1T

The S2-only data of XENON1T [9] can also set non-trivial constraints on the DM models. In this study, we use the datasets, response matrices, and background models provided by XENON1T collaboration [9]. According to [9], we will use the ER data and CEvNS background models for the present analysis, whereas the cathode backgrounds is ignored.

The physical spectra of the electron recoil events include the DM-electron scattering and the Migdal effect, which are given by Eqs. (3.8) and (3.14) respectively. To extract the S2 signals, we first apply the energy cutoff at 0.186 keV, and then convert the physical event rate to the binned S2 rate using the response matrix. In Fig. 4, we present a sample of the predicted S2 rates for the XENON1T detector with DM mass values, $m_X = (0.1,\ 1,\ 10)\,\text{GeV}$, respectively. Here the color of each curve does not correspond to the benchmark models (a)-(i) defined in Table 1. Note that the maximum S2 area is 3000 PE which translates to about 4 keV, thus for the current analysis of this subsection the DM mss-splitting Δm varies in the range $(0.1 - 5)\,\text{keV}$.

The nuclear recoil contribution is always negligible for $m_X = 0.1\,\text{GeV}$ and $m_X = 1\,\text{GeV}$, with a detection threshold of $O(\text{keV})$. As for $m_X = 10\,\text{GeV}$, the nuclear recoil signal is significant and the XENON1T collaboration has derived a bound, $\sigma_N < 4 \times 10^{-45}\text{cm}^2$ for the elastic DM case [9]. For the

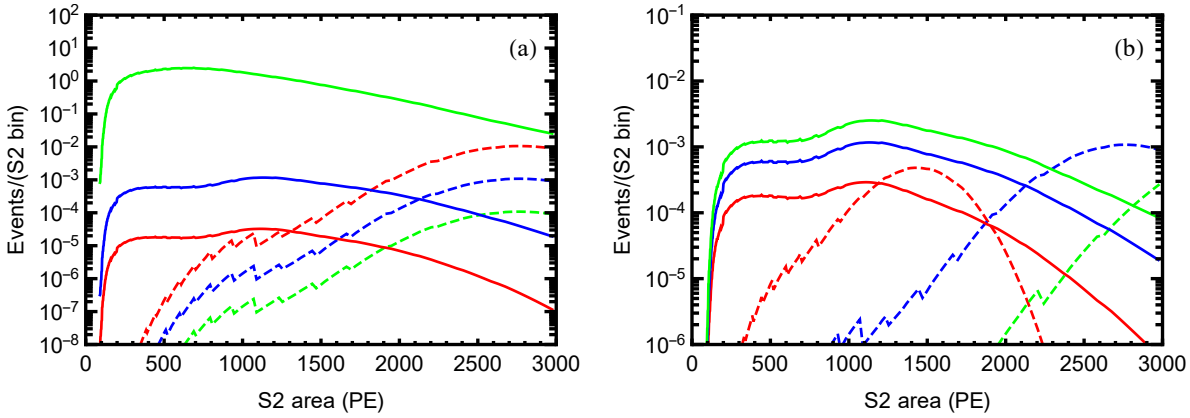


Figure 4: Recoil signals from inelastic DM scattering by using the XENON1T S2-only data. The solid curves present contributions by the Migdal effect, and the dashed curves are given by contributions from the DM-electron scattering. We set the cutoff scale $\Lambda = 500\,\text{GeV}$, and choose the dark charges $(q_e, q_n, q_p) = (1, 1, -1)$. Plot-(a): The mass-splitting is set as $\Delta m = 3\,\text{keV}$. The (red, blue, green) curves correspond to $m_X = (0.1,\, 1,\, 10)\,\text{GeV}$, respectively. Plot-(b): The DM mass is set as $m_X = 1\,\text{GeV}$. The (red, blue, green) curves correspond to $\Delta m = (1,\, 3,\, 5)\,\text{keV}$, respectively.

inelastic DM case with $\Delta m < 5\,\text{keV}$, we always have

$$\frac{m_X}{m_N}\Delta m < \text{keV}, \quad \text{and} \quad \frac{\Delta m}{m_X v_{\text{DM}}^2} < 1. \tag{4.4}$$

This implies that the contribution from Δm to nuclear recoil is always below the threshold and sub-dominant as compared to the contribution from the kinetic energy of the incoming DM particle. Thus, the bound set by the XENON1T experiment [9] should remain unchanged for the case of $\Delta m < 5\,\text{keV}$.

To derive the constraint for each model and each parameter set of $(m_X, \Delta m)$, we choose a custom S2 region of interest (ROI) before analyzing the search data of XENON1T. As required in Ref. [9], the lower (upper) end of an ROI must lie between the 5th and 60th (40th and 95th) percentile of the S2 spectrum to contain sufficient signals, and should never be below 150 PE. We first scan over all such ROIs on the training dataset and determine the optimized ROI that gives the lowest bound. Then, we apply this ROI on the search dataset (which is independent of the training dataset). The exclusion region (at 95% C.L.) for the parameter $\boldsymbol{\theta}$ of a general probabilistic model is determined by the formula:

$$p(\boldsymbol{\theta}) \equiv \sum_{n=0}^{n_{\text{obs}}} \frac{\mu(\boldsymbol{\theta})^n}{n!} e^{-\mu(\boldsymbol{\theta})} \leqslant 0.05\,, \tag{4.5}$$

where μ is the expected event number in the chosen ROI including the background and signal events, and n_{obs} denotes the observed event number in the chosen ROI. In the excluded region, the probability that more events would have been produced than what are actually observed (i.e., $n > n_{\text{obs}}$) is above 95%. For our scenario under consideration, there is only one free parameter $\boldsymbol{\theta} = \Lambda$.

In Fig. 5, we present the results from analyzing the XENON1T S2-only data with inputs of $m_X = (0.1,\, 1,\, 10)\,\text{GeV}$, respectively. The plots are arranged in the same way as in Fig. 2. In addition, we derive the constraints for $\Delta m = 3\,\text{keV}$ over the DM mass range of $0.1\,\text{GeV} \leqslant m_X \leqslant 10\,\text{GeV}$, as

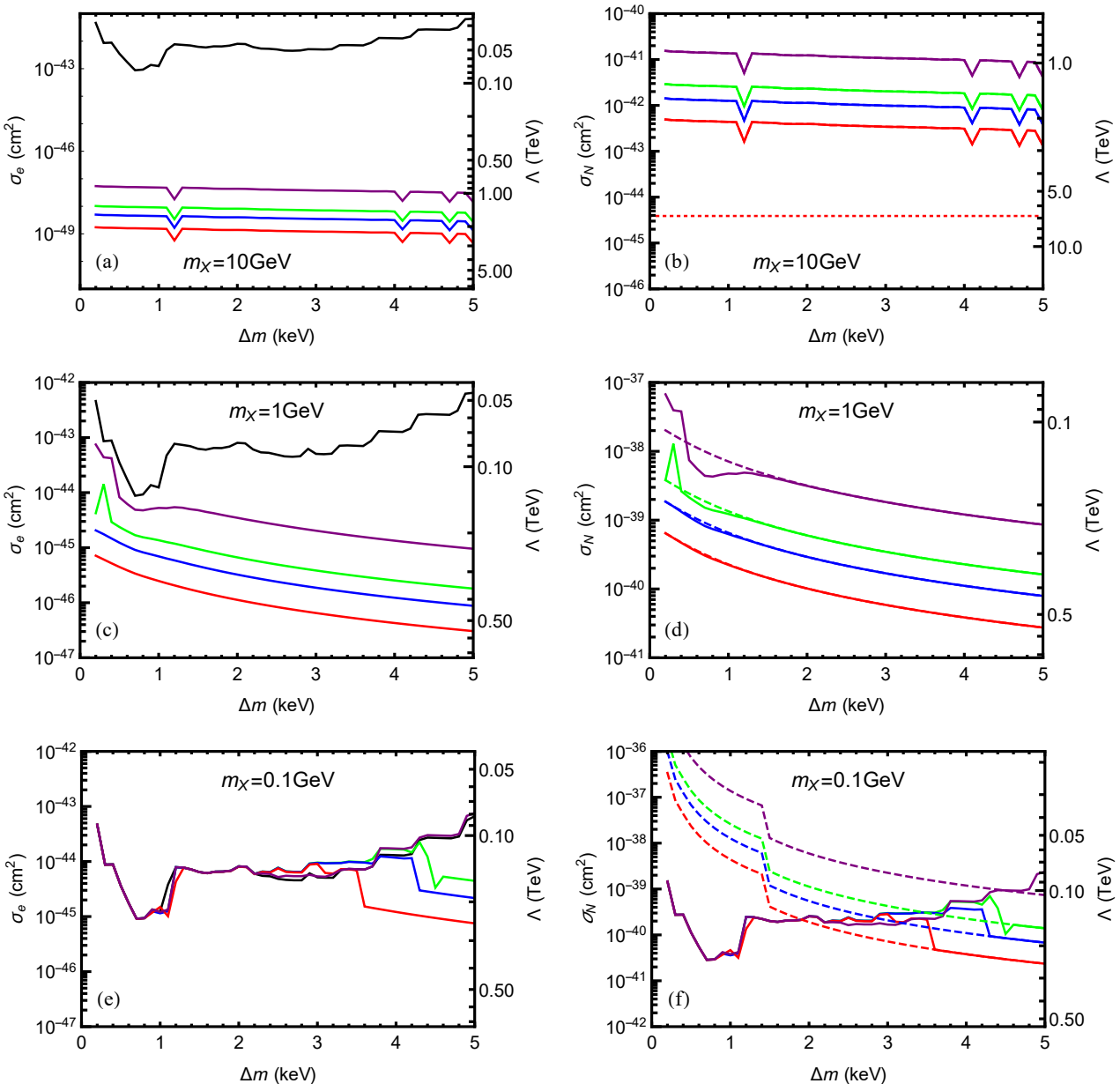


Figure 5: Limits on the DM-electron cross section (left panels) and on the DM-nucleon scattering cross sections (right panels) by using XENON1T S2-only data. The plots from top to bottom choose the DM mass $m_X = \{10, 1, 0.1\}$ GeV, respectively. The color of each curve matches the corresponding benchmark scenario (as indicated) in Table 1 (Section 2), i.e., dashed curves for $q_e = 0$ and solid curves for $q_e = 1$, whereas green curves for $(q_n, q_p) = (0, 1)$, blue curves for $(q_n, q_p) = (1, 0)$, red curves for $(q_n, q_p) = (1, 1)$, purple curves for $(q_n, q_p) = (1, -1)$, and black curves for $(q_n, q_p) = (0, 0)$. The region above each curve is excluded. The red dotted curve in plot-(b) is taken from Ref. [9]. It shows the 90% C.L. upper limit on spin-independent DM-nucleon cross section by NR signals at $m_X = 10$ GeV.

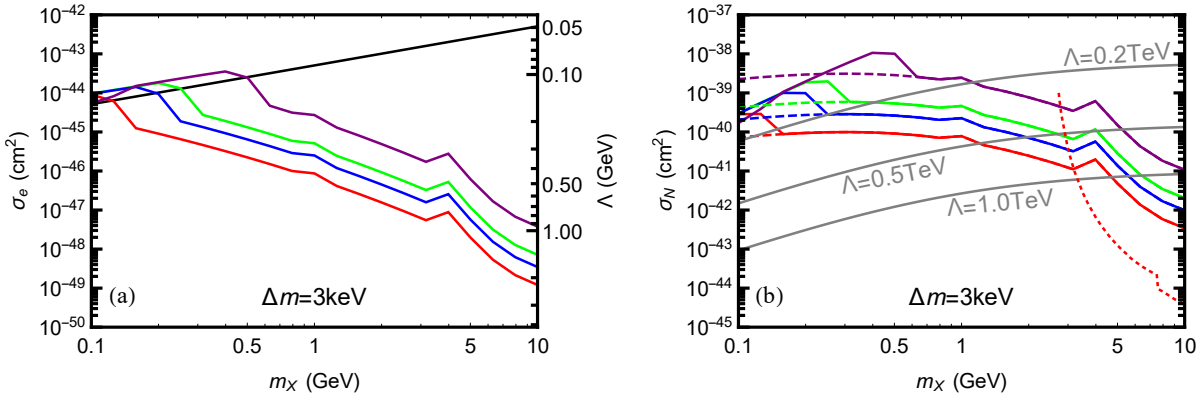


Figure 6: Limits on the DM-electron cross section (left panel) and on the DM-nucleon scattering cross sections (right panel) by using XENON1T S2-only data. The color of each curve matches the corresponding benchmark scenario (as indicated) in Table 1 (Section 2), i.e., dashed curves for $q_e = 0$ and solid curves for $q_e = 1$, whereas green curves for $(q_n, q_p) = (0, 1)$, blue curves for $(q_n, q_p) = (1, 0)$, red curves for $(q_n, q_p) = (1, 1)$, purple curves for $(q_n, q_p) = (1, -1)$, and black curves for $(q_n, q_p) = (0, 0)$. In plot-(b), the gray curves from top to bottom correspond to $\Lambda = (0.2, 0.5, 1.0)\,\text{TeV}$, respectively. The red dotted curve is taken from Ref. [9]. It stands for the 90% C.L. upper limit on spin-independent DM-nucleon cross section given by NR signals. In both plots the region above each curve is excluded.

shown in Fig. 6. We see that the same pattern appears as in the results from the XENONnT ER data, namely, the dashed curves are smooth, whereas for small DM mass m_X the solid curves are twisty. Because the S2-only event numbers of XENON1T are much smaller than that in the ER data of XENONnT, the statistic fluctuations are more significant. This also leads to the non-smoothness of the ROI choices, which further enlarges the fluctuations in these curves.[1] As we have confirmed, the Migdal effect is more important than DM-electron scattering for larger m_X and/or larger Δm. The red dotted curves in Fig. 5(b) and Fig. 6(b) are the 90% C.L. upper limit on spin-independent DM-nucleon cross section taken from Ref. [9]. We use red color for the dotted curves because this limit corresponds to the $q_n = q_p = 1$ case. This limit is determined solely by elastic nuclear recoil signals, which is neglected in this study. As discussed in Eq. (4.4), the limits are unchanged for inelastic DM with $\Delta m < 5\,\text{keV}$. In Fig. 6(b) we see that this limit gets weakened rapidly as m_X decreases. In consequence, for larger DM mass ($m_X \gtrsim 5\,\text{GeV}$), the nuclear recoil signals dominates over that of the electron recoils, whereas for $m_X \lesssim 5\,\text{GeV}$, the nuclear recoil effects are negligible.

5. Probing Inelastic DM with Dark Photon Mediator

Based upon the above model-independent study, we further construct an inelastic DM model with dark photon mediator via kinetic mixing, which can exhibit the features as we studied in the previous sections. Then, we systematically derive the cosmological bounds and laboratory bounds on

[1] Most notably in Fig. 5(f), for $2\,\text{keV} \lesssim \Delta m \lesssim 4\,\text{keV}$, the ROIs for the solid curves (chosen by the training dataset) are in regions with higher S2 area. The search dataset in this region contains slightly more observed events above the backgrounds and imposes weaker limits than the dashed curves, whose ROIs are in the regions with lower S2 area which contains zero events in the search dataset [9].

this minimal inelastic DM model.

5.1. Model Realization: Inelastic DM with Dark Photon Mediator

In this model the SM is extended with a dark $U(1)_X$ gauge group, which connects to the SM through kinetic mixing between the dark $U(1)_X$ gauge field $\bar{A}'_\mu$ and the SM $U(1)_Y$ gauge field B_μ. Thus, the kinematic terms of the dark $U(1)_X$ and the SM $U(1)_Y$ are given by

$$\mathcal{L} \supset -\frac{1}{4}\bar{\mathcal{A}}'_{\mu\nu}\bar{\mathcal{A}}'^{\mu\nu} - \frac{1}{4}B_{\mu\nu}B^{\mu\nu} - \frac{\kappa}{2}\bar{\mathcal{A}}'_{\mu\nu}B^{\mu\nu}, \tag{5.1}$$

where the dark gauge field strength $\bar{\mathcal{A}}'_{\mu\nu} = \partial_\mu \bar{A}'_\nu - \partial_\nu \bar{A}'_\mu$. The dark $U(1)_X$ gauge group is spontaneously broken by the vacuum expectation values (VEVs) of two singlet scalar fields S and ϕ,

$$\Delta\mathcal{L} \supset |D^\mu S|^2 + M_S^2|S|^2 - \lambda_S|S|^4 + |D^\mu\phi|^2 - M_\phi^2|\phi|^2 + \left(\lambda_{S\phi}S^3\phi + \text{h.c.}\right), \tag{5.2}$$

where the dark charges of S and ϕ are $1/3$ and -1, respectively. This generates a mass term for $\bar{A}'_\mu$ through the Higgs mechanism,

$$m_{\bar{A}'}^2 = 2g_X^2\left(v_\phi^2 + \tfrac{1}{9}v_S^2\right), \tag{5.3}$$

where g_X is the $U(1)_X$ coupling, and the VEVs are $v_S = M_S/\sqrt{2\lambda_S}$ and $v_\phi = \lambda_{S\phi}v_S^3/M_\phi^2$. Taking $M_\phi \gg v_S$, we have $v_\phi \ll v_S$. This further gives, $m_{\bar{A}'} \simeq \sqrt{2}g_X v_S/3$ and $v_\phi = 27\lambda_{S\phi}m_{\bar{A}'}^3/(2\sqrt{2}g_X^3 M_\phi^2)$.

After the spontaneous breaking of the electroweak gauge group $SU(2)_L \otimes U(1)_Y$, the neutral gauge boson component W_μ^3 of $SU(2)_L$ and the $U(1)_Y$ gauge boson B_μ form their mass eigenstates, $\bar{A}_\mu = B_\mu\cos\theta_W + W_\mu^3\sin\theta_W$ and $\bar{Z}_\mu = W_\mu^3\cos\theta_W - B_\mu\sin\theta_W$, where θ_W is the weak mixing angle. Thus, including the W_μ^3 part and all mass terms, we can rewrite the kinetic terms (5.1) as follows:

$$\begin{aligned}\mathcal{L} \supset & -\frac{1}{4}\bar{\mathcal{A}}'_{\mu\nu}\bar{\mathcal{A}}'^{\mu\nu} - \frac{1}{4}\bar{\mathcal{A}}_{\mu\nu}\bar{\mathcal{A}}^{\mu\nu} - \frac{1}{4}\bar{\mathcal{Z}}_{\mu\nu}\bar{\mathcal{Z}}^{\mu\nu} - \frac{\kappa}{2}\bar{\mathcal{A}}'_{\mu\nu}\left(\bar{\mathcal{A}}^{\mu\nu}\cos\theta_W - \bar{\mathcal{Z}}^{\mu\nu}\sin\theta_W\right) \\ & + \frac{1}{2}m_{\bar{A}'}^2\bar{A}'_\mu\bar{A}'^\mu + \frac{1}{2}M_{\bar{Z}}^2\bar{Z}_\mu\bar{Z}^\mu,\end{aligned} \tag{5.4}$$

where the gauge field strengths $\bar{\mathcal{A}}_{\mu\nu} = \partial_\mu\bar{A}_\nu - \partial_\nu\bar{A}_\mu$ and $\bar{\mathcal{Z}}_{\mu\nu} = \partial_\mu\bar{Z}_\nu - \partial_\nu\bar{Z}_\mu$. Then, we can write the interaction terms of the gauge fields $(\bar{A}'_\mu, \bar{A}_\mu, \bar{Z}_\mu)$ with matter currents:

$$\mathcal{L}_{\text{Int}} \supset g_X\bar{A}'_\mu J_X^\mu + e\bar{A}_\mu J_{\text{em}}^\mu + \frac{g}{\cos\theta_W}\bar{Z}_\mu J_Z^\mu, \tag{5.5}$$

where J_X^μ is the dark current as in Eq. (2.1), J_{em}^μ the electromagnetic current, and J_Z^μ the weak neutral current.

To diagonalize these kinetic mixing terms and mass terms in Eq.(5.4), we transform the gauge fields from the basis $(\bar{A}'_\mu, \bar{A}_\mu, \bar{Z}_\mu)$ to the non-mixing mass-eigenbasis (A'_μ, A_μ, Z_μ). For the present study, we consider kinetic mixing parameter $\kappa \lesssim O(10^{-3})$ and dark photon mass $m_{\bar{A}'} \lesssim O(\text{GeV})$. Thus, to the leading order of the mixing parameter κ and the mass ratio $m_{\bar{A}'}^2/M_{\bar{Z}}^2$, we derive

$$\begin{pmatrix}\bar{A}'_\mu \\ \bar{A}_\mu \\ \bar{Z}_\mu\end{pmatrix} \simeq \begin{pmatrix}1 & 0 & \kappa s_W \\ -\kappa c_W & 1 & 0 \\ -\frac{m_{\bar{A}'}^2}{M_{\bar{Z}}^2}\kappa s_W & 0 & 1\end{pmatrix}\begin{pmatrix}A'_\mu \\ A_\mu \\ Z_\mu\end{pmatrix}, \tag{5.6}$$

where we denote $(s_W, c_W) = (\sin\theta_W, \cos\theta_W)$. Accordingly, we derive the mass spectrum of the neutral gauge bosons (A'_μ, A_μ, Z_μ) as follows:

$$m_{A'} \simeq m_{\bar{A}'}\big(1+\kappa^2 c_W^2\big)^{\frac{1}{2}}, \qquad m_A = 0\,, \qquad M_Z^2 \simeq M_{\bar{Z}}\big(1+\kappa^2 s_W^2\big)^{\frac{1}{2}}. \tag{5.7}$$

After the diagonalization of the gauge bosons, the interaction Lagrangian (5.5) becomes:

$$\begin{aligned}\mathcal{L}_{\rm Int} \supset\ & g_X\big(A'_\mu + \kappa s_W Z_\mu\big)J_X^\mu + e\left(A_\mu - \kappa c_W A'_\mu\right)J_{\rm em}^\mu \\ & + \frac{g}{c_W}\left(Z_\mu - \frac{m_{\bar{A}'}^2}{M_{\bar{Z}}^2}\kappa s_W A'_\mu\right)J_Z^\mu + O(\kappa^2)\,,\end{aligned} \tag{5.8}$$

In the following, we define $\epsilon = \kappa\cos\theta_W$ as the mixing parameter.

The inelastic DM consists of two nearly degenerate long-lived states. These states can be formulated by either a pseudo-complex scalar $\widehat{X} = (X + \mathtt{i}X')/\sqrt{2}$ or a pseudo-Dirac spinor $\widehat{\chi} = (\chi_1, \chi_2^\dagger)^T$, which are charged under the dark gauge group $U(1)_X$ with dark charge $+1$ for $\widehat{X}$ or dark charge $+\frac{1}{2}$ for $\widehat{\chi}$. (This means that the Weyl spinors χ_1 and χ_2 have dark charges $+\frac{1}{2}$ and $-\frac{1}{2}$ respectively.) The mass-splitting Δm between the two DM components can be generated naturally by a seesaw mechanism. For the scalar dark matter $\widehat{X}$, the DM Lagrangian takes the following form:

$$\begin{aligned}\Delta\mathcal{L}_{\rm DM} \supset\ & |D^\mu\widehat{X}|^2 - m_{\widehat{X}}^2|\widehat{X}|^2 - \lambda_X|\widehat{X}|^4 + \left(\lambda_\delta \widehat{X}^2\phi^2 + \text{h.c.}\right) \\ & - \lambda_{X\phi}|\widehat{X}|^2|\phi|^2 - \lambda_{XS}|\widehat{X}|^2|S|^2\,.\end{aligned} \tag{5.9}$$

The DM mass is mainly determined by the DM quadratic mass term and the DM couplings to $|S|^2$ and $|\phi|^2$, so the DM mass term is given by

$$\begin{aligned}\Delta\mathcal{L}_{\rm DM} \supset\ & -\tfrac{1}{2}\big(m_{\widehat{X}}^2 + \lambda_{XS}v_S^2 + \lambda_{X\phi}v_\phi^2\big)(X^2 + X'^2) + \lambda_\delta v_\phi^2(X^2 - X'^2) \\ =\ & -\tfrac{1}{2}\overline{m}_X^2(X^2 + X'^2) + \tfrac{1}{2}\delta m^2(X^2 - X'^2)\,,\end{aligned} \tag{5.10}$$

where the mass parameters $\overline{m}_X = (m_{\widehat{X}}^2 + \lambda_{XS}v_S^2 + \lambda_{X\phi}v_\phi^2)^{1/2}$ and $\delta m^2 = 2\lambda_\delta v_\phi^2 \ll \overline{m}_X^2$. The mass-splitting Δm_X between the two DM components is determined by the unique quartic interaction $\widehat{X}^2\phi^2$ which gives rise to the mass-squared difference δm^2, as shown above. Since $v_\phi \ll v_S, \overline{m}_X$ and thus $\delta m^2 \ll \overline{m}_X^2$, we have

$$m_{X,X'} \simeq \overline{m}_X \mp \frac{\delta m^2}{2\overline{m}_X}\,. \tag{5.11}$$

With these, we derive the scalar DM mass-splitting as follows:

$$\Delta m_X \simeq \frac{\delta m^2}{\overline{m}_X} \simeq \frac{729\lambda_\delta\lambda_{S\phi}^2 m_{A'}^6}{4g_X^6 M_\phi^4 m_X}\,. \tag{5.12}$$

By setting the sample inputs $(\lambda_\delta, \lambda_{S\phi}) = O(1)$, $g_X = O(10^{-2})$, $(m_X, m_{A'}) = O(\text{GeV})$, and $M_\phi = O(10^2\,\text{TeV})$, we can readily achieve a naturally small mass-splitting $\Delta m_X = O(\text{keV})$.

For the fermionic DM $\widehat{\chi}$, the scalar potential (5.2) remains the same and the fermionic DM has the following gauge-invariant Lagrangian terms:

$$\Delta\mathcal{L} \supset \chi_1^\dagger \mathtt{i}\bar{\sigma}^\mu D_\mu\chi_1 + \chi_2^\dagger \mathtt{i}\bar{\sigma}^\mu D_\mu\chi_2 - (m_{\widehat{\chi}}\chi_1\chi_2 + \text{h.c.})$$

$$+\left(y_{\phi\chi_1}\chi_1\chi_1\phi + y_{\phi\chi_2}\chi_2\chi_2\phi^* + \text{h.c.}\right), \tag{5.13}$$

where the Majorana mass $m_{\widehat{\chi}}$ and Yukawa couplings $(y_{\phi\chi_1},\, y_{\phi\chi_2})$ are positive after proper phase rotations of ϕ and (χ_1, χ_2). The small VEV v_ϕ induces additional Majorana masses for $(\chi_1,\, \chi_2)$ through the Yukawa interactions in Eq.(5.13). Thus, we have the following DM mass terms:

$$\mathcal{L}_{\chi_1\chi_2} \supset -m_{\widehat{\chi}}\chi_1\chi_2 + \delta m_1\chi_1\chi_1 + \delta m_2\chi_2\chi_2 + \text{h.c.}\,, \tag{5.14}$$

where $(\delta m_1,\, \delta m_2) = (y_{\phi\chi_1}v_\phi,\, y_{\phi\chi_2}v_\phi)$. To transform $(\chi_1,\, \chi_2)$ into the mass-eigenstates $(\chi,\, \chi')$, we make the following decompositions:

$$\chi_1 = \frac{1}{\sqrt{2}}(\chi - \mathtt{i}\chi'), \qquad \chi_2 = \frac{1}{\sqrt{2}}(\chi + \mathtt{i}\chi'). \tag{5.15}$$

Since $v_\phi \ll m_{\widehat{\chi}}$, we derive the following Majorana masses for the DM mass-eigenstates $(\chi,\, \chi')$:

$$m_\chi \simeq m_{\widehat{\chi}} - (\delta m_1 + \delta m_2)\,, \tag{5.16a}$$

$$m_{\chi'} \simeq m_{\widehat{\chi}} + (\delta m_1 + \delta m_2)\,, \tag{5.16b}$$

which have a mass-splitting,

$$\Delta m_\chi \simeq 2(\delta m_1 + \delta m_2)\,. \tag{5.17}$$

We choose the sample input parameters, $\lambda_{S\phi},\, y_{\phi\chi_1},\, y_{\phi\chi_2} = O(0.01)$, $v_S = O(20)\,\text{GeV}$, and $M_\phi = O(\text{TeV})$. With these, we can readily derive a small VEV $v_\phi = O(0.1)\text{MeV}$, and thus realize the desired mass-splitting $\Delta m_\chi = O(\text{keV})$.

From Eq.(5.9), we deduce the $U(1)_X$ gauge interactions for the scalar DM fields $(X,\, X')$:

$$\mathcal{L}_{\text{int}} \supset g_X\left(X^\dagger\partial_\mu X' - X'^\dagger\partial_\mu X\right)\bar{A}'^\mu\,, \tag{5.18}$$

which is consistent with the effective theory formulation in Section 2. We note that the diagonal vertices X-X-A'^μ and X'-X'-A'^μ vanish, whereas the above non-diagonal vertices can induce the desired inelastic scattering. Similar behavior holds for the case of fermionic inelastic DM.

At leading order, the cross sections of DM-electron and DM-nucleon scattering are mediated by the dark photon A'_μ. The contribution from Z-boson exchange is suppressed by $m^4_{A'}/m^4_Z$. Thus, we derive the following cross section formulas:

$$\sigma_{XN} = Z^2\frac{4\alpha g_X^2\epsilon^2\mu^2}{m^4_{A'}}\,, \tag{5.19a}$$

$$\sigma_{Xe} = \frac{4\alpha g_X^2\epsilon^2 m_e^2}{m^4_{A'}}\,. \tag{5.19b}$$

This should correspond to the scenario-(f) in Table 1 of Section 2, where $q_n = 0$ and $|q_p| = |q_e| = 1$, and the effective cutoff scale is given by

$$\Lambda = m_{A'}/\sqrt{g_X\,\epsilon}\,. \tag{5.20}$$

In the above formula, we have considered that the momentum transfer $q^2 \ll m_{A'}^2$. This is always true in the DM-electron scattering for $m_{A'} > O(\text{MeV})$, because the atomic form factors are peaked at $q \sim O(10\text{keV})$ as we discussed earlier. But, for the DM-nucleon scattering, we have $|q| \sim m_X v_{\text{DM}} \sim 10^{-3} m_X$. Thus, we will focus on $m_{A'} > 10^{-2} m_X$ in the following analysis.

5.2. Cosmological and Laboratory Constraints on Inelastic DM

Such exothermic inelastic scattering of DM particles with target atoms in the detector requires a significant local abundance of the heavier DM component X'. The conversion between X' and X is mainly due to X' decay, of which the only kinematically allowed channels are $X' \to X\gamma\gamma\gamma$ and $X' \to X\nu\bar{\nu}$. Since the 3γ decay channel is one-loop suppressed, the dominant decay channel is $X' \to X\nu\bar{\nu}$, which occurs through the A'/Z exchange due to the neutral gauge boson mixings in Eq.(5.6). We can estimate the X' decay width as follows:

$$\begin{aligned} \Gamma_{X' \to X\nu\bar{\nu}} &= \frac{e^2}{1260\pi^3 M_Z^4 \cos^4\theta_W} \frac{g_X^2 \epsilon^2}{m_{A'}^4} \Delta m^9 \\ &\approx \left(4 \times 10^{34}\text{yrs}\right)^{-1} \left(\frac{\Lambda}{100\,\text{GeV}}\right)^{-4} \left(\frac{\Delta m}{10\,\text{keV}}\right)^9 , \end{aligned} \tag{5.21}$$

where we have included the contributions of the final state neutrinos from all three families of the SM. Note that this width is much narrower than that in our previous model [21], because in this model the coupling between A' and $\nu\bar{\nu}$ is suppressed by $m_{A'}^2/M_Z^2$ and cancels the contribution from Z exchange at leading order, resulting in a tiny factor $\Delta m^4/M_Z^4 \simeq 10^{-28}$ in the decay width for $\Delta m = 10\,\text{keV}$. This makes the lifetime of X' much longer than the age of the universe. Hence, assuming equal initial abundance of X and X', we have $\rho_X = \rho_{X'} = \rho_{\text{DM}}/2$ at the present. Consequently, the limits on the cutoff Λ in Figs. 2-3 and Figs. 5-6 should be rescaled by a factor of $2^{-1/4} \simeq 0.84$.

This minimal inelastic DM model is also constrained by cosmological observations. The Planck Collaboration measured the present DM relic abundance [36], $\Omega_X h^2 = 0.120 \pm 0.001$, which can be achieved through the freeze-out mechanism. Since $\Delta m \ll m_X$, the inelastic DM components X and X' are equally abundant in the thermal bath before exiting the equilibrium. For $m_X > m_{A'}$, the dominant annihilation channel is $\hat{X}^\dagger \hat{X} \to A'A'$. The annihilation cross section scales as g_X^4 and is independent of mixing parameter ϵ, hence the bounds on $\Lambda \propto (g_X \epsilon)^{-1/2}$ from direct detection experiments are irrelevant to the annihilation process. In fact, we can in turn derive the bounds on ϵ by combining the g_X values required by the DM relic density and the bounds on Λ from direct detection experiments. But for $m_X < m_{A'}$, the leading annihilation channel is $\hat{X}^\dagger \hat{X} \to A'^* \to f\bar{f}$, where f and $\bar{f}$ are charged SM fermions. The relic abundance of the DM can be estimated as follows [37–39]:

$$\Omega_X h^2 \simeq 0.1 \left(\frac{x_f}{20}\right)\left(\frac{10^{-8}\text{GeV}^{-2}}{\sigma_X}\right), \tag{5.22}$$

where $x_f \equiv T_f/m_X$ with T_f the freeze-out temperature. The DM annihilation cross section $\sigma_X \sim \alpha m_X^2/\Lambda^4$ is highly constrained by direct detection experiments, since the green solid curves in Figs. 2-

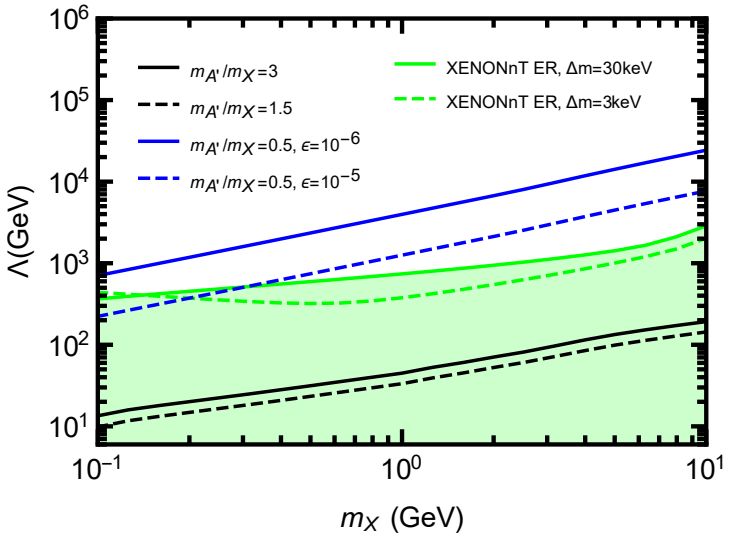


Figure 7: Allowed parameter space of $(m_X,\,\Lambda)$ as given by imposing the DM relic density bound together with XENONnT electron recoil bounds of Fig. 3. The parameter space of the black and blue curves can provide the observed DM relic density today, whereas the green region displays the excluded parameter space at 95% C.L. The blue dashed (solid) curve corresponds to the sample inputs of $m_{A'}/m_X = 0.5$ and $\epsilon = 10^{-5}$ ($\epsilon = 10^{-6}$). The black dashed (solid) curve corresponds to the sample input of $m_{A'}/m_X = 1.5$ ($m_{A'}/m_X = 3$); and the green dashed (solid) curve corresponds to the sample input of $\Delta m = 3\,\text{keV}$ ($\Delta m = 30\,\text{keV}$) for XENONnT ER bounds with the green shaded area being excluded.

3 and Figs. 5-6 have set $\Lambda \gtrsim O(10^2\,\text{GeV})$. This always results in an overproduction of DM, so that the case of $m_X < m_{A'}$ is disfavored.

To demonstrate this, we present in Fig. 7 the Λ values required by the inelastic DM relic density and compare them to the constraints from direct detection experiments. The green dashed (solid) curve corresponds to the sample inputs of $\Delta m = 3\,\text{keV}$ ($\Delta m = 30\,\text{keV}$) for XENONnT ER bounds with the green shaded area being excluded. We compute the DM relic density numerically by using the package `MicrOMEGAs` [40]. We see that for the case of $m_X < m_{A'}$, the sample input of $m_{A'}/m_X = 1.5$ ($m_{A'}/m_X = 3$) is excluded by XENONnT bounds, as shown by the black dashed (solid) curve. As mentioned earlier, the bounds on $\Lambda \propto (g_X \epsilon)^{-1/2}$ are irrelevant to the case of $m_X > m_{A'}$. In order to translate the values of g_X given by imposing DM relic density to Λ, we choose sample inputs of $\epsilon = 10^{-5}$ and 10^{-6} which correspond to the blue dashed and solid curves in Fig. 7, respectively. Since ϵ does not receive any lower bound, we can always choose small enough values of ϵ such that the blue curve is fully above the green shaded region of Fig. 7 and thus escape the constraints.

Another cosmological constraint comes from the CMB anisotropy [41][42]. After the DM freezes out, the annihilation is largely diluted but not completely shut down. The electron/positron injection from A' decay contributes to the CMB anisotropy, which is already constrained by the CMB measurements including Planck [36]. The leading annihilation channel $\hat{X}^\dagger \hat{X} \to A'A' \to \ell\bar{\ell}\ell\bar{\ell}$ is s-wave dominant. Its thermally averaged cross section receives an upper bound from the Planck data [36]:

$$f_{\text{eff}} \frac{\langle \sigma v \rangle}{m_X} \;<\; 3.2 \times 10^{-28} \text{cm}^3 \text{s}^{-1} \text{GeV}^{-1}, \tag{5.23}$$

where the efficiency factor $f_{\rm eff}$ is the fraction of the DM rest mass energy deposited into the gas [42]. In general, $f_{\rm eff} \gtrsim 0.1$ and it depends on the lepton energy injected into the gas. This excludes the full parameter space determined by the freeze-out analysis, and would exclude the minimal model for the inelastic DM scenario with dark photon mediator (via kinetic mixing). The same conclusion applies to the case of fermionic DM.

But we note that the dark sector may contain several species of particles and mediators like the visible sector. Thus in this case the CMB anisotropy constraint can be readily relaxed if A' predominantly decays into light particles in the dark sector (rather than leptons) [23]. For instance, the dark sector may contain a light Dirac fermion f' charged under a new gauge group $U(1)_{X'}$ with gauge field A''_μ. The gauge boson A''_μ obtains a mass $m_{A''}$ through either the Higgs mechanism or the Stueckelberg mechanism, of which the detail is irrelevant to the discussion below. The kinetic mixing between $U(1)_{X'}$ and $U(1)_Y$ induces a small coupling between the electromagnetic current and A''_μ as parameterized by $\epsilon' e \ll 1$. The dark fermion f' is charged under both $U(1)_X$ and $U(1)_{X'}$, with a mass that satisfies $m_{A'} > 2m_{f'}$. The interactions of various currents takes the form,

$$\mathcal{L} \supset -g_X \bar{f}'\gamma^\mu f' A'_\mu - g_{X'} \bar{f}'\gamma^\mu f' A''_\mu - \epsilon' e \mathcal{A}''_\mu J^\mu_{\rm em} \,, \tag{5.24}$$

where $g_{X'}$ denotes the gauge coupling of $U(1)_{X'}$. There is possible mixing between $U(1)_X$ and $U(1)_{X'}$, which is set to be small (or vanishing), so the coupling between $\hat{X}$ and A'' is always suppressed and thus has negligible effect. In this setup, the ratio between the branching fractions $\mathrm{Br}[A' \to \ell\bar{\ell}]$ and $\mathrm{Br}[A' \to f'\bar{f}']$ is suppressed by the tiny factor of ϵ^2, thus this setup can readily evade the stringent bound from the CMB measurements.[2] Regarding the density of the stable particles f', it is depleted by the efficient freeze-out process $f'\bar{f}' \to A'' \to \ell\bar{\ell}$.[3] This leads to $n_{f'} \ll n_X$, so f' contributes to neither the DM abundance nor the CMB anisotropy. Also, this setup brings a new annihilation channel $\hat{X}^\dagger \hat{X} \to A'^* \to f'\bar{f}'$. For $m_X > m_{A'}$, since it is p-wave dominant, i.e., suppressed by $x_f \sim 1/20$ as compared to $\hat{X}^\dagger \hat{X} \to A'A'$, it barely affects the DM relic density. But for $m_X < m_{A'}$, it becomes the dominant channel because it receives no suppression by ϵ^2, as compared to $\hat{X}^\dagger \hat{X} \to A'^* \to f\,\bar{f}$. Hence, unlike the minimal model, this setup allows the $m_X < m_{A'}$ case to produce the correct DM relic density, as well as avoiding the CMB anisotropy constraint. Hence, in this simple setup of the dark sector, the interesting interplay between the constraints of the DM relic density and the direct detection still holds as in the minimal model, whereas the cosmological bounds from CMB and BBN are satisfied.

We use the the package `MicrOMEGAs` [40] to compute the inelastic DM relic density for this setup. To be concrete, we choose the inputs $m_X > m_{A'} > 50\,\mathrm{MeV}$, $m_{f'} = 15\,\mathrm{MeV}$, and $m_{A''} = 45\,\mathrm{MeV}$. Hence the freeze-out ends before the BBN at which $T \sim 1\,\mathrm{MeV}$. We set the coupling input $g_{X'} = \sqrt{2\pi}$ (and thus $\alpha_{X'} = g^2_{X'}/4\pi = 0.5$) and the mixing parameter $\epsilon' = 10^{-4}$ (which is allowed by the NA64 bound [43]).

[2] The annihilation cross section of $XX' \to \ell\bar{\ell}\ell\bar{\ell}$ through two virtual A' is suppressed by ϵ^4 and satisfies the constraint (5.23) easily.

[3] The annihilation $f'\bar{f}' \to \ell\bar{\ell}$ through a virtual A' is insufficient to deplete the f' density based on a similar relation to Eq.(5.22).

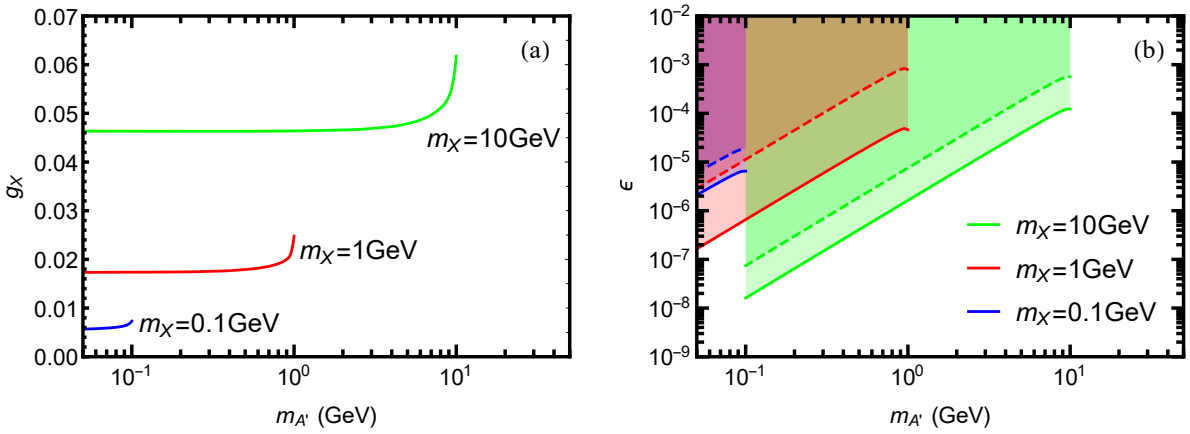


Figure 8: Plot-(a): Predicted $U(1)_X$ coupling g_X versus the dark photon mass $m_{A'}$ as derived by imposing today's DM relic abundance $\Omega h^2 = 0.120$. Plot-(b): Bounds in the $(\epsilon, m_{A'})$ plane. The (green, red, blue) colors denote the DM masses $m_X = (10,\ 1,\ 0.1)\,\text{GeV}$, respectively. The solid (dashed) curves are derived from combining the DM direct detection and the DM relic density, with input $\Delta m = 30\,\text{keV}\,(1\,\text{keV})$.

In Fig. 8(a), we present the g_X values that can give the correct DM relic density. Fig. 8(b) shows the constraints on the dark photon from the direct detection experiments and cosmological observations. In this figure, the (green, red, blue) curves correspond to the DM mass $m_X = (10,\ 1,\ 0.1)\,\text{GeV}$, respectively. They are derived from $\epsilon = g_X^{-1} m_{A'}^2 \Lambda^{-2}$, where the coupling g_X is constrained in Fig. 8(a) as a function of $m_{A'}$, and the cutoff scale Λ is constrained by the direct detection constraints as in Fig. 2. The solid (dashed) curves corresponds to $\Delta m = 30\,\text{keV}\,(1\,\text{keV})$. Note that the green curves only cover the mass region $10^{-2} m_X < m_{A'} < m_X$ as is required in Section 5.1. Throughout the parameter space, we affirm that the relic abundance of f' is always small, $\Omega_f h^2 < 10^{-3}$.

We see that for a given DM mass, the dark coupling g_X is a nonzero constant as $m_{A'} \to 0$. Thus, we derive the bound on ϵ [shown as solid and dashed curves in Fig. 8(b)] which scales as $m_{A'}^2$ for small dark photon mass. This ensures a high sensitivity to the mixing parameter ϵ, and allows a probe towards the parameter space $10^{-7} < \epsilon < 10^{-3}$ and $0.01\,\text{GeV} < m_{A'} < 10\,\text{GeV}$, where a large portion is previously viable as it is not constrained by other experiments such as the fixed-target experiments [44, 45] and the collider searches [46].

Before concluding this subsection, we also comment on an inelastic DM model with dark photon mediator as introduced in Ref. [21]. In this model, the inelastic DM and the right-handed first generation SM fermions are charged under a $U(1)_R$ gauge group. The electroweak symmetry is spontaneously broken by two Higgs doublets, whose VEVs (v_1, v_2) satisfy $v_h = \sqrt{v_1^2 + v_2^2} \simeq 174\,\text{GeV}$ and $v_1^2 \ll v_2^2$. The dark photon mass is generated by the $U(1)_R$ symmetry breaking.

The DM relic abundance can be provided by the freeze-out mechanism. To obtain the observed DM relic density, a proper DM annihilation rate is needed. Since $\Delta m \ll m_X$, X and X' are equally abundant in the thermal bath before exiting the equilibrium. Thus, the dominant annihilation channel is $XX' \to A'A'$ when $m_{A'} < m_X$ and $XX' \to A' \to f\bar{f}$ when $m_{A'} > m_X$. Since the interactions are suppressed by Λ, the annihilation rate is sufficient only when the channel $XX' \to A'A'$ is near the

resonance during freeze-out. This requires $m_{A'} \gtrsim 2m_X$.

After the freeze-out, the total DM abundance is already fixed, but the ratio between X and X' can still evolve. As discussed in [21], the leading channel for the conversion $X' \to X$ is the decay $X' \to X\nu\bar{\nu}$ decay, which has the decay width,

$$\Gamma \simeq \frac{q_{\rm DM}^2 g_X^4}{160\pi^3} \frac{v_1^4 \Delta m_X^5}{v_h^4 m_{A'}^4}. \tag{5.25}$$

Ref. [21] sets the mass-splitting around 2.8 keV, whereas in the present study we allow the mass-splitting to vary up to 30 keV, which reduces the value of v_1 to $O(1)$ GeV scale and requires a high VEV ratio $\tan\beta \sim 10^2$.

Although the bounds in this work as imposed by current direct detection experiments are stronger than that of [21], the collider constraints remain unchanged. As is discussed in [21], the case of $m_{A'} > 2m_X$ is disfavored by collider searches. Since it is the only allowed case by the DM relic density constraint, so most parameter space in this model is excluded.

6. Conclusions

The origin and nature of dark matter (DM) remain largely unknown so far except its participation in the gravitational interaction. It is therefore important to probe the DM particles in both large and small mass ranges, and through all possible means including the direct detection, indirect detection, and collider searches.

In this work, we focus on studying the light inelastic DM with mass around (sub-)GeV scale. In Section 2, we gave a generic parameterization of the light inelastic DM interactions. For studying both the DM-electron scattering and DM-nucleus scattering (with Migdal effect) as well as their interplay, we presented the benchmark scenarios of the dark charge assignments as shown in Table 1. Then, in Section 3, we studied the electron recoil signatures from both the direct DM-electron scattering and the Migdal effect (induced by DM-nucleus scattering).

In Section 4, we analyzed the nature of the exothermic inelastic DM scattering process and demonstrated how direct detection experiments (such as XENON1T and XENONnT) can distinguish the signals from the light inelastic DM, as shown in Fig. 1 and Fig. 4. For the different benchmark scenarios of the dark charge assignments, we derived the experimental bounds on the light inelastic DM from the XENONnT ER data and the XENON1T S2-only data as shown in Figs. 2-3 and Figs. 5-6. These bounds depend sensitively on the dark charges (q_e, q_n, q_p) and the mass parameters $(m_X, \Delta m)$. We found that for larger DM mass m_X and/or vanishing dark charge q_e, in which case the DM-nucleon scattering dominates, the bounds are set mainly by the amplitudes of Migdal effect with the electron recoil energy around $(1-2)$ keV range, whereas in the case with direct DM-electron scattering being dominant, the signals are concentrated around the $E_R = \Delta m$ region. These facts suggest that a lower energy threshold in the detector can benefit the sensitivity for the DM-nucleon scattering with Migdal effect, and a higher energy resolution can increase the sensitivity to the DM-electron scattering. The

Migdal effect dominates over the direct electron scattering for larger m_X or larger Δm. But, for a general input of $(m_X, \Delta m)$, we demonstrated that it is highly nontrivial to determine which of the two effects is dominant. Hence, it is important to perform a combined analysis of both effects.

Finally, in Section 5, we studied a model realization of such light inelastic DM with the dark photon mediator, and applied the bounds of our benchmark scenarios to constrain this model as shown in Figs. 7 and 8. We further studied the cosmological and laboratory constraints on the inelastic DM.

Acknowledgements

We thank Jingqiang Ye for discussing the XENON1T and XENONnT data analysis. This research was supported in part by the National NSF of China under grants 12175136 and 11835005.

References

[1] A. H. Abdelhameed *et al.* [CRESST Collaboration], "First results from the CRESST-III low-mass dark matter program," Phys. Rev. D 100 (2019) no.10, 102002 [arXiv:1904.00498 [astro-ph.CO]].

[2] Z. Z. Liu *et al.* [CDEX Collaboration], "Constraints on Spin-Independent Nucleus Scattering with sub-GeV Weakly Interacting Massive Particle Dark Matter from the CDEX-1B Experiment at the China Jinping Underground Laboratory," Phys. Rev. Lett. 123 (2019) no.16, 161301 [arXiv:1905.00354 [hep-ex]].

[3] Y. Meng *et al.* [PandaX-4T Collaboration], "Dark Matter Search Results from the PandaX-4T Commissioning Run," Phys. Rev. Lett. 127 (2021) no.26, 261802 [arXiv:2107.13438 [hep-ex]].

[4] E. Aprile *et al.* [XENON Collaboration], "First Dark Matter Search with Nuclear Recoils from the XENONnT Experiment," Phys. Rev. Lett. 131 (2023) no.4, 041003 [arXiv:2303.14729 [hep-ex]].

[5] J. Aalbers *et al.* [LZ Collaboration], "First Dark Matter Search Results from the LUX-ZEPLIN (LZ) Experiment," Phys. Rev. Lett. 131 (2023) no.4, 041002 [arXiv:2207.03764 [hep-ex]].

[6] C. Cheng *et al.* [PandaX-II Collaboration], "Search for Light Dark Matter-Electron Scatterings in the PandaX-II Experiment," Phys. Rev. Lett. 126 (2021) no.21, 211803 [arXiv:2101.07479 [hep-ex]].

[7] E. Aprile *et al.* [XENON Collaboration], "Search for New Physics in Electronic Recoil Data from XENONnT," Phys. Rev. Lett. 129 (2022) no.16, 161805 [arXiv:2207.11330 [hep-ex]].

[8] Z. Y. Zhang *et al.* [CDEX Collaboration], "Constraints on Sub-GeV Dark Matter–Electron Scattering from the CDEX-10 Experiment," Phys. Rev. Lett. 129 (2022) no.22, 221301 [arXiv:2206.04128 [hep-ex]].

[9] E. Aprile *et al.* [XENON Collaboration], "Light Dark Matter Search with Ionization Signals in XENON1T," Phys. Rev. Lett. 123 (2019) no.25, 251801 [arXiv:1907.11485 [hep-ex]].

[10] R. Essig, J. Mardon and T. Volansky, "Direct Detection of Sub-GeV Dark Matter," Phys. Rev. D 85 (2012), 076007 [arXiv:1108.5383 [hep-ph]].

[11] A. B. Migdal, J. Phys. (USSR) 4 (1941) 449;

[12] M. Ibe, W. Nakano, Y. Shoji, and K. Suzuki, "Migdal Effect in Dark Matter Direct Detection Experiments," JHEP 03 (2018) 194 [arXiv:1707.07258 [hep-ph]].

[13] M. J. Dolan, F. Kahlhoefer, C. McCabe, "Directly detecting sub-GeV dark matter with electrons from nuclear scattering," Phys. Rev. Lett. 121 (2018) 101801, [arXiv: 1711.09906 [hep-ph]].

[14] N. F. Bell, J. B. Dent, J. L. Newstead, S. Sabharwal and T. J. Weiler, "Migdal effect and photon bremsstrahlung in effective field theories of dark atter direct detection and coherent elastic neutrino-nucleus scattering," Phys. Rev. D 101 (2020) no.1, 015012 [arXiv:1905.00046 [hep-ph]].

[15] R. Essig, J. Pradler, M. Sholapurkar and T. T. Yu, "Relation between the Migdal Effect and Dark Matter-Electron Scattering in Isolated Atoms and Semiconductors," Phys. Rev. Lett. 124 (2020) no.2, 021801 [arXiv:1908.10881 [hep-ph]].

[16] K. D. Nakamura, K. Miuchi, S. Kazama, Y. Shoji, M. Ibe and W. Nakano, "Detection capability of the Migdal effect for argon and xenon nuclei with position-sensitive gaseous detectors," PTEP 2021 (2021) no.1, 013C01 [arXiv:2009.05939 [physics.ins-det]].

[17] S. Knapen, J. Kozaczuk and T. Lin, "Migdal Effect in Semiconductors," Phys. Rev. Lett. 127 (2021) no.8, 081805 [arXiv:2011.09496 [hep-ph]].

[18] W. Wang, K. Y. Wu, L. Wu, and B. Zhu, "Direct detection of spin-dependent sub-GeV dark matter via Migdal effect," Nucl. Phys. B 983 (2022) 115907 [arXiv:2112.06492 [hep-ph]].

[19] P. W. Graham, R. Harnik, S. Rajendran and P. Saraswat, "Exothermic Dark Matter," Phys. Rev. D 82 (2010) 063512 [arXiv:1004.0937 [hep-ph]]; G. Barello, S. Chang and C. A. Newby, "A Model Independent Approach to Inelastic Dark Matter Scattering," Phys. Rev. D 90 (2014) 094027 [arXiv:1409.0536 [hep-ph]]; E. Del Nobile, G. B. Gelmini, A. Georgescu and J. H. Huh, "Reevaluation of spin-dependent WIMP-proton interactions as an explanation of the DAMA data," JCAP 1508 (2015) 046 [arXiv:1502.07682 [hep-ph]]; M. Baryakhtar, A. Berlin, H. Liu and N. Weiner, "Electromagnetic signals of inelastic dark matter scattering," JHEP 06 (2022) 047 [arXiv:2006.13918 [hep-ph]]; M. Carrillo González and N. Toro, "Cosmology and signals of light pseudo-Dirac dark matter," JHEP 04 (2022) 060 [arXiv:2108.13422 [hep-ph]].

[20] H. J. He, Y. C. Wang and J. Zheng, "EFT Approach of Inelastic Dark Matter for Xenon Electron Recoil Detection", JCAP 01 (2021) 042 [arXiv:2007.04963 [hep-ph]].

[21] H. J. He, Y. C. Wang and J. Zheng, "GeV-scale inelastic dark matter with dark photon mediator via direct detection and cosmological and laboratory constraints", Phys. Rev. D 104 (2021) no.11, 115033 [arXiv:2012.05891 [hep-ph]].

[22] I. M. Bloch, A. Caputo, R. Essig, D. Redigolo, M. Sholapurkar and T. Volansky, "Exploring new physics with O(keV) electron recoils in direct detection experiments," JHEP 01 (2021) 178 [arXiv:2006.14521 [hep-ph]].

[23] J. Bramante and N. Song, "Electric But Not Eclectic: Thermal Relic Dark Matter for the XENON1T Excess," Phys. Rev. Lett. 125 (2020) no.16, 161805 [arXiv:2006.14089 [hep-ph]].

[24] J. Engel and P. Vogel, "Spin dependent cross-sections of weakly interacting massive particles on nuclei," Phys. Rev. D 40 (1989) 3132-3135; J. Engel, "Nuclear form-factors for the scattering of weakly interacting massive particles," Phys. Lett. B 264 (1991) 114-119; F. Iachello, L. M. Krauss and G. Maino, "Spin Dependent Scattering of Weakly Interacting Massive Particles in Heavy Nuclei," Phys. Lett. B 254 (1991) 220-224.

[25] G. Jungman, M. Kamionkowski and K. Griest, "Supersymmetric dark matter," Phys. Rept. 267 (1996) 195-373 [arXiv:hep-ph/9506380].

[26] K. Griest, "Cross-Sections, Relic Abundance and Detection Rates for Neutralino Dark Matter," Phys. Rev. D 38 (1988) 2357 [erratum: D 39 (1989) 3802].

[27] J. D. Lewin and P. F. Smith, "Review of mathematics, numerical factors, and corrections for dark matter experiments based on elastic nuclear recoil," Astropart. Phys. 6 (1996) 87-112.

[28] B. M. Roberts, V. A. Dzuba, V. V. Flambaum, M. Pospelov and Y. V. Stadnik, "Dark matter scattering on electrons: Accurate calculations of atomic excitations and implications for the DAMA signal", Phys. Rev. D 93 (2016) 115037, no.11 [arXiv:1604.04559 [hep-ph]].

[29] B. M. Roberts and V. V. Flambaum, "Electron-interacting dark matter: Implications from DAMA/LIBRA-phase2 and prospects for liquid xenon detectors and NaI detectors", Phys. Rev. D 100 (2019) 063017, no.6 [arXiv:1904.07127 [hep-ph]].

[30] C. F. Bunge, J. A. Barrientos, and A. V. Bunge, Atomic Data and Nuclear Data Tables 53 (1993) 113.

[31] C. McCabe, "The Astrophysical Uncertainties Of Dark Matter Direct Detection Experiments," Phys. Rev. D 82 (2010) 023530 [arXiv:1005.0579 [hep-ph]].

[32] C. Savage, K. Freese and P. Gondolo, "Annual Modulation of Dark Matter in the Presence of Streams," Phys. Rev. D 74 (2006) 043531 [arXiv:astro-ph/0607121].

[33] N. F. Bell, J. B. Dent, B. Dutta, S. Ghosh, J. Kumar and J. L. Newstead, "Low-mass inelastic dark matter direct detection via the Migdal effect," Phys. Rev. D 104 (2021) no.7, 7 [arXiv:2103.05890 [hep-ph]].

[34] J. Li, L. Su, L. Wu, and B. Zhu, "Spin-dependent sub-GeV inelastic dark matter-electron scattering and Migdal effect. Part I. Velocity independent operator," JCAP 04 (2023) 020 [arXiv: 2210.15474 [hep-ph]].

[35] E. Aprile *et al.* [XENON Collaboration], "Low-energy Calibration of XENON1T with an Internal ^{37}Ar Source", Eur. Phys. J. C 83 (2023) no.6, 542 [arXiv:2211.14191 [physics.ins-det]].

[36] N. Aghanim *et al.* [Planck Collaboration], "Planck 2018 results. VI. Cosmological parameters," Astron. Astrophys. 641 (2020) A6 [erratum: Astron. Astrophys. 652 (2021) C4] [arXiv:1807.06209 [astro-ph.CO]].

[37] M. Srednicki, R. Watkins and K. A. Olive, "Calculations of Relic Densities in the Early Universe," Nucl. Phys. B 310 (1988) 693.

[38] P. Gondolo and G. Gelmini, "Cosmic abundances of stable particles: Improved analysis," Nucl. Phys. B 360 (1991) 145.

[39] R.L. Workman *et al.* [Particle Data Group], "Review of Particle Physics," Prog. Theor. Exp. Phys. 2022 (2022) 083C01.

[40] G. Belanger, A. Mjallal and A. Pukhov, "Recasting direct detection limits within micrOMEGAs and implication for non-standard Dark Matter scenarios," Eur. Phys. J. C 81 (2021) no.3, 239 [arXiv:2003.08621 [hep-ph]].

[41] T. R. Slatyer, N. Padmanabhan and D. P. Finkbeiner, "CMB Constraints on WIMP Annihilation: Energy Absorption During the Recombination Epoch," Phys. Rev. D 80 (2009) no.4, 043526 [arXiv:0906.1197 [astro-ph.CO]].

[42] T. R. Slatyer, "Indirect dark matter signatures in the cosmic dark ages. I. Generalizing the bound on s-wave dark matter annihilation from Planck results," Phys. Rev. D 93 (2016) no.2, 023527 [arXiv:1506.03811 [hep-ph]].

[43] Y. M. Andreev *et al.* [NA64 Collaboration], "Search for Light Dark Matter with NA64 at CERN," Phys. Rev. Lett. 131 (2023) no.16, 161801 [arXiv:2307.02404 [hep-ex]].

[44] J. P. Lees *et al.* [BaBar Collaboration], "Search for a Dark Photon in e^+e^- Collisions at BaBar," Phys. Rev. Lett. 113 (2014) no.20, 201801 [arXiv:1406.2980 [hep-ex]].

[45] A. Anastasi *et al.* [KLOE-2 Collaboration], "Limit on the production of a new vector boson in $e^+e^- \to \mathrm{U}\gamma$, $\mathrm{U} \to \pi^+\pi^-$ with the KLOE experiment," Phys. Lett. B 757 (2016) 356-361 [arXiv: 1603.06086 [hep-ex]].

[46] R. Aaij *et al.* [LHCb Collaboration], "Search for $A' \to \mu^+\mu^-$ Decays," Phys. Rev. Lett. 124 (2020) no.4, 041801 [arXiv:1910.06926 [hep-ex]].

Prepared for submission to JHEP

TTP24-004, P3H-24-014

arXiv:2403.03078v1 [hep-ph] 5 Mar 2024

N-jettiness soft function at next-to-next-to-leading order in perturbative QCD

Prem Agarwal,[a] Kirill Melnikov,[a] and Ivan Pedron[a,b]

[a] *Institute for Theoretical Particle Physics, KIT, 76128 Karlsruhe, Germany*
[b] *Institute for Astroparticle Physics, KIT, 76344 Eggenstein-Leopoldshafen, Germany*

Abstract: We derive a compact representation of the *renormalized* N-jettiness soft function that is free of infrared and collinear divergences through next-to-next-to-leading order in perturbative QCD. The number of hard partons N is a parameter in the formula for the finite remainder. Cancellation of all infrared and collinear singularities between the bare soft function and its renormalization matrix in color space is demonstrated analytically.

Contents

1 Introduction **1**

2 Definitions of basic quantities **2**

3 Renormalization of the soft function **4**

4 N-jettiness soft function at NLO **5**

5 N-jettiness soft function at NNLO **7**

6 Uncorrelated emissions of two soft gluons **9**

7 Terms with three color charges **10**

8 The remaining contributions **12**

9 Correlated emissions of two soft gluons: the strongly ordered limit **13**

10 Collinear subtractions **17**
10.1 The double-collinear $\mathfrak{m}||\mathfrak{n}$ contribution with N-jettiness constraint 20
10.2 The triple-collinear subtraction term with N-jettiness constraint 24

11 Correlated emissions without N-jettiness constraint **27**
11.1 Strongly-ordered limit without N-jettiness constraint 27
11.2 Double-collinear limit without N-jettiness constraint 29
11.3 Triple-collinear limit without N-jettiness constraint 29
11.4 Extracting the required combinations of the various contributions 30

12 Final-state fermions **32**

13 The renormalized N-jettiness soft function **36**

14 Numerical implementations and checks **38**

15 Conclusions **39**

A Renormalization of the soft function **40**

B Useful phase space integrals **40**

C Eikonal functions **41**

D Numerical Checks of N-Jettiness Soft Functions **41**
D.1 1-Jettiness 42
D.2 2-jettiness 42
D.3 3-jettiness 43

1 Introduction

The need for precise description of high-multiplicity final states produced in hard processes at the Large Hadron Collider (LHC) led to many studies of the so-called subtraction and slicing schemes for perturbative QCD computations [1–30]. The role of these schemes is to enable cancellation of infrared and collinear divergences between virtual and real contributions to cross sections without compromising the fully-differential nature of theoretical predictions.

In spite of the fact that slicing and subtraction schemes aim at achieving identical goals, their discussions in the literature proceed quite differently. Indeed, a typical pathway to the construction of a subtraction scheme involves studies of how factorization of matrix elements in the soft and collinear limits, and factorization of phase spaces for final-state particles can be combined to make the subtraction terms both observable-independent and analytically (or numerically) integrable in d-dimensions.[1] On the contrary, advanced slicing schemes start from the choice of an observable for which physical cross sections factorize into universal quantities, in the limit where the selected observable is small.

In spite of a somewhat different philosophy, it is clear that a very tight connection between slicing and subtraction approaches must exist since variables employed for slicing calculations are infrared safe. It follows that a differential cross section for the small value of the selected slicing parameter – which can be considered as the major quantity to understand in order to enable the construction of a slicing scheme – should be computable with subtractions.

We believe that existing computations in the context of existing slicing schemes do not make this connection sufficiently clear and do not exploit it. To see this, consider available computations of the N-jettiness soft function at next-to-leading (NLO) [16] and at next-to-next-to-leading order (NNLO) [17, 18, 31–37] in perturbative QCD. These computations are performed by mapping the available phase space of soft-gluon emissions onto hemispheres along the different hard directions, computing many of the required integrals numerically, and studying cancellation of infrared and collinear divergences against the soft-function renormalization matrix *a posteriori*. Furthermore, the soft-function renormalization matrix is constructed from the *consistency requirement* that soft and collinear divergences cancel when different elements of the factorization theorem (the hard function, the beam function, the jet function and the soft function) are combined to produce a physical cross section. While this computational method works fine in practice, it is in stark contrast with the

[1] We use dimensional regularization throughout this paper and assume that $d = 4 - 2\epsilon$.

current developments in understanding subtraction schemes where one attempts to find suitable subtraction terms for a generic N-jet problem, integrate them over unresolved phase spaces, show analytically the cancellation of all the $1/\epsilon$ poles and derive a compact representation for the finite remainder [24, 38].

The goal of this paper is to show that borrowing certain ideas from the recent developments in constructing generic NNLO QCD subtraction schemes [38] is beneficial for computing essential ingredients for modern slicing computations. Our prime example is the N-jettiness soft function [16] at NNLO QCD that we study for a *generic value of* N. We analytically demonstrate the cancellation of all soft and collinear $1/\epsilon$ divergences that appear in the calculation of the N-jettiness soft function against the corresponding renormalization constant, and derive a simple formula for the finite remainder that is valid in four space-time dimensions. We note that very recently a calculation of N-jettiness soft function for arbitrary N was reported in Ref. [37]. The computational method used in that reference is, however, very different from ours since it relies on the extension of numerical methods developed in Refs. [35, 39–41].

The remainder of the paper is organized as follows. In the next Section we define the N-jettiness variable [42] and the soft function that we study in this paper. In Section 3 we discuss the renormalization of the soft function. We continue with the calculation of the N-jettiness soft function at NLO QCD in Section 4. We then proceed to the analysis of the NNLO case. We start by discussing in Section 5 how the NNLO QCD computation of the N-jettiness soft function can be organized. We first focus on the two-gluon final state. We discuss the contribution of the uncorrelated emissions of two soft gluons in Section 6. We analyze the triple-color correlated terms in N-jettiness soft function in Section 7. Correlated emissions of two gluons are discussed in Sections 8, 9, 10 and 11. We study the contribution of the soft $q\bar{q}$ pair to N-jettiness soft function in Section 12. The final result for the soft function can be found in Section 13. Numerical implementation and comparison with results available in the literature is described in Section 14. We conclude in Section 15. Some useful formulas are collected in appendices.

2 Definitions of basic quantities

We consider partonic processes with an arbitrary number of hard color-charged partons that we denote by N

$$\begin{aligned} &0 \to h_1 + h_2 + h_3 + h_4 + \cdots h_N, \\ &h_1 \to h_2 + h_3 + h_4 + \cdots h_N, \\ &h_1 + h_2 \to h_3 + h_4 + \cdots h_N. \end{aligned} \tag{2.1}$$

The first process refers to e^+e^- annihilation, the second to deep-inelastic scattering and the third to hadron collisions. Each parton in Eq. (2.1) carries a four-momentum p_i and a color charge $\mathbf{T_i}$. All partons are assumed to be massless.

The cross sections of processes shown in Eq. (2.1) are affected by the radiation of soft quarks and gluons, both real and virtual. To quantify their impact, an observable that

controls the softness of the radiation is needed. In this paper, we will use the N-jettiness $\mathcal{T}$ [42] for this purpose.

To define $\mathcal{T}$, we proceed as follows. For a generic process, we split all final-state partons that we have to consider in a particular order of perturbation theory into resolved $\mathcal{R}$ and unresolved $\mathcal{U}$ ones. We define a list

$$L_x = \left\{ \frac{2p_x p_{h_1}}{P_{h_1}}, \frac{2p_x p_{h_2}}{P_{h_2}}, \frac{2p_x p_{h_3}}{P_{h_3}} ... \right\}, \tag{2.2}$$

where $x \in \mathcal{U}$ and $h_i \in \mathcal{R}$. Quantities P_{h_i} are arbitrary normalization constants. We then define the N-jettiness variable as [42]

$$\mathcal{T}(\mathcal{R},\mathcal{U}) = \sum_{x\in\mathcal{U}} \min\left[L_x\right]. \tag{2.3}$$

To compute radiative corrections to processes in Eq. (2.1), we need to consider virtual and real-emission corrections. Since we work through next-to-next-to-leading order, we need to include virtual corrections up to two loops, one-loop corrections with and without one soft parton and the real emission processes with up to two soft partons. For virtual corrections to processes without additional soft radiation, $\mathcal{U}$ is an empty set and so $\mathcal{T}$ is zero. The same is true for leading order processes shown in Eq. (2.1).

We note that virtual corrections do not need to be computed explicitly. Indeed, since infrared and collinear singularities of a generic two-loop amplitude are known [43–45], it is customary to separate them from the short-distance contribution to the two-loop amplitude known as the "hard function" and include them into the renormalization constant of the soft function, that we discuss in the next section. Hence, to compute the soft function at NNLO we need to study contributions with one or two soft partons to cross sections of processes in Eq. (2.1), subject to N-jettiness constraint.

The perturbative expansion of the *bare* soft function can be written as

$$S_\tau(\tau) = \delta(\tau) + a_s S_{\tau,1}(\tau) + a_s^2 S_{\tau,2}(\tau) + \cdots, \tag{2.4}$$

where τ is the value of N-jettiness and $a_s = \alpha_s(\mu)/(2\pi)$ is the renormalized QCD coupling constant. The quantities $S_{\tau,i}(\tau)$, $i = 1, 2$, can be computed starting from universal functions that describe the behaviour of QCD matrix elements when some of the radiated partons are soft.

Before proceeding, it is useful to point out that it is very convenient to work with the Laplace transform of the soft function [37]. The Laplace transform is defined as follows

$$S(u) = \int_0^\infty \mathrm{d}\tau\; S_\tau(\tau) e^{-u\tau}. \tag{2.5}$$

As we will see from the explicit computations described below, the dependence of functions $S_{\tau,i}$, $i = 1, 2$, on τ is very particular and is given by simple powers $\tau^{-1-n\epsilon}$, where $n = 2, 4$

etc. For these functions, the Laplace transform evaluates to

$$\int_0^\infty \mathrm{d}\tau\ \tau^{-1-n\epsilon} e^{-u\tau} = -u^{n\epsilon}\frac{\Gamma(1-n\epsilon)}{n\epsilon} = -\frac{\bar{u}^{n\epsilon} e^{-\epsilon n\gamma_{\mathrm{E}}}\Gamma(1-n\epsilon)}{n\epsilon}. \tag{2.6}$$

Note that in the last step we introduced a variable $\bar{u} = ue^{\gamma_E}$ to simplify the expansion of the corresponding Γ-functions in ϵ. In what follows we will use Eq. (2.6) to compute the Laplace transform of the perturbative expansion of the bare soft function.

3 Renormalization of the soft function

Perturbative computations of the soft function lead to expressions that contain soft and collinear divergences that manifest themselves through $1/\epsilon$ poles. These divergences are removed by a dedicated renormalization [16].

The renormalization of the soft function is a multiplicative (matrix) renormalization in the Laplace space [37]. We denote the Laplace transforms of the bare and renormalized soft functions by S and $\tilde{S}$, respectively. The two functions are related by the following equation

$$S = Z\tilde{S}Z^{+}, \tag{3.1}$$

where Z is a matrix in color space, see Appendix A. While it is entirely possible to compute the unrenormalized soft function S and then remove the divergences by using Eq. (3.1), it is beneficial to study suitable combinations of Z and S that are actually needed for computing $\tilde{S}$.

To find these combinations, we write expansions of Z, S and $\tilde{S}$ in powers of α_s

$$\begin{aligned} Z &= 1 + Z_1 + Z_2, \\ S &= 1 + S_1 + S_2, \\ \tilde{S} &= 1 + \tilde{S}_1 + \tilde{S}_2, \end{aligned} \tag{3.2}$$

substitute them into Eq. (3.1) and solve for $\tilde{S}_{1,2}$. We find

$$\begin{aligned} \tilde{S}_1 &= S_1 - Z_1 - Z_1^{+}, \\ \tilde{S}_2 &= S_2 - Z_2 - Z_2^{+} + Z_1 Z_1 + Z_1^{+} Z_1^{+} - Z_1 S_1 - S_1 Z_1^{+} + Z_1 Z_1^{+}. \end{aligned} \tag{3.3}$$

It was recently pointed out in Ref. [38], in the context of the application of the nested soft-collinear subtraction scheme to arbitrary multi-jet processes, that it is beneficial to separate iterations of $\mathcal{O}(\alpha_s)$ soft, soft-collinear and virtual contributions to cross sections from the rest of NNLO contributions. Following the same logic, we write

$$S_2 = \frac{1}{2} S_1 S_1 + S_{2,r}. \tag{3.4}$$

It is useful to do the same for the NNLO contribution to the renormalization matrix

$$Z_2 = \frac{1}{2} Z_1 Z_1 + Z_{2,r}. \tag{3.5}$$

It is then easy to see that $\tilde{S}_2$ can be written as

$$\tilde{S}_2 = \frac{1}{2}\tilde{S}_1\tilde{S}_1 + \frac{1}{2}[Z_1, Z_1^+] + \frac{1}{2}\left[S_1, Z_1 - Z_1^+\right] + S_{2,r} - Z_{2,r} - Z_{2,r}^+. \tag{3.6}$$

We will show below that this representation is beneficial for computing the renormalized N-jettiness soft function. Indeed, when representation in Eq. (3.6) is used, the required effort is minimized because cancellations of $1/\epsilon$ poles between the different quantities are identified relatively early in the course of the computation. However, before discussing how the NNLO computation is performed, we will illustrate our approach by calculating the NLO contribution to the N-jettiness soft function.

4 N-jettiness soft function at NLO

We will explain main ideas of our approach by considering N-jettiness soft function at NLO. Since one-loop virtual corrections to N-jettiness soft function do not need to be considered, we focus on the single real-emission contribution below. We use label $\mathfrak{m}$ to denote a soft gluon and write its momentum as $p_\mathfrak{m}$. The gluon $\mathfrak{m}$ is the only unresolved parton, therefore $\mathcal{U} = \{\mathfrak{m}\}$.

We choose $P_{h_i} = E_i$, where E_i is the energy of the parton h_i in the chosen reference frame, and obtain (c.f. Eqs. (2.2,2.3))

$$\mathcal{T}(\mathfrak{m}) = E_\mathfrak{m}\psi_\mathfrak{m}. \tag{4.1}$$

In Eq. (4.1) $E_\mathfrak{m}$ is the energy of the unresolved gluon $\mathfrak{m}$ and $\psi_\mathfrak{m}$ is a function defined as

$$\psi_\mathfrak{m} = \min\{\rho_{1\mathfrak{m}}, \rho_{2\mathfrak{m}}, \rho_{3\mathfrak{m}}, ..., \rho_{N\mathfrak{m}}\}, \tag{4.2}$$

where $\rho_{ij} = 1 - \vec{n}_i \cdot \vec{n}_j$ and $\vec{n}_i$ is a unit vector which points in the direction of the three-momentum of parton i.

The real-emission single-gluon soft contribution at fixed N-jettiness τ reads

$$S_{\tau,1}(\tau) = -\sum_{(ij)} \mathbf{T}_i \cdot \mathbf{T}_j \, I^{(1)}_{S,ij}(\tau), \tag{4.3}$$

where we use the notation (ij) to indicate that the sum runs over all $i, j \in \mathcal{R}$ with the constraint $i \neq j$. Furthermore, $\mathbf{T}_i$ is the color charge operator of parton i,

$$I^{(1)}_{S,ij} = g_s^2 \int [\mathrm{d}p_\mathfrak{m}] \, \delta(\tau - E_\mathfrak{m}\psi_\mathfrak{m}) \, S_{ij}(\mathfrak{m}), \tag{4.4}$$

g_s is the bare QCD coupling constant and

$$S_{ij}(\mathfrak{m}) = \frac{p_i p_j}{(p_i p_\mathfrak{m})(p_j p_\mathfrak{m})} = \frac{1}{E_\mathfrak{m}^2} \frac{\rho_{ij}}{\rho_{i\mathfrak{m}}\rho_{j\mathfrak{m}}}, \tag{4.5}$$

is the soft eikonal function. It is convenient to write the phase space element of the gluon $\mathfrak{m}$ as follows

$$[\mathrm{d}p_m] = \frac{\mathrm{d}\Omega_\mathfrak{m}^{(d-1)}}{2(2\pi)^{d-1}} \frac{\mathrm{d}E_\mathfrak{m}}{E_\mathfrak{m}^{1+2\epsilon}} E_\mathfrak{m}^2 = \frac{\Omega^{(d-2)}}{2(2\pi)^{d-1}} [\mathrm{d}\Omega_\mathfrak{m}^{(d-1)}] \frac{\mathrm{d}E_\mathfrak{m}}{E_\mathfrak{m}^{1+2\epsilon}} E_\mathfrak{m}^2. \tag{4.6}$$

We then combine the coupling constant squared with the remnant of phase space normalization factor

$$g_s^2 \frac{\Omega^{(d-2)}}{2(2\pi)^{d-1}} = [\alpha_s], \tag{4.7}$$

and note that

$$[\alpha_s] = a_s(\mu)\, \mu^{2\epsilon} \frac{e^{\gamma_E \epsilon}}{\Gamma(1-\epsilon)} \left(1 + \mathcal{O}(a_s)\right), \tag{4.8}$$

where $a_s(\mu) = \alpha_s(\mu)/(2\pi)$ and $\alpha_s(\mu)$ is the QCD coupling constant renormalized in the $\overline{\text{MS}}$ scheme.

We work to first order in a_s and use Eq. (4.6) to integrate over energy of the gluon $E_{\mathfrak{m}}$ in Eq. (4.4). We find

$$I^{(1)}_{S,ij}(\tau) = \frac{[\alpha_s]}{\tau^{1+2\epsilon}} \int [\mathrm{d}\Omega^{(d-1)}_{\mathfrak{m}}]\; \psi_{\mathfrak{m}}^{2\epsilon} \frac{\rho_{ij}}{\rho_{i\mathfrak{m}}\rho_{j\mathfrak{m}}} = \frac{[\alpha_s]}{\tau^{1+2\epsilon}} \left\langle \psi_{\mathfrak{m}}^{2\epsilon} \frac{\rho_{ij}}{\rho_{i\mathfrak{m}}\rho_{j\mathfrak{m}}} \right\rangle_{\mathfrak{m}}, \tag{4.9}$$

where $\langle .. \rangle_{\mathfrak{m}}$ indicates integration over directions of the vector $\vec{n}_{\mathfrak{m}}$.

To proceed further, we compute the Laplace transform of the soft function and obtain

$$S_1 = \frac{\bar{u}^{2\epsilon} e^{-2\epsilon\gamma_{\mathrm{E}}} \Gamma(1-2\epsilon)}{2\epsilon} [\alpha_s] \sum_{(ij)} \mathbf{T}_i \cdot \mathbf{T}_j \left\langle \psi_{\mathfrak{m}}^{2\epsilon} \frac{\rho_{ij}}{\rho_{i\mathfrak{m}}\rho_{j\mathfrak{m}}} \right\rangle_{\mathfrak{m}}. \tag{4.10}$$

Integration over directions of the vector $\vec{n}_{\mathfrak{m}}$ induces collinear singularities when $\vec{n}_{\mathfrak{m}} || \vec{n}_i$ and $\vec{n}_{\mathfrak{m}} || \vec{n}_j$. To isolate them, we make use of the fact that collinear singularities of the integrand are fully controlled by the remnants of the eikonal function in Eq. (4.10) and that the collinear limits of the function $\psi_{\mathfrak{m}}$ can be predicted for an *arbitrary hard process*.

Indeed, consider the collinear limit $\mathfrak{m}||i$ as an example. In that limit, $\rho_{i\mathfrak{m}}$ is the smallest ρ-value so that

$$\lim_{\mathfrak{m}||i} \psi_{\mathfrak{m}} = \rho_{i\mathfrak{m}}. \tag{4.11}$$

It turns out useful to rewrite the integrand in Eq. (4.9) as follows

$$\psi_{\mathfrak{m}}^{2\epsilon} \frac{\rho_{ij}}{\rho_{i\mathfrak{m}}\rho_{j\mathfrak{m}}} = \left(\frac{\psi_{\mathfrak{m}}\rho_{ij}}{\rho_{i\mathfrak{m}}\rho_{j\mathfrak{m}}}\right)^{2\epsilon} \frac{\rho_{ij}^{1-2\epsilon}}{\rho_{i\mathfrak{m}}^{1-2\epsilon}\rho_{j\mathfrak{m}}^{1-2\epsilon}}. \tag{4.12}$$

We then define

$$\left(\frac{\psi_{\mathfrak{m}}\rho_{ij}}{\rho_{i\mathfrak{m}}\rho_{j\mathfrak{m}}}\right)^{2\epsilon} = 1 + 2\epsilon g^{(2)}_{ij,\mathfrak{m}}, \tag{4.13}$$

where the function $g^{(\alpha)}_{ij,\mathfrak{m}}$ contains higher powers of ϵ in addition to the first power shown explicitly. Hence, we write

$$\left\langle \psi_{\mathfrak{m}}^{2\epsilon} \frac{\rho_{ij}}{\rho_{i\mathfrak{m}}\rho_{j\mathfrak{m}}} \right\rangle_{\mathfrak{m}} = \left\langle \left(1 + 2\epsilon g^{(2)}_{ij,\mathfrak{m}}\right) \frac{\rho_{ij}^{1-2\epsilon}}{\rho_{i\mathfrak{m}}^{1-2\epsilon}\rho_{j\mathfrak{m}}^{1-2\epsilon}} \right\rangle_{\mathfrak{m}}. \tag{4.14}$$

Since the function $\epsilon g^{(2)}_{ij,m}$ vanishes in all collinear limits and is $\mathcal{O}(\epsilon)$, it only provides a finite contribution to the N-jettiness soft function that will have to be computed numerically for

a given configuration of hard partons. On the contrary, the first integral in the right-hand side of Eq. (4.14) can be computed explicitly, see Eq. (B.5). We write

$$\left\langle \frac{\rho_{ij}^{1-2\epsilon}}{\rho_{i\mathfrak{m}}^{1-2\epsilon}\rho_{j\mathfrak{m}}^{1-2\epsilon}} \right\rangle_{\mathfrak{m}} = \frac{2\eta_{ij}^{\epsilon}}{\epsilon} K_{ij}^{(2)}, \tag{4.15}$$

where $\eta_{ij} = \rho_{ij}/2$ and

$$K_{ij}^{(2)} = \frac{\Gamma(1+\epsilon)^2}{\Gamma(1+2\epsilon)}\, {}_2F_1\left(\epsilon, \epsilon, 1-\epsilon, 1-\eta_{ij}\right). \tag{4.16}$$

Putting everything together, we find

$$S_1 = a_s\, (\mu\bar{u})^{2\epsilon}\, \frac{\Gamma(1-2\epsilon)}{\Gamma(1-\epsilon)e^{\epsilon\gamma_E}} \sum_{(ij)} \mathbf{T}_i \cdot \mathbf{T}_j \left[\frac{\eta_{ij}^{\epsilon}}{\epsilon^2} K_{ij}^{(2)} + \left\langle g_{ij,\mathfrak{m}}^{(2)}\, \frac{\rho_{ij}^{1-2\epsilon}}{\rho_{i\mathfrak{m}}^{1-2\epsilon}\rho_{j\mathfrak{m}}^{1-2\epsilon}} \right\rangle_{\mathfrak{m}} \right], \tag{4.17}$$

It follows from the above equation that all $1/\epsilon$ poles have been separated from the finite remainder and that the remnant of the complicated N-jettiness function appears in the finite remainder *only*.

It remains to combine S_1 with the renormalization matrices Z_1 and Z_1^+, c.f. Eq. (3.3). The expression for Z_1 can be found in Appendix A; similar to the NLO soft function shown in Eq. (4.17), it is given by the sum of products of the color-charge operators with some coefficients. Combining the different contributions and discarding all terms beyond $\mathcal{O}(\epsilon^0)$, we find

$$\tilde{S}_1 = a_s \sum_{(ij)} \mathbf{T}_i \cdot \mathbf{T}_j \left[2L_{ij}^2 + \mathrm{Li}_2(1-\eta_{ij}) + \frac{\pi^2}{12} + \left\langle \ln\left(\frac{\psi_{\mathfrak{m}}\rho_{ij}}{\rho_{i\mathfrak{m}}\rho_{j\mathfrak{m}}}\right) \frac{\rho_{ij}}{\rho_{i\mathfrak{m}}\rho_{j\mathfrak{m}}} \right\rangle_{\mathfrak{m}} + \mathcal{O}(\epsilon) \right], \tag{4.18}$$

where

$$L_{ij} = \ln\left(\mu\bar{u}\sqrt{\eta_{ij}}\right). \tag{4.19}$$

This result can be easily evaluated numerically for an arbitrary number of hard partons N. The logarithm $\ln(\psi_{\mathfrak{m}}\rho_{ij}/(\rho_{i\mathfrak{m}}\rho_{j\mathfrak{m}}))$ provides an infrared regulator for an integral that would have exhibited collinear divergencies without it.

5 *N*-jettiness soft function at NNLO

We will now explain how to extend the above approach to compute the NNLO contribution to the N-jettiness soft function. It is clear that the NNLO computation is significantly more complex than the NLO one. However, we will show that it is possible to split the calculation into several independent parts making the entire problem simpler.

The NNLO contribution to the bare soft function reads

$$S_2 = S_{2,RR} + S_{2,RV} - a_s\, \frac{\beta_0}{\epsilon} S_1, \tag{5.1}$$

where $S_{2,RR}$ is the double real-emission contribution, $S_{2,RV}$ is the real-virtual contribution and the last term arises because of the renormalization of the strong coupling constant in the NLO soft function. The leading order QCD β-function is defined as

$$\beta_0 = \frac{11}{6}C_A - \frac{2}{3}n_F T_R, \tag{5.2}$$

where $C_A = N_c$ is the Casimir of the group $SU(N_c)$, $T_R = 1/2$ and n_f is the number of massless quarks.

The double-real emission contribution is obtained by integrating the double-soft eikonal current [46] over the phase space of two soft gluons subject to the N-jettiness constraint. Following Ref. [46], we further split the double-real contribution into correlated and uncorrelated pieces

$$S_{2,RR,\tau} = S_{2,RR,\tau,T^4} + S_{2,RR,\tau,T^2}. \tag{5.3}$$

We note that the subscript τ indicates that the Laplace transform of the corresponding quantities has not yet been computed.

The uncorrelated contribution reads

$$S_{2,RR,\tau,T^4} = \frac{1}{2}\sum_{(ij),(k,l)} \{\mathbf{T}_i\cdot\mathbf{T}_j, \mathbf{T}_k\cdot\mathbf{T}_l\}\, I_{T^4,ij,kl}, \tag{5.4}$$

where

$$I_{T^4,ij,kl} = \frac{g_s^4}{2}\int [\mathrm{d}p_{\mathfrak{m}}]\,[\mathrm{d}p_{\mathfrak{n}}]\delta(\tau - E_{\mathfrak{m}}\psi_{\mathfrak{m}} - E_{\mathfrak{n}}\psi_{\mathfrak{n}})\, S_{ij}(\mathfrak{m})\, S_{kl}(\mathfrak{n}), \tag{5.5}$$

and the eikonal functions $S_{ij}(\mathfrak{m})$ and $S_{kl}(\mathfrak{n})$ are defined in Eq. (4.5). The correlated contribution S_{2,RR,T^2} reads

$$S_{2,RR,\tau,T^2} = -\frac{C_A}{2}\sum_{(ij)} \mathbf{T}_i\cdot\mathbf{T}_j\, I_{T^2,ij}, \tag{5.6}$$

where

$$I_{T^2,ij} = \frac{g_s^4}{2}\int [\mathrm{d}p_{\mathfrak{m}}][\mathrm{d}p_{\mathfrak{n}}]\delta(\tau - E_{\mathfrak{m}}\psi_{\mathfrak{m}} - E_{\mathfrak{n}}\psi_{\mathfrak{n}})\tilde{S}_{ij}^{gg}(\mathfrak{m},\mathfrak{n}). \tag{5.7}$$

The eikonal function $\tilde{S}_{ij}^{gg}(\mathfrak{m},\mathfrak{n})$ can be found in Appendix C.

The real-virtual contribution reads [46]

$$S_{2,RV,\tau} = \frac{[\alpha_s]\,2^{-\epsilon}}{\epsilon^2}C_A A_K(\epsilon)\sum_{(ij)} \mathbf{T}_i\cdot\mathbf{T}_j\, I_{RV,ij} + [\alpha_s]\frac{4\pi N_\epsilon}{\epsilon}\sum_{(kij)}\kappa_{ij}F^{kij}I_{kij}. \tag{5.8}$$

where

$$\kappa_{ij} = \lambda_{ij} - \lambda_{i\mathfrak{m}} - \lambda_{j\mathfrak{m}}, \tag{5.9}$$

and $\lambda_{ij} = 1$ if both i and j refer to incoming or outgoing partons and zero otherwise. Furthermore, the normalization factors in Eq. (5.8) read

$$A_K(\epsilon) = \frac{\Gamma^3(1+\epsilon)\Gamma^5(1-\epsilon)}{\Gamma(1+2\epsilon)\Gamma^2(1-2\epsilon)}, \quad N_\epsilon = \frac{\Gamma(1+\epsilon)\Gamma^3(1-\epsilon)}{\Gamma(1-2\epsilon)}, \tag{5.10}$$

and we have defined $F^{kij} = f_{abc}T_k^a T_i^b T_j^c$ to describe anti-symmetrized product of three color charge operators. Finally, the functions $I_{RV,ij}$ and I_{kij} read

$$I_{RV,ij} = g_s^2 \int [\mathrm{d}p_{\mathfrak{m}}]\delta(\tau - E_{\mathfrak{m}}\psi_{\mathfrak{m}})(S_{ij}^{gg}(\mathfrak{m}))^{1+\epsilon}, \tag{5.11}$$

and

$$I_{kij} = g_s^2 \int [\mathrm{d}p_{\mathfrak{m}}]\delta(\tau - E_{\mathfrak{m}}\psi_{\mathfrak{m}})S_{ki}(\mathfrak{m})(S_{ij}^{gg}(\mathfrak{m}))^{\epsilon}. \tag{5.12}$$

In the next section we will show that

$$S_{2,RR,T^4} = \frac{1}{2}S_1 S_1. \tag{5.13}$$

Therefore, the quantity $S_{2,r}$ introduced in Eq. (3.4) reads

$$S_{2,r} = S_{2,RR,T^2} + S_{2,RV} - \frac{a_s\beta_0}{\epsilon}S_1. \tag{5.14}$$

6 Uncorrelated emissions of two soft gluons

We have argued that S_2 contains an iterated contribution of the next-to-leading order soft function S_1 and that it is beneficial to separate it from the rest of S_2, c.f. Eq. (3.4). We will now show that this iteration can be identified with the Laplace transform of the term S_{2,RR,τ,T^4} in Eq. (5.4). To this end, we write

$$I_{T^4,ij,kl} = \frac{[\alpha_s]^2}{2}\left\langle \int_0^\infty \frac{\mathrm{d}E_{\mathfrak{m}}}{E_{\mathfrak{m}}^{1+2\epsilon}}\frac{\mathrm{d}E_{\mathfrak{n}}}{E_{\mathfrak{n}}^{1+2\epsilon}}\,\delta(\tau - E_{\mathfrak{m}}\psi_{\mathfrak{m}} - E_{\mathfrak{n}}\psi_{\mathfrak{n}})\frac{\rho_{ij}}{\rho_{i\mathfrak{m}}\rho_{j\mathfrak{m}}}\frac{\rho_{kl}}{\rho_{k\mathfrak{n}}\rho_{l\mathfrak{n}}}\right\rangle_{\mathfrak{m}\mathfrak{n}}. \tag{6.1}$$

It is straightforward to integrate over energies of two gluons $E_{\mathfrak{m},\mathfrak{n}}$. Indeed, the first integration (say over $E_{\mathfrak{n}}$) is elementary since it just removes the δ-function. The second integration over $E_{\mathfrak{m}}$ extends from 0 to $E_{\mathfrak{m}}^{\max} = \tau/\psi_{\mathfrak{m}}$, i.e. the energy of the gluon $\mathfrak{m}$ which corresponds to $E_{\mathfrak{n}} = 0$. The integral turns out to be of a Beta-function type, and we obtain

$$\int_0^\infty \frac{\mathrm{d}E_{\mathfrak{m}}}{E_{\mathfrak{m}}^{1+2\epsilon}}\frac{\mathrm{d}E_{\mathfrak{n}}}{E_{\mathfrak{n}}^{1+2\epsilon}}\,\delta(\tau - E_{\mathfrak{m}}\psi_{\mathfrak{m}} - E_{\mathfrak{n}}\psi_{\mathfrak{n}}) = \frac{\tau^{-1-4\epsilon}}{\Gamma(-4\epsilon)}\frac{\psi_{\mathfrak{m}}^{2\epsilon}\Gamma(1-2\epsilon)}{2\epsilon}\frac{\psi_{\mathfrak{n}}^{2\epsilon}\Gamma(1-2\epsilon)}{2\epsilon}. \tag{6.2}$$

Using this result, and performing the Laplace transform, we derive

$$\begin{aligned} S_{2,RR,T^4} = \frac{[\alpha_s]^2}{4}\sum_{(ij),(kl)}\{\mathbf{T}_i\cdot\mathbf{T}_j, \mathbf{T}_k\cdot\mathbf{T}_l\}\left(\frac{u^{2\epsilon}\Gamma(1-2\epsilon)}{2\epsilon}\right)^2 \\ \times\left\langle \psi_{\mathfrak{m}}^{2\epsilon}\frac{\rho_{ij}}{\rho_{i\mathfrak{m}}\rho_{j\mathfrak{m}}}\right\rangle_{\mathfrak{m}}\left\langle \psi_{\mathfrak{n}}^{2\epsilon}\frac{\rho_{kl}}{\rho_{k\mathfrak{n}}\rho_{l\mathfrak{n}}}\right\rangle_{\mathfrak{n}} = \frac{1}{2}\,S_1 S_1, \end{aligned} \tag{6.3}$$

where the last step follows from the symmetry between (ij) and (kl) summation indices, and from the comparison with the results for the NLO N-jettiness soft function derived in Section 4. As we already explained in Section 3, it is straightforward to combine the above result with the iterated contribution of the renormalization constants to arrive at the relevant contribution to the renormalized soft function.

7 Terms with three color charges

We will next discuss the computation of the contribution that depends on triple products of color charges. It originates from the following terms in the expression for $\tilde{S}_2$

$$\tilde{S}_2^{tc} = \frac{1}{2}\left[Z_1, Z_1^+\right] + \frac{1}{2}\left[S_1, Z_1 - Z_1^+\right] + S_{RV,tc}, \tag{7.1}$$

where the real-virtual triple-color correlated contribution is given by the Laplace transform of the last term in Eq. (5.8).

The commutators are easy to compute using a general formula in Ref. [38].[2] We find

$$\frac{1}{2}[Z_1, Z_1^+] = -\frac{2\pi a_s^2}{\epsilon^2}\sum_{(kij)} \lambda_{kj} L_{ij} F^{kij} = -\frac{\pi a_s^2}{\epsilon^2}\sum_{(kij)} \lambda_{kj} \ln \eta_{ij}\; F^{kij}, \tag{7.2}$$

where the last step follows from the definition of L_{ij} in Eq. (4.19) and the (anti)-symmetry of F^{kij} with respect to permutations of its indices.

The second commutator reads

$$\begin{aligned}\frac{1}{2}[S_1, Z_1 - Z_1^+] &= \frac{a_s^2\pi(\mu u)^{2\epsilon}}{\epsilon^2}\frac{e^{\gamma_E\epsilon}\Gamma(1-2\epsilon)}{\Gamma(1-\epsilon)}\sum_{(kij)} \lambda_{kj}\left\langle \psi_{\mathfrak{m}}^{2\epsilon}\frac{\rho_{ij}}{\rho_{i\mathfrak{m}}\rho_{j\mathfrak{m}}}\right\rangle_{\mathfrak{m}} F^{kij} \\ &= -\frac{a_s^2\pi(\mu u)^{2\epsilon}}{\epsilon^2}\frac{e^{\gamma_E\epsilon}\Gamma(1-2\epsilon)}{\Gamma(1-\epsilon)}\sum_{(kij)} \lambda_{kj}\left\langle \psi_{\mathfrak{m}}^{2\epsilon}\frac{\rho_{ki}}{\rho_{k\mathfrak{m}}\rho_{i\mathfrak{m}}}\right\rangle_{\mathfrak{m}} F^{kij},\end{aligned} \tag{7.3}$$

where in the last step we replaced $k \leftrightarrow j$ and used the symmetry of λ_{kj} and the anti-symmetry of F^{kij}. Furthermore, it is convenient to replace λ_{kj} in the above expression with κ_{kj} defined in Eq. (5.9). This is possible because

$$\sum_{(kij)} \lambda_{j\mathfrak{m}}\left\langle \psi_{\mathfrak{m}}^{2\epsilon}\frac{\rho_{ki}}{\rho_{k\mathfrak{m}}\rho_{i\mathfrak{m}}}\right\rangle_{\mathfrak{m}} F^{kij} = \sum_{(kij)} \lambda_{k\mathfrak{m}}\left\langle \psi_{\mathfrak{m}}^{2\epsilon}\frac{\rho_{ki}}{\rho_{k\mathfrak{m}}\rho_{i\mathfrak{m}}}\right\rangle_{\mathfrak{m}} F^{kij} = 0. \tag{7.4}$$

The first of these equation holds because the summation over i and k involves a symmetric and an anti-symmetric tensor. The second is fulfilled because one can sum over j using conservation of color charges and use the antisymmetry of F^{kij} to set the resulting terms to zero. Hence, we can write

$$\frac{1}{2}[S_1, Z_1 - Z_1^+] = -\frac{a_s^2\pi(\mu u)^{2\epsilon}}{\epsilon^2}\frac{e^{\gamma_E\epsilon}\Gamma(1-2\epsilon)}{\Gamma(1-\epsilon)}\sum_{(kij)} \kappa_{kj}\left\langle \psi_{\mathfrak{m}}^{2\epsilon}\frac{\rho_{ki}}{\rho_{k\mathfrak{m}}\rho_{i\mathfrak{m}}}\right\rangle_{\mathfrak{m}} F^{kij}. \tag{7.5}$$

The real-virtual triple-color correlated contribution evaluates to

$$S_{RV,tc} = \frac{a_s^2\pi(\mu\,\bar{u})^{4\epsilon}N_\epsilon 2^{-\epsilon}}{2\epsilon^2}\frac{\Gamma(1-4\epsilon)}{\Gamma^2(1-\epsilon)e^{2\gamma_E\epsilon}}\sum_{(kij)} \kappa_{kj}\left\langle \psi_{\mathfrak{m}}^{4\epsilon}\frac{\rho_{ki}}{\rho_{k\mathfrak{m}}\rho_{i\mathfrak{m}}}\left(\frac{\rho_{kj}}{\rho_{k\mathfrak{m}}\rho_{j\mathfrak{m}}}\right)^{\epsilon}\right\rangle_{\mathfrak{m}} F^{kij}\,. \tag{7.6}$$

We need to combine the three contributions to $\tilde{S}_2^{tc}$ shown above, demonstrate that all $1/\epsilon$ poles cancel and derive a representation for the finite remainder. We will do this

[2] See Eqs. (4.142, 4.143).

in steps starting from contributions that exhibit dependence on the N-jettiness function. There are two such contributions – the commutator in Eq. (7.5) and $S_{RV,tc}$. We define

$$\Sigma^{\psi}_{\rm tcc} = \frac{1}{2}[S_1, Z_1 - Z_1^+] + S_{RV,tc}. \tag{7.7}$$

Both terms in Eq. (7.7) involve integrals of various combinations of ρ_{ij}'s and $\psi_{\mathfrak{m}}$ over the directions of the momentum of the gluon $\mathfrak{m}$. Following the discussion of the NLO contribution to the soft function, we write

$$\begin{aligned}
\left\langle \psi_{\mathfrak{m}}^{2\epsilon} \frac{\rho_{ki}}{\rho_{k\mathfrak{m}}\rho_{i\mathfrak{m}}} \right\rangle_{\mathfrak{m}} &= \left\langle (1 + 2\epsilon g^{(2)}_{ki,\mathfrak{m}}) \frac{\rho_{ki}^{1-2\epsilon}}{\rho_{k\mathfrak{m}}^{1-2\epsilon}\rho_{i\mathfrak{m}}^{1-2\epsilon}} \right\rangle_{\mathfrak{m}}, \\
\left\langle \psi_{\mathfrak{m}}^{4\epsilon} \frac{\rho_{ki}}{\rho_{k\mathfrak{m}}\rho_{i\mathfrak{m}}} \left(\frac{\rho_{kj}}{\rho_{k\mathfrak{m}}\rho_{j\mathfrak{m}}}\right)^{\epsilon} \right\rangle_{\mathfrak{m}} &= \left\langle \left(1 + 4\epsilon g^{(4)}_{ki,\mathfrak{m}}\right) \frac{\rho_{ki}^{1-4\epsilon}}{\rho_{k\mathfrak{m}}^{1-4\epsilon}\rho_{i\mathfrak{m}}^{1-4\epsilon}} \left(\frac{\rho_{kj}}{\rho_{k\mathfrak{m}}\rho_{j\mathfrak{m}}}\right)^{\epsilon} \right\rangle_{\mathfrak{m}}.
\end{aligned} \tag{7.8}$$

Using Eq. (7.8), and focusing on the *divergent* contributions that contain $g^{(2)}$ and $g^{(4)}$, we find

$$\Sigma^{\psi}_{\rm tcc} \to -\frac{2a_s^2\pi}{\epsilon} \sum_{(kij)} \kappa_{kj} \left\langle \frac{\rho_{ik}}{\rho_{i\mathfrak{m}}\rho_{k\mathfrak{m}}} \left(g^{(2)}_{ki,\mathfrak{m}} - g^{(4)}_{ki,\mathfrak{m}}\right) \right\rangle_{\mathfrak{m}} F^{kij} = \mathcal{O}(\epsilon^0), \tag{7.9}$$

where the last step follows from the equality $g^{(2)} = g^{(4)}$ through order $\mathcal{O}(\epsilon^0)$.

Extending the above computation in a straightforward way, we derive the finite N-jettiness-dependent triple-color correlated remainder. We obtain

$$\Sigma^{\psi}_{\rm tcc} \to 2a_s^2\pi \sum_{(kij)} \kappa_{kj} \left\langle \frac{\rho_{ki}}{\rho_{i\mathfrak{m}}\rho_{k\mathfrak{m}}} \ln\left(\frac{\psi_{\mathfrak{m}}\rho_{ki}}{\rho_{k\mathfrak{m}}\rho_{i\mathfrak{m}}}\right) \ln\left(\frac{(\bar{u}\mu)^2\psi_{\mathfrak{m}}\rho_{i\mathfrak{m}}\rho_{kj}}{2\rho_{j\mathfrak{m}}\rho_{ki}}\right) \right\rangle_{\mathfrak{m}} F^{kij}. \tag{7.10}$$

Next, we discuss triple-color correlated contributions that do not involve jettiness functions. The first one is given in Eq. (7.2); it contains explicit $1/\epsilon^2$ divergence and does not require further discussion. The second contribution is extracted from Eq. (7.5) using Eq. (7.8). The required angular integral is straightforward to compute and we do not discuss it further.

It is slightly more challenging to calculate a similar contribution to $S_{RV,tc}$. However, we can cast it into a form that allows us to expand it in powers of ϵ. The corresponding expression reads

$$\begin{aligned}
\left\langle \frac{\rho_{ki}^{1-4\epsilon}}{\rho_{k\mathfrak{m}}^{1-4\epsilon}\rho_{i\mathfrak{m}}^{1-4\epsilon}} \left(\frac{\rho_{kj}}{\rho_{k\mathfrak{m}}\rho_{j\mathfrak{m}}}\right)^{\epsilon} \right\rangle_{\mathfrak{m}} &= \left\langle \frac{\rho_{ki}^{1-4\epsilon}}{\rho_{k\mathfrak{m}}^{1-3\epsilon}\rho_{i\mathfrak{m}}^{1-4\epsilon}} \right\rangle_{\mathfrak{m}} + \left\langle \frac{\rho_{ki}^{-\epsilon}}{\rho_{i\mathfrak{m}}^{1-4\epsilon}} \left(\left(\frac{\rho_{kj}}{\rho_{ij}}\right)^{\epsilon} - 1\right) \right\rangle_{\mathfrak{m}} \\
&+ \left\langle \frac{\rho_{ki}^{1-4\epsilon}}{\rho_{k\mathfrak{m}}^{1-3\epsilon}\rho_{i\mathfrak{m}}^{1-4\epsilon}} \left(\left(\frac{\rho_{kj}}{\rho_{j\mathfrak{m}}}\right)^{\epsilon} - 1\right) - \frac{\rho_{ki}^{-\epsilon}}{\rho_{i\mathfrak{m}}^{1-4\epsilon}} \left(\left(\frac{\rho_{kj}}{\rho_{ij}}\right)^{\epsilon} - 1\right) \right\rangle_{\mathfrak{m}}.
\end{aligned} \tag{7.11}$$

The first two integrals on the right-hand side are straightforward to compute but the last one is challenging. Since this integral is $\mathcal{O}(\epsilon)$, it contributes to the divergence of the triple-color correlated term so that we need to analytically compute it.

The simplest way to do this is to use the results of Ref. [38] where the analytic expression for the following integral

$$\left\langle \frac{\rho_{ki}}{\rho_{k\mathfrak{m}}\rho_{i\mathfrak{m}}} \left(\frac{\rho_{kj}}{\rho_{k\mathfrak{m}}\rho_{j\mathfrak{m}}} \right)^{\epsilon} \right\rangle_{\mathfrak{m}}, \tag{7.12}$$

was derived. The idea is to rewrite the integral in Eq. (7.12) in the same way as the integral in Eq. (7.11) and then take the difference of the two results. Upon doing that, one finds that the complicated finite integral appears at order $\mathcal{O}(\epsilon^2)$ only; this integral can be computed *numerically* alongside with N-jettiness dependent contributions.

Putting everything together, we find that all divergences in triple-color correlated contributions cancel, and a finite result is obtained. It reads

$$\frac{1}{2}[Z_1, Z_1^+] + \frac{1}{2}[S_1, Z_1 - Z_1^+] + S_{RV,tc} = a_s^2 \pi \sum_{(kij)} F^{kij}\, \kappa_{kj} G_{kij}^{\text{triple}}, \tag{7.13}$$

where

$$\begin{aligned} G_{kij}^{\text{triple}} = \Bigg[& \frac{8}{3} L_{ki}^3 + 4 L_{ki} \left(\text{Li}_2(1-\eta_{ki}) + \frac{\pi^2}{12} + \left\langle \frac{\rho_{ki}}{\rho_{i\mathfrak{m}}\rho_{k\mathfrak{m}}} \ln\left(\frac{\psi_{\mathfrak{m}}\rho_{ki}}{\rho_{k\mathfrak{m}}\rho_{i\mathfrak{m}}} \right) \right\rangle_{\mathfrak{m}} \right) \\ & + 2\text{Li}_3(1-\eta_{ki}) - 6\text{Li}_3(\eta_{ki}) + \text{Li}_2(1-\eta_{ki})(2\ln 2 - 8\ln(\eta_{ki})) - \ln^3(\eta_{ki}) \\ & - 3\ln(1-\eta_{ki})\ln^2(\eta_{ki}) - \ln 2 \ln^2(\eta_{ki}) + \frac{\pi^2}{6}\ln(\eta_{ki}) - \bar{G}_{r,\text{fin}}^{ikj} - 2W_{kij} \\ & + 2\left\langle \frac{\rho_{ki}}{\rho_{i\mathfrak{m}}\rho_{k\mathfrak{m}}} \ln\left(\frac{\psi_{\mathfrak{m}}\rho_{ki}}{\rho_{k\mathfrak{m}}\rho_{i\mathfrak{m}}} \right) \ln\left(\frac{\psi_{\mathfrak{m}}\rho_{i\mathfrak{m}}\rho_{kj}}{\rho_{j\mathfrak{m}}\rho_{ki}^2} \right) \right\rangle_{\mathfrak{m}} + \mathcal{O}(\epsilon) \Bigg]. \end{aligned} \tag{7.14}$$

We note that the function L_{ki} is given in Eq. (4.19), the function W_{kij} reads

$$W_{kij} = \left\langle \frac{\rho_{ki}}{\rho_{i\mathfrak{m}}\rho_{k\mathfrak{m}}} \ln\frac{\rho_{kj}}{\rho_{j\mathfrak{m}}} \ln\frac{\rho_{ki}}{\rho_{i\mathfrak{m}}\rho_{k\mathfrak{m}}} + \frac{1}{\rho_{i\mathfrak{m}}} \ln\rho_{i\mathfrak{m}} \ln\frac{\rho_{kj}}{\rho_{ij}} \right\rangle_{\mathfrak{m}}, \tag{7.15}$$

and the function $\bar{G}_{r,\text{fin}}^{ikj}$ can be found in Eq. (H.16) of Ref. [38].

8 The remaining contributions

We are left with the discussion of the contributions to the soft function that are not iterations of next-to-leading order terms, and do not contain triple-color correlators. We write them as

$$S_{2,RR,T^2} + S_{RV,T^2} - Z_{2,r} - Z_{2,r}^+ - \frac{a_s\beta_0}{\epsilon} S_1, \tag{8.1}$$

where S_{2,RR,T^2} is defined in Eq. (5.6) and

$$S_{RV,T^2,\tau} = \frac{[\alpha_s]2^{-\epsilon}}{\epsilon^2} C_A A_K(\epsilon) \sum_{(ij)} \mathbf{T}_i \cdot \mathbf{T}_j\, I_{RV,ij}, \tag{8.2}$$

is the part of the real-virtual contribution that depends on the products of two color-charge operators.

The calculation of $I_{RV,ij}$ is straightforward. We obtain

$$I_{RV,ij} = \frac{[\alpha_s]}{\tau^{1+4\epsilon}} \left\langle \psi_{\mathfrak{m}}^{4\epsilon} \left(\frac{\rho_{ij}}{\rho_{i\mathfrak{m}}\rho_{j\mathfrak{m}}} \right)^{1+\epsilon} \right\rangle_{\mathfrak{m}} . \tag{8.3}$$

Next, we perform the Laplace transform and find

$$S_{RV,T^2} = -\frac{[\alpha_s]^2(\bar{u})^{4\epsilon} e^{-4\gamma_E\epsilon}\Gamma(1-4\epsilon)}{2^{2+\epsilon}\,\epsilon^3} C_A A_K(\epsilon) \sum_{(ij)} \mathbf{T}_i \cdot \mathbf{T}_j \left\langle \psi_{\mathfrak{m}}^{4\epsilon} \left(\frac{\rho_{ij}}{\rho_{i\mathfrak{m}}\rho_{j\mathfrak{m}}} \right)^{1+\epsilon} \right\rangle_{\mathfrak{m}} . \tag{8.4}$$

This contribution contains both explicit $1/\epsilon$ terms and collinear divergences that arise after integration over directions of the gluon $\mathfrak{m}$. The latter can be isolated by following what has been done for computing the soft function at next-to-leading order. We also note that terms that involve the jettiness function $\psi_{\mathfrak{m}}$ start contributing at order $1/\epsilon^2$. We will discuss how the jettiness-dependent divergent contributions cancel out once we isolate similar terms in S_{2,RR,T^2} in the next Section.

9 Correlated emissions of two soft gluons: the strongly ordered limit

We consider the remaining contribution to S_{2,RR,T^2}. It reads

$$S_{2,RR,T^2,\tau} = -\frac{C_A}{2} \sum_{(ij)} \mathbf{T}_i \cdot \mathbf{T}_j \; I_{ij,\tau}, \tag{9.1}$$

where

$$I_{ij,\tau} = \frac{g_s^4}{2} \int [\mathrm{d}p_{\mathfrak{m}}][\mathrm{d}p_{\mathfrak{n}}] \;\; \delta\left(\tau - E_{\mathfrak{m}}\psi_{\mathfrak{m}} - E_{\mathfrak{n}}\psi_{\mathfrak{n}}\right) \tilde{S}_{ij}^{gg}(\mathfrak{m},\mathfrak{n}). \tag{9.2}$$

Since the function $\tilde{S}_{ij}^{gg}$ is symmetric under the permutation of $\mathfrak{m}$ and $\mathfrak{n}$, we can introduce the energy-ordering $E_{\mathfrak{n}} < E_{\mathfrak{m}}$ ($E_{\mathfrak{n}} = \omega E_{\mathfrak{m}}$) and use the fact that the scaling of $\tilde{S}_{ij}^{gg}$ with the common gluon energy "scale" $E_{\mathfrak{m}}$ is uniform. We then write

$$\begin{aligned} I_{ij,\tau} &= g_s^4 \int [\mathrm{d}p_{\mathfrak{m}}][\mathrm{d}p_{\mathfrak{n}}]\; \theta(E_{\mathfrak{m}} - E_{\mathfrak{n}})\; \delta\left(\tau - E_{\mathfrak{m}}\psi_{\mathfrak{m}} - E_{\mathfrak{n}}\psi_{\mathfrak{n}}\right) \tilde{S}_{ij}^{gg}(\mathfrak{m},\mathfrak{n}) \\ &= [\alpha_s]^2 \int_0^1 \frac{\mathrm{d}\omega}{\omega^{1+2\epsilon}} \left\langle \int_0^\infty \frac{\mathrm{d}E_{\mathfrak{m}}}{E_{\mathfrak{m}}^{1+4\epsilon}} \delta(\tau - E_{\mathfrak{m}}\psi_{\mathfrak{mn}}) \;\; \left[\omega^2\; \tilde{S}_{ij}^{gg}(\mathfrak{m},\mathfrak{n})\right]_{E_{\mathfrak{m}}\to 1, E_{\mathfrak{n}}\to\omega} \right\rangle_{\mathfrak{mn}} \\ &= \frac{[\alpha_s]^2}{\tau^{1+4\epsilon}} \int_0^1 \frac{\mathrm{d}\omega}{\omega^{1+2\epsilon}} \left\langle \psi_{\mathfrak{mn}}^{4\epsilon} \;\; \left[\omega^2 \tilde{S}^{gg}(\mathfrak{m},\mathfrak{n})\right] \right\rangle_{\mathfrak{mn}}, \end{aligned} \tag{9.3}$$

where $\psi_{\mathfrak{mn}} = \psi_{\mathfrak{m}} + \omega\psi_{\mathfrak{n}}$. We note that from now on, for simplicity of notation, we will always assume that in the evaluation of $\tilde{S}^{gg}(\mathfrak{m},\mathfrak{n})$ the energy of the gluon $\mathfrak{m}$ is set to 1 and the energy of the gluon $\mathfrak{n}$ is set to ω. Finally, we perform the Laplace transform and find

$$I_{ij} = \frac{N_u}{\epsilon} \int_0^1 \frac{\mathrm{d}\omega}{\omega^{1+2\epsilon}} \left\langle \psi_{\mathfrak{mn}}^{4\epsilon} \;\; \left[\omega^2 \tilde{S}_{ij}^{gg}(\mathfrak{m},\mathfrak{n})\right] \right\rangle_{\mathfrak{mn}}, \tag{9.4}$$

where

$$N_u = -\frac{[\alpha_s]^2 \bar{u}^{4\epsilon} e^{-4\epsilon\gamma_E}\Gamma(1-4\epsilon)}{4}. \tag{9.5}$$

The representation of function I_{ij} in Eq. (9.4) is the starting point of our analysis of the correlated emissions of two gluons. To compute I_{ij} we identify and subtract various singular limits of the integrand in Eq. (9.4). We begin with the $\omega \to 0$ limit which we will refer to as the "strongly-ordered" one, in the sense of the energy ordering. The strongly-ordered limit of $\tilde{S}_{ij}^{gg}$ evaluates to

$$\lim_{\omega\to 0}\left[\omega^2 \tilde{S}_{ij}^{gg}(\mathfrak{m},\mathfrak{n})\right] = \left[\frac{2\rho_{ij}}{\rho_{\mathfrak{m}\mathfrak{n}}\rho_{i\mathfrak{m}}\rho_{j\mathfrak{n}}} + \frac{2\rho_{ij}}{\rho_{\mathfrak{m}\mathfrak{n}}\rho_{i\mathfrak{n}}\rho_{j\mathfrak{m}}} - \frac{2\rho_{ij}^2}{\rho_{i\mathfrak{m}}\rho_{i\mathfrak{n}}\rho_{j\mathfrak{m}}\rho_{j\mathfrak{n}}}\right] = F_{ij}(\mathfrak{m},\mathfrak{n}). \tag{9.6}$$

We then need to compute

$$I_{ij}^{\text{so}} = \frac{N_u}{\epsilon}\int_0^1 \frac{\mathrm{d}\omega}{\omega^{1+2\epsilon}}\left\langle (\psi_{\mathfrak{m}} + \omega\psi_{\mathfrak{n}})^{4\epsilon}\ F_{ij}(\mathfrak{m},\mathfrak{n})\right\rangle_{\mathfrak{m}\mathfrak{n}}. \tag{9.7}$$

To integrate over ω, we change the integration variable $\omega \to 1/\omega$ and find

$$I_{ij}^{\text{so}} = \frac{N_u}{\epsilon}\int_1^\infty \frac{\mathrm{d}\omega}{\omega^{1+2\epsilon}}\left\langle (\omega\psi_{\mathfrak{m}} + \psi_{\mathfrak{n}})^{4\epsilon}\ F_{ij}(\mathfrak{m},\mathfrak{n})\right\rangle_{\mathfrak{m}\mathfrak{n}}. \tag{9.8}$$

We then rename $\mathfrak{m} \leftrightarrow \mathfrak{n}$ and obtain

$$I_{ij}^{\text{so}} = \frac{N_u}{\epsilon}\int_1^\infty \frac{\mathrm{d}\omega}{\omega^{1+2\epsilon}}\left\langle (\psi_{\mathfrak{m}} + \omega\psi_{\mathfrak{n}})^{4\epsilon}\ F_{ij}(\mathfrak{n},\mathfrak{m})\right\rangle_{\mathfrak{m}\mathfrak{n}}. \tag{9.9}$$

Since $F_{ij}(\mathfrak{n},\mathfrak{m}) = F_{ij}(\mathfrak{m},\mathfrak{n})$, we finally find

$$\begin{aligned} I_{ij}^{\text{so}} &= \frac{N_u}{2\epsilon}\int_0^\infty \frac{\mathrm{d}\omega}{\omega^{1+2\epsilon}}\left\langle (\psi_{\mathfrak{m}} + \omega\psi_{\mathfrak{n}})^{4\epsilon}\ F_{ij}(\mathfrak{m},\mathfrak{n})\right\rangle_{\mathfrak{m}\mathfrak{n}} \\ &= -\frac{N_u\Gamma[1-2\epsilon]^2}{2\epsilon^2\Gamma[1-4\epsilon]}\left\langle \psi_{\mathfrak{m}}^{2\epsilon}\ \psi_{\mathfrak{n}}^{2\epsilon}\ F_{ij}(\mathfrak{m},\mathfrak{n})\right\rangle_{\mathfrak{m}\mathfrak{n}} \\ &= -\frac{N_u\Gamma[1-2\epsilon]^2}{\epsilon^2\Gamma[1-4\epsilon]}\left\langle \psi_{\mathfrak{m}}^{2\epsilon}\ \psi_{\mathfrak{n}}^{2\epsilon}\left[\frac{2\rho_{ij}}{\rho_{\mathfrak{m}\mathfrak{n}}\rho_{i\mathfrak{m}}\rho_{j\mathfrak{n}}} - \frac{\rho_{ij}^2}{\rho_{i\mathfrak{m}}\rho_{i\mathfrak{n}}\rho_{j\mathfrak{m}}\rho_{j\mathfrak{n}}}\right]\right\rangle_{\mathfrak{m}\mathfrak{n}}. \end{aligned} \tag{9.10}$$

The last term in Eq. (9.10) is fully factorized and can be computed in the same way as the uncorrelated contribution. We only need to understand how to deal with the first term in Eq. (9.10).

To this end, we note that the angular integral

$$\left\langle \psi_{\mathfrak{m}}^{2\epsilon}\ \psi_{\mathfrak{n}}^{2\epsilon}\frac{\rho_{ij}}{\rho_{\mathfrak{m}\mathfrak{n}}\ \rho_{i\mathfrak{m}}\ \rho_{j\mathfrak{n}}}\right\rangle_{\mathfrak{m}\mathfrak{n}}, \tag{9.11}$$

is singular in the three collinear limits $\mathfrak{m}||i$, $\mathfrak{n}||j$ and $\mathfrak{m}||\mathfrak{n}$. To regulate the first two, we define the following functions

$$\left(\frac{\psi_{\mathfrak{m}}}{\rho_{i\mathfrak{m}}}\right)^{2\epsilon} = 1 + \epsilon f_{i\mathfrak{m}}, \quad \left(\frac{\psi_{\mathfrak{n}}}{\rho_{j\mathfrak{n}}}\right)^{2\epsilon} = 1 + \epsilon f_{j\mathfrak{n}}. \tag{9.12}$$

Then, we split the integral into contributions with and without functions $f_{i\mathfrak{m}}$ and $f_{j\mathfrak{n}}$. This splitting introduces unregulated singularities in some integrals; to address this issue, we modify the integral in Eq. (9.11) by incorporating an additional (analytic) regulator, and write it as

$$\left\langle \psi_{\mathfrak{m}}^{2\epsilon}\, \psi_{\mathfrak{n}}^{2\epsilon} \frac{\rho_{ij}}{\rho_{\mathfrak{mn}}\, \rho_{i\mathfrak{m}}^{1+\nu}\, \rho_{j\mathfrak{n}}^{1+\nu}} \right\rangle_{\mathfrak{mn}}. \tag{9.13}$$

Using the functions $f_{i\mathfrak{m}}, f_{j\mathfrak{n}}$ defined in Eq. (9.12), we rewrite it as follows

$$\begin{aligned} &\left\langle \psi_{\mathfrak{m}}^{2\epsilon}\, \psi_{\mathfrak{n}}^{2\epsilon} \frac{\rho_{ij}}{\rho_{\mathfrak{mn}}\, \rho_{i\mathfrak{m}}^{1+\nu}\, \rho_{j\mathfrak{n}}^{1+\nu}} \right\rangle_{\mathfrak{mn}} \\ &= \left\langle \left(\epsilon^2 f_{i\mathfrak{m}} f_{j\mathfrak{n}} + \left(\frac{\psi_{\mathfrak{m}}}{\rho_{i\mathfrak{m}}}\right)^{2\epsilon} + \left(\frac{\psi_{\mathfrak{n}}}{\rho_{j\mathfrak{n}}}\right)^{2\epsilon} - 1 \right) \frac{\rho_{ij}}{\rho_{\mathfrak{mn}}\, \rho_{i\mathfrak{m}}^{1+\nu-2\epsilon}\, \rho_{j\mathfrak{n}}^{1+\nu-2\epsilon}} \right\rangle_{\mathfrak{mn}}. \end{aligned} \tag{9.14}$$

We need to compute the above integral and take the limit $\nu \to 0$ *before* the expansion around $\epsilon = 0$ is performed.

It is clear that in the second, the third and the forth terms in the right-hand side in Eq. (9.14), we can integrate over directions of $\mathfrak{n}$ or directions of $\mathfrak{m}$ or directions of both. We begin with the computation of the last integral in the right-hand side of Eq. (9.14) where we first integrate over $\mathfrak{n}$. The integration is straightforward [47] and we obtain

$$\begin{aligned} \left\langle \frac{\rho_{ij}}{\rho_{\mathfrak{mn}}\, \rho_{i\mathfrak{m}}^{1+\nu-2\epsilon}\, \rho_{j\mathfrak{n}}^{1+\nu-2\epsilon}} \right\rangle_{\mathfrak{mn}} &= \frac{2^{-\epsilon}\Gamma(-\epsilon)\Gamma(\epsilon-\nu)}{\Gamma(-\nu)} \\ &\times \left\langle {}_2F_1(-\epsilon, \epsilon-\nu, 1-\epsilon, 1-\eta_{j\mathfrak{m}}) \frac{\rho_{ij}}{\rho_{i\mathfrak{m}}^{1-2\epsilon+\nu}\, \rho_{j\mathfrak{m}}^{1-\epsilon+\nu}} \right\rangle_{\mathfrak{m}}. \end{aligned} \tag{9.15}$$

Since $1/\Gamma(-\nu) = -\nu/\Gamma(1-\nu)$, this integral appears to be proportional to the analytic regulator. Because we are supposed to take the $\nu \to 0$ limit at fixed ϵ, it is tempting to conclude that the whole integral vanishes. However, this conclusion is wrong because *the remaining integral over directions of $\vec{n}_{\mathfrak{m}}$ is ill-defined for $\nu = 0$.*

To extract the $1/\nu$ singularity from the remaining integration over $\vec{n}_{\mathfrak{m}}$ in Eq. (9.15) we note that it originates from a kinematic configuration where $\mathfrak{m}||j$. Hence, to extract it, we take the collinear limit in all quantities of the integrand except $1/\rho_{j\mathfrak{m}}^{1-\epsilon+\nu}$, whose integration produces the $1/\nu$ singularity. Taking the $\nu \to 0$ limit, we find

$$\lim_{\nu\to 0} \left\langle \frac{\rho_{ij}}{\rho_{\mathfrak{mn}}\, \rho_{i\mathfrak{m}}^{1+\nu-2\epsilon}\, \rho_{j\mathfrak{n}}^{1+\nu-2\epsilon}} \right\rangle_{\mathfrak{mn}} = -\frac{\eta_{ij}^{2\epsilon}\Gamma(1+\epsilon)\Gamma^3(1-\epsilon)}{\epsilon^2\Gamma(1-2\epsilon)}. \tag{9.16}$$

It is easy to convince oneself that the second and the third integrals in Eq. (9.14) cannot be rescued using this mechanism and just vanish, and the first integral does not need the analytic regulator since all divergences are dimensionally regularized.

Hence, we conclude that the angular integral needed to describe the strongly-ordered soft limit is given by the following equation

$$\left\langle \psi_{\mathfrak{m}}^{2\epsilon}\,\psi_{\mathfrak{n}}^{2\epsilon}\frac{\rho_{ij}}{\rho_{\mathfrak{mn}}\,\rho_{i\mathfrak{m}}\,\rho_{j\mathfrak{n}}}\right\rangle_{\mathfrak{mn}} = \epsilon^2\left\langle f_{i\mathfrak{m}}f_{j\mathfrak{n}}\frac{\rho_{ij}}{\rho_{\mathfrak{mn}}\,\rho_{i\mathfrak{m}}^{1-2\epsilon}\,\rho_{j\mathfrak{n}}^{1-2\epsilon}}\right\rangle_{\mathfrak{mn}} + \frac{\eta_{ij}^{2\epsilon}\Gamma(1+\epsilon)\Gamma^3(1-\epsilon)}{\epsilon^2\Gamma(1-2\epsilon)}. \quad (9.17)$$

The usefulness of this representation stems from the fact that in the remaining integral on the right-hand side $\mathfrak{m}||i$ and $\mathfrak{n}||j$ collinear singularities are regulated since $f_{i\mathfrak{m}}$ and $f_{j\mathfrak{n}}$ vanish in these limits. The singular limit which remains is the $\mathfrak{m}||\mathfrak{n}$ one. We therefore subtract the $\mathfrak{m}||\mathfrak{n}$ singularity and write[3]

$$\begin{aligned}\left\langle f_{i\mathfrak{m}}f_{j\mathfrak{n}}\frac{\rho_{ij}}{\rho_{\mathfrak{mn}}\,\rho_{i\mathfrak{m}}^{1-2\epsilon}\,\rho_{j\mathfrak{n}}^{1-2\epsilon}}\right\rangle_{\mathfrak{mn}} &= \left\langle \bar{C}_{\mathfrak{mn}}f_{i\mathfrak{m}}f_{j\mathfrak{n}}\frac{\rho_{ij}}{\rho_{\mathfrak{mn}}\,\rho_{i\mathfrak{m}}^{1-2\epsilon}\,\rho_{j\mathfrak{n}}^{1-2\epsilon}}\right\rangle_{\mathfrak{mn}} \\ &\quad + \left\langle C_{\mathfrak{mn}}f_{i\mathfrak{m}}f_{j\mathfrak{n}}\frac{\rho_{ij}}{\rho_{\mathfrak{mn}}\,\rho_{i\mathfrak{m}}^{1-2\epsilon}\,\rho_{j\mathfrak{n}}^{1-2\epsilon}}\right\rangle_{\mathfrak{mn}},\end{aligned} \quad (9.18)$$

where $\bar{C}_{\mathfrak{mn}} = I - C_{\mathfrak{mn}}$. We then simplify the last term. We write

$$\begin{aligned}\left\langle C_{\mathfrak{mn}}f_{i\mathfrak{m}}f_{j\mathfrak{n}}\frac{\rho_{ij}}{\rho_{\mathfrak{mn}}\,\rho_{i\mathfrak{m}}^{1-2\epsilon}\,\rho_{j\mathfrak{n}}^{1-2\epsilon}}\right\rangle_{\mathfrak{mn}} &= \left\langle f_{i\mathfrak{m}}f_{j\mathfrak{m}}\frac{\rho_{ij}}{\rho_{\mathfrak{mn}}\,\rho_{i\mathfrak{m}}^{1-2\epsilon}\,\rho_{j\mathfrak{m}}^{1-2\epsilon}}\right\rangle_{\mathfrak{mn}} \\ &= -\frac{2^{-2\epsilon}}{\epsilon}\frac{\Gamma^2(1-\epsilon)}{\Gamma(1-2\epsilon)}\left\langle f_{i\mathfrak{m}}f_{j\mathfrak{m}}\frac{\rho_{ij}}{\rho_{i\mathfrak{m}}^{1-2\epsilon}\,\rho_{j\mathfrak{m}}^{1-2\epsilon}}\right\rangle_{\mathfrak{m}}.\end{aligned} \quad (9.19)$$

The final result for the integral I_{ij}^{so} defined in Eq. (9.10) reads

$$\begin{aligned}I_{ij}^{\mathrm{so}} = -\frac{N_u\,\Gamma(1-2\epsilon)^2}{\epsilon^2\Gamma(1-4\epsilon)}\Bigg[&\epsilon^2\left\langle \bar{C}_{\mathfrak{mn}}\,f_{i\mathfrak{m}}f_{j\mathfrak{n}}\,\frac{2\rho_{ij}}{\rho_{\mathfrak{mn}}\,\rho_{i\mathfrak{m}}^{1-2\epsilon}\,\rho_{j\mathfrak{n}}^{1-2\epsilon}}\right\rangle_{\mathfrak{mn}} \\ &+ \frac{2\eta_{ij}^{2\epsilon}\Gamma(1+\epsilon)\Gamma^3(1-\epsilon)}{\epsilon^2\Gamma(1-2\epsilon)} - \frac{2^{1-2\epsilon}}{\epsilon}\frac{\Gamma^2(1-\epsilon)}{\Gamma(1-2\epsilon)}\left\langle \epsilon^2\,f_{i\mathfrak{m}}f_{j\mathfrak{m}}\,\frac{\rho_{ij}}{\rho_{i\mathfrak{m}}^{1-2\epsilon}\,\rho_{j\mathfrak{m}}^{1-2\epsilon}}\right\rangle_{\mathfrak{m}} \\ &- \left\langle \psi_{\mathfrak{m}}^{2\epsilon}\frac{\rho_{ij}}{\rho_{i\mathfrak{m}}\rho_{j\mathfrak{m}}}\right\rangle_{\mathfrak{m}}\left\langle \psi_{\mathfrak{n}}^{2\epsilon}\frac{\rho_{ij}}{\rho_{i\mathfrak{n}}\rho_{j\mathfrak{n}}}\right\rangle_{\mathfrak{n}}\Bigg].\end{aligned} \quad (9.20)$$

We use this result to write the strongly-ordered contribution to the uncorrelated real-emission part of the N-jettiness soft function as follows

$$\begin{aligned}S_{2,RR,T^2}^{\mathrm{so}} = \frac{C_A N_u\Gamma^2(1-2\epsilon)}{2\epsilon^2\,\Gamma(1-4\epsilon)}\sum_{(ij)}\mathbf{T}_i\cdot\mathbf{T}_j\Bigg[&\epsilon^2\left\langle \bar{C}_{\mathfrak{mn}}\,f_{i\mathfrak{m}}f_{j\mathfrak{n}}\,\frac{2\rho_{ij}}{\rho_{\mathfrak{mn}}\,\rho_{i\mathfrak{m}}^{1-2\epsilon}\,\rho_{j\mathfrak{n}}^{1-2\epsilon}}\right\rangle_{\mathfrak{mn}} \\ &+ \frac{2\eta_{ij}^{2\epsilon}\Gamma(1+\epsilon)\Gamma^3(1-\epsilon)}{\epsilon^2\Gamma(1-2\epsilon)} - \frac{2^{1-2\epsilon}}{\epsilon}\frac{\Gamma^2(1-\epsilon)}{\Gamma(1-2\epsilon)}\left\langle \epsilon^2\,f_{i\mathfrak{m}}f_{j\mathfrak{m}}\,\frac{\rho_{ij}}{\rho_{i\mathfrak{m}}^{1-2\epsilon}\,\rho_{j\mathfrak{m}}^{1-2\epsilon}}\right\rangle_{\mathfrak{m}} \\ &- \left\langle \psi_{\mathfrak{m}}^{2\epsilon}\frac{\rho_{ij}}{\rho_{i\mathfrak{m}}\rho_{j\mathfrak{m}}}\right\rangle_{\mathfrak{m}}\left\langle \psi_{\mathfrak{n}}^{2\epsilon}\frac{\rho_{ij}}{\rho_{i\mathfrak{n}}\rho_{j\mathfrak{n}}}\right\rangle_{\mathfrak{n}}\Bigg].\end{aligned} \quad (9.21)$$

[3] As we will see later, sometimes it is useful to take the collinear limit of the phase space as well. If this is the case, we indicate this explicitly.

We continue with the discussion of how to extract divergences from $S^{\rm so}_{2,RR,T^2}$. We note that the first term in the sum on the r.h.s. in Eq. (9.21) is already finite because functions $f_{\mathfrak{m}i} \sim f_{\mathfrak{n}j} \sim \mathcal{O}(1)$ vanish in the collinear limits $\mathfrak{m}||i$, $\mathfrak{n}||j$, respectively and the singularity at $\mathfrak{m}||\mathfrak{n}$ is regulated by $\bar{C}_{\mathfrak{m}\mathfrak{n}}$ operator. Since the ϵ-dependence of the second term on the right-hand side in Eq. (9.21) is explicit, we need to focus on the remaining two terms. We rewrite them to make their dependencies on the N-jettiness constraint explicit. We find

$$\begin{aligned}\left\langle \epsilon^2 f_{i\mathfrak{m}} f_{j\mathfrak{m}} \frac{\rho_{ij}}{\rho_{i\mathfrak{m}}^{1-2\epsilon}\rho_{j\mathfrak{m}}^{1-2\epsilon}} \right\rangle_{\mathfrak{m}} &= \left\langle \frac{\rho_{ij}^{1-4\epsilon}}{\rho_{i\mathfrak{m}}^{1-4\epsilon}\rho_{j\mathfrak{m}}^{1-4\epsilon}} + \frac{\rho_{ij}}{\rho_{i\mathfrak{m}}^{1-2\epsilon}\rho_{j\mathfrak{m}}^{1-2\epsilon}} - 2\frac{\rho_{ij}^{1-2\epsilon}}{\rho_{i\mathfrak{m}}^{1-2\epsilon}\rho_{j\mathfrak{m}}^{1-4\epsilon}} \right\rangle_{\mathfrak{m}} \\ &+ 4\epsilon \left\langle g^{(4)}_{ij,\mathfrak{m}} \frac{\rho_{ij}^{1-4\epsilon}}{\rho_{i\mathfrak{m}}^{1-4\epsilon}\rho_{j\mathfrak{m}}^{1-4\epsilon}} - g^{(2)}_{ij,\mathfrak{m}} \frac{\rho_{ij}^{1-2\epsilon}}{\rho_{i\mathfrak{m}}^{1-2\epsilon}\rho_{j\mathfrak{m}}^{1-4\epsilon}} \right\rangle_{\mathfrak{m}},\end{aligned} \tag{9.22}$$

and

$$\begin{aligned}\left\langle \psi_{\mathfrak{m}}^{2\epsilon} \frac{\rho_{ij}}{\rho_{\mathfrak{m}i}\rho_{\mathfrak{m}j}} \right\rangle_{\mathfrak{m}} \left\langle \psi_{\mathfrak{n}}^{2\epsilon} \frac{\rho_{ij}}{\rho_{\mathfrak{n}i}\rho_{\mathfrak{n}j}} \right\rangle_{\mathfrak{n}} &= \left\langle \frac{\rho_{ij}^{1-2\epsilon}}{\rho_{\mathfrak{m}i}^{1-2\epsilon}\rho_{\mathfrak{m}j}^{1-2\epsilon}} \right\rangle_{\mathfrak{m}}^2 \\ &+ 4\epsilon \left\langle g^{(2)}_{ij,\mathfrak{m}} \frac{\rho_{ij}^{1-2\epsilon}}{\rho_{\mathfrak{m}i}^{1-2\epsilon}\rho_{\mathfrak{m}j}^{1-2\epsilon}} \right\rangle_{\mathfrak{m}} \left\langle \frac{\rho_{ij}^{1-2\epsilon}}{\rho_{\mathfrak{n}i}^{1-2\epsilon}\rho_{\mathfrak{n}j}^{1-2\epsilon}} \right\rangle_{\mathfrak{n}} + 4\epsilon^2 \left\langle g^{(2)}_{ij,\mathfrak{m}} \frac{\rho_{ij}^{1-2\epsilon}}{\rho_{\mathfrak{m}i}^{1-2\epsilon}\rho_{\mathfrak{m}j}^{1-2\epsilon}} \right\rangle_{\mathfrak{m}}^2.\end{aligned} \tag{9.23}$$

When these equations are used in Eq. (9.21), higher order terms in the expansion of functions $g^{(4)}$ and $g^{(2)}$ in ϵ become necessary. Fortunately, it is easy to compute them since

$$g^{(k)}_{ij,\mathfrak{m}} = \frac{1}{k\epsilon}\left[\left(\frac{\psi_{\mathfrak{m}}\rho_{ij}}{\rho_{i\mathfrak{m}}\rho_{j\mathfrak{m}}}\right)^{k\epsilon} - 1\right]. \tag{9.24}$$

Furthermore, since these functions regulate all divergences in the angular integrals where they appear, Eq. (9.24) can be expanded in powers of ϵ *before integration over directions of the momentum of gluon* $\mathfrak{m}$ *is performed*. Comparing the divergent contributions of *all* ψ*-dependent terms* in Eq. (9.21) with similar contributions to the real-virtual soft limit in Eq. (8.4), we find that they cancel. The remaining strongly-ordered contributions are accounted for when the final result for the soft function is assembled.

10 Collinear subtractions

We continue with the discussion of the uncorrelated contribution to N-jettiness soft function. Our starting point is Eq. (9.4). We have computed the *strongly-ordered* contribution to that equation and we will consider the remaining contribution in this section. Hence, we write

$$\bar{S}_\omega[I_{ij}] = \frac{N_u}{\epsilon}\int_0^1 \frac{\mathrm{d}\omega}{\omega^{1+2\epsilon}} \left\langle \psi_{\mathfrak{m}\mathfrak{n}}^{4\epsilon}\ \bar{S}_\omega\left[\omega^2 \tilde{S}^{gg}_{ij(\mathfrak{m},\mathfrak{n})}\right]\right\rangle_{\mathfrak{m}\mathfrak{n}}, \tag{10.1}$$

where N_u can be found in Eq. (9.5), $\bar{S}_\omega = I - S_\omega$ and S_ω is the operator that enforces the strongly-ordered limit. Furthermore, the eikonal function in Eq. (10.1) should be evaluated

assuming that the four-momentum of the gluon $\mathfrak{m}$ is $(1, \vec{n}_\mathfrak{m})$ and the four-momentum of the gluon $\mathfrak{n}$ is $\omega(1, \vec{n}_\mathfrak{n})$.

The integrand in Eq. (10.1) possesses a complicated singularity structure. We separate double-collinear and triple-collinear singularities introducing partition functions (see e.g. Ref. [38]) and write

$$\bar{S}_\omega[I_{ij}] = \bar{S}_\omega[I_{ij}^{dc}] + \bar{S}_\omega[I_{ij}^{tc}], \tag{10.2}$$

where the first term describes the contribution of the double-collinear and the second one – of the triple-collinear partition. We will discuss them in turn.

We begin with the double-collinear contribution. It reads

$$\bar{S}_\omega[I_{ij}^{dc}] = \frac{N_u}{\epsilon} \int\limits_0^1 \frac{\mathrm{d}\omega}{\omega^{1+2\epsilon}} \left\langle \psi_{\mathfrak{mn}}^{4\epsilon} \left(w^{\mathfrak{m}i,\mathfrak{n}j} + w^{\mathfrak{n}i,\mathfrak{m}j}\right) \bar{S}_\omega \left[\omega^2 \tilde{S}_{ij}^{gg}(\mathfrak{m},\mathfrak{n})\right] \right\rangle_{\mathfrak{mn}}. \tag{10.3}$$

By construction, the partitions ensure that the only allowed singularities are $\mathfrak{m}||i$, $\mathfrak{n}||j$, and $\mathfrak{m}||j$ and $\mathfrak{n}||i$, respectively. However, it is easy to see that the integrand is not singular in these limits. Hence, we can expand $\psi_{\mathfrak{mn}}^{4\epsilon}$ in powers of ϵ in Eq. (10.3). The first term of this expansion corresponds to the contribution of double-collinear partitions to the soft-subtracted integral of $\omega^2 \tilde{S}_{ij}^{gg}$ *without the N-jettiness constraint*. Since this term is multiplied by $1/\epsilon$, we need to compute it analytically if we want to show the cancellation of all ϵ-singular terms without relying on numerical calculations. We will show that it is possible to extract this contribution from the result of Ref. [48], so that its computation is not required. The jettiness-dependent term that arises in the expansion of Eq. (10.3) in powers of ϵ, contains a factor $4\epsilon \ln \psi_{\mathfrak{mn}}$ and, thus, only provides an ϵ-finite contribution that we evaluate numerically.

The term I_{ij}^{tc} is a triple-collinear contribution. In this case we write

$$\bar{S}_\omega[I_{ij}^{tc}] = \frac{N_u}{\epsilon} \int\limits_0^1 \frac{\mathrm{d}\omega}{\omega^{1+2\epsilon}} \left\langle \psi_{\mathfrak{mn}}^{4\epsilon}\, w^{tc}\, \bar{S}_\omega \left[\omega^2 \tilde{S}_{ij}^{gg}(\mathfrak{m},\mathfrak{n})\right] \right\rangle_{\mathfrak{mn}}, \tag{10.4}$$

where

$$w^{tc} = w^{\mathfrak{m}i,\mathfrak{n}i} + w^{\mathfrak{m}j,\mathfrak{n}j}. \tag{10.5}$$

To facilitate the computation of $\bar{S}_\omega[I_{ij}^{tc}]$, we introduce the standard sectors to further partition angular integrations, see e.g. Refs. [1, 9, 10, 38]. We also assume that when we subtract $\mathfrak{m}||\mathfrak{n}$ singularity, we need to simplify the phase space but a similar simplification is not needed for the triple-collinear limit. Finally, we note that there are no double-collinear $\mathfrak{m}||i$, $\mathfrak{n}||i$ and similar singularities. Hence, we only need to subtract triple-collinear and $\mathfrak{m}||\mathfrak{n}$ double-collinear singularities in the integrand in Eq. (10.4). With this in mind, we

write[4]

$$\bar{S}_\omega[I_{ij}^{tc}] = \frac{N_u}{\epsilon}\int_0^1 \frac{\mathrm{d}\omega}{\omega^{1+2\epsilon}} \left\langle C_{\mathfrak{mn}}\,[\mathrm{d}\Omega_{\mathfrak{mn}}]\,\theta^{b+d} w^{tc}\psi_{\mathfrak{mn}}^{4\epsilon}\bar{S}_\omega\left[w^2\tilde{S}_{ij}^{gg}(\mathfrak{m},\mathfrak{n})\right]\right\rangle_{\mathfrak{mn}}$$
$$+\frac{N_u}{\epsilon}\sum_{x\in\{i,j\}}\int_0^1 \frac{\mathrm{d}\omega}{\omega^{1+2\epsilon}} \left\langle (1-\theta^{b+d}C_{\mathfrak{mn}})\,[\mathrm{d}\Omega_{\mathfrak{mn}}]\,C_{x\mathfrak{mn}} w^{tc}\psi_{\mathfrak{mn}}^{4\epsilon}\bar{S}_\omega\left[w^2\tilde{S}_{ij}^{gg}(\mathfrak{m},\mathfrak{n})\right]\right\rangle_{\mathfrak{mn}} \tag{10.6}$$
$$+\frac{N_u}{\epsilon}\sum_{x\in\{i,j\}}\int_0^1 \frac{\mathrm{d}\omega}{\omega^{1+2\epsilon}} \left\langle (1-\theta^{b+d}C_{\mathfrak{mn}})\,[\mathrm{d}\Omega_{\mathfrak{mn}}]\,\bar{C}_{x\mathfrak{mn}}\; w^{\mathfrak{m}x,\mathfrak{n}x}\psi_{\mathfrak{mn}}^{4\epsilon}\bar{S}_\omega\left[w^2\tilde{S}_{ij}^{gg}(\mathfrak{m},\mathfrak{n})\right]\right\rangle_{\mathfrak{mn}},$$

where $\bar{C}_{x\mathfrak{mn}} = I - C_{x\mathfrak{mn}}$ and $[\mathrm{d}\Omega_{\mathfrak{mn}}] = [\mathrm{d}\Omega_{\mathfrak{m}}][\mathrm{d}\Omega_{\mathfrak{n}}]$. We expect that the first term in Eq. (10.6) contains an $\mathcal{O}(1/\epsilon^3)$ singularity, the second term an $\mathcal{O}(1/\epsilon^2)$ one and the last term is $\mathcal{O}(1/\epsilon)$ because its collinear and soft singularities are fully subtracted.

Since the $1/\epsilon$ divergence in the last term in Eq. (10.6) arises from a prefactor, we can expand the integrand in powers of ϵ. In particular, we apply the expansion to the function $\psi_{\mathfrak{mn}}^{4\epsilon}$. The term with $\ln\psi_{\mathfrak{mn}}$ is $\mathcal{O}(\epsilon^0)$ and the term without it provides an $\mathcal{O}(1/\epsilon)$ divergent contribution. However, this contribution is the same as in the case when no N-jettiness constraint is imposed. To make this more explicit, we combine double- and triple-collinear partitions, and write

$$\bar{S}_\omega[I_{ij}] = \frac{N_u}{\epsilon}\int_0^1 \frac{\mathrm{d}\omega}{\omega^{1+2\epsilon}} \left\langle C_{\mathfrak{mn}}\,[\mathrm{d}\Omega_{\mathfrak{mn}}]\,\theta^{b+d} w^{tc}\psi_{\mathfrak{mn}}^{4\epsilon}\bar{S}_\omega\left[w^2\tilde{S}_{ij}^{gg}(\mathfrak{m},\mathfrak{n})\right]\right\rangle_{\mathfrak{mn}}$$
$$+\frac{N_u}{\epsilon}\sum_{x\in\{i,j\}}\int_0^1 \frac{\mathrm{d}\omega}{\omega^{1+2\epsilon}} \left\langle (1-\theta^{b+d}C_{\mathfrak{mn}})\,[\mathrm{d}\Omega_{\mathfrak{mn}}]\,C_{x\mathfrak{mn}} w^{tc}\psi_{\mathfrak{mn}}^{4\epsilon}\bar{S}_\omega\left[w^2\tilde{S}_{ij}^{gg}(\mathfrak{m},\mathfrak{n})\right]\right\rangle_{\mathfrak{mn}}$$
$$+\frac{N_u}{\epsilon}\sum_{x\in\{i,j\}}\int_0^1 \frac{\mathrm{d}\omega}{\omega^{1+2\epsilon}} \left\langle (1-\theta^{b+d}C_{\mathfrak{mn}})\,[\mathrm{d}\Omega_{\mathfrak{mn}}]\,\bar{C}_{x\mathfrak{mn}} w^{x\mathfrak{m},x\mathfrak{n}}\;\bar{S}_\omega\left[w^2\tilde{S}_{ij}^{gg}(\mathfrak{m},\mathfrak{n})\right]\right\rangle_{\mathfrak{mn}}$$
$$+\frac{N_u}{\epsilon}\int_0^1 \frac{\mathrm{d}\omega}{\omega^{1+2\epsilon}} \left\langle \left(w^{\mathfrak{m}i,\mathfrak{n}j}+w^{\mathfrak{m}j,\mathfrak{n}i}\right)\;\bar{S}_\omega\left[w^2\tilde{S}_{ij}^{gg}(\mathfrak{m},\mathfrak{n})\right]\right\rangle_{\mathfrak{mn}} \tag{10.7}$$
$$+4N_u\sum_{x\in\{i,j\}}\int_0^1 \frac{\mathrm{d}\omega}{\omega^{1+2\epsilon}} \left\langle (1-\theta^{b+d}C_{\mathfrak{mn}})\,[\mathrm{d}\Omega_{\mathfrak{mn}}]\,\bar{C}_{x\mathfrak{mn}}\; w^{x\mathfrak{m},x\mathfrak{n}}\;\ln\psi_{\mathfrak{mn}}\;\bar{S}_\omega\left[w^2\tilde{S}_{ij}^{gg}(\mathfrak{m},\mathfrak{n})\right]\right\rangle_{\mathfrak{mn}}$$
$$+4N_u\sum_{x\in\{i,j\}}\int_0^1 \frac{\mathrm{d}\omega}{\omega^{1+2\epsilon}} \left\langle (w^{i\mathfrak{m},j\mathfrak{n}}+w^{i\mathfrak{n},j\mathfrak{m}})\ln\psi_{\mathfrak{mn}}\;\bar{S}_\omega\left[w^2\tilde{S}_{ij}^{gg}(\mathfrak{m},\mathfrak{n})\right]\right\rangle_{\mathfrak{mn}}.$$

[4] As is customary, c.f. Refs. [1, 38], we use the convention that collinear operators act on everything that appears to the right of them. The angular phase space appears to the right of $C_{\mathfrak{mn}}$ and to the left of $C_{x\mathfrak{mn}}$ indicating that the first operator acts on it and the second does not.

In the above formula, the first, the second, the third and the fourth terms are divergent. Our strategy will be to compute the first and the second terms explicitly, and extract the third and the fourth terms from the result in Ref. [48] making use of the fact that they do not depend on the N-jettiness function $\psi_{\mathfrak{mn}}$.

To make this connection explicit, we write a formula that describes the extraction of singularities of the integral of the double-eikonal function in a situation when *no N-jettiness constraint is imposed*. This quantity, computed in Ref. [48], can be cast into the following form

$$J_{ij} = \frac{N_E}{\epsilon} \int_0^1 \frac{\mathrm{d}\omega}{\omega^{1+2\epsilon}} \left\langle \omega^2 \tilde{S}_{ij}(\mathfrak{m},\mathfrak{n}) \right\rangle_{\mathfrak{mn}}, \tag{10.8}$$

where

$$N_E = -\frac{E_{\max}^{-4\epsilon}[\alpha_s]^2}{4}. \tag{10.9}$$

We can now write an expression for J_{ij}, where the various singularities are extracted. We obtain

$$\begin{aligned}
J_{ij} = {} & \frac{N_E}{\epsilon} \int_0^1 \frac{\mathrm{d}\omega}{\omega^{1+2\epsilon}} \left\langle S_\omega \left[\omega^2 \tilde{S}_{ij}(\mathfrak{m},\mathfrak{n})\right] \right\rangle_{\mathfrak{mn}} \\
& + \frac{N_E}{\epsilon} \int_0^1 \frac{\mathrm{d}\omega}{\omega^{1+2\epsilon}} \left\langle C_{\mathfrak{mn}} \left[\mathrm{d}\Omega_{\mathfrak{mn}}\right] \theta^{b+d} w^{tc} \bar{S}_\omega \left[w^2 \tilde{S}_{ij}^{gg}(\mathfrak{m},\mathfrak{n})\right] \right\rangle_{\mathfrak{mn}} \\
& + \frac{N_E}{\epsilon} \sum_{x\in\{i,j\}} \int_0^1 \frac{\mathrm{d}\omega}{\omega^{1+2\epsilon}} \left\langle (1-\theta^{b+d} C_{\mathfrak{mn}}) \left[\mathrm{d}\Omega_{\mathfrak{mn}}\right] C_{x\mathfrak{mn}} w^{tc} \bar{S}_\omega \left[w^2 \tilde{S}_{ij}^{gg}(\mathfrak{m},\mathfrak{n})\right] \right\rangle_{\mathfrak{mn}} \\
& + \frac{N_E}{\epsilon} \sum_{x\in\{i,j\}} \int_0^1 \frac{\mathrm{d}\omega}{\omega^{1+2\epsilon}} \left\langle (1-\theta^{b+d} C_{\mathfrak{mn}}) \left[\mathrm{d}\Omega_{\mathfrak{mn}}\right] \bar{C}_{x\mathfrak{mn}}\, w^{\mathfrak{m}x,\mathfrak{n}x} \bar{S}_\omega \left[w^2 \tilde{S}_{ij}^{gg}(\mathfrak{m},\mathfrak{n})\right] \right\rangle_{\mathfrak{mn}} \\
& + \frac{N_E}{\epsilon} \int_0^1 \frac{\mathrm{d}\omega}{\omega^{1+2\epsilon}} \left\langle \left(w^{\mathfrak{m}i,\mathfrak{n}j} + w^{\mathfrak{m}j,\mathfrak{n}i}\right)\, \bar{S}_\omega \left[w^2 \tilde{S}_{ij}^{gg}(\mathfrak{m},\mathfrak{n})\right] \right\rangle_{\mathfrak{mn}}.
\end{aligned} \tag{10.10}$$

Since the left-hand side of the above equation was computed through $\mathcal{O}(\epsilon^0)$ in Ref. [48], we can use this result to determine the last two terms that appear on the right-hand side in Eq. (10.10) and *also* enter Eq. (10.7). This is a sensible thing to do because their computation appears to be particularly challenging. Clearly, to make this happen, we have to compute all the other terms that appear in Eqs. (10.7,10.10) through finite terms in the expansion in ϵ. We describe details of the required computations in what follows.

10.1 The double-collinear $\mathfrak{m}||\mathfrak{n}$ contribution with N-jettiness constraint

To proceed, we need to compute the $\mathfrak{m}||\mathfrak{n}$ limit of the soft-subtracted eikonal function $\tilde{S}_{ij}$, given by the first term in Eq. (10.7). In principle, this is straightforward, except for the fact that the $\mathfrak{m}||\mathfrak{n}$ singularity appears to be stronger than logarithmic. Although this is

not the case, it implies that the corresponding contribution needs to be carefully extracted. We find

$$C_{\mathfrak{mn}}\overline{S}_{\omega}\ \left[\omega^2\tilde{S}^{gg}_{ij}(\mathfrak{m},\mathfrak{n})\right]=\frac{4\omega\rho_{ij}}{(1+\omega)^2\rho_{\mathfrak{mn}}\rho_{i\mathfrak{m}}\rho_{j\mathfrak{m}}}\Bigg\{-2 + \frac{(1-\epsilon)\omega\rho_{i\mathfrak{m}}\rho_{j\mathfrak{m}}}{(1+\omega)^2\rho_{ij}}\left(\frac{n_j\kappa_{\mathfrak{n}}}{\rho_{j\mathfrak{m}}}-\frac{n_i\kappa_{\mathfrak{n}}}{\rho_{i\mathfrak{m}}}\right)^2\Bigg\}, \tag{10.11}$$

where the three-vector $\kappa_{\mathfrak{n}}$ is defined through the following equation

$$\vec{n}_{\mathfrak{n}}=\cos\theta_{\mathfrak{mn}}\vec{n}_{\mathfrak{m}}+\sin\theta_{\mathfrak{mn}}\ \vec{\kappa}_{\mathfrak{n}}, \tag{10.12}$$

with the additional constraints

$$\vec{n}_{\mathfrak{m}}\cdot\vec{\kappa}_{\mathfrak{n}}=0,\quad \vec{\kappa}^2_{\mathfrak{n}}=1. \tag{10.13}$$

We also need the collinear limit of the phase space in b- and d-sectors. The corresponding parametrization can be found in Refs. [1, 38]. We obtain

$$\begin{aligned}&C_{\mathfrak{mn}}\ [\mathrm{d}\Omega_{\mathfrak{mn}}]\ \theta^{(b)}\ w^{\mathfrak{m}i,\mathfrak{n}i}\dots\\&=N^{(b,d)}_{\epsilon}\ w^{\mathfrak{m}i,\mathfrak{n}i}_{\mathfrak{m}||\mathfrak{n}}\ \eta^{-\epsilon}_{i\mathfrak{m}}\ (1-\eta_{i\mathfrak{m}})^{\epsilon}\ \left[\mathrm{d}\Omega^{(d-1)}_{\mathfrak{m}}\right]\ \left[\rho_{\mathfrak{mn}}\frac{\mathrm{d}x_4}{x_4^{1+2\epsilon}}\frac{[\mathrm{d}\Omega^{(d-3)}_a]}{[\Omega^{(d-3),a}]}\mathrm{d}\Lambda\right]\ C_{\mathfrak{mn}}\cdots,\end{aligned} \tag{10.14}$$

where

$$N^{(b,d)}_{\epsilon}=\frac{\Gamma(1-\epsilon)\Gamma(1+2\epsilon)}{\Gamma(1+\epsilon)}. \tag{10.15}$$

As the next step, we need to integrate over azimuthal angles parameterized by $\mathrm{d}\Omega^{(d-3)}_a$ and $\mathrm{d}\Lambda$ in Eq. (10.14). To facilitate this, we write

$$\left(\frac{(n_j\kappa_{\mathfrak{n}})}{\rho_{j\mathfrak{m}}}-\frac{(n_i\kappa_{\mathfrak{n}})}{\rho_{i\mathfrak{m}}}\right)^2=v_\mu v_\nu\kappa^\mu_{\mathfrak{n}}\kappa^\nu_{\mathfrak{n}}, \tag{10.16}$$

where $v^\mu=(n^\mu_i/\rho_{i\mathfrak{m}}-n^\mu_j/\rho_{j\mathfrak{m}})$, and the four-vector κ satisfies

$$\kappa_\mu t^\mu=0,\quad \kappa_\mu e^\mu_{\mathfrak{m}}=0, \tag{10.17}$$

where $t^\mu=(1,\vec{0})$ and $e^\mu_{\mathfrak{m}}=(0,\vec{n}_{\mathfrak{m}})$. The averaging of $\kappa^\mu\kappa^\nu$ over $[\mathrm{d}\Omega^{(d-3)}_a]/[\mathrm{d}\Omega^{(d-3),a}]\ \mathrm{d}\Lambda$ gives

$$\langle\kappa^\mu\kappa^\nu\rangle=-\frac{1}{2}g^{\mu\nu}_{\perp,d-2}+\epsilon r^\mu_i r^\nu_i. \tag{10.18}$$

The derivation of this formula as well as the definition of vector r^μ_i are given in Appendix F in Ref. [38].

To further simplify this expression, we write the metric tensor of the transverse space as follows

$$g^{\mu\nu}_{\perp,d-2}=g^{\mu\nu}-t^\mu t^\nu+e^\mu_{\mathfrak{m}}e^\nu_{\mathfrak{m}}. \tag{10.19}$$

Since

$$n^{\mu}_{\mathfrak{m}} v_{\mu} = 0, \tag{10.20}$$

we find

$$t_{\mu} v^{\mu} = -e_{\mathfrak{m},\mu} v^{\mu}. \tag{10.21}$$

This allows us to write

$$v_{\mu} v_{\nu} \left\langle \kappa^{\mu} \kappa^{\nu} \right\rangle = v_{\mu} v_{\nu} \left(-\frac{1}{2} g^{\mu\nu}_{\perp,d-2} + \epsilon r_i^{\mu} r_i^{\nu} \right) = -\frac{1}{2} v_{\mu} v^{\mu} + \epsilon (r_i \cdot v)^2. \tag{10.22}$$

A straightforward computation gives

$$v_{\mu} v^{\mu} = -\frac{2\rho_{ij}}{\rho_{i\mathfrak{m}} \rho_{j\mathfrak{m}}}, \tag{10.23}$$

and

$$(r_i v)^2 = \frac{(\rho_{ij} - \rho_{i\mathfrak{m}} + \rho_{j\mathfrak{m}})^2}{(2 - \rho_{i\mathfrak{m}}) \rho_{i\mathfrak{m}} \rho_{j\mathfrak{m}}^2} = 2 \left(\frac{1}{\rho_{i\mathfrak{m}}} + \frac{1}{\rho_{j\mathfrak{m}}} \right) + W_{ij}^{\mathfrak{m}}. \tag{10.24}$$

We note that the function $W_{ij}^{\mathfrak{m}}$ develops a singularity in the limit $\mathfrak{m}||j$ but this singularity is regulated by the partition function.

Finally, we note that the contributions of sectors b and d are equal. Integrating over x_4 and adding the two sectors, we obtain

$$\begin{aligned} \Sigma^{(i)}_{\mathfrak{m}||\mathfrak{n}} &= \frac{N_u}{\epsilon} \int_0^1 \frac{\mathrm{d}\omega}{\omega^{1+2\epsilon}} \left\langle C_{\mathfrak{mn}} [\mathrm{d}\Omega_{\mathfrak{mn}}] \theta^{b+d} w^{\mathfrak{m}i,\mathfrak{n}i} \psi^{4\epsilon}_{\mathfrak{mn}} \left[w^2 \tilde{S}^{gg}_{ij}(\mathfrak{m},\mathfrak{n}) \right] \right\rangle_{\mathfrak{mn}} \\ &= -\frac{N_u N_{\epsilon}^{b,d}}{\epsilon^2} \left\langle \frac{\eta_{i\mathfrak{m}}^{-\epsilon}}{(1-\eta_{i\mathfrak{m}})^{-\epsilon}} \, \psi^{4\epsilon}_{\mathfrak{m}} \, w^{\mathfrak{m}i,\mathfrak{n}i}_{\mathfrak{m}||\mathfrak{n}} \left[\gamma_g \, A^{(i)} + \epsilon \delta_g \, B^{(i)} \right] \right\rangle_{\mathfrak{m}}. \end{aligned} \tag{10.25}$$

In Eq. (10.25), we introduced the following quantities

$$A^{(i)} = \frac{\rho_{ij}}{\rho_{i\mathfrak{m}} \rho_{j\mathfrak{m}}}, \qquad B^{(i)} = \left(2 \frac{\rho_{i\mathfrak{m}} + \rho_{j\mathfrak{m}}}{\rho_{i\mathfrak{m}} \rho_{j\mathfrak{m}}} + W_{ij}^{\mathfrak{m}} \right), \tag{10.26}$$

and the analogs of the cusp anomalous dimension

$$\begin{aligned} \gamma_g &= \int_0^1 \frac{\mathrm{d}\omega}{\omega^{1+2\epsilon}} \frac{4\omega}{(1+\omega)^{2-4\epsilon}} \left(-2 + \frac{(1-\epsilon)\omega}{(1+\omega)^2} \right) = -\frac{11}{3} - \frac{137}{9}\epsilon \\ &\quad + \left(\frac{22\pi^2}{9} - \frac{1646}{27} \right) \epsilon^2 + \left(\frac{176}{3}\zeta_3 + \frac{274}{27}\pi^2 - \frac{19760}{81} \right) \epsilon^3 + \mathcal{O}(\epsilon^4), \\ \delta_g &= (1-\epsilon) \int_0^1 \frac{\mathrm{d}\omega}{\omega^{1+2\epsilon}} \frac{4\omega^2}{(1+\omega)^{4-4\epsilon}} = \frac{1}{3} + \frac{7}{9}\epsilon + \left(\frac{82}{27} - \frac{2\pi^2}{9} \right) \epsilon^2 + \mathcal{O}(\epsilon^3). \end{aligned} \tag{10.27}$$

It is convenient to write the result for the sum of i- and j-partitions. To do this in an optimal way, we need to rearrange contributions that appear in Eq. (10.25). The key point

in this rearrangement is to make the divergent contribution symmetric with respect to the replacement $i \leftrightarrow j$. We illustrate how this is done by considering the term proportional to γ_g in Eq. (10.25). We write

$$\begin{aligned}
&\left\langle \eta_{i\mathfrak{m}}^{-\epsilon}(1-\eta_{i\mathfrak{m}})^{\epsilon}\,\psi_{\mathfrak{m}}^{4\epsilon} w_{\mathfrak{m}||\mathfrak{n}}^{\mathfrak{m}i,\mathfrak{n}i}\,\frac{\rho_{ij}}{\rho_{i\mathfrak{m}}\rho_{j\mathfrak{m}}}\right\rangle_{\mathfrak{m}} \\
&= 2^{\epsilon}\left\langle \psi_{\mathfrak{m}}^{4\epsilon} w_{\mathfrak{m}||\mathfrak{n}}^{\mathfrak{m}i,\mathfrak{n}i}\,\frac{\rho_{ij}^{1+\epsilon}}{\rho_{i\mathfrak{m}}^{1+\epsilon}\rho_{j\mathfrak{m}}^{1+\epsilon}}\,(1-\eta_{i\mathfrak{m}})^{\epsilon}\left(\frac{\eta_{j\mathfrak{m}}}{\eta_{ij}}\right)^{\epsilon}\right\rangle_{\mathfrak{m}} = 2^{\epsilon}\left\langle \psi_{\mathfrak{m}}^{4\epsilon} w_{\mathfrak{m}||\mathfrak{n}}^{\mathfrak{m}i,\mathfrak{n}i}\,\frac{\rho_{ij}^{1+\epsilon}}{\rho_{i\mathfrak{m}}^{1+\epsilon}\rho_{j\mathfrak{m}}^{1+\epsilon}}\right\rangle_{\mathfrak{m}} \\
&+ 2^{\epsilon}\left\langle \psi_{\mathfrak{m}}^{4\epsilon} w_{\mathfrak{m}||\mathfrak{n}}^{\mathfrak{m}i,\mathfrak{n}i}\,\frac{\rho_{ij}^{1+\epsilon}}{\rho_{i\mathfrak{m}}^{1+\epsilon}\rho_{j\mathfrak{m}}^{1+\epsilon}}\left[(1-\eta_{i\mathfrak{m}})^{\epsilon}\left(\frac{\eta_{j\mathfrak{m}}}{\eta_{ij}}\right)^{\epsilon}-1\right]\right\rangle_{\mathfrak{m}},
\end{aligned} \tag{10.28}$$

and observe that the first term in the right-hand side of Eq. (10.28) can be easily combined with the $\mathfrak{m}||j,\mathfrak{n}||j$ partition and the last term is finite. Therefore, it can be computed by expanding in ϵ before integration. Note that in this term the $\psi_{\mathfrak{m}}$-dependent contribution appears at order $\mathcal{O}(\epsilon^2)$ which, given the $1/\epsilon^2$ prefactor in Eq. (10.25) is the last (finite) order in the ϵ-expansion that we care about.

Using these considerations, we combine contributions of the $\mathfrak{m}||i,\mathfrak{n}||i$ and $\mathfrak{m}||j,\mathfrak{n}||j$ partitions and obtain

$$\Sigma_{\mathfrak{m}||\mathfrak{n}}^{(i+j)} = -\frac{N_u N_\epsilon^{b,d}}{\epsilon^2}\left[\gamma_g A^{(ij)} + \epsilon\delta_g B^{(ij)}\right]. \tag{10.29}$$

We note that we have used

$$w_{\mathfrak{m}||\mathfrak{n}}^{\mathfrak{m}i,\mathfrak{n}i} + w_{\mathfrak{m}||\mathfrak{n}}^{\mathfrak{m}j,\mathfrak{n}j} = 1. \tag{10.30}$$

The term A^{ij} reads

$$\begin{aligned}
A^{(ij)} &= 2^{\epsilon}\left\langle\left(1+4\epsilon g_{ij,\mathfrak{m}}^{(4)}\right)\frac{\rho_{ij}^{1-3\epsilon}}{\rho_{i\mathfrak{m}}^{1-3\epsilon}\rho_{j\mathfrak{m}}^{1-3\epsilon}}\right\rangle \\
&+ 2^{\epsilon}\left\langle\frac{\rho_{ij}^{1+\epsilon}}{\rho_{i\mathfrak{m}}^{1+\epsilon}\rho_{j\mathfrak{m}}^{1+\epsilon}} w_{\mathfrak{m}||\mathfrak{n}}^{\mathfrak{m}i,\mathfrak{n}i}\psi_{\mathfrak{m}}^{4\epsilon}\left[\left(\frac{\eta_{j\mathfrak{m}}}{\eta_{ij}}\right)^{\epsilon}(1-\eta_{i\mathfrak{m}})^{\epsilon}-1\right]\right\rangle \\
&+ 2^{\epsilon}\left\langle\frac{\rho_{ij}^{1+\epsilon}}{\rho_{i\mathfrak{m}}^{1+\epsilon}\rho_{j\mathfrak{m}}^{1+\epsilon}} w_{\mathfrak{m}||\mathfrak{n}}^{\mathfrak{m}j,\mathfrak{n}j}\psi_{\mathfrak{m}}^{4\epsilon}\left[\left(\frac{\eta_{i\mathfrak{m}}}{\eta_{ij}}\right)^{\epsilon}(1-\eta_{j\mathfrak{m}})^{\epsilon}-1\right]\right\rangle.
\end{aligned} \tag{10.31}$$

As we already mentioned, the second and third terms on the right-hand side of Eq. (10.31) can be expanded in ϵ because expressions in square brackets protect the integrands from developing collinear singularities. Furthermore, since the expressions in square brackets start contributing at $\mathcal{O}(\epsilon)$, the N-jettiness dependence that arises from factors $\psi_{\mathfrak{m}}^{4\epsilon}$, only appears in $\mathcal{O}(\epsilon^0)$ contributions to the soft function.

Next, we discuss the $B^{(ij)}$ term in Eq. (10.29). In this case terms with W_{ij}^m provide integrable contributions. Taking this into account and repeating the steps we employed to

rewrite A^{ij}, we find

$$\begin{aligned}
B^{(ij)} &= 2^{1+\epsilon}\left\langle\left(1+4\epsilon g^{(4)}_{ij,\mathfrak{m}}\right)\frac{\rho_{ij}^{-3\epsilon}(\rho_{i\mathfrak{m}}+\rho_{j\mathfrak{m}})}{\rho_{i\mathfrak{m}}^{1-3\epsilon}\rho_{j\mathfrak{m}}^{1-3\epsilon}}\right\rangle \\
&+ 2^{1+\epsilon}\left\langle\frac{\rho_{ij}^{\epsilon}(\rho_{i\mathfrak{m}}+\rho_{j\mathfrak{m}})}{\rho_{i\mathfrak{m}}^{1+\epsilon}\rho_{j\mathfrak{m}}^{1+\epsilon}}\omega^{\mathfrak{m}i,\mathfrak{n}i}_{\mathfrak{m}||\mathfrak{n}}\psi^{4\epsilon}_{\mathfrak{m}}\left[\left(\frac{\eta_{j\mathfrak{m}}}{\eta_{ij}}\right)^{\epsilon}(1-\eta_{i\mathfrak{m}})^{\epsilon}-1\right]\right\rangle \\
&+ 2^{1+\epsilon}\left\langle\frac{\rho_{ij}^{\epsilon}(\rho_{i\mathfrak{m}}+\rho_{j\mathfrak{m}})}{\rho_{i\mathfrak{m}}^{1+\epsilon}\rho_{j\mathfrak{m}}^{1+\epsilon}}\omega^{\mathfrak{m}j,\mathfrak{n}j}_{\mathfrak{m}||\mathfrak{n}}\psi^{4\epsilon}_{\mathfrak{m}}\left[\left(\frac{\eta_{i\mathfrak{m}}}{\eta_{ij}}\right)^{\epsilon}(1-\eta_{j\mathfrak{m}})^{\epsilon}-1\right]\right\rangle \\
&+ \left\langle\eta_{i\mathfrak{m}}^{-\epsilon}(1-\eta_{i\mathfrak{m}})^{\epsilon}\psi^{4\epsilon}_{\mathfrak{m}}\omega^{\mathfrak{m}i,\mathfrak{n}i}_{\mathfrak{m}||\mathfrak{n}}W^{\mathfrak{m}}_{ij}\right\rangle + \left\langle\eta_{j\mathfrak{m}}^{-\epsilon}(1-\eta_{j\mathfrak{m}})^{\epsilon}\psi^{4\epsilon}_{\mathfrak{m}}\omega^{\mathfrak{m}j,\mathfrak{n}j}_{\mathfrak{m}||\mathfrak{n}}W^{\mathfrak{m}}_{ji}\right\rangle.
\end{aligned} \tag{10.32}$$

It follows from Eq. (10.29) that B^{ij} is needed through $\mathcal{O}(\epsilon)$ to compute the relevant contributions to the soft function. Therefore, for the analysis of the *divergent* contributions to the soft function, in Eq. (10.32) we require the first term without $g^{(4)}$ and the last term at $\epsilon = 0$.

10.2 The triple-collinear subtraction term with N-jettiness constraint

The second term we require is the triple-collinear limit of the eikonal function subject to the N-jettiness constraint. The corresponding equation reads

$$\frac{N_u}{\epsilon}\sum_{x\in\{i,j\}}\int_0^1\frac{\mathrm{d}\omega}{\omega^{1+2\epsilon}}\left\langle(1-\theta^{b+d}C_{\mathfrak{mn}})\,[\mathrm{d}\Omega_{\mathfrak{mn}}]\,C_{x\mathfrak{mn}}\;w^{tc}\;\psi^{4\epsilon}_{\mathfrak{mn}}\;\bar{S}_\omega\;\left[w^2\tilde{S}^{gg}_{ij}(\mathfrak{m},\mathfrak{n})\right]\right\rangle_{\mathfrak{mn}}. \tag{10.33}$$

There are four contributions to the above equation – the i- and j-triple-collinear partitions and the $\mathfrak{m}||\mathfrak{n}$ subtractions terms applied to the triple-collinear limit to remove subdivergences. The calculation of all these terms is similar, so that we take the i-triple-collinear partition and discuss first the triple-collinear limit.

For further reference, we define

$$\Sigma^{(i,tc)} = \frac{N_u}{\epsilon}\int_0^1\frac{\mathrm{d}\omega}{\omega^{1+2\epsilon}}\left\langle(\rho_{i\mathfrak{m}}+\omega\rho_{i\mathfrak{n}})^{4\epsilon}\;C_{i\mathfrak{mn}}\;\bar{S}_\omega\;\left[w^2\tilde{S}^{gg}_{ij}(\mathfrak{m},\mathfrak{n})\right]\right\rangle_{\mathfrak{mn}}, \tag{10.34}$$

where we have used

$$C_{i\mathfrak{mn}}w^{tc}=1,\quad C_{i\mathfrak{mn}}\;\psi^{4\epsilon}_{\mathfrak{mn}}=(\rho_{i\mathfrak{m}}+\omega\rho_{i\mathfrak{n}})^{4\epsilon}. \tag{10.35}$$

It follows from this equation that in the triple-collinear limits the dependence on the N-jettiness function disappears since we only need its limiting expression.

To proceed, we require the triple-collinear limit of the soft-subtracted eikonal function. It is straightforward to obtain it; we find

$$\begin{aligned}
C_{i\mathfrak{mn}}\overline{S}_\omega\;\left[\omega^2\tilde{S}_{ij}\right] &= \frac{2\omega^2(1-\epsilon)(\rho_{i\mathfrak{m}}-\rho_{i\mathfrak{n}})^2}{(\omega+1)^2\rho^2_{\mathfrak{mn}}(\rho_{i\mathfrak{m}}+\omega\rho_{i\mathfrak{n}})^2} - \frac{\omega\left(\rho^2_{i\mathfrak{m}}+6\rho_{i\mathfrak{n}}\rho_{i\mathfrak{m}}+\rho^2_{i\mathfrak{n}}\right)}{(\omega+1)\rho_{\mathfrak{mn}}\rho_{i\mathfrak{m}}\rho_{i\mathfrak{n}}(\rho_{i\mathfrak{m}}+\omega\rho_{i\mathfrak{n}})} \\
&+ \frac{\omega(\rho_{i\mathfrak{m}}+\rho_{i\mathfrak{n}})}{(\omega+1)\rho_{i\mathfrak{m}}\rho_{i\mathfrak{n}}(\rho_{i\mathfrak{m}}+\omega\rho_{i\mathfrak{n}})}.
\end{aligned} \tag{10.36}$$

We then write

$$\Sigma^{(i,tc)} = \frac{N_u}{\epsilon} B_{gg}^{(i,tc)}, \tag{10.37}$$

where

$$\begin{aligned} B_{gg}^{(i,tc)} = \int_0^1 \frac{\mathrm{d}\omega}{\omega^{1+2\epsilon}} \Bigg\langle \frac{1}{(\rho_{i\mathfrak{m}} + \omega\rho_{i\mathfrak{n}})^{1-4\epsilon}} \Bigg[\frac{2\omega^2(1-\epsilon)(\rho_{i\mathfrak{m}} - \rho_{i\mathfrak{n}})^2}{(\omega+1)^2 \rho_{\mathfrak{mn}}^2 (\rho_{i\mathfrak{m}} + \omega\rho_{i\mathfrak{n}})} \\ - \frac{\omega\left(\rho_{i\mathfrak{m}}^2 + 6\rho_{i\mathfrak{n}}\rho_{i\mathfrak{m}} + \rho_{i\mathfrak{n}}^2\right)}{(\omega+1)\rho_{\mathfrak{mn}}\rho_{i\mathfrak{m}}\rho_{i\mathfrak{n}}} + \frac{\omega(\rho_{i\mathfrak{m}} + \rho_{i\mathfrak{n}})}{(\omega+1)\rho_{i\mathfrak{m}}\rho_{i\mathfrak{n}}} \Bigg] \Bigg\rangle_{\mathfrak{mn}}. \end{aligned} \tag{10.38}$$

To simplify the calculation of this quantity we use the (partial) symmetry of the integrand under $\omega \to 1/\omega$ transformation as well as the invariance of the integration measure under $\mathfrak{m} \leftrightarrow \mathfrak{n}$, to extend the integration over ω in Eq. (10.38) to $\omega = \infty$ and to simplify the integrand. We find

$$\begin{aligned} B_{gg}^{(i,tc)} = \int_0^\infty \frac{\mathrm{d}\omega}{\omega^{1+2\epsilon}} \Bigg\langle \frac{1}{(\rho_{i\mathfrak{m}} + \omega\rho_{i\mathfrak{n}})^{1-4\epsilon}} \Bigg[\frac{2\omega^2(1-\epsilon)\rho_{i\mathfrak{m}}(\rho_{i\mathfrak{m}} - \rho_{i\mathfrak{n}})}{(\omega+1)^2 \rho_{\mathfrak{mn}}^2 (\rho_{i\mathfrak{m}} + \omega\rho_{i\mathfrak{n}})} \\ - \frac{\omega\left(\rho_{i\mathfrak{m}} + 3\rho_{i\mathfrak{n}}\right)}{(\omega+1)\rho_{\mathfrak{mn}}\rho_{i\mathfrak{n}}} + \frac{\omega}{(\omega+1)\rho_{i\mathfrak{n}}} \Bigg] \Bigg\rangle_{\mathfrak{mn}}. \end{aligned} \tag{10.39}$$

It turns out that it is relatively straightforward to compute $B_{gg}^{(i,tc)}$. To do that, it is convenient to employ a Mellin-Barnes representation [49] for $1/(\rho_{i\mathfrak{m}} + \omega\rho_{i\mathfrak{n}})^{1-4\epsilon}$ and then integrate over ω and the directions of $\mathfrak{m}$ and $\mathfrak{n}$. We note that this requires the introduction of a second Mellin-Barnes representation for integrals that involve $\rho_{\mathfrak{mn}}$. This is typically done using a particular Mellin-Barnes representation for the hypergeometric function

$$\begin{aligned} {}_2F_1(a,b,c,x) = \frac{\Gamma(c)}{\Gamma(c-b)\Gamma(a)\Gamma(b)\Gamma(c-a)} \\ \times \int \frac{\mathrm{d}z}{2\pi i} \Gamma(-z)\Gamma(a+z)\Gamma(b+z)\Gamma(c-a-b-z)\,(1-x)^z. \end{aligned} \tag{10.40}$$

The two-dimensional Mellin-Barnes integrals that one obtains are relatively simple as one integration can always be performed using the second Barnes lemma. The remaining integration is either performed using the first Barnes lemma or by mapping appropriate products of Gamma-functions onto parametric integrals using Euler's representation of a Beta function [49]. To perform the parametric integrals we use Hyperint [50]. We find

$$\begin{aligned} \Sigma^{i,tc} = \frac{N_u}{\epsilon} B_{gg}^{i,tc} = \frac{N_u}{\epsilon} \Bigg[\frac{11}{6\epsilon^2} + \frac{1}{\epsilon}\left(\frac{73}{18} + \frac{\pi^2}{6}\right) + 3\zeta_3 + \frac{11\pi^2}{18} + \frac{217}{27} \\ + \epsilon\left(\frac{73\pi^2}{54} - \frac{22\zeta_3}{3} + \frac{7\pi^4}{45} + \frac{1298}{81}\right) + \mathcal{O}(\epsilon^2) \Bigg]. \end{aligned} \tag{10.41}$$

We continue with the discussion of the double-collinear subtraction of the triple-collinear contribution. Focusing on the i-collinear partition, the corresponding expression reads

$$\Sigma_{dc}^{i,tc} = \frac{N_u}{\epsilon} \int_0^1 \frac{\mathrm{d}\omega}{\omega^{1+2\epsilon}} \left\langle \theta^{b+d}\, C_{\mathfrak{mn}}\, [\mathrm{d}\Omega_{\mathfrak{mn}}]\, C_{i\mathfrak{mn}}\, \psi_{\mathfrak{mn}}^{4\epsilon}\, \bar{S}_\omega \, \left[w^2 \tilde{S}_{ij}^{gg}(\mathfrak{m},\mathfrak{n}) \right] \right\rangle_{\mathfrak{mn}}. \tag{10.42}$$

We now discuss how to compute the required limits. Our starting point is Eq. (10.36) where we are supposed to take $\mathfrak{m}||\mathfrak{n}$ limit; this limit is made specific through the parametrization of scalar products in b and d sectors. The challenge in taking the limit is related to the fact that $1/\rho_{\mathfrak{mn}}^2$ appears in the first term in Eq. (10.36) which is too strong a singularity and so an expansion around the limit is needed. Fortunately, this can be avoided if we recall that in b and d sectors the following equation holds (c.f. Refs. [1, 38])

$$\frac{(\rho_{i\mathfrak{m}} - \rho_{i\mathfrak{n}})^2}{\rho_{\mathfrak{mn}}} = 2x_3\, N(x_3, 1 - x_4/2, \lambda). \tag{10.43}$$

Here N is the function that appears in the phase-space parametrization of b and d sectors [1, 38]. For the purposes of computing the double-collinear limit of a triple-collinear limit, we need to take $x_4 \to 0$ in Eq. (10.43). Upon doing that, we find [1, 38]

$$\lim_{x_4\to 0} \frac{(\rho_{i\mathfrak{m}} - \rho_{i\mathfrak{n}})^2}{\rho_{\mathfrak{mn}}} = 8x_3(1-x_3)\lambda = 2\rho_{i\mathfrak{m}}(2-\rho_{i\mathfrak{m}})\,\lambda. \tag{10.44}$$

If we combined the above expression together with Eq. (10.14), we easily obtain

$$\begin{aligned} &\theta^b\, C_{\mathfrak{mn}}\, [\mathrm{d}\Omega_{\mathfrak{mn}}]\, C_{i\mathfrak{mn}}\, \psi_{\mathfrak{mn}}^{4\epsilon}\, \bar{S}_\omega \, \left[w^2 \tilde{S}_{ij}^{gg}(\mathfrak{m},\mathfrak{n}) \right] = N_\epsilon^{(b,d)} [\mathrm{d}\Omega_{\mathfrak{m}}^{(d-1)}] \frac{\mathrm{d}x_4}{x_4^{1+2\epsilon}} \\ &\times \frac{\eta_{i\mathfrak{m}}^{-\epsilon}(1-\eta_{i\mathfrak{m}})^\epsilon}{\rho_{i\mathfrak{m}}^{1-4\epsilon}} \frac{4\omega}{(1+\omega)^{2-4\epsilon}} \left(-2 + \frac{\omega(1-\epsilon)(1+2\epsilon)}{(1+\omega)^2}\,(1-\eta_{i\mathfrak{m}}) \right). \end{aligned} \tag{10.45}$$

Note that we have used $\int \mathrm{d}\Lambda\, \lambda = (1+2\epsilon)/2$, see Refs. [1, 38] for details. We also note that the contribution of the sector d is identical.

The rest of the calculation is straightforward. Integrating over directions of $\mathfrak{m}$ and over the energy parameter ω, and combining contributions of sectors b and d we find

$$\begin{aligned} \Sigma_{dc}^{i,tc} = -\frac{N_u N_\epsilon^{(b,d)}}{\epsilon^2} \Bigg[&-\frac{11}{6\epsilon} - \frac{137}{18} - \frac{11\ln 2}{3} + \epsilon\Big(\frac{11\pi^2}{9} - \frac{823}{27} \\ &- \frac{11}{3}\ln^2 2 - \frac{137\ln 2}{9}\Big) + \epsilon^2\Big(\frac{88\zeta_3}{3} + \frac{137\pi^2}{27} - \frac{9880}{81} \\ &- \frac{22}{9}\ln^3 2 - \frac{137\ln^2 2}{9} + \frac{22}{9}\pi^2 \ln 2 - \frac{1646\ln 2}{27}\Big) + \mathcal{O}(\epsilon^3) \Bigg]. \end{aligned} \tag{10.46}$$

The quantity $N_\epsilon^{(b,d)}$ is defined in Eq. (10.15).

Combining the different results, we obtain

$$\begin{aligned}
&\frac{N_u}{\epsilon}\sum_{x\in\{i,j\}}\int_0^1\frac{\mathrm{d}\omega}{\omega^{1+2\epsilon}}\left\langle(1-\theta^{b+d}C_{\mathfrak{mn}})\,[\mathrm{d}\Omega_{\mathfrak{mn}}]\,C_{x\mathfrak{mn}}\,w^{tc}\,\psi^{4\epsilon}_{\mathfrak{mn}}\,\bar{S}_\omega\,\left[w^2\tilde{S}^{gg}_{ij}(\mathfrak{m},\mathfrak{n})\right]\right\rangle_{\mathfrak{mn}}\\
&=N_u\left[\frac{1}{\epsilon^2}\left(\frac{\pi^2}{6}-\frac{32}{9}-\frac{11}{3}\ln 2\right)+\frac{1}{\epsilon}\left(3\zeta_3+\frac{11\pi^2}{9}-\frac{202}{9}-\frac{11}{3}\ln^2 2-\frac{137\ln 2}{9}\right)\right.\\
&\left.+\frac{77}{3}\zeta_3+\frac{182\pi^2}{45}-\frac{8582}{81}-\frac{22}{9}\ln^3 2-\frac{137\ln^2 2}{9}+\left(\frac{11}{9}\pi^2-\frac{1646}{27}\right)\ln 2+\mathcal{O}(\epsilon)\right].
\end{aligned}\tag{10.47}$$

As expected, we observe the cancellation of the leading $\mathcal{O}(1/\epsilon^3)$ singularities between the triple-collinear contribution and its double-collinear limit, indicating that the subtraction of $\mathfrak{m}||\mathfrak{n}$ subdivergences was properly performed.

11 Correlated emissions without N-jettiness constraint

As we mentioned earlier, we would like to use the result of Ref. [48] to deduce certain contributions to the N-jettiness soft function. The corresponding expression is given in Eq. (10.10); our goal is to determine the sum of the fourth and the fifth terms in the right-hand side of that equation from the known result for J_{ij}. It is clear that this is only possible if all other terms on the right-hand side of Eq. (10.10) are known. Below we describe the calculation of the strongly-ordered, double-collinear $\mathfrak{m}||\mathfrak{n}$ and the triple-collinear limits of the correlated emissions without the N-jettiness constraint.

11.1 Strongly-ordered limit without N-jettiness constraint

We begin by considering the following integral

$$J^{\mathrm{so}}_{ij}=\frac{N_E}{\epsilon}\int_0^1\frac{\mathrm{d}\omega}{\omega^{1+2\epsilon}}\left\langle S_\omega[\omega^2\tilde{S}^{gg}_{ij}(\mathfrak{m},\mathfrak{n})]\right\rangle_{\mathfrak{mn}}.\tag{11.1}$$

Using the result for the soft limit of the eikonal function $\tilde{S}^{gg}_{ij}$, we find

$$J^{\mathrm{so}}_{ij}=-\frac{N_E}{\epsilon^2}\left\langle\frac{2\rho_{ij}}{\rho_{\mathfrak{mn}}\rho_{i\mathfrak{m}}\rho_{j\mathfrak{n}}}-\frac{\rho^2_{ij}}{\rho_{i\mathfrak{m}}\rho_{j\mathfrak{m}}\rho_{i\mathfrak{n}}\rho_{j\mathfrak{n}}}\right\rangle_{\mathfrak{mn}}.\tag{11.2}$$

The two terms that need to be integrated in Eq. (11.2) are quite different. The second one is easy to compute because integrations over directions of $\mathfrak{m}$ and $\mathfrak{n}$ factorize. For each of the integrals we use

$$\left\langle\frac{\rho_{ij}}{\rho_{i\mathfrak{n}}\rho_{j\mathfrak{n}}}\right\rangle_{\mathfrak{n}}=-\frac{2^{1-2\epsilon}\,\eta_{ij}^{-\epsilon}}{\epsilon}K_{ij},\tag{11.3}$$

where

$$K_{ij}=\frac{\Gamma(1-\epsilon)^2}{\Gamma(1-2\epsilon)}{}_2F_1(-\epsilon,-\epsilon,1-\epsilon,1-\eta_{ij}).\tag{11.4}$$

Integration of the first term on the right-hand side in Eq. (11.2) requires more effort. We first use the result in Eq. (B.5) to integrate over $\mathfrak{n}$, then write the obtained hypergeometric function using the representation in Eq. (10.40) and integrate over directions of $\mathfrak{m}$. This gives another hypergeometric function for which we introduce Mellin-Barnes representation again. Finally, we find

$$\begin{aligned}\left\langle \frac{\rho_{ij}}{\rho_{\mathfrak{mn}}\rho_{i\mathfrak{m}}\rho_{j\mathfrak{n}}} \right\rangle_{\mathfrak{mn}} &= \frac{\Gamma(1-\epsilon)^2}{\Gamma(-2\epsilon)} \int \frac{\mathrm{d}z_2}{2\pi i} \frac{\rho_{ij}^{1+z_2}}{2^{1+z_2+4\epsilon}} \Gamma(-z_2)\Gamma(1+z_2) \\ &\times \int \frac{\mathrm{d}z_1}{2\pi i} \frac{\Gamma(-z_1)\Gamma(z_1-\epsilon)\Gamma^2(1+z_1+z_2)\Gamma(-1-\epsilon-z_1-z_2)}{\Gamma(1-2\epsilon+z_1+z_2)}.\end{aligned} \tag{11.5}$$

The integration over z_1 can be performed with the help of the Barnes' second lemma. Once this is done, the resulting integral can be transformed to a parametric integral using Euler's integral representation of Beta-functions. This gives

$$\left\langle \frac{\rho_{ij}}{\rho_{\mathfrak{mn}}\rho_{i\mathfrak{m}}\rho_{j\mathfrak{n}}} \right\rangle_{\mathfrak{mn}} = -\frac{6\,\eta_{ij}\,2^{-4\epsilon}\Gamma^5(1-\epsilon)}{\epsilon\,\Gamma(1-3\epsilon)\Gamma(1-2\epsilon)} \int_0^1 \mathrm{d}x\, \frac{x^{-1-2\epsilon}{}_2F_1(-2\epsilon,-\epsilon,-3\epsilon,x)}{x+(1-x)\eta_{ij}}, \tag{11.6}$$

where $\eta_{ij} = \rho_{ij}/2$. The resulting integral over x is straightforward to compute using the program Hyperint [50].

Performing the integration, combining the results for the two integrals that appear in Eq. (11.2) and expanding in powers of ϵ, we find

$$\begin{aligned}J_{ij}^{\mathrm{so}} = [\alpha_s]^2\, \frac{E_{\max}^{-4\epsilon}\,2^{-4\epsilon}}{2\epsilon^4} \Bigg[& 1 - 2\epsilon \ln(\eta_{ij}) + \epsilon^2 \left(4\mathrm{Li}_2(1-\eta_{ij}) + 2\ln^2(\eta_{ij}) - \frac{2\pi^2}{3} \right) \\ & + \epsilon^3 \Big(4\mathrm{Li}_3(1-\eta_{ij}) + 12\mathrm{Li}_3(\eta_{ij}) + 4\mathrm{Li}_2(1-\eta_{ij})\ln(\eta_{ij}) - \frac{4}{3}\ln^3(\eta_{ij}) \\ & + 6\ln(1-\eta_{ij})\ln^2(\eta_{ij}) - \frac{2}{3}\pi^2\ln(\eta_{ij}) - 26\zeta_3 \Big) + \epsilon^4 \Big(-\frac{19}{45}\pi^4 + \frac{2}{3}\ln^4(\eta_{ij}) \\ & - \frac{2}{3}\ln^3(\eta_{ij})\ln(1-\eta_{ij}) + 10\ln^2(\eta_{ij})\ln^2(1-\eta_{ij}) - \frac{10}{3}\pi^2\ln(\eta_{ij})\ln(1-\eta_{ij}) \\ & + 2[\pi^2 + 2\ln(\eta_{ij})\ln(1-\eta_{ij}) + \ln^2(\eta_{ij})]\mathrm{Li}_2(\eta_{ij}) + 2\mathrm{Li}_2^2(\eta_{ij}) - 28\mathrm{Li}_4(\eta_{ij}) \\ & + 4\mathrm{Li}_4(1-\eta_{ij}) + 32S_{2,2}(\eta_{ij}) + 4S_{2,2}(1-\eta_{ij}) + 32\ln(1-\eta_{ij})[\mathrm{Li}_3(\eta_{ij}) - \zeta_3] \\ & + 4\ln(\eta_{ij})[\mathrm{Li}_3(\eta_{ij}) + 6\mathrm{Li}_3(1-\eta_{ij}) + 5\zeta_3] \Big) + \mathcal{O}(\epsilon^5) \Bigg].\end{aligned} \tag{11.7}$$

In addition to standard polylogarithms, also the Nielsen polylogarithm $S_{2,2}(x)$ appears in the above formula.

11.2 Double-collinear limit without N-jettiness constraint

The easiest contribution to compute is the double-collinear $\mathfrak{m}||\mathfrak{n}$ subtraction term since we can borrow the calculation from Section 10.1 nearly verbatim. We then find

$$\begin{aligned}\frac{N_E}{\epsilon}\int_0^1 \frac{\mathrm{d}\omega}{\omega^{1+2\epsilon}}\left\langle C_{\mathfrak{mn}}\left[\mathrm{d}\Omega_{\mathfrak{mn}}\right]\theta^{b+d}\omega^{tc}\bar{S}_\omega\left[w^2\tilde{S}_{ij}^{gg}(\mathfrak{m},\mathfrak{n})\right]\right\rangle_{\mathfrak{mn}} \\ = -\frac{N_E N_\epsilon^{b,d}}{\epsilon^2}\left[\gamma_{gJ}A_J^{(ij)}+\epsilon\delta_{gJ}B_J^{(ij)}\right].\end{aligned} \tag{11.8}$$

The various quantities in this expression differ from similar quantities when the N-jettiness constraint is imposed. In particular,

$$\begin{aligned}A_J^{(ij)} = 2^\epsilon\left\langle\frac{\rho_{ij}^{1+\epsilon}}{\rho_{i\mathfrak{m}}^{1+\epsilon}\rho_{j\mathfrak{m}}^{1+\epsilon}}\right\rangle_{\mathfrak{mn}} + 2^\epsilon\left\langle\frac{\rho_{ij}^{1+\epsilon}}{\rho_{i\mathfrak{m}}^{1+\epsilon}\rho_{j\mathfrak{m}}^{1+\epsilon}}\omega_{\mathfrak{m}||\mathfrak{n}}^{\mathfrak{m}i,\mathfrak{n}i}\left[\left(\frac{\eta_{j\mathfrak{m}}}{\eta_{ij}}\right)^\epsilon(1-\eta_{i\mathfrak{m}})^\epsilon-1\right]\right\rangle \\ + 2^\epsilon\left\langle\frac{\rho_{ij}^{1+\epsilon}}{\rho_{i\mathfrak{m}}^{1+\epsilon}\rho_{j\mathfrak{m}}^{1+\epsilon}}\omega_{\mathfrak{m}||\mathfrak{n}}^{\mathfrak{m}j,\mathfrak{n}j}\left[\left(\frac{\eta_{i\mathfrak{m}}}{\eta_{ij}}\right)^\epsilon(1-\eta_{j\mathfrak{m}})^\epsilon-1\right]\right\rangle,\end{aligned} \tag{11.9}$$

and

$$\begin{aligned}B_J^{(ij)} &= 2^{1+\epsilon}\left\langle\frac{\rho_{ij}^{\epsilon}(\rho_{i\mathfrak{m}}+\rho_{j\mathfrak{m}})}{\rho_{i\mathfrak{m}}^{1+\epsilon}\rho_{j\mathfrak{m}}^{1+\epsilon}}\right\rangle_{\mathfrak{mn}} \\ &+ 2^{1+\epsilon}\left\langle\frac{\rho_{ij}^{\epsilon}(\rho_{i\mathfrak{m}}+\rho_{j\mathfrak{m}})}{\rho_{i\mathfrak{m}}^{1+\epsilon}\rho_{j\mathfrak{m}}^{1+\epsilon}}\omega_{\mathfrak{m}||\mathfrak{n}}^{\mathfrak{m}i,\mathfrak{n}i}\left[\left(\frac{\eta_{j\mathfrak{m}}}{\eta_{ij}}\right)^\epsilon(1-\eta_{i\mathfrak{m}})^\epsilon-1\right]\right\rangle \\ &+ 2^{1+\epsilon}\left\langle\frac{\rho_{ij}^{\epsilon}(\rho_{i\mathfrak{m}}+\rho_{j\mathfrak{m}})}{\rho_{i\mathfrak{m}}^{1+\epsilon}\rho_{j\mathfrak{m}}^{1+\epsilon}}\omega_{\mathfrak{m}||\mathfrak{n}}^{\mathfrak{m}j,\mathfrak{n}j}\left[\left(\frac{\eta_{i\mathfrak{m}}}{\eta_{ij}}\right)^\epsilon(1-\eta_{j\mathfrak{m}})^\epsilon-1\right]\right\rangle \\ &+ \left\langle\eta_{i\mathfrak{m}}^{-\epsilon}(1-\eta_{i\mathfrak{m}})^\epsilon\omega_{\mathfrak{m}||\mathfrak{n}}^{\mathfrak{m}i,\mathfrak{n}i}W_{ij}^{\mathfrak{m}}\right\rangle + \left\langle\eta_{j\mathfrak{m}}^{-\epsilon}(1-\eta_{j\mathfrak{m}})^\epsilon\omega_{\mathfrak{m}||\mathfrak{n}}^{\mathfrak{m}j,\mathfrak{n}j}W_{ji}^{\mathfrak{m}}\right\rangle.\end{aligned} \tag{11.10}$$

Furthermore, the anomalous dimensions read in this case

$$\begin{aligned}\gamma_{gJ} &= -\frac{11}{3}+\epsilon\left(-\frac{2}{3}-\frac{44}{3}\ln 2\right)+\epsilon^2\left(-\frac{22\pi^2}{9}-1-\frac{4}{3}\ln 2\right) \\ &\quad+\epsilon^3\left(-44\zeta_3-\frac{2\pi^2}{9}+\frac{4}{3}-\frac{16}{3}\ln 2\right)+\mathcal{O}(\epsilon^4), \\ \delta_{gJ} &= \frac{1}{3}+\epsilon\left(\frac{4\ln 2}{3}-\frac{2}{3}\right)+\epsilon^2\left(\frac{2\pi^2}{9}-1-\frac{1}{3}4\ln 2\right)+\mathcal{O}(\epsilon^3).\end{aligned} \tag{11.11}$$

11.3 Triple-collinear limit without N-jettiness constraint

The next contribution that we require is the triple-collinear one, from which the double-collinear limit is to be subtracted. Similar to the calculation with the N-jettiness constraint, we find it to be convenient to calculate the two terms separately and then subtract them from each other. Furthermore, the two triple collinear configurations, $\mathfrak{m}||\mathfrak{n}||i$ and $\mathfrak{m}||\mathfrak{n}||j$, are the same. Hence, we consider one of them and multiply the result by a factor two to account for the other one.

An important difference with respect to a similar computation with the N-jettiness constraint is the fact that the $\omega \to 1/\omega$ transformation is not a symmetry anymore. For this reason the closed-form integration over ω becomes impossible. Hence, we proceed as follows. We first employ the Mellin-Barnes representations to integrate over angles of $\mathfrak{m}$ and $\mathfrak{n}$. Similar to the N-jettiness case, we find that one of the Mellin-Barnes integrations can be performed using the second Barnes lemma. We then map the remaining Mellin-Barnes integrals onto multi-variable integrals using Euler's integral representation of Beta-functions and then integrate over the new (Euler) variables as well as over ω. We find

$$\begin{aligned}
&\frac{N_E}{\epsilon}\sum_{x\in\{i,j\}}\int_0^1\frac{\mathrm{d}\omega}{\omega^{1+2\epsilon}}\left\langle C_{x\mathfrak{mn}}\,w^{tc}\,\bar{S}_\omega\,\left[\omega^2\tilde{S}^{gg}_{ij}(\mathfrak{m},\mathfrak{n})\right]\right\rangle_{\mathfrak{mn}}=[\alpha_s]^2E_{\max}^{-4\epsilon}\Bigg[\frac{11}{12\epsilon^3}\\
&+\frac{1}{\epsilon^2}\left(\frac{\pi^2}{12}-\frac{35}{18}\right)+\frac{1}{\epsilon}\left(\frac{11\zeta_3}{4}-\frac{11\pi^2}{36}+\frac{205}{54}-11\ln^2 2-\frac{1}{3}\pi^2\ln 2-\frac{\ln 2}{2}\right)\\
&+4\mathrm{Li}_4\left(\frac{1}{2}\right)-\frac{275\zeta_3}{12}-\frac{15}{2}\zeta_3\ln 2+\frac{\pi^4}{80}+\frac{137\pi^2}{216}-\frac{1463}{162}+\frac{\ln^4 2}{6}+\frac{110\ln^3 2}{3}\\
&+\frac{1}{2}\pi^2\ln^2 2+\frac{155\ln^2 2}{6}-\frac{11}{18}\pi^2\ln 2-\ln 2+\mathcal{O}(\epsilon)\Bigg].
\end{aligned}\tag{11.12}$$

The next step is to compute the double-collinear limit of the triple-collinear subtraction term without the N-jettiness constraint. The calculation follows the same steps as what is discussed in the previous Section where the N-jettiness constraint was taken into account. We find the following representation of the corresponding quantity

$$\begin{aligned}
&\left\langle C_{\mathfrak{mn}}[\mathrm{d}\Omega_{\mathfrak{mn}}]\theta^{(b+d)}C_{i\mathfrak{mn}}\,\omega^{tc}\,\bar{S}_\omega\,\left[\omega^2\tilde{S}^{gg}_{ij}(\mathfrak{m},\mathfrak{n})\right]\right\rangle_{\mathfrak{mn}}\\
&=-\frac{N_\epsilon^{(b,d)}}{2\epsilon}\left\langle\eta_{i\mathfrak{m}}^{-\epsilon-1}(1-\eta_{i\mathfrak{m}})^\epsilon\frac{4\omega}{(1+\omega)^2}\left[-2+\frac{(1-\epsilon)(1+2\epsilon)\omega}{(1+\omega)^2}\,(1-\eta_{i\mathfrak{m}})\right]\right\rangle_{\mathfrak{m}}.
\end{aligned}\tag{11.13}$$

The remaining integration over the directions of parton $\mathfrak{m}$ is straightforward. We find

$$\begin{aligned}
&\frac{N_E}{\epsilon}\sum_{x\in\{i,j\}}\int_0^1\frac{\mathrm{d}\omega}{\omega^{1+2\epsilon}}\left\langle\theta^{(b+d)}\,C_{\mathfrak{mn}})\;[\mathrm{d}\Omega_{\mathfrak{mn}}]\;C_{x\mathfrak{mn}}\,\omega^{tc}\bar{S}_\omega\;\left[\omega^2\tilde{S}^{gg}_{ij}(\mathfrak{m},\mathfrak{n})\right]\right\rangle_{\mathfrak{mn}}=\\
&[\alpha_s]^2E_{\max}^{-4\epsilon}\Bigg[\frac{11}{12\epsilon^3}+\frac{1}{\epsilon^2}\left(\frac{11\ln 2}{6}-\frac{1}{6}\right)+\frac{1}{\epsilon}\left(\frac{11\pi^2}{12}+\frac{1}{4}-\frac{1}{2}11\ln^2 2-\frac{2\ln 2}{3}\right)\\
&+\frac{55\zeta_3}{6}+\frac{2}{3}-\frac{2\pi^2}{9}+\frac{55\ln^3 2}{9}+\frac{5\ln^2 2}{3}-\frac{11}{18}\pi^2\ln 2-\frac{\ln 2}{2}+\mathcal{O}(\epsilon)\Bigg].
\end{aligned}\tag{11.14}$$

11.4 Extracting the required combinations of the various contributions

As we already mentioned, J_{ij} defined in Eq. (10.10) was computed in Ref. [48]. We can use this result, supplemented with our computation of the various limits without the N-jettiness constraint, to derive analytic results for the quantity that is needed for computations with the N-jettiness constraint.

Specifically, we use Eq. (10.10) to write

$$
\begin{aligned}
&\frac{N_E}{\epsilon}\sum_{x\in\{i,j\}}\int_0^1\frac{\mathrm{d}\omega}{\omega^{1+2\epsilon}}\left\langle(1-\theta^{b+d}C_{\mathfrak{mn}})\,[\mathrm{d}\Omega_{\mathfrak{mn}}]\,\bar{C}_{x\mathfrak{mn}}\;w^{x\mathfrak{m},x\mathfrak{n}}\;\bar{S}_\omega\left[w^2\tilde{S}_{ij}^{gg}(\mathfrak{m},\mathfrak{n})\right]\right\rangle_{\mathfrak{mn}}\\
&+\frac{N_E}{\epsilon}\int_0^1\frac{\mathrm{d}\omega}{\omega^{1+2\epsilon}}\left\langle\left(w^{\mathfrak{m}i,\mathfrak{n}j}+w^{\mathfrak{m}j,\mathfrak{n}i}\right)\;\bar{S}_\omega\left[w^2\tilde{S}_{ij}^{gg}(\mathfrak{m},\mathfrak{n})\right]\right\rangle_{\mathfrak{mn}}\\
&\quad=J_{ij}-\frac{N_E}{\epsilon}\int_0^1\frac{\mathrm{d}\omega}{\omega^{1+2\epsilon}}\left\langle S_\omega\left[\omega^2\tilde{S}_{ij}(\mathfrak{m},\mathfrak{n})\right]\right\rangle_{\mathfrak{mn}}\\
&\quad-\frac{N_E}{\epsilon}\int_0^1\frac{\mathrm{d}\omega}{\omega^{1+2\epsilon}}\left\langle C_{\mathfrak{mn}}\,[\mathrm{d}\Omega_{\mathfrak{mn}}]\,\theta^{b+d}\omega^{tc}\bar{S}_\omega\left[w^2\tilde{S}_{ij}^{gg}(\mathfrak{m},\mathfrak{n})\right]\right\rangle_{\mathfrak{mn}}\\
&\quad-\frac{N_E}{\epsilon}\sum_{x\in\{i,j\}}\int_0^1\frac{\mathrm{d}\omega}{\omega^{1+2\epsilon}}\left\langle(1-\theta^{b+d}C_{\mathfrak{mn}})\,[\mathrm{d}\Omega_{\mathfrak{mn}}]\,C_{x\mathfrak{mn}}\omega^{tc}\bar{S}_\omega\left[w^2\tilde{S}_{ij}^{gg}(\mathfrak{m},\mathfrak{n})\right]\right\rangle_{\mathfrak{mn}}.
\end{aligned}
\tag{11.15}
$$

Using the results of the calculation discussed earlier, we obtain

$$
\begin{aligned}
&\frac{N_E}{\epsilon}\sum_{x\in\{i,j\}}\int_0^1\frac{\mathrm{d}\omega}{\omega^{1+2\epsilon}}\left\langle(1-\theta^{b+d}C_{\mathfrak{mn}})\,[\mathrm{d}\Omega_{\mathfrak{mn}}]\,\bar{C}_{x\mathfrak{mn}}\;\bar{S}_\omega\left[w^2\tilde{S}_{ij}^{gg}(\mathfrak{m},\mathfrak{n})\right]\right\rangle_{\mathfrak{mn}}\\
&+\frac{N_E}{\epsilon}\int_0^1\frac{\mathrm{d}\omega}{\omega^{1+2\epsilon}}\left\langle\left(w^{\mathfrak{m}i,\mathfrak{n}j}+w^{\mathfrak{m}j,\mathfrak{n}i}\right)\;\bar{S}_\omega\left[w^2\tilde{S}_{ij}^{gg}(\mathfrak{m},\mathfrak{n})\right]\right\rangle_{\mathfrak{mn}}\\
&=\frac{1}{\epsilon}\left(\frac{11}{12}A_{ij}^{\mathrm{fin}}-\frac{1}{12}B_{ij}^{\mathrm{fin}}-\frac{\pi^2}{6}\ln(\eta_{ij})+\frac{11}{3}\ln 2\ln(\eta_{ij})+\frac{35\ln(\eta_{ij})}{9}\right.\\
&\quad\left.+\frac{11\pi^2}{18}-\zeta_3-\frac{1}{9}-\frac{1}{3}\ln 2\right)+\mathcal{O}(\epsilon^0),
\end{aligned}
\tag{11.16}
$$

where

$$
\begin{aligned}
A_{ij}^{\mathrm{fin}}&=\left\langle\frac{\rho_{ij}}{\rho_{i\mathfrak{m}}\rho_{j\mathfrak{m}}}\left[\omega_{\mathfrak{m}i,\mathfrak{n}i}^{\mathfrak{m}||\mathfrak{n}}\ln\left(\frac{\eta_{j\mathfrak{m}}(1-\eta_{i\mathfrak{m}})}{\eta_{ij}}\right)+\omega_{\mathfrak{m}j,\mathfrak{n}j}^{\mathfrak{m}||\mathfrak{n}}\ln\left(\frac{\eta_{i\mathfrak{m}}(1-\eta_{j\mathfrak{m}})}{\eta_{ij}}\right)\right]\right\rangle_{\mathfrak{m}},\\
B_{ij}^{\mathrm{fin}}&=\left\langle\omega_{\mathfrak{m}||\mathfrak{n}}^{\mathfrak{m}i,\mathfrak{n}i}\;W_{ij}^{\mathfrak{m}}+\omega_{\mathfrak{m}||\mathfrak{n}}^{\mathfrak{m}j,\mathfrak{n}j}\;W_{ji}^{\mathfrak{m}}\right\rangle_{\mathfrak{m}}.
\end{aligned}
\tag{11.17}
$$

To save space, we do not show $\mathcal{O}(\epsilon^0)$ terms in Eq. (11.16) although they are needed for the final result. It is, however, straightforward to compute them following the preceding discussion.

We can use the result shown in Eq. (11.16) to compute the remaining contribution to the N-jettiness soft functions that originates from correlated emissions. Upon doing that, we find that the divergent contributions cancel and a finite remainder is obtained. We present the corresponding results in Section 13.

12 Final-state fermions

We continue with the discussion of the contribution of the soft $q\bar{q}$ pair to the N-jettiness soft function. In this case, the entire contribution comes from correlated emissions. It reads

$$S^{q\bar{q}}_{2,RR,T^2,\tau} = \frac{n_f T_R}{2} \sum_{(ij)} \mathbf{T}_i \cdot \mathbf{T}_j \; I^{q\bar{q}}_{ij,\tau}, \tag{12.1}$$

where

$$I^{q\bar{q}}_{ij,\tau} = g_s^4 \int [\mathrm{d}p]_{\mathfrak{m}} [\mathrm{d}p]_{\mathfrak{n}} \delta(\tau - E_{\mathfrak{m}}\psi_{\mathfrak{m}} - E_{\mathfrak{n}}\psi_{\mathfrak{n}}) \; \tilde{S}^{q\bar{q}}_{ij}(\mathfrak{m},\mathfrak{n}). \tag{12.2}$$

The eikonal function $\tilde{S}^{q\bar{q}}_{ij}$ is symmetric under the interchange of q and $\bar{q}$ momenta; it can be found in Appendix C. Hence, we proceed in exactly the same way as with the gluons in that we introduce the energy ordering $E_{\mathfrak{n}} < E_{\mathfrak{m}}$, write $E_{\mathfrak{n}} = \omega E_{\mathfrak{m}}$, with $0 < \omega < 1$, and integrate over $E_{\mathfrak{m}}$. After the Laplace transform, we obtain

$$I^{q\bar{q}}_{ij} = \frac{2N_u}{\epsilon} \int_0^1 \frac{\mathrm{d}\omega}{\omega^{1+2\epsilon}} \left\langle \psi^{4\epsilon}_{\mathfrak{mn}} \omega^2 \tilde{S}^{q\bar{q}}_{ij}(\mathfrak{m},\mathfrak{n}) \right\rangle_{\mathfrak{mn}}, \tag{12.3}$$

where we have to set $E_{\mathfrak{m}}$ to one and $E_{\mathfrak{n}}$ to ω when computing $\tilde{S}^{q\bar{q}}_{ij}(\mathfrak{m},\mathfrak{n})$ in the last equation.

We continue with the investigation of the various limits of the above equation. In principle, these limits are identical to the ones in the gluon case except that the $q\bar{q}$ eikonal function does not possess a strongly-ordered singular limit. Accounting for this and following what has been done for the two-gluon final state, we write

$$\begin{aligned}
I^{q\bar{q}}_{ij} = {} & \frac{2N_u}{\epsilon} \int_0^1 \frac{\mathrm{d}\omega}{\omega^{1+2\epsilon}} \left\langle C_{\mathfrak{mn}} \, [\mathrm{d}\Omega_{\mathfrak{mn}}] \, \theta^{b+d} w^{tc} \psi^{4\epsilon}_{\mathfrak{mn}} [\omega^2 \tilde{S}^{q\bar{q}}_{ij}(\mathfrak{m},\mathfrak{n})] \right\rangle_{\mathfrak{mn}} \\
& + \frac{2N_u}{\epsilon} \sum_{x\in\{i,j\}} \int_0^1 \frac{\mathrm{d}\omega}{\omega^{1+2\epsilon}} \left\langle (1 - \theta^{b+d} C_{\mathfrak{mn}}) \, [\mathrm{d}\Omega_{\mathfrak{mn}}] \, C_{x\mathfrak{mn}} \psi^{4\epsilon}_{\mathfrak{mn}} [\omega^2 \tilde{S}^{q\bar{q}}_{ij}(\mathfrak{m},\mathfrak{n})] \right\rangle_{\mathfrak{mn}} \\
& + \frac{2N_u}{\epsilon} \sum_{x\in\{i,j\}} \int_0^1 \frac{\mathrm{d}\omega}{\omega^{1+2\epsilon}} \left\langle (1 - \theta^{b+d} C_{\mathfrak{mn}}) \, [\mathrm{d}\Omega_{\mathfrak{mn}}] \, \bar{C}_{x\mathfrak{mn}} \; w^{x\mathfrak{m},x\mathfrak{n}} \; [\omega^2 \tilde{S}^{q\bar{q}}_{ij}(\mathfrak{m},\mathfrak{n})] \right\rangle_{\mathfrak{mn}} \\
& + \frac{2N_u}{\epsilon} \sum_{x\in\{i,j\}} \int_0^1 \frac{\mathrm{d}\omega}{\omega^{1+2\epsilon}} \left\langle \left(w^{i\mathfrak{m},j\mathfrak{n}} + w^{j\mathfrak{m},i\mathfrak{n}} \right) \; [\omega^2 \tilde{S}^{q\bar{q}}_{ij}(\mathfrak{m},\mathfrak{n})] \right\rangle_{\mathfrak{mn}} \\
& + 8N_u \sum_{x\in\{i,j\}} \int_0^1 \frac{\mathrm{d}\omega}{\omega^{1+2\epsilon}} \left\langle (1 - \theta^{b+d} C_{\mathfrak{mn}}) \, [\mathrm{d}\Omega_{\mathfrak{mn}}] \, \bar{C}_{x\mathfrak{mn}} \; w^{x\mathfrak{m},x\mathfrak{n}} \; \ln\psi_{\mathfrak{mn}} \; [\omega^2 \tilde{S}^{q\bar{q}}_{ij}(\mathfrak{m},\mathfrak{n})] \right\rangle_{\mathfrak{mn}} \\
& + 8N_u \sum_{x\in\{i,j\}} \int_0^1 \frac{\mathrm{d}\omega}{\omega^{1+2\epsilon}} \left\langle \left(w^{i\mathfrak{m},j\mathfrak{n}} + w^{j\mathfrak{m},i\mathfrak{n}} \right) \ln\psi_{\mathfrak{mn}} \; [\omega^2 \tilde{S}^{q\bar{q}}_{ij}(\mathfrak{m},\mathfrak{n})] \right\rangle_{\mathfrak{mn}}.
\end{aligned} \tag{12.4}$$

We continue with the discussion of the individual terms. The first one is the double-collinear $\mathfrak{m}||\mathfrak{n}$ limit. It reads

$$C_{\mathfrak{mn}}[\omega^2 \tilde{S}_{ij}^{q\bar{q}}(\mathfrak{m},\mathfrak{n})] = \frac{2\omega\rho_{ij}}{(1+\omega)^2\rho_{\mathfrak{mn}}\rho_{i\mathfrak{m}}\rho_{j\mathfrak{m}}}\left(-1+\frac{2\omega}{(1+\omega)^2}\,\frac{\rho_{i\mathfrak{m}}\rho_{j\mathfrak{m}}}{\rho_{ij}}\,v_\mu v_\nu \kappa_{\mathfrak{n}}^\mu \kappa_{\mathfrak{n}}^\nu,\right). \tag{12.5}$$

The vectors v^μ and $\kappa_{\mathfrak{n}}^\nu$ are defined in Eq. (10.16). We compute this contribution following the discussion of the two-gluon case. Borrowing most of the calculation from there, we write the result for the sum of b and d sectors

$$\begin{aligned}\Sigma_{\mathfrak{m}||\mathfrak{n}}^{(i)} &= \frac{N_u}{\epsilon}\int_0^1 \frac{\mathrm{d}\omega}{\omega^{1+2\epsilon}}\left\langle C_{\mathfrak{mn}}[\mathrm{d}\Omega_{\mathfrak{mn}}]\theta^{b+d}\omega^{\mathfrak{m}i,\mathfrak{n}i}\psi_{\mathfrak{mn}}^{4\epsilon}\left[w^2\tilde{S}_{ij}^{q\bar{q}}(\mathfrak{m},\mathfrak{n})\right]\right\rangle_{\mathfrak{mn}} \\ &= -\frac{N_u N_\epsilon^{b,d}}{\epsilon^2}\left\langle \frac{\eta_{i\mathfrak{m}}^{-\epsilon}}{(1-\eta_{i\mathfrak{m}})^{-\epsilon}}\,\psi_{\mathfrak{m}}^{4\epsilon}\,\omega_{\mathfrak{m}||\mathfrak{n}}^{\mathfrak{m}i,\mathfrak{n}i}\left[\gamma_{q\bar{q}}\,A_{q\bar{q}}^{(i)}+\epsilon\delta_{q\bar{q}}\,B_{q\bar{q}}^{(i)}\right]\right\rangle_{\mathfrak{m}},\end{aligned} \tag{12.6}$$

with

$$A_{q\bar{q}}^{(i)} = \frac{\rho_{ij}}{\rho_{i\mathfrak{m}}\rho_{j\mathfrak{m}}}, \quad B_{q\bar{q}}^{(i)} = \left(2\frac{\rho_{i\mathfrak{m}}+\rho_{j\mathfrak{m}}}{\rho_{i\mathfrak{m}}\rho_{j\mathfrak{m}}}+W_{ij}^{\mathfrak{m}}\right), \tag{12.7}$$

and

$$\begin{aligned}\gamma_{q\bar{q}} &= \int_0^1 \frac{\mathrm{d}\omega}{\omega^{1+2\epsilon}}\frac{2\omega}{(1+\omega)^{2-4\epsilon}}\left(-1+\frac{2\omega}{(1+\omega)^2}\right) = -\frac{2}{3}-\frac{26}{9}\epsilon \\ &+\left(\frac{4\pi^2}{9}-\frac{320}{27}\right)\epsilon^2+\left(\frac{32}{3}\zeta_3+\frac{52}{27}\pi^2-\frac{3872}{81}\right)\epsilon^3+\mathcal{O}(\epsilon^4), \\ \delta_{q\bar{q}} &= \int_0^1 \frac{\mathrm{d}\omega}{\omega^{1+2\epsilon}}\frac{4\omega^2}{(1+\omega)^{4-4\epsilon}} = \frac{1}{3}+\frac{10}{9}\epsilon+\left(\frac{112}{27}-\frac{2\pi^2}{9}\right)\epsilon^2+\mathcal{O}(\epsilon^3).\end{aligned} \tag{12.8}$$

Structurally, this result is identical to the $\mathfrak{m}||\mathfrak{n}$ contribution in the two-gluon case except that different collinear anomalous dimensions appear. The analysis, therefore, proceeds along identical lines and the result can be written in the same way as in the two-gluon case, c.f. Eqs. (10.29, 10.31, 10.32) up to the change in the anomalous dimensions and the overall normalization factor.

As the next step, we need to compute the triple-collinear limit of the $q\bar{q}$ eikonal function. The calculation follows what has already been done for the two-gluon case. We obtain

$$C_{i\mathfrak{mn}}[\omega^2\tilde{S}_{ij}^{q\bar{q}}(\mathfrak{m},\mathfrak{n})] = \frac{2\omega^2}{(1+\omega)^2}\,\frac{(\rho_{i\mathfrak{m}}-\rho_{i\mathfrak{n}})^2}{\rho_{\mathfrak{mn}}^2(\rho_{i\mathfrak{m}}+\omega\rho_{i\mathfrak{n}})^2}-\frac{2\omega}{(1+\omega)}\,\frac{1}{\rho_{\mathfrak{mn}}(\rho_{i\mathfrak{m}}+\omega\rho_{i\mathfrak{n}})}. \tag{12.9}$$

Since this expression is also very similar to the two-gluon case, we proceed accordingly. As the first step, we change the integration variable $\omega \to 1/\omega$ and extend the integration over ω to $\omega = \infty$ using the symmetry of the integrand. We then write

$$\Sigma_{q\bar{q}}^{i,tc} = \frac{N_u}{\epsilon}B_{q\bar{q}}^i, \tag{12.10}$$

where

$$B^i_{q\bar{q}} = \int_0^\infty \frac{\mathrm{d}\omega}{\omega^{1+2\epsilon}} \left\langle \frac{2\omega}{(1+\omega)(\rho_{i\mathfrak{m}}+\omega\rho_{i\mathfrak{n}})^{1-4\epsilon}} \left(\frac{\omega}{(1+\omega)} \frac{(\rho_{i\mathfrak{m}}-\rho_{i\mathfrak{n}})^2}{\rho^2_{\mathfrak{mn}}(\rho_{i\mathfrak{m}}+\omega\rho_{i\mathfrak{n}})} - \frac{1}{\rho_{\mathfrak{mn}}} \right) \right\rangle_{\mathfrak{mn}} . \quad (12.11)$$

Using the $\mathfrak{m} \leftrightarrow \mathfrak{n}$ and $\omega \to 1/\omega$ transformations, we rewrite the above expression as

$$B^i_{q\bar{q}} = \int_0^\infty \frac{\mathrm{d}\omega}{\omega^{1+2\epsilon}} \left\langle \frac{2\omega}{(1+\omega)(\rho_{i\mathfrak{m}}+\omega\rho_{i\mathfrak{n}})^{1-4\epsilon}} \left(\frac{2\omega}{(1+\omega)} \frac{\rho_{i\mathfrak{m}}(\rho_{i\mathfrak{m}}-\rho_{i\mathfrak{n}})}{\rho^2_{\mathfrak{mn}}(\rho_{i\mathfrak{m}}+\omega\rho_{i\mathfrak{n}})} - \frac{1}{\rho_{\mathfrak{mn}}} \right) \right\rangle_{\mathfrak{mn}} . \quad (12.12)$$

The calculation proceeds along the same lines as in the two-gluon case. We obtain

$$\Sigma^{i,tc}_{q\bar{q}} = \frac{N_u}{\epsilon} \left[\frac{2}{3\epsilon^2} + \frac{16}{9\epsilon} + \frac{2\pi^2}{9} + \frac{104}{27} + \epsilon \left(-\frac{8\zeta_3}{3} + \frac{16\pi^2}{27} + \frac{640}{81} \right) + \mathcal{O}(\epsilon^2) \right] . \quad (12.13)$$

The double-collinear subtraction term of the triple-collinear contribution reads

$$\Sigma^{i,tc}_{dc,q\bar{q}} = \frac{N_u}{\epsilon} \int_0^1 \frac{\mathrm{d}\omega}{\omega^{1+2\epsilon}} \left\langle \theta^{b+d}\, C_{\mathfrak{mn}}\, [\mathrm{d}\Omega_{\mathfrak{mn}}]\, C_{i\mathfrak{mn}}\, \psi^{4\epsilon}_{\mathfrak{mn}} \left[w^2 \tilde{S}^{q\bar{q}}_{ij}(\mathfrak{m},\mathfrak{n}) \right] \right\rangle_{\mathfrak{mn}} . \quad (12.14)$$

Following the very same procedure as in the two-gluon case, we arrive at

$$\begin{aligned} \Sigma^{i,tc}_{dc,q\bar{q}} = \frac{N_u N^{(b,d)}_\epsilon}{\epsilon^2} \Bigg[& \frac{2}{3\epsilon} + \frac{4\ln 2}{3} + \frac{26}{9} + \epsilon \left(\frac{4\ln^2 2}{3} + \frac{52\ln 2}{9} - \frac{4\pi^2}{9} + \frac{320}{27} \right) \\ & + \epsilon^2 \Bigg(-\frac{32\zeta_3}{3} + \frac{8\ln^3 2}{9} + \frac{52\ln^2 2}{9} - \left(\frac{8\pi^2}{9} - \frac{640}{27} \right) \ln 2 \\ & - \frac{52\pi^2}{27} + \frac{3872}{81} \Bigg) + \mathcal{O}(\epsilon^3) \Bigg] . \end{aligned} \quad (12.15)$$

Combining the above results and accounting for the contribution of the second partition function, we obtain the result for the triple-collinear limit of the $q\bar{q}$ contribution to the integrated eikonal function subject to N-jettiness constraint

$$\begin{aligned} & \frac{2N_u}{\epsilon} \sum_{x\in\{i,j\}} \int_0^1 \frac{\mathrm{d}\omega}{\omega^{1+2\epsilon}} \left\langle (1-\theta^{b+d} C_{\mathfrak{mn}})\, [\mathrm{d}\Omega_{\mathfrak{mn}}]\, C_{x\mathfrak{mn}} \omega^{tc} \psi^{4\epsilon}_{\mathfrak{mn}} [\omega^2 \tilde{S}^{q\bar{q}}_{ij}(\mathfrak{m},\mathfrak{n})] \right\rangle_{\mathfrak{mn}} = \\ & N_u \Bigg[\frac{1}{\epsilon^2} \left(-\frac{10}{9} - \frac{4}{3}\ln 2 \right) + \frac{1}{\epsilon} \left(\frac{4\pi^2}{9} - 8 - \frac{4}{3}\ln^2 2 - \frac{52\ln 2}{9} \right) \\ & + \frac{28}{3}\zeta_3 + \frac{14\pi^2}{9} - \frac{3232}{81} - \frac{8}{9}\ln^3 2 - \frac{52\ln^2 2}{9} + \frac{4}{9}\pi^2 \ln 2 - \frac{640}{27}\ln 2 + \mathcal{O}(\epsilon) \Bigg] . \end{aligned} \quad (12.16)$$

To determine the collinear-regulated contribution in Eq. (12.4), we proceed in the same way as in the two-gluon case. Namely, we write a similar representation for the "energy-regulated" integral of the $q\bar{q}$ contribution to the soft function computed in Ref. [48]. It

reads

$$
\begin{aligned}
J_{ij}^{q\bar{q}} = &\frac{2N_E}{\epsilon}\int_0^1 \frac{\mathrm{d}\omega}{\omega^{1+2\epsilon}} \left\langle C_{\mathfrak{mn}}\,[\mathrm{d}\Omega_{\mathfrak{mn}}]\,\theta^{b+d}\omega^{tc}[\omega^2\tilde{S}_{ij}^{q\bar{q}}(\mathfrak{m},\mathfrak{n})]\right\rangle_{\mathfrak{mn}} \\
&+\frac{2N_E}{\epsilon}\sum_{x\in\{i,j\}}\int_0^1 \frac{\mathrm{d}\omega}{\omega^{1+2\epsilon}} \left\langle (1-\theta^{b+d}C_{\mathfrak{mn}})\,[\mathrm{d}\Omega_{\mathfrak{mn}}]\,C_{x\mathfrak{mn}}\omega^{tc}[\omega^2\tilde{S}_{ij}^{q\bar{q}}(\mathfrak{m},\mathfrak{n})]\right\rangle_{\mathfrak{mn}} \\
&+\frac{2N_E}{\epsilon}\sum_{x\in\{i,j\}}\int_0^1 \frac{\mathrm{d}\omega}{\omega^{1+2\epsilon}} \left\langle (1-\theta^{b+d}C_{\mathfrak{mn}})\,[\mathrm{d}\Omega_{\mathfrak{mn}}]\,\bar{C}_{x\mathfrak{mn}}\,w^{x\mathfrak{m},x\mathfrak{n}}\,[\omega^2\tilde{S}_{ij}^{q\bar{q}}(\mathfrak{m},\mathfrak{n})]\right\rangle_{\mathfrak{mn}} \\
&+\frac{2N_E}{\epsilon}\sum_{x\in\{i,j\}}\int_0^1 \frac{\mathrm{d}\omega}{\omega^{1+2\epsilon}} \left\langle \left(w^{i\mathfrak{m},j\mathfrak{n}}+w^{j\mathfrak{m},i\mathfrak{n}}\right)\,[\omega^2\tilde{S}_{ij}^{q\bar{q}}(\mathfrak{m},\mathfrak{n})]\right\rangle_{\mathfrak{mn}}.
\end{aligned}
\tag{12.17}
$$

We observe that, up to a normalization factor, the last two contributions are the same as the missing divergent ones in Eq. (12.4). Since the result for $J_{ij}^{q\bar{q}}$ is known [48], we can extract the contribution of the last two terms in Eq. (12.17) if the first two terms are known. We note that these terms are similar but not identical to the ones that we already computed because the N-jettiness function $\psi_{\mathfrak{mn}}$ does not appear in Eq. (12.17). However, their computation is nearly identical to what has been discussed in the two-gluon case and for this reason we do not repeat it. We find

$$
\begin{aligned}
&\frac{2N_E}{\epsilon}\sum_{x\in\{i,j\}}\int_0^1 \frac{\mathrm{d}\omega}{\omega^{1+2\epsilon}} \left\langle (1-\theta^{b+d}C_{\mathfrak{mn}})\,[\mathrm{d}\Omega_{\mathfrak{mn}}]\,\bar{C}_{x\mathfrak{mn}}w^{x\mathfrak{m},x\mathfrak{n}}\,\left[w^2\tilde{S}_{ij}^{q\bar{q}}(\mathfrak{m},\mathfrak{n})\right]\right\rangle_{\mathfrak{mn}} \\
&+\frac{2N_E}{\epsilon}\sum_{x\in\{i,j\}}\int_0^1 \frac{\mathrm{d}\omega}{\omega^{1+2\epsilon}} \left\langle \left(w^{i\mathfrak{m},j\mathfrak{n}}+w^{j\mathfrak{m},i\mathfrak{n}}\right)\,[\omega^2\tilde{S}_{ij}^{q\bar{q}}(\mathfrak{m},\mathfrak{n})]\right\rangle_{\mathfrak{mn}} \\
&=\frac{1}{\epsilon}\left(\frac{A_{ij}^{\mathrm{fin}}}{6}-\frac{B_{ij}^{\mathrm{fin}}}{12}+\frac{2}{3}\ln 2\ln(\eta_{ij})+\frac{\pi^2}{9}+\frac{8\ln(\eta_{ij})}{9}-\frac{1}{9}-\frac{\ln 2}{3}+\mathcal{O}(\epsilon)\right).
\end{aligned}
\tag{12.18}
$$

To obtain the above formula, we used the following result for the triple-collinear contribution in the case without the N-jettiness constraint.

$$
\begin{aligned}
\frac{2N_E}{\epsilon}\int_0^1 \frac{\mathrm{d}\omega}{\omega^{1+2\epsilon}} \left\langle C_{x\mathfrak{mn}}\omega^{tc,i}\left[w^2\tilde{S}_{ij}^{q\bar{q}}(\mathfrak{m},\mathfrak{n})\right]\right\rangle_{\mathfrak{mn}} = \frac{2N_E}{\epsilon}\Bigg[&-\frac{1}{3\epsilon^2}+\frac{19}{18\epsilon} \\
&+\frac{\pi^2}{9}-\frac{83}{54}+4\ln^2 2+\ln 2+\epsilon\Big(\frac{25\zeta_3}{3}-\frac{35\pi^2}{108}+\frac{1057}{162} \\
&-\frac{1}{3}40\ln^3 2-\frac{53\ln^2 2}{3}+\frac{2}{9}\pi^2\ln 2+3\ln 2\Big)+\mathcal{O}(\epsilon^2)\Bigg].
\end{aligned}
\tag{12.19}
$$

The corresponding result for the double-collinear subtracted contribution without the N-jettiness constraint reads

$$\begin{aligned}
&\frac{2N_E}{\epsilon}\int\limits_0^1 \frac{\mathrm{d}\omega}{\omega^{1+2\epsilon}}\left\langle \theta^{b+d} C_{\mathfrak{mn}}\left[\mathrm{d}\Omega_{\mathfrak{mn}}\right] C_{x\mathfrak{mn}}\omega^{tc,i}\left[w^2\tilde{S}_{ij}^{q\bar{q}}(\mathfrak{m},\mathfrak{n})\right]\right\rangle_{\mathfrak{mn}} = \\
&\frac{2N_E}{\epsilon}\Bigg[-\frac{1}{3\epsilon^2}+\frac{1}{\epsilon}\left(\frac{1}{2}-\frac{2\ln 2}{3}\right)-\frac{\pi^2}{3}+2\ln^2 2+\frac{5\ln 2}{3} \\
&+\epsilon\left(-\frac{10\zeta_3}{3}+\frac{11\pi^2}{18}-\frac{4}{3}-\frac{20}{9}\ln^3 2-\frac{13}{3}\ln^2 2+\left(\frac{8}{3}+\frac{2\pi^2}{9}\right)\ln 2\right)+\mathcal{O}(\epsilon^2)\Bigg].
\end{aligned} \tag{12.20}$$

13 The renormalized N-jettiness soft function

We are now in a position to present the renormalized N-jettiness soft function through NNLO in the perturbative expansion in QCD. We write

$$\tilde{S} = 1 + \tilde{S}_1 + \tilde{S}_2 + \mathcal{O}(\alpha_s^3). \tag{13.1}$$

It is convenient to introduce the following short-hand notations

$$L_{ij} = \ln(\bar{u}\sqrt{\eta_{ij}}\mu), \quad L^{\psi}_{ij,\mathfrak{m}} = \ln\left(\frac{\psi_{\mathfrak{m}}\rho_{ij}}{\rho_{i\mathfrak{m}}\rho_{j\mathfrak{m}}}\right). \tag{13.2}$$

The NLO contribution reads

$$\tilde{S}_1 = a_s\sum_{(ij)}\mathbf{T}_i\cdot\mathbf{T}_j\left[2L_{ij}^2+\mathrm{Li}_2(1-\eta_{ij})+\frac{\pi^2}{12}+\left\langle L^{\psi}_{ij,\mathfrak{m}}\frac{\rho_{ij}}{\rho_{i\mathfrak{m}}\rho_{j\mathfrak{m}}}\right\rangle_{\mathfrak{m}}\right]. \tag{13.3}$$

The NNLO contribution is constructed from different pieces. We write

$$\tilde{S}_2 = \frac{1}{2}\,\tilde{S}_1^2 + a_s^2 C_A\sum_{(ij)}\mathbf{T}_i\cdot\mathbf{T}_j\,G_{ij} + a_s^2\,n_f\,T_R\sum_{(ij)}\mathbf{T}_i\cdot\mathbf{T}_j\,Q_{ij} + a_s^2\pi\sum_{(kij)}F^{kij}\,\kappa_{kj}G^{\mathrm{triple}}_{kij}. \tag{13.4}$$

The function G_{ij} reads

$$\begin{aligned}
G_{ij} = {}& \frac{22}{9}L_{ij}^3+\left(\frac{67}{9}-\frac{\pi^2}{3}\right)L_{ij}^2+L_{ij}\Bigg(\frac{11}{3}\left\langle L^{\psi}_{ij,\mathfrak{m}}\frac{\rho_{ij}}{\rho_{i\mathfrak{m}}\rho_{j\mathfrak{m}}}\right\rangle_{\mathfrak{m}}+\frac{11}{3}\mathrm{Li}_2(1-\eta_{ij}) \\
&+\frac{202}{27}-7\zeta_3\Bigg)+\left\langle\frac{\rho_{ij}}{\rho_{i\mathfrak{m}}\rho_{j\mathfrak{m}}}\Bigg(\left(L^{\psi}_{ij,\mathfrak{m}}\right)^2\left(\frac{11}{6}-\ln\left(\frac{\eta_{ij}}{\eta_{i\mathfrak{m}}\eta_{j\mathfrak{m}}}\right)\right)\right. \\
&+L^{\psi}_{ij,\mathfrak{m}}\Bigg(2\ln^2\left(\frac{\eta_{ij}}{\eta_{i\mathfrak{m}}\eta_{j\mathfrak{m}}}\right)+\ln\left(\frac{\eta_{ij}}{\eta_{i\mathfrak{m}}\eta_{j\mathfrak{m}}}\right)\left(-\frac{11}{3}+\ln(\eta_{i\mathfrak{m}}\eta_{j\mathfrak{m}})\right)+\frac{137}{18}-\frac{\pi^2}{2} \\
&-\frac{1}{2}\ln^2\left(\frac{\eta_{i\mathfrak{m}}}{\eta_{j\mathfrak{m}}}\right)+\mathrm{Li}_2(1-\eta_{ij})+\frac{11}{3}\ln 2-\frac{11}{6}\ln(\eta_{i\mathfrak{m}}\eta_{j\mathfrak{m}})-\frac{(\rho_{i\mathfrak{m}}+\rho_{j\mathfrak{m}})}{3\rho_{ij}}\Bigg)\Bigg)\Bigg\rangle_{\mathfrak{m}} \\
&+\left\langle A^{\mathrm{fin}}_{ij,\mathfrak{m}}\left(\frac{11}{6}L^{\psi}_{ij,\mathfrak{m}}-\frac{11}{6}\ln\frac{\eta_{ij}}{\eta_{i\mathfrak{m}}\eta_{j\mathfrak{m}}}+\frac{131}{72}\right)\right\rangle_{\mathfrak{m}}
\end{aligned}$$

$$
\begin{aligned}
&+\left\langle B^{\rm fin}_{ij,\mathfrak{m}}\left(-\frac{1}{6}L^{\psi}_{ij,\mathfrak{m}}+\frac{1}{6}\ln\frac{\eta_{ij}}{\eta_{i\mathfrak{m}}\eta_{j\mathfrak{m}}}-\frac{13}{72}\right)\right\rangle_{\mathfrak{m}}-2G_{-1,0,0,1}(\eta_{ij})+\frac{7}{2}G_{0,1,0,1}(\eta_{ij})\\
&-\frac{11}{3}\mathrm{Ci}_3(2\delta_{ij})-\frac{1}{6\tan(\delta_{ij})}\mathrm{Si}_2(2\delta_{ij})+17S_{2,2}(\eta_{ij})-\frac{1}{2}\mathrm{Li}_4\left(1-\eta_{ij}^2\right)\\
&-2\mathrm{Li}_4\left(\frac{1}{\eta_{ij}+1}\right)+\mathrm{Li}_4\left(\frac{1-\eta_{ij}}{1+\eta_{ij}}\right)-\mathrm{Li}_4\left(\frac{\eta_{ij}-1}{1+\eta_{ij}}\right)-12\mathrm{Li}_4(\eta_{ij})\\
&+\mathrm{Li}_3(\eta_{ij})\left(-\frac{11}{6}+10\ln(1-\eta_{ij})+10\ln(\eta_{ij})-2\ln(1+\eta_{ij})\right)\\
&+\mathrm{Li}_3(1-\eta_{ij})\Big(10\ln(\eta_{ij})+2\ln(1+\eta_{ij})\Big)-2\mathrm{Li}_3(-\eta_{ij})\ln(1-\eta_{ij})\\
&+\frac{5\mathrm{Li}_2(\eta_{ij})^2}{4}+\mathrm{Li}_2(\eta_{ij})\Big(-2\mathrm{Li}_2(-\eta_{ij})-4\ln^2(\eta_{ij})\\
&+6\ln(1-\eta_{ij})\ln(\eta_{ij})+\frac{11\ln(\eta_{ij})}{6}+\frac{\pi^2}{3}-11\ln 2-\frac{131}{12}\Big)\\
&-\frac{1}{12}\ln^4(1+\eta_{ij})-\ln^3(\eta_{ij})\ln(1-\eta_{ij})+\frac{\pi^2}{12}\ln^2(1+\eta_{ij})\\
&+\ln^2(\eta_{ij})\left(\frac{11}{2}\ln^2(1-\eta_{ij})+\frac{11}{12}\ln(1-\eta_{ij})-\frac{\pi^2}{6}+\frac{11\ln 2}{3}+\frac{32}{9}\right)\\
&+\ln(1-\eta_{ij})\left(-11\ln 2\ln(\eta_{ij})-\frac{4\pi^2\ln(\eta_{ij})}{3}-\frac{131\ln(\eta_{ij})}{12}-\frac{23\zeta_3}{2}\right)\\
&+\ln(\eta_{ij})\left(-\frac{11\ln^2 2}{3}-\frac{\pi^2\ln 2}{3}+\frac{64\ln 2}{9}-\frac{27\zeta_3}{4}-\frac{11\pi^2}{18}+\frac{1631}{108}\right)\\
&-\frac{7}{4}\zeta_3\ln(1+\eta_{ij})+\frac{1}{3}\ln^4 2+\ln^2 2\left(\frac{1}{3}-\frac{\pi^2}{3}\right)+\ln 2\left(5\zeta_3+\frac{11\pi^2}{18}-\frac{2}{9}\right)\\
&+8\mathrm{Li}_4\left(\frac{1}{2}\right)-\frac{11}{9}\zeta_3-\frac{11}{80}\pi^4+\frac{937}{432}\pi^2+\frac{403}{162}\\
&-\left\langle\bar{C}_{\mathfrak{mn}}\ln\left(\frac{\psi_m}{\rho_{im}}\right)\ln\left(\frac{\psi_n}{\rho_{jn}}\right)\frac{\rho_{ij}}{\rho_{\mathfrak{mn}}\rho_{i\mathfrak{m}}\rho_{j\mathfrak{n}}}\right\rangle_{\mathfrak{mn}}+\frac{1}{2}\left\langle L^{\psi}_{ij,\mathfrak{m}}\frac{\rho_{ij}}{\rho_{i\mathfrak{m}}\rho_{j\mathfrak{m}}}\right\rangle^2_{\mathfrak{m}}\\
&+\frac{1}{2}\sum_{x\in\{i,j\}}\int_0^1\frac{\mathrm{d}\omega}{\omega}\left\langle(1-\theta^{b+d}C_{\mathfrak{mn}})\left[\mathrm{d}\Omega_{\mathfrak{mn}}\right]\bar{C}_{x\mathfrak{mn}}\;w^{x\mathfrak{m},x\mathfrak{n}}\;\ln\psi_{\mathfrak{mn}}\;\bar{S}_{\omega}\left[\omega^2\tilde{S}_{ij}(\mathfrak{m},\mathfrak{n})\right]\right\rangle_{\mathfrak{mn}}\\
&+\frac{1}{2}\int_0^1\frac{\mathrm{d}\omega}{\omega}\left\langle(w^{i\mathfrak{m},j\mathfrak{n}}+w^{j\mathfrak{m},i\mathfrak{n}})\;\ln\psi_{\mathfrak{mn}}\;\bar{S}_{\omega}\left[\omega^2\tilde{S}_{ij}(\mathfrak{m},\mathfrak{n})\right]\right\rangle_{\mathfrak{mn}}.
\end{aligned}
\tag{13.5}
$$

In the above formula $\delta_{ij}=\theta_{ij}/2$ and θ_{ij} is the relative angle between partons i and j. The Clausen functions are defined through their relation to complex-valued polylogarithms

$$
\begin{aligned}
\mathrm{Ci}_n(z)&=\frac{1}{2}\left(\mathrm{Li}_n(e^{iz})+\mathrm{Li}_n(e^{-iz})\right),\\
\mathrm{Si}_n(z)&=\frac{1}{2i}\left(\mathrm{Li}_n(e^{iz})-\mathrm{Li}_n(e^{-iz})\right).
\end{aligned}
\tag{13.6}
$$

The functions S_{a_1,a_2} and $G_{a_1,a_2,\ldots,a_m}(x)$ are the Nielsen and Goncharov [51] polylogarithms, respectively. The auxiliary functions that we employed while writing the above formula

read

$$
\begin{aligned}
A^{\rm fin}_{ij,\mathfrak{m}} &= \frac{\rho_{ij}}{\rho_{i\mathfrak{m}}\rho_{j\mathfrak{m}}}\left[\omega^{\mathfrak{m}i,\mathfrak{n}i}_{\mathfrak{m}||\mathfrak{n}}\ln\left(\frac{\eta_{j\mathfrak{m}}(1-\eta_{i\mathfrak{m}})}{\eta_{ij}}\right)+\omega^{\mathfrak{m}j,\mathfrak{n}j}_{\mathfrak{m}||\mathfrak{n}}\ln\left(\frac{\eta_{i\mathfrak{m}}(1-\eta_{j\mathfrak{m}})}{\eta_{ij}}\right)\right],\\
B^{\rm fin}_{ij,\mathfrak{m}} &= \omega^{\mathfrak{m}i,\mathfrak{n}i}_{\mathfrak{m}||\mathfrak{n}}\,W^{\mathfrak{m}}_{ij}+\omega^{\mathfrak{m}j,\mathfrak{n}j}_{\mathfrak{m}||\mathfrak{n}}\,W^{\mathfrak{m}}_{ji}.
\end{aligned}
\tag{13.7}
$$

The function Q_{ij} evaluates to

$$
\begin{aligned}
Q_{ij} = &-\frac{8}{9}L_{ij}^3-\frac{20}{9}L_{ij}^2-L_{ij}\left(\frac{4}{3}\left\langle L^{\psi}_{ij,\mathfrak{m}}\frac{\rho_{ij}}{\rho_{i\mathfrak{m}}\rho_{j\mathfrak{m}}}\right\rangle_{\mathfrak{m}}+\frac{4}{3}\,\mathrm{Li}_2(1-\eta_{ij})+\frac{56}{27}\right)\\
&-\left\langle\frac{\rho_{ij}}{\rho_{i\mathfrak{m}}\rho_{j\mathfrak{m}}}\left(\frac{2}{3}\left(L^{\psi}_{ij,\mathfrak{m}}\right)^2-L^{\psi}_{ij,\mathfrak{m}}\left(\frac{2}{3}\ln\left(\frac{\eta_{ij}^2}{4\eta_{i\mathfrak{m}}\eta_{j\mathfrak{m}}}\right)-\frac{26}{9}+\frac{2(\rho_{i\mathfrak{m}}+\rho_{j\mathfrak{m}})}{3\rho_{ij}}\right)\right)\right\rangle_{\mathfrak{m}}\\
&+\left\langle A^{\rm fin}_{ij,\mathfrak{m}}\left(-\frac{2}{3}L^{\psi}_{ij,\mathfrak{m}}+\frac{2}{3}\ln\left(\frac{\eta_{ij}}{\eta_{i\mathfrak{m}}\eta_{j\mathfrak{m}}}\right)-\frac{23}{36}\right)\right\rangle_{\mathfrak{m}}\\
&+\left\langle B^{\rm fin}_{ij,\mathfrak{m}}\left(\frac{1}{3}L^{\psi}_{ij,\mathfrak{m}}-\frac{1}{3}\ln\left(\frac{\eta_{ij}}{\eta_{i\mathfrak{m}}\eta_{j\mathfrak{m}}}\right)+\frac{13}{36}\right)\right\rangle_{\mathfrak{m}}+\frac{2}{3}\mathrm{Li}_3(\eta_{ij})\\
&+\mathrm{Li}_2(1-\eta_{ij})\left(\frac{2\ln(\eta_{ij})}{3}-\frac{7}{2}-4\ln 2\right)+\ln^2 2\left(-\frac{2}{3}+\frac{4}{3}\ln(\eta_{ij})\right)\\
&+\ln 2\left(-\frac{4}{3}\ln^2(\eta_{ij})-\frac{20}{9}\ln(\eta_{ij})+\frac{4\pi^2}{9}+\frac{4}{9}\right)\\
&-\ln^2(\eta_{ij})\left(\frac{10}{9}-\frac{1}{3}\ln(1-\eta_{ij})\right)+\ln(\eta_{ij})\left(\frac{\pi^2}{9}-\frac{335}{54}\right)\\
&+\frac{4\zeta_3}{9}+\frac{122}{81}-\frac{47\pi^2}{108}+\frac{4}{3}\mathrm{Ci}_3(2\delta_{ij})+\frac{1}{3\tan(\delta_{ij})}\mathrm{Si}_2(2\delta_{ij})\\
&-\sum_{x\in\{i,j\}}\int_0^1\frac{\mathrm{d}\omega}{\omega}\left\langle(1-\theta^{b+d}C_{\mathfrak{mn}})\,[\mathrm{d}\Omega_{\mathfrak{mn}}]\,\bar{C}_{x\mathfrak{mn}}\;w^{x\mathfrak{m},x\mathfrak{n}}\;\ln\psi_{\mathfrak{mn}}\;[\omega^2\tilde{S}^{q\bar{q}}_{ij}(\mathfrak{m},\mathfrak{n})]\right\rangle_{\mathfrak{mn}}\\
&-\int_0^1\frac{\mathrm{d}\omega}{\omega}\left\langle(w^{i\mathfrak{m},j\mathfrak{n}}+w^{j\mathfrak{m},i\mathfrak{n}})\;\ln\psi_{\mathfrak{mn}}\;[\omega^2\tilde{S}^{q\bar{q}}_{ij}(\mathfrak{m},\mathfrak{n})]\right\rangle_{\mathfrak{mn}},
\end{aligned}
\tag{13.8}
$$

The function $G^{\rm triple}_{kij}$, defined in Eq. (7.14), corresponds to the finite remainder of the triple-color correlation terms.

14 Numerical implementations and checks

We have implemented the above formulas into a Fortran code. The implementation is, in principle, straightforward. To compute terms that require integration over directions of gluons' momenta, we use the phase space parametrization described in Ref. [1, 9, 10]. A possible choice of partition functions can be found in Ref. [52].

As we already mentioned, the N-jettiness soft function was recently discussed in Ref. [37] where a plethora of numerical results for various kinematic configurations have

been presented. We have checked many of the presented results for various values of the parameter N and found excellent agreement. We present some examples of such a comparison in Appendix D.

We note that to obtain the high-precision numbers shown in Appendix D, we have used a very large number of sample points which results in runtimes that can be as large as a few minutes per dipole per kinematic point. However, to obtain the same numbers with a better-than-percent precision, we need a relatively small number of sampling points which results in runtimes of an order of a few seconds per dipole per phase space point. We note that runtimes for individual dipoles are largely *independent* of N. Since $(N+2)(N+1)/2$ dipoles need to be calculated to determine the N-jettiness soft function for a given phase space point, $\mathcal{O}(1-2)$ minutes will be required to do that in case of three- or four-jet production at a hadron collider, or six-jet production at an e^+e^- collider.

The situation with triple-color correlated terms is quite similar. Since in this case integration over the direction of a single gluon is required, the integration converges rather fast. In general, for an N-jettiness case, the evaluation of $(N+2)(N+1)N$ independent functions G_{kij}^{triple} is required from which a smaller number of independent color-correlated contributions can be constructed. We need about twenty seconds to compute all the required G_{kij}^{triple} functions for $N=2$ and, therefore, we will need about a minute to compute them for $N=3$ and about two minutes for $N=4$.

15 Conclusions

We have described the computation of the N-jettiness soft function through NNLO in QCD. Keeping N as the parameter, we demonstrated the cancellation of all $1/\epsilon$ poles *analytically* against the soft-function renormalization matrix. Furthermore, we derived a simple representation for the finite, jettiness-dependent remainder valid for an arbitrary number of hard partons N. We compared our numerical results for $N=1,2$ and $N=3$ with the ones recently presented in Ref. [37] and found excellent agreement. We have also found that the representation of the finite remainder that is derived in this paper leads to fast and rapidly convergent integration which is important if the results for N-jettiness soft function are to be used for the computation of higher-order corrections for multi-jet production at colliders.

From a more general perspective, this study was motivated by a question of how advances in developing NNLO subtraction schemes for generic processes at the LHC can be used to derive representations for the building blocks of modern slicing methods that rely on choosing observables to define suitable slicing variables. We have shown that, at least for N-jettiness, the benefits of applying subtraction-inspired methods are significant. We note that the application of the subtraction-inspired methods for computing the N-jettiness soft function becomes possible if one departs from the (by now) standard approach [16, 18, 34] to such computations where hemisphere soft functions are used as elementary building blocks and, instead, interprets N-jettiness as one of the many infrared safe observables that can be studied using available subtraction schemes.

Acknowledgments

We are grateful to G. Bell for useful exchanges and R. K. Ellis for helpful conversations. This research was supported by the German Research Foundation (DFG, Deutsche Forschungsgemeinschaft) under grant 396021762-TRR 257.

A Renormalization of the soft function

A suitable expression for the renormalization of the N-jettiness soft function was recently given in Ref. [37]. It reads

$$Z = 1 + Z_1 + \frac{1}{2} Z_1 Z_1 + Z_{2,r}, \tag{A.1}$$

where

$$Z_1 = a_s \sum_{(ij)} \mathbf{T}_i \cdot \mathbf{T}_j \left(\frac{1}{2\epsilon^2} + \frac{2L_{ij} + i\pi\lambda_{ij}}{2\epsilon} \right), \tag{A.2}$$

and

$$Z_{2,r} = a_s^2 \sum_{(ij)} \mathbf{T}_i \cdot \mathbf{T}_j \left(-\frac{3\beta_0}{8\epsilon^3} + \frac{\Gamma_1 - 4\beta_0(2L_{ij} + i\pi\lambda_{ij})}{16\epsilon^2} + \frac{\Gamma_1(2L_{ij} + i\pi\lambda_{ij}) + \gamma_1^S}{8\epsilon} \right), \tag{A.3}$$

with

$$L_{ij} = \ln(\bar{u}\sqrt{\eta_{ij}}\mu), \tag{A.4}$$

$$\Gamma_1 = \left(\frac{67}{9} - \frac{\pi^2}{3} \right) C_A - \frac{20}{9} T_R n_f, \tag{A.5}$$

and

$$\gamma_1^S = \left(\frac{202}{27} - \frac{11\pi^2}{36} - 7\zeta_3 \right) C_A + \left(-\frac{56}{27} + \frac{\pi^2}{9} \right) T_R n_f. \tag{A.6}$$

where Γ_1 is the cusp anomalous dimension and the non-cusp anomalous dimension γ_1^S is known to two-loop order [53]. Furthermore, $\lambda_{ij} = 1$ if both i and j are incoming or outgoing and $\lambda_{ij} = 0$ otherwise.

B Useful phase space integrals

We define measures of angular integration as

$$[\mathrm{d}\Omega^{(d-1)}] = \frac{\mathrm{d}\Omega^{(d-1)}}{\Omega^{(d-2)}}. \tag{B.1}$$

Then

$$\frac{\mathrm{d}\Omega^{(d-1)}}{2(2\pi)^{d-1}} = \frac{\Omega^{(d-2)}}{2(2\pi)^{d-1}} [\mathrm{d}\Omega^{(d-1)}], \tag{B.2}$$

where

$$\frac{\Omega^{(d-2)}}{2(2\pi)^{d-1}} = \left[\frac{(4\pi)^\epsilon}{8\pi^2 \Gamma(1-\epsilon)} \right]. \tag{B.3}$$

With this integration measure, we find [47]

$$\left\langle \frac{1}{\rho_{i\mathfrak{m}}^{\alpha}} \right\rangle_{\mathfrak{m}} = 2^{1-\alpha-2\epsilon} \frac{\Gamma(1-\epsilon)\Gamma(1-\alpha-\epsilon)}{\Gamma(2-\alpha-2\epsilon)}, \tag{B.4}$$

$$\left\langle \frac{1}{\rho_{i\mathfrak{m}}^{\alpha}\rho_{j\mathfrak{m}}^{\beta}} \right\rangle_{\mathfrak{m}} = 2^{1-\alpha-\beta-2\epsilon} \frac{\Gamma(1-\beta-\epsilon)\Gamma(1-\alpha-\epsilon)}{\Gamma(2-\alpha-\beta-2\epsilon)} \times {}_2F_1(\alpha,\beta,1-\epsilon,1-\eta_{ij}), \tag{B.5}$$

where brackets $\langle ... \rangle_{\mathfrak{m}}$ indicate integration over $[\mathrm{d}\Omega_{\mathfrak{m}}^{(d-1)}]$.

C Eikonal functions

For completeness, we provide the double real-emission eikonal functions that we use to compute the relevant contributions to the N-jettiness soft function. Following Ref. [46], for two soft gluons, we define

$$\tilde{S}_{ij}^{gg}(\mathfrak{m},\mathfrak{n}) = 2S_{ij}^{gg}(\mathfrak{m},\mathfrak{n}) - S_{ii}^{gg}(\mathfrak{m},\mathfrak{n}) - S_{jj}^{gg}(\mathfrak{m},\mathfrak{n}). \tag{C.1}$$

The function $S_{ij}^{gg}(\mathfrak{m},\mathfrak{n})$ reads

$$\begin{aligned} S_{ij}^{gg}(\mathfrak{m},\mathfrak{n}) = S_{ij}^{gg,\mathrm{so}}(\mathfrak{m},\mathfrak{n}) &- \frac{2p_i\cdot p_j}{p_{\mathfrak{m}}\cdot p_{\mathfrak{n}}[p_i\cdot(p_{\mathfrak{m}}+p_{\mathfrak{n}})][p_j\cdot(p_{\mathfrak{m}}+p_{\mathfrak{n}})]} \\ &+ \frac{(p_i\cdot p_{\mathfrak{m}})(p_j\cdot p_{\mathfrak{n}})+(p_i\cdot p_{\mathfrak{n}})(p_i\cdot p_{\mathfrak{m}})}{[p_i\cdot(p_{\mathfrak{m}}+p_{\mathfrak{n}})p_j\cdot(p_{\mathfrak{m}}+p_{\mathfrak{n}})]}\left[\frac{1-\epsilon}{(p_{\mathfrak{m}}\cdot p_{\mathfrak{n}})^2} - \frac{1}{2}S_{ij}^{gg,\mathrm{so}}(\mathfrak{m},\mathfrak{n})\right], \end{aligned} \tag{C.2}$$

where

$$\begin{aligned} S_{ij}^{gg,\mathrm{so}}(\mathfrak{m},\mathfrak{n}) = &\frac{p_i\cdot p_j}{p_{\mathfrak{m}}\cdot p_{\mathfrak{n}}}\left(\frac{1}{(p_i\cdot p_{\mathfrak{m}})(p_j\cdot p_{\mathfrak{n}})}+\frac{1}{(p_i\cdot p_{\mathfrak{n}})(p_j\cdot p_{\mathfrak{m}})}\right) \\ &- \frac{(p_i\cdot p_j)^2}{(p_i\cdot p_{\mathfrak{m}})(p_j\cdot p_{\mathfrak{m}})(p_i\cdot p_{\mathfrak{n}})(p_j\cdot p_{\mathfrak{n}})}. \end{aligned} \tag{C.3}$$

In case the soft partons are a quark and an anti-quark, we write

$$\tilde{S}_{ij}^{q\bar{q}}(\mathfrak{m},\mathfrak{n}) = 2S_{ij}^{q\bar{q}}(\mathfrak{m},\mathfrak{n}) - S_{ii}^{q\bar{q}}(\mathfrak{m},\mathfrak{n}) - S_{jj}^{q\bar{q}}(\mathfrak{m},\mathfrak{n}), \tag{C.4}$$

where [46]

$$S_{ij}^{q\bar{q}}(\mathfrak{m},\mathfrak{n}) = \frac{(p_i\cdot p_{\mathfrak{m}})(p_j\cdot p_{\mathfrak{n}})+(p_i\cdot p_{\mathfrak{n}})(p_j\cdot p_{\mathfrak{m}})-(p_i\cdot p_j)(p_{\mathfrak{m}}\cdot p_{\mathfrak{n}})}{(p_{\mathfrak{m}}\cdot p_{\mathfrak{n}})^2[p_i\cdot(p_{\mathfrak{m}}+p_{\mathfrak{n}})][p_j\cdot(p_{\mathfrak{m}}+p_{\mathfrak{n}})]}. \tag{C.5}$$

D Numerical Checks of N-Jettiness Soft Functions

In this section, we compare results for the N-Jettiness soft function obtained in this paper with those in Ref. [37]. For this comparison, we define two functions G_{ij}^{nl} and Q_{ij}^{nl} that are obtained from G_{ij} and Q_{ij} by setting all terms with L_{ij} to zero

$$\begin{aligned} G_{ij} = &\frac{22}{9}L_{ij}^3 + \left(\frac{67}{9}-\frac{\pi^2}{3}\right)L_{ij}^2 + L_{ij}\Bigg(\frac{11}{3}\left\langle L_{ij,\mathfrak{m}}^{\psi}\frac{\rho_{ij}}{\rho_{i\mathfrak{m}}\rho_{j\mathfrak{m}}}\right\rangle_{\mathfrak{m}} + \frac{11}{3}\mathrm{Li}_2(1-\eta_{ij}) \\ &+ \frac{202}{27} - 7\zeta_3\Bigg) + G_{ij}^{nl} \end{aligned}, \tag{D.1}$$

$$Q_{ij} = -\frac{8}{9}L_{ij}^3 - \frac{20}{9}L_{ij}^2 - L_{ij}\left(\frac{4}{3}\left\langle L_{ij,\mathfrak{m}}^{\psi}\frac{\rho_{ij}}{\rho_{i\mathfrak{m}}\rho_{j\mathfrak{m}}}\right\rangle_{\mathfrak{m}} + \frac{4}{3}\,\mathrm{Li}_2(1-\eta_{ij}) + \frac{56}{27}\right) + Q_{ij}^{nl}. \quad \text{(D.2)}$$

We also note that for the comparison of the triple-color correlated contributions, we do not set these logarithms to zero but take $\bar{u} = \mu = 1$ instead. As the result, we should set $L_{ki} \to 1/2 \ln \eta_{ki}$ in Eq. (7.14).

D.1 1-Jettiness

In order to compare our numerical results, we parameterize our phase space in a similar way as done in Ref. [37]. In the case where there are two back-to-back beams and one jet confined in a plane, we parameterize the scattering by the angle θ_{13} using the following momenta,

$$n_1 = (0, 0, 1), \quad n_2 = (0, 0, -1), \quad n_3 = (\sin\theta_{13}, 0, \cos\theta_{13}). \quad \text{(D.3)}$$

In order to compare a phase space point where the jet is separated from the beams, we take

$$\theta_{13} = \frac{12\pi}{25}. \quad \text{(D.4)}$$

In Table 1 we present the results for the non-logarithmic coefficient of the renormalized 1-jettiness soft function, which are in agreement with the ones in Ref. [37].

Dipoles	Gluons		Quarks	
	G_{ij}^{nl}	Ref. [37]	Q_{ij}^{nl}	Ref. [37]
12	48.10 ± 0.01	48.04 ± 0.07	-23.504 ± 0.001	-23.503 ± 0.010
13	36.81 ± 0.02	36.82 ± 0.04	-21.871 ± 0.003	-21.875 ± 0.009
23	38.14 ± 0.01	38.13 ± 0.05	-22.039 ± 0.002	-22.031 ± 0.009

Table 1. Comparison of the selected results for the 1-jettiness soft function for the kinematic point in Eq. (D.4). When quoting results for functions G_{ij}^{nl}, Q_{ij}^{nl}, we show Vegas integration errors which, most likely, underestimate the true uncertainties of the result.

D.2 2-jettiness

We again consider the configuration where there are two back-to-back beams. We parameterize the scattering of the two jets by θ_{13}, θ_{14} and ϕ_4 as

$$\begin{aligned} n_1 &= (0, 0, 1), \quad n_2 = (0, 0, -1), \\ n_3 &= (\sin\theta_{13}, 0, \cos\theta_{13}), \quad n_4 = (\sin\theta_{14}\cos\phi_4, \sin\theta_{14}\sin\phi_4, \cos\theta_{14}). \end{aligned} \quad \text{(D.5)}$$

Considering a generic phase space point where the beams and jets are separated from each other, we take

$$\theta_{13} = \frac{6\pi}{25}, \quad \theta_{14} = \frac{13\pi}{25}, \quad \phi_4 = \frac{\pi}{5}. \quad \text{(D.6)}$$

Results for all possible dipole coefficients are presented on Table 2. In the case of 2-jettiness, the tripole contribution can be reduced to a single color structure, $f_{ABC}\, T_1^A T_2^B T_3^C$. The renormalized sum of all tripole contributions in this configuration is 1064.77 ± 0.08, which is in agreement with the value (1064.6 ± 0.1) reported in [37].

Dipoles	Gluons		Quarks	
	G_{ij}^{nl}	Ref. [37]	Q_{ij}^{nl}	Ref. [37]
12	71.15 ± 0.05	71.11 ± 0.12	-27.837 ± 0.001	-27.841 ± 0.011
13	36.27 ± 0.02	36.17 ± 0.07	-21.719 ± 0.005	-21.724 ± 0.009
23	75.79 ± 0.01	75.62 ± 0.09	-27.804 ± 0.002	-27.807 ± 0.011
14	65.48 ± 0.02	65.38 ± 0.09	-25.660 ± 0.003	-25.666 ± 0.010
24	46.25 ± 0.01	46.15 ± 0.06	-22.933 ± 0.005	-22.908 ± 0.009
34	44.86 ± 0.02	44.72 ± 0.09	-22.513 ± 0.004	-22.518 ± 0.009

Table 2. Comparison of the selected results for the 2-jettiness soft function for the kinematic point in Eq. (D.6). When quoting results for functions G_{ij}^{nl}, Q_{ij}^{nl}, we show Vegas integration errors which, most likely, underestimate the true uncertainties of the result.

D.3 3-jettiness

We parameterize the scattering of the additional jet by θ_{15} and ϕ_5

$$n_5 = (\sin\theta_{15}\cos\phi_5, \sin\theta_{15}\sin\phi_5, \cos\theta_{15}). \tag{D.7}$$

We compare in Table 3 our 3-jettiness dipole contributions to the benchmark result in [37] by taking the following phase space point

$$\theta_{13} = \frac{3\pi}{10}, \quad \theta_{14} = \frac{6\pi}{10}, \quad \theta_{15} = \frac{9\pi}{10}, \quad \phi_4 = \frac{3\pi}{5}, \quad \phi_5 = \frac{6\pi}{5}. \tag{D.8}$$

Dipoles	Gluons		Quarks	
	G_{ij}^{nl}	Ref. [37]	Q_{ij}^{nl}	Ref. [37]
12	116.20 ± 0.01	116.20 ± 0.16	-36.249 ± 0.001	-36.244 ± 0.009
13	38.13 ± 0.03	37.63 ± 0.03	-21.717 ± 0.007	-21.732 ± 0.005
14	63.63 ± 0.01	63.66 ± 0.06	-25.189 ± 0.003	-25.192 ± 0.006
15	107.17 ± 0.01	106.99 ± 0.12	-35.268 ± 0.001	-35.256 ± 0.009
23	97.11 ± 0.01	96.97 ± 0.10	-32.875 ± 0.002	-32.872 ± 0.008
24	67.36 ± 0.02	67.51 ± 0.08	-26.821 ± 0.003	-26.815 ± 0.007
25	30.87 ± 0.03	30.73 ± 0.04	-21.561 ± 0.009	-21.561 ± 0.005
34	69.43 ± 0.01	69.24 ± 0.07	-25.854 ± 0.002	-25.861 ± 0.006
35	106.13 ± 0.02	105.97 ± 0.13	-34.799 ± 0.002	-34.796 ± 0.008
45	74.45 ± 0.02	74.36 ± 0.09	-28.247 ± 0.004	-28.251 ± 0.007

Table 3. Comparison of the selected results for the 3-jettiness soft function for the kinematic point in Eq. (D.8). When quoting results for functions G_{ij}^{nl}, Q_{ij}^{nl}, we show Vegas integration errors which, most likely, underestimate the true uncertainties of the result.

For the tripole contribution in this configuration, there are four independent color structures. In Table 4 we present our results for each of these configurations, as defined in [37].

	$\tilde{c}^{(2,124)}_{\text{tripoles}}$	$\tilde{c}^{(2,125)}_{\text{tripoles}}$	$\tilde{c}^{(2,145)}_{\text{tripoles}}$	$\tilde{c}^{(2,245)}_{\text{tripoles}}$
$\tilde{c}_{\text{tripoles}}$	-683.25 ± 0.01	-2203.3 ± 0.2	-6.324 ± 0.004	-0.837 ± 0.008
Ref. [37]	-683.23 ± 0.04	-2203.5 ± 0.1	-6.325 ± 0.04	-0.830 ± 0.039

Table 4. Same as in Table 3 for the four independent triple-color correlated contributions.

References

[1] F. Caola, K. Melnikov and R. Röntsch, *Nested soft-collinear subtractions in NNLO QCD computations*, *Eur. Phys. J. C* **77** (2017) 248 [1702.01352].

[2] S. Frixione and M. Grazzini, *Subtraction at NNLO*, *JHEP* **06** (2005) 010 [hep-ph/0411399].

[3] A. Gehrmann-De Ridder, T. Gehrmann and E.W.N. Glover, *Antenna subtraction at NNLO*, *JHEP* **09** (2005) 056 [hep-ph/0505111].

[4] J. Currie, E.W.N. Glover and S. Wells, *Infrared Structure at NNLO Using Antenna Subtraction*, *JHEP* **04** (2013) 066 [1301.4693].

[5] G. Somogyi, Z. Trocsanyi and V. Del Duca, *Matching of singly- and doubly-unresolved limits of tree-level QCD squared matrix elements*, *JHEP* **06** (2005) 024 [hep-ph/0502226].

[6] G. Somogyi and Z. Trocsanyi, *A Subtraction scheme for computing QCD jet cross sections at NNLO: Regularization of real-virtual emission*, *JHEP* **01** (2007) 052 [hep-ph/0609043].

[7] V. Del Duca, C. Duhr, A. Kardos, G. Somogyi and Z. Trócsányi, *Three-Jet Production in Electron-Positron Collisions at Next-to-Next-to-Leading Order Accuracy*, *Phys. Rev. Lett.* **117** (2016) 152004 [1603.08927].

[8] V. Del Duca, C. Duhr, A. Kardos, G. Somogyi, Z. Szőr, Z. Trócsányi et al., *Jet production in the CoLoRFulNNLO method: event shapes in electron-positron collisions*, *Phys. Rev. D* **94** (2016) 074019 [1606.03453].

[9] M. Czakon, *A novel subtraction scheme for double-real radiation at NNLO*, *Phys. Lett. B* **693** (2010) 259 [1005.0274].

[10] M. Czakon, *Double-real radiation in hadronic top quark pair production as a proof of a certain concept*, *Nucl. Phys. B* **849** (2011) 250 [1101.0642].

[11] M. Czakon and D. Heymes, *Four-dimensional formulation of the sector-improved residue subtraction scheme*, *Nucl. Phys. B* **890** (2014) 152 [1408.2500].

[12] C. Anastasiou, K. Melnikov and F. Petriello, *A new method for real radiation at NNLO*, *Phys. Rev. D* **69** (2004) 076010 [hep-ph/0311311].

[13] S. Catani and M. Grazzini, *An NNLO subtraction formalism in hadron collisions and its application to Higgs boson production at the LHC*, *Phys. Rev. Lett.* **98** (2007) 222002 [hep-ph/0703012].

[14] R. Boughezal, K. Melnikov and F. Petriello, *A subtraction scheme for NNLO computations*, *Phys. Rev. D* **85** (2012) 034025 [1111.7041].

[15] M. Grazzini, S. Kallweit and M. Wiesemann, *Fully differential NNLO computations with MATRIX*, *Eur. Phys. J. C* **78** (2018) 537 [1711.06631].

[16] T.T. Jouttenus, I.W. Stewart, F.J. Tackmann and W.J. Waalewijn, *The Soft Function for Exclusive N-Jet Production at Hadron Colliders*, *Phys. Rev. D* **83** (2011) 114030 [1102.4344].

[17] J. Gaunt, M. Stahlhofen, F.J. Tackmann and J.R. Walsh, *N-jettiness Subtractions for NNLO QCD Calculations*, *JHEP* **09** (2015) 058 [1505.04794].

[18] R. Boughezal, X. Liu and F. Petriello, *N-jettiness soft function at next-to-next-to-leading order*, *Phys. Rev. D* **91** (2015) 094035 [1504.02540].

[19] G.F.R. Sborlini, F. Driencourt-Mangin and G. Rodrigo, *Four-dimensional unsubtraction with massive particles*, *JHEP* **10** (2016) 162 [1608.01584].

[20] F. Herzog, *Geometric IR subtraction for final state real radiation*, *JHEP* **08** (2018) 006 [1804.07949].

[21] L. Magnea, E. Maina, G. Pelliccioli, C. Signorile-Signorile, P. Torrielli and S. Uccirati, *Local analytic sector subtraction at NNLO*, *JHEP* **12** (2018) 107 [1806.09570].

[22] Z. Capatti, V. Hirschi, D. Kermanschah and B. Ruijl, *Loop-Tree Duality for Multiloop Numerical Integration*, *Phys. Rev. Lett.* **123** (2019) 151602 [1906.06138].

[23] W.J. Torres Bobadilla et al., *May the four be with you: Novel IR-subtraction methods to tackle NNLO calculations*, *Eur. Phys. J. C* **81** (2021) 250 [2012.02567].

[24] G. Bertolotti, L. Magnea, G. Pelliccioli, A. Ratti, C. Signorile-Signorile, P. Torrielli et al., *NNLO subtraction for any massless final state: a complete analytic expression*, *JHEP* **07** (2023) 140 [2212.11190].

[25] I. Moult, L. Rothen, I.W. Stewart, F.J. Tackmann and H.X. Zhu, *Subleading Power Corrections for N-Jettiness Subtractions*, *Phys. Rev. D* **95** (2017) 074023 [1612.00450].

[26] R. Boughezal, X. Liu and F. Petriello, *Power Corrections in the N-jettiness Subtraction Scheme*, *JHEP* **03** (2017) 160 [1612.02911].

[27] I. Moult, L. Rothen, I.W. Stewart, F.J. Tackmann and H.X. Zhu, *N -jettiness subtractions for $gg \to H$ at subleading power*, *Phys. Rev. D* **97** (2018) 014013 [1710.03227].

[28] R. Boughezal, A. Isgrò and F. Petriello, *Next-to-leading-logarithmic power corrections for N-jettiness subtraction in color-singlet production*, *Phys. Rev. D* **97** (2018) 076006 [1802.00456].

[29] M.A. Ebert, I. Moult, I.W. Stewart, F.J. Tackmann, G. Vita and H.X. Zhu, *Power Corrections for N-Jettiness Subtractions at $\mathcal{O}(\alpha_s)$*, *JHEP* **12** (2018) 084 [1807.10764].

[30] R. Boughezal, A. Isgrò and F. Petriello, *Next-to-leading power corrections to $V + 1$ jet production in N-jettiness subtraction*, *Phys. Rev. D* **101** (2020) 016005 [1907.12213].

[31] R. Kelley, M.D. Schwartz, R.M. Schabinger and H.X. Zhu, *The two-loop hemisphere soft function*, *Phys. Rev. D* **84** (2011) 045022 [1105.3676].

[32] P.F. Monni, T. Gehrmann and G. Luisoni, *Two-Loop Soft Corrections and Resummation of the Thrust Distribution in the Dijet Region*, *JHEP* **08** (2011) 010 [1105.4560].

[33] A. Hornig, C. Lee, I.W. Stewart, J.R. Walsh and S. Zuberi, *Non-global Structure of the $\mathcal{O}(\alpha_s^2)$ Dijet Soft Function*, *JHEP* **08** (2011) 054 [1105.4628].

[34] J.M. Campbell, R.K. Ellis, R. Mondini and C. Williams, *The NNLO QCD soft function for 1-jettiness*, *Eur. Phys. J. C* **78** (2018) 234 [1711.09984].

[35] G. Bell, B. Dehnadi, T. Mohrmann and R. Rahn, *Automated Calculation of $\boldsymbol{N}$-jet Soft Functions*, *PoS* **LL2018** (2018) 044 [1808.07427].

[36] S. Jin and X. Liu, *Two-loop N-jettiness soft function for $pp \to 2j$ production*, Phys. Rev. D **99** (2019) 114017 [1901.10935].

[37] G. Bell, B. Dehnadi, T. Mohrmann and R. Rahn, *The NNLO soft function for N-jettiness in hadronic collisions*, 2312.11626.

[38] F. Devoto, K. Melnikov, R. Röntsch, C. Signorile-Signorile and D.M. Tagliabue, *A fresh look at the nested soft-collinear subtraction scheme: NNLO QCD corrections to N-gluon final states in $q\bar{q}$ annihilation*, JHEP **02** (2024) 016 [2310.17598].

[39] G. Bell, R. Rahn and J. Talbert, *Two-loop anomalous dimensions of generic dijet soft functions*, Nucl. Phys. B **936** (2018) 520 [1805.12414].

[40] G. Bell, R. Rahn and J. Talbert, *Generic dijet soft functions at two-loop order: correlated emissions*, JHEP **07** (2019) 101 [1812.08690].

[41] G. Bell, R. Rahn and J. Talbert, *Generic dijet soft functions at two-loop order: uncorrelated emissions*, JHEP **09** (2020) 015 [2004.08396].

[42] I.W. Stewart, F.J. Tackmann and W.J. Waalewijn, *N-Jettiness: An Inclusive Event Shape to Veto Jets*, Phys. Rev. Lett. **105** (2010) 092002 [1004.2489].

[43] S. Catani, *The Singular behavior of QCD amplitudes at two loop order*, Phys. Lett. B **427** (1998) 161 [hep-ph/9802439].

[44] T. Becher and M. Neubert, *On the Structure of Infrared Singularities of Gauge-Theory Amplitudes*, JHEP **06** (2009) 081 [0903.1126].

[45] T. Becher, G. Bell, C. Lorentzen and S. Marti, *Transverse-momentum spectra of electroweak bosons near threshold at NNLO*, JHEP **02** (2014) 004 [1309.3245].

[46] S. Catani and M. Grazzini, *Infrared factorization of tree level QCD amplitudes at the next-to-next-to-leading order and beyond*, Nucl. Phys. B **570** (2000) 287 [hep-ph/9908523].

[47] G. Somogyi, *Angular integrals in d dimensions*, J. Math. Phys. **52** (2011) 083501 [1101.3557].

[48] F. Caola, M. Delto, H. Frellesvig and K. Melnikov, *The double-soft integral for an arbitrary angle between hard radiators*, Eur. Phys. J. C **78** (2018) 687 [1807.05835].

[49] I. Dubovyk, J. Gluza and G. Somogyi, *Mellin-Barnes Integrals: A Primer on Particle Physics Applications*, Lect. Notes Phys. **1008** (2022) pp. [2211.13733].

[50] E. Panzer, *Algorithms for the symbolic integration of hyperlogarithms with applications to Feynman integrals*, Comput. Phys. Commun. **188** (2015) 148 [1403.3385].

[51] A.B. Goncharov, *Multiple polylogarithms, cyclotomy and modular complexes*, Math. Res. Lett. **5** (1998) 497 [1105.2076].

[52] K. Asteriadis, F. Caola, K. Melnikov and R. Röntsch, *Analytic results for deep-inelastic scattering at NNLO QCD with the nested soft-collinear subtraction scheme*, Eur. Phys. J. C **80** (2020) 8 [1910.13761].

[53] I.W. Stewart, F.J. Tackmann and W.J. Waalewijn, *The Quark Beam Function at NNLL*, JHEP **09** (2010) 005 [1002.2213].

Higgs couplings in SMEFT via Zh production at the HL-LHC

Subhaditya Bhattacharya,[a] **Abhik Sarkar,**[a] **Sanjoy Biswas**[b]

[a] *Department of Physics, Indian Institute of Technology Guwahati, Assam 781039, India*

[b] *Department of Physics, Ramakrishna Mission Vivekananda Educational and Research Institute, Belur Math, Howrah 711202, India*

E-mail: subhab@iitg.ac.in, sarkar.abhik@iitg.ac.in, sanjoy.phy@gm.rkmvu.ac.in

Abstract: We study the Higgs couplings present in the Zh associated production mode at the Large Hadron Collider (LHC) in presence of both CP even and CP odd dimension 6 Standard Model Effective Theory (SMEFT) operators. The analysis is performed mainly in context of the HL-LHC (with $\sqrt{s}$ =14 TeV and luminosity 3000 fb^{-1}) setup using cut based as well as machine learning techniques. The analysis shows significant betterment in the signal significance by using the machine learning technique. We also do a χ^2 analysis, which reveals a significant change in the sensitivity of the coupling modifiers due to the presence of effective operators, in particular due to the four point $qqZh$ interaction. The presence of dimension six CP odd four point operators, which contributes at $\mathcal{O}(\Lambda^{-4})$ order due to lack of interference with the SM contributions, can only have sensitivity with smaller NP scale at the HL-LHC, after addressing the effective limit and constraints.

Keywords: Higgs production, Higgs properties, SMEFT

arXiv:2403.03001v1 [hep-ph] 5 Mar 2024

Contents

1 Introduction **1**

2 EFT framework **3**
- 2.1 SMEFT operators relevant to Zh production 3
- 2.2 Parametrization of production cross sections 5
- 2.3 Comparison with other Higgs production modes 8

3 Constraints on the HZZ coupling from current data **9**
- 3.1 Constraints on the effective coupling coefficients 10

4 Collider analysis: Current and future runs **11**
- 4.1 Cut based analysis 11
- 4.2 BDT based analysis 14
- 4.3 Two parameter χ^2 analysis 17

5 Summary and Conclusion **18**

A Details of BDT analysis parameters **20**

1 Introduction

The Higgs boson discovery at the LHC provided the first conclusive portrait of the Electroweak Symmetry Breaking (EWSB) mechanism [1] and mass generation of the SM particles. Over a decade since the Higgs discovery, we have been able to probe many of its properties, some of which are precise and closely mimic that of a SM-like isodoublet (H), some are not, allowing for New Physics (NP) studies via Higgs sector. One standard way of parametrizing the Higgs couplings beyond the SM is to use the κ framework [2], where any deviation from the SM is taken into consideration by variation of the κ parameter, where $\kappa = 1$ depicts SM. Most of the Higgs studies at the LHC uses such parametrisation and so do we. However, one needs to be vigilant about the possible sources of NP that generates such contributions and need to be consistent with null observation of NP searches while scanning the possible values that κ can acquire[1].

The couplings of our interest for this study are the $qqZ/qqZh$ and hZZ vertices which appear in both VBF as well as Zh production modes of the Higgs boson. The entire set of operators involved in the modification of the SM counterpart of Z vertices are written in equations (1.1) and (1.2). Note here in writing (1.1) and (1.2), we have adhered to the

[1] We will address this issue later in a specific context.

vertices after EWSB, when $H = \begin{pmatrix} 0 \\ \frac{(v+h)}{\sqrt{2}} \end{pmatrix}$. $\kappa_Z \neq 1$ takes into account the deviation of the SM hZZ expectation.

$$\begin{aligned}\mathcal{L}_{SM} = \kappa_Z \frac{m_Z^2}{v}\, Z_\mu Z^\mu h + g_{uL}^{\mathtt{SM}}\, Z_\mu \overline{u_L}\gamma^\mu u_L + g_{uR}^{\mathtt{SM}}\, Z_\mu \overline{u_R}\gamma^\mu u_R + g_{dL}^{\mathtt{SM}}\, Z_\mu \overline{d_L}\gamma^\mu d_L \\ + g_{dR}^{\mathtt{SM}}\, Z_\mu \overline{d_R}\gamma^\mu d_R\,;\end{aligned} \tag{1.1}$$

$$\begin{aligned}\mathcal{L}_{NP} = g_{ZZ}\, \frac{h}{v} Z^{\mu\nu} Z_{\mu\nu} + g_{Z\widetilde{Z}}\, \frac{h}{v} Z^{\mu\nu} \widetilde{Z_{\mu\nu}} + g_{Z\gamma}\, \frac{h}{v} A^{\mu\nu} Z_{\mu\nu} + g_{\widetilde{Z}\gamma}\, \frac{h}{v} A^{\mu\nu} \widetilde{Z_{\mu\nu}} \\ + g_u^L\, Z_\mu \overline{u_L}\gamma^\mu u_L + g_u^R\, Z_\mu \overline{u_R}\gamma^\mu u_R + g_d^L\, Z_\mu \overline{d_L}\gamma^\mu d_L + g_d^R\, Z_\mu \overline{d_R}\gamma^\mu d_R \\ + \delta_u^L\, \frac{h}{v} Z_\mu \overline{u_L}\gamma^\mu u_L + \delta_u^R\, \frac{h}{v} Z_\mu \overline{u_R}\gamma^\mu u_R + \delta_d^L\, \frac{h}{v} Z_\mu \overline{d_L}\gamma^\mu d_L + \delta_d^R\, \frac{h}{v} Z_\mu \overline{d_R}\gamma^\mu d_R \\ + g_u\, \frac{1}{v}(\overline{u_L}\sigma^{\mu\nu} u_R + \overline{u_R}\sigma^{\mu\nu} u_L) Z_{\mu\nu} + g_d\, \frac{1}{v}(\overline{d_L}\sigma^{\mu\nu} d_R + \overline{d_R}\sigma^{\mu\nu} d_L) Z_{\mu\nu} \\ + \delta_u\, \frac{h}{v^2}(\overline{u_L}\sigma^{\mu\nu} u_R + \overline{u_R}\sigma^{\mu\nu} u_L) Z_{\mu\nu} + \delta_d\, \frac{h}{v^2}(\overline{d_L}\sigma^{\mu\nu} d_R + \overline{d_R}\sigma^{\mu\nu} d_L) Z_{\mu\nu}\,.\end{aligned} \tag{1.2}$$

In the above equations, the notations have usual meaning, particularly note $Z_{\mu\nu} = \partial_\mu Z_\nu - \partial_\nu Z_\mu$, $\widetilde{Z_{\mu\nu}} = \epsilon_{\mu\nu\alpha\beta} Z^{\alpha\beta}$ where Z_μ denotes the physical Z boson, $\epsilon_{\mu\nu\alpha\beta}$ is a completely antisymmetric tensor and $\sigma^{\mu\nu} = \{\gamma^\mu, \gamma^\nu\}$. We will provide a detailed matching with the standard Warsaw basis [3] later.

Over the last two runs, LHC experiments, ATLAS [4] and CMS [5] have almost pinned down the Higgs couplings to less than 10% uncertainty, however, the High Luminosity (HL) run will prove to be significant for establishing a clearer picture of Higgs characteristics. The Higgs couplings associated with gauge bosons has been studied extensively in the existing literature from various point of views. They include bounds on the anomalous couplings [6–9], Higgs CP properties [10–14], etc. The procedure involves dedicated signal observables as well as in the effective theory (EFT) framework [15–22] in variety of production and decay channels in context of the current and future colliders.

In this analysis, we study the NP effects in hZZ and qqZ couplings as well as the fully NP induced $qqZh$ coupling in the Zh associated production mode, within the realm of the Standard Model Effective Field Theory (SMEFT) [23] at the High Luminosity (HL) LHC frontier. SMEFT framework is arguably the best motivated scenario for searching NP in a model independent way, either via deviations in the signal pattern or excess in the cross-section predicted from the SM, given the absence of a specific hint for NP in current scenarios.

Out of the different channels of Higgs production, the Higgs-strahlung or Vh ($V = W, Z$) production modes turn out to be more sensitive to the variation of effective operators concerned in the modification of the aforementioned couplings. We limit ourselves to the Zh channel, but a similar analysis is possible for the WH channel and estimation of hWW coupling, however, the SM background turns indomitable to make a reasonable prediction in such circumstances. There have been a number of analysis concerning the Zh production mode [16–18]. However, the effect of CP odd operators in context of the

$qqZ/qqZh$ couplings (dipole operators) have been neglected. We show that the presence of both CP even as well as CP odd effective operators significantly alter the existing bounds on the concerned couplings at the present and projected LHC sensitivities.

The organization of the paper is as follows: we discuss SMEFT operators relevant for our analysis and their sensitivities in section 2, constraints on the coupling modifiers as well as SMEFT coefficients from current data in section 3, detailed collider analysis in section 4 and concluding remarks in 5.

2 EFT framework

In absence of a direct observational evidence of NP signal at current experiments, one of the best possible ways to gauge the effects of NP is through higher dimensional effective operators constructed out of the SM fields respecting the SM gauge symmetry. They are popularly referred as SMEFT operators. Note here that SMEFT operators also include the Higgs field as isodoublet under the SM gauge group, while there are efforts to keep it beyond, for example, in HEFT [24] , but given the Higgs properties closely mimicking that of a SM doublet, we choose SMEFT framework to explore the limit of NP[2]. These operators are suppressed by an appropriate power of a heavy NP mass scale (Λ) integrated out, depending on the mass-scale of the operator. Understandably the effects of such operators diminish with higher mass dimension of the operators, hence we will constrict ourselves to the lowest dimension operators that contribute to the Zh associated production, which appears in dimension six; operators of dimension 8 [30, 31] may also contribute, but will be suppressed[3].

2.1 SMEFT operators relevant to Zh production

The SMEFT Lagrangian can be written as:

$$\mathcal{L} = \mathcal{L}_{SM} + \sum_{i,(n>4)} \frac{c_i}{\Lambda^{(n-4)}} \mathcal{O}_i^{(n)} \,, \tag{2.1}$$

Here, $\mathcal{O}_i^{(n)}$ represents operators of dimension n and c_i represents dimensionless couplings or Wilson's coefficients. Throughout this analysis, the effective scale is taken as $\Lambda = 1$ TeV, while the resulting bound or the sensitivity is obtained for the corresponding Wilson coefficient c_i. However, it is simple to understand that the limit on c_i can be rescaled easily for different choices of Λ, following, $\frac{c_i}{\Lambda^2} = \frac{c_i'}{\Lambda'^2}$. Although, the validity of effective limit depends on the choice of Λ, strictly speaking the CM energy of the reaction should abide by $\sqrt{s} < \Lambda$. At hadron collider, it is difficult to ensure such a condition, we elaborate upon the possibility later.

There is no unique basis for the choice of these operators and all the different bases are equivalent. We choose Warsaw basis for our representation. The SMEFT operators

[2] Apart, operators with two Higgs doublets [25, 26], or a right handed neutrino [27–29] have also been done.

[3] It is well known that the only SMEFT operator in dimension 5 is the Weinberg operator $\bar{N}N^c$; $N = H^\dagger \epsilon \ell$, which generates Majorana neutrino mass.

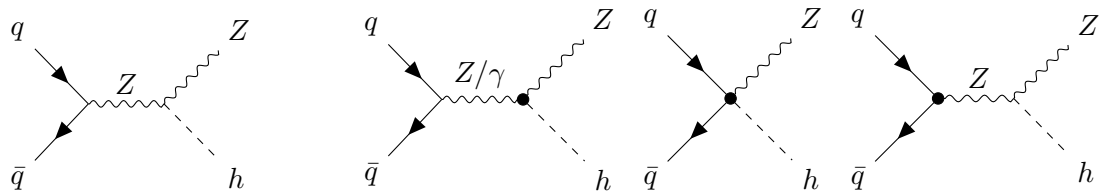


Figure 1: SM and EFT contributions to the Zh associated production mode at the LHC. Dotted vertices refer to the presence of EFT operators.

relevant to ZH associated production mode are tabulated in Table 1 and the corresponding Feynman diagrams are shown in Figure 1. The vertices with a blob represent effective operator contribution, which modifies ZZh, qqh vertices and additional contributions are obtained via γZh and $qqZh$ vertices.

Before moving forward, it should be noted that operators are classified majorly into two categories, those generated at loop level (LG operators) or potential tree generated (PTG operators) for NPs those which are weakly coupled and decoupling [32]. The LG operators are suppressed additionally by a factor of $(4\pi)^2$ coming from the loops and hence their contributions are expected to be suppressed in comparison to the PTG operators if the underlying NP scale is the same. However, this additional suppression factor for the LG operators is not intrinsically incorporated in most SMEFT studies in order to maintain uniformity of the nomenclature, we will however use the operator classification as in [3].

Operators (hZZ vertex, CP even)
$\mathcal{O}_{H\Box} = (H^\dagger H)\Box(H^\dagger H)$
$\mathcal{O}_{HDD} = (H^\dagger D_\mu H)(H^\dagger D^\mu H)$
$\mathcal{O}_{HW} = (H^\dagger H)W^i_{\mu\nu}W^{i\mu\nu}$
$\mathcal{O}_{HB} = (H^\dagger H)B_{\mu\nu}B^{\mu\nu}$
$\mathcal{O}_{HWB} = (H^\dagger \tau^i H)W^i_{\mu\nu}B^{\mu\nu}$
Operators (hZZ vertex, CP odd)
$\mathcal{O}_{H\widetilde{W}} = (H^\dagger H)\widetilde{W^i_{\mu\nu}}W^{i\mu\nu}$
$\mathcal{O}_{H\widetilde{B}} = (H^\dagger H)\widetilde{B_{\mu\nu}}B^{\mu\nu}$
$\mathcal{O}_{H\widetilde{W}B} = (H^\dagger \tau^i H)\widetilde{W^i_{\mu\nu}}B^{\mu\nu}$

Operators ($qqZ/qqZh$ vertex, CP even)
$\mathcal{O}^{(1)}_{Hq} = (H^\dagger i\overleftrightarrow{D_\mu} H)(\bar{q}_p\gamma^\mu q_r)$
$\mathcal{O}^{(3)}_{Hq} = (H^\dagger i\overleftrightarrow{D^i_\mu} H)(\bar{q}_p\tau^i\gamma^\mu q_r)$
$\mathcal{O}_{Hu} = (H^\dagger i\overleftrightarrow{D_\mu} H)(\bar{u}_p\gamma^\mu u_r)$
$\mathcal{O}_{Hd} = (H^\dagger i\overleftrightarrow{D_\mu} H)(\bar{d}_p\gamma^\mu d_r)$
Operators ($qqZ/qqZh$ vertex, CP odd)
$\mathcal{O}_{uW} = (\bar{q}_p\sigma^{\mu\nu}u_r)\tau^i\widetilde{H}W^i_{\mu\nu}$
$\mathcal{O}_{uB} = (\bar{q}_p\sigma^{\mu\nu}u_r)\widetilde{H}B_{\mu\nu}$
$\mathcal{O}_{dW} = (\bar{q}_p\sigma^{\mu\nu}d_r)\tau^i HW^i_{\mu\nu}$
$\mathcal{O}_{dB} = (\bar{q}_p\sigma^{\mu\nu}d_r)HB_{\mu\nu}$

Table 1: Dimension 6 SMEFT operators (in Warsaw basis) relevant to VH associated production at the LHC. Here, p and r are quark family indices. For complex operators, the presence of respective hermitian conjugates is assumed. For relevance: $D_\mu = \partial_\mu + ig\frac{\tau^i}{2}W^i_\mu + ig'\frac{1}{2}B_\mu$, $W^i_{\mu\nu} = \partial_\mu W^i_\nu - \partial_\nu W^i_\mu + g\epsilon^{ijk}W^j_\mu W^k_\nu$, $B_{\mu\nu} = \partial_\mu B_\nu - \partial_\nu B_\mu$, $H^\dagger i\overleftrightarrow{D_\mu}H = iH^\dagger D_\mu H - i(D_\mu H)^\dagger H$, $H^\dagger i\overleftrightarrow{D^i_\mu}H = iH^\dagger\tau^i D_\mu H - i(D_\mu H)^\dagger\tau^i H$, $\widetilde{V_{\mu\nu}} = \epsilon_{\mu\nu\rho\sigma}V^{\rho\sigma}$ $(V = W^i, B)$.

A few observations related to the operators as mentioned in Table 1:

- The operators $\mathcal{O}_{H\Box}$ and $\mathcal{O}_{HDD}$ modify the Higgs gauge boson coupling by a mul-

tiplicative factor without introducing any new Lorentz structure, amounting to a renormalization of the Higgs field. As such the contribution can be absorbed in the coupling modifier.

- The operators $\mathcal{O}_{HW}$, $\mathcal{O}_{HB}$ and $\mathcal{O}_{HWB}$ contribute in the modification of the HVV vertex. These amounts to the CP conserving anomalous Higgs gauge boson coupling.
- The operators $\mathcal{O}_{H\widetilde{W}}$, $\mathcal{O}_{H\widetilde{B}}$ and $\mathcal{O}_{H\widetilde{W}B}$ contribute in the modification of the hZZ vertex. These amounts to the CP violating anomalous Higgs gauge boson coupling.
- The operators $\mathcal{O}^{(1)}_{Hq}$, $\mathcal{O}^{(3)}_{Hq}$, $\mathcal{O}_{Hu}$ and $\mathcal{O}_{Hd}$ are the CP even contributions to the four field contact interaction $qqZh$. These operators also contribute to qqZ vertex.
- The operators $\mathcal{O}_{uW}$, $\mathcal{O}_{uB}$, $\mathcal{O}_{dW}$ and $\mathcal{O}_{dB}$ are the CP odd contributions to the four field contact interaction $qqZh$. These operators also contribute to qqZ vertex. These operators contribute to the dipole moments of quarks and hence can be referred to as dipole operators.

A complete matching between the coefficients in Eq.1.2 and the SMEFT coefficients as in Table 1 are shown in Table 2.

Coefficient	Warsaw equivalent
g_{ZZ}	$2\left(c_w^2 c_{HW} + s_w^2 c_{HB} + s_w c_w c_{HWB}\right) v^2/\Lambda^2$
$g_{Z\gamma}$	$\left(2 s_w c_w^2 (c_{HW} - c_{HB}) + (s_w^2 - c_w^2) c_{HWB}\right) v^2/\Lambda^2$
$g_{Z\widetilde{Z}}$	$2\left(c_w^2 c_{H\widetilde{W}} + s_w^2 c_{H\widetilde{B}} + s_w c_w c_{H\widetilde{W}B}\right) v^2/\Lambda^2$
$g_{\widetilde{Z}\gamma}$	$\left(2 s_w c_w^2 (c_{H\widetilde{W}} - c_{H\widetilde{B}}) + (s_w^2 - c_w^2) c_{H\widetilde{W}B}\right) v^2/\Lambda^2$
g_u^L	$-\left(c^{(1)}_{Hq} + c^{(3)}_{Hq}\right) ev^2/\left(2\Lambda^2 s_w c_w\right)$
g_d^L	$-\left(c^{(1)}_{Hq} - c^{(3)}_{Hq}\right) ev^2/\left(2\Lambda^2 s_w c_w\right)$
g_u^R	$-c_{Hu} ev^2/\left(2\Lambda^2 s_w c_w\right)$
g_d^R	$-c_{Hd} ev^2/\left(2\Lambda^2 s_w c_w\right)$
δ_u^L	$-\left(c^{(1)}_{Hq} + c^{(3)}_{Hq}\right) ev^2/\left(\Lambda^2 s_w c_w\right)$
δ_d^L	$-\left(c^{(1)}_{Hq} - c^{(3)}_{Hq}\right) ev^2/\left(\Lambda^2 s_w c_w\right)$
δ_u^R	$-c_{Hu} ev^2/\left(\Lambda^2 s_w c_w\right)$
δ_d^R	$-c_{Hd} ev^2/\left(\Lambda^2 s_w c_w\right)$
g_u	$\left(s_w c_{uB} - c_w c_{uW}\right) ev^2/\sqrt{2}\Lambda^2$
g_d	$\left(s_w c_{dB} + c_w c_{dW}\right) ev^2/\sqrt{2}\Lambda^2$
δ_u	$\sqrt{2}\left(s_w c_{uB} - c_w c_{uW}\right) ev^2/\Lambda^2$
δ_d	$\sqrt{2}\left(s_w c_{dB} + c_w c_{dW}\right) ev^2/\Lambda^2$

Table 2: Matching between coefficients in equation (1.2) and the SMEFT coefficients. s_w and c_w are the sine and cosine of the Weinberg angle.

2.2 Parametrization of production cross sections

When SMEFT effects are included, the cross section consists of three types of terms viz. the pure SM contribution, the SM plus EFT interference ($\propto \Lambda^{-2}$ from dimension six operators)

and the pure EFT contribution ($\propto \Lambda^{-4}$). Inclusion of dimension 8 operators would result in SM plus EFT interference contribution $\propto \Lambda^{-4}$ which is comparable to the pure EFT contribution from dimension 6 terms, however, we do not consider them in this analysis. The production cross section in presence of SMEFT operators takes the form:

$$\sigma = \sigma^{(SM)} + \sum_{i=1}^{n_L} c_i \sigma_i^{(L)} + \sum_{i<j}^{n_Q} c_i c_j \sigma_{ij}^{(Q)} \,, \tag{2.2}$$

where, n_L and n_Q refers to the number of linear and quadratic SMEFT contributions. The effective scales Λ^{-2} and Λ^{-4} are absorbed in the cross sections $\sigma_i^{(L)}$ and $\sigma_{ij}^{(Q)}$ respectively. In presence of coupling modifiers κ, the cross section in equation (2.2) takes the form as below,

$$\sigma = \kappa^2\, \sigma^{(SM)} + \sum_{i=1}^{n_L} (\alpha_i^{(L)}\kappa + \beta_i^{(L)}\kappa^2)\, c_i \sigma_i^{(L)} + \sum_{i<j}^{n_Q} (1 + \alpha_{ij}^{(Q)}\kappa + \beta_{ij}^{(Q)}\kappa^2)\, c_i c_j \sigma_{ij}^{(Q)} \,. \tag{2.3}$$

At the hadron collider, an analytical form of the cross section is difficult to write due to the uncertainty of the incoming momenta of the partons. However, we can numerically fit the cross section as a function of the parameters and this turns out to be equally useful for gauging the effects of NP. In the following, we fit the operator coefficients following (2.3) at 14 TeV LHC for the Zh associated production processes are performed considering one operator at a time. The variation of the total production cross section are shown in Figure 2 (for CP even operators) and 3 (for CP odd operators). The ratio of the total production cross section for moving from 13 TeV to 14 TeV are also shown. We adopt the following methodology, the effective Lagrangian is implemented in `FeynRules` [33] to generate the `UFO` model [34] file. This model file is then fed into the event generator `MG5_aMC` [35] to obtain the above cross sections at the leading order (LO). The NP scale is chosen as $\Lambda =$ 1 TeV. A few key points observed are as follows:

- The CP even operators associated with the $qqZ/qqZh$ vertices have significant quadratic contributions indicating large pure EFT contribution. The enhancement of the EFT terms result from the absence of propagator suppression in the production process.

- The CP odd operators concerning $qqZ/qqZh$ vertices have weak linear contribution. This is because they bind fermions with different chiralities and hence do not interfere with the SM process. Due to the negligible linear dependence, they cause variation in the cross section only in the positive direction.

- All the operators except $\mathcal{O}_{Hq}^{(3)}$ shows near symmetric behaviour along the positive and negative side. The operator $\mathcal{O}_{Hq}^{(3)}$ dips around $c_{Hq}^{(3)} = -0.2$ and then continues to rise as we go further in the negative direction. This is due to strong linear as well as quadratic dependence and the trade off between them happens away from $c_{Hq}^{(3)} = 0$ towards the negative axis.

- When moving from 13 TeV to 14 TeV LHC, the contact operators i.e. operators associated with $qqZ/qqZh$ vertices, significantly boost the production cross sections. The other operators are less sensitive.

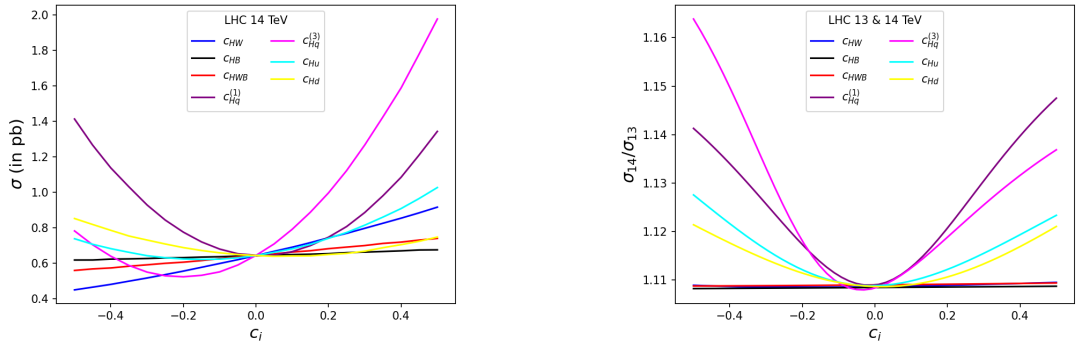


Figure 2: Left: Variation of Zh associated production cross section with variation in CP even effective operator coefficients at the 14 TeV LHC. Right: Variation in the ratio of production cross section of the 14 TeV LHC to the 13 TeV LHC with variation in the effective operator coefficients. See figure inset for the colour codes.

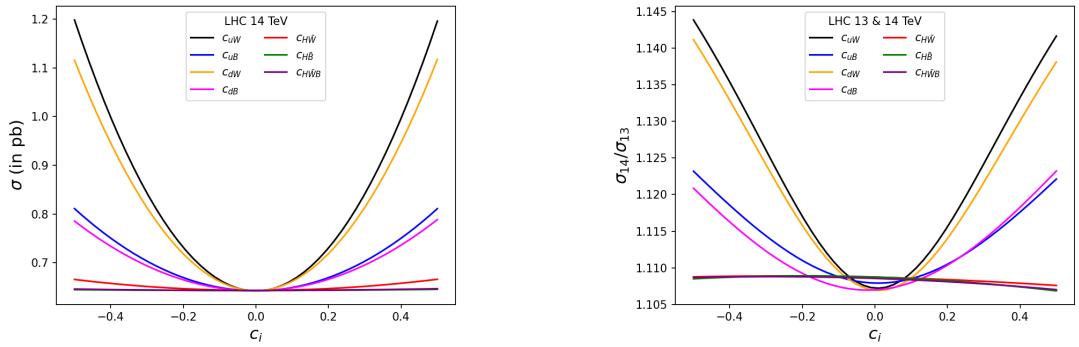


Figure 3: Left: Variation of Zh associated production cross section with change in CP odd effective operator coefficients at the 14 TeV (Left) LHC. Right: Variation in the ratio of production cross section of the 14 TeV LHC to the 13 TeV LHC with change in effective operator coefficients. See figure inset for the colour codes.

It is observed that the most significant change to the cross section is obtained from $\mathcal{O}_{Hq}^{(3)}$ among the CP even operators and $\mathcal{O}_{uW}$ among the CP odd operators. We will consider these two operators for our study. Along with the coupling modifier κ_Z, this form our EFT parameter space: $\{\kappa_Z,\, c_{uW},\, c_{Hq}^{(3)}\}$. The parametrized coefficients for Zh production with these operators following Eqn. (2.3) are tabulated in Table 3. Coefficients of linear terms in 1, κ_Z, c_{uW} and $c_{Hq}^{(3)}$ are not present in our parametrization. Further, the coefficients of $k_Z\, c_{uW}$, $k_Z^2\, c_{uW}$, $c_{uW}\, c_{Hq}^{(3)}$, $k_Z\, c_{uW}\, c_{Hq}^{(3)}$ and $k_Z^2\, c_{uW}\, c_{Hq}^{(3)}$ vanish because of no interference between the SM and $\mathcal{O}_{Hq}^{(3)}$ operators with diagrams with $\mathcal{O}_{uW}$ operator.

We shall also note that the variation of the cross-section presented here with EFT operator coefficients, have been done without considering the constraints on these operators. We shall do it in the next section. We get the dominant physics contribution to the process under consideration and the resultant parametrisation, which remains intact with the modified range of the operator coefficients that will be used for scanning the parameter space.

Coefficients	1×1	$1 \times c_{uW}$	$1 \times c_{Hq}^{(3)}$	$c_{uW} \times c_{uW}$	$c_{Hq}^{(3)} \times c_{Hq}^{(3)}$	$c_{uW} \times c_{Hq}^{(3)}$
1×1	-	-	-	1.9456	2.7265	-
$1 \times \kappa_Z$	-	-	1.0963	0.1353	0.2493	-
$\kappa_Z \times \kappa_Z$	0.6426	-	0.0925	0.1285	-0.0303	-

Table 3: The parametrized coefficients for operators $\mathcal{O}_{Hq}^{(3)}$, $\mathcal{O}_{uW}$ and κ_Z contributing to Zh production at 14 TeV LHC, following equation (2.3).

2.3 Comparison with other Higgs production modes

The operators $\mathcal{O}_{uW}$ and $\mathcal{O}_{Hq}^{(3)}$ are not unique to the Vh ($V = W, Z$) associated production mode. It appears in the vector boson fusion (VBF) and single top production in association with Higgs (thj) as well. The thj process has a comparatively smaller cross section and it is not ideal for the study of these operators, but the VBF mode has a larger cross section compared to VH associated production mode, as considered here. These operators are also associated with the diboson production ($VV = WW, WZ, ZZ$) processes. However, it is the sensitivity of the effective operators where VH associated production mode is superior in comparison to the VBF mode as well as VV processes. This has been illustrated in Figure 4 for the operators $\mathcal{O}_{Hq}^{(3)}$ and $\mathcal{O}_{uW}$. For the study of $qqZ/qqZh$ vertices, Zh production fares over ZBF, ZZ or WZ modes.

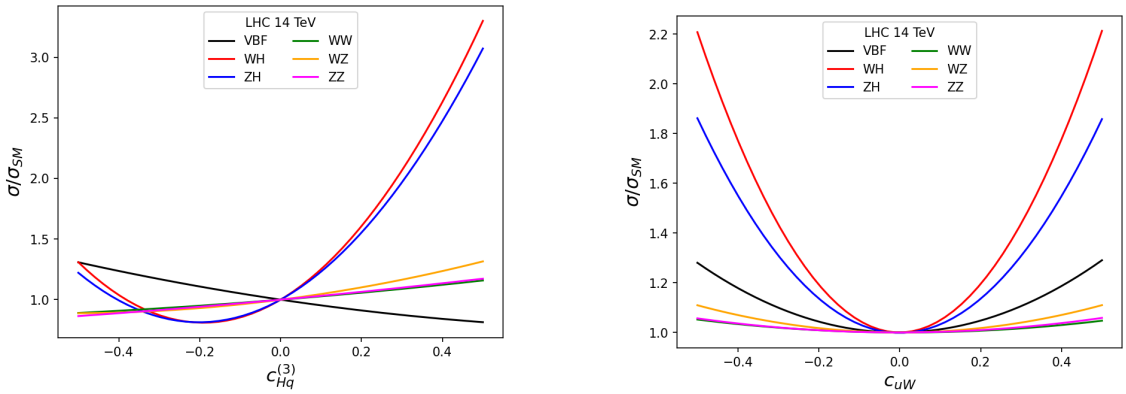


Figure 4: Variation in the ratio of production cross section to the SM cross section in VBF, VH and VV processes at the 14 TeV LHC with variation in effective coefficients: $c_{Hq}^{(3)}$ (Left) and c_{uW}(Right).

3 Constraints on the HZZ coupling from current data

The κ framework is the most preferred way to incorporate uncertainties in the measurement of Higgs couplings. This has been adopted in most of the experimental results reported so far, and we will also follow the same here. The current uncorrelated bounds from ATLAS (**139** fb^{-1}) and CMS (**138** fb^{-1}) are based on Run II data and involves global fit over the main five production and decay channels. Since we intend to study Zh associated production with H subsequently decaying to bottom pair, the bottom Higgs coupling modifier, κ_B is also important for this analysis. Higgs decay to bottom pair has been studied intensely at the LHC across several channels and the bounds are given in terms of signal strength (μ), i.e. the ratio of the observed signal to the SM predicted value. In Table 5 we list out the uncorrelated bounds on the coupling modifiers as well as the signal strengths of the Higgs decay to bottom pair in the Zh production channel.

Measurable	Bound	Source
κ_Z	[0.97, 1.11]	CMS ($pp \to h$) [5]
	[0.94, 1.05]	ATLAS ($pp \to h$) [4]
κ_B	[0.85, 1.11]	CMS ($pp \to h$) [5]
	[0.79, 1.01]	ATLAS ($pp \to h$) [4]
μ^{Zh}_{Hbb}	[0.59, 1.17]	CMS ($pp \to Zh, h \to b\bar{b}$) [36]
	[0.85, 1.33]	ATLAS ($pp \to Zh, h \to b\bar{b}$) [37]

Table 4: Constraints on κ_Z, κ_B and μ^{Zh}_{Hbb} (at 95% C.L.) from ATLAS and CMS experiments.

Considering the bounds on the signal strength, we can limit the coupling modifiers using the measured signal strengths as shown in Eqn. 3.1.

$$\mu^{Zh}_{hbb} = \frac{(\sigma^{Zh} \times (B.R.)^{hbb})}{(\sigma^{Zh} \times (B.R.)^{hbb})_{SM}} = \frac{\kappa_Z^2 \kappa_B^2}{0.1775 + 0.5809\kappa_B^2 + (0.2152 + 0.0264)\kappa_Z^2} \,. \tag{3.1}$$

In evaluating Eqn. 3.1, both the Higgs couplings with the bottom quark as well as with Z bosons have been modified keeping coupling with other fermions unchanged. κ_Z appears from the production cross-section, while κ_B appears from the decay branching fraction, pertaining to the fact that Higgs production and decay modes are those predicted in the SM, the NP effects only enters via rescaling of the Higgs coupling strength. The denominator comes from the modification of the Higgs decay width, which is easily adjusted within the observed total Higgs decay width at LHC for moderate values of κ parameters. We can see that for $\kappa_Z = \kappa_B = 1$, the signal strength turns one. We further invoke the custodial symmetry requirement $\kappa_W = \kappa_Z$. The bounded region is shown in Figure 5. Additionally, superimposing the current correlated bound on the $\kappa_V - \kappa_F$ space from the combined Higgs measurement gives the status of the most accurate constraint from the current data. The uncertainties are less than 10% from the SM prediction.

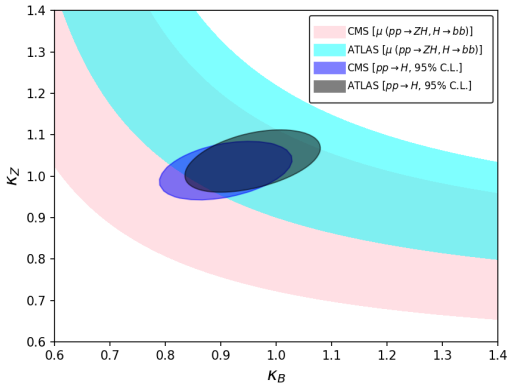


Figure 5: Constraints on coupling modifiers κ_Z and κ_B based on combined limit on $pp \to Zh$, $h \to b\bar{b}$ production signal strength (bands) [36, 37] as well as the combined experimental best fit for all Higgs production and decay processes (ellipses) [4, 5] at ATLAS and CMS experiments.

3.1 Constraints on the effective coupling coefficients

In context of the study of Higgs couplings in effective framework, the SMEFiT collaboration [38] has attempted to provide global bounds based on Higgs, Top and Diboson data from Tevatron, LHC and LEP. Similar fits have been done including B-Physics data with LHC top and bottom quark studies [39, 40]. Similarly, global fits have also been performed based on Electroweak Precision data as well as Δ_{CKM} measurement [41]. Customarily, both ATLAS and CMS have done a number of studies on constraining the EFT operators across various channels using latest data. While ATLAS uses SMEFT, CMS uses HEL parametrization, we will consider bounds from ATLAS [37, 42, 43] only. Also, there has been numerous studies concerning SMEFT, projecting constraints for future collider experiments. We tabulate the constraints on the coefficients c_{uW} and $c_{Hq}^{(3)}$ from current data in Table 5.

Coefficient	Bound	Combined	C.L.	Source
c_{uW}	[-0.375, 0.375]	[-0.01, 0.05]	95%	[44]
	[-0.01, 0.05]		90%	[40]
$c_{Hq}^{(3)}$	[-0.432, 0.062]	[-0.02, 0.04]	95%	[38]
	[-0.7024, 0.1036]		68%	[41]
	[-0.08, 0.1]		95%	[43]
	[-0.23, -0.19] $\cup$ [-0.04, 0.04]		95%	[37]
	[-0.15, 0.52]		95%	[42]
	[-0.02, 0.05]		90%	[40]

Table 5: Constraints on the effective operator coefficients c_{uW} and $c_{Hq}^{(3)}$ from existing studies, see the references for details.

A few comments and clarifications on the existing bounds:

- The bound on c_{uW} from the EFT analysis [44] based on existing LHC Drell-Yan process provides a constraint of $[-6.0, 6.0]$ at $\Lambda = 4$ TeV. Scaling Λ down to 1 TeV, the bound stands at $[-0.375, 0.375]$.

- The bounds on the operator coefficients in [40] are provided for the coefficients $\tilde{C}_i = c_i \left(\frac{v^2}{\Lambda^2}\right)$. Correspondingly, the bounds on c_{uW} and $c_{Hq}^{(3)}$ in Table 5 are obtained for $v = 246$ GeV and $\Lambda = 1$ TeV.

- The CP-violating gauge-Higgs operators listed in Table 1 are constrained by the fermion dipole moment observables, such as electron and neutron dipole moments, as they contribute at one loop to dipole operators. The current limits on the electron and neutron dipole moments are 1.1×10^{-29} and 3.0×10^{-26} (in units of e cm), respectively [45]. These operators are also constrained by the measurements of the triple gauge-interactions of the form $WW\gamma$ and WWZ at LEP and the CP asymmetry measured in the $B \to X_s\gamma$ decay. The CP asymmetry measured in $B \to X_s\gamma$ decay is $A_{B\to X_s\gamma} = 0.015(20)$.

4 Collider analysis: Current and future runs

In this section, we will discuss the event generation and analysis in the context of the current and future HL LHC data. We have simulated $pp \to Zh \to (\ell\ell)(\bar{b}b)$ process at the LHC 13 TeV and 14 TeV center of mass energies. The PDF set used is `NN23LO1` [46] and the renormalization and factorization scales are set at the default dynamical scale choice of MadGraph. The signal and background informations will be detailed in Section 4.1. Before proceeding for a collider analysis in presence of the EFT operators, it is important to check validity of the effective approximation for the collider setup. The validity condition is $\sqrt{\hat{s}} < \Lambda$, where $\sqrt{\hat{s}}$ is the partonic centre of mass energy. However, ensuring this criteria is difficult in hadron colliders like LHC, where collisions between partons happen at variable centre of mass energies. One way to deal with this is to construct the invariant mass of the final state particles, $M_{Zh}^2 = (p_Z + p_h)^2$ here ($p_{h,Z}$ represent reconstructed four momenta), to guess the energy scale at which the partonic collisions take place. This is depicted in Figure 6, for the production process at a particular EFT benchmark point and we observe that almost all the events obey the effective validation criteria, when $\Lambda = 1$ TeV. Now, the generated signal and background events are fed in `Pythia8` [47] for parton showering. The showered events are fed in `Fastjet3` [48] for jet clustering using the `anti` k_t algorithm [49] with jet radius 0.5 and jet $p_T \geq 20$ GeV. Finally, the events are processed through `Delphes3` to take into account finite detector resolution effects, as well as particle identification, reconstruction and jet tagging. The b-tagging efficiency is around 0.6 and the light-jet mistagging efficiency is considered to be one in 100. The processed events are analyzed using `MadAnalysis5` [50].

4.1 Cut based analysis

We consider the signal to be $pp \to Z(l^+l^-)H(b\bar{b})$ i.e. a dilepton di-bjet signal. This signal is comparatively clean due to the presence of charged leptons with invariant mass

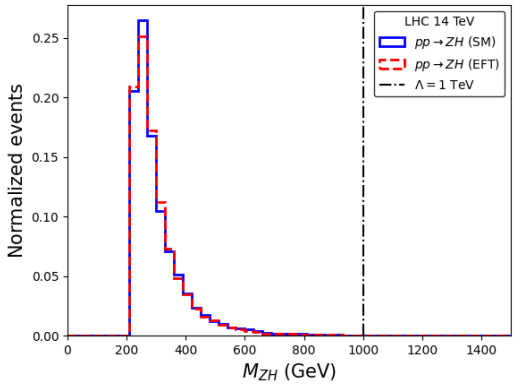


Figure 6: Invariant mass of Zh for the parton level processes in absence as well as presence of EFT operators at $\Lambda = 1$ TeV.. Here we consider the EFT benchmark point corresponding to $\kappa_Z = 1.0$, $c_{uW} = 0.05$ and $c_{Hq}^{(3)} = 0.04$.

of the dilepton system peaking around Z-mass. The possible SM backgrounds for this signal process are $pp \to t\bar{t}$, $pp \to ZZ$, $gg \to Zh$ and $pp \to Zb\bar{b}$. NLO corrections to both signal and background processes are taken into account by multiplying the production cross sections for each process by its NLO K factor, where $K = \sigma_{NLO}/\sigma_{LO}$. The LO and NLO cross sections are calculated using `MG5_aMC@NLO` at LHC 13 TeV and the K factors for different processes are: Zh: 1.288 (for $pp \to Zh$), 2.000 (for $gg \to Zh$), $Zb\bar{b}$: 1.230, $t\bar{t}$: 1.338 and ZZ: 1.461 [51–53].

We perform the analysis for two different setups viz. LHC 13 TeV 139 fb^{-1} (equivalent to Run II) and LHC 14 TeV 3000 fb^{-1} (future HL-LHC projection). We introduce some basic cuts common for all the analysis. These can be detailed as: $P_T^j > 20.0$ GeV, $P_T^l > 10.0$ GeV, $-5.0 < \eta_j < 5.0$, $-2.5 < \eta_l < 2.5$, $\Delta R_{jj} > 0.4$, $\Delta R_{lj} > 0.4$, $\Delta R_{ll} > 0.4$, where, subscripts j and l refer to jets and leptons respectively, and the kinematic variables have their usual definitions as in collider literature [54]. Apart from these, to ensure exclusive $l^+l^-b\bar{b}$ signal we select events with $N_b = 2$ and $N_l = 2$. The relevant distributions of kinematic variables and observables are plotted in Figure 7 for 13 TeV and 14 TeV LHC. Choosing $N_j < 5$ for Zh considerably reduces the pure hadronic backgrounds at LHC. We further choose a wide M_{bb} cut around the Higgs mass to make sure that we retain most of the signal while eliminating the backgrounds. The presence of dileptons enables us to use some additional cuts. Owing to the better detectability of leptons, a narrow cut on M_{ll} around the Z mass significantly reduces the $t\bar{t}$ background. Finally due to the absence of invisible particles in the final state (a part from neutrinos possibly coming b-decay) rejecting events with large MET (MET$>$ 30 GeV) removes backgrounds with neutrinos in final state like leptonic $t\bar{t}$ mode. The entire cut flow for SM Zh process (in absence of EFT contributions) is tabulated in Table 6.

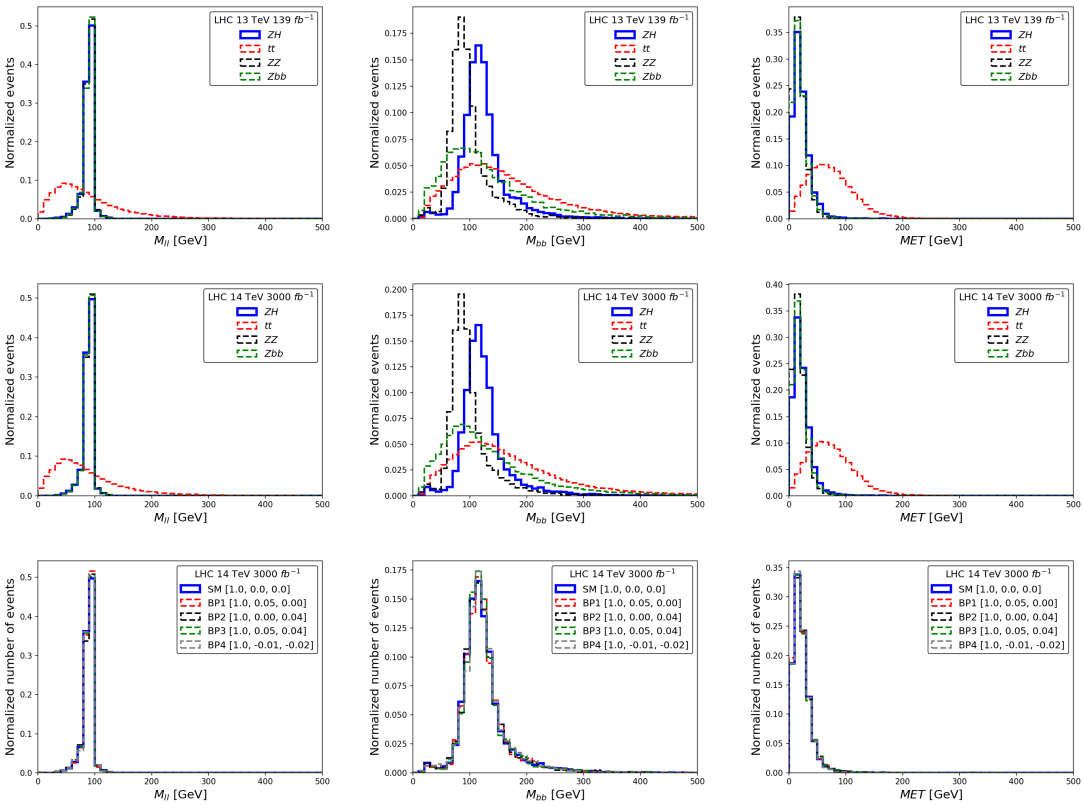


Figure 7: Invariant mass of dilepton (Left), invariant mass of di-bjet (Center) and missing transverse energy (Right) corresponding to the SM signal and background processes in $Z(l^+l^-)h(b\bar{b})$ associated production at the LHC for $\sqrt{s}$ =13 TeV, luminosity of 139 fb^{-1} (Top layer), $\sqrt{s}$ =14 TeV, luminosity of 3000 fb^{-1} (Middle layer) analysis. The Bottom layer consists of the same distributions at different EFT benchmark points shown in Table 7 at $\sqrt{s}$ =14 TeV, luminosity of 3000 fb^{-1}.

	LHC 13 TeV 139 fb^{-1}				LHC 14 TeV 3000 fb^{-1}			
Cuts	S	B	S/B	z	S	B	S/B	z
Basic Cuts	569	1016890	0.0006	0.56	13327	25581580	0.0005	2.63
$N_j < 5$	309	369549	0.0008	0.51	7054	9079825	0.0008	2.34
110.0 GeV $< M_{bb} <$ 140.0 GeV	126	56059	0.0022	0.53	2858	1382411	0.0021	2.43
80.0 GeV$< M_{ll} <$ 100.0 GeV	107	11674	0.0092	0.99	2456	285269	0.0086	4.59
MET $<$ 30 GeV	91	5472	0.0166	1.23	2026	129095	0.0156	5.62

Table 6: Cut flow and signal significance (z) for the SM $Z(l^+l^-)h(b\bar{b})$ associated production signal with the SM background processes at LHC with $\sqrt{s}$ =13 TeV and luminosity of 139 fb^{-1} and at LHC with $\sqrt{s}$ = 14 TeV and integrated luminosity of 3000 fb^{-1}. Apart, we use the following notations, S: Signal events, B: Background events, S/B: Signal to background ratio.

BPs $\left(\kappa_Z, c_{uW}, c_{Hq}^{(3)}\right)$	S	B	S/B	z	ϵ_s	ϵ_b
SM (1.0, 0.0, 0.0)	2026		0.0156	5.62	2.09×10^{-2}	
BP1 (1.0, 0.05, 0.0)	2142		0.0166	5.94	2.19×10^{-2}	
BP2 (1.0, 0.00, 0.04)	2203	129095	0.0171	6.11	2.10×10^{-2}	8.72×10^{-4}
BP3 (1.0, 0.05, 0.04)	2290		0.0177	6.35	2.17×10^{-2}	
BP4 (1.0, -0.01, -0.02)	1954		0.0151	5.42	2.09×10^{-2}	

Table 7: Signal significance of the $Z(l^+l^-)h(b\bar{b})$ production process (at LHC with $\sqrt{s}$ =14 TeV and luminosity 3000 fb^{-1}) from cut based analysis at different benchmark points (BPs) in presence of effective operators, along with signal (ϵ_s) and background (ϵ_b) efficiencies.

For signal significance, we use the Asimov definition [55]:

$$z = \sqrt{2\left((S+B)\ln\left(1+\frac{S}{B}\right) - S\right)}\,, \tag{4.1}$$

where S is the number of signal events and B is the number of background events. The Asimov definition turns out to be better representative of the significance of a signal. On Taylor expansion in the limit $S \ll B$, the Asimov significance approximates to $S/\sqrt{B}$, which is the more common definition. However, when the signal and background numbers are comparable, it is sensible to use the Asimov definition. The number of signal and background events can further be parametrized in terms of the coupling modifiers and the effective operator coefficients as shown in Eqn. 4.2 .

$$\begin{aligned} S &= \mathcal{L} \times \sigma^S_{SM+EFT}(\kappa_V, c_i) \times BR^S(\kappa_B) \times \epsilon_S\,, \\ B &= \mathcal{L} \times \sigma^B_{SM} \times BR^B \times \epsilon_B\,; \end{aligned} \tag{4.2}$$

where, $\mathcal{L}$ is the integrated luminosity, ϵ_S and ϵ_B are the signal and background cut efficiencies respectively. From Table 6, it is clear that the signal significance improves significantly as we move to the high luminosity frontier.

The second part of the analysis features inclusion of EFT operators. In presence of EFT operators, there is further boost in the signal significance. This has been illustrated in Table 7 in presence of SMEFT operators at some benchmark values. The relevant kinematic variables and observables for the different benchmark points are shown in Figure 7. The variation from the SM signal are minuscule. The benchmarks are chosen at the limiting values of the bounds discussed in section 3.

4.2 BDT based analysis

With the advent of modern machine learning tools, multivariate analysis has become a norm in collider analysis [56, 57]. Among the machine learning techniques, boosted decisions trees (BDT) based algorithms are extremely popular due to their stability as well as accuracy even for smaller datasets. With an aim to improved the signal background separation with more accuracy, we perform an analysis using the `XGBoost` classifier [58]. The core setup of the analysis is kept similar to the cut based counterpart. Since, we observed

higher significance at 14 TeV, 3000 fb^{-1} LHC, we will perform the BDT based analysis exclusively for the HL-LHC run. The training sets for signal ($pp \to Z(l^+l^-)H(b\bar{b})$) and backgrounds ($pp \to t\bar{t}$, $pp \to ZZ$, $gg \to Zh$ and $pp \to Zb\bar{b}$) are prepared and weighted according to its number strength at 3000 fb^{-1}. This weighted data is subjected to the same basic cuts as used in the cut based analysis. The feature selection is done in similar line with the VH, $H \to b\bar{b}$ analysis at ATLAS [37]. The features are detailed below:

- Transverse momentum of the leading lepton: p_T^l
- Transverse momentum of the leading b-jet: p_T^b
- Number of jets (inclusive of b-jets): N_j
- Missing transverse energy: MET
- Transverse momentum of the dilepton system: p_T^{ll}
- Transverse momentum of the di-b-jet system: p_T^{bb}
- Invariant mass of the dilepton system: M_{ll}
- Invariant mass of the di-b-jet system: M_{bb}
- Separation in (η, ϕ) space between the leptons: ΔR^{ll}
- Separation in (η, ϕ) space between the b-jets: ΔR^{bb}
- Difference in η between the dilepton and di-b-jet system: $\Delta\eta^{ll,bb}$
- Difference in ϕ between the dilepton and di-b-jet system: $\Delta\phi^{ll,bb}$

The detailed correlation heatmap between the features is shown in Appendix A. To prevent features with large magnitudes (like p_T, MET, etc) to dominate over small valued features (like $\Delta\eta$, ΔR, etc), all the features are scaled about their mean value by their standard deviation. This ensures all features are more or less at equal footing at the beginning of the training process. The signal and background events are divided in 1:1 ratio for training and testing each process. For training, the overall signal weight is equated with the overall background weight ensuring equal number of signal and background events entering the training process. The BDT model is constructed using `XGBClassifier` and the hyperparamter tuning is done using `GridSearchCV` [59]. The details of the optimal hyperparameters is listed in Table 9 in Appendix A. The model is 3 fold cross validated using `StratifiedKFold` [59]. Since, the distributions for the SM plus EFT benchmarks vary very little from the SM distributions, we train only the SM signal and backgrounds and test on the SM as well as on SM plus EFT benchmarks.

The highlights of the BDT analysis are shown in Figure 8. As a metric for evaluation of our model, we use the ROC AUC. The AUC value for the training set is 0.9827. For the test sets, the AUC obtained are 0.9715, 0.9714, 0.9716, 0.9733 and 0.9719 respectively for SM, BP1, BP2, BP3 and BP4. This indicate that there was very little overfitting and the BPs

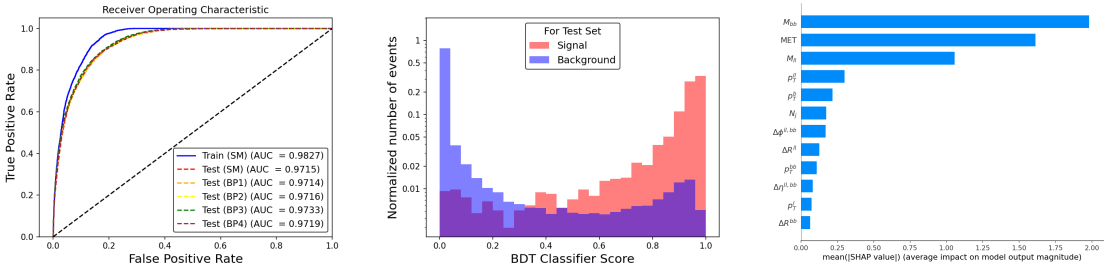


Figure 8: The Receiver Operating Characteristic (ROC) curve for the training and testing (SM as well as BPs) data. (Left) The distribution of the BDT classifier score for the SM signal and backgrounds. (Center) The mean absolute SHAP values for the features used for training the BDT model. (Right)

fared very well on the model trained with SM inputs. To enhance the signal significance, we've set the threshold classifier score at 0.95. This means we'll only keep events with a BDT classifier score greater than or equal to 0.95. By doing this, we maintain a roughly similar background efficiency as in the cut-based analysis, making it easier to compare signal efficiencies between the two methods. The feature importance of a machine learning model can be realized using SHAP (SHapley Additive exPlanations) [60] values for the features. SHAP values show how each feature affects each final prediction, the significance of each feature compared to others, and the model's reliance on the interaction between features. The SHAP values for the model are plotted in Figure 8 using `shap` module. It is distinctly observed that M_{bb} turns out to be the best discriminating feature. MET, M_{ll} and p_T^{ll} turns out to be the other important features which was also taken into account in the cut based analysis. Corresponding to the threshold value of 0.95, the significance and cut efficiencies of the signal and background processes for the BDT analysis are detailed in Table 8. It is observed that for similar background numbers, there is a significant boost in the signal numbers for both SM and other EFT benchmark points, compared to the cut based analysis.

BPs (κ_Z, c_{uW}, $c_{Hq}^{(3)}$)	S	B	S/B	z	ϵ_s	ϵ_b
SM (1.0, 0.0, 0.0)	3822	137574	0.0278	10.26	3.94×10^{-2}	9.29×10^{-4}
BP1 (1.0, 0.05, 0.00)	4066		0.0296	10.91	4.16×10^{-2}	
BP2 (1.0, 0.00, 0.04)	4523		0.0329	12.19	4.63×10^{-2}	
BP3 (1.0, 0.05, 0.04)	4620		0.0336	12.39	4.38×10^{-2}	
BP4 (1.0, -0.01, -0.02)	3702		0.0269	9.94	3.96×10^{-2}	

Table 8: Signal significance of the $Z(l^+l^-)h(b\bar{b})$ production process (at LHC 14 TeV 3000 fb^{-1}) from BDT based analysis (with threshold: 0.95) at different benchmark points (BPs) in presence of effective operators, along with signal (ϵ_s) and background (ϵ_b) efficiencies.

4.3 Two parameter χ^2 analysis

The χ^2 test [2] serves as a statistical measure to evaluate the degree of conformity between empirical observations and theoretical expectations within the framework of a contingency table. In statistical literature, there exist a number of definitions for the χ^2 function. These definitions are more or less equivalent and can be used interchangeably. For our case, we shall use Pearson's definition where the χ^2 is defined as follows:

$$\chi^2 = \sum_{j}^{bins} \left(\frac{(S^j(\kappa_i, c_i) + B^j_{SM}) - (S^j_{SM} + B^j_{SM})}{\Delta N^j(\kappa_i, c_i)} \right)^2 = \sum_{j}^{bins} \left(\frac{\Delta S^j(\kappa_i, c_i)}{\Delta N^j(\kappa_i, c_i)} \right)^2 . \tag{4.3}$$

For our analysis, we define $\Delta S^j(\kappa_i, c_i) = S^j(\kappa_i, c_i) - S^j_{SM}$, where $S^j(\kappa_i, c_i)$ corresponds to signal events in the j^{th} bin of a kinematic distribution, in presence of effective operators and coupling modifiers and S^j_{SM} corresponds to signal events in the same bin under the SM process. $\Delta N^j(\kappa_i, c_i)$ is the statistical uncertainty in the number of events for that bin. Now, assuming a Poisson distributed counting experiment, $\Delta N^j(\kappa_i, c_i) = \sqrt{S^j(\kappa_i, c_i) + B^j_{SM}}$, where B^j_{SM} corresponds to the background events in the j^{th} bin. The detailed parametrizations of signal and background numbers are shown in Eqn. 4.4.

$$\begin{aligned} S(\kappa_i, c_i) &= \mathcal{L} \times \sigma^S_{SM+EFT}(\kappa_Z, c_i) \times BR^S(\kappa_B) \times \epsilon_S \,, \\ S_{SM} &= \mathcal{L} \times \sigma^S_{SM} \times BR^S \times \epsilon_S \,, \\ B_{SM} &= \mathcal{L} \times \sigma^B_{SM} \times BR^B \times \epsilon_B \,. \end{aligned} \tag{4.4}$$

Considering the better performance of the BDT analysis over the cut based analysis, we use the signal and background efficiencies based on the BDT analysis. The χ^2 analysis is performed corresponding to the binned p_T distribution of the leading lepton. The dataset post the threshold cut is divided into 10 bins from 0-250 GeV in intervals of 25 GeV. The events with $p^l_T > 250$ GeV is dumped into an excess bin. The number of events for signal and background in each bin is tabulated in Table 10. For a Poisson distributed binned data, the number of degrees of freedom is given by $D = N - M$, where N is the number of bins and M is the number of fitted parameters. In this case, $D = 11 - 2 = 9$. Usually the constraints on the parameter space of physical parameters are reported in terms of confidence levels (C.L.). The confidence levels can be interpreted from the χ^2 values. The 68% C.L. for $D = 9$ corresponds to $\chi^2 \approx 10.388$. The χ^2 for different parameter benchmarks in κ_Z - κ_B plane are shown in Figure 9.

Fig. 9 shows that the 68% C.L. bounds are very sensitive to the parameter $c^{(3)}_{Hq}$ corresponding to the CP even contact interaction. This is because $\frac{\sigma}{\sigma_{SM}}$ changes significantly under the variation of $c^{(3)}_{Hq}$ in the Vh channel (see Fig. 4 left). However, despite the fact that the variation of $\frac{\sigma}{\sigma_{SM}}$ as function of c_{uW} is quite prominent (as can be seen from Fig. 4 right) the same is not reflected in the χ^2 plots. This is mostly due to the fact that the CP-odd operators contribute at $\frac{1}{\Lambda^2}$ order and the variation of (c_{uW} considered over a range (-0.01, 0.05) which is very narrow to produce any significant impact at that order.

The 68% C.L. bounds on the EFT couplings are shown in Fig. 10, which shows similar

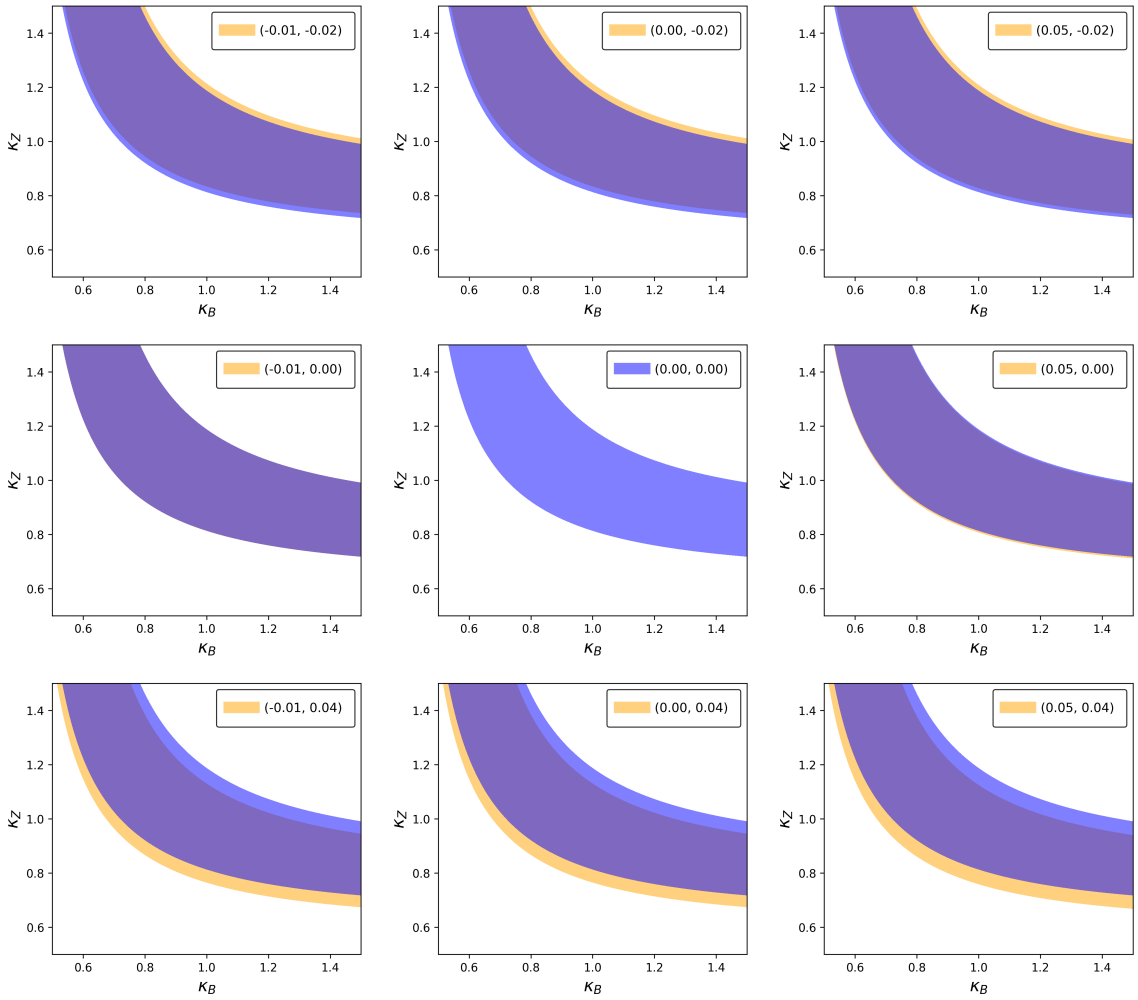


Figure 9: χ^2 plots showing 68% C.L. bounds in the κ_Z - κ_B space at LHC 14 TeV 3000 fb^{-1} for different values of effective coefficients. The values in the legends refer to effective coefficient $\left(c_{uW}, c_{Hq}^{(3)}\right)$.

sensitivities of the EFT operators and modifiers as in Fig. 9.

5 Summary and Conclusion

We have presented an analysis of Zh associated production at LHC in presence of dimension six SMEFT operators and coupling modifiers. We choose a simple parametrisation to match the coupling modifiers that stem from dimension six SMEFT operators in Warsaw basis. We analysed the signal and background contributions at various benchmark points, which allows maximum cross-section within the allowed values of the EFT parameters and coupling modifiers. We do both cut-based and BDT analysis using kinematic variables relevant for the process. NP scale is safely chosen at $\Lambda = 1$ TeV, which abides by effective limit having the invariant mass distribution peaks below it.

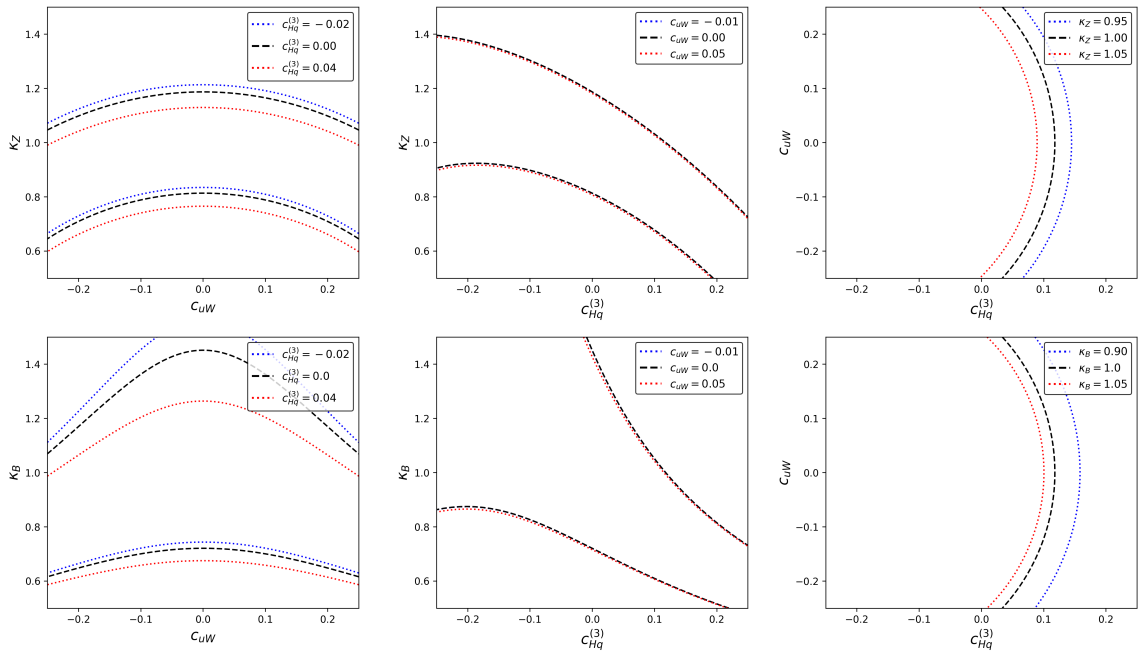


Figure 10: 68% C.L. bounds on effective coefficients at the 14 TeV 3000 fb^{-1} LHC. $\kappa_B = 1.0$ for the plots on the top layer and $\kappa_Z = 1.0$ for the plots in the bottom layer.

A comparison of Table 7 and 8 shows that the BDT analysis perform better than the cut based analysis presented in previous section as expected. One obtains almost factor 2 enhancement in the estimation of the significances for the various BP's considered in our analysis. This is due to the fact that BDT comes with better efficiency for the signal events even though the background efficiency remains almost the same. We have obtained more than 9σ (5σ) significance using BDT (cut based) analysis for all our chosen benchmark points. We further note that the corresponding background contributions have limited sensitivity to the EFT operators introduced here, hence we do not include them in our analysis.

A χ^2 analysis is performed in the two dimensional parameter space of the EFT operator coefficients as well as in coupling modifiers. All the plots show a bounded region which is not entirely closed. This is because the analysis is primarily done in a single channel. Based on the plots in Figure 9 and Figure: 10, it is evident that the inclusion of EFT contributions significantly alter the bounds on the $\kappa_Z - \kappa_B$ plane. It is observed that even with the tight constraints on the operators, presence of CP even operator $\mathcal{O}^{(3)}_{Hq}$ results in visible changes on the bounds in $\kappa_Z - \kappa_B$ plane. The individual impact of the CP odd operator $\mathcal{O}_{uW}$ is relatively small and do not show any significant deviation from the SM predictions. This is mainly because, they do not interfere with SM and the contributions are obtained only at $1/\Lambda^4$ order. However, if we choose a smaller NP scale, for example, $\Lambda = 500$ GeV, which still remains okay with the effective theory limit as seen from the Fig. 6 after taking care of the already existing constraints, the effect from CP odd contributions

enhance roughly by a factor of 16 and has a larger contribution. Similar arguments hold for dimension eight operators, whose inclusion will not affect the conclusions significantly at least with a large NP scale. However, the contributions from $\mathcal{O}_{Hq}^{(3)}$ will still dominate. Therefore, for detecting CP violating NP, dedicated observables are required.

Acknowledgments

SB would like to acknowledge the grant CRG/2019/004078 from DST-SERB, Govt. of India.

A Details of BDT analysis parameters

Feature selection is a integral and significant part of any machine learning analysis. Presence of too many redundant features causes a model to learn unnecessary characteristics, as such we expect the features to have little dependence on one another. The correlation matrix captures the interdependnce among the features very accurately. For our BDT model, the feature correlation heatmap is plotted in Figure 11. Darker patches refer to high correlation. Apart from features likes p_T^l and p_T^{ll}, p_T^b and p_T^{bb}, where correlation is expected, most of the features show little to no correlation, enhancing the model's learnability against general data. Apart from feature selection, another important aspect of model tuning is the hyperparameter optimization. Proper tuning prevents the model from overfitting, resulting in better performance on new data. The optimized hyperparameters for the model are detailed in Table 9.

Hyperparameters for the XGBClassifier model	Optimal value
Number of boosting rounds (`n_estimators`)	50
Maximum depth of a tree (`max_depth`)	5
Learning rate for the model (`learning_rate`)	0.15
Fraction of samples used each tree (`subsample`)	0.8
Fraction of features used for each tree (`colsmaple_bytree`)	1.0
Minimum sum of instance weight in a child (`min_child_weight`)	50
Minimum loss reduction for further partition (`gamma`)	0.75
L1 regularization term on weights (`reg_alpha`)	8
L2 regularization term on weights (`reg_lambda`)	60
Maximum step size for each iteration (`max_delta_step`)	2

Table 9: The optimal hyperparameter values for the model mined using `GridSearchCV`. The `objective` hyperparameter is fixed at `"binary:logistic"`.

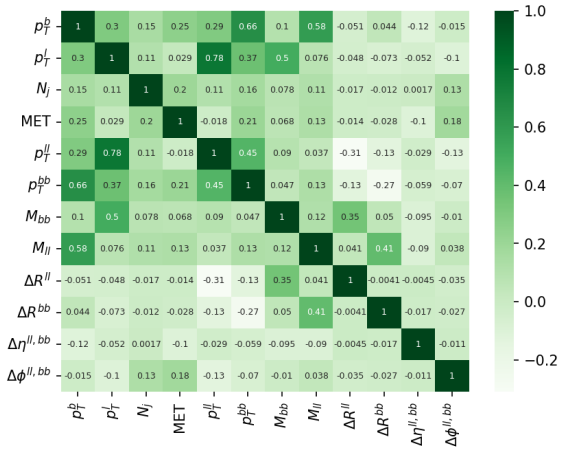


Figure 11: Correlation matrix for the features used in training the XGBoost model.

p_T^l (GeV)	Signal (S)	Background (B)
0 - 25	15	180
25 - 50	244	11933
50 - 75	942	33769
75 - 100	764	37304
100 - 125	732	25895
125 - 150	399	12402
150 - 175	240	6652
175 - 200	167	4323
200 - 225	120	1913
225 - 250	46	863
> 250	153	1810

Table 10: Transverse momentum of the leading lepton for signal and background processes in different bins for a threshold selection of 0.95.

References

[1] H.E. Logan, *TASI 2013 lectures on Higgs physics within and beyond the Standard Model*, 1406.1786.

[2] Particle Data Group collaboration, *Review of Particle Physics*, *PTEP* **2022** (2022) 083C01.

[3] B. Grzadkowski, M. Iskrzynski, M. Misiak and J. Rosiek, *Dimension-Six Terms in the Standard Model Lagrangian*, *JHEP* **10** (2010) 085 [1008.4884].

[4] ATLAS collaboration, *A detailed map of Higgs boson interactions by the ATLAS experiment ten years after the discovery*, *Nature* **607** (2022) 52 [2207.00092].

[5] CMS collaboration, *A portrait of the Higgs boson by the CMS experiment ten years after the discovery.*, *Nature* **607** (2022) 60 [2207.00043].

[6] CMS collaboration, *Constraints on anomalous HVV couplings from the production of Higgs bosons decaying to τ lepton pairs*, *Phys. Rev. D* **100** (2019) 112002 [1903.06973].

[7] I. Anderson et al., *Constraining Anomalous HVV Interactions at Proton and Lepton Colliders*, *Phys. Rev. D* **89** (2014) 035007 [1309.4819].

[8] P. Sharma and A. Shivaji, *Probing non-standard HVV (V = W, Z) couplings in single Higgs production at future electron-proton collider*, *JHEP* **10** (2022) 108 [2207.03862].

[9] S. Dutta, K. Hagiwara and Y. Matsumoto, *Measuring the Higgs-Vector boson Couplings at Linear e^+e^- Collider*, *Phys. Rev. D* **78** (2008) 115016 [0808.0477].

[10] N. Desai, D.K. Ghosh and B. Mukhopadhyaya, *CP-violating HWW couplings at the Large Hadron Collider*, *Phys. Rev. D* **83** (2011) 113004 [1104.3327].

[11] N.D. Christensen, T. Han and Y. Li, *Testing CP Violation in ZZH Interactions at the LHC*, *Phys. Lett. B* **693** (2010) 28 [1005.5393].

[12] S. Dwivedi, D.K. Ghosh, B. Mukhopadhyaya and A. Shivaji, *Distinguishing CP-odd couplings of the Higgs boson to weak boson pairs*, *Phys. Rev. D* **93** (2016) 115039 [1603.06195].

[13] F.U. Bernlochner, C. Englert, C. Hays, K. Lohwasser, H. Mildner, A. Pilkington et al., *Angles on CP-violation in Higgs boson interactions*, *Phys. Lett. B* **790** (2019) 372 [1808.06577].

[14] J. Brehmer, F. Kling, T. Plehn and T.M.P. Tait, *Better Higgs-CP Tests Through Information Geometry*, *Phys. Rev. D* **97** (2018) 095017 [1712.02350].

[15] S. Banerjee, T. Mandal, B. Mellado and B. Mukhopadhyaya, *Cornering dimension-6 HVV interactions at high luminosity LHC: the role of event ratios*, *JHEP* **09** (2015) 057 [1505.00226].

[16] S. Banerjee, C. Englert, R.S. Gupta and M. Spannowsky, *Probing Electroweak Precision Physics via boosted Higgs-strahlung at the LHC*, *Phys. Rev. D* **98** (2018) 095012 [1807.01796].

[17] S. Banerjee, R.S. Gupta, J.Y. Reiness and M. Spannowsky, *Resolving the tensor structure of the Higgs coupling to Z-bosons via Higgs-strahlung*, *Phys. Rev. D* **100** (2019) 115004 [1905.02728].

[18] S. Banerjee, R.S. Gupta, J.Y. Reiness, S. Seth and M. Spannowsky, *Towards the ultimate differential SMEFT analysis*, *JHEP* **09** (2020) 170 [1912.07628].

[19] S. Banerjee, R.S. Gupta, O. Ochoa-Valeriano, M. Spannowsky and E. Venturini, *A fully differential SMEFT analysis of the golden channel using the method of moments*, *JHEP* **06** (2021) 031 [2012.11631].

[20] S. Banerjee, R.S. Gupta, O. Ochoa-Valeriano and M. Spannowsky, *High energy lepton colliders as the ultimate Higgs microscopes*, *JHEP* **02** (2022) 176 [2109.14634].

[21] T. Biswas, A. Datta and B. Mukhopadhyaya, *Following the trail of new physics via the vector boson fusion Higgs boson signal at the Large Hadron Collider*, *Phys. Rev. D* **105** (2022) 055028 [2107.05503].

[22] J.Y. Araz, S. Banerjee, R.S. Gupta and M. Spannowsky, *Precision SMEFT bounds from the VBF Higgs at high transverse momentum*, *JHEP* **04** (2021) 125 [2011.03555].

[23] I. Brivio and M. Trott, *The Standard Model as an Effective Field Theory*, *Phys. Rept.* **793** (2019) 1 [1706.08945].

[24] R. Alonso, E.E. Jenkins and A.V. Manohar, *A Geometric Formulation of Higgs Effective*

Field Theory: Measuring the Curvature of Scalar Field Space, Phys. Lett. B **754** (2016) 335 [1511.00724].

[25] A. Crivellin, M. Ghezzi and M. Procura, *Effective Field Theory with Two Higgs Doublets*, JHEP **09** (2016) 160 [1608.00975].

[26] Anisha, S. Das Bakshi, J. Chakrabortty and S. Prakash, *Hilbert Series and Plethystics: Paving the path towards 2HDM- and MLRSM-EFT*, JHEP **09** (2019) 035 [1905.11047].

[27] F. del Aguila, S. Bar-Shalom, A. Soni and J. Wudka, *Heavy Majorana Neutrinos in the Effective Lagrangian Description: Application to Hadron Colliders*, Phys. Lett. B **670** (2009) 399 [0806.0876].

[28] A. Aparici, K. Kim, A. Santamaria and J. Wudka, *Right-handed neutrino magnetic moments*, Phys. Rev. D **80** (2009) 013010 [0904.3244].

[29] S. Bhattacharya and J. Wudka, *Dimension-seven operators in the standard model with right handed neutrinos*, Phys. Rev. D **94** (2016) 055022 [1505.05264].

[30] H.-L. Li, Z. Ren, J. Shu, M.-L. Xiao, J.-H. Yu and Y.-H. Zheng, *Complete set of dimension-eight operators in the standard model effective field theory*, Phys. Rev. D **104** (2021) 015026 [2005.00008].

[31] C.W. Murphy, *Dimension-8 operators in the Standard Model Eective Field Theory*, JHEP **10** (2020) 174 [2005.00059].

[32] S. Bhattacharya and J. Wudka, *Effective theories with dark matter applications*, Int. J. Mod. Phys. D **30** (2021) 2130004 [2104.01788].

[33] A. Alloul, N.D. Christensen, C. Degrande, C. Duhr and B. Fuks, *FeynRules 2.0 - A complete toolbox for tree-level phenomenology*, Comput. Phys. Commun. **185** (2014) 2250 [1310.1921].

[34] C. Degrande, C. Duhr, B. Fuks, D. Grellscheid, O. Mattelaer and T. Reiter, *UFO - The Universal FeynRules Output*, Comput. Phys. Commun. **183** (2012) 1201 [1108.2040].

[35] J. Alwall, M. Herquet, F. Maltoni, O. Mattelaer and T. Stelzer, *MadGraph 5 : Going Beyond*, JHEP **06** (2011) 128 [1106.0522].

[36] CMS collaboration, *Observation of Higgs boson decay to bottom quarks*, Phys. Rev. Lett. **121** (2018) 121801 [1808.08242].

[37] ATLAS collaboration, *Measurements of WH and ZH production in the $H \to b\bar{b}$ decay channel in pp collisions at 13 TeV with the ATLAS detector*, Eur. Phys. J. C **81** (2021) 178 [2007.02873].

[38] SMEFiT collaboration, *Combined SMEFT interpretation of Higgs, diboson, and top quark data from the LHC*, JHEP **11** (2021) 089 [2105.00006].

[39] S. Bißmann, C. Grunwald, G. Hiller and K. Kröninger, *Top and Beauty synergies in SMEFT-fits at present and future colliders*, JHEP **06** (2021) 010 [2012.10456].

[40] C. Grunwald, G. Hiller, K. Kröninger and L. Nollen, *More synergies from beauty, top, Z and Drell-Yan measurements in SMEFT*, JHEP **11** (2023) 110 [2304.12837].

[41] M. Thomas Arun, K. Deka and T. Srivastava, *Constraining SMEFT BSM scenarios with EWPO and Δ_{CKM}*, 2301.09273.

[42] ATLAS collaboration, *Measurements of differential cross-sections in four-lepton events in 13 TeV proton-proton collisions with the ATLAS detector*, JHEP **07** (2021) 005 [2103.01918].

[43] ATLAS collaboration, *Combined measurements of Higgs boson production and decay using up to 139 fb^{-1} of proton-proton collision data at $\sqrt{s} = 13$ TeV collected with the ATLAS experiment*, .

[44] R. Boughezal, E. Mereghetti and F. Petriello, *Dilepton production in the SMEFT at O(1/Λ4)*, *Phys. Rev. D* **104** (2021) 095022 [2106.05337].

[45] V. Cirigliano, A. Crivellin, W. Dekens, J. de Vries, M. Hoferichter and E. Mereghetti, *CP Violation in Higgs-Gauge Interactions: From Tabletop Experiments to the LHC*, *Phys. Rev. Lett.* **123** (2019) 051801 [1903.03625].

[46] R.D. Ball et al., *Parton distributions with LHC data*, *Nucl. Phys. B* **867** (2013) 244 [1207.1303].

[47] T. Sjostrand, S. Mrenna and P.Z. Skands, *A Brief Introduction to PYTHIA 8.1*, *Comput. Phys. Commun.* **178** (2008) 852 [0710.3820].

[48] M. Cacciari, G.P. Salam and G. Soyez, *FastJet User Manual*, *Eur. Phys. J. C* **72** (2012) 1896 [1111.6097].

[49] M. Cacciari, G.P. Salam and G. Soyez, *The anti-k_t jet clustering algorithm*, *JHEP* **04** (2008) 063 [0802.1189].

[50] E. Conte, B. Fuks and G. Serret, *MadAnalysis 5, A User-Friendly Framework for Collider Phenomenology*, *Comput. Phys. Commun.* **184** (2013) 222 [1206.1599].

[51] F. Cascioli, T. Gehrmann, M. Grazzini, S. Kallweit, P. Maierhöfer, A. von Manteuffel et al., *ZZ production at hadron colliders in NNLO QCD*, *Phys. Lett. B* **735** (2014) 311 [1405.2219].

[52] L. Chen, J. Davies, G. Heinrich, S.P. Jones, M. Kerner, G. Mishima et al., *ZH production in gluon fusion at NLO in QCD*, *JHEP* **08** (2022) 056 [2204.05225].

[53] J.M. Campbell, J.W. Huston and W.J. Stirling, *Hard Interactions of Quarks and Gluons: A Primer for LHC Physics*, *Rept. Prog. Phys.* **70** (2007) 89 [hep-ph/0611148].

[54] M.D. Schwartz, *TASI Lectures on Collider Physics*, in *Proceedings, Theoretical Advanced Study Institute in Elementary Particle Physics : Anticipating the Next Discoveries in Particle Physics (TASI 2016): Boulder, CO, USA, June 6-July 1, 2016*, R. Essig and I. Low, eds., pp. 65–100 (2018), DOI [1709.04533].

[55] G. Cowan, K. Cranmer, E. Gross and O. Vitells, *Asymptotic formulae for likelihood-based tests of new physics*, *Eur. Phys. J. C* **71** (2011) 1554 [1007.1727].

[56] Y. Coadou, *Boosted decision trees*, 2206.09645.

[57] A.S. Cornell, W. Doorsamy, B. Fuks, G. Harmsen and L. Mason, *Boosted decision trees in the era of new physics: a smuon analysis case study*, *JHEP* **04** (2022) 015 [2109.11815].

[58] T. Chen and C. Guestrin, *Xgboost: A scalable tree boosting system*, in *Proceedings of the 22nd ACM SIGKDD International Conference on Knowledge Discovery and Data Mining*, KDD '16, ACM, Aug., 2016, DOI.

[59] F. Pedregosa, G. Varoquaux, A. Gramfort, V. Michel, B. Thirion, O. Grisel et al., *Scikit-learn: Machine learning in Python*, *Journal of Machine Learning Research* **12** (2011) 2825.

[60] S. Lundberg and S.-I. Lee, *A unified approach to interpreting model predictions*, 2017.

Microscopic parametrization of the near threshold oscillations of the nucleon time-like effective electromagnetic form factors

Francesco Rosini* and Simone Pacetti
Dipartimento di Fisica e Geologia, INFN Sezione di Perugia, 06123 Perugia, Italy

Olga Shekhovtsova
INFN Sezione di Perugia, 06123 Perugia, Italy and
National Science Centre, Kharkov Institute of Physics and Technology, Akademicheskaya, Ukraine

Egle Tomasi-Gustafsson
DPhN, IRFU, CEA, Université Paris-Saclay, 91191 Gif-sur-Yvette Cedex, France

arXiv:2403.02916v1 [hep-ph] 5 Mar 2024

We present an analysis of the recent near threshold BESIII data for the nucleon time-like effective form factors. The damped oscillation emerging from the subtraction of the dipole formula is treated in non-perturbative-QCD, making use of the light cone distribution amplitudes expansion. Non-perturbative effects are accounted for by considering Q^2-dependent coefficients in such expansions, whose free parameters are determined by fitting to the proton and neutron data. Possible implications and future analysis have been discussed.

I. INTRODUCTION

The theoretical impossibility of describing the nucleon internal structure in terms of strongly interacting quarks and gluons, which are the fundamental fields of quantum chromodynamics, enhances the electromagnetic form factors (EMFFs) to the role of unique and privileged tools to unravel the dynamics underlying the electromagnetic interaction of nucleons. They provide the most effective description of the mechanisms that determine and rule the dynamic and static properties of nucleons. In specific reference frames, EMFFs represent the Fourier transforms of spatial charge and magnetic momentum densities.

Recently, the BESIII [1] experiment measured the time-like nucleon form factors (FFs) at center-of-mass energies between 2.0 GeV and 3.5 GeV [2–6]. These data present an oscillating behavior [7–12], which manifests itself as a periodic, exponentially dumped component over the typical dipolar carrier, usually identified as the only contribution. The nature of such an oscillating component is still unknown. Possible explanations rely either on the final state interaction between the baryon and the antibaryon, or in a phenomenon intrinsic to the baryon structure. In the latter case, the invoked phenomenon would be encoded by the EMFFs of nucleons.

In order to investigate this eventuality we propose a parametrization for the EMFFs defined by considering the nucleons as triplets of collinear quarks lying at light-like distances in the light-front framework [13].

The matrix element of the "+" component of the hadronic current J^μ, which depends directly on the EMFFs, evaluated between the baryon and antibaryon particle states, can then be expanded using the Lorentz invariance of the three quark Fock state's matrix elements.

The resulting form depends on a set of functions of the four momentum squared fractions, called light cone distribution amplitudes (LCDAs), and a deep knowledge of their expression can provide further information about the form factors shape. Using the $\mathcal{L}_{\rm QCD}$ conformal symmetry [14], the LCDAs are expanded on a polynomial basis, the most common choice being represented by the orthonormal Appell polynomials, defined on the triangle $T(x_1, x_3) = \{(x_1, x_3) \in \mathbb{R} : x_1 > 0, x_3 > 0, x_1 + x_3 < 1\}$, where $x_i = k_i^+/P^+$ are the quark's light front momentum fractions along is the $(^+)$ direction and so the following relation holds: $\sum_{i=1}^{3} x_i = 1$. The only unknown quantities now are the expansion coefficients, which have to be determined considering the phenomenology of the problem. The nonperturbative coefficients admit an evolution equation in the conformal symmetry framework, and their values can be determined theoretically by QCD sum rules. On the other hand, we are considering a center of mass energy of the system between 2.0 GeV and 3.5 GeV, so we are not allowed to use perturbative methods. What we propose then is to perform a truncated Laurent expansion of the non-perturbative coefficients over the negative powers of the four momentum squared, subsequently performing a fit over the recent BESIII experimental data to determine these coefficients. The final goal of this description is to find whether the oscillations of the EMFFs can be described by the model functions.

II. THE MICROSCOPIC MODEL

One of the most effective ways to describe subnuclear processes is to work on a light front framework, expanding the involved particle states in a free particle state basis, commonly known as Fock states. For a baryon we

* francesco.rosini@studenti.unipg.it

have

$$|\text{baryon}\rangle = |0\rangle + |qqq\rangle + |qqqg\rangle + |qqqq\bar{q}\rangle + \dots , \quad (1)$$

where the three-quark state can be expanded in a Lorentz series of its matrix element between the vacuum and the particle states. The expansion has already been performed in Ref. [15], e.g., for the proton has the form

$$\begin{aligned} &\langle 0|\, \varepsilon^{ijk} u^i_\alpha (a_1 z)\, u^j_\beta (a_2 z)\, d^k_\gamma (a_3 z)\, |P\rangle \\ &= \frac{1}{4}\Big[S_1 M C_{\alpha\beta} \left(\gamma_5 N^+\right)_\gamma + V_1 \left(\not{p} C\right)_{\alpha\beta} \left(\gamma_5 N^+\right)_\gamma \\ &\quad + P_1 M \left(\gamma_5 C\right)_{\alpha\beta} N^+_\gamma + A_1 \left(\not{p}\gamma_5 C\right)_{\alpha\beta} N^+_\gamma \\ &\quad + T_1 \left(i\sigma_{\perp p} C\right)_{\alpha\beta} \left(\gamma^\perp \gamma_5 N^+\right)_\gamma + \dots \Big] , \end{aligned} \quad (2)$$

where the functions S_1, V_1, P_1, A_1 and T_1 are called light cone distribution amplitudes, they are functions of the scalar product $P \cdot z$, z being a light like four-vector. The dots in Eq. (2) indicate that the expansion has been written explicitly only for twist-3 LCDAs, while the complete expansion includes 24 LCDAs.

Considering now the whole expansion, we can find some conditions for the LCDAs imposing that the nucleon state isospin is 1/2. For example, for twist-3 LCDAs, the following equation holds

$$\begin{aligned} 2T_1 (x_1, x_2, x_3) &= [V_1 - A_1] (x_1, x_3, x_2) \\ &\quad + [V_1 - A_1] (x_2, x_3, x_1) , \end{aligned}$$

which allows to restrict the study of twist-3 LCDAs to a single function, which is chosen to be

$$\varphi_N (\mathbf{x}) = V_1 (\mathbf{x}) - A_1 (\mathbf{x}) ,$$

where $\mathbf{x}$ is 3-vector (x_1, x_2, x_3). Taking advantage from the conformal symmetry of the Lagrangian density $\mathcal{L}_{\text{QCD}}$, the twist-3 LCDA φ_N can be expanded over the orthonormalized Appell polynomials set $\{P_n (\mathbf{x})\}_n$ as follows

$$\varphi_N \left(\mathbf{x}, Q^2\right) = 120 x_1 x_2 x_3 \sum_n B_n \left(Q^2\right) P_n (\mathbf{x}) .$$

The set of non-perturbative coefficients $\{B_n\}_n$ is unknown and contains all the information about the form factor for the leading twist.

Each coefficient B_n is linked to the φ_N LCDA's momenta. The first coefficient B_0 is fixed being linked to the normalization of φ_N, i.e.,

$$B_0 = \int_0^1 dx_1 \int_0^1 dx_2 \int_0^1 dx_3 \varphi_N \left(\mathbf{x}, Q^2\right) = 1 .$$

As already stated, since we are considering the non perturbative aspect of the LCDAs, we can perform an expansion over the negative powers of the four-momentum squared,

$$B_n \left(Q^2\right) = \sum_{k=0}^{M_n} b_k^{(n)} Q^{-2k}, \quad (3)$$

where $Q^2 = -q^2$, $\left\{ \{b_k^{(n)}\}_{k=0}^{M_n} \right\}_n$ is the set of coefficients and M_n is the maximum power of Q^{-2} in the expansion of the n^{th} parameter B_n.

III. LEADING ORDER CONTRIBUTING DIAGRAMS

Taking the leading order into account, the minimum number of contributing diagrams has been evaluated in Ref. [15], where fourteen diagrams have been considered. The Sachs form factors which we are interested in are related to the Pauli and Dirac ones by the relations

$$\begin{aligned} G_E \left(Q^2\right) &= F_1 \left(Q^2\right) - \tau F_2 \left(Q^2\right) , \\ G_M \left(Q^2\right) &= F_1 \left(Q^2\right) + F_2 \left(Q^2\right) , \end{aligned}$$

where $\tau = Q^2 / \left(4M_B^2\right)$. We performed our fit over the effective form factor data, which is linked to the Sachs form factors by the relation

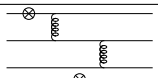
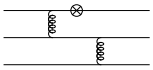
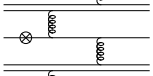
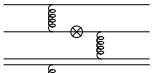
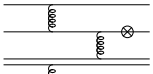
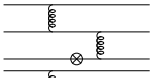
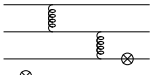
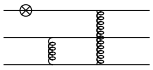
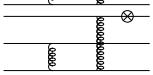
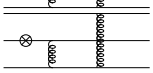
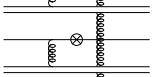
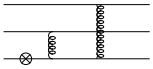
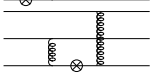
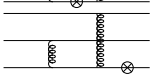
$$|G_{\text{eff}}| = \sqrt{\frac{|G_E|^2 + 2\tau |G_M|^2}{1 + 2\tau}} .$$

Following the works of Brodsky and Lepage [16], the light front EMFF can be written as the convolution of three probabilities, namely the probability of describing the baryon and antibaryon as a system of three collinear quarks, $\varphi_N \left(\mathbf{x}, Q^2\right)$, and the probability of finding a certain strong interaction, known as *hard scattering kernel* K_H. At the leading order, each of the fourteen contributing diagrams corresponds to a hard scattering kernel $K_i (\mathbf{x}, \mathbf{y})$, here $\varphi_N (\mathbf{x}) = V_1 (\mathbf{x}) - A_1 (\mathbf{x})$, and $T (\mathbf{x}) = T_1 (\mathbf{x})$ are the light cone distribution amplitudes involved in the calculation.
In order to evaluate the form factor G_M, we used the Chernyak-Zhitnitsky [15] asymptotic formula

$$\begin{aligned} q^4 G_M \left(q^2\right) \to \frac{\left(4\pi\bar{\alpha}_s\right)^2}{54} |f_N|^2 \\ \int [dx] \int [dy] \left(2 \sum_{i=1}^{7} e_i K_i (\mathbf{x}, \mathbf{y}) + \sum_{i=8}^{14} e_i K_i (\mathbf{x}, \mathbf{y}) \right) , \end{aligned} \quad (4)$$

where $[dx] = \delta \left(1 - \sum_{i=1}^3 x_i\right) dx_1 dx_2 dx_3$ and $\bar{\alpha}_s$ is the modified coupling constant. For the evaluation of the modified coupling constant $\bar{\alpha}_s^2$, we follow the procedure proposed by Chernyak and Zhitnitsky in Ref. [15]. The value of $\bar{\alpha}_s^2$ is given by the product of the coupling constants for the two subprocesses, namely the two gluon exchanges which appear in the tree-level diagrams shown in Table I. The average virtuality $\bar{q}_1^2$ of the lightest gluon is $\bar{x}_3 \bar{y}_3 q^2$, while the rest gluon has an averaged virtuality $\bar{q}_2^2 = \overline{(1 - x_1)}\, \overline{(1 - y_1)} q^2$. The typical values of a realistic nucleon wave function for the $\bar{x}_i$ are $\bar{x}_1 \simeq 2/3$, $\bar{x}_2 \simeq \bar{x}_3 \simeq 1/6$. Therefore $\bar{\alpha}_s^2 \left(q^2\right) = \alpha_s \left(\frac{1}{36} q^2\right) \alpha_s \left(\frac{1}{9} q^2\right)$.

TABLE I. Diagrams and leading twist baryon wave functions [15].

Index i	Diagram	$K_i(\mathbf{x},\mathbf{y})$
1		$\dfrac{\varphi_N(\mathbf{x})\varphi_N(\mathbf{y})+4T(\mathbf{x})T(\mathbf{y})}{(1-x_1)^2x_3(1-y_1)^2y_3}$
2		0
3		$\dfrac{-4T(\mathbf{x})T(\mathbf{y})}{x_1x_3(1-x_2)y_1y_3(1-y_1)}$
4		$\dfrac{\varphi_N(\mathbf{x})\varphi_N(\mathbf{y})}{x_1x_3(1-x_3)y_1y_3(1-y_1)}$
5		$\dfrac{-\varphi_N(\mathbf{x})\varphi_N(\mathbf{y})}{x_2x_3(1-x_3)y_2y_3(1-y_1)}$
6		0
7		$\left(\dfrac{1}{x_1y_1}+\dfrac{1}{x_2y_2}\right)\dfrac{\varphi_N(\mathbf{x})\varphi_N(\mathbf{y})}{(1-x_3)^2(1-y_3)^2}$
8		0
9		$\dfrac{\varphi_N(\mathbf{x})\varphi_N(\mathbf{y})+4T(\mathbf{x})T(\mathbf{y})}{(1-x_1)^2x_2(1-y_1)^2y_2}$
10		$\dfrac{\varphi_N(\mathbf{x})\varphi_N(\mathbf{y})+4T(\mathbf{x})T(\mathbf{y})}{(1-x_1)^2x_2(1-y_1)^2y_2}$
11		0
12		$\dfrac{-\varphi_N(\mathbf{x})\varphi_N(\mathbf{y})}{x_1x_2(1-x_3)y_1y_2(1-y_1)}$
13		$\dfrac{4T(\mathbf{x})T(\mathbf{y})}{x_1x_2(1-x_1)y_1y_2(1-y_2)}$
14		$\dfrac{-\varphi_N(\mathbf{x})\varphi_N(\mathbf{y})}{x_1x_2(1-x_1)y_1y_2(1-y_3)}$

The integrals in Eq. (4) are (weakly) convergent, it is possible to solve them analytically. The results have already been obtained in Ref. [14], and are reported in Appendix C. Non-perturbative-QCD effects are accounted for by considering the Q^2-dependence of the B_n defined in Eq. (3) as truncated expansions in powers of Q^{-2}. The first parameter B_0 is fixed to 1 and is related to the zero order of the LCDA φ_N, so it is considered a constant. As for the other parameters, we are for now limiting our discussion to the LCDA's second order momenta, so we are only interested in the first six parameters, namely those of the set $\{B_n\}_{n=0}^5$.

For the truncated expansion, we propose $M_0 = 0$, $M_1 = M_2 = 1$, $M_3 = M_4 = M_5 = 2$, so that

$$\begin{aligned} B_0 &= 1\,, \\ B_n(Q^2) &= b_0^{(n)} + \frac{b_1^{(n)}}{Q^2}\,, \quad n = 1,2\,, \\ B_m(Q^2) &= b_0^{(m)} + \frac{b_1^{(m)}}{Q^2} + \frac{b_2^{(m)}}{(Q^2)^2}\,, \quad m = 3,4,5\,. \end{aligned} \tag{5}$$

We obtain a closed expression of the form factor G_M depending only on the non-perturbative parameters for the proton and the neutron. Since the nucleons are related by the isospin symmetry, their parameters are the same we can performed a simultaneous fit to the recent BESIII data on proton and neutron cross sections to determine the sets of coefficients $\left\{\{b_k^{(n)}\}_{k=0}^{M_n}\right\}_{n=0}^{5}$. The fit is performed using the ROOT Data Analysis Framework [17] program.

IV. RESULTS AND DISCUSSION

Figure 1 shows the results for the effective proton (upper panel) and neutron (lower panel) form factors in comparison with the experimental values measured by the BESIII experiment [2–4]. The fit functions depend on 13 free parameters, which are the coefficients of the expressions of Eq. (5). The normalized minimum χ^2 is

$$\frac{\chi^2}{n_{\mathrm{DoF}}} = \frac{79.93}{43} \simeq 1.79\,.$$

It has been obtained by using 48 data points of the proton cross section and 18 of the neutron one. The error bands have been determined by considering both the errors of data, and the theoretical systematic error of the model, which has ben estimated by using expressions for the $B_n(Q^2)$ parameters with the additional power $\left(Q^{-2}\right)^{M_n+1}$.

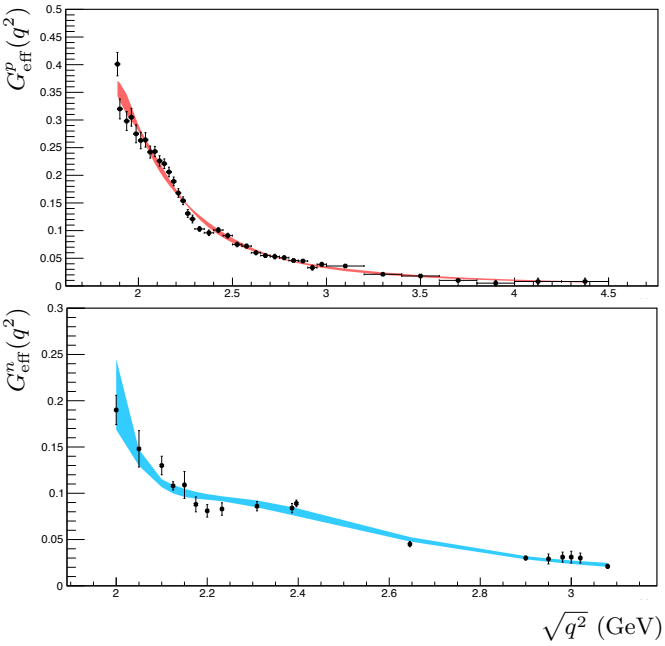


FIG. 1. The bands represent the fit results for the proton (upper panel) and neutron (lower panel) effective form factor. The data are from the BESIII experiment [2–4].

Figure 2 shows the twist-3 nucleon distribution amplitude

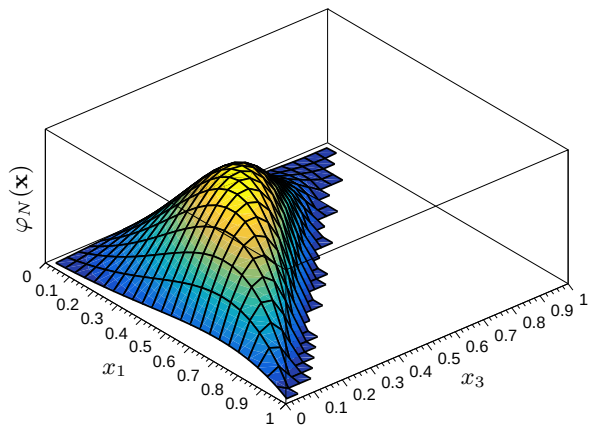


FIG. 2. The nucleon distribution function $\varphi_N(\mathbf{x})$ obtained at $\sqrt{-Q^2} = 2.5$ GeV as a function of x_1 and x_3.

$\varphi_N(\mathbf{x})$ evaluated at $\sqrt{-Q^2} = 2.5$ GeV. The maximum value is reached at the light-cone momentum fractions

$$x_1 \simeq 0.49\,, \qquad x_2 \simeq 0.24\,, \qquad x_3 \simeq 0.27\,,$$

which agree with the assumption made in the Chernyak-Zhitnitsky formula [15] that the first quark has a momentum fraction about 50% larger than the other two, which equally divide the remaining momentum fraction.

Summarizing, a coherent model has been developed to reproduce the data on proton and neutron EMFFs, recently obtained by the BESIII collaboration. The model is based on a parameterization of the light-cone distribution amplitudes, and obeys conformal symmetry of the QCD Lagrangian.

The light-front quantization allows us to express the three-quark operator, occurring in the expression of the hard scattering kernel, as the Fourier transform of the light-cone distribution amplitudes, which, in turn, describe the behaviour of the three valence quarks constituting the baryon in a light-cone system. Always under the aegis of the QCD-Lagrangian conformal symmetry we expanded the leading-twist baryon distribution amplitudes over a set of Appell polynomials, which diagonalize the one gluon exchange kernel. The non-perturbative nature of the baryon distribution amplitudes is implemented by considering a Q^2-dependence of the expansion parameters $\{B_n\}_n$. We have restricted our calculations to the first six Appell polynomials.

These distribution amplitudes have been used to calculate the near threshold behaviour of the nucleon effective form factors, extending the valence of an asymptotic formula to the low-momentum transfer region. Such a near-threshold extension has been obtained by considering a Q^2-dependence of the expansion parameters $\left\{B_n(Q^2)\right\}_n$, as polynomials of zero, first and second degree of Q^{-2}.

Moreover, since the nucleon EMFFs are linked by the isospin symmetry, the same set $\left\{B_n(Q^2)\right\}_n$ can be used and the free coefficients of their power series can be determined by means a simultaneous fit to the proton and neutron data. The error bands of the near-threshold effective nucleon form factors, have been obtained by considering the experimental uncertainties of the data, used to determine the free parameters of the model and the theoretical systematic uncertainties due to the particular parametrization used.

This study aims to identify the origin or at least the dominant cause of the oscillatory behaviour of the effective nucleon form factors. In particular, we would like to distinguish between two hypotheses about the oscillation phenomenon: the intrinsic dynamical origin and the final state interaction. In the first case, the oscillations appear at the form factor level, while in the second case, they are due to re-scattering reactions that happen when the nucleons are already formed. A necessary condition in favour of the intrinsic origin is that there exists a microscopic model of nucleons that can give oscillatory form factors.

Even though for the neutron effective form factor the model reproduces quite well the oscillatory behaviour, it seems to fail in the case of the proton. Indeed, the obtained behaviour of the effective proton form factor, the orange band shown in the upper panel of Fig. 1, is compatible with the so-called regular background of Refs. [7, 8, 11]. It can be interpreted as the contribution due to the short distance quark-level dynamics [18, 19], i. e., the $p\bar{p}$ final state is produced by the creation of quark-antiquark pairs within a small volume, with a linear dimension much smaller than the standard hadron size of about 1 fm.

Nevertheless, the model has the added value of proving that a unique parametrization in all the kinematical ranges where data are present is effective both for proton and neutron FFs. This is in contrast to previous works, where a common fit could only be achieved either in a restricted kinematical region, concluding in a change of the phase [3], or at the price of three different models applicable in different kinematical regions [5].

Appendix A: Contributing diagrams computation

Using the expressions [15]

$$\begin{aligned}\varphi_N(\mathbf{x}) &= 120x_1x_2x_3\left(ax_1^2+bx_2^2+cx_3^2+dx_3+e\right),\\ T(\mathbf{x}) &= 120x_1x_2x_3\left[\frac{a+c}{2}\left(x_1^2+x_2^2\right)+bp_3^2+\right.\\ &\left.\frac{d}{2}(1-x_3)+e\right],\end{aligned} \tag{A1}$$

where the values of the coefficients a, b, c, d, e and f are given in Ref. [15], the analytic solutions of the integrals of Eq. (4), namely the ten non-vanishing expressions

$$\mathcal{K}_i = \int [dx] \int [dy] K_i(\mathbf{x},\mathbf{y}), \tag{A2}$$

where the functions $K_i(\mathbf{x},\mathbf{y})$ are given in Table I, with $i \in \{1,3,4,5,7,9,10,12,13,14\}$, are:

$$\begin{aligned}\mathcal{K}_1 &= \left(I_1^{(1)}\right)^2+4\left(I_1^{(2)}\right)^2,\\ I_1^{(1)} &= \frac{5}{12}(36a+6b+2c+12d+72e),\\ I_1^{(2)} &= \frac{5}{12}(21a+20b+3c+32d+72e);\end{aligned} \tag{A3}$$

$$\begin{aligned}\mathcal{K}_3 &= -4I_3^{(1)}I_3^{(2)},\\ I_3^{(1)} &= \frac{5}{3}(10a+2b+10c+15d+36e),\\ I_3^{(2)} &= \frac{5}{12}(15a+6b+15c+28d+72e);\end{aligned} \tag{A4}$$

$$\begin{aligned}\mathcal{K}_4 &= I_4^{(1)}I_4^{(2)},\\ I_4^{(1)} &= \frac{5}{2}(a+3b+2(c+2d+6e)),\\ I_4^{(2)} &= \frac{5}{6}(6a+9b+3c+8d+36e);\end{aligned} \tag{A5}$$

$$\begin{aligned}\mathcal{K}_5 &= -I_5^{(1)}I_5^{(2)},\\ I_5^{(1)} &= \frac{5}{2}(3a+b+2(c+2d+6e))\\ I_5^{(2)} &= \frac{10}{3}(9a+b+c+3d+18e);\end{aligned} \tag{A6}$$

$$\begin{aligned}\mathcal{K}_7 &= \left(I_7^{(1)}\right)^2+\left(I_7^{(2)}\right)^2,\\ I_7^{(1)} &= \frac{5}{6}(a+3(b+6c+8d+12e)),\\ I_7^{(2)} &= \frac{5}{6}(3a+b+6(3c+4d+6e));\end{aligned} \tag{A7}$$

$$\begin{aligned}\mathcal{K}_9 &= \mathcal{K}_{10} = \left(I_9^{(1)}\right)^2+4\left(I_9^{(2)}\right)^2,\\ I_9^{(1)} &= \frac{5}{6}(18a+b+3c+8d+36e),\\ I_9^{(2)} &= \frac{5}{12}(19a+6b+19c+28d+72e);\end{aligned} \tag{A8}$$

$$\begin{aligned}\mathcal{K}_{12} &= -I_{12}^{(1)}I_{12}^{(2)};\\ I_{12}^{(1)} &= \frac{10}{3}(a+b+9c+12d+18e),\\ I_{12}^{(2)} &= \frac{5}{6}(6a+3b+9c+16d+36e);\end{aligned} \tag{A9}$$

$$\begin{aligned}\mathcal{K}_{13} &= 4I_{13}^{(1)}I_{13}^{(2)}\\ I_{13}^{(1)} &= \frac{5}{12}(-3a+90b-3c+100d+360e),\\ I_{13}^{(2)} &= \frac{5}{12}(9a+18b+9c+20d+72e);\end{aligned} \tag{A10}$$

$$\begin{aligned}\mathcal{K}_{14} &= -I_{14}^{(1)}I_{14}^{(2)},\\ I_{14}^{(1)} &= \frac{5}{6}(6a+3b+9c+16d+36e),\\ I_{14}^{(2)} &= \frac{10}{3}(a+b+9c+12d+18e).\end{aligned} \tag{A11}$$

Appendix B: Distribution amplitudes computation

1. Quark distribution amplitudes complex conjugate computation

Omitting the color and current indices, there is a proportionality between the hadronic current matrix element and the quark distribution amplitudes, given by

$$\langle P'|J|P\rangle \propto \langle P'|\bar{u}_\mu\bar{u}_\nu\bar{d}_\rho|0\rangle\,\langle 0|K_H^{\mu\nu\rho\alpha\beta\gamma}|0\rangle\,\langle 0|u_\alpha u_\beta d_\gamma|P\rangle, \tag{B1}$$

so that the transition amplitude is proportional to the vacuum expectation value of the hard scattering kernel. The Feynman diagram is depicted in Fig. 3.

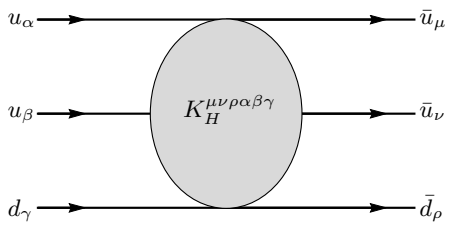


FIG. 3. Basic graph for the hard scattering kernel.

The hard scattering structure $K_H^{\mu\nu\rho\alpha\beta\gamma}$ is given by a product of the three Lorentz structures which give the coupling of the three fermion lines:

$$K_H^{\mu\nu\rho\alpha\beta\gamma} = \Gamma_1^{\alpha\mu}\Gamma_2^{\beta\nu}\Gamma_3^{\gamma\rho}. \tag{B2}$$

First of all, we need to write the complex conjugate of the matrix element representing the distribution amplitude $\varphi_N(\mathbf{x})$. We calculate this directly as we can take the complex conjugate of the three parts composing the matrix element expansion:

$$\begin{aligned}\langle 0|\,u_\alpha u_\beta d_\gamma\,|P\rangle^* &= \langle P|\,d_\gamma^\dagger u_\beta^\dagger u_\alpha^\dagger\,|0\rangle\\ &= \langle P|\,\bar{d}_i\bar{u}_j\bar{u}_k\,|0\rangle\,\gamma^0_{i\gamma}\gamma^0_{j\beta}\gamma^0_{k\alpha}.\end{aligned} \tag{B3}$$

For the axial component we have

$$\begin{aligned}\langle P|\,\bar{d}_i\bar{u}_j\bar{u}_k\,|0\rangle_A &= A_1^*\left(\not{P}\gamma_5 C\right)^*_{\alpha\beta} N\left(P\right)^*_\gamma \gamma^0_{\gamma i}\gamma^0_{\beta j}\gamma^0_{\alpha k}\\ &= A_1^*\left(\left(\not{P}\gamma_5 C\right)^\dagger\right)_{\beta\alpha}\bar{N}\left(P\right)_i\gamma^0_{\beta j}\gamma^0_{\alpha k}\\ &= A_1^*\left(C\gamma_5\not{P}\right)_{jk}\bar{N}\left(P\right)_i\,, \end{aligned} \tag{B4}$$

for the vector one

$$\begin{aligned}\langle P|\,\bar{d}_i\bar{u}_j\bar{u}_k\,|0\rangle_V &= V_1^*\left(\not{P}C\right)^*_{\alpha\beta}\left(\gamma_5 N\left(P\right)\right)^*_\gamma \gamma^0_{\gamma i}\gamma^0_{\beta j}\gamma^0_{\alpha k}\\ &= -V_1^*\left(\left(\not{P}C\right)^\dagger\right)_{\beta\alpha}\left(\bar{N}\left(P\right)\gamma_5\right)_i\gamma^0_{\beta j}\gamma^0_{\alpha k}\\ &= -V_1^*\left(C\not{P}\right)_{jk}\left(\bar{N}\left(P\right)\gamma_5\right)_i\,, \end{aligned} \tag{B5}$$

and finally for the tensorial part

$$\begin{aligned}\langle P|\,\bar{d}_i\bar{u}_j\bar{u}_k\,|0\rangle_T &= T_1^*\left(\overleftrightarrow{\sigma}^{\mu\nu}P_\nu C\right)^*_{\alpha\beta}\left(\gamma_\mu\gamma_5 N\left(P\right)\right)^*_\gamma\\ &\quad\gamma^0_{\gamma i}\gamma^0_{\beta j}\gamma^0_{\alpha k}\\ &= -T_1^*\left(\left(\overleftrightarrow{\sigma}^{\mu\nu}P_\nu C\right)^\dagger\right)_{\beta\alpha}\left(\bar{N}\left(P\right)\gamma_5\gamma_\mu\right)_i\\ &\quad\gamma^0_{\beta j}\gamma^0_{\alpha k}\\ &= -T_1^*\left(CP_\nu\overleftrightarrow{\sigma}^{\mu\nu}\right)_{jk}\left(\bar{N}\left(P\right)\gamma_5\gamma_\mu\right)_i\,. \end{aligned} \tag{B6}$$

2. Distribution amplitudes convolutions

Here we compute the convolution of the distribution amplitudes used for the evaluation of the contributing diagrams. In each of the following calculations we use the anti-commutative properties of the gamma matrices, in particular the fact that the γ_5 matrix anti commutes with every component of the matrix four-vector γ^μ, while for the charge conjugation matrix C the following rule holds:

$$C\gamma^\mu C = -\left(\gamma^\mu\right)^T\,. \tag{B7}$$

The axial, vector, tensor, and axial-vector components of the hadronic-current matrix element are, respectively,

$$\begin{aligned}\langle P'|J|P\rangle_A &= \langle P'|\bar{u}_\mu\bar{u}_\nu\bar{d}_\rho|0\rangle_A\langle 0|K_H^{\mu\nu\rho\alpha\beta\gamma}|0\rangle\langle 0|u_\alpha u_\beta d_\gamma|P\rangle_A\\ &= A_1^*\left(C\gamma_5\not{P}'\right)_{\mu\nu}\left(\bar{N}P'\right)_\rho\Gamma_1^{\mu\alpha}\Gamma_2^{\nu\beta}\Gamma_3^{\rho\gamma}A_1\\ &\quad\left(\not{P}\gamma_5 C\right)_{\alpha\beta}N\left(P\right)_\gamma\\ &= \left|A_1\right|^2\bar{N}\left(P'\right)\Gamma_3 N\left(P\right)\\ &\quad\left[-\Gamma_1^{\mu\alpha}\left(\not{P}\gamma_5 C\right)_{\alpha\beta}\left(\Gamma_2^T\right)^{\beta\nu}\left(C\gamma_5\not{P}'\right)_{\nu\mu}\right]\\ &= -\left|A_1\right|^2\bar{N}\left(P'\right)\Gamma_3 N\left(P\right)\\ &\quad\mathrm{Tr}\left[\Gamma_1\not{P}\gamma_5 C\Gamma_2^T C\gamma_5\not{P}'\right]\\ &= \left(-1\right)^{1+2n_2}\left|A_1\right|^2\bar{N}\left(P'\right)\Gamma_3 N\left(P\right)\\ &\quad\mathrm{Tr}\left[\Gamma_1\not{P}\overleftrightarrow{\Gamma}_2\not{P}'\right]\,; \end{aligned} \tag{B8}$$

$$\begin{aligned}\langle P'|J|P\rangle_V &= \langle P'|\bar{u}_\mu\bar{u}_\nu\bar{d}_\rho|0\rangle_V\langle 0|K_H^{\mu\nu\rho\alpha\beta\gamma}|0\rangle\,\langle 0|u_\alpha u_\beta d_\gamma|P\rangle_V\\ &= -V_1^*\left(C\not{P}'\right)_{\mu\nu}\left(\bar{N}\left(P'\right)\gamma_5\right)_\rho\Gamma_1^{\mu\alpha}\Gamma_2^{\nu\beta}\Gamma_3^{\rho\gamma}\\ &\quad V_1\left(\not{P}C\right)_{\alpha\beta}\left(N\left(P\right)\gamma_5\right)_\gamma\\ &= \left(-1\right)^{1+n_3}\left|V_1\right|^2\bar{N}\left(P'\right)\Gamma_3 N\left(P\right)\\ &\quad\left[\left(\Gamma_1\right)_{\mu\alpha}\left(\not{P}C\right)_{\alpha\beta}\left(\Gamma_2^T\right)_{\beta\nu}\left(C\not{P}'\right)_{\nu\mu}\right]\\ &= \left(-1\right)^{1+n_3}\left|V_1\right|^2\bar{N}\left(P'\right)\Gamma_3 N\left(P\right)\\ &\quad\mathrm{Tr}\left[\Gamma_1\not{P}C\Gamma_2^T C\not{P}'\right]\\ &= \left(-1\right)^{1+n_2+n_3}\left|V_1\right|^2\bar{N}\left(P'\right)\Gamma_3 N\left(P\right)\\ &\quad\mathrm{Tr}\left[\Gamma_1\not{P}\overleftrightarrow{\Gamma}_2\not{P}'\right]\\ &= -\left|V_1\right|^2\bar{N}\left(P'\right)\Gamma_3 N\left(P\right)\mathrm{Tr}\left[\Gamma_1\not{P}\overleftrightarrow{\Gamma}_2\not{P}'\right]\,; \end{aligned} \tag{B9}$$

$$\begin{aligned}\langle P'|J|P\rangle_T &= \langle P'|\bar{u}_\mu\bar{u}_\nu\bar{d}_\rho|0\rangle_T\langle 0|K_H^{\mu\nu\rho\alpha\beta\gamma}|0\rangle\langle 0|u_\alpha u_\beta d_\gamma|P\rangle_T\\ &= T_1^*\left(CP'_\lambda\overleftrightarrow{\sigma}^{\delta\lambda}\right)_{\mu\nu}\left(\bar{N}\left(P'\right)\gamma_5\gamma_\delta\right)_\rho\Gamma_1^{\mu\alpha}\Gamma_2^{\nu\beta}\Gamma_3^{\rho\gamma}\\ &\quad T_1\left(\overleftrightarrow{\sigma}^{\eta\kappa}P_\kappa C\right)_{\alpha\beta}\left(\gamma_\eta\gamma_5\left(N\left(P\right)\right)\right)_\gamma\\ &= \left|T_1\right|^2 P'_\lambda P_\kappa\bar{N}\left(P'\right)\gamma_\delta\Gamma_3\gamma_\eta N\left(P\right)\\ &\quad\left[\Gamma_1^{\mu\alpha}\left(\overleftrightarrow{\sigma}^{\eta\kappa}C\right)_{\alpha\beta}\left(\Gamma_2^T\right)_{\beta\nu}\left(C\overleftrightarrow{\sigma}^{\delta\lambda}\right)_{\nu\mu}\right]\\ &= \left|T_1\right|^2 P'_\lambda P_\kappa\bar{N}\left(P'\right)\gamma_\delta\Gamma_3\gamma_\eta N\left(P\right)\\ &\quad\mathrm{Tr}\left[\Gamma_1\overleftrightarrow{\sigma}^{\eta\kappa}C\Gamma_2^T C\overleftrightarrow{\sigma}^{\delta\lambda}\right]\\ &= \left|T_1\right|^2 P'_\lambda P_\kappa\bar{N}\left(P'\right)\gamma_\delta\Gamma_3\gamma_\eta N\left(P\right)\\ &\quad\mathrm{Tr}\left[\Gamma_1\overleftrightarrow{\sigma}^{\eta\kappa}\overleftrightarrow{\Gamma}_2\overleftrightarrow{\sigma}^{\delta\lambda}\right]\,; \end{aligned} \tag{B10}$$

$$\begin{aligned}&\langle P'|\,\bar{u}_\mu\bar{u}_\nu\bar{d}_\rho\,|0\rangle_A\,\langle 0|\,K_H^{\mu\nu\rho\alpha\beta\gamma}\,|0\rangle\,\langle 0|\,u_\alpha u_\beta d_\gamma\,|P\rangle_V\\ &+\langle P'|\,\bar{u}_\mu\bar{u}_\nu\bar{d}_\rho\,|0\rangle_V\,\langle 0|\,K_H^{\mu\nu\rho\alpha\beta\gamma}\,|0\rangle\,\langle 0|\,u_\alpha u_\beta d_\gamma\,|P\rangle_A\\ =\;&\left[A_1^*\left(C\gamma_5\not{P}'\right)_{\mu\nu}\left(\bar{N}\left(P'\right)\right)_\rho V_1\left(\not{P}C\right)_{\alpha\beta}\left(N\left(P\right)\gamma_5\right)_\gamma\right.\\ &\left.-V_1^*\left(C\not{P}'\right)_{\mu\nu}\left(\bar{N}\left(P'\right)\gamma_5\right)_\rho A_1\left(\not{P}\gamma_5 C\right)_{\alpha\beta}N\left(P\right)_\gamma\right]\\ &\Gamma_1^{\mu\alpha}\Gamma_2^{\nu\beta}\Gamma_3^{\rho\gamma}\\ =\;&-\left(V_1A_1^*+V_1^*A_1\right)\bar{N}\left(P'\right)\Gamma_3\gamma_5 N\left(P\right)\mathrm{Tr}\left[\Gamma_1\not{P}\overleftrightarrow{\Gamma}_2\not{P}'\right]\,. \end{aligned} \tag{B11}$$

Appendix C: Contributing diagrams in terms of the non-perturbative parameters

Here we write the integrals used for the calculation of the nucleon form factors $G_M^{p,n}$. The Chernyak-Zhitnitsky formula is

$$q^4 G_M^{p,n}\left(q^2\right)\to\frac{\left(4\pi\bar{\alpha}_s\right)^2}{54}\left|f_N\right|^2 I^{p,n}\,, \tag{C1}$$

where the integrals $I^{p,n}$ up to the second degree polynomials are

$$
\begin{aligned}
I^p &= 1400B_0B_1 + \frac{2000}{9}B_1^2 + 1800B_0B_2 + \frac{2800}{3}B_1B_2 \\
&\quad +1200B_2^2 + 6600B_0B_3 + \frac{22000}{9}B_1B_3 + 4800B_2B_3 \\
&\quad +\frac{18800}{3}B_3^2 - \frac{1000}{3}B_0B_4 - \frac{2600}{27}B_1B_4 - \frac{2200}{9}B_2B_4 \\
&\quad -\frac{4600}{9}B_3B_5 + \frac{2600}{243}B_4^2 - 1400B_0B_5 - \frac{3500}{9}B_1B_5 \\
&\quad -\frac{1100}{3}B_2B_5 - \frac{5900}{3}B_3B_5 + \frac{4100}{81}B_4B_5 + \frac{7700}{27}B_5^2\,; \\
I^n &= 1800B_0^2 - 1400B_0B_1 + \frac{2000}{9}B_1^2 - 1800B_0B_2 \\
&\quad -\frac{2800}{3}B_1B_2 - 200B_2^2 - 1000B_0B_3 - \frac{22000}{9}B_1B_3 \\
&\quad -2000B_2B_3 - \frac{17000}{9}B_3^2 + \frac{1000}{3}B_0B_4 - \frac{2600}{27}B_1B_4 \\
&\quad +\frac{2200}{9}B_2B_4 + \frac{4600}{9}B_3B_5 + \frac{2600}{243}B_4^2 + \frac{2000}{3}B_0B_5 \\
&\quad +\frac{3500}{9}B_1B_5 + \frac{500}{9}B_2B_5 + \frac{6500}{9}B_3B_5 - \frac{4100}{81}B_4B_5 \\
&\quad -\frac{7250}{81}B_5^2\,, \qquad \text{(C2)}
\end{aligned}
$$

where the coefficients $\{B_n\}_{n=0}^5$ are the ones appearing in the expansion of the LCDA $\varphi_N\left(\mathbf{x}, Q^2\right)$, and their operative form is given in Eq. (5).

[1] Institute of high energy physics chinese academy of sciences, https://web.archive.org/web/20160316234203/http://www.ihep.ac.cn/english/E-Bepc/.

[2] M. Ablikim, M. N. Achasov, P. Adlarson, and N. Amhed (BESIII Collaboration), Study of the process $e^+e^- \to p\overline{p}$ via initial state radiation at besiii, Phys. Rev. D **99**, 092002 (2019).

[3] M. Ablikim, M. N. Achasov, P. Adlarson, S. Ahmed, and M. Albrecht, Oscillating features in the electromagnetic structure of the neutron, Nature Physics **17**, 1200 (2021).

[4] M. Ablikim, M. N. Achasov, P. Adlarson, and N. Amhed (BESIII Collaboration), Measurement of proton electromagnetic form factors in $e^+e^- \to p\overline{p}$ in the energy region 2.00–3.08 gev, Phys. Rev. Lett. **124**, 042001 (2020).

[5] Q.-H. Yang, D. Guo, L.-Y. Dai, J. Haidenbauer, X.-W. Kang, and U.-G. Meißner, New insights into the oscillations of the nucleon electromagnetic form factors, Science Bulletin **68**, 2729 (2023).

[6] M. Ablikim, M. Achasov, P. Adlarson, S. Ahmed, and M. Albrecht, Measurement of proton electromagnetic form factors in the time-like region using initial state radiation at besiii, Physics Letters B **817**, 136328 (2021).

[7] A. Bianconi and E. Tomasi-Gustafsson, Periodic interference structures in the timelike proton form factor, Phys. Rev. Lett. **114**, 232301 (2015), arXiv:1503.02140 [nucl-th].

[8] A. Bianconi and E. Tomasi-Gustafsson, Phenomenological analysis of near threshold periodic modulations of the proton timelike form factor, Phys. Rev. C **93**, 035201 (2016), arXiv:1510.06338 [nucl-th].

[9] A. Bianconi and E. Tomasi-Gustafsson, Fourth dimension of the nucleon structure: Spacetime analysis of the timelike electromagnetic proton form factors, Phys. Rev. C **95**, 015204 (2017), arXiv:1611.02149 [hep-ph].

[10] A. Bianconi and E. Tomasi-Gustafsson, Soft rescattering in the timelike proton form factor within a spacetime scheme, Phys. Rev. C **98**, 055204 (2018), arXiv:1809.05709 [nucl-th].

[11] E. Tomasi-Gustafsson, A. Bianconi, and S. Pacetti, New fit of timelike proton electromagnetic form factors from e^+e^- colliders, Phys. Rev. C **103**, 035203 (2021), arXiv:2012.14656 [hep-ph].

[12] E. Tomasi-Gustafsson, A. Bianconi, and S. Pacetti, Dynamical Properties of Baryons, Symmetry **13**, 1480 (2021).

[13] S. J. Brodsky, H.-C. Pauli, and S. S. Pinsky, Quantum chromodynamics and other field theories on the light cone, Physics Reports **301**, 299 (1998).

[14] V. Braun, S. Derkachov, G. Korchemsky, and A. Manashov, Baryon distribution amplitudes in QCD, Nuclear Physics B **553**, 355 (1999).

[15] V. Chernyak and I. Zhitnitsky, Nucleon wave function and nucleon form factors in qcd, Nuclear Physics B **246**, 52 (1984).

[16] G. P. Lepage and S. J. Brodsky, Exclusive processes in perturbative quantum chromodynamics, Phys. Rev. D **22**, 2157 (1980).

[17] R. Brun and F. Rademakers, Root — an object oriented data analysis framework, Nuclear Instruments and Methods in Physics Research Section A: Accelerators, Spectrometers, Detectors and Associated Equipment **389**, 81 (1997), new Computing Techniques in Physics Research

V.
[18] V. A. Matveev, R. M. Muradian, and A. N. Tavkhelidze, Automodellism in the large - angle elastic scattering and structure of hadrons, Lett. Nuovo Cim. **7**, 719 (1973).
[19] S. J. Brodsky and G. R. Farrar, Scaling Laws at Large Transverse Momentum, Phys. Rev. Lett. **31**, 1153 (1973).

arXiv:2403.02897v1 [hep-ph] 5 Mar 2024

Rare B and K decays in a scotogenic model

Chuan-Hung Chen[1, 2, *] and Cheng-Wei Chiang[3, 2, †]

[1]*Department of Physics, National Cheng-Kung University, Tainan 70101, Taiwan*

[2]*Physics Division, National Center for Theoretical Sciences, Taipei 10617, Taiwan*

[3]*Department of Physics and Center for Theoretical Physics, National Taiwan University, Taipei 10617, Taiwan*

(Dated: March 6, 2024)

Abstract

A scotogenic model can radiatively generate the observed neutrino mass, provide a dark matter candidate, and lead to rare lepton flavor-violating processes. We aim to extend the model to establish a potential connection to the quark flavor-related processes within the framework of scotogenesis, enhancing the unexpectedly large branching ratio (BR) of $B^+ \to K^+\nu\bar{\nu}$, observed by Belle II Collaboration. Meanwhile, the model can address tensions between some experimental measurements and standard model (SM) predictions in flavor physics, such as the muon $g-2$ excess and the higher BR of $B_s \to \mu^-\mu^+$. We introduce in the model the following dark particles: a neutral singlet Dirac-type lepton (N); two inert Higgs doublets ($\eta_{1,2}$), with one of which carrying a lepton number; a charged singlet dark scalar (χ^+), and a singlet vector-like up-type dark quark (T). The first two entities are responsible for the radiative neutrino mass, and χ^+ couples to right-handed quarks and leptons and can resolve the tensions existing in muon $g-2$ and $B_s \to \mu^-\mu^+$. Furthermore, the BR of $B^+ \to K^+\nu\bar{\nu}$ can be enhanced up to a factor of 2 compared to the SM prediction through the mediations of the dark T and the charged scalars. In addition, we also study the impacts on the $K \to \pi\nu\bar{\nu}$ decays.

*E-mail: physchen@mail.ncku.edu.tw

†E-mail: chengwei@phys.ntu.edu.tw

I. INTRODUCTION

Under an enormous number of experimental tests and with great success in most of them, the standard model (SM) has been established as a very good effective theory at and below the electroweak scale. However, certain empirical observations, such as the existence of neutrino mass and dark matter (DM), still await definitive resolutions. In addition, a long-standing issue in the anomalous magnetic dipole moment of muon (muon $g-2$), observed in BNL [1] and further confirmed by Fermilab experiments [2], strongly hints at possibly a new interaction in the lepton sector.

Recently, the Belle II Collaboration with 362 fb^{-1} of data has observed the first evidence of $B^+ \to K^+\nu\bar{\nu}$ decay, and the resulting branching ratio (BR) is reported as [3]:

$$\mathcal{B}(B^+ \to K^+\nu\bar{\nu}) = [2.3 \pm 0.5\,(\text{stat})\,^{+0.5}_{-0.4}\,(\text{syst})] \times 10^{-5} = (2.3 \pm 0.7) \times 10^{-5}\,. \tag{1}$$

When combined with earlier results measured by BaBar [4, 5] and Belle [6, 7], the weighted average is given by $\mathcal{B}(B^+ \to K^+\nu\bar{\nu}) = (1.3 \pm 0.4) \times 10^{-5}$. Compared to the SM prediction of $\mathcal{B}(B^+ \to K^+\nu\bar{\nu})^{\rm SM} = (4.92 \pm 0.30) \times 10^{-6}$ [8], the current data shows a 2.7σ deviation. This difference hints at the possibility of some peculiar interactions, predominantly manifesting in the $b \to s\nu\bar{\nu}$ or $b \to s +$ invisible transitions [9–23], rather than in $b \to s\ell^-\ell^+$ that is subject to strict constraints from $B \to X_s\ell^-\ell^+$ and $B_s \to \mu^-\mu^+$ decays.

A primary motivation of this study is to extend the existing scotogenic model [24] to enhance the $d_i \to d_j\nu\bar{\nu}$ decays and muon $g-2$ while simultaneously explaining the observed neutrino data and dark matter relic density. To radiatively generate Majorana neutrino mass in a scotogenic model, lepton number-violating couplings are essential. Such violation of the lepton number could stem from the leptonic right-handed Majorana neutrino mass term, like in the type-I seesaw mechanism [25–28]. However, to prevent the mass scale of the introduced Majorana fermion from reaching an undetectable energy scale when the Yukawa couplings are of $O(m_\tau/v)$, either the Majorana fermion does not carry a lepton number [24] or a Dirac-type neutral fermion should be used instead [29]. In other words, the new heavy fermion mass term is unrelated to or retains the lepton number conservation. Therefore, within the framework of scotogenesis, the lepton number symmetry should be violated in some scalar coupling, for instance, a non-Hermitian quartic term, where the involved exotic scalar field carries a dark charge and is assigned a lepton number as proposed in the Ma model [24]. Since the lepton number symmetry will be restored when the scalar coupling,

which violates the lepton number, approaches zero, it can be considered as a technical naturalness if the scalar coupling is small [30].

If we focus on leptonic processes, one Higgs doublet, which carries a dark charge and lepton number, associated with 2 or 3 dark right-handed Majorana fermions in the Ma model can successfully account for the neutrino data observed from the neutrino oscillation experiments [24]. For simplicity, we will refer to a scalar carrying a dark charge as an inert scalar. As a result, this model has implications for rare leptonic decays, such as $\mu \to e\gamma$, $\mu \to 3e$, $\mu - e$ conversion in nucleus processes [31, 32], and DM candidate [24]. However, due to the absence of the lepton quantum number in quarks, the lepton number-carrying Higgs doublet in the Ma model has no interactions with the quarks. This remains true even with the introduction of a new heavy quark carrying a dark charge; otherwise, the lepton number violation will occur in the quark Yukawa couplings, leading to the breakdown of R_p-parity, defined as $R_p = (-1)^{3B+L+2S}$, where B, L, and S denote the baryon, lepton, and spin quantum numbers of a particle.

To incorporate the effects responsible for the loop-induced neutrino mass into the rare flavor-changing neutral-current (FCNC) B and K decay processes, a suitable extension of the Ma model is called for. We, therefore, aim to identify a minimal extension that not only addresses the issues of neutrino mass, DM relic density, and muon $g-2$ but also significantly enhances the BRs in the $d_i \to d_j \nu\bar{\nu}$ decays.

We find that the essential part to achieve our goal is the introduction of an inert Higgs doublet in the absence of the lepton number association. To preserve the lepton number conservation in the Yukawa sector, it is imperative to replace the Majorana-type neutral fermion used in the Ma model with a vector-like Dirac-type neutral lepton. Furthermore, to establish the connection between the SM quarks and the particles within the dark sector through the non-leptonic inert Higgs, it is necessary to introduce a new quark with an appropriate dark charge. For the sake of gauge anomaly-free conditions, the minimal choice of the new dark quark is an $SU(2)_L$ singlet vector-like up-type quark.

Since the non-leptonic inert Higgs is an $SU(2)_L$ doublet, the Yukawa couplings only involve the left-handed SM quarks. In other words, when $d_i \to d_j \nu\bar{\nu}$ are enhanced, the effects contributing to $B_s \to \mu^-\mu^+$ align with the SM contribution and could result in constructive interference and pushing its BR above the current experimental data. To address the constraint arising from $B_s \to \mu^-\mu^+$, a right-handed quark current used to cancel the effect from

the left-handed current in the $b \to s$ transition becomes helpful. What is more is that in fact, the SM predicts $\mathcal{B}(B_s \to \mu^-\mu^+) = 3.78^{+0.15}_{-0.10} \times 10^{-9}$ [8], slightly higher than the current experimental measurement $\mathcal{B}(B_s \to \mu^-\mu^+) = (3.01 \pm 0.35) \times 10^{-9}$ [33]. The introduction of right-handed quark currents helps alleviate this tension.

Because the right-handed quarks and leptons in the SM and the introduced dark quark are $SU(2)_L$ singlet, we can employ an $SU(2)_L$ singlet electrically charged dark scalar to couple these particles. As a result, the right-handed currents for the $b \to s$ transition can be generated from one-loop Feynman diagrams. Moreover, through mixing with the inert Higgs doublet, the left- and right-handed leptons can couple to the physical inert charged scalars. This results in the corrections to lepton $g-2$ being linear in the lepton mass. Therefore, the muon $g-2$ can be significantly enhanced in the model. Based on the above analysis, the additional dark particles introduced in the model to explain the neutrino measurements and the muon $g-2$, to fit $\mathcal{B}(B_s \to \mu^-\mu^+)$, and to enhance the $d_i \to d_j \nu\bar{\nu}$ processes are: the non-leptonic inert Higgs doublet, the singlet vector-like up-type dark quark, and the singlet dark-charged scalar.

The paper is structured as follows. We set up the scotogenic model and derive the Yukawa and relevant gauge couplings in Sec. II. Utilizing the obtained Yukawa couplings and scalar mixings, we formulate the loop-induced neutrino mass matrix and lepton $g-2$ in Sec. III. The constraints from $b \to s\gamma$ and $|\Delta F| = 2$ arising from box diagrams are analyzed. In addition, the effective Hamiltonian for $d_i \to d_j(\nu\bar{\nu}, \mu^-\mu^+)$, which arises from the Z-penguin diagrams, is derived in this section. Based on the new interactions, the BRs for $B \to K^{(*)}\nu\bar{\nu}$, $K \to \pi\nu\bar{\nu}$, $B \to X_s\ell^-\ell^+$, and $B_s \to \mu^-\mu^+$ are computed in Sec. IV. The detailed numerical analysis and discussions of the phenomenological results are shown in Sec. V. The findings of this study are summarized in Sec. VI.

II. THE MODEL AND COUPLINGS

As stated in the introduction, the Majorana neutrino mass can be radiatively generated in the scotogenic model if lepton number violation originates from the coupling of the leptonic inert Higgs doublet to the non-leptonic inert Higgs and the SM Higgs doublets in the scalar potential. Moreover, by introducing an $SU(2)_L$ singlet vector-like up-type quark, we can have interesting phenomenological contributions to the FCNC B and K decays. Therefore,

to investigate the impacts of new physics on the processes of $d_i \to d_j(\nu\bar{\nu}, \ell^-\ell^+)$ while avoiding the strict constraints from the $B \to X_s\ell^-\ell^+$ and $B_s \to \mu^+\mu^-$ decays, we extend the SM by adding two Higgs doublet $\eta_{1,2}$, one charged scalar $\chi^\pm$, and singlet vector-like neutral leptons $N_{L,R}$ and up-type quarks $T_{L,R}$, one for each chirality.

It is found that with appropriate charge assignment to the new particles, a global $U(1)_X$ dark symmetry exists in the model. Since a Z'-guage boson is not necessary for the study, we do not gauge the $U(1)_X$ symmetry. For clarity, we show the representations and assignments of $U(1)_X$ charge and lepton number as follows:

$$\begin{aligned} \eta_1 \sim (2,\, 1,\, q_X,\, 0)\,,\ \eta_2 \sim (2,\, 1,\, -q_X, -2)\ , \\ N_{L,R} \sim (1,\, 0,\, q_X,\, 1)\,,\ T_{L,R} \sim (1,\, 4/3,\, q_X,\, 0)\,,\ \chi^+ \sim (1,\, 2,\, q_X,\, 0)\,, \end{aligned} \tag{2}$$

where the numbers in the parentheses denote in sequence the $SU(2)_L$ representation, the $U(1)_Y$ charge, the $U(1)_X$ charge, and the lepton number. We note that both η_2 and N carry the lepton number. Moreover, to ensure the stability of a DM candidate in the model, we assume that the $U(1)_X$ is exact, and the $\eta_{1,2}$ are assumed to have no nonzero vacuum expectation values (VEVs). Hence, the masses of the dark-charged scalars do not originate from the electroweak symmetry breaking.

We will focus on the loop-induced quark flavor-changing processes in this work. Details of the scalar potential, the scalar mixings, and the scalar mass spectra are presented in Appendix A. The main free parameters associated with the scalar sector are the masses of the inert charged Higgs bosons.

A. Yukawa couplings

Based on the representations and charge assignments in Eq. (2), the Yukawa couplings for the new particles are given by:

$$\begin{aligned} -\mathcal{L}_Y =& \overline{L}\,\mathbf{y}_1\,\tilde{\eta}_1 N_R + \overline{L}\,\mathbf{y}_2\,\tilde{\eta}_2 N_L^C + \overline{\ell_R}\,\mathbf{y}_\ell\, N_L\chi^- + m_N\overline{N}_L N_R \\ &+ \overline{Q_L}\,\mathbf{y}_T^R\,\tilde{\eta}_1 T_R + \overline{d_R}\,\mathbf{y}_T^L\, T_L\chi^- + m_T\overline{T_L}T_R + \text{H.c.}\ , \end{aligned} \tag{3}$$

where the flavor indices are suppressed, L and Q_L denote respectively the left-handed lepton and quark doublets in the SM, $\tilde{\eta}_j = i\tau_2\eta_j^*$, $N^C = C\bar{N}^T$ is the charge conjugation of N, and m_N (m_T) is the mass of N (T). After electroweak symmetry breaking, we introduce the unitary flavor-mixing matrices $V_{R,L}^\ell$ and $V_{R,L}^q$ to diagonalize the charged lepton and quark

mass matrices. Since the neutrinos are still massless at the tree level, we can absorb the lepton flavor-mixing matrices to the Yukawa couplings $\mathbf{y}_{1,2,\ell}$. If we rotate away the weak phase of $\mathbf{y}_1$, both $\mathbf{y}_2$ and $\mathbf{y}_\ell$ in general contain complex parameters. Thus, $\mathbf{y}_2$ can lead to a complex Majorana neutrino mass matrix through radiative corrections. Using the physical charged and neutral scalar states defined in Eqs. (A5) and (A9), the lepton Yukawa couplings can be obtained as:

$$\begin{aligned}-\mathcal{L}_Y^\ell =& \overline{\nu_L}\,\mathbf{y}_1\,N_R\,\left(c_\phi(S_1-iA_1)-s_\phi(S_2+iA_2)\right)\\ &+\overline{\nu_L}\,\mathbf{y}_2\,N_L^C\,\left(s_\phi(S_1+iA_1)+c_\phi(S_2-iA_2)\right)-\overline{\ell_L}\,\mathbf{y}_2\,N_L^C\,\eta_2^-\\ &-\overline{\ell_L}\,\mathbf{y}_1\,N_R\left(c_\theta H_1^- - s_\theta H_2^-\right)+\overline{\ell_R}\,\mathbf{y}_\ell\,N_L\left(s_\theta H_1^- + c_\theta H_2^-\right)+m_N\overline{N_L}N_R+\text{H.c.}\,,\end{aligned} \tag{4}$$

where θ denotes the mixing angle between $\eta_1^\pm$ and $\chi^\pm$. Besides the masses of neutral scalars, we will show later that the loop-induced Majorana neutrino mass matrix depends on $\mathbf{y}_{1,2}$ and the angle θ.

Before electroweak symmetry breaking, the weak phases of $\mathbf{y}_T^{R,T}$ can be rotated away by redefining the phases of the quark fields u_L and $d_{L,R}$. After the symmetry breaking, when the quark-flavor mixing matrices are introduced for diagonalizing the quark mass matrices, we can redefine $V_L^u\mathbf{y}_T^R$ as $\mathbf{y}_T^R$ in the $\bar{u}_L\mathbf{y}_T^R T_R\eta_1^{0*}$ term. As a result, the term related to the left-handed down-type quark becomes $\bar{d}_L V^\dagger\mathbf{y}_T^R T_R\eta_1^-$, where $V=V_L^u V_L^{d\dagger}$ represents the Cabibbo-Kobayashi-Maskawa (CKM) matrix. In terms of physical quark and scalar states, the Yukawa couplings of the new quark in the model are expressed as:

$$\begin{aligned}-\mathcal{L}_Y^q =& \overline{u_L}\,\mathbf{y}_T^R\,T_R\,\left[c_\phi(S_1-iA_1)-s_\phi(S_2+iA_2)\right]\\ &+\bar{d}\,\left(\mathbf{C}_{Ti}^{Rk}P_R+\mathbf{C}_T^{Lk}P_L\right)T H_k^- + m_T\overline{T_L}T_R+\text{H.c.}\end{aligned} \tag{5}$$

Here, $\mathbf{C}_T^{R1(2)}=-c_\theta(s_\theta)\mathbf{Y}_T^R$, and $\mathbf{C}_T^{L1(2)}=s_\theta(c_\theta)\mathbf{Y}_T^L$, with

$$\mathbf{Y}_T^R=V^\dagger\mathbf{y}_T^R\,,\ \mathbf{Y}_T^L=V_R^d\,\mathbf{y}_T^L\,. \tag{6}$$

From Eq. (5), it can be seen that the down-type quarks only couple to the charged Higgses. Although the Yukawa couplings $\mathbf{y}_T^{R,L}$ can be tightly restrained by the up-type quark processes mediated by the scalars S_i and pseudoscalars A_i, such as $D-\bar{D}$ mixing, the constraint is essentially close to that from the $K-\bar{K}$ mixing. Without loss of generality, we will focus on the charged Higgs-mediated phenomena.

If the up-type quarks in the weak eigenstates are initially aligned with their physical states (i.e., $V_L^u=\mathbb{1}$), we then have $V=V_L^{d\dagger}$, which is well-determined in experiments. Since there

is no information on the right-handed quark flavor mixings, V_R^d is essentially an unspecified unitary matrix. To reduce the number of free parameters, we adopt the assumption that $V_R^d = V_L^d$. Indeed, the assumption can be realized in the left-right symmetric model or model with a Hermitian quark mass matrix. The unique CP-violating phase in the quark sector then arises from the Kobayashi-Maskawa (KM) phase in the CKM matrix. We will apply the assumption in the numerical analysis.

B. Gauge couplings

In addition to the Yukawa couplings, the alternative interactions essential for the study of the FCNC B and K decays are the gauge couplings of the photon (A_μ) and Z-boson to T, $\chi^\pm$, and η_1^+. Being an $SU(2)_L$ singlet and charged under $U(1)_X$, T does not mix with the SM quarks or couple with the W boson.

To obtain the relevant guage interactions, we write the covariant derivatives of T, $\chi^\pm$ and η_i as:

$$\begin{aligned} D_\mu T &= (\partial_\mu + iQ_T g' B_\mu) T \ , \\ D_\mu \chi^+ &= (\partial_\mu + ig' B_\mu)\chi^+ \ , \\ D_\mu \eta_1 &= \left(\partial_\mu + i\frac{g}{2}\vec{\tau}\cdot\vec{W}_\mu + i\frac{g'}{2}B_\mu\right)\eta_1 \ , \end{aligned} \tag{7}$$

where the hypercharges of $Y_T = 4/3 = 2Q_T$, $Y_{\chi^+} = 2$ and $Y_{\eta_1} = 1$ have been explicitly used. Because η_2 does not couple to quarks, we refrain from showing its gauge couplings. Using the weak mixing angle, defined by $\cos\theta_W = g/\sqrt{g^2+g'^2}$ and $\sin\theta_W = g'/\sqrt{g^2+g'^2}$, and the relation of $g\sin\theta_W = g'\cos\theta_W = e$, we parametrize the photon and Z-boson states as:

$$\begin{aligned} A_\mu &= c_W B_\mu + s_W W_\mu^3 \ , \\ Z_\mu &= -s_W B_\mu + c_W W_\mu^3 \ , \end{aligned} \tag{8}$$

with $c_W \equiv \cos\theta_W$ and $s_W \equiv \sin\theta_W$. The gauge couplings of A_μ and Z_μ to the heavy new quark can be found as:

$$\mathcal{L}_{TTV} = -eQ_T\bar{T}\gamma_\mu T A^\mu - \frac{g}{2c_W}\left(-2Q_T s_W^2\right)\bar{T}\gamma_\mu T Z^\mu \ . \tag{9}$$

Note that as T is a vector-like quark, it has a vectorial coupling to the Z gauge boson.

For the gauge couplings of the charged scalars $H_i^\pm$, they can be obtained as:

$$\mathcal{L}_{H^-H^+V} = ieA^\mu \sum_{i=1}^{2} (H_i^+ \partial_\mu H_i^- - H_i^- \partial_\mu H_i^+) + i\frac{g}{2c_W} c_{ij}^Z Z^\mu \left((\partial_\mu H_i^-) H_j^+ - H_i^- \partial_\mu H_j^+ \right) , \tag{10}$$

where $c_{11}^Z = c_\theta^2 - 2s_W^2$, $c_{12}^Z = c_{21}^Z = c_\theta s_\theta$, and $c_{22}^Z = s_\theta^2 - 2s_W^2$. Because $\eta_1^\pm$ and $\chi^\pm$ mix together and belong to different $SU(2)_L$ representations, the Z couplings to these charged Higgs fields are not diagonal. We note that the gauge couplings of scalars S_i and pseudoscalars A_i to the Z gauge boson can be expressed as $\mathcal{L}_{\rm kin} \supset g/(2c_W)\,(A_i \partial_\mu S_i - S_i \partial_\mu A_i)\, Z^\mu$. From the results shown in Appendix A, S_i and A_i are degenerate due to the $U(1)_X$ symmetry. Therefore, these bosons cannot be the DM candidates; otherwise, the scalar boson scattering off the nucleon, $S_i \mathcal{N} \to A_i \mathcal{N}$ or its inverse process, mediated by the Z gauge boson will lead to too large a cross section that has already been excluded by the DM direct detection. Thus, the neutral Dirac fermion N is the DM candidate in this model. Utilizing the Yukawa couplings in Eq. (4), the annihilation cross section of $N\bar{N} \to f_{\rm SM}\bar{f}_{\rm SM}$ can accommodate the observed DM relic density when $m_N \lesssim 600$ GeV, as detailed in Ref. [29].

III. LOOP-INDUCED PROCESSES

In the following, we examine various loop-mediated processes that receive additional contributions from the new particles in the model.

A. Radiative neutrino mass and muon $g-2$

According to the lepton Yukawa couplings shown in Eq. (4), the Majorana neutrino mass matrix elements mediated by the neutral scalars and N can be obtained as:

$$m_{ij}^\nu = \frac{\sin(2\phi)}{32\pi^2} \overline{y}_{ij} m_N \left[\frac{m_{S_1}^2}{m_{S_1}^2 - m_N^2} \ln\left(\frac{m_{S_1}^2}{m_N^2}\right) - \frac{m_{S_2}^2}{m_{S_2}^2 - m_N^2} \ln\left(\frac{m_{S_2}^2}{m_N^2}\right) \right] , \tag{11}$$

where we have included the pseudoscalar A_i contributions, used the mass relation $m_{A_i} = m_{S_i}$, and defined the symmetric Yukawa couplings $\overline{y}_{ij}$ in flavor indices as $\overline{y}_{ij} = y_{1i}^* y_{2j}^* + y_{2i}^* y_{1j}^*$. For illustration purposes, we take $m_{S_1} = 600$ GeV, $m_{S_2} = 800$ GeV, $m_N = 300$ GeV, $\phi \sim \mathcal{O}(10^{-7})$, and $\mathbf{y}_{1,2} \sim \mathcal{O}(10^{-2})$ which is the order of τ lepton Yukawa coupling in the SM, and obtain $m_{ij}^\nu \sim \mathcal{O}(10^{-2})$ eV. To have more impacts on the lepton flavor-violating

processes, such $\mu \to e\gamma$, $\mu \to 3e$, and $\mu - e$ conversion, one can take $\mathbf{y}_{1,2}$ of $\mathcal{O}(1)$ while keeping $\phi \sim 10^{-11}$ or $\lambda_5 \sim \mathcal{O}(10^{-10})$. In the limit of $\lambda_5 = 0$, the lepton number symmetry is restored. Therefore, a small λ_5 can be regarded as technically natural [30].

When considering the scheme with $\mathbf{y}_1 \sim \mathcal{O}(1)$, one might anticipate significant effects on $d_i \to s(\nu\bar{\nu}, \ell^-\ell^+)$ from box diagrams, where the T-quark, N-lepton, and charged Higgses run inside the loops. However, unlike the Z-penguin diagrams that induce dimension-4 d_i-s-Z^* couplings, the effective operators arising from the box diagrams for $d_i \to s(\nu\bar{\nu}, \ell^-\ell^+)$ are of dimension-6. In other words, the effective Wilson coefficients resulting from $\mathbf{y}_1$ are suppressed by m_W^2/m_T^2. Consequently, the lepton Yukawa couplings cannot have a significant effect on the quark flavor-changing processes.

Using the Yukawa couplings in Eq. (4), the radiative corrections to the muon magnetic dipole moment mediated by $H^+_{1,2}$ and N can be obtained as:

$$\Delta a_\mu = -\frac{m_\mu s_{2\theta}}{16\pi^2} m_N \,\mathrm{Re}(y_{\ell 2} y_{12}^*) \left(\frac{J_1(w_{H_1^+})}{m^2_{H_1^+}} - \frac{J_1(w_{H_2^+})}{m^2_{H_2^+}} \right) , \tag{12}$$

where $w_{H_i^+} \equiv m_N^2/m^2_{H_i^+}$, and J_1 is a loop integral, defined as:

$$J_1(w) = \frac{1+w}{2(1-w)^2} + \frac{w \ln w}{(1-w)^3} . \tag{13}$$

Because η_1^+ and χ^+ couple to the left-handed and right-handed leptons, respectively, the resulting Δa_μ is proportional to m_μ. The mass insertion factor occurring in the N propagator further enhances Δa_μ. In addition, without introducing χ^+, the contribution to Δa_μ from η_1^+ would always have a negative sign. Assuming $m_{H_1^+} = 600$ GeV, $m_{\chi_1^+} = 800$ GeV, $m_N = 300$ GeV, $s_\theta = 0.1$, and $\mathrm{Re}(y_{\ell 2} y_{12}^*) = 0.2$ as an illustration, we obtain $\Delta a_\mu \simeq 2.2\times 10^{-9}$.

The above numerical estimate demonstrates that the model can readily accommodate the observed neutrino mass and the muon $g-2$ anomaly. Since the purely lepton-related processes in the model are similar to the study in Ref. [29], a detailed analysis can be found therein. This study primarily focuses on exploring rare quark flavor-changing processes.

B. $b \to s\gamma$

Due to the precision measurement of $b \to s\gamma$ decays, the new physics effects contributing to $b \to s(\nu\bar{\nu},\, \ell^-\ell^+)$ are severely constrained. In this subsection, we examine the influence of new couplings on the $b \to s\gamma$ decays.

The effective Hamiltonian for $b \to s\gamma^{(*)}$ from photon-penguin diagrams mediated by $H^{\pm}_{1,2}$ and T can be parametrized as:

$$\mathcal{H}^{NP}_{b\to s\gamma} = k^2\, \bar{s}\, \gamma^\mu \left(A_L P_L + A_R P_R\right) b\, A_\mu + \bar{s}\, \sigma^{\mu\nu} \left(B_L P_L + B_R P_R\right) b\, F_{\mu\nu}\,, \tag{14}$$

where k_μ is the momentum of the emitted photon, and $F_{\mu\nu}$ is the field strength tensor of the electromagnetic field. For an on-shell photon, i.e., $k^2 = 0$, only the dipole operators contribute. By dimensional analysis, since A_L and A_R are associated with vector currents and the chiralities in the initial and final states of quarks are the same, A_L and A_R are proportional to $1/m_T^2$ if T-quark is the heaviest particle in the model. As a result, the processes $b \to s\,\ell^-\,\ell^+$ from the off-shell photon are indeed suppressed and negligible.

The situation for the dipole operators is more complicated. By dimensional analysis, $B_{L,R}$ can depend on m_b/m_T^2 and $1/m_T$, where m_b arises from the application of the equation of motion or chirality flip in the b-quark propagator. Since $m_s \ll m_b$, we take $m_s \approx 0$. In terms of the weak states of η_1^+ and χ^+, one can easily understand that the contribution from each of η_1^+ and χ^+ results in the dependence of m_b/m_T^2. Since η_1^+ and χ^+ only couple to the left-handed and the right-handed quarks, respectively, to flip the chirality of the b-quark in the tensor-type weak currents, the mass effect of b-quark must appear. Hence, the dimension-4 Hamiltonian mediated by η_1^+/χ^+ leads to $B_{R,L} \propto m_b/m_T^2$.

When considering the mixing effect of η_1^+ and χ^+, the chirality flip in the tensor-type current is automatically satisfied. Moreover, instead of the m_b effect, a mass insertion factor appears in the propagator of T that runs in the photon-penguin loop. Consequently, the contributions from the η_1^+-χ^+ mixing are expected to be $B_{L,R} \propto c_\theta s_\theta/m_T$, which are larger than those from the individual η_1^+ and χ^+ contributions. The dominant effects of $B_{L,R}$ can then be expressed as:

$$\begin{aligned} B_L &= \frac{(2+Q_T)c_\theta s_\theta}{32\pi^2 m_T} Y^L_{T2} Y^{R*}_{T3} \left(J_1(z_{H_2^+}) - J(z_{H_1^+})\right)\,, \\ B_R &= \frac{(2+Q_T)c_\theta s_\theta}{32\pi^2 m_T} Y^R_{T2} Y^{L*}_{T3} \left(J_1(z_{H_2^+}) - J(z_{H_1^+})\right)\,, \end{aligned} \tag{15}$$

with $z_{H_i^+} \equiv m^2_{H_i^+}/m_T^2$. To avoid the constraint on $\mathbf{Y}_T^{R,L}$ from $b \to s\gamma$, we can either consider s_θ to be sufficiently small or $m_{H_1^+} \sim m_{H_2^+}$ for a subtle cancellation in $J_1(z_{H_2^+}) - J(z_{H_1^+})$. For numerical illustration purposes, we rewrite Eq. (14) in terms of the standard magnetic

dipole operators as:

$$\mathcal{H}^{\rm NP}_{b\to s\gamma} = -\frac{G_F V^*_{ts} V_{tb}}{\sqrt{2}} \left(C^{\rm NP}_7 O_{7\gamma} + C'^{\rm NP}_{7\gamma} O'_{7\gamma} \right) , \tag{16}$$
$$O^{(\prime)}_{7\gamma} = \frac{e m_b}{4\pi^2} \bar{s}\, \sigma_{\mu\nu} P_{R(L)}\, b\, F^{\mu\nu} .$$

The SM results are $C^{\rm SM}_{7\gamma} \approx -0.3$ and $C'^{\rm SM}_{7\gamma} \approx 0$. Using the typical values of the parameters: $m_T = 1.2$ TeV, $m_{H^+_1} = 0.6$ TeV, $m_{H^+_2} = 0.8$ TeV, $s_\theta = 0.1$, and $Y^L_{T2} Y^{R*}_{T3} \sim Y^L_{T2} Y^{R*}_{T3} \sim 0.1$, we obtain $|C^{(\prime)\rm NP}_{7\gamma}/C^{SM}_{7\gamma}| \sim 0.19$. As no anomalous signals are found in the $b \to s\gamma$ processes, we can simply suppress $C^{(\prime)\rm NP}_{7\gamma}$ without further limiting the Yukawa couplings $\mathbf{Y}^{R,L}_T$, which are the primary factors contributing to the $|\Delta F| = 1$ and $|\Delta F| = 2$ ($F = K$, B_d, and B_s) processes in the model.

C. $|\Delta F| = 2$ from box diagrams

Among loop-induced FCNCs involving the down-type quarks, the essential and most well-measured processes are K and B_q ($q = d, s$) meson oscillations, characterized by the mass differences between their mass eigenstate, denoted by $\Delta m_{K,\, B_q}$. To evaluate the impact of new physics effects in the model on the $|\Delta F| = 2$ processes, we derive the Δm_F, including the SM contributions, as follows.

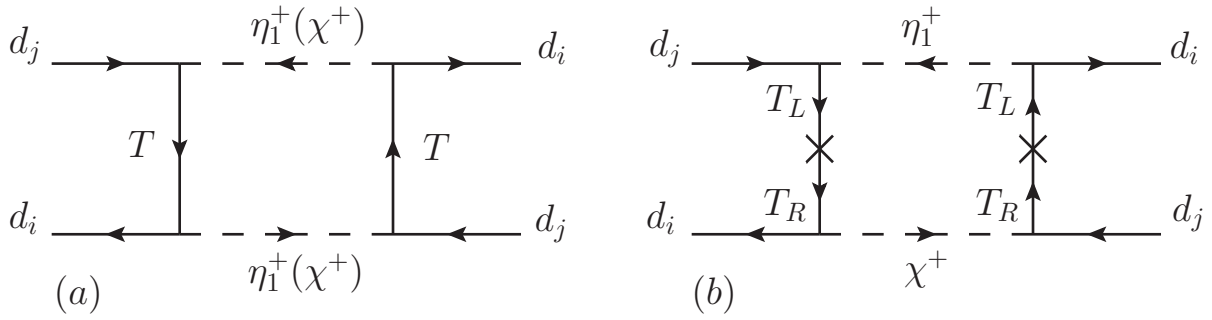


FIG. 1: Selected Feynman diagrams for $|\Delta F| = 2$ processes.

Since there is no FCNC coupling at the tree level, the $|\Delta F| = 2$ processes have to arise from the box diagrams, and the representative Feynman diagrams are sketched in Fig. 1, where the left-handed plot shows the mediation of η^+_1-η^+_1 and χ^+-χ^+, and the right-handed plot shows that of η^+_1-χ^+. Since the four fermions in the external legs of the box diagrams

lead to dimension-6 operators, the associated effective coefficients in the induced Hamiltonian have to be proportional to $1/m_T^2$. Although a m_T^2 factor appears at the propagators of T via the mass insertions, the dependence of $1/m_T^2$ is not changed in Fig. 1(b) because the denominator of the loop integrand has an eighth power of momentum in four-dimensional momentum integral. Therefore, the final result still shows the dependence of $1/m_T^2$. Using the Yukawa couplings shown in Eq. (5), the effective Hamiltonian for $|\Delta F| = 2$ can be obtained as:

$$\begin{aligned}\mathcal{H}^{\rm NP}(|\Delta F|=2) =& \frac{c_\theta^4}{4(4\pi)^2 m_T^2}(Y_{Ti}^R Y_{Tj}^{R*})^2 J_1(z_{H_1^+})\,\overline{d_i}\gamma_\mu P_L d_j\,\overline{d_i}\gamma^\mu P_L d_j \\ &+ \frac{c_\theta^4}{4(4\pi)^2 m_T^2}(Y_{Ti}^L Y_{Tj}^{L*})^2 J_1(z_{H_2^+})\,\overline{d_i}\gamma_\mu P_R d_j\,\overline{d_i}\gamma^\mu P_R d_j \\ &- \frac{c_\theta^4}{(4\pi)^2 m_T^2}\left(Y_{Ti}^L Y_{Tj}^{L*} Y_{Ti}^R Y_{Tj}^{R*}\right) J_2(z_{H_1^+}, z_{H_2^+})\,\overline{d_i}P_L d_j\,\overline{d_i}P_R d_j\,,\end{aligned} \tag{17}$$

where all involved Feynman diagrams have been considered, the small contributions from the dependence of s_θ and m_b are neglected, and the flavor index pairs $(i,\, j) = (2,\, 1)$, $(3,\, 1)$, and $(3,\, 2)$ correspond to the K, B_d, and B_s mesons, respectively. The loop integral function J_1 is the same as that in Eq. (13), and J_2 is given by

$$J_2(w,x) = -\frac{1}{(1-w)(1-x)} - \frac{1}{w-x}\left[\frac{w\ln w}{(1-w)^2} - \frac{x\ln x}{(1-x)^2}\right]. \tag{18}$$

The mass differences between the heavy and light neutral K/B_q mesons are defined as:

$$\begin{aligned}\Delta m_K &= 2\ {\rm Re}(M_{12}^K) = 2\ {\rm Re}(\langle \bar{K}|\mathcal{H}(|\Delta S|=2)|K\rangle)\,, \\ \Delta m_{B_q} &= 2\,|M_{12}^{B_q}| = 2\,|\langle \bar{B}_q|\mathcal{H}(|\Delta S|=2)|B_q\rangle|\,.\end{aligned} \tag{19}$$

To estimate the matrix elements of M_{12}^K and $M_{12}^{B_q}$ contributed from the new physics effects, we apply the results obtained in Ref. [34], where the QCD renormalization group effects from a high energy scale to a low μ scale are included. To apply the results from Ref. [34], the $|\Delta F| = 2$ Hamiltonian is parametrized by

$$\mathcal{H}(|\Delta F|=2) = \frac{G_F^2}{16\pi^2} m_W^2 \sum_i C_i(\mu) Q_i\,, \tag{20}$$

where the operators Q_i are defined as [34]:

$$Q_1^{\rm VLL} = (\overline{d_i}\gamma_\mu P_L d_j)(\overline{d_i}\gamma^\mu P_L d_j)\,, \tag{21a}$$

$$Q_1^{\rm LR} = (\overline{d_i}\gamma_\mu P_L d_j)(\overline{d_i}\gamma^\mu P_R d_j)\,, \tag{21b}$$

$$Q_2^{\rm LR} = (\overline{d_i} P_L d_j)(\overline{d_i} P_R d_j)\,, \tag{21c}$$

$$Q_1^{\rm SLL} = (\overline{d_i} P_L d_j)(\overline{d_i} P_L d_j)\,, \tag{21d}$$

$$Q_2^{\rm SLL} = (\overline{d_i}\sigma_{\mu\nu} P_L d_j)(\overline{d_i}\sigma^{\mu\nu} P_L d_j)\,. \tag{21e}$$

Here we have suppressed the color indices. Since the matrix elements of the operators VRR and SRR are the same as those of VLL and SLL, we do not explicitly show these operators in Eq. (21). The master formula for the meson-antimeson matrix element is expressed as [34]:

$$\begin{aligned} M_{12}^{\rm F,NP} =& \frac{G_F^2}{16\pi^2} m_W^2 \frac{F_F^2 m_F}{3} \left[P_1^{\rm VLL} \left(C_1^{\rm VLL} + C_1^{\rm RLL} \right) + P_1^{\rm LR} C_1^{\rm LR} + P_2^{\rm LR} C_2^{LR} \right. \\ & \left. + P_1^{\rm SLL} \left(C_1^{\rm SLL} + C_1^{\rm SRR} \right) + P_2^{\rm SLL} \left(C_2^{\rm SLL} + C_2^{\rm SRR} \right) \right] , \end{aligned} \tag{22}$$

where P_i^α include the non-perturbative bag parameters and QCD running factors, C_i^α denote the effective coefficients at the high energy scale, and F_F is the decay constant of meson F. The values of P_i^α are shown in Table I [34]. We note that with the exception of $P_1^{\rm VLL}$, the values of P_i^α in the K meson are one order of magnitude larger than those in the B_q meson due to the factor of $m_F^2/(m_{d_i} + m_{d_j})^2$. This factor in K is approximately 20 times larger than that in B_q.

TABLE I: Values of P_i^α used to estimate the matrix elements of the K, B_d, and B_s mesons.

	$P_1^{\rm VLL}$	P_1^{LR}	$P_2^{\rm LR}$	P_1^{SLL}	P_2^{SLL}
K	0.48	-36.1	59.2	-18.1	-32.2
B_d	0.84	-1.62	2.46	-1.47	-2.98
B_s	0.94	-1.83	2.78	-1.66	-3.37

From Eq. (17), the involved four-fermion operators are $Q_1^{\rm VLL,VRR}$ and Q_2^{LR}. Using the master formula in Eq. (22), the resulting mixing matrix element for F transition to $\bar{F}$ can

then be written as:

$$M_{12}^{\rm F,NP} = \frac{F_F^2 m_F c_\theta^4}{48\pi^2 m_T^2}\left[\frac{P_1^{VLL}}{4}\left((Y_{Ti}^R T_{Tj}^{R*})^2 J_1(z_{H_1^+}) + (Y_{Ti}^L T_{Tj}^{L*})^2 J_1(z_{H_2^+})\right)\right.$$
$$\left. -\ P_2^{LR}\left(Y_{Ti}^R Y_{Tj}^{R*}\right)\left(Y_{Ti}^L Y_{Tj}^{L*}\right) J_2(z_{H_1^+}, z_{H_2^+})\right]. \tag{23}$$

In order to combine the SM contributions, we write the SM results as [35]:

$$M_{12}^{\rm K,SM} = \frac{G_F^2 m_W^2}{12\pi^2} F_K^2 m_K \hat{B}_K \left[\lambda_c^2 \xi_1 S_0(x_c) + \lambda_t^2 \xi_2 S_0(x_t) + 2\lambda_c\lambda_t \xi_3 S_0(x_c,\, x_t)\right]$$
$$M_{12}^{\rm B_q,SM} = \frac{G_F^2 m_W^2}{12\pi^2} \lambda_t^2 F_{B_q}^2 m_{B_q} \hat{B}_{B_q} \xi_B S_0(x_t)\,, \tag{24}$$

where $\lambda_k = V_{ki}^* V_{kj}$; $\xi_{1,2,3} = (1.87 \pm 0.76,\, 0.5765 \pm 0.0065,\, 0.496 \pm 0.047)$ [36] and $\xi_B = 0.5510 \pm 0.0022$ [37, 38] are the QCD correction factors, and $\hat{B}_F$ is the renormalization scale-independent bag parameter. With $x_f \equiv m_f^2/m_W^2$, the S_0 functions are read as [35]:

$$S_0(x_c) = x_c\,,$$
$$S_0(x_t) = \frac{4x_t - 11x_t^2 + x_t^3}{4(1-x_t)^2} - \frac{3x_t^3 \ln x_t}{2(1-x_t)^3}\,, \tag{25}$$
$$S_0(x_c, x_t) = x_c\left(\ln\frac{x_t}{x_c} - \frac{3x_t}{4(1-x_t)} - \frac{3x_t^2 \ln x_t}{4(1-x_t)^2}\right).$$

Accordingly, the transition matrix element by combining the SM result and the charged-Higgs mediated effects is given by $M_{12}^F = M_{12}^{\rm F,SM} + M_{12}^{\rm F,NP}$. Using Eq. (19), we can obtain Δm_F.

D. Z-penguin induced $d_i \to d_j(\nu\bar{\nu}, \ell^-\ell^+)$

As alluded to earlier, the $d_i \to d_j \ell^-\ell^+$ processes mediated through the photon-penguin diagrams have negligible contributions due to the $1/m_T^2$ suppression. Box diagrams, mediated by T and N and governed by the Yukawa couplings $\mathbf{y}_1$, can also induce $d_i \to d_j \ell^-\ell^+$. However, similar to the $|\Delta F| = 2$ case, the induced dimension-6 four-fermion operators of $d_i d_j \ell^-\ell^+$ are suppressed by $1/m_T^2$. Therefore, the primary contributions to $d_i \to d_j \ell'\overline{\ell'}$ ($\ell' = \nu_\ell, \ell^\pm$) in the model are predominantly from the Z-penguin diagrams. The dominant Feynman diagram is depicted in Fig. 2.

Analogous to Eq. (14), the loop-induced $d_i d_j Z^*$ vertices generally contain structures of vector and tensor currents. Through dimensional analysis and consideration of quark

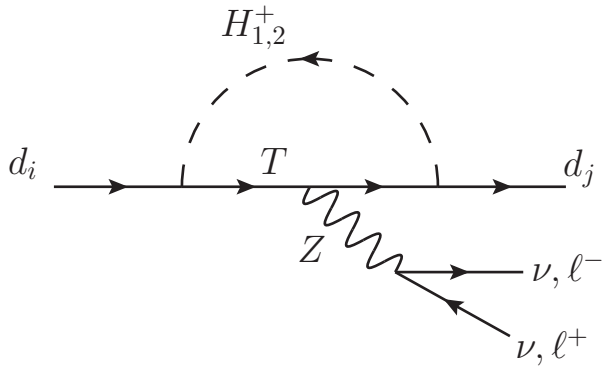


FIG. 2: Dominant Z-penguin Feynman diagrams for $d_i \to d_j(\nu\bar{\nu},\, \ell^-\ell^+)$.

chirality, it can be found that the effective coefficients associated with the tensor currents are proportional to $c_\theta\, m_{d_i}/m_T^2$ and s_θ/m_T, where the former corresponds to the contributions from $\eta_1^+(\chi^+)$, and the latter is from the mixing of η_1^+ and χ^+. As the tensor operator $\overline{d_j}\sigma_{\mu\nu}d_i Z^{\mu\nu}$ relates to the transition momentum $k_\mu = p_i - p_j$, roughly of the order of m_{d_i}, its contributions to $d_i \to d_j\ell'\overline{\ell'}$ are indeed suppressed by $c_\theta\, m_{d_i}\mathcal{O}(m_{d_i})/m_T^2$ and $s_\theta\mathcal{O}(m_{d_i})/m_T$. Hence, we can neglect the effects of the tensor operators.

Furthermore, when all Feynman diagrams, including self-energy diagrams, are considered to cancel the ultraviolet divergences, the dominant effects of Fig. 2 arise from the vector currents. Retaining the same chirality in the initial and final quarks requires a double mass insertion in the T-quark propagator; thus, the suppression factor of $1/m_T^2$ is replaced by the factor of m_T^2 in the induced effective coefficients. As a result, the effective Hamiltonian for $d_i \to d_j\ell\overline{\ell'}$ can be derived as:

$$\mathcal{H}^{\rm NP}_{d_i\to d_j\ell'\overline{\ell'}} = -\sqrt{2}\, G_F\, \overline{d_j}\gamma_\mu \left(C^L_{Zji}P_L + C^R_{ji}P_R\right) d_i\, \overline{\ell'}\gamma^\mu \left(c_V^{\ell'} - c_A^{\ell'}\gamma_5\right)\ell'\,, \tag{26}$$

where $c_V^{\ell'} = I^3_{\ell'} - 2s_W^2 Q_{\ell'}$ and $c_A^{\ell'} = I^3_{\ell'}$ with $I^3_{\ell'}$ being the third weak isospin of ℓ', and the induced coefficients $C_Z^{L,R}$ and loop integral function J_Z are given as:

$$\begin{aligned} C^L_{Zji} &= \frac{2Q_T s_W^2 c_\theta^2}{16\pi^2} Y^R_{Tj} Y^{R*}_{Ti} J_Z\left(z_{H_1^+}\right)\,, \\ C^R_{Zji} &= \frac{2Q_T s_W^2 c_\theta^2}{16\pi^2} Y^L_{Tj} Y^{L*}_{Ti} J_Z\left(z_{H_2^+}\right)\,, \\ J_Z(x) &= \frac{1}{1-x} + \frac{x\ln x}{(1-x)^2}\,. \end{aligned} \tag{27}$$

When $x \to 0$ and $x \to 1$, the asymptotic values of $J_Z(x)$ are 1 and 1/2, respectively.

Therefore, if we take the scheme of $s_\theta \ll 1$, the primary free parameters in the matrices $\mathbf{C}_Z^{L,R}$ are $\mathbf{Y}_T^{L,R}$.

IV. OBSERVABLES IN RARE B AND K DECAYS

Based on the Z-mediated interactions shown in Eq. (26), we discuss their contributions to the rare B and K decays in this section. The processes of interest inlcude $B \to K^{(*)}\nu\bar{\nu}$, $K^+ \to \pi^+\nu\bar{\nu}$, $K_L \to \pi^0\nu\bar{\nu}$, $B_s \to \mu^-\mu^+$, and inclusive $B \to X_s\ell^-\ell^+$ decays. Since the influence on the angular observables of $B \to K^*\ell^-\ell^+$ is found to be insignificant for the parameters that enhance the BR of $B^+ \to K^+\nu\bar{\nu}$, we do not discuss them in this study.

A. $B \to (K, K^*)\nu\bar{\nu}$

Combining Eq. (26) with the interactions in the SM, the effective Hamiltonian for $b \to s\nu\bar{\nu}$ is written as:

$$\begin{aligned}\mathcal{H}_{b\to s\nu\bar{\nu}} =& \frac{4G_F}{\sqrt{2}}\frac{\alpha}{2\pi s_W^2}\left[\left(V_{ts}^*V_{tb}X_t - \frac{\sqrt{2}G_F C_{Z23}^L}{C_{\rm SM}^\nu}\right)\bar{s}\gamma^\mu P_L b\bar{\nu}\gamma_\mu P_L\nu\right.\\ &\left. - \frac{\sqrt{2}G_F C_{Z23}^R}{C_{\rm SM}^\nu}\bar{s}\gamma^\mu P_R b\bar{\nu}\gamma_\mu P_L\nu\right] ,\end{aligned} \tag{28}$$

where the neutrino flavors are suppressed, $\alpha = e^2/4\pi$, $X_t = 1.481 \pm 0.009$ [39], and $C_{\rm SM}^\nu = 2G_F\alpha/(\sqrt{2}\pi s_W^2)$. The q^2-dependent differential decay rate of $B \to K\nu\bar{\nu}$ is obatined as:

$$\frac{d\Gamma}{dq^2}(\bar{B} \to K\nu\bar{\nu}) = \frac{d\Gamma^{\rm SM}}{dq^2}(B \to K\nu\bar{\nu})\left|1 - \frac{\sqrt{2}G_F(C_{Z23}^L + C_{Z23}^R)}{V_{ts}^*V_{tb}X_tC_{\rm SM}^\nu}\right|^2 . \tag{29}$$

Since the new interactions are lepton flavor-conserving and involve only the vector currents, we can factorize the new physics effects as a q^2-independent scalar factor. Therefore, the ratio of BR in the model to the SM prediction can be simplified as:

$$R_K^\nu = \frac{\mathcal{B}(B^+ \to K^+\nu\bar{\nu})}{\mathcal{B}(B^+ \to K^+\nu\bar{\nu})^{\rm SM}} = \left|1 - \frac{\sqrt{2}G_F(C_{Z23}^L + C_{Z23}^R)}{V_{ts}^*V_{tb}X_tC_{\rm SM}^\nu}\right|^2 . \tag{30}$$

Using the form factors of $\bar{B} \to K^*$ defined in Appendix B, the partial differential decay

rate for $B \to K^* \nu\bar{\nu}$ is

$$\begin{aligned}\frac{d\Gamma}{dq^2}(B \to K^* \nu\bar{\nu}) =& \frac{G_F^2 \alpha^2}{256\pi^5 s_W^4 m_B^3} q^2 \sqrt{\lambda_{K^*}} \left[\left| V_{ts}^* V_{tb} X_t + \frac{\sqrt{2} G_F}{C_{\rm SM}^\nu} (C_{Z23}^L - C_{Z23}^R) \right|^2 H_{V,0}^2 \right. \\ &+ \left(\left| V_{ts}^* V_{tb} X_t + \frac{\sqrt{2} G_F C_{Z23}^L}{C_{\rm SM}^\nu} \right|^2 + \left| \frac{\sqrt{2} G_F C_{Z23}^R}{C_{\rm SM}^\nu} \right|^2 \right) \left(H_{V,+}^2 + H_{V-}^2 \right) \\ &\left. -4\,{\rm Re} \left(\left(V_{ts}^* V_{tb} X_t + \frac{\sqrt{2} G_F C_{Z23}^L}{C_{\rm SM}^\nu} \right) \frac{\sqrt{2} G_F C_{Z23}^R}{C_{\rm SM}^\nu} \right) H_{V,+}\, H_{V,-} \right] ,\end{aligned} \tag{31}$$

where the q^2-dependent λ_{K^*} and polarization factors $H_{V,0(\pm)}$ of K^* are defined as [10]:

$$\lambda_P(q^2) = m_B^4 + m_P^4 + q^4 - 2m_B^2 m_P^2 - 2m_P^2 q^2 - 2m_B^2 q^2 \,, \tag{32a}$$

$$H_{V,0}(q^2) = \frac{8}{\sqrt{q^2}} m_B m_{K^*} A_{12}(q^2) \,, \tag{32b}$$

$$H_{V,\pm}(q^2) = (m_B + m_{K^*}) A_1(q^2) \mp \frac{\sqrt{\lambda_{K^*}}}{m_B + m_{K^*}} V(q^2) \,, \tag{32c}$$

with $A_{12}(q^2)$, $A_1(q^2)$, and $V(q^2)$ being the $\bar{B} \to K^*$ transition form factors. In our numerical estimates, we use the $\bar{B} \to K$ form factors obtained from the lattice QCD calculations [40], and the $\bar{B} \to K^*$ form factors obtained from the combination of light-cone sum rule and lattice QCD calculations [41]. To illustrate the influence of new physics, we define analogous to Eq. (30) the ratio:

$$R_{K^*}^\nu = \frac{\mathcal{B}(B_d \to K^{*0} \nu\bar{\nu})}{\mathcal{B}(B_d \to K^{*0} \nu\bar{\nu})^{\rm SM}} \,. \tag{33}$$

B. $K^+ \to \pi^+ \nu\bar{\nu}$ and $K_L \to \pi\nu\bar{\nu}$

The effective Hamiltonian for $d \to s\nu\bar{\nu}$ in the model is written as:

$$\begin{aligned}\mathcal{H}_{d\to s\nu\bar{\nu}} =& C_{\rm SM}^\nu \sum_{\ell=e,\mu\tau} \left[\left(V_{cs}^* V_{cd} X_{\rm NNL}^\ell + V_{ts}^* V_{td} X_t - \frac{\sqrt{2} G_F C_{Z21}^L}{C_{\rm SM}^\nu} \right) \bar{s}\gamma^\mu P_L d \right. \\ &\left. - \frac{\sqrt{2} G_F C_{Z21}^R}{C_{\rm SM}^\nu} \bar{s}\gamma^\mu P_R d \right] \bar{\nu}_\ell \gamma_\mu P_L \nu_\ell \,,\end{aligned} \tag{34}$$

where $X_{\rm NNL}^\ell$ denotes the contributions from the charm quark with the QCD corrections calculated up to next-to-next-to-leading (NNL) order [42, 43], and the two-loop electroweak corrections also included [44]. Using the results formulated in Refs. [39, 45], the BRs of the

$K^+ \to \pi^+ \nu\bar{\nu}$ and $K_L \to \pi^0 \nu\bar{\nu}$ decays can be obtained respectively as:

$$\begin{aligned}
\mathcal{B}(K^+ \to \pi^+ \nu\bar{\nu}) &= \kappa_+ (1 + \Delta_{\rm EM}) \left[\left(\frac{{\rm Im} X_{\rm eff}}{\lambda^5} \right)^2 + \left(\frac{{\rm Re}(V_{cs}^* V_{cd})}{\lambda} P_c(X) + \frac{{\rm Re}(X_{\rm eff})}{\lambda^5} \right)^2 \right] , \\
\mathcal{B}(K_L \to \pi^0 \nu\bar{\nu}) &= \mathcal{B}(K_L \to \pi^0 \nu\bar{\nu})^{\rm SM} \left| 1 - \frac{\sqrt{2} G_F \, {\rm Im}(C_{Z21}^L + C_{Z21}^R)}{{\rm Im}(V_{ts}^* V_{td}) X_t C_{\rm SM}^\nu} \right|^2 ,
\end{aligned} \tag{35}$$

where $\Delta_{\rm EM} = -0.003$ is the electromagnetic radiative corrections, and $\kappa_+ = (5.173 \pm 0.025) \times 10^{-11} (\lambda/0.225)^8$. Here $P_c(X) = P_c^{\rm SD}(X) + \delta P_{c,u} = 0.405 \pm 0.024$ denotes the charm-quark loop contributions, in which the short-distance part is given by [39]:

$$P_c^{\rm SD}(X) = \frac{1}{\lambda^4} \left(\frac{2}{3} X_{\rm NNL}^e + \frac{1}{3} X_{\rm NNL}^\tau \right) = 0.365 \pm 0.012 \, , \tag{36}$$

and the long-distance contribution is estimated as $\delta P_{c,u} = 0.04 \pm 0.02$ [46]. The factor $X_{\rm eff}$ that combines the SM and new physics effects is:

$$X_{\rm eff} = V_{ts}^* V_{td} X_t - \frac{\sqrt{2} G_F}{C_{\rm SM}^\nu} (C_{Z21}^L + C_{Z21}^R) \, . \tag{37}$$

Similar to R_{K,K^*}^ν, we will explore the new physics effects contributing to rare K decays by using the ratio of the BR in the model to the SM prediction, defined as:

$$R_\pi^\nu = \frac{\mathcal{B}(K \to \pi \nu\bar{\nu})}{\mathcal{B}(K \to \pi \nu\bar{\nu})^{\rm SM}} \, , \tag{38}$$

where $\pi = \pi^+(\pi^0)$ when $K = K^+(K_L)$.

It is worth mentioning that the new physics effects on $B^+ \to K^+ \nu\bar{\nu}$ and $K_L \to \pi^0 \nu\bar{\nu}$ can be factorized as a multiplicative factor as shown in Eqs. (30) and (35). Since we adopt $V_R^d = V_{\rm CKM}$ in this study, the multiplicative factor in both equations indeed is approximately the same when the Yukawa couplings follow the hierarchy of $y_{T1}^{R(L)} \ll y_{T2}^{R(L)} \ll y_{T3}^{R(L)}$ due to the constraints from the $|\Delta F| = 2$ processes. If the small CP phase of V_{ts} is neglected, the new physics effect in Eqs. (30) and (35) can be expressed as:

$$\frac{(C_{Z23}^L + C_{Z23}^R)}{V_{ts}^* V_{tb}} \approx \frac{{\rm Im}(C_{Z21}^L + C_{Z21}^R)}{Im(V_{ts}^* V_{td})} \approx \frac{2 Q_T s_W^2 c_\theta^2}{16\pi^2} \left[\left(y_{T3}^R + \frac{y_{T2}^R}{V_{ts}} \right) y_{T3}^R + R \to L \right] . \tag{39}$$

That is, we obtain $R_K^\nu \simeq R_{\pi^0}^\nu$ in the model. We will explicitly demonstrate the relationship in the numerical analysis.

C. $B \to X_s \ell^- \ell^+$ and $B_s \to \mu^- \mu^+$

The effective Hamiltonian for the inclusive and exclusive $b \to s\ell^-\ell^+$ decays, including the loop matrix element effects that arise from the tree- and penguin-induced four-quark operators, is given as:

$$\mathcal{H}_{b\to s\ell^-\ell^+} = -\frac{4G_F}{\sqrt{2}}\frac{\alpha}{4\pi}V_{ts}^*V_{tb}\left[\sum_{k=9,10}\left(C_k^{\rm eff}\mathcal{O}_k + C_k^{\prime\rm eff}\mathcal{O}_k'\right) - \frac{2m_b}{q^2}C_7^{\rm eff}\mathcal{O}_7\right] . \tag{40}$$

The effective operators in the model are

$$\mathcal{O}_9^{(\prime)} = \left(\bar{s}\gamma_\mu P_{L(R)}b\right)\left(\bar{\ell}\gamma^\mu\ell\right) \ , \tag{41a}$$

$$\mathcal{O}_{10}^{(\prime)} = \left(\bar{s}\gamma_\mu P_{L(R)}b\right)\left(\bar{\ell}\gamma^\mu\gamma_5\ell\right) \ , \tag{41b}$$

$$\mathcal{O}_7 = \left(\bar{s}i\sigma_{\mu\nu}q^\nu P_R b\right)\left(\bar{\ell}\gamma^\mu\ell\right) \ , \tag{41c}$$

and the effective coefficients, combining the SM contributions and the effects from the new Z-penguin diagrams, are given as:

$$C_9^{\rm eff} = C_9^{\rm eff,SM} + \frac{\sqrt{2}G_F}{C_{\rm SM}^\ell}c_V^\ell C_{Z23}^L \ , \tag{42a}$$

$$C_9^{\prime\rm eff} = \frac{\sqrt{2}G_F}{C_{\rm SM}^\ell}c_V^\ell C_{Z23}^R \ , \tag{42b}$$

$$C_{10}^{\rm eff} = C_{10}^{\rm eff,SM} - \frac{\sqrt{2}G_F}{C_{\rm SM}^\ell}c_A^\ell C_{Z23}^L \ , \tag{42c}$$

$$C_{10}^{\prime\rm eff} = -\frac{\sqrt{2}G_F}{C_{\rm SM}^\ell}c_A^\ell C_{Z23}^R \ , \tag{42d}$$

with $C_{SM}^\ell = G_F\alpha V_{ts}^*V_{tb}/(\sqrt{2}\pi)$. The SM results, obtained by ignoring the q^2-dependence at the energy scale of $\mu_b = 4.2$ GeV, are $C_9^{\rm eff,SM} \approx 4.114$, $C_{10}^{\rm eff,SM} \approx -4.193$, and $C_7^{\rm eff} = C_7^{\rm eff,SM} \approx -0.2957$ [47]. Their detailed NNLO results can be found in Refs. [48–50].

Since the new Z-mediated contributions to the angular observables of $B \to K^*\ell^-\ell^+$ are insignificant for the effects that enhance the $d_i \to s\nu\bar{\nu}$ processes, our attention focuses on the contributions to the $B \to X_s\ell^-\ell^+$ and $B_s \to \mu^-\mu^+$ processes, where both processes play a crucial role in constraining the parameters related to the $b \to s$ transition. Applying the interactions in Eq. (40), the differential decay rate for $b \to X_s\ell^-\ell^+$ as a function of

$s = q^2/m_b^2$ can be obtained as:

$$\frac{\Gamma(b \to X_s \ell^- \ell^+)}{ds} = \left(\frac{\alpha}{4\pi}\right)^2 \frac{G_F^2 m_b^5}{48\pi^3} |V_{ts}^* V_{tb}|^2 (1-s)^2 \Bigg[\left(4 + \frac{8}{s}\right) |C_7^{\rm eff}|^2 + (1+2s) \left(|C_9^{\rm eff}|^2 + |C_9^{\prime \rm eff}|^2 + |C_{10}^{\rm eff}|^2 + |C_{10}^{\prime \rm eff}|^2\right) + 12 C_7^{\rm eff} Re(C_9^{\rm eff} + C_9^{\prime \rm eff}) \Bigg] . \tag{43}$$

Notably, $\mathcal{O}_9^{(\prime)}$ and $\mathcal{O}_7$ do not contribute to the chirality suppression process $B_s \to \mu^- \mu^+$. The BR for $B_s \to \mu^- \mu^+$ arising from $\mathcal{O}_{10}^{(\prime)}$ is given as [54–56]:

$$\mathcal{B}(B_s \to \mu^- \mu^+) = \tau_{\mu^- \mu^-} \frac{G_F^2}{\pi} \left| \frac{\alpha V_{ts}^* V_{tb}}{4\pi} \right|^2 F_{B_s}^2 m_{B_s} m_\mu^2 \sqrt{1 - \frac{4m_\mu^2}{m_{B_s}}} \left| C_{10}' - C_{10} \right|^2 , \tag{44}$$

where $\tau_{\mu^- \mu^+}$ is the effective lifetime of B_s in the time-dependent $B_s \to \mu^- \mu^+$ decay and is related to the width difference between heavy and light B_s mesons. The simplified relation can be written as $\tau_{\mu^- \mu^+} = \tau_{B_s}/(1 - y_s)$ with $2y_s = \tau_{B_s} \Delta\Gamma_s = 0.128 \pm 0.007$ [51] and τ_{B_s} being the B_s lifetime. The Wilson coefficients $C_{10}^{(\prime)}$ are $C_{10}' = C_{10}^{\prime \rm eff}$ and

$$C_{10} = \eta_{\rm eff} \frac{0.315 x_t^{0.78}}{s_W^2} - \frac{\sqrt{2} G_F}{C_{\rm SM}^\ell} c_A^\ell C_{Z23}^L , \tag{45}$$

where $\eta_{\rm eff} = 0.9882 \pm 0.00024$ represents the QCD and electroweak corrections [52, 53].

V. NUMERICAL ANALYSIS AND DISCUSSIONS

There are only seven observables measured from the neutrino oscillation experiments. Therefore, the free parameters in the one-loop induced neutrino mass matrix given in Eq. (11), such as $m_{S_{1,2,N}}$, ϕ, and $y_{1i,2i}$, cannot be completely fixed. More related processes, such as $\ell_i \to \ell_j \gamma$, $\mu \to 3e$, $\mu - e$ conversion, and muon $g-2$, should be included and analyzed together. Since the m_N, ϕ, and $y_{1i,2i}$ parameters are irrelevant to the semileptonic B and K decays, we don't repeat the numerical analysis of the neutrino physics and lepton flavor-violating processes in this work. The relevant study with detailed analysis can be found in Ref. [29]. Hence, we focus on the contributions from the parameters $\mathbf{y}_T^{R,L}$, $m_{H_{1,2}^+}$ and their mixing angle θ, and m_T.

A. Numerical inputs and parameter constraints

As discussed earlier, the weak phases of $\mathbf{y}_T^{R,L}$ can be rotated away; therefore, six free parameters are involved in the quark Yukawa couplings. To satisfy the perturbativity re-

quirement, we assume their upper limits to be $|\mathbf{y}_{Ti}^{R,L}| < \sqrt{4\pi}$. According to the fact that $\Delta m_K \ll \Delta m_{B_d} < \Delta m_{B_s}$ and $\Delta m_{B_d}^{\rm exp}/\Delta m_{B_s}^{\rm exp} \sim \Delta m_{B_d}^{\rm SM}/\Delta m_{B_s}^{\rm SM} \sim \lambda^2$ with $\lambda \approx 0.225$ being one of the Wolfenstein parameters, we further restrict the upper bounds on the parameters to be $|y_{T3}^{R,L}| \lesssim 3.5$, $|y_{T2}^{R,L}| \lesssim 1$, and $|y_{T1}^{R,L}| \lesssim 0.5$ in the numerical calculations.

For the mass limit of the heavy quark T, we adopt the constraints based on the stop searches in R-parity conserving supersymmetry (SUSY). The data, obtained with an integrated luminosity of 139 fb^{-1} at $\sqrt{s} = 13$ TeV by ATLAS [57], show that mass below 1 TeV has been excluded when the neutralino mass is around 100 GeV. Since the lightest neutral inert scalar cannot be the DM in the model, i.e., $m_{S_{1,2}} > m_N$, the inert charged scalar should also be heavier than N. Thus, to reduce the number of free parameters in our numerical analysis, we fix the masses as follows: $m_T = 1.2$ TeV, $m_{H_1^+}^2/m_T^2 = 0.3$, and $m_{H_2^+}^2/m_T^2 = 0.4$. For the scenario with a small mixing angle θ, we fix $s_\theta = 0.1$ in the numerical estimates.

With the above-specified values of m_T and $m_{H_{1,2}^+}$, more than six experimental observables are required to determine the allowed ranges of $\mathbf{y}_T^{R,L}$. Since we want to consider the processes of $B \to K^{(*)}\nu\bar{\nu}$ and $K_L \to \pi^0\nu\bar{\nu}$ as predictions in the model, they should be excluded from the inputs. Based on the discussions in Secs. III and IV, the experimental inputs can be $\Delta m_{K,B_q}$, $B_s \to \mu^-\mu^+$, $B \to X_s\ell^-\ell^+$, $K^+ \to \pi^+\nu\bar{\nu}$ as well as the CP asymmetry in the $B \to J/\Psi K$ decay, denoted as $S_{J/\Psi K^0}$. Thus, we can use these seven observables to put bounds on the six free parameters. Their SM predictions and current experimental values are shown in Table II.

TABLE II: The experimental measurements and the SM predictions.

Obs.	$\Delta m_K \cdot 10^{15}$ [GeV]	$\Delta m_{B_d} \cdot 10^{13}$ [GeV]	$\Delta m_{B_s} \cdot 10^{12}$ [GeV]	$S_{J/\Psi K^0}$
Exp [33]	3.482 ± 0.006	3.332 ± 0.013	11.688 ± 0.004	0.699 ± 0.017
SM	5.8 ± 2.4 [58]	$3.618^{+1.052}_{-0.987}$ [38]	$11.053^{+3.618}_{-2.237}$ [38]	0.831 ± 0.116 [38]
Obs.	$\mathcal{B}(B_s \to \mu^-\mu^+) \cdot 10^9$	$\mathcal{B}(b \to X_s\ell^-\ell^+) \cdot 10^6$	$\mathcal{B}(K^+ \to \pi^+\nu\bar{\nu}) \cdot 10^{11}$	$\mathcal{B}(K_L \to \pi^0\nu\bar{\nu}) \cdot 10^{11}$
Exp	3.01 ± 0.35 [33]	5.8 ± 1.3 [33]	$11.4^{+4.0}_{-3.3}$ [33]	$< 2 \times 10^{-9}$ [59]
SM	$3.78^{+0.15}_{-0.10}$ [8]	4.15 ± 0.7 [60]	8.60 ± 0.42 [8]	2.94 ± 0.15 [8]

To determine the ranges of the free parameters that are consistent with the chosen ex-

perimental data, we employ the minimum chi-square approach, where the weighted χ^2 is defined as follows:

$$\chi^2 = \sum_i \frac{(O_i^{\rm th} - O_i^{\rm exp})^2}{\sigma_i^2} \,. \tag{46}$$

Here $O_i^{\rm th}$ and $O_i^{\rm exp}$ represent the central values of the i-th observable predicted by the model and measured in experiments, respectively. The weight factor $\sigma_i^2 = (\sigma_i^{\rm SM})^2 + (\sigma_i^{\rm exp})^2$ [61] combines the uncertainties from both SM predictions and experimental data.

With the assumed values of masses and ranges of Yukawa couplings, the minimum value of the weighted χ^2 for the seven observable inputs is $\chi^2_{\rm min} = 0.23$, while the χ^2 value in the SM is $\chi^2_{\rm SM} = 4.93$. The best-fit parameter values are $\mathbf{y}_T^{L,\rm min} \simeq (0.032,\, 0.150,\, 0.893)$ and $\mathbf{y}_T^{R,\rm min} = (0.024,\, 0.111,\, 0.813)$. To clearly understand the parameter correlations, we show contours of the χ^2 function in the planes of y^R_{T3}-y^R_{T2}, y^R_{T3}-y^R_{T1}, y^L_{T3}-y^L_{T2}, and y^L_{T3}-y^L_{T1} in Fig. 3(a)-(d), where the shaded areas represent probabilities of the χ^2 distribution within 68.27%, 95.45%, and 99.73% confidence level (CL), respectively. Note that when two parameters are selected as variables for the two-dimensional contours, the other parameters are held fixed at their best-fit values.

B. Numerical analysis of observables in rare B and K processes

Based on the results in Figs. 3(b) and (d), it is seen that the ranges of $y_{T1}^{R,L}$ are localized in narrow regions at around $y_{T1}^{R,\rm min}$ and $y_{T1}^{L,\rm min}$. To efficiently illustrate numerical results for the studied processes in two-dimensional contour plots, we always fix $y^R_{T1} = y^{R,\rm min}_{T1}$ and $y^L_{T1} = y^{L,\rm min}_{T1}$. Since the areas within 2σ CL in the y^R_{T3}-y^R_{T2} and y^L_{T3}-y^L_{T2} planes with $y^{R,T}_{T3} > 0$ have similar patterns and regions of parameters, we will demonstrate the observables in the rare B and K meson decays in the y^R_{T3}-y^R_{T2} and y^L_{T3}-y^R_{T3} planes. When we vary the parameters in the planes of y^R_{T3}-y^R_{T2} and y^L_{T3}-y^R_{T3} within the above-mentioned contour regions, the other parameters including $y_{T1}^{R,L}$ are fixed at $\mathbf{y}_T^{R,\rm min}$ and $\mathbf{y}_T^{L,\rm min}$.

According to R^ν_K and $R^\nu_{K^*}$ defined in Eqs. (30) and (33), the contours for R^ν_K (dashed) and $R^\nu_{K^*}$ (dot-dashed) in the y^R_{T3}-y^R_{T2} plane are shown in Fig. 4(a), with the values $R^\nu_K = (1, 5,\, 1.8,\, 2.0)$ and $R^\nu_{K^*} = (0.9,\, 1.0,\, 1.1,\, 1.2)$. The results indicate that R^ν_K can reach up to a factor of 2, while the influence of new physics effects in the model on $B \to K^*\nu\bar{\nu}$ is mild. Additionally, we show the BR of $B_s \to \mu^-\mu^+$ within the 1σ error of the experimental value in dotted curves. As stated in the introduction, a tension exists between the experimental

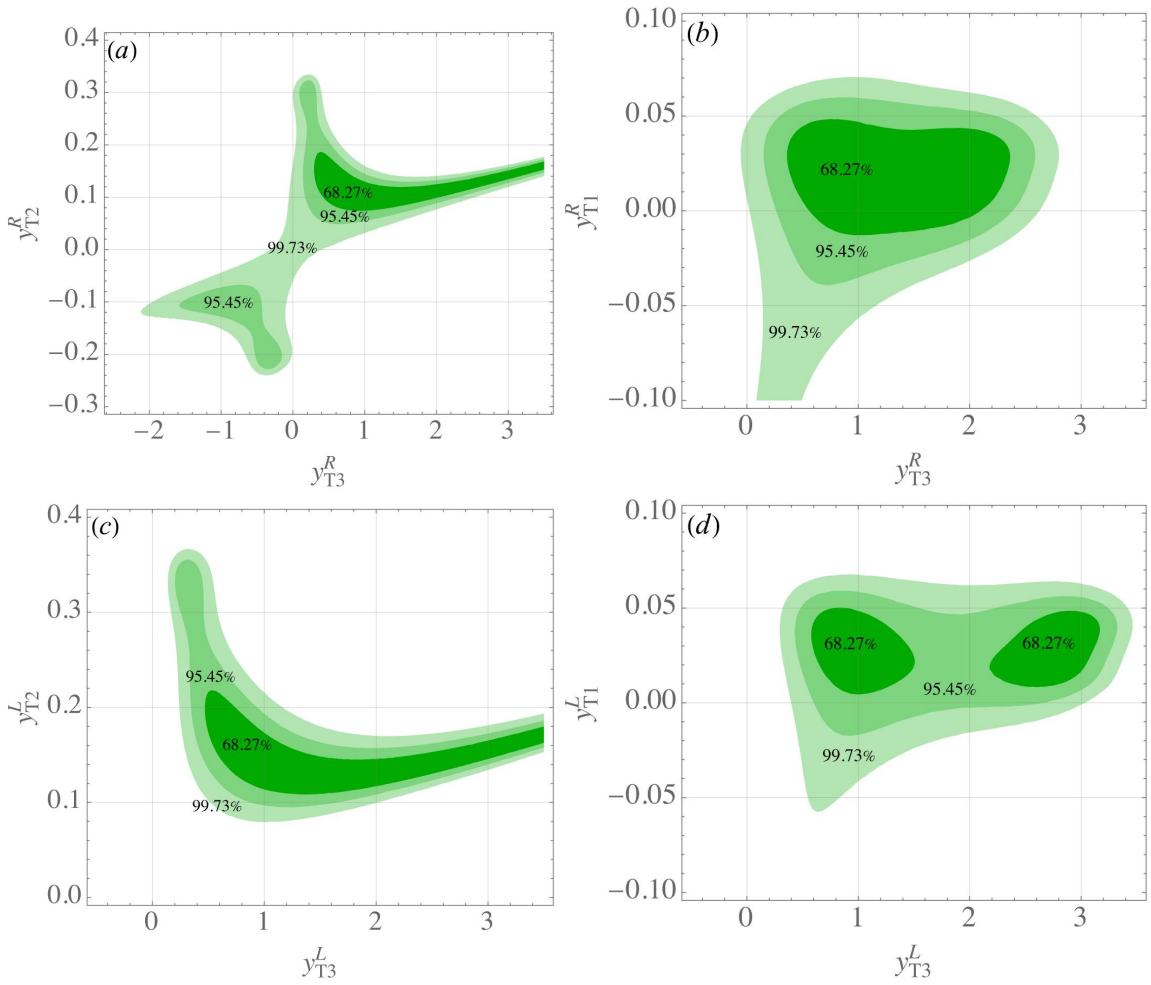


FIG. 3: Probabilities of χ^2 distribution within 68.27%, 95.45%, and 99.73% shown in the planes of (a) y^R_{T3}-y^R_{T2}, (b) y^R_{T3}-y^R_{T1}, (c) y^L_{T3}-y^L_{T2}, and (d) y^L_{T3}-y^L_{T1}.

data and SM prediction for $\mathcal{B}(B_s \to \mu^-\mu^+)$. Interestingly, the Z-penguin diagrams mediated by the inert charged scalars can resolve this tension and significantly enhance R^ν_K. For comparison, we show the χ^2 contours within the 3σ CL in the plot.

From the definition in Eq. (38), we show the contours for $R^\nu_{\pi^+}$ (dot-dashed) and $R^\nu_{\pi^0}$ (double-dot-dashed) in the plane of y^R_{T3} and y^R_{T2} in Fig. 4(b), with the values $R^\nu_{\pi^+} =$ (0.9, 1.3, 1.8) and $R^\nu_{\pi^0} =$ (1.2, 1.4, 1.8, 2.0), where the values of $R^\nu_{\pi^+}$ correspond the current experimental data with the 1σ error. The results indicate that $R^\nu_{\pi^0} = 2$ can be achieved within the 3σ CL in the model, and the BR for $K^+ \to \pi^+\nu\bar{\nu}$ can be enahnced up to the $+1\sigma$ upper value of $\mathcal{B}(K^+ \to \pi^+\nu\bar{\nu}) \simeq 15.4 \times 10^{-11}$ at $y^R_{T2} \sim 0.3$ and -0.2.

In Figs. 4(c) and (d), we project the allowed parameter space onto the y^R_{T3}-y^L_{T3} plane

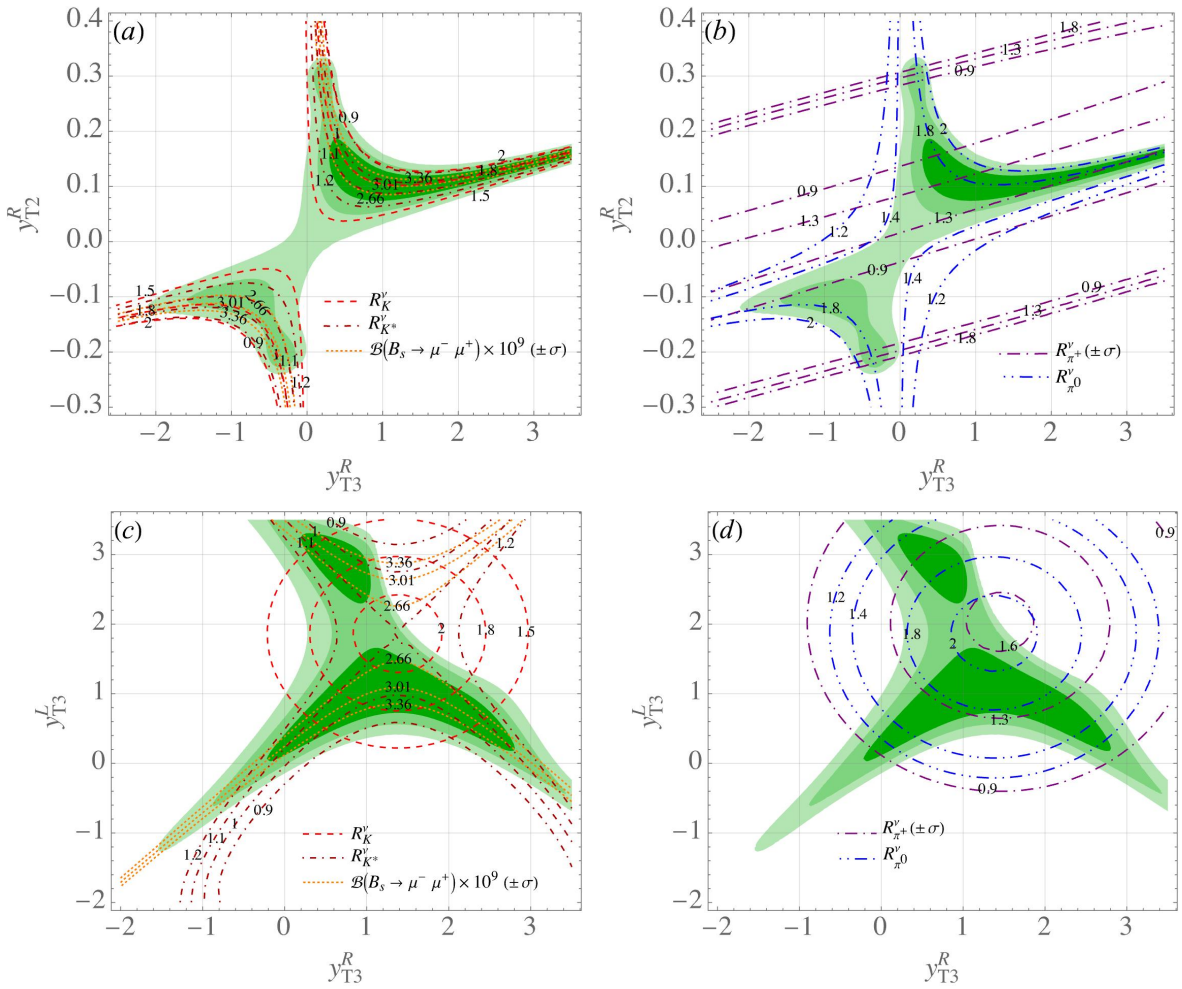


FIG. 4: Contours in the y^R_{T3}-y^R_{T2} plane for the observables of (a) R^ν, $R^\nu_{K^*}$, and $\mathcal{B}(B_s \to \mu^-\mu^+)$ and of (b) $R^\nu_{\pi^+}$ and $R^\nu_{\pi^0}$, where values of the parameters other than $y^R_{T3,T2}$ are taken to be their best-fit values at $\chi^2_{\rm min}$. In the plots, $\pm\sigma$ denotes that the experimental data within one standard deviation are applied. Plots (c) and (d) resemble plots (a) and (b), but in the y^L_{T3}-y^R_{T3} plane.

the same physical quantities as those shown in Figs. 4(a) and (b), where $y^{L,R}_{T3}$ are the only Yukawa couplings that can be of $\mathcal{O}(1)$ in our setting. Note that the contour of the $+1\sigma$ upper value $R^\nu_{\pi^+} = 1.8$ is outside the range, and we use $R^\nu_{\pi^+} = 1.6$ instead. It is observed that the contours of these observables in the y^R_{T3}-y^L_{T3} plane exhibit distinct patterns. $R^\nu_{K^*}$ and $\mathcal{B}(B_s \to \mu^-\mu^+)$ behave like hyperbolic curves, while R^ν_K and R^ν_π exhibit circular patterns. In Fig. 4(b), the $R^\nu_{\pi^0} = 1.2$ and 1.4 contours do not overlap with the parameter region within the 3σ CL; however, the $R^\nu_{\pi^0} = 1.2$ and 1.4 contours do cross over the region when viewed in the y^R_{T3}-y^L_{T3} plane of Fig. 4(d).

According to the results in Fig. 4, we observe that when $y_{T3}^{R(L)} \sim y_{T3}^{R(L),\min}$, R^{ν}_{K,π^+,π^0} can be significantly enhanced and that $\mathcal{B}(B_s \to \mu^-\mu^+)$ can fit the experimental central value. Thus, it is interesting to explore the dependence of the considered processes on the $y_{T2}^{R,L}$ parameters, with the other parameter values fixed at $\mathbf{y}_T^{R,\min}$ and $\mathbf{y}_T^{L,\mini}$. For illustration purposes, we show the contours as functions of y_{T2}^L and y_{T2}^R for R^{ν}_{K,K^*} and $\mathcal{B}(B_s \to \mu^-\mu^+)$ in Fig. 5(a) and for $R^{\nu}_{\pi^+,\pi^0}$ in Fig. 5(b). From the plots, it is evident that each observable in the selected values of contours can match the area within the 3σ CL. However, from Fig. 5(a), the curves of $R^{\nu}_{K^*} = 0.9$ and 1.2 do not overlap with the contours of $B_s \to \mu^-\mu^+$ in the R^{ν}_K-enhanced region within the 1σ error. The same behavior is also shown in Fig. 4(c). Hence, $R^{\nu}_{K^*}$ can be strictly bound by the measurement of $\mathcal{B}(B_s \to \mu^-\mu^+)$.

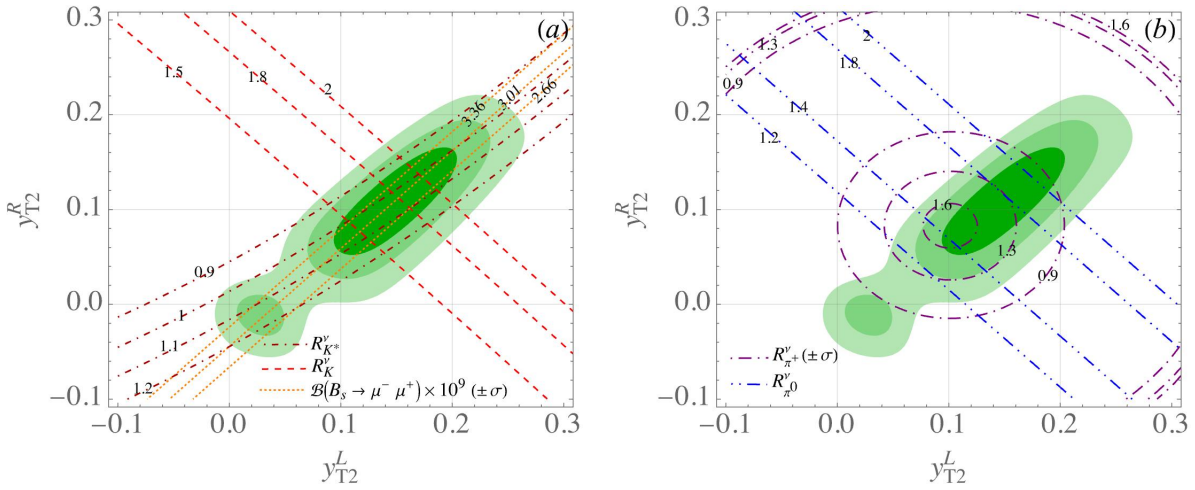


FIG. 5: Contours in the y_{T2}^L-y_{T2}^R plane for the observables of (a) R^{ν}, $R^{\nu}_{K^*}$, and $\mathcal{B}(B_s \to \mu^-\mu^+)$ and of (b) $R^{\nu}_{\pi^+}$ and $R^{\nu}_{\pi^0}$, where the parameter values, except for $y_{T2}^{L,R}$, are set to be $\mathbf{y}_T^{R(L),\min}$. In the plots, $\pm\sigma$ denotes that the experimental data within one standard deviation are applied.

To examine the correlations between observables, we need to vary all parameters simultaneously instead of merely varying two parameters as before. Based on the above analysis, except for $y_{T1}^{R(L)}$, which are fixed at the values of $y_{T1}^{R(L),\min}$, we set the ranges of the other parameters around $\mathbf{y}_T^{R(L),\min}$. We scan the parameters assuming a normal distribution with $\mathbf{y}_T^{R(L),\min}$ as the mean and setting the standard deviations as $\sigma(y_{T2}^{R(L)}) = y_{T2}^{R(L),\min}$ and $\sigma(y_{T3}^{R(L)}) = 0.1$. In addition to the 1σ experimental constraints shown in Table II, we further require that $\chi^2 - \chi^2_{\min} \lesssim 3.84$.

Using 10^7 sampling points, Fig. 6 shows the scatter plot depicting the correlations between

R_K^ν and R_M^ν with $M = K^*, \pi^+, \pi^0$ at 95% CL. As alluded to before, the result of $R_K^\nu \simeq R_{\pi^0}^\nu$ given in Eq. (39) is numerically verified. Both ratios can be enhanced up to a factor of 2. As expected, due to the introduction of right-handed quark currents, which are used to fit the observed BR for $B_s \to \mu^-\mu^+$, the influence of new physics effects on $R_{K^*}^\nu$ in the model is mild. It is observed that both $R_{\pi^+}^\nu$ and R_K^ν increase simultaneously when $R_K^\nu \lesssim 1.4$. Subsequently, when $R_K^\nu > 1.4$, $R_{\pi^+}^\nu$ decreases as R_K^ν increases. This behavior of $R_{\pi^+}^\nu$ can be understood as follows. The imaginary part of $X_{\rm eff}$, which also contributes to $K_L \to \pi^0\nu\bar{\nu}$ and is defined in Eq. (37), increases linearly with R_K^ν. However, the real part of $X_{\rm eff}$ decreases after $R_K^\nu \simeq 1.4$. Since $K^+ \to \pi^+\nu\bar{\nu}$ is dominated by the CP-conserving effect, this leads to a decrease in $\mathcal{B}(K^+ \to \pi^+\nu\bar{\nu})$ for $R_K^\nu > 1.4$, although the BR of the CP-violating process $K_L \to \pi^0\nu\bar{\nu}$ continues to increase. Since the resulting $\mathcal{B}(B_s \to \mu^-\mu^+)$ can be within 1σ errors of experimental data for any value of R_K^ν in the region of (1.2, 2.2), the scatter plot for the correlation between $\mathcal{B}(B_s \to \mu^-\mu^+)$ and R_K^ν is not shown. In all interesting regions of R_K^ν, the Z-penguin diagrams mediated by the charged Higgs bosons can alleviate the tension observed in $B_s \to \mu^-\mu^+$ between the experimental measurement and the SM prediction.

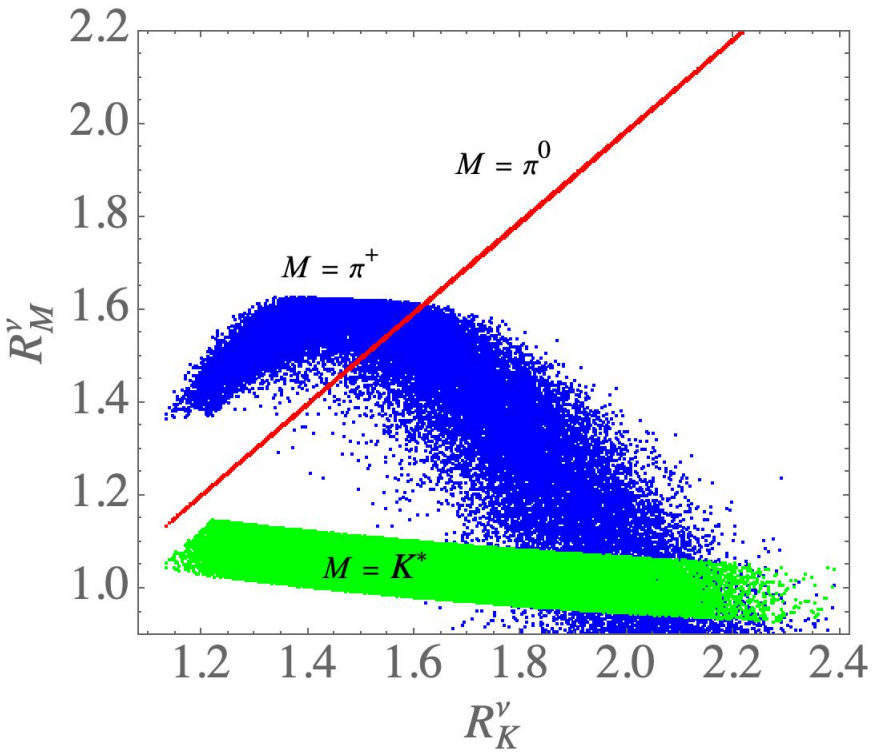


FIG. 6: Scatter plot illustrating the correlations between R_K^ν and R_M^ν with $M = K^*, \pi^+$, and π^0.

VI. SUMMARY

Scotogenesis, typically used for lepton-related phenomena such as neutrino mass and dark matter candidate, is rarely studied in the context of the quark flavor-related processes. Moreover, the minimal scotogenic model [24] cannot accommodate the muon $g-2$ anomaly. To apply the mechanisms in a scotogenic model to the quark FCNC processes and preserve the characteristic features of scotogenesis, we propose in this work a scotogenic model whose dark particles include a neutral Dirac-type dark lepton, two inert Higgs doublets with one carrying a dark charge, a charged singlet dark scalar, and a singlet vector-like up-type dark quark. As demonstrated above, each of these particles plays a crucial role in this study.

With appropriate dark charge assignments, the model has a dark $U(1)$ symmetry with which the scalar and pseudoscalar in the same inert Higgs doublet are degenerate in mass. Consequently, the inert scalars cannot be dark matter candidates. Nevertheless, the singlet dark neutral lepton does not couple to the Z boson and the SM Higgs boson, and can self-scatter into the SM particles through the Yukawa couplings; thus, it can be dark matter in the model.

With the introduction of a dark up-type quark, the SM quarks can couple to this dark quark via the non-leptonic inert Higgs doublet. As a result, the loop-induced Z-penguin diagrams make significant contributions to the $B^+ \to K^+\nu\bar{\nu}$ and $K \to \pi\nu\bar{\nu}$ processes. Furthermore, with the introduction of a singlet dark-charged scalar, not only can muon $g-2$ be enhanced, but also the right-handed quark current for the $b \to s$ transition can be induced. As a result, the tension in $B_s \to \mu^-\mu^+$ between the experimental measurement and the SM prediction can be resolved.

Acknowledgments

C.-W. C would like to thank the High Energy Physics Theory Group at the University of Tokyo for their hospitality during his visit when part of this work was finished. This work was supported in part by the National Science and Technology Council, Taiwan, under Grant Nos. NSTC-110-2112-M-006-010-MY2 (C.-H. Chen) and NSTC-111-2112-M-002-018-MY3 (C.-W. Chiang).

Appendix A: Saclar potential and masses of scalars

The scalar potential for the SM Higgs H, $\eta_{1,2}$, and χ^+ is written as:

$$\begin{aligned}
V =& V_{\rm SM} + V(H,\eta_1,\eta_2,\chi^\pm) \ , \\
V_{\rm SM} =& -\mu_H^2 H^\dagger H + \lambda_H (H^\dagger H)^2 \ , \\
V(H,\eta_1,\eta_2,\chi^\pm) =& \mu_1^2 \eta_1^\dagger \eta_1 + \mu_2^2 \eta_2^\dagger \eta_2 + \mu_3^2 \chi^- \chi^+ + (\mu_\chi \eta_1^T i\tau_2 H \chi^- + \text{H.c.}) + \lambda_1 (\eta_1^\dagger \eta_1)^2 \\
&+ \lambda_2 (\eta_2^\dagger \eta_2)^2 + \lambda_3 (\eta_1^\dagger \eta_1)(\eta_2^\dagger \eta_2) + \lambda_4 (\eta_1^\dagger \eta_2)(\eta_2^\dagger \eta_1) \\
&+ \left(\lambda_5 (H^\dagger \eta_1)(H^\dagger \eta_2) + \text{H.c.}\right) + \lambda_6 (H^\dagger \eta_1)(\eta_1^\dagger H) + \lambda_7 (H^\dagger \eta_2)(\eta_2^\dagger H) \\
&+ \lambda_8 (H^\dagger H)(\eta_1^\dagger \eta_1) + \lambda_9 (H^\dagger H)(\eta_2^\dagger \eta_2) + \lambda_{10} (\chi^- \chi^+)^2 \\
&+ (\chi^- \chi^+)(\lambda_{11} H^\dagger H + \lambda_{12} \eta_1^\dagger \eta_1 + \lambda_{13} \eta_2^\dagger \eta_2) \ .
\end{aligned} \tag{A1}$$

It can be seen that the non-self-Hermitian terms are the λ_5 and μ_χ terms, where the former violates the lepton number by two units and plays an important role in the radiative generation of the Majorana neutrino mass, and the latter leads to the mixing between $\eta_1^\pm$ and $\chi^\pm$. In addition to the leptonic Yukawa couplings shown in Eq. (3), the tiny neutrino mass can be achieved when $\lambda_5 \ll 1$. To spontaneously break the electroweak gauge symmetry, we take $\mu_H^2, \lambda_H > 0$ as in the SM. The masses of $\eta_{1,2}$ can be irrelevant to the electroweak symmetry breaking, and we thus require $\mu_{1,2}^2(\lambda_{1,2}) > 0$. Using the charge assignment shown in Eq. (2), the scalar potential in Eq. (A1) has an unbroken global $U(1)_X$ symmetry. To preserve the global $U(1)_X$ symmetry, the VEVs of $\eta_{1,2}$ are kept zero. Therefore, the components of the three doublet scalars are parametrized as follows ($j = 1, 2$):

$$H = \begin{pmatrix} G^+ \\ \frac{1}{\sqrt{2}}(v + h + iG^0) \end{pmatrix} \ , \quad \eta_j = \begin{pmatrix} \eta_j^+ \\ \frac{1}{\sqrt{2}}(\eta_j^0 + i a_j) \end{pmatrix} \ , \tag{A2}$$

where $G^{\pm,0}$ are the Goldstone bosons, v is the VEV of H, and h is the SM Higgs boson.

From Eq. (A1), $\eta_2^\pm$ does not mix with the other charged scalars. Its mass is given by:

$$m^2_{\eta_2^\pm} = \mu_2^2 + \frac{\lambda_9 v^2}{2} \ . \tag{A3}$$

Because $\eta_1^\pm$ mixes with $\chi^\pm$ via the μ_χ term, their mass-squared matrix is found to be:

$$\begin{aligned}
&(\eta_1^-, \chi^-) \begin{pmatrix} m_{11}^2 & m_{12}^2 \\ m_{12}^2 & m_{22}^2 \end{pmatrix} \begin{pmatrix} \eta_1^+ \\ \chi^+ \end{pmatrix} \ , \\
&\text{with } m_{11}^2 = \mu_1^2 + \frac{\lambda_8 v^2}{2} \ , \ m_{12}^2 = \frac{\mu_\chi v}{\sqrt{2}} \ , \ m_{22}^2 = \mu_3^2 + \frac{\lambda_{11} v^2}{2} \ .
\end{aligned} \tag{A4}$$

The mass matrix can be diagonalized by a 2×2 orthogonal rotation defined by

$$\begin{pmatrix} H_1^+ \\ H_2^+ \end{pmatrix} = \begin{pmatrix} c_\theta & s_\theta \\ -s_\theta & c_\theta \end{pmatrix} \begin{pmatrix} \eta_1^+ \\ \chi^+ \end{pmatrix} , \tag{A5}$$

where $c_\theta \equiv \cos\theta$ and $s_\theta \equiv \sin\theta$. As a result, the mass eigenvalues and the mixing angle are obtained as:

$$\begin{aligned} m^2_{1(2)} &= \frac{m^2_{11} + m^2_{22}}{2} \pm \frac{1}{2}\sqrt{(m^2_{22} - m^2_{11})^2 + 4(m^2_{12})^2}\,, \\ s_{2\theta} &= -\frac{2m^2_{12}}{m^2_2 - m^2_1}\,, \end{aligned} \tag{A6}$$

where $s_{2\theta} \equiv \sin 2\theta$.

Since the terms $(H^\dagger \eta_j)^2$ are forbidden by the $U(1)_X$ symmetry, the scalar η_j^0 and pseudoscalar a_j are degenerate in mass. Although the λ_5 term would mix $\eta_1^0(a_1)$ and $\eta_2^0(a_2)$, it will not lift the degeneracy. To obtain the mass spectrum of the neutral scalar bosons, we write the mass matrices for (η_1^0, η_2^0) and (a_1, a_2) as follows:

$$m_S^2 = \begin{pmatrix} \bar{m}^2_{11} & \bar{m}^2_{12} \\ \bar{m}^2_{12} & \bar{m}^2_{22} \end{pmatrix} , \quad m_A^2 = \begin{pmatrix} \bar{m}^2_{11} & -\bar{m}^2_{12} \\ -\bar{m}^2_{12} & \bar{m}^2_{22} \end{pmatrix} , \tag{A7}$$

where the matrix elements are:

$$\begin{aligned} \bar{m}^2_{11} &= \mu_1^2 + \frac{v^2}{2}(\lambda_6 + \lambda_8) \,, \\ \bar{m}^2_{22} &= \mu_2^2 + \frac{v^2}{2}\left(\lambda_7 + \lambda_9\right) \,, \\ \bar{m}^2_{12} &= \frac{v^2}{2}\lambda_5 \,. \end{aligned} \tag{A8}$$

Analogous to the case of the charged scalar mass matrix, each of the two 2×2 mass-squared matrices can be diagonalized by the corresponding orthogonal matrix $O(\theta_\zeta)$ $(\zeta = S, A)$ through $O(\theta_\zeta) m^2_\zeta O^T(\theta_\zeta)$, where

$$O(\theta_\zeta) = \begin{pmatrix} \cos\theta_\zeta & \sin\theta_\zeta \\ -\sin\theta_\zeta & \cos\theta_\zeta \end{pmatrix} . \tag{A9}$$

Since the matrix elements in m_A^2 are the same as those in m_S^2 except for the sign change in the off-diagonal elements, we therefore take $\theta_S = -\theta_A \equiv \phi$. The eigenvalues of m_S^2 are found to be:

$$m^2_{S_{1,2}} = \frac{1}{2}\left[\bar{m}^2_{11} + \bar{m}^2_{22} \pm \sqrt{(\bar{m}^2_{22} - \bar{m}^2_{11})^2 - 4(\bar{m}^4_{12})}\right] . \tag{A10}$$

For the physical pseudoscalars $A_{1,2}$, we have $m^2_{A_{1(2)}} = m^2_{S_{1(2)}}$. The mixing angle ϕ is defined by:

$$\sin 2\phi = -\frac{\lambda_5 v^2}{m^2_{S_2} - m^2_{S_1}} \ . \tag{A11}$$

Since the λ_5 term violates the lepton number and eventually leads to the Majorana mass, its value has to be sufficiently small, i.e., $\lambda_5 \ll 1$. As a result, the off-diagonal mass matrix element $|\bar{m}^2_{12}|$ is suppressed and the mixing angle $\phi \ll 1$.

Appendix B: Form factors for $\bar{B} \to (K, K^*)$

The q^2-dependent form factors for $\bar{B} \to K$ are defined through the following relations:

$$\begin{aligned}
\langle K(p_2)|V_\mu|\bar{B}(p_1)\rangle &= f_+(q^2)\left(P_\mu - \frac{P\cdot q}{q^2}\right) + \frac{P\cdot q}{q^2} f_0(q^2)\, q_\mu, \\
\langle K(p_2)|T_{\mu\nu}q^\nu|\bar{B}(p_1)\rangle &= \frac{f_T(q^2)}{m_B + m_K}\left(P\cdot q\, q_\mu - q^2 P_\mu\right) \ ,
\end{aligned} \tag{B1}$$

where $P = p_1 + p_2$, $q = p_1 - p_2$; $V_\mu = \bar{s}\gamma_\mu b$, and $T_{\mu\nu} = \bar{s} i\sigma_{\mu\nu} b$. For $\bar{B} \to K^*$, the form factors are parametrized as:

$$\begin{aligned}
\langle K^*(p_2,\epsilon)|V_\mu|\bar{B}(p_1)\rangle =& i\frac{V(q^2)}{m_B + m_{K^*}}\varepsilon_{\mu\alpha\beta\rho}\epsilon^{*\alpha}P^\beta q^\rho \ , \\
\langle K^*(p_2,\epsilon)|A_\mu|\bar{B}(p_1)\rangle =& 2m_{K^*}A_0(q^2)\frac{\epsilon^*\cdot q}{q^2}q_\mu + (m_B + m_{K^*})A_1(q^2)\left(\epsilon^*_\mu - \frac{\epsilon^*\cdot q}{q^2}q_\mu\right) \\
& - A_2(q^2)\frac{\epsilon^*\cdot q}{m_B + m_{K^*}}\left(P_\mu - \frac{P\cdot q}{q^2}q_\mu\right) \ , \\
\langle K^*(p_2,\epsilon)|T_{\mu\nu}q^\nu|\bar{B}(p_1)\rangle =& -iT_1(q^2)\varepsilon_{\mu\alpha\beta\rho}\epsilon^{*\alpha}P^\beta q^\rho \ , \\
\langle K^*(p_2,\epsilon)|T^5_{\mu\nu}q^\nu|\bar{B}(p_1)\rangle =& T_2(q^2)\left(\epsilon^*_\mu P\cdot q - \epsilon^*\cdot q P_\mu\right) + T_3(q^2)\epsilon^*\cdot q\left(q_\mu - \frac{q^2}{P\cdot q}P_\mu\right) \ .
\end{aligned} \tag{B2}$$

Here ϵ denotes the polarization vector of K^*, $A_\mu = \bar{s}\gamma_\mu\gamma_5 b$, and $T^5_{\mu\nu} = \bar{s} i\sigma_{\mu\nu}\gamma_5 b$. It is useful to define additional form factors $A_{12}(q^2)$ and $T_{23}(q^2)$:

$$16 m_B m^2_{K^*} A_{12}(q^2) = (m_B + m_{K^*})(m_B^2 - m^2_{K^*} - q^2)A_1(q^2) - \frac{\lambda_{K^*}(q^2)}{m_B + m_{K^*}}A_2(q^2) \ , \tag{B3}$$

$$8 m_B m^2_{K^*} T_{23}(q^2) = (m_B + m_{K^*})(m_B^2 + 3m^2_{K^*} - q^2)T_2(q^2) - \frac{\lambda_{K^*}(q^2)}{m_B - m_{K^*}}T_3(q^2) \ . \tag{B4}$$

---

[1] G. W. Bennett *et al.* [Muon g-2], Phys. Rev. D **73**, 072003 (2006) [arXiv:hep-ex/0602035 [hep-ex]].

[2] D. P. Aguillard *et al.* [Muon g-2], Phys. Rev. Lett. **131**, no.16, 161802 (2023) [arXiv:2308.06230 [hep-ex]].

[3] I. Adachi *et al.* [Belle-II], [arXiv:2311.14647 [hep-ex]].

[4] P. del Amo Sanchez *et al.* [BaBar], Phys. Rev. D **82**, 112002 (2010) [arXiv:1009.1529 [hep-ex]].

[5] J. P. Lees *et al.* [BaBar], Phys. Rev. D **87**, no.11, 112005 (2013) [arXiv:1303.7465 [hep-ex]].

[6] O. Lutz *et al.* [Belle], Phys. Rev. D **87**, no.11, 111103 (2013) [arXiv:1303.3719 [hep-ex]].

[7] J. Grygier *et al.* [Belle], Phys. Rev. D **96**, no.9, 091101 (2017) [arXiv:1702.03224 [hep-ex]].

[8] A. J. Buras, Eur. Phys. J. C **83**, no.1, 66 (2023) [arXiv:2209.03968 [hep-ph]].

[9] A. J. Buras, J. Girrbach-Noe, C. Niehoff and D. M. Straub, JHEP **02**, 184 (2015) [arXiv:1409.4557 [hep-ph]].

[10] T. E. Browder, N. G. Deshpande, R. Mandal and R. Sinha, Phys. Rev. D **104**, no.5, 053007 (2021) [arXiv:2107.01080 [hep-ph]].

[11] P. Asadi, A. Bhattacharya, K. Fraser, S. Homiller and A. Parikh, [arXiv:2308.01340 [hep-ph]].

[12] P. Athron, R. Martinez and C. Sierra, [arXiv:2308.13426 [hep-ph]].

[13] R. Bause, H. Gisbert and G. Hiller, [arXiv:2309.00075 [hep-ph]].

[14] L. Allwicher, D. Becirevic, G. Piazza, S. Rosauro-Alcaraz and O. Sumensari, [arXiv:2309.02246 [hep-ph]].

[15] T. Felkl, A. Giri, R. Mohanta and M. A. Schmidt, [arXiv:2309.02940 [hep-ph]].

[16] H. K. Dreiner, J. Y. Günther and Z. S. Wang, [arXiv:2309.03727 [hep-ph]].

[17] Y. Amhis, M. Kenzie, M. Reboud and A. R. Wiederhold, [arXiv:2309.11353 [hep-ex]].

[18] X. G. He, X. D. Ma and G. Valencia, [arXiv:2309.12741 [hep-ph]].

[19] C. H. Chen and C. W. Chiang, [arXiv:2309.12904 [hep-ph]].

[20] A. Datta, D. Marfatia and L. Mukherjee, Phys. Rev. D **109**, no.3, L031701 (2024) [arXiv:2310.15136 [hep-ph]].

[21] W. Altmannshofer, A. Crivellin, H. Haigh, G. Inguglia and J. Martin Camalich, [arXiv:2311.14629 [hep-ph]].

[22] F. Z. Chen, Q. Wen and F. Xu, [arXiv:2401.11552 [hep-ph]].

[23] B. F. Hou, X. Q. Li, M. Shen, Y. D. Yang and X. B. Yuan, [arXiv:2402.19208 [hep-ph]].

[24] E. Ma, Phys. Rev. D **73**, 077301 (2006) [hep-ph/0601225].

[25] P. Minkowski, Phys. Lett. B **67**, 421-428 (1977).

[26] T. Yanagida, Conf. Proc. C **7902131**, 95-99 (1979) KEK-79-18-95.

[27] M. Gell-Mann, P. Ramond and R. Slansky, Conf. Proc. C **790927**, 315-321 (1979) [arXiv:1306.4669 [hep-th]].

[28] R. N. Mohapatra and G. Senjanovic, Phys. Rev. Lett. **44**, 912 (1980).

[29] C. H. Chen, C. W. Chiang, T. Nomura and C. W. Su, JHEP **09**, 166 (2022) [arXiv:2201.10759 [hep-ph]].

[30] G. 't Hooft, "Naturalness, chiral symmetry, and spontaneous chiral symmetry breaking," NATO Sci. Ser. B **59**, 135-157 (1980).

[31] T. Toma and A. Vicente, JHEP **01**, 160 (2014) [arXiv:1312.2840 [hep-ph]].

[32] C. H. Chen and T. Nomura, JHEP **09**, 090 (2021) [arXiv:2001.07515 [hep-ph]].

[33] R. L. Workman *et al.* [Particle Data Group], PTEP **2022**, 083C01 (2022).

[34] A. J. Buras, S. Jager and J. Urban, Nucl. Phys. B **605**, 600-624 (2001) [arXiv:hep-ph/0102316 [hep-ph]].

[35] G. Buchalla, A. J. Buras and M. E. Lautenbacher, Rev. Mod. Phys. **68**, 1125-1144 (1996) [arXiv:hep-ph/9512380 [hep-ph]].

[36] J. Brod, M. Gorbahn and E. Stamou, Phys. Rev. Lett. **125**, no.17, 171803 (2020) [arXiv:1911.06822 [hep-ph]].

[37] A. J. Buras, M. Jamin and P. H. Weisz, Nucl. Phys. B **347**, 491-536 (1990).

[38] A. Lenz, U. Nierste, J. Charles, S. Descotes-Genon, A. Jantsch, C. Kaufhold, H. Lacker, S. Monteil, V. Niess and S. T'Jampens, Phys. Rev. D **83**, 036004 (2011) [arXiv:1008.1593 [hep-ph]].

[39] A. J. Buras, D. Buttazzo, J. Girrbach-Noe and R. Knegjens, JHEP **11**, 033 (2015) [arXiv:1503.02693 [hep-ph]].

[40] J. A. Bailey, A. Bazavov, C. Bernard, C. M. Bouchard, C. DeTar, D. Du, A. X. El-Khadra, J. Foley, E. D. Freeland and E. Gámiz, *et al.* Phys. Rev. D **93**, no.2, 025026 (2016) [arXiv:1509.06235 [hep-lat]].

[41] A. Bharucha, D. M. Straub and R. Zwicky, JHEP **08**, 098 (2016) [arXiv:1503.05534 [hep-ph]].

[42] A. J. Buras, M. Gorbahn, U. Haisch and U. Nierste, Phys. Rev. Lett. **95**, 261805 (2005) [arXiv:hep-ph/0508165 [hep-ph]].

[43] A. J. Buras, M. Gorbahn, U. Haisch and U. Nierste, JHEP **11**, 002 (2006) [erratum: JHEP **11**, 167 (2012)] [arXiv:hep-ph/0603079 [hep-ph]].

[44] J. Brod and M. Gorbahn, Phys. Rev. D **78**, 034006 (2008) [arXiv:0805.4119 [hep-ph]].

[45] F. Mescia and C. Smith, Phys. Rev. D **76**, 034017 (2007) [arXiv:0705.2025 [hep-ph]].

[46] G. Isidori, F. Mescia and C. Smith, Nucl. Phys. B **718**, 319 (2005) [hep-ph/0503107].

[47] T. Blake, G. Lanfranchi and D. M. Straub, Prog. Part. Nucl. Phys. **92**, 50-91 (2017) [arXiv:1606.00916 [hep-ph]].

[48] C. Bobeth, M. Misiak and J. Urban, Nucl. Phys. B **574**, 291-330 (2000) [arXiv:hep-ph/9910220 [hep-ph]].

[49] C. Bobeth, P. Gambino, M. Gorbahn and U. Haisch, JHEP **04**, 071 (2004) [arXiv:hep-ph/0312090 [hep-ph]].

[50] T. Huber, E. Lunghi, M. Misiak and D. Wyler, Nucl. Phys. B **740**, 105-137 (2006) [arXiv:hep-ph/0512066 [hep-ph]].

[51] Y. S. Amhis *et al.* [HFLAV], Phys. Rev. D **107**, no.5, 052008 (2023) [arXiv:2206.07501 [hep-ex]].

[52] C. Bobeth, M. Gorbahn, T. Hermann, M. Misiak, E. Stamou and M. Steinhauser, Phys. Rev. Lett. **112**, 101801 (2014) [arXiv:1311.0903 [hep-ph]].

[53] A. J. Buras, F. De Fazio and J. Girrbach, JHEP **02**, 112 (2014) [arXiv:1311.6729 [hep-ph]].

[54] K. De Bruyn, R. Fleischer, R. Knegjens, P. Koppenburg, M. Merk, A. Pellegrino and N. Tuning, Phys. Rev. Lett. **109**, 041801 (2012) [arXiv:1204.1737 [hep-ph]].

[55] R. Fleischer, Nucl. Phys. B Proc. Suppl. **241-242**, 135-140 (2013) [arXiv:1208.2843 [hep-ph]].

[56] A. J. Buras, R. Fleischer, J. Girrbach and R. Knegjens, JHEP **07**, 077 (2013) [arXiv:1303.3820 [hep-ph]].

[57] G. Aad *et al.* [ATLAS], JHEP **04**, 165 (2021) [arXiv:2102.01444 [hep-ex]].

[58] B. Wang, PoS **LATTICE2021**, 141 (2022) [arXiv:2301.01387 [hep-lat]].

[59] Koji Shiomi, on behalf of KOTO Collaboration, talk presented at KEK IPNS and J-PARC Joint Seminar, 6th Sep 2023.

[60] C. Bobeth, G. Hiller and G. Piranishvili, JHEP **12**, 040 (2007) [arXiv:0709.4174 [hep-ph]].

[61] S. Descotes-Genon, J. Matias, M. Ramon and J. Virto, JHEP **01**, 048 (2013) [arXiv:1207.2753 [hep-ph]].

On instabilities of perturbations in some homogeneous color-electric and -magnetic backgrounds in $SU(2)$ gauge theory.

Divyarani C. Geetha,[1] and Anders Tranberg[1]

[1] *Faculty of Science and Technology, University of Stavanger, 4036 Stavanger, Norway*

(Dated: March 2024)

We consider the instabilities of field perturbations around a homogeneous background color-electric and/or -magnetic field in SU(2) pure gauge theory. We investigate a number of distinct cases of background magnetic and electric fields, and compute the dispersion relations in the linearised theory, identifying stable and unstable momentum modes. In the case of a net homogenous non-abelian B-field, we compute the non-linear (quadratic and cubic) corrections to the equation of motion, and quantify to what extent the instabilities are tempered by these non-linearities.

arXiv:2403.02859v1 [hep-ph] 5 Mar 2024

I. INTRODUCTION

The thermalisation process of non-abelian gauge fields has been the subject of intense study, in particular in the context of heavy ion collisions (HIC) (see [1] for a comprehensive review). In the initial stages of the collision, anisotropic particle distributions along and perpendicular to the beam line may create large anisotropic classical fields [2–6]. In this background, which is not necessarily homogeneous, perturbations may under certain conditions grow (semi-)exponentially. These (plasma) instabilities may result in long-wavelength fluctuations with very large occupation numbers, that may impact the equilibration process as well [1, 7–9]. It turns out that fast hydrodynamization may likely be understood from kinetic theory with input from perturbation theory [10–18], but a thorough understanding of also the non-perturbative dynamics is still of great interest.

Instabilities in anisotropic backgrounds are well-known from both abelian and non-abelian gauge theory [19]. While a U(1) theory produces linear field equations of motion for the gauge field instabilities, which could then in principle grow very large, for QCD the equations of motion are non-linear and the instabilities could turn out to be short-lived and irrelevant. The abelianization phenomenon [20] implies that there will may be directions in field space, where non-linear contributions vanish, and where the instability could continue unhindered for some time. Ultimately, this will depend on the relative magnitude of the non-linearities, the range of modes that become unstable and the self-coupling. Substantial work has been performed analytically and numerically on plasma instabilities in QCD and QCD-like theories (see for instance [21–25]), both in a HIC context and for simplified models.

In the present work we will explore the instabilities of gauge field perturbations around homogeneous and constant E and B fields in pure classical SU(2) gauge theory. For simplicity, we will ignore any fermions coupled to the gauge fields, which may feel and enhance the anisotropy. Our approach is inspired by [26, 27], where the authors investigated the dispersion relations of perturbations in the linearized theory, in a variety of gauge field backgrounds. Part of the present work is an extension of their analysis, while later parts attempts to go beyond the linear approximation.

A. The equations of motion order by order

The classical equation of motion for pure SU(2) gauge theory reads

$$D^{ab}_\mu F^{\mu\nu,b} = j^{\nu,a}, \tag{1}$$

where the covariant derivative is

$$D^{ab}_\mu = \partial_\mu \delta^{ab} - g\epsilon^{abc} A^c_\mu, \tag{2}$$

and the field strength tensor is

$$F^{\mu\nu,a} = \partial^\mu A^{\nu,a} - \partial^\nu A^{\mu,a} + g\epsilon^{abc} A^{\mu,b} A^{\nu,c}. \tag{3}$$

The gauge field $A_{\mu,a}$ is a 12-component vector, corresponding to colour indices $a = 1, 2, 3$ and Lorentz indices $\mu = 0, 1, 2, 3$. Because of gauge invariance, there is some redundancy in these degrees of freedom, and we will make use of this point shortly. The metric signature is taken to be $(+---)$, so that $x_0 = x^0 = t$ and $-x_i = x^i = (x, y, z)$, and $\partial^0 = \partial_0 = \partial/\partial t$, $-\partial^i = \partial_i = \partial/\partial x^i$. Then $E^{i,a} = F^{i0,a}$, while $B^{i,a} = \frac{1}{2}\epsilon^{ijk} F^{kj,a}$.

We will assume that the gauge field may be decomposed into a background field and a fluctuation, with the notation

$$A^\mu_a(x,t) = \bar{A}^\mu_a(x,t) + h^\mu_a(x,t), \tag{4}$$

and with an assumption that the fluctuations are in some sense "small", $h^\mu_a \ll \bar{A}^\mu_a$. It then makes sense to expand order by order in h^μ_a.

Background field

The equation of motion for the background field (expanding to zero'th order in the fluctuation h^μ_a) is simply

$$\bar{D}^{ab}_\mu \bar{F}^{\mu\nu,b} = j^{\nu,a}, \tag{5}$$

where the bar on $\bar{D}^{ab}_\mu$ and $\bar{F}^{\mu\nu,b}$ indicate that they are expressed only in terms of the background field $\bar{A}$. We have

assumed that the external current enters in this background field equation in its entirety. In practice, we will in the following state the background field $\bar{A}^\mu_a$ and simply infer what the current j^ν_a is required to be to generate such a field. In principle, this current may be taken to arise from some distribution of colour-charged particles, but we will not discuss this further.

Linear in fluctuations

To linear order in fluctuations, one finds

$$\begin{aligned}&\partial_\mu\partial^\mu h^\nu_a + g\epsilon_{abc}\left(2\partial^\nu \bar{A}^b_\mu h^\mu_c + 2\partial_\mu \bar{A}^\nu_c h^\mu_b + 2\bar{A}^\mu_b \partial_\mu h^\nu_c\right)\\ &-g^2\left(2\bar{A}^c_\mu \bar{A}^\nu_a h^\mu_c - 2\bar{A}^\nu_c \bar{A}^a_\mu h^\mu_c + \bar{A}^c_\mu \bar{A}^\mu_c h^\nu_a - \bar{A}^c_\mu \bar{A}^\mu_a h^\nu_c\right) = 0.\end{aligned} \tag{6}$$

We adopt the Lorenz gauge $\partial_\mu \bar{A}^\mu_a = 0$ for the background field, and have imposed the background gauge fixing condition on the fluctuations, $\bar{D}^{ab}_\mu h^{\mu,b} = 0$, where $\bar{D}^{ab}_\mu$ again denotes the covariant derivative in terms of the background field $\bar{A}^b_\mu$ only. In a more compact notation, this may be rewritten as

$$\left[g^{\mu\nu}(\bar{D}_\rho \bar{D}^\rho)_{ac} + 2g\epsilon_{abc}\bar{F}^{\mu\nu}_b\right] h_{\nu,c} = \mathcal{M}^{\mu\nu}_{ac}[12\times 12]h_{\nu,c} = 0. \tag{7}$$

As we will see, in momentum space this turns into a $[12\times 12]$ matrix equation for h^μ_a, which has unstable modes for certain choices of $\bar{A}^\mu_a$. Some of these correspond to non-zero homogeneous colour-electric and/or -magnetic fields, and we will in section II consider a fairly broad subset. Given $\bar{A}^\mu_a$, one may compute the dispersion relations for these modes.

Quadratic in fluctuations

At early times, when h^μ_a is truly $\ll \bar{A}^\mu_a$, the linear approximation is valid and unstable modes grow exponentially. However, non-linearities will eventually impact the evolution. At second order in fluctuations, we have

$$\begin{aligned}&g\epsilon_{abc}\left(2\partial_\mu h^\nu_c h^\mu_b + \partial^\nu h^b_\mu h^\mu_c\right)\\ &-g^2\left(2\bar{A}^\mu_c h^c_\mu h^\nu_a - 2\bar{A}^\mu_a h^c_\mu h^\nu_c + \bar{A}^\nu_a h^c_\mu h^\mu_c - \bar{A}^\nu_c h^c_\mu h^\mu_a\right).\end{aligned} \tag{8}$$

which upon taking the expectation values for the fluctuations, and truncating at quadratic order, naturally adds to the background equation of motion (5). Defining

$$C^{\mu\nu}_{ab} = \langle h^\mu_a h^\nu_b\rangle, \quad \bar{j}^\nu_a = g\epsilon_{abc}\langle 2\partial_\mu h^\nu_c h^\mu_b + \partial^\nu h^b_\mu h^\mu_c\rangle, \tag{9}$$

we have schematically

$$\bar{D}^{ab}_\mu \bar{F}^{\mu\nu,b} - g^2 \bar{M}^{\nu\mu}_{ab}[C]\bar{A}_{\mu,b} = j^\nu_a - \bar{j}^\nu_a. \tag{10}$$

where $\bar{M}$ is some matrix involving the C correlators in (9). This in effect changes both the background equation of motion and the effective current, and if j^ν_a is constant will eventually ruin the assumption of a constant background electric/magnetic fields. We will investigate the effect of this non-linear back reaction below.

Cubic in fluctuations

Finally, the equation of motion has cubic contributions in the fluctuations, which read

$$-g^2\left[h^\nu_a h^c_\mu h^\mu_c - h^\mu_a h^c_\mu h^\nu_c\right], \tag{11}$$

and which again upon taking expectation values naturally add to the linear equation for the modes as

$$\left[g^{\mu\nu}(\bar{D}_\rho \bar{D}^\rho)_{ac} + 2g\epsilon_{abc}\bar{F}^{\mu\nu}_b - g^2\hat{M}^{\mu\nu}_{ac}(C)\right] h_{\nu,c} = 0. \tag{12}$$

The matrix $\hat{M}$ is expressed in terms if the C correlators, providing a corrected linear equation for the fluctuations h^μ_a. This gives rise to new time-dependent dispersion relations, altering the pattern of instabilities.

B. This work

In section II, we will consider a fairly general set of homogeneous, anisotropic field backgrounds. For three of these we will in section A compute the dispersion relations of the fluctuation modes explicitly, and establish for which momentum regions the fluctuations are unstable. The remaining cases are more involved, and we will simply sketch how one would go about finding dispersion relations for them in Appendix B, relying heavily on [26, 27]. In section III we choose one of the three cases and compute the eigenmodes explicitly, in order to compute the C correlators. This will in turn allow us to compute the cubic correction matrix $\hat{M}$ and the quadratic corrections $\bar{M}$ and $\bar{J}$, from which we will be able to study the evolution of the instabilities. We provide some discussion, conclusions and suggestions for future work in section IV.

II. ANISOTROPIC BACKGROUNDS WITH CONSTANT, HOMOGENEOUS ELECTRIC/MAGNETIC FIELDS

A. Electric field only

We will first consider a constant, homogeneous colour-electric field only, and set up our procedure and notation. Firstly, without loss of generality, we can choose the electric field in the $i = 1$, $a = 1$ direction. We hence require that

$$\bar{F}^{i0}_a = E^i_a = \delta^{i1}_{a1}E. \tag{13}$$

Since

$$\bar{F}^{i0}_a = \partial^i \bar{A}^0_a - \partial^0 \bar{A}^i_a + g\epsilon_{abc}\bar{A}^i_b\bar{A}^0_c, \tag{14}$$

such an electric field may correspond to a multitude of choices for $\bar{A}^\mu_a$ (some of which may be gauge-equivalent). We choose to restrict ourselves to two cases: One where only the linear-in-A ("Abelian") derivative part of $\bar{F}$ is non-zero. And one where only the quadratic-in-A ("non-Abelian") part is non-zero. A homogeneous, time-independent *Abelian* electric field may then be written (in a compact notation we will use repeatedly for the 12-component objects such as $\bar{A}^\mu_a$, j^μ_a), as

$$\begin{aligned}\bar{A}^\mu_a &= \left[\begin{pmatrix}\bar{A}^0_1\\ \bar{A}^0_2\\ \bar{A}^0_3\end{pmatrix}\begin{pmatrix}\bar{A}^1_1\\ \bar{A}^1_2\\ \bar{A}^1_3\end{pmatrix}\begin{pmatrix}\bar{A}^2_1\\ \bar{A}^2_2\\ \bar{A}^2_3\end{pmatrix}\begin{pmatrix}\bar{A}^3_1\\ \bar{A}^3_2\\ \bar{A}^3_3\end{pmatrix}\right]\\ &= \left[\begin{pmatrix}-x\,C_1\\ 0\\ 0\end{pmatrix}\begin{pmatrix}-t\,C_2\\ 0\\ 0\end{pmatrix}\begin{pmatrix}0\\ 0\\ 0\end{pmatrix}\begin{pmatrix}0\\ 0\\ 0\end{pmatrix}\right],\end{aligned} \tag{15}$$

so that

$$E^1_1 \equiv E = C_1 + C_2. \tag{16}$$

This corresponds to a vanishing current $j^{\nu,a} = 0$. Similarly a homogeneous time-independent *non-Abelian* electric field may be written as

$$\bar{A}^\mu_a = \left[\begin{pmatrix}0\\ D_2\\ D_1\end{pmatrix}\begin{pmatrix}0\\ D_4\\ D_3\end{pmatrix}\begin{pmatrix}0\\ 0\\ 0\end{pmatrix}\begin{pmatrix}0\\ 0\\ 0\end{pmatrix}\right], \tag{17}$$

to find

$$E^1_1 \equiv E = g(D_4D_1 - D_3D_2). \tag{18}$$

This corresponds to a current with four non-vanishing components:

$$j^\nu_a = -gE\left[\begin{pmatrix}0\\ D_3\\ -D_4\end{pmatrix}\begin{pmatrix}0\\ D_1\\ -D_2\end{pmatrix}\begin{pmatrix}0\\ 0\\ 0\end{pmatrix}\begin{pmatrix}0\\ 0\\ 0\end{pmatrix}\right]. \tag{19}$$

B. Magnetic field only

For a homogeneous magnetic field we can again choose the $\mu = 1$, $a = 1$ direction, and write

$$\frac{1}{2}\epsilon^{ijk}F^{kj}_a = B^i_a = \delta^{i1}_{a1}B. \tag{20}$$

An *Abelian* background field can be parametrized as

$$\bar{A}^\mu_a = \left[\begin{pmatrix}0\\ 0\\ 0\end{pmatrix}\begin{pmatrix}0\\ 0\\ 0\end{pmatrix}\begin{pmatrix}-z\,C_4\\ 0\\ 0\end{pmatrix}\begin{pmatrix}y\,C_3\\ 0\\ 0\end{pmatrix}\right], \tag{21}$$

so that

$$B^1_1 = B = C_3 + C_4. \tag{22}$$

This again corresponds to a vanishing current $j^{\nu,a} = 0$. The *non-Abelian* realisation is

$$\bar{A}^\mu_a = \left[\begin{pmatrix}0\\ 0\\ 0\end{pmatrix}\begin{pmatrix}0\\ 0\\ 0\end{pmatrix}\begin{pmatrix}0\\ D_6\\ D_5\end{pmatrix}\begin{pmatrix}0\\ D_8\\ D_7\end{pmatrix}\right], \tag{23}$$

with

$$B^1_1 = B = g(D_5D_8 - D_6D_7). \tag{24}$$

This again corresponds to a current with four non-vanishing components:

$$j^\nu_a = -gB\left[\begin{pmatrix}0\\ 0\\ 0\end{pmatrix}\begin{pmatrix}0\\ 0\\ 0\end{pmatrix}\begin{pmatrix}0\\ D_7\\ -D_8\end{pmatrix}\begin{pmatrix}0\\ -D_5\\ D_6\end{pmatrix}\right]. \tag{25}$$

These expressions are minor generalisations to [26], where the authors consider Abelian E with $C_1 = E$, $C_2 = 0$, Abelian B with $C_3 = B$, $C_4 = 0$, non-Abelian E with $D_2 = -D_3 = \sqrt{E/g}$, $D_1 = D_4 = 0$ and non-Abelian B with $D_5 = D_8 = \sqrt{B/g}$, $D_6 = D_7 = 0$. In [27] the same authors in addition considered arbitrary D_2, D_3, and D_5, D_8, respectively. We see, that there are a host of other possibilities for choosing the C_i or the D_i for a given E or B. It will not be possible to keep full generality in the following, but we will further investigate some of the combinations in terms of the resulting dispersion relations.

C. Electric and magnetic fields, combined

The natural generalisation is to consider the combination of an electric field E^1_1 together with a magnetic field that is/is not aligned in space and/or colour. Allowing for all combinations of Abelian/non-Abelian $\bar{A}^\mu_a$ one might expect 16 distinct cases. Some combinations are however not possible since additional components of magnetic and electric field are sourced. The task is therefore to identify vector potentials with the property that they generate only E^1_1 and then some combination of B^i_a, enforcing that they are either of Abelian or non-Abelian type, and that E and B are constant in space and time. One then finds a limited set of options, which we will briefly review in the following.

Abelian E and Abelian B

Choosing a vector potential of the form

$$\bar{A}^\mu_a = \left[\begin{pmatrix}-x\,C_1\\ \\ \\ 0\\ 0\end{pmatrix}\begin{pmatrix}-t\,C_2 - y\,C_{16}\\ +z\,C_9\\ \\ 0\\ 0\end{pmatrix}\begin{pmatrix}-z\,C_4\\ +x\,C_{15}\\ \\ 0\\ 0\end{pmatrix}\begin{pmatrix}-x\,C_{10}\\ +y\,C_3\\ \\ 0\\ 0\end{pmatrix}\right], \tag{26}$$

gives Abelian E- and B-fields aligned in colour, with

$$E_1^1 = C_1 + C_2,$$
$$B_a^i = g\left[\begin{pmatrix} C_3+C_4 \\ 0 \\ 0 \end{pmatrix}\begin{pmatrix} C_9+C_{10} \\ 0 \\ 0 \end{pmatrix}\begin{pmatrix} C_{15}+C_{16} \\ 0 \\ 0 \end{pmatrix}\right]. \tag{27}$$

Explicitly setting $\bar{A}_1^0 = 0$ ($C_1 = 0$), this opens up a few more options:

$$\bar{A}_a^\mu = \left[\begin{pmatrix} 0 \\ 0 \\ 0 \end{pmatrix}\begin{pmatrix} -t\,C_2 - y\,C_{16} + z\,C_9 \\ -y\,C_{18} + z\,C_{11} \\ -y\,C_{20} + z\,C_{13} \end{pmatrix}\begin{pmatrix} 0 \\ 0 \\ 0 \end{pmatrix}\begin{pmatrix} 0 \\ 0 \\ 0 \end{pmatrix}\right], \tag{28}$$

which gives Abelian E- and B-fields orthogonal in space:

$$E_1^1 = C_2,$$
$$B_a^i = g\left[\begin{pmatrix} 0 \\ 0 \\ 0 \end{pmatrix}\begin{pmatrix} C_9 \\ C_{11} \\ C_{13} \end{pmatrix}\begin{pmatrix} C_{16} \\ C_{18} \\ C_{20} \end{pmatrix}\right]. \tag{29}$$

Abelian E and non-Abelian B

A vector potential of the form

$$\bar{A}_a^\mu = \left[\begin{pmatrix} 0 \\ 0 \\ 0 \end{pmatrix}\begin{pmatrix} -tC_2 \\ D_4 \\ D_3 \end{pmatrix}\begin{pmatrix} D_{11} \\ 0 \\ 0 \end{pmatrix}\begin{pmatrix} D_{12} \\ 0 \\ 0 \end{pmatrix}\right], \tag{30}$$

gives Abelian E- and non-Abelian B-fields orthogonal in space and colour:

$$E_1^1 = C_2,$$
$$B_a^i = g\left[\begin{pmatrix} 0 \\ 0 \\ 0 \end{pmatrix}\begin{pmatrix} 0 \\ D_3D_{12} \\ -D_4D_{12} \end{pmatrix}\begin{pmatrix} 0 \\ -D_3D_{11} \\ D_4D_{11} \end{pmatrix}\right]. \tag{31}$$

Non-Abelian E and non-Abelian B

Finally, we may choose

$$\bar{A}_a^\mu = \left[\begin{pmatrix} 0 \\ 0 \\ D_1 \end{pmatrix}\begin{pmatrix} 0 \\ D_4 \\ 0 \end{pmatrix}\begin{pmatrix} 0 \\ 0 \\ D_5 \end{pmatrix}\begin{pmatrix} 0 \\ 0 \\ D_7 \end{pmatrix}\right], \tag{32}$$

which gives non-Abelian E- and B-fields orthogonal in colour, but aligned in space.

$$E_1^1 = gD_1D_4,$$
$$B_a^i = g\left[\begin{pmatrix} 0 \\ 0 \\ 0 \end{pmatrix}\begin{pmatrix} D_4D_7 \\ 0 \\ 0 \end{pmatrix}\begin{pmatrix} -D_4D_5 \\ 0 \\ 0 \end{pmatrix}\right]. \tag{33}$$

The combination

$$\bar{A}_a^\mu = \left[\begin{pmatrix} 0 \\ D_2 \\ 0 \end{pmatrix}\begin{pmatrix} 0 \\ 0 \\ D_3 \end{pmatrix}\begin{pmatrix} 0 \\ D_6 \\ 0 \end{pmatrix}\begin{pmatrix} 0 \\ D_8 \\ 0 \end{pmatrix}\right], \tag{34}$$

is equivalent.

In summary, we have seen that we can find:

- Abelian E or B, or non-Abelian E or B with a somewhat generalised parametrisation of what was reported in [26].
- Space-aligned, colour-aligned E and B: Possible as an Abelian/Abelian combination. $C_1 \neq 0$, $C_3 \neq 0$ is the special case reported in [26].
- Space-aligned, colour-orthogonal E and B: Can not be realised in our setup.
- Space-orthogonal, colour-aligned E and B: Possible as Abelian/Abelian and non-Abelian/non-Abelian combinations.
- Space-orthogonal, colour-orthogonal E and B: Possible as Abelian/Abelian and Abelian/non-Abelian combinations.

We also see that there are several computationally distinct cases, depending on whether the vector potential is itself space- and/or time-dependent. We will press on with the three purely non-Abelian cases (E only, B only, E and B), where $\bar{A}_a^\mu$ is homogeneous and constant. We refer to Appendix B for a brief discussion of the issues involved for the Abelian vector potentials.

D. Non-Abelian B, E=0

Let us return to the case of a non-Abelian B-field and zero E-field. In 4-dimensional momentum space, the linear equation for the modes of the fluctuations reduce to a set of 12 coupled linear algebraic equations for h_a^μ, which however split into 3 independent sections.

$$\mathcal{M}_{ac}^{\mu\nu}\,[12\times 12]\,h_\nu^c = \begin{pmatrix} M_{00} & 0 & 0 & 0 \\ 0 & M_{11} & 0 & 0 \\ 0 & 0 & M_{22} & M_{23} \\ 0 & 0 & M_{32} & M_{33} \end{pmatrix}\begin{pmatrix} h^0_{1,2,3} \\ h^1_{1,2,3} \\ h^2_{1,2,3} \\ h^3_{1,2,3} \end{pmatrix}, \tag{35}$$

where in addition $M_{00} = M_{11} = M_{22} = M_{33}$ are all hermitian, and $M_{23} = M_{32}^\dagger$, so that the whole matrix M is hermitian. Hence the equations for $h^0_{1,2,3}$ (M_{00}) and $h^1_{1,2,3}$ (M_{11}) are identical

$$\begin{pmatrix} \Box_k + D_5^2 + D_6^2 + D_7^2 + D_8^2 & 2i(D_5k_y + D_7k_z) & -2i(D_6k_y + D_8k_z) \\ -2i(D_5k_y + D_7k_z) & \Box_k + D_5^2 + D_7^2 & -(D_5D_6 + D_7D_8) \\ 2i(D_6k_y + D_8k_z) & -(D_5D_6 + D_7D_8) & \Box_k + D_6^2 + D_8^2 \end{pmatrix} \begin{pmatrix} h_1^{0,1} \\ h_2^{0,1} \\ h_3^{0,1} \end{pmatrix} = 0, \tag{36}$$

while the $h^{2,3}_{1,2,3}$-sections mix ($M_{22,23,32,33}$)

$$\begin{pmatrix} \Box_k + D_5^2 + D_6^2 + D_7^2 + D_8^2 & 2i(D_5k_y + D_7k_z) & -2i(D_6k_y + D_8k_z) \\ -2i(D_5k_y + D_7k_z) & \Box_k + D_5^2 + D_7^2 & -(D_5D_6 + D_7D_8) \\ 2i(D_6k_y + D_8k_z) & -(D_5D_6 + D_7D_8) & \Box_k + D_6^2 + D_8^2 \end{pmatrix} \begin{pmatrix} h_1^2 \\ h_2^2 \\ h_3^2 \end{pmatrix} + \begin{pmatrix} 0 & 0 & 0 \\ 0 & 0 & -2B \\ 0 & 2B & 0 \end{pmatrix} \begin{pmatrix} h_1^3 \\ h_2^3 \\ h_3^3 \end{pmatrix} = 0, \tag{37}$$

and

$$\begin{pmatrix} \Box_k + D_5^2 + D_6^2 + D_7^2 + D_8^2 & 2i(D_5k_y + D_7k_z) & -2i(D_6k_y + D_8k_z) \\ -2i(D_5k_y + D_7k_z) & \Box_k + D_5^2 + D_7^2 & -(D_5D_6 + D_7D_8) \\ 2i(D_6k_y + D_8k_z) & -(D_5D_6 + D_7D_8) & \Box_k + D_6^2 + D_8^2 \end{pmatrix} \begin{pmatrix} h_1^3 \\ h_2^3 \\ h_3^3 \end{pmatrix} + \begin{pmatrix} 0 & 0 & 0 \\ 0 & 0 & 2B \\ 0 & -2B & 0 \end{pmatrix} \begin{pmatrix} h_1^2 \\ h_2^2 \\ h_3^2 \end{pmatrix} = 0. \tag{38}$$

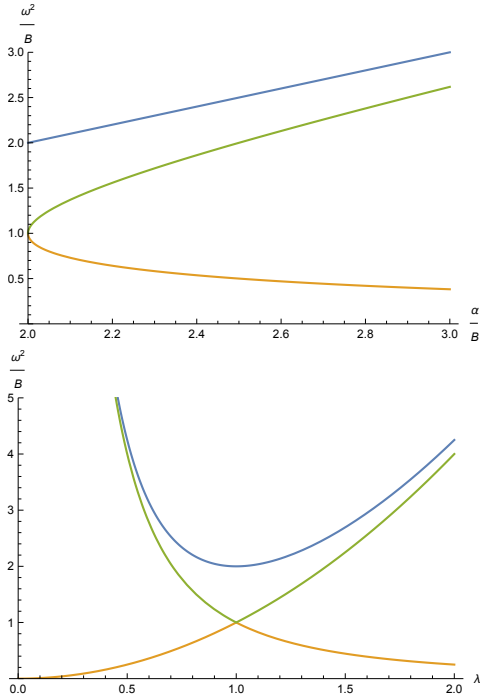


FIG. 1. Non-Abelian B: The three eigenvalues in the 0, 1 sectors for $\mathbf{k} = 0$, general D_i (top) and for $\sqrt{B} = D_6/\lambda = -D_7\lambda$ (bottom).

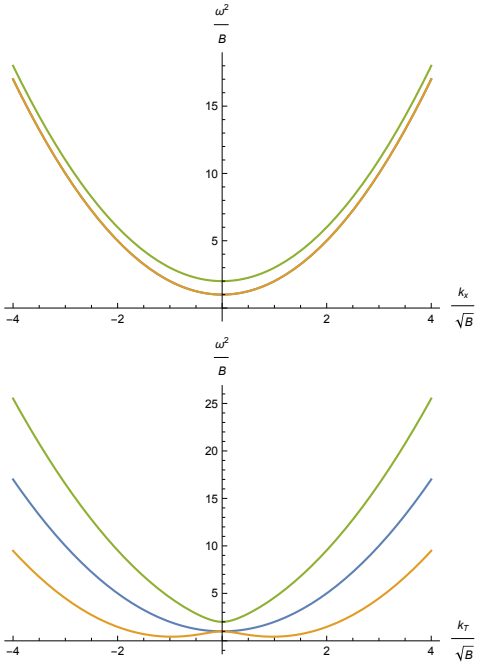


FIG. 2. Non-Abelian B: The three eigenvalues in the 0, 1 sectors for $\sqrt{B} = D_6 = -D_7$, with $k_T = 0$ (top) and $k_x = 0$ (bottom).

To somewhat mitigate notational clutter we have absorbed g into $\bar{A}$, $gD_i \to D_i$, and defined the box operator in momentum space $\Box_k = -\omega^2 + k_x^2 + k_T^2$, with $k_T^2 = k_y^2 + k_z^2$. We note that the $D_{5,6,7,8}$ do not only appear in the combination $B = D_5D_8 - D_6D_7$, but depend on the D_i individually.

Non-Abelian B: 0 and 1 sector

The condition on ω to satisfy the equation is that $\mathrm{Det}[M_{00}] = 0 = \mathrm{Det}[M_{11}]$, which reduces to the cubic equation

$$\Box_k^3 + 2\alpha_B\Box_k^2 + \beta_B\Box_k + \gamma_B = 0, \tag{39}$$

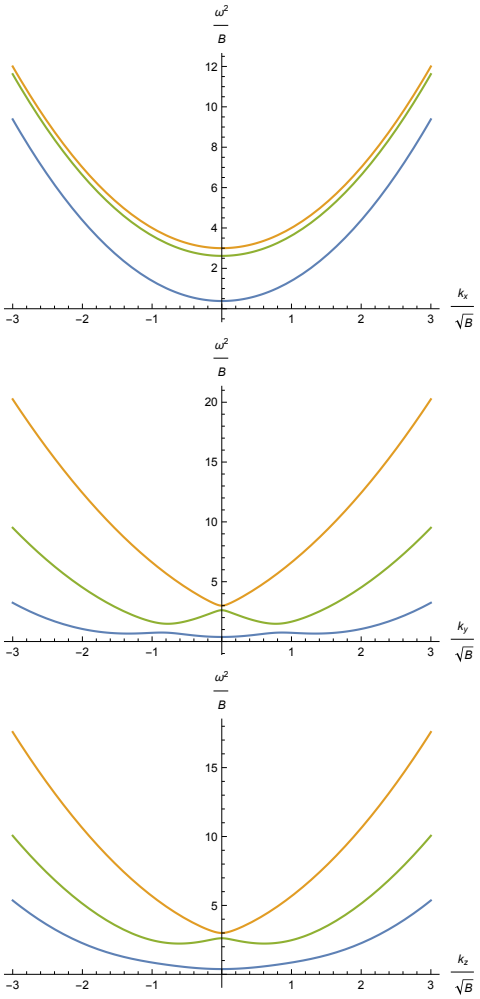


FIG. 3. Non-Abelian B: The three eigenvalues in the 0, 1 sectors for $\sqrt{B} = D_6 = -D_7$, with non-zero $D_5 = \sqrt{nB}$, $n = 1$. For non-zero k_x (top), k_y (middle) and k_z (bottom).

with

$$\alpha_B = (D_5^2 + D_6^2 + D_7^2 + D_8^2) \geq 2B, \tag{40}$$

$$\beta_B = \alpha_B^2 + B^2 - 4\left((D_5 k_y + D_7 k_z)^2 + (D_6 k_y + D_8 k_z)^2\right), \tag{41}$$

$$\gamma_B = B^2(\alpha_B - 4k_T^2). \tag{42}$$

Let us first consider the zero-momentum case $k_T = k_x = 0$, so that $\omega^2 = -\Box_k$, and

$$-\left(\omega^2\right)^3 + 2\alpha_B\left(\omega^2\right)^2 - \left(\alpha_B^2 + B^2\right)\omega^2 + B^2\alpha_B = 0. \tag{43}$$

The solutions for ω^2 only depend on the combination α_B/B,

$$\frac{\omega^2}{B} = \frac{\alpha_B}{B}, \quad \frac{\omega^2}{B} = \frac{1}{2}\left(\frac{\alpha_B}{B} \pm \sqrt{\frac{\alpha_B^2}{B^2} - 4}\right), \tag{44}$$

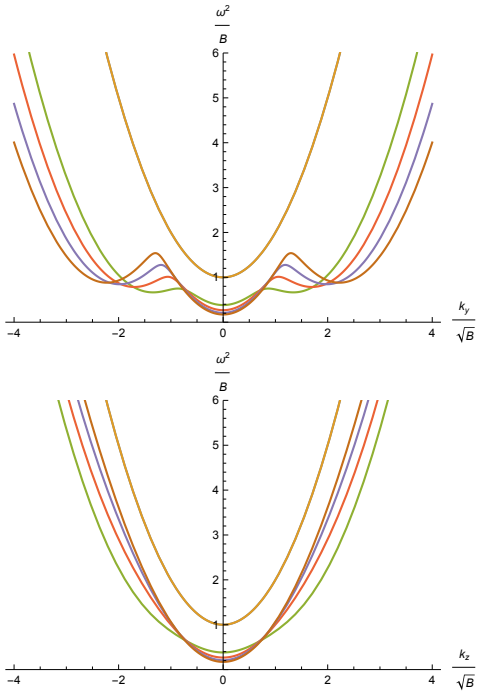


FIG. 4. Non-Abelian B: The lowest eigenvalues in the 0, 1 sectors for $\sqrt{B} = D_6 = -D_7$, with non-zero $D_5 = \sqrt{nB}$, $n = 0, 1, 2, 3, 4$. For non-zero k_y (top) and k_z (bottom).

and they are all real and positive (see Figure 1, top). For instance in the case $D_5 = D_8 = 0$, $D_6 = -D_7 = \sqrt{B}$, we find $\alpha_B/B = 2$ so that the eigenvalues reduce to $\omega^2 = (2B, B, B)$. For the more general case $D_6 = \sqrt{B}\lambda$, $-D_7 = \sqrt{B}/\lambda$ for some λ [26], $\alpha_B/B = \lambda^2 + \lambda^{-2} \geq 2$, and the solutions are again real and positive (see Figure 1, bottom). As a sanity check, we note that when $B = 0$, the eigenvalues are $\omega^2 = (0, \alpha_B, \alpha_B)$. These are real and positive, and only zero when all the D_i are zero.

For non-zero momentum k_T, k_x, the explicit realisation of $D_{5,..,8}$ becomes more important. Again for the case $D_6 = -D_7 = \sqrt{B}$ one finds ($\alpha_B/B = 2$, $\beta_B/B^2 = 5 - 4k_T^2/B$, $\gamma_B/B^3 = 2 - 4k_T^2/B$),

$$\left(-\frac{\omega^2}{B} + \frac{k_T^2}{B} + \frac{k_x^2}{B}\right)^3 + 4\left(-\frac{\omega^2}{B} + \frac{k_T^2}{B} + \frac{k_x^2}{B}\right)^2 + \left(5 - 4\frac{k_T^2}{B}\right)\left(-\frac{\omega^2}{B} + \frac{k_T^2}{B} + \frac{k_x^2}{B}\right) + 2 - 4\frac{k_T^2}{B} = 0, \tag{45}$$

which has the solutions (see Figure 2)

$$\frac{\omega^2}{B} = 1 + \frac{k_x^2}{B} + \frac{k_T^2}{B}, \quad \frac{\omega^2}{B} = \frac{3}{2} + \frac{k_x^2}{B} + \frac{k_T^2}{B} \pm \frac{1}{2}\sqrt{1 + 16\frac{k_T^2}{B}}. \tag{46}$$

These are real and positive for all B, k_x, k_T, and hence the 0 and 1 components of the fluctuations are stable for this choice of $D_{5,..,8}$.

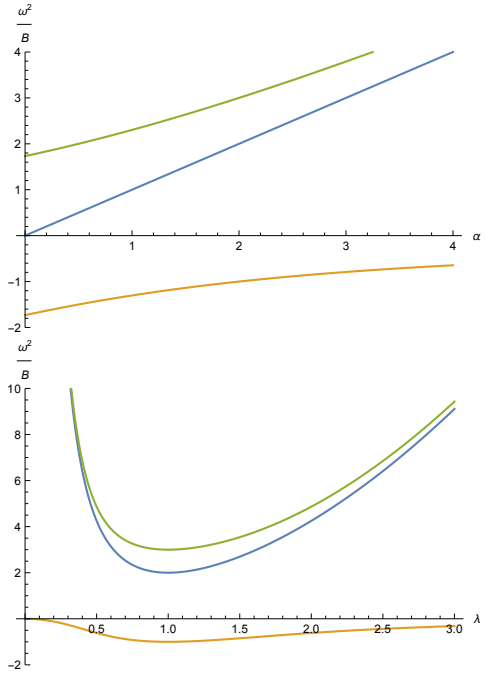


FIG. 5. Non-Abelian B: The three double eigenvalues in the 2, 3 sectors for $\mathbf{k}=0$, general D_i (top) and for $\sqrt{B}=D_6/\lambda=-D_7\lambda$ (bottom).

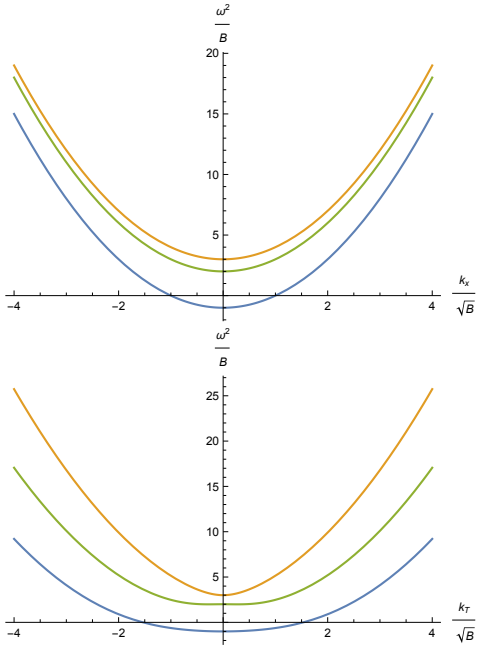


FIG. 6. Non-Abelian B: The three eigenvalues in the 2, 3 sectors for $\sqrt{B}=D_6=-D_7$, with $k_T=0$ (top) and $k_x=0$ (bottom).

For fixed B, a 3-dimensional space of realisations of $D_{5,..,8}$ is available, which we will not fully explore here. We will however briefly consider again the case $D_6=-D_7=\sqrt{B}$, fixing $D_8=0$, allowing us to choose any value for D_5 without changing B. We choose $D_5=\sqrt{nB}$, and vary n. In Figure 3 we show the eigenvalues for $n=1$, and their dependence on $k_{x,y,z}$ (respectively, keeping the other two constant). We note how the $k_T=\sqrt{k_y^2+k_z^2}$-dependence in Figure 2 is resolved into different dependence on k_y and k_z. We can further examine the n-dependence of the lowest eigenvalue, as function of k_y and k_z, shown in Figure 4. We see a non-trivial dependence, but the eigenvalue remains real and positive.

Non-Abelian B: 2 and 3 sector

For the 2-3 component, the requirement $\mathrm{Det}[M_{22,23,32,33}]=0$ amounts to (compare to (39))

$$\left[\Box_k^3+2\alpha_B\Box_k^2+(\beta_B-4B^2)\Box_k+\gamma_B-4B^2\alpha_B.\right]^2=0, \tag{47}$$

We may focus on the expression inside the square bracket, and infer that any solution is a double solution. For $k_T,k_x=0$ this becomes

$$-(\omega^2)^3+2\alpha_B(\omega^2)^2-(\alpha_B^2-3B^2)\omega^2-3B^2\alpha_B=0, \tag{48}$$

which has solutions

$$\frac{\omega^2}{B}=\frac{\alpha_B}{B},\quad \omega^2=\frac{1}{2}\left(\frac{\alpha_B}{B}\pm\sqrt{\frac{\alpha_B^2}{B^2}+12}\right). \tag{49}$$

One of these eigenvalues is negative for all α_B/B (see Figure 5, top). In particular for $D_5=D_8=0$, $D_6=-D_7=\sqrt{B}$ we find $\omega^2=(3B,2B,-B)$, while the parametrization $D_6=\sqrt{B}\lambda$, $-D_7=\sqrt{B}/\lambda$ gives the negative eigenvalue for ω^2 in the interval $[-1,0]$ (see Figure 5, bottom). Again, when $B=0$, $\omega^2=(0,\alpha_B,\alpha_B)$.

For non-zero momentum, we consider again $D_6=-D_7=\sqrt{B}$, for which we need to solve

$$\left(-\frac{\omega^2}{B}+\frac{k_T^2}{B}+\frac{k_x^2}{B}\right)^3+4\left(-\frac{\omega^2}{B}+\frac{k_T^2}{B}+\frac{k_x^2}{B}\right)^2 +\left(1-4\frac{k_T^2}{B}\right)\left(-\frac{\omega^2}{B}+\frac{k_T^2}{B}+\frac{k_x^2}{B}\right)-6-4\frac{k_T^2}{B}=0, \tag{50}$$

This is a general cubic equation, which may be solved straightforwardly, to reveal (Figure 6) that the (double) unstable mode becomes stable as k_x and/or k_T increase. Explicitly, for $k_T=0$, the unstable region is $|k_x|<1$, while for $k_x=0$ it is $|k_T|<\sqrt{(3-\sqrt{8})^{1/3}+(3+\sqrt{8})^{1/3}}\simeq 1.53$.

We can again extend our analysis somewhat, by allowing $D_5=\sqrt{n}B$, while keeping $D_8=0$. In Figure 7 we show the negative eigenvalue and its momentum dependence (nonzero k_x, k_y or k_z, respectively), for different

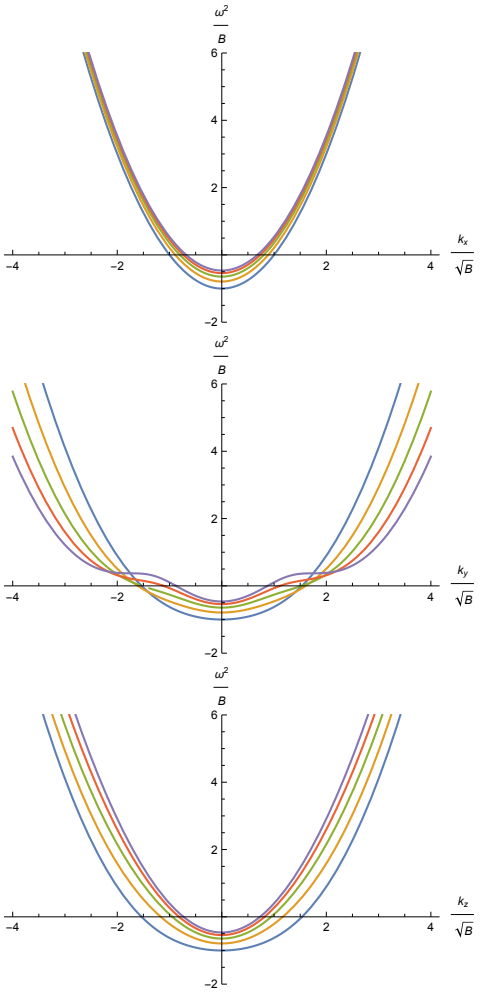


FIG. 7. Non-Abelian B: The lowest (negative) eigenvalue in the 2, 3 sectors for $\sqrt{B} = D_6 = -D_7$, with non-zero $D_5 = \sqrt{nB}$, $n = 0, 1, 2, 3, 4$. For non-zero k_x (top) k_y (middle) and k_z (bottom).

values of $n = 0, 1, 2, 3, 4$. We see that larger n reduces the region of instability, and we find that for $n \to \infty$, $\omega^2(\mathbf{k} = \mathbf{0}) \to 0$.

Hence, in the presence of a constant, homogeneous non-Abelian magnetic field, for this choice of $D_{5,..,8}$, of the 12 sets of momentum modes present, two are potentially unstable, growing as

$$\propto \exp(\pm|\omega|t), \tag{51}$$

with an ω given by the two lowest, degenerate solutions to (47) (exemplified by the $-$ solution in the special case of (49)). Furthermore, the region of instabilibity is centered around the origin ($\mathbf{k} = 0$), and that for large enough $\mathbf{k}$, these modes are again stable. Hence only a finite IR region of momentum modes are unstable, and this region is not only dependent on B, but also on the concrete choice of $D_{5,..,8}$, exemplified here by varying D_5.

In section III we will further find the eigenmodes of the system for non-Abelian B only, with $\sqrt{B} = D_6 = -D_7$, $D_5 = D_8 = 0$, compute the quadratic and cubic corrections to the evolution equations and solve them including these corrections.

E. Non-Abelian E, B=0

For a non-Abelian background E-field and zero B-field, the linear equation for the Fourier modes again splits into 3 independent sections. The section for $h^2_{1,2,3}$ (M_2) and $h^3_{1,2,3}$ (M_3) are now identical and decoupled from each other, and read (absorbing again g as $gD_i \to D_i$)

$$\begin{pmatrix} \Box_k - D_1^2 - D_2^2 + D_3^2 + D_4^2 & -2i(D_1\omega - D_3k_x) & 2i(D_2\omega - D_4k_x) \\ +2i(D_1\omega - D_3k_x) & \Box_k - D_1^2 + D_3^2 & D_1D_2 - D_3D_4 \\ -2i(D_2\omega - D_4k_x) & D_1D_2 - D_3D_4 & \Box_k - D_2^2 + D_4^2 \end{pmatrix} \begin{pmatrix} h_1^{2,3} \\ h_2^{2,3} \\ h_3^{2,3} \end{pmatrix} = 0. \tag{52}$$

while the $h^{0,1}_{1,2,3}$-sections mix ($M_{00}, M_{01}, M_{10}, M_{11}$)

$$\begin{pmatrix} \Box_k - D_1^2 - D_2^2 + D_3^2 + D_4^2 & -2i(D_1\omega - D_3k_x) & 2i(D_2\omega - D_4k_x) \\ 2i(D_1\omega - D_3k_x) & \Box_k - D_1^2 + D_3^2 & D_1D_2 - D_3D_4 \\ -2i(D_2\omega - D_4k_x) & D_1D_2 - D_3D_4 & \Box_k - D_2^2 + D_4^2 \end{pmatrix} \begin{pmatrix} h_1^0 \\ h_2^0 \\ h_3^0 \end{pmatrix} + \begin{pmatrix} 0 & 0 & 0 \\ 0 & 0 & -2E \\ 0 & 2E & 0 \end{pmatrix} \begin{pmatrix} h_1^1 \\ h_2^1 \\ h_3^1 \end{pmatrix} = 0, \tag{53}$$

and

$$\begin{pmatrix} \Box_k - D_1^2 - D_2^2 + D_3^2 + D_4^2 & -2i(D_1\omega - D_3k_x) & 2i(D_2\omega - D_4k_x) \\ 2i(D_1\omega - D_3k_x) & \Box_k - D_1^2 + D_3^2 & D_1D_2 - D_3D_4 \\ -2i(D_2\omega - D_4k_x) & D_1D_2 - D_3D_4 & \Box_k - D_2^2 + D_4^2 \end{pmatrix} \begin{pmatrix} h_1^1 \\ h_2^1 \\ h_3^1 \end{pmatrix} + \begin{pmatrix} 0 & 0 & 0 \\ 0 & 0 & -2E \\ 0 & 2E & 0 \end{pmatrix} \begin{pmatrix} h_1^0 \\ h_2^0 \\ h_3^0 \end{pmatrix} = 0. \tag{54}$$

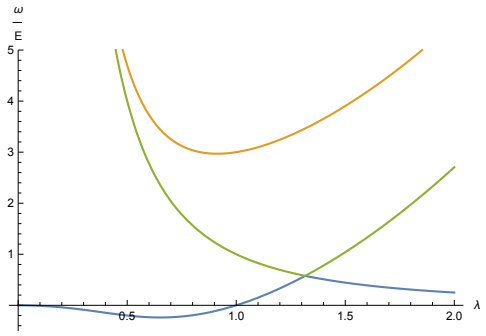


FIG. 8. Non-Abelian E: The three eigenvalues in the 2, 3 sectors for $\sqrt{E} = D_1/\lambda = D_4\lambda$.

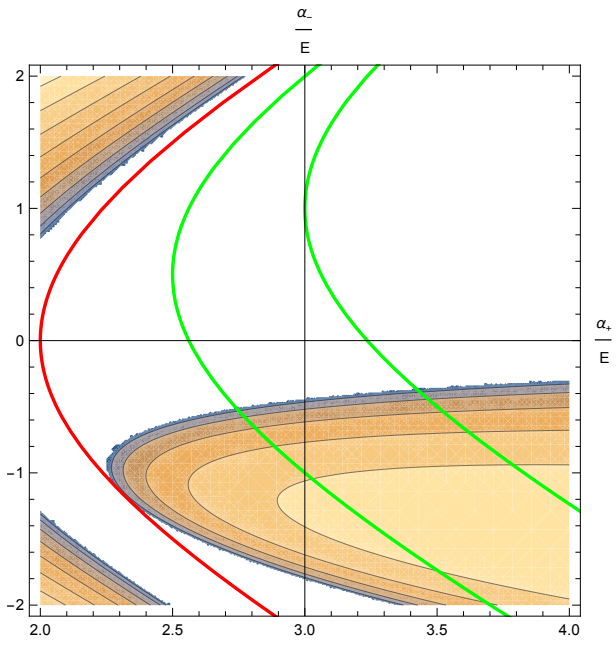


FIG. 9. Non-Abelian E: Regions of non-zero imaginary part of the eigenvalues in α_+/α_- space. Overlaid the curve $\sqrt{E} = D_1/\lambda = D_4\lambda$ (red) and curves when further adding non-zero $D_3 = \sqrt{nB}$, $n = 0.5$, 1 (green).

Non-Abelian E: 2 and 3 sector

The condition on ω is now that $\mathrm{Det}[M_{22}] = 0 = \mathrm{Det}[M_{33}]$, which is again a cubic equation of the form

$$\Box_k^3 + 2\alpha_-\Box_k^2 + \beta_E\Box_k + \gamma_E = 0, \tag{55}$$

where still $\Box_k = -\omega^2 + k_x^2 + k_T^2$, $k_T^2 = k_y^2 + k_z^2$, and

$$\alpha_- = -D_1^2 - D_2^2 + D_3^2 + D_4^2, \tag{56}$$
$$\alpha_+ = D_1^2 + D_2^2 + D_3^2 + D_4^2, \tag{57}$$
$$\beta_E = \alpha_-^2 - E^2 - 4\left((D_1\omega - D_3k_x)^2 + (D_2\omega - D_4k_x)^2\right), \tag{58}$$
$$\gamma_E = -E^2(\alpha_- - 4(k_x^2 - \omega^2)), \tag{59}$$

keeping in mind that $E = D_1D_4 - D_2D_3$. For $k_T = k_x = 0$, we obtain[**?**]

$$-(\omega^2)^3 + 2\alpha_+(\omega^2)^2 - (\alpha_-^2 + 3E^2)\omega^2 - E^2\alpha_- = 0. \tag{60}$$

There is now one real solution for ω^2, while the other two solutions are in general non-real. Hence already in the 2 and 3 sectors, there are unstable modes in the presence of finite E. However, for the special case $D_1 = D_4 = \sqrt{E}$, $D_2 = D_3 = 0$, the eigenvalues are $\omega^2 = (0, E, 3E)$, while for the generalisation $D_1 = \sqrt{E}\lambda$, $D_4 = \sqrt{E}/\lambda$, one of the eigenvalues is negative in the interval $\lambda \in [0, 1]$ and the other two are real and positive (see Figure 8). It appears that the curve traced out by $D_1D_4 = E$ in the space of $D_{1,..,4}$ is quite special, avoiding the regions where the eigenvalues are non-real. In Figure 9, we show the α_+/α_- plane, and the contours of non-zero imaginary value of the eigenvalues. Overlaid in red, the curve traced out at λ is varied, which precisely avoids those regions. Overlaid in green, the curves traced out by adding non-zero $D_3 = \sqrt{nE}$, $n = 0.5, 1$. As another sanity check, we note that for $E = 0$, $\omega^2 = (0, \alpha_+ \pm \sqrt{\alpha_+^2 - \alpha_-^2})$, which is real and positive, but non-zero whenever the D_i are.

For non-zero momentum, we immediately specialize to $D_1 = D_4 = \sqrt{E}$, $D_2 = D_3 = 0$, so that we need to solve

$$\left(-\frac{\omega^2}{E} + \frac{k_T^2}{E} + \frac{k_x^2}{E}\right) \times \left[\left(-\frac{\omega^2}{E} + \frac{k_T^2}{E} + \frac{k_x^2}{E}\right)^2 - 4\left(\frac{\omega^2}{E} + \frac{k_x^2}{E}\right) - 1\right] - 4\left(\frac{\omega^2}{E} - \frac{k_x^2}{E}\right) = 0. \tag{61}$$

The solutions are real, and one of them is negative for some regions of (k_x, k_T^2), as shown in Figure 10.

Non-Abelian E: 0 and 1 sector

We compute $\mathrm{Det}[M_{00,01,10,11}] = 0$ to find (compare (55)):

$$\left[\Box_k^3 + 2\alpha_-\Box_k^2 + \left(\beta_E + 4E^2\right)\Box_k + \gamma_e + 4E^2\alpha_-\right]^2 = 0, \tag{62}$$

and so we may consider the expression inside the square, and treat each solution as a double root. We again first consider the case $k_x = k_T = 0$, for which we have

$$-(\omega^2)^3 + 2\alpha_+(\omega^2)^2 - (\alpha_-^2 + 7E^2)\omega^2 + 3E^2\alpha_- = 0. \tag{63}$$

Again, we have one real solution and two solutions that are non-real in part of the parameter space, shown in

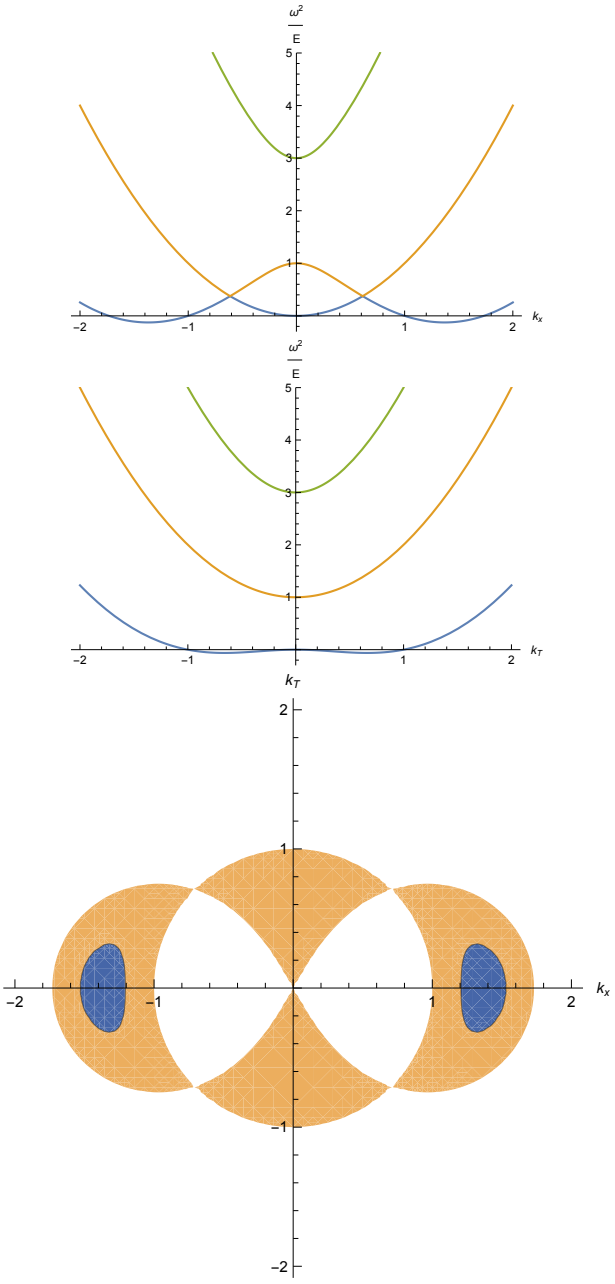


FIG. 10. Non-Abelian E: The three eigenvalues in the 2, 3 sectors for $\sqrt{E} = D_1 = D_4$, as a function k_x (top) and k_T (middle), and the region in the k_x/k_T-plane, where the lowest eigenvalue is negative (bottom).

Figure 11 as a function of α_+ and α_-. Overlaid is the now-familiar curve parametrised by $D_1 = \sqrt{E}\lambda$, $D_4 = \sqrt{E}/\lambda$, $D_2 = D_3 = 0$ which lies fully in the region of non-real eigenvalues. For $\lambda = 1$, the eigenvalues are $\omega^2 = (0, (2 \pm i\sqrt{3})E)$. The real part of two eigenvalues is always positive, while the third has negative real part whenever α_- is negative.

For non-zero momentum and $D_1 = D_4 = \sqrt{E}$, we need

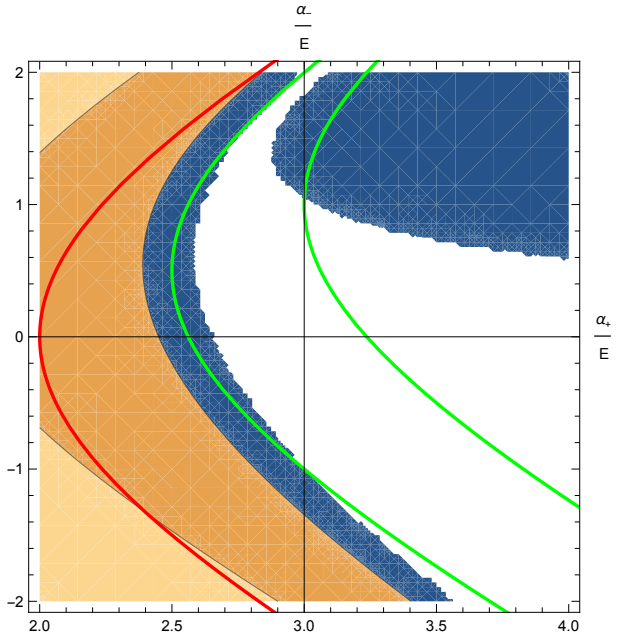


FIG. 11. Non-Abelian E: Regions of non-zero imaginary part of the eigenvalues in the 0, 1 sector in α_+/α_- space (shaded). Overlaid the curve $\sqrt{E} = D_1/\lambda = D_4\lambda$ (red) and curves when further adding non-zero D_3 (green).

to solve

$$\left(-\frac{\omega^2}{E} + \frac{k_T^2}{E} + \frac{k_x^2}{E}\right) \times \left[\left(-\frac{\omega^2}{E} + \frac{k_T^2}{E} + \frac{k_x^2}{E}\right)^2 - 4\left(\frac{\omega^2}{E} + \frac{k_x^2}{E}\right) + 3\right] - 4\left(\frac{\omega^2}{E} - \frac{k_x^2}{E}\right) = 0. \tag{64}$$

which provides one real solution and two solutions that are in general non-real. In Figure 12 we show the real and imaginary parts of these eigenvalues as a function of k_x (top) and k_T (bottom), respectively. We see that the eigenvalues are real and positive everywhere except a finite region near the origin (an ellipse in the $k_x - k_T$-plane).

And so the non-Abelian electric field only, of the set of 12 momentum modes present, several are potentially unstable, depending on the precise choice of $D_{1,..,4}$. For the special case of $D_1 = D_4 = \sqrt{E}$, the 0,1 sector has a finite momentum region with two unstable modes near the origin with non-real eigenvalues, while in the 2, 3 sector there are two unstable modes in certain momentum regions with real, negative eigenvalues (imaginary ω).

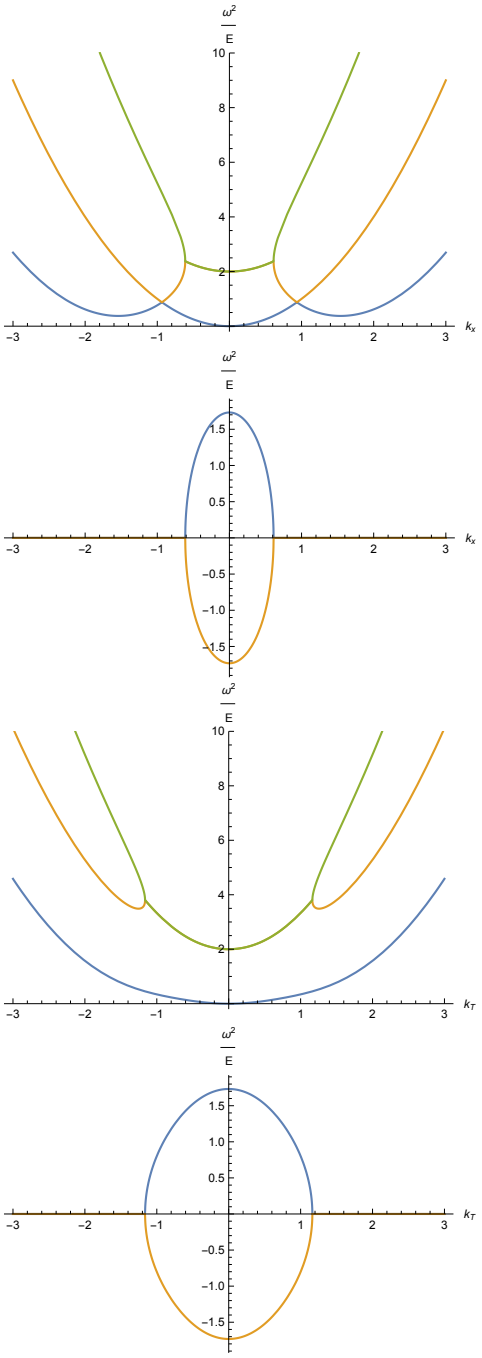


FIG. 12. Non-Abelian E: Real part and imaginary part for the three (double) eigenvalues in the 0,1 sector, as a function of k_x (top two) and k_T (bottom two), for $k_{T,x} = 0$, respectively.

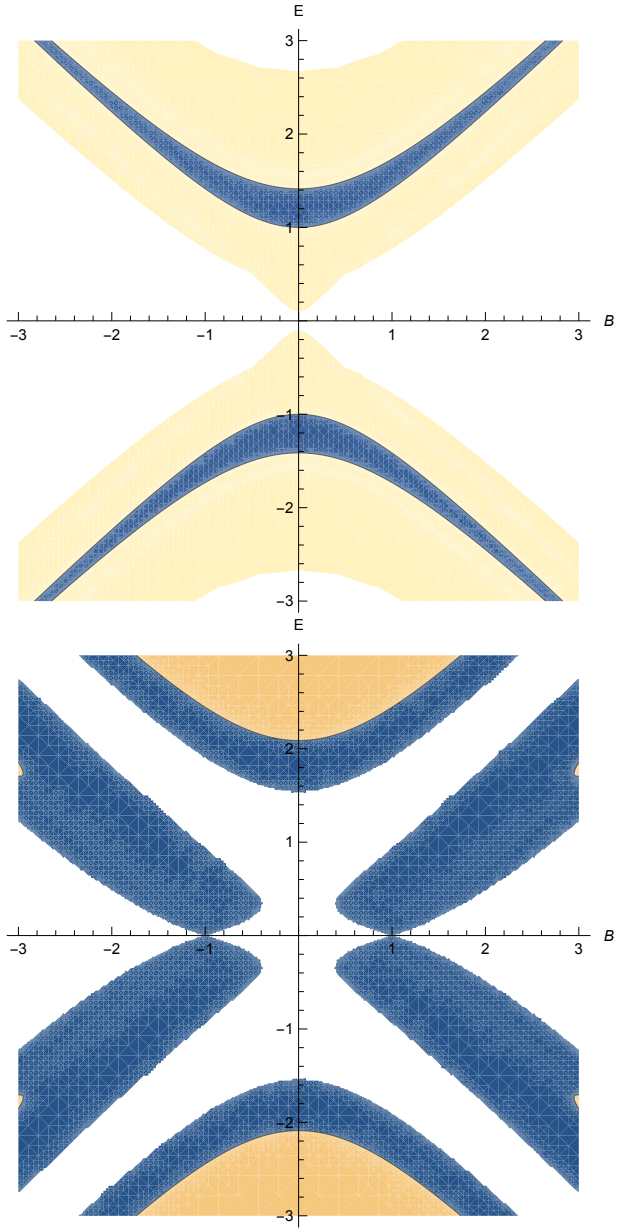


FIG. 13. Non-Abelian E and B: Regions in the E-B plane, where one or more of the first three (double) eigenvalues has negative real part (top) or non-zero imaginary part (bottom).

F. Non-Abelian E and B

Including both an electric and a magnetic field allows us to specify two directions in space, and hence completely break isotropy. We recall the non-Abelian/non-Abelian configuration

$$\bar{A}_3^0 = D_1, \quad \bar{A}_2^1 = D_4, \quad \bar{A}_3^3 = D_7, \tag{65}$$

which gives

$$E_1^1 = gD_1D_4, \quad B_1^2 = gD_4D_7. \tag{66}$$

The linear equation in momentum space is again a 12-by-12 matrix, but now the sectors are coupled. Introducing

a shorthand, where we absorb g as before and define

$$M_{\rm diag} = \begin{pmatrix} \Box_k - D_1^2 + D_4^2 + D_7^2 & 2i\,(D_7 k_z - D_1\omega) & -2iD_4 k_x \\ -2i\,(D_7 k_z - D_1\omega) & \Box_k - D_1^2 + D_7^2 & 0 \\ 2iD_4 k_x & 0 & \Box_k + D_4^2 \end{pmatrix}, \tag{67}$$

and

$$M_E = \begin{pmatrix} 0 & 0 & 0 \\ 0 & 0 & -2E \\ 0 & 2E & 0 \end{pmatrix}, \quad M_B = \begin{pmatrix} 0 & 0 & 0 \\ 0 & 0 & 2B \\ 0 & -2B & 0 \end{pmatrix}, \tag{68}$$

We have schematically

$$\begin{pmatrix} M_{\rm diag} & M_E & 0 & 0 \\ -M_E^T & M_{\rm diag} & 0 & M_B \\ 0 & 0 & M_{\rm diag} & 0 \\ 0 & M_B^T & 0 & M_{\rm diag} \end{pmatrix} \begin{pmatrix} h^0_{1,2,3} \\ h^1_{1,2,3} \\ h^2_{1,2,3} \\ h^3_{1,2,3} \end{pmatrix} = 0, \tag{69}$$

This couples the 0,1 and 3 sectors, while the 2-sector is decoupled. Note that this is not simply combining the non-Abelian E and the non-Abelian B that we considered above.

We write $D_1 = E/D_4$ and $D_7 = B/D_4$, in which case the determinant of the entire matrix may be conveniently written as

$$\frac{1}{D_4^{16}}\left[D_4^4\Box_k^3 + 2D_4^2\alpha_3\Box_k^2 + \beta_3\Box_k + \gamma_3\right]^2 \times \left[D_4^4\Box_k^3 + 2D_4^2\alpha_3\Box_k^2 + (\beta_3 - 4D_4^4(\alpha_3 - D_4^4))\Box_k + \gamma_3 - 4D_4^2\alpha_3(\alpha_3 - D_4^4)\right]^2 = 0, \tag{70}$$

with

$$\alpha_3 = B^2 - E^2 + D_4^4, \tag{71}$$

$$\beta_3 = \alpha_3(\alpha_3 + D_4^4) - D_4^8 - 4D_4^6 k_x^2 - 4D_4^2(Bk_z - E\omega)^2, \tag{72}$$

$$\gamma_3 = D_4^2\left[\alpha_3(\alpha_3 - D_4^4) - 4D_4^2(\alpha_3 - D_4^4)k_x^2 - 4D_4^2(Bk_z - E\omega)^2\right], \tag{73}$$

which reduces to (56) in the limit $B = 0$ ($D_7 = 0$). We see that the 12 roots split up into 6 double roots, 3 for each term.

We can again specialise to zero momentum, and we will rescale all quantities with the appropriate power of D_4 (ω/D_4, B/D_4^2, E/D_4^2, α_3/D_4^4 and so on, which amounts to setting $D_4 = 1$) to find the requirements

$$-(\omega^2)^3 + 2(B^2 + E^2 + 1)(\omega^2)^2 - ((B^2 - E^2)^2 + 3B^2 + E^2 + 1)\omega^2 + (B^2 - E^2)(B^2 - E^2 + 1) = 0, \tag{74}$$

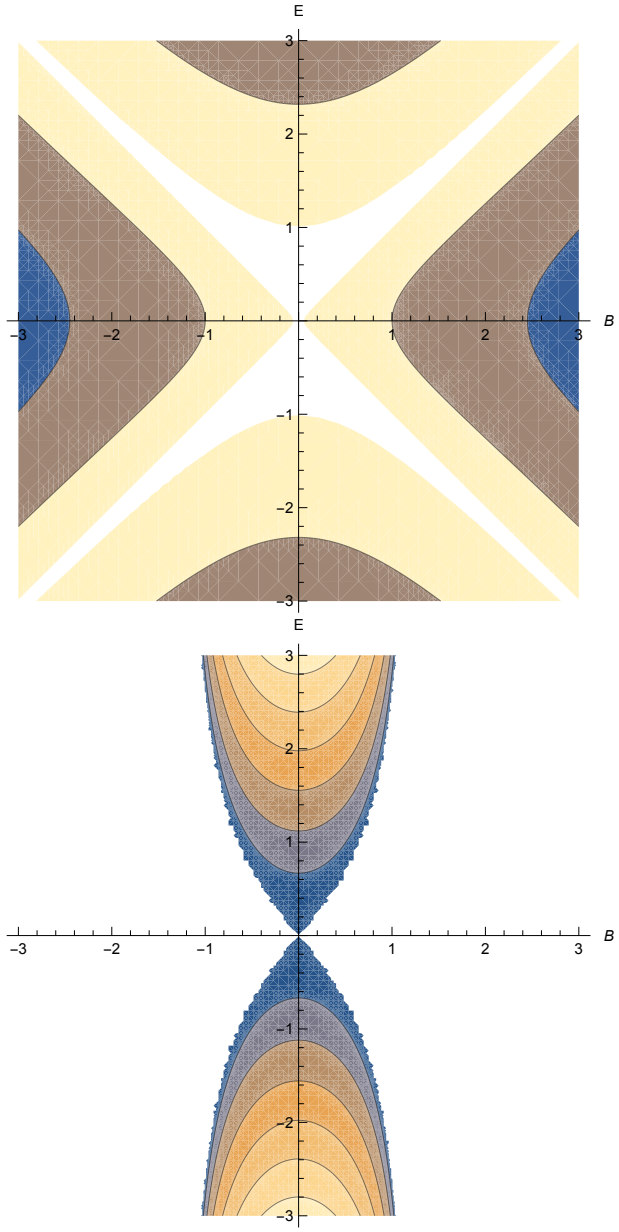


FIG. 14. Non-Abelian E and B: Regions in the E-B plane, where one or more of the second set of three (double) eigenvalues has negative real part (top) or non-zero imaginary part (bottom).

and

$$-(\omega^2)^3 + 2(B^2 + E^2 + 1)(\omega^2)^2 - ((B^2 - E^2)^2 - B^2 + 5E^2 + 1)\omega^2 - 3(B^2 - E^2)(B^2 - E^2 + 1) = 0, \tag{75}$$

These provide 6 distinct (double) eigenvalues for ω^2/D_4^2. Figure 13 shows the regions in E-B space, where one or more has negative real part (top) or non-zero imaginary part (bottom). Figure 14 show the same for the second set of three eigenvalues (solutions of (75)). Ten of twelve

eigenmodes are subject to instability in some part of momentum space.

The solutions for non-zero momentum now involves k_x, k_y and k_z independently, in addition to E and B, and it is perhaps not so helpful attempting to display the eigenvalues in all generality. But for instance for $k_y \neq 0$, we simply get the same relations but with $\omega^2 \to \omega^2 - k_y^2$. Hence all solutions for ω^2 are shifted by $+k_y^2$, so that unstable, but real-ω solutions become stable for large k_y. For $k_x \neq 0$, a similar shift appears, but there are additional terms involving k_x^2 as well in both equations

$$+4k_x^2(\omega^2 - k_x^2 - B^2 + E^2). \tag{76}$$

Something new happens for $k_z \neq 0$, where in addition to the shift $\omega^2 \to \omega^2 - k_z^2$, we pick up terms linear in ω, k_z, and proportional to BE

$$+4(B^2k_z^2 - 2BEk_z\omega)(\omega^2 - k_z^2 - 1), \tag{77}$$

so that the (relative) signs of E, B, k_z matter for determining ω.

We will not pursue this further, but simply note that there is much fun to be had in this large parameter space.

III. COMPUTING THE QUADRATIC AND CUBIC CONTRIBUTIONS FOR NON-ABELIAN B

A. Setting up the matrix structures: Mode equation

Having completed our survey of realisations of instabilities, we now return to Eq. (12), which implies that the equation of motion for the fluctuations h_a^μ including self-interaction at leading order takes the form

$$\left[g^{\mu\nu}(\bar{D}_\rho\bar{D}^\rho)_{ac} + 2g\epsilon_{abc}\bar{F}_b^{\mu\nu}\right]h_{\nu,c} - g^2\hat{M}_{ab}^{\mu\nu}(C)h_{\nu,b} = 0, \tag{78}$$

where the matrix $\hat{M}_{ab}^{\mu\nu}$ is expressed in terms of the expectation values of the fluctuation fields themselves

$$C_{a,b}^{\mu,\nu} = \langle h_a^\mu(x,t)h_b^\nu(x,t)\rangle = \int \frac{d^3k}{(2\pi)^3}\langle h_a^\mu(k,t)(h_b^\nu(k,t))^\dagger\rangle. \tag{79}$$

For the case of a non-Abelian B-field, the matrix structure is as follows (in the 2-3 sector)

$$\hat{M}_{j,ab}^i = \begin{bmatrix} -\hat{M}_{11} & 0 & 0 & 0 & 0 & 0 \\ 0 & -\hat{M}_{22} & -\hat{M}_{23} & 0 & 0 & -\hat{M}_{26} \\ 0 & -\hat{M}_{32} & -\hat{M}_{33} & 0 & -\hat{M}_{35} & 0 \\ 0 & 0 & 0 & -\hat{M}_{44} & 0 & 0 \\ 0 & 0 & -\hat{M}_{53} & 0 & -\hat{M}_{55} & -\hat{M}_{56} \\ 0 & -\hat{M}_{62} & 0 & 0 & -\hat{M}_{65} & -\hat{M}_{66} \end{bmatrix}, \tag{80}$$

where

$$\hat{M}_{11} = C_{2,2}^{3,3} + C_{3,3}^{3,3}, \quad \hat{M}_{22} = C_{3,3}^{3,3} + C_{1,1}^{3,3}, \tag{81}$$

$$\hat{M}_{33} = C_{1,1}^{3,3} + C_{2,2}^{3,3}, \quad \hat{M}_{44} = C_{2,2}^{2,2} + C_{3,3}^{2,2}, \tag{82}$$

$$\hat{M}_{55} = C_{3,3}^{2,2} + C_{1,1}^{2,2}, \quad \hat{M}_{66} = C_{1,1}^{2,2} + C_{2,2}^{2,2}, \tag{83}$$

and

$$\hat{M}_{23} = \hat{M}_{32} \ = -C_{3,2}^{3,3} = -C_{2,3}^{3,3}, \tag{84}$$

$$\hat{M}_{56} = \hat{M}_{65} \ = -C_{3,2}^{2,2} = -C_{2,3}^{2,2}, \tag{85}$$

$$\hat{M}_{26} = \hat{M}_{62} \ \ = 2C_{2,3}^{2,3} - C_{3,2}^{2,3}, \tag{86}$$

$$\hat{M}_{35} = \hat{M}_{53} \ \ = 2C_{3,2}^{2,3} - C_{2,3}^{2,3}. \tag{87}$$

We have at this point already implemented that several correlators vanish identically, and we have for simplicity by hand set to zero all correlators involving the modes in the 0-1 sector, since they are stable. The 0-1 sector of the matrix has the same structure as the 2-3 sector, but without the sector-mixing components $\hat{M}_{26,62,35,53}$. In our particular setup, we in addition find that $\hat{M}_{11} = \hat{M}_{44}$, $\hat{M}_{22} = \hat{M}_{33} = \hat{M}_{55} = \hat{M}_{66}$, $\hat{M}_{23} = \hat{M}_{32} = \hat{M}_{56} = \hat{M}_{65}$ and $\hat{M}_{35} = \hat{M}_{53} = -\hat{M}_{26} = -\hat{M}_{62}$, as there are only four distinct correlators to take into account, $C_{1,1}^{2,2}, C_{2,2}^{2,2}, C_{2,3}^{2,3}, C_{2,3}^{2,2}$.

Our task is then to compute these time-dependent correlators, and solving again the eigenvalue equations ($\mathrm{Det}[\mathcal{M} - g^2\hat{M}] = 0$) to find corrected, time-dependent values of ω^2. We will do this below, but already at this stage, we note that in the limit where $\hat{M} \gg \mathcal{M}$, the corrected system now has three double eigenvalues $\hat{M}_{11}, \hat{M}_{22} \pm \sqrt{\hat{M}_{23}^2 + \hat{M}_{26}^2}$, of which one is negative whenever $\hat{M}_{23}^2 + \hat{M}_{26}^2 > \hat{M}_{22}^2$. This means that (some of) the instabilities remain even at late times, provided the background field remains constant. In the 0-1 sector, all modes remain stable, since $\hat{M}_{26} \to 0$ and as we will see, $\hat{M}_{22} > \hat{M}_{23}$.

B. Setting up the matrix structures: Background equation

Similarly, we can express the quadratic contribution (10) in terms of correlators,

$$\bar{D}_\mu^{ab}\bar{F}^{\mu\nu,b} = j_a^\nu - \bar{M}_{ab}^{\nu\mu}[C]\bar{A}_{\mu,b}. \tag{88}$$

Again, in our specific setup the space-derivative terms in the correction to the current $\bar{j}_a^\nu$ vanishes because the correlators are space-independent. The time-derivative terms also vanish because they either act on a stable correlator (in the 0-μ sector, which we neglect) or because of antisymmetrization. We are therefore left with the matrix $\bar{M}(C)$ which multiplies $\bar{A}$, and we find that this matrix has the same structure as $\hat{M}$. Since there is no original current in the 0-1 sector, it is consistent to set $\bar{A}_a^{0,1} = 0$ throughout, and we will consider it no further.

In the 2-3 sector, however, we would have to solve the full Yang-Mills equation with a time-dependent current.

We will not attempt this here, but simply estimate at which time the assumption of constant $\bar{A}$ is likely to break down. We quantify this as when the correction is larger than the original current

$$\bar{M}^{\nu\mu}_{ab}[C]\bar{A}_{\mu,b} > j^{\nu}_{a}. \tag{89}$$

Recall, that

$$j^{\nu}_{a} = -gB\left[\begin{pmatrix}0\\0\\0\end{pmatrix}\begin{pmatrix}0\\0\\0\end{pmatrix}\begin{pmatrix}0\\D_7\\-D_8\end{pmatrix}\begin{pmatrix}0\\-D_5\\D_6\end{pmatrix}\right]. \tag{90}$$

with $D_6 = -D_7 = \sqrt{B/g}$, and $D_5 = D_8 = 0$. The correction simply becomes

$$\left(\bar{M}\bar{A}\right)^{\nu}_{a} = -gB\left[\begin{pmatrix}0\\0\\0\end{pmatrix}\begin{pmatrix}0\\0\\0\end{pmatrix}\begin{pmatrix}0\\J_7\\-J_8\end{pmatrix}\begin{pmatrix}0\\-J_5\\J_6\end{pmatrix}\right]. \tag{91}$$

with

$$J_6 = -J_7 = \sqrt{\frac{B}{g}}\frac{g\left(C^{33}_{11} + C^{33}_{33} - 3C^{23}_{23}\right)}{B},$$
$$J_5 = -J_8 = \sqrt{\frac{B}{g}}\frac{g\,C^{22}_{23}}{B}, \tag{92}$$

so that the form of the total current is unchanged, and will still generate a B field in the $\mu = 1$, $a = 1$ direction. This B-field is however now time dependent, and the time-dependence of $\bar{A}^{\mu}_{a}$ could also potentially source an Abelian E-field. This means that as soon as either of the correlators is larger than B/g, our approximation breaks down. We will now estimate when that happens.

C. Eigenvectors, quantization and correlators

The 2-3 sector of the linear system has 6 eigenvalues for each set of momenta $k_{x,y,z}$, $\omega^2_i(k)$, corresponding to 6 eigenvectors $\phi_i(k,t)$ which are solutions to

$$\partial^2_t\phi_i(k,t) = -\omega^2_i(k)\phi_i(k,t), \quad i = 1,...,6, \tag{93}$$
$$\rightarrow \quad \phi_i(k,t) = \alpha^i_k e^{i\omega_i(k)t} + \beta^i_k e^{-i\omega_i(k)t}. \tag{94}$$

In order to define the state in which to compute the expectation values, we will assume that the system is prepared in a vanishing background $\bar{A}^{\mu}_{a} = 0$ for $t < 0$, and that $\bar{A}^{\mu}_{a}$ is instantaneously turned on at $t = 0$, remaining constant for $t > 0$. Then we may write for $t < 0$

$$\phi_i(k,t) = \frac{1}{\sqrt{2\omega^0_k}}\left(a^i_k e^{i\omega^0_k t} + (a^i_{-k})^{\dagger}e^{-i\omega^0_k t}\right), \tag{95}$$
$$\partial_t\phi_i(k,t) = \frac{i\omega^0_k}{\sqrt{2\omega^0_k}}\left(a^i_k e^{i\omega^0_k t} - (a^i_{-k})^{\dagger}e^{-i\omega^0_k t}\right), \tag{96}$$

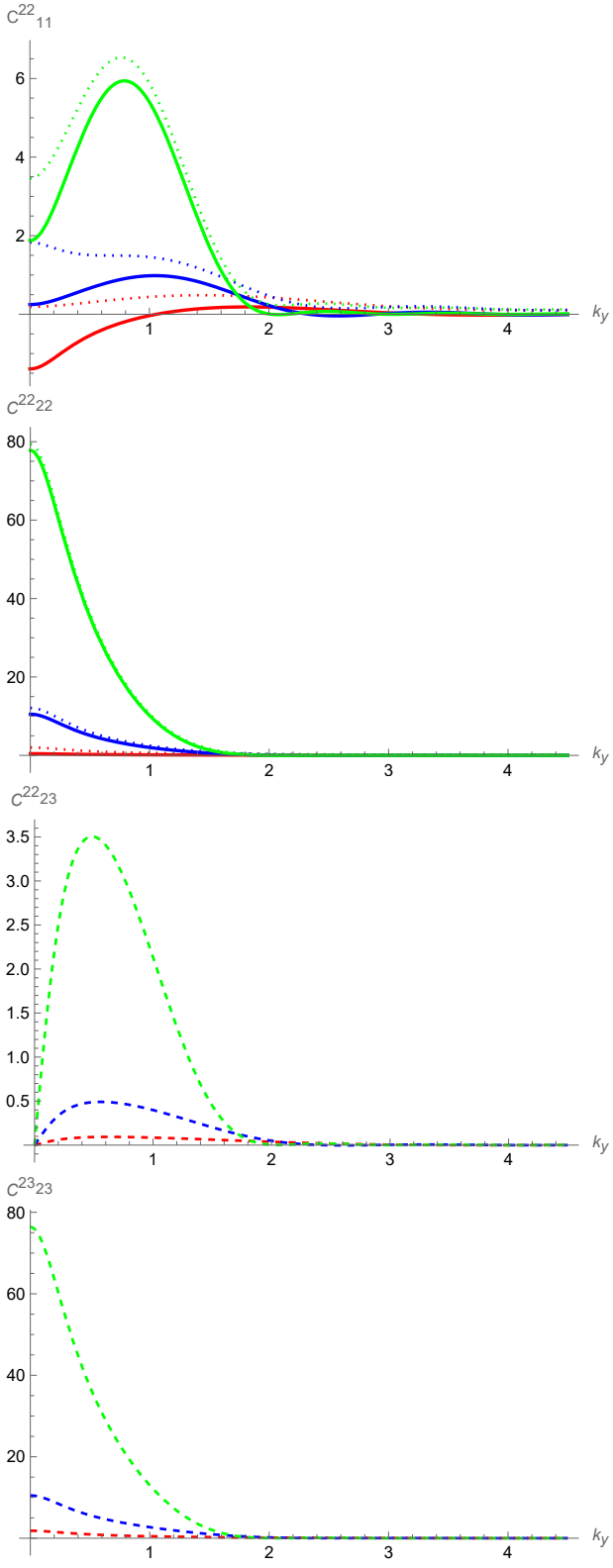


FIG. 15. Non-Abelian B: The correlators C^{22}_{11}, C^{22}_{22}, C^{22}_{23} and C^{23}_{23} (top to bottom) as a function of k_y for time $gBt = 1, 2, 3$ (red, blue, green). Renormalised (full lines) and unrenormalised (dotted lines).

where we note that for $\bar{A}^\mu_a = 0$, all the eigenvalues coincide $\omega_i(k) \to \omega^0_k = |\mathbf{k}|$.

For $t > 0$, we may write in general

$$\phi_i(k,t) = \alpha^i_k e^{i\omega^i_k t} + \beta^i_k e^{-i\omega^i_k t}, \quad (97)$$

$$\partial_t \phi_i(k,t) = i\omega^i_k \left(\alpha^i_k e^{i\omega^i_k t} - \beta^i_k e^{-i\omega^i_k t}\right). \quad (98)$$

Matching the expressions at $t = 0$, we can express α^i_k and β^i_k in terms of a^i_k and a^i_{-k} as,

$$\alpha^i_k = \frac{1}{\sqrt{2\omega^0_k}}\left[a^i_k\left(1+\frac{\omega^0_k}{\omega^i_k}\right) + (a^i_{-k})^\dagger\left(1-\frac{\omega^0_k}{\omega^i_k}\right)\right], \quad (99)$$

$$\beta^i_k = \frac{1}{\sqrt{2\omega^0_k}}\left[a^i_k\left(1-\frac{\omega^0_k}{\omega^i_k}\right) + (a^i_{-k})^\dagger\left(1+\frac{\omega^0_k}{\omega^i_k}\right)\right]. \quad (100)$$

Choosing our initial state as the vacuum at $t < 0$, $a^i_k|0\rangle = 0$ and using the standard commutation relations $[a^i_k, (a^j_{k'})^\dagger] = (2\pi)^3\delta^{ij}\delta^3(k-k')$, we can straightforwardly compute expectation values of any combination of α^i_k, β^i_k.

The fluctuation fields $h^\mu_a(k)$ in the 2-3 sector are linear combinations of the eigenmodes $\phi_i(k)$, written in terms of a unitary matrix $U^{ij}(k)$. With ($\mu = 2,3$, $a = 1,2,3 \to 1,..,6$) so that

$$\begin{aligned}\langle h^i(k)(h^j(k))^\dagger\rangle &= \langle U_{ir}\phi^r(k)[U_{js}\phi^s(k)]^\dagger\rangle \\ &= U^{ir}[U^\dagger]_{rj}\langle\phi^r(k)[\phi^r(k)]^\dagger\rangle, \end{aligned} \quad (101)$$

since $\langle\phi^r(k)[\phi^s(k)]^\dagger\rangle \propto \delta^{rs}$. We wish to compute the correlators

$$\begin{aligned} C^{\mu,\nu}_{a,b} &= \int \frac{d^3k}{(2\pi)^3}\langle h^\mu_a(k)h^\nu_b(-k)\rangle \\ &= \int \frac{d^3k}{(2\pi)^3}\frac{\langle h^i(k)[h^j(k)]^\dagger + [h^i(k)]^\dagger h^j(k)\rangle}{2}. \end{aligned} \quad (102)$$

Which follow from combining (94, 100, 101), and using these we can construct the non-linear correction to the linear mode equation (80).

One final complication is that the diagonal correlators are (IR and UV) divergent, and so in order to gauge the effect of the instability, we will in practice compute

$$C^{\mu,\nu}_{a,b;ren} = \int \frac{d^3k}{(2\pi)^3}\left[\langle h^\mu_a(k,t)h^\nu_b(-k,t)\rangle - \langle h^\mu_a(k,0)h^\nu_b(-k,0)\rangle\right]. \quad (103)$$

In Figure 15 we show the four distinct (renormalised) correlators in momentum space at times $t = 1,2,3$ (in units where $gB = 1$). We see that the C^{22}_{22} and C^{23}_{23} are substantially larger than the other two.

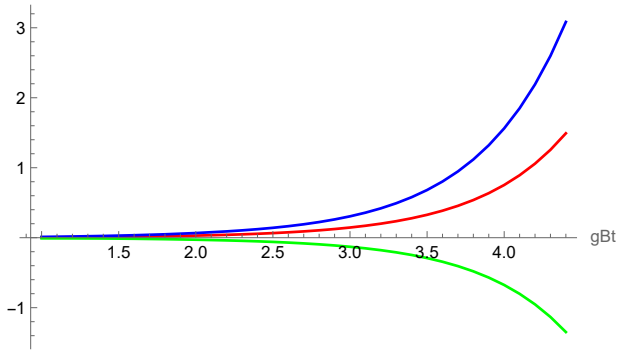


FIG. 16. Non-Abelian B: The three eigenvalues M_{11}, $M_{22} \pm \sqrt{M_2 3^2 - M^2_{26}}$.

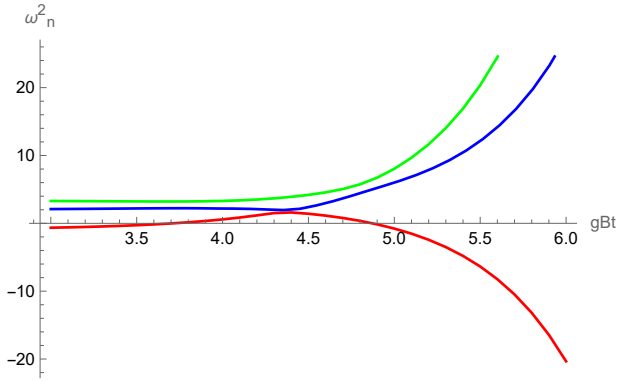


FIG. 17. Non-Abelian B: The corrected eigenvalues ω_i as a function of time.

D. Corrected dispersion relations

In Figure 16, we show M_{11}, $M_{22} \pm \sqrt{M^2_{23} + M^2_{26}}$, which was our late-time estimate for the eigenvalues in section III A. The lowest eigenvalue is indeed negative throughout, and so for any momentum, for late enough time, instabilities remain if they are not switched off for other reasons.

We can do better, and simply compute the eigenvalues at $k = 0$ of the whole matrix $\mathcal{M} - g^2\hat{M}$, as a function of time. Figure 17 shows the 6 eigenvalues in the 2-3 sector as a function of time. The initially unstable mode is briefly stabilized around $gBt = 3.5$, but by 4.7 the late time behaviour takes over and the eigenvalue becomes negative again.

E. Corrected current

In a similar way, we can insert the correlators into the effective current. Figure 18 shows the quantities $J_{5,6,7,8}$ (92) in time. We see that $J_6 = -J_7$ grow fastest, and become order 1 (our criterion for $g = B = 1$) around $gBt = 4-5$. At this time, we can then no longer assume

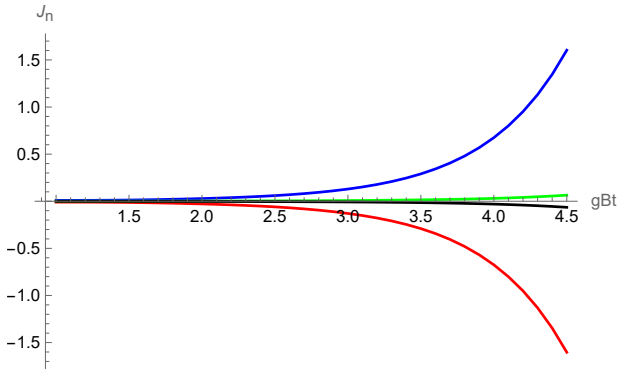


FIG. 18. Non-Abelian B: The quantities $J_{5,6,7,8}/\sqrt{B/g}$ in time.

a constant background field. Whether this leads to stability is beyond our approach here, but may be readily studied using numerical simulations.

IV. CONCLUSIONS

To summarize, we have investigated the instabilities of field fluctuations in pure SU(2) classical gauge theory with a constant homogeneous background E and/or B field. We first in section II presented a fairly general set of background vector potentials, generalising the setup of [26, 27]. We then in section A focused on non-Abelian E and B field backgrounds, and derived the dispersion relation that the fluctuations obey. Non-real instances of frequencies $\omega(k)$ signal unstable modes in the linear theory, and we confirmed that these arise for homogeneous E fields, B fields and when combining the two. As an aside, we also found that the instability does not simply depend on the B or E-field, but on the vector field components $\bar{A}^\mu_a$ separately.

Of particular interest is to understand to what extent these instabilities shut themselves off, due to the non-linearities of the theory. To that end, we computed the non-linear (Gaussian) corrections to both the background field equation and the linear fluctuation equation. We found that the corrections certainly influence the instabilities of the fluctuations, but that rather than turning them off, they can make them stronger. This however assumes that the background field stays constant and homogeneous throughout, which is spoiled by the non-linearities in the background field equation. We estimated the time when the background field is no longer a constant non-Abelian B field to be $gBt \simeq 4$, but further details of how this comes about, and the explicit effect on the instabilities is likely better adressed numerically.

Although the context of this type of instabilities is the thermalisation of the plasma in HICs, anisotropic gauge fields are not unique to QCD. Anisotropic conditions also appear in cosmology, for instance in the context of first order phase transitions. In that case, the walls of nucleated bubbles sweep through the ambient plasma, so that immediately in front and behind the advancing wall, the plasma is anisotropic (see for instance [28–30]). Although it is not clear to what extent net E and B fields are produced, it would be worth investigating whether an anisotropic out-of-equilibrium background could potentially source similar instabilities.

The obvious continuation of this work is to make a full investigation the other realisations of background E and B fields presented in Appendix B. This could also readily be compared to direct numerical simulations of the pure gauge SU(2) system, going beyond the Gaussian approximation to the non-linearities. Further generalising to SU(3) gauge theory involves writing down a $\mathcal{M}(32\times 32)$ matrix equation and solving for the dispersion relations and then unstable modes there. This is ongoing work, but we note that the results for SU(2) presented here naturally arise as a subsector in the SU(3) theory.

ACKNOWLEDGMENTS

We thank Aleksi Kurkela and Germano Nardini for enlightening discussions and Alexander Rothkopf for many useful comments. This work is funded by the grant Project. No. 302640 funded by the Research Council of Norway.

Appendix A: Linear equations of motion in momentum space

If the background field $\bar{A}^\mu_a$ has no space dependence, we can simply Fourier transform in three dimensions and write

$$h^\mu_a(x,y,z,t) = \int \frac{dk_x dk_y dk_z}{(2\pi)^3} e^{-ik_x x - ik_y y - ik_z z} h^\mu_a(k_x,k_y,k_z,t). \tag{A1}$$

Then the equation of motion in momentum space reads

$$\mathcal{M}(\partial_t^2, \partial_t, k_x, k_y, k_z, \bar{A}) h^\mu_a = 0, \tag{A2}$$

which can be solved as a set of coupled linear differential equations. One may further Fourier transform in time, in the sense that

$$h^\mu_a(k_x,k_y,k_z,t) = \int \frac{d\omega}{2\pi} h^\mu_a(k_x,k_y,k_z,\omega) e^{i\omega t}, \tag{A3}$$

in which case one may substitute $\partial_t \to i\omega$ in (A2). The expectation is that for some of the modes (for certain values of $k_x, k_y, k_z, \bar{A}$) ω_k has a non-zero imaginary part, and the mode grows (or decays) exponentially in time.

If the background field depends on a spatial coordinate, we can only Fourier transform in the remaining

coordinates (say y, z), to find

$$h_a^\mu(x,y,z,t) = \int \frac{dk_y dk_z}{(2\pi)^2} e^{-ik_y y - ik_z z} h_a^\mu(x,k_y,k_z,t), \tag{A4}$$

and we are led to a relation of the form

$$\mathcal{M}(\partial_t^2, \partial_t, \partial_x^2, \partial_x, k_y, k_z, \bar{A}) h_a^\mu = 0. \tag{A5}$$

This implies that the field profile is not a product of plane waves in x, y, z but that the x-dependence is some other function to be solved for explicitly. Similary, if the background field depends on two spatial coordinate, we can only Fourier transform in the remaining coordinates (say, z), to find

$$h_a^\mu(x,y,z,t) = \int \frac{dk_z}{(2\pi)} e^{-ik_z z} h_a^\mu(x,y,k_z,t). \tag{A6}$$

Neither the x- and y-dependence can then be expressed as plane waves. Finally, if $\bar{A}_a^\mu$ is a function of t, also the Fourier transform in time fails, and the field has a non-trivial time evolution. We again refer to [26] and Appendix B for a discussion on this.

Appendix B: Space- or time-dependent vector potentials

For completeness, we now briefly present a few cases of Abelian vector potentials, and how one might go about solving the linearised equations of motion.

1. Abelian Configuration of B field ($C_3 = B \neq 0$)

Consider a potential $\bar{A}_a^\mu$ in the $\mu = 3$ direction with a constant homogeneous magnetic field in the $i = 2$ direction and in the $a = 1$ color direction,

$$\bar{A}_a^\mu = \left[\begin{pmatrix} 0 \\ 0 \\ 0 \end{pmatrix} \begin{pmatrix} 0 \\ 0 \\ 0 \end{pmatrix} \begin{pmatrix} 0 \\ 0 \\ 0 \end{pmatrix} \begin{pmatrix} By \\ 0 \\ 0 \end{pmatrix} \right]. \tag{B1}$$

The linearized Y-M equation becomes

$$\Box h_a^\mu - 2gBy\epsilon^{ab1}\partial_z h_b^\mu - 2gB\epsilon^{ab1}(\delta^{\mu y} h_b^z - \delta^{\mu z} h_b^y) - g^2 B^2 y^2 \epsilon^{ac1}\epsilon^{cb1} h_b^\mu = 0. \tag{B2}$$

Let us define the functions

$$T^\pm = h_2^0 \pm i h_3^0, \qquad X^\pm = h_2^x \pm i h_3^x,$$
$$Y^\pm = h_2^y \pm i h_3^y, \qquad Z^\pm = h_2^z \pm i h_3^z.$$

Modifying Eq. (B2) and then solving for each modes in Fourier space, we obtain the dispersion relations such as

$$\left(-\omega^2 + k_x^2 + (k_z \mp gBy)^2 - \frac{d^2}{dy^2} \right) T^\pm(y) = 0, \tag{B3}$$

$$\left(-\omega^2 + k_x^2 + (k_z \mp gBy)^2 - \frac{d^2}{dy^2} \right) X^\pm(y) = 0, \tag{B4}$$

$$\left(-\omega^2 \pm 2gB + k_x^2 + (k_z - gBy)^2 - \frac{d^2}{dy^2} \right) U^\pm(y) = 0, \tag{B5}$$

$$\left(-\omega^2 \mp 2gB + k_x^2 + (k_z + gBy)^2 - \frac{d^2}{dy^2} \right) W^\pm(y) = 0. \tag{B6}$$

where

$$U^\pm \equiv Y^+ \pm iZ^+, \qquad W^\pm \equiv Y^- \pm iZ^-.$$

The above equations resemble a Schrödinger equation for a harmonic oscillator, and have a discrete spectrum of frequencies. We can solve for the frequencies for W^+ and U^-, to find

$$\omega_0^2 = 2gB\left(n + \frac{1}{2}\right) + k_x^2. \tag{B7}$$

and

$$\omega_\pm^2 = 2gB\left(n + \frac{1}{2}\right) \pm 2gB + k_x^2. \tag{B8}$$

for discrete $n = 0, 1, 2, \ldots$ and continuous k_x.

It is clear that ω_0^2 and ω_+^2 are always positive (≥ 0) for any values of n, but ω_-^2 is negative whenever $n < \frac{1}{2} - \frac{k_x^2}{2gB}$. That means there are unstable modes of U^- and W^+ which grow exponentially. The remaining modes $T^\pm$ and $X^\pm$, U^+ and W^- are stable for all k_x. We see that the dependence of k_z is absorbed in a redefinition of the y-coordinate.

2. Abelian Configuration of E field ($C_1 = E \neq 0$)

Consider instead a potential $\bar{A}_a^\mu$ in the $\mu = 0$ direction with a constant homogeneous electric field in the $i = 1$ direction and in the $a = 1$ color direction

$$\bar{A}_a^\mu = \left[\begin{pmatrix} -Ex \\ 0 \\ 0 \end{pmatrix} \begin{pmatrix} 0 \\ 0 \\ 0 \end{pmatrix} \begin{pmatrix} 0 \\ 0 \\ 0 \end{pmatrix} \begin{pmatrix} 0 \\ 0 \\ 0 \end{pmatrix} \right]. \tag{B9}$$

The linearized Y-M equation becomes

$$g^{\mu\nu}\left[(\partial_\rho \delta^{ad} - g f^{ade} \bar{A}_\rho^e)(\partial^\rho \delta_{dc} - g f_{dcf} \bar{A}_f^\rho) h_\nu^c \right] + 2g f^{abc} \bar{F}_b^{\mu\nu} h_\nu^c = 0. \tag{B10}$$

Solving Eq. (B10) for the modes in Fourier space give us dispersion relations such as

$$\left(k_y^2 + k_z^2 \pm 2igE - (\omega + gEx)^2 - \frac{d^2}{dx^2} \right) G^\pm(x) = 0, \tag{B11}$$

$$\left(k_y^2+k_z^2\mp 2igE-(\omega-gEx)^2-\frac{d^2}{dx^2}\right)H^{\pm}(x)=0, \tag{B12}$$

$$\left(k_y^2+k_z^2-(\omega\pm gEx)^2-\frac{d^2}{dx^2}\right)Y^{\pm}(x)=0, \tag{B13}$$

$$\left(k_y^2+k_z^2-(\omega\mp gEx)^2-\frac{d^2}{dx^2}\right)Z^{\pm}(x)=0. \tag{B14}$$

where the functions $G^{\pm}$ and $H^{\pm}$ are defined as

$$G^{\pm}\equiv T^{+}\pm X^{+}, \qquad H^{\pm}\equiv T^{-}\pm X^{-}.$$

The above equations again resemble an inverted Schrödinger equation, an "upside-down" harmonic oscillator. This does not have any normalizable solutions.

3. Abelian E and Abelian B ($C_1 \neq 0 \neq C_3$)

Consider a potential $\bar{A}^{\mu}_a$ corresponding to a constant homogeneous electric field in the x direction and a constant homogeneous magnetic field in the y direction,

$$\bar{A}^{\mu}_a=\left[\begin{pmatrix}-Ex\\0\\0\end{pmatrix}\begin{pmatrix}0\\0\\0\end{pmatrix}\begin{pmatrix}0\\0\\0\end{pmatrix}\begin{pmatrix}By\\0\\0\end{pmatrix}\right]. \tag{B15}$$

The linearized Y-M equation in this case becomes

$$\left((k_z-gBy)^2-(\omega+gEx)^2\pm 2igE-\frac{d^2}{dx^2}-\frac{d^2}{dy^2}\right)\times G^{\pm}(x,y)=0, \tag{B16}$$

$$\left((k_z+gBy)^2-(\omega-gEx)^2\mp 2igE-\frac{d^2}{dx^2}-\frac{d^2}{dy^2}\right)\times H^{\pm}(x,y)=0, \tag{B17}$$

$$\left((k_z-gBy)^2-(\omega+gEx)^2\pm 2gB-\frac{d^2}{dx^2}-\frac{d^2}{dy^2}\right)\times U^{\pm}(x,y)=0, \tag{B18}$$

$$\left((k_z+gBy)^2-(\omega-gEx)^2\mp 2gB-\frac{d^2}{dx^2}-\frac{d^2}{dy^2}\right)\times W^{\pm}(x,y)=0. \tag{B19}$$

Since there is explicit dependence on x and y we are left with a partial differential equation in both coordinates. The equations (B16) − (B19) can be further solved variable separation. For example, considering Eq. (B18), we can write

$$U^{\pm}(x,y)=U^{\pm}_E(x)U^{\pm}_B(y). \tag{B20}$$

We can split them into two equations such as

$$\left[Q^{\pm}_U-\frac{d^2}{dx^2}-g^2E^2\left(\frac{\omega}{gE}+x\right)^2\right]U^{\pm}_E(x)=0, \tag{B21}$$

$$\left[-Q^{\pm}_U\pm 2gB-\frac{d^2}{dy^2}+g^2B^2\left(\frac{k_z}{gB}-y\right)^2\right]U^{\pm}_B(y)=0. \tag{B22}$$

where $Q^{\pm}_U$ is the separation constant. Equation (B22) is another Schrödinger equation with the following replacements, $Q^{\pm}_U\mp 2gB\rightarrow 2m\varepsilon$, $gB\rightarrow m\bar{\omega}$, $\frac{k_z}{gB}\rightarrow y_0$. Since the oscillator energy $\varepsilon_n=(n+\frac{1}{2})\bar{\omega}$, $n=0,1,2,3,...$

$$Q^{\pm}_U=gB(2n+1)\pm 2gB. \tag{B23}$$

Equation (B21) is an inverted Schrödinger equation with the following replacements, $Q^{\pm}_U\rightarrow -2m\varepsilon$, $gE\rightarrow m\bar{\omega}$, $\frac{\omega}{gE}\rightarrow x_0$. It has no normalizable solutions.

Similary, separating variables one can write

$$W^{\pm}(x,y)=W^{\pm}_E(x)W^{\pm}_B(y). \tag{B24}$$

It can also be split into two equations such as

$$\left[Q^{\pm}_W-\frac{d^2}{dx^2}-g^2E^2\left(\frac{\omega}{gE}-x\right)^2\right]W^{\pm}_E(x)=0, \tag{B25}$$

$$\left[-Q^{\pm}_W\mp 2gB-\frac{d^2}{dy^2}+g^2B^2\left(\frac{k_z}{gB}+y\right)^2\right]W^{\pm}_B(y)=0. \tag{B26}$$

where $Q^{\pm}_W$ is the separation constant. Similarly one can solve the remaining two equations.

4. Abelian E and non-Abelian B ($C_2 = E$, $D_3 = \lambda\sqrt{B/g}$ and $D_{12}=\frac{1}{\lambda}\sqrt{B/g}$)

Consider a potential $\bar{A}^{\mu}_a$ corresponding to a constant homogeneous electric field in the x direction and constant homogenous magnetic field components in the x and z directions

$$\bar{A}^{\mu}_a=\left[\begin{pmatrix}0\\0\\0\end{pmatrix}\begin{pmatrix}-tC_2\\0\\D_3\end{pmatrix}\begin{pmatrix}0\\0\\0\end{pmatrix}\begin{pmatrix}D_{12}\\0\\0\end{pmatrix}\right]. \tag{B27}$$

In this case, the linearized Yang-Mills equation reduces to

$$\begin{aligned}&\Box h^{\mu}_a+2g\epsilon^{a1b}(D_{12}\partial_z-tC_2\partial_x)h^{\mu}_b\\&\quad+2g\epsilon^{a3b}D_3\partial_x h^{\mu}_b-g^2\epsilon^{a1d}\epsilon^{d1b}(t^2C_2^2+D_{12}^2)h^{\mu}_b\\&\quad+g^2tC_2D_3h^{\mu}_b(\epsilon^{a1d}\epsilon^{d3b}+\epsilon^{a3d}\epsilon^{d1b})-g^2\epsilon^{a3d}\epsilon^{d3b}D_3^2h^{\mu}_b\\&\quad+2g^2\epsilon^{a2b}(\delta^{\mu 3}D_{12}D_3h^{x}_b-\delta^{\mu 1}D_3D_{12}h^{z}_b)=0.\end{aligned} \tag{B28}$$

We may now Fourier transform in space, but not in time, and the linear equation for the modes of the fluctuations reduce to a set of 12 coupled linear differential equations which we can split into four 3×3 matrices corresponding to the $\mu = 0, 1, 2, 3$ sectors introduced earlier, with cross-terms coupling the 0 and 1 sectors. The diagonal 3×3 matrix has the form

$$M^t_{ANA} = \begin{bmatrix} (\Box + g^2 D_3^2) & 2igk_x D_3 & g^2 t D_3 C_2 \\ -2igk_x D_3 & \Box + g^2(t^2 C_2^2 + D_{12}^2 + D_3^2) & 2ig(D_{12}k_z - tC_2 k_x) \\ g^2 t D_3 C_2 & -2ig(D_{12}k_z - tC_2 k_x) & \Box + g^2(t^2 C_2^2 + D_{12}^2) \end{bmatrix} \tag{B29}$$

where $\Box = \frac{\partial^2}{\partial t^2} + \mathbf{k}^2$, $\mathbf{k}^2 = k_x^2 + k_y^2 + k_z^2$. Diagonalizing this set of equations is non-trivial, but would result in a set of 12 non-linear differential equations in t, which most likely require numerical evaluation.

[1] S. Mrowczynski, B. Schenke and M. Strickland, Phys. Rept. **682** (2017), 1-97 doi:10.1016/j.physrep.2017.03.003 [arXiv:1603.08946 [hep-ph]].

[2] T. Epelbaum and F. Gelis, Phys. Rev. Lett. **111** (2013), 232301 doi:10.1103/PhysRevLett.111.232301 [arXiv:1307.2214 [hep-ph]].

[3] T. Epelbaum and F. Gelis, Phys. Rev. D **88** (2013), 085015 doi:10.1103/PhysRevD.88.085015 [arXiv:1307.1765 [hep-ph]].

[4] T. Lappi, Phys. Rev. C **67** (2003), 054903 doi:10.1103/PhysRevC.67.054903 [arXiv:hep-ph/0303076 [hep-ph]].

[5] T. Lappi and L. McLerran, Nucl. Phys. A **772** (2006), 200-212 doi:10.1016/j.nuclphysa.2006.04.001 [arXiv:hep-ph/0602189 [hep-ph]].

[6] F. Gelis, K. Kajantie and T. Lappi, Phys. Rev. Lett. **96** (2006), 032304 doi:10.1103/PhysRevLett.96.032304 [arXiv:hep-ph/0508229 [hep-ph]].

[7] R. Baier, A. H. Mueller, D. Schiff and D. T. Son, Phys. Lett. B **502** (2001), 51-58 doi:10.1016/S0370-2693(01)00191-5 [arXiv:hep-ph/0009237 [hep-ph]].

[8] S. Mrowczynski, Phys. Lett. B **314** (1993), 118-121 doi:10.1016/0370-2693(93)91330-P

[9] S. Mrowczynski, Acta Phys. Polon. B **37** (2006), 427-454 [arXiv:hep-ph/0511052 [hep-ph]].

[10] A. Kurkela and G. D. Moore, JHEP **12** (2011), 044 doi:10.1007/JHEP12(2011)044 [arXiv:1107.5050 [hep-ph]].

[11] A. Kurkela and G. D. Moore, JHEP **11** (2011), 120 doi:10.1007/JHEP11(2011)120 [arXiv:1108.4684 [hep-ph]].

[12] J. Berges, K. Boguslavski, S. Schlichting and R. Venugopalan, Phys. Rev. D **89** (2014) no.7, 074011 doi:10.1103/PhysRevD.89.074011 [arXiv:1303.5650 [hep-ph]].

[13] A. Kurkela, A. Mazeliauskas, J. F. Paquet, S. Schlichting and D. Teaney, Phys. Rev. Lett. **122** (2019) no.12, 122302 doi:10.1103/PhysRevLett.122.122302 [arXiv:1805.01604 [hep-ph]].

[14] A. Kurkela, A. Mazeliauskas, J. F. Paquet, S. Schlichting and D. Teaney, Phys. Rev. C **99** (2019) no.3, 034910 doi:10.1103/PhysRevC.99.034910 [arXiv:1805.00961 [hep-ph]].

[15] A. Kurkela and Y. Zhu, Phys. Rev. Lett. **115** (2015) no.18, 182301 doi:10.1103/PhysRevLett.115.182301 [arXiv:1506.06647 [hep-ph]].

[16] J. Berges and S. Schlichting, Phys. Rev. D **87** (2013) no.1, 014026 doi:10.1103/PhysRevD.87.014026 [arXiv:1209.0817 [hep-ph]].

[17] J. Berges, S. Scheffler, S. Schlichting and D. Sexty, Phys. Rev. D **85** (2012), 034507 doi:10.1103/PhysRevD.85.034507 [arXiv:1111.2751 [hep-ph]].

[18] J. Berges, K. Boguslavski, S. Schlichting and R. Venugopalan, Phys. Rev. D **89** (2014) no.7, 074011 doi:10.1103/PhysRevD.89.074011 [arXiv:1303.5650 [hep-ph]].

[19] J. Randrup and S. Mrowczynski, Phys. Rev. C **68** (2003), 034909 doi:10.1103/PhysRevC.68.034909 [arXiv:nucl-th/0303021 [nucl-th]].

[20] P. B. Arnold and J. Lenaghan, Phys. Rev. D **70** (2004), 114007 doi:10.1103/PhysRevD.70.114007 [arXiv:hep-ph/0408052 [hep-ph]].

[21] P. B. Arnold, J. Lenaghan, G. D. Moore and L. G. Yaffe, Phys. Rev. Lett. **94** (2005), 072302 doi:10.1103/PhysRevLett.94.072302 [arXiv:nucl-th/0409068 [nucl-th]].

[22] A. Rebhan, P. Romatschke and M. Strickland, Phys. Rev. Lett. **94** (2005), 102303 doi:10.1103/PhysRevLett.94.102303 [arXiv:hep-ph/0412016 [hep-ph]].

[23] P. B. Arnold, G. D. Moore and L. G. Yaffe, Phys. Rev. D **72** (2005), 054003 doi:10.1103/PhysRevD.72.054003 [arXiv:hep-ph/0505212 [hep-ph]].

[24] P. Romatschke and A. Rebhan, Phys. Rev. Lett. **97** (2006), 252301 doi:10.1103/PhysRevLett.97.252301 [arXiv:hep-ph/0605064 [hep-ph]].

[25] D. Bodeker and K. Rummukainen, JHEP **07** (2007), 022 doi:10.1088/1126-6708/2007/07/022 [arXiv:0705.0180 [hep-ph]].

[26] S. Bazak and S. Mrowczynski, Phys. Rev. D **105** (2022) no.3, 034023 doi:10.1103/PhysRevD.105.034023 [arXiv:2111.11396 [hep-ph]].

[27] S. Bazak and S. Mrowczynski, Phys. Rev. D **106** (2022) no.3, 034031 doi:10.1103/PhysRevD.106.034031

[arXiv:2205.08282 [hep-ph]].

[28] Z. G. Mou, P. M. Saffin and A. Tranberg, JHEP **02** (2021), 189 doi:10.1007/JHEP02(2021)189 [arXiv:2006.13620 [hep-th]].

[29] M. Hindmarsh, S. J. Huber, K. Rummukainen and D. J. Weir, Phys. Rev. Lett. **112** (2014), 041301 doi:10.1103/PhysRevLett.112.041301 [arXiv:1304.2433 [hep-ph]].

[30] C. Caprini, M. Chala, G. C. Dorsch, M. Hindmarsh, S. J. Huber, T. Konstandin, J. Kozaczuk, G. Nardini, J. M. No and K. Rummukainen, *et al.* JCAP **03** (2020), 024 doi:10.1088/1475-7516/2020/03/024 [arXiv:1910.13125 [astro-ph.CO]].

NITEP 202

Attempt Constructing a Model of Grand Gauge-Higgs Unification with Family Unification

arXiv:2403.02731v1 [hep-ph] 5 Mar 2024

Nobuhito Maru[a,b] and Ryujiro Nago[a]

[a] *Department of Physics, Osaka Metropolitan University, Osaka 558-8585, Japan*

[b] *Nambu Yoichiro Institute of Theoretical and Experimental Physics (NITEP), Osaka Metropolitan University, Osaka 558-8585, Japan*

Abstract

We discuss a possibility whether a model of grand gauge-Higgs unification incorporating family unification in higher dimensions can be constructed. We first extend a five dimensional $SU(6)$ grand gauge-Higgs unification model to a five dimensional $SU(7)$ grand gauge-Higgs unification model compactified on an orbifold S^1/Z_2 to obtain three generations of quarks and leptons after symmetry breaking of the larger family unified gauge group. A prescription of constructing a six dimensional $SU(N)$ grand gauge-Higgs unification model including a five dimensional $SU(7)$ grand gauge-Higgs unification after compactifying the sixth dimension on an orbifold S^1/Z_2 is given. We find a six dimensional $SU(14)$ grand gauge-Higgs unification model with a set of representations containing three generations of quarks and leptons.

1 Introduction

One of the mysteries in the Standard Model (SM) of particle physics is the origin of three generations of quarks and leptons, where quarks and leptons with the same representations and charges have a triple copy structure. Understanding whether three generations are inevitable or accidental is a very nontrivial problem. One of the approaches to solve this problem has been known as "family unification". In this scenario, quarks and leptons are embedded into fermions (desirably one fermion) in some non-repetitive representations of a large group which has the grand unified theory (GUT) gauge group or the SM gauge group as a subgroup and three generations of quarks and leptons appear after symmetry breaking. The study of family unification has a very long history and has been done from various viewpoints [1–23].

A pioneering work was given by Georgi [1]. Three copies of fermions in $\overline{\mathbf{5}}$ and $\mathbf{10}$ of $SU(5)$ representations were obtained from some non-repetitive and anomaly-free set of totally anti-symmetric representations in $SU(11)$ theory. In a process of symmetry breaking, one might worry that there might appear many extra and unwanted massless fermions. If the representations of the fermions are vector-like or real under the unbroken subgroup, such fermions would have masses of the order of symmetry breaking scale and are decoupled in the low energy theory. Taking into account this point, three generations were obtained.

This line of thought has also applied to the higher dimensional theory [15]. The advantages of this application are as follows. In odd dimensional theories, the anomaly constraints for the representations of fermions are relaxed. This greatly helps the possibility of model building extended. In even dimensional theories, the anomaly constraints certainly exist in general, but it is not so serious if we consider only the Dirac fermions from the beginning. The other advantage is that it is relatively easy to consider symmetry breaking in higher dimensional theory compactified on an orbifold. In such theories, symmetry breaking can be realized by boundary conditions and we have no need to introduce a complicated and unnatural Higgs potential as in four dimensional theories.

On the other hand, it has been known that the SM gauge fields and the SM Higgs field can be unified in higher dimensional gauge theory, which is called as "gauge-Higgs unification". In the scenario, the SM Higgs field is identified with extra spatial components of the higher dimensional gauge field. Regardless of the non-renormalizability, the quantum corrections of the physical quantities as Higgs mass and potential are predicted to be finite, which solves the hierarchy problem. The GUT extension of this scenario have been also considered and are very interesting, which has been paid much attention [24–26, 28]. One of authors has proposed a five dimensional (5D) $SU(6)$ grand gauge-Higgs unification (GGHU). It is remarkable in this model that quarks and leptons of one generation can be

embedded into two $\overline{\mathbf{6}}$ and single $\mathbf{20}$ representations of $SU(6)$ without exotic fermions.

In this paper, we attempt to incorporate the family unification into grand gauge-Higgs unification. Employing the above $SU(6)$ model, we immediately notice that we have to extend the $SU(6)$ model since the $\mathbf{20}$ representation is self-conjugate to $\overline{\mathbf{20}}$ and even if three $\mathbf{20}$ are obtained, a pair of them makes a mass term, which implies that three generations are impossible in the approach of [1]. Therefore, we first extend the 5D $SU(6)$ GGHU model to an $SU(7)$ model to circumvent this problem. Then, we search for a six dimensional (6D) GGHU model with family unification following the approach [1], which includes the 5D $SU(7)$ GGHU model with three generations after compactification to 5D. We find a 6D $SU(14)$ GGHU model with family unification.

The organization of this paper is as follows. In section 2, 5D $SU(7)$ GGHU model is constructed as a simple extension of 5D $SU(6)$ GGHU model. In section 3, we investigate a GGHU model with family unification in 6D following the approach by [1]. We find an $SU(14)$ GGHU model with family unification. Conclusion is given in the last section.

2 5D $SU(7)$ theory

In this section, we point out some problems of our previous 5D $SU(6)$ GGHU model in the contest of family unification and propose an $SU(7)$ model as a simple extension before discussing a 6D GGHU model of family unification.

In [24], a GGHU model of 5D $SU(6)$ gauge theory compactified on S^1/Z_2 was proposed, where the gauge fields and the Higgs fields in GUT are unified in the 5D gauge field. One of the remarkable features of this model is that one generation of quarks and leptons are embedded into a set of representations $2 \times \overline{\mathbf{6}} \oplus \mathbf{20}$ of $SU(6)$ and furthermore no massless exotic fermions are left after compactification. However, we immediately notice that three generations of quarks and leptons cannot be obtained from this $SU(6)$ model in the approach of [1] since the $\mathbf{20}$ is self-conjugate to $\overline{\mathbf{20}}$ under $SU(6)$ and therefore a pair of them should be massive.

To improve this point, we propose a 5D $SU(7)$ model compactified on S^1/Z_2 including the $SU(6)$ model. Z_2 parity matrices are given on each fixed points $y = 0, \pi R$ as

$$\begin{aligned} P_0 &= \mathrm{diag}(+1,+1,+1,+1,+1,-1,-1) \quad \text{at} \quad y = 0, \\ P_1 &= \mathrm{diag}(+1,+1,-1,-1,-1,-1,+1) \quad \text{at} \quad y = \pi R, \end{aligned} \tag{1}$$

where y, R are the coordinate of the fifth dimension and a radius of the S^1, respectively. For the gauge fields, the Z_2 parity boundary conditions are taken as follows.

$$A_\mu(x^\mu, -y) = P_{0,1} A_\mu(x^\mu, y) P_{0,1}^\dagger, \quad A_5(x^\mu, -y) = -P_{0,1} A_\mu(x^\mu, y) P_{0,1}^\dagger. \tag{2}$$

$x^\mu = 0, 1, 2, 3$ denotes the four dimensional spacetime coordinate.

More explicitly, the parities of $A_{\mu,5}$ can be expressed in a matrix form.

$$A_\mu = \left(\begin{array}{cc|ccc|c|c} (+,+) & (+,+) & (+,-) & (+,-) & (+,-) & (-,-) & (-,+) \\ (+,+) & (+,+) & (+,-) & (+,-) & (+,-) & (-,-) & (-,+) \\ \hline (+,-) & (+,-) & (+,+) & (+,+) & (+,+) & (-,+) & (-,-) \\ (+,-) & (+,-) & (+,+) & (+,+) & (+,+) & (-,+) & (-,-) \\ (+,-) & (+,-) & (+,+) & (+,+) & (+,+) & (-,+) & (-,-) \\ \hline (-,-) & (-,-) & (-,+) & (-,+) & (-,+) & (+,+) & (+,-) \\ \hline (-,+) & (-,+) & (-,-) & (-,-) & (-,-) & (+,-) & (+,+) \end{array}\right), \tag{3}$$

$$A_5 = \left(\begin{array}{cc|ccc|c|c} (-,-) & (-,-) & (-,+) & (-,+) & (-,+) & (+,+) & (+,-) \\ (-,-) & (-,-) & (-,+) & (-,+) & (-,+) & (+,+) & (+,-) \\ \hline (-,+) & (-,+) & (+,-) & (+,-) & (+,-) & (+,-) & (+,+) \\ (-,+) & (-,+) & (+,-) & (+,-) & (+,-) & (+,-) & (+,+) \\ (-,+) & (-,+) & (+,-) & (+,-) & (+,-) & (+,-) & (+,+) \\ \hline (+,+) & (+,+) & (+,-) & (+,-) & (+,-) & (-,-) & (-,+) \\ \hline (+,-) & (+,-) & (+,+) & (+,+) & (+,+) & (-,+) & (-,-) \end{array}\right), \tag{4}$$

where the matrix elements mean a set of Z_2 parities (P_0, P_1).

Noting that Kaluza-Klein (KK) mode expansions of the five dimensional field Φ with Z_2 parity (P_0, P_1) are given by

$$\begin{aligned} \Phi^{(+,+)}(x,y) &= \frac{1}{\sqrt{2\pi R}}\phi_0(x) + \frac{1}{\sqrt{\pi R}}\sum_{n=1}^{\infty}\phi_n^{(+,+)}(x)\cos\left(\frac{n}{R}\,y\right), \\ \Phi^{(+,-)}(x,y) &= \frac{1}{\sqrt{\pi R}}\sum_{n=0}^{\infty}\phi_n^{(+,-)}(x)\cos\left(\frac{n+1/2}{R}\,y\right), \\ \Phi^{(-,+)}(x,y) &= \frac{1}{\sqrt{\pi R}}\sum_{n=0}^{\infty}\phi_n^{(-,+)}(x)\sin\left(\frac{n+1/2}{R}\,y\right), \\ \Phi^{(-,-)}(x,y) &= \frac{1}{\sqrt{\pi R}}\sum_{n=0}^{\infty}\phi_n^{(-,-)}(x)\sin\left(\frac{n}{R}\,y\right), \end{aligned} \tag{5}$$

$\phi_0(x)$ in $\Phi^{(+,+)}(x,y)$ only remain massless in 4D. From this observation, we find the symmetry breaking pattern $SU(7) \to SU(3)_c \times SU(2)_L \times U(1)_Y \times U(1)_\alpha \times U(1)_\beta$ from A_μ and the SM Higgs doublet is indeed embedded in A_5. Generators of $U(1)_\alpha$ and $U(1)_\beta$ are contained in the $SU(7)$ generators as

$$U(1)_\alpha : \begin{pmatrix} 1 & & & & & & \\ & 1 & & & & & \\ & & 1 & & & & \\ & & & 1 & & & \\ & & & & 1 & & \\ & & & & & -5 & \\ & & & & & & 0 \end{pmatrix}, \quad U(1)_\beta : \begin{pmatrix} 1 & & & & & & \\ & 1 & & & & & \\ & & 1 & & & & \\ & & & 1 & & & \\ & & & & 1 & & \\ & & & & & 1 & \\ & & & & & & -6 \end{pmatrix}.$$

Looking at A_5, we find the colored Higgs field to be massless at tree level. Taking into account quantum corrections, its mass squared is expected to be $\mathcal{O}(\alpha_s/R^2)$. Since a typical order of the compactification scale is $\mathcal{O}(10\text{TeV})$ in GHU, the colored Higgs mass will be at most $\mathcal{O}(10\text{TeV})$. For proton stability, the baryon number violating operators by the colored Higgs exchange have to be forbidden or suppressed enough by some mechanism, which will not be discussed in this paper.

In the $SU(7)$ theory, $2\times\overline{\mathbf{6}}\oplus\mathbf{20}$ are embedded in $2\times\overline{\mathbf{7}}\oplus\overline{\mathbf{35}}$:

$$\begin{aligned}\overline{\mathbf{7}}&=\overline{\mathbf{6}}\oplus\mathbf{1},\\ \overline{\mathbf{35}}&=\mathbf{20}\oplus\overline{\mathbf{15}}.\end{aligned}\tag{6}$$

More explicitly, one generation of quarks and leptons are contained as follows

$$\overline{\mathbf{7}}=\begin{cases}\overline{\mathbf{7}}_L=\underbrace{(\overline{\mathbf{3}},\mathbf{1})^{(+,-)}_{(\frac{1}{3},-1,-1)}\oplus l_L(\mathbf{1},\mathbf{2})^{(+,+)}_{(-\frac{1}{2},-1,-1)}\oplus(\mathbf{1},\mathbf{1})^{(-,-)}_{(0,5,-1)}}_{\overline{\mathbf{6}}}\oplus\underbrace{(\mathbf{1},\mathbf{1})^{(-,+)}_{(0,0,6)}}_{\mathbf{1}}\\ \overline{\mathbf{7}}_R=\underbrace{(\overline{\mathbf{3}},\mathbf{1})^{(-,+)}_{(\frac{1}{3},-1,-1)}\oplus(\mathbf{1},\mathbf{2})^{(-,-)}_{(-\frac{1}{2},-1,-1)}\oplus\nu_R(\mathbf{1},\mathbf{1})^{(+,+)}_{(0,5,-1)}}_{\overline{\mathbf{6}}}\oplus\underbrace{(\mathbf{1},\mathbf{1})^{(+,-)}_{(0,0,6)}}_{\mathbf{1}}\end{cases}$$

$$\overline{\mathbf{7}}=\begin{cases}\overline{\mathbf{7}}_L=\underbrace{(\overline{\mathbf{3}},\mathbf{1})^{(-,-)}_{(\frac{1}{3},-1,-1)}\oplus l_L(\mathbf{1},\mathbf{2})^{(-,+)}_{(-\frac{1}{2},-1,-1)}\oplus(\mathbf{1},\mathbf{1})^{(+,-)}_{(0,5,-1)}}_{\overline{\mathbf{6}}}\oplus\underbrace{\chi_1(\mathbf{1},\mathbf{1})^{(+,+)}_{(0,0,6)}}_{\mathbf{1}}\\ \overline{\mathbf{7}}_R=\underbrace{\overline{d}_R(\overline{\mathbf{3}},\mathbf{1})^{(+,+)}_{(\frac{1}{3},-1,-1)}\oplus(\mathbf{1},\mathbf{2})^{(+,-)}_{(-\frac{1}{2},-1,-1)}\oplus(\mathbf{1},\mathbf{1})^{(-,+)}_{(0,5,-1)}}_{\overline{\mathbf{6}}}\oplus\underbrace{(\mathbf{1},\mathbf{1})^{(-,-)}_{(0,0,6)}}_{\mathbf{1}}\end{cases}$$

$$\overline{\mathbf{35}}=\begin{cases}\overline{\mathbf{35}}_L=\underbrace{q_L(\mathbf{3},\mathbf{2})^{(+,+)}_{(\frac{1}{6},-3,-3)}\oplus(\overline{\mathbf{3}},\mathbf{1})^{(+,-)}_{(-\frac{2}{3},-3,-3)}\oplus(\mathbf{1},\mathbf{1})^{(+,-)}_{(1,-3,-3)}}_{\mathbf{20}}\\ \qquad\underbrace{\oplus(\overline{\mathbf{3}},\mathbf{2})^{(-,+)}_{(-\frac{1}{6},3,-3)}\oplus(\mathbf{3},\mathbf{1})^{(-,-)}_{(\frac{2}{3},3.,-3)}\oplus(\mathbf{1},\mathbf{1})^{(-,-)}_{(-1,3,-3)}}_{\mathbf{20}}\\ \qquad\underbrace{\oplus(\overline{\mathbf{3}},\mathbf{2})^{(-,-)}_{(-\frac{1}{6},-2,4)}\oplus(\mathbf{3},\mathbf{1})^{(-,+)}_{(\frac{2}{3},-2.,4)}\oplus\chi_2(\overline{\mathbf{3}},\mathbf{1})^{(+,+)}_{(\frac{1}{3},4,4)}\oplus(\mathbf{1},\mathbf{2})^{(+,-)}_{(-\frac{1}{2},4,4)}\oplus(\mathbf{1},\mathbf{1})^{(-,+)}_{(-1,-2,4)}}_{\overline{\mathbf{15}}}\\ \overline{\mathbf{35}}_R=\underbrace{(\mathbf{3},\mathbf{2})^{(-,-)}_{(\frac{1}{6},-3,-3)}\oplus(\overline{\mathbf{3}},\mathbf{1})^{(-,+)}_{(-\frac{2}{3},-3,-3)}\oplus(\mathbf{1},\mathbf{1})^{(-,+)}_{(1,-3)}}_{\mathbf{20}}\\ \qquad\underbrace{\oplus(\overline{\mathbf{3}},\mathbf{2})^{(+,-)}_{(-\frac{1}{6},3,-3)}\oplus u_R(\mathbf{3},\mathbf{1})^{(+,+)}_{(\frac{2}{3},3,-3)}\oplus e_R(\mathbf{1},\mathbf{1})^{(+,+)}_{(-1,3,-3)}}_{\mathbf{20}}\\ \qquad\underbrace{\oplus\chi_3(\overline{\mathbf{3}},\mathbf{2})^{(+,+)}_{(-\frac{1}{6},-2,4)}\oplus(\mathbf{3},\mathbf{1})^{(+,-)}_{(\frac{2}{3},-2.,4)}\oplus(\overline{\mathbf{3}},\mathbf{1})^{(-,-)}_{(\frac{1}{3},4,4)}\oplus(\mathbf{1},\mathbf{2})^{(-,+)}_{(-\frac{1}{2},4,4)}\oplus(\mathbf{1},\mathbf{1})^{(+,-)}_{(-1,-2,4)}}_{\overline{\mathbf{15}}}\end{cases}$$

where the bold face numbers in the right-hand side are the representations under $SU(3)_c\times SU(2)_L$ and the numbers in the subscript are the charges of $U(1)_Y\times U(1)_\alpha\times U(1)_\beta$. $L(R)$ means 4D left(right)-handed chiralities.

Furthermore, we must note that these representations have exotic fermions $\chi_i (i = 1, 2, 3)$ absent in the Standard Model as the price of extending the gauge group $SU(6)$ to $SU(7)$. These exotic fermions can be massive and removed by introducing the 4D fermions $\overline{\chi}_i$ with conjugate representations and opposite chirality to χ_i and Dirac mass terms $m_i \overline{\chi}_i \chi_i$ on the fixed point.

3 6D $SU(N)$ theory

In this section, we attempt constructing a six dimensional (6D) $SU(N)$ theory on S^1/Z_2 to realize a family unification of the previous 5D $SU(7)$ theory. Our strategy is based on an approach by Georgi [1] and its applications to higher dimensional theory by Kawamura et al [15, 16, 18, 20, 21]. In [1], the 4D theory of the gauge group $SU(N)$ including $SU(5)$ as a subgroup with fermions in only antisymmetric tensor representation of $SU(N)$ was considered and a possibility that three generations of quarks and leptons are obtained after symmetry breaking was explored. This is a very nontrivial requirement since all of antisymmetric tensor representations are not replicated and the fermion content has to be anomaly-free. Furthermore, if some fermions are vector-like or real representations under $SU(5)$ after symmetry breaking, they will have a mass of order of the symmetry breaking scale. In [15, 16, 18, 20, 21], the argument by Georgi was applied to the higher dimensional theory. The advantages of this application are as follows. There is no anomaly-free conditions in the case of odd dimensions. If the Dirac fermions are considered, the anomaly is cancelled even in even dimensions. Moreover, the symmetry breaking can be easily realized by boundary conditions in extra spatial dimensions. Following approaches by [1] and [15,16,18,20,21], we would like to attempt constructing a 6D model where both gauge-Higgs unification and family unification are incorporated.

In 6D theory, gamma matrices Γ^M $(M = 0, 1, 2, 3, 5, 6)$ are 8×8 matrices satisfying Clifford algebra,

$$\left\{\Gamma^M, \Gamma^N\right\} = 2\eta^{MN} \quad (M, N = 0, 1, 2, 3, 5, 6), \tag{7}$$

where η^{MN} is metric and $\eta = \mathrm{diag}(+1, -1, -1, -1, -1, -1)$. In addition, Γ^7 is defined as

$$\Gamma^7 \coloneqq i\Gamma^0\Gamma^1\Gamma^2\Gamma^3\Gamma^5\Gamma^6. \tag{8}$$

In our notation, the 6D Weyl fermions $\Psi_\pm$ are eigenstates of Γ^7 with eigenvalue ± 1, respectively and are decomposed into 4D Weyl fermions ψ_L and ψ_R,

$$\Psi = \begin{pmatrix} \Psi_+ \\ \Psi_- \end{pmatrix} = \begin{pmatrix} \psi_{+L} \\ \psi_{+R} \\ \psi_{-L} \\ \psi_{-R} \end{pmatrix}. \tag{9}$$

By compactifying the sixth dimension z to S^1/Z_2 orbifold with a radius R' of S^1, we consider a symmetry breaking $SU(N) \to SU(7) \times SU(p) \times SU(q) \times U(1)^2$ realized by the following Z_2 parities P'_0 and P'_1,

$$\begin{aligned} P'_0 &= \mathrm{diag}\overbrace{(+1, \cdots, +1,\ +1, \cdots, +1,\ -1, \cdots, -1)}^{N} \quad \text{at} \quad z = 0, \\ P'_1 &= \mathrm{diag}(\underbrace{+1, \cdots, +1}_{7},\ \underbrace{-1, \cdots, -1}_{p},\ \underbrace{+1, \cdots, +1}_{q}) \quad \text{at} \quad z = \pi R', \end{aligned} \tag{10}$$

where the rank of the gauge symmetries are unchanged by the symmetry breaking, $7+p+q = N$. We introduce here a symbol $[k]_N$, which means the rank k totally antisymmetric tensor representation of $SU(N)$. This is decomposed into multiplets of $SU(7) \times SU(p) \times SU(q)$ as

$$[k]_N = \sum_{l=0}^{k} \sum_{m=0}^{k-l} \sum_{n=0}^{k-l-m} ([\,l\,]_7, [m]_p, [n]_q). \tag{11}$$

We note that $[k]_N$ does not exist for the case of $k > N$. $[k]_N$ can be expressed as an antisymmetric part of the tensor product of k fundamental representations $\boldsymbol{N}$:

$$[k]_N = (\boldsymbol{N} \times \cdots \times \boldsymbol{N})_a \tag{12}$$

where a means an antisymmetric part. The Z_2 transformations at $z = 0, \pi R$ of the 6D Dirac fermion in the $[k]_N$ representation are given as follows.

$$\begin{aligned} (\boldsymbol{N} \times \cdots \times \boldsymbol{N})_a &\to \eta_k (P'_0 \boldsymbol{N} \times \cdots \times P'_0 \boldsymbol{N})_a \quad \text{at} \quad z = 0, \\ (\boldsymbol{N} \times \cdots \times \boldsymbol{N})_a &\to \eta'_k (P'_1 \boldsymbol{N} \times \cdots \times P'_1 \boldsymbol{N})_a \quad \text{at} \quad z = \pi R', \end{aligned} \tag{13}$$

where $\eta_k, \eta'_k = \pm 1$. For example, $[1]_N = \boldsymbol{N}$ is decomposed as

$$\boldsymbol{N} = (\boldsymbol{7}, \boldsymbol{1}, \boldsymbol{1}) \oplus (\boldsymbol{1}, \boldsymbol{p}, \boldsymbol{1}) \oplus (\boldsymbol{1}, \boldsymbol{1}, \boldsymbol{q}), \tag{14}$$

and the Z_2 transformation at $z = 0$ can be read as

$$\boldsymbol{N} \to \eta_k P'_0 \boldsymbol{N} = \eta_k (\boldsymbol{7}, \boldsymbol{1}, \boldsymbol{1}) \oplus +\eta_k (\boldsymbol{1}, \boldsymbol{p}, \boldsymbol{1}) \oplus -\eta_k (\boldsymbol{1}, \boldsymbol{1}, \boldsymbol{q}). \tag{15}$$

In this way, we obtain the Z_2 parities $\mathcal{P}'_0$ and $\mathcal{P}'_1$ of the representation $([\,l\,]_7, [m]_p, [n]_q)$

$$\begin{aligned} \mathcal{P}'_0 &= (-1)^n \eta_k = (-1)^{l+m} (-1)^k \eta_k, \\ \mathcal{P}'_1 &= (-1)^m \eta'_k = (-1)^{l+n} (-1)^k \eta'_k, \end{aligned} \tag{16}$$

where a condition $l + m + n = k$ is taken into account in the second quality.

Here we can define "LH" fermion Ψ_- has η_k, η'_k factor, and "RH" fermion Ψ_+ has $-\eta_k, -\eta'_k$ factor, more explicitly,

$$\Psi_- : (-1)^{l+m} (-1)^k \eta_k, \quad (-1)^{l+m} (-1)^k \eta'_k, \tag{17}$$

$$\Psi_+ : -(-1)^{l+m} (-1)^k \eta_k, \quad -(-1)^{l+m} (-1)^k \eta'_k. \tag{18}$$

This relative sign is due to that of the chiral operator in 6D.

Now choosing as $\left((-1)^k\eta_k, (-1)^k\eta'_k\right) = (+1,+1)$ for simplicity, we obtain the Z_2 parity assignment for $\mathbf{7}, \mathbf{21}$ and $\mathbf{35}$ representations of $SU(7)$ by putting $l = 1,2,3$ as in the following Table 1.

	$\mathcal{P}'_0$	$\mathcal{P}'_1$
$\mathbf{7}_\pm$	$\pm(-1)^m$	$\pm(-1)^n$
$\mathbf{21}_\pm$	$\mp(-1)^m$	$\mp(-1)^n$
$\mathbf{35}_\pm$	$\pm(-1)^m$	$\pm(-1)^n$
$\overline{\mathbf{35}}_\pm$	$\mp(-1)^m$	$\mp(-1)^n$
$\overline{\mathbf{21}}_\pm$	$\pm(-1)^m$	$\pm(-1)^n$
$\overline{\mathbf{7}}_\pm$	$\mp(-1)^m$	$\mp(-1)^n$

Table 1: Z_2 parity assignment of $\mathbf{7}, \mathbf{21}$ and $\mathbf{35}$ (and their conjugate) representations of $SU(7)$. $\pm$ are given by the corresponding Γ_7 eigenvalues.

From the information of Z_2 parities listed in Table 1, we can obtain the numbers of massless fermions with Z_2 even parity in the representations of $\bar{\mathbf{7}}_-, \mathbf{21}_-$ and $\overline{\mathbf{35}}_-$

$$
\begin{aligned}
n^{(+,+)}_{\overline{\mathbf{7}}_-,k} &= \sum_{m,n=\text{even}} {}_pC_m \cdot {}_qC_n \cdot (\delta_{k,1+m+n} + \delta_{k,6+m+n}) \\
&\quad - \sum_{m,n=\text{odd}} {}_pC_m \cdot {}_qC_n \cdot (\delta_{k,1+m+n} + \delta_{k,6+m+n}), \\
n^{(+,+)}_{\mathbf{21}_-,k} &= \sum_{m,n=\text{even}} {}_pC_m \cdot {}_qC_n \cdot (\delta_{k,2+m+n} + \delta_{k,5+m+n}) \\
&\quad - \sum_{m,n=\text{odd}} {}_pC_m \cdot {}_qC_n \cdot (\delta_{k,2+m+n} + \delta_{k,5+m+n}), \\
n^{(+,+)}_{\overline{\mathbf{35}}_-,k} &= \sum_{m,n=\text{even}} {}_pC_m \cdot {}_qC_n \cdot (\delta_{k,3+m+n} + \delta_{k,4+m+n}) \\
&\quad - \sum_{m,n=\text{odd}} {}_pC_m \cdot {}_qC_n \cdot (\delta_{k,3+m+n} + \delta_{k,4+m+n})
\end{aligned}
\tag{19}
$$

where $\delta_{k,l+m+n}$ expresses $k = l+m+n$. For the case of $\bar{\mathbf{7}}_-$, the breakdown of the number of massless 5D fermions is that the sum with respect to even (odd) m, n come from $\bar{\mathbf{7}}_-$ and $\mathbf{7}_+$ ($\mathbf{7}_-$ and $\bar{\mathbf{7}}_+$), respectively. Similar arguments for $\mathbf{21}_-$ and $\overline{\mathbf{35}}_-$ are also applied.

Now, we would like to find a 6D family unified model of 5D SU(7) grand gauge-Higgs unification with three replicated $2 \times \overline{\mathbf{7}} \oplus \overline{\mathbf{35}}$ representations including three families of quarks and leptons.

Taking $N = 14$, $p = 5$, and $q = 2$ of our interest, (19) is rewritten as

$$\begin{aligned}
n^{(+,+)}_{\overline{\mathbf{7}}_-,k} &= \sum_{m=0,2,4}\sum_{n=0,2} {}_5C_m \cdot {}_2C_n \cdot (\delta_{k,1+m+n} + \delta_{k,6+m+n}) \\
&\quad - \sum_{m=1,3,5}\sum_{n=1} {}_5C_m \cdot {}_2C_n \cdot (\delta_{k,1+m+n} + \delta_{k,6+m+n}), \\
n^{(+,+)}_{\mathbf{21}_-,k} &= \sum_{m=0,2,4}\sum_{n=0,2} {}_5C_m \cdot {}_2C_n \cdot (\delta_{k,2+m+n} + \delta_{k,5+m+n}) \\
&\quad - \sum_{m=1,3,5}\sum_{n=1} {}_5C_m \cdot {}_2C_n \cdot (\delta_{k,2+m+n} + \delta_{k,5+m+n}), \\
n^{(+,+)}_{\overline{\mathbf{35}}_-,k} &= \sum_{m=0,2,4}\sum_{n=0,2} {}_5C_m \cdot {}_2C_n \cdot (\delta_{k,3+m+n} + \delta_{k,4+m+n}) \\
&\quad - \sum_{m=1,3,5}\sum_{n=1} {}_5C_m \cdot {}_2C_n \cdot (\delta_{k,3+m+n} + \delta_{k,4+m+n}).
\end{aligned} \tag{20}$$

From these results, the list of $n^{(+,+)}_{\overline{\mathbf{7}}_-,k}, n^{(+,+)}_{\mathbf{21}_-,k}$ and $n^{(+,+)}_{\overline{\mathbf{35}}_-,k}$ for various values of k in Table 2 are obtained. We note that $n^{(+,+)}_{R_-,k} = -5$ means $n^{(+,+)}_{R_+,k} = 5$ because of $n^{(+,+)}_{R_-,k} = -n^{(+,+)}_{R_+,k}$($R =$

k	$n^{(+,+)}_{\overline{\mathbf{7}}_-,k}$	$n^{(+,+)}_{\mathbf{21}_-,k}$	$n^{(+,+)}_{\overline{\mathbf{35}}_-,k}$
1	1	0	0
2	0	1	0
3	1	0	1
4	0	1	1
5	−5	1	1
6	1	−5	1
7	3	1	−5
8	1	3	−5
9	0	−5	3
10	−5	0	3
11	0	3	0
12	3	0	0
13	0	0	0

Table 2: Numbers of massless fermions in $\overline{\mathbf{7}}_-, \mathbf{21}_-, \overline{\mathbf{35}}_-$ representations for various k-rank totally anti-symmetric tensors of $SU(14)$.

$\overline{\mathbf{7}}, \mathbf{21}, \overline{\mathbf{35}}$). Consider a set of representations $[1]_{14} \oplus [2]_{14} \oplus [3]_{14} \oplus [4]_{14} \oplus [6]_{14} \oplus [11]_{14} \oplus [12]_{14}$,

all numbers of $\bar{\mathbf{7}}_-, \mathbf{21}_-$ and $\overline{\mathbf{35}}_-$ are given by

$$\begin{aligned} n_{\overline{\mathbf{7}}_-} &:= \sum_{k=1,2,3,4,6,11,12} n^{(+,+)}_{\overline{\mathbf{7}}_-,k} = 1+0+1+0+1+0+3 = 6, \\ n_{\mathbf{21}_-} &:= \sum_{k=1,2,3,4,6,11,12} n^{(+,+)}_{\mathbf{21}_+,k} = 0+1+0+1-5+3+0 = 0, \\ n_{\overline{\mathbf{35}}_-} &:= \sum_{k=1,2,3,4,6,11,12} n^{(+,+)}_{\overline{\mathbf{35}}_-,k} = 0+0+1+1+1+0+0 = 3. \end{aligned} \tag{21}$$

Remarkably, we have succeeded in obtaining a desirable set of massless fermions in the representations $3 \times (2 \times \overline{\mathbf{7}} \oplus \overline{\mathbf{35}})$, which contain three families of quarks and leptons. We think this result to be very nontrivial since the number of massless **21** representations has to be vanished in addition to $3\times(2\times\overline{\mathbf{7}}\oplus\overline{\mathbf{35}})$ to realize three generations. We have investigated various models up to $SU(14)$, the above $SU(14)$ model was an only satisfactory solution. One might think that other models can obtained if larger gauge groups are considered. However, it seems to be difficult to find other GGHU models with family unification since the representations and the number of massless fermions become more complicated in such cases. It is therefore plausible to conclude that our 6D $SU(14)$ theory obtained in this paper is a simplest GGHU model with family unification in a class of SU theories although we cannot prove it formally.

Some comments on anomaly cancellation are given. A chiral gauge theory in even dimensions, in general, is possible to have gauge anomalies and global anomaly. Fermions in the representations $[k]_{14}$ $(k = 1, 2, 3, 4, 6, 11, 12)$ we introduced are massless 6D Dirac fermions, that is, both of $[k]_{14+}$ and $[k]_{14-}$ are introduced. Therefore, the gauge anomalies are canceled. As for the global anomaly, the global anomaly is absent since the sixth homotopy group of $SU(14)$, $\Pi_6(SU(14))$, is known to be vanished [29].

4 Conclusion

We have attempted constructing a grand gauge-Higgs unification model with family unification in this paper. A 6D $SU(14)$ GGHU theory as a family unified 5D $SU(7)$ GGHU theory was found, where the set of representations $[1]_{14} \oplus [2]_{14} \oplus [3]_{14} \oplus [4]_{14} \oplus [6]_{14} \oplus [11]_{14} \oplus [12]_{14}$ are decomposed into $3\times(2\times\overline{\mathbf{7}}\oplus\overline{\mathbf{35}})$ after symmetry breaking $SU(14) \to SU(7)\times SU(5)\times SU(2)\times U(1)^2$. Three generations of quarks and leptons are obtained from $3\times(2\times\overline{\mathbf{7}}\oplus\overline{\mathbf{35}})$ after compactification to 4D. As far as we know, this is the first GGHU model unifying three generations of quarks and leptons, which is expected to be a guideline of a model building along this line.

We have many issues to be explored since our work done in this paper is still a first step towards a construction of realistic model of GGHU with family unification.

In our model, we have unfortunately some massless exotic fermions. It is of course desirable to find a model without them. In order to realize it, it would be interesting to study the theories with other gauge groups and fermion matter content. In this paper, we have set $\left((-1)^k\eta_k, (-1)^k\eta'_k\right) = (+1, +1)$ for all k for simplicity. Considering other patterns for $\left((-1)^k\eta_k, (-1)^k\eta'_k\right)$ might help reducing the number of massless exotic fermions.

In our family unified 6D $SU(14)$ model, two step compactification is considered. It would be interesting to investigate a possibility that three generations of quarks and leptons are directly obtained from the compactification of 6D GGHU theory to 4D one such as [20].

As one of the other interesting directions, it would be interesting to consider models of SO gauge theory. The family unification via the spinor representation in SO theory has been much studied since the work [6]. Although several irreducible representations are necessary to realize the family unification in SU theory, the family unification in SO theory is expected to be realized by fewer irreducible representations than SU theory since the dimension of spinor representation is exponentially large with respect to the size of the gauge group.

There are many phenomenological issues to be studied, generating the realistic Yukawa hierarchy, the study of electroweak symmetry breaking, the flavor physics, the gauge coupling unification and the proton decay analysis and so on.

All of them are left for our future study.

References

[1] H. Georgi, "Towards a Grand Unified Theory of Flavor," Nucl. Phys. B **156** (1979), 126-134.

[2] P. H. Frampton, "SU(N) Grand Unification With Several Quark - Lepton Generations," Phys. Lett. B **88** (1979), 299-301.

[3] P. Frampton and S. Nandi, "SU(9) Grand Unification of Flavor With Three Generations," Phys. Rev. Lett. **43** (1979), 1460.

[4] P. H. Frampton, "Unification of Flavor," Phys. Lett. B **89** (1980), 352-354.

[5] M. Ida, Y. Kayama and T. Kitazoe, "Inclusion of Generations in SO(14)," Prog. Theor. Phys. **64** (1980), 1745.

[6] F. Wilczek and A. Zee, "Families from Spinors," Phys. Rev. D **25** (1982), 553.

[7] S. Nandi, A. Stern and E. C. G. Sudarshan, "Structure of Proton Decay in SO(n) Family Unification," Phys. Rev. D **26** (1982), 1653.

[8] Y. Fujimoto, "SO(18) Unification," Phys. Rev. D **26** (1982), 3183.

[9] J. Bagger, S. Dimopoulos and E. Masso, "Proton Lifetime in Orthogonal Theories of Family Unification," Phys. Lett. B **145** (1984), 211-215.

[10] J. A. Bagger, S. Dimopoulos, E. Masso and M. H. Reno, "A realistic theory of family unification," Nucl. Phys. B **258** (1985), 565-600.

[11] S. M. Barr, "E_8 family unification, mirror fermions, and new low-energy physics," Phys. Rev. D **37** (1988), 204.

[12] P. H. Frampton and T. W. Kephart, "Minimal family unification," Phys. Rev. D **51** (1995) no.1, R1-R4 [arXiv:hep-ph/9409324 [hep-ph]].

[13] K. S. Babu, S. M. Barr and B. Kyae, "Family unification in five-dimensions and six-dimensions," Phys. Rev. D **65** (2002), 115008, [arXiv:hep-ph/0202178 [hep-ph]].

[14] Z. y. Han and W. Skiba, "Family unification on an orbifold," Phys. Rev. D **70** (2004), 035013, [arXiv:hep-ph/0405199 [hep-ph]].

[15] Y. Kawamura, T. Kinami and K. y. Oda, "Orbifold family unification," Phys. Rev. D **76** (2007), 035001, [arXiv:hep-ph/0703195 [hep-ph]].

[16] Y. Kawamura and T. Kinami, "Sfermion mass relations in orbifold family unification," Prog. Theor. Phys. **119** (2008), 285-301, [arXiv:0709.1524 [hep-ph]].

[17] P. H. Frampton and T. W. Kephart, "Fermion Mixings in SU(9) Family Unification," Phys. Lett. B **681** (2009), 343-346, [arXiv:0904.3084 [hep-ph]].

[18] Y. Kawamura and T. Miura, Phys. Rev. D **81** (2010), 075011, [arXiv:0912.0776 [hep-ph]].

[19] C. H. Albright, Robert. P. Feger and Thomas. W/ Kephart, "An explicit SU(12) family and flavor unification model with natural fermion masses and mixings," Phys. Rev. D **86** (2012), 015012, [arXiv:1204.5471 [hep-ph]].

[20] Y. Goto, Y. Kawamura and T. Miura, "Orbifold family unification on six dimensions," Phys. Rev. D **88** (2013) no.5, 055016, [arXiv:1307.2631 [hep-ph]].

[21] Y. Goto and Y. Kawamura, "Predictions of SU (9) orbifold family unification," Phys. Lett. B **752** (2016), 252-257, [arXiv:1508.06357 [hep-ph]].

[22] M. Reig, J. W. F. Valle, C. A. Vaquera-Araujo and F. Wilczek, "A Model of Comprehensive Unification," Phys. Lett. B **774** (2017), 667-670, [arXiv:1706.03116 [hep-ph]].

[23] N. Yamatsu, "Family Unification in Special Grand Unification," PTEP **2018** (2018) no.9, 091B01, [arXiv:1807.10855 [hep-ph]].

[24] C. S. Lim and N. Maru, "Towards a realistic grand gauge-Higgs unification," Phys. Lett. B **653** (2007), 320-324, [arXiv:0706.1397 [hep-ph]].

[25] K. Kojima, K. Takenaga and T. Yamashita, "Grand Gauge-Higgs Unification," Phys. Rev. D **84** (2011), 051701, [arXiv:1103.1234 [hep-ph]]; "Gauge symmetry breaking patterns in an SU(5) grand gauge-Higgs unification model," Phys. Rev. D **95** (2017) no.1, 015021, [arXiv:1608.05496 [hep-ph]]; "The Standard Model Gauge Symmetry from Higher-Rank Unified Groups in Grand Gauge-Higgs Unification Models," JHEP **06** (2017), 018, [arXiv:1704.04840 [hep-ph]]; Phys. Rev. D **108** (2023) no.3, 035031, [arXiv:2304.05701 [hep-ph]].

[26] Y. Hosotani and N. Yamatsu, "Gauge-Higgs grand unification," PTEP **2015** (2015), 111B01, [arXiv:1504.03817 [hep-ph]]; A. Furui, Y. Hosotani and N. Yamatsu, "Toward Realistic Gauge-Higgs Grand Unification," PTEP **2016** (2016) no.9, 093B01 [arXiv:1606.07222 [hep-ph]]; Y. Hosotani and N. Yamatsu, "Gauge-Higgs seesaw mechanism in 6-dimensional grand unification," PTEP **2017** (2017) no.9, 091B01, [arXiv:1706.03503 [hep-ph]]; Y. Hosotani and N. Yamatsu, "Electroweak symmetry breaking and mass spectra in six-dimensional gauge–Higgs grand unification," PTEP **2018** (2018) no.2, 023B05, [arXiv:1710.04811 [hep-ph]].

[27] N. Maru and Y. Yatagai, "Fermion Mass Hierarchy in Grand Gauge-Higgs Unification," PTEP **2019** (2019) no.8, 083B03, [arXiv:1903.08359 [hep-ph]]; N. Maru and Y. Yatagai, "Improving fermion mass hierarchy in grand gauge–Higgs unification with localized gauge kinetic terms," Eur. Phys. J. C **80** (2020) no.10, 933, [arXiv:1911.03465 [hep-ph]]; N. Maru, H. Takahashi and Y. Yatagai, "Gauge coupling unification in simplified grand gauge-Higgs unification," Phys. Rev. D **106** (2022) no.5, 055033, [arXiv:2207.10253 [hep-ph]].

[28] A. Angelescu, A. Bally, S. Blasi and F. Goertz, "Minimal SU(6) gauge-Higgs grand unification," Phys. Rev. D **105** (2022) no.3, 035026 [arXiv:2104.07366 [hep-ph]]; A. Angelescu, A. Bally, F. Goertz and S. Weber, "SU(6) gauge-Higgs grand unification: minimal viable models and flavor," JHEP **04** (2023), 012, [arXiv:2208.13782 [hep-ph]].

[29] B. A. Dobrescu and E. Poppitz, "Number of fermion generations derived from anomaly cancellation," Phys. Rev. Lett. **87** (2001), 031801, [arXiv:hep-ph/0102010 [hep-ph]].

arXiv:2403.02721v1 [hep-ph] 5 Mar 2024

Light Thermal Dark Matter Beyond p-Wave Annihilation in Minimal Higgs Portal Model

Yu-Tong Chen[a,b], Shigeki Matsumoto[c],
Tian-Peng Tang[a], Yue-Lin Sming Tsai[a,d], and Lei Wu[b]

[a] *Key Laboratory of Dark Matter and Space Astronomy, Purple Mountain Observatory, Chinese Academy of Sciences, Nanjing 210033, China*

[b] *Department of Physics and Institute of Theoretical Physics, Nanjing Normal University, Nanjing, 210023, China*

[c] *Kavli IPMU (WPI), UTIAS, U. Tokyo, Kashiwa 277-8583, Chiba, Japan and*

[d] *School of Astronomy and Space Science, University of Science and Technology of China, Hefei, Anhui 230026, China*

(Dated: March 6, 2024)

Abstract

This study explores a minimal renormalizable dark matter (DM) model, incorporating a sub-GeV Majorana DM and a singlet scalar particle ϕ. Using scalar and pseudo-scalar interactions (couplings c_s and c_p), we investigate implications for DM detection, considering s-wave, p-wave, and combined (s+p wave) contributions in DM annihilation cross-section, as well as loop-correction contributions to DM-nucleon elastic scattering. Identifying a broad parameter space ($10\,\mathrm{MeV} < m_\chi \lesssim m_\phi$) within the 2σ allowed region, we explore scenarios ($|c_s| \gg |c_p|$, $|c_s| \ll |c_p|$, and $|c_s| \approx |c_p|$). We find that (i) a non-zero pseudo-scalar coupling alleviates direct detection constraints as a comparison with the previous pure scalar coupling case; (ii) CMB observations set stringent limits on pseudo-scalar interaction dominant cases, making s-wave annihilation viable only for $m_\chi > 1\,\mathrm{GeV}$; (iii) the preferred ϕ-resonance region can be tested in the future indirect detection experiments, such as e-ASTROGAM.

I. INTRODUCTION

The nature of dark matter (DM) is one of the most fundamental problems in modern physics, and revealing its physical properties could lead to substantial progress in fundamental physics. Among the various candidates for DM, the thermal DM model stands out for its natural explanation of the observed DM relic abundance. This model relies on the freeze-out mechanism, a powerful framework that not only sheds light on the DM nature, but also provides a successful explanation for the history of Big Bang Nucleosynthesis (BBN).

The mass range of thermal DM is theoretically predicted to span from a few MeV to several hundreds of TeV [1–5]. The upper and lower bounds of DM mass are both related to the constraints of the relic density and are based on different assumptions. The mass upper bound comes from the joint constraint of the unitarity condition for s-wave annihilation [6], and the relic density. On the other hand, the lower bound of the DM mass depends on the particles involved in DM annihilation. If DM only annihilates into a pair of standard model (SM) particles mediated by any SM particle, then the relic density constraint requires DM mass to be heavier than 2 GeV, called Lee-Weinberg bound [7]. However, if the DM annihilates to a pair of new light scalar particles, as discussed in this work, the scalar particles must be larger than MeV to be consistent with the allowed relativistic degrees of freedom in the BBN era [8–13]. Thus, the DM mass has to be heavier than $\mathcal{O}(10\,\mathrm{MeV})$ to simultaneously fulfill the relic density constraint and the allowed relativistic degrees of freedom.

Direct detection, a primary strategy for weakly interacting massive particle (WIMP) DM exploration through scattering interactions with nuclei, is constrained to DM masses above a few GeV due to the required kinetic energy for nuclear recoil through elastic scattering. Recent experiments like XENON [14], LZ [15], and PandaX-4T [16] have ruled out a large portion of the parameter space for conventional GeV-scale WIMP DM, leaving a vast region of sub-GeV thermal DM untested. Detecting nuclear recoil energy in sub-GeV thermal DM using conventional methods poses challenges. Methods for DM direct detection with masses ranging from eV to 100 MeV are to search for electron recoils, with active pursuit by various groups [17–21]. This study aims to explore the unknown parameter space of a minimal renormalizable DM model including a sub-GeV Majorana DM and a singlet scalar particle [22]. In this Higgs portal DM model, the DM-electron interaction is suppressed by

the small electron Yukawa coupling and a tiny mixing angle, which simply escapes from the experimental constraints involving electron recoils.

In the early universe, charged particles interacted with CMB photons, altering their black-body spectrum [23]. After recombination, injected energy affected gas temperature and ionization fraction, leaving imprints on CMB temperature and polarization power spectra [24–27]. CMB measurements, evolving from pre-WMAP to the Planck satellite era, independently constrain DM annihilation cross-sections, particularly in the sub-GeV mass range. Other indirect detection experiments like Fermi-LAT and AMS-02 lose sensitivity in the low-mass regime due to instrumental thresholds [28–32]. Overall, CMB serves as a distinct and complementary probe for understanding thermal DM, crucial for low-mass DM and models with non-velocity-suppressed s-wave annihilation [27, 33–38]. Beyond s-wave annihilation, several mechanisms can simultaneously meet CMB constraints and yield the correct relic abundance, such as p-wave DM annihilation [39–45], forbidden DM mechanisms [46–50], self-interaction DM [51–54], and other alternatives [55–62].

In this study, our goal is to identify a parameter space of the minimal Higgs portal DM model that mitigates constraints from direct detection and CMB, while remaining testable in future indirect detection experiments like e-ASTROGAM [63, 64]. The DM candidate in this minimal model is singlet under the SM gauge group and interacts with the SM sector via a singlet scalar [22]. We conduct a comprehensive Markov chain Monte Carlo (MCMC) analysis, considering constraints from cosmology, astrophysics, direct detection experiments, collider experiments, DM self-interaction, and CMB observations. Our findings indicate that thermal light DM, annihilating through an s-wave process, fails to simultaneously satisfy relic density and CMB constraints, if DM mass is lighter than 1 GeV. Although p-wave annihilation may evade CMB constraints, the small annihilation cross-section poses a challenge for future indirect detection experiments. Fortunately, upcoming experiments, such as e-ASTROGAM, COSI [65, 66], and GECOO [67, 68], designed for the MeV-Gap, offer promising prospects to explore ϕ-resonance annihilation regions of sub-GeV DM and enhance sensitivity by 2-3 orders of magnitude compared to current limits [69, 70].

The remaining sections of the paper are organized as follows. In Sec. II, we present the minimal Higgs portal DM model featuring a light Majorana DM coupled with a singlet scalar. We provide a comprehensive overview of the interactions and the decay of this new scalar. In Sec. III, we outline all the constraints incorporated into our likelihood, along with

a detailed discussion of the updated constraints. The outcomes of our likelihood analysis are presented in Sec. IV. Finally, we summarize our findings in Sec. V.

II. A MINIMAL HIGGS PORTAL DM MODEL

We consider an SM singlet Majorana DM χ interacting with the SM sector via an SM singlet real scalar boson Φ [22]. For DM mass m_χ, the minimal but renormalizable Lagrangian can be written as

$$\mathcal{L} = \mathcal{L}_{\rm SM} + \frac{1}{2}\bar{\chi}(i\partial\!\!\!/ - m_\chi)\chi + \frac{1}{2}(\partial\Phi)^2 - \frac{c_s}{2}\Phi\bar{\chi}\chi - \frac{c_p}{2}\Phi\bar{\chi}i\gamma_5\chi - V(\Phi, H), \tag{1}$$

where $\mathcal{L}_{\rm SM}$ and H are the SM Lagrangian and SM Higgs doublet, respectively. The coupling coefficients of DM with scalar and pseudo-scalar are denoted as c_s and c_p. To preserve a stable DM, χ is the Z_2-odd particle, while other particles are Z_2-even. The scalar potential of the model is composed of $V(\Phi, H) \equiv V_\Phi(\Phi) + V_{\Phi H}(\Phi, H)$ and $V_H(H)$, where $V_H(H)$ is the SM Higgs potential. Their explicit forms are

$$\begin{aligned} V_H(H) &= \mu_H^2 H^\dagger H + \frac{\lambda_H}{2}(H^\dagger H)^2, \\ V_\Phi(\Phi) &= \mu_1^3\Phi + \frac{\mu_\Phi^2}{2}\Phi^2 + \frac{\mu_3}{3!}\Phi^3 + \frac{\lambda_\Phi}{4!}\Phi^4, \\ V_{\Phi H}(\Phi, H) &= A_{\Phi H}\Phi H^\dagger H + \frac{\lambda_{\Phi H}}{2}\Phi^2 H^\dagger H, \end{aligned} \tag{2}$$

where λ_is are dimensionless coupling constants of quartic terms while others $\mu_{1,2,3}$ and $A_{\Phi H}$ are dimensional couplings for quadratic and cubic scalar interactions.

A. The properties of the scalar particles

In this subsection, we summarize the properties of the new scalar particle ϕ and the SM Higgs, including their masses, interactions, and decay channels.

1. Masses of the scalars

We denote the vacuum expectation value (VEV) of H and Φ are v_H and v_Φ, respectively. By expanding $H = [0, (v_H + h')/\sqrt{2}]^T$ and $\Phi = v_\Phi + \phi'$, we then rewrite the mass matrix of

the scalars with the flavor basis (h', ϕ') as

$$U \begin{pmatrix} m^2_{h'h'} & m^2_{h'\phi'} \\ m^2_{h'\phi'} & m^2_{\phi'\phi'} \end{pmatrix} U^\dagger = \begin{pmatrix} m^2_h & 0 \\ 0 & m^2_\phi \end{pmatrix}, \qquad U = \begin{pmatrix} \cos\theta & -\sin\theta \\ \sin\theta & \cos\theta \end{pmatrix}, \tag{3}$$

where we define the $m^2_{h'h'} = \lambda_H v_H^2$, $m^2_{h'\phi'} = A_{\Phi H} v_H$, and $m^2_{\phi'\phi'} = \mu^2_\Phi + \lambda_{\Phi H} v_H^2/2$. The mixing angle θ in the matrix U controls the magnitude of interactions between the mediator particle ϕ and SM particles. Note that the physical mass m_h and m_ϕ can be obtained by the eigenvalue of the mass matrix. In addition, $\sin\theta$ is a common variable used in the Higgs portal DM model. Hence, instead of using $A_{\Phi H}$ and $\lambda_{\Phi H}$, we take m_ϕ and $\sin\theta$ as our model inputs.

2. Scalar interactions and DM annihilations

The interactions between the scalar sector (h and ϕ) with DM sector are

$$\mathcal{L}_{\rm int} \supset -\frac{\cos\theta}{2}(c_s\, \phi\, \bar\chi\chi + c_p\, \phi\, \bar\chi i\gamma_5\chi) + \frac{\sin\theta}{2}(c_s\, h\, \bar\chi\chi + c_p\, h\, \bar\chi i\gamma_5\chi). \tag{4}$$

Clearly, the interactions between h and χ are suppressed by $\sin\theta$. On the other hand, $\cos\theta$ is roughly equal to 1, and ϕ interacts with the dark sector only depending on c_s and c_p.

We can rewrite the triple and quartic scalar interactions with the mixing angle,

$$\begin{aligned} \mathcal{L} \supset\ & -\frac{c_{hhh}}{3!}h^3 - \frac{c_{\phi hh}}{2}\phi h^2 - \frac{c_{\phi\phi h}}{2}\phi^2 h - \frac{c_{\phi\phi\phi}}{3!}\phi^3, \\ & -\frac{c_{hhhh}}{4!}h^4 - \frac{c_{\phi hhh}}{3!}\phi h^3 - \frac{c_{\phi\phi hh}}{4}\phi^2 h^2 - \frac{c_{\phi\phi\phi h}}{3!}\phi^3 h - \frac{c_{\phi\phi\phi\phi}}{4!}\phi^4, \end{aligned} \tag{5}$$

where all the relevant couplings can be found in appendix A. We would like to note that the couplings $c_{\phi\phi h}$ and $c_{\phi\phi hh}$ are not suppressed even when the mixing angle is very suppressed (namely, $|\sin\theta| \ll 1$), as they originate in the quartic term $\Phi^2|H|^2$.

The new scalar boson ϕ plays an important role in DM annihilation. Compared with Ref. [22], our work considers the non-zero pseudo-scalar coupling c_p. The newly introduced interaction may induce an s-wave DM annihilation cross-section, which remains unsuppressed in the present universe. This aspect has been explored in Refs. [71–74] for investigating various phenomenological possibilities [56, 75–87]. Therefore, the two main annihilation channels are:

- $\chi\chi \to \text{SM} + \text{SM}$

  The s-channel with ϕ-exchange is dominant in the relevant Feynman diagrams. If $m_\chi \approx m_\phi/2$, the resonance mechanism takes over the annihilations. In principle, resonance annihilation can happen at any time. We will show that the resonance mechanism can be detected in future MeV gamma-ray telescopes but fulfill the relic density and escape from the CMB constraints if DM resonance annihilation appears in the present Universe.

  To understand the velocity dependence of the DM annihilation cross-section, we can expand the cross-section of DM annihilating to a pair of SM particles as $\langle\sigma v\rangle \propto c_p^2 a + (c_s^2 b_1 + c_p^2 b_2)v^2$, where the coefficients a, b_1 and b_2 are determined by the m_χ, m_ϕ, $\sin\theta$ and the mass of the SM particles. Clearly, if $c_p = 0$ but $c_s \neq 0$, the cross-section $\langle\sigma v\rangle$ remains v^2-dependence, namely p-wave component. On the contrary, in the case of $c_p \neq 0$ and $c_s = 0$, the expansion of $\langle\sigma v\rangle$ posses both s-wave and p-wave contributions, but the s-wave one can be enhanced by a small velocity.

  It is important to clarify that the aforementioned expansion and velocity-dependence are not applicable to the ϕ resonance. As demonstrated in Ref. [88] (see Eq. (13) and Table I therein), the resonance peak and velocity-dependence strongly depend on the numerator of the cross-section. Given these considerations, we will address the ϕ resonance as a separate case in this study.

- $\chi\chi \to \phi + \phi$

  There are two diagrams of this channel. The first one is t-channel with χ-exchange and the second one is s-channel with ϕ exchange. The former usually relates to the forbidden DM scenarios ($m_\phi \gtrsim m_\chi$) or secluded DM scenarios ($m_\phi \ll m_\chi$). The latter cannot be resonance annihilation, but its relevant coupling $c_{\phi\phi h}$ and $c_{\phi\phi hh}$ are not suppressed as aforementioned.

  Similar to the SM final state, the annihilation cross-section to a pair of ϕ also has a velocity suppression if $c_p = 0$, while the case $c_s = 0$ includes both s-wave and p-wave contributions. Note that the s-wave cross-section in this channel can be obtained by setting $|c_s| \approx |c_p|$. Qualitatively, the complete annihilation cross-section of this channel exhibits p-wave dominant contribution at high velocities, while it becomes s-wave dominant if velocity is small.

3. *Decay width of the scalars*

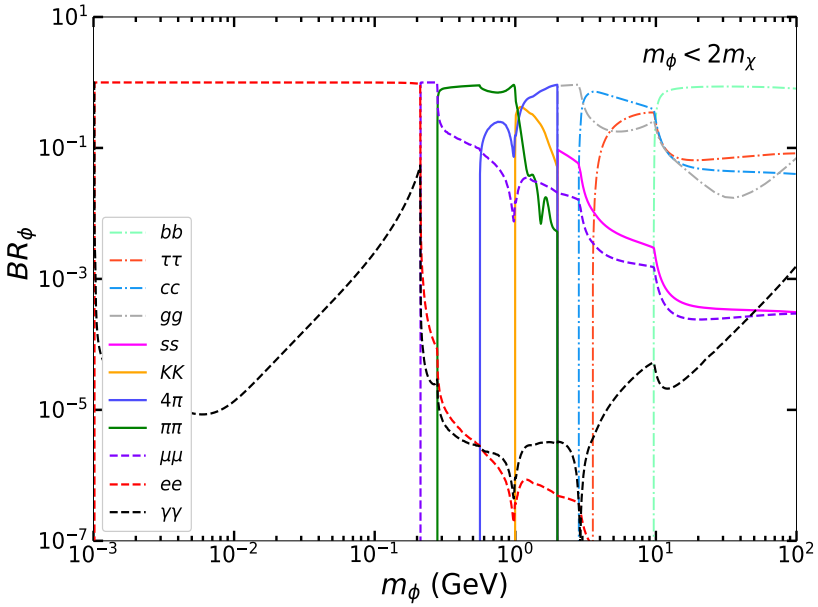


FIG. 1: The main decay branching ratio of mediator ϕ. Here, we let $m_\chi > m_\phi$, thus ϕ does not decay into a DM pair.

Because of $h-\phi$ mixing, the ϕ decay width of $\phi \to \mathrm{SM}+\mathrm{SM}$ can be directly rewritten as

$$\Gamma\left(\phi \to \mathrm{SM}+\mathrm{SM}\right) = \sin^2\theta \times \left[\Gamma\left(h \to \mathrm{SM}+\mathrm{SM}\right)\right]_{m_h \to m_\phi}. \tag{6}$$

If ϕ decays to a pair of the SM fermions $f\bar{f}$, the decay width is

$$\Gamma\left(\phi \to f\bar{f}\right) = \sin^2\theta \times \frac{m_f^2 m_\phi}{8\pi v_H^2}\left(1-\frac{4m_f^2}{m_\phi^2}\right)^{3/2}. \tag{7}$$

Fig. 1 depicts the decay branching ratio of several major channels of the mediator ϕ, where the mediator mass is less than twice the DM mass [43, 89]. For $m_\phi < 2m_\mu$, the decay channel of ϕ will be dominated by electron and photon pairs. Instead, more hadron channels can open as the m_ϕ increases. Moreover, for invisible ϕ decay ($\phi \to \chi\chi$), the partial decay width can be calculated as

$$\Gamma(\phi \to \chi\chi) = \cos^2\theta \frac{m_\phi}{16\pi}\left[c_s^2\left(1-\frac{4m_\chi^2}{m_\phi^2}\right)^{3/2} + c_p^2\left(1-\frac{4m_\chi^2}{m_\phi^2}\right)^{1/2}\right]. \tag{8}$$

Similar to ϕ decay, the expressions of the SM Higgs decay widths can be obtained by replacing $\cos\theta \to \sin\theta$ and $m_\phi \to m_h$. However, when $m_h > m_\phi$, the decay width of $h \to \phi\phi$ is given by

$$\Gamma(h \to \phi\phi) = \frac{c^2_{\phi\phi h}}{32\pi m_h}\left(1 - \frac{4m^2_\phi}{m^2_h}\right)^{1/2}, \tag{9}$$

with the couplings $c_{\phi\phi h}$ given in appendix A

B. The model parameters

There are only eight free parameters from the scalar potential, namely μ^2_H, μ^3_1, μ^2_Φ, μ_3, λ_H, λ_Φ, $\lambda_{\Phi H}$, $A_{\Phi H}$. In addition, only three parameters (m_χ, c_s, c_p) are in the dark sector. In Sec. II A 1, we have chosen m_ϕ and $\sin\theta$ instead of $A_{\Phi H}$ and $\lambda_{\Phi H}$ as the inputs. Similarly, the parameter λ_H can be determined by the Higgs mass measurement $m_h \simeq 125\,\text{GeV}$. Using the minimum condition with given the vacuum expectation values ($v_H \simeq 246\,\text{GeV}$ and $v_\Phi = 0$), we can further reduce two parameters from equations $\mu^2_H + \lambda_H v^2_H/2 = 0$ and $\mu^3_1 + A_{\Phi H} v^2_H/2 = 0$. Finally, we have five free parameters to describe the scalar potential (m_ϕ, $\sin\theta$, μ^2_ϕ, μ_3, λ_Φ), and three parameters (m_χ, c_s, c_p) to describe the dark sector.

Including these eight parameters, our prior ranges are

$$\begin{aligned}
1\ \text{MeV} \le\ & m_\chi\ \le 30\,\text{GeV},\\
-1 \le\ & c_p\ \le 1,\\
-1 \le\ & c_s\ \le 1,\\
1\ \text{MeV} \le\ & m_\phi\ \le 60\,\text{GeV},\\
-\pi/6 \le\ & \theta\ \le \pi/6,\\
-1\,\text{TeV}^2 \le\ & \mu^2_\Phi\ \le 1\,\text{TeV}^2,\\
-1\,\text{TeV} \le\ & \mu_3\ \le 1\,\text{TeV},\\
-1 \le\ & \lambda_\Phi\ \le 1.
\end{aligned} \tag{10}$$

As suggested by Ref. [22], except for turning on the pseudo-scalar coupling c_p, we set the mixing angle $|\theta| \le \pi/6$ and enhance the DM and mediator mass lower limits to 1 MeV. We conservatively assume those dimensionless couplings $|c_s| \le 1$, $|c_p| \le 1$ and $|\lambda_\Phi| \le 1$. Additionally, we can restrict those dimensionful parameters (m_ϕ, $|\mu_\Phi|$, μ_3) to be less than

1 TeV. Beyond the 1 TeV scale, an effective theory shall be applied, but it is not in our interest. However, we only consider the light DM mass region $m_\chi < 30\,\mathrm{GeV}$ in this work.

III. CONSTRAINTS

In this section, we summarize the likelihoods used in our analysis. Particularly, we focus on those updated constraints not included in the previous literature. Because s-wave annihilating DM, especially for $m_\chi < 1\,\mathrm{GeV}$, may be hard to satisfy the relic density and the constraints from the CMB power spectrum simultaneously, we have to take Planck CMB measurement into account. Moreover, the current constraints from colliders and DM direct detection experiments strongly restrict a large $\sin\theta$, so that the DM self-interaction can be enhanced to satisfy the relic density. Hence, we also use bullet cluster constraints to prevent such a scenario.

Except for the vacuum stability criterion for the Higgs potential as implemented in Ref. [22], we classify other constraints into four groups: (i) the cosmological and astrophysical constraints in Sec. III A, (ii) the collider constraints in Sec. III B, (iii) the constraints from the CMB power spectrum in Sec. III C, and (iv) the bullet cluster constraints for the DM self-interaction in Sec. III D.

A. Cosmological and astrophysical constraints

In Table I, we summarize the cosmological and astrophysical constraints of the DM and the mediator used in this work. The Planck measurement $\Omega_\chi^{\mathrm{exp}}h^2$ together with σ_{sys} mainly determine the shape of parameter space. The Boltzmann solver `MicrOMEGAs` [95] is hired to compute the predicted relic density, and 10% of theoretical computation $\Omega_\chi^{\mathrm{th}}h^2$ is then taken as the systematic uncertainties σ_{sys} for conservative treatment. In most model parameter space, the relic density is lower than the measurement, corresponding to the low DM annihilation rate. For $m_\phi > m_\chi$, the DM annihilation to SM particles is mainly via s-channel by the exchange of ϕ and h. However, these processes are suppressed due to small Yukawa couplings and the mixing angle. Therefore, only at the resonant region ($2m_\chi \approx m_\phi$) the DM annihilation cross-section can be significantly enhanced to fulfill the Planck measurement. If $m_\phi < m_\chi$, DM can annihilate to a pair of mediators, and the allowed parameter space

	Likelihood	Constraints
Relic abundance	Gaussian	$\Omega_\chi^{\rm exp}h^2 = 0.1193 \pm 0.0014$ [90]; $\sigma_{\rm sys} = 10\% \times \Omega_\chi^{\rm th}h^2$.
Equilibrium	Conditions	either ($\Gamma^{\rm FO}_{\chi{\rm SM}} \geq H_{\rm FO}$), or ($\Gamma^{\rm FO}_{\phi{\rm SM}} \geq H_{\rm FO}$ and $\Gamma^{\rm FO}_{\chi\phi} \geq H_{\rm FO}$)
DM direct detection	Half Gaussian	$9\,{\rm GeV} < m_\phi < 10\,{\rm TeV}$ (LZ [91]), $3.5\,{\rm GeV} < m_\phi < 9\,{\rm GeV}$ (PANDAX-4T [16]), $60\,{\rm MeV} < m_\phi < 5\,{\rm GeV}$ (DarkSide [92]).
$\triangle N_{\rm eff}$	Half Gaussian	$\triangle N_{\rm eff} < 0.17$ for 95% C.L. [90]
BBN	Conditions	if ($m_\phi \geq 2m_\pi$) then $\tau_\phi \leq 1$ s [93], if ($m_\phi \leq 2m_\pi$) then $\tau_\phi \leq 10^5$ s [94].

TABLE I: Cosmological and astrophysical conditions and constraints implemented in our likelihoods. The interaction rates at the freeze-out are denoted as $\Gamma^{\rm FO}$, while the universe expansion at the freeze-out is $H_{\rm FO}$.

can be more extended. There are two possible solutions: $m_\chi \sim m_\phi$ with a large $\sin\theta$ for a kinematic suppression or $m_\phi \ll m_\chi$ with a tiny $\sin\theta$. We note those DM annihilation mechanisms may result in the temperature of the dark sector being different from the SM sector before the DM freeze-out. This implies that the assumption of the thermal DM can be incorrect for some parameter space. To maintain the thermal DM assumption, we force the allowed parameter space to obey the conditions given in Table I. If the interaction rate between the dark sector and the SM sector is stronger than the Universe expansion rate at the freeze-out, namely $\Gamma^{\rm FO}_{\chi{\rm SM}} \geq H_{\rm FO}$, the temperatures of the two sectors can be still the same. Once $\Gamma^{\rm FO}_{\chi{\rm SM}} < H_{\rm FO}$, the thermal equilibrium can be maintained as long as the conditions $\Gamma^{\rm FO}_{\phi{\rm SM}} \geq H_{\rm FO}$ and $\Gamma^{\rm FO}_{\chi\phi} \geq H_{\rm FO}$ hold.

The null signal measurement of DM direct detection (DD) experiments provides stringent upper limits on the DM-proton interactions, especially for m_χ around GeV. Due to the different materials of detectors, different experiments are sensitive to different DM mass ranges, such as $60\,{\rm MeV} < m_\phi < 5\,{\rm GeV}$ for DarkSide-50 [92], $3.5\,{\rm GeV} < m_\phi < 9\,{\rm GeV}$ for PANDAX-4T [16], and $9\,{\rm GeV} < m_\phi < 10\,{\rm TeV}$ for LZ [91]. We incorporate these latest

upper limits in our likelihood analysis.[1] Our theoretical predictions for DM-nucleon elastic scattering cross-section $\sigma_p^{\rm SI}$ at tree-level are mainly computed by using `MicrOMEGAs`. In principle, at the tree-level calculation, only the scalar interaction c_s contributes to the cross-section, but the pseudo-scalar interaction c_p is velocity suppressed. However, in this work, the loop-level cross-section has to be considered if $c_s \approx 0$. The expression of the loop-level contribution can be found in Ref. [96],

$$\sigma_{\rm SI}^{\rm loop} = c_p^4 \cos^2\theta \frac{m_\chi^4 m_N^4 f_N^2 c_{\phi\phi h}^2}{16\pi^3 v_H^2 m_h^4 (m_N + m_\chi)^2} \left[\frac{\partial B_0(m_\chi, m_\phi, m_\chi)}{\partial p^2}\right]^2, \tag{11}$$

where m_N is the mass of a nucleon and $f_N = f_{Tu} + f_{Td} + f_{Ts} + \left(\frac{2}{9}\right) f_{TG}$, with $f_{Tu} \simeq 0.0153$, $f_{Td} \simeq 0.0191$, $f_{Ts} \simeq 0.0447$, and $f_{TG} \simeq 0.921$, respectively. The loop function can be written as

$$\frac{\partial B_0\left(m_\chi, m_\phi, m_\chi\right)}{\partial p^2} = \int_0^1 {\rm d}x \frac{x\left(1-x\right)}{m_\phi^2 x + m_\chi^2 (1-x)^2}, \tag{12}$$

and the coupling $c_{\phi\phi h}$ is given in appendix A. Hence, we consider the tree-level cross-section for c_s coupling while the loop-level cross-section is computed for c_p coupling.

Finally, a light ϕ may contribute the relativistic degree of freedom $\Delta N_{\rm eff}$. Following Ref. [90, 97], we apply a 95% upper limit $N_{\rm eff} < 0.17$ [98] as a half Gaussian likelihood. This upper limit and the relic density measurements can jointly exclude the region m_ϕ and m_χ below a few MeV. Moreover, ϕ decaying into the SM particles can also spoil the successful BBN history. This can put a stringent limit on the decay time τ_ϕ. In this work, we adopt a conservative way to implement BBN constraints. For the light mass $m_\phi < 2m_\pi$, because ϕ can only decay to leptons, we set a condition $\tau_\phi < 10^5$ s [94]. For the heavier mass $m_\phi > 2m_\pi$, the ϕ hadronic decay can alter the BBN history if its lifetime is shorter than one second [93].

B. Constraints from collider experiments

The model has two new particles χ and ϕ. Both of them only interact with the SM sector via the Higgs portal. The condition $m_\phi < m_h$ allows us to explore the properties of ϕ from

[1] We incorporate experimental cross-section upper limits from various collaborations into our likelihood analysis. The local DM density is typically assumed to be $0.3\,{\rm GeVcm}^{-3}$ by experimental collaborations. However, a higher value of $0.4\,{\rm GeVcm}^{-3}$ is frequently used, which leads to stronger exclusion limits in our study.

	ϕ signature	Constraints
Higgs decay	Prompt*	See the upper limits of $\mathrm{BR}(h \to \phi\phi)\mathrm{BR}(\phi \to ll)^2$ from Fig. 12 of Ref. [99] and Fig. 7 of Ref. [100].
	Displaced*	See Ref. [101, 102]
	Long-lived*	$\mathrm{BR}(h \to \mathrm{inv.})_{\mathrm{BSM}} \leq 0.145$ [103]
B decay	Prompt	$\mathrm{BR}(B^{\pm} \to K^{\pm}\mu^{-}\mu^{+}) \lesssim 3 \times 10^{-7}$ [104]
	Displaced	(1) $\sin^2\theta \gtrsim 2 \times 10^{-8}$ for the region $0.5 < m_\phi/\,\mathrm{GeV} < 1.5$ and $1 < c\tau_\phi/\mathrm{cm} < 20$ [105] (2) See Fig. 5 of Ref. [106] for details.
	Long-lived*	$P_p\ \mathrm{BR}(B^{\pm} \to K^{\pm}\nu\bar{\nu}) = (2.3 \pm 0.7) \times 10^{-5}$ [107]
Kaon decay	Prompt	(1) $\mathrm{BR}(K^{+} \to \pi^{+}\mu^{-}\mu^{+}) \leq 4 \times 10^{-8}$ [108] (2) $\mathrm{BR}\big(K_L \to \pi^0 e^{-} e^{+}\big) \leq 2.8 \times 10^{-10}$ [109] (3) $\mathrm{BR}\big(K_L \to \pi^0 \mu^{-} \mu^{+}\big) \leq 3 \times 10^{-10}$ [110]
	Displaced	CHARM detected events $\gtrsim 2.3$ [111]
	Long-lived*	(1) $\mathrm{BR}\big(K_L \to \pi^0 \nu\bar{\nu}\big) \leq 3.0 \times 10^{-9}$[112] (2) See $\mathrm{BR}(K^{+} \to \pi^{+}\nu\bar{\nu})$ limits from Fig. 18 of Ref. [113] and Fig. 4 of Ref. [114] for details.

TABLE II: The constraints from collider experiments. Most of them are imposed in our likelihood in the same manner as the former work [22], but those starred columns are the updated constraints.

the precision measurement of Higgs decay at the colliders. It also depends on the lifetime of ϕ, and there are three possible signatures in the detectors. The first one is a prompt signal for the case that ϕ immediately decays to some SM charge particles after production, and these new charged particles can be recognized in the detectors. The second potential signal associated with ϕ decay is the observation of displaced vertices. When ϕ propagates a long distance but decays within the range of the detector, the signal can be treated as a displaced vertex. The third method to search for ϕ relies on detecting missing energy signals, similar to searching for DM production in the final state. This approach assumes that ϕ has a long enough lifetime to escape from the detectors.

Moreover, in a sizeable $\sin\theta$, ϕ can be produced by the meson decay. Hence, the precise

measurements of Kaon and B meson decay can largely probe the parameter space of m_ϕ and $\sin\theta$. Like Higgs decay, we divide these meson decay searches into prompt signals, displaced vertices, and missing energy signals. Table II lists all the constraints used in this work. The majority are the same as the former work [22], but the starred columns are the updated likelihoods described in the following paragraphs.

To compute the likelihood of the colliders, we first take the Higgs decay as an example, while the likelihoods for K and B decay can be obtained similarly. As shown in Table II, we update all the Higgs relevant likelihoods.

- Prompt ϕ decay:

  By assuming instantaneous decay of ϕ, the ATLAS collaboration has updated to a new upper limit on $\mathrm{BR}(h\to\phi\phi)\mathrm{BR}(\phi\to ll)^2$ [99]. After taking the surviving probability of ϕ, namely $\mathcal{P}_\phi = \exp[-\sigma/(\gamma\beta c\tau_\phi)]$, into account, the limit shall be modified by including $\mathcal{P}_\phi$ as

  $$(1-\mathcal{P}_\phi)^2\,\mathrm{Br}\,(h\to\phi\phi)\,\mathrm{Br}\,(\phi\to ll)^2\,, \tag{13}$$

  with $\sigma = 1$ mm and $\gamma\beta = m_h/(2m_\phi)\sqrt{1-(2m_\phi/m_h)^2}$ [99].

- Displaced ϕ decay:

  The ATLAS collaboration [101] have updated the constraint on the dark photon decaying into collimated leptons or light hadrons of the process $h\to\gamma_\mathrm{d}\gamma_\mathrm{d}+X$, where the γ_d and X refer to the dark photon and the lightest dark particle. With the null result, we can simply modify the limit to $h\to\phi\phi$ process. Compared with the 95% limits of total dark photon events in the detector, we reconstruct the allowed limits as

  $$\frac{N^\phi_\mathrm{dec}}{N^{\gamma_\mathrm{d},95\%}_\mathrm{dec}} = \frac{\mathcal{P}_\phi\times\mathrm{BR}\,(gg\to h)\times\mathrm{BR}\,(h\to\phi\phi)}{\mathcal{P}^{95\%}_{\gamma_\mathrm{d}}\times\mathrm{BR}\,(gg\to h)\times\mathrm{BR}\,(h\to\gamma_d\gamma_d+X)}\leq 1, \tag{14}$$

  where $\mathcal{P}^{95\%}_{\gamma_\mathrm{d}}$ is the 95% limit of the dark photon decaying probability in the beam dump,

  $$\mathcal{P}^{95\%}_{\gamma_\mathrm{d}} = \exp\left[\frac{-l_\mathrm{min}}{\beta_{\gamma_\mathrm{d}}\gamma_{\gamma_\mathrm{d}}c\tau_{\gamma_d}}\right]-\exp\left[\frac{-l_\mathrm{max}}{\beta_{\gamma_\mathrm{d}}\gamma_{\gamma_\mathrm{d}}c\tau_{\gamma_d}}\right]. \tag{15}$$

  Similarly, we can compute the ϕ decaying probability $\mathcal{P}_\phi$ with the replacement $\gamma_\mathrm{d}\to\phi$.

  The lifetimes for γ_d and ϕ are τ_{γ_d} and τ_ϕ, respectively. The value of τ_{γ_d} is obtained from the contour in Figure 7 of Ref. [101]. Here, we fix the branch ratio $\mathrm{BR}(h\to\gamma_d\gamma_d+X)$ to be 20%, while $\mathrm{BR}(h\to\phi\phi)$ is function of m_ϕ and $\sin\theta$. The detector parameters

are $l_{\rm min} = 1.5$ mm and $l_{\rm max} = 307$ mm. The $\beta_{\gamma_{\rm d}} = E/m_{\gamma_{\rm d}}$, Also, the constraints from Ref. [102] are included in our likelihood.

- Long-lived ϕ:

  In the case of a very long-lived ϕ, the signature is the complete missing energy, namely the Higgs invisible decay branching ration BR($h \to$ inv.). We use the latest result from the ATLAS collaboration [103], which has improved the upper limit to BR($h \to$ inv.) $\leq$ 0.145 at the 90% confidence limit.

If m_ϕ is smaller than B or Kaon, we can also search for ϕ produced by B or Kaon decay. As given in Table II, we update the likelihoods of the long-lived ϕ signature for both B and Kaon decay, while their likelihoods from prompt and displaced ϕ decay are the same as previous work [22].

- Long-lived ϕ from B decay:

  The Belle II collaboration has released their latest measurement for BR($B^\pm \to K^\pm \nu\bar{\nu}$), with a measurement BR($B^\pm \to K^\pm \nu\bar{\nu}$) $= (2.3 \pm 0.7) \times 10^{-5}$[107]. This constraint is significantly stronger than the previous upper limits provided by Belle and Babar. We interpret it as P_lBR $(B^\pm \to K^\pm \phi)$+P_p BR $(B^\pm \to K^\pm \phi)$ BR $(\phi \to \chi\chi) = (2.3 \pm 0.7) \times 10^{-5}$. Here P_l is the probability that the ϕ decays outside the detector and the expression can be written as

$$P_l \equiv \frac{1}{2} \int_0^\pi {\rm d}\theta_\phi \sin\theta_\phi \exp\left[-\frac{l_{xy}}{\sin\theta_\phi} \frac{1}{\gamma\beta c\tau_\phi} \right], \tag{16}$$

  with the size of the detector $l_{xy} \simeq 25$ cm and the boost factor $\gamma\beta = m_B/(2m_\phi)\sqrt{1-(2m_\phi/m_B)^2}$.

- Long-lived ϕ from Kaon decay:

  The NA62 collaboration has reported a stringent limit on the branching fraction BR($K^+ \to \pi^+ \phi$) [114]. We modify this limit as $P_l^{'}$Br $(K^+ \to \pi^+ \phi)$ + $\left(1 - P_l^{'}\right)$ Br $(K^+ \to \pi^+ \phi)$ Br $(\phi \to \chi\chi)$[114], where the probability of mediator decays outside the detector is $P_l^{'} = e^{-l_z/c\gamma\beta\tau_\phi}$ with the size of detector $l_z = 65$ cm and the boost factor $\gamma\beta = 37.5$ GeV$/m_\phi$. The upper limits on the branch fraction at 90% can be found in Fig. 9 of Ref. [114]. However, the constraint on the same branching fraction provided by the E949 collaboration[113], as mentioned in Ref. [22], is more

stringent compared to the updated constraint from the NA62 collaboration within certain mass intervals. Therefore, we include this constraint in our analysis as well.

On the other hand, the neutral Kaon decay, $K_L \to \pi^0$+missing, is also used to find such a very long-lived mediator. However, the SM process, $K_L \to \pi^0 + \nu\bar{\nu}$, is a background against the signal. At present, the KOTO experiment put a stringent constraint on the branching fraction as $P_l \mathrm{Br}\,(K_L \to \pi^0\phi) + (1 - P_l)\,\mathrm{Br}\,(K_L \to \pi^0\phi)\,\mathrm{Br}\,(\phi \to \chi\chi) \leq 3.0\times10^{-9}$. Here the P_l is the same as in Eq. 16, with the size of the detector $l_{xy} \simeq 145$cm and the boost factor $\gamma\beta \simeq 1$.

All of the above constraints from the charged and neutral Kaon decays are included in our likelihood analysis.

C. CMB constraints

In the early universe, around $600 \lesssim z \lesssim 1100$, DM annihilation into SM particles can inject energy into the gas, affecting its temperature and ionization. This energy injection can modify the CMB matter power spectra, as determined by the precise measurements from the Planck experiment [90]. That implies that, for thermal sub-GeV DM where the number density is greater than the case of $m_\chi > 1\,\mathrm{GeV}$, the 95% upper limit on the s-wave annihilation cross-section is $\langle\sigma v\rangle \lesssim 10^{-27}\ \mathrm{cm}^3\ \mathrm{s}^{-1}$.

In our minimal DM model, we consider two annihilation channels. One involves SM pair production through an s-channel exchange mediator, denoted as $\chi\chi \to$ SM SM, while the other channel involves DM annihilating into a pair of light mediators, denoted as $\chi\chi \to \phi\phi$, resulting in four SM particles. As the CMB constraints are only sensitive to the energy injection, we adopt the same upper limit at the same m_χ for both two and four SM final state particles. The decay width of mediator ϕ is given by Eq. (6), and the estimation of χ^2 for CMB is described as a Half-Gaussian distribution

$$\chi^2_{\mathrm{CMB}} = \left[\frac{\langle\sigma v\rangle_{\mathrm{CMB}}}{\langle\sigma v\rangle^{\mathrm{Planck,90\%}}_{\mathrm{CMB}}/1.64}\right]^2, \tag{17}$$

where $\langle\sigma v\rangle^{\mathrm{Planck,90\%}}_{\mathrm{CMB}}$ is the upper limits of the cross-section for a given DM mass at 95% confidence level from Planck 2018 data [90]. Therefore, we take the DM annihilation cross-

section during the CMB period as

$$\langle\sigma v\rangle_{\rm CMB} = \begin{cases} \langle\sigma v\rangle_{\rm SMs} & \text{for } \chi\chi \to \text{SM SM}, \\ \langle\sigma v\rangle_{\phi\phi} \times [\text{BR}(\phi \to \text{SM SM})]^2 & \text{for } \chi\chi \to \phi\phi, \end{cases} \tag{18}$$

where $\langle\sigma v\rangle$ is the velocity-averaged annihilation cross-section

$$\langle\sigma v\rangle = \int \sigma v f(v) \mathrm{d}v, \text{ with } f(v) = \frac{v^2}{2\sqrt{\pi} v_{\rm CMB}^3} e^{-\frac{v^2}{4v_{\rm CMB}^2}}. \tag{19}$$

Here, we adopt the relative velocity distribution $f(v)$ described by the Maxwell-Boltzmann distribution [115]. We employ the numerical code `CalcHEP` [95] to calculate the annihilation cross-section σv. The DM velocity at recombination epoch $v_{\rm CMB}$ is given by $v_{\rm CMB}^2 = 3x \left(T_\gamma^{\rm CMB}/m_\chi\right)^2$, where we relate the DM temperature $T_\chi^{\rm CMB}$ to $v_{\rm CMB}$ as $T_\chi^{\rm CMB} = m_\chi v_{\rm CMB}^2/3$. The dimensionless temperature parameter $x = \max[x_F, x_{\rm kd}]$ depends on the freeze-out temperature parameter x_F obtained by `micrOMEGAs` [95] and kinematic decoupling temperature parameter $x_{\rm kd}$.

If kinematic decoupling occurs after freeze-out ($x_{\rm kd} > x_F$), the value of the parameter $x_{\rm kd}$ is only relevant for CMB constraints in the range $x_F < x_{\rm kd} \leq m_\chi/T_\gamma^{\rm CMB}$. Solving at least two Boltzmann equations tracking DM temperature and density evolution is necessary to determine $x_{\rm kd}$ accurately [116, 117]. We would like to comment on the impacts of $x_{\rm kd}$ on CMB constraints for s-wave, p-wave, and ϕ-resonance annihilation if $x_F < x_{\rm kd} \leq m_\chi/T_\gamma^{\rm CMB}$.

- s-wave annihilation:

  The annihilation cross-section is independent of x, so the CMB constraints are entirely unrelated to the value of $x_{\rm kd}$.

- p-wave annihilation:

  The value of $\langle\sigma v\rangle$ strongly depends on $x_{\rm kd}$ but is greatly suppressed by the tiny DM velocity, well below the Planck upper limits.

- ϕ-resonance annihilation:

  The impacts of $x_{\rm kd}$ on this annihilation are intricate [44]. Only the annihilation peaks within the range $x_F < x_{\rm kd} \leq m_\chi/T_\gamma^{\rm CMB}$ can be examined in the Planck CMB data. However, such large values of $x_{\rm kd}$ correspond to an extremely narrow range of $1 - 4m_\chi^2/m_\phi^2$, spanning approximately from 10^{-16} to 10^{-9} for $m_\chi \approx 100\,\text{MeV}$. As this extremely fine-tuned range, its indirect detection signal may not be testable or it can

be already ruled out by constraints from relic density and CMB data. Hence, we do not consider this parameter space.

D. Self Interaction constraints

One important fact of the MeV scale DM is that the vertex between ϕ and the SM particles ($\sin\theta$ part) is suppressed by experimental measurements such as collider searches and DM direct detection. However, the vertex between ϕ and the DM particles ($\cos\theta$ part) have to be large enough to maintain the right size of $\langle\sigma v\rangle$ and correct relic abundance in the early Universe. Consequently, the self-scattering cross-section, namely $\sigma(\chi\chi \to \chi\chi)$, will be significantly enhanced. This resulting self-scattering cross-section may excess the upper limit given by Bullet Cluster limit [118],

$$\sigma_{\chi\chi\to\chi\chi}/m_\chi < 1.0 \text{ cm}^2/\text{g}. \tag{20}$$

Here, the incident velocity of DM is set to be 4000 km/s. Hence, we assume the likelihood is a half Gaussian distribution with the central value at zero as a conservative test. We compute $\sigma(\chi\chi \to \chi\chi)$ by using `CalcHEP`, but find that the predicted values are much smaller than the limit.

IV. RESULT

In our study, we apply the methodology established in our previous works [88, 119–123]. We utilize the likelihood distribution detailed in Sec. III within our Markov Chain Monte Carlo scan. By employing `emcee` package [124], we conduct 24 Markov chains with several focusing scans to assess good coverage in an eight-dimensional parameter space as Eq. 10. To illustrate our findings, we employ the Profile Likelihood method to eliminate the nuisance parameters and project the results onto a two-dimensional plane based on the total three million collected data points. We assume an approximate Gaussian likelihood for our total likelihood function, thus the 95% (2σ) allowed region is defined by $\delta\chi^2 < 5.99$.

In Fig. 2, we display the 95% confidence region of our total likelihood in two panels, showing the correlations between m_χ and μ_3 (left panel) and between m_χ and m_ϕ (right panel). The shape of the likelihood distribution is determined by the Planck relic density

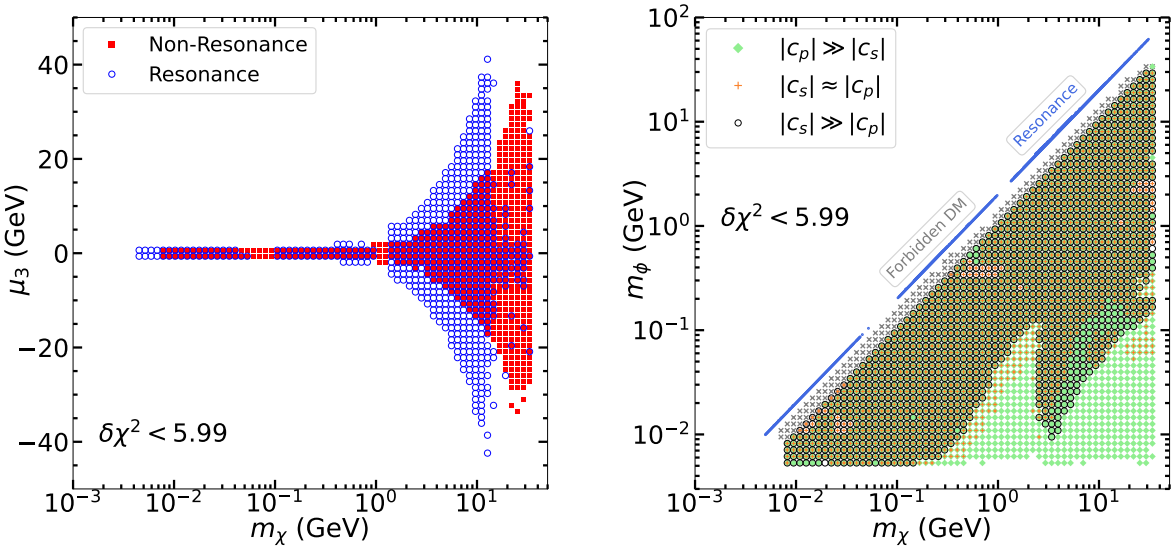


FIG. 2: The 95% confidence region in the (m_χ, μ_3) plane (left panel) and the (m_χ, m_ϕ) plane (right panel). The colors used for the left panel are the non-resonance annihilations (red solid square) and the resonance annihilations (blue unfilled circle). For the right panel, blue and grey regions represent the resonance and forbidden DM mechanisms, respectively. For the $m_\chi > m_\phi$ cases, the layer for c_s or c_p domination is marked in black circle or green diamond, while the scenario of $|c_s| \approx |c_p|$ is indicated in orange plus.

measurement and thermal equilibrium conditions. In the left panel, we divide the 95% confidence region into two groups: one for non-resonance annihilation (red solid squares) and the other for resonance annihilation (blue unfilled circles). As depicted in the right panel, the relic density constraint favors the non-resonance regions $m_\chi \gtrsim m_\phi$ and the resonance regions $m_\chi \approx m_\phi/2$ (indicated by blue lines). For $m_\chi > 1\,\text{GeV}$, the resonance region corresponds to a wider range of μ_3 and a heavier ϕ compared to the non-resonance region, due to the vacuum stability criterion [2]. In the mass region $m_\phi < 1\,\text{GeV}$ where m_χ must be less than $\mathcal{O}(\,\text{GeV})$, collider constraints impose an upper limit of $\sin\theta < 10^{-2}$, which requires sufficiently small values of $|\mu_3|$ to satisfy the vacuum stability condition.

In the right panel of Fig. 2, we divide the 95% confidence region based on the coupling relative size, namely $|c_s| > 10 \times |c_p|$ (black unfilled circles), $|c_s| < 0.1 \times |c_p|$ (green solid

[2] The parameter correlations can be referenced in Fig. 6 of Ref. [22].

diamonds), and the rest region $|c_s| \approx |c_p|$ (orange pluses). We denote $|c_s| > 10 \times |c_p|$ as $|c_s| \gg |c_p|$, $0.1 \times |c_p| \leq |c_s| \leq 10 \times |c_p|$ as $|c_s| \approx |c_p|$, and $|c_s| < 0.1 \times |c_p|$ as $|c_s| \ll |c_p|$. We can see that if $|c_s|$ is sufficiently large, in either $|c_s| \gg |c_p|$ or $|c_s| \approx |c_p|$, two exclusions appear in $300\,\mathrm{MeV} < m_\chi < 30\,\mathrm{GeV}$. As discussed in Sec. III regarding the constraints on DM direct detection, the spin-independent scattering cross-section of DM-nucleon, dominated by c_p, is loop-level suppressed. Conversely, if c_s is involved, it contributes at the tree level. Therefore, the identified exclusions associated with c_s are mainly imposed by DM direct detection experiments.

We also depict the resonance region $2m_\chi \approx m_\phi$ with a blue line. Two distinct gaps appear around $m_\phi \sim 0.1\,\mathrm{GeV}$ and $m_\phi \sim 2\,\mathrm{GeV}$. The exclusion in the former case is a result of the long-lived ϕ constraint from Kaon experiments, while the latter is ruled out by the Planck relic density and CMB constraints arising from the hadronic ϕ decay. Moreover, the grey region corresponds to the forbidden DM [46], namely m_ϕ slightly heavier than m_χ. In this region, DM particles only annihilate to a pair of ϕ before freeze-out, because of the higher DM temperature in the early universe. However, the forbidden DM mechanism lacks a visible signal in indirect detection, unless accounting for other specialized DM acceleration mechanisms [46, 47, 49, 50, 125].

In Fig. 3, we present the 2σ allowed parameter regions on the $(m_\phi, |\sin\theta|)$ planes (two upper panels) and the $(m_\chi, |\sin\theta|)$ planes (two lower panels). The color scheme is identical to the right panel of Fig. 2. Furthermore, we assign appropriate tags of experimental constraints to the exclusion regions. Those updated constraints are denoted as "red tags" in comparison to those mentioned in Ref. [22]. We summarize our findings as follows:

- For $m_\phi < 500\,\mathrm{MeV}$, Kaon experiments such as CHARM and E949 can probe $|\sin\theta| \gtrsim 10^{-3}$.

- For the range $500\,\mathrm{MeV} \leq m_\phi \leq 5\,\mathrm{GeV}$, the upper limit is determined by B meson experiments. Note that the upper limits for m_ϕ in the range of $\sim 0.3 - 4\,\mathrm{GeV}$ exhibit rapid changes. This behavior is attributed to the dominant ϕ decay channel, which involves transitions between final states such as $\pi\pi$, KK, 4π, gg, $c\bar{c}$, and $\tau^+\tau^-$, as depicted in Fig. 1.

- In the mass region $m_\phi \geq 5\,\mathrm{GeV}$, stringent constraints on $\sin\theta$ are imposed by DM direct detection experiments, particularly in cases where c_s dominates. For cases

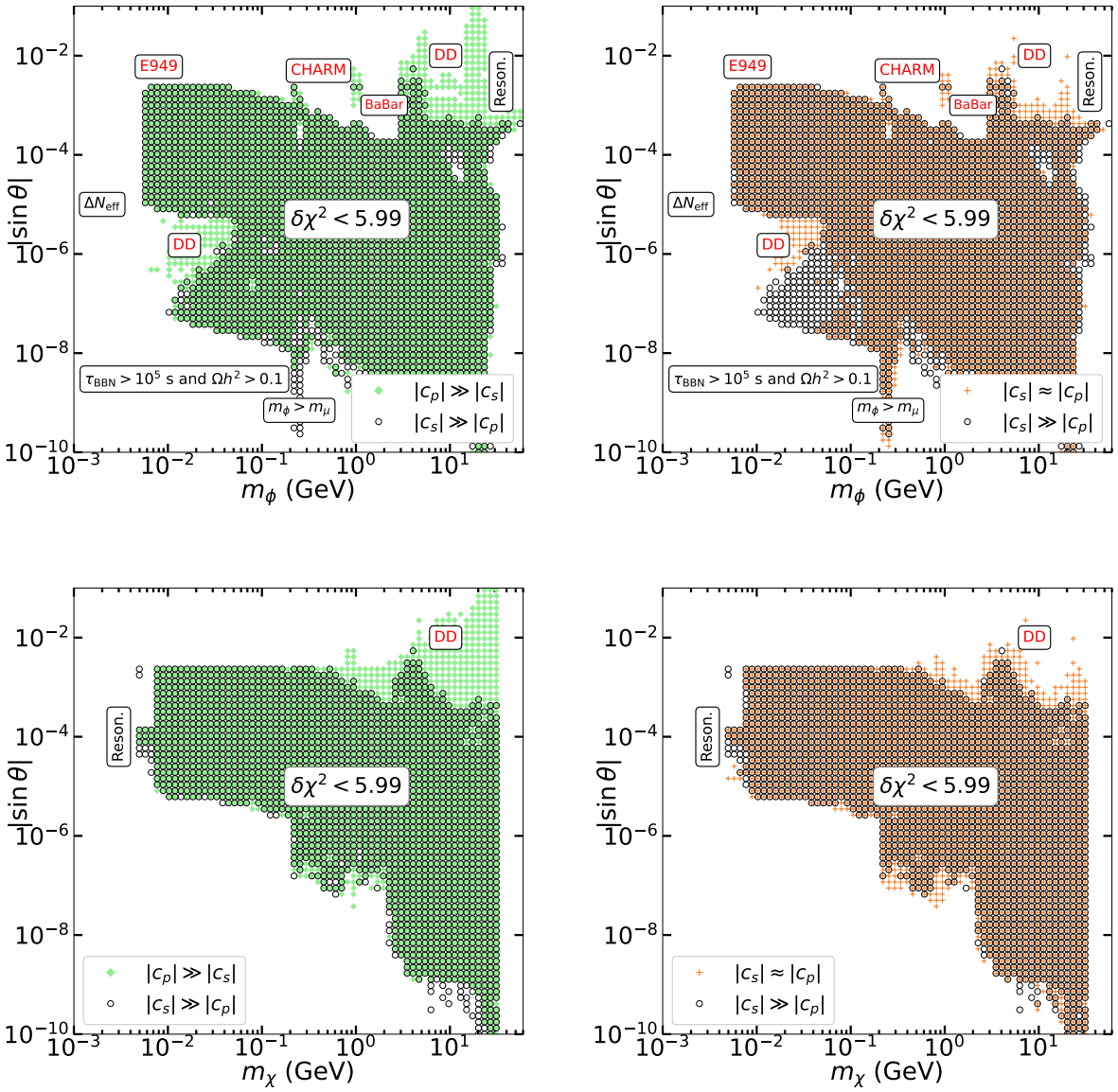


FIG. 3: The 95% allowed regions on the panels of m_ϕ versus $|\sin\theta|$ (two upper panels), and m_χ versus $|\sin\theta|$ (two lower panels). The color schemes are the same as the right panel of Fig. 2. The red labels indicate the updated constraints from collider and direct detection experiments.

dominated by c_p (green diamonds), the weaker limit is due to loop suppression. Additionally, this region corresponds to $m_\chi > 1\,\text{GeV}$, as illustrated in the two bottom panels.

- For $m_\phi > 30\,\text{GeV}$, only the resonance region $m_\phi \approx 2m_\chi$ survives.

- The lower bound on m_ϕ is determined by $\Delta N_{\rm eff}$ measurement.

- The lower limit on $|\sin\theta|$ is derived from the combined constraints of BBN and the observed DM relic density. The peak around $m_\phi \approx 200\,\text{MeV}$ corresponds to the opening of the $\chi\chi \to \mu^+\mu^-$ channel. In the $|c_p| \gg |c_s|$ scenario, the cross-section of this channel exhibits s-wave behavior, a result of the simultaneous presence of $\chi\bar{\chi}i\gamma_5\phi$ and $\Phi|H|^2$ interactions, which break CP symmetry. Consequently, the parameter space of the $|c_p| \gg |c_s|$ scenario is partially excluded from the constraints imposed by the Planck CMB constraints.

- The joint contribution of $|c_s| \approx |c_p|$ leads to s-wave annihilation of $\chi\chi \to \phi\phi$, in contrast to scenarios where $|c_s| \gg |c_p|$ or $|c_s| \ll |c_p|$, as discussed in Sec.II A. The s-wave annihilation cross-section of this process scales as $\langle\sigma v\rangle \propto (c_s \times c_p)^2$. In the case where $|c_s| \approx |c_p|$ scenario, this results in exclusion for $m_\phi < 100\,\text{MeV}$ and $|\sin\theta| \lesssim 10^{-6}$, based on the Planck CMB constraints.

Finally, we explore the possibilities of testing various DM annihilation mechanisms in upcoming DM indirect detection experiments. Fig.4 illustrates the 95% favored regions of the annihilation cross-section in the present Universe, as a function of m_χ for all mechanisms (left panel) and specifically for annihilation via ϕ-resonance (right panel).

In the left panel, we distinguish DM annihilation channels, including s-wave (red triangles) and p or s+p-wave (green squares). For ϕ-resonance annihilation, unfilled blue circles are employed. The solid red line represents the 95% projected upper limit of e-ASTROGAM [126] on gamma-ray emissions from DM annihilating to e^+e^- in the Galactic Center (GC). The projected sensitivities for the $\chi\chi \to e^+e^-$ channel from COSI [66] and GECOO [68] are represented by dashed orange and black lines, respectively.

Considering the constraints from the CMB and the relic density, pure DM s-wave annihilation only survives at the region $m_\chi > 1\,\text{GeV}$. Future indirect detection experiments may probe this region. On the other hand, the DM p and s+p-wave annihilation cross-section can naturally escape the CMB constraint due to its dependence on velocity squared. Therefore, only a small fraction of the parameter space is observable in future indirect detection experiments.

The resonance results present intriguing possibilities for indirect detection. In this study, we utilize the Breit-Wigner resonance formula, as outlined in Eq. (1) of Ref.[127], to compute

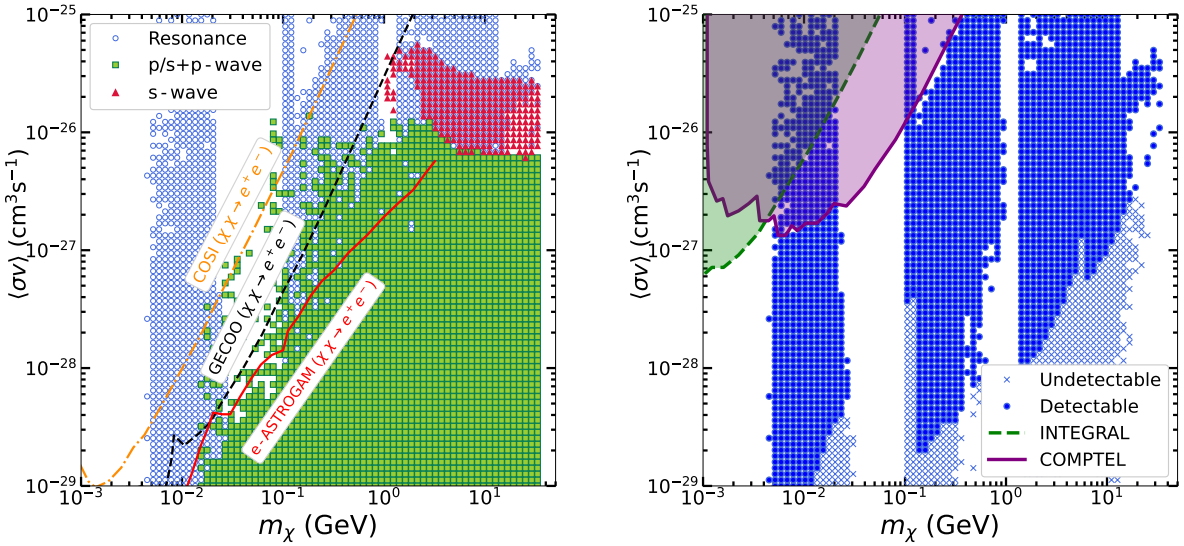


FIG. 4: The 95% favored regions of $\langle\sigma v\rangle$ as a function of DM mass m_χ. The red triangles and green squares represent the DM annihilation mechanisms dominated by s-wave and p or s+p-wave, respectively. The ϕ-resonance annihilation regions are marked with blue circles. The solid red line represents the 95% projected upper limit on gamma-ray emission from DM annihilating to e^+e^- in the GC, as determined by e-ASTROGAM [126]. The DM density profile utilizes the Navarro-Frenk-White (NFW) model. The dashed orange and black lines represent the expectations from COSI [66] and GECOO [68] for the $\chi\chi \to e^+e^-$ channel, respectively. In addition, the green and purple shades in the right panel are from INTEGRAL and COMPTEL limits [69].

the DM annihilation cross-section for $m_\phi \approx 2m_\chi$. Our resonance result is given in the right panel of Fig. 4. Note that the e-ASTROGAM illustrates the detection capability of $\chi\chi \to e^+e^-$, but ϕ can decay into various channels beyond e^+e^-, depending on its mass, as depicted in Fig. 1.

To reconstruct the future sensitivity of the e-ASTROGAM for any given annihilation final state, we adopt the approach developed in Ref. [128] to compute the 95% upper limit on the photon flux induced by DM annihilation. Assuming the branching ratio BR($\chi\chi \to e^+e^-$)=1, the total flux of DM annihilation-induced γ-rays predicted by a 95% upper limit $\langle\sigma v\rangle_{\rm ann,95}$ is expressed as

$$\int_{\rm E_{min}}^{\rm E_{max}} \Phi_{95}\,(E)\,dE = \frac{N_{e^+e^-}\,\langle\sigma v\rangle_{e^+e^-,95}\,J}{8\pi m_\chi^2}. \tag{21}$$

Here, $\rm E_{min}$ is the minimum threshold energy of e-ASTROGAM, and $\rm E_{max}$ is the smaller

value between the DM mass and the e-ASTROGAM upper threshold energy. The number $N_{e^+e^-}$ represents the integral of the photon energy distribution per DM annihilation, i.e. $N_{e^+e^-} = \int_{\mathrm{E_{min}}}^{\mathrm{E_{max}}} \frac{dN_\gamma}{dE_\gamma}(\chi\chi \to e^+e^-)dE_\gamma$. The astrophysical factor J can be determined, once the DM halo profile is given. The bound on the total DM annihilation photons is

$$\int_{\mathrm{E_{min}}}^{\mathrm{E_{max}}} \Phi_{95}(E)\, dE = \frac{\left(\sum_i \mathrm{BR}_i N_i\right) \langle\sigma v\rangle_{\mathrm{ann},95}\, J}{8\pi m_\chi^2}. \tag{22}$$

By combining Eq.21 and Eq.22, we can obtain the total DM annihilation cross-section

$$\langle\sigma v\rangle_{\mathrm{ann},95} = \frac{\langle\sigma v\rangle_{e^+e^-,95}\, N_{e^+e^-}}{\sum_i \mathrm{BR}_i N_i}. \tag{23}$$

Here, $\langle\sigma v\rangle_{e^+e^-,95}$ is obtained from the e-ASTROGAM upper limit of the DM annihilation cross-section (the red solid line in the left panel of Fig. 4). We employ `HAZMA` [129] and `PPPC4` [130] to calculate the photon spectrum, such as $N_\gamma^{e^+e^-}(E)$, for each DM annihilation channel. We sum the branching ratios BR_i over all the ϕ decay channels.

In the right panel of Fig. 4, we depict the expected sensitivity of e-ASTROGAM in detecting DM annihilation through ϕ-resonance. The green and purple shaded regions show constraints on the DM annihilation cross-section from the current MeV gamma-ray telescopes, INTEGRAL and COMPTEL [69]. The detectable regions are denoted by blue solid circles, whereas regions marked with blue crosses present challenges in probing with e-ASTROGAM. The distinct spike structures at $m_\chi \sim 1.05$ GeV and $m_\chi \sim 4.18$ GeV correspond to the thresholds of the $\chi\chi \to \mu^+\mu^-$ and $\chi\chi \to b\bar{b}$ channels, respectively.

V. CONCLUSION

In this comprehensive study, we investigated a minimal renormalizable DM model, by including a sub-GeV Majorana DM and a singlet scalar particle. Building upon the setup of Ref. [22], we extended our analysis by incorporating both scalar and pseudo-scalar interactions (c_s and c_p) between the DM and the newly introduced scalar. In comparison to the scenario where c_p is absent, the new c_p interaction yields intriguing implications for DM direct and indirect detection.

For DM indirect detection, the interplay between c_s and c_p coupling predicts that DM annihilation cross-section can be dominated by s-wave, p-wave, or a combination of both (s+p-wave) contributions. In the context of DM direct detection, the role of c_p is limited

to the loop-correction contribution of DM-nucleon elastic scattering. Thanks to nonzero DM-nucleon elastic scattering cross-section, even in the absence of c_s, this scenario remains testable.

Our analysis takes into account these new model features and incorporates updated constraints. We include constraints from DM direct detection experiments, Planck CMB power spectrum measurements, and collider searches in our likelihood, providing a more comprehensive analysis in light of the latest experimental data.

We have identified a broad parameter space within the 2σ allowed region, specifically $10\,\mathrm{MeV} < m_\chi \lesssim m_\phi$ and $2m_\chi \approx m_\phi$ (ϕ-resonance region). Additionally, we explore three distinct scenarios: $|c_s| \gg |c_p|$, $|c_s| \ll |c_p|$, and $|c_s| \approx |c_p|$. Our findings indicate that the presence of a non-zero pseudo-scalar coupling coefficient effectively alleviates constraints from direct detection. However, CMB observations impose rigorous limits on scenarios where c_p dominates, particularly for DM masses lighter than 1 GeV. Consequently, the scenario with only s-wave annihilation remains viable only for $m_\chi > 1\,\mathrm{GeV}$.

Finally, we explored the detectability prospects for this minimal DM model in future indirect detection experiments. Our findings suggest challenges for thermal sub-GeV DM annihilating via s-wave processes to meet both relic density and CMB constraints, whereas p-wave annihilation fits these criteria but is hard to be detected by indirect detection experiments. Fortunately, a significant portion of the parameter space associated with ϕ-resonance can be probed by future indirect detection experiments, such as e-ASTROGAM.

Acknowledgments

We express our gratitude to Mei-Wen Yang for her invaluable numerical support. YST is supported by the National Key Research and Development Program of China (No. 2022YFF0503304), and the Project for Young Scientists in Basic Research of the Chinese Academy of Sciences (No. YSBR-092). LW is supported by the National Natural Science Foundation of China (NNSFC) No. 12275134, No. 12335005, and No. 12147228. SM is supported by Grant-in-Aid for Scientific Research from the MEXT, Japan (20H01895, 20H00153, 19H05810, 18H05542, JPJSCCA20200002) and by World Premier International Research Center Initiative (WPI), MEXT, Japan (Kavli IPMU).

Appendix A: Scalar Interactions

Here we show the explicit expression for the scalar interactions between h and ϕ.

$$
\begin{aligned}
c_{hhh} &= 3\lambda_H v_H c_\theta^3 - 3A_{\Phi H} c_\theta^2 s_\theta - \mu_3 s_\theta^3 + 3\lambda_{\Phi H} v_H s_\theta^2 c_\theta, \\
c_{\phi hh} &= 3\lambda_H v_H c_\theta^2 s_\theta + A_{\Phi H}(c_\theta^3 - 2c_\theta s_\theta^2) + \mu_3 c_\theta s_\theta^2 + \lambda_{\Phi H} v_H (s_\theta^3 - 2c_\theta^2 s_\theta), \\
c_{\phi\phi h} &= 3\lambda_H v_H c_\theta s_\theta^2 + A_{\Phi H}(2c_\theta^2 s_\theta - s_\theta^3) - \mu_3 c_\theta^2 s_\theta + \lambda_{\Phi H} v_H (c_\theta^3 - 2c_\theta s_\theta^2), \\
c_{\phi\phi\phi} &= 3\lambda_H v_H s_\theta^3 + 3A_{\Phi H} c_\theta s_\theta^2 + \mu_3 c_\theta^3 + 3\lambda_{\Phi H} v_H c_\theta^2 s_\theta, \\
c_{hhhh} &= 3\lambda_H c_\theta^4 + 6\lambda_{\Phi H} c_\theta^2 s_\theta^2 + \lambda_\Phi s_\theta^4, \\
c_{\phi hhh} &= 3\lambda_H c_\theta^3 s_\theta - 3\lambda_{\Phi H}(c_\theta^3 s_\theta - c_\theta s_\theta^3) - \lambda_\Phi c_\theta s_\theta^3, \\
c_{\phi\phi hh} &= 3\lambda_H c_\theta^2 s_\theta^2 + \lambda_{\Phi H}(c_\theta^4 - 4c_\theta^2 s_\theta^2 + s_\theta^4) + \lambda_\Phi c_\theta^2 s_\theta^2, \\
c_{\phi\phi\phi h} &= 3\lambda_H c_\theta s_\theta^3 + 3\lambda_{\Phi H}(c_\theta^3 s_\theta - c_\theta s_\theta^3) - \lambda_\Phi c_\theta^3 s_\theta, \\
c_{\phi\phi\phi\phi} &= 3\lambda_H s_\theta^4 + 6\lambda_{\Phi H} c_\theta^2 s_\theta^2 + \lambda_\Phi c_\theta^4,
\end{aligned}
\tag{A1}
$$

where parameters s_θ and c_θ are defined as $s_\theta \equiv \sin\theta$ and $c_\theta \equiv \cos\theta$, respectively.

---

[1] C. Boehm, D. Hooper, J. Silk, M. Casse and J. Paul, Phys. Rev. Lett. **92**, 101301 (2004) doi:10.1103/PhysRevLett.92.101301 [arXiv:astro-ph/0309686 [astro-ph]].

[2] C. Boehm, T. A. Ensslin and J. Silk, J. Phys. G **30**, 279-286 (2004) doi:10.1088/0954-3899/30/3/004 [arXiv:astro-ph/0208458 [astro-ph]].

[3] H. Murayama and J. Shu, Phys. Lett. B **686**, 162-165 (2010) doi:10.1016/j.physletb.2010.02.037 [arXiv:0905.1720 [hep-ph]].

[4] T. Hambye and M. H. G. Tytgat, Phys. Lett. B **683**, 39-41 (2010) doi:10.1016/j.physletb.2009.11.050 [arXiv:0907.1007 [hep-ph]].

[5] C. Boehm, M. J. Dolan and C. McCabe, JCAP **08**, 041 (2013) doi:10.1088/1475-7516/2013/08/041 [arXiv:1303.6270 [hep-ph]].

[6] K. Griest and M. Kamionkowski, Phys. Rev. Lett. **64**, 615 (1990) doi:10.1103/PhysRevLett.64.615

[7] B. W. Lee and S. Weinberg, Phys. Rev. Lett. **39**, 165-168 (1977) doi:10.1103/PhysRevLett.39.165

[8] P. F. Depta, M. Hufnagel, K. Schmidt-Hoberg and S. Wild, JCAP **04**, 029 (2019) doi:10.1088/1475-7516/2019/04/029 [arXiv:1901.06944 [hep-ph]].

[9] R. H. Cyburt, J. R. Ellis, B. D. Fields and K. A. Olive, Phys. Rev. D **67**, 103521 (2003) doi:10.1103/PhysRevD.67.103521 [arXiv:astro-ph/0211258 [astro-ph]].

[10] K. Jedamzik and M. Pospelov, New J. Phys. **11**, 105028 (2009) doi:10.1088/1367-2630/11/10/105028 [arXiv:0906.2087 [hep-ph]].

[11] M. Hufnagel, K. Schmidt-Hoberg and S. Wild, JCAP **11**, 032 (2018) doi:10.1088/1475-7516/2018/11/032 [arXiv:1808.09324 [hep-ph]].

[12] M. Kawasaki, K. Kohri, T. Moroi, K. Murai and H. Murayama, JCAP **12**, 048 (2020) doi:10.1088/1475-7516/2020/12/048 [arXiv:2006.14803 [hep-ph]].

[13] P. F. Depta, M. Hufnagel and K. Schmidt-Hoberg, JCAP **04**, 011 (2021) doi:10.1088/1475-7516/2021/04/011 [arXiv:2011.06519 [hep-ph]].

[14] E. Aprile *et al.* [XENON], Phys. Rev. Lett. **131**, no.4, 041003 (2023) doi:10.1103/PhysRevLett.131.041003 [arXiv:2303.14729 [hep-ex]].

[15] J. Aalbers *et al.* [LZ], Phys. Rev. Lett. **131**, no.4, 041002 (2023) doi:10.1103/PhysRevLett.131.041002 [arXiv:2207.03764 [hep-ex]].

[16] Y. Meng *et al.* [PandaX-4T], Phys. Rev. Lett. **127**, no.26, 261802 (2021) doi:10.1103/PhysRevLett.127.261802 [arXiv:2107.13438 [hep-ex]].

[17] R. Agnese *et al.* [SuperCDMS], Phys. Rev. Lett. **121**, no.5, 051301 (2018) [erratum: Phys. Rev. Lett. **122**, no.6, 069901 (2019)] doi:10.1103/PhysRevLett.121.051301 [arXiv:1804.10697 [hep-ex]].

[18] A. Aguilar-Arevalo *et al.* [DAMIC], Phys. Rev. Lett. **123**, no.18, 181802 (2019) doi:10.1103/PhysRevLett.123.181802 [arXiv:1907.12628 [astro-ph.CO]].

[19] C. Cheng *et al.* [PandaX-II], Phys. Rev. Lett. **126**, no.21, 211803 (2021) doi:10.1103/PhysRevLett.126.211803 [arXiv:2101.07479 [hep-ex]].

[20] Z. Y. Zhang *et al.* [CDEX], Phys. Rev. Lett. **129**, no.22, 221301 (2022) doi:10.1103/PhysRevLett.129.221301 [arXiv:2206.04128 [hep-ex]].

[21] P. Adari *et al.* [SENSEI], [arXiv:2312.13342 [astro-ph.CO]].

[22] S. Matsumoto, Y. L. S. Tsai and P. Y. Tseng, JHEP **07**, 050 (2019) doi:10.1007/JHEP07(2019)050 [arXiv:1811.03292 [hep-ph]].

[23] J. Chluba and R. A. Sunyaev, Mon. Not. Roy. Astron. Soc. **419**, 1294-1314 (2012)

doi:10.1111/j.1365-2966.2011.19786.x [arXiv:1109.6552 [astro-ph.CO]].

[24] J. A. Adams, S. Sarkar and D. W. Sciama, Mon. Not. Roy. Astron. Soc. **301**, 210-214 (1998) doi:10.1046/j.1365-8711.1998.02017.x [arXiv:astro-ph/9805108 [astro-ph]].

[25] X. L. Chen and M. Kamionkowski, Phys. Rev. D **70**, 043502 (2004) doi:10.1103/PhysRevD.70.043502 [arXiv:astro-ph/0310473 [astro-ph]].

[26] N. Padmanabhan and D. P. Finkbeiner, Phys. Rev. D **72**, 023508 (2005) doi:10.1103/PhysRevD.72.023508 [arXiv:astro-ph/0503486 [astro-ph]].

[27] T. R. Slatyer, N. Padmanabhan and D. P. Finkbeiner, Phys. Rev. D **80**, 043526 (2009) doi:10.1103/PhysRevD.80.043526 [arXiv:0906.1197 [astro-ph.CO]].

[28] M. Ackermann *et al.* [Fermi-LAT], Phys. Rev. Lett. **115**, no.23, 231301 (2015) doi:10.1103/PhysRevLett.115.231301 [arXiv:1503.02641 [astro-ph.HE]].

[29] S. Hoof, A. Geringer-Sameth and R. Trotta, JCAP **02**, 012 (2020) doi:10.1088/1475-7516/2020/02/012 [arXiv:1812.06986 [astro-ph.CO]].

[30] L. Oakes *et al.* [Fermi-LAT, HAWC, H.E.S.S., MAGIC and VERITAS], PoS **ICRC2019**, 012 (2021) doi:10.22323/1.358.0012 [arXiv:1909.06310 [astro-ph.HE]].

[31] M. Boudaud, J. Lavalle and P. Salati, Phys. Rev. Lett. **119**, no.2, 021103 (2017) doi:10.1103/PhysRevLett.119.021103 [arXiv:1612.07698 [astro-ph.HE]].

[32] L. Roszkowski, E. M. Sessolo and S. Trojanowski, Rept. Prog. Phys. **81**, no.6, 066201 (2018) doi:10.1088/1361-6633/aab913 [arXiv:1707.06277 [hep-ph]].

[33] T. R. Slatyer, Phys. Rev. D **93**, no.2, 023527 (2016) doi:10.1103/PhysRevD.93.023527 [arXiv:1506.03811 [hep-ph]].

[34] G. Steigman, Phys. Rev. D **91**, no.8, 083538 (2015) doi:10.1103/PhysRevD.91.083538 [arXiv:1502.01884 [astro-ph.CO]].

[35] N. Aghanim *et al.* [Planck], Astron. Astrophys. **641**, A1 (2020) doi:10.1051/0004-6361/201833880 [arXiv:1807.06205 [astro-ph.CO]].

[36] J. Cang, Y. Gao and Y. Z. Ma, Phys. Rev. D **102**, no.10, 103005 (2020) doi:10.1103/PhysRevD.102.103005 [arXiv:2002.03380 [astro-ph.CO]].

[37] M. Kawasaki, H. Nakatsuka, K. Nakayama and T. Sekiguchi, JCAP **12**, no.12, 015 (2021) doi:10.1088/1475-7516/2021/12/015 [arXiv:2105.08334 [astro-ph.CO]].

[38] S. Matsumoto, Y. Watanabe, Y. Watanabe and G. White, JHEP **09**, 015 (2023) doi:10.1007/JHEP09(2023)015 [arXiv:2212.10739 [hep-ph]].

[39] R. Diamanti, L. Lopez-Honorez, O. Mena, S. Palomares-Ruiz and A. C. Vincent, JCAP **02**, 017 (2014) doi:10.1088/1475-7516/2014/02/017 [arXiv:1308.2578 [astro-ph.CO]].

[40] K. Bondarenko, A. Boyarsky, T. Bringmann, M. Hufnagel, K. Schmidt-Hoberg and A. Sokolenko, JHEP **03**, 118 (2020) doi:10.1007/JHEP03(2020)118 [arXiv:1909.08632 [hep-ph]].

[41] D. Croon, G. Elor, R. Houtz, H. Murayama and G. White, Phys. Rev. D **105**, no.6, L061303 (2022) doi:10.1103/PhysRevD.105.L061303 [arXiv:2012.15284 [hep-ph]].

[42] Y. C. Ding, Y. L. Ku, C. C. Wei and Y. F. Zhou, Eur. Phys. J. C **82**, no.2, 126 (2022) doi:10.1140/epjc/s10052-022-10048-y [arXiv:2110.10388 [hep-ph]].

[43] T. Binder, S. Chakraborti, S. Matsumoto and Y. Watanabe, JHEP **01**, 106 (2023) doi:10.1007/JHEP01(2023)106 [arXiv:2205.10149 [hep-ph]].

[44] G. Bélanger, S. Chakraborti, Y. Génolini and P. Salati, [arXiv:2401.02513 [hep-ph]].

[45] T. Siegert, F. Calore and P. D. Serpico, Mon. Not. Roy. Astron. Soc. **528**, no.2, 3433-3440 (2024) doi:10.1093/mnras/stae104 [arXiv:2401.03795 [astro-ph.HE]].

[46] R. T. D'Agnolo and J. T. Ruderman, Phys. Rev. Lett. **115**, no.6, 061301 (2015) doi:10.1103/PhysRevLett.115.061301 [arXiv:1505.07107 [hep-ph]].

[47] R. T. D'Agnolo, D. Liu, J. T. Ruderman and P. J. Wang, JHEP **06**, 103 (2021) doi:10.1007/JHEP06(2021)103 [arXiv:2012.11766 [hep-ph]].

[48] T. Hara, S. Kanemura and T. Katayose, Phys. Rev. D **105**, no.3, 035035 (2022) doi:10.1103/PhysRevD.105.035035 [arXiv:2109.03553 [hep-ph]].

[49] G. N. Wojcik and T. G. Rizzo, JHEP **04**, 033 (2022) doi:10.1007/JHEP04(2022)033 [arXiv:2109.07369 [hep-ph]].

[50] Y. Cheng, S. F. Ge, X. G. He and J. Sheng, Phys. Lett. B **847**, 138294 (2023) doi:10.1016/j.physletb.2023.138294 [arXiv:2211.05643 [hep-ph]].

[51] C. Boehm and P. Fayet, Nucl. Phys. B **683**, 219-263 (2004) doi:10.1016/j.nuclphysb.2004.01.015 [arXiv:hep-ph/0305261 [hep-ph]].

[52] T. Lin, H. B. Yu and K. M. Zurek, Phys. Rev. D **85**, 063503 (2012) doi:10.1103/PhysRevD.85.063503 [arXiv:1111.0293 [hep-ph]].

[53] X. Chu, C. Garcia-Cely and T. Hambye, JHEP **11**, 048 (2016) doi:10.1007/JHEP11(2016)048 [arXiv:1609.00399 [hep-ph]].

[54] S. Tulin and H. B. Yu, Phys. Rept. **730**, 1-57 (2018) doi:10.1016/j.physrep.2017.11.004

[arXiv:1705.02358 [hep-ph]].

[55] S. Mizuta and M. Yamaguchi, Phys. Lett. B **298**, 120-126 (1993) doi:10.1016/0370-2693(93)91717-2 [arXiv:hep-ph/9208251 [hep-ph]].

[56] M. Pospelov, A. Ritz and M. B. Voloshin, Phys. Lett. B **662**, 53-61 (2008) doi:10.1016/j.physletb.2008.02.052 [arXiv:0711.4866 [hep-ph]].

[57] J. L. Feng, H. Tu and H. B. Yu, JCAP **10**, 043 (2008) doi:10.1088/1475-7516/2008/10/043 [arXiv:0808.2318 [hep-ph]].

[58] J. L. Feng, M. Kaplinghat and H. B. Yu, Phys. Rev. D **82**, 083525 (2010) doi:10.1103/PhysRevD.82.083525 [arXiv:1005.4678 [hep-ph]].

[59] Y. Hochberg, E. Kuflik, T. Volansky and J. G. Wacker, Phys. Rev. Lett. **113**, 171301 (2014) doi:10.1103/PhysRevLett.113.171301 [arXiv:1402.5143 [hep-ph]].

[60] Y. Hochberg, E. Kuflik, H. Murayama, T. Volansky and J. G. Wacker, Phys. Rev. Lett. **115**, no.2, 021301 (2015) doi:10.1103/PhysRevLett.115.021301 [arXiv:1411.3727 [hep-ph]].

[61] E. Bernreuther, S. Heeba and F. Kahlhoefer, JCAP **03**, 040 (2021) doi:10.1088/1475-7516/2021/03/040 [arXiv:2010.14522 [hep-ph]].

[62] J. Guo, L. Wu and B. Zhu, Phys. Lett. B **840**, 137853 (2023) doi:10.1016/j.physletb.2023.137853 [arXiv:2302.06159 [hep-ph]].

[63] A. De Angelis *et al.* [e-ASTROGAM], Exper. Astron. **44**, no.1, 25-82 (2017) doi:10.1007/s10686-017-9533-6 [arXiv:1611.02232 [astro-ph.HE]].

[64] A. De Angelis, V. Tatischeff, A. Argan, S. Brandt, A. Bulgarelli, A. Bykov, E. Costantini, R. Curado da Silva, I. A. Grenier and L. Hanlon, *et al.* Exper. Astron. **51**, no.3, 1225-1254 (2021) doi:10.1007/s10686-021-09706-y [arXiv:2102.02460 [astro-ph.IM]].

[65] J. A. Tomsick, A. Zoglauer, C. Sleator, H. Lazar, J. Beechert, S. Boggs, J. Roberts, T. Siegert, A. Lowell and E. Wulf, *et al.* [arXiv:1908.04334 [astro-ph.IM]].

[66] A. Caputo, M. Negro, M. Regis and M. Taoso, JCAP **02**, 006 (2023) doi:10.1088/1475-7516/2023/02/006 [arXiv:2210.09310 [hep-ph]].

[67] E. Orlando, E. Bottacini, A. Moiseev, A. Bodaghee, W. Collmar, T. Ensslin, I. V. Moskalenko, M. Negro, S. Profumo and M. G. Baring, *et al.* JCAP **07**, no.07, 036 (2022) doi:10.1088/1475-7516/2022/07/036 [arXiv:2112.07190 [astro-ph.HE]].

[68] A. Coogan, A. Moiseev, L. Morrison, S. Profumo, M. G. Baring, A. Bolotnikov, G. A. Carini, S. C. Herrmann, F. Longo and F. W. Stecker, *et al.* Phys. Rev. D **107**, no.2, 023022 (2023)

doi:10.1103/PhysRevD.107.023022 [arXiv:2101.10370 [astro-ph.HE]].

[69] R. Essig, E. Kuflik, S. D. McDermott, T. Volansky and K. M. Zurek, JHEP **11**, 193 (2013) doi:10.1007/JHEP11(2013)193 [arXiv:1309.4091 [hep-ph]].

[70] K. K. Boddy and J. Kumar, Phys. Rev. D **92**, no.2, 023533 (2015) doi:10.1103/PhysRevD.92.023533 [arXiv:1504.04024 [astro-ph.CO]].

[71] S. Matsumoto, S. Mukhopadhyay and Y. L. S. Tsai, JHEP **10**, 155 (2014) doi:10.1007/JHEP10(2014)155 [arXiv:1407.1859 [hep-ph]].

[72] A. Berlin, S. Gori, T. Lin and L. T. Wang, Phys. Rev. D **92**, 015005 (2015) doi:10.1103/PhysRevD.92.015005 [arXiv:1502.06000 [hep-ph]].

[73] S. Matsumoto, S. Mukhopadhyay and Y. L. S. Tsai, Phys. Rev. D **94**, no.6, 065034 (2016) doi:10.1103/PhysRevD.94.065034 [arXiv:1604.02230 [hep-ph]].

[74] B. Díaz Sáez, P. Escalona, S. Norero and A. R. Zerwekh, JHEP **10**, 233 (2021) doi:10.1007/JHEP10(2021)233 [arXiv:2105.04255 [hep-ph]].

[75] L. Lopez-Honorez, T. Schwetz and J. Zupan, Phys. Lett. B **716**, 179-185 (2012) doi:10.1016/j.physletb.2012.07.017 [arXiv:1203.2064 [hep-ph]].

[76] M. Heikinheimo, A. Racioppi, M. Raidal, C. Spethmann and K. Tuominen, Nucl. Phys. B **876**, 201-214 (2013) doi:10.1016/j.nuclphysb.2013.08.006 [arXiv:1305.4182 [hep-ph]].

[77] K. Ghorbani, JCAP **01**, 015 (2015) doi:10.1088/1475-7516/2015/01/015 [arXiv:1408.4929 [hep-ph]].

[78] Y. G. Kim, K. Y. Lee, C. B. Park and S. Shin, Phys. Rev. D **93**, no.7, 075023 (2016) doi:10.1103/PhysRevD.93.075023 [arXiv:1601.05089 [hep-ph]].

[79] S. Esch, M. Klasen and C. E. Yaguna, Phys. Rev. D **88**, 075017 (2013) doi:10.1103/PhysRevD.88.075017 [arXiv:1308.0951 [hep-ph]].

[80] S. Esch, M. Klasen and C. E. Yaguna, JHEP **09**, 108 (2014) doi:10.1007/JHEP09(2014)108 [arXiv:1406.0617 [hep-ph]].

[81] S. Ipek, D. McKeen and A. E. Nelson, Phys. Rev. D **90**, no.5, 055021 (2014) doi:10.1103/PhysRevD.90.055021 [arXiv:1404.3716 [hep-ph]].

[82] F. Kahlhoefer, K. Schmidt-Hoberg and S. Wild, JCAP **08**, 003 (2017) doi:10.1088/1475-7516/2017/08/003 [arXiv:1704.02149 [hep-ph]].

[83] S. Baek, P. Ko and J. Li, Phys. Rev. D **95**, no.7, 075011 (2017) doi:10.1103/PhysRevD.95.075011 [arXiv:1701.04131 [hep-ph]].

[84] G. Arcadi, M. Lindner, F. S. Queiroz, W. Rodejohann and S. Vogl, JCAP **03**, 042 (2018) doi:10.1088/1475-7516/2018/03/042 [arXiv:1711.02110 [hep-ph]].

[85] N. F. Bell, Y. Cai, J. B. Dent, R. K. Leane and T. J. Weiler, Phys. Rev. D **96**, no.2, 023011 (2017) doi:10.1103/PhysRevD.96.023011 [arXiv:1705.01105 [hep-ph]].

[86] K. Ghorbani and P. H. Ghorbani, JHEP **05**, 096 (2019) doi:10.1007/JHEP05(2019)096 [arXiv:1812.04092 [hep-ph]].

[87] S. Banerjee, G. Bélanger, D. Bhatia, B. Fuks and S. Raychaudhuri, JHEP **07**, 111 (2022) doi:10.1007/JHEP07(2022)111 [arXiv:2110.15391 [hep-ph]].

[88] M. Abdughani, Y. Z. Fan, C. T. Lu, T. P. Tang and Y. L. S. Tsai, JHEP **07**, 127 (2022) doi:10.1007/JHEP07(2022)127 [arXiv:2111.02946 [astro-ph.HE]].

[89] M. W. Winkler, Phys. Rev. D **99**, no.1, 015018 (2019) doi:10.1103/PhysRevD.99.015018 [arXiv:1809.01876 [hep-ph]].

[90] N. Aghanim *et al.* [Planck], Astron. Astrophys. **641**, A6 (2020) [erratum: Astron. Astrophys. **652**, C4 (2021)] doi:10.1051/0004-6361/201833910 [arXiv:1807.06209 [astro-ph.CO]].

[91] J. Aalbers *et al.* [LZ], Phys. Rev. Lett. **131**, no.4, 041002 (2023) doi:10.1103/PhysRevLett.131.041002 [arXiv:2207.03764 [hep-ex]].

[92] P. Agnes *et al.* [DarkSide-50], Eur. Phys. J. C **83**, 322 (2023) doi:10.1140/epjc/s10052-023-11410-4 [arXiv:2302.01830 [hep-ex]].

[93] J. Berger, K. Jedamzik and D. G. E. Walker, JCAP **11**, 032 (2016) doi:10.1088/1475-7516/2016/11/032 [arXiv:1605.07195 [hep-ph]].

[94] G. Krnjaic, Phys. Rev. D **94**, no.7, 073009 (2016) doi:10.1103/PhysRevD.94.073009 [arXiv:1512.04119 [hep-ph]].

[95] G. Belanger, F. Boudjema and A. Pukhov, doi:10.1142/9789814390163_0012 [arXiv:1402.0787 [hep-ph]].

[96] T. Abe, M. Fujiwara and J. Hisano, JHEP **02**, 028 (2019) doi:10.1007/JHEP02(2019)028 [arXiv:1810.01039 [hep-ph]].

[97] A. D. Dolgov, Phys. Rept. **370**, 333-535 (2002) doi:10.1016/S0370-1573(02)00139-4 [arXiv:hep-ph/0202122 [hep-ph]].

[98] P. A. R. Ade *et al.* [Planck], Astron. Astrophys. **571**, A16 (2014) doi:10.1051/0004-6361/201321591 [arXiv:1303.5076 [astro-ph.CO]].

[99] G. Aad *et al.* [ATLAS], JHEP **03**, 041 (2022) doi:10.1007/JHEP03(2022)041

[arXiv:2110.13673 [hep-ex]].

[100] V. Khachatryan *et al.* [CMS], JHEP **10**, 076 (2017) doi:10.1007/JHEP10(2017)076 [arXiv:1701.02032 [hep-ex]].

[101] G. Aad *et al.* [ATLAS], Eur. Phys. J. C **80**, no.5, 450 (2020) doi:10.1140/epjc/s10052-020-7997-4 [arXiv:1909.01246 [hep-ex]].

[102] J. D. Clarke, JHEP **10**, 061 (2015) doi:10.1007/JHEP10(2015)061 [arXiv:1505.00063 [hep-ph]].

[103] G. Aad *et al.* [ATLAS], JHEP **08**, 104 (2022) doi:10.1007/JHEP08(2022)104 [arXiv:2202.07953 [hep-ex]].

[104] R. Aaij *et al.* [LHCb], JHEP **02**, 105 (2013) doi:10.1007/JHEP02(2013)105 [arXiv:1209.4284 [hep-ex]].

[105] J. P. Lees *et al.* [BaBar], Phys. Rev. Lett. **114**, no.17, 171801 (2015) doi:10.1103/PhysRevLett.114.171801 [arXiv:1502.02580 [hep-ex]].

[106] R. Aaij *et al.* [LHCb], Phys. Rev. D **95**, no.7, 071101 (2017) doi:10.1103/PhysRevD.95.071101 [arXiv:1612.07818 [hep-ex]].

[107] I. Adachi *et al.* [Belle-II], [arXiv:2311.14647 [hep-ex]].

[108] J. R. Batley *et al.* [NA48/2], Phys. Lett. B **697**, 107-115 (2011) doi:10.1016/j.physletb.2011.01.042 [arXiv:1011.4817 [hep-ex]].

[109] A. Alavi-Harati *et al.* [KTEV], Phys. Rev. Lett. **84**, 5279-5282 (2000) doi:10.1103/PhysRevLett.84.5279 [arXiv:hep-ex/0001006 [hep-ex]].

[110] A. Alavi-Harati *et al.* [KTeV], Phys. Rev. Lett. **93**, 021805 (2004) doi:10.1103/PhysRevLett.93.021805 [arXiv:hep-ex/0309072 [hep-ex]].

[111] F. Bezrukov and D. Gorbunov, JHEP **05**, 010 (2010) doi:10.1007/JHEP05(2010)010 [arXiv:0912.0390 [hep-ph]].

[112] J. K. Ahn *et al.* [KOTO], Phys. Rev. Lett. **122**, no.2, 021802 (2019) doi:10.1103/PhysRevLett.122.021802 [arXiv:1810.09655 [hep-ex]].

[113] A. V. Artamonov *et al.* [BNL-E949], Phys. Rev. D **79**, 092004 (2009) doi:10.1103/PhysRevD.79.092004 [arXiv:0903.0030 [hep-ex]].

[114] E. Cortina Gil *et al.* [NA62], JHEP **03**, 058 (2021) doi:10.1007/JHEP03(2021)058 [arXiv:2011.11329 [hep-ex]].

[115] F. Ferrer and D. R. Hunter, JCAP **09**, 005 (2013) doi:10.1088/1475-7516/2013/09/005

[arXiv:1306.6586 [astro-ph.HE]].

[116] T. Binder, T. Bringmann, M. Gustafsson and A. Hryczuk, Phys. Rev. D **96**, no.11, 115010 (2017) [erratum: Phys. Rev. D **101**, no.9, 099901 (2020)] doi:10.1103/PhysRevD.96.115010 [arXiv:1706.07433 [astro-ph.CO]].

[117] T. Binder, T. Bringmann, M. Gustafsson and A. Hryczuk, Eur. Phys. J. C **81**, 577 (2021) doi:10.1140/epjc/s10052-021-09357-5 [arXiv:2103.01944 [hep-ph]].

[118] S. W. Randall, M. Markevitch, D. Clowe, A. H. Gonzalez and M. Bradac, Astrophys. J. **679**, 1173-1180 (2008) doi:10.1086/587859 [arXiv:0704.0261 [astro-ph]].

[119] A. Arhrib, Y. L. S. Tsai, Q. Yuan and T. C. Yuan, JCAP **06**, 030 (2014) doi:10.1088/1475-7516/2014/06/030 [arXiv:1310.0358 [hep-ph]].

[120] A. Fowlie, K. Kowalska, L. Roszkowski, E. M. Sessolo and Y. L. S. Tsai, Phys. Rev. D **88**, 055012 (2013) doi:10.1103/PhysRevD.88.055012 [arXiv:1306.1567 [hep-ph]].

[121] Y. L. S. Tsai, V. Tran and C. T. Lu, JHEP **06**, 033 (2020) doi:10.1007/JHEP06(2020)033 [arXiv:1912.08875 [hep-ph]].

[122] Y. Z. Fan, T. P. Tang, Y. L. S. Tsai and L. Wu, Phys. Rev. Lett. **129**, no.9, 091802 (2022) doi:10.1103/PhysRevLett.129.091802 [arXiv:2204.03693 [hep-ph]].

[123] T. P. Tang, M. Abdughani, L. Feng, Y. L. S. Tsai, J. Wu and Y. Z. Fan, Sci. China Phys. Mech. Astron. **66**, no.3, 239512 (2023) doi:10.1007/s11433-022-2046-y [arXiv:2204.04356 [hep-ph]].

[124] D. Foreman-Mackey, D. W. Hogg, D. Lang and J. Goodman, Publ. Astron. Soc. Pac. **125**, 306-312 (2013) doi:10.1086/670067 [arXiv:1202.3665 [astro-ph.IM]].

[125] A. Delgado, A. Martin and N. Raj, Phys. Rev. D **95**, no.3, 035002 (2017) doi:10.1103/PhysRevD.95.035002 [arXiv:1608.05345 [hep-ph]].

[126] A. W. Strong, I. V. Moskalenko and O. Reimer, Astrophys. J. **613**, 962-976 (2004) doi:10.1086/423193 [arXiv:astro-ph/0406254 [astro-ph]].

[127] M. Ibe, H. Murayama and T. T. Yanagida, Phys. Rev. D **79**, 095009 (2009) doi:10.1103/PhysRevD.79.095009 [arXiv:0812.0072 [hep-ph]].

[128] L. Roszkowski, E. M. Sessolo and Y. L. S. Tsai, Phys. Rev. D **86**, 095005 (2012) doi:10.1103/PhysRevD.86.095005 [arXiv:1202.1503 [hep-ph]].

[129] A. Coogan, L. Morrison and S. Profumo, JCAP **01**, 056 (2020) doi:10.1088/1475-7516/2020/01/056 [arXiv:1907.11846 [hep-ph]].

[130] M. Cirelli, G. Corcella, A. Hektor, G. Hutsi, M. Kadastik, P. Panci, M. Raidal, F. Sala and A. Strumia, JCAP **03**, 051 (2011) [erratum: JCAP **10**, E01 (2012)] doi:10.1088/1475-7516/2012/10/E01 [arXiv:1012.4515 [hep-ph]].

arXiv:2403.02685v1 [hep-ph] 5 Mar 2024

Limits on scalar dark matter interactions from radiative corrections

V. V. Flambaum* and I. B. Samsonov†
School of Physics, University of New South Wales, Sydney 2052, Australia

There is limited information about interaction strength of scalar dark matter candidate with hadrons and leptons for scalar particle mass exceeding 10^{-3} eV while its interaction with photon is well-studied. The scalar-photon coupling constant receives quantum corrections from one-loop Feynman diagrams which involve the scalar-lepton, scalar-quark and scalar-W boson vertices. We calculate these one-loop quantum corrections and find new limits on the scalar particle interactions with electron, muon, tau, quarks, nucleons, gluons and W boson for $m_\phi < 15$ MeV by re-purposing the results of experiments measuring the scalar-photon interaction. Limits on interactions with heavy leptons and quarks have been obtained for the first time, limits on other interactions in certain mass intervals are 2 to 15 orders of magnitude stronger than those presented in previous publications.

I. INTRODUCTION

Scalar and pseudoscalar fields are very promising candidates for dark matter (DM) particles. The pseudoscalar DM candidates are exemplified by the QCD axion which represents a consistent extension of the Standard Model and helps resolving the strong CP problem (see, e.g., [1] for a review). The CP-even counterpart of the axion field is a dilaton ϕ [2], which is strongly motivated by superstring theory, see, e.g., Refs. [3–8]. Scalar field DM candidates appear also in chameleon models of gravity, see, e.g., Ref. [9].

Since the preferred interaction channel between the scalar field and the visible matter particles is not known, it is generally assumed that all types of interactions are allowed, and the strengths of these interactions should be measured experimentally. The leading interaction vertices should be linear with respect to the scalar field, although quadratic interactions are also of interest, see, e.g., Refs. [10–12]. Therefore, the majority of experiments searching for the scalar DM candidates focus on measurements of coupling constants of this scalar field to photon, $g_{\phi\gamma}$ and electron $g_{\phi e}$. The results of these measurements are summarized in Refs. [13, 14]. The channel of hadronic interactions of this scalar field remains less studied.

This paper is devoted to the study of interaction of the scalar field with leptons, quarks and W boson. We show that it is possible to re-purpose the results of the experiments measuring the scalar-photon interaction constant for obtaining new limits on strength of interaction of the scalar field with leptons, quarks and W boson. The main idea is that the scalar-photon coupling constant $g_{\phi\gamma}$ receives quantum corrections from one-loop Feynman diagrams involving the scalar-fermion and scalar-W boson vertices. In other words, the scalar field can decay into two photons via fermionic and W boson loops. Thus, using the relation between the scalar-photon and scalar-fermion or scalar-W interaction constants allows us to find new constraints on the scalar-lepton, scalar-quark and scalar-W boson interactions.

In the next section, we present the general expression for quantum corrections to the scalar-photon interaction constant from one-loop Feynman graphs. This process is analogous to the decay of the Higgs field into two photons mediated by quarks, leptons or W bosons calculated in Refs. [15, 16]. In Sec. II we apply the one-loop relation between the coupling constants for obtaining new limits on the interaction of the scalar DM candidate with leptons, quarks, nucleons, W boson and gluons. A short summary of the results is given in the last section.

In this paper, we use natural units with $\hbar = c = 1$.

II. ONE-LOOP CONTRIBUTION TO SCALAR-PHOTON COUPLING

Let ϕ be a real scalar field representing DM particles with mass m_ϕ. In the model of dilaton-like DM [11, 12, 17, 18], this field may have the following interaction vertices to the photon field with Maxwell field strength $F_{\mu\nu}$, to quarks or leptons described by Dirac fermions f, ($f = e, \mu, \tau, u, d, s, c, b, t$ for electron, muon, tau, up, down, strange, charm, bottom and top quarks, respectively), to gluons $G^a_{\mu\nu}$ and to $W^\pm_\mu$ bosons

$$\mathcal{L}_{\rm int} = \frac{1}{4} g_{\phi\gamma}\phi F^{\mu\nu}F_{\mu\nu} - \sum_f g_{\phi f}\phi\bar{f}f + \frac{1}{4} g_{\phi g}\phi G^{\mu\nu a}G^a_{\mu\nu} + g_{\phi W} m_W \phi W^{+\mu}W^-_\mu \,. \tag{1}$$

The coupling constant $g_{\phi\gamma}$ receives quantum corrections from fermionic loop diagrams with the scalar-fermion interaction quantified by the coupling constant $g_{\phi f}$ and from W-boson loop involving the vertex with $g_{\phi W}$ coupling. The leading contributions are represented by the triangle Feynman graphs in Fig. 1. The corresponding

* v.flambaum@unsw.edu.au
† igor.samsonov@unsw.edu.au

scattering amplitude $\mathcal{M}$ reads

$$\mathcal{M} = \frac{\alpha}{2\pi}\left(\frac{g_{\phi f}}{m_f}A_{1/2} + \frac{g_{\phi W}}{2m_W}A_1\right) \times (k_1^\rho k_{2\rho} g^{\mu\nu} - k_1^\mu k_2^\nu) e_{1\mu} e_{2\nu}\,, \tag{2}$$

where m_f and m_W are the fermion particle and W boson rest masses, respectively, k_1^μ, k_2^ν and $e_{1\mu}$, $e_{2\nu}$ are four-momenta and polarization four-vectors of the photons. The dimensionless functions $A_{1/2}$ and A_1 were calculated in Refs. [15, 16] where decay of the Higgs boson into two photons was considered (see also Ref. [19] for a review),

$$A_{1/2}(\tau_f) = \sum_f N_c Q_f^2 2[\tau_f + (\tau_f - 1) f(\tau_f)]\tau_f^{-2}\,, \tag{3a}$$

$$A_1(\tau_W) = -[2\tau_W^2 + 3\tau_W + 3(2\tau_W - 1) f(\tau_W)]\tau_W^{-2}\,, \tag{3b}$$

where $\tau_f = m_\phi^2/(4m_f^2)$, $\tau_W = m_\phi^2/(4m_W^2)$ and

$$f(\tau) = \begin{cases} \arcsin^2\sqrt{\tau} & (\tau \le 1) \\ -\frac{1}{4}\left[\log\frac{1+\sqrt{1-\tau^{-1}}}{1-\sqrt{1-\tau^{-1}}} - i\pi\right]^2 & (\tau > 1)\,. \end{cases} \tag{4}$$

In Eq. (3a), N_c is the number of colors ($N_c = 3$ for quarks and $N_c = 1$ for leptons) and Q_f are fractional quark and lepton charges ($Q_f = +\frac{3}{2}$ for u, c and t quarks, $Q_f = -\frac{1}{3}$ for d, s and b quarks, and $Q_f = -1$ for electron, muon and tau).

Note that in the limit of light scalar field as compared with the fermion or W boson mass the functions (3) simplify drastically,

$$A_{1/2} \approx \frac{4}{3}\sum_f N_c Q_f^2 \qquad (m_\phi \ll m_f), \tag{5a}$$

$$A_1 \approx -7 \qquad (m_\phi \ll m_W). \tag{5b}$$

The expression for the scattering amplitude (2) provides the one-loop contribution to the scalar-photon coupling constant $g_{\phi\gamma}$:

$$g_{\phi\gamma} = \frac{\alpha}{2\pi}\left(\frac{g_{\phi f}}{m_f}A_{1/2} + \frac{g_{\phi W}}{2m_W}A_1\right). \tag{6}$$

Below, we will use this relation for extracting limits on $g_{\phi f}$ and $g_{\phi W}$ from known experimental constraints on the scalar-photon coupling $g_{\phi\gamma}$.

We point out that the relation (6) may be extended to quadratic couplings of the scalar field with photon $g^{(2)}_{\phi\gamma}$ and fermions $g^{(2)}_{\phi f}$,

$$g^{(2)}_{\phi\gamma} = \frac{\alpha}{2\pi}\left(\frac{g^{(2)}_{\phi f}}{m_f}A_{1/2} + \frac{g^{(2)}_{\phi W}}{2m_W}A_1\right). \tag{7}$$

Implication of this relation for studying constants of interaction of ϕ^2 with visible matter requires separate considerations.

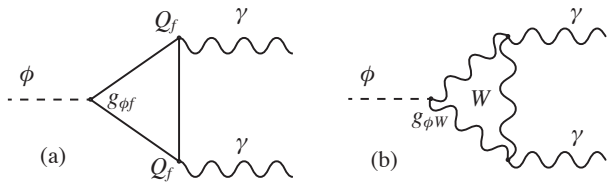


FIG. 1. Feynman graph representing leading one-loop quantum correction to the scalar-photon coupling. (a) Contribution from fermion (quark or lepton) fields with charges Q_f. (b) Contribution from W boson loop.

III. LIMITS ON SCALAR FIELD INTERACTIONS

In this section, we will study limits on the coupling constants of the scalar DM particle with leptons, quarks and W boson given in Eq. (1). These limits will be obtained by applying Eq. (6) to known experimental and theoretical constraints on the scalar-photon interaction [20–40].

A. Scalar-electron interaction

Since the mass of the scalar field ϕ is unknown, it is necessary to search for scalar DM signal in a wide range of masses, spanning from ultralight fields with masses $m_\phi \sim 10^{-24}\,\text{eV}$ to MeV-GeV region. Let us first discuss ultralight scalar fields, with masses $10^{-24}\,\text{eV} < m_\phi \lesssim 10^{-6}\,\text{eV}$, because the scalar-photon interaction in this region has been studied in a series of works [20–40], see also Ref. [13] for a recent review.

If the scalar field is much lighter than the electron, $m_\phi \ll m_e$, the identity (5a) applies with $N_c = 1$ and $Q_f^2 = 1$. In this case, the one-loop contribution to the scalar-photon coupling constant from the electron loop (6) reads

$$g_{\phi\gamma} = \frac{2\alpha}{3\pi m_e} g_{\phi e}\,. \tag{8}$$

This relation allows us to find the limits on $g_{\phi e}$ from the known constraints on the coupling constant $g_{\phi\gamma}$ presented in Refs. [20–38] in the mass region $10^{-24}\,\text{eV} < m_\phi \lesssim 10^{-6}\,\text{eV}$. These limits are, however, 1-2 orders in magnitude weaker than the direct limits on the scalar-electron interaction obtained in the works [23, 24, 27–31, 33–38, 41–44] through direct measurements of this coupling. Therefore, we do not present these limits in this paper and turn to considering heavier scalars.

If the mass of the scalar particle is comparable with the electron mass, $m_\phi \sim m_e$, the general expression (3a) for the function $A_{1/2}$ should be used with $N_c = 1$ and $Q_f^2 = 1$. Substituting this function into Eq. (6), we find the following relation for the absolute value of the scalar-

electron coupling constant,

$$|g_{\phi e}| = \frac{\pi m_e}{\alpha}\left|\frac{g_{\phi\gamma}\tau^2}{\tau+(\tau-1)f(\tau)}\right|, \tag{9}$$

with the function $f(\tau)$ given by Eq. (4) and $\tau = m_\phi^2/(4m_e^2)$.

Scalar particles with mass in the eV to MeV range can decay into photons and create emission lines potentially observable with the aid of space-based optical, x-ray and gamma-ray telescopes. The decay rate of these scalars is the same as that for the axion-like particles. Therefore, making use of the identity (9) we re-purpose the results of the works [45–61] to obtain the limits on the scalar-photon $g_{\phi\gamma}$ and scalar-electron $g_{\phi e}$ coupling constants. These limits are shown in Fig. 2 as a consolidated pink area in the range of scalar filed masses $0.8\,\mathrm{eV} < m_\phi < 1\,\mathrm{MeV}$. Numerical data for limits on the scalar-photon interaction constant are taken from Ref. [14].

Fig. 2 includes also limits on $g_{\phi\gamma}$ and $g_{\phi e}$ in the interval $10^{-4}\,\mathrm{eV} < m_\phi < 1\,\mathrm{eV}$ which originate from the limits of the CAST experiment [62] on the axion-photon interaction $g_{a\gamma}$. In Ref. [63], it was shown that the results of this experiment apply to the scalar-photon interaction with direct substitution $g_{a\gamma} \to g_{\phi\gamma}$. Thus, making use of Eq. (8), we re-purpose the results of the CAST experiment [62] to obtain the limits on the scalar-electron interaction constant $g_{\phi e}$.

If the mass of the scalar field exceeds twice the electron mass, $m_\phi > 2m_e$, the scalar can decay directly into electron-positron pairs. The tree-level decay rate of this process is [64] (see also Ref. [19])

$$\Gamma(\phi \to e^+e^-) = \frac{1}{8\pi}g_{\phi e}^2 m_\phi\left(1-\frac{4m_e^2}{m_\phi^2}\right)^{3/2}. \tag{10}$$

The electrons and positrons ejected in the decays of scalar DM particles serve as an additional source of diffuse photons produced by the interaction with interstellar medium. The ejected positrons annihilate in the interstellar medium and produce the 511 keV photon line in gamma-ray detectors such as the SPI/INTEGRAL telescope. The reported flux of 511 keV photons from the Galactic bulge is [65]

$$\Phi \simeq 10^{-3}\mathrm{cm}^{-2}\mathrm{s}^{-1}. \tag{11}$$

Assuming that a fraction of this photon flux is produced by decays of the scalar dark matter particles, we can set an upper bound on the value of the coupling $g_{\phi e}$ in Eq. (10).

To estimate the flux of 511-keV photons from the Galactic center we consider a DM distribution in our Galaxy given by the generalized Navarro-Frenk-White profile

$$\rho_{\rm DM}(r) = \frac{C}{r^\gamma(1+r/R_s)^{3-\gamma}}, \tag{12}$$

where $R_s = 20\,\mathrm{kpc}$ is the scale radius. Following Ref. [66], we set the values of the parameters $\gamma = 1.1$ and $C = 2.4\times10^8 M_\odot \mathrm{kpc}^{-1.9}$ so that Eq. (12) reproduces the estimated mass of dark matter in the Galactic bulge, see, e.g., Ref. [67], and provides the correct value for local DM density of $\rho_{\rm DM}(8.5\,\mathrm{kpc}) \approx 0.4\,\mathrm{GeV/cm}^3$. Thus, given the DM density distribution (12) we find the photon flux at the observation point on Earth from the Galactic bulge,

$$\Phi = \frac{1}{4\pi(8.5\,\mathrm{kpc})^2}\int_{\rm bulge}\frac{\rho_{\rm DM}\Gamma}{m_\phi}d^3r\,. \tag{13}$$

The Galactic bulge here is roughly taken as a spherical region with radius 2 kpc around the Galactic center. Substituting the decay rate (10) into Eq. (13) and equating it to the observed flux (11) we find the upper limit on the coupling constant $g_{\phi e}$. The corresponding excluded region is represented by the blue area in Fig. 2. Note that in this plot we restrict the mass of the scalar $m_\phi < 15\,\mathrm{MeV}$ because, according to our estimates, the corresponding positrons are likely to be stopped by interaction with the interstellar medium within the bulge and eventually annihilate.

B. Scalar-muon and tau interactions

Equation (8) may be easily generalized to accommodate one-loop contributions from the muon and tau loops,

$$g_{\phi\gamma} = \frac{2\alpha}{3\pi}\left(\frac{g_{\phi\mu}}{m_\mu}+\frac{g_{\phi\tau}}{m_\tau}\right), \tag{14}$$

where m_μ and m_τ are muon and tau rest masses, respectively. Note that these masses are significantly larger than the upper bound on the scalar field mass considered in the present study, $m_\phi < 15\,\mathrm{MeV}$. Therefore, we do not need to consider direct decay of the scalar into muon and tau pairs as in Eq. (10). In Fig. 3a we present the limits on the coupling constants $g_{\phi\mu}$ and $g_{\phi\tau}$ obtained by applying Eq. (14) to the results of the works [20–40] and [46–62].

Note that our limits on the scalar-muon coupling represent a 8-15 orders in magnitude improvement over the results of the works [64, 68]. Limits on the scalar-tau interaction are presented for the first time to the best of our knowledge.

C. Scalar-W boson interaction

In this subsection, we assume that the dominant one-loop contribution to the scalar-photon coupling arises from the loop of W bosons shown in Fig. 1b. Noting that in the case under consideration the W-boson mass is always much larger than the scalar field mass, Eqs. (5b) and (6) may be cast in the form

$$g_{\phi\gamma} = -\frac{7\alpha}{4\pi m_W}g_{\phi W}\,. \tag{15}$$

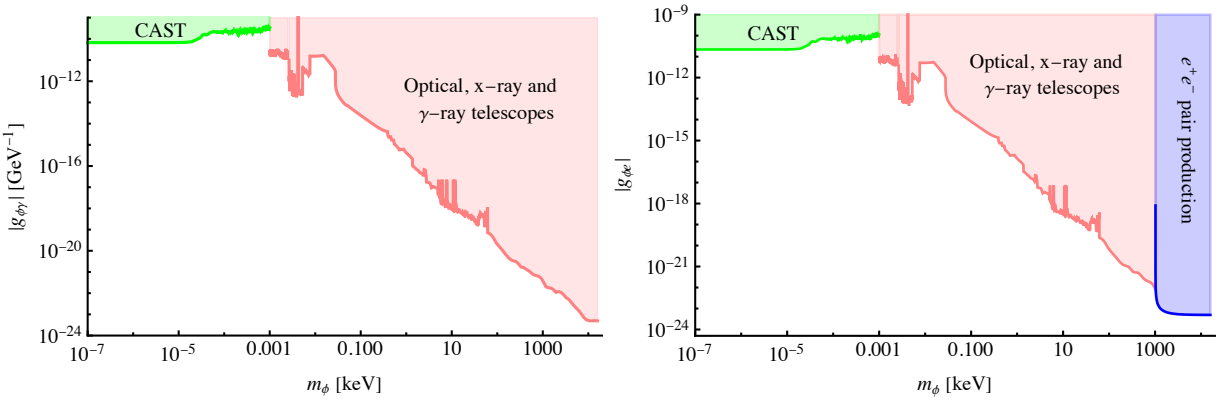


FIG. 2. Limits on the scalar-photon $g_{\phi\gamma}$ and scalar-electron $g_{\phi e}$ interaction constants. Green excluded area originates from re-purposing the results of CAST experiment [62]. Pink area represents the consolidated excluded region arising from application of the relation (9) to the results of the works [45–61]. Blue area sets an upper limit on the scalar-electron coupling constant from direct tree-level decay of scalars into electron-positron pairs. Limits on the scalar-gluon interaction constant $g_{\phi g}$ are about three orders in magnitude weaker than limits on $g_{\phi\gamma}$.

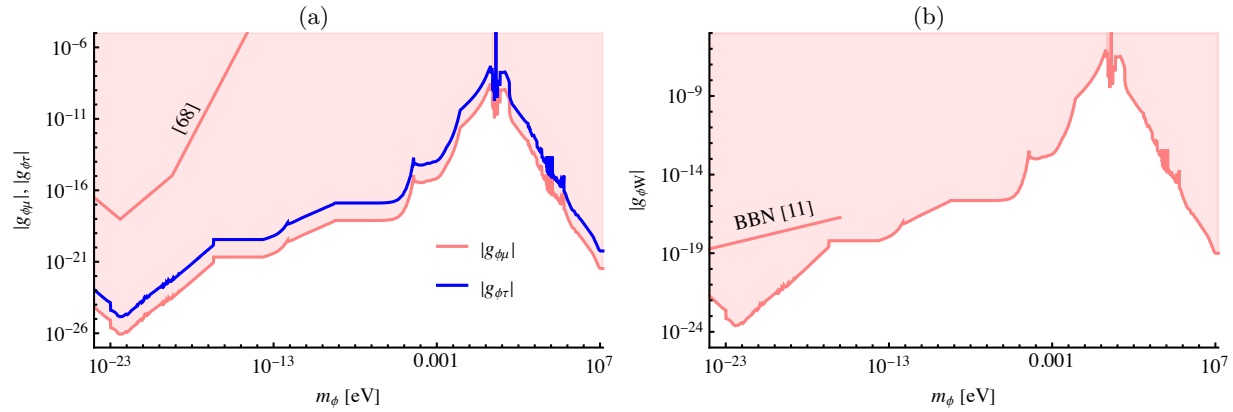


FIG. 3. (a) Limits on scalar-muon (pink curve) and scalar-tau (blue curve) coupling constants obtained by applying the relation (14) to the results of the works [20–38] and [45–60]. (b) Analogous limits on the scalar-W boson interaction.

This relation allows us to find limits on $g_{\phi W}$ from known constraints on the scalar-photon interaction presented in Refs. [20–38, 45–60], see Fig. 3b. Our limits on $g_{\phi W}$ are 2-5 orders in magnitude stronger than those found earlier in Ref. [11] for $m_\phi < 10^{-16}$ eV from the analysis of Big Bang nucleosynthesis.

D. Scalar-quark interaction

One-loop contributions to $g_{\phi\gamma}$ from "light" u, d, s and "heavy" c, b, t quarks should be considered slightly different. Let us start with the light quarks first.

For the contribution from the u, d and s quark loops, the relations (3a) and (6) cannot be applied naively, because they do not take into account the effect of strong coupling of quarks at low energies. The most important effect here is a significant increase of the hadron masses relative to the bare quark masses. The minimum effective hadron mass in the intermediate state on the Feynamn graph in Fig. 1a actually corresponds to two pions. This effect may be roughly taken into account by replacing the bare u and d quark masses with the effective mass $m_f \to m_\pi \approx 140\,\text{MeV}$ in Eq. (6). In the contribution of s quark we should take $m_f \to m_K \approx 494$ MeV. Substituting the values of quark charges and $N_c = 3$ into Eq. (3a), we find the following relation between the scalar-photon and scalar-quark coupling constants:

$$g_{\phi\gamma} = \frac{2\alpha}{\pi}\left[\frac{4}{9}\frac{g_{\phi u}}{m_\pi} + \frac{1}{9}\frac{g_{\phi d}}{m_\pi} + \frac{1}{9}\frac{g_{\phi s}}{m_K}\right] \approx [0.015 g_{\phi u} + 0.0037 g_{\phi d} + 0.0010 g_{\phi s}]\text{GeV}^{-1}\,. \quad (16)$$

This allows us to derive limits on either of the constants $g_{\phi u}$, $g_{\phi d}$ and $g_{\phi s}$ assuming that it gives a dominant contribution to $g_{\phi\gamma}$.

The limits on $g_{\phi u}$ are represented by pink area in Fig. 4a. These limits are obtained by re-purposing the results of works [46–62] where the constraints on the axion-photon interaction constant $g_{a\gamma}$ were retrieved from the

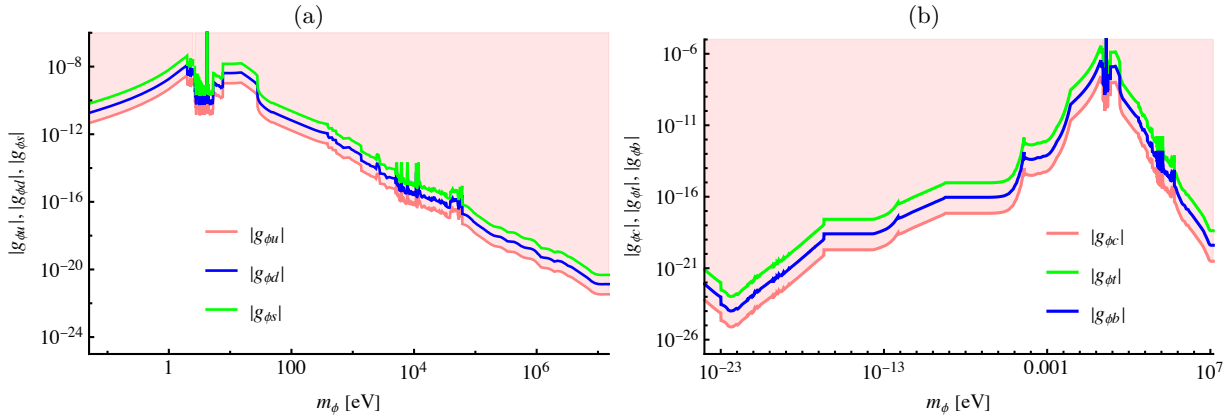


FIG. 4. Limits on scalar-quark interaction.

data of various telescopes and laboratories. The latter constraints directly apply to the scalar-photon interaction with a simple substitution $g_{a\gamma} \to g_{\phi\gamma}$ because the two-photon decay rates of the axion a and the scalar ϕ are the same.

In Fig. 4a we do not consider ultralight scalars with $m_\phi \lesssim 0.05\,\text{eV}$ because, in this region, the relation (16) gives us the constraints which are 3-5 orders in magnitude weaker than the existing ones obtained directly from the torsion-balance and equivalence principle test experiments [23, 25, 69–75], as well as from analysis of atomic clock frequency shifts [20–22, 25–27].

For the one-loop contributions to $g_{\phi\gamma}$ from heavy quarks c, b and t the effects of strong interaction are not as important as for the light ones. Therefore, bare masses of these quarks may be used in Eq. (6),

$$g_{\phi\gamma} = \frac{2\alpha}{\pi}\left[\frac{4}{9}\frac{g_{\phi c}}{m_c} + \frac{1}{9}\frac{g_{\phi b}}{m_b} + \frac{4}{9}\frac{g_{\phi t}}{m_t}\right]. \qquad (17)$$

This relation allows us to find limits on $g_{\phi c}$, $g_{\phi b}$ and $g_{\phi t}$ from the constraints on $g_{\phi\gamma}$ assuming that either of these interactions is dominant. There limits are presented in Fig. 4b.

E. Scalar-nucleon interaction

The couplings $g_{\phi u}$ and $g_{\phi d}$ may be related with the scalar-proton $g_{\phi p}$ and scalar-neutron $g_{\phi n}$ ones,

$$g_{\phi p} = 2g_{\phi u} + g_{\phi d}\,, \qquad g_{\phi n} = g_{\phi u} + 2g_{\phi d}\,. \qquad (18)$$

Substituting these relations into Eq. (16) and ignoring contributions from $g_{\phi s}$, we find

$$g_{\phi\gamma} = (8.6g_{\phi p} - 1.2g_{\phi n})10^{-3}\,\text{GeV}^{-1}\,. \qquad (19)$$

This equation allows us to set limits on the scalar-nucleon interaction constants $g_{\phi p}$ and $g_{\phi n}$ assuming that either of these contributions is dominant. These limits are very close to the ones for the scalar-quark interaction in Fig. 4a. Therefore, we do not present here dedicated plots for the scalar-nucleon constants but we point out that these limits are about 4 orders in magnitude stronger than the ones obtained in Ref. [76] from the analysis of results of liquid noble gas DM search experiments.

F. Order-of-magnitude estimate of scalar-gluon interaction

The contribution of the scalar-gluon vertex in Eq. (1) to the scalar-photon interaction constant starts from two loops. This contribution may be roughly estimated as

$$g_{\phi\gamma} = K\frac{\alpha}{\pi}\frac{\alpha_s}{\pi}g_{\phi g}\,, \qquad (20)$$

where K is a $O(1)$ numeric coefficient and $\alpha_s \sim 1$ is the strong interaction constant. Eq. (20) gives an order-of-magnitude estimate for the scalar-gluon coupling constant from experimentally measured value of $g_{\phi\gamma}$. An accurate calculation of the coefficient K in Eq. (20) goes beyond the scope of this paper since it involves non-perturbative aspects of QCD at low energy.

IV. SUMMARY

In this paper, we studied the interaction strength of hypothetical scalar dark matter particles with leptons, quarks, nucleons, gluons and W boson. We have shown that the scalar-photon interaction constant $g_{\phi\gamma}$ receives one-loop quantum corrections from Feynman graphs with $g_{\phi e}$, $g_{\phi\mu}$, $g_{\phi\tau}$ $g_{\phi q}$, $g_{\phi W}$ and $g_{\phi g}$ vertices. As a result, we find limits on the scalar-lepton, scalar-quark, scalar-gluon and scalar-W boson interaction constants from the known limits on $g_{\phi\gamma}$ obtained in a series of experimental and theoretical works [20–38], see Figs. 2, 3 and 4.

New limits on the scalar-electron coupling constant $g_{\phi e}$ are found for scalar field mass ranging from $10^{-4}\,\text{eV}$ to $15\,\text{MeV}$. If the mass of the scalar field exceeds twice

the electron mass, $m_\phi > 2m_e$, the scalar can decay directly into electron-positron pairs. The ejected positrons should produce observable 511 keV photon line in the space gamma-ray telescopes like SPI/INTEGRAL [65]. By considering the observed photon flux from the Galactic bulge we set a new upper limit on $g_{\phi e}$ for $m_\phi > 2m_e$, $g_{\phi e} \lesssim 5 \times 10^{-24}$.

We found limits on the scalar-muon and scalar-tau lepton couplings in the interval $10^{-24}\,\mathrm{eV} < m_\phi < 15\,\mathrm{MeV}$. Our limits on the scalar-muon interaction represent a 8-15 orders improvement over the ones reported in Ref. [68]. The scalar-tau constants is limited in this interval for the first time to the best of our knowledge.

For the scalar-quark and scalar-nucleon coupling constants we find strong limits in the interval $0.05\,\mathrm{eV} < m_\phi < 15\,\mathrm{MeV}$, see Fig. 4. These limits are many orders in magnitude stronger than the ones in Refs. [77–82] derived from non-observation of shifts of atomic and molecular spectra due to interactions beyond the Standard Model. The limits on the interaction of the scalar to heavy c, b and t quarks are obtained for the first time in the interval $10^{-24}\,\mathrm{eV} < m_\phi < 15\,\mathrm{MeV}$.

Finally, we find one-loop contributions to the scalar-photon coupling constant from the W boson loop, see Eq. (15). This relation allows us to set upper limit on the scalar-W boson coupling constant in the mass range $10^{-24}\,\mathrm{eV} < m_\phi < 15\,\mathrm{MeV}$. Ref. [11] provided limits derived from the analysis of Big Bang nucleosynthesis for ultralight scalars with mass $m_\phi < 10^{-16}\,\mathrm{eV}$, however our constraints are 2-5 orders in magnitude stronger.

Acknowledgements.— We are grateful to Hooman Davoudiasl for stimulating discussions. The work was supported by the Australian Research Council Grants No. DP230101058 and No. DP200100150.

[1] C. B. Adams *et al.*, Axion Dark Matter (2022), arXiv:2203.14923 [hep-ex].
[2] K. Allison, C. T. Hill, and G. G. Ross, Nucl. Phys. B **891**, 613 (2015), arXiv:1409.4029 [hep-ph].
[3] T. Taylor and G. Veneziano, Phys. Lett. B **213**, 450 (1988).
[4] T. Damour and A. Polyakov, Nucl. Phys. B **423**, 532 (1994), arXiv:hep-th/9401069.
[5] T. Damour and A. M. Polyakov, Gen. Rel. Grav. **26**, 1171 (1994), arXiv:gr-qc/9411069.
[6] T. Damour, F. Piazza, and G. Veneziano, Phys. Rev. Lett. **89**, 081601 (2002), arXiv:gr-qc/0204094.
[7] T. Damour, F. Piazza, and G. Veneziano, Phys. Rev. D **66**, 046007 (2002), arXiv:hep-th/0205111.
[8] D. B. Kaplan and M. B. Wise, J. High Ener. Phys. **2000**, 037 (2000), arXiv:hep-ph/0008116.
[9] C. Burrage and J. Sakstein, Living Rev. Rel. **21**, 1 (2018), arXiv:1709.09071 [astro-ph.CO].
[10] A. Derevianko and M. Pospelov, Nature Phys. **10**, 933 (2014), arXiv:1311.1244 [physics.atom-ph].
[11] Y. V. Stadnik and V. V. Flambaum, Phys. Rev. Lett. **115**, 201301 (2015), arXiv:1503.08540 [astro-ph.CO].
[12] Y. V. Stadnik and V. V. Flambaum, Phys. Rev. Lett. **114**, 161301 (2015), arXiv:1412.7801 [hep-ph].
[13] D. Antypas *et al.*, New Horizons: Scalar and Vector Ultralight Dark Matter (2022), arXiv:2203.14915 [hep-ex].
[14] C. O'Hare, cajohare/axionlimits: Axionlimits, `https://cajohare.github.io/AxionLimits/` (2020).
[15] J. R. Ellis, M. K. Gaillard, and D. V. Nanopoulos, Nucl. Phys. B **106**, 292 (1976).
[16] M. A. Shifman, A. I. Vainshtein, M. B. Voloshin, and V. I. Zakharov, Sov. J. Nucl. Phys. **30**, 711 (1979).
[17] T. Damour and J. F. Donoghue, Phys. Rev. D **82**, 084033 (2010), arXiv:1007.2792 [gr-qc].
[18] A. Arvanitaki, J. Huang, and K. Van Tilburg, Phys. Rev. D **91**, 015015 (2015), arXiv:1405.2925 [hep-ph].
[19] A. Djouadi, Phys. Rep. **457**, 1 (2008), arXiv:hep-ph/0503172.
[20] A. Hees, J. Guéna, M. Abgrall, S. Bize, and P. Wolf, Phys. Rev. Lett. **117**, 061301 (2016), arXiv:1604.08514 [gr-qc].
[21] M. Filzinger, S. Dörscher, R. Lange, J. Klose, M. Steinel, E. Benkler, E. Peik, C. Lisdat, and N. Huntemann, Phys. Rev. Lett. **130**, 253001 (2023), arXiv:2301.03433 [physics.atom-ph].
[22] N. Sherrill *et al.*, New J. Phys. **25**, 093012 (2023), arXiv:2302.04565 [physics.atom-ph].
[23] J. Bergé, P. Brax, G. Métris, M. Pernot-Borràs, P. Touboul, and J.-P. Uzan, Phys. Rev. Lett. **120**, 141101 (2018), arXiv:1712.00483 [gr-qc].
[24] A. Hees, O. Minazzoli, E. Savalle, Y. V. Stadnik, and P. Wolf, Phys. Rev. D **98**, 064051 (2018), arXiv:1807.04512 [gr-qc].
[25] K. Van Tilburg, N. Leefer, L. Bougas, and D. Budker, Phys. Rev. Lett. **115**, 011802 (2015), arXiv:1503.06886 [physics.atom-ph].
[26] K. Beloy *et al.* (BACON), Nature **591**, 564 (2021), arXiv:2005.14694 [physics.atom-ph].
[27] C. J. Kennedy, E. Oelker, J. M. Robinson, T. Bothwell, D. Kedar, W. R. Milner, G. E. Marti, A. Derevianko, and J. Ye, Phys. Rev. Lett. **125**, 201302 (2020), arXiv:2008.08773 [physics.atom-ph].
[28] E. G. Adelberger, B. R. Heckel, and A. E. Nelson, Ann. Rev. Nucl. Part. Sci. **53**, 77 (2003), arXiv:hep-ph/0307284.
[29] E. Fischbach and C. Talmadge, in *31st Rencontres de Moriond: Dark Matter and Cosmology, Quantum Measurements and Experimental Gravitation* (1996) pp. 443–451, arXiv:hep-ph/9606249.
[30] W. M. Campbell, B. T. McAllister, M. Goryachev, E. N. Ivanov, and M. E. Tobar, Phys. Rev. Lett. **126**, 071301 (2021), arXiv:2010.08107 [hep-ex].
[31] X. Zhang, A. Banerjee, M. Leyser, G. Perez, S. Schiller, D. Budker, and D. Antypas, Phys. Rev. Lett. **130**, 251002 (2023), arXiv:2212.04413 [physics.atom-ph].
[32] S. Aharony, N. Akerman, R. Ozeri, G. Perez, I. Savoray, and R. Shaniv, Phys. Rev. D **103**, 075017 (2021), arXiv:1902.02788 [hep-ph].
[33] R. Oswald *et al.*, Phys. Rev. Lett. **129**, 031302 (2022), arXiv:2111.06883 [hep-ph].

[34] K. Fukusumi, S. Morisaki, and T. Suyama, Phys. Rev. D **108**, 095054 (2023), arXiv:2303.13088 [hep-ph].

[35] S. Vermeulen *et al.*, Nature **600**, 424 (2021), arXiv:2103.03783 [gr-qc].

[36] E. Savalle, A. Hees, F. Frank, E. Cantin, P.-E. Pottie, B. M. Roberts, L. Cros, B. T. Mcallister, and P. Wolf, Phys. Rev. Lett. **126**, 051301 (2021), arXiv:2006.07055 [gr-qc].

[37] L. Aiello, J. W. Richardson, S. M. Vermeulen, H. Grote, C. Hogan, O. Kwon, and C. Stoughton, Phys. Rev. Lett. **128**, 121101 (2022), arXiv:2108.04746 [gr-qc].

[38] O. Tretiak, X. Zhang, N. L. Figueroa, D. Antypas, A. Brogna, A. Banerjee, G. Perez, and D. Budker, Phys. Rev. Lett. **129**, 031301 (2022), arXiv:2201.02042 [hep-ph].

[39] V. V. Flambaum, A. J. Mansour, I. B. Samsonov, and C. Weitenberg, Phys. Rev. D **107**, 015008 (2023), arXiv:2210.08778 [hep-ph].

[40] I. M. Bloch, D. Budker, V. V. Flambaum, I. B. Samsonov, A. O. Sushkov, and O. Tretiak, Phys. Rev. D **107**, 075033 (2023), arXiv:2301.08514 [hep-ph].

[41] A. Branca *et al.*, Phys. Rev. Lett. **118**, 021302 (2017), arXiv:1607.07327 [hep-ex].

[42] M. Filzinger, A. R. Caddell, D. Jani, M. Steinel, L. Giani, N. Huntemann, and B. M. Roberts, Ultralight dark matter search with space-time separated atomic clocks and cavities (2023), arXiv:2312.13723 [hep-ph].

[43] T. Kobayashi *et al.*, Phys. Rev. Lett. **129**, 241301 (2022), arXiv:2212.05721 [physics.atom-ph].

[44] A. Afzal *et al.* (NANOGrav), Astrophys. J. Lett. **951**, L11 (2023), arXiv:2306.16219 [astro-ph.HE].

[45] D. Cadamuro and J. Redondo, J. Cosm. Astropart. Phys. **2012**, 032 (2012), arXiv:1110.2895 [hep-ph].

[46] J. W. Foster, M. Kongsore, C. Dessert, Y. Park, N. L. Rodd, K. Cranmer, and B. R. Safdi, Phys. Rev. Lett. **127**, 051101 (2021), arXiv:2102.02207 [astro-ph.CO].

[47] K. Perez, K. C. Y. Ng, J. F. Beacom, C. Hersh, S. Horiuchi, and R. Krivonos, Phys. Rev. D **95**, 123002 (2017), arXiv:1609.00667 [astro-ph.HE].

[48] B. M. Roach *et al.*, Phys. Rev. D **107**, 023009 (2023), arXiv:2207.04572 [astro-ph.HE].

[49] K. C. Y. Ng, B. M. Roach, K. Perez, J. F. Beacom, S. Horiuchi, R. Krivonos, and D. R. Wik, Phys. Rev. D **99**, 083005 (2019), arXiv:1901.01262 [astro-ph.HE].

[50] F. Calore, A. Dekker, P. D. Serpico, and T. Siegert, Mon. Not. Roy. Astron. Soc. **520**, 4167 (2023), arXiv:2209.06299 [hep-ph].

[51] D. Wadekar and Z. Wang, Phys. Rev. D **106**, 075007 (2022), arXiv:2111.08025 [hep-ph].

[52] J. L. Bernal, A. Caputo, G. Sato-Polito, J. Mirocha, and M. Kamionkowski, Phys. Rev. D **107**, 103046 (2023), arXiv:2208.13794 [astro-ph.CO].

[53] P. Carenza, G. Lucente, and E. Vitagliano, Phys. Rev. D **107**, 083032 (2023), arXiv:2301.06560 [hep-ph].

[54] K. Nakayama and W. Yin, Phys. Rev. D **106**, 103505 (2022), arXiv:2205.01079 [hep-ph].

[55] D. Grin, G. Covone, J.-P. Kneib, M. Kamionkowski, A. Blain, and E. Jullo, Phys. Rev. D **75**, 105018 (2007), arXiv:astro-ph/0611502.

[56] H. Liu, W. Qin, G. W. Ridgway, and T. R. Slatyer, Phys. Rev. D **108**, 043531 (2023), arXiv:2303.07370 [astro-ph.CO].

[57] F. Capozzi, R. Z. Ferreira, L. Lopez-Honorez, and O. Mena, JCAP **06**, 060, arXiv:2303.07426 [astro-ph.CO].

[58] E. Todarello, M. Regis, J. Reynoso-Cordova, M. Taoso, D. Vaz, J. Brinchmann, M. Steinmetz, and S. L. Zoutendijke, Robust bounds on ALP dark matter from dwarf spheroidal galaxies in the optical MUSE-Faint survey (2023), arXiv:2307.07403 [astro-ph.CO].

[59] M. Regis, M. Taoso, D. Vaz, J. Brinchmann, S. L. Zoutendijk, N. F. Bouché, and M. Steinmetz, Phys. Lett. B **814**, 136075 (2021), arXiv:2009.01310 [astro-ph.CO].

[60] R. Janish and E. Pinetti, Hunting dark matter lines in the infrared background with the James Webb Space Telescope (2023), arXiv:2310.15395 [hep-ph].

[61] C. Fong, K. C. Y. Ng, and Q. Liu, PoS **TAUP2023**, 172 (2024), arXiv:2401.16747 [hep-ph].

[62] V. Anastassopoulos *et al.* (CAST), Nature Phys. **13**, 584 (2017), arXiv:1705.02290 [hep-ex].

[63] V. V. Flambaum, B. T. McAllister, I. B. Samsonov, and M. E. Tobar, Phys. Rev. D **106**, 055037 (2022), arXiv:2207.14437 [hep-ph].

[64] C.-Y. Chen, M. Pospelov, and Y.-M. Zhong, Phys. Rev. D **95**, 115005 (2017), arXiv:1701.07437 [hep-ph].

[65] P. Jean *et al.*, Astron. Astrophys. **407**, L55 (2003), arXiv:astro-ph/0309484.

[66] V. V. Flambaum and I. B. Samsonov, Phys. Rev. D **104**, 063042 (2021), arXiv:2108.00652 [hep-ph].

[67] D. Hooper, Phys. Dark Univ. **15**, 53 (2017), arXiv:1608.00003 [astro-ph.HE].

[68] Y. V. Stadnik, Phys. Rev. Lett. **131**, 011001 (2023), arXiv:2206.10808 [hep-ph].

[69] J. G. Lee, E. G. Adelberger, T. S. Cook, S. M. Fleischer, and B. R. Heckel, Phys. Rev. Lett. **124**, 101101 (2020), arXiv:2002.11761 [hep-ex].

[70] D. J. Kapner, T. S. Cook, E. G. Adelberger, J. H. Gundlach, B. R. Heckel, C. D. Hoyle, and H. E. Swanson, Phys. Rev. Lett. **98**, 021101 (2007), arXiv:hep-ph/0611184.

[71] E. G. Adelberger, B. R. Heckel, S. Hoedl, C. D. Hoyle, D. J. Kapner, and A. Upadhye, Phys. Rev. Lett. **98**, 131104 (2007), arXiv:hep-ph/0611223.

[72] C. D. Hoyle, D. J. Kapner, B. R. Heckel, E. G. Adelberger, J. H. Gundlach, U. Schmidt, and H. E. Swanson, Phys. Rev. D **70**, 042004 (2004), arXiv:hep-ph/0405262.

[73] C. D. Hoyle, U. Schmidt, B. R. Heckel, E. G. Adelberger, J. H. Gundlach, D. J. Kapner, and H. E. Swanson, Phys. Rev. Lett. **86**, 1418 (2001), arXiv:hep-ph/0011014.

[74] G. L. Smith, C. D. Hoyle, J. H. Gundlach, E. G. Adelberger, B. R. Heckel, and H. E. Swanson, Phys. Rev. D **61**, 022001 (2000).

[75] N. Leefer, A. Gerhardus, D. Budker, V. V. Flambaum, and Y. V. Stadnik, Phys. Rev. Lett. **117**, 271601 (2016), arXiv:1607.04956 [physics.atom-ph].

[76] V. A. Dzuba, V. V. Flambaum, and I. B. Samsonov, Sensitivity of dark matter detectors to scalar-nucleon coupling (2023), arXiv:2312.10566 [hep-ph].

[77] E. J. Salumbides, J. C. J. Koelemeij, J. Komasa, K. Pachucki, K. S. E. Eikema, and W. Ubachs, Phys. Rev. D **87**, 112008 (2013), arXiv:1304.6560 [physics.atom-ph].

[78] E. J. Salumbides, W. Ubachs, and V. I. Korobov, J. Molec. Spectrosc. **300**, 65 (2014), arXiv:1308.1711 [hep-ph].

[79] P. Munro-Laylim, V. Dzuba, and V. Flambaum, Molecular Physics **121**, e2160385 (2023), arXiv:2207.07325 [physics.atom-ph].

[80] N. L. Figueroa, J. C. Berengut, V. A. Dzuba, V. V. Flambaum, D. Budker, and D. Antypas, Phys. Rev. Lett. **128**,

073001 (2022).
[81] J. Hur *et al.*, Phys. Rev. Lett. **128**, 163201 (2022), arXiv:2201.03578 [physics.atom-ph].
[82] N.-H. Rehbehn, M. K. Rosner, J. C. Berengut, P. O. Schmidt, T. Pfeifer, M. F. Gu, and J. R. Crespo López-Urrutia, Phys. Rev. Lett. **131**, 161803 (2023), arXiv:2309.17141 [physics.atom-ph].

Femtoscopy analysis of ultra-soft pion trap at LHC energies

W. Rzesa[1], G. Kornakov[1], A.R. Kisiel[1], Yu.M. Sinyukov[1,2], V.M. Shapoval[2]
[1] *Warsaw University of Technology, Faculty of Physics, ul. Koszykowa 75, 00-662, Warsaw, Poland*
[2] *Bogolyubov Institute for Theoretical Physics, 14b Metrolohichna street, Kyiv 03143, Ukraine*
(Dated: March 6, 2024)

Femtoscopy studies of pion radiation in heavy-ion collisions have been conducted extensively at all available collider energies, both theoretically and experimentally. In all these studies a special interest is given to m_T dependency of pion femtoscopy radii, usually approximated by a power-law function at transverse momenta above 200 MeV/c. However, the radii behaviour has been much less explored for the ultra-soft pions, possessing the transverse momentum comparable to or lower than the pion mass. For many experimental setups this region is difficult to measure. In this work we present theoretical calculations of pion emission in the ultra-soft region in the two hybrid models — iHKM and LHYQUID+THERMINATOR2. Along with the particle transverse momentum spectra, we present the calculated femtoscopy radii, both in one-dimensional and three-dimensional representations. We investigate the radii dependence on pair m_T and observe, in particular, a departure from the power-law behaviour at ultra-soft momenta, potentially reflecting a decoupling of such slow pions from the rest of collectively expanding system. We provide the theoretical interpretation of this result and discuss its significance, in particular, for the ongoing non-identical particle femtoscopy analysis for pairs consisting of a pion and a baryon (or of a pion and a charmed meson).

arXiv:2403.02551v1 [hep-ph] 5 Mar 2024

I. INTRODUCTION

The interferometry of particles emitted from the small radiating source enables one to study the evolving geometry of that source. The particle interferometry has originated from the experimental paper [1] and theoretical works [2, 3]. In the latter it was also found that the results for the quantum statistics correlation effect for two close sources of identical particle emission in collision physics are formally similar to those for classical intensity correlations of the light radiation coming from different parts of the star, known in astronomy as the Hanbury Brown – Twiss (HBT) effect [4–6]. The similarity, as well as the difference between the quantum correlations in identical-particle pairs and the classical HBT effect are analyzed, e.g., in [7]. Note, that the correlation femtoscopy method, initially developed for finding the overall *size* of identical quantum particles' source, now is considered to measure the *homogeneity lengths* [8] of such femto-small sources. This general interpretation is especially important for the studies of the space-time structure of expanding sources, such as those created in proton/antiproton and heavy-ion collisions [1–3, 9–14].

The homogeneity lengths, defined as a result of correlation femtoscopy analysis, reflect the spatial dimensions of the region within the entire strongly interacting system formed in the collision, from which particles are emitted with similar velocities (having close, nearly coinciding values and directions) [8, 15]. Gaussian parameterization for the particle emission source function (SF) and the two-particle correlation function (CF) are usually used in femtoscopy studies, although the realistic source shape differs from a perfect Gaussian — e.g., resonance decay contributions cause the exponential behaviour near the peak of the correlation function. The conventional use of the Gaussian shape allows one to standardize the description of experimental data and easily compare the results of different femtoscopy measurements, as well as to interpret the obtained radii as the homogeneity lengths. It is also well-motivated experimentally in heavy-ion collisions, where correlation shapes for pions in 3D analyses are universally observed to be Gaussian in a wide range of centralities and pair transverse momenta. The study of the dependence of the radii on the particle species, collision type and collision energy is the main objective of the femtoscopic analysis of heavy-ion collisions.

In experimental studies, one clearly observes certain types of universal scaling behaviour for the measured femtoscopy scales. For a given colliding system and collision energy a linear scaling of the femtoscopic radii is universally observed versus cube root of the final state mean particle multiplicity $\langle dN_{ch}/d\eta\rangle^{1/3}$ [16–22]. A similar scaling across collision energies and colliding systems is only approximate [23, 24]. The radii versus the pair transverse momentum exhibit a power-law-like scaling in pair transverse mass m_T ($m_T = \sqrt{k_T^2 + m^2}$, where k_T is pair mean transverse momentum, $k_T = |\mathbf{p}_{T1} + \mathbf{p}_{T2}|/2$, and m is particle mass) [16, 17, 25–30]. In heavy-ion collisions both these scalings are predicted by hydrodynamic models [31]. Specifically, the m_T scaling is explained as a direct consequence and one of the main signatures of the collective radial flow of the system.

The observed m_T power-law scaling means a decrease of the radii with growing m_T that is a signature of hydrodynamic collectivity, typical for all particle species affected by the same flow field. Such dependence can be helpful for the prediction of the source size at certain m_T through the interpolation between radii measured at different m_T values. Nonetheless, the m_T range of experimental radii measurement depends on the acceptance of the detectors used in the study, and the very-low-m_T region has not been reached yet via such measurements.

Therefore, the femto-scale predictions in that region can come only from the extrapolation, which following the commonly used power-law function, shows a very rapid growth of the radii with decreasing m_T. The theoretical studies, by contrast, do not face such problems and so, simulations within a realistic collision model can help estimate the possible character of the femtoscopy radii behaviour in ultra-soft momentum region.

The knowledge of femtoscopic radii for ultra-soft pions is becoming increasingly important in the context of rapidly developing experimental analyses of femtoscopic correlations of non-identical particles [32, 33]. In the case of such pairs the correlation occurs between two particles with similar velocity. If the pair in question contains a pion and a relatively massive particle (e.g. a deuteron or a charmed meson), then the pion in the pair needs to be ultra-soft in order to be correlated. The femtoscopic radius of the pair is directly related to the size of emission regions of both particles in the pair. Therefore, in order to study the non-identical correlations between pions and massive particles, the knowledge of femtoscopic radii of ultra-soft pions becomes essential.

Several previous theoretical studies of the ultra-low momentum pions were motivated by the experimental evidence of enhanced production [34, 35]. These observations could be addressed by non-equilibrium models [36]. In addition to the semi-classical models, pure quantum effects such as pion condensation and Bose-Einstein enhancement were also explored [37]. However, none of these studies addressed the pion femtoscopic radii nor their scaling at very low transverse momenta.

Thus, in this paper, we focus on studying the pion femtoscopic radii dependence on pair m_T, including the region of very low transverse masses, in Pb-Pb collisions at the LHC energy $\sqrt{s_{NN}} = 5.02$ TeV simulated within the integrated HydroKinetic Model (iHKM) [31, 38, 39] and the hydrodynamics model [40] coupled to the statistical hadronisation code THERMINATOR2 (LHYQUID + THERMINATOR2) [41]– (LQTH).

II. MODELS' DESCRIPTION

The collisions of heavy ions at ultra-relativistic energies allow to create quark-gluon plasma (QGP) — a new state of strongly interacting matter, where quarks and gluons are no longer confined within individual nucleons. The evolution of such matter can be successfully described in complicated models realized in the form of codes for labor-consuming computer simulations. Such codes typically include modules describing the initial state formation, relativistic hydrodynamics expansion of liquid-like QGP at the intermediate stage of the system's evolution, its subsequent particlization (turning into a set of hadrons) and, finally, the hadron-resonance gas expansion. As a result of typical calculation, one obtains from the model a set of created hadrons, characterized by the space-time points of their last collision and 4-momenta. Based on these data one can construct different observables, like spectra, correlation functions etc.

The data analyzed in this study were generated using two such models, iHKM and LQTH, each having its own characteristics.

The iHKM is one of the most complete models, describing all the essential phases of the matter evolution in the course of a relativistic A+A collision (see [31, 38] for details). The initial conditions (IC) for each simulation include the energy density spatial distribution at the starting time τ_0, usually close to 0.1 fm/c (for the high-energy collisions we use GLISSANDO code [42] to generate it), and anisotropic momentum distribution, inspired by the Color Glass Condensate model. These IC correspond to the very initial non-equilibrium partonic state right after the two nuclei collision. At the next stage of the system's evolution, it gradually thermalizes and approaches to a nearly hydrodynamical state. Then (starting from the thermalization time $\tau_{th} \approx 1$ fm/c) follows a continuous medium expansion described in the Israel-Stewart viscous hydrodynamics formalism. As the matter expands and cools down, it eventually reaches the "particlization temperature" $T_p \approx 160$ MeV (depending on the QGP equation of state used at the hydrodynamics stage), when one switches to the description of the system in terms of hadrons (here the Cornelius routine [43] is applied). Produced hadrons are then fed to the UrQMD hadron cascade code [44, 45], performing multiple hadronic rescatterings and resonance decays taking place at this final "afterburner" phase of the collision. The model is calibrated based on the experimental mean charged particle multiplicity and pion p_T spectrum slope in the most central collisions of a given type. In this paper, we use the iHKM tuning, used for the LHC 5.02A TeV Pb-Pb collisions simulation described in detail in [39].

The LQTH approach assumes the ideal (3+1)D hydrodynamics evolution of the created fireball (however, bulk and shear viscosity can be implemented as well) until the single (both chemical and kinetic) freeze-out at certain temperature ($T_p \approx 140$ MeV), where statistical hadronization takes place, and the system's chemical composition and momentum spectra do not change anymore, except for the resonance decays. As well as the iHKM, for the current study the model is properly calibrated to describe the $\sqrt{s_{NN}} = 5.02$ TeV Pb-Pb collisions at the LHC.

Both models describe well the experimental results for pion, kaon and proton transverse momentum spectra, including the region of very soft momenta (see Fig. 1). Note, that such a description is achieved without the implementation of additional specific mechanisms of the soft pion emission, like the Bose-Einstein condensation, discussed, e.g., in [37]. Also, the two utilized models were previously used to successfully describe the LHC data on 2.76A TeV Pb-Pb collisions [38, 39, 46, 47].

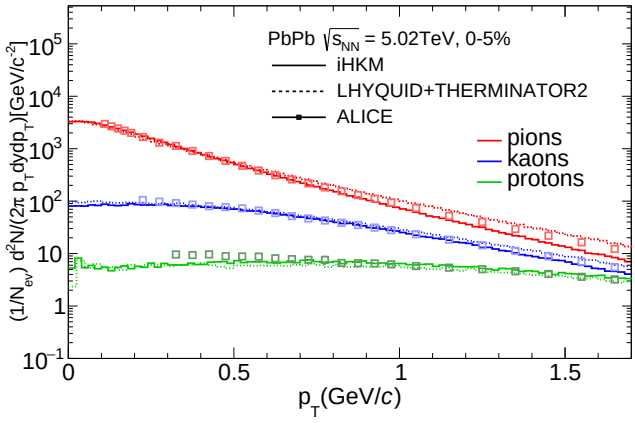


FIG. 1. Pion, kaon and proton transverse momentum spectra calculated in the iHKM (solid lines) and in the LQTH models (dashed lines) for the most central $\sqrt{s_{NN}} = 5.02$ TeV Pb-Pb collisions at the LHC [48].

III. CONSTRUCTION OF THE CORRELATION FUNCTION

The femtoscopic radii constituting the main subject of this study are typically defined from the Gaussian fits to the correlation functions depending on pair relative momentum $q = p_1 - p_2$. Here we consider the correlations in pairs of identical charged pions (π^+ and π^-), performing 1D and 3D analysis. The 1D correlation of identical particles is calculated as a function of $q_{\rm inv} = \sqrt{q_0^2 - \mathbf{q}^2}$ in the Pair Rest Frame (PRF) and requires minimal statistics in contrast to the 3D study. However, the radius $R_{\rm inv}$, in this case, is the only length extracted, so that the emission source is assumed to be a spherically symmetric Gaussian one. The 3D study is based on relative momentum components $q_{\rm out}$, $q_{\rm side}$, and $q_{\rm long}$ calculated in the Longitudinally Co-Moving System (LCMS), where the longitudinal direction is along the beam axis, the outward direction is along the pair transverse momentum and the sideward direction is perpendicular to the other two. Accordingly, the three radii $R_{\rm out}$, $R_{\rm side}$, and $R_{\rm long}$ are extracted from the CF fit in this case.

The correlation function is generally defined as

$$C(p_1, p_2) = \frac{P_{12}(p_1, p_2)}{P_1(p_1)P_2(p_2)}, \qquad (1)$$

and can be understood as the ratio of conditional probability to detect a pair of particles with the specific momentum values, $P_{12}(p_1, p_2)$, to the probability of finding them with such momenta independently, $P_1(p_1)P_2(p_2)$.

In experimental analysis, the procedure of obtaining the correlation function consists of making pairs of particles coming from the same event to build the correlated distribution (numerator), and for the background distribution (denominator) pairs are created using particles coming from different events (meaning that they retain all aspects of experimental acceptance, while not being correlated due to the mutual interaction).

In simulation studies, one usually fills two histograms (1D or 3D, depending on the analysis type) representing the corresponding particle pairs' relative momentum q distribution — one histogram for the numerator and another one for the denominator in Eq. (1) — based on the generated model output (set of hadrons). However, since in all currently available heavy-ion collision models the quantum statistical effects (including the Bose-Einstein symmetrization of the two identical bosons' wave-function) are not implemented directly, on a microscopic level, one usually introduces a weight factor

$$w = 1 + \cos(qr), \qquad (2)$$

coming from the Bose-Einstein interference at the so-called "afterburner" stage (to simplify the presentation, Coulomb and strong final-state interactions are not considered here). This factor w is taken as a weight for the pairs entering the correlated distribution histogram (a numerator one). For the background distribution (denominator) the weight is equal to 1. In this study, we also use the rapidity cut, $|y| < 1$, during the identical charged pion pairs selection to reproduce the acceptance of the ALICE detector.

To obtain a fitting formula for the CF, which will allow us to define the desired femtoscopy radii, one can consider the 7D (if particles are on the mass shell) particle emission functions $S_i(x, p)$ for each particle species i and derive the approximate expressions for single-particle and two-particle momentum spectra, and then using Eq. (1) obtain the well known Bertsch-Pratt [49, 50] representation for the correlation function of two identical bosons in LCMS:

$$C(\mathbf{k},\mathbf{q}) = 1 + \lambda_{3D}(\mathbf{k}) \exp(-R^2_{\rm out}(\mathbf{k})q^2_{\rm out} - R^2_{\rm side}(\mathbf{k})q^2_{\rm side} - R^2_{\rm long}(\mathbf{k})q^2_{\rm long}), \qquad (3)$$

where femto-radii R_i depend on mean pair momenta $\mathbf{k}$, and λ_{3D} are referred to as correlation strength factors.

The invariant one-dimensional form of the correlation function Gaussian parameterization is

$$C(k, q_{\rm inv}) = 1 + \lambda_{1D}(k) \exp(-R^2_{\rm inv}(k)q^2_{\rm inv}). \qquad (4)$$

IV. PION FEMTOSCOPY SCALES

This section presents the results on pion femto-radii obtained as a result of correlation function fitting for identical pions in 1D and 3D studies using the two models (iHKM and LQTH). The correlation functions were calculated separately for the six centrality classes $(0-5\%, 5-10\%, 10-20\%, 20-30\%, 30-40\%$ and $40-50\%)$ and the ten k_T ranges $(0.00-0.05, 0.05-0.10, 0.10-0.15, 0.15-0.20, 0.20-0.25, 0.25-0.30, 0.30-0.35, 0.35-0.45, 0.45-0.60, 0.60-0.80)$ GeV/c.

In Fig.2 all the radii for identical pion pairs, corresponding to 1D and 3D calculations in the two models

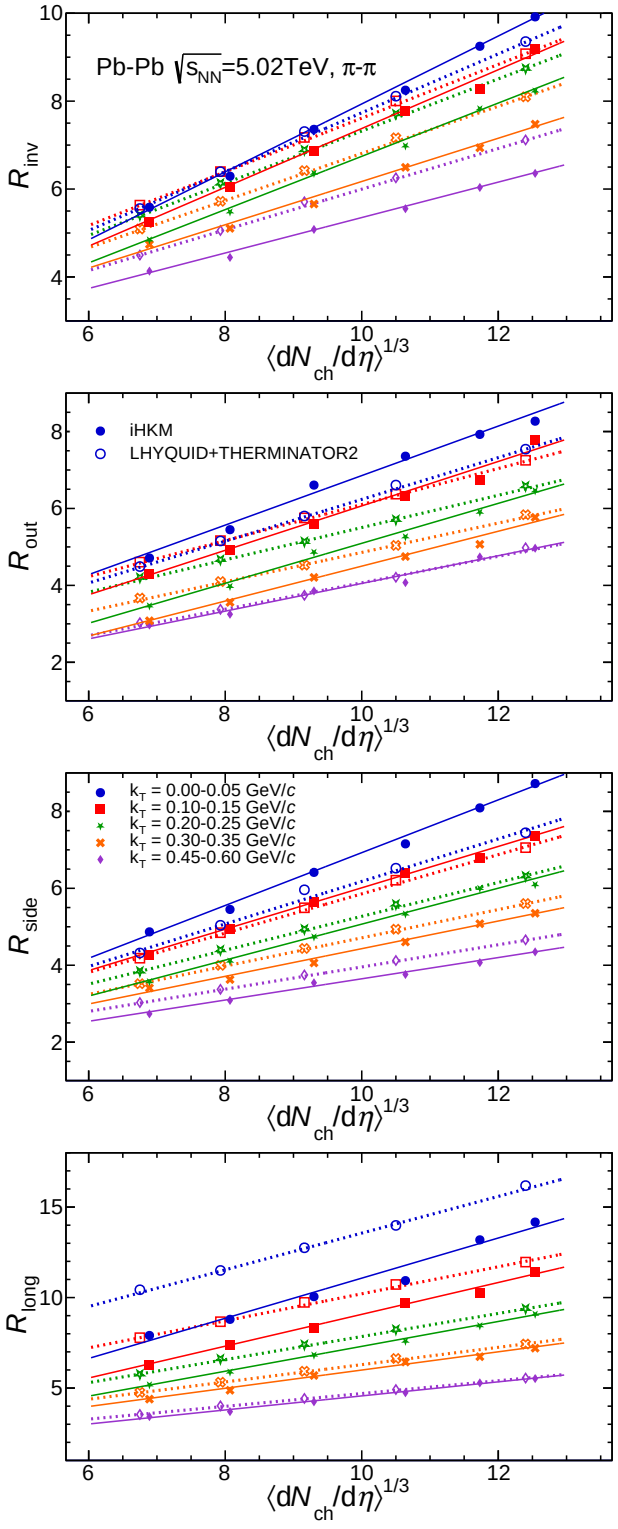


FIG. 2. Femtoscopic radii of charged identical pions as functions of $\langle dN_{ch}/d\eta\rangle^{1/3}$ calculated using iHKM (full markers) and LQTH (empty markers) models, for 5 k_T ranges (from top to bottom: $0.00-0.05, 0.10-0.15, 0.20-0.25, 0.30-0.35, 0.45-0.60$ GeV/c). Different panels from top to bottom correspond to 1D $R_{\rm inv}$, and 3D $R_{\rm out}$, $R_{\rm side}$, and $R_{\rm long}$ radii respectively. Lines correspond to linear fits to the radii dependencies. Symbols are slightly shifted in the x direction for visibility.

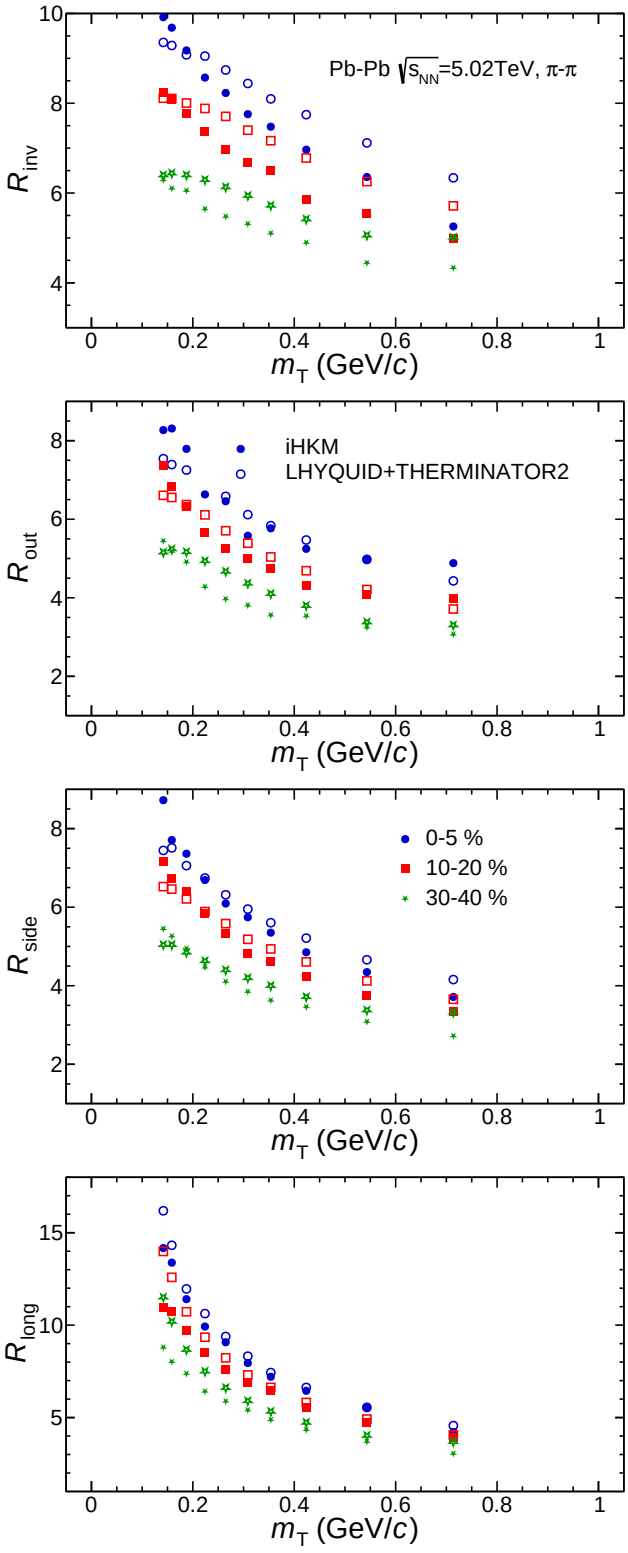


FIG. 3. Femtoscopic radii of charged identical pions as functions of m_T calculated using iHKM (full markers) and LQTH (empty markers) models, for the three centrality classes ($0-5\%$ — blue, $10-20\%$ — red, $30-40\%$ — green). Different panels from top to bottom correspond to 1D $R_{\rm inv}$, and 3D $R_{\rm out}$, $R_{\rm side}$, and $R_{\rm long}$ radii respectively.

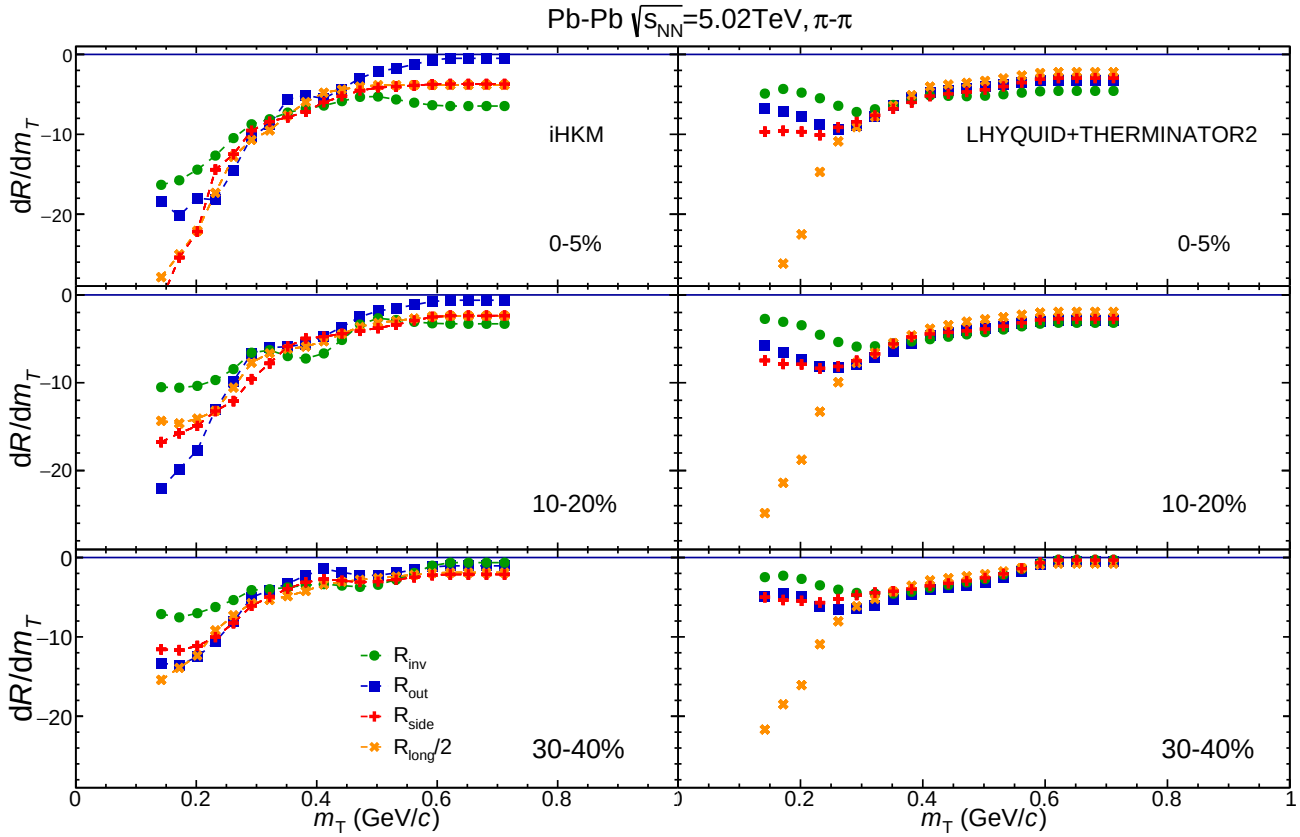


FIG. 4. First-order derivative of the charged identical pions femtoscopic radii m_T dependency, dR/dm_T, in the HKM (left) and the LQTH (right) models, for the three collision centralities (from top to bottom: $0-5\%, 10-20\%, 30-40\%$). Each panel contains derivatives of the three radii from the 3D study ($R_{\rm out}$ — blue, $R_{\rm side}$ — red, $R_{\rm long}$ — orange) and $R_{\rm inv}$ from the 1D study (green).

are demonstrated as functions of $\langle dN_{ch}/d\eta\rangle^{1/3}$. The results for the five of all ten m_T bins are shown for better visibility since the radii in all bins follow a monotonic trend. The radii values vary in the range from about 15 fm ($R_{\rm long}$ for the lowest m_T and the highest multiplicity in LQTH) to about 2 fm ($R_{\rm side}$ for high m_T and low multiplicity in iHKM). All the radii universally grow linearly with the cube root of final-state multiplicity. The multiplicity dependencies for various m_T ranges generally show m_T ordering, except for 1D and transverse 3D results from the LQTH model, where the first bins of m_T overlap. This is because in the LQTH model, radii of the first m_T bins take similar values. Fig. 3, where femto-radii are shown as functions of m_T presents it more clearly. All the measured radii decrease with increasing m_T. However, in the case of the LQTH model, we can observe a small plateau for the 1D and the transverse 3D radii at low m_T. The iHKM results, however, mostly fall monotonically in the lowest m_T region. The Figure 3 also exhibits an expected ordering with respect to analysed centrality — the more peripheral collision, the smaller the radii. In both figures 2 and 3, the difference in femto-scales between the two models is also evident.

One can see from Fig. 3 that the femto-radii in the iHKM model decrease faster than in the LQTH one. This is likely due to a very early, at $\tau_0 = 0.1$ fm/c, expansion starts in the iHKM, leading to stronger velocity gradients at the final stage. This is the main reason for the reduction of the femto-radii: the homogeneity lengths are reduced with the growing flow intensity. So, at the intermediate and high k_T the iHKM radii are smaller, than those in the LQTH model with a later start of the expansion ($\tau_0 \approx 0.6$ fm/c). As for the radii values at ultra-soft transverse momenta, the situation becomes even more complicated. At very small k_T the transverse radii are larger in the iHKM approach (the mentioned gradient could be the reason), while the longitudinal ones are larger in the LQTH model. The physics of pion production in the very-low-k_T region appears to be non-trivial and worthy of further study and better understanding.

To better investigate the character of the radii m_T dependencies, they were differentiated, and the obtained derivatives are presented in Fig. 4 (for the three centrality classes). The derivative has been extracted in the range ± 0.07 GeV/c around each point in the figure. Most of the functions show similar behaviour, with a clear change in the derivative value at certain momenta.

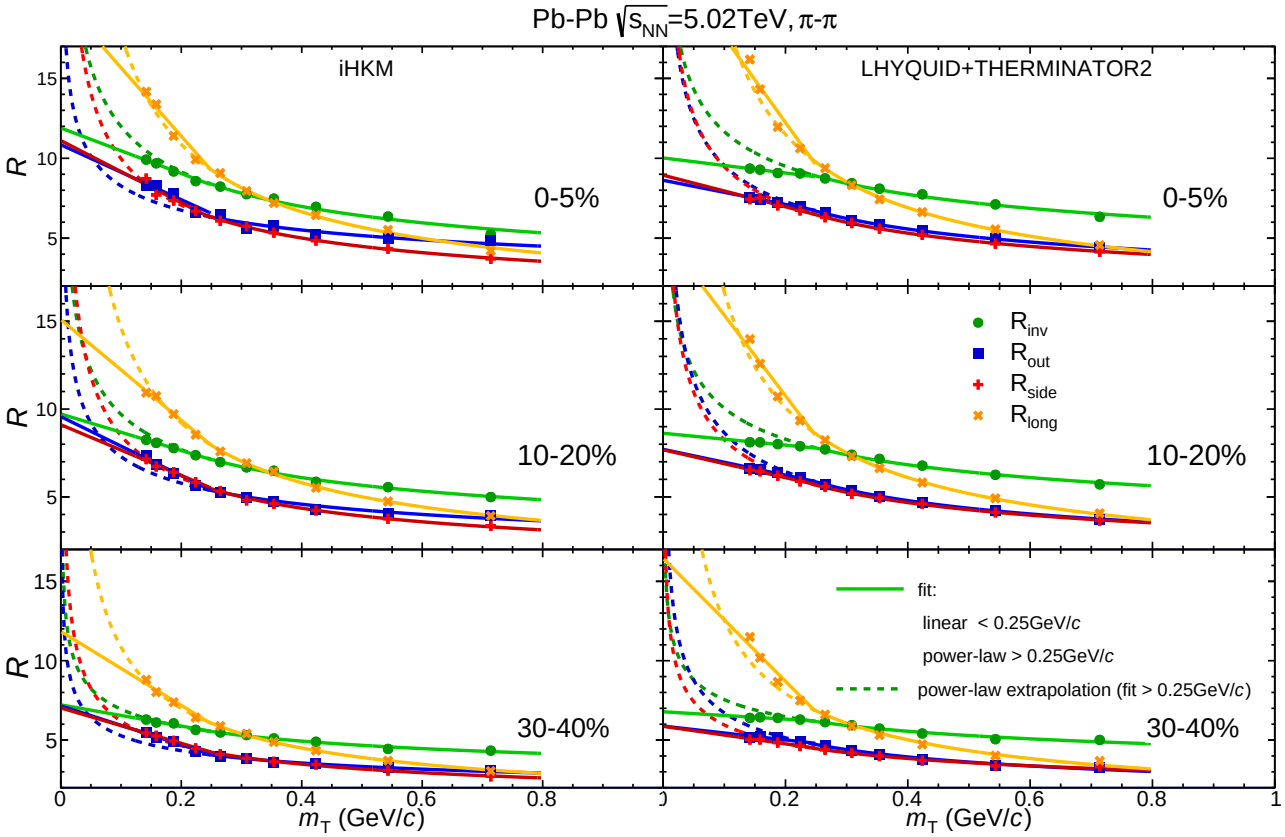


FIG. 5. Pion femtoscopic radii dependencies on m_T calculated in iHKM (left) and LQTH (right) models, for the three centrality classes (from top to bottom: $0-5\%, 10-20\%, 30-40\%$). Each panel contains results for the three radii from the 3D study ($R_{\rm out}$ — squares, $R_{\rm side}$ — crosses, $R_{\rm long}$ — tilted crosses) and for $R_{\rm inv}$ from the 1D study (cicles). Lines correspond to power-law fits am_T^{-b} to radii dependencies in the range above 0.25 GeV/c.

The iHKM model shows a constant derivative at low momentum (especially for the 1D study), then a systematic rise and again a higher constant value at large momenta. Flat parts of the curves correspond to constant slopes of the radii decrease approximated by a linear function. The rising/falling parts indicate a change in the radii dependency slope. The low-m_T flat part ends around 0.25 GeV/c. The LQTH model, in turn, shows for the 1D and the 3D transverse radii derivatives a constant or decreasing behaviour up to 0.3 GeV/c, then the dependence starts rising to end up with a constant value at large momentum. The initial decrease reflects the change of a nearly constant $R(m_T)$ dependence to a to decreasing one, while the next rising dR/dm_T part is connected with more gentle radii change at growing m_T. The *long* direction, by contrast, shows growing behaviour ending up with a plateau without any clear flat beginning.

To interpret above mentioned results, one can use a very recent iHKM femto-analysis [51] as follows. When the system is just formed (at times near 0.1 fm/c), huge gradients of density in the transverse direction take place, since the system is essentially finite and borders with vacuum. The gradient is not equal locally along the radial directions: it is more strong at the periphery, and less strong in the center, where soft hadrons mostly come from. In the vicinity of the geometrical center of the system, its decay into free particles happens at significantly later proper times than for the most of other parts of the system. Such a difference in proper times of spectra formation can be up to 5 fm/c [51]. Thus, in the context of the present study, one can expect that maximal formation times (about 15 fm/c) should be typical for the ultra-soft pions with transverse momenta less than 0.3 GeV/c, that are emitted from the central region of the fireball. Whereas for the pions radiated from other parts of the decaying expanding system and having higher transverse momenta, $0.45-2$ GeV/c, the (proper) time of maximal emission is close to 10 fm/c [51]. The situation looks like a pion trap formed in the center of the created quark-gluon — hadron system. The hadrons stay together (cannot leave the system) for a longer time in the system's center because of the following:

- firstly, very low (close to zero) transverse collective velocity;
- secondly, smaller density gradient in the center during almost the entire duration of the evolution, as compared to non-central and periphery parts.

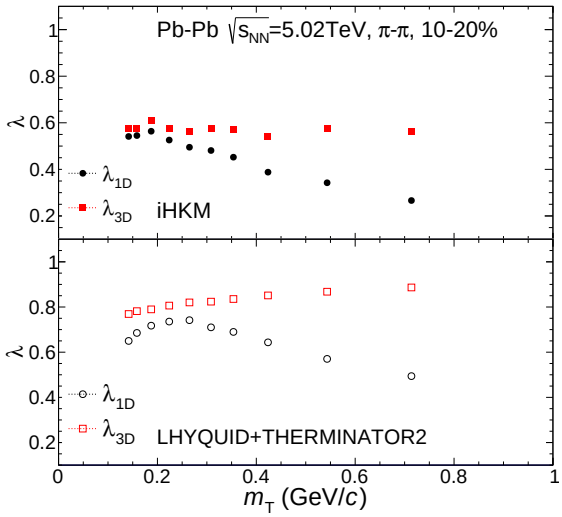


FIG. 6. The correlation strength λ parameters from 1D (black) and 3D (red) fits to the two-pion CF functions for the ten m_T bins. The iHKM (top) and the LQTH (bottom) results are shown for $c = 10 - 20\%$ Pb-Pb collisions at $\sqrt{s_{NN}} = 5.02$ TeV.

- thirdly, the initially highest density in the geometrical center in central and semi-central nucleus-nucleus collisions. Therefore, for this high-mass-density region, it is difficult to expand because of the relatively small transverse pressure gradient in the center.

Note, that we see the mentioned effects of relative flattening of the transverse radii behaviour in the ultra-soft momentum region in "hydro plus hadronic cascade" models, where the dynamics is built in quasi-classical approximation. The Bose-Einstein quantum statistics effect is taken into account in the very final stage only, but even this way, using the femtoscopy method, one can see specific (delayed freeze-out) behaviour of emission in the ultra-low-momentum region (see also Fig. 1 from [51]). In particular, as we already mentioned, the femtoscopy analysis brings us the signal about a long-lived ultra-soft pion trap formed in the central part of the system created in ultra-relativistic heavy ion collision.

The dependencies of the radii on m_T, together with the power-law fits, are presented for the three centrality classes in Fig. 5. The fitting was performed outside the plateau region observed in Fig. 4 (above 0.25 GeV/c). As one can see from this figure, the power-law function in the form am_T^{-b} works well, especially for all three R_i in the 3D case in the iHKM model and for the *long* direction of the LQTH model. As for the transverse radii from the LQTH, the first 2-3 corresponding points are mostly below expectations. In both models, the behaviour most different from the power-law in the low-m_T region is observed for the 1D $R_{\rm inv}$ points, which lie, up to 0.25 GeV/c, below the extrapolated line.

In Fig. 5 the fall of 1D radii is less prominent than the fall for radii from 3D studies. This can be connected with the shape of the respective correlation functions. The 1D functions are less Gaussian than the 3D functions, and therefore the fitting has to compensate for this by reducing the correlation strength parameter λ. The m_T dependencies of lambda in the two applied models are shown in Fig. 6. In the low m_T region the lambda behaves similarly in both cases, whereas with growing m_T it tends to go down in the 1D case.

Finally, we analyzed the femto-radii dependence on pair velocity, see Fig. 7 for different centrality intervals and for both used model approaches. In all cases, we notice a slow radii falling at low velocities. All the distributions were fitted with the analytic formula

$$R(\beta) = a + \frac{b}{e^{(\beta - c)/d} + 1}, \tag{5}$$

where $\beta = k_T/m_T$ is pair velocity, and a, b, c, d are free parameters of the fit. As particle velocity decreases, the radii seem to reach a saturated value, similar in a very broad range of β. Therefore such value could be used to determine an extrapolated value of the radii for ultra-soft pions, instead of the historically used dependence based on power-law m_T scaling.

V. SUMMARY

In this paper, the model study of femtoscopic radii obtained from simulated data of iHKM and LQTH were shown. The results point out that the power-law character of the femtoscopic m_T-scaling is no longer valid for 1D studies in the low m_T region (below 250 MeV/c). In the case of 3D studies, the radii are better described by the power-law dependence than 1D radii, however, the final conclusions are model-dependent. The iHKM model follows a power-law description in all 3 directions. On the other hand, for the LQTH model power-law description holds only in the longitudinal direction. Both models show that in low-m_T region radii distribution tends to be more linear than power-law or even flat in some cases. This results in smaller radii than expected from the extrapolation of the power-law scaling from intermediate and high $m_{\rm T}$.

This modification of the behaviour is motivated by the capacity of the ultra-soft pions to decouple from the energetic and dense core of the expanding system, resulting in longer emission times but from the centre of the created system. This can be interpreted as both spatial and kinematic trapping of the ultra-soft pions by the more dense part of the created system. Such pions cannot escape this phase-space region until this confining mechanism is released. This finding is fundamental for addressing experimentally the expected pion radii in non-identical femtoscopic studies when the second particle has a large mass difference with the pion mass, *e.g.*, pion–deuteron, pion–omega, or pion–charm hadron pairs.

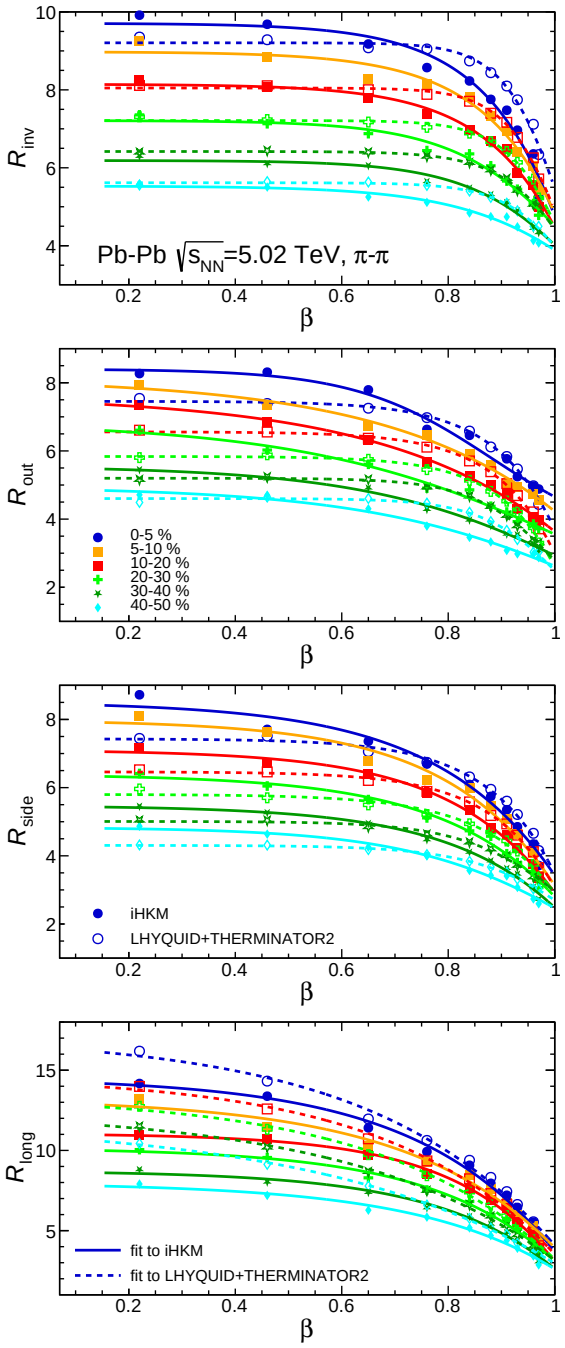


FIG. 7. The identical pion femtoscopy radii dependencies on pair velocity β in the iHKM (full markers) and the LQTH (empty markers) models. The results for the six centrality classes are shown. The lines represent fits to the radii by the formula (5).

The observations of the non-monotonic behaviour of ultra-soft pions obtained from semi-classical models should also be explored from the quantum perspective. The role of confinement and its connection to the direct photon puzzle [52–56] might as well influence the pion homogeneity lengths and should be studied further.

VI. ACKNOWLEDGMENTS

This work is funded by the Research University – Excellence Initiative of Warsaw University of Technology via the strategic funds of the Priority Research Centre of High Energy Physics and Experimental Techniques, the IDUB POSTDOC programme, the IDUB YOUNG-PW programme, Scientific Council of the discipline grant programme and by the Polish National Science Centre under agreements no. 2022/45/B/ST2/02029, and no. 2023/49/N/ST2/03525.

[1] G. Goldhaber, S. Goldhaber, W. Lee, and A. Pais, Influence of Bose-Einstein Statistics on the Antiproton-Proton Annihilation Process, Phys. Rev. **120**, 300 (1960).
[2] G. I. Kopylov and M. I. Podgoretsky, Correlations of identical particles emitted by highly excited nuclei, Sov. J. Nucl. Phys. **15**, 219 (1972).
[3] G. I. Kopylov, Like particle correlations as a tool to study the multiple production mechanism, Phys. Lett. B **50**, 472 (1974).

[4] R. Hanbury Brown and R. Q. Twiss, LXXIV. A new type of interferometer for use in radio astronomy, The London, Edinburgh, and Dublin Philosophical Magazine and Journal of Science **45**, 663 (1954), https://doi.org/10.1080/14786440708520475.

[5] R. Q. Twiss and R. Hanbury Brown, Correlation between photons in two coherent beams of light, Nature **177**, 27 (1956).

[6] R. Q. Twiss, A. G. Little, and R. Hanbury Brown, Correlation between photons, in coherent beams of light, detected by a coincidence counting technique, Nature **180**, 324 (1957).

[7] Yu. M. Sinyukov and V. M. Shapoval, Correlation femtoscopy of small systems, Phys. Rev. D **87**, 094024 (2013).

[8] S. V. Akkelin and Yu. M. Sinyukov, The HBT-interferometry of expanding sources, Phys. Lett. B **356**, 525 (1995).

[9] S. E. Koonin, Proton pictures of high-energy nuclear collisions, Phys. Lett. B **70**, 43 (1977).

[10] M. Gyulassy, S. K. Kauffmann, and L. W. Wilson, Pion interferometry of nuclear collisions. I. Theory, Phys. Rev. C **20**, 2267 (1979).

[11] W. A. Zajc, J. A. Bistirlich, R. R. Bossingham, H. R. Bowman, C. W. Clawson, K. M. Crowe, K. A. Frankel, J. G. Ingersoll, J. M. Kurck, C. J. Martoff, *et al.*, Two-pion correlations in heavy ion collisions, Phys. Rev. C **29**, 2173 (1984).

[12] A. N. Makhlin and Yu. M. Sinyukov, The pion interferometry theory for the hydrodynamic stage of multiple processes, Sov. J. Nucl. Phys **46**, 345 (1987).

[13] A. N. Makhlin and Yu. M. Sinyukov, Hydrodynamics of hadron matter under pion interferometric microscope, Z. Phys. C **39**, 69 (1988).

[14] H. U. Gersch, Coulomb final state interaction in identical boson interferometry, Zeitschrift für Physik A Atomic Nuclei **327**, 115 (1987).

[15] Yu. M. Sinyukov, Spectra and correlations in locally equilibrium hadron and quark-gluon systems, Nucl. Phys. A **566**, 589 (1994).

[16] K. Aamodt, A. Abrahantes, D. Adamova, M. Aggarwal, G. Aglieri Rinella, A. Agocs, S. Salazar, Z. Ahammed, N. Ahmad, A. Masoodi, *et al.* (ALICE Collaboration), Two-pion Bose-Einstein correlations in central Pb-Pb collisions at $\sqrt{s_{NN}} = 2.76$ TeV, Phys. Lett. B **696**, 328 (2011).

[17] J. Adam, D. Adamová, M. M. Aggarwal, G. Aglieri Rinella, M. Agnello, N. Agrawal, Z. Ahammed, S. U. Ahn, I. Aimo, S. Aiola, *et al.* (ALICE Collaboration), One-dimensional pion, kaon, and proton femtoscopy in Pb-Pb collisions at $\sqrt{s_{NN}} = 2.76$ TeV, Phys. Rev. C **92**, 054908 (2015).

[18] K. Aamodt *et al.* (ALICE Collaboration), Two-pion Bose-Einstein correlations in *pp* collisions at $\sqrt{s} = 900$ GeV, Phys. Rev. D **82**, 052001 (2010), arXiv:1007.0516 [hep-ex].

[19] J. Adam *et al.* (ALICE Collaboration), Two-pion femtoscopy in p-Pb collisions at $\sqrt{s_{\rm NN}} = 5.02$ TeV, Phys. Rev. C **91**, 034906 (2015), arXiv:1502.00559 [nucl-ex].

[20] K. Aamodt *et al.* (ALICE Collaboration), Femtoscopy of *pp* collisions at $\sqrt{s} = 0.9$ and 7 TeV at the LHC with two-pion Bose-Einstein correlations, Phys. Rev. D **84**, 112004 (2011), arXiv:1101.3665 [hep-ex].

[21] J. Adam *et al.* (ALICE Collaboration), Centrality dependence of pion freeze-out radii in Pb-Pb collisions at $\sqrt{s_{NN}} = 2.76$ TeV, Phys. Rev. C **93**, 024905 (2016), arXiv:1507.06842 [nucl-ex].

[22] S. Acharya *et al.* (ALICE Collaboration), Pion-kaon femtoscopy and the lifetime of the hadronic phase in Pb−Pb collisions at $\sqrt{s_{\rm NN}} = 2.76$ TeV, Phys. Lett. B **813**, 136030 (2021), arXiv:2007.08315 [nucl-ex].

[23] S. V. Akkelin and Yu. M. Sinyukov, Phase-space densities and effects of resonance decays in a hydrodynamic approach to heavy ion collisions, Phys. Rev. C **70**, 064901 (2004).

[24] V. M. Shapoval, P. Braun-Munzinger, Iu. A. Karpenko, and Yu. M. Sinyukov, Femtoscopic scales in p+p and p+Pb collisions in view of the uncertainty principle, Phys. Lett. B **725**, 139 (2013).

[25] C. Adler *et al.* (STAR Collaboration), Pion interferometry of $\sqrt{s_{NN}} = 130$ GeV Au+Au collisions at RHIC, Phys. Rev. Lett. **87**, 082301 (2001), arXiv:nucl-ex/0107008.

[26] S. S. Adler *et al.* (PHENIX Collaboration), Bose-Einstein Correlations of Charged Pion Pairs in Au + Au Collisions at $\sqrt{s_{NN}} = 200$ GeV, Phys. Rev. Lett. **93**, 152302 (2004).

[27] J. Adams *et al.* (STAR Collaboration), Pion interferometry in Au+Au collisions at $\sqrt{s_{NN}} = 200$ GeV, Phys. Rev. C **71**, 044906 (2005), arXiv:nucl-ex/0411036.

[28] M. A. Lisa, S. Pratt, R. Soltz, and U. Wiedemann, Femtoscopy in relativistic heavy ion collisions: Two decades of progress, Annual Review of Nuclear and Particle Science **55**, 357 (2005), https://doi.org/10.1146/annurev.nucl.55.090704.151533.

[29] B. Abelev, M. Aggarwal, Z. Ahammed, B. Anderson, D. Arkhipkin, G. Averichev, J. Balewski, O. Barannikova, L. Barnby, J. Baudot, *et al.* (STAR Collaboration), Pion interferometry in Au+Au and Cu+Cu collisions at $\sqrt{s_{NN}} = 62.4$ and 200 GeV, Phys. Rev. C **80**, 024905 (2009).

[30] S. Acharya, D. Adamová, A. Adler, J. Adolfsson, M. M. Aggarwal, G. Aglieri Rinella, M. Agnello, N. Agrawal, Z. Ahammed, S. Ahmad, *et al.* (ALICE Collaboration), Search for a common baryon source in high-multiplicity pp collisions at the LHC, Phys. Lett. B **811**, 135849 (2020).

[31] V. Yu. Naboka, S. V. Akkelin, Iu. A. Karpenko, and Yu. M. Sinyukov, Initialization of hydrodynamics in relativistic heavy ion collisions with an energy-momentum transport model, Phys. Rev. C **91**, 014906 (2015).

[32] R. Lednicky, Finite-size effects on two-particle production in continuous and discrete spectrum, Phys. Part. Nucl. **40**, 307 (2009), arXiv:nucl-th/0501065.

[33] A. Kisiel, Non-identical particle femtoscopy at s(NN)**(1/2) = 200-AGeV in hydrodynamics with statistical hadronization, Phys. Rev. C **81**, 064906 (2010), arXiv:0909.5349 [nucl-th].

[34] B. Abelev *et al.* (ALICE), Pion, Kaon, and Proton Production in Central Pb–Pb Collisions at $\sqrt{s_{NN}} = 2.76$ TeV, Phys. Rev. Lett. **109**, 252301 (2012), arXiv:1208.1974 [hep-ex].

[35] B. Abelev *et al.* (ALICE), Centrality dependence of π, K, p production in Pb-Pb collisions at $\sqrt{s_{NN}} = 2.76$ TeV, Phys. Rev. C **88**, 044910 (2013), arXiv:1303.0737 [hep-ex].

[36] V. Begun, W. Florkowski, and M. Rybczynski, Explanation of hadron transverse-momentum spectra in heavy-ion collisions at $\sqrt{s}_{NN} = 2.76$ TeV within chemical non-equilibrium statistical hadronization model, Phys. Rev. C **90**, 014906 (2014), arXiv:1312.1487 [nucl-th].

[37] V. Begun and W. Florkowski, Bose-Einstein condensation of pions in heavy-ion collisions at the CERN Large Hadron Collider (LHC) energies, Phys. Rev. C **91**, 054909 (2015), arXiv:1503.04040 [nucl-th].

[38] V. Yu. Naboka, Iu. A. Karpenko, and Yu. M. Sinyukov, Thermalization, evolution, and observables at energies available at the CERN Large Hadron Collider in an integrated hydrokinetic model of A+A collisions, Phys. Rev. C **93**, 024902 (2016).

[39] V. M. Shapoval and Yu. M. Sinyukov, Bulk observables in Pb + Pb collisions at $\sqrt{s_{NN}} = 5.02$ TeV at the CERN Large Hadron Collider within the integrated hydrokinetic model, Phys. Rev. C **100**, 044905 (2019).

[40] P. Bożek and I. Wyskiel-Piekarska, Particle spectra in Pb-Pb collisions at $\sqrt{\mathbf{s_{NN}}} = \mathbf{2.76}$ TeV, Phys. Rev. C **85**, 064915 (2012).

[41] M. Chojnacki, A. Kisiel, W. Florkowski, and W. Broniowski, THERMINATOR 2: THERMal heavy IoN generATOR 2, Comput. Phys. Commun. **183**, 746 (2012).

[42] P. Bozek, W. Broniowski, M. Rybczynski, and G. Stefanek, GLISSANDO 3: GLauber Initial-State Simulation AND mOre..., ver. 3., Comput. Phys. Commun. **245**, 106850 (2019).

[43] P. Huovinen and H. Petersen, Particlization in hybrid models, Eur. Phys. J. A **48**, 171 (2012).

[44] S. A. Bass *et al.*, Microscopic Models for Ultrarelativistic Heavy Ion Collisions, Prog. Part. Nucl. Phys. **41**, 225–370 (1998).

[45] M. Bleicher *et al.*, Relativistic Hadron-Hadron Collisions in the Ultra-Relativistic Quantum Molecular Dynamics Model, J. Phys. G: Nucl. Part. Phys. **25**, 1859–1896 (1999).

[46] A. Kisiel, M. Gałażyn, and P. Bożek, Pion, kaon, and proton femtoscopy in Pb-Pb collisions at $\sqrt{s_{NN}} = 2.76$ TeV modeled in (3+1)D hydrodynamics, Phys. Rev. C **90**, 064914 (2014).

[47] A. Kisiel, Pion-kaon femtoscopy in Pb–Pb collisions at $\sqrt{s_{NN}} = 2.76$ TeV modeled in (3+1)D hydrodynamics coupled to Therminator 2 and the effect of delayed kaon emission, Phys. Rev. C **98**, 044909 (2018).

[48] S. Acharya, D. Adamová, S. P. Adhya, A. Adler, J. Adolfsson, M. M. Aggarwal, G. Aglieri Rinella, M. Agnello, N. Agrawal, *et al.* (ALICE Collaboration), Production of charged pions, kaons, and (anti-)protons in pb-pb and inelastic *pp* collisions at $\sqrt{s_{NN}} = 5.02$ tev, Phys. Rev. C **101**, 044907 (2020).

[49] S. Pratt, Pion interferometry of quark-gluon plasma, Phys. Rev. D **33**, 1314 (1986).

[50] G. Bertsch and G. E. Brown, Temporal development of the plasma phase transition, Phys. Rev. C **40**, 1830 (1989).

[51] Yu. M. Sinyukov, V. M. Shapoval, and M. D. Adzhymambetov, Space-time structure of particle emission and femtoscopy scales in ultrarelativistic heavy-ion collisions, Universe **9**, 433 (2023), arXiv:2310.16233 [nucl-th].

[52] J.-F. Paquet, C. Shen, G. S. Denicol, M. Luzum, B. Schenke, S. Jeon, and C. Gale, Production of photons in relativistic heavy-ion collisions, Phys. Rev. C **93**, 044906 (2016).

[53] A. Adare, S. Afanasiev, C. Aidala, N. Ajitanand, Y. Akiba, R. Akimoto, H. Al-Bataineh, H. Al-Ta'ani, J. Alexander, A. Angerami, *et al.* (PHENIX Collaboration), Centrality dependence of low-momentum direct-photon production in Au+Au collisions at $\sqrt{s_{NN}} = 200$ GeV, Phys. Rev. C **91**, 064904 (2015).

[54] J. Adam, D. Adamová, M. M. Aggarwal, G. Aglieri Rinella, M. Agnello, N. Agrawal, Z. Ahammed, S. U. Ahn, S. Aiola, A. Akindinov, *et al.* (ALICE Collaboration), Direct photon production in Pb–Pb collisions at $\sqrt{s_{NN}} = 2.76$ TeV, Phys. Lett. B **754**, 235 (2016).

[55] V. Yu. Naboka, Yu. M. Sinyukov, and G. M. Zinovjev, Photon spectra and anisotropic flow in heavy ion collisions at the top RHIC energy within the integrated hydrokinetic model with photon hadronization emission, Nucl. Phys. A **1000**, 121843 (2020).

[56] H. Fujii, K. Itakura, and C. Nonaka, Photon emission at hadronization, Nucl. Phys. A **967**, 704 (2017).

arXiv:2403.02538v1 [hep-ph] 4 Mar 2024

Thermal effects on sound velocity peak and conformality in isospin QCD

Ryuji Chiba,[1,*] Toru Kojo,[1,†] and Daiki Suenaga[2,3,‡]

[1] *Department of Physics, Tohoku University, Sendai 980-8578, Japan*
[2] *Kobayashi-Maskawa Institute for the Origin of Particles and the Universe, Nagoya University, Nagoya, 464-8602, Japan*
[3] *Research Center for Nuclear Physics, Osaka University, Ibaraki 567-0048, Japan*

(Dated: March 6, 2024)

We study thermal effects on equations of state (EOS) in isospin QCD, utilizing a quark-meson model coupled to a Polyakov loop. The quark-meson model is analyzed at one-loop that is the minimal order to include quark substructure constraints on pions which condense at finite isospin density. In the previous study we showed that the quark-meson model at zero temperature produces the sound velocity peak and the negative trace anomaly in the domain between the chiral effective theory regime at low density and the perturbative QCD regime at high density, in reasonable agreement with lattice simulations. We now include thermal effects from quarks in the Polyakov loop background and examine EOS, especially the sound velocity and trace anomaly along isentropic trajectories. At large isospin density, there are three temperature windows; (i) the pion condensed region with almost vanishing Polyakov loops, (ii) the pion condensed region with finite Polyakov loops, and (iii) the quark gas without pion condensates. In the domain (i), the gap associated with the pion condensate strongly quenches thermal excitations. As the system approaches the domain (ii), thermal quarks, which behave as non-relativistic particles, add energy density but little pressure, substantially reducing the sound velocity to the value less than the conformal value while increasing the trace anomaly toward the positive value. Approaching the domain (iii), thermal quarks become more relativistic as pion condensates melt, increasing sound velocity toward the conformal limit. Corrections from thermal pions are also briefly discussed.

I. INTRODUCTION

Recent observations for two-solar mass neutron stars (NSs) [1–6] and the inferred radii of $\sim$ 12-13 km [7–10], together with the low density nuclear constraints [11–13], imply that the equation of state (EOS) in QCD exhibits rapid soft-to-stiff evolution [14], i.e., the pressure grows rapidly as density increases. A useful measure for the evolution of stiffness is (adiabatic) sound velocity $c_s = (\partial P/\partial\varepsilon)^{1/2}$ where the derivative is taken for a fixed entropy. In the dilute regime, nuclear theories predict small c_s^2 of ~ 0.1 at baryon density $n_B \simeq n_0$ [11] ($n_0 \simeq 0.16\,\mathrm{fm}^{-3}$: nuclear saturation density), while in the high density limit c_s^2 approaches 1/3. In the intermediate regime, there is a domain where c_s^2 makes a peak whose height exceeding 1/3. In addition, recently the trace anomaly [15], $\Delta_{\rm tr} = 1/3 - P/\varepsilon$, attracts attention which contains information about the absolute value of P, in addition to the slope, at a given ε. The vanishing of the trace anomaly implies the system being in the conformal limit. The sound velocity peak and trace anomaly are the key quantities to infer the relevant degrees of freedom, quarks or hadrons or else, and hence have crucial importance to characterize the state of matter.

To test theoretical conceptions in dense QCD, it is useful to study QCD-like theories such as two-color or isospin QCD [16–18], for which lattice simulations are doable without suffering from the sign problem. For example, lattice simulations for two-color QCD [19, 20] have demonstrated the existence of the sound velocity peak, and subsequently other simulations in isospin QCD also have confirmed it [21, 22].

In a recent work [23], we have analyzed a quark-meson model for isospin QCD which should be suitable for the regime intermediate between hadronic and weakly coupled quark matter. More precisely, a dense matter starts with the Bose-Einstein-Condensation (BEC) phase of pions and smoothly changes into the Bardeen-Cooper-Schrieffer (BCS) phase with the pion condensates on top of the quark Fermi sea. This can be regarded as the hadron-to-quark crossover in which the condensates (order parameters) have the same quantum number but the qualitative features change. We delineated the microphysics relevant to the sound velocity peak and trace anomaly. Respecting the symmetry, the model results at low density are in good agreement with those from the Chiral effective field theory (ChEFT) [24–26] and lattice simulations [21, 22]. In the transient regime from hadronic to quark matter, we found that the sound velocity peak is developed and remains larger than 1/3 until the density reaches the pQCD domain, $\mu_I \sim 1$ GeV. One of possible explanations for such slow reduction of c_s^2 is non-perturbative power corrections of $\sim +\Lambda_{\rm QCD}^2\mu_I^2$ to the pressure, where the BCS gap of $\Delta \sim$ 200-300 MeV appears in place of $\Lambda_{\rm QCD}$ [23]. The power corrections add negative contributions to the trace anomaly, and hence the trace anomaly may be usable as a measure of non-

* rjchiba@nucl.phys.tohoku.ac.jp
† toru.kojo.b1@tohoku.ac.jp
‡ daiki.suenaga@kmi.nagoya-u.ac.jp

perturbative effects in quark matter. These conceptions are found to be qualitatively consistent with the lattice results of Ref. [22], and, in some density interval, work even at quantitative level.

Based on our zero temperature analyses, we now proceed to analyses at finite temperature. We add thermal quark contributions which couple to a Polyakov loop, a measure of thermally generated color-field backgrounds. Understanding the relationship between thermal effects and the phase structure should be important in the context of supernovae and binary NS mergers, and also in heavy ion collisions at low energy, see Refs. [27, 28] for reviews and e.g., Refs. [29, 30] for up-to-date analyses. How quark degrees of freedom affects these phenomena has been studied most typically in models with first phase transitions from hadronic to quark matter [31]. In the phase transition region, a matter has $c_s^2 = 0$ and produces a latent heat. In contrast, models with a crossover [32–39], which we are exploring, lead to the sound velocity peak that leaves the astrophysical signatures differing from what we expect from purely nuclear or hybrid models with first order phase transitions [40–43]. How stiffening, rather than softening, affects the above-mentioned phenomena is an important question related to the structure of the QCD phase diagram. We examine the sound velocity and trace anomaly along isentropic trajectories on which the s/n_B is constant.

This paper is organized as follows. In Sec. II we briefly review the quark-meson model and the renormalization procedures. The Polyakov loops are coupled. In Sec. III B we examine equations of state of isospin QCD, especially the behaviors of the sound velocity and trace anomaly along isentropic trajectories.

II. MODEL

A. Renormalization

The quark-meson model for isospin QCD, including the renormalization procedures, was discussed in our last paper [23] (which follows the original works in Refs. [44, 45]), so here we only briefly review the model and then discuss the modification for finite temperature.

In our treatment we include only the leading order of the $1/N_c$ expansion. Our thermodynamic potential is dominated by quarks and condensed mesons of $O(N_c)$. We neglect quantum and thermal meson fluctuations which give $O(1)$ contributions; although the structure of mesonic excitations is affected at the leading order of $1/N_c$ expansion, such feedback does not show up in the thermodynamics of $O(N_c)$. Our setup and approximation are the same as Refs. [44, 45] which put focus on the structure of the phase diagram, while in our study we examine the EOS in detail.

The Lagrangian of the two-flavor quark-meson model at finite isospin chemical potential μ_I, which appears in place of up- and down-quark chemical potentials, $\mu_u = \mu_I$ and $\mu_d = -\mu_I$, is

$$\begin{aligned}\mathcal{L}(\vec{\phi}) = &\frac{1}{2}\left[(\partial_\mu\sigma)^2 + (\partial_\mu\pi_3)^2\right] \\ &+ (\partial_\mu + 2\mathrm{i}\mu_I\delta^0_\mu)\pi^+ (\partial^\mu - 2\mathrm{i}\mu_I\delta^\mu_0)\,\pi^- \\ &- \frac{m_0^2}{2}\vec{\phi}^2 - \frac{\lambda}{24}(\vec{\phi}^2)^2 + h\sigma \\ &+ \overline{\psi}\left[\mathrm{i}\partial\!\!\!/ + \mu_I\tau_3\gamma^0 - g(\sigma + \mathrm{i}\gamma^5\vec{\tau}\cdot\vec{\pi})\right]\psi\,. \end{aligned} \tag{1}$$

We explain the values of parameters at the end of this section. Here ψ is a quark field with up- and down-quark components $\psi = (u, d)^T$. The $\vec{\phi} = (\sigma, \vec{\pi})$ are meson fields which correspond to the isospin **1** and **3** representations. The τ_i's are the Pauli matrices in flavor space. We note that our definition of μ_I gives $n_I = n_u - n_d$, a factor 2 larger than the other conventional definition $n_I^{\rm conventional} = (n_u - n_d)/2$.

The model at $\mu_I = 0$ and $m_\pi \neq 0$ has the flavor $U(2)_V$. With $0 < \mu_I < m_\pi/2$, we are left with the $U(1)_{I_3}\otimes U(1)_B$ symmetry. For $\mu_I \geq m_\pi/2$, the $U(1)_{I_3}$ symmetry is further broken down, yielding a single massless mode. The dynamics of such a mode at low energy can be efficiently described by the effective field theory of the $U(1)_{I_3}$ breaking.

At tree level, we can already see that the μ_I favors the nonzero values of $\pi_{1,2}$, the pion condensates. Without loss of generality one can choose $\langle\pi_1\rangle \neq 0$ and $\langle\pi_2\rangle = 0$. Including one-loop corrections from quarks changes the response of pion condensates to μ_I especially at high density, since quarks become responsible for quantities such as isospin density which, at tree level, are solely carried by condensed pions. The condensed mesons affect the quark energy through the Dirac mass and gap as

$$M_q = g\langle\sigma\rangle\,, \qquad \Delta = g\langle\pi_1\rangle\,, \tag{2}$$

which, in the large N_c limit, is renormalization group (RG) invariant, while g and σ are separately RG variant [23, 44, 45]. The quark energies are

$$E_u = E_{\overline{d}} = E(\mu_I)\,, \quad E_d = E_{\overline{u}} = E(-\mu_I)\,, \tag{3}$$

where

$$E(\mu_I) = \sqrt{(E_D - \mu_I)^2 + \Delta^2}\,, \tag{4}$$

with $E_D = \sqrt{\boldsymbol{p}^2 + M_q^2}$.

The effective potential can be concisely written in the $\overline{\rm MS}$ renormalization scheme,

$$\begin{aligned} V_{1-\rm loop} &= \frac{m^2}{2g^2}\left(M_q^2 + \Delta^2\right) + \frac{\lambda}{24g^4}\left(M_q^2 + \Delta^2\right)^2 - \frac{h}{g}M_q \\ &+ \frac{2N_c}{(4\pi)^2}\left(\frac{3}{2} - \ln\frac{M_q^2 + \Delta^2}{M_0^2}\right)\left(M_q^2 + \Delta^2\right)^2 \\ &- 2\mu_I^2\left(\frac{1}{g^2} - \frac{4N_c}{(4\pi)^2}\ln\frac{M_q^2 + \Delta^2}{M_0^2}\right)\Delta^2 \\ &+ V_q^R(\mu_I, M_q, \Delta)\,, \end{aligned} \tag{5}$$

where M_0 is the Dirac mass in vacuum and (m, g, λ) are parameters evaluated in the $\overline{\rm MS}$ scheme at a scale M_0. The V_q^R is the subtracted single particle energy, $V_q^R = V_q - V_q^{(0)} - V_q^{(2)}$, where

$$\begin{aligned} V_q &= -N_c \int_{\boldsymbol{p}} \left(E_u + E_d + E_{\overline{u}} + E_{\overline{d}}\right), \\ V_q^{(0)} &= -4N_{\rm c} \int_{\boldsymbol{p}} \sqrt{E_D^2 + \Delta^2}, \\ V_q^{(2)} &= -2N_{\rm c} \int_{\boldsymbol{p}} \frac{\mu_I^2 \Delta^2}{(E_D^2 + \Delta^2)^{3/2}}. \end{aligned} \tag{6}$$

The potential V_q^R is well-saturated by μ_I^4 terms and contains vanishing μ_I^2 contributions.

The parameters in the $\overline{\rm MS}$ effective potential can be related to the physical parameters in the on-shell scheme, and we use the effective potential rewritten with the on-shell parameters, see Ref. [23] for the full expression. We determine the parameters so as to reproduce $m_\pi = 140$ MeV, $m_\sigma = 600$ MeV, $f_\pi = 90$ MeV, and $M_q = 300$ MeV. The details can be found in Ref. [23].

B. Thermal contributions

As we have stated at the beginning of this section, we do not explicitly calculate the thermal mesonic contributions within our model. The only contributions we take into account are thermal quark contributions. In principle mesonic excitations at low baryon density may be calculated within the hadron resonance gas picture [46], while excitations in the pion condensed phase, where the isospin and parity symmetry are broken, require coupled channel calculations among π's and σ. In order to include the latter into the thermodynamics, we need not only the masses but also the full momentum dependence and discussions for the dissociation scale of excitations. Such extensive analyses are beyond the scope in this paper. Instead, to gain some insights we give rough estimates of mesonic contributions in the pion condensed phase in Sec. III E.

The quark contributions are potentially $O(N_{\rm c})$ but there are two important effects that suppress the thermal quark effects. The first is the condensation effects with which quark excitations are gapped and acquire the Boltzmann factor of $\sim {\rm e}^{-\Delta/T}$. With a naive BCS estimate, $\Delta \sim T_c/0.57 \sim 300$ MeV where $T_c \sim 170$ MeV is the estimate from the lattice simulations [21].

Even without the pion condensation, an isolated quark excitation costs the large energy associated with a color electric flux (QCD string) emerging from the quark. At high enough temperature, such a QCD string can be connected with color fields supplied by either thermally excited hadrons or a quark-gluon-plasma. Those colored background can be found when the entropic effects dominate over the energetic cost. A measure of such colored background is a Polyakov loop; it becomes finite at large temperature where QCD strings condense [47].

Quark models coupled to Polyakov loops have given successful descriptions for the thermodynamics at zero chemical potential, see Ref. [48] for a review. At low temperature, Polyakov loops offer extra suppression factors for thermal quark excitations, reflecting the extra energy cost associated with an isolated quark excitation. This delays the chiral restoration and improves the agreement between quark model calculations and the lattice simulation results (at $\mu_B = 0$).

In the following we add the thermal contribution to the zero temperature expression as

$$V_{1-\rm loop}^T \equiv V_{1-\rm loop} + V_q^T + V_L, \tag{7}$$

where V_q^T is the thermal quark contribution and V_L is the Polyakov loop potential.

The thermal quark part contains the coupling with the Polyakov loop and has the form

$$V_q^T = -2T \sum_{f=u,d,\bar{u},\bar{d}} \int_{\boldsymbol{p}} \ln w_f, \tag{8}$$

with the Boltzman factors coupled to the Polyakov loop

$$\begin{aligned} w_{u,d} &= 1 + 3\Phi {\rm e}^{-\beta E_{u,d}} + 3\bar{\Phi} {\rm e}^{-2\beta E_{u,d}} + {\rm e}^{-3\beta E_{u,d}}, \\ w_{\bar{u},\bar{d}} &= 1 + 3\bar{\Phi} {\rm e}^{-\beta E_{\bar{u},\bar{d}}} + 3\Phi {\rm e}^{-2\beta E_{\bar{u},\bar{d}}} + {\rm e}^{-3\beta E_{\bar{u},\bar{d}}}. \end{aligned} \tag{9}$$

For $\Phi \to 0$ at $T \to 0$, only the last term survives while, at $\Phi \to 1$ at large T, the factor is summarized into $w \to (1 + {\rm e}^{-\beta E})^3$, recovering the usual form for deconfined quarks.

For the Polyakov loop potential, we use the parametrization motivated by the Haar measure [49, 50]

$$\begin{aligned} T^{-4} V_L(\Phi, \Phi^*, T) &= -a(T)\bar{\Phi}\Phi/2 \\ &+ b(T) \ln\left[1 - 6\bar{\Phi}\Phi + 4\left(\bar{\Phi}^3 + \Phi^3\right) - 3\left(\bar{\Phi}\Phi\right)^2\right], \end{aligned} \tag{10}$$

where the Φ's are mean field values of the traced Polyakov loop,

$$\Phi = \frac{1}{N_{\rm c}} \langle {\rm tr}_{\rm c} L \rangle, \qquad L = \mathcal{P} {\rm e}^{{\rm i} \int_0^\beta {\rm d}x_0 A_0}. \tag{11}$$

The parameters $a(T)$ and $b(T)$ is assumed to be

$$a(T) = a_0 + a_1/t + a_2/t^2, \qquad b(T) = b_0/t^3, \tag{12}$$

with $t = T/T_0$. The parameters are given as [50]

$$a_0 = 3.51, \; a_1 = -2.47, \; a_2 = 15.2, \; b_0 = -1.75. \tag{13}$$

The parameter T_0 is chosen to be [51]

$$T_0(N_{\rm f}) = T_\tau {\rm e}^{-1/\alpha_0 \gamma}, \qquad \gamma = \frac{11N_{\rm c} - 2N_{\rm f}}{6\pi}, \tag{14}$$

with $\alpha_0 = 0.304$ and $T_\tau = 1.77$ GeV. The present parameterization leads to $T_0(N_{\rm f} = 0) = 270$ MeV for

the pure glue theory, $T_0(N_{\rm f}=2)=208$ MeV, and $T_0(N_{\rm f}=3)=178$ MeV for finite quark flavors. With these parameters, the critical temperature for the chiral restoration in $N_{\rm f}=2$ theories appears to be $T_c\sim 180$ MeV [51].

In our analyses at finite density, we use the same parameter sets as the vacuum case unless otherwise stated. In the literatures there are versions with the μ_I dependence of γ, e.g., $\gamma\to\gamma-16N_{\rm f}\mu_I^2/\pi T_\tau^2$, originally introduced in Ref. [51] with considerations based on the hard-dense loop. In the normal phase, this introduces $\sim 10\%$ reduction of the critical temperature. Meanwhile the situation may change in the pion condensed phase; the back reaction from quarks to the gluon sector is expected to be suppressed due to the color-singlet BCS gap. This conjecture has been tested for the gluon propagators in two-color QCD [52–55]. There it is found crucial to use quark propagators with the BCS gap to explain the lattice data [56, 57]. Combining gluon propagators weakly depending on μ_I with the computation of the effective potential for Polyakov loops [58], we expect that the μ_I dependence to be included in the parameter γ should be modest. In what follows, we have checked that using the μ_I-dependent T_0 introduces $\sim 10\%$ enhancement in the critical temperature for the domain of our interest (see also Ref. [45]), and we present only the simplest version of the model with T_0 fixed as the vacuum case.

III. EQUATIONS OF STATE

We first examine the gross features of the phase digram in the μ_I-T plane and look into the equations of state.

A. Phase structure

First we take a look at the chiral and pion condensates and Polyakov loop at given (μ_I, T). Up to $\mu_I\simeq m_\pi/2$, the phase structure is similar to what has been calculated for the hadronic phase. As shown in Fig. 1, at $T=0$ and beyond $\mu_I=m_\pi/2$, the charged pions condense while the chiral condensates begin to dissociate but approach zero only asymptotically. The phase transition line at $\mu_I\sim m_\pi/2$ is almost constant up to $T\sim 150$ MeV. In the mean field calculations, the transition lines separating the pion condensed phase and the others are the second order phase transition lines.

Without the Polyakov loops, the critical temperature for the pion condensate, T_c^π, is $\simeq 170$ MeV. Including the Polyakov loop enhances T_c^π to $\simeq 200$ MeV, about 30 MeV larger than the lattice simulation results. This overestimate is in part duel to our neglect of thermal contributions from in-medium hadrons. In Sec. III E we try to give rough estimates for hadronic excitations. Another problem in our current modeling is that we are not including the medium modifications of the Polyakov loop potential which we have mentioned in the previous sec-

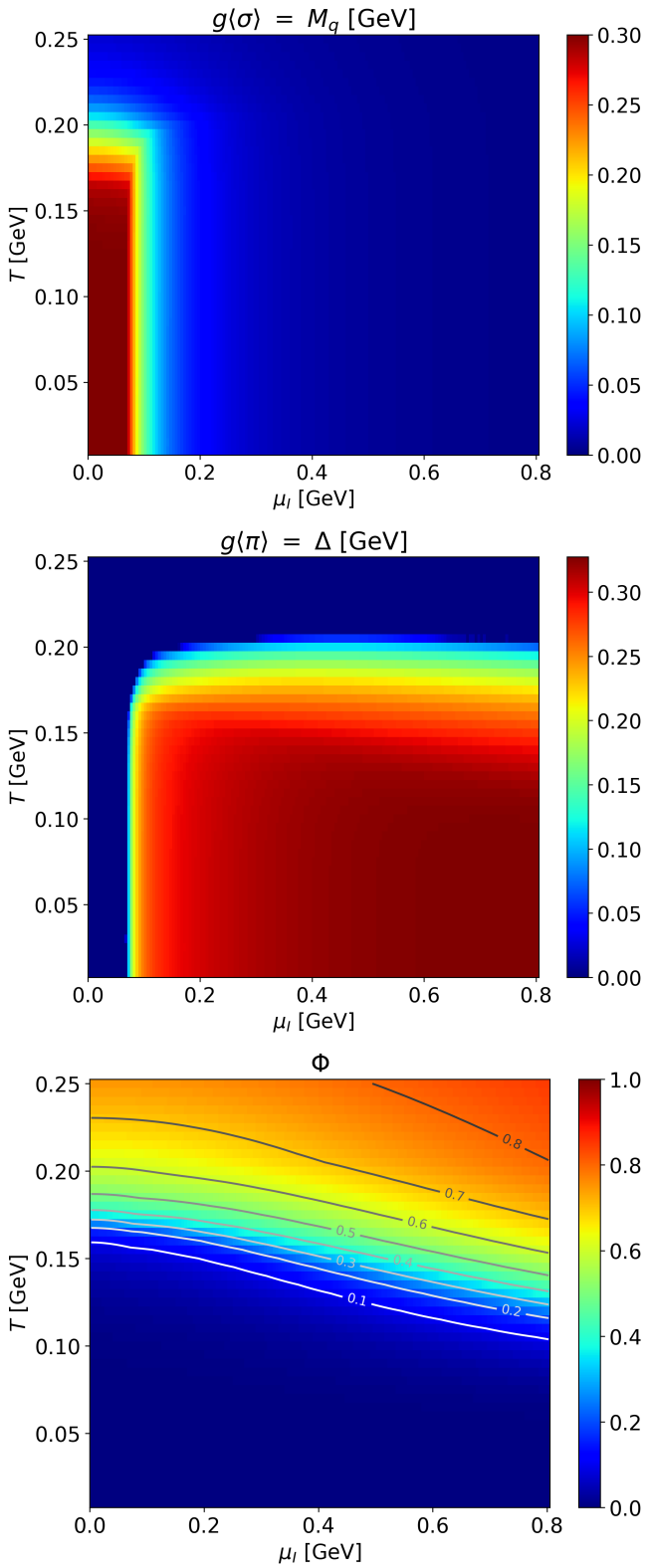


FIG. 1. The phase structure: **Top**: dynamical quark mass $M_q=g\langle\sigma\rangle$; **Middle**: quark mass gap $\Delta=g\langle\pi_1\rangle$; **Bottom**: Polyakov loop.

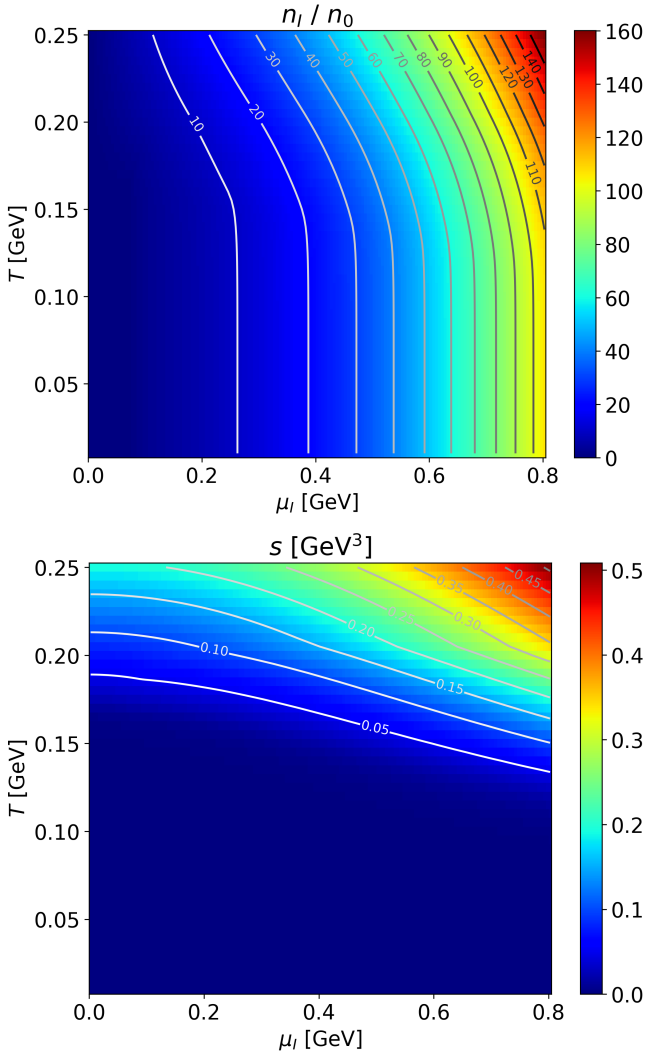


FIG. 2. The n_I/n_0 (top) and s (bottom) in the μ_I-T plane.

tion. In what follows we proceed with the current setup while keeping in mind that thermal corrections to EOS would be underestimated.

At a fixed temperature, the Polyakov loop values decrease as μ_I increases. Within our one-loop computations in the large N_c treatment, such reduction at larger μ_I is due to the phase space enhancement of $\sim 4\pi p_F^2$ ($p_F \sim n_I^{1/3}$: the quark Fermi momentum) for thermal quarks, provided that the excitation gaps remain similar from low to high μ_I. Actually in our model such a constant gap is realized at low temperature.

B. Equations of state

We study EOS mainly for the isentropic trajectories, i.e., EOS at fixed s/n_I. Before doing so, we first show n_I and s as functions of μ_I for several T as a preparation.

Shown in Fig. 2 are the isospin density n_I/n_0 and entropy density s. For n_I, in Fig. 3 we also show the same plot but with more focus on the low density domain at $\mu_I \leq 2m_\pi$. The experimental determination based on the πe scattering and the $e^+e^- \to \pi^+\pi^-$ process [59] yields the estimate $r_\pi^V = \sqrt{\langle r^2\rangle_V} \simeq 0.66\,\mathrm{fm}$ [60] which has been reproduced by lattice calculations [61, 62]. The isospin density where pions overlap is estimated as (reminder: our definition of n_I is $n_u - n_d$, so $n_I/2$ should be equated with the inverse volume of pions with isospin 1)

$$n_I^{\rm overlap} = 2 \times \left(4\pi r_\pi^3/3\right)^{-1} \simeq 10.4 n_0\,, \tag{15}$$

which corresponds to $\mu_I \simeq 0.26\,\mathrm{GeV}$.

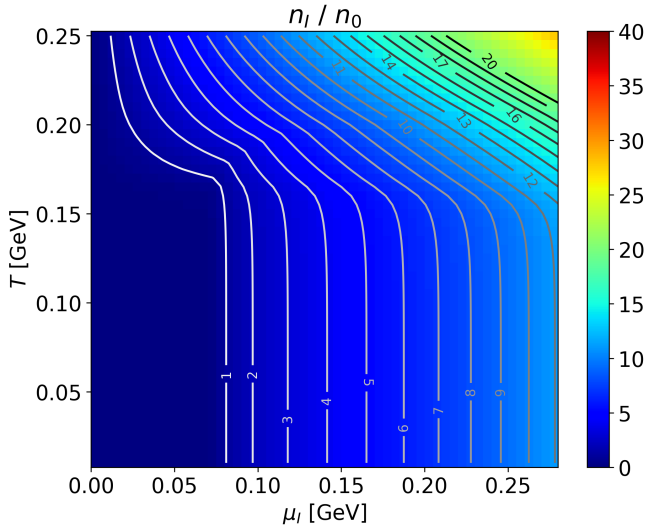


FIG. 3. The n_I/n_0 with more focus on the low density region at $\mu_I \leq 2m_\pi$.

At finite temperature and low density, the overlap of thermally excited hadrons is roughly characterized by the entropy of 2-3 fm^{-3}, supposing that a single meson or baryon including two or three quarks is available within a volume $\sim 1\,\mathrm{fm}^3$. That is, at $s \sim$ 2-3 fm^{-3} thermally excited hadrons should begin to overlap each other. Lattice simulations at $\mu_I = 0$ show that the entropy density around the critical temperature $T_c \simeq 155$ MeV is $s \sim 0.02\,\mathrm{GeV}^3 \simeq 2.6\,\mathrm{fm}^{-3}$ which seems consistent with the naive estimate.

Next we consider the entropy at high density. As a guide we first consider the entropy in the Stefan-Boltzmann limit ($N_c = 3, N_f = 2$),

$$s_q^{\rm SB} = \frac{N_c N_f}{6}\left(\mu_I^2 T + \frac{7\pi^2 T^3}{15}\right), \tag{16}$$

where quarks are treated as gapless. The μ_I^2 factor in the first term reflects the phase space around the Fermi surface. For $\mu_I = 1$ GeV $\simeq 7m_\pi$, the entropy of $s \simeq$ 2-3 fm^{-3} would be reached at $T \sim 20$ MeV with gapless quarks; a large entropy could be reached at very low temperature.

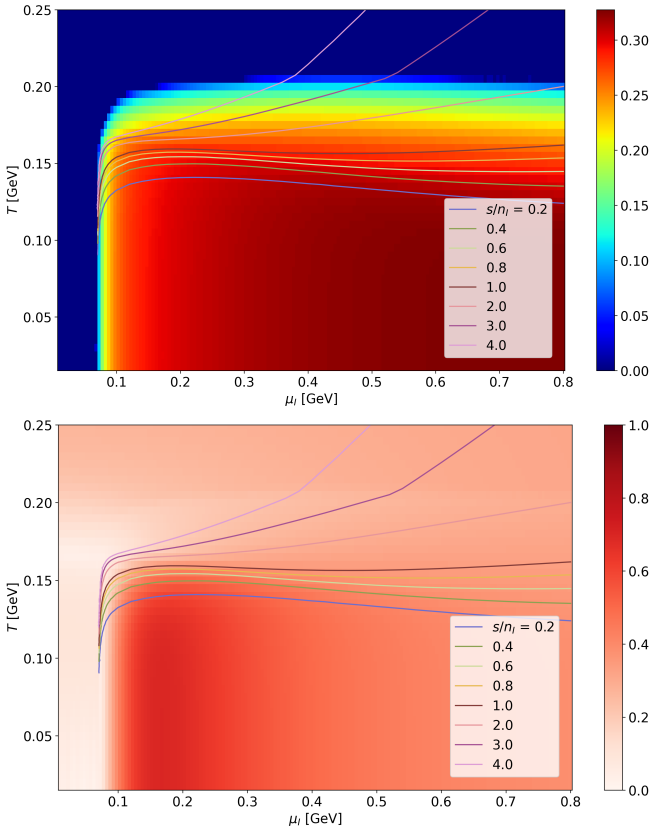


FIG. 4. The contour for Δ (top) and c^2_{s/n_I} (bottom) and isentropic (fixed s/n_I) trajectories in the μ_I-T plane. The thickness of the cells represents the size of Δ and c_s^2. The kinks in the isentropic trajectories around $T \simeq 200$ MeV are due to the dissociation of pion condensates (the second order phase transition).

The situation is very different in the pion condensed phase. Here thermal quark excitations are suppressed by the gaps. The entropy at low T parametrically scales as $s_q \sim \mu_I^2 T \mathrm{e}^{-\Delta/T}$. Hence EOS at low temperature, up to $T \sim 150$ MeV, and $\mu_I \lesssim 7m_\pi$ remain almost the same as the $T = 0$ case.

Now we examine the isentropic trajectories in the μ_I-T plane, as shown for $s/n_I = 0.2$ to 4.0, together with the squared sound velocity along the trajectory, $c^2_{s/n_I} = (\partial P/\partial\varepsilon)|_{s/n_I \text{ fixed}}$, in Fig. 4. These relatively low s/n_I are achieved only when s is very low or n_I is large.

First we examine the low μ_I region with $\mu_I \sim m_\pi/2$ where the trajectories go from low to high T without much change in μ_I. This domain is slightly above the threshold of the pion condensation beyond which n_I grows as $\sim f_\pi^2 \mu_I$, as can be derived from the ChEFT. Meanwhile the entropy calculated based on thermal quark excitations (without thermal pions) is controlled by a factor $\sim \mathrm{e}^{-\Delta(\mu_I,T)/T}$ where the gap near $\mu_I = m_\pi/2$ is sensitive to μ_I. A parametric expression is

$$s/n_I \simeq (\text{phase space}) \times \mathrm{e}^{-\Delta(\mu_I,T)/T}\,, \tag{17}$$

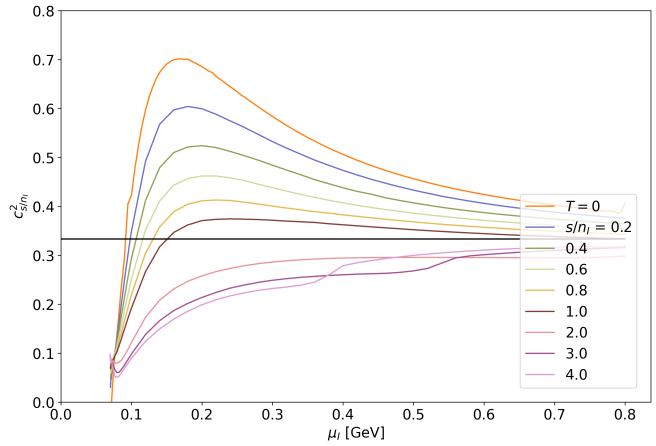


FIG. 5. The squared isentropic sound velocity c^2_{s/n_I} on isentropic trajectories. At low s/n_I, a c_s^2 makes a peak as in the $T = 0$ result. As s/n_I increases, the height of the peak decreases, and the entire curve goes below the conformal limit $c_s^2 = 1/3$ for $s/n_I \simeq 1.5$.

that is, the entropy becomes sizable only when T is as large as Δ. More explicitly, the temperature scales as

$$T(\mu_I)|_{s/n_I} \simeq \frac{\Delta(\mu_I, T)}{\ln\left[\,(\text{phase space}) \times (n_I/s)|_{\text{fixed}}\,\right]} \tag{18}$$

where the denominator is logarithmic and its variation with respect to μ_I, T, and $(s/n_I)_{\text{fixed}}$ is modest. Then, along the isentropic trajectories the μ_I-dependence of T is primarily determined by the behavior of the gap.

Next we consider the pion condensed domain at large μ_I. Until thermal corrections to Δ become substantial, Δ is almost constant for changes in μ_I. Applying the same discussion as the above, we conclude that T in the isentropic trajectories shows the weak μ_I-dependence, as seen in e.g., $s/n_I \sim 0.8$ trajectory. Meanwhile, when $\Delta \ll T$, the Boltzmann factor is approximately $\mathrm{e}^{-\Delta/T} \sim 1$. At large μ_I, $s \sim \mu_I^2 T$ and $n_I \sim \mu_I^3$ so that along the isentropic trajectories $T \propto \mu_I$. This behavior is clearly seen in Fig. 4.

C. Sound velocity

Shown in Fig. 5 are the squared sound velocity c_s^2 along various isentropic trajectories, from $s/n_I = 0.2$ to 3.5. For a small s/n_I, the sound velocity in the BEC-BCS crossover region has a peak with the height greater than the conformal value $c^2_{s/n_I} = 1/3$. Increasing s/n_I, the trajectories leave the pion condensed domain, and the peak structure disappears.

For a normal quark gas, the c^2_{s/n_I} does not exceed the conformal limit 1/3 but asymptotically approaches it from below. The same is true for a pure pion gas. Thus, the c^2_{s/n_I} exceeding 1/3 should be related to condensed

pions [63].[1] Leaving from the pion condensed phase, the behaviors of c^2_{s/n_I} approach the quark gas behavior (reminder: we have not included thermal pions yet).

Thus, what is nontrivial is the c^2_{s/n_I} in the pion condensed phase. The sound velocity at $T = 0$ is found to have a peak around $\mu_I \sim m_\pi$. Parametrically, the existence of the peak can be inferred by combining the ChEFT at LO and the relativistic limit. Near $\mu_I \sim 0.5m_\pi$, one can use the EOS derived from the ChEFT at leading oder,

$$P^{\rm LO}_{\rm EFT} = 2f_\pi^2\mu_I^2\left(1 - \frac{m_\pi^2}{4\mu_I^2}\right)^2, \tag{19}$$

with which the sound velocity behaves as

$$c_s^2\big|_{\rm EFT} = \frac{\left(2\mu_I\right)^4 - m_\pi^4}{\left(2\mu_I\right)^4 + 3m_\pi^4}\,. \tag{20}$$

The c_s^2 reaches 1/3 at $\mu_I = m_\pi/(2\times 3^{1/4}) \simeq 0.7m_\pi$ and asymptotically approaches 1 toward very large μ_I. But the ChEFT should lose the validity at $\mu_I \gg m_\pi$ and the EOS should be replaced with the quark EOS. A useful measure to examine the impact of the quark substructure is the occupation probability of quark states [23, 65–67]; the existence of the upper bound imposes a constraint which is invisible from purely hadronic models and yields statistical repulsion among hadrons.

At asymptotically large μ_I, the quark kinetic energy should dominate over interactions and then $c_s^2 = 1/3$ follows. Reducing μ_I toward $\mu_I \sim m_\pi$, the pQCD corrections predict c_s^2 is reduced from 1/3. To describe growing c_s^2 toward low density, we need other elements. One possible candidate is the non-perturbative power corrections producing $+\Lambda^2_{\rm QCD}\mu_I^2$ terms with $\Lambda_{\rm QCD} \sim$ 200-300 MeV. The BCS gap Δ can appear in the place of $\Lambda_{\rm QCD}$. Now parameterizing ($a \sim O(1) > 0$)

$$P_{\rm BCS}(\mu_I) = C\left(\mu_I^4 + a\Delta^2\mu_I^2\right), \tag{21}$$

we obtain

$$c_s^2\big|_{\rm BCS} = \frac{2\mu_I^2 + a\Delta^2}{6\mu_I^2 + a\Delta^2}\,. \tag{22}$$

At $\mu_I \sim \Delta$, the c_s^2 can be substantially larger than 1/3.

The quark-meson model covers both low and high density characteristics. At low density condensed pions dominate the EOS, while at high density condensed pions become responsible for the BCS gaps for quarks.

Finally, we notice that enhancement of c^2_{s/n_I} at large $s/n_I \gtrsim 2.0$ and large $\mu_I \gtrsim 300$ MeV which is related to melting of pion condensates. As can be seen in Fig. 4, these trajectories start with $T \gtrsim 150$ MeV at low density and have larger temperatures for larger μ_I, eventually crossing the critical line for pion condensed phase. For these trajectories with $T \gtrsim 150$ MeV, there are already substantial thermal quark excitations and sizable Polyakov loop contributions. It is worth mentioning that, with a larger Δ, thermal excitations are closer to the non-relativistic regime

$$\sqrt{(E_q - \mu_I)^2 + \Delta^2} \simeq \Delta + \frac{v_F^2\boldsymbol{p}^2}{2\Delta} \tag{23}$$

where we use an approximation $|E_q - \mu_I| \simeq v_F|\boldsymbol{p}|$ for excitations near the Fermi surface. Thus, while the presence of Δ enhances c_s^2 in the zero temperature EOS, it acts oppositely for thermal corrections. When Δ vanishes, thermal quarks become more relativistic and increases c_s^2.

D. Trace Anomaly

A useful quantity to examine the conformality of the system is the trace anomaly divided by the energy density [15]

$$\Delta_{\rm tr} = \frac{\langle T^\mu_\mu\rangle}{3\varepsilon} = \frac{1}{3} - \frac{P}{\varepsilon}\,. \tag{24}$$

The $\Delta_{\rm tr}$ is vanishing in the conformal limit. We are mainly interested in the sign.

This quantity in isospin QCD has been studied at $T = 0$ in Ref. [23]. Within pQCD, the perturbative corrections favor positive trace anomaly. Then, we examine parametrized non-perturbative corrections. The bag constant favors positive trace anomaly. On the other hand, we found that attractive correlations near the Fermi surface yield positive power corrections of $\Delta^2\mu_I^2$ that favor the negative trace anomaly. Our prediction of the negative trace anomaly to high density turns out to be consistent with the lattice calculations in Ref. [22] in which the trace anomaly is negative up to $\mu_I \sim 7.5m_\pi \simeq 1.28$ GeV, to very high density where pQCD has been supposed to be valid. This deviation from pQCD suggests that non-perturbative effects survive from the hadronic to weakly coupled quark matter domain.

In this work we extend the analyses to finite temperature. For $\mu_I \simeq 0$ and finite T, it has been known that the trace anomaly is positive and has a peak along T-axis around where a hadron resonance gas transforms into a QGP. We examine when and how the negative trace anomaly found at $T = 0$ changes the trend toward high temperature.

First we consider a normal phase at $\mu_I \lesssim m_\pi/2$. In the non-relativistic regime with $\varepsilon \gg P$, the trace anomaly is approximately $\langle T^\mu_\mu\rangle \simeq \varepsilon - 3P \simeq \varepsilon$ and hence is positive. At low μ_I and low T, thermal quark excitations with the mass m are highly suppressed by $\sim {\rm e}^{-m/T}$. Increasing

[1] Relations between the sound velocity peak and the chiral-partner contributions on top of the condensates in two-color QCD are discussed in Ref. [64].

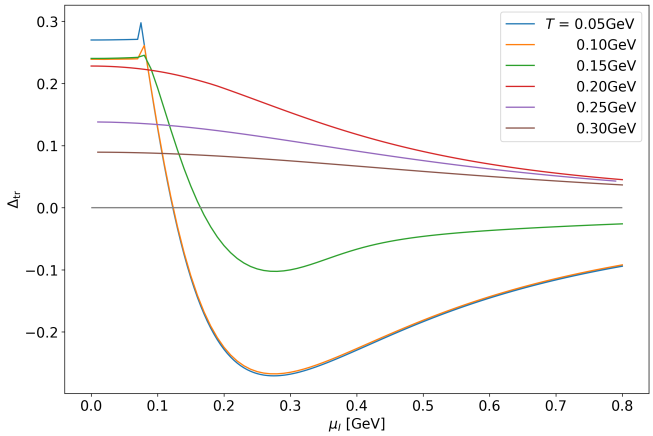


FIG. 6. The trace anomaly $\Delta_{\rm tr}$ as a function of μ_I at various temperatures. In the non-relativistic limit, $\Delta_{\rm tr} \simeq 1/3$.

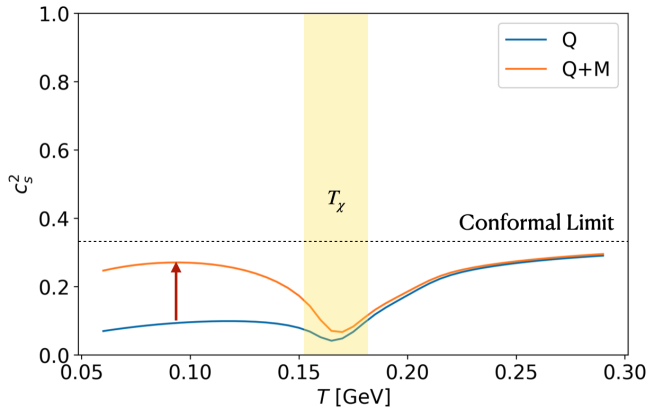


FIG. 7. The squared sound velocity c_s^2 at $\mu_I = 0$ and various temperatures. At low temperature, the EOS including only thermal quarks underestimate c_s^2 and including thermal pions significantly enhance it. The window for the chiral restoration is shown as a guidance. The window for deconfinement, characterized by the Polyakov loop, appears to be in the same range as T_χ and hence is not shown explicitly.

T, each excitation becomes more relativistic so that the pressure becomes larger and $\Delta_{\rm tr}$ approaches the conformal limit from above, $\Delta_{\rm tr} \propto \varepsilon - 3P \to 0^+$.

For $\mu_I \gtrsim m_\pi/2$ and low T, pion condensates are formed. Near the onset, $\varepsilon \sim m_\pi n_I \gg P$ so that the trace anomaly is positive. But with slight increase of μ_I, the pressure develops rapidly exceeding the conformal value $\varepsilon/3$, and then stays beyond the conformal limit for a wide interval. Increasing T, the trace anomaly does not change much within the pion condensates, but begins to increase as the condensates melt. In the range of $T = 0.15$-0.20 GeV, the trace anomaly becomes positive everywhere.

E. Thermal pions: rough estimates

Our quark-meson model within the one-loop approximation misses thermal hadronic contributions. At low density, this causes serious errors in estimating the thermodynamic quantities. In fact, it has been known that thermal pions are dominant at low temperature. Indeed, typical quark models lead to too small sound velocity at low temperature since thermal quarks are massive and stay within the non-relativistic regime (Fig. 7). Pions, which are lighter than quarks, reach the relativistic regime earlier and hence increase c_s^2 to the value close to the conformal limit. Approaching the chiral restoration temperature $T_\chi \simeq 160$ MeV, the massive quarks dominate over pions in the EOS and the system goes back to the non-relativistic regime, creating a dip in c_s^2 before reaching the relativistic or conformal limit.

Then, it is natural to ask how much our results including only thermal quarks can be affected by thermal hadronic excitations at finite density. In the crossover regime, which we are most interested in, there can be thermal hadronic excitations.

Computing hadron spectra in the pion condensed phase requires multi-channel coupling analyses, as the condensed pions serve isospin and change the parity when other particles propagate. Three pion modes all mix and even sigma mode couples due to the violation of the parity in medium. Because of these complications, in this paper we do not directly calculate the spectra within our model but simply quote the results from the EFT of the I_3 symmetry breaking to get rough estimates.

To avoid artificial jumps in thermodynamics from the hadronic phase to the pion condensed phase, we keep track of adiabatic changes from three pions in the hadronic phase to three modes in the pion condensed phase. The other possible hadronic excitations are neglected, consistently in the normal and pion condensed phases. The spectra are continuous because the phase transition is the second order in mean field theories. Among the three modes in the pion condensed phase, one mode is massless while the other two modes are massive.

The spectra in the normal hadronic phase are

$$\begin{aligned} E_{\pi_\pm} &= \sqrt{m_\pi^2 + \boldsymbol{p}^2} \mp 2\mu_I \,, \\ E_{\pi_0} &= \sqrt{m_\pi^2 + \boldsymbol{p}^2} \,. \end{aligned} \tag{25}$$

The π_+ becomes massless at $\mu_I = m_\pi/2$.

In the pion condensed phase, we use the labels $\tilde\pi_i$ which are smoothly connected with π_i. The spectra are (see Appendix A)

$$\begin{aligned} E_{\tilde\pi_+} &= |\boldsymbol{p}| \sqrt{\frac{4\mu_I^2 - m_\pi^2}{12\mu_I^2 - m_\pi^2}} \equiv v_\pi |\boldsymbol{p}| \,, \\ E_{\tilde\pi_-} &= \sqrt{m_-^2 + \left(1 + \frac{16\mu_I^2}{m_-^2}\right)\boldsymbol{p}^2} \,, \\ E_{\tilde\pi_0} &= \sqrt{4\mu_I^2 + \boldsymbol{p}^2} \,, \end{aligned} \tag{26}$$

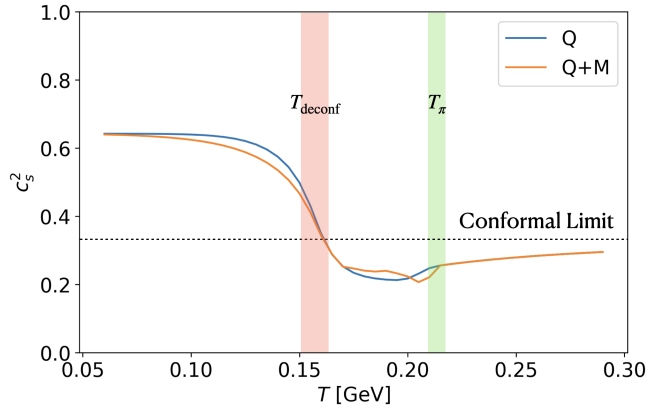


FIG. 8. The squared sound velocity c_s^2 at $\mu_I = 0$ and various temperatures at $\mu_I = 240$ MeV. Results with and without thermal pions are compared. The quick reduction of c_s^2 occurs in the interval $T = 140$-170 MeV which coincides with the domain where the Polyakov loop rises quickly.

where $m_-^2 = 24\mu_I^2 - 2m_\pi^2$ whose derivation is model dependent. One can check the spectra at $\mu_I = m_\pi/2$ coincides with the spectra in the normal phase.

We note that at large μ_I, the velocity of the massless mode approaches $\sqrt{1/3}$. Meanwhile, at the onset of the pion condensation, $\Delta \to 0$, the velocity v_π of $\tilde{\pi}_+$ vanishes. As shown in the Appendix A, the velocity scales as $v_\pi \sim \Delta$. This is the critical slowing down.

When we try to include the massless mode in the thermodynamics, some additional considerations are necessary for the applicability of the EFT. Formally we find

$$P_{\tilde{\pi}_+} = -T \int_{\boldsymbol{p}} \ln\left(1 - \mathrm{e}^{-\beta v_\pi |\boldsymbol{p}|}\right). \tag{27}$$

If we take this expression at its face value, we run into troubles near the threshold; $P_{\tilde{\pi}_+}$ diverges as $\left(T/v_\pi\right)^3 \to \infty$ for $\mu_I \to m_\pi/2 + 0^+$. This divergence is fictitious because the phase space where the EFT is applicable is limited to $\sim \Delta$. Including such cutoff scale in the momentum integral, the change of variable as $\sim v_\pi \boldsymbol{p} \to \boldsymbol{p}'$ yields the pressure which parametrically behaves as

$$P_{\tilde{\pi}_+} \sim T\Delta^3, \tag{28}$$

and is harmless for $\mu_I \to m_\pi/2 + 0^+$ or $\Delta \to 0$. In practice, we integrate momenta of $\tilde{\pi}_+$ up to 2Δ beyond which pions may decay to a quark and a quark-hole.

Shown in Fig. 8 is c_s^2 at $\mu_I = 240$ MeV at various temperatures. The isospin density is $\sim 9n_0$ which is smaller than the density where pions are supposed to overlap. Results with and without thermal pions are compared. To moderate temperature ~ 100 MeV, thermal pions give minor corrections, reflecting that the cold matter pressure at $T = 0$ is already substantial.

IV. SUMMARY

We study the EOS of the isospin QCD within a quark-meson model with the Polyakov loop at finite μ_I and T, especially along isentropic trajectories where s/n_I is fixed. The model describes the BEC-BCS crossover of pion condensates. At low density the condensed pions dominate the EOS while at high density they play roles of the BCS gaps for quarks. Based on the previous analyses for the sound velocity peak and trace anomaly at $T = 0$ [23], in this work we examine corrections from thermally excited quarks in the Polyakov loop background. The thermal corrections smear out the sound velocity peak and eventually bring the trace anomaly to the positive value. The sound velocity becomes smaller than the conformal value when thermal quarks, which appear to be non-relativistic, are liberated. This changes occur within pion condensed phase whose melting temperature is greater than the temperature for quark liberation (with substantial Polyakov loops).

In this work we include only thermal quarks but neglected thermally excited dynamical gluons and hadrons. A part of gluons are included in the form of Polyakov loop potential, but in a QGP thermal gluons should be manifestly taken into account. A more qualitatively nontrivial question is the impact of hadronic excitations in the pion condensed phases. In this paper we gave only rough estimates in the region close to the quark matter domain and concluded that thermal hadronic contributions give minor corrections to the zero temperature EOS. But more quantitative discussions are necessary in the domain closer to the hadronic domain where zero temperature EOS can be comparable to thermal contributions. The description requires the understanding of spectra, momentum dependence, and the dissociation scale. In the pion condensed phase, all pions and σ mesons are mixed so that the coupled channel computations based on quarks are necessary. In addition to the impacts on EOS, studying the properties of hadronic excitations in dense matter is of interest by its own (see Refs. [68–70] for two-color QCD), as they are relevant for transport phenomena. In future we plan to perform extensive analyses based on quark degrees of freedom.

Another interesting question is how gluons and the Polyokov loop potential are modified by the medium effects. In two-color QCD, lattice QCD simulations indicate that modifications to gluon propagators are modest even at quark chemical potential of $\mu_q \sim 1$ GeV [52–57]. The Polyakov loop potential calculated from such gluon propagators should also show modest response to changes in μ_I. Since the non-perturbative power corrections are very important for c_s^2 to exceed the conformal value $1/3$, it is crucial to understand how the non-perturbative effects become irrelevant at high density. Such analyses will allows us to judge which conceptions in QCD-like theories can be transferred to QCD at finite μ_B.

ACKNOWLEDGMENTS

We thank Drs. Brandt and Endrodi for kindly providing us with their lattice data in Ref. [21], and Dr. Abbott and his collaborators for their kindness of sending the lattice data in Ref. [22]. We thank Drs. E. Itou, Y. Fujimoto for discussions. This work was supported by JSPS KAKENHI Grant No. 23K03377. TK is also supported by the Graduate Program on Physics for the Universe (GPPU) at Tohoku university; D.S. by the RIKEN special postdoctoral researcher program and the JSPS KAKENHI Grant No. 23H05439.

Appendix A: Pion spectra in the pion condensed phase

We consider an EFT_{I_3} for charged pions,

$$\mathcal{L} = (\partial_\mu + 2\mathrm{i}\mu_I\delta^0_\mu)\pi^+ (\partial^\mu - 2\mathrm{i}\mu_I\delta^\mu_0)\,\pi^- - \frac{m_\pi^2}{2}\left(\pi_1^2+\pi_2^2\right) - \frac{\lambda'}{24}\left(\pi_1^2+\pi_2^2\right)^2 + \cdots \tag{A1}$$

We assume that quark and σ are integrated out and hence λ' may be modified from the parameters in the quark-meson model. Pions here are just treated as ordinary massive mesons with the mass m_π. The following calculations do not refer to the chiral symmetry in the underlying theories. The condensates are given by

$$\bar\pi^2 = \frac{6}{\lambda'}\left(4\mu_I^2 - m_\pi^2\right). \tag{A2}$$

With this background, the fluctuation of pions are given by

$$\mathcal{L}_{1,2} = \frac{1}{2}\left[(\partial_\mu\pi_1)^2 + (\partial_\mu\pi_2)^2\right] - 2\mu_I\left[(\partial_0\pi_1)\pi_2 - (\partial_0\pi_2)\pi_1\right] - \frac{\lambda'\bar\pi^2}{6}\pi_1^2 . \tag{A3}$$

The spectra for $\tilde\pi_\pm$ are obtained by finding p_0 such that

$$\det\begin{bmatrix} p_0^2 - \boldsymbol{p}^2 + \frac{\lambda'}{3}\bar\pi^2 & 4\mathrm{i}\mu_I p_0 \\ -4\mathrm{i}\mu_I p_0 & p_0^2 - \boldsymbol{p}^2 \end{bmatrix} = 0\,. \tag{A4}$$

For $\boldsymbol{p} = 0$, it is clear $p_0 = 0$ satisfies the equation, i.e., there is massless mode. Meanwhile, a massive mode has the squared mass

$$m_-^2 = 16\mu_I^2 + \frac{\lambda'}{3}\bar\pi^2 = 24\mu_I^2 - 2m_\pi^2\,. \tag{A5}$$

At finite $\boldsymbol{p}$, the spectra are given by

$$E_{\tilde\pi_-} = \sqrt{m_-^2 + \left(1 + \frac{16\mu_I^2}{m_-^2}\right)\boldsymbol{p}^2} \tag{A6}$$

for a massive mode, and

$$E_{\tilde\pi_+} = v_\pi|\boldsymbol{p}|\,, \tag{A7}$$

with

$$v_\pi \equiv \sqrt{\frac{4\mu_I^2 - m_\pi^2}{12\mu_I^2 - m_\pi^2}} = \bar\pi\sqrt{\frac{\lambda'}{3m_-^2}}\,. \tag{A8}$$

We note that at large μ_I, the velocity of the massless mode approaches $\sqrt{1/3}$. Meanwhile, at the onset of the pion condensation, $\bar\pi \to 0$, the velocity v_π of $\tilde\pi_+$ vanishes. This is the critical slowing down.

[1] Z. Arzoumanian et al. (NANOGrav), The NANOGrav 11-year Data Set: High-precision timing of 45 Millisecond Pulsars, Astrophys. J. Suppl. **235**, 37 (2018), arXiv:1801.01837 [astro-ph.HE].

[2] E. Fonseca et al., The NANOGrav Nine-year Data Set: Mass and Geometric Measurements of Binary Millisecond Pulsars, Astrophys. J. **832**, 167 (2016), arXiv:1603.00545 [astro-ph.HE].

[3] P. Demorest, T. Pennucci, S. Ransom, M. Roberts, and J. Hessels, Shapiro Delay Measurement of A Two Solar Mass Neutron Star, Nature **467**, 1081 (2010), arXiv:1010.5788 [astro-ph.HE].

[4] H. T. Cromartie et al., Relativistic Shapiro delay measurements of an extremely massive millisecond pulsar, Nature Astron. **4**, 72 (2019), arXiv:1904.06759 [astro-ph.HE].

[5] E. Fonseca et al., Refined Mass and Geometric Measurements of the High-mass PSR J0740+6620, Astrophys. J. Lett. **915**, L12 (2021), arXiv:2104.00880 [astro-ph.HE].

[6] J. Antoniadis et al., A Massive Pulsar in a Compact Relativistic Binary, Science **340**, 6131 (2013), arXiv:1304.6875 [astro-ph.HE].

[7] B. Abbott et al. (LIGO Scientific, Virgo), GW170817: Observation of Gravitational Waves from a Binary Neutron Star Inspiral, Phys. Rev. Lett. **119**, 161101 (2017), arXiv:1710.05832 [gr-qc].

[8] M. C. Miller et al., The Radius of PSR J0740+6620 from NICER and XMM-Newton Data, Astrophys. J. Lett. **918**, L28 (2021), arXiv:2105.06979 [astro-ph.HE].

[9] T. E. Riley et al., A NICER View of the Massive Pulsar PSR J0740+6620 Informed by Radio Timing and XMM-Newton Spectroscopy, Astrophys. J. Lett. **918**, L27 (2021), arXiv:2105.06980 [astro-ph.HE].

[10] G. Raaijmakers, S. K. Greif, K. Hebeler, T. Hinderer, S. Nissanke, A. Schwenk, T. E. Riley, A. L. Watts, J. M. Lattimer, and W. C. G. Ho, Constraints on the dense matter equation of state and neutron star properties from NICER's mass-radius estimate of PSR J0740+6620 and

multimessenger observations, (2021), arXiv:2105.06981 [astro-ph.HE].
[11] C. Drischler, S. Han, and S. Reddy, Large and massive neutron stars: Implications for the sound speed within QCD of dense matter, Phys. Rev. C **105**, 035808 (2022), arXiv:2110.14896 [nucl-th].
[12] B. Sun, S. Bhattiprolu, and J. M. Lattimer, Compiled Properties of Nucleonic Matter and Nuclear and Neutron Star Models from Non-Relativistic and Relativistic Interactions, (2023), arXiv:2311.00843 [nucl-th].
[13] H. Togashi, K. Nakazato, Y. Takehara, S. Yamamuro, H. Suzuki, and M. Takano, Nuclear equation of state for core-collapse supernova simulations with realistic nuclear forces, Nucl. Phys. A **961**, 78 (2017), arXiv:1702.05324 [nucl-th].
[14] T. Kojo, QCD equations of state and speed of sound in neutron stars, AAPPS Bull. **31**, 11 (2021), arXiv:2011.10940 [nucl-th].
[15] Y. Fujimoto, K. Fukushima, L. D. McLerran, and M. Praszalowicz, Trace Anomaly as Signature of Conformality in Neutron Stars, Phys. Rev. Lett. **129**, 252702 (2022), arXiv:2207.06753 [nucl-th].
[16] D. T. Son and M. A. Stephanov, QCD at finite isospin density, Phys. Rev. Lett. **86**, 592 (2001), arXiv:hep-ph/0005225.
[17] D. T. Son and M. A. Stephanov, QCD at finite isospin density: From pion to quark - anti-quark condensation, Phys. Atom. Nucl. **64**, 834 (2001), arXiv:hep-ph/0011365.
[18] K. Splittorff, D. T. Son, and M. A. Stephanov, QCD - like theories at finite baryon and isospin density, Phys. Rev. D **64**, 016003 (2001), arXiv:hep-ph/0012274.
[19] K. Iida and E. Itou, Velocity of sound beyond the high-density relativistic limit from lattice simulation of dense two-color QCD, PTEP **2022**, 111B01 (2022), arXiv:2207.01253 [hep-ph].
[20] E. Itou and K. Iida, Speed of sound exceeding the conformal bound in dense 2-color QCD, in 40th International Symposium on Lattice Field Theory (2023) arXiv:2311.15259 [hep-lat].
[21] .
[22] R. Abbott, W. Detmold, F. Romero-López, Z. Davoudi, M. Illa, A. Parreño, R. J. Perry, P. E. Shanahan, and M. L. Wagman, Lattice quantum chromodynamics at large isospin density: 6144 pions in a box, (2023), arXiv:2307.15014 [hep-lat].
[23] R. Chiba and T. Kojo, Sound velocity peak and conformality in isospin QCD, (2023), arXiv:2304.13920 [hep-ph].
[24] P. Adhikari, J. O. Andersen, and M. A. Mojahed, Quark, pion and axial condensates in three-flavor finite isospin chiral perturbation theory, Eur. Phys. J. C **81**, 449 (2021), arXiv:2012.04339 [hep-ph].
[25] Z.-Y. Lu, C.-J. Xia, and M. Ruggieri, Thermodynamics and susceptibilities of isospin imbalanced QCD matter, Eur. Phys. J. C **80**, 46 (2020), arXiv:1907.11497 [hep-ph].
[26] A. Gómez Nicola and A. Vioque-Rodríguez, Effective Lagrangian at nonzero isospin chemical potential, Phys. Rev. D **106**, 114017 (2022), arXiv:2205.14609 [hep-ph].
[27] A. Sorensen et al., Dense Nuclear Matter Equation of State from Heavy-Ion Collisions, (2023), arXiv:2301.13253 [nucl-th].
[28] A. Lovato et al., Long Range Plan: Dense matter theory for heavy-ion collisions and neutron stars, (2022), arXiv:2211.02224 [nucl-th].
[29] M. Omana Kuttan, J. Steinheimer, K. Zhou, and H. Stoecker, QCD Equation of State of Dense Nuclear Matter from a Bayesian Analysis of Heavy-Ion Collision Data, Phys. Rev. Lett. **131**, 202303 (2023), arXiv:2211.11670 [hep-ph].
[30] N. Yao, A. Sorensen, V. Dexheimer, and J. Noronha-Hostler, Structure in the speed of sound: from neutron stars to heavy-ion collisions, (2023), arXiv:2311.18819 [nucl-th].
[31] S. Blacker, A. Bauswein, and S. Typel, Exploring thermal effects of the hadron-quark matter transition in neutron star mergers, Phys. Rev. D **108**, 063032 (2023), arXiv:2304.01971 [astro-ph.HE].
[32] K. Masuda, T. Hatsuda, and T. Takatsuka, Hadron-Quark Crossover and Massive Hybrid Stars with Strangeness, Astrophys. J. **764**, 12 (2013), arXiv:1205.3621 [nucl-th].
[33] K. Masuda, T. Hatsuda, and T. Takatsuka, Hadron–quark crossover and massive hybrid stars, PTEP **2013**, 073D01 (2013), arXiv:1212.6803 [nucl-th].
[34] K. Masuda, T. Hatsuda, and T. Takatsuka, Hyperon Puzzle, Hadron-Quark Crossover and Massive Neutron Stars, Eur. Phys. J. A **52**, 65 (2016), arXiv:1508.04861 [nucl-th].
[35] T. Kojo, P. D. Powell, Y. Song, and G. Baym, Phenomenological QCD equation of state for massive neutron stars, Phys. Rev. D **91**, 045003 (2015), arXiv:1412.1108 [hep-ph].
[36] T. Kojo, Phenomenological neutron star equations of state: 3-window modeling of QCD matter, Eur. Phys. J. A **52**, 51 (2016), arXiv:1508.04408 [hep-ph].
[37] G. Baym, T. Hatsuda, T. Kojo, P. D. Powell, Y. Song, and T. Takatsuka, From hadrons to quarks in neutron stars: a review, Rept. Prog. Phys. **81**, 056902 (2018), arXiv:1707.04966 [astro-ph.HE].
[38] G. Baym, S. Furusawa, T. Hatsuda, T. Kojo, and H. Togashi, New Neutron Star Equation of State with Quark-Hadron Crossover, Astrophys. J. **885**, 42 (2019), arXiv:1903.08963 [astro-ph.HE].
[39] T. Kojo, G. Baym, and T. Hatsuda, Implications of NICER for Neutron Star Matter: The QHC21 Equation of State, Astrophys. J. **934**, 46 (2022), arXiv:2111.11919 [astro-ph.HE].
[40] Y.-J. Huang, L. Baiotti, T. Kojo, K. Takami, H. Sotani, H. Togashi, T. Hatsuda, S. Nagataki, and Y.-Z. Fan, Merger and Postmerger of Binary Neutron Stars with a Quark-Hadron Crossover Equation of State, Phys. Rev. Lett. **129**, 181101 (2022), arXiv:2203.04528 [astro-ph.HE].
[41] Y. Fujimoto, K. Fukushima, K. Hotokezaka, and K. Kyutoku, Gravitational Wave Signal for Quark Matter with Realistic Phase Transition, Phys. Rev. Lett. **130**, 091404 (2023), arXiv:2205.03882 [astro-ph.HE].
[42] A. Kedia, H. I. Kim, I.-S. Suh, and G. J. Mathews, Binary neutron star mergers as a probe of quark-hadron crossover equations of state, Phys. Rev. D **106**, 103027 (2022), arXiv:2203.05461 [gr-qc].
[43] R. Harada, K. Cannon, K. Hotokezaka, and K. Kyutoku, On the Testability of the Quark-Hadron Transition Using Gravitational Waves From Merging Binary Neutron Stars, (2023), arXiv:2310.13603 [astro-ph.HE].
[44] P. Adhikari, J. O. Andersen, and P. Kneschke, On-shell parameter fixing in the quark-meson model, Phys. Rev. D **95**, 036017 (2017), arXiv:1612.03668 [hep-ph].

[45] P. Adhikari, J. O. Andersen, and P. Kneschke, Pion condensation and phase diagram in the Polyakov-loop quark-meson model, Phys. Rev. D **98**, 074016 (2018), arXiv:1805.08599 [hep-ph].

[46] S. Roessner, T. Hell, C. Ratti, and W. Weise, The chiral and deconfinement crossover transitions: PNJL model beyond mean field, Nucl. Phys. A **814**, 118 (2008), arXiv:0712.3152 [hep-ph].

[47] A. M. Polyakov, Thermal Properties of Gauge Fields and Quark Liberation, Phys. Lett. B **72**, 477 (1978).

[48] K. Fukushima and V. Skokov, Polyakov loop modeling for hot QCD, Prog. Part. Nucl. Phys. **96**, 154 (2017), arXiv:1705.00718 [hep-ph].

[49] K. Fukushima, Chiral effective model with the Polyakov loop, Phys. Lett. B **591**, 277 (2004), arXiv:hep-ph/0310121.

[50] S. Roessner, C. Ratti, and W. Weise, Polyakov loop, diquarks and the two-flavour phase diagram, Phys. Rev. D **75**, 034007 (2007), arXiv:hep-ph/0609281.

[51] B.-J. Schaefer, J. M. Pawlowski, and J. Wambach, The Phase Structure of the Polyakov–Quark-Meson Model, Phys. Rev. D **76**, 074023 (2007), arXiv:0704.3234 [hep-ph].

[52] T. Kojo and G. Baym, Color screening in cold quark matter, Phys. Rev. D **89**, 125008 (2014), arXiv:1404.1346 [hep-ph].

[53] D. Suenaga and T. Kojo, Gluon propagator in two-color dense QCD: Massive Yang-Mills approach at one-loop, Phys. Rev. D **100**, 076017 (2019), arXiv:1905.08751 [hep-ph].

[54] T. Kojo and D. Suenaga, Thermal quarks and gluon propagators in two-color dense QCD, Phys. Rev. D **103**, 094008 (2021), arXiv:2102.07231 [hep-ph].

[55] R. Contant and M. Q. Huber, Dense two-color QCD from Dyson-Schwinger equations, Phys. Rev. D **101**, 014016 (2020), arXiv:1909.12796 [hep-ph].

[56] T. Boz, O. Hajizadeh, A. Maas, and J.-I. Skullerud, Finite-density gauge correlation functions in QC2D, Phys. Rev. D **99**, 074514 (2019), arXiv:1812.08517 [hep-lat].

[57] V. G. Bornyakov, V. V. Braguta, A. A. Nikolaev, and R. N. Rogalyov, Effects of Dense Quark Matter on Gluon Propagators in Lattice QC_2D, Phys. Rev. D **102**, 114511 (2020), arXiv:2003.00232 [hep-lat].

[58] K. Fukushima and K. Kashiwa, Polyakov loop and QCD thermodynamics from the gluon and ghost propagators, Phys. Lett. B **723**, 360 (2013), arXiv:1206.0685 [hep-ph].

[59] B. Ananthanarayan, I. Caprini, and D. Das, Electromagnetic charge radius of the pion at high precision, Phys. Rev. Lett. **119**, 132002 (2017), arXiv:1706.04020 [hep-ph].

[60] M. Tanabashi *et al.* (Particle Data Group), Review of particle physics, Phys. Rev. D **98**, 030001 (2018).

[61] J. Koponen, F. Bursa, C. T. H. Davies, R. J. Dowdall, and G. P. Lepage, Size of the pion from full lattice QCD with physical u , d , s and c quarks, Phys. Rev. D **93**, 054503 (2016), arXiv:1511.07382 [hep-lat].

[62] G. Wang, J. Liang, T. Draper, K.-F. Liu, and Y.-B. Yang (chiQCD), Lattice Calculation of Pion Form Factor with Overlap Fermions, Phys. Rev. D **104**, 074502 (2021), arXiv:2006.05431 [hep-ph].

[63] M. Hippert, E. S. Fraga, and J. Noronha, Insights on the peak in the speed of sound of ultradense matter, Phys. Rev. D **104**, 034011 (2021), arXiv:2105.04535 [nucl-th].

[64] M. Kawaguchi and D. Suenaga, Sound velocity peak induced by the chiral partner in dense two-color QCD, (2024), arXiv:2402.00430 [hep-ph].

[65] T. Kojo, Stiffening of matter in quark-hadron continuity, Phys. Rev. D **104**, 074005 (2021), arXiv:2106.06687 [nucl-th].

[66] T. Kojo and D. Suenaga, Peaks of sound velocity in two color dense QCD: Quark saturation effects and semishort range correlations, Phys. Rev. D **105**, 076001 (2022), arXiv:2110.02100 [hep-ph].

[67] Y. Fujimoto, T. Kojo, and L. D. McLerran, Momentum Shell in Quarkyonic Matter from Explicit Duality: A Solvable Model Analysis, (2023), arXiv:2306.04304 [nucl-th].

[68] D. Suenaga, K. Murakami, E. Itou, and K. Iida, Probing the hadron mass spectrum in dense two-color QCD with the linear sigma model, Phys. Rev. D **107**, 054001 (2023), arXiv:2211.01789 [hep-ph].

[69] K. Murakami, D. Suenaga, K. Iida, and E. Itou, Measurement of hadron masses in 2-color finite density QCD, PoS **LATTICE2022**, 154 (2023), arXiv:2211.13472 [hep-lat].

[70] D. Suenaga, K. Murakami, E. Itou, and K. Iida, Mass spectrum of spin-one hadrons in dense two-color QCD: Novel predictions by extended linear sigma model, (2023), arXiv:2312.17017 [hep-ph].

Electroweak metastability and Higgs inflation

Isabella Masina *[1,2] and Mariano Quiros †[3]

[1] *Dept. of Physics and Earth Science, Ferrara University, Via Saragat 1, 44122 Ferrara, Italy*
[2] *Istituto Nazionale di Fisica Nucleare (INFN), Sez. di Ferrara, Via Saragat 1, 44122 Ferrara, Italy*
[3] *Institut de Física d'Altes Energies (IFAE) and The Barcelona Institute of Science and Technology (BIST), Campus UAB, 08193 Bellaterra (Barcelona) Spain*

arXiv:2403.02461v1 [hep-ph] 4 Mar 2024

Abstract

Extrapolating the Standard Model Higgs potential at high energies, we study the barrier between the electroweak and Planck scale minima. The barrier arises by taking the central values of the relevant experimental inputs, that is the strong coupling constant and the top quark and Higgs masses. We then extend the Standard Model by including a non-minimal coupling to gravity, and explore the phenomenology of the Higgs inflation model. We point out that even configurations that would be metastable in the Standard Model, become viable for inflation if the non-minimal coupling is large enough to flatten the Higgs potential at field values below the barrier; we find that the required value of the non-minimal coupling is smaller than the one needed for the conventional Higgs inflation scenario (which relies on a stable Standard Model Higgs potential, without any barrier); in addition, values of the top mass which are slightly larger than those required in the conventional scenario are allowed.

1 Introduction

In the pure Standard Model (SM), and depending on the value of the electroweak parameters, there is the possibility of having a second minimum at high energies [1–3]. As it is well known, the experimental data suggest that the electroweak vacuum is likely to be metastable rather than stable [4–7], although it will be difficult to exclude stability in future [8, 9]. The study of the shape of the Higgs effective potential at high energy is a relevant issue, also in view of the possible role of the Higgs field as the inflaton; for this sake, a region where the Higgs potential becomes sufficiently flat, for large enough values of the Higgs field, to meet the slow-roll conditions would be required.

In this paper, we will first reconsider the analysis of stability and metastability of the SM electroweak vacuum, in view of the most recent experimental results and theoretical developments; and secondly, we will do it for the case where the Higgs is non-minimally coupled to gravity. For the central values of the relevant experimental inputs, which are the strong coupling constant with five flavors, $\alpha_s^{(5)}$, the top quark pole mass, m_t, and the Higgs mass, m_H, in the SM potential a barrier arises between the electroweak minimum and a second high scale minimum. We study in detail the phenomenology of such a barrier, as its height and position. Fixing $\alpha_s^{(5)}$

*masina@fe.infn.it
†quiros@ifae.es

and m_H to their central values, there is a particular value of the top mass, m_t^i, corresponding to a stable inflection point configuration: for any $m_t > m_t^i$ the barrier thus takes place [10]. In particular, the electroweak and Planck scale vacua are degenerate for the critical value m_t^c [3].

The possibility of having an inflection point, or a shallow vacuum configuration, attracted interest in view of cosmological applications: rolling down [11, 12], or being trapped into such configurations [13–16], the Higgs field might in principle induce a stage of primordial inflation. It was shown that this scenario cannot however account for the observed cosmological parameters [17] (see also [18] for previous related ideas). Extensions of the SM are thus needed. For instance, by introducing a non-minimal coupling to gravity, ξ, that flattens the Higgs potential at field values larger than about $M_P/\sqrt{\xi}$, where $M_P = 1/\sqrt{8\pi G_N}$ is the reduced Planck scale; in this way, the Higgs might successfully play the role of the inflaton [19].

We thus secondly introduce a non-minimal coupling to gravity, $\xi|\mathcal{H}|^2 R$, and study in detail how the Higgs potential is modified. We do this for stable configurations without any barrier ($m_t < m_t^i$), as traditionally done in the previous literature [19–28], as well as for configurations with the barrier. The latter are both the stable configurations where the second minimum is higher than the electroweak one (such that $m_t^c > m_t > m_t^i$), and the metastable configurations where the second minimum is rather deeper than the electroweak one ($m_t > m_t^c$).

SM stable configurations without barrier require low values of the top pole mass, m_t; according to our analysis, they correspond to the lower 2σ range of the PDG 2022 world average $m_t = 172.5$ GeV [29]. In this case, as well known, large values of $\xi = O(10^4)$ are required in order to fit the cosmological observables derived from the cosmic microwave background (CMB) data [19–28]. We revisit this calculation and study in detail the dependence of ξ on the top mass.

For SM stable configurations with the barrier, *i.e.* for $m_t^c > m_t > m_i^t$, we find that the barrier at its maximum turns out to be larger than the upper limit on the inflaton potential coming from CMB data. Then, configurations as an inflection point, or a shallow minimum, are not viable for inflation [17], unless modifying the potential. We show that, including a non-minimal coupling to gravity, these configurations can be flattened at field values smaller than those of the barrier, and Higgs inflation can successfully be realized.

For SM metastable configurations, *i.e.* for $m_t > m_t^c$, we find that, for a suitable range of values of the non-minimal coupling ξ, it is possible to avoid the second high energy minimum of the Higgs potential: this happens when the potential is flattened before the barrier, so that it stays frozen to positive values in the region where the high energy minimum would take place. We then focus on Higgs inflation in the case of metastable configurations, a scenario that, to the best of our knowledge, has not been previously studied. In particular, we find that the values of ξ which are required for successful inflation are even slightly smaller than those required in the well-studied case of stable configurations without barriers. As a result, values of the top mass which are slightly larger than those required in the conventional Higgs inflation scenario are allowed.

The paper is organized as follows. In Sec. 2 we study the running of the SM parameters and review the derivation of the Higgs effective potential. In Sec. 3 we discuss the phenomenology of the barrier between the electroweak and Planck scale minimum. In Sec. 4 we review the SM extension with a non-minimal coupling to gravity, including radiative corrections. In Sec. 5 the values of ξ required to avoid metastability are discussed. In Sec. 6 we discuss the phenomenology of Higgs inflation for both stable and metastable configurations. In Sec. 7 we draw our conclusions.

2 The running SM parameters

In this section we review the steps required to extrapolate the SM couplings at high energies. The physical Higgs boson field ϕ belongs to the complex scalar Higgs doublet, $\mathcal{H} = e^{i\vec{\chi}\cdot\vec{\sigma}}(0, (\phi + v)/\sqrt{2})^T$, where $\vec{\chi}$ are the Goldstone bosons and v is the electroweak scale. The tree-level Higgs potential is given by

$$V(\phi) = \frac{\lambda}{6}\left(|\mathcal{H}|^2 - \frac{v^2}{2}\right)^2 = \frac{\lambda}{24}\phi^4 + \frac{\lambda}{6}\phi^3 v + \frac{\lambda}{6}\phi^2 v^2 \,, \tag{1}$$

where we adopt Ford, Jack and Jones conventions for the Higgs quartic coupling λ in Ref. [30]. The tree-level relations for the masses of the Higgs boson and fermions f are given by $m_H^2 = \lambda v^2/3$ and $m_f = h_f v/\sqrt{2}$, where h_f denotes the fermion Yukawa coupling.

To go beyond the tree-level, we adopt the $\overline{\text{MS}}$ scheme and extrapolate the Higgs effective potential, $V_{\text{eff}}(\phi)$, at very high energies. We will consider the matching and the renormalization group equations (RGE) evolution of the relevant couplings which, in addition to λ, are: the three gauge couplings, g, g', g_s, the top Yukawa coupling, h_t, and the anomalous dimension of the Higgs field, γ. In the effective potential at large values of ϕ, potentially large logarithms appear of the type $\log(\phi/\mu)$, where μ is the renormalization scale. To not spoil the applicability of perturbation theory, they are treated by means of the renormalization group equations. For fixed values of the bare parameters, the effective potential must be independent of the renormalization scale μ [31]. The formal solution of the RGE is

$$V_{\text{eff}}(\mu, \lambda_i, \phi) = V_{\text{eff}}(\mu(t), \lambda_i(t), \phi(t)) \,, \tag{2}$$

where i stands for each one of the SM couplings λ_i, γ is the background field anomalous dimension and

$$\mu(t) = e^t \mu \,,\ \phi(t) = e^{\Gamma(t)}\phi \,,\ \Gamma(t) = -\int_0^t \gamma(\lambda(t'))dt' \,. \tag{3}$$

The running of the SM couplings, $\lambda_i(t)$, is thus specified by the β-function equations

$$\frac{d\lambda_i(t)}{dt} = \beta_i(\lambda_i(t)) \,, \tag{4}$$

and subject to the boundary conditions $\lambda_i(0) = \lambda_i$. We now turn to the issue of the boundary conditions to be given at the low energy matching scale $\mu(0) = \mu$.

2.1 Matching

In order to obtain the values of the relevant parameters (g, g', g_s, h_t and λ) at the matching scale $\mu(0)$, we exploit the results of a recent detailed analysis performed by Alam and Martin in Ref. [32], where $\mu(0) = 200$ GeV and the data from the PDG 2022 review are considered [29]. While uncertainties in the matching of $g(0)$ and $g'(0)$ are negligible, the most significant uncertainties are those associated with $g_s(0)$, $h_t(0)$ and $\lambda(0)$.

Simplified expressions which capture the dominant dependences and sources of uncertainty for the latter three couplings can be found in [32], and each of them is at present dominated by the experimental error in the related observable. In this way, the uncertainty in the value of $g_s(0)$ is dominated by the experimental error on the value of the strong coupling constant at m_Z in the SM with five flavors, $\alpha_s^{(5)}$; the uncertainties in $\lambda(0)$ and $h_t(0)$ are dominated by the

experimental error respectively on the Higgs mass, m_H, and the top pole mass, m_t. One gets from [32]:

$$g_s(0) \simeq 1.15251 \left(1 + 0.00378 \, \frac{\alpha_s^{(5)} - 0.1179}{10^{-3}}\right) \ , \tag{5}$$

$$\lambda(0)/6 \simeq 0.123533 \left(1 + 0.001682 \, \frac{m_H - 125.25\,\text{GeV}}{0.1\,\text{GeV}}\right) \ , \tag{6}$$

$$h_t(0) \simeq 0.23777 \left(1 + 0.006352 \, \frac{m_t - 172.5\,\text{GeV}}{1\,\text{GeV}}\right) \ . \tag{7}$$

In the present work, we use the PDG 2022 [29] world averages for the mean values and 1σ errors: $\alpha_s^{(5)\,\text{exp}} = 0.1179$ and $\Delta\alpha_s^{(5)} = 0.0009$; $m_H^{\text{exp}} = 125.25$ GeV and $\Delta m_H = 0.17$ GeV; $m_t^{\text{exp}} = 172.5$ and $\Delta m_t = 0.7$ GeV. Our lower 2σ and 3σ values for m_t are thus respectively 171.1 GeV and 170.4 GeV.

As it is well known, the experimental determination of the top pole mass is a delicate and debated issue. Considering direct measurements, the PDG 2022 world average in the Top Quark Listings [29] is $m_t = 172.76 \pm 0.30$ GeV. In addition to the latter experimental error one should also include the theoretical error taking into account any difference between the top pole mass, m_t, and the mass parameter implemented in the Monte Carlo event generators employed by the experimental groups, estimated to be $\Delta m_t^{MC} = \pm 0.52$ GeV [29]. The September 2023 ATLAS and CMS combined analysis from data collected at $\sqrt{s} = 7$ and 8 TeV gave $m_t = 172.52 \pm 0.33$ GeV [33]. Considering instead cross-section measurements, the PDG 2022 world average in the Top Quark Listings [29] is $m_t = 172.5 \pm 0.7$ GeV. According to the recent analysis by [34], the updated result from cross-section measurements gives a smaller value, $m_t = 171.54^{+0.28}_{-0.31}$ GeV; the central value of the latter being about 1.5σ below the corresponding PDG 2022 central value.

2.2 Running

The β-functions can be organized as a sum of contributions with increasing number of loops:

$$\frac{d}{dt}\lambda_i(t) = \kappa\beta_{\lambda_i}^{(1)} + \kappa^2\beta_{\lambda_i}^{(2)} + \kappa^3\beta_{\lambda_i}^{(3)} + \dots \, , \tag{8}$$

where $\kappa = 1/(16\pi^2)$ and the apex on the β-functions represents the loop order. Here, we are interested in the RGE dependence of the couplings g, g', g_s, h_t, λ, γ.

The one-loop and two-loop expressions for the β-functions in the SM are well known and can be found, for instance, in Ref. [30]. The complete three-loop β-functions for the SM have been computed in Refs. [35–42]. The dominant four-loop contribution to the running of the strong gauge coupling has also been computed in Refs. [43, 44]. There are recent results about the four-loop β-functions: the leading four-loop QCD contribution to the β-function of the Higgs self coupling has been derived in [45], while the full four-loop β-functions for the gauge couplings have been given in [46]. We checked that, for the sake of our analysis, it is enough to work up to three-loop, as the four-loop contribution has a negligible impact.

As it is well known, the central values of m_t, $\alpha_s^{(5)}$ and m_H suggest that λ has a small negative minimum at high energies. The left panel of Fig. 1 shows the behavior of λ for the central values previously mentioned (solid central line), and its variation associated to the 1σ range for m_t (blue), $\alpha_s^{(5)}$ (orange) and m_H (green). Notice that the variation associated to the 1σ error in m_H is the less significant one. An increase by $+(-)1\sigma$ in a parameter corresponds to the corresponding solid (dashed) curve. Although the central values of the input parameters favor negative values for λ above $\mu(t) \sim 10^{11}$ GeV, one can see that stability is allowed within 2σ.

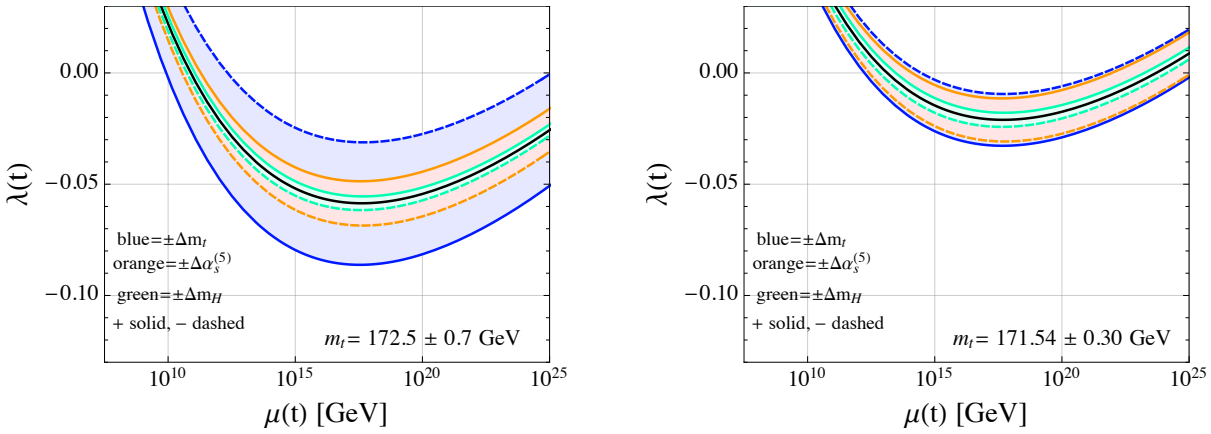


Figure 1: *Evolution of λ and its experimental variations. Left: We use the PGD 2022 [29] world averages for the mean values and the 1σ errors. Right: The same, but adopting the range for m_t suggested in [34].*

Stability is even more favored adopting the results for m_t according to the analysis by Garzelli et al. in Ref. [34], as shown in the right plot of Fig. 1. In the future it might be difficult to exclude stability in a robust way, given the challenges associated to a precise determination of m_t [8].

It is common to identify the instability scale with the scale where $\lambda(t)$ goes negative. However, the instability scale is, strictly speaking, the renormalization scale where the effective potential turns negative, so that a detailed calculation of the effective potential is relevant.

2.3 The Higgs effective potential

The RGE-improved effective potential at high field values can be expanded as a sum of tree-level plus increasing loop contributions. The one-loop contribution has been computed by Coleman and Weinberg in Ref. [47]; the two-loop contribution was derived by Ford, Jack and Jones in Ref. [30] and cast in a more compact form in Refs. [4, 6]. Recently, there have been additional refinements extending the calculation of the effective potential to three-loop [48] and to the leading four-loop QCD contribution [49].

We adopt here the procedure outlined in [50]; however (as already done in Refs. [10, 17], to which we refer for more details), we prefer to work with the wave-function renormalized field, $\phi(t)$, instead of the classical one, ϕ. Explicitly, in the Landau gauge:

$$V_{\rm eff} = V^{(0)} + V^{(1)} + V^{(2)} + \dots \ , \tag{9}$$

where

$$V^{(0)} = \frac{\lambda(t)}{24}\phi^4(t) \ , \tag{10}$$

$$\begin{aligned} V^{(1)} &= \frac{1}{24}\frac{6}{(4\pi)^2}\left[6\left(\frac{g^2(t)}{4}\right)^2\left(\log\frac{\frac{g^2(t)}{4}\phi^2(t)}{\mu^2(t)} - \frac{5}{6}\right)\right. \\ &+ 3\left(\frac{g^2(t)+g'^2(t)}{4}\right)^2\left(\log\frac{\frac{g^2(t)+g'^2(t)}{4}\phi^2(t)}{\mu^2(t)} - \frac{5}{6}\right) \\ &- \left. 12\left(\frac{h_t^2(t)}{2}\right)^2\left(\log\frac{\frac{h_t^2(t)}{2}\phi^2(t)}{\mu^2(t)} - \frac{3}{2}\right)\right]\phi^4(t)\,, \end{aligned} \tag{11}$$

while $V^{(2)}$ can be explicitly found in [4, 6]. For large values of the Higgs field $\phi(t) \gg v$ we are only keeping the quartic coupling in the tree-level potential.

The RGE-improved effective potential is gauge dependent. However the Nielsen identity [51] guarantees that the effective potential is gauge independent where it is stationary. This happens for instance for the critical configuration with two degenerate vacua [3], and for an inflection point configuration. On the other hand, the values of the low energy input parameters, as m_t, m_H and $\alpha_s^{(5)}$, ensuring stationary configurations are gauge independent [10]. Thus, working in the Landau gauge is perfectly consistent in order to calculate the value of the effective potential at a stationary point, call it V_s, or the value of the input parameters providing it.

Nevertheless, one has to be aware that the truncation of the effective potential loop expansion, at some loop order, introduces an unavoidable theoretical error both in V_s and in the input parameters. For this sake, it is useful to introduce the parameter α via $\mu(t) = \alpha\,\phi(t)$ and study how the observables depend on it [52]. The higher the order of the considered loop expansion, the milder the V_s dependence on α, as shown explicitly in [10] for the cases of two degenerate vacua and a rising inflection point; in particular, the value of α for which the one-loop and two-loop (which is almost α-independent) expressions for V_s (and the input parameters) agree is $\alpha \simeq 0.3$. In the following we work at two-loop order taking $\alpha = 1$.

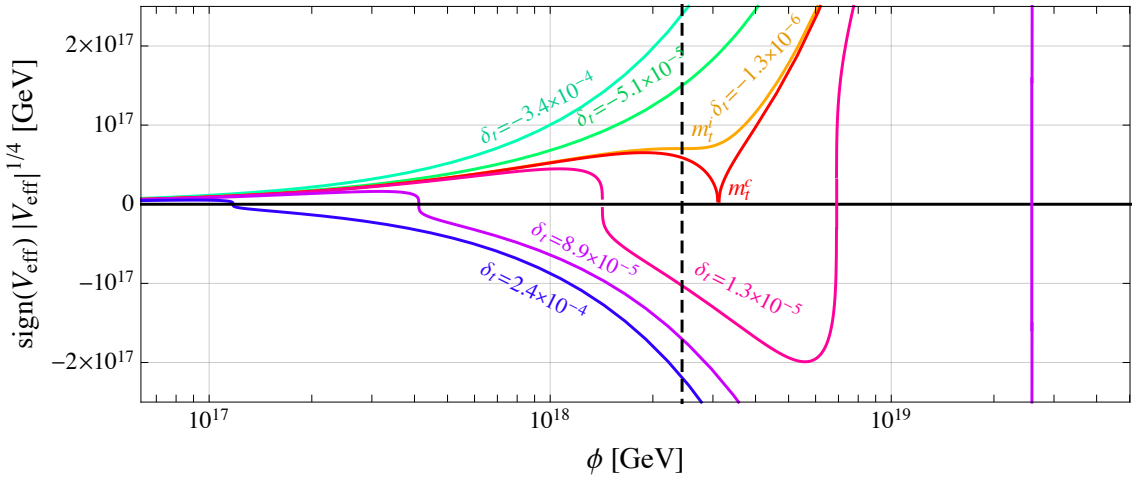


Figure 2: *Illustrative shapes for the effective potential at high energies. Central values of m_H and $\alpha_s^{(5)}$ are assumed; various values of the top mass are considered, which increase going from top to bottom. The vertical dashed line shows the value of the reduced Planck mass.*

Possible shapes of the effective potential are illustrated in Fig. 2, for central values of m_H and $\alpha_s^{(5)}$ and increasing values of the top mass, going from top to bottom. The selected values of the top mass include the critical value m_t^c corresponding to two degenerate vacua and the value corresponding to an inflection point, m_t^i. Since a tiny variation in the top mass corresponds to a drastic change in the shape of the potential for values of m_t close to m_t^c, it is useful to introduce the fractional deviation from criticality, δ_t, as

$$m_t = m_t^c\,(1 + \delta_t) \quad . \tag{12}$$

Focussing on the critical configuration (for the central values of m_H and $\alpha_s^{(5)}$ discussed previously and considered in Fig. 2), it turns out that: $m_t^c \simeq 171.0588$ GeV, close to the lower 2σ value of the PDG 2022, that is 171.1 GeV; the second degenerate minimum takes place

at $\phi_c \approx 3 \times 10^{18}$ GeV, slightly beyond the reduced Planck mass (vertical dashed line); the maximum of the potential barrier between the electroweak and second degenerate minimum is $V_B^{1/4} \approx 6 \times 10^{16}$ GeV and takes place at $\phi_B \approx 2 \times 10^{18}$ GeV. For an inflection point configuration one has $\delta_t \simeq -1.3 \times 10^{-6}$. Notice that the PDG 2022 central and lower 2σ values of m_t correspond respectively to $\delta_t = 8.4 \times 10^{-3}$ and $\delta_t = 2.4 \times 10^{-4}$; the latter corresponds to the bottom curve in Fig. 2.

3 The barrier between the two minima

For $m_t \leq m_t^i$, the Higgs effective potential is stable and monotonously increasing with ϕ. For $m_t \geq m_t^i$, the potential displays a second minimum at high energies. We now study in detail the features of the barrier separating the two minima. This applies to stable ($m_t^i \leq m_t \leq m_t^c$) as well as to metastable ($m_t > m_t^c$) configurations, for which the high energy minimum is higher or deeper than the electroweak one, respectively.

3.1 The barrier for metastable configurations

The (non gauge invariant) value where the deepest minimum takes place, ϕ_B, is shown in the left plot of Fig. 3 as a function of m_t. The central line corresponds to the mean values of the inputs as discussed previously, and the band shows the impact of the 1σ experimental errors. As for the instability scale, one defines the parameter t_V by means of the constraint $V_{eff}(t_V) = 0$. The corresponding value of the Higgs field is $\phi(t_V)$ (which is not gauge invariant); it turns out that $\phi(t_V) = 1.29\,\phi_B$. The value of the Higgs potential at the top of a barrier, V_B, is a gauge

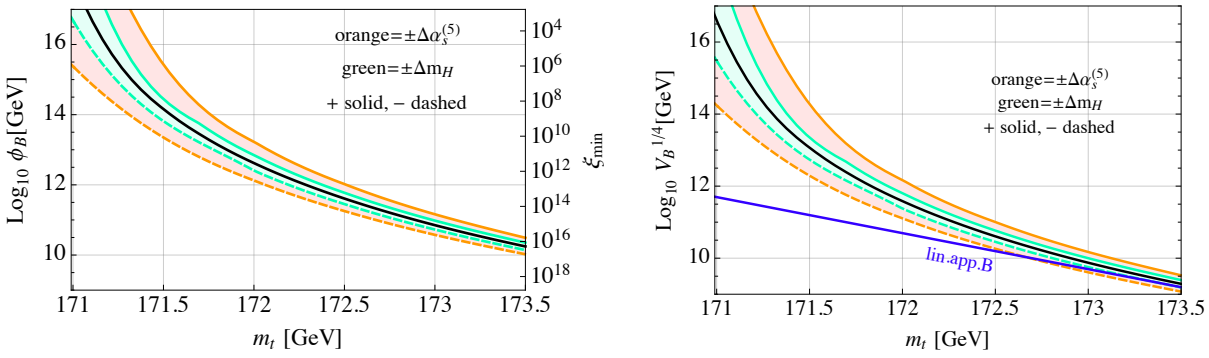


Figure 3: *The position (left) and the value (right) of the barrier between the electroweak and high energy minima. The solid line corresponds to the central values of the inputs according to PDG 2022 [29]; the inner (green) and the outer (orange) bands show the effect of the* 1σ *variation in* m_H *and* $\alpha_s^{(5)}$ *respectively. Also shown is the linear approximation of Buttazzo et al. [6]. The quantity* ξ_{min} *(right vertical axis of the left plot) will be introduced in the following.*

invariant quantity, as it corresponds to a stationary configuration. We plot it in the right panel of Fig. 3, as a function of m_t. To the best of our knowledge, the dependence of V_B on m_t has not been studied in such detail so far. Previously, a linear approximation was derived by Buttazzo et al. [6] (see also [8]), which is included for comparison in the plot; such approximation was derived in view of large values of m_t, so it fails for $m_t \lesssim 172.5$ GeV.

The magnitude of V_B is relevant in view of applications of the Higgs potential in the context of Higgs inflation. It is tempting to precisely exploit the Higgs potential for inflation, and interpret the Higgs directly as the inflaton. There are already constraints on this hypothesis: from the CMB data one can derive an upper bound on the potential responsible for inflation. We briefly review this argument later in this section.

3.2 The barrier for stable configurations

We now focus on stable configurations, *i.e.* from the configuration with two degenerate vacua to the configuration with an inflection point. Once m_H and $\alpha_s^{(5)}$ have been fixed, the critical value of m_t for which the SM displays two degenerate vacua, m_t^c, is a gauge invariant quantity. This value has been studied in many works, often showing the critical top mass line (separating the stability and metastability regions) as a function of the Higgs mass [4–7].

Given the impressive precision achieved on m_H, it is by now more useful to plot the critical top mass line as a function of $\alpha_s^{(5)}$, as done in the upper panel of Fig. 4, where we can see the mild variation induced by varying m_H within 1σ. The shaded rectangles display the 1σ and 2σ variations in m_t and in $\alpha_s^{(5)}$, according to the PDG 2022. The criticality line is inside the lower right corner of the 2σ rectangle [1]. This shows that stability is at present compatible with experimental data, and that it will be challenging to robustly support metastability in future [8].

In the left bottom panel of Fig. 4 we display, always for a critical configuration, the value of ϕ_c, where the high energy minimum takes place (notice that it can be slightly beyond the reduced Planck scale, which is about 2.4×10^{18} GeV). The barrier separating the electroweak and the second degenerate minimum at ϕ_c has a maximum at ϕ_B, which is also displayed in the same panel (and turns out to be slightly lower than the reduced Planck scale). The height of the barrier, $V_B^{1/4}$, is displayed in the right bottom panel of Fig. 4; it turns out to be just below the Planck scale. Notice that $V_B^{1/4}$, ϕ_c and ϕ_B all decrease when increasing $\alpha_s^{(5)}$. As can be seen from the plots, the central values for the parameters characterizing a critical configuration are: $\phi_c \approx 3 \times 10^{18}$ GeV, $\phi_B \approx 2 \times 10^{18}$ GeV, $V_B^{1/4} \approx 6 \times 10^{16}$ GeV. The latter scale cannot be much reduced by changing the input parameters: considering the upper 2σ value of $\alpha_s^{(5)}$, one cannot achieve a value smaller than $V_B^{1/4} \approx 4.5 \times 10^{16}$ GeV.

Notice that, for any value of the top mass in the range $m_t^i \leq m_t \leq m_t^c$ (from a degenerate second minimum to the case of an inflection point configuration), the values of ϕ_B and V_B are practically the same as those indicated in Fig. 4.

3.3 Constraints on the height of the barrier from CMB

In the following, we review the constraints provided by the CMB on the inflationary potential, U_i, in view of a possible identification of the Higgs with the inflaton field. We introduce a bar over a quantity to indicate that it is written in units of the reduced Planck mass, $M_P \simeq 2.43 \times 10^{18}$ GeV, and introduce the subscript i for a quantity to be calculated at the beginning of inflation, say $50-60$ e-folds before its end. According to the PDG 2022 review on cosmological parameters [29], the observed amplitude of the density fluctuations is given by

$$2.1 \times 10^{-9} \approx \Delta_R^2 = \frac{\bar{H}_i^2}{8\pi^2 \epsilon_i} = \frac{2\bar{U}_i}{3\pi^2 r} \ , \tag{13}$$

where in the last equality we exploited the relation $\bar{H}_i^2 = \bar{U}_i/3$, where H_i is the Hubble constant, and assumed a slow-roll phase, for which the tensor-to-scalar ratio is $r = 16\,\epsilon_i$. The constraint

[1] Our results agree with the recent work [9].

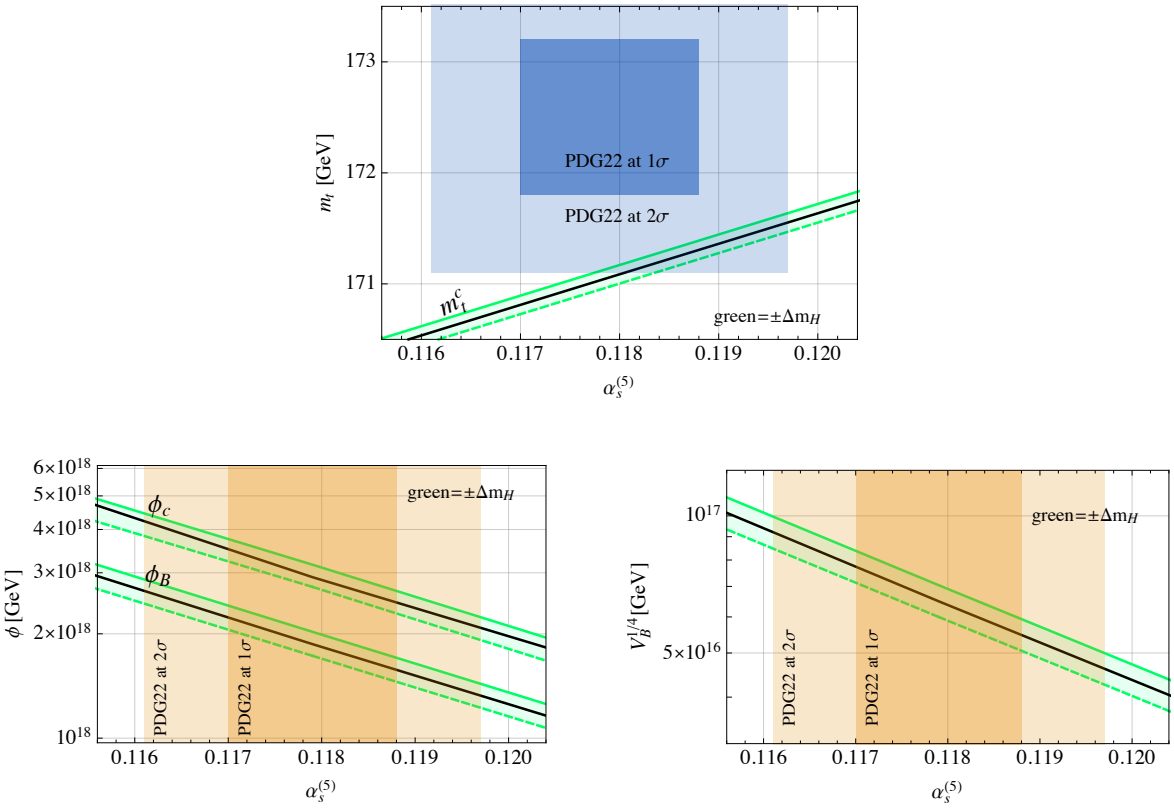


Figure 4: *Two degenerate vacua (critical configuration). As a function of* $\alpha_s^{(5)}$*, we display* m_t^c *(top panel),* ϕ_c *and* ϕ_B *(bottom left panel),* $V_B^{1/4}$ *(bottom right panel). The solid lines correspond to the central values of the inputs according to PDG 2022 [29]; the (green) band shows the impact of the* 1σ *experimental error in* m_H*. The shaded (blue and orange) regions display the* 1σ *and* 2σ *ranges for* m_t *and* $\alpha_s^{(5)}$ *respectively.*

on the inflationary potential is thus

$$\bar{U}_i^{1/4} \equiv \frac{U_i^{1/4}}{M_P} = \left(\frac{3}{2}\pi^2\, r\, \Delta_R^2\right)^{1/4} \approx 1.3 \times 10^{-2}\; r^{1/4}\;. \tag{14}$$

The most recent analysis of the BICEP, Keck Array and Planck data [53] places an upper bound on the tensor-to-scalar ratio $r < 0.036$ at the 95% CL, so that from the equation above one gets $U_i^{1/4} < 2.5 \times 10^{16}$ GeV. Assuming that r is not far from being detected, the scale of $U_i^{1/4}$ should correspond to the GUT scale.

It is worth emphasizing that the previous quantities like ϕ_c, ϕ_B and V_B do depend just on the SM parameters, and have nothing to do with gravity. For metastable configurations Fig. 3 shows for which values of the input parameters $V_B^{1/4}$ is in the GUT range: this requires low values of m_t, close to the 2σ lower range.

For $m_t \lesssim 171.5$ GeV, the values of $V_B^{1/4}$ can even exceed the GUT scale. In order to be exploited for inflation, the Higgs potential would thus require a modification, as for instance a flattening by means of a non-minimal coupling to gravity. As it is well known (and will be reviewed in the following), the Higgs inflation model predicts $r = 12/N^2 = 0.0033 - 0.0048$ for $N = 60 - 50$, so that CMB data would suggest the value $U_i^{1/4} = (7.8 - 8.5) \times 10^{15}$ GeV (or equivalently, $\bar{U}_i^{1/4} \approx 10^{-2.5}$ as shown in Fig. 6).

For values of $m_t \gtrsim 171.5$ GeV, the values of $V_B^{1/4}$ are smaller than the GUT scale. The introduction of a non-minimal coupling to achieve Higgs inflation is thus useless in this case, as the flattened potential would stay in any case below the desired value, $U_i^{1/4} = (7.8 - 8.5) \times 10^{15}$ GeV. Other modifications of the SM Higgs potential would be required in view of inflation, as for instance: *i)* introducing new physics to increase $V_B^{1/4}$, like adding another scalar field [54, 55] or in R^2-Higgs inflation [56]; *ii)* considering a model with very small r, allowing for values of $V_B^{1/4}$ much smaller than the GUT scale (see [57] for a related attempt).

For a stable configuration instead, as stressed previously while commenting Fig. 4, one has $V_B^{1/4} \gtrsim 4.5 \times 10^{16}$ GeV, which is in tension with the constraint from CMB, $U_i^{1/4} < 2.5 \times 10^{16}$ GeV. Models with a shallow vacuum [13–16] and inflection point Higgs inflation (also called critical Higgs inflation) [11, 12] are thus in tension with CMB data [17], unless invoking modifications to the Higgs effective potential.

4 The Higgs potential with a non-minimal coupling

We now modify the Higgs potential by introducing a non-minimal gravitational coupling ξ between the SM Higgs doublet $\mathcal{H}$ and the Ricci scalar R [19]. The classical action for Higgs inflation is

$$\mathcal{S} = \int d^4x \sqrt{-g} \left[\mathcal{L}_{SM} - \frac{M^2}{2} R - \xi \left| \mathcal{H} \right|^2 R \right] , \tag{15}$$

where g is the determinant of the FLRW metric, $\mathcal{L}_{SM}$ is the SM Lagrangian and M is a parameter with the dimension of a mass, to be identified with the reduced Planck mass, $M_P = 1/(8\pi G_N)^{1/2}$, where G_N is the Newton constant, in order to obtain the equations of general relativity.

From a cosmological point of view, the relevant part of the action above is

$$\mathcal{S}_J = \int d^4x \sqrt{-g} \left[(\partial_\mu \mathcal{H})^\dagger (\partial^\mu \mathcal{H}) - \frac{M_P^2}{2} R - \xi \left| \mathcal{H} \right|^2 R - V \right] , \tag{16}$$

where V is the SM potential of Eq. (1) and the subscript J means that the action is evaluated in the Jordan frame. In order to remove the non-minimal coupling we introduce a conformal (or Weyl) transformation:

$$\tilde{g}_{\mu\nu} = \Omega^2 g_{\mu\nu}, \qquad \Omega^2 \equiv 1 + 2\xi \frac{|\mathcal{H}|^2}{M_P^2} = 1 + \xi \bar{\phi}^2 \, . \tag{17}$$

where the last equality holds in the Higgs representation $\mathcal{H} = e^{i\vec{\chi}\cdot\vec{\sigma}}(0, (\phi + v)/\sqrt{2})^T$, where $\vec{\chi}$ are the Goldstone bosons and ϕ is the radial mode. The Einstein frame action is obtained when gravity is canonically normalized, in the metric formulation, by

$$\mathcal{S}_E = \int d^4x \sqrt{-\tilde{g}} \left[K \frac{(\partial\phi)^2}{2} - \frac{M_P^2}{2} \tilde{R} - \frac{V}{\Omega^4} \right] \, , \; K = \frac{\Omega^2 + \frac{3}{2} \left(\frac{d\Omega^2}{d\phi} \right)^2}{\Omega^4} \, . \tag{18}$$

The kinetic term for the classical Higgs field ϕ is made canonical by the redefinition $\phi = \phi(\chi)$ such that

$$\frac{d\chi}{d\phi} = \sqrt{K} = \frac{\sqrt{1 + \xi\bar{\phi}^2 + 6(\frac{1}{2}\frac{d\xi}{d\bar{\phi}}\bar{\phi} + \xi)^2 \bar{\phi}^2}}{1 + \xi\bar{\phi}^2} \, , \qquad \chi(\phi = 0) = 0 \, , \tag{19}$$

so that the final expression for the Einstein frame action and the potential U felt by χ are

$$\mathcal{S}_E = \int d^4x \sqrt{-\tilde{g}} \left[\frac{(\partial\chi)^2}{2} - \frac{M_P^2}{2}\tilde{R} - U(\chi) \right] \ , \ U(\chi) = \frac{V}{\Omega^4} \simeq \frac{\lambda}{24} \frac{\phi^4(\chi)}{(1+\xi\bar{\phi}^2(\chi))^2} \quad . \tag{20}$$

The potential is flat for large field values, $\phi > M_P/\sqrt{\xi}$, and can in principle provide a slow-roll inflationary phase.

4.1 Radiative corrections

We turn to consider the inclusion of radiative corrections: the running of the couplings, now also including the running of the non-minimal coupling ξ, and the loop corrections to the effective potential.

The expressions for the β-functions of the relevant SM couplings, including $\xi(t)$, can be found *e.g.* in Refs. [26, 58]. The non-minimal coupling affects the running through the appearance of a factor s that suppresses the contribution of the physical Higgs to the RGEs [21, 26]:

$$s(\phi(t)) = \frac{1+\xi(t)\bar{\phi}^2(t)}{1+(1+6\xi(t))\xi(t)\bar{\phi}^2(t)} \, . \tag{21}$$

For small field values $\bar{\phi}(t) \ll 1/\xi(t)$, $s \simeq 1$, recovering the SM case; in the inflationary regime $\bar{\phi}(t) \gg 1/\xi(t)$, the RGEs differ from those of the SM as quantum loops involving the Higgs field are suppressed by $s \simeq 1/(1+6\xi(t))$.

The RGE-improved effective potential is given by

$$U_{\text{eff}} = U^{(0)} + U^{(1)} + U^{(2)} + \dots \, , \tag{22}$$

with all the involved running couplings evaluated at some renormalization scale $\mu(t)$, conveniently chosen in order to minimize the effect of the logarithms, for the benefit of perturbation theory.

We will then consider the quantum corrections to the effective potential [26, 59] after the transformation (17) has been done, *i.e.* in the Einstein frame [19], where gravitons have canonical kinetic term [2]. First, the tree-level RGE-improved potential is rewritten in the Einstein frame, giving at leading order

$$U^{(0)} = \frac{\lambda(t)}{24} \frac{\phi^4(t)}{\Omega^4(t)} \ , \ \Omega^2(t) = 1 + \xi(t)\,\bar{\phi}^2(t) \, . \tag{23}$$

As for the one-loop potential, the relevant terms for the gauge bosons V and fermions ψ in the tree level action are given in the Jordan frame by

$$S_J = \int d^4x \sqrt{-g} \left[-\frac{1}{4}\text{tr}\, F_{\mu\nu}F^{\mu\nu} - \frac{1}{2}\frac{M^2(v)}{v^2}\phi^2 V_\mu V^\mu + \bar{\psi} i D_\mu \gamma^\mu \psi - \frac{\lambda_\psi}{\sqrt{2}}\bar{\psi}_L \phi \psi_R + \dots \right] \tag{24}$$

and in the Einstein frame by

$$S_E = \int d^4x \sqrt{-\tilde{g}} \left[-\frac{1}{4}\text{tr}\, F_{\mu\nu}F^{\mu\nu} - \frac{1}{2}\frac{M^2(v)}{v^2}\frac{\phi^2}{\Omega^2} V_\mu V^\mu + \bar{\chi} i D_\mu \tilde{\gamma}^\mu \chi - \frac{\lambda_\psi}{\sqrt{2}}\bar{\chi}_L \frac{\phi}{\Omega}\chi_R + \dots \right] \tag{25}$$

where $\chi \equiv \Omega^{-3/2}\psi$ and $\tilde{\gamma}^\mu \equiv \Omega^{-1}\gamma^\mu$ satisfies the anticommutation relation $\{\tilde{\gamma}^\mu, \tilde{\gamma}^\nu\} = 2\tilde{g}^{\mu\nu}$. In these expressions we are neglecting the variation of $\Omega(\phi)$ which is motivated during inflation

[2] We will neglect quantum gravity effects, as they are not expected to be important at the scales where inflation will take place [19]. In particular, higher dimensional operators as ϕ^{4+2n}/M_P will have a small impact as inflation happens for field values $\phi \ll M_P$.

when slow-roll conditions are fulfilled for the inflaton ϕ. Notice that the kinetic terms of gauge bosons is scale invariant, so gauge bosons do not need any field redefinition.

The one-loop corrections take the form of Eq. (11), but particle masses are computed from the tree-level action above in the Einstein frame (25). The two-loop radiative corrections $U^{(2)}$ can be found in the same way, operating on the explicit form given in Refs. [4,6]. The appropriate scale for minimizing the effect of the logarithms is given by $\phi(t)/\Omega(t)$. Following the argument illustrated in the previous section, we define the parameter α via $\mu(t) = \alpha\phi(t)/\Omega(t)$ [3], which give for the one-loop potential

$$\begin{aligned} U^{(0)} + U^{(1)} &= \frac{1}{24}\left(\lambda(t) + \frac{6}{(4\pi)^2}\left[6\left(\frac{g^2(t)}{4}\right)^2\left(\log\frac{g^2(t)}{4\alpha^2} - \frac{5}{6}\right)\right.\right. \\ &+ 3\left(\frac{g^2(t)+g'^2(t)}{4}\right)^2\left(\log\frac{g^2(t)+g'^2(t)}{4\alpha^2} - \frac{5}{6}\right) \\ &- \left.\left. 12\left(\frac{h_t^2(t)}{2}\right)^2\left(\log\frac{h_t^2(t)}{2\alpha^2} - \frac{3}{2}\right)\right]\right)\frac{\phi^4(t)}{(1+\xi(t)\,\bar{\phi}^2(t))^2}\,. \end{aligned} \tag{26}$$

Notice that the explicit dependence on the field values $\phi(t)$ has disappeared as we are making the choice for the scale $\mu(t)$

$$\mu(t) = \alpha\,\frac{\phi(t)}{\sqrt{1+\xi(t)\bar{\phi}^2(t)}}\,. \tag{27}$$

For small field values, $\bar{\phi}(t) \ll 1/\sqrt{\xi(t)}$, we get the same result as in this case $\Omega \approx 1$, so that:

$$t = \log\left(\frac{\alpha\phi(t)}{\mu(0)}\right)\ . \tag{28}$$

For large field values, $\bar{\phi}(t) \gg 1/\sqrt{\xi(t)}$, the situation changes as t approaches a nearly constant value, approximately given by

$$t_{\rm lim} \approx \log\left(\frac{\alpha}{\sqrt{\xi(t_{\rm lim})}}\frac{M_P}{\mu(0)}\right)\ , \tag{29}$$

and hence so do the couplings $g(t), g'(t), \lambda(t)$, etc. As a result, the effective potential approaches a constant value in the inflationary region (even after including radiative corrections). The constant limit for the potential is thus expected to be

$$U_{\rm lim} \approx \frac{1}{24}\lambda(t_{\rm lim})\frac{M_P^4}{\xi^2(t_{\rm lim})}\ . \tag{30}$$

In the following, we study how to modify the SM potential by exploiting the flattening induced by the non-minimal coupling ξ. As discussed above, the transition from small to large field values of $\bar{\phi}(t)$ happens at $1/\sqrt{\xi(t)} \approx 1/\sqrt{\xi(0)} \equiv 1/\sqrt{\xi} \equiv \bar{\phi}_\xi$, as the running of the parameter $\xi(t)$ is very slow and one can safely neglect it. It will thus be important to compare $\bar{\phi}_\xi$ with the

[3] It was proposed in Ref. [20] to compute quantum effects in the Jordan frame, so that radiative corrections are evaluated directly from masses provided by the Jordan frame, Eq. (24), before the conformal transformation: they are thus given by $V^{(1)}$ of Eq. (11). In this case the scale factor $\mu_J(t)$ in the Jordan frame is related to the scale factor in the Einstein frame $\mu(t)$ by the anomaly relation $\mu_J(t) = \mu(t)\Omega(t)$, providing the manifestation of the conformal anomaly in both frames [24]. Even if the choice of the renormalization scale is relevant when a truncated series in perturbation theory is considered, as the former is not physical, and the effective action is renormalization scale invariant, the physical observables do not depend on the renormalization scale choice.

parameters characterizing the potential, especially with $\bar{\phi}_B$. It is also important to understand the size of the theoretical error associated to the truncation of the effective potential at a certain loop order. This error can be estimated by varying α, as done in [10]. In the following we thus use the one-loop approximation with $\alpha = 0.3$, as it gives nearly the same results as the two-loop one, which we have checked to essentially be α-independent. In particular the critical value of the top quark mass is given by $m_t^c = 171.0549$. To illustrate the different behaviors we will consider the benchmark configurations that are shown in Tab. 1.

Point	P_{1a}	P_{1b}	P_i	P_{2a}	P_{2b}	P_{3a}	P_{3b}
δ_t	$-3.8 \cdot 10^{-3}$	$-1.5 \cdot 10^{-3}$	$-1.4 \cdot 10^{-6}$	$6.2 \cdot 10^{-6}$	$1.5 \cdot 10^{-4}$	$2.6 \cdot 10^{-4}$	$2.8 \cdot 10^{-3}$

Table 1: *The benchmark points used in this paper. The value of δ_t parameterizes the deviation with respect to the critical configuration P_c, see Eq. (12), for which $\delta_t = 0$. Top quark masses below and above the critical configuration are separated by a double line.*

4.2 The canonical field and its equation of motion

As a last step, we have to generalize the relation between ϕ and the canonical field χ to the case of running couplings. As discussed in Refs. [59, 60], the kinetic term for the wave-function renormalized Higgs field, $\phi(t)$, can be made canonical by defining the field $\chi(\phi(t))$ by means of a generalization of Eq. (19). We numerically integrate such equation as done in Ref. [17], to which we refer for more details. Once the shape of $U(\chi)$ is known, it is possible to wonder about primordial inflation. One has to distinguish between the possibilities of single and multi-field inflation.

In the case of single-field inflation, the Higgs field itself plays the role of the inflaton and, as it is well known, the inflationary observables are calculated as follows. By identifying t with the cosmological time, the equation of motion of the field $\chi(t)$ is given by

$$\chi''(t) + 3\,H(t)\,\chi'(t) = -\frac{dU}{d\chi}(\chi(t)) \ , \ H^2(t) = \frac{1}{3M_P^2}\left(U(\chi(t)) + \frac{1}{2}\chi'^2(t)\right) \ , \tag{31}$$

where the initial conditions are $\chi(t_0) = \chi_0$, $\chi'(t_0) = \chi_0'$, and t_0 is some initial time. The time duration of the inflationary phase is represented by the number of e-folds,

$$N = \int_{t_i}^{t_e} dt\, H(t) \ , \tag{32}$$

where t_e is the time at the end of inflation and $t_i > t_0$ is the time when the inflationary CMB observables, like the density fluctuations Δ_R, the spectral index n_s and the tensor-to-scalar ratio r, are measured. It is known that t_i should be such that $N \approx 50 - 60$.

In the case of multi-field inflation instead, the Higgs field is not the inflaton and one introduces another scalar field, acting as inflaton, so that the Hubble parameter is dominated by the potential of the latter field.

5 Avoiding metastability by a non-minimal coupling

Studies of the Higgs potential in de Sitter background, during the cosmological inflation period triggered by some other inflaton field, shows that the minimal probability for the Higgs to

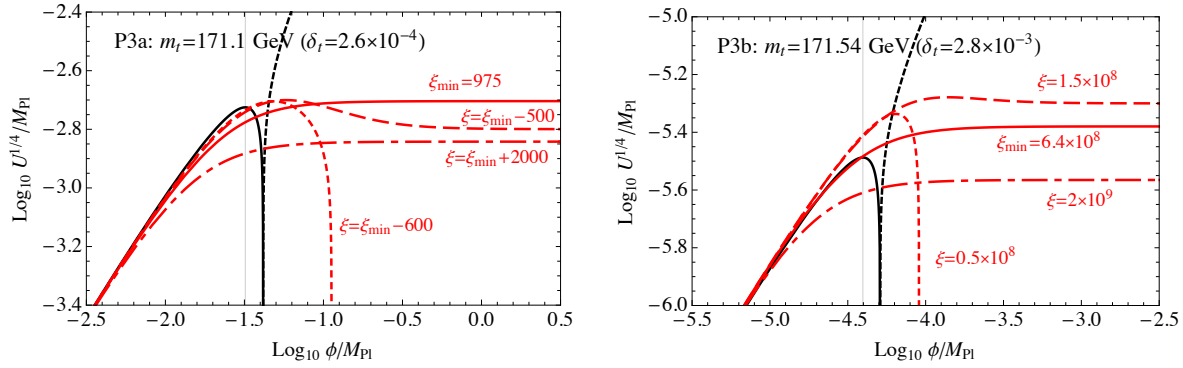


Figure 5: *Left panel: study of the configurations with* $m_t = 171.1$ *GeV, for the indicated values of* ξ*. The solid line refers to* $\xi = \xi_{min} = 975$*; the short and long dashed lines to* $\xi = \xi_{min} - 600$ *and* $\xi = \xi_{min} - 500$ *respectively; the dot-dashed line to* $\xi = \xi_{min} + 2000$*. Right panel: study of the configurations with* $m_t = 171.54$ *GeV, as suggested in [34], for the indicated values of* ξ*, including* $\xi_{min} = 6.4 \times 10^8$*.*

overcome the top of the barrier after N e-folds of inflation is [60]

$$p(\phi > \phi_B) \simeq 1 - \mathrm{erf}\left(\frac{\sqrt{2}\pi\phi_B}{\sqrt{N}H}\right) \ , \tag{33}$$

where erf(x) is the error function. Imposing that this does not happen in any of the e^{3N} causally disconnected regions that are made during inflation, *i.e.* $p(\phi > \phi_B) < e^{-3N}$ imposes the condition

$$H_e \gtrsim 0.04\,\phi_B \tag{34}$$

where H_e is the Hubble parameter at the end of inflation, and the value of ϕ_B for different values of m_t is plotted in the left panel of Fig. 3. This imposes a strong bound on the value of the Hubble parameter during the inflationary period and, in particular, excludes the case of high-scale inflation. For instance for the central experimental value of the top quark mass, for which $\phi_B \simeq 3 \times 10^{11}$ GeV, the scale of inflation is bounded by $H_e \lesssim 10^{10}$ GeV.

Of course if the Higgs field is identified with the inflaton, the existence of a metastable minimum precludes inflation unless $\phi_i \lesssim \phi_B$, ϕ_i being the Higgs field at the beginning of inflation.

A non-minimal coupling to gravity can naturally allow to avoid such metastable minimum if ξ is sufficiently large, so that $1/\sqrt{\xi} = \bar{\phi}_\xi \lesssim \bar{\phi}_B$. The lower bound on the non-minimal coupling is thus

$$\xi_{\rm min} \equiv \frac{1}{\bar{\phi}_B^2} \lesssim \xi \ , \tag{35}$$

which we display in the right vertical axis of the left panel of Fig. 3. Clearly, very large values of ξ are required to avoid metastability, unless m_t is close to the PDG 2022 lower 2σ range, $m_t = 171.1$ GeV [29].

As an illustrative example, we precisely fix $m_t = 171.1$ GeV, case P_{3a} in Tab. 1, take central values for m_H and $\alpha_s^{(5)}$ given by the PDG 2022 [29], and display the SM Higgs potential, $|V_{eff}|^{1/4}$, in the left plot of Fig. 5; the black solid (dashed) curve refers to positive (negative) values of the potential. As can be seen, in this case one has $\phi_B \simeq 7.8 \times 10^{16}$ GeV and $V_B^{1/4} \simeq 4.6 \times 10^{15}$ GeV (barely satisfying condition (34)), below the upper bound from CMB, $U_i^{1/4} < 2.5 \times 10^{16}$ GeV.

We study how the potential gets modified for various values of the non-minimal coupling ξ. The upper solid (red) curve is obtained by taking $\xi = \xi_{\rm min} = 975$; metastability is indeed avoided, because the potential gets flattened at field values below ϕ_B. The other curves show the shape of the potential for other values of ξ. The short and long dashed curves are obtained by taking $\xi = \xi_{\rm min} - 600$ and $\xi = \xi_{\rm min} - 500$, respectively. In the latter case metastability is avoided, but the potential is not monotonously increasing; still it is stable and there is no unphysical deep minimum. The lower dot-dashed curve is obtained by taking $\xi - \xi_{\rm min} = 2000$, so that the flattening takes place at slightly smaller values than ϕ_B, whose value is indicated by the vertical grey line.

Notice that all these configurations, although displaying a plateau and stabilizing the Higgs potential, cannot work for Higgs inflation. As already mentioned, Higgs inflation would require $U_i^{1/4} = (7.8 - 8.5) \times 10^{15}$ GeV, while here the plateau is at most as high as the barrier, $V_B^{1/4} \simeq 4.6 \times 10^{15}$ GeV. This shows that a slightly smaller value of m_t with respect to the one adopted in Fig. 5 might, instead, provide viable Higgs inflation for a configuration that would have been metastable in the pure SM, without the non-minimal coupling.

In the right plot of Fig. 5, as another illustrative example, we fix $m_t = 171.54$ GeV, case P_{3b} in Tab. 1, as suggested in [34], and show the effect of varying ξ around $\xi_{min} = 6.4 \times 10^8$.

6 Higgs Inflation: the model and its phenomenology

Here we study the various configurations of the Higgs potential flattened by a non-minimal coupling that allow for viable Higgs inflation.

6.1 Slow-roll parameters for Higgs inflation

The slow-roll parameters are given by

$$\epsilon(t) = \frac{1}{2}\left(\frac{dU(\bar\phi(t))}{d\bar\phi(t)}\frac{1}{U(\bar\phi(t))}\right)^2\left(\frac{d\bar\chi(t)}{d\bar\phi(t))}\right)^{-2} \tag{36}$$

$$\eta(t) = \frac{d^2U(\bar\phi(t))}{d\bar\phi^2(t)}\frac{1}{U(\bar\phi(t))}\left(\frac{d\bar\chi(t)}{d\bar\phi(t))}\right)^{-2} - \frac{dU(\bar\phi(t))}{d\bar\phi(t)}\frac{1}{U(\bar\phi(t))}\left(\frac{d\bar\chi(t)}{d\bar\phi(t))}\right)^{-3}\frac{d^2\bar\chi(t)}{d\bar\phi^2(t)}\ , \tag{37}$$

from which one can easily derive the following approximate expressions

$$\epsilon(t) \approx \frac{4}{3}\frac{1}{\xi^2}\frac{1}{\bar\phi^4(t)}\ \ ,\ \ \eta(t) \approx -\frac{4}{3}\frac{1}{\xi}\frac{1}{\bar\phi^2(t)}\ . \tag{38}$$

Since inflation ends when $\epsilon \approx 1$, namely $\bar\phi_e^2 \approx \sqrt{\frac{4}{3}\frac{1}{\xi}}$, we get

$$N = \frac{1}{\sqrt{2}}\int_{\bar\phi_i}^{\bar\phi_e} d\bar\phi\frac{1}{\epsilon^{1/2}}\frac{d\bar\chi}{d\bar\phi} \approx \frac{3}{4}\xi\bar\phi_i^2 \ \Rightarrow\ \bar\phi_i^2 \approx \frac{4}{3}\frac{N}{\xi}\ . \tag{39}$$

At the beginning of inflation the slow roll parameters are approximately given by

$$\epsilon_i \approx \frac{3}{4}\frac{1}{N^2}\ \ ,\ \ \eta_i \approx -\frac{1}{N}\ ,\quad \text{with}\quad |\eta_i| \gg \epsilon_i\,, \tag{40}$$

so that there are quite sharp predictions for the observable parameters

$$n_s \approx 1 - 6\epsilon_i + 2\eta_i \approx 1 - \frac{2}{N}\ \ ,\ \ r \approx 16\epsilon_i \approx \frac{12}{N^2}\ . \tag{41}$$

Taking $N = 50 - 60$, the model prediction for n_s is in the range $0.960 - 0.967$, which is well compatible with the cosmological data. Indeed, according to Ref. [61], observationally one has $n_s = 0.9649 \pm 0.0042$ at 68% CL. Taking $N = 50 - 60$, the model prediction for r is the range $0.0048 - 0.0033$; this is below the present Planck limit, $r_{0.002} < 0.056$ at 95% CL [61], and below the most stringent recent combined analysis of the BICEP, Keck Array and Planck data, which places an upper bound on the tensor-to-scalar ratio $r < 0.036$ at the 95% CL [53].

As already mentioned, the amplitude of perturbations is

$$2.1 \times 10^{-9} \approx \Delta_R^2 \approx \frac{2}{3\pi^2}\frac{\bar{U}_i}{r} \approx \frac{1}{432\pi^2}\lambda(t_{\rm lim})\left(\frac{N}{\xi(t_{\rm lim})}\right)^2 , \tag{42}$$

where the last approximation was obtained exploiting the approximation $r \approx 12/N^2$, and taking $\bar{U}_i \approx \bar{U}_{\rm lim}$. In our analysis we find numerically the value of ξ that gives the right value for the amplitude of perturbations, and then calculate the parameters r and n_s. We checked that the right-hand side of the previous equation is a good approximation for such value of ξ.

6.2 Higgs inflation phenomenology for stable and metastable configurations

We now study in more detail how the SM Higgs effective potential gets modified, by exploiting the flattening induced by the non-minimal coupling, to account for successful inflation. The transition from small to large field values happens when $\bar{\phi}(t) \sim \bar{\phi}_\xi = 1/\sqrt{\xi}$. Let us study in turn the various scenarios for m_t, considering increasing values of the latter, going from stability to metastability as in Fig. 2, for the benchmark points shown in Tab. 1.

- $m_t < m_t^i$.

  This is the traditional approach of Higgs inflation, suggested in [19]. The idea is to consider a stable configuration (without minima at high field values) for the Higgs potential, and flatten it with a value of ξ that correctly reproduces the observational data from CMB, in particular the amplitude of perturbations (while n_s and r do not depend on ξ). It is well known that such value is quite high, $\xi = \mathcal{O}(10^4)$, as derived in the pioneering tree-level calculation of [19]. Our more sophisticated analysis indicates slightly smaller values, in particular for stable configurations not far from the inflection point configuration. Indeed, from Eq. (42) one realizes that for $\lambda \approx 10^{-2}$ (typical of a stable configuration, see Fig. 1), one needs $\xi \approx 3 \times 10^3$.

  Let us now numerically inspect this situation, taking central values for m_H and $\alpha_s^{(5)}$ and choosing two values for the top mass: $m_t = 170.4$ GeV, which is the lower 3σ value according to PDG 2022 [29], and $m_t = 170.8$ GeV. These values correspond respectively to $\delta_t = -3.8 \times 10^{-3}$ $\delta_t = -1.5 \times 10^{-3}$ in the notation of Eq. (12). We call P_{1a} and P_{1b} these configurations in Tab. 1 and study them in the upper panels of Fig. 6. The solid (black) curve shows $|\bar{V}_{eff}|^{1/4}$, while the dashed (red) curve shows $\bar{U}^{1/4}$ for the indicated value of ξ, which accounts for the observed density perturbations, taking $N = 60$. It turns out that $\xi \approx 3000$ for P_{1a}, and decreases to $\xi \approx 2000$ for P_{1b}; this is related to the fact that ϕ_ξ (shown in the upper horizontal axis) increases, when going from P_{1a} to P_{1b}. The dashed (pink) horizontal line represents the value of $\bar{U}_i^{1/4}$ required by Higgs inflation, that is the value obtained by taking $r = 12/N^2 = 0.0031$ in Eq. (14). The value $\bar{\phi}_\xi = 1/\sqrt{\xi}$, where the flattening starts to be effective, is shown in the upper horizontal axes. The vertical grey lines correspond to the beginning and the end of inflation, which are also emphasized with circles in top of the curve of $\bar{U}_i^{1/4}$. Inflation thus takes place at field values slightly below the Planck scale, starting at $\bar{\phi}_i$ and ending at $\bar{\phi}_e$. The predictions for

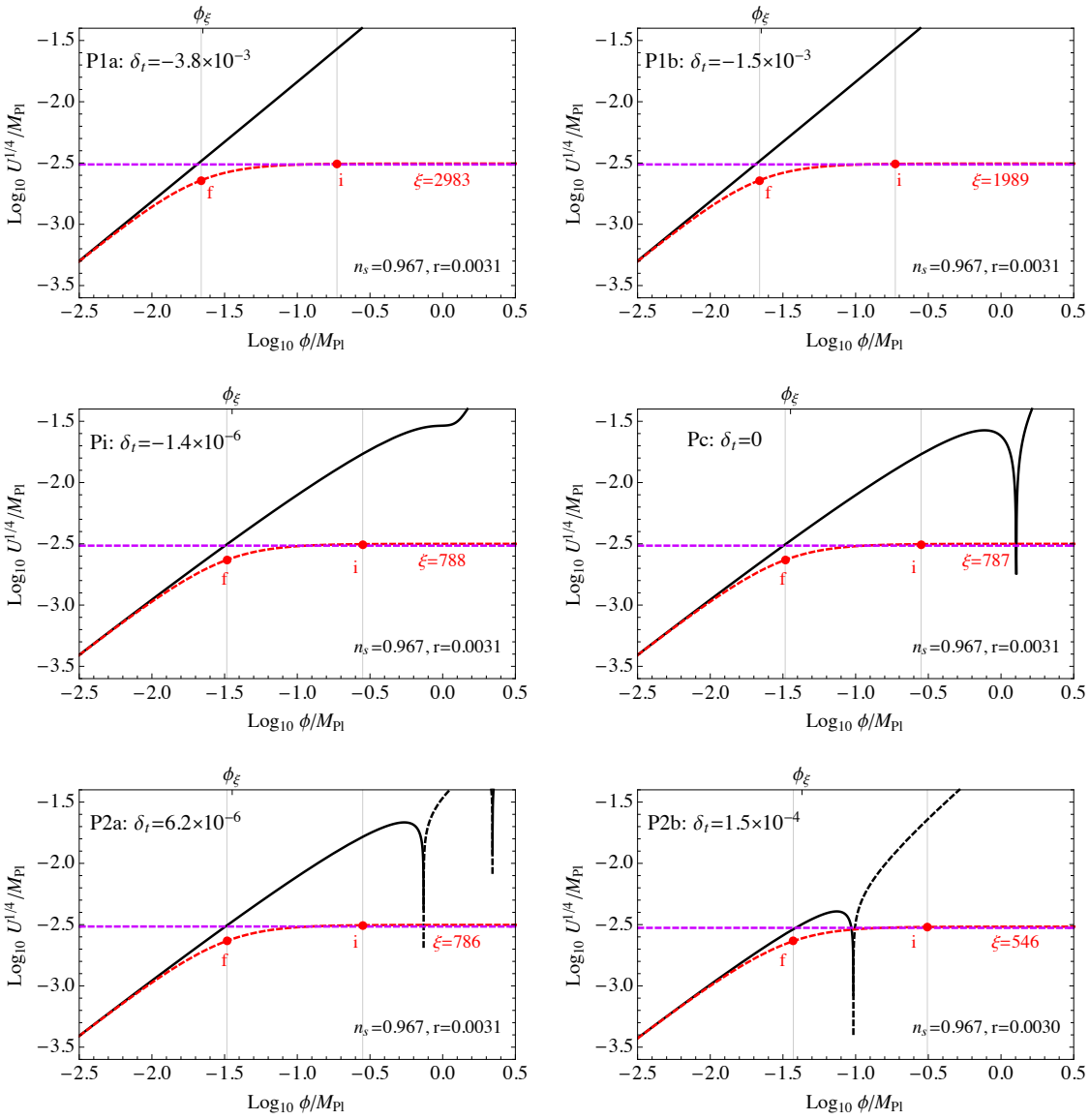


Figure 6: *Various configurations, using central values for m_H and $\alpha_s^{(5)}$. Increasing values of the top mass, as indicated. The shape of $|\bar{V}_{eff}|^{1/4}$ (solid black when positive, dashed black when negative) is shown, together with the shape of $\bar{U}^{1/4}$ (dashed red) for the indicated value of ξ, accounting for the observed density perturbations and taking $N = 60$.*

n_s and r, showed in the lower right corner of the plot, are consistent with those expected from the approximations in Eq. (41) and are perfectly compatible with observational data from CMB, as already discussed.

- $m_t = m_t^i$.

  Slightly rising m_t with respect to P_{1b}, we find a configuration that corresponds to an inflection point, and which we call P_i in Tab. 1, as displayed in the left middle panel of Fig. 6. In this case, $\delta_t = -1.6 \times 10^{-6}$. Essentially, one can envisage two scenarios which essentially depend on the value of the parameter ξ.

i) The potential is flattened at field values larger than those of the inflection point, that is larger than ϕ_B. This requires $\bar{\phi}_\xi > \bar{\phi}_B \approx 2 \times 10^{18}$ GeV, as can be seen from Fig. 4. Hence, one expects $\xi \lesssim \mathcal{O}(1)$, which might appear very interesting for inflation [11]; in addition, one might achieve a two-plateau potential [4]. The inflationary plateau is at least as high as the inflection point of V_{eff}, since for field values up to ϕ_ξ, and in particular around ϕ_B, one has $U \approx V_{eff}$. This configuration however cannot account for the observational data from CMB [17]: numerically, $V_B^{1/4} \approx 6 \times 10^{16}$ GeV is larger than the CMB constraint, $U_i^{1/4} < 2.5 \times 10^{16}$ GeV, as can be seen from the left middle plot in Fig. 6.

ii) The potential is flattened at values smaller than ϕ_B, that is $\bar{\phi}_\xi < \bar{\phi}_B$. In this case, the shape of the Higgs potential around the inflection point is drastically affected: the inflection point is simply not there anymore. For the sake of Higgs inflation, this configuration is quite similar to the former cases, P_{1a} and P_{1b}; notice however that in this case $\xi \approx 800$, which is a significantly smaller value with respect to the configurations P_{1a} and P_{1b}. Indeed, $\lambda(t_{\rm lim})$ gets smaller increasing m_t, so that also $\xi \approx \xi(t_{\rm lim})$ gets smaller according to Eq. (42). Notice also that inflation starts and ends at slightly larger field values with respect to P_{1a} and P_{1b}.

- $m_t^i < m_t \leq m_t^c$.

  This range corresponds to a configuration displaying a second high energy minimum close to the Planck scale, which can be shallow or quite deep but, in any case, not lower than the electroweak minimum. All the arguments of the previous case P_i apply here too. One thus needs $\bar{\phi}_\xi < \bar{\phi}_B$ and a further very mild reduction of ξ is achieved. We display in the right middle panel of Fig. 6 the critical configuration corresponding to two degenerate minima, denoted as P_c. For the sake of inflation, essentially P_c is equivalent to P_i.

- $m_t > m_t^c$.

  For metastable configurations, the potential has to be flattened before the appearance of the deepest minimum at high energies, so that again we need $\bar{\phi}_\xi < \bar{\phi}_B$. Increasing slightly m_t with respect to P_c, we reach a configuration displaying a tiny metastability, which we denote by P_{2a} in Tab. 1, such that $\delta_t = 6.2 \times 10^{-6}$. The barrier between the two minima is slightly smaller than it was for P_c, as can be seen in the left bottom panel of Fig. 6; the solid (dashed) black line refers to positive (negative) values for V_{eff}. The value of ξ allowing for successful Higgs inflation is thus negligibly smaller with respect to the case of P_c, and the cosmological observables are unchanged.

  Increasing further the top mass to the value $m_t = 171.08$ GeV, corresponding to $\delta_t = 1.5 \times 10^{-4}$, we reach the most metastable configuration P_{2b} in Tab. 1, shown in the right bottom panel of Fig. 6. Now the top of the barrier, $V_B^{1/4}$, is significantly reduced with respect to P_{2a}, getting closer to the value of the inflationary potential required by Higgs inflation, corresponding to the horizontal (pink) dashed line. The flattening of the potential, associated to $\bar{\phi}_\xi$, takes place just before the barrier; in this case $\bar{\phi}_\xi$ slightly moves to the right with respect to P_{2a}; as an effect, we have a further reduction of the non-minimal coupling, $\xi \approx 550$. Notice that inflation stars at field values where one would have had a negative potential in the SM. Notice also that by further increasing the value of m_t one could go to lower values of the parameter ξ, although without reaching the potential value required by density perturbations, in which case one should introduce a scalaron scalar

[4] It was suggested one could exploit the highest plateau induced by the non-minimal coupling at field values larger than ϕ_ξ for inflation, and to exploit the inflection point (around 20-30 e-folds after the beginning of inflation) to trigger the production of primordial black holes [12].

taking care of the CMB data, or else the Higgs, with a stable potential, is not a good candidate for inflaton.

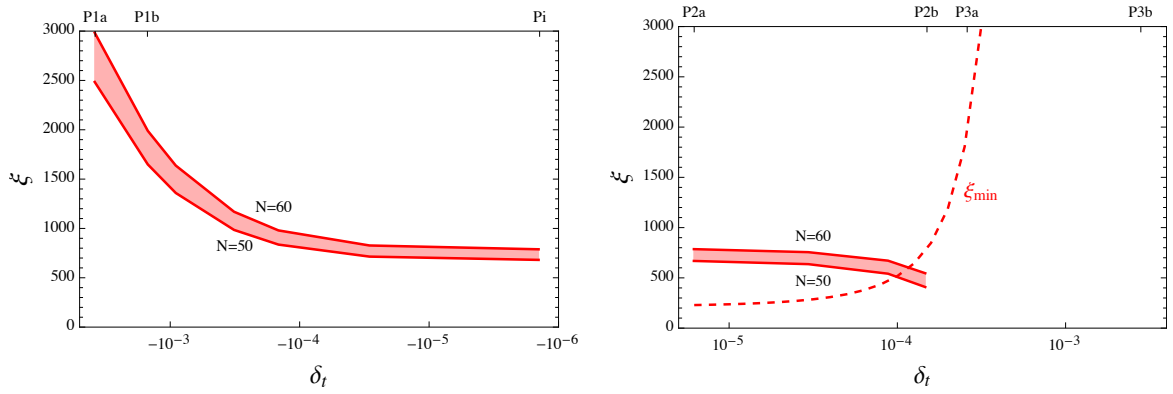


Figure 7: *The value of the non-minimal coupling for stability (left panel) and metastability (right panel), for* $N = 50, 60$ *and taking the central values of the inputs, as in the PDG 2022 [29]. For comparison, the dashed line* $\xi_{\rm min}$ *reproduces the values shown in the left panel of Fig. 3.*

We finally summarize the dependence of ξ on the top quark mass in Fig. 7 for values of the top mass corresponding to stability (left panel) and metastability (right panel). Notice that, while we are finding smaller ξ values for the cases of potential stability, we can deal with cases where the Higgs potential is metastable so that the right panel in Fig. 7 constitutes the main finding in this paper. Moreover the dashed line in the right panel of Fig. 7 corresponds to the values of the parameter ξ stabilizing the Higgs effective potential, without any relation with Higgs inflation.

7 Discussion and conclusions

As cosmological inflation is supposed to be driven by a scalar field, and the only elementary scalar field in nature is the Higgs boson, identifying the inflaton with the Higgs boson has constituted a fascinating possibility, which is nevertheless in tension with CMB data on the amplitude of density perturbations. However, it was proven that such a problem can be solved if the Higgs is non-minimally coupled to gravity with a large coupling ξ, a theory dubbed Higgs inflation, in which case for large field values the Higgs potential is flattened and proportional to $\lambda(\mu)/\xi^2$, and one can cope with CMB data with a large enough value of ξ. Notice that this is just a tree-level flattening, as λ runs with ϕ at loop level, according to the renormalization group equations. Thus this mechanism is jeopardized when including radiative corrections on the Higgs effective potential, as depending on the value of the quark top pole mass and the strong coupling constant, the effective potential, and the Higgs quartic coupling, become negative at some value of the Higgs field ϕ_B, detecting the existence of a deep minimum at high field values, and making the electroweak minimum metastable. This explains why Higgs inflation was originally proposed for stable configurations.

In this paper we have first reanalyzed the issue of the stability vs. metastability of the Higgs effective potential using the most recent experimental data on the top quark and Higgs masses

as well as the strong coupling, mainly in view of the capabilities of the Higgs to be identified with the inflaton triggering cosmological inflation and the seed of density perturbations in the early Universe.

Further, we have exploited a particular feature of the Higgs effective potential in the Einstein frame, in cases where the Higgs is non-minimally coupled to gravity in the Jordan frame. In fact while for minimal coupling, $\xi = 0$, perturbation theory in the effective potential is optimized for the choice of the renormalization scale $\bar{\mu} = \alpha\bar{\phi}$, for non minimal coupling it is optimized by the choice $\bar{\mu} = \alpha\bar{\phi}/\sqrt{1+\xi\bar{\phi}^2}$. This means that there is a limiting value of the renormalization scale given by $\bar{\mu}_{\rm lim} = \alpha/\sqrt{\xi}$ achieved for field values $\bar{\phi} > \bar{\phi}_\xi = 1/\sqrt{\xi}$, and the effective potential is flattened to a value $\propto \lambda(\bar{\mu}_{\rm lim})/\xi^2$. Therefore a non-minimal coupling to gravity can naturally avoid a metastable minimum if $\xi \gtrsim \xi_{\rm min}$, where $\xi_{\rm min} \equiv 1/\bar{\phi}_B^2$.

Using the above tools we have (re)examined Higgs inflation for the cases where:

i) The electroweak vacuum is the only minimum of the effective potential (stability without barrier): the original proposal for Higgs inflation, valid for $m_t < m_t^i$.

ii) The electroweak vacuum is the true minimum, but there is either an inflection point or a second fake minimum, separated from the electroweak one by a potential barrier (stability with a barrier): valid for $m_t^i < m_t < m_t^c$.

iii) The electroweak vacuum is a fake minimum, separated by a barrier from the true non-physical AdS minimum (metastability): valid for $m_t > m_t^c$.

For a successful inflationary scenario two conditions are required:

a) The potential should be flattened for values of the field $\phi \lesssim \phi_B$, which requires a non-minimal coupling $\xi \gtrsim \xi_{\rm min}$.

b) The potential should reproduce the CMB condition on the amplitude of density perturbations.

We have then re-examined the different cases. For the case *i)* above, stability without barrier, condition a) is trivial as $\xi_{\rm min} = 0$ so only condition b) applies, by which the flattening must take place about two orders of magnitude below the Planck scale, which yields values of $\xi \sim 3000$. For the case *ii)*, with an inflection point or a barrier between the electroweak minimum and a local minimum, again $\xi_{\rm min} = 0$ so that condition a) does not apply, while condition b) implies that the flattening of the potential must take place before the inflection point, or before the value of the field corresponding to the maximum of the barrier, respectively, leading to values $\xi \sim 800$. In particular for a value of the top quark mass equal to the critical value Higgs inflation can take place (critical Higgs inflation) for a value of the non minimal coupling $\xi = 787$. Finally even metastable configurations, case *iii)*, can satisfy conditions a) and b) above, and are viable for inflation. They require smaller values of ξ, down to $\xi \sim 500$. However, only metastable configurations close to critical configuration are allowed, as the barrier between the two vacua must anyway be larger than the value of the inflaton potential suggested by CMB data for this model (see the dashed purple lines in Fig. 6). This corresponds to just a tiny increase for m_t, ~ 0.03 GeV, with respect to m_t^c, corresponding to $\delta_t \lesssim 1.5 \times 10^{-4}$ GeV.

In summary we have re-analyzed Higgs inflation in the presence of non-minimal coupling to gravity, beyond the stable configurations usually considered in the literature. We have proven that inflection and critical Higgs inflation are rescued as viable possibilities for suitable values of the non-minimal coupling. Moreover we have proven that even metastable configurations, going beyod the critical case, are viable possibilities for Higgs inflation. Even this tiny extension of the allowed range for m_t is however relevant in principle, as it opens up to metastable configurations.

For larger values of the top quark mass cosmological inflation can take place but the predicted amplitude of density perturbations at CMB are too small, motivating the presence of a scalaron from the R^2 term in the Jordan frame.

To conclude, considering the central values for the top quark pole mass and strong coupling constant quoted by the PDG 2022 data, the maximum value of the top quark mass consistent with Higgs inflation is 2σ away from its central value. However taking into account the error in the strong coupling, the maximum allowed value deviates around 1.5σ from the central experimental value of the top quark mass. Moreover, considering recent analyses [34] based on measurements of the top quark pole mass from differential cross sections by ATLAS and CMS, the deviation can shrink to around less than 1σ. So, ultimately while Higgs inflation cannot be excluded by present data, its viability will depend on future experimental measurements of the top quark mass and the strong coupling constant.

Acknowledgments

We thank the CERN Theory Department for kind hospitality and support during the completion of this work. IM acknowledges partial support by the research project TAsP (Theoretical Astroparticle Physics) funded by the Istituto Nazionale di Fisica Nucleare (INFN). The work of MQ is supported by the Departament d'Empresa i Coneixement, Generalitat de Catalunya, Grant No. 2021 SGR 00649, and by the Ministerio de Economía y Competitividad, Grant No. PID2020-115845GB-I00. IFAE is partially funded by the CERCA program of the Generalitat de Catalunya.

References

[1] P. Q. Hung, Vacuum Instability and New Constraints on Fermion Masses, Phys. Rev. Lett. 42 (1979) 873. doi:10.1103/PhysRevLett.42.873.

[2] N. Cabibbo, L. Maiani, G. Parisi, R. Petronzio, Bounds on the Fermions and Higgs Boson Masses in Grand Unified Theories, Nucl. Phys. B158 (1979) 295–305. doi:10.1016/0550-3213(79)90167-6.

[3] C. D. Froggatt, H. B. Nielsen, Standard model criticality prediction: Top mass 173 ± 5 GeV and Higgs mass 135 ± 9 GeV, Phys. Lett. B368 (1996) 96–102. arXiv:hep-ph/9511371, doi:10.1016/0370-2693(95)01480-2.

[4] G. Degrassi, S. Di Vita, J. Elias-Miro, J. R. Espinosa, G. F. Giudice, et al., Higgs mass and vacuum stability in the Standard Model at NNLO, JHEP 1208 (2012) 098. arXiv:1205.6497, doi:10.1007/JHEP08(2012)098.

[5] I. Masina, Higgs boson and top quark masses as tests of electroweak vacuum stability, Phys. Rev. D87 (5) (2013) 053001. arXiv:1209.0393, doi:10.1103/PhysRevD.87.053001.

[6] D. Buttazzo, G. Degrassi, P. P. Giardino, G. F. Giudice, F. Sala, A. Salvio, A. Strumia, Investigating the near-criticality of the Higgs boson, JHEP 12 (2013) 089. arXiv:1307.3536, doi:10.1007/JHEP12(2013)089.

[7] A. V. Bednyakov, B. A. Kniehl, A. F. Pikelner, O. L. Veretin, Stability of the Electroweak Vacuum: Gauge Independence and Advanced Precision, Phys. Rev. Lett. 115 (20) (2015) 201802. arXiv:1507.08833, doi:10.1103/PhysRevLett.115.201802.

[8] R. Franceschini, A. Strumia, A. Wulzer, The collider landscape: which collider for establishing the SM instability?, JHEP 08 (2022) 229, [Erratum: JHEP 03, 167 (2023)]. arXiv:2203.17197, doi:10.1007/JHEP08(2022)229.

[9] G. Hiller, T. Höhne, D. F. Litim, T. Steudtner, Vacuum Stability in the Standard Model and Beyond (1 2024). arXiv:2401.08811.

[10] G. Iacobellis, I. Masina, Stationary configurations of the Standard Model Higgs potential: electroweak stability and rising inflection point, Phys. Rev. D94 (7) (2016) 073005. arXiv:1604.06046, doi:10.1103/PhysRevD.94.073005.

[11] F. Bezrukov, M. Shaposhnikov, Higgs inflation at the critical point, Phys. Lett. B734 (2014) 249–254. arXiv:1403.6078, doi:10.1016/j.physletb.2014.05.074.

[12] J. M. Ezquiaga, J. Garcia-Bellido, E. Ruiz Morales, Primordial Black Hole production in Critical Higgs Inflation, Phys. Lett. B776 (2018) 345–349. arXiv:1705.04861, doi:10.1016/j.physletb.2017.11.039.

[13] I. Masina, A. Notari, The Higgs mass range from Standard Model false vacuum Inflation in scalar-tensor gravity, Phys.Rev. D85 (2012) 123506. arXiv:1112.2659, doi:10.1103/PhysRevD.85.123506.

[14] I. Masina, A. Notari, Standard Model False Vacuum Inflation: Correlating the Tensor-to-Scalar Ratio to the Top Quark and Higgs Boson masses, Phys.Rev.Lett. 108 (2012) 191302. arXiv:1112.5430, doi:10.1103/PhysRevLett.108.191302.

[15] I. Masina, A. Notari, Inflation from the Higgs field false vacuum with hybrid potential, JCAP 1211 (2012) 031. arXiv:1204.4155, doi:10.1088/1475-7516/2012/11/031.

[16] I. Masina, The Gravitational wave background and Higgs false vacuum inflation, Phys. Rev. D 89 (12) (2014) 123505. arXiv:1403.5244, doi:10.1103/PhysRevD.89.123505.

[17] I. Masina, Ruling out Critical Higgs Inflation?, Phys. Rev. D 98 (4) (2018) 043536. arXiv:1805.02160, doi:10.1103/PhysRevD.98.043536.

[18] G. Isidori, V. S. Rychkov, A. Strumia, N. Tetradis, Gravitational corrections to standard model vacuum decay, Phys. Rev. D 77 (2008) 025034. arXiv:0712.0242, doi:10.1103/PhysRevD.77.025034.

[19] F. Bezrukov, M. Shaposhnikov, The Standard Model Higgs boson as the inflaton, Phys.Lett. B659 (2008) 703–706. arXiv:0710.3755, doi:10.1016/j.physletb.2007.11.072.

[20] A. Barvinsky, A. Y. Kamenshchik, A. Starobinsky, Inflation scenario via the Standard Model Higgs boson and LHC, JCAP 0811 (2008) 021. arXiv:0809.2104, doi:10.1088/1475-7516/2008/11/021.

[21] A. De Simone, M. P. Hertzberg, F. Wilczek, Running Inflation in the Standard Model, Phys. Lett. B678 (2009) 1–8. arXiv:0812.4946, doi:10.1016/j.physletb.2009.05.054.

[22] F. Bezrukov, M. Shaposhnikov, Standard Model Higgs boson mass from inflation: Two loop analysis, JHEP 0907 (2009) 089. arXiv:0904.1537, doi:10.1088/1126-6708/2009/07/089.

[23] A. Barvinsky, A. Y. Kamenshchik, C. Kiefer, A. Starobinsky, C. Steinwachs, Higgs boson, renormalization group, and naturalness in cosmology, Eur.Phys.J. C72 (2012) 2219. arXiv:0910.1041, doi:10.1140/epjc/s10052-012-2219-3.

[24] F. Bezrukov, A. Magnin, M. Shaposhnikov, S. Sibiryakov, Higgs inflation: consistency and generalisations, JHEP 01 (2011) 016. arXiv:1008.5157, doi:10.1007/JHEP01(2011)016.

[25] F. Bezrukov, M. Yu. Kalmykov, B. A. Kniehl, M. Shaposhnikov, Higgs Boson Mass and New Physics, JHEP 10 (2012) 140. arXiv:1205.2893, doi:10.1007/JHEP10(2012)140.

[26] K. Allison, Higgs xi-inflation for the 125-126 GeV Higgs: a two-loop analysis, JHEP 1402 (2014) 040. arXiv:1306.6931, doi:10.1007/JHEP02(2014)040.

[27] F. Bezrukov, M. Shaposhnikov, Why should we care about the top quark Yukawa coupling?, J. Exp. Theor. Phys. 120 (2015) 335–343, [Zh. Eksp. Teor. Fiz.147,389(2015)]. arXiv:1411.1923, doi:10.1134/S1063776115030152.

[28] F. Bezrukov, M. Pauly, J. Rubio, On the robustness of the primordial power spectrum in renormalized Higgs inflation, JCAP 1802 (02) (2018) 040. arXiv:1706.05007, doi:10.1088/1475-7516/2018/02/040.

[29] R. L. Workman, et al., The review of particle physics, 2022 and 2023 update, Prog. Theor. Exp. Phys. 083C01 (2022).

[30] C. Ford, I. Jack, D. R. T. Jones, The Standard model effective potential at two loops, Nucl. Phys. B387 (1992) 373–390, [Erratum: Nucl. Phys.B504,551(1997)]. arXiv:hep-ph/0111190, doi:10.1016/0550-3213(92)90165-8.

[31] S. Coleman, E. Weinberg, Radiative Corrections as the Origin of Spontaneous Symmetry Breaking, Phys. Rev. D 7 (1973) 1888–1910. doi:10.1103/PhysRevD.7.1888.

[32] Z. Alam, S. P. Martin, Standard model at 200 GeV, Phys. Rev. D 107 (1) (2023) 013010. arXiv:2211.08576, doi:10.1103/PhysRevD.107.013010.

[33] Combination of measurements of the top quark mass from data collected by the ATLAS and CMS experiments at $\sqrt{s} = 7$ and 8 TeV (2023).

[34] M. V. Garzelli, J. Mazzitelli, S. O. Moch, O. Zenaiev, Top-quark pole mass extraction at NNLO accuracy, from total, single- and double-differential cross sections for $t\bar{t} + X$ production at the LHC (11 2023). arXiv:2311.05509.

[35] L. N. Mihaila, J. Salomon, M. Steinhauser, Gauge Coupling β-functions in the Standard Model to Three Loops, Phys. Rev. Lett. 108 (2012) 151602. arXiv:1201.5868, doi:10.1103/PhysRevLett.108.151602.

[36] L. N. Mihaila, J. Salomon, M. Steinhauser, Renormalization constants and β-functions for the gauge couplings of the Standard Model to three-loop order, Phys. Rev. D86 (2012) 096008. arXiv:1208.3357, doi:10.1103/PhysRevD.86.096008.

[37] K. G. Chetyrkin, M. F. Zoller, Three-loop β-functions for top-Yukawa and the Higgs self-interaction in the Standard Model, JHEP 06 (2012) 033. arXiv:1205.2892, doi:10.1007/JHEP06(2012)033.

[38] K. G. Chetyrkin, M. F. Zoller, β-function for the Higgs self-interaction in the Standard Model at three-loop level, JHEP 04 (2013) 091, [Erratum: JHEP09,155(2013)]. arXiv:1303.2890, doi:10.1007/JHEP04(2013)091,10.1007/JHEP09(2013)155.

[39] A. V. Bednyakov, A. F. Pikelner, V. N. Velizhanin, Higgs self-coupling β-function in the Standard Model at three loops, Nucl. Phys. B875 (2013) 552–565. arXiv:1303.4364, doi:10.1016/j.nuclphysb.2013.07.015.

[40] A. V. Bednyakov, A. F. Pikelner, V. N. Velizhanin, Yukawa coupling β-functions in the Standard Model at three loops, Phys. Lett. B722 (2013) 336–340. arXiv:1212.6829, doi:10.1016/j.physletb.2013.04.038.

[41] A. V. Bednyakov, A. F. Pikelner, V. N. Velizhanin, Three-loop Higgs self-coupling β-function in the Standard Model with complex Yukawa matrices, Nucl. Phys. B879 (2014) 256–267. arXiv:1310.3806, doi:10.1016/j.nuclphysb.2013.12.012.

[42] A. V. Bednyakov, A. F. Pikelner, V. N. Velizhanin, Three-loop SM β-functions for matrix Yukawa couplings, Phys. Lett. B737 (2014) 129–134. arXiv:1406.7171, doi:10.1016/j.physletb.2014.08.049.

[43] M. F. Zoller, Top-Yukawa effects on the β-function of the strong coupling in the SM at four-loop level, JHEP 02 (2016) 095. arXiv:1508.03624, doi:10.1007/JHEP02(2016)095.

[44] A. V. Bednyakov, A. F. Pikelner, Four-loop strong coupling β-function in the Standard Model. , Physics Letters B 762 (2016) 151–156. arXiv:1508.02680.

[45] K. G. Chetyrkin, M. F. Zoller, Leading QCD-induced four-loop contributions to the β-function of the Higgs self-coupling in the SM and vacuum stability., J. High Energ. Phys. 175 (2016). arXiv:1604.00853.

[46] J. Davies, F. Herren, C. Poole, M. Steinhauser, E. Thomsen, A. Gauge coupling β functions to four-loop order in the standard model, Phys. Rev. Lett. 124 (2020) 071803.

[47] S. R. Coleman, E. J. Weinberg, Radiative Corrections as the Origin of Spontaneous Symmetry Breaking, Phys. Rev. D7 (1973) 1888–1910. doi:10.1103/PhysRevD.7.1888.

[48] S. P. Martin, Effective potential at three loops, Phys. Rev. D 96 (9) (2017) 096005. arXiv:1709.02397, doi:10.1103/PhysRevD.96.096005.

[49] S. P. Martin, Four-Loop Standard Model Effective Potential at Leading Order in QCD, Phys. Rev. D 92 (5) (2015) 054029. arXiv:1508.00912, doi:10.1103/PhysRevD.92.054029.

[50] A. Andreassen, W. Frost, M. D. Schwartz, Consistent Use of the Standard Model Effective Potential, Phys. Rev. Lett. 113 (24) (2014) 241801. arXiv:1408.0292, doi:10.1103/PhysRevLett.113.241801.

[51] N. K. Nielsen, On the Gauge Dependence of Spontaneous Symmetry Breaking in Gauge Theories, Nucl. Phys. B101 (1975) 173. doi:10.1016/0550-3213(75)90301-6.

[52] J. A. Casas, J. R. Espinosa, M. Quiros, Standard model stability bounds for new physics within LHC reach, Phys. Lett. B382 (1996) 374–382. arXiv:hep-ph/9603227, doi:10.1016/0370-2693(96)00682-X.

[53] P. A. R. Ade, et al., Improved Constraints on Primordial Gravitational Waves using Planck, WMAP, and BICEP/Keck Observations through the 2018 Observing Season, Phys. Rev. Lett. 127 (15) (2021) 151301. arXiv:2110.00483, doi:10.1103/PhysRevLett.127.151301.

[54] J. Elias-Miro, J. R. Espinosa, G. F. Giudice, H. M. Lee, A. Strumia, Stabilization of the Electroweak Vacuum by a Scalar Threshold Effect, JHEP 06 (2012) 031. arXiv:1203.0237, doi:10.1007/JHEP06(2012)031.

[55] Y. Cado, M. Quirós, Baryogenesis from combined Higgs–scalar field inflation, Phys. Rev. D 106 (5) (2022) 055018. arXiv:2201.06422, doi:10.1103/PhysRevD.106.055018.

[56] Y. Cado, C. Englert, T. Modak, M. Quirós, Baryogenesis in R^2-Higgs Inflation: the Gravitational Connection, (12 2023). arXiv:2312.10414.

[57] W. Yin, Weak-Scale Higgs Inflation, (10 2022). arXiv:2210.15680.

[58] D. P. George, S. Mooij, M. Postma, Quantum corrections in Higgs inflation: the Standard Model case, JCAP 1604 (04) (2016) 006. arXiv:1508.04660, doi:10.1088/1475-7516/2016/04/006.

[59] J. Fumagalli, M. Postma, UV (in)sensitivity of Higgs inflation, JHEP 05 (2016) 049. arXiv:1602.07234, doi:10.1007/JHEP05(2016)049.

[60] J. R. Espinosa, G. F. Giudice, E. Morgante, A. Riotto, L. Senatore, A. Strumia, N. Tetradis, The cosmological Higgstory of the vacuum instability, JHEP 09 (2015) 174. arXiv:1505.04825, doi:10.1007/JHEP09(2015)174.

[61] Y. Akrami, et al., Planck 2018 results. X. Constraints on inflation, Astron. Astrophys. 641 (2020) A10. arXiv:1807.06211, doi:10.1051/0004-6361/201833887.

CFTP/24-001

Prepared for submission to JHEP

Impact of New Experimental Data on the C2HDM: the Strong Interdependence between LHC Higgs Data and the Electron EDM

Thomas Biekötter,[a] **Duarte Fontes,**[b] **Margarete Mühlleitner,**[a] **Jorge C. Romão,**[c] **Rui Santos,**[d,e] **and João P. Silva**[c]

[a] *Institute for Theoretical Physics, Karlsruhe Institute of Technology, 76128 Karlsruhe, Germany*

[b] *Department of Physics, Brookhaven National Laboratory, Upton, N.Y., 11973, U.S.A.*

[c] *Departamento de Física and CFTP, Instituto Superior Técnico, Universidade de Lisboa, Avenida Rovisco Pais 1, 1049-001 Lisboa, Portugal*

[d] *ISEL - Instituto Superior de Engenharia de Lisboa, Instituto Politécnico de Lisboa 1959-007 Lisboa, Portugal*

[e] *Centro de Física Teórica e Computacional, Faculdade de Ciências, Universidade de Lisboa, Campo Grande, Edifício C8, 1749-016 Lisboa, Portugal*

E-mail: thomas.biekoetter@kit.edu, dfontes@bnl.gov, margarete.muehlleitner@kit.edu, jorge.romao@tecnico.ulisboa.pt, rasantos@fc.ul.pt, jpsilva@cftp.ist.utl.pt

arXiv:2403.02425v1 [hep-ph] 4 Mar 2024

Abstract: The complex two-Higgs doublet model (C2HDM) is one of the simplest extensions of the Standard Model with a source of CP-violation in the scalar sector. It has a $\mathbb{Z}_2$ symmetry, softly broken by a complex coefficient. There are four ways to implement this symmetry in the fermion sector, leading to models known as Type-I, Type-II, Lepton-Specific and Flipped. In the latter three models, there is *a priori* the surprising possibility that the 125 GeV Higgs boson couples mostly as a scalar to top quarks, while it couples mostly as a pseudoscalar to bottom quarks. This "maximal" scenario was still possible with the data available in 2017. Since then, there have been more data on the 125 GeV Higgs boson, direct searches for CP-violation in angular correlations of τ-leptons produced in Higgs boson decays, new results on the electron electric dipole moment, new constraints from LHC searches for additional Higgs bosons and new results on $b \to s\gamma$ transitions. Highlighting the crucial importance of the physics results of LHC's Run 2, we combine all these experiments and show that the "maximal" scenario is now excluded in all models. Still, one can have a pseudoscalar component in $h\tau\bar{\tau}$ couplings in the Lepton-Specific case as large as 87% of the scalar component for all mass orderings of the neutral scalar bosons.

Contents

1 Introduction **1**

2 The C2HDM **3**
2.1 Physical parameters 3
2.2 Theoretical and Experimental Constraints 5

3 Searching for large CP-odd couplings **6**
3.1 Type-II 7
3.2 Lepton-Specific 12
3.2.1 $h_1 = h_{125}$ 12
3.2.2 $h_2 = h_{125}$ 14
3.2.3 $h_3 = h_{125}$ 14
3.3 Flipped 14

4 Conclusions **16**

1 Introduction

The discovery of a 125 GeV neutral scalar (h_{125}) by the ATLAS [1] and CMS [2] collaborations at the Large Hadron Collider (LHC) opened a window into the scalar sector. The subsequent Run 2 stage has greatly improved our knowledge, as will become apparent in this article. However, there is still much to uncover, as we start Run 3 and peer into the scalar sector with unprecedented precision.

One interesting example concerns the CP properties of the h_{125}. The early detection of the $h_{125} \to ZZ^*$ decay meant that the Higgs boson could not be a pure CP-odd state [3, 4]. But maybe it can be a mixture of CP-even and CP-odd components. More surprisingly, the h_{125} can couple as mostly CP-even to some states and as mostly CP-odd to others. Consider a two-Higgs doublet model with a $\Phi_1 \to \Phi_1$, $\Phi_2 \to -\Phi_2$ symmetry, softly broken in the potential by a term,

$$V_{\text{soft}} = m_{12}^2 \Phi_1^\dagger \Phi_2 + m_{12}^{2*} \Phi_2^\dagger \Phi_1 \,, \tag{1.1}$$

where m_{12}^2 is a complex coefficient. This is known as the complex two-Higgs doublet model (C2HDM). We will denote by "real 2HDM" the model obtained when all coefficients in the scalar potential (including m_{12}^2) are real[1]; for reviews, see Refs. [6, 7]. The real 2HDM was introduced by T. D. Lee in order to show that one can have a spontaneous symmetry

[1] In Ref. [5] it is argued that, since neutral meson observables require explicit complex CP-violating dimension-four Yukawa couplings to quarks, the real 2HDM might not be a fully consistent theory.

breaking origin for CP-violation [8]. In contrast, in the C2HDM investigated here the CP-violation appears explicitly in the potential [9, 10].

Due to the presence of additional sources of CP-violation and the possibility of accommodating a strong first-order electroweak phase transition, the C2HDM is a suitable framework for an explanation of the baryon asymmetry of the Universe by means of electroweak baryogenesis. This model has been studied extensively in the literature; see, for example, Refs. [11–40]. In particular, a full analysis was performed of the C2HDM parameter space consistent with the experimental data available at the end of 2017 [26]. The 2017 analysis introduced a new code, `C2HDM_HDECAY`, implementing the C2HDM in the well-known `HDECAY` program [41, 42], and used also:

- Signal strength constraints on h_{125} from the combination of ATLAS and CMS data collected at 7 TeV and 8 TeV [43];
- HiggsBounds 4.3.1 [44], for data from searches for additional scalars;
- The electron electric dipole moment (eEDM) limit of 8.7×10^{-29} e.cm [45];
- The lower bound of 580 GeV on the charged Higgs boson mass, $m_{H^\pm}$, from radiative B-meson decays in the Type-II and Flipped models (introduced below) [46].

Since then, the experimental situation improved considerably on all four fronts. In fact, there are new data on both the properties of the h_{125} and the searches for additional scalar states, a factor of roughly 20 improvement on the eEDM, and improved lower bounds on $m_{H^\pm}$ in Type-II and Flipped. In this paper, we analyze the impact of the new experimental data on the parameter space of the C2HDM. Specifically, we address the question whether it is still experimentally viable that the detected Higgs boson at 125 GeV could be coupled to down-type quarks and/or charged leptons as a dominantly CP-odd state.[2] To this end, we confront the model with the following set of recent measurements:

- The latest LHC data on the h_{125} signal strengths, including the full Run 2 data collected at 13 TeV, for the different production and decay modes that have so far been detected. We specifically use the ATLAS results summarized in Fig. 3 of Ref. [52], demanding that the predicted signal rates agree within 2σ with each individual signal-rate measurement. The ATLAS measurements are well in agreement with the corresponding CMS results, such that all our conclusions would remain unchanged if instead the CMS results or a combination of ATLAS+CMS results were used;
- The impact of the latest data of direct searches for CP-violation by CMS using angular correlations in decay planes of τ leptons produced in Higgs boson decays $h_{125} \to \tau\bar{\tau}$ [53], setting an upper limit of $\alpha_{h\tau\tau} < 41^\circ$ on the effective mixing angle between the

[2] Similar analyses focusing on the LHC Higgs data have been carried out in the past within an effective field theory framework to describe the Higgs-boson couplings, see, e.g. Refs. [47–51].

CP-even and CP-odd τ-Yukawa coupling at the 2σ confidence level (which, as we will show, has a very strong impact on our analysis);[3]

- The impact of new searches for additional scalars, as compiled in `HiggsBounds` 5.7.1 and 5.9.1 [44, 55–57] and in the newest `HiggsTools` 1.1.3 [58], incorporating the newest version 6 of `HiggsBounds`, extending the previous versions by a large set of searches that were performed including the full Run 2 data collected at 13 TeV;

- The recent 90% confidence-level limit on the eEDM of 1.1×10^{-29} e.cm reported by the ACME collaboration [59] and the most recent limit of 4.1×10^{-30} e.cm measured at JILA [60];

- Updated bounds on the mass of the charged Higgs bosons from measurements of radiative B-meson decays (see the discussion in Sec. 3.1).

We note that in the C2HDM the stringent eEDM bounds can only be evaded either close to the CP-conserving limit of the model, or in scenarios where cancellations between diagrams with different neutral scalar particles occur [61–63].[4] Also, henceforth HB stands for `HiggsBounds` and HT for `HiggsTools`.

The paper is organised as follows. In Section 2, we describe the parameter space of the model and the couplings of the scalars to fermions and gauge bosons, and we present the theoretical and experimental constraints used in our analysis. In Section 3, we discuss the current situation concerning the possibility that the CP-odd components in the couplings of fermions to h_{125} are sizable compared to the respective CP-even components, and thus potentially directly detectable at the LHC. We summarize our conclusions in Section 4.

2 The C2HDM

2.1 Physical parameters

We follow closely the notation of Ref. [26]. In our notation, the vacuum expectation values (vevs) of the neutral components of the scalar doublets are $\langle \Phi_i^0 \rangle = v_i/\sqrt{2}$ $(i = 1, 2)$, where the parameters v_i can be set to be real and positive without loss of generality due to the freedom of field re-definitions of the doublet fields Φ_i, and $v^2 = v_1^2 + v_2^2 \simeq 246\,\text{GeV}$, $\tan\beta = v_2/v_1$. The mixing of the neutral scalar particles can be described by three angles α_k $(k = 1, 2, 3)$, combined in the mixing matrix

$$R = \begin{pmatrix} c_1 c_2 & s_1 c_2 & s_2 \\ -(c_1 s_2 s_3 + s_1 c_3) & c_1 c_3 - s_1 s_2 s_3 & c_2 s_3 \\ -c_1 s_2 c_3 + s_1 s_3 & -(c_1 s_3 + s_1 s_2 c_3) & c_2 c_3 \end{pmatrix}, \tag{2.1}$$

[3] Our analysis uses the CMS results, which was published earlier than the corresponding ATLAS results. ATLAS recently published a similar upper limit of $\alpha_{h\tau\tau} < 34^\circ$ [54]. Our conclusions would remain unchanged if a combined CMS+ATLAS limit would be considered.

[4] The contributions from the muon EDM and from non-leptonic EDMs are currently less stringent [26] and will not be considered here.

where the short-hand notation $s_k \equiv \sin\alpha_k$ and $c_k \equiv \cos\alpha_k$ has been used, and, without loss of generality,

$$-\pi/2 < \alpha_1 \leq \pi/2, \qquad -\pi/2 < \alpha_2 \leq \pi/2, \qquad -\pi/2 \leq \alpha_3 \leq \pi/2. \tag{2.2}$$

We will make use of a mass-ordered notation in which the neutral scalar masses obey $m_1 < m_2 < m_3$. Following Ref. [26], we will describe the scalar sector of the C2HDM in terms of 9 independent parameters:

$$v,\ \tan\beta,\ \alpha_1,\ \alpha_2,\ \alpha_3,\ m_{H^\pm},\ m_1,\ m_2,\ \text{and}\ \mathrm{Re}(m_{12}^2)\ . \tag{2.3}$$

With this choice of independent parameters, the mass of the heaviest neutral scalar, m_3, is a dependent parameter, given by

$$m_3^2 = \frac{m_1^2\, R_{13}(R_{12}\, t_\beta - R_{11}) + m_2^2\ R_{23}(R_{22}\, t_\beta - R_{21})}{R_{33}(R_{31} - R_{32}\, t_\beta)}\,, \tag{2.4}$$

with $t_\beta \equiv \tan\beta$. Any of the three neutral scalars, denoted h_1, h_2, h_3 in the following, can in principle coincide with h_{125}; we will thus explore the three possibilities: $m_{h_{125}} = m_1$, $m_{h_{125}} = m_2$, and $m_{h_{125}} = m_3$.

The most general 2HDM suffers from potentially large flavour-changing neutral scalar interactions with quarks, which could contribute to the neutral meson mixing observables at levels much above what is experimentally allowed. This can be cured by the so-called natural flavour conservation mechanism, which uses a $\mathbb{Z}_2$ symmetry, $\Phi_1 \to \Phi_1$, $\Phi_2 \to -\Phi_2$ extended to the fermion sector in such a way that each of the three families of fermions (up-type quarks, down-type quarks, charged leptons) couples to one and only one scalar field [64, 65]. Denoting by Φ_u, Φ_d, and Φ_ℓ the doublet Φ_i $(i = 1, 2)$ that couples to up-type quarks, down-type quarks, and charged leptons, respectively, there are the following four possibilities:[5]

- Type-I: $\Phi_u = \Phi_d = \Phi_\ell \equiv \Phi_2$;
- Type-II: $\Phi_u \equiv \Phi_2 \neq \Phi_d = \Phi_\ell \equiv \Phi_1$;
- Lepton-Specific (LS): $\Phi_u = \Phi_d \equiv \Phi_2 \neq \Phi_\ell \equiv \Phi_1$;
- Flipped $\Phi_u = \Phi_\ell \equiv \Phi_2 \neq \Phi_d \equiv \Phi_1$.

In the fermion and scalar mass bases, the Yukawa Lagrangian for the neutral scalars may be written as

$$\mathcal{L}_Y = -\sum_{i=1}^{3} \frac{m_f}{v}\, \bar{f}\left[c^e(h_i f\bar{f}) + i c^o(h_i f\bar{f})\gamma_5\right] f\, h_i\,, \tag{2.5}$$

where f denotes the fermion field with mass m_f. The real coefficients $c^e(h_i f\bar{f})$ and $c^o(h_i f\bar{f})$ describe the CP-even and CP-odd parts of the Yukawa couplings, respectively; we list them in Table 1 in terms of the mixing matrix elements R_{ij} (see Eq. (2.1)) and the mixing angle β.

	u-type	d-type	leptons
Type-I	$\frac{R_{i2}}{s_\beta} - i\frac{R_{i3}}{t_\beta}\gamma_5$	$\frac{R_{i2}}{s_\beta} + i\frac{R_{i3}}{t_\beta}\gamma_5$	$\frac{R_{i2}}{s_\beta} + i\frac{R_{i3}}{t_\beta}\gamma_5$
Type-II	$\frac{R_{i2}}{s_\beta} - i\frac{R_{i3}}{t_\beta}\gamma_5$	$\frac{R_{i1}}{c_\beta} - it_\beta R_{i3}\gamma_5$	$\frac{R_{i1}}{c_\beta} - it_\beta R_{i3}\gamma_5$
Lepton-Specific	$\frac{R_{i2}}{s_\beta} - i\frac{R_{i3}}{t_\beta}\gamma_5$	$\frac{R_{i2}}{s_\beta} + i\frac{R_{i3}}{t_\beta}\gamma_5$	$\frac{R_{i1}}{c_\beta} - it_\beta R_{i3}\gamma_5$
Flipped	$\frac{R_{i2}}{s_\beta} - i\frac{R_{i3}}{t_\beta}\gamma_5$	$\frac{R_{i1}}{c_\beta} - it_\beta R_{i3}\gamma_5$	$\frac{R_{i2}}{s_\beta} + i\frac{R_{i3}}{t_\beta}\gamma_5$

Table 1: Yukawa couplings of the Higgs bosons h_i in the C2HDM, divided by the corresponding Standard Model Higgs couplings. The expressions correspond to $[c^e(h_i f\bar{f}) + ic^o(h_i f\bar{f})\gamma_5]$ from Eq. (2.5).

In the following, $c^e(h_{125}f\bar{f})$ and $c^o(h_{125}f\bar{f})$ are abbreviated by c_f^e and c_f^o, respectively. Moreover, we represent the different families of up-type quarks, down-type quarks and leptons by identifying f with the generic labels t, b and τ, respectively. The effective mixing angle between CP-even and CP-odd τ-Yukawa couplings introduced in Sec. 1 is then given by

$$\alpha_{h\tau\tau} = \tan^{-1}|c_\tau^o|/|c_\tau^e| \,. \tag{2.6}$$

The LHC signal-rate measurements of h_{125} indicate that the couplings of h_{125} to the massive gauge bosons $V = W, Z$ agree within about 10% with their Standard Model (SM) values [52, 66]. This favors the alignment limit of the 2HDM, in which the couplings of the neutral scalar h_i identified with h_{125}, mimic the ones of the Higgs boson as predicted by the SM. The deviations of the couplings of each neutral scalar h_i from that limit are parameterized by

$$c(h_i VV) = c_\beta R_{i1} + s_\beta R_{i2} \,, \tag{2.7}$$

where in the exact alignment limit one finds $c(h_i VV) = 1$ for one of the three states $h_i = h_{125}$ and $c(h_i VV) = 0$ for the other two $h_i \neq h_{125}$, and outside of the alignment limit $c(h_i VV) < 1$ for all three neutral scalars. For reference, the full set of couplings in the C2HDM using our notation is presented on the web page [67].

2.2 Theoretical and Experimental Constraints

Our input parameters are chosen as follows. One of the neutral scalars is identified with h_{125}; the masses of the remaining neutral scalars are kept in the interval 30 GeV $\leq m_i <$ 1 TeV. As for $m_{H^\pm}$, we implement the bounds on the $m_{H^\pm} - t_\beta$ plane arising from B physics, most notably those implied by the measurements of $B \to X_s\gamma$ [46, 68–72]. We follow Ref. [26] in using 80 GeV $\leq m_{H^\pm} <$ 1 TeV for the Type-I and LS models, and 580 GeV $\leq m_{H^\pm} <$ 1 TeV for both Type-II and Flipped models (although we will discuss the impact of the new bounds

[5] For all four possibilities, the Yukawa coupling matrices of fermions with all neutral scalars are diagonal and proportional to the fermion masses. Thus, besides the parameters for the scalar sector, only fermion masses and the parameters of the Cabibbo-Kobayashi-Maskawa (CKM) matrix (for the coupling to charged scalars) are needed to specify a parameter point.

in the two latter types). As for the remaining input parameters, we also follow Ref. [26], by choosing the intervals: $0.8 \leq t_\beta \leq 35$, $-\frac{\pi}{2} \leq \alpha_{1,2,3} < \frac{\pi}{2}$ and $0 \leq \mathrm{Re}(m_{12}^2) < 500000$ GeV^2. We then require our points to comply with the measured values of the oblique parameters S, T and U [7] within 2σ of the experimental results quoted in Ref. [73], comparing against the theoretically predicted values for the oblique parameters at the one-loop level. Finally, for each plot shown below, we will explicitly mention which LHC constraints on h_{125} are being used (whether those from Ref. [43] or those from Ref. [52]), which LHC constraints on extra scalars are being used (whether HB-4.3.1 [44], HB-5.9.1 [57] or HT-1.1.3 [58]), which eEDM constraints are being used (whether 8.7×10^{-29} e.cm [45, 74], 1.1×10^{-29} e.cm [59] or 4.1×10^{-30} e.cm [60]), and if the constraint on CP-violating couplings coming from angular correlations in the decays $h_{125} \to \tau\bar{\tau}$ [53] is being used. For the theoretical predictions of the eEDM in the C2HDM, we follow Ref. [16].

In all plots, we impose the known theoretical constraints, namely boundedness from below and the non-existence of a lower lying minimum [75] to ensure the absolute stability of the EW vacuum, and we demand perturbative unitarity [76–78], applying an upper limit of 8π on the eigenvalues of the scalar four-point scattering matrix in the high-energy limit.

3 Searching for large CP-odd couplings

We perform an update of Ref. [26] of some of the authors of this paper, looking in particular at the possibility that the $h_{125}b\bar{b}$ and/or the $h_{125}\tau\bar{\tau}$ coupling might be mostly CP-odd; that is, $|c_b^o| \gg |c_b^e|$ and/or $|c_\tau^o| \gg |c_\tau^e|$. In Ref. [26], we found the situation summarized in Table 2.

Type	I	II	LS	Flipped
$h_1 = h_{125}$	×	×	✓	✓
$h_2 = h_{125}$	×	✓	✓	×
$h_3 = h_{125}$	×	×	✓	×

Table 2: Results for the possibility of sizable CP-odd components in the couplings of the Higgs boson at 125 GeV from Ref. [26]. A checkmark (cross) means that it was (not) possible to have large CP-odd components $|c_f^o| > |c_f^e|$ ($f = b, \tau$) in the couplings of h_{125}.

The impossibility to accommodate mostly CP-odd couplings of h_{125} found in all Type-I cases is easy to understand. As can be seen in the first row of Table 1, the CP-odd coupling components in that Type are always proportional to R_{i3}/t_β. Now, on the one hand, the B physics constraints force $t_\beta > 1$. On the other hand, R_{i3} is just a product of sine and cosine of the rotation angles matrix of Eq. (2.1), so that $|R_{i3}| \leq 1$. More than this, $|R_{i3}|$ is further constrained by μ_{VV} (the ratio between the new physics and the SM value of the product between Higgs-boson production and its decay to vector bosons); the reason is that $|R_{i3}|$ is a measure of the CP-odd admixture of the state h_i, thus suppressing the couplings to gauge bosons [22]. Finally, since in Type-I all fermions couple as the top quark to the

scalars, this Type is precluded from large CP-odd components.[6] As a consequence, in the following discussion we do not consider the Type-I anymore and focus on the other three Yukawa types of the C2HDM.

In the following subsections, we present several figures. In all of them, the light green points are consistent with the old eEDM of 8.7×10^{-29} e.cm, the dark green points with the more recent result 1.1×10^{-29} e.cm and the dark red points with the new result, 4.1×10^{-30} e.cm. Also, the signs of c_f^e and c_f^o have no absolute meaning; they are relative to the sign of $k_V \equiv c(h_{125}VV)$, which is thus also taken into account in the plots by always plotting $\text{sgn}(k_V)c_f^o$ *vs.* $\text{sgn}(k_V)c_f^e$.

3.1 Type-II

Reference [26] found that, in Type-II, it was possible to have sizable CP-odd components in the Yukawa couplings of h_{125} for the case of $h_2 = h_{125}$ (and only in this case). In the following figures, we reproduce this result, and investigate the impact of recent LHC data. We thus assume $h_2 = h_{125}$, and we use the bound of $m_{H^\pm} > 580$ GeV [46] resulting from measurements of $b \to s\gamma$ transitions, which was the limit applied in Ref. [26]. Meanwhile, there was an updated NNLO calculation of the inclusive $b \to s\gamma$ branching ratios, giving rise to a limit of $m_{H^\pm} > 800$ GeV [72]. This limit was based on the HFLAV average value $\text{BR}(b \to s\gamma) = (3.32 \pm 0.15) \times 10^{-4}$ from 2019 [85]. The current average value from HFLAV 2022 [86], $\text{BR}(b \to s\gamma) = (3.49 \pm 0.19) \times 10^{-4}$, is slightly larger and has a larger uncertainty.[7] A reanalysis of the impact of this new result by the group that provided the previous limits [46, 72] lowers the limit on the charged Higgs-boson mass to $m_{H^\pm} > 500$ GeV at 2σ confidence level [88]. Since the underlying experimental data has undergone significant changes in recent years, leading to substantial fluctuations in the lower limit on the mass of the charged Higgs bosons, we decided to keep the somewhat stronger limit of $m_{H^\pm} > 580$ GeV [46] applied in the previous analysis [26] to facilitate a better comparison and a more direct analysis of the impact of the other experimental constraints applied in our analysis. We have verified that our conclusions regarding the possibility of accommodating sizable CP-odd components in the couplings of h_{125} in the Type-II and the Flipped Type do not depend on whether a lower limit of 500 GeV or 580 GeV is applied.

Figure 1 shows the allowed parameter space in the plane CP-odd (c_b^o) *vs.* CP-even (c_b^e) component of the $h_{125}b\bar{b}$ coupling. The left panel considers the 7 and 8 TeV LHC data for h_{125} collected until 2017 [43] and the cross-section limits from BSM scalar searches as implemented in HB-4.3.1 [44], which are the limits that were applied in the previous analysis [26]. The right one considers additionally the 13 TeV LHC data for h_{125} collected during Run 2 [52] and the cross-section limits from BSM scalar searches at 13 TeV

[6] There are also direct measurements on the CP-odd *vs.* CP-even components of the top coupling coming from $pp \to t\bar{t}(h_{125} \to \gamma\gamma)$ [79], giving rise to $\alpha_{htt} < 43^\circ$ at 95% confidence level, thus directly excluding the maximally CP-odd scenario with $|c_t^o| \gg |c_t^e|$. We also point out that the valid cases shown in Table 2 also allowed for the so-called wrong-sign regime, in which the Yukawa coupling is real but has the opposite sign it would have in the SM [19, 80–84].

[7] Not including the most recent Belle-II measurement [87], the HFLAV 2022 average value is in good agreement with this latest experimental result.

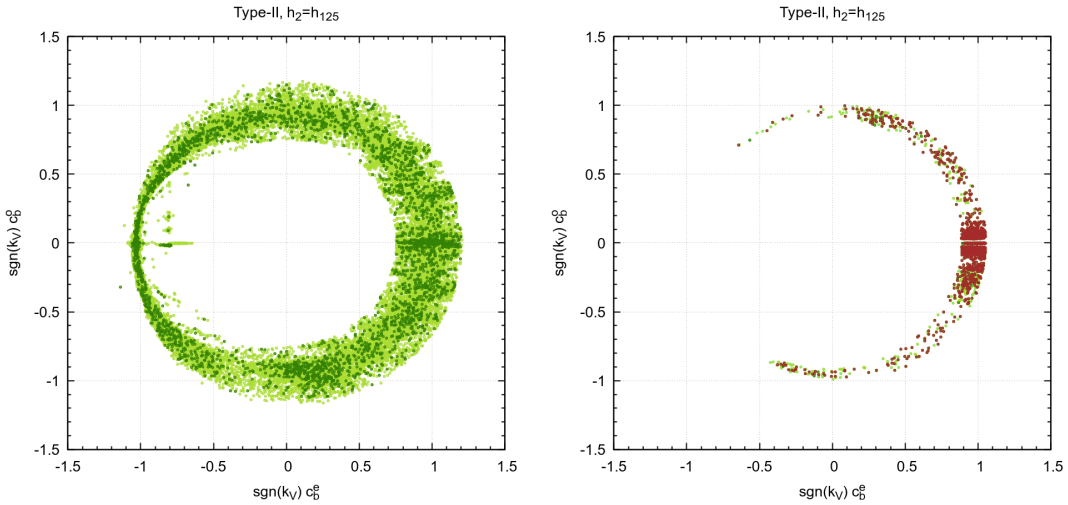


Figure 1: CP-odd *vs.* CP-even component in the $h_{125}b\bar{b}$ coupling of allowed parameter points in Type-II, assuming $h_2 = h_{125}$. Left panel: LHC 2017 data on h_{125} and constraints from beyond-SM (BSM) scalar searches at 7 and 8 TeV using HB-4.3.1. Right panel: LHC 2022 data on h_{125} and constraints from BSM scalars including 13 TeV data using HT-1.1.3. The light green points are consistent with the old eEDM of 8.7×10^{-29} e.cm [45, 74], the dark green points with the more recent ACME result 1.1×10^{-29} e.cm [59]. The dark red points obey the currently strongest limit on the eEDM 4.1×10^{-30} e.cm reported by JILA [60]. The fermion masses in the loops of diagrams contributing to the eEDM were taken as pole masses. The limit $\alpha_{h\tau\tau} < 41^\circ$ [53] from searches for CP-violation in angular correlations of τ leptons in $h_{125} \to \tau\bar{\tau}$ decays has not been applied in either of the plots in this figure.

as implemented in HT-1.1.3 [58]. The light green points are in agreement with the old eEDM of 8.7×10^{-29} e.cm [45, 74], the dark green points with the more recent result 1.1×10^{-29} e.cm [59]. The dark red points obey the current limit on the eEDM [60]. The considerable reduction of the allowed parameter space in the transition from the left to the right plot is mainly caused by the 13 TeV data on h_{125} collected until 2022 (and to a lesser extend by improved searches for heavier scalars involved in the different versions of HB). The width of the rings is related to the decay width $\Gamma(h_{125} \to b\bar{b}) \propto (c_b^e)^2 + (c_b^o)^2$, which is the largest contribution to the total width and can thus also be responsible for modifications in other decay channels, and the new data reduces the allowed range for $(c_b^e)^2 + (c_b^o)^2$. Note also that the points close to the wrong sign limit in the left panel of Fig. 1 disappear with the new data, which is mainly related to more precise measurements in the gluon-fusion production channels of h_{125}.[8] Yet, even after applying all current constraints except for the direct limit on the effective mixing angle $\alpha_{h\tau\tau}$ (see discussion below), but including the new limit on the eEDM [60], we find allowed parameter points in the Type-II with a large pseudoscalar component in the couplings of h_{125} to bottom quarks.

So far, we have not yet applied the recent direct bound on a CP-odd coupling component from the angular correlations of τ leptons in $h_{125} \to \tau\bar{\tau}$ decays [53, 54]. In the Type-II

[8] See Refs. [89–91] for more detailed discussions about the wrong sign limit in view of the 13 TeV LHC Higgs data.

model, the down-type quarks are coupled to the neutral scalars in the same way as the charged leptons, such that $c_b^{e,o} = c_\tau^{e,o}$. It follows that, in this type, the recent bound $\alpha_{h\tau\tau} < 41^\circ$ has to be taken into account in the study of the CP properties of $h_{125}b\bar{b}$. The limit on $\alpha_{h\tau\tau}$ has not been applied in either of the plots in Fig. 1. Requiring that $\alpha_{hbb} < 41^\circ$, with $\alpha_{hbb} = \tan^{-1}|c_b^o|/|c_b^e| = \alpha_{h\tau\tau}$, excludes the possibility of $|c_b^o| \gg |c_b^e|$ in the right panel of Fig. 1. Nevertheless, the interesting possibility that $|c_b^o| \simeq |c_b^e|$ (and therefore also $|c_\tau^o| \simeq |c_\tau^e|$) would still be allowed.

The above conclusions in the Type-II crucially depend on a significant fine-tuning of the model parameters in order to be compatible with the stringent experimental upper bounds on the eEDM. These limits can be evaded only as a result of a cancellation between different contributions to the eEDM at two-loop level in the perturbative expansion (as discussed in more detail below). This cancellation gives rise to a strong dependence of the predicted eEDM on the model parameters, including the values for the masses of the fermions that appear as virtual particles in the loops of Barr-Zee type diagrams [92]. The corresponding amplitudes are proportional to the mass of the fermion appearing in the loop. Consequently, the numerically relevant contributions stem from diagrams with an internal top quark, bottom quark, or τ lepton. At the two-loop level, it is formally consistent to choose different renomalization prescriptions for the fermion masses [93], and different approaches have been applied in the literature. The two most common choices have been to use either $\overline{\text{MS}}$ running masses at the scale M_Z $(\overline{m}_t(M_Z), \overline{m}_b(M_Z), \overline{m}_\tau(M_Z))$, see e.g. Refs. [16, 33, 94], or pole masses for top quark and τ lepton in combination with the running bottom-quark mass at the scale $\overline{m}_b$ $(m_t, \overline{m}_b(\overline{m}_b), m_\tau)$, see e.g. Refs. [26, 27, 35, 40, 51]. In the analysis discussed above, we have used the latter possibility for the eEDM predictions. In the following, we will discuss the modifications resulting from choosing the running masses at the scale M_Z.

To this end, we generated a new set of parameter points in the Type-II which all satisfy the current experimental limit on the eEDM with the eEDM computed using the running masses at M_Z. Moreover, the parameter points fulfill the other experimental and theoretical constraints discussed in Sec. 2.2, with the exception of the constraints from BSM scalar searches at the LHC and from direct searches for CP-violation in $h_{125} \to \tau\bar{\tau}$ decays. The resulting parameter points are shown in the plane of CP-odd *vs.* CP-even components of the $h_{125}b\bar{b}$ coupling in the left plot of Fig. 2. One can see that, before the cross-section limits from the LHC searches are applied, the results are very similar to the case shown in the right plot of Fig. 1, where the eEDM was computed using the on-shell (OS) prescription for the top-quark and τ-lepton masses in combination with $\overline{m}_b(\overline{m}_b)$. However, after applying the LHC constraints from searches for additional scalars (see the discussion below for details), the only still viable parameter points are situated very close to the alignment limit, as is shown in the right plot of Fig. 2. Hence, if the eEDM is computed using the running masses at the scale M_Z, we find that it is incompatible to have both sizable CP-odd components in the $h_{125}b\bar{b}$ coupling and agreement with the experimental upper limit on the eEDM and with cross-section limits from BSM scalar searches. This is in clear contrast to our observations using pole masses m_t and m_τ in combination with $\overline{m}_b(\overline{m}_b)$ for the eEDM predictions, as becomes apparent by comparing the right plot of Fig. 2 to the right plot of Fig. 1.

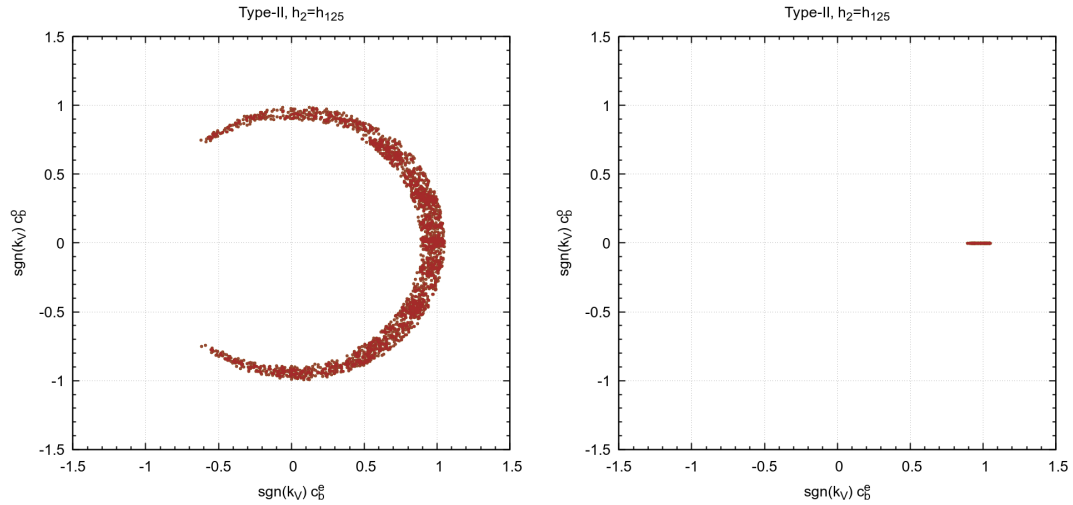


Figure 2: CP-odd *vs.* CP-even component in the $h_{125}b\bar{b}$ coupling of allowed parameter points in Type-II, assuming $h_2 = h_{125}$. All points obey the current experimental limit on the eEDM [60], where here the masses of the fermions in the loops of diagrams contributing to the eEDM were taken to be the running masses at the M_Z scale (see text for details). Also applied are the constraints from the h_{125} cross section measurements using LHC 2022 data collected at 13 TeV. The left panel does not include the LHC constraints on the extra scalars while in the right panel these constraints are applied including the most recent searches at 13 TeV using HT-1.1.3.

To gain more insight as to why the conclusions in the Type-II model depend so strongly on the choice of the parameters (such as the precise values for the fermion masses), we investigated the individual Barr-Zee contributions to the eEDM. Following the nomenclature of Ref. [16], these can be divided into four classes denoted "fermion loops", "charged Higgs loops", "W loops" and "$H^{\mp}W^{\pm}\gamma$ loops". In our scans, we observed that, for parameter points that satisfy the experimental upper limit of $4.1 \cdot 10^{-30}$ e.cm, the contributions from the individual pieces can still be of the order of 10^{-28} e.cm. This is illustrated in the left plot of Fig. 3, where we show in green the contribution from one of the diagrams in the W-loop class, which typically is the numerically most important piece, and in red the sum of the other three contributions. Finally, we show in blue the total eEDM containing all four pieces, confirming the very significant fine-tuning between the different components.

In our scans, this fine-tuning is achieved by carefully adjusting the parameters of the model. If one changes the fermion masses in the loops (e.g. as a result of choosing different renormalization prescriptions as discussed above), one has to adjust the other parameters of the model in order to maintain the fine-tuning in the eEDM prediction. This concerns mainly the masses of the BSM scalars, which then turns out to have a large impact on the LHC phenomenology and corresponding constraints on the C2HDM. The difference of results in Type-II according to the different prescription of the fermion masses, as discussed above, has its origin in the application of cross-section limits from LHC searches — more specifically, searches for scalar resonances produced via gluon-fusion with subsequent decay

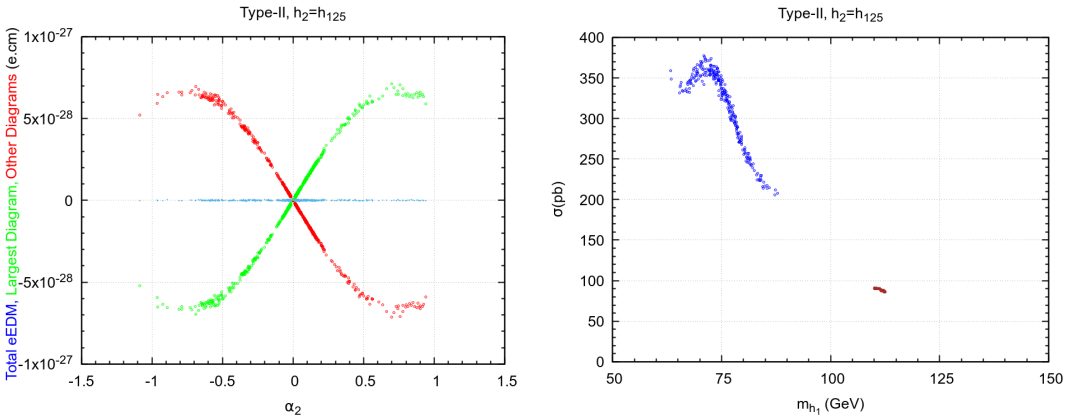


Figure 3: Left panel: Individual contributions to the eEDM taken into our account in our analysis. The green points show the contribution from one of the diagrams in the W-loop class, which gives the largest contribution to the eEDM, and the red points show the sum of the remaining three contributions. The blue points show the total eEDM (see text for the details). Right panel: LHC 13 TeV cross section for the gluon-fusion production of h_1 as a function of m_{h_1}. Blue and brown points are the subset of the points shown in the right plot of Fig. 1 and in the left plot of Fig. 2, respectively, that additionally satisfy the condition $|c_b^e| < 0.1$.

in $\tau\bar{\tau}$ final states performed by CMS at 13 TeV [95].[9] In the right plot of Fig. 3, we show the parameter points from the two scans that we have performed in Type-II, with the lightest scalar mass m_{h_1} on the horizontal axis and the gluon-fusion production cross section for h_1 at 13 TeV on the vertical axis. Note that we only show the points that satisfy the additional condition $|c_b^e| < 0.1$, which ensures that, for the shown parameter points, the $h_{125}b\bar{b}$ coupling is mainly CP-odd. The brown points are from the scan in which we used the pole masses m_t and m_τ and the $\overline{\text{MS}}$ mass $\overline{m}_b(\overline{m}_b)$ in the computation of the eEDM (corresponding to a subset of the points depicted in the right plot of Fig. 1), and the blue points are from the scan in which the running fermion masses at the weak scale were used (corresponding to a subset of the points depicted in the left plot of Fig. 2). One can see that, for the latter set of parameter points, the masses of the lightest scalar h_1 are lower compared to the points for which the pole masses m_t and m_τ in combination with $\overline{m}_b(\overline{m}_b)$ were used for the eEDM. As a consequence, h_1 has substantially larger production cross sections at the LHC, and would have been observed in searches for low-mass scalar resonances decaying into τ-lepton pairs.[10] The application of the corresponding cross-section limits gives rise not only to the difference between the left and the right plot of Fig. 2, but also to the different conclusions (regarding the possibility of detectable CP-odd components in the couplings of h_{125}) according to the mass renormalization of the virtual fermions in diagrams contributing to the eEDM.

[9] The corresponding ATLAS search [96] does not include the mass region below 125 GeV that is relevant in this discussion.

[10] The branching ratios of the decay $h_1 \to \tau\bar{\tau}$ have values in the interval 8.6% to 9.7% for the brown points and 8.6% to 9.2% for the blue points. Therefore, the exclusion comes mainly from the differences in the production cross section.

3.2 Lepton-Specific

In the LS model, the down-type quarks are coupled to the scalars in the same way as the up-type quarks. As a consequence, given that (as discussed above) the $h_{125}t\bar{t}$ coupling is measured to be mainly CP-even, one can only find sizable CP-odd components in the LS model in the coupling to leptons, i.e. $|c_\tau^o| \gg |c_\tau^e|$. In the following, we consider the three possible mass hierarchies with the lightest, the second-lightest or the heaviest neutral scalar playing the role of h_{125}. With the 7 and 8 TeV LHC Higgs data collected until 2017 and for the LS case, all placements of h_{125} in the neutral scalar mass orderings were still consistent with a mostly CP-odd $h_{125}\tau\bar{\tau}$ coupling [26].

In view of the discussion in Sec. 3.1, we computed the eEDM in the LS model using the running fermion masses at the M_Z scale. However, we note that, in contrast to the Type-II model, the LS model is such that the fine-tuning of parameters required to satisfy the upper bounds on the eEDM is not very severe. It follows that our findings are unchanged if, instead of the running fermion masses at the M_Z scale, we were to use the pole masses for the top quark and the τ lepton as well as $\overline{m}_b(\overline{m}_b)$ (we verified this explicitly with dedicated scans). The LS model has a further advantage over the Type-II model, which concerns the fact that constraints from collider experiments are less severe. As discussed in Sec. 2.2, in fact, the lower limit $m_{H^\pm} > 580$ GeV on the charged Higgs-boson mass from measurements of $b \to s\gamma$ transitions applicable in Type-II is not valid for the LS model. Moreover, the LS model can realize CP-violating effects only in the couplings of the 125 GeV Higgs boson to leptons, whereas its couplings to quarks can remain at the same time approximately CP-conserving. As a result, the LS model allows for a sizable amount of CP-violation in the couplings of the h_{125} to leptons, without modifications from CP-violating effects to the most important production and decay channels at the LHC. Thus, there is more freedom in this type for the presence of CP-violating couplings in regards to the cross-section measurements of the detected Higgs boson.

In the following, we will analyze separately the three possible mass hierarchies in the LS model.

3.2.1 $h_1 = h_{125}$

The results for the LS model with $h_1 = h_{125}$ are shown in Fig. 4. This figures takes into account up-to-date constraints from LHC searches for additional Higgs bosons and the signal rate measurements of h_{125}. Whereas in the left panel we exclude the constraints on the CP-violating phase $\alpha_{h\tau\tau}$ coming from direct searches for CP-violation in angular variables of τ leptons in $h_{125} \to \tau\bar{\tau}$ decays, reported by CMS [53], in the right panel we include them. We see that, in the left panel, even though we are including the latest eEDM data, there is still a large allowed parameter region consistent with $|c_\tau^o| \gg |c_\tau^e|$. On the other hand, the right panel shows that the constraints on $\alpha_{h\tau\tau}$ exclude this scenario. Therefore, in the LS type of the C2HDM, the direct LHC measurements of CP-violation in angular variables in $h_{125} \to \tau\bar{\tau}$ decays are able to exclude regions of the parameter space that would otherwise be allowed by all other theoretical and experimental constraints. In particular, we find parameter points which are in agreement with the experimental upper bounds on the

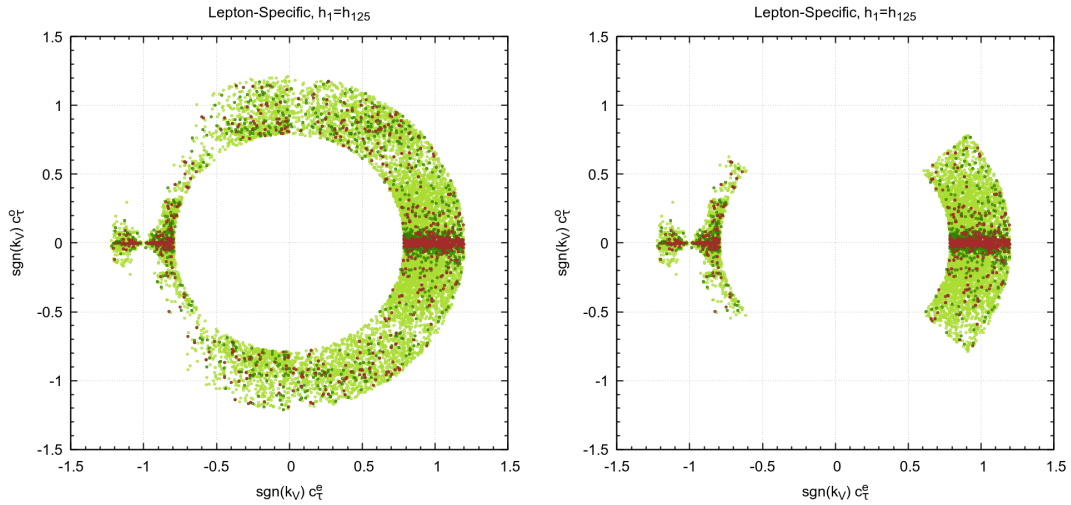


Figure 4: CP-odd *vs.* CP-even component in the $h_{125}\tau\bar{\tau}$ coupling for the allowed parameter points in the LS model, assuming $h_1 = h_{125}$, using 13 TeV LHC Higgs data on h_{125} collected until 2022 and constraints from BSM scalar searches included in HT-1.1.3. In the left panel, the limit $\alpha_{h\tau\tau} < 41^\circ$ from angular correlations of τ leptons in $h_{125} \to \tau\bar{\tau}$ decays is not applied, whereas the right panel includes this limit. Colour code as in Fig. 1.

eEDM (dark red points in Fig. 4), and which are excluded only by the LHC measurements of CP-violation in decays of the h_{125} to τ leptons. This demonstrates the complementarity of probing possible CP-violation in extended Higgs-sector models at low-energies in terms of eEDMs and at high-energy at the LHC.

Even though the direct limits on $\alpha_{h\tau\tau}$ substantially restrict the possible amount of CP-violation in the $h_{125}\tau\bar{\tau}$ coupling, they do not exclude the interesting possibility $|c_\tau^o| \simeq |c_\tau^e|$, as can be seen in the right panel of Fig. 4. This has important consequences for the possibility of explaining the baryon asymmetry of the Universe in the framework of the C2HDM by means of electroweak baryogenesis. It has recently been shown that a sizable amount of CP-violation in the $h_{125}\tau\bar{\tau}$ coupling might be sufficient to accommodate the baryon asymmetry without the presence of additional CP-violation in the other couplings of the h_{125} [51].[11] As such, the LS C2HDM can still be regarded as a possible framework for an explanation of the matter-antimatter asymmetry of the Universe. We note, however, that a successful realization of electroweak baryogenesis also requires a sufficiently strong first-order electroweak phase transition. We leave for future work an analysis of whether the allowed parameter points in our scan sample that feature sizable CP-odd components in the $h_{125}\tau\bar{\tau}$ coupling can additionally accommodate such a phase transition.

[11] Compare, however, also with Ref. [35]. Note furthermore that it is still under debate if the amount of generated baryon asymmetry is sufficiently large to be in agreement with the observed value because of large theory uncertainties in the prediction for the baryon asymmetry, which strongly depends on the approach that is used to compute the source term for the baryon asymmetry, see Ref. [97] for a recent discussion.

3.2.2 $h_2 = h_{125}$

The case with the second lightest neutral scalar h_2 acting as h_{125} is similar to the case where $h_1 = h_{125}$, as can be seen in Fig. 5. Here, we show the same as in Fig. 4, but now for $h_2 = h_{125}$. As in the previous case, a parameter region with $|c_\tau^o| \gg |c_\tau^e|$ still remains after the application of all current experimental constraints from the LHC and the eEDM. Consequently, also the mass hierarchy with $h_2 = h_{125}$ is subject to new constraints on the

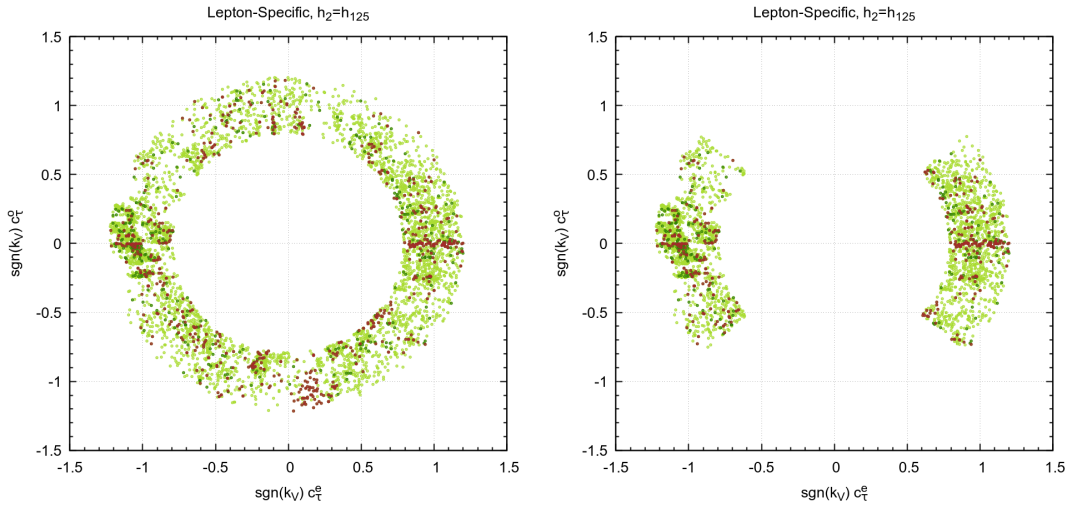


Figure 5: Same as in Fig. 4, but for $h_2 = h_{125}$.

parameter space coming from the LHC measurement of CP violating effects in $h_{125} \to \tau\bar{\tau}$ decays, still leaving the interesting possibility of $|c_\tau^o| \simeq |c_\tau^e|$ though.

3.2.3 $h_3 = h_{125}$

The situation for the mass hierarchy with $h_3 = h_{125}$, is shown in Fig. 6, where the color of the points is defined as in Figs. 4 and 5. Likewise, the limit on $\alpha_{\tau\tau}$ has been applied in the right plot only, whereas all other constraints have been applied in both plots according to the discussion above. The main conclusions are the same as in the previous two cases. Since all mass hierarchies in the LS model are compatible with CP-odd components in the $h_{125}\tau\bar{\tau}$ coupling that are sufficiently large to be directly observable at the LHC, a possible future detection of CP-violation in $h_{125} \to \tau\bar{\tau}$ decays via angular correlations of the τ leptons would not allow for a distinction between the different mass hierarchies.

3.3 Flipped

We have seen that that Higgs data related to μ_{VV} (as well as direct searches [79]) forbid values of $|c_t^0| \gtrsim |c_t^e|$, and that the latest data of searches for CP-violation in angular correlations of the τ leptons in $h_{125} \to \tau\bar{\tau}$ decays precludes $|c_\tau^o| \simeq 1$ [53, 54]. The Flipped type, with $\Phi_u = \Phi_\ell \neq \Phi_d$, might still be a promising candidate for large CP-odd components, as it in principle allows the possibility of large $|c_b^o|$. Moreover, since this type was shown in 2017 (after the 7 and 8 TeV Runs of the LHC) to be able to accommodate sizable CP-odd

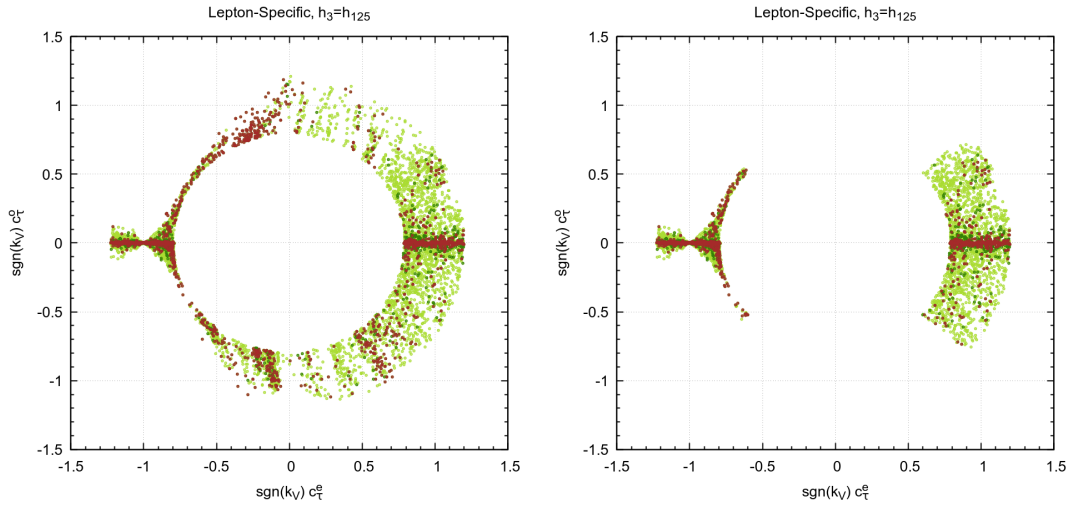


Figure 6: Same as in Fig. 4, but for $h_3 = h_{125}$.

components with the mass hierarchy in which the detected Higgs boson at 125 GeV is the lightest scalar [26], the impact of the more stringent lower bounds on $m_{H^\pm}$ from $b \to s\gamma$ transitions can be expected to be less severe compared to the situation in Type-II (see discussion in Sec. 3.1).

It turns out that this possibility is now excluded. Indeed, the status of the Flipped type changed significantly with respect to Ref. [26]. This is not because of the LHC 2022 data on the signal strengths of h_{125}, but because of the additional constraints imposed by the searches for extra scalars at 13 TeV, as implemented in the most recent version of HB (now incorporated in HT). This is shown in Fig. 7, which takes $h_1 = h_{125}$. In the left panel, we use the old 2017 data on h_{125} and the old HB-4.3.1 bounds. In the right panel, we use HT-1.1.3 and the latest LHC 2022 data on searches for additional Higgs bosons, as well as the most recent limit on the eEDM [60] (not used with the old data on the left panel). The main impact of taking into account the 13 TeV signal-rate measurements of h_{125} is that it decreases the width of the rings on which allowed parameter points can be found. We see a more significant difference between the left and the right plot of Fig. 7 as a result of new constraints from LHC searches for additional scalars at 13 TeV. In particular, searches for one heavy Higgs boson decaying into a Z and another Higgs boson, both by ATLAS [98] and CMS [99], together with the latest eEDM results — precludes the situation where $c_b^e \simeq 0$, which is thus not visible in the right panel of Fig. 7. One should note here that, in the CP-conserving limit of the 2HDM with h_{125} predicted to be CP-even as in the SM, the decay $h_i \to Zh_{125}$ is only allowed for a CP-odd state h_i, whereas there is no coupling between a Z boson and two CP-even scalars. If, on the other hand, h_{125} carries a CP-odd admixture, both heavier neutral scalars h_2 and h_3 can decay into a Z boson and h_{125}. It follows that searches for heavier Higgs bosons decaying into the 125 GeV Higgs boson and a Z-boson are exceptionally important if CP-violation is present in the scalar sector (see also Refs. [21, 23, 24]). In our case, indeed, they exclude large parts of Fig. 7 with $|c_b^e| < 1$. This is a confirmation of the important physical insight gained during Run 2 and, in this

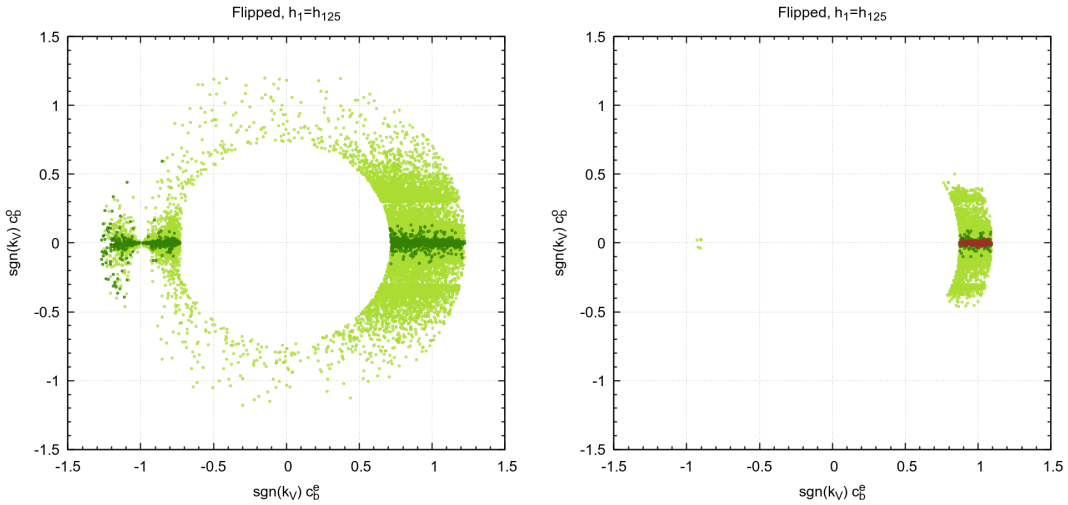


Figure 7: CP-odd *vs.* CP-even component in the $h_{125}b\bar{b}$ coupling for allowed parameter points in the Flipped model, assuming $h_1 = h_{125}$. Left panel: LHC 2017 data on h_{125} and constraints from BSM scalar searches at 7 and 8 TeV included in HB-4.3.1. Right panel: LHC 2022 data on h_{125}, constraints from BSM scalar searches including searches at 13 TeV using HT-1.1.3 and the latest eEDM limit. Colour code as in Fig. 1.

particular instance, on the crucial new bounds placed on the production of additional Higgs bosons.

As a result of the application of the 13 TeV BSM scalar searches, there is no further impact from the CMS constraints on $\alpha_{h\tau\tau}$ [53]. We observe that, at the current level of experimental precision, the direct limit on $\alpha_{h\tau\tau}$ does not yet play a role in the CP properties of the coupling $h_{125}b\bar{b}$. This is expected by the fact that, in the Flipped type, the $h_{125}\tau\bar{\tau}$ and the $h_{125}b\bar{b}$ couplings are independent parameters, according to $\Phi_u = \Phi_\ell \neq \Phi_d$. In the end, then, the situation that was shown to be possible in Ref. [26] (left panel of Fig. 7) is reduced to almost vanishing CP-odd components, c_b^o. These would not be observable directly at the LHC, due to the combination of the new results from the eEDM (dark red points) and searches for additional scalars at the LHC.

4 Conclusions

The C2HDM is one of the simplest extensions of the SM with one new CP-violating parameter, which arises from the scalar sector. The experimental data available in 2017, in particular the LHC data collected at 7 and 8 TeV, still allowed for the striking possibility that the CP-odd components (c^o) of the h_{125} couplings to down-type quarks and/or charged leptons were much larger than the corresponding CP-even components (c^e). This was possible for all types, except Type-I [26]. The possible presence of sizable CP-odd coupling components would be a clear indication of physics beyond the SM, and it could give rise to important phenomenological consequences. For instance, the viability of a realization of electroweak baryogenesis in generic extensions of the SM by a second Higgs doublet field relies on additional sources of CP-violation according to the Sakharov conditions [100].

In this paper, we re-analyze the situation in light of the most recent experimental constraints, namely: up-to-date results from LHC's Run 2 at 13 TeV regarding searches for additional scalars and the signal-rate measurements of the Higgs boson at 125 GeV, new eEDM results, data from direct searches for CP-violation in angular correlations of final state τ-leptons in $h_{125} \to \tau\bar{\tau}$ decays in terms of the effective mixing angle $\alpha_{h\tau\tau}$ and, finally, discussing the bounds on $m_{H^\pm}$ coming from the $b \to s\gamma$ constraints. The current situation is summarized in Table 3. This can be compared with Table 2 summarizing the status in

Type	I	II	LS	Flipped
$h_1 = h_{125}$	×	×	τ	$\underline{\times}$
$h_2 = h_{125}$	×	$\underline{\times}$	τ	×
$h_3 = h_{125}$	×	×	τ	×

Table 3: Current results for the large Yukawa couplings. A cross means that it is not possible to have large CP-odd couplings, i.e. $|c^0| \gtrsim |c^e|$. The notation τ means that c^o/c^e is limited by the direct searches for CP-violating angular correlations of τ leptons in $h_{125} \to \tau\bar{\tau}$ decays [53]. Underlined crosses indicate a change from allowed (✓) to excluded (×) compared to the previous analysis carried out in 2017 [26].

2017 found in a previous analysis [26]. The most important conclusions of the updated analysis presented here are the following:

Type-II: Previously, the possibility of sizable CP-odd components in the couplings of h_{125}, $|c_b^o| \gg |c_b^e|$, remained experimentally viable for the mass hierarchy with h_{125} being the second lightest neutral scalar ($h_2 = h_{125}$) [26]. This possibility is now practically excluded, as we discussed in Sec. 3.1. This exclusion follows from the combination of stringent eEDM constraints and limits from LHC searches for additional Higgs bosons at 13 TeV, most notably from searches for di-τ resonances below 125 GeV [95]. The only still viable option for sizable $|c_b^o|$ happens if two conditions are verified: first, if the parameters are very fine-tuned, such that cancellations between different contributions to the eEDM occur at (or below) the percent-level; second, if the pole masses for top-quark and τ-lepton and the running bottom-quark mass $\overline{m}_b(\overline{m}_b)$ are used for the computation of the eEDM. If both conditions are met, the LHC measurements of $\alpha_{h\tau\tau}$ exclude otherwise allowed parameter space. If, however, the running fermion masses at the scale M_Z are used for the computation of the eEDM, no parameter points can be found that simultaneously evade the experimental upper bound on the eEDM, and comply with the LHC cross-section limits from BSM scalar searches. This strong dependence on the fermion masses emphasizes that, in order to conclude whether Type-II can accomodate sizable CP-violating Higgs-boson couplings, one needs a proper understanding of which prescription to use for the fermion masses in the calculation of the eEDM.

LS: This Yukawa type is the only one that can still accommodate sizable CP-odd components in the couplings of h_{125} to charged leptons, while being in agreement with all theoretical and experimental constraints. In particular, the possibility of $|c_\tau^o| \simeq |c_\tau^e|$

is still allowed in the LS case, and only in this case. We find values of $\alpha_{h\tau\tau}$ that would be directly observable at the LHC by measurements of angular correlations of final state τ leptons in $h_{125} \to \tau\bar{\tau}$ decays. Consequently, in the LS type, the recently reported 2σ confidence-level limits of $\alpha_{h\tau\tau} < 41°$ from CMS [53] and of $\alpha_{h\tau\tau} < 34°$ from ATLAS [54] give rise to new constraints on the C2HDM parameter space, excluding previously allowed parameter space regions. According to our findings, if in the future a non-vanishing value of $\alpha_{h\tau\tau}$ were measured at the LHC, this would point towards the LS type, allowing to experimentally distinguish this type from the other Yukawa types of the C2HDM. Since all possible mass hierarchies of neutral scalars were shown to be compatible with sizable values of $\alpha_{h\tau\tau}$, a possible future detection of a CP-violating $h_{125}\tau\bar{\tau}$ coupling would not decide whether the detected Higgs boson at 125 GeV would correspond to the lightest, the second-lightest or the heaviest neutral scalar of the C2HDM.

Flipped: In this type, one has $c_\tau^o = c_t^o$. Hence, the circumstance that $|c_t^o|$ is already stringently constrained from signal-rate measurements of h_{125} renders the aforementioned constraints on $\alpha_{h\tau\tau}$ irrelevant. On the other hand, the possibility $|c_b^o| > |c_b^e|$ was previously allowed, assuming that the 125 GeV Higgs boson is the lightest neutral scalar. Here, we demonstrated that this possibility is now also forbidden in this type of the C2HDM, due to the LHC's improved bounds from searches for extra scalars (in combination with the other experimental constraints). The most relevant searches are those involving one heavy Higgs boson decaying into a Z and another Higgs boson, both by ATLAS [98] and CMS [99]. Additionally, the more recent eEDM bounds [60] constrain c_b^o to lie very close to zero.

In summary, we have shown that the possibility of sizable CP-odd components $|c^o| \simeq |c^e|$ in the couplings of the 125 GeV Higgs boson is only allowed in the LS cases (all mass orderings), where the CP-violation appears in the couplings of the Higgs boson to τ leptons. The possible amount of CP-violation is then limited ultimately by the direct searches for CP-violation in angular correlations between τ leptons produced in Higgs boson decays. These measurements have been performed by both ATLAS and CMS utilizing the full Run 2 dataset. The measurements are currently statistically limited. The anticipated future improvements on their experimental precision will be paramount to our understanding of the C2HDM and its phenomenology at the LHC, as well as of the extent to which the shortcomings of the SM can be addressed in this model.

Acknowledgments

T.B. thanks Henning Bahl for useful discussions. The work of J.C.R. and J.P.S. is supported in part by the Portuguese Fundação para a Ciência e Tecnologia (FCT) under Contracts CERN/FIS-PAR/0002/2021, UIDB/00777/2020, and UIDP/00777/2020; these projects are partially funded through POCTI (FEDER), COMPETE, QREN, and the EU. D.F. is supported by the U.S. Department of Energy under Grant Contract No. DE-SC0012704. R.S. is partially supported by FCT under Contracts

no. UIDB/00618/2020, UIDP/00618/2020, CERN/FIS-PAR/0025/2021, CERN/FIS-PAR/0021/2021 and CERN/FIS-PAR/0037/2021. M.M. acknowledges financial support from the Deutsche Forschungsgemeinschaft (DFG, German Research Foundation) under grant 396021762 - TRR 257. The work of T.B. is supported by the German Bundesministerium für Bildung und Forschung (BMBF, Federal Ministry of Education and Research) – project 05H21VKCCA.

References

[1] G. Aad et al., *Observation of a new particle in the search for the Standard Model Higgs boson with the ATLAS detector at the LHC*, *Phys. Lett. B* **716** (2012) 1–29.

[2] S. Chatrchyan et al., *Observation of a New Boson at a Mass of 125 GeV with the CMS Experiment at the LHC*, *Phys. Lett. B* **716** (2012) 30–61.

[3] ATLAS collaboration, *Measurements of the properties of the Higgs-like boson in the four lepton decay channel with the ATLAS detector using 25 fb^{-1} of proton-proton collision data*, Tech. Rep. ATLAS-CONF-2013-013, CERN, Geneva, 2013.

[4] CMS collaboration, S. Chatrchyan et al., *Measurement of the Properties of a Higgs Boson in the Four-Lepton Final State*, *Phys. Rev. D* **89** (2014) 092007, [1312.5353].

[5] D. Fontes, M. Löschner, J. C. Romão and J. P. Silva, *Leaks of CP violation in the real two-Higgs-doublet model*, *Eur. Phys. J. C* **81** (2021) 541.

[6] J. F. Gunion, H. E. Haber, G. L. Kane and S. Dawson, *The Higgs hunter's guide*. Westview Press, 1990.

[7] G. C. Branco, P. M. Ferreira, L. Lavoura, M. N. Rebelo, M. Sher and J. P. Silva, *Theory and phenomenology of two-Higgs-doublet models*, *Phys. Rept.* **516** (2012) 1–102.

[8] T. D. Lee, *A Theory of Spontaneous T Violation*, *Phys. Rev. D* **8** (1973) 1226–1239.

[9] I. F. Ginzburg, M. Krawczyk and P. Osland, *Two Higgs doublet models with CP violation*, in *International Workshop on Linear Colliders (LCWS 2002)*, pp. 703–706, 11, 2002, hep-ph/0211371.

[10] S. Weinberg, *Unitarity Constraints on CP Nonconservation in Higgs Exchange*, *Phys. Rev. D* **42** (1990) 860–866.

[11] W. Khater and P. Osland, *CP violation in top quark production at the LHC and two Higgs doublet models*, *Nucl. Phys. B* **661** (2003) 209–234.

[12] A. W. El Kaffas, P. Osland and O. M. Ogreid, *CP violation, stability and unitarity of the two Higgs doublet model*, *Nonlin. Phenom. Complex Syst.* **10** (2007) 347–357, [hep-ph/0702097].

[13] B. Grzadkowski and P. Osland, *Tempered Two-Higgs-Doublet Model*, *Phys. Rev. D* **82** (2010) 125026.

[14] A. Arhrib, E. Christova, H. Eberl and E. Ginina, *CP violation in charged Higgs production and decays in the Complex Two Higgs Doublet Model*, *JHEP* **04** (2011) 089.

[15] A. Barroso, P. M. Ferreira, R. Santos and J. P. Silva, *Probing the scalar-pseudoscalar mixing in the 125 GeV Higgs particle with current data*, *Phys. Rev. D* **86** (2012) 015022.

[16] T. Abe, J. Hisano, T. Kitahara and K. Tobioka, *Gauge invariant Barr-Zee type contributions to fermionic EDMs in the two-Higgs doublet models*, *JHEP* **01** (2014) 106, [1311.4704]. [Erratum: JHEP 04, 161 (2016)].

[17] S. Inoue, M. J. Ramsey-Musolf and Y. Zhang, *CP-violating phenomenology of flavor conserving two Higgs doublet models*, *Phys.Rev.* **D89** (2014) 115023.

[18] K. Cheung, J. S. Lee, E. Senaha and P.-Y. Tseng, *Confronting Higgcision with Electric Dipole Moments*, *JHEP* **06** (2014) 149.

[19] D. Fontes, J. C. Romão and J. P. Silva, *$h \to Z\gamma$ in the complex two Higgs doublet model*, *JHEP* **12** (2014) 043.

[20] R. Grober, M. Muhlleitner and M. Spira, *Higgs Pair Production at NLO QCD for CP-violating Higgs Sectors*, *Nucl. Phys. B* **925** (2017) 1–27, [1705.05314].

[21] D. Fontes, J. C. Romão, R. Santos and J. a. P. Silva, *Undoubtable signs of CP-violation in Higgs boson decays at the LHC run 2*, *Phys. Rev. D* **92** (2015) 055014, [1506.06755].

[22] D. Fontes, J. C. Romão, R. Santos and J. P. Silva, *Large pseudoscalar Yukawa couplings in the complex 2HDM*, *JHEP* **06** (2015) 060.

[23] C.-Y. Chen, S. Dawson and Y. Zhang, *Complementarity of LHC and EDMs for Exploring Higgs CP Violation*, *JHEP* **06** (2015) 056.

[24] C.-Y. Chen, H.-L. Li and M. Ramsey-Musolf, *CP-Violation in the Two Higgs Doublet Model: from the LHC to EDMs*, *Phys. Rev. D* **97** (2018) 015020.

[25] M. Mühlleitner, M. O. P. Sampaio, R. Santos and J. Wittbrodt, *Phenomenological Comparison of Models with Extended Higgs Sectors*, *JHEP* **08** (2017) 132, [1703.07750].

[26] D. Fontes, M. Mühlleitner, J. C. Romão, R. Santos, J. P. Silva and J. Wittbrodt, *The C2HDM revisited*, *JHEP* **02** (2018) 073.

[27] P. Basler, M. Mühlleitner and J. Wittbrodt, *The CP-Violating 2HDM in Light of a Strong First Order Electroweak Phase Transition and Implications for Higgs Pair Production*, *JHEP* **03** (2018) 061.

[28] M. Aoki, K. Hashino, D. Kaneko, S. Kanemura and M. Kubota, *Probing CP violating Higgs sectors via the precision measurement of coupling constants*, *PTEP* **2019** (2019) 053B02.

[29] P. Basler, M. Mühlleitner and J. Müller, *Electroweak Phase Transition in Non-Minimal Higgs Sectors*, *JHEP* **05** (2020) 016, [1912.10477].

[30] X. Wang, F. P. Huang and X. Zhang, *Gravitational wave and collider signals in complex two-Higgs doublet model with dynamical CP-violation at finite temperature*, *Phys. Rev. D* **101** (2020) 015015.

[31] R. Boto, T. V. Fernandes, H. E. Haber, J. C. Romão and J. P. Silva, *Basis-independent treatment of the complex 2HDM*, *Phys. Rev. D* **101** (2020) 055023.

[32] K. Cheung, A. Jueid, Y.-N. Mao and S. Moretti, *Two-Higgs-doublet model with soft CP violation confronting electric dipole moments and colliders*, *Phys. Rev. D* **102** (2020) 075029.

[33] W. Altmannshofer, S. Gori, N. Hamer and H. H. Patel, *Electron EDM in the complex two-Higgs doublet model*, *Phys. Rev. D* **102** (2020) 115042.

[34] D. Fontes and J. C. Romão, *Renormalization of the C2HDM with FeynMaster 2*, *JHEP* **06** (2021) 016.

[35] P. Basler, L. Biermann, M. Mühlleitner and J. Müller, *Electroweak baryogenesis in the CP-violating two-Higgs doublet model*, *Eur. Phys. J. C* **83** (2023) 57.

[36] M. Frank, E. G. Fuakye and M. Toharia, *Restricting the parameter space of type-II two-Higgs-doublet models with CP violation*, *Phys. Rev. D* **106** (2022) 035010.

[37] H. Abouabid, A. Arhrib, D. Azevedo, J. E. Falaki, P. M. Ferreira, M. Mühlleitner et al., *Benchmarking di-Higgs production in various extended Higgs sector models*, *JHEP* **09** (2022) 011, [2112.12515].

[38] D. Fontes and J. C. Romão, *The one-loop impact of a dependent mass: the role of m_3 in the C2HDM*, *JHEP* **03** (2022) 144.

[39] D. Azevedo, T. Biekötter and P. M. Ferreira, *2HDM interpretations of the CMS diphoton excess at 95 GeV*, *JHEP* **11** (2023) 017, [2305.19716].

[40] D. Gonçalves, A. Kaladharan and Y. Wu, *Gravitational waves, bubble profile, and baryon asymmetry in the complex 2HDM*, *Phys. Rev. D* **108** (2023) 075010, [2307.03224].

[41] A. Djouadi, J. Kalinowski and M. Spira, *HDECAY: A Program for Higgs boson decays in the standard model and its supersymmetric extension*, *Comput. Phys. Commun.* **108** (1998) 56–74.

[42] A. Djouadi, J. Kalinowski, M. Muehlleitner and M. Spira, *HDECAY: Twenty$_{++}$ years after*, *Comput. Phys. Commun.* **238** (2019) 214–231.

[43] G. Aad et al., *Measurements of the Higgs boson production and decay rates and constraints on its couplings from a combined ATLAS and CMS analysis of the LHC pp collision data at $\sqrt{s} = 7$ and 8 TeV*, *JHEP* **08** (2016) 045.

[44] P. Bechtle, O. Brein, S. Heinemeyer, O. Stål, T. Stefaniak, G. Weiglein et al., HiggsBounds – 4*: Improved Tests of Extended Higgs Sectors against Exclusion Bounds from LEP, the Tevatron and the LHC*, *Eur. Phys. J. C* **74** (2014) 2693.

[45] J. Baron et al., *Order of Magnitude Smaller Limit on the Electric Dipole Moment of the Electron*, *Science* **343** (2014) 269–272.

[46] M. Misiak and M. Steinhauser, *Weak radiative decays of the B meson and bounds on $M_{H^\pm}$ in the Two-Higgs-Doublet Model*, *Eur. Phys. J. C* **77** (2017) 201.

[47] A. Freitas and P. Schwaller, *Higgs CP Properties From Early LHC Data*, *Phys. Rev. D* **87** (2013) 055014, [1211.1980].

[48] A. Djouadi and G. Moreau, *The couplings of the Higgs boson and its CP properties from fits of the signal strengths and their ratios at the 7+8 TeV LHC*, *Eur. Phys. J. C* **73** (2013) 2512, [1303.6591].

[49] F. Ferreira, B. Fuks, V. Sanz and D. Sengupta, *Probing CP-violating Higgs and gauge-boson couplings in the Standard Model effective field theory*, *Eur. Phys. J. C* **77** (2017) 675, [1612.01808].

[50] E. Fuchs, M. Losada, Y. Nir and Y. Viernik, *CP violation from τ, t and b dimension-6 Yukawa couplings - interplay of baryogenesis, EDM and Higgs physics*, *JHEP* **05** (2020) 056, [2003.00099].

[51] H. Bahl, E. Fuchs, S. Heinemeyer, J. Katzy, M. Menen, K. Peters et al., *Constraining the $\mathcal{CP}$ structure of Higgs-fermion couplings with a global LHC fit, the electron EDM and baryogenesis*, *Eur. Phys. J. C* **82** (2022) 604, [2202.11753].

[52] *A detailed map of Higgs boson interactions by the ATLAS experiment ten years after the discovery*, *Nature* **607** (2022) 52–59. [Erratum: Nature 612, E24 (2022)].

[53] A. Tumasyan et al., *Analysis of the CP structure of the Yukawa coupling between the Higgs boson and τ leptons in proton-proton collisions at $\sqrt{s}$ = 13 TeV*, *JHEP* **06** (2022) 012.

[54] G. Aad et al., *Measurement of the CP properties of Higgs boson interactions with τ-leptons with the ATLAS detector*, *Eur. Phys. J. C* **83** (2023) 563.

[55] P. Bechtle, O. Brein, S. Heinemeyer, G. Weiglein and K. E. Williams, *HiggsBounds: Confronting Arbitrary Higgs Sectors with Exclusion Bounds from LEP and the Tevatron*, *Comput. Phys. Commun.* **181** (2010) 138–167.

[56] P. Bechtle, O. Brein, S. Heinemeyer, G. Weiglein and K. E. Williams, *HiggsBounds 2.0.0: Confronting Neutral and Charged Higgs Sector Predictions with Exclusion Bounds from LEP and the Tevatron*, *Comput. Phys. Commun.* **182** (2011) 2605–2631.

[57] P. Bechtle, D. Dercks, S. Heinemeyer, T. Klingl, T. Stefaniak, G. Weiglein et al., *HiggsBounds-5: Testing Higgs Sectors in the LHC 13 TeV Era*, *Eur. Phys. J. C* **80** (2020) 1211.

[58] H. Bahl, T. Biekötter, S. Heinemeyer, C. Li, S. Paasch, G. Weiglein et al., *HiggsTools: BSM scalar phenomenology with new versions of HiggsBounds and HiggsSignals*, *Comput. Phys. Commun.* **291** (2023) 108803, [2210.09332].

[59] V. Andreev et al., *Improved limit on the electric dipole moment of the electron*, *Nature* **562** (2018) 355–360.

[60] T. S. Roussy et al., *An improved bound on the electron's electric dipole moment*, *Science* **381** (2023) adg4084, [2212.11841].

[61] M. Jung and A. Pich, *Electric Dipole Moments in Two-Higgs-Doublet Models*, *JHEP* **04** (2014) 076.

[62] J. Shu and Y. Zhang, *Impact of a CP Violating Higgs Sector: From LHC to Baryogenesis*, *Phys. Rev. Lett.* **111** (2013) 091801.

[63] W.-S. Hou, G. Kumar and S. Teunissen, *Discovery prospects for electron and neutron electric dipole moments in the general two Higgs doublet model*, *Phys. Rev. D* **109** (2024) L011703, [2308.04841].

[64] S. L. Glashow and S. Weinberg, *Natural Conservation Laws for Neutral Currents*, *Phys. Rev. D* **15** (1977) 1958.

[65] E. A. Paschos, *Diagonal Neutral Currents*, *Phys. Rev. D* **15** (1977) 1966.

[66] A. Tumasyan et al., *A portrait of the Higgs boson by the CMS experiment ten years after the discovery*, *Nature* **607** (2022) 60–68.

[67] D. Fontes, M. Muhlleitner, J. C. Romão, R. Santos, J. P. Silva and J. Wittbrodt, *Couplings of the C2HDM: `http://porthos.tecnico.ulisboa.pt/arXiv/C2HDM/`*, October, 2017.

[68] O. Deschamps, S. Descotes-Genon, S. Monteil, V. Niess, S. T'Jampens and V. Tisserand, *The Two Higgs Doublet of Type II facing flavour physics data*, *Phys. Rev. D* **82** (2010) 073012.

[69] F. Mahmoudi and O. Stal, *Flavor constraints on the two-Higgs-doublet model with general Yukawa couplings*, *Phys. Rev. D* **81** (2010) 035016.

[70] T. Hermann, M. Misiak and M. Steinhauser, *$\bar{B} \to X_s\gamma$ in the Two Higgs Doublet Model up to Next-to-Next-to-Leading Order in QCD*, *JHEP* **11** (2012) 036.

[71] M. Misiak et al., *Updated NNLO QCD predictions for the weak radiative B-meson decays*, *Phys. Rev. Lett.* **114** (2015) 221801.

[72] M. Misiak, A. Rehman and M. Steinhauser, *Towards $\overline{B} \to X_s\gamma$ at the NNLO in QCD without interpolation in m_c*, *JHEP* **06** (2020) 175, [2002.01548].

[73] M. Baak, J. Cúth, J. Haller, A. Hoecker, R. Kogler, K. Mönig et al., *The global electroweak fit at NNLO and prospects for the LHC and ILC*, *Eur. Phys. J. C* **74** (2014) 3046.

[74] P. W. Hess, *Improving the Limit on the Electron EDM: Data Acquisition and Systematics Studies in the ACME Experiment*, Ph.D. thesis, Harvard U. (main), 2014.

[75] I. P. Ivanov and J. P. Silva, *Tree-level metastability bounds for the most general two Higgs doublet model*, *Phys. Rev.* **D92** (2015) 055017.

[76] S. Kanemura, T. Kubota and E. Takasugi, *Lee-Quigg-Thacker bounds for Higgs boson masses in a two doublet model*, *Phys. Lett. B* **313** (1993) 155–160.

[77] A. G. Akeroyd, A. Arhrib and E.-M. Naimi, *Note on tree level unitarity in the general two Higgs doublet model*, *Phys. Lett. B* **490** (2000) 119–124.

[78] I. F. Ginzburg and I. P. Ivanov, *Tree level unitarity constraints in the 2HDM with CP violation*, hep-ph/0312374.

[79] G. Aad et al., *CP Properties of Higgs Boson Interactions with Top Quarks in the $t\bar{t}H$ and tH Processes Using $H \to \gamma\gamma$ with the ATLAS Detector*, *Phys. Rev. Lett.* **125** (2020) 061802.

[80] D. Carmi, A. Falkowski, E. Kuflik and T. Volansky, *Interpreting LHC Higgs Results from Natural New Physics Perspective*, *JHEP* **07** (2012) 136.

[81] C.-W. Chiang and K. Yagyu, *Implications of Higgs boson search data on the two-Higgs doublet models with a softly broken Z_2 symmetry*, *JHEP* **07** (2013) 160.

[82] P. M. Ferreira, J. F. Gunion, H. E. Haber and R. Santos, *Probing wrong-sign Yukawa couplings at the LHC and a future linear collider*, *Phys. Rev. D* **89** (2014) 115003.

[83] D. Fontes, J. C. Romão and J. P. Silva, *A reappraisal of the wrong-sign $hb\bar{b}$ coupling and the study of $h \to Z\gamma$*, *Phys. Rev.* **D90** (2014) 015021.

[84] P. M. Ferreira, R. Guedes, M. O. P. Sampaio and R. Santos, *Wrong sign and symmetric limits and non-decoupling in 2HDMs*, *JHEP* **12** (2014) 067.

[85] Y. S. Amhis et al., *Averages of b-hadron, c-hadron, and τ-lepton properties as of 2018*, *Eur. Phys. J. C* **81** (2021) 226.

[86] Y. S. Amhis et al., *Averages of b-hadron, c-hadron, and τ-lepton properties as of 2021*, *Phys. Rev. D* **107** (2023) 052008.

[87] Belle-II collaboration, F. Abudinén et al., *Measurement of the photon-energy spectrum in inclusive $B \to X_s\gamma$ decays identified using hadronic decays of the recoil B meson in 2019-2021 Belle II data*, 2210.10220.

[88] M. Steinhauser, Private communication, 2023.

[89] W. Su, *Probing loop effects in wrong-sign Yukawa coupling region of Type-II 2HDM*, *Eur. Phys. J. C* **81** (2021) 404, [1910.06269].

[90] T. Biekötter and M. Pierre, *Higgs-boson visible and invisible constraints on hidden sectors*, *Eur. Phys. J. C* **82** (2022) 1026, [2208.05505].

[91] ATLAS collaboration, G. Aad et al., *Interpretations of the ATLAS measurements of Higgs boson production and decay rates and differential cross-sections in pp collisions at* $\sqrt{s} = 13$ *TeV*, 2402.05742.

[92] S. M. Barr and A. Zee, *Electric Dipole Moment of the Electron and of the Neutron*, *Phys. Rev. Lett.* **65** (1990) 21–24. [Erratum: Phys.Rev.Lett. 65, 2920 (1990)].

[93] P. Athron, C. Balazs, A. Cherchiglia, D. H. J. Jacob, D. Stöckinger, H. Stöckinger-Kim et al., *Two-loop prediction of the anomalous magnetic moment of the muon in the Two-Higgs Doublet Model with GM2Calc 2*, *Eur. Phys. J. C* **82** (2022) 229, [2110.13238].

[94] S. F. King, M. Muhlleitner, R. Nevzorov and K. Walz, *Exploring the CP-violating NMSSM: EDM Constraints and Phenomenology*, *Nucl. Phys. B* **901** (2015) 526–555, [1508.03255].

[95] A. Tumasyan et al., *Searches for additional Higgs bosons and for vector leptoquarks in* $\tau\tau$ *final states in proton-proton collisions at* $\sqrt{s} = 13$ *TeV*, *JHEP* **07** (2023) 073.

[96] ATLAS collaboration, G. Aad et al., *Search for heavy Higgs bosons decaying into two tau leptons with the ATLAS detector using pp collisions at* $\sqrt{s} = 13$ *TeV*, *Phys. Rev. Lett.* **125** (2020) 051801, [2002.12223].

[97] M. Postma, J. van de Vis and G. White, *Resummation and cancellation of the VIA source in electroweak baryogenesis*, *JHEP* **12** (2022) 121, [2206.01120].

[98] M. Aaboud et al., *Search for a heavy Higgs boson decaying into a Z boson and another heavy Higgs boson in the* $\ell\ell bb$ *final state in pp collisions at* $\sqrt{s} = 13$ *TeV with the ATLAS detector*, *Phys. Lett. B* **783** (2018) 392–414.

[99] A. M. Sirunyan et al., *Search for a heavy pseudoscalar boson decaying to a Z and a Higgs boson at* $\sqrt{s} = 13$ *TeV*, *Eur. Phys. J. C* **79** (2019) 564.

[100] A. D. Sakharov, *Violation of CP Invariance, C asymmetry, and baryon asymmetry of the universe*, *Pisma Zh. Eksp. Teor. Fiz.* **5** (1967) 32–35.

CTPU-PTC-24-06

Cogenesis of baryon and dark matter with PBH and QCD axion

Debasish Borah,[1,*] Nayan Das,[1,†] Suruj Jyoti Das,[2,‡] and Rome Samanta[3,4,5,§]

[1] *Department of Physics, Indian Institute of Technology Guwahati, Assam 781039, India*

[2] *Particle Theory and Cosmology Group, Center for Theoretical Physics of the Universe, Institute for Basic Science (IBS), Daejeon, 34126, Korea*

[3] *CEICO, Institute of Physics of the Czech Academy of Sciences, Na Slovance 1999/2, 182 21 Prague 8, Czech Republic*

[4] *Scuola Superiore Meridionale, Largo S. Marcellino 10, I-80138 Napoli, Italy*

[5] *Istituto Nazionale di Fisica Nucleare (INFN), sez. di Napoli, Via Cinthia 9, I-80126 Napoli, Italy*

arXiv:2403.02401v1 [hep-ph] 4 Mar 2024

Abstract

We study the role of an ultra-light primordial black hole (PBH) dominated phase on the generation of baryon asymmetry of the Universe (BAU) and dark matter (DM) in a type-I seesaw framework augmented by Peccei-Quinn (PQ) symmetry which solves the strong CP problem. While the BAU is generated via leptogenesis from the decay of heavy right-handed neutrino (RHN) at the seesaw scale dictated by the PQ scale, DM can arise either from QCD axion or one of the RHNs depending upon the PQ scale. The ultra-light PBH not only affects the axion DM production via misalignment mechanism, but can also produce superheavy RHN DM via evaporation. Depending upon the PBH parameters and relative abundance of axion DM, axion mass can vary over a wide range from sub-μeV to sub-eV keeping the detection prospects promising across a wide range of experiments. While hot axions produced from PBH evaporation can lead to observable $\Delta N_{\rm eff}$ to be probed at future cosmic microwave background (CMB) experiments, stochastic gravitational waves (GW) produced from PBH density fluctuations can be observed at future detectors like CE, DECIGO, LISA and even future runs of LIGO-VIRGO.

*Electronic address: dborah@iitg.ac.in

†Electronic address: nayan.das@iitg.ac.in

‡Electronic address: surujjd@gmail.com

§Electronic address: romesamanta@gmail.com

I. INTRODUCTION

Strong upper limits on the electric dipole moment of neutron show that strong interactions are CP symmetric [1], although the standard model (SM) entirely is not. The CP violation in the strong interaction is characterized by the angle $\bar{\theta}$, which is bounded from above: $\bar{\theta} < 10^{-10}$. The required vanishingly small value of the $\bar{\theta}$ parameter is the strong CP problem. The classic solution to this is to promote $\bar{\theta}$ as a pseudoscalar axion field resulting from a global $U(1)$ symmetry breaking – the Peccei-Quinn (PQ) mechanism [2–5]. When axion obtains its potential through QCD effects, remarkably, $\bar{\theta}$ relaxes to zero (ground state of the potential) and solves the strong-CP problem. Besides solving the strong-CP problem, axions could constitute the entire cold dark matter (DM) energy density if they are incredibly light; $m_a \simeq 10^{-5}$ eV [6–8]. The key UV parameter in any QCD axion model is the scale of the PQ phase transition f_a; also known as the axion decay constant. In the models of light QCD axions, the quantity f_a is bounded from below by astrophysical observations as $f_a \gtrsim 10^{8\div 9}$ GeV [9]. On the other hand, the misalignment mechanism offers a stringent window [1] for the decay constant around $f_a \sim 10^{11}$ GeV to produce the correct dark matter relic [14]. This simple PQ solution to the strong CP problem thus renders dark matter physics and evades astrophysical constraints, generically for a high-scale phase transition (PQ symmetry breaking). We might wonder then whether any other cosmological puzzles that are attributed to high-scale physics in their simplest theoretical form share common ground with axion physics. This article discusses one such possibility, where the generation of the baryon asymmetry of the Universe (BAU) through leptogenesis [15] shares a common origin with axion physics. While there are several ways that one couples the axion physics to the baryogenesis [16–19], our interest aligns with the SMASH [20] like scenarios, where the right-handed neutrinos which are introduced in the SM to generate light neutrino mass via seesaw mechanism and provide leptogenesis, get mass from the PQ phase transition. The motivation is, of course, that the framework couples neutrino physics with axions–one of the aspects of SMASH-like scenarios. In addition, as we shall discuss, given a proper cosmological setup, such a framework offers the testability of the vanilla regime of leptogenesis ($T_{\rm lepto} \gtrsim 10^{12}$

[1] Depending on the IR models, e.g., Dine-Fischler-Srednicki-Zhitnitsky (DFSZ) [10, 11] and Kim-Shifman-Vainshtein-Zakharov (KSVZ) [12, 13], additional contributions from the topological defects can alter this window less than an order of magnitude [14]

GeV), which otherwise is not testable, because of its sequestration from low-energy neutrino mixing parameters[2]. Having said that, besides considering the unification of the seesaw and PQ scale, here we explore and exploit the cosmological setup, that before the Big Bang nucleosynthesis (BBN), the early universe went through a non-standard cosmological expansion in the primordial ages which is unconstrained with any observable signature. As we shall discuss, considering such a cosmological framework not only opens up new testable parameter space of baryogenesis via leptogenesis with axion searches, it may provide a complementary probe with detectable stochastic primordial gravitational waves (GW). To this end, we focus on ultra-light primordial black holes (PBH)[3] providing such a non-standard phase. Such ultra-light PBH mass remains confined to the window $0.1\,\mathrm{g} \lesssim m_{\rm in} \lesssim 3.4 \times 10^8\,\mathrm{g}$ where the lower bound comes from cosmic microwave background (CMB) upper bound on the scale of inflation while the upper bound comes from the requirement that PBH evaporate by emitting Hawking radiation [27, 28] before the BBN epoch. These PBH also induce very sharply peaked stochastic GW signals via density fluctuations [29–33]. Let us also mention that evaporation of ultra-light PBH can also lead to the production of dark matter (DM) [34–51] and play non-trivial role in baryogenesis [27, 43–46, 52–61]. The role of PBH on axion DM has also been discussed in [62, 63].

In this unified scenario of the seesaw and the PQ scale subjected to a non-standard PBH epoch, we first consider axion to constitute the entire DM and study the impact of PBH on axion abundance which also decides the PQ scale–equivalent to the scale of seesaw or leptogenesis in our setup. Secondly, we consider the DM to be multi-component such that one of the three RHNs can also contribute to the DM abundance. We discuss the production of such RHN DM from PBH evaporation, axion portal, and Yukawa interactions and find the shift in axion or PQ scale depending upon relative axion DM abundance. Due to appreciable changes in the PQ scale in these two scenarios, the axion detection prospects become more promising due to sensitivity across a wide range of experiments. While RHN DM can have some indirect detection signatures if it remains light, hot axion production from PBH evaporation can lead to dark radiation within the reach of future CMB experiments. In both the cases we study here, the density fluctuations of ultra-light PBH lead to a stochastic GW

[2] Recently there have been some efforts to probe high-scale leptogenesis (including vanilla regime) with primordial gravitational waves e.g., topological defects [21–25].

[3] See [26] for a recent review of PBH.

background within reach of several GW detectors.

This paper is organised as follows. In section II we briefly discuss our model followed by a discussion of axion DM in section III. In section IV we discuss the interplay of leptogenesis and axion DM followed by studying another possibility in section V where one of the RHNs introduced for generating neutrino mass can also play the role of DM either fully or partially. In section VI and section VII, we mention the detection prospects of our model in gravitational wave and axion experiments, respectively. Finally, we conclude in section VIII.

II. THE FRAMEWORK

We consider a type-I seesaw framework [64–68] extended by Peccei-Quinn symmetry [2, 3]. A recent review of QCD axion models can be found in [69]. In addition to the heavy RHNs (here we consider three RHNs) required for the seesaw, the other field content and PQ charges are kept similar to a KSVZ type model [12, 13] in which $v_{\rm PQ} = f_a$, where $v_{\rm PQ}$ is the vacuum expectation value (VEV) of the PQ scalar field σ and f_a is the axion decay constant. Thus, the BSM field content is constituted by a complex PQ scalar field $\sigma \equiv \frac{v_{\rm PQ}+\rho}{\sqrt{2}}\, e^{ia/f_a}$ ($\sigma \sim (1,1,0)$), a heavy quark $Q \sim (3,1,0)$ and three right-handed neutrinos $N_R \sim (1,1,0)$ where the numbers in brackets denote their charges under the SM gauge symmetry $SU(3)_c \times SU(2)_L \times U(1)_Y$. The transformation of these fields and leptons under PQ symmetry are

$$\sigma \to e^{i\alpha}\,\sigma;\quad N_R \to e^{-i\alpha/2}\,N_R;\quad l_R, L \to e^{-i\alpha/2}\,l_R, L;\quad Q_L \to e^{i\alpha/2}\,Q_L;\quad Q_R \to e^{-i\alpha/2}\,Q_R.$$

The SM quarks have vanishing PQ charges. The Yukawa coupling part of the PQ invariant Lagrangian can be written as

$$\mathcal{L}_{\mathcal{Y}} = -\left[y\overline{Q}_L \sigma Q_R + G_{ij}\overline{L_i} H l_{jR} + F_{ij}\overline{L_i}\tilde{H} N_{jR} + \frac{1}{2}\, y_{ij}\, \overline{N}^c_{iR}\sigma N_{jR}\right] + \text{h.c.} \tag{1}$$

with H being the SM Higgs. The scalar potential of the model is given by

$$V(H,\sigma) = \lambda_H\left(H^\dagger H - \frac{v^2}{2}\right)^2 + \lambda_\sigma\left(|\sigma|^2 - \frac{v_{\rm PQ}^2}{2}\right)^2 + \lambda_{H\sigma}\left(H^\dagger H - \frac{v^2}{2}\right)\left(|\sigma|^2 - \frac{v_{\rm PQ}^2}{2}\right) \tag{2}$$

with v being the VEV of the SM Higgs H. After PQ symmetry breaking the first and the last terms in $\mathcal{L}_y$ give rise to

$$\begin{aligned} y\bar{Q}_L\sigma Q_R &\to \frac{y}{\sqrt{2}}\rho\bar{Q}_L Q_R e^{ia/f_a} + \frac{y}{\sqrt{2}}v_{PQ}\bar{Q}_L Q_R e^{ia/f_a} \\ \frac{1}{2}\,y_{ij}\,\bar{N}^c_{iR}\sigma N_{jR} &\to \frac{1}{2}\,\frac{y_{ij}}{\sqrt{2}}\rho\,\bar{N}^c_{iR}N_{jR}e^{ia/f_a} + \frac{1}{2}\,\frac{y_{ij}}{\sqrt{2}}v_{PQ}\,\bar{N}^c_{iR}N_{jR}e^{ia/f_a}. \end{aligned} \tag{3}$$

The phase part can be absorbed by the transformation $Q_R \to e^{-i\frac{a}{2f_a}}Q_R$ and $N_R \to e^{-i\frac{a}{2f_a}}N_R$. As the chiral transformation on Q is anomalous under QCD, one gets the term $\frac{g_s^2}{32\pi^2}\frac{a}{f_a}G_{\mu\nu}\tilde{G}^{\mu\nu}$ with $G_{\mu\nu}\,(\tilde{G}^{\mu\nu})$ being (dual) field strength tensor of QCD. Simultaneously, from the kinetic term $\overline{Q}i\gamma^\mu\partial_\mu Q$, after transformation one gets the term $-\frac{\partial_\mu a}{2f_a}\overline{Q}\gamma^\mu\gamma_5 Q$. Similarly, from the kinetic term of RHN $\frac{i}{2}\overline{N}\gamma^\mu\partial_\mu N$, one gets the term $-\frac{1}{4}\,\frac{\partial_\mu a}{f_a}\,\overline{N}\gamma^\mu\gamma_5 N$. Now using the Dirac equation and the fact that the total derivative is zero at the boundary, we get

$$\begin{aligned} -\frac{\partial_\mu a}{2f_a}\overline{Q}\gamma^\mu\gamma_5 Q &= -i\frac{M_Q}{f_a}a\overline{Q}\gamma_5 Q \\ -\frac{1}{4}\,\frac{\partial_\mu a}{f_a}\,\overline{N}\gamma^\mu\gamma_5 N &= -\frac{i}{2}\,\frac{M_i}{f_a}\,a\,\overline{N}\gamma_5 N \end{aligned} \tag{4}$$

which define axion couplings to RHN and heavy quark Q. We have also dropped the chirality index from RHN notation and will denote them only by N_i with mass M_i hereafter.

III. AXION DARK MATTER IN THE PRESENCE OF PBH

The effect of PBH on the axion dark matter relic abundance was studied in detail in [62, 63]. Here, we revisit the dynamics of axion in the presence of PBH domination and their subsequent evaporation, and point out the differences we obtain compared to the case of standard cosmology without PBH. We consider PBH to be formed in the early radiation-dominated Universe at a temperature $T_{\rm in}$, with an initial mass related to the particle horizon size as [43, 70]

$$m_{\rm in} = \frac{4}{3}\,\pi\,\gamma\left(\frac{1}{\mathcal{H}\,(T_{\rm in})}\right)^3\rho_{\rm R}\,(T_{\rm in}) \tag{5}$$

with $\rho_{\rm R}$, $\mathcal{H}$ indicating the radiation energy density and the Hubble parameter respectively. $\gamma \simeq 0.2$ is a numerical factor which contains the uncertainty of the PBH formation. The

initial abundance of PBH during their formation is denoted by

$$\beta = \frac{\rho_{\rm PBH}\left(T_{\rm in}\right)}{\rho_{\rm R}\left(T_{\rm in}\right)} \tag{6}$$

where $\rho_{\rm PBH}$ represents the PBH energy density. After their production, PBH evolves as matter and can dominate the energy density of the early Universe, if their initial energy density is greater than a critical value given by

$$\beta \geq \beta_{\rm crit} \simeq 2.5 \times 10^{-14} \gamma^{-\frac{1}{2}} \left(\frac{m_{\rm in}}{10^8 {\rm g}}\right)^{-1} . \tag{7}$$

Finally, PBH lose their mass through Hawking radiation and completely evaporates away when the Universe reaches a temperature

$$T_{\rm ev} \simeq \left(\frac{9 g_{*,B}(T_{\rm BH})}{10240}\right)^{\frac{1}{4}} \left(\frac{M_{\rm P}^5}{m_{\rm in}^3}\right)^{\frac{1}{2}} . \tag{8}$$

Here, M_P denotes reduced Planck mass and $g_{*,B}(T_{\rm BH}) \simeq 100$ denotes the relativistic degrees of freedom below $T_{\rm BH}$. Now, for QCD axions, the zero temperature mass ($T \leq T_{\rm QCD} \simeq 150$ MeV) is related to PQ symmetry breaking scale, f_a as

$$m_a \simeq 5.7 \left(\frac{10^{12}\ {\rm GeV}}{f_a}\right) \mu{\rm eV}. \tag{9}$$

Above $T > T_{\rm QCD}$, the temperature-dependent axion mass is given as

$$m_a(T) = m_a \left(\frac{T_{\rm QCD}}{T}\right)^4 . \tag{10}$$

As indicated by lattice simulation, the power of 4 is not precise [69], but it does not affect our overall results significantly. If the PQ symmetry breaks in post inflationary era, the initial misalignment angle, $\theta_i = a_i/f_a$ takes the average value $\theta_i = \frac{\pi}{\sqrt{3}} \sim 1.81$. At high temperatures, the axion evolution is friction-dominated and frozen at θ_i. It then starts to oscillate at a temperature $T_{\rm osc}$, when the Hubble rate becomes comparable to axion mass: $\mathcal{H}(T_{\rm osc}) \sim 3 m_a(T_{\rm osc})$. From the onset of oscillations temperature, axion starts behaving as matter, and from conservation of comoving number density, its number density at a later epoch can be written as

$$n_a(T) = n_a(T_{\rm osc}) \frac{s(T)}{s(T_{\rm osc})}. \tag{11}$$

Here $s(T)$ denotes the comoving entropy density at a temperature T. The axion behaves as cold matter and can make all the observed dark matter abundance with total abundance

$$\Omega_a h^2 = \frac{\rho_a(T_0)}{\rho_c} h^2 = \frac{m_a(T_0)}{\rho_c} \left(\frac{\rho_a(T_{\rm osc})}{m_a(T_{\rm osc})} \frac{s(T)}{s(T_{\rm osc})} \right) h^2. \tag{12}$$

If axion constitutes all the dark matter, it should have a mass around $\sim$ 14 μeV, when produced via the misalignment mechanism [69].

The presence of PBH can modify the axion dark matter abundance in two different ways [62, 63] namely, (1) PBH can change the oscillation temperature $T_{\rm osc}$, because of its contribution to the Hubble expansion rate $\mathcal{H}$; (2) PBH evaporation can dilute the existing abundance of axions via entropy injection. In addition to affecting the axion dark matter abundance, evaporation of PBH itself can also produces axions. However, due to the high energy of these evaporating particles, the axions generated from evaporation instead behave as dark radiation and do not contribute to cold dark matter abundance. These axions can contribute to the effective number of relativistic species denoted by $N_{\rm eff}$.

We numerically study the evolution of the PBH-axion system, closely following Ref. [63]. We numerically solve a set of coupled Boltzmann equations (see Appendix A) for the axions, PBH and the radiation energy density.

IV. THE INTERPLAY BETWEEN LEPTOGENESIS AND AXION

Lepton asymmetry can be generated thermally (with the thermal production of RHNs mediated by Yukawa couplings) at a high scale via the CP-violating decays of RHNs, which can be converted to the baryon asymmetry through the electroweak sphaleron processes [15]. At a temperature $T \sim M_i$, lepton asymmetry produced by ith RH neutrino freezes out; therefore, M_i is typically the 'scale of thermal leptogenesis'. In the high-scale leptogenesis scenario, there are three distinct regimes of leptogenesis. Generally, the RH neutrinos produce lepton doublets as a coherent superposition of flavours: $|L_i\rangle = A_{i\alpha} |L_{\alpha i}\rangle$, where $\alpha = e, \mu, \tau$ and $A_{i\alpha}$ is the corresponding amplitude determined by $F_{i\alpha}$. For temperatures $T \gtrsim 10^{12}$, all the charged lepton Yukawa couplings are out of equilibrium (the interaction strength is given by $\Gamma_\alpha \sim 5 \times 10^{-3} T h_\alpha$, with h_α being the charged lepton Yukawa coupling) and do not participate in the leptogenesis process. This is the unflavour or the vanilla regime of leptogenesis. In this regime, leptogenesis is not sensitive to the neutrino mixing

matrix, e.g., mixing angles and low-energy CP phases. When the temperature drops down to $T \lesssim 10^{12}$ GeV, the τ flavored charged lepton interaction comes into equilibrium and breaks the coherent $|L_i\rangle$ state into τ and a composition of $e+\mu$ flavour (two flavour regime). Likewise, the later composition is broken once $T \lesssim 10^{9}$, when the μ flavoured charged lepton interaction comes into equilibrium (three flavour regime). In both these flavoured regimes, leptogenesis may be sensitive to the low-energy neutrino parameters because the neutrino mixing matrix cannot be eliminated from the CP asymmetry parameter. Therefore, for $T \sim M_i \gtrsim 10^{12}$, practically there are no ways to test high-scale thermal leptogenesis, barring some recent effort with gravitational waves from topological defects [21–25]. Here we show, in the unified setup of axion and seesaw, the vanilla regime is testable with axion physics for the hierarchical mass spectrum of RHNs, and interestingly, if the RHNs are quasi-degenerate, the vanilla regime is testable additionally with gravitational waves from PBH density fluctuations.

Note also that the lepton asymmetry can be generated non-thermally from the decay of RHNs produced by PBH evaporation (see [43], for example). However, for the mass range of PBH we consider in this work, they evaporate after the sphaleron decoupling temperature $T_{\rm sph} \sim 132$ GeV, and therefore cannot lead to baryon asymmetry via leptogenesis. Such a mass range of PBH nonetheless affects axion evolution non-trivially and leads to observable gravitational wave signatures in near-future detectors, as we discuss below.

As mentioned earlier, in our scenario, since we propose that the scale of RHN mass generation be the same order as that of the PQ symmetry-breaking, i.e., $M_i \sim f_a$, the RHN masses are connected to m_a via f_a. For hierarchical RHNs, the CP asymmetry parameter can be estimated as [71, 72]

$$\epsilon_1 = \frac{3M_1\sqrt{(\Delta m_{\rm atm})^2}}{4\pi v^2}, \tag{13}$$

with $v/\sqrt{2} = 174$ GeV is the VEV of the SM Higgs and $(\Delta m_{\rm atm})^2 \simeq 2.4 \times 10^{-3}{\rm eV}^2$ is the active neutrino atmospheric mass-squared difference. The resulting baryon asymmetry from the decay of N_1 can be approximately written in terms of baryon-to-photon ratio as [73]

$$\eta_B \approx 10^{-2}\kappa_1 \frac{\epsilon_1}{\xi}\,. \tag{14}$$

Here ξ denotes the entropy dilution due to PBH evaporation, estimated as [73]

$$\xi = 233\,\beta \left(\frac{m_{\rm in}}{M_{\rm Pl}}\right)\left(\frac{\gamma}{g_{*,B}(T_{\rm BH})\mathcal{G}}\right)^{1/2}, \tag{15}$$

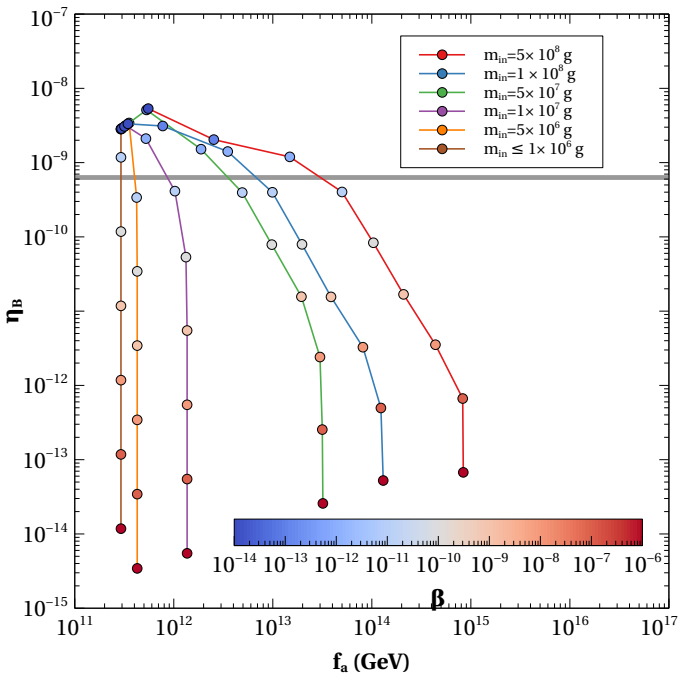


FIG. 1: Baryon to photon ratio, η_B vs f_a for different PBH mass and initial fractional abundance, β. Here, the contours satisfy the correct DM relic. Initial misalignment angle is taken to be $\theta_i = \frac{\pi}{\sqrt{3}} \sim 1.81$. The horizontal gray line denotes the observed value of η_B. The effective number of relativistic species due to hot QCD axion from PBH evaporation is mentioned for each PBH mass. Here, we take $M_1 = f_a$ which gives $\beta = 5.7 \times 10^{-12} \left(\frac{M_{\rm Pl}}{m_{\rm in}}\right) \left(\frac{f_a}{\rm GeV}\right)$ for correct asymmetry.

and $\kappa_1 \simeq 10^{-2}$ is the efficiency of lepton asymmetry production. $\mathcal{G} \sim 3.8$ is the greybody factor and $M_{\rm Pl} = \sqrt{8\pi} M_{\rm P}$ is the Planck mass. The extra factor 10^{-2} on the right-hand side of Eq. (14) accounts for the combined effects of sphaleron conversion of the leptons to baryons plus the photon dilution [71]. Now, since the axion and RHN mass originate from the same symmetry breaking, we replace[4] $f_a \simeq M_1$. This gives us the following condition on β to satisfy the observed baryon asymmetry (similar expression as in Ref. [73], but now M_1 is replaced by f_a)

$$\beta \simeq 5.7 \times 10^{-12} \left(\frac{M_{\rm Pl}}{m_{\rm in}}\right) \frac{f_a}{\rm GeV} \simeq 32.3 \left(\frac{M_{\rm Pl}}{m_{\rm in}}\right) \left(\frac{1\mu{\rm eV}}{m_a}\right) . \tag{16}$$

In Fig. 1, we show the baryon asymmetry as a function of the PQ scale f_a, for different

[4] Note that here we use the formula for the CP asymmetry parameter valid only for a hierarchical mass spectrum of RHNs, and we consider a N_1-dominated leptogenesis scenario. In this case, although the heavier RHNs do not have any significant role to play, their masses are constrained as $M_{i=2,3} < f_a\sqrt{4\pi}$.

values of initial PBH mass. The given contours are also consistent with the observed DM relic from axion oscillation. If PBH evaporates before the axion oscillation temperature $T_{\rm osc}$, they do not affect the axion dynamics. It turns out that for $m_{\rm in} \lesssim 10^6$ g, the PBH evaporation temperature remains higher than $T_{\rm osc}$ leading to the standard axion results with $f_a \simeq 3 \times 10^{11}$ GeV, generating the correct DM relic. This is indicated by the left-most brown colored contour in Fig. 1. Along this contour, β is varied, as per the color bar, which changes the baryon asymmetry because of entropy dilution, following Eq. (15). Increasing the PBH mass beyond 10^6 g decreases the oscillation temperature and also leads to dilution of the axion abundance because of entropy dilution, resulting in a higher f_a to obtain the observed DM abundance. With a decrease in β, this cumulative effect of PBH starts to diminish and hence the contours move towards the standard case of $f_a \simeq 3 \times 10^{11}$ GeV. On the other hand, decreasing f_a and β has opposite effects on the baryon asymmetry η_B, with the former decreasing the asymmetry by decreasing M_1 (cf. Eq. (13)), while the latter increasing the asymmetry because of lesser entropy dilution. The latter effect turns out to be more dominant which leads to an increase in the value of η_B.

The lepton asymmetry can be significantly enhanced if two of the RHNs are quasi-degenerate, i.e., $\Delta M = M_2 - M_1 \ll \overline{M} = (M_1 + M_2)/2$ leading to the resonant leptogenesis scenario [74, 75]. For $\Delta M \simeq \Gamma$, the CP asymmetry parameter can reach upto $\mathcal{O}(1)$, where Γ indicates the decay width of the RHN. For the resonant scenario, the expression for β can be written as -

$$\beta = 2.9 \times 10^4 \epsilon_1 \left(\frac{M_{\rm Pl}}{m_{\rm in}} \right) . \tag{17}$$

We will discuss the difference in our results for hierarchical and resonant leptogenesis scenarios as we proceed.

For QCD axion to be dark matter in the absence of PBH, we only get a particular value of axion mass. In presence of PBH, due to two extra parameters $m_{\rm in}$ and β, new parameter space opens up. Fig. 2 shows the different axion mass in color bar as a function of β and $m_{\rm in}$ so that DM abundance is satisfied. For PBH mass around $m_{\rm in} \lesssim 10^{6.5}$ g, the evaporation of PBH occurs before the onset of axion oscillation. Hence for that PBH mass range, presence of PBH does not change axion abundance. Similarly, in the radiation domination region, PBH has no effect on axion mass. This is visible in the left and left-bottom triangular regions from the plot, where mass of axion remains fixed at $\sim 10^{-5}$ eV. For PBH masses greater

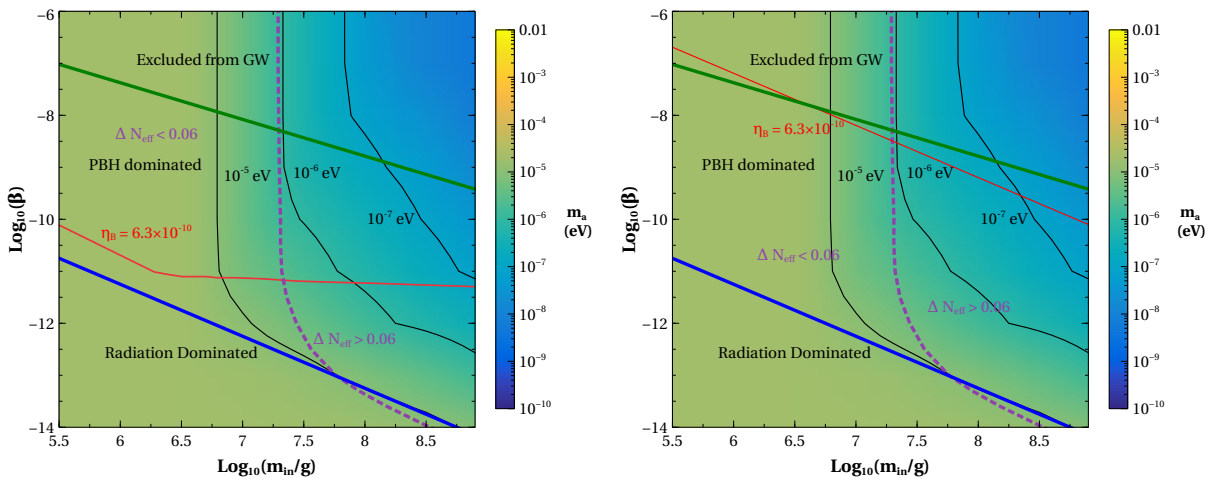


FIG. 2: Constraint on $m_{\rm in}$ vs β plane considering a hierarchical N_1-dominated leptogenesis scenario (left plot) and a resonant leptogenesis scenario (right plot). The color bar represent axion mass that satisfy the observed DM abundance. The red color lines in both the plots denote the parameter space that is consistent with both DM relic and baryon asymmetry. The region excluded from GW is separated by solid green line. The magenta dashed line separates the regions that can be probed by future CMB-S4 experiment due to contribution of hot axion on $N_{\rm eff}$.

than $\gtrsim 10^{6.5}$ g, presence of PBH not only delays the oscillation temperature but also dilute the axion abundance. So one needs ample amount of axions before PBH evaporation so that correct DM relic is satisfied. This is achieved by reducing the axion mass (or increasing the PQ symmetry breaking scale, f_a). The overall variation of axion mass as a function of PBH mass and initial fractional abundance can be seen from Fig. 2. Thus, the presence of PBH opens up more parameter space for axion mass to be in agreement with total DM abundance.

We now discuss the difference between left and right panel plots of Fig. 2 and the parameter space consistent with successful leptogenesis. The left panel of this figure considers the hierarchical N_1-dominated leptogenesis scenario where we use Eq. (13) for CP asymmetry parameter along with Eq. (14). The solid red colored line corresponds to the parameter space consistent with successful leptogenesis. For the PBH mass range, $10^{5.5}$g $\lesssim$ m$_{\rm in}$ $\lesssim$ $10^{6.5}$g, CP asymmetry parameter remains constant as $M_1 \sim f_a$ does not change from axion DM abudance criteria. Therefore, the only factor which affects baryon asymmetry is the dilution factor in Eq.(14). So, for a constant η_B, the parameters $m_{\rm in}$ and β are anti-correlated.

This gives a decrease in β as PBH mass is increased for the range $10^{5.5}$g $\lesssim$ m$_{\rm in}$ $\lesssim 10^{6.5}$g. For PBH masses above $m_{\rm in} \gtrsim 10^{6.5}$ g, increase in PBH mass increases the axion scale f_a. Due to this, CP asymmetry parameter takes a larger value. Hence, for the mass range $m_{\rm in} \gtrsim 10^{6.5}$ g, as PBH mass increases, the decrease in β is not as sharp as for the mass range $10^{5.5}$g $\lesssim$ m$_{\rm in}$ $\lesssim 10^{6.5}$g. The region below the red line gives $\eta_B > 6.3 \times 10^{-10}$, i.e. it produces more baryon asymmetry than the observed value. The region above the red line gives $\eta_B < 6.3 \times 10^{-10}$ However, for this scenario, it turns out that the parameter space that satisfies the observed baryon asymmetry and DM abundance is out of reach from near future gravitational waves experiment sensitivities, to be discussed later.

In the right panel plot of Fig. 2, we consider the resonant leptogenesis scenario. Instead of Eq. (13) for hierarchical leptogenesis, here we have considered a maximal CP asymmetry $\epsilon = 0.1$, achievable with resonant enhancement. This makes the CP asymmetry parameter independent of the PQ scale (because now the expression of CP asymmetry parameter in Eq.13, is scaled by a free parameter $\delta^{-1} \equiv M/\Delta M$). At the same time, due to the larger CP asymmetry parameter, one needs a large amount of entropy dilution. This requires a larger value of β for a given PBH mass compared to the vanilla leptogenesis scenario. This is evident from the upward shift of the solid red line consistent with the observed BAU compared to the one in the left panel. Also, due to a larger value to β, this region of parameter space can be probed from future gravitational wave experiments. In both the plots, we also indicate the parameter space within reach future CMB experiments like CMB-S4 [76] which can measure additional relativistic degrees of freedom $\Delta N_{\rm eff}$. Such non-zero $\Delta N_{\rm eff}$ or dark radiation arises in our setup due to the production of hot axions from PBH evaporation. Note, remarkably, that in both the plots, the $T \sim M_i \sim f_a \gtrsim 10^{12}$ GeV is testable, with either axion physics or combinedly with GW experiments.

A. Sub-dominant axion DM

If axion does not constitute the entire DM, the parameter space can change significantly offering interesting detection prospects. The deficit in total DM abundance can be filled up by one of the RHNs, details of which will be discussed later. Fig. 3 shows the parameter space for PBH initial mass, initial energy fraction, and axion mass for different percentages of total DM constituted by axion. The top left panel plot shows the hierarchical leptogenesis and

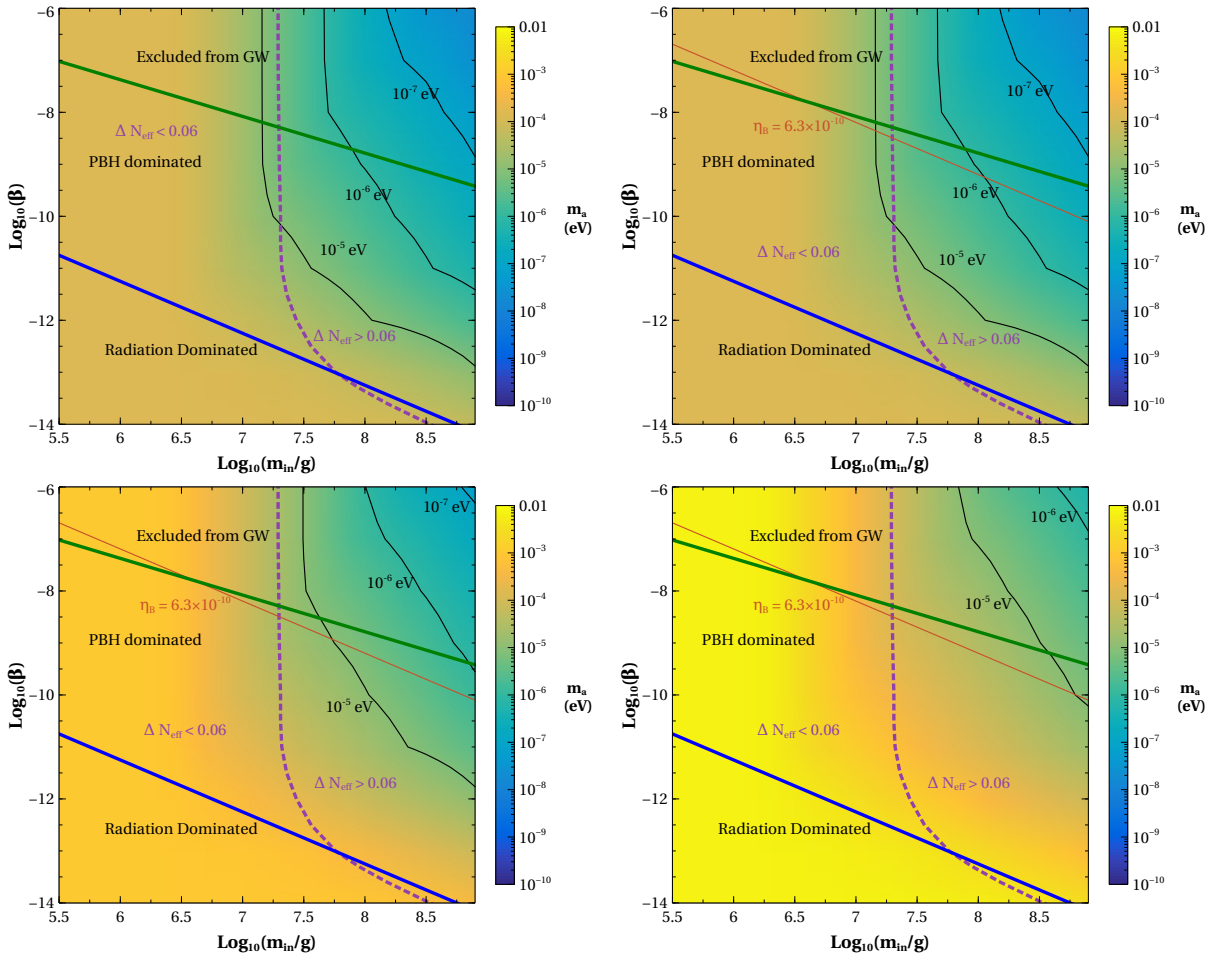


FIG. 3: Constraint on $m_{\rm in}$ vs β plane considering vanilla leptogenesis and (top left panel) and leptogenesis with resonant (top right and bottom panels). Axion constitutes $10\%, 1\%, 0.1\%$ of total DM abundance in top panels, bottom left and bottom right panels respectively. The red solid lines in the plots denote the parameter space that is consistent with both DM relic and baryon asymmetry. The region excluded from GW is separated by solid green line. The magenta dashed line separate the regions that can be probed by future CMB-S4 experiment due to contribution of hot axion on $N_{\rm eff}$.

axion result, constituting 10% of total DM abundance. Compared to the left panel of Fig.2, for a particular value of $m_{\rm in}$ and β, one needs a larger value of axion mass (correspondingly smaller value of f_a) here. This is visible from the color code and the black solid contours for different axion masses. However, at the same time, a smaller value of f_a also reduces the CP asymmetry parameter according to Eq. (13). As a result, baryon asymmetry also reduces. Thus, for a particular PBH mass, one needs to consider a smaller value β so that dilution is

also less to obtain correct baryon asymmetry. However, it turns out that for this particular scenario, even if one reduces β to β_c (where β_c distinguishes PBH-dominated and radiation-dominated region), the correct baryon asymmetry can not be obtained. The maximum baryon asymmetry that can be obtained is $\sim 4 \times 10^{-10}$ which is less than the observed asymmetry, viz., 6.3×10^{-10}. All the region above the $\beta = \beta_c$ line gives $\eta_{\rm B} < 4 \times 10^{-10}$. A similar conclusion can be obtained for smaller relative abundances of axion DM as well. For sub-dominant axion DM scenario, one has to consider resonant leptogenesis approach to generate correct BAU. As seen from top right panel and bottom panel plots of Fig. 3, corresponding to maximal CP asymmetry $\epsilon = 0.1$, there exist parameter space, indicated by the solid red line, consistent with the observed BAU. As the relative abundance of axion DM changes from 10% to 0.1% in these plots, the axion parameter changes while the red solid line indicating the BAU satisfied criteria stays at the same position as CP asymmetry no longer depends upon the axion parameters in the resonant leptogenesis scenario.

Note that, in this model, we can have smaller f_a values, and consequently, axion mass range in the solar axion ballpark [77, 78]. At the same time, the model can offer the observed dark matter abundance. However, in this case, the dark matter will be in a multi-component form constituting axions and one of the RHNs, as discussed below. We nonetheless would like to mention that there have been efforts to obtain the entire dark matter relic only in the form of axions for a smaller value of decay constant ($f_a \sim 10^{8\div 9}$GeV) via parametric resonance production of axions. see. e.g., [79–81].

V. RIGHT HANDED NEUTRINO DARK MATTER

As two RHNs are sufficient to generate neutrino mass and BAU via leptogenesis, the other RHN, if sufficiently long-lived, can constitute some part of the total DM abundance. Due to the presence of PBH and RHN coupling to axion as well as SM leptons, we can have three[5] different production channels for RHN DM namely, (i) gravitational production from PBH evaporation [34–51], (ii) production via axion portal interactions [84–86], (iii) freeze-in production via Yukawa portal interactions [87, 88]. For the axion decay constant we have in our setup, superheavy RHN DM is more natural which is produced dominantly via PBH

[5] It is also possible to generate light RHN DM via active-sterile neutrino oscillation [82], though it faces severe X-ray constraints. See [83] for a review.

evaporation. However, if we allow fine-tuning of RHN DM mass, keeping it much lower than the PQ scale, other production mechanisms can dominate. For the sake of completeness, we briefly discuss all these production channels below.

Gravitational production from PBH: For RHN DM production from the evaporation of PBH, we can have two different situations depending of whether DM mass $M_{\rm DM}$ is more or less compared to the initial Hawking temperature of PBH $T_{\rm BH}^{\rm in}$ or equivalently $M_{\rm DM} < T_{\rm BH}^{\rm in}$ or $M_{\rm DM} > T_{\rm BH}^{\rm in}$. The total DM abundance of both the cases (assuming PBH domination in the early Universe) are given as

$$\Omega_{\rm DM}h^2 \simeq M_{\rm DM}\frac{T_{\rm ev}}{m_{\rm in}}\begin{cases}\left(\frac{m_{\rm in}}{M_{\rm P}}\right)^2, & \text{for } M_{\rm DM} < T_{\rm BH}^{\rm in}\\ \left(\frac{M_{\rm P}}{M_{\rm DM}}\right)^2, & \text{for } M_{\rm DM} > T_{\rm BH}^{\rm in}.\end{cases} \tag{18}$$

For the case when $M_{\rm DM} < T_{\rm BH}^{\rm in}$, correct relic abundance needs DM mass in the range of $\sim$ GeV. However, for this mass range of DM produced by PBH evaporation, the DM turns out to be hot and hence disfavored from structure formation constraints. For the other limiting case $M_{\rm DM} > T_{\rm BH}^{\rm in}$, the DM mass is greater than 10^9 GeV, keeping it in the superheavy ballpark, a natural consequence of the high PQ symmetry breaking scale.

Axion portal production: The RHN DM can also be produced via the axion portal interactions due to its non-zero PQ charge. Since, axion portal coupling of RHN will be suppressed for allowed mass range of thermal DM below unitarity limit [89], such production is likely to occur via freeze-in mechanism from the SM bath. Here, for simplicity, we consider only the gluon initiated production channel $gg \to N_1 N_1$ with the interaction $\frac{1}{4}\frac{\partial_\mu a}{f_a}\bar{N}\gamma^\mu\gamma_5 N$ and $\frac{g_s^2}{32\pi^2}\frac{a}{f_a}G_{\mu\nu}\tilde{G}^{\mu\nu}$. With this, the comoving abundance of DM, produced from UV freeze-in can be estimated as [84, 85]

$$Y_{\rm DM} = \frac{16\times 45}{2\times\pi^7\times 1.66\times g_*^s\sqrt{g_*^\rho}}\left(\frac{1}{4f_a}\right)^2\left(\frac{g_s^2}{32\pi^2 f_a}\right)^2 M_{\rm DM}^2 M_{\rm Pl}\,\max(f_a, T_{\rm RH}). \tag{19}$$

Here g_s^s and g_*^ρ denotes the effective number of degrees of freedoms for entropy and energy density respectively and $T_{\rm RH}$ denotes the reheating temperature. For $f_a, T_{\rm RH} \sim 10^{12}$ GeV, we require DM mass to be around 10^5 GeV to produce the observed DM abundance. For heavier DM mass, it is likely to be overproduced via axion portal interactions as long as $T_{\rm RH} > M_{\rm DM}$. On the other hand, RHN DM of mass $\sim 10^5$ GeV will also be overproduced from PBH evaporation as mentioned above. This pushes RHN DM to low mass where it can be produced efficiently via Yukawa portal interactions.

Yukawa portal production: From the above discussion, we see that the due to the presence of both gravitational production and axion portal production, RHN DM mass has to be smaller than $\sim$ 1 GeV if $T_{\rm RH} > M_{\rm DM}$. So one requires the DM with masses less than $\sim$ 1 GeV where both the gravitational production and axion portal production are subdominant. This can be achieved via IR freeze-in production of N_1 from the SM bath. As shown in earlier works [87, 88], such freeze-in production is dominated by $W^{\pm}, Z$ and SM Higgs decays facilitated via active-sterile neutrino mixing. The light neutrino mass matrix is given as $m_\nu = -M_D M^{-1} M_D^T$, where $(M_D)_{ij} = F_{ij}\frac{v}{\sqrt{2}}$ and $M_{ij} = y_{ij}\frac{f_a}{\sqrt{2}}\delta_{ij}$. The light neutrino mass matrix m_ν can be diagonalized by the Pontecorvo-Maki-Nakagawa-Sakata (PMNS) leptonic mixing matrix U as $U^\dagger m_\nu U^* = \text{diag}\ (m_1, m_2, m_3)$ with m_i's being the light neutrino mass eigenvalues (assuming diagonal charged lepton matrix). From the decay of $W^{\pm}, Z$ and h to N_1 via the relevant active sterile neutrino mixing $(M_D)_{i1}/M_1 = V_{i1}$, sufficient amount of N_1 can be produced. It turns out that the freeze-in value of comoving number density of N_1, Y_{N_1} is proportional to $\frac{m_1}{M_1}$. Hence N_1 abundance $\Omega_{N_1}h^2 \propto M_1 Y_{N_1}$ is independent of M_1 [88] whereas it is directly proportional to m_1. As a result, m_1 is uniquely determined for a given N_1 abundance. On the other hand, due to active sterile neutrino mixing, N_1 can decay to SM particles. It turns out that the radiative decay of $N_1 \to \gamma\nu$ is the most dominant one and its decay rate is given by [88]

$$\Gamma_{N_1\to\gamma\nu} = \frac{9\alpha G_{\rm F}^2}{1024\pi^4}\sin^2(2\theta_1)M_1^5, \tag{20}$$

where α, G_F are fine structure and Fermi constants respectively with

$$\theta_1^2 = \sum_{i=e,\mu,\tau}\frac{|(M_D)_{i1}|^2}{M_1^2} = \sum_{i=e,\mu,\tau}\frac{|V_{i1}|^2}{M_1}. \tag{21}$$

So, although the abundance of N_1 only depends on m_1, the decay rate of N_1 depends on both m_1 and M_1. This gives a constraint on the N_1 mass, as shown in the left panel of Fig. 4. The magenta colored line represents the situation where PBH does not dominate the energy density of the Universe (i.e. no additional entropy dilution). The brown colored line denotes the situation where entropy dilution is present from PBH evaporation. Due to presence of entropy dilution, N_1 should be produced over-abundantly requiring a larger value of active-sterile mixing angle. As the decay of N_1 is also dependent of θ_1^2, so M_1 is more tightly constraint in presence of entropy dilution as seen from left plot of figure 4. Here both the magenta and the brown color lines give correct relic density. In the right panel

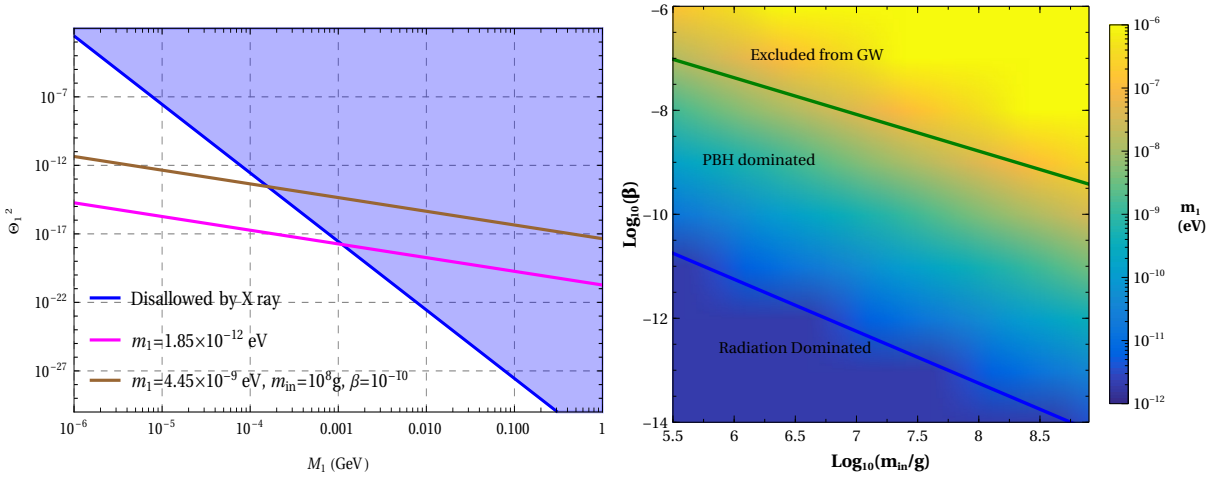


FIG. 4: Left plot : θ_1^2 vs M_1 for two different scenarios : without PBH and with PBH ($m_{\rm in} = 10^8$ g and $\beta = 10^{-10}$) shown by magenta and brown color respectively. The shaded blue color region represents excluded region by X-ray experiments. Right plot : Lightest neutrino mass m_1 in PBH parameter space $\beta - m_{\rm in}$ with N_1 abundance $\Omega_{N_1}h^2 = 0.12$.

plot, m_1 is shown in the $\beta - m_{\rm in}$ plane for $\Omega_{N_1}h^2 = 0.12$, correlating neutrino mass with PBH parameters from correct DM relic criteria.

A. RHN DM with $T_{\rm RH} < M_{\rm DM}$

As noticed in the above discussions, the RHN DM parameter space produced from PBH evaporation and axion portal interactions is anti-correlated, forcing the RHN DM mass to sub-GeV ballpark where it can be efficiently produced from Yukawa portal freeze-in mechanisms. However, this requires severe fine-tuning of RHN coupling with the PQ scalar such that $M_1 \equiv M_{\rm DM} \ll f_a$. Such unnatural fine-tuning can, however, be avoided if we consider the heaviest RHN N_3 to be DM with mass $M_3 = f_a > T_{\rm RH}$ which can not be produced from the bath. Leptogenesis is obtained from N_1 and N_2 with $M_1 \simeq M_2$. For thermal leptogenesis, we assume $M_1 \simeq M_2 < T_{\rm RH} \ll M_3 = f_a$. Although the PQ symmetry gets broken after e.g., slow-roll inflation, a non-instantaneous reheating phase [90] can lead to a reheat temperature $T_{\rm RH} \ll f_a$. This leads to purely gravitational production of RHN DM from PBH evaporation. The DM mass produced from PBH evaporation is given by

$$M_{\rm DM} \simeq 4.5 \times 10^3 \left(\frac{0.12}{\Omega_{N_3}h^2}\right)\left(\frac{m_{\rm in}}{M_{\rm Pl}}\right)^{-5/2}\frac{M_{\rm Pl}^2}{\rm GeV}. \tag{22}$$

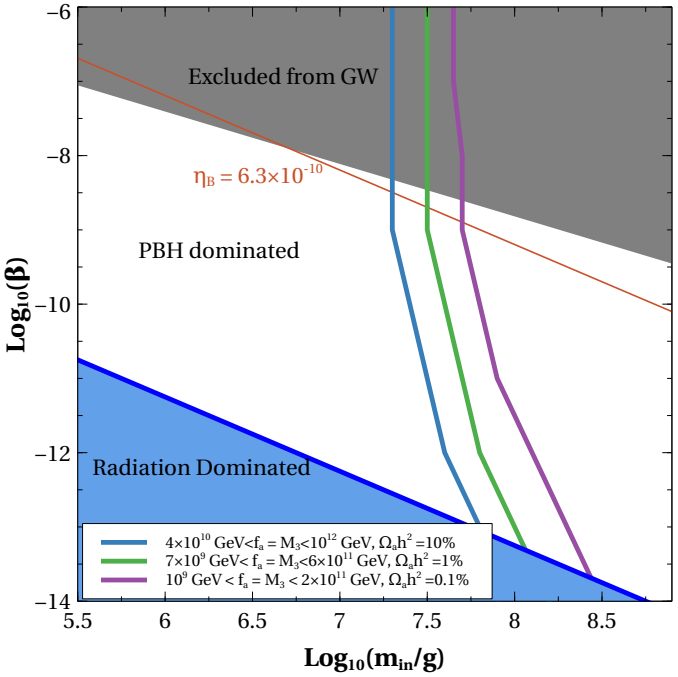


FIG. 5: For $M_3 \gg T_{\rm RH} > M_2 \sim M_3$. Blue, green and magenta colored lines denote the different situation where $\Omega_{\rm a}h^2 = 10\%, \Omega_{\rm a}h^2 = 1\%$ and $\Omega_{\rm a}h^2 = 0.1\%$ respectively and $f_a = M_3$. The RHN N_3 constitutes the rest of DM abundance. The brown colored solid line denotes the parameter space consistent with the baryon asymmetry for maximal CP asymmetry.

As $M_{\rm DM} = f_a$, this gives a line in the $\beta - m_{\rm in}$ plane. In Fig. 5, blue, green and magenta colorued lines correspond to the situations where $\Omega_a h^2 = 10\%, 1\%$ and 0.1% of total DM abundance respectively. Note that $M_3 = M_{\rm DM} = f_a$ changes along these contours, following Eq. (22). The rest of the DM abundance is constituted by N_3. The observed BAU can be generated from resonant leptogenesis as discussed earlier. The parameter space satisfying the observed BAU for maximal CP asymmetry $\epsilon = 0.1$ is indicated by the brown colored solid line in Fig. 5.

VI. GRAVITATIONAL WAVES DETECTION PROSPECT

The presence of ultra-light PBH not only affects the production of DM and BAU but also opens up interesting detection prospects at gravitational wave frontiers. Of many different ways to connect GW with PBH, we focus on the GW production from the inhomogeneity in the PBH distribution after they are formed [29–33]. This particular source of GW remains

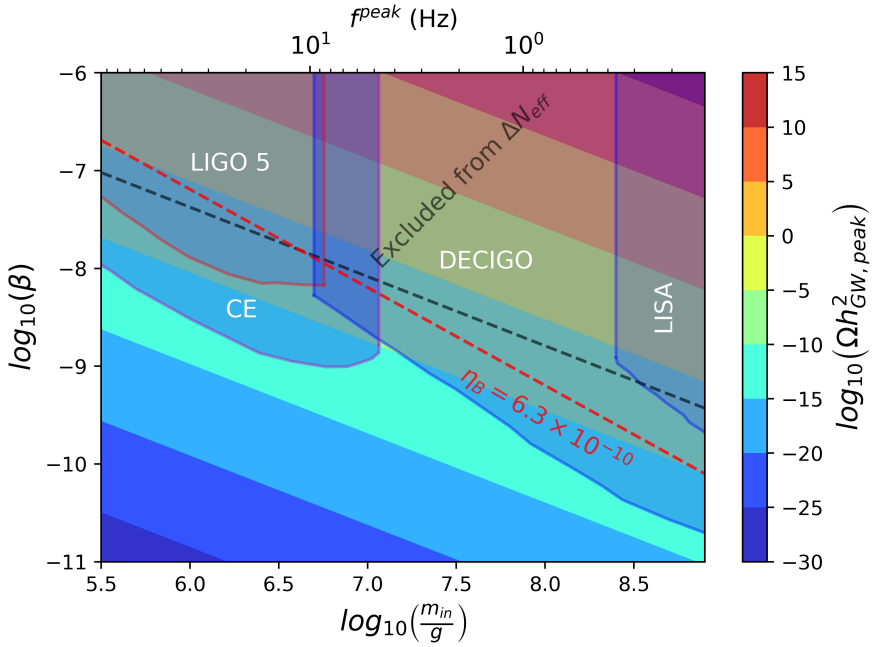


FIG. 6: Peak Gravitational Waves amplitude as a function of $m_{\rm in}$ and β with different experimental sensitivities. The red dashed line denotes the correct baryon asymmetry value for resonant leptogenesis ($\epsilon = 0.1$).

unaffected by the production mechanism of PBH and also lead to observable GW within reach of near future detectors as we briefly discuss here.

PBH typically follows an inhomogeneous spatial distribution after formation obeying Poisson statistics [29]. Such spatial inhomogeneities induce GW at second order once PBH dominates the energy density of the Universe [29, 30] and then gets further enhanced during PBH evaporation [30]. The peak amplitude of gravitational wave production produced due to PBH evaporation is given as [30, 31, 48, 73]

$$\Omega_{\rm gw}(t_0, f) \simeq \Omega_{\rm gw}^{\rm peak} \left(\frac{f}{f^{\rm peak}}\right)^{11/3} \Theta\left(f^{\rm peak} - f\right), \tag{23}$$

where $\Omega_{\rm gw}^{\rm peak}$ indicates the peak amplitude and is given by

$$\Omega_{\rm gw}^{\rm peak} \simeq 2 \times 10^{-6} \left(\frac{\beta}{10^{-8}}\right)^{16/3} \left(\frac{m_{\rm in}}{10^7 {\rm g}}\right)^{34/9}. \tag{24}$$

The peak frequency of gravitational waves which is related to the mean separation between PBH is

$$f^{\rm peak} \simeq 1.7 \times 10^3 \, {\rm Hz} \left(\frac{m_{\rm in}}{10^4 {\rm g}}\right)^{-5/6}. \tag{25}$$

From the contribution of GW to effective number of relativistic species, bound on β can be obtained as

$$\beta \lesssim 1.1 \times 10^{-6} \left(\frac{m_{\rm in}}{10^4 {\rm g}}\right)^{-17/24}. \tag{26}$$

in order to be consistent with the limits on $N_{\rm eff}$ from BBN and CMB observations.

Fig. 6 shows the sensitivity of different GW experiments like advanced LIGO-VIRGO or LIGO 5 [91], LISA [92], DECIGO [93] and CE [94] to the parameter space in $\beta - m_{\rm in} - f^{\rm peak}$ plane with the color code indicating the peak amplitude. Clearly, the parameter space consistent with successful leptogenesis and BBN, CMB limits on $\Delta N_{\rm eff}$ remains within reach of several near future GW detectors.

Note also that, although arguable [95], one can potentially have GWs from axion-strings [96] in this model. Due to the PBH domination, our scenario can marginally access the values $f_a \gtrsim 10^{14}$ GeV to produce GWs from axion cosmic strings. However, we do not discuss this spectrum because, in the presence of PBH, a string-PBH network evolution requires numerical simulation [97].

VII. AXIONS DETECTION PROSPECT

The axion detection prospects in most experiments primarily rely on axion-photon coupling. The axion-photon coupling leading to $\frac{1}{4} g_{a\gamma} a F \tilde{F}$ is given by (same as KSVZ model) [98]

$$g_{a\gamma} = -\frac{\alpha}{2\pi f_a}\left(\frac{2}{3}\frac{4m_d + m_u}{m_u + m_d}\right) = -1.92\frac{\alpha}{2\pi f_a}. \tag{27}$$

Fig. 7 shows the axion-photon coupling with axion mass including the bounds and sensitivities of different experiments. The current experimental bound on the axion-photon coupling from various experiments or observables are shown by the solid color lines (CAST [99, 100], SN87A [101–103], NGC 1275 [104], ADMX [105–107]) whereas future experimental sensitivies are shown by the dashed lines (CASPEr [108], KLASH [109, 110], ABRACADABRA [111, 112], CULTASK [113, 114], MADMAX [115], IAXO [77, 116], Fermi-LAT [117], BH superradiance [118]).

The left panel of Fig.7 shows the constraint on $g_{a\gamma}$ without PBH with the color bar indicating the relative axion abundance compared to total DM relic. The right panel of the

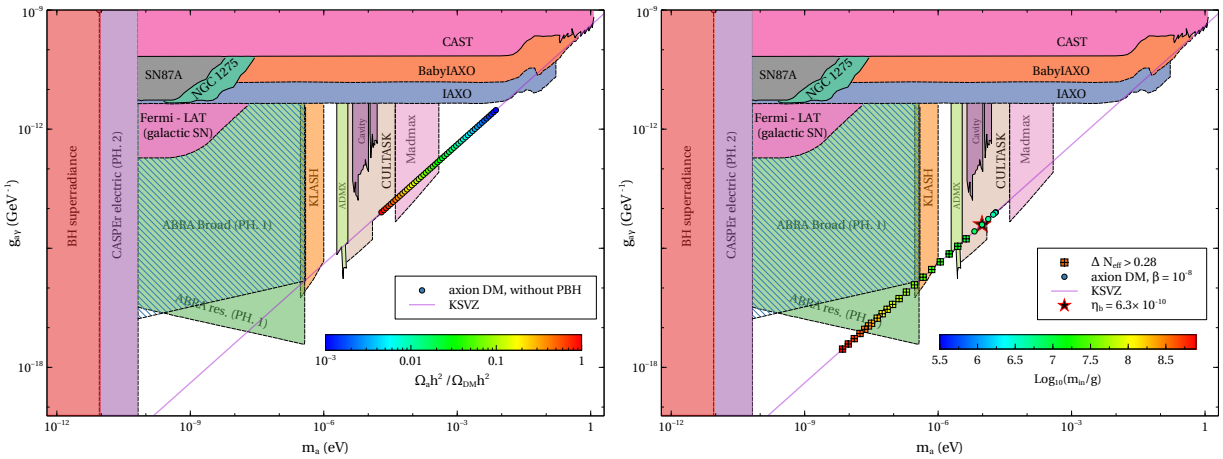


FIG. 7: Axion-photon coupling versus axion mass without PBH (top left panel), with PBH and axion giving rise to total DM (top right panel).

TABLE I:

DM composition	$m_{a,min}$ (eV)	$m_{a,max}$ (eV)	$f_{a,max}$ (GeV)	$f_{a,min}$ (GeV)
RHN 0%, axion 100%	4×10^{-8}	2×10^{-5}	1.4×10^{14}	2.9×10^{11}
RHN 90.0%, axion 10.0%	3×10^{-7}	1.4×10^{-4}	1.9×10^{13}	4.1×10^{10}
RHN 99.0%, axion 1.0%	2×10^{-6}	1×10^{-3}	2.9×10^{12}	5.8×10^{9}
RHN 99.9%, axion 0.1%	1×10^{-5}	7×10^{-3}	5.8×10^{11}	8.3×10^{8}

same figure shows the constraint on $g_{a\gamma}$ in the presence of PBH with $\beta = 10^{-8}$ and the color bar indicating the initial mass of PBH. As we have already seen that presence of PBH requires a smaller axion mass, so the dotted color points shift towards left as PBH mass increases. The points indicated by ♦ are ruled out by $\Delta N_{\rm eff}$ contribution coming from GW (cf. Eq. (26)). ★ indicates the point satisfying the observed baryon asymmetry, considering the resonant case. Note that for a smaller value of β (cf. left panel of Fig. 2), the scenario of hierarchical leptogenesis can also be within the sensitivity of axion experiments. Fig. 8 shows the constraint for four different situations where axion contribution to DM are 100%, 10%, 1% and 0.1% denoted by red, blue, green and cyan line respectively. The minimum f_a is obtained for the PBH mass with $T_{\rm ev} > T_{\rm osc}$ (i.e. $m_{\rm in} \lesssim 10^{6.5}$g). The maximum f_a is obtained for PBH mass with $T_{\rm ev} \sim T_{\rm BBN}$ and for maximum allowed β from Eq. (26) (i.e. $m_{\rm in} \sim 10^{8.6}$ g and $\beta \sim 6 \times 10^{-10}$). These limits on axion mass and decay constants are also summarised in table I.

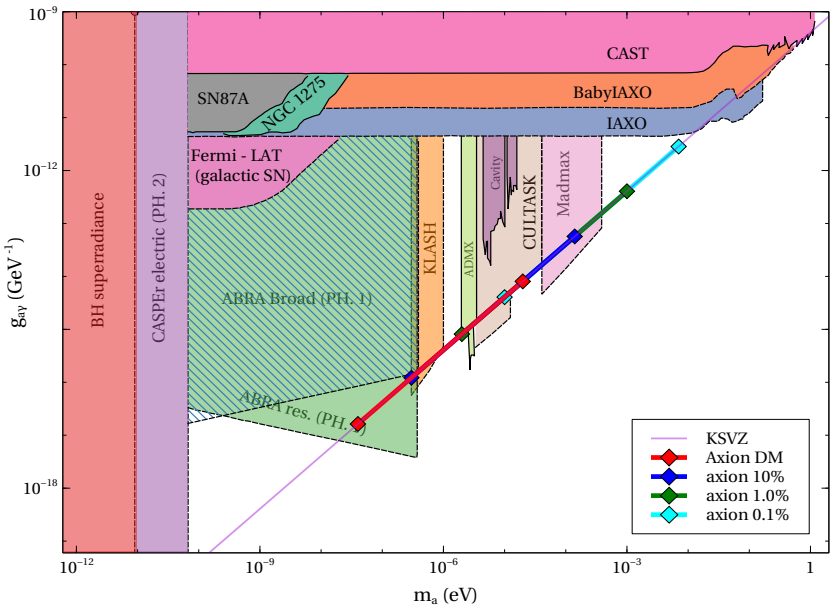


FIG. 8: Constraints on axion-photon coupling in presence of PBH for four different axion contribution to DM.

VIII. CONCLUSION

We have studied the possibility of generating dark matter and baryon asymmetry in the Universe by considering a Peccei-Quinn symmetric framework solving the strong CP problem and the presence of a non-standard cosmological phase arising from ultra-light primordial black holes. The popular type-I seesaw framework for generating non-zero neutrino mass is augmented by a $U(1)_{\rm PQ}$ symmetry leading to a KSVZ-type axion model where the PQ symmetry breaking scale also generates the seesaw scale or mass of right-handed neutrinos. While the BAU is generated via leptogenesis from RHNs, DM can arise either from QCD axion or from one of the RHNs or a combination of both. The presence of PBH as well as the possibility of sub-dominant axion DM changes the axion parameter space significantly keeping the axion detection prospects promising across a wide range of axion mass and couplings. In the absence of fine-tuning in RHN DM mass, it is naturally produced from PBH evaporation. Additionally, PBH also produces dark radiation in terms of hot axions which can be observed at next generation CMB experiments. The PBH parameter space considered in this work also leads to stochastic gravitational waves from PBH density fluctuations within reach of several near future detectors like LISA, CE as well as advanced LIGO-VIRGO. The detection prospects of the setup at a variety of experiments like low energy axion detection

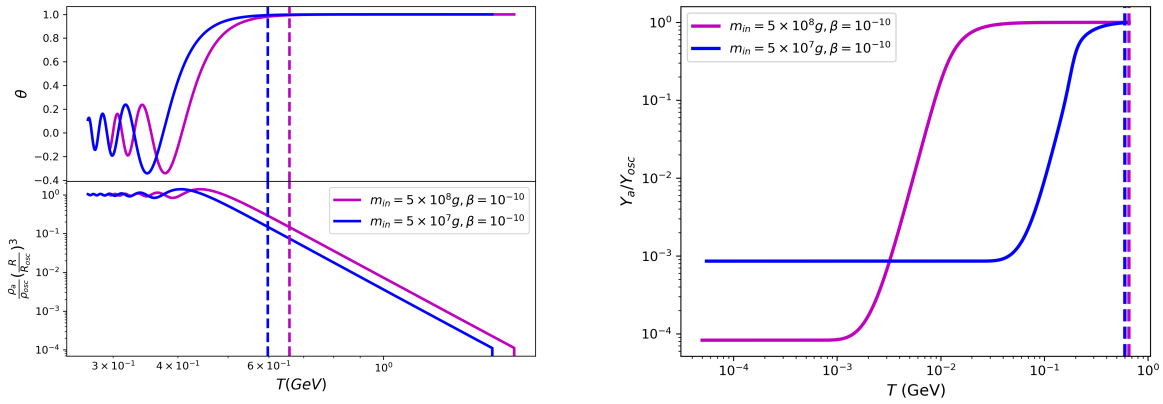


FIG. 9: Evolution of axions in presence of primordial black hole. The red and blue color denote PBH mass of 5×10^8 g and 5×10^7 g respectively. The rest of the parameters are kept constant : $\beta = 10^{-10}$, $\theta_i = 1$ and $m_1 = 10^{-6}$ eV. The vertical dotted line shows the condition when $\mathcal{H}(T) = m_a(T)$.

ones to CMB and GW detectors keep it verifiable in near future.

Acknowledgements

We thank Satyabrata Datta for the discussion at the initial stages of this work. The work of DB is supported by the Science and Engineering Research Board (SERB), Government of India grants MTR/2022/000575 and CRG/2022/000603. The work of ND is supported by the Ministry of Education, Government of India via the Prime Minister's Research Fellowship (PMRF) December 2021 scheme. ND would like to thank Disha Bandyopadhyay for useful discussions. The work of SJD was supported by IBS under the project code, IBS-R018-D1. SJD would also like to thank the support and hospitality of the Tata Institute of Fundamental Research (TIFR), Mumbai, where a part of this project was carried out.

Appendix A: Axion field evolution

PBH after formation loses its energy via Hawking evaporation. The combined Boltamzann equations for the system can be written as -

$$\frac{d\rho_{\rm in}}{dt} + 3\mathcal{H}\rho_{\rm BH} = \frac{1}{m_{\rm BH}}\frac{dm_{\rm BH}}{dt}\rho_{\rm BH} \tag{A1}$$

$$\frac{d\rho_{\rm r}}{dt} + 4\mathcal{H}\rho_r = -\frac{1}{m_{in}}\frac{dm_{\rm BH}}{dt}\rho_{\rm BH}, \tag{A2}$$

where Hubble expansion rate

$$3M_{\rm p}\mathcal{H}^2 = \rho_r + \rho_{\rm BH} \tag{A3}$$

and mass loss rate

$$\frac{1}{m_{\rm BH}}\frac{dm_{\rm BH}}{dt} = -\frac{\mathcal{G}g_H(T_H)}{30720\pi G^2 m_{\rm BH}^3}. \tag{A4}$$

Due to PBH evaporation, entropy injection takes place, leading to non-conservation of entropy. The entropy injection can be tracked via -

$$\frac{ds}{dt} + 3\mathcal{H}s = -\frac{1}{m_{\rm BH}}\frac{dm_{\rm BH}}{dt}\frac{\rho_{\rm BH}}{T}. \tag{A5}$$

The evolution of axion field a in the early universe can be written as -

$$\ddot{a} + 3\mathcal{H}\dot{a} + \frac{1}{R^2(t)}\nabla^2 a + \frac{\partial V(a,T)}{\partial a} = 0, \tag{A6}$$

where

$$V(a,t) = f_a^2 m_a^2(T)\left(1 - \cos\left(\frac{a}{f_a}\right)\right) \tag{A7}$$

and R denotes the scale factor. The initial axion angle, $\theta = \frac{a}{f_a}$ is frozen in until the oscillation temperature of axion which can be estimated by comparing Hubble expansion rate to the temperature dependent axion mass -

$$\mathcal{H}(T_{\rm osc}) = m_a(T_{\rm osc}). \tag{A8}$$

To get the present contribution of axion to the current energy budget, we solve the above equations following the procedure in the reference [63]. The procedure is to first estimate

the oscillation temperature $T_{\rm osc}$ in presence of PBH. With this, number density of axion at $T_{\rm osc}$ can be calculated following

$$n_a(T_{\rm osc}) = \frac{\rho_a(T_{\rm osc})}{m_a(T_{\rm osc})} = \frac{1}{m_a(T_{\rm osc})}\left(\frac{1}{2}\dot{a}^2 + \frac{1}{2}|\nabla a|^2 + V(a)\right). \tag{A9}$$

Due to entropy dilution, the equation for n_a becomes

$$\frac{1}{n_a}\frac{d(n_a/s)}{dt} = \frac{1}{m_{\rm BH}}\frac{dm_{\rm BH}}{dt}\frac{\rho_{\rm BH}}{Ts^2}. \tag{A10}$$

The above equation is solved from $T \gtrsim T_{\rm osc}$ to a sufficiently small temperature when PBH completely evaporates. Fig. 9 shows the evolution of axions in presence of two different masses of PBH $m_{\rm in} = 5\times10^8$ g and $m_{\rm in} = 5\times10^7$ g. The initial fractional abundance β, initial misalignment angle and axion mass are kept fixed at $10^{-10}, 1$ and 10^{-6} eV respectively. In the left plot, the change is oscillation temperatures is shown. The vertical dashed lines represent the rough estimation of oscillation temperature $\mathcal{H}(\mathcal{T}) = m_a(T)$. Due to larger Hubble expansion rate for blue line than the red line at a particular temperature, the oscillation for the blue line takes place at a later time. In the right plot, we can see the effect of entropy dilution for both the PBH masses. Due to higher PBH mass, the relative final abundance ($Y_a \equiv \frac{n_a}{s}, Y_{\rm osc} \equiv \frac{n_a}{s}|_{\rm osc}$) in the red color line is smaller compared to the blue color line.

[1] C. Abel et al., *Measurement of the Permanent Electric Dipole Moment of the Neutron*, *Phys. Rev. Lett.* **124** (2020), no. 8 081803, [arXiv:2001.11966].

[2] R. D. Peccei and H. R. Quinn, *CP Conservation in the Presence of Instantons*, *Phys. Rev. Lett.* **38** (1977) 1440–1443.

[3] R. D. Peccei and H. R. Quinn, *Constraints Imposed by CP Conservation in the Presence of Instantons*, *Phys. Rev. D* **16** (1977) 1791–1797.

[4] F. Wilczek, *Problem of Strong P and T Invariance in the Presence of Instantons*, *Phys. Rev. Lett.* **40** (1978) 279–282.

[5] S. Weinberg, *A New Light Boson?*, *Phys. Rev. Lett.* **40** (1978) 223–226.

[6] J. Preskill, M. B. Wise, and F. Wilczek, *Cosmology of the Invisible Axion*, *Phys. Lett. B* **120** (1983) 127–132.

[7] L. F. Abbott and P. Sikivie, *A Cosmological Bound on the Invisible Axion*, *Phys. Lett. B* **120** (1983) 133–136.

[8] M. Dine and W. Fischler, *The Not So Harmless Axion*, *Phys. Lett. B* **120** (1983) 137–141.

[9] G. G. Raffelt, *Astrophysical axion bounds*, *Lect. Notes Phys.* **741** (2008) 51–71, [hep-ph/0611350].

[10] M. Dine, W. Fischler, and M. Srednicki, *A Simple Solution to the Strong CP Problem with a Harmless Axion*, *Phys. Lett. B* **104** (1981) 199–202.

[11] A. R. Zhitnitsky, *On Possible Suppression of the Axion Hadron Interactions. (In Russian)*, *Sov. J. Nucl. Phys.* **31** (1980) 260.

[12] J. E. Kim, *Weak Interaction Singlet and Strong CP Invariance*, *Phys. Rev. Lett.* **43** (1979) 103.

[13] M. A. Shifman, A. I. Vainshtein, and V. I. Zakharov, *Can Confinement Ensure Natural CP Invariance of Strong Interactions?*, *Nucl. Phys. B* **166** (1980) 493–506.

[14] M. Kawasaki and K. Nakayama, *Axions: Theory and Cosmological Role*, *Ann. Rev. Nucl. Part. Sci.* **63** (2013) 69–95, [arXiv:1301.1123].

[15] M. Fukugita and T. Yanagida, *Baryogenesis Without Grand Unification*, *Phys. Lett. B* **174** (1986) 45–47.

[16] G. Servant, *Baryogenesis from Strong CP Violation and the QCD Axion*, *Phys. Rev. Lett.* **113** (2014), no. 17 171803, [arXiv:1407.0030].

[17] S. Ipek and T. M. P. Tait, *Early Cosmological Period of QCD Confinement*, *Phys. Rev. Lett.* **122** (2019), no. 11 112001, [arXiv:1811.00559].

[18] D. Croon, J. N. Howard, S. Ipek, and T. M. P. Tait, *QCD baryogenesis*, *Phys. Rev. D* **101** (2020), no. 5 055042, [arXiv:1911.01432].

[19] R. T. Co and K. Harigaya, *Axiogenesis*, *Phys. Rev. Lett.* **124** (2020), no. 11 111602, [arXiv:1910.02080].

[20] G. Ballesteros, J. Redondo, A. Ringwald, and C. Tamarit, *Standard Model—axion—seesaw—Higgs portal inflation. Five problems of particle physics and cosmology solved in one stroke*, *JCAP* **08** (2017) 001, [arXiv:1610.01639].

[21] J. A. Dror, T. Hiramatsu, K. Kohri, H. Murayama, and G. White, *Testing the Seesaw Mechanism and Leptogenesis with Gravitational Waves*, *Phys. Rev. Lett.* **124** (2020), no. 4 041804, [arXiv:1908.03227].

[22] S. Blasi, V. Brdar, and K. Schmitz, *Fingerprint of low-scale leptogenesis in the primordial gravitational-wave spectrum*, *Phys. Rev. Res.* **2** (2020), no. 4 043321, [arXiv:2004.02889].

[23] B. Fornal and B. Shams Es Haghi, *Baryon and Lepton Number Violation from Gravitational Waves*, *Phys. Rev. D* **102** (2020), no. 11 115037, [arXiv:2008.05111].

[24] R. Samanta and S. Datta, *Gravitational wave complementarity and impact of NANOGrav data on gravitational leptogenesis*, *JHEP* **05** (2021) 211, [arXiv:2009.13452].

[25] B. Barman, D. Borah, A. Dasgupta, and A. Ghoshal, *Probing High Scale Dirac Leptogenesis via Gravitational Waves from Domain Walls*, arXiv:2205.03422.

[26] B. Carr, K. Kohri, Y. Sendouda, and J. Yokoyama, *Constraints on primordial black holes*, *Rept. Prog. Phys.* **84** (2021), no. 11 116902, [arXiv:2002.12778].

[27] S. W. Hawking, *Black hole explosions*, *Nature* **248** (1974) 30–31.

[28] S. W. Hawking, *Particle Creation by Black Holes*, *Commun. Math. Phys.* **43** (1975) 199–220. [Erratum: Commun.Math.Phys. 46, 206 (1976)].

[29] T. Papanikolaou, V. Vennin, and D. Langlois, *Gravitational waves from a universe filled with primordial black holes*, *JCAP* **03** (2021) 053, [arXiv:2010.11573].

[30] G. Domènech, C. Lin, and M. Sasaki, *Gravitational wave constraints on the primordial black hole dominated early universe*, *JCAP* **04** (2021) 062, [arXiv:2012.08151]. [Erratum: JCAP 11, E01 (2021)].

[31] G. Domènech, V. Takhistov, and M. Sasaki, *Exploring evaporating primordial black holes with gravitational waves*, *Phys. Lett. B* **823** (2021) 136722, [arXiv:2105.06816].

[32] G. Domènech, *Scalar Induced Gravitational Waves Review*, *Universe* **7** (2021), no. 11 398, [arXiv:2109.01398].

[33] T. Papanikolaou, *Gravitational waves induced from primordial black hole fluctuations: the effect of an extended mass function*, *JCAP* **10** (2022) 089, [arXiv:2207.11041].

[34] P. Gondolo, P. Sandick, and B. Shams Es Haghi, *Effects of primordial black holes on dark matter models*, *Phys. Rev. D* **102** (2020), no. 9 095018, [arXiv:2009.02424].

[35] N. Bernal and O. Zapata, *Dark Matter in the Time of Primordial Black Holes*, *JCAP* **03** (2021) 015, [arXiv:2011.12306].

[36] A. M. Green, *Supersymmetry and primordial black hole abundance constraints*, *Phys. Rev. D* **60** (1999) 063516, [astro-ph/9903484].

[37] M. Y. Khlopov, A. Barrau, and J. Grain, *Gravitino production by primordial black hole evaporation and constraints on the inhomogeneity of the early universe*, *Class. Quant. Grav.* **23** (2006) 1875–1882, [astro-ph/0406621].

[38] D.-C. Dai, K. Freese, and D. Stojkovic, *Constraints on dark matter particles charged under a hidden gauge group from primordial black holes*, *JCAP* **06** (2009) 023, [arXiv:0904.3331].

[39] R. Allahverdi, J. Dent, and J. Osinski, *Nonthermal production of dark matter from primordial black holes*, *Phys. Rev. D* **97** (2018), no. 5 055013, [arXiv:1711.10511].

[40] O. Lennon, J. March-Russell, R. Petrossian-Byrne, and H. Tillim, *Black Hole Genesis of Dark Matter*, *JCAP* **04** (2018) 009, [arXiv:1712.07664].

[41] D. Hooper, G. Krnjaic, and S. D. McDermott, *Dark Radiation and Superheavy Dark Matter from Black Hole Domination*, *JHEP* **08** (2019) 001, [arXiv:1905.01301].

[42] P. Sandick, B. S. Es Haghi, and K. Sinha, *Asymmetric reheating by primordial black holes*, *Phys. Rev. D* **104** (2021), no. 8 083523, [arXiv:2108.08329].

[43] T. Fujita, M. Kawasaki, K. Harigaya, and R. Matsuda, *Baryon asymmetry, dark matter, and density perturbation from primordial black holes*, *Phys. Rev. D* **89** (2014), no. 10 103501, [arXiv:1401.1909].

[44] S. Datta, A. Ghosal, and R. Samanta, *Baryogenesis from ultralight primordial black holes and strong gravitational waves from cosmic strings*, *JCAP* **08** (2021) 021, [arXiv:2012.14981].

[45] S. Jyoti Das, D. Mahanta, and D. Borah, *Low scale leptogenesis and dark matter in the presence of primordial black holes*, arXiv:2104.14496.

[46] B. Barman, D. Borah, S. J. Das, and R. Roshan, *Non-thermal origin of asymmetric dark matter from inflaton and primordial black holes*, *JCAP* **03** (2022), no. 03 031, [arXiv:2111.08034].

[47] B. Barman, D. Borah, S. Das Jyoti, and R. Roshan, *Cogenesis of Baryon Asymmetry and Gravitational Dark Matter from PBH*, arXiv:2204.10339.

[48] B. Barman, D. Borah, S. Jyoti Das, and R. Roshan, *Gravitational wave signatures of a PBH-generated baryon-dark matter coincidence*, *Phys. Rev. D* **107** (2023), no. 9 095002, [arXiv:2212.00052].

[49] A. Cheek, L. Heurtier, Y. F. Perez-Gonzalez, and J. Turner, *Primordial Black Hole Evaporation and Dark Matter Production: I. Solely Hawking radiation*, arXiv:2107.00013.

[50] A. Chaudhuri, B. Coleppa, and K. Loho, *Dark matter production from two evaporating PBH distributions*, *Phys. Rev. D* **108** (2023), no. 3 035040, [arXiv:2301.08588].

[51] D. Borah, S. Jyoti Das, and I. Saha, *Dark matter from phase transition generated PBH*

evaporation with gravitational waves signatures, arXiv:2401.12282.

[52] B. J. Carr, *Some cosmological consequences of primordial black-hole evaporations*, *Astrophys. J.* **206** (1976) 8–25.

[53] D. Baumann, P. J. Steinhardt, and N. Turok, *Primordial Black Hole Baryogenesis*, hep-th/0703250.

[54] A. Hook, *Baryogenesis from Hawking Radiation*, *Phys. Rev. D* **90** (2014), no. 8 083535, [arXiv:1404.0113].

[55] Y. Hamada and S. Iso, *Baryon asymmetry from primordial black holes*, *PTEP* **2017** (2017), no. 3 033B02, [arXiv:1610.02586].

[56] L. Morrison, S. Profumo, and Y. Yu, *Melanopogenesis: Dark Matter of (almost) any Mass and Baryonic Matter from the Evaporation of Primordial Black Holes weighing a Ton (or less)*, *JCAP* **05** (2019) 005, [arXiv:1812.10606].

[57] D. Hooper and G. Krnjaic, *GUT Baryogenesis With Primordial Black Holes*, *Phys. Rev. D* **103** (2021), no. 4 043504, [arXiv:2010.01134].

[58] Y. F. Perez-Gonzalez and J. Turner, *Assessing the tension between a black hole dominated early universe and leptogenesis*, arXiv:2010.03565.

[59] N. Smyth, L. Santos-Olmsted, and S. Profumo, *Gravitational Baryogenesis and Dark Matter from Light Black Holes*, arXiv:2110.14660.

[60] N. Bernal, C. S. Fong, Y. F. Perez-Gonzalez, and J. Turner, *Rescuing High-Scale Leptogenesis using Primordial Black Holes*, arXiv:2203.08823.

[61] A. Ambrosone, R. Calabrese, D. F. G. Fiorillo, G. Miele, and S. Morisi, *Towards baryogenesis via absorption from primordial black holes*, *Phys. Rev. D* **105** (2022), no. 4 045001, [arXiv:2106.11980].

[62] N. Bernal, F. Hajkarim, and Y. Xu, *Axion Dark Matter in the Time of Primordial Black Holes*, *Phys. Rev. D* **104** (2021) 075007, [arXiv:2107.13575].

[63] K. Mazde and L. Visinelli, *The interplay between the dark matter axion and primordial black holes*, *JCAP* **01** (2023) 021, [arXiv:2209.14307].

[64] P. Minkowski, $\mu \to e\gamma$ *at a Rate of One Out of* 10^9 *Muon Decays?*, *Phys. Lett. B* **67** (1977) 421–428.

[65] M. Gell-Mann, P. Ramond, and R. Slansky, *Complex Spinors and Unified Theories*, *Conf. Proc. C* **790927** (1979) 315–321, [arXiv:1306.4669].

[66] R. N. Mohapatra and G. Senjanovic, *Neutrino Mass and Spontaneous Parity Nonconservation*, *Phys. Rev. Lett.* **44** (1980) 912.

[67] T. Yanagida, *Horizontal Symmetry and Masses of Neutrinos*, *Prog. Theor. Phys.* **64** (1980) 1103.

[68] J. Schechter and J. Valle, *Neutrino Masses in SU(2) x U(1) Theories*, *Phys. Rev. D* **22** (1980) 2227.

[69] L. Di Luzio, M. Giannotti, E. Nardi, and L. Visinelli, *The landscape of QCD axion models*, *Phys. Rept.* **870** (2020) 1–117, [arXiv:2003.01100].

[70] I. Masina, *Dark matter and dark radiation from evaporating primordial black holes*, *Eur. Phys. J. Plus* **135** (2020), no. 7 552, [arXiv:2004.04740].

[71] W. Buchmuller, P. Di Bari, and M. Plumacher, *Leptogenesis for pedestrians*, *Annals Phys.* **315** (2005) 305–351, [hep-ph/0401240].

[72] S. Davidson, E. Nardi, and Y. Nir, *Leptogenesis*, *Phys. Rept.* **466** (2008) 105–177, [arXiv:0802.2962].

[73] D. Borah, S. Jyoti Das, R. Samanta, and F. R. Urban, *PBH-infused seesaw origin of matter and unique gravitational waves*, *JHEP* **03** (2023) 127, [arXiv:2211.15726].

[74] A. Pilaftsis and T. E. J. Underwood, *Resonant leptogenesis*, *Nucl. Phys. B* **692** (2004) 303–345, [hep-ph/0309342].

[75] P. S. B. Dev, M. Garny, J. Klaric, P. Millington, and D. Teresi, *Resonant enhancement in leptogenesis*, *Int. J. Mod. Phys.* **A33** (2018) 1842003, [arXiv:1711.02863].

[76] K. Abazajian et al., *CMB-S4 Science Case, Reference Design, and Project Plan*, arXiv:1907.04473.

[77] **IAXO** Collaboration, E. Armengaud et al., *Physics potential of the International Axion Observatory (IAXO)*, *JCAP* **06** (2019) 047, [arXiv:1904.09155].

[78] **TASTE** Collaboration, V. Anastassopoulos et al., *Towards a medium-scale axion helioscope and haloscope*, *JINST* **12** (2017), no. 11 P11019, [arXiv:1706.09378].

[79] R. T. Co, L. J. Hall, and K. Harigaya, *QCD Axion Dark Matter with a Small Decay Constant*, *Phys. Rev. Lett.* **120** (2018), no. 21 211602, [arXiv:1711.10486].

[80] R. T. Co, L. J. Hall, K. Harigaya, K. A. Olive, and S. Verner, *Axion Kinetic Misalignment and Parametric Resonance from Inflation*, *JCAP* **08** (2020) 036, [arXiv:2004.00629].

[81] S. Ramazanov and R. Samanta, *Heating up Peccei-Quinn scale*, *JCAP* **05** (2023) 048,

[arXiv:2210.08407].

[82] S. Dodelson and L. M. Widrow, *Sterile-neutrinos as dark matter*, *Phys. Rev. Lett.* **72** (1994) 17–20, [hep-ph/9303287].

[83] M. Drewes et al., *A White Paper on keV Sterile Neutrino Dark Matter*, *JCAP* **01** (2017) 025, [arXiv:1602.04816].

[84] D. K. Ghosh, A. Ghoshal, and S. Jeesun, *Axion-like particle (ALP) portal freeze-in dark matter confronting ALP search experiments*, *JHEP* **01** (2024) 026, [arXiv:2305.09188].

[85] A. Bharucha, F. Brümmer, N. Desai, and S. Mutzel, *Axion-like particles as mediators for dark matter: beyond freeze-out*, *JHEP* **02** (2023) 141, [arXiv:2209.03932].

[86] P. J. Fitzpatrick, Y. Hochberg, E. Kuflik, R. Ovadia, and Y. Soreq, *Dark matter through the axion-gluon portal*, *Phys. Rev. D* **108** (2023), no. 7 075003, [arXiv:2306.03128].

[87] D. Borah, S. Jyoti Das, and A. K. Saha, *Cosmic inflation in minimal $U(1)_{B-L}$ model: implications for (non) thermal dark matter and leptogenesis*, *Eur. Phys. J. C* **81** (2021), no. 2 169, [arXiv:2005.11328].

[88] A. Datta, R. Roshan, and A. Sil, *Imprint of the Seesaw Mechanism on Feebly Interacting Dark Matter and the Baryon Asymmetry*, *Phys. Rev. Lett.* **127** (2021), no. 23 231801, [arXiv:2104.02030].

[89] K. Griest and M. Kamionkowski, *Unitarity Limits on the Mass and Radius of Dark Matter Particles*, *Phys. Rev. Lett.* **64** (1990) 615.

[90] G. F. Giudice, E. W. Kolb, and A. Riotto, *Largest temperature of the radiation era and its cosmological implications*, *Phys. Rev. D* **64** (2001) 023508, [hep-ph/0005123].

[91] **LIGO Scientific** Collaboration, J. Aasi et al., *Advanced LIGO*, *Class. Quant. Grav.* **32** (2015) 074001, [arXiv:1411.4547].

[92] **LISA** Collaboration, P. Amaro-Seoane et al, *Laser Interferometer Space Antenna*, *arXiv e-prints* (Feb., 2017) arXiv:1702.00786, [arXiv:1702.00786].

[93] S. Kawamura et al., *The Japanese space gravitational wave antenna DECIGO*, *Class. Quant. Grav.* **23** (2006) S125–S132.

[94] **LIGO Scientific** Collaboration, B. P. Abbott et al., *Exploring the Sensitivity of Next Generation Gravitational Wave Detectors*, *Class. Quant. Grav.* **34** (2017), no. 4 044001, [arXiv:1607.08697].

[95] J. Baeza-Ballesteros, E. J. Copeland, D. G. Figueroa, and J. Lizarraga, *Gravitational Wave*

Emission from a Cosmic String Loop, I: Global Case, arXiv:2308.08456.

[96] M. Gorghetto, E. Hardy, and H. Nicolaescu, *Observing invisible axions with gravitational waves*, *JCAP* **06** (2021) 034, [arXiv:2101.11007].

[97] A. Vilenkin, Y. Levin, and A. Gruzinov, *Cosmic strings and primordial black holes*, *JCAP* **11** (2018) 008, [arXiv:1808.00670].

[98] M. Srednicki, *Axion Couplings to Matter. 1. CP Conserving Parts*, *Nucl. Phys. B* **260** (1985) 689–700.

[99] **CAST** Collaboration, S. Andriamonje et al., *An Improved limit on the axion-photon coupling from the CAST experiment*, *JCAP* **04** (2007) 010, [hep-ex/0702006].

[100] **CAST** Collaboration, V. Anastassopoulos et al., *New CAST Limit on the Axion-Photon Interaction*, *Nature Phys.* **13** (2017) 584–590, [arXiv:1705.02290].

[101] M. S. Turner, *Axions from sn1987a*, *Phys. Rev. Lett.* **60** (May, 1988) 1797–1800.

[102] A. Burrows, M. S. Turner, and R. P. Brinkmann, *Axions and sn 1987a*, *Phys. Rev. D* **39** (Feb, 1989) 1020–1028.

[103] G. Raffelt and D. Seckel, *Bounds on exotic-particle interactions from sn1987a*, *Phys. Rev. Lett.* **60** (May, 1988) 1793–1796.

[104] **Fermi-LAT** Collaboration, M. Ajello et al., *Search for Spectral Irregularities due to Photon–Axionlike-Particle Oscillations with the Fermi Large Area Telescope*, *Phys. Rev. Lett.* **116** (2016), no. 16 161101, [arXiv:1603.06978].

[105] **ADMX** Collaboration, L. D. Duffy, P. Sikivie, D. B. Tanner, S. J. Asztalos, C. Hagmann, D. Kinion, L. J. Rosenberg, K. van Bibber, D. B. Yu, and R. F. Bradley, *A high resolution search for dark-matter axions*, *Phys. Rev. D* **74** (2006) 012006, [astro-ph/0603108].

[106] I. Stern, *ADMX Status*, *PoS* **ICHEP2016** (2016) 198, [arXiv:1612.08296].

[107] **ADMX** Collaboration, T. Braine et al., *Extended Search for the Invisible Axion with the Axion Dark Matter Experiment*, *Phys. Rev. Lett.* **124** (2020), no. 10 101303, [arXiv:1910.08638].

[108] D. Budker, P. W. Graham, M. Ledbetter, S. Rajendran, and A. Sushkov, *Proposal for a Cosmic Axion Spin Precession Experiment (CASPEr)*, *Phys. Rev. X* **4** (2014), no. 2 021030, [arXiv:1306.6089].

[109] D. Alesini, D. Babusci, D. Di Gioacchino, C. Gatti, G. Lamanna, and C. Ligi, *The KLASH Proposal*, arXiv:1707.06010.

[110] D. Alesini et al., *KLASH Conceptual Design Report*, arXiv:1911.02427.

[111] Y. Kahn, B. R. Safdi, and J. Thaler, *Broadband and Resonant Approaches to Axion Dark Matter Detection*, *Phys. Rev. Lett.* **117** (2016), no. 14 141801, [arXiv:1602.01086].

[112] J. L. Ouellet et al., *First Results from ABRACADABRA-10 cm: A Search for Sub-μeV Axion Dark Matter*, *Phys. Rev. Lett.* **122** (2019), no. 12 121802, [arXiv:1810.12257].

[113] S. Lee, S. Ahn, J. Choi, B. R. Ko, and Y. K. Semertzidis, *Axion Dark Matter Search around 6.7 μeV*, *Phys. Rev. Lett.* **124** (2020), no. 10 101802, [arXiv:2001.05102].

[114] Y. K. Semertzidis et al., *Axion Dark Matter Research with IBS/CAPP*, arXiv:1910.11591.

[115] **MADMAX Working Group** Collaboration, A. Caldwell, G. Dvali, B. Majorovits, A. Millar, G. Raffelt, J. Redondo, O. Reimann, F. Simon, and F. Steffen, *Dielectric Haloscopes: A New Way to Detect Axion Dark Matter*, *Phys. Rev. Lett.* **118** (2017), no. 9 091801, [arXiv:1611.05865].

[116] J. K. Vogel et al., *IAXO - The International Axion Observatory*, in *8th Patras Workshop on Axions, WIMPs and WISPs*, 2, 2013. arXiv:1302.3273.

[117] M. Meyer, M. Giannotti, A. Mirizzi, J. Conrad, and M. A. Sánchez-Conde, *Fermi Large Area Telescope as a Galactic Supernovae Axionscope*, *Phys. Rev. Lett.* **118** (2017), no. 1 011103, [arXiv:1609.02350].

[118] V. Cardoso, O. J. C. Dias, G. S. Hartnett, M. Middleton, P. Pani, and J. E. Santos, *Constraining the mass of dark photons and axion-like particles through black-hole superradiance*, *JCAP* **03** (2018) 043, [arXiv:1801.01420].



MAX-PLANCK-MEDAILLE

Expedition to the Zeptouniverse

Flavour experiments promise insights into energy scales as high as 200 TeV and distances as small as 10^{-21} meter and offer the chance to identify New Physics.

Andrzej J. Buras

The Large Hadron Collider (LHC) at CERN will directly probe distance scales as short as 10^{-19} m, corresponding to energy scales at the level of a few TeV. Presently, higher resolution can only be achieved with the help of quantum fluctuations caused by new particles and new forces that act at very short distance scales and modify the predictions of the Standard Model of particle physics for very rare processes. In this context, weak decays of mesons and leptons play the prominent role besides the transitions between particles and antiparticles in which flavours of quarks and leptons are changed. In this manner, information about the Zeptouniverse corresponding to energy scales as high as 200 TeV or distances as small as 10^{-21} m can be obtained.

The year 1676 was very important for humanity, because Antoni van Leeuwenhoek discovered the empire of bacteria. He called these small creatures *animalcula* (small animals). His discovery was a milestone in our civilization for at least two reasons: He discovered creatures invisible to us which have been killing humans for thousands of years, often responsible for millions of deaths in one year. While Antoni van Leeuwenhoek did not know that bacteria could be dangerous for humans, his followers like Louis Pasteur, Robert Koch and other „microbe hunters" realized the danger coming from these tiny creatures and also developed weapons against this empire [1].

Van Leeuwenhoek was the first human who looked at short distance scales invisible to us and discovered thereby

© 2020 Wiley-VCH GmbH

a new underground world. At that time, researchers looked mainly at large distances, discovering new planets and finding laws, such as the Kepler laws which Isaac Newton was able to derive from his mechanics.

While van Leeuwenhoek could reach a resolution of roughly 10^{-6} m, this could be improved by twelve orders of magnitude over the last 344 years. On the way down to shortest distance scales, scientists discovered the nanouniverse (10^{-9} m), the femtouniverse (10^{-15} m) relevant for nuclear particle physics and low-energy elementary particle physics and finally the attouniverse (10^{-18} m) which is the territory of contemporary high-energy elementary-particle physics.

Using this overture, I have opened my lecture at the 50th Cracow School of Theoretical Physics held in Zakopane, Poland, in June 2010. At that time, it was strongly believed that the LHC in addition to discovering the only then missing particle of the Standard Model, the Higgs boson, would discover a plethora of new particles, in particular supersymmetric particles or those related to the existence of large extra dimensions like Kaluza-Klein gluons. The Higgs boson was indeed discovered two years later at CERN. But even tremendous efforts of experimentalists and theorists to find New Physics beyond the Standard Model did not result in the discovery of any new particles at the LHC. Thereby, as of August 2020, shifting the masses of supersymmetric particles and Kaluza-Klein gluons significantly above the 1 TeV scale.[1)]

Yet, we know that new particles and new forces beyond those present in the Standard Model must exist. The most convincing arguments are based on the following questions, none of which can be answered within the Standard Model:

- What is the dark matter that occupies 27 percent of our universe?
- Why is our universe dominated by matter? This is clearly required for our existence, but the size of the violation of CP symmetry required for the dominance of matter over antimatter soon after the Big Bang is much larger than the one found within the Standard Model.
- Why is the neutron heavier than the proton? This question is significant for our existence.
- What is the origin of neutrino masses and why are they by nine orders of magnitude smaller than the proton mass?
- Why is the mass of the heaviest quark, the top quark, by five orders of magnitude larger than the mass of the lightest quark, the up quark?

It is not the goal of this article to address these questions. Rather, being motivated by them and knowing that New Physics must exist at scales much shorter than explored by now, I would like to concentrate on the following questions:

- Can quantum fluctuations help us with getting some insight into the dynamics at very short distance scales. Could they answer some of these questions, if no direct clear signal of New Physics will be seen at the LHC, i.e., no new particles with masses below 6 TeV will be discovered?
- Can we reach the Zeptouniverse, i.e., a resolution as high as 10^{-21} m or energies as large as 200 TeV, by means of quark flavour physics and lepton flavour violating processes in this decade well before this will be possible by means of any collider built in this century?

The photo opening this paper was chosen to illustrate that I am much more optimistic about the future of particle physics than Christoph Wetterich, the winner of Gentner-Kastler-Prize 2019 [2]. Christoph is an esteemed colleague of mine but, in my view, his vision of a desert between the LHC scales and the Planck scale cannot be correct and will be disproved in this decade precisely by flavour physics. In the landscape, photographed by my son Allan during one of his expeditions to the far north, first the Standard Model (our Base Camp) is placed and the energy gap which we are already crossing with the help of the renormalization group equations of the so-called Standard Model Effective Field Theory (SMEFT). However, in order to reach New Physics summits in the far distance, we have to cross the crevasses representing very difficult experiments and difficult theoretical calculations. To this end, we will need brilliant ideas which will guide us through these crevasses so that one day we will reach the summits that will help us to answer at least some of the questions listed above.

After a brief review of the particle content of the Standard Model and of the properties of strong and electroweak interactions described by it, I will present a number of strategies which, with the help of quantum fluctuations, should indeed allow us to get a view of the Zeptouniverse before the advent of future colliders. Subsequently, we will have a brief look at the most interesting anomalies, the departures of the experimental findings from Standard Model expectations. They can be considered as footprints of new particles and new interactions that appear to be beyond the reach of the LHC, although one should not give up the hope that some hints for them will be seen in the next LHC run.

It should be mentioned that this indirect search for new phenomena is by no means new. A classical analogy is the

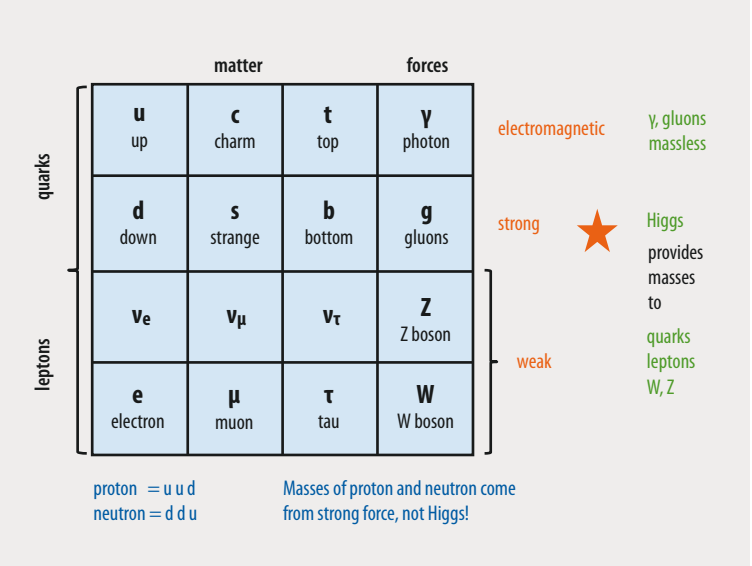


Fig. 1 The particle content of the Standard Model

1) Of course, one cannot exclude the existence of very light particles, like axions, that being very weakly coupled to standard matter could not be detected until now.

© 2020 Wiley-VCH GmbH

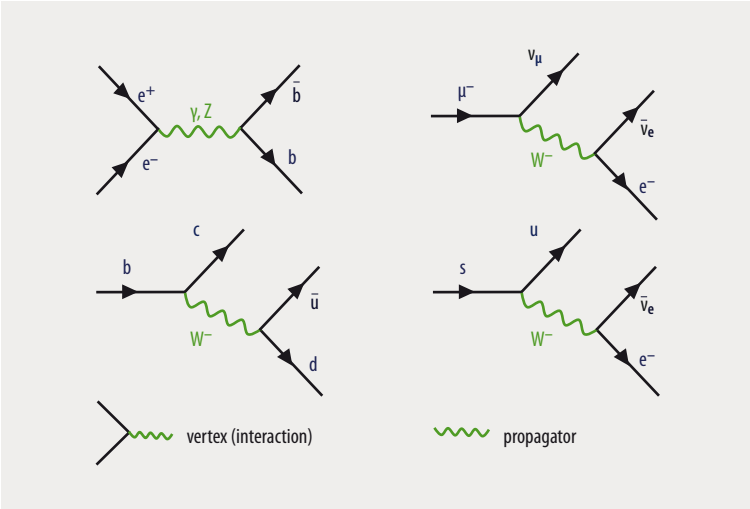


Fig. 2 The world of Feynman Diagrams: more complicated diagrams can be constructed and probabilities for a given process evaluated.

prediction of the existence of the planet Neptune in 1846 by Urbain Le Verrier based on an anomaly in the orbit of the Uranus. Neptune's existence was soon after confirmed by the German astronomer Johann Gottfried Galle. The gauge bosons $W^{\pm}$ and Z^0 were seen indirectly in lower-energy experiments well before their discovery in 1983 at CERN. The presence of the $W^{\pm}$ bosons was actually felt already in the 1930s in the context of the Fermi theory of β-decays even if only in the 1960s theorists realized what are the elementary particles mediating these decays. Z boson was seen first in 1973 through the discovery of neutral currents at CERN – ten years before this boson was discovered also at CERN.

Express Review of the Standard Model

In the Standard Model matter consists of four fermion families (**Fig. 1**): up quark (u,c,t), down quark (d,s,b), neutrino (ν_e,ν_μ,ν_τ) and electron (e,μ,τ). They correspond to the four rows in the table. Particles in a given family have the same quantum numbers, in particular similar electric charges: 2/3, –1/3, 0 and –1, respectively. Their antiparticles have opposite electric charges. The members of a given family can only be distinguished by their masses which increase in the table from left to right. The columns in this table correspond to three generations of these elementary particles and the different names of quarks and leptons are called flavours: six quark flavours and six lepton flavours.

The interactions between the matter fields are mediated by gauge bosons with spin 1. For strong interactions (Quantum Chromodynamics, QCD), these are the electrically neutral massless gluons (G^a). For the electroweak interactions (Quantum Flavourdynamics) these are the electrically neutral massless photon (γ), the electrically neutral heavy Z boson and finally the charged heavy $W^{\pm}$. The masses of all these particles, according to the Standard Model, are generated through their interactions with an electrically neutral scalar particle (Spin 0), the Higgs boson.

The strong and electroweak interactions have a number of properties encoded in the Lagrangian of the Standard Model that can be found in any textbook on particle physics. The following four properties of these interactions (**Fig. 2**) will be relevant for us:

- By themselves, neutral gauge bosons (G^a,γ,Z) and the Higgs boson cannot transfer a fermion with one flavour into another fermion with a different flavour. There are simply no vertices in any Feynman diagram that involve any of these bosons and two fermions (quarks or leptons) with different flavours. For instance, a vertex with Z boson, b quark and a s quark does not exist. This is assured by the so-called Glashow-Iliopoulos-Maiani (GIM) mechanism. Needless to say, Standard Model gauge bosons cannot transfer a lepton into a quark or vice versa. This is already evident from charge conservation. The interactions mediated by these bosons also conserve parity (P), charge conjugation (C) and CP-parity. The charged gauge bosons $W^{\pm}$ change flavour and violate maximally parity and charge conjugation implying that only left-handed quarks and left-handed leptons take part in the charged current weak interactions. These interactions are parametrized in the case of quarks by the unitary Cabibbo-Kobayashi-Maskawa (CKM) matrix which depends on three real parameters (the so-called mixing angles) and one complex phase responsible for CP-violation in the Standard Model. In the case of leptons, $W^{\pm}$ interactions are parametrized by the unitary Pontecorvo-Maki-Nakagawa-Sakata (PMNS) matrix which can have two additional phases relative to the CKM matrix, the so-called Majorana phases, related to special properties of neutrinos, the only neutral fermions we know.
- The gauge interactions mediated by neutral G^a, Z and γ are universal in a given family. In particular the interactions of Z with e, μ and τ are the same.
- While electroweak interactions are weak and can be calculated within perturbation theory, the strong interactions are strong at scales below 1 GeV in order to bind quarks inside hadrons like mesons, the proton and the neutron. At these scales, only non-perturbative methods are useful. These are in particular the numerical Lattice QCD and analytical methods like Dual QCD and Chiral Perturbation Theory. For scales above 1 GeV, strong interactions are sufficiently weak due to the property of asymptotic freedom in QCD, so that their effect can be calculated within perturbation theory. Yet, in the presence of vastly different energy scales, like the hadronic scale $\mathcal{O}$(1 GeV), the electroweak scale (246 GeV) and New Physics scales often well above 1 TeV, the appearance of large logarithms of the ratios of these scales multiplying the gauge couplings requires their summation to all order of perturbation theory. To this end, very efficient renormalization group methods, known also in the field of phase transitions, are used. They are discussed in much more detail in my recent book [3].

We have seen that, within the Standard Model, neutral gauge bosons are not able to change flavour by themselves. However, one can construct complicated Feynman diagrams (loop diagrams) involving these bosons together with $W^{\pm}$ that do change flavour. One example of such a diagram is called penguin diagram (**Fig. 3**). But such loop diagrams can have a different shape like the so-called box diagrams, in which the neutral gauge boson is replaced by the pair W^{+}

© 2020 Wiley-VCH GmbH

and W^- that has zero charge. Processes of this type are called Flavour Changing Neutral Current (FCNC) processes and are very important for our discussion. Prominent examples are the decays $B_s^0 \to \mu^+\mu^-$, $K^+ \to \pi^+\nu\bar{\nu}$ and particle-antiparticle transitions like $(B_{s,d}^0 - \bar{B}_{s,d}^0)$ mixings.

According to the usual Feynman-diagram calculus, the probability for a given process to occur is proportional to the product of couplings present in the vertices of the diagrams governing this process. Involving several weak couplings and often small elements of the CKM matrix present in the vertices in one-loop diagrams, FCNC processes are strongly suppressed within the Standard Model. This suppression is partly lifted if the top-quark is present inside the loop and the contributions of such diagrams grow quadratically with the top-quark mass. This is only the case with the decays of K and B mesons but not for the D mesons and leptons, so that most interesting measurements of FCNCs to date come from weak decays of K and B mesons, $(B_{s,d}^0 - \bar{B}_{s,d}^0)$ mixings and $(K^0 - \bar{K}^0)$ mixing. But as these processes are very strongly suppressed in the Standard Model, they are more powerful in the search for New Physics than processes that are possible within the Standard Model through the exchange of a simple $W^\pm$ (**Fig. 2**). In this way, the Standard Model contributions represent a significant background in the search for New Physics.

On the other hand, and beyond the Standard Model, the GIM mechanism is often absent and FCNC processes can be governed by simpler diagrams involving new heavy particles. For example, a very heavy neutral gauge boson Z' contributes to $(B_{s,d}^0 - \bar{B}_{s,d}^0)$ mixing (**Fig. 4**). Although its propagator $(1/M_{Z'}^2)$ strongly suppresses this contribution, the absence of several weak couplings relatively to one-loop diagrams partly lifts this suppression. Consequently, such contributions can be relevant and play often significant roles in finding new phenomena as we will explain now. Quantum fluctuations involving new particles can also generate flavour changing vertices in which Z bosons changes an s or d quark into the b quark (**Fig. 4**).

The Technology to Reach the Zeptouniverse

Main players in indirect searches for New Physics are presently the mesons, quark-antiquark bound states

$$B_d^0 = (\bar{b}d),\ B_s^0 = (\bar{b}s),\ B^+ = (\bar{b}u),\ K^+ = (\bar{s}u),\ K_L = (\bar{s}d),\ \pi^+ = (\bar{d}u),$$

but also leptons and mesons with charm quark will surely play important roles in the search for New Physics in this decade. In order to reach high resolution at short distance scales, one has to produce many of these mesons in high energy collisions. They subsequently decay into lighter particles. The goal of experimentalists is then to measure very accurately the probability with which a given meson decays into a particular final state such as $\mu^+\mu^-$, $\pi^+\nu\bar{\nu}$, $\pi^+\pi^-$ among many possible final states. These probabilities, normalized to unity (100 percent), are called branching ratios.

The goal of theorists is to calculate these with high precision within the Standard Model and compare them with the experimentally measured branching ratios. Any difference between the experimental branching ratio and the one predicted by the Standard Model is a hint at the existence of new particles that are often too massive to be produced at the LHC. But through quantum fluctuations represented by propagators in Feynman diagrams they can affect various branching ratios so that the latter can differ from the ones predicted in the Standard Model.

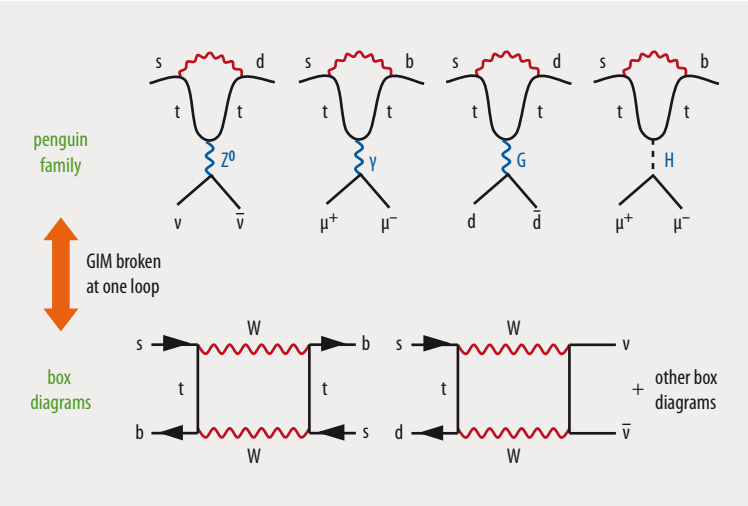


Fig. 3 Penguin diagrams and box diagrams

To identify new particles in this indirect manner, it is crucial to test many different branching ratios for the meson decays listed above. The Particle Data Group (PDG) collects the experimental values of these branching ratios and this collection amounts to thousands of different numbers. In the case of lepton decays, only upper limits on the branching ratios are known, because to date, no FCNC process in the lepton sector has been observed experimentally. Yet, they must exist at a certain level because of non-vanishing neutrino masses. However, these masses are tiny, and in the Standard Model, such processes are predicted to have very small branching ratios like $\mu \to e\gamma$ in the ballpark of 10^{-54}. Any observation of such decays would be a clear signal of New Physics.

As far as flavour expedition to the Zeptouniverse is concerned, only a fraction of the branching ratios collected by the PDG is of interest to us. These are the ones which are predicted to be very small in the Standard Model, because

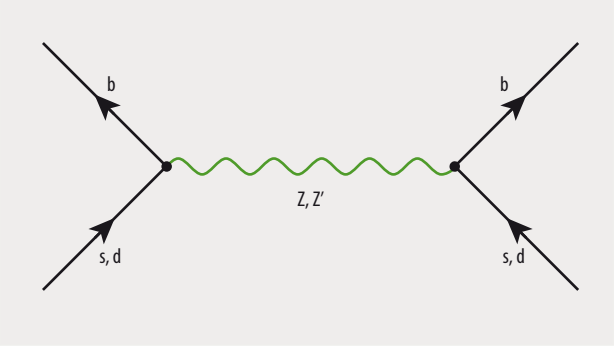


Fig. 4 This Feynman diagram shows a FCNC process mediated by a heavy neutral gauge boson Z' and/or Z.

© 2020 Wiley-VCH GmbH

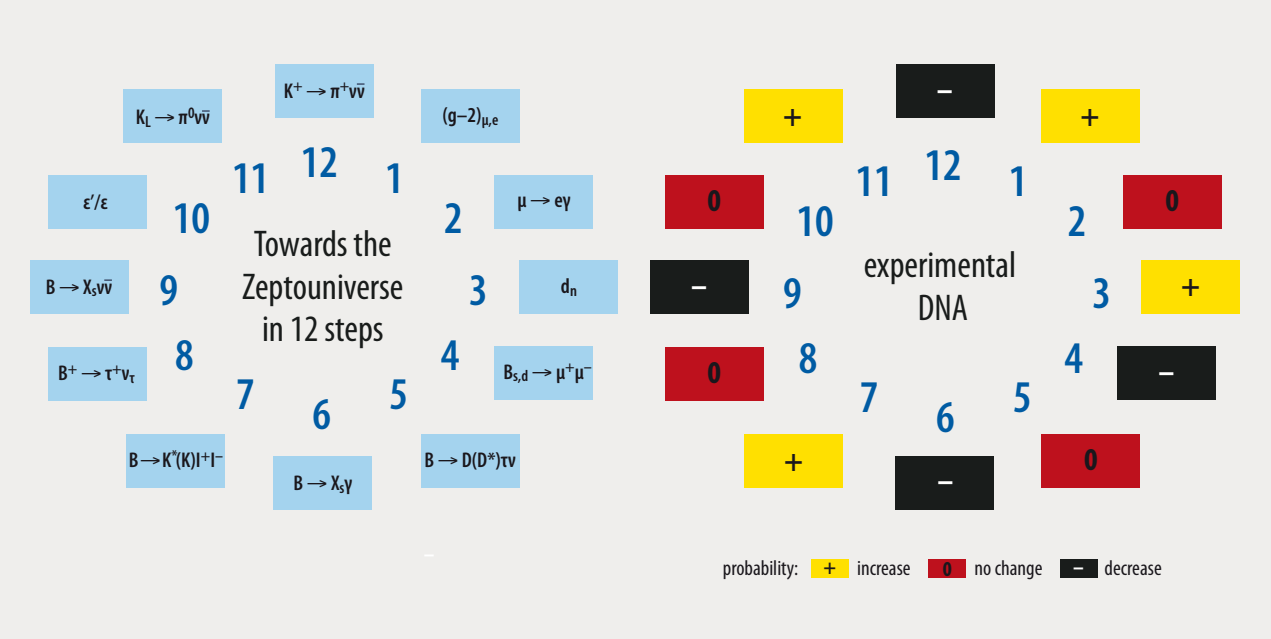


Fig. 5 General Structure of DNA: considered processes (left) and experimental DNA (right).

then the background from the Standard Model does not prevent seeing new phenomena. Very small does not mean 0.01 or 0.001 but often 10^{-6}, 10^{-9} and even 10^{-11} in the case of meson decays. For leptons, such branching ratios are even smaller as already stated above. For instance, the present experimental upper bound on the branching ratio of $\mu \to e\gamma$ amounts to 10^{-13} and it is amazing that experimentalists can measure such tiny values.

Let us assume that one day we will have hundreds of very precise measurements of various branching ratios for decays of mesons and leptons and very precise Standard Model predictions for them. This will allow us to construct a series of differences between experimental and theoretical branching ratios calculated in the Standard Model. These differences will be generally positive, negative or consistent with zero. A positive difference means that there is a New Physics contribution enhancing the branching ratio, while a negative one signals New Physics which suppresses the branching ratio relative to the one predicted by the Standard Model. An example is given in **Fig. 5** where a selected number of processes is shown compared to the coding for differences between Standard Model predictions and experimental data found in the possible future.

These twelve examples are representatives of the hundreds of branching ratios at our disposal one day, among them many that will correspond to yellow or black

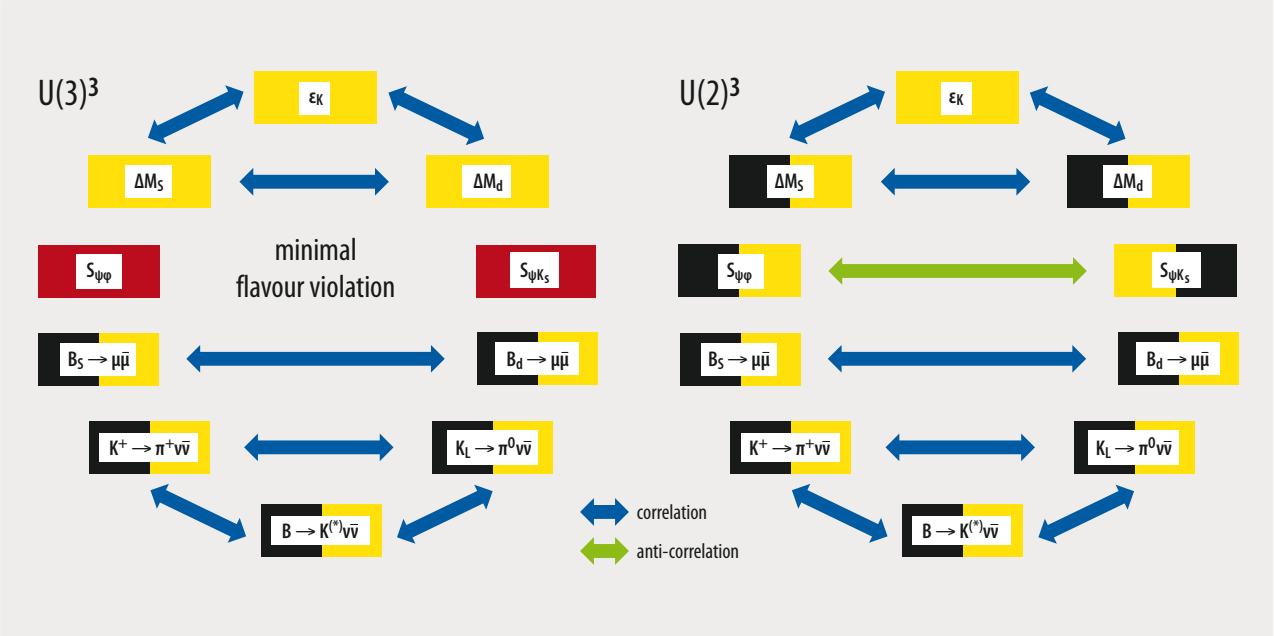


Fig. 6 DNA-chart of Minimal Flavour Violation models and DNA-chart of $U(2)^3$ models

© 2020 Wiley-VCH GmbH

colours thereby indicating the presence of New Physics. This is similar to having a DNA of a criminal, represented here by New Physics, and our goal is to identify him or her in the most efficient manner. Of course, there are many criminals behind these numbers, in general complicating this search.

Without any theoretical input, this goal cannot be realized. In addition to finding these new particles, we would obviously like to know their interactions which could again be mediated by gluons, photons and a Z boson. But generally new Feynman diagrams will include additional gauge bosons, new fermions and scalars that is brothers and sisters of Standard Model particles which could be both electrically neutral or charged. One restriction comes from the observation that for energy scales much larger than the scale of spontaneous breakdown of the Standard Model gauge symmetry $SU(3)_C \times SU(2)_L \times U(1)_Y$, this symmetry must be exact which reduces the number of possible theories. Yet, without additional dynamical assumptions, the New Physics contributions in full generality turn out to depend on 1350 real parameters and 1149 complex phases. This number becomes smaller if one considers a specific class of processes, but still it is not possible to determine all these parameters in low-energy experiments without some specific simplifying assumptions about the structure of New Physics. This fact is fortunately key to reduce the number of possibilities for physics beyond the Standard Model.

In my view the most efficient strategy in this context is to consider many concrete New Physics models or some simplified versions of them and calculate within each of them as many observables as possible. Most of my younger colleagues would then just put these results into a computer code to calculate χ^2 or a p number for each model. Others would present multi-dimensional plots in the space of the parameters of the model to identify the range of parameters that is ruled out by experiment, often leaving small oases where a given model can still survive. These are valid procedures, but in my view not sufficiently transparent as far as the nature of the New Physics we are searching for is concerned. In my view, it is better to first construct for each model its DNA consisting of +, 0 and – as explained above , and then compare it to the DNA of the criminal(s) determined by experiment as given in **Fig. 5**.

However, it is rare for a given observable in a given theory to be uniquely suppressed or enhanced relative to the Standard Model. Frequently, two observables are correlated or uncorrelated with each other. Thus, the enhancement of one observable implies uniquely an enhancement (correlation) or suppression (anticorrelation) of another observable. Among further possibilities, it can also happen that a change in the value of a given observable implies no change in another observable. After adjusting the parameters of a given theory in order to reproduce the enhancement of a given branching ratio, this theory predicts also enhanced or suppressed values for other observables and sometimes there is no effect of New Physics on some other branching ratios.

Applying then the information from a given theory requires sometimes further significant theoretical work. The strategy, developed in collaboration with Jennifer Girrbach-Noe [4], is to connect a given pair of branching ratios that are correlated or anticorrelated with each other by a line in a DNA-chart. The absence of a line means that two given observables are uncorrelated.

This strategy is illustrated with four simplified models discussed in detail in [3, 4]. In the left part of **Fig. 6**, we show the DNA-chart of the so-called Minimal Flavour Violation New Physics scenario which is based on the flavour symmetry $U(3)^3$. It is the minimal extension of the Standard Model. The right part of this figure shows the DNA of models with reduced flavour symmetry $U(2)^3$. **Fig. 7** shows two theories with a heavy neutral Z', which only interacts with

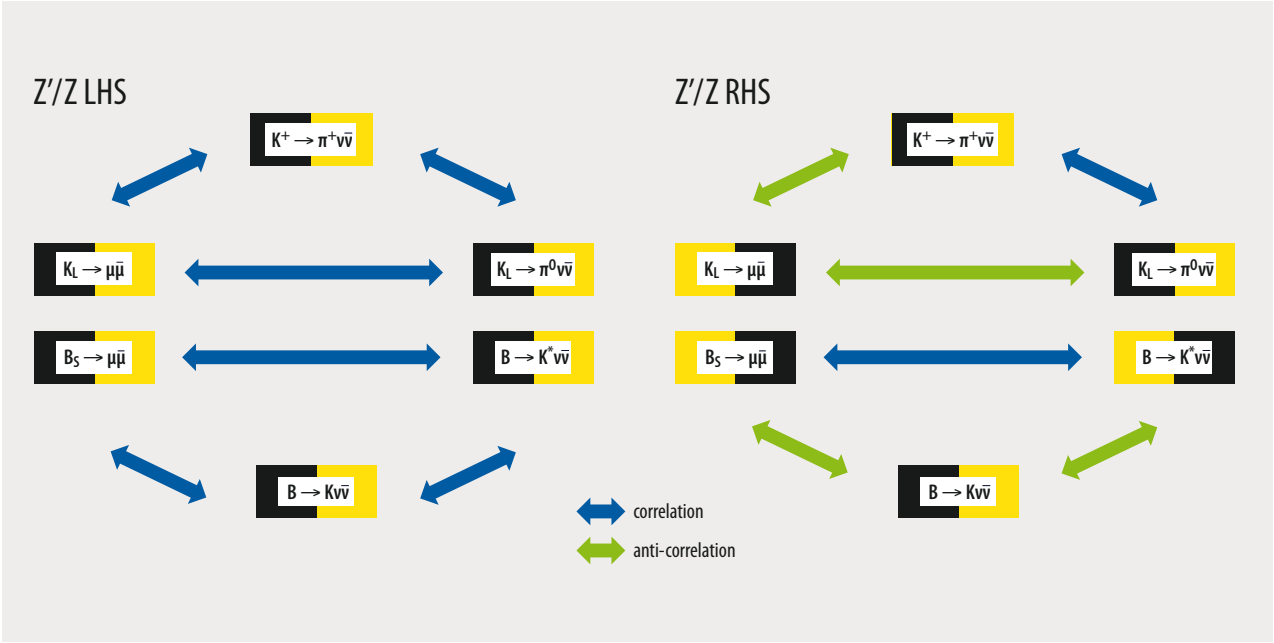


Fig. 7 DNA-charts of Z' models with LH and RH currents

© 2020 Wiley-VCH GmbH

left-handed and right-handed quarks, respectively. This two charts can also represent the Standard Model Z boson, which acquired flavour-changing interactions through New Physics. It should be noted that all four charts differ from each other. As soon as experiments favour one model, one can begin to investigate it in more detail within the chosen theory, calculating χ^2 and p-numbers. If neither is favoured by nature, new DNAs for other theories have to be constructed.

Anomalies

During the last ten years a number of deviations from Standard Model predictions have been measured by experimentalists. The most popular ones are presently the so-called B-physics anomalies observed in the BaBar, LHCb, CMS, ATLAS, and Belle experiments. The observed data imply that the lepton flavour universality breaks down, i.e., the branching ratios for rare decays of B mesons with muons and electrons in the final state differ from each other by 2 to 3 standard deviations. A similar phenomenon is observed when a B meson decays into muons compared with decays into τ leptons. The prime criminals behind such phenomena are leptoquarks, heavy bosons with spin 0 or 1 changing quarks into leptons or vice versa. In the case of the violation of the $\mu - e$ universality, a heavy gauge boson Z' could be responsible for this anomaly as well. Yet, we still have to wait for more precise data and in some cases for more precise calculations to be confident that these effects are indeed more than statistical fluctuations.

Another anomaly found already twenty years ago at the Brookhaven National Laboratory is the deviation of the anomalous magnetic moment of the muon, $(g-2)_\mu$, from its rather precise Standard Model value. A new experiment at FNAL and an independent experiment at J-PARC in Japan should clarify whether new physics is hidden in this finding. Again, leptoquarks could be responsible for this anomaly.

The study of the violation of CP symmetry in $K \to \pi\pi$ decays represented by the so-called ratio ϵ'/ϵ is also of considerable importance. Unfortunately, the calculation of this ratio is subject to large non-perturbative uncertainties. Presently, we do not know whether new phases beyond the CKM phase are necessary to explain the existing data from NA48 at CERN and KTeV at Fermilab, known to us already for twenty years. Such new phases, if required, could in principle explain the dominance of the matter over the antimatter in the universe. If that is the case the criminals among other possibilities could be a heavy Z' and heavy vector-like quarks in which left and right components transform identically under $SU(2)_L$. Leptoquarks turn out to be less useful in this case: Even the explanation of a moderate ϵ'/ϵ anomaly would imply very large branching ratios for rare Kaon decays, which are experimentally excluded. This result highlights the importance of correlations between various processes. Such correlations should be very powerful when the rare decays $K^+ \to \pi^+ \nu\bar{\nu}$ and $K_L \to \pi^0 \nu\bar{\nu}$ will be accurately measured by the NA62 experiment at CERN and by the KOTO experiment in Japan, respectively. In addition, the CLEVER experiment at CERN should contribute in the future to the study of $K_L \to \pi^0 \nu\bar{\nu}$.

Conclusions

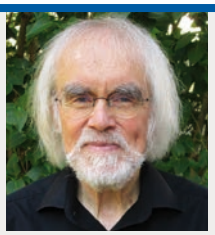
Detailed studies of the ability of flavour physics to provide information about new physics beyond 100 TeV have been performed in [5, 6]. They show that the particle-antiparticle mixings are most efficient to reach these scales [5], but a detailed picture of the Zeptouniverse can only be obtained through the study of rare K and $B_{s,d}$ decays [6] and lepton flavour violating decays like $\mu \to e\gamma$ and $\mu^- \to e^- e^+ e^-$ [7]. Additionally, electric dipole moments of the neutron and of various atoms are very important in the search for new phenomena [8].

There is no question that flavour physics has a great future through experiments in Europe, Japan and USA. I am looking forward to the year 2030, when hopefully a concrete picture of the Zeptouniverse will be known.

References

[1] *Paul de Kruif*, Microbe Hunters, Mariner Books, Boston (2002); the book was first published in 1926.
[2] *Ch. Wetterich*, Physik Journal, August/September 2019, S. 67
[3] *A. J. Buras*, Gauge Theory of Weak Decays, Cambridge University Press, Cambridge (2020)
[4] *A. J. Buras* and *J. Girrbach*, Rep. Prog. Phys. **77**, 086201 (2014)
[5] *G. Isidori*, *Y. Nir* and *G. Perez*, Ann. Rev. Nucl. Part. Sci. **60**, 355 (2010)
[6] *A. J. Buras*, *D. Buttazzo*, *J. Girrbach-Noe* and *R. Knegjens*, JHEP **1411**, 121 (2014)
[7] *M. Lindner*, *M. Platscher* and *F. S. Queiroz*, Phys. Rep. **731**, 1 (2018)
[8] *T. Chupp*, *P. Fierlinger*, *M. Ramsey-Musolf* and *J. Singh*, Rev. Mod. Phys. **91**, 015001 (2019)

The Author



Andrzej J. Buras studied physics in Warsaw. He received his doctorate in 1972 at the Niels Bohr Institute (Copenhagen). Postdoctoral years at CERN (Geneva), Fermilab (Chicago) and SLAC (Stanford University) were followed by a position at the Max Planck Institute for Physics in Munich. In 1988, he was appointed full professor at the Physics Department of the TU Munich. Since 2012, he is Emeritus of Excellence of the TUM and heads a group on Fundamental Physics at the Institute for Advanced Study of the university. Andrzej J. Buras was awarded the Smoluchowski-Warburg Medal of the German and Polish Physical Societies in 2007. From 2011 to 2016, he was funded by an ERC Advanced Grant. He is a full member of the Bavarian Academy of Sciences (2010), foreign member of the Polish Academy of Sciences (2013) and of the Polska Akademia Umiejętności in Cracow.

Prof. Dr. Andrzej J. Buras, TUM Institute for Advanced Study, Lichtenbergstraße 2a, 85748 Garching, Germany

© 2020 Wiley-VCH GmbH

KCL-PH-TH/2024-09

Vector Wave Dark Matter and Terrestrial Quantum Sensors

arXiv:2403.02381v1 [hep-ph] 4 Mar 2024

Dorian W. P. Amaral[a*] , **Mudit Jain**[a,b*]
Mustafa A. Amin[a] , **and Christopher Tunnell**[a]

[a] *Department of Physics and Astronomy, Rice University, Houston, TX, 77005, U.S.A.*
[b] *Theoretical Particle Physics and Cosmology, King's College London, Strand, London, WC2R 2LS, United Kingdom*
[*] *These authors contributed approximately equally to this work.*
E-mail: dorian.amaral@rice.edu, mudit.jain@kcl.ac.uk, mustafa.a.amin@rice.edu, christopher.tunnell@rice.edu

Abstract: (Ultra)light spin-1 particles—dark photons—can constitute all of dark matter (DM) and have beyond Standard Model couplings. This can lead to a coherent, oscillatory signature in terrestrial detectors that depends on the coupling strength. We provide a signal analysis and statistical framework for inferring the properties of such DM by taking into account (i) the stochastic and (ii) the vector nature of the underlying field, along with (iii) the effects due to the Earth's rotation. On time scales shorter than the coherence time, the DM field vector typically traces out a fixed ellipse. Taking this ellipse and the rotation of the Earth into account, we highlight a distinctive three-peak signal in Fourier space that can be used to constrain DM coupling strengths. Accounting for all three peaks, we derive latitude-independent constraints on such DM couplings, unlike those stemming from single-peak studies. We apply our framework to the search for ultralight $B-L$ DM using optomechanical sensors, demonstrating the ability to delve into previously unprobed regions of this DM candidate's parameter space.

Contents

1 Introduction **2**

2 Calculating the Stochastic Wave Vector Dark Matter Signal **4**
2.1 The Dark Photon Field 4
2.1.1 Equipartion and Ellipses 5
2.2 The Detector Signal 6

3 Statistical Analysis **10**
3.1 Signal Likelihood 10
3.2 Projected Exclusions 12

4 Application to Accelerometer Studies **15**
4.1 Recasting Generalised Limits onto $B - L$ Dark Matter 16

5 Future Directions **20**
5.1 Longer Observation Times 20
5.2 Expanding the Mass Window 20

6 Conclusions **21**

A Equipartition between Longitudinal and Transverse Modes **28**

B Derivation of Marginal Likelihood with Stochastic Field Amplitude **30**

C Covariance Matrix **31**

D The Case of the Gradient of a Scalar **32**

1 Introduction

Dark matter (DM) dominates the non-relativistic matter content in our cosmos. However, we know exceptionally little about the constituent particles/fields of DM. Apart from the fact that they must interact gravitationally, we do not know their mass, spin, and other potential interactions [1, 2]. Astrophysical observations allow for a broad range of masses for the dark matter "particles": $10^{-19}\text{eV} \lesssim \text{few} \times M_\odot$ [3, 4]. Theoretical models include particle masses that span this range, with ultralight bosons at the lower end and composite particles/primordial black holes at the upper end [5–10].

Among the variety of possibilities, the case of ultralight, bosonic dark matter is particularly intriguing. These include, for instance, the QCD axion [11–13], axion-like particles and other scalars [14–17], and vector particles [18, 19]. A wide-ranging observational and experimental program is currently exploring models that can be tested with contemporary technology. Assuming a local dark matter density $\rho \sim \text{GeV cm}^{-3}$ with a typical virial velocity of $v_0 \sim 10^{-3}c$, for particle masses smaller than a few eV, the typical particle number within a de Broglie volume becomes sufficiently large, allowing for a classical field theory description: $N_{\rm dB} \simeq \rho/m\,(h/mv_0)^3 \sim 10^{66}\left(10^{-15}\,\text{eV}/m\right)^4$.

A widely pursued DM candidate is the light/ultralight vector dark matter (VDM) particle. Several early-universe production mechanisms exist for such dark matter [20–30] and, recently, numerical simulations of structure formation of light, vector dark matter in the nonlinear regime have been carried out (e.g. [31–33]). Our focus here is on the detection prospects of this kind of dark matter. Many dedicated studies have been conducted on the detection or exclusion of vectors [34–42] as well as scalars [35, 39, 42–49]. However, for the vector case, the analyses focusing on the Fourier space signal did not fully account for the vector nature and stochastic aspects of the field in their statistical treatment, and nor did they model the effect of the rotation of the Earth [36, 38]. In this work, we take these effects into account when studying the sensitivity of mono-directional accelerometers to ultralight vector dark matter.

In our detection scheme, the sensor points in a fixed direction relative to the local tangent plane of the experiment, rotating with the Earth at an angular frequency $\omega_\oplus \equiv 2\pi/(1\text{ sidereal day}) \approx 7.5\times10^{-5}\,\text{Hz}$. We will show that the signal in Fourier space contains three distinct peaks located at the angular frequencies m, $m-\omega_\oplus$, and $m+\omega_\oplus$, with the last two arising due to the Earth's rotation. Since $\omega_\oplus$ corresponds to a mass scale of $\sim 5\times10^{-20}\,\text{eV}$, which is already outside of the allowed mass window, we naturally have $m > \omega_\oplus$. To resolve these three distinct peaks, we shall therefore enforce that the observation time always satisfies $T_{\rm obs} > 1\,\text{d}$. With this basic setup, we will concentrate on the short observation time regime in this paper: experimental expedition timescales which are much smaller than the coherent timescale of the wave DM field, $T_{\rm obs} \ll \tau_{\rm coh} \equiv h/mv_0^2$. Thus, our observation time will always lie between

$$1\,\text{d} \lesssim T_{\rm obs} \ll 10\,\text{d}\left(\frac{5\times10^{-15}\,\text{eV}}{m}\right). \tag{1.1}$$

This means that, at most, our framework is valid for masses that give a coherence time of at least 1 d, corresponding to $m \lesssim 5\times10^{-15}$ eV. For longer expedition times, this upper mass

limit decreases: for example, for a runtime of 1 yr, we have that $m \lesssim 10^{-16}\,\mathrm{eV}$. This gives us the mass range of $5 \times 10^{-20}\,\mathrm{eV} \lesssim m \lesssim 5 \times 10^{-15}\,\mathrm{eV}$ where our analysis is appropriate[1].

Given the recent and substantial research and development efforts in quantum technologies, we are specifically interested in timely studies aimed at understanding the potential of quantum optomechanical sensors in the direct detection of dark matter. Mechanical detectors have a rich history in tests of gravity, including LIGO, and in recent years there has been a surge in efforts to explore their potential in quantum sensing for fundamental physics investigations (see reviews [50–52]). We are only beginning to understand the new opportunities for dark matter searches [53–58] in light of significant advances in quantum readout and control of mechanical sensing devices using optical or microwave light [59–61]. Accurately modeling the dark matter signal and the associated statistics is crucial for drawing representative inferences, guiding these quantum research and development efforts and aiding in experimental design. This is particularly relevant for large-scale accelerometer projects, such as the one proposed by the Windchime collaboration [62]. Such sensors have demonstrated potential as powerful probes for the wavelike signature produced by ultralight dark matter [63].

In this paper, we devise the analysis strategy for ultralight vector dark matter in the coherent regime to draw more representative exclusion inferences in the future. We begin by laying the theoretical groundwork for this DM paradigm in Section 2, where we derive the DM signal in both the time and frequency domains, taking into account both its stochastic and polarization properties, as well as accounting for the rotation of the Earth. We then perform statistical analyses of the DM signal in the frequency domain in Section 3. We derive a limit on a generalised parameter that is independent of the vector dark matter model and experimental parameters, which can be recast to concrete choices of them. Unlike other studies that focus solely on a single peak, our findings reveal that the signal power is distributed across three distinct peaks. Accounting for this distribution ensures the retention of constraining power, regardless of the experiment's location on Earth. Finally, in Section 4, we apply our framework to a concrete dark matter model and sensor: $B - L$ dark matter and the canonical optomechanical light cavity.

We have also included 4 appendices in the paper. In Appendix A, we discuss the equipartition between longitudinal and transverse modes. In Appendix B, we derive the marginal likelihood for the three-peak signal. In Appendix C, we show that the peaks are uncorrelated. Finally, in Appendix D, we discuss the applicability of our results in the context of the gradient of a scalar, deriving limits on the appropriate generalized parameter. Throughout the rest of this paper, we will work in natural units, whereby $\hbar = c = 1$. Moreover, we sometimes quote the DM mass in units of Hz where it is more appropriate to treat it as an angular frequency. The conversion from Hz to eV is given by the relation $m = \hbar\omega/c^2 \approx 4.14 \times 10^{-15}\,\mathrm{eV}[\omega/(2\pi\,\mathrm{Hz})]$.

[1] Later, in Section 5.2, we shall discuss a plausible detection scheme where the sensor is instead made to rotate manually at higher frequencies, allowing us to probe masses above $\sim 5 \times 10^{-15}$ eV.

2 Calculating the Stochastic Wave Vector Dark Matter Signal

2.1 The Dark Photon Field

The random vector field $\hat{\boldsymbol{A}}$ of mass m, at any given location and time, can be decomposed as

$$\hat{\boldsymbol{A}}(\boldsymbol{x},t) = \frac{1}{\sqrt{2m}} e^{-imt}\hat{\boldsymbol{\Psi}}(\boldsymbol{x},t) + \text{c.c.}\,, \tag{2.1}$$

where, in the non-relativistic limit and assuming free field evolution, each Fourier mode of the complex 3-vector field $\hat{\boldsymbol{\Psi}}(\boldsymbol{x},t)$ evolves as $\hat{\boldsymbol{\Psi}}_{\boldsymbol{k}}(t) = \hat{\boldsymbol{\Psi}}_{\boldsymbol{k}}\, e^{-i\frac{k^2}{2m}t}$.

With non-linear gravitational clustering, we expect an equipartition of longitudinal and transverse *helicities* of the plane waves in our vicinity, regardless of whether the early universe production mechanism favors one over the other.

Given this equipartition, the spectrum $\langle \hat{\boldsymbol{\Psi}}^\dagger_{\boldsymbol{k}} \cdot \hat{\boldsymbol{\Psi}}_{\boldsymbol{p}} \rangle = \delta_{\boldsymbol{k},\boldsymbol{p}}\, f_{\boldsymbol{k}}$, where $f_{\boldsymbol{k}}$ is the Milky Way halo distribution function[2] with $V^{-1}\sum_{\boldsymbol{k}} f_{\boldsymbol{k}} = \rho/m$ (here, V is the volume and ρ is the local mass density), we can define $\hat{\boldsymbol{\Psi}}_{\boldsymbol{k}} = \sqrt{f_{\boldsymbol{k}}}\,\hat{\boldsymbol{\epsilon}}_{\boldsymbol{k}}$ such that for every $\boldsymbol{k}$, $\hat{\boldsymbol{\epsilon}}_{\boldsymbol{k}}$ is a set of 6 real (3 complex) i.i.d.s (independent and identically distributed random variables) with unit norm $\langle \hat{\boldsymbol{\epsilon}}^\dagger_{\boldsymbol{k}} \cdot \hat{\boldsymbol{\epsilon}}_{\boldsymbol{p}} \rangle = \delta_{\boldsymbol{k},\boldsymbol{p}}$. In other words, for every $\boldsymbol{k}$ there are 5 real random numbers that are uniformly distributed on a unit S_5. With this, a realization of the random vector field is

$$\hat{\boldsymbol{A}}(\boldsymbol{x},t) = \sqrt{\frac{2}{m}}\,\Re\left\{\frac{1}{\sqrt{V}}\sum_{\boldsymbol{k}} e^{i\boldsymbol{k}\cdot\boldsymbol{x}}\,\sqrt{f_{\boldsymbol{k}}}\,\hat{\boldsymbol{\epsilon}}_{\boldsymbol{k}}\, e^{-i\left(m+\frac{k^2}{2m}\right)t}\right\}. \tag{2.2}$$

In this paper, we are interested in the short observation time limit, $T_{\rm obs} \ll \tau_{\rm coh} = m/k_0^2$ (where $k_0 = mv_0$ denotes the typical wavenumber). In this case, we can neglect the $k^2/2m$ factor from the time-varying sinusoid. Subsequently, we have a summation over many monochromatic waves (all oscillating with frequency m), with different amplitudes and phases for different values of $\boldsymbol{k}$. Assuming that the halo function is well behaved (meaning any $n^{\rm th}$ moment $\sum_{\boldsymbol{k}} k^n\, f_{\boldsymbol{k}}$ is finite), we can use the central limit theorem to arrive at the following:

$$\begin{aligned} &\hat{\boldsymbol{A}}(\boldsymbol{x},t)\Big|_{t\ll\tau_{\rm coh}} \approx \sqrt{\frac{2}{m}}\,\Re\left\{e^{-imt}\,\hat{\boldsymbol{w}}(\boldsymbol{x})\right\}, \\ \text{where}\qquad &\langle \hat{\boldsymbol{w}}(\boldsymbol{x})\rangle = 0 \quad\text{and}\quad \langle \hat{w}^{i\,*}(\boldsymbol{x})\hat{w}^j(\boldsymbol{y})\rangle = \frac{\delta^{ij}}{3}\times\frac{1}{V}\sum_{\boldsymbol{k}} e^{i\boldsymbol{k}\cdot(\boldsymbol{x}-\boldsymbol{y})} f_{\boldsymbol{k}}\,. \end{aligned} \tag{2.3}$$

For $T_{\rm obs} \ll \tau_{\rm coh}$, we can also safely assume that the distance Earth sweeps during the observation time is negligible compared to the de Broglie length. As such, we shall set $\boldsymbol{x} = \boldsymbol{y}$

[2]The halo function can be given as $f_{\boldsymbol{k}} = [\mathcal{N}(2\pi/(m\sigma V^{1/3}))]^{-3}(\rho V/m)e^{-(\boldsymbol{k}-\bar{\boldsymbol{k}})^2/(2m^2\sigma^2)}$ where $\mathcal{N}(x) = \text{ET}(3,\,0,\,e^{-x^2/2})$ is the elliptic theta function (which goes as $\sqrt{2\pi}/x$ as $x\to 0$). Here, $\bar{\boldsymbol{k}}/m$ is our velocity w.r.t. the rest frame of the halo, and σ is the velocity dispersion.

and further set $\boldsymbol{x} = 0$ assuming statistical homogeneity of the DM field. Decomposing the complex Gaussian random variables $\hat{\boldsymbol{w}}$ into Euler form, $\hat{w}^j = \hat{\alpha}^j\, e^{-i\hat{\varphi}^j}$, we may write

$$\hat{A}^j(t)\Big|_{t\ll\tau_{\rm coh}} \approx \sqrt{\frac{2\rho}{3m^2}}\,\hat{\alpha}^j \cos\left(mt + \hat{\varphi}^j\right) . \tag{2.4}$$

The three $\hat{\alpha}^j$ are independent Rayleigh distributed random variables, while the three φ^j are independent uniformly distributed angles (ranging from 0 to 2π):

$$P(\alpha^j) = 2\alpha^j e^{-(\alpha^j)^2} \qquad \text{and} \qquad P(\varphi^j) = \frac{1}{2\pi} . \tag{2.5}$$

The three components become statistically independent, mimicking three independent scalars.[3] Also note that our result is similar to the case of the gradient of a scalar [45], in the sense that there are 6 independent normal random variables to describe the DM field at a given location and short time scales.

2.1.1 Equipartion and Ellipses

In this subsection, we further justify our assumption of equipartition in the previous section.

Equipartion and Vector Field Ellipses: There exist various production mechanisms where disparate amounts of longitudinal (spin-0) and transverse (spin-1) helicities are produced [20, 21, 23, 25]. That is, for every $\boldsymbol{k}$, there could be different amounts of longitudinal and transverse components of $\boldsymbol{\Psi}_{\boldsymbol{k}}$[4]. However, owing to non-linear gravitational clustering, such disparity within the two sectors is expected to have disappeared by now within our local cosmic vicinity. With non-linear gravitational clustering, we expect virialization, leading to the *equipartition* of energy within all three degrees of freedom (dof). This would result in 2/3 of the total power being contained within the (two) transverse dof and the remaining 1/3 within the longitudinal ones. In this case, the vector field at each point (within a coherence region), which is formed out of a sum over a large number of Fourier modes, roughly traces out a *randomly oriented ellipse* (as opposed to oscillating along some fixed direction). This can be seen by noting that within time scales and length scales much smaller than the coherent ones, the spin current [31, 64] is negligible since it scales with the typical speed σ. Hence, the local spin density (given by $\boldsymbol{s} = \boldsymbol{A} \times \dot{\boldsymbol{A}}$) is conserved, implying that the local field vector $\boldsymbol{A}$ can execute a two-dimensional sinusoidal motion in general, i.e. it sweeps an ellipse. See Fig. 1 for a visualization and a description of this evolution. Such elliptical motion is appropriately used in, for example, [65–67].

In Appendix A, we discuss equipartition in greater detail, providing evidence for it via concrete halo-formation 3D simulations of the Schrödinger field $\boldsymbol{\Psi}$.

[3] This can be generalized to the many-components case. In particular, for multi-component scalar dark matter (with naturally different masses and also different energy densities for each component), we can simply replace the mass and density by their respective values, m^j and ρ^j.

[4] With the transverse and longitudinal projection operators $\mathcal{P}^{ij}_{\boldsymbol{k}_\perp}$ and $\mathcal{P}^{ij}_{\boldsymbol{k}_{||}}$, the respective components are $\mathcal{P}^{ij}_{\boldsymbol{k}_\perp}\,\Psi^j_{\boldsymbol{k}}$ and $\mathcal{P}^{ij}_{\boldsymbol{k}_{||}}\,\Psi^j_{\boldsymbol{k}}$. See Appendix A for some more details.

Random Linear Polarization: Some studies make the assumption of linear polarization; i.e. the vector field oscillates along a line in a fixed direction with this direction changing randomly every coherence time (see for example [40, 68–70]). However, as we argued above based on equipartition, an elliptical motion of the vector field is what one should expect. Nevertheless, we note that a preference for linear (circular) polarization could be generated by allowing for a non-gravitational attractive (repulsive) self-interaction [71–73]. While these works argue for such a preference in isolated soliton-like configurations, whether a significant preference for linear (circular) polarization within each coherence patch can be achieved dynamically remains to be seen.

Fixed Direction: There could exist a misalignment production mechanism for vectors where the entire observable Universe (or at least a large portion of it) has the vector field oscillating in a fixed direction [74, 75]. Such setups indeed lead to a fixed direction of oscillation of the vector field (apart from randomly oriented small perturbations). This would be distinct from the equipartition case we consider. However, there are difficulties associated with their production mechanisms [76–78].

2.2 The Detector Signal

Let $\boldsymbol{\zeta}(t)$ be the "antenna" direction—the time series signal is then given by $\hat{\mathcal{S}}(t) = g\,\boldsymbol{\zeta}(t)\cdot\hat{\boldsymbol{E}}(t) \approx g\,\boldsymbol{\zeta}(t)\cdot\partial_t\hat{\boldsymbol{A}}(t)$. Here, g is some overall coefficient containing the coupling constant and any other possible model parameters, and we have used the fact that the produced dark electric field is approximately given by $\boldsymbol{E} \approx \partial_t\boldsymbol{A}$ in the non-relativistic limit of the vector DM field. In this work, we will take the antenna to always point towards the zenith; however, we will comment on this assumption in Section 3. With ϕ denoting the latitude (where $\phi = 0°$ and $\phi = 90°$ respectively correspond to the equator and poles), and $\omega_\oplus$ denoting the angular rotation frequency of the Earth, we have $\boldsymbol{\zeta}(t) = (\cos\phi\cos(\omega_\oplus t),\, \cos\phi\sin(\omega_\oplus t),\, \sin\phi)^\intercal$. Then, the signal $\hat{\mathcal{S}}(t)$ is

$$\hat{\mathcal{S}}(t)|_{T\ll\tau_{\rm coh}} \approx g\sqrt{2\rho/3}\Big[\hat{\alpha}_x\cos\phi\cos\left(mt+\hat{\varphi}_x\right)\cos(\omega_\oplus t) + \hat{\alpha}_y\cos\phi\cos\left(mt+\hat{\varphi}_y\right)\sin(\omega_\oplus t) + \hat{\alpha}_z\sin\phi\cos\left(mt+\hat{\varphi}_z\right)\Big]\,. \tag{2.6}$$

Ultimately, we perform our analysis in Fourier space, considering the (one-sided) periodogram generated by Eq. (2.6). This is proportional to the mod-square of the discrete Fourier transform of $\hat{\mathcal{S}}(t)$ and is given by

$$\mathcal{P}(\omega) \equiv 2\frac{(\Delta t)^2}{T_{\rm obs}}\left|\sum_{n=0}^{N-1}\hat{\mathcal{S}}(t_n)e^{i\omega n\Delta t}\right|^2\,. \tag{2.7}$$

Here, ω is the angular frequency, N is the number of points sampled in the time domain, and $\Delta t \equiv T_{\rm obs}/N$ is the sampling frequency. The factor of two accounts for the 'folding' of the result from negative angular frequencies to positive angular frequencies, producing the one-sided periodogram that ignores the former. We define the dimensionless parameter

$$\beta \equiv \sqrt{\frac{\mathcal{A}^2 T_{\rm obs}}{2\sigma^2}}\,, \quad \text{with} \quad \mathcal{A} \equiv g\sqrt{2\rho/3}\,, \tag{2.8}$$

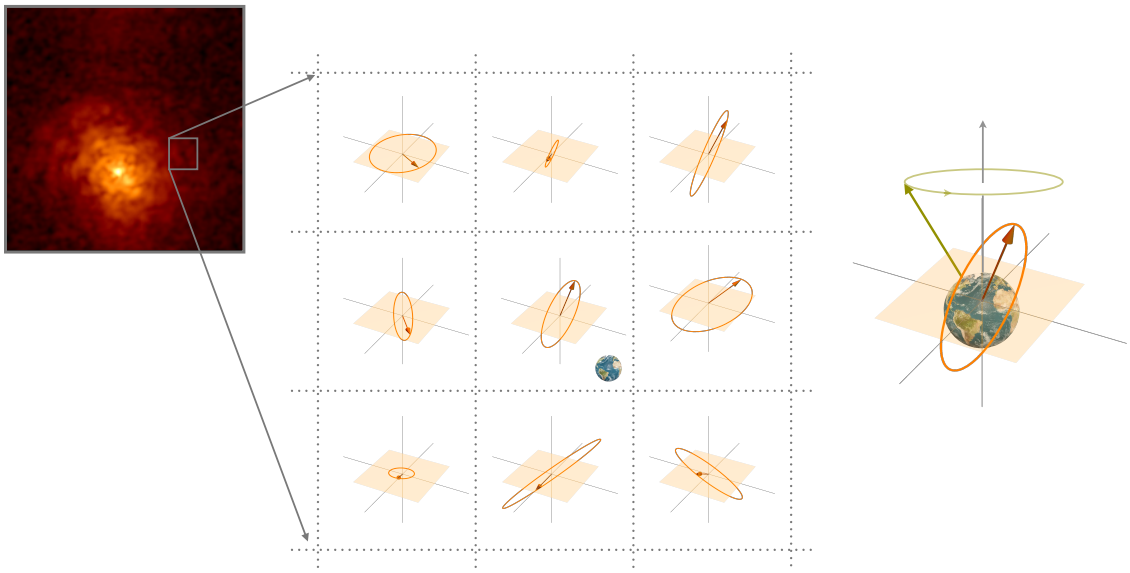


Figure 1: At each spatial point with a coherence region of size $2\pi/mv_0$ (scale of interference "granules"), the dark matter field $\boldsymbol{A}$ (orange vector) traces out an approximately fixed ellipse (for $2\pi/mc^2 = \tau_{\rm Comp} \ll t \ll \tau_{\rm coh} = 2\pi/mv_0^2$). These "random" ellipses change their size and orientations on the coherence time scale and smoothly connect with each other from one coherence region to another. For the duration of the measurement, we expect to find ourselves within one such coherence region. The detection signal $\mathcal{S}(t)$ is proportional to the dot product of the dark electric field $\boldsymbol{E} \simeq \partial_t \boldsymbol{A}$ and the detector orientation $\boldsymbol{\zeta}(t)$ (green arrow). Also see Fig. 2. Snapshot of the actual simulated field—leftmost panel—taken from [31].

where σ is the noise power spectral density (PSD). Typically, $\mathcal{A}$ is an acceleration or a force for accelerometer studies. With these definitions, the signal periodogram, normalised by the noise PSD (which we call the excess power λ), is given by

$$\begin{aligned}\lambda(\omega) \equiv \frac{\mathcal{P}(\omega)}{\sigma^2} = \frac{\beta^2}{4}\Big\{ &\left[\alpha_x^2 + \alpha_y^2 + 2\alpha_x\alpha_y \sin(\varphi_y - \varphi_x)\right]\cos^2\phi\,\delta_{\omega,\,s} \\ &+ \left[\alpha_x^2 + \alpha_y^2 - 2\alpha_x\alpha_y \sin(\varphi_y - \varphi_x)\right]\cos^2\phi\,\delta_{\omega,\,d} \\ &+ 4\,\alpha_z^2 \sin^2\phi\,\delta_{\omega,\,m}\Big\}\,.\end{aligned} \tag{2.9}$$

Here, we have defined the 'sum' and 'difference' angular frequencies, $s \equiv m + \omega_\oplus$ and $d \equiv m - \omega_\oplus$, respectively. The $\delta_{a,\,b}$ are Kronecker delta functions over angular frequencies.

We note that σ can be frequency dependent. This means that the expected noise PSD within each signal-containing bin can be different. However, for the remainder of this work, we take σ to be approximately constant, which is a good approximation in the frequency range of the signal, $\Delta\omega \sim \omega_\oplus \equiv 2\pi/T_\oplus \approx 7.3 \times 10^{-5}\,$Hz, where $T_\oplus = 23.93\,$h is the Earth's

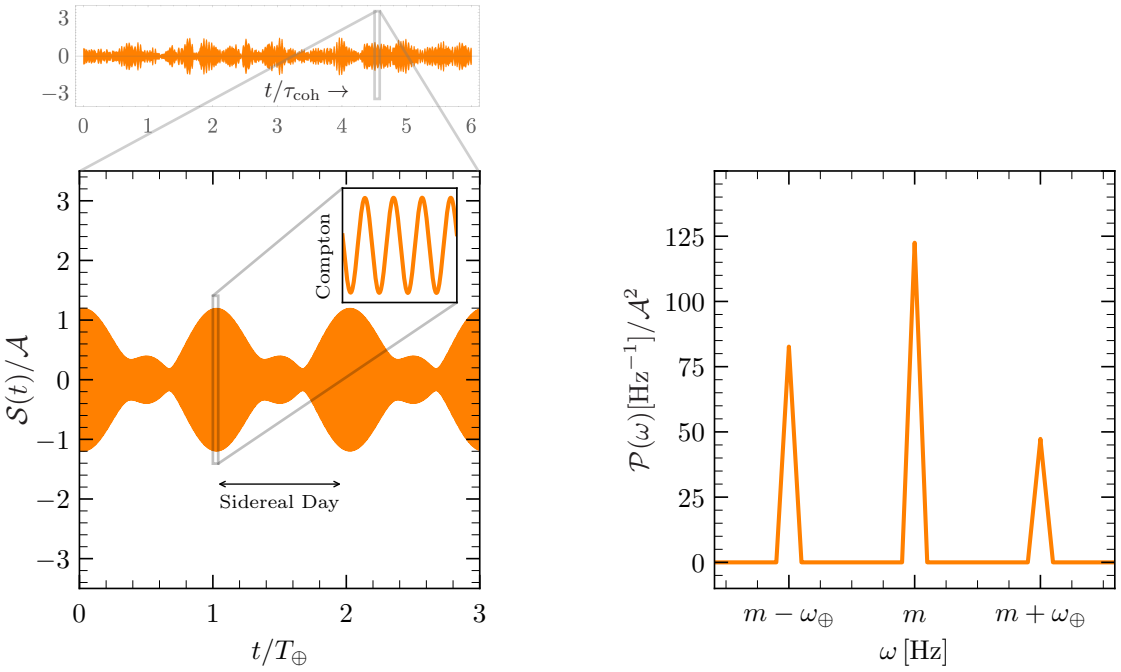


Figure 2: An example of the expected signal $\mathcal{S}(t) \approx g\boldsymbol{\zeta}(t) \cdot \partial_t \boldsymbol{A}(t)$. This depends on the shape, orientation and period of the vector field $\boldsymbol{A}(t)$, as well as the detector axis $\boldsymbol{\zeta}(t)$, which rotates with the Earth, and a model-dependent coupling g. Also refer to Fig. 1. We show the signal in the time (**left**) and Fourier (**right**) domains. For the time domain signal, we show its behaviour over several coherent times (**upper**) and sidereal days (**lower**), the latter of which is the expected observed signal in our sensor. The inset shows the oscillation of the signal over several Compton times. Note the appearance of three peaks: a single Compton peak at frequency m in the middle and two additional ones appearing due to Earth's rotation—a *difference* peak at $d \equiv m - \omega_\oplus$ and a *sum* peak at $s \equiv m + \omega_\oplus$. The time domain signal is simulated from Eq. (2.6), the periodogram of which is taken via Eq. (2.7). For the simulation, we have used the observation time $T_{\rm obs} = 10T_\oplus$, and the results are expressed in terms $\mathcal{A} \equiv g\sqrt{2\rho/3}$ (where ρ is the local DM density). For additional details on the simulation, see text. The peaks are contained within bins whose widths correspond to the resolution of the frequency space data, given by $\Delta\omega = 2\pi/T_{\rm obs}$. Note that the general elliptical behavior of the DM field allows for different power in the sum and difference peaks. In contrast, the linearly polarized DM field would lead to equal power in these peaks.

sidereal period. We comment on this approximation further in Section 4 when we consider a concrete sensor and DM model.

Fig. 2 shows an example of a signal in the short observation time regime, in both the time (Eq. (2.6)) and Fourier (Eq. (2.9)) domain. To generate them, we have taken $\mathcal{A} = 1\,[\mathcal{A}]$, $m = 2\pi\,\text{Hz}$, $\phi = 45°$, $T_{\rm obs} = 10T_\oplus$, and, for the purposes of fast convergence, $T_\oplus = 100\,\text{s}$. Here, $[\mathcal{A}]$ are the units of $\mathcal{A}$, which depend on the quantity being measured by the experiment. We have also taken $\boldsymbol{\alpha} \equiv (\alpha_x, \alpha_y, \alpha_z)^\intercal = (1, 0.7, 0.2)^\intercal$ and $\boldsymbol{\varphi} \equiv (\varphi_x, \varphi_y, \varphi_z)^\intercal = (\pi/2, \pi/4, \pi/3)^\intercal$. When running our future simulations, we sample these six variables independently from their respective distributions.

There are three characteristic timescales within the signal: the Compton scale, the Earth's rotation period, and the coherent (de Broglie) scale. The first two of these are present in the larger panels of Fig. 2. The Earth's rotation period is evident from the time domain signal, which we have shown for three full rotation periods. The Compton scale is much faster than this scale (see inset), making the signal appear solid in shape. Crucially, we see that the vector ULDM field leaves a characteristic three-peak signal in the Fourier domain[5]. One peak is present at the Compton frequency $\omega = m$, which previous frequency-space analyses have focused on [36, 38]. However, a further two peaks manifest as a result of the Earth's rotation, which are spaced $\omega_\oplus$ away from the Compton peak. These additional peaks, the use of which has been ignored in previous accelerometer analyses[6], only appear as $T_{\rm obs} \geq T_\oplus$; shorter observation times do not give us enough resolution in the frequency domain to resolve them[7]. We call the peak at the Compton frequency the *Compton* peak, that at s the *sum* peak, and that at d the *difference* peak.

We argued earlier that, within a coherence patch, we expect the vector field to undergo an elliptical motion with period $2\pi/m$ (see Fig. 1), as opposed to a linear one commonly used in the literature. In both the linear and elliptical cases, the time domain signal, $\mathcal{S}(t)$, is sinusoidal and contains the angular frequencies m and $m \pm \omega_\oplus$. Repeating the analysis of [40] in the time domain, but without the linear polarization assumption, we expect qualitatively similar results (with more statistical spread on the time averaged power). However, there are some important differences when analysing the expected signal in Fourier space.

In the elliptical case, the power contained in the m and $m \pm \omega_\oplus$ peaks is statistically uncorrelated (see Appendix C). On the other hand, for the linear polarization case, the power at m and $m \pm \omega_\oplus$ is correlated, with equal power in the sum and difference peaks. This can be seen by noting that, in this case, all the components of the vector are in phase. The statistical independence in the elliptical case significantly simplifies our analysis pipeline for projected sensitivities. Furthermore, the distinction in power at $m \pm \omega_\oplus$ is also relevant in case of a detection since we would expect different powers in the elliptical case.

[5] Such a signal would also be seen in the case of the gradient of a scalar field, as mentioned in Ref. [45], and its form is similar to that of Eq. (2.6). See Appendix D for details.

[6] Ref. [36] also noted this spectral splitting; however, the focus was on the Compton peak for the purposes of that analysis. In Ref. [67], this splitting as it relates to a global network of magnetometers was used.

[7] For us, the observation time is defined as the amount of time that data are continuously taken. As such, the total expedition time of the entire experiment is equivalent to $T_{\rm obs}$.

3 Statistical Analysis

We now consider the projected exclusion limits that a generic experiment would be able to set using our three-peak analysis. To do this, we use a series of likelihood-ratio tests.

3.1 Signal Likelihood

For our likelihood, we follow a hybrid frequentist-Bayesian approach, defining a marginalized likelihood in which all nuisance parameters are integrated out. In our case, these are the random Rayleigh parameters, $\boldsymbol{\alpha}$, and random uniform DM phases, $\boldsymbol{\varphi}$. Such a hybrid approach has already been used in the context of ultralight bosonic dark matter [42, 79]. Our work differs from Ref. [79] since they focused on an axion-like signal as opposed to that from vector DM. It goes beyond Ref. [42] since they did not consider the peaks arising from the rotation of the Earth in their analysis.

The full likelihood in Fourier space is well-known to follow a non-central χ^2 with two degrees of freedom [80]. In our case, the non-centrality parameter is the total signal amplitude in Eq. (2.9). The marginalized likelihood is then given by

$$\mathcal{L}_{\rm marg}(\beta,\, \phi;\, p) = \int \chi^2_{\rm nc}\left(p;\; k=2,\, \lambda(\beta,\, \phi,\, \boldsymbol{\alpha},\, \boldsymbol{\varphi})\right)\, \Pi(\boldsymbol{\alpha},\, \boldsymbol{\varphi})\, \mathrm{d}^3\boldsymbol{\alpha}\, \mathrm{d}^3\boldsymbol{\varphi}\,, \tag{3.1}$$

where Π describes the priors of our random parameters and p is the random variable we expect to measure in an experiment. We can express the result of Eq. (3.1) completely analytically and provide a full derivation of it in Appendix B, only quoting the final result here. The likelihoods in the signal-containing bins, which we call the Compton and sum/difference likelihoods, are respectively

$$\begin{aligned}
\mathcal{L}_m(\beta,\, \phi;\, p) &= \frac{1}{2+\beta^2\sin^2\phi}\exp\left[-\frac{p}{2+\beta^2\sin^2\phi}\right]\,, \\
\mathcal{L}_{s/d}(\beta,\, \phi;\, p) &= \frac{1}{2+(\beta^2\cos^2\phi)/2}\exp\left[-\frac{p}{2+(\beta^2\cos^2\phi)/2}\right]\,.
\end{aligned} \tag{3.2}$$

Note that, when $\beta = 0$, we correctly retrieve central χ^2 distributions in each bin, corresponding to the background-only case. The result for the Compton peak matches that of Refs. [42, 79]. The result for the sum/difference peaks is new.

In Fig. 3, we show a comparison between a numerical simulation of the signal likelihoods and the analytical results of Eq. (3.2). For the former, we begin from Eq. (2.6), simulating 10^6 realisations of the time-domain signal. We take $\mathcal{A} = 1\,[\mathcal{A}]$, $T_{\rm obs} = 10T_\oplus$, $\sigma^2 = 5\,[\mathcal{A}]^2\,\mathrm{Hz}^{-1}$, and $\phi = 45°$. For the purposes of fast convergence in our simulations, we take $m = 2\pi\,\mathrm{Hz}$ and $T_\oplus = 100\,\mathrm{s}$. For each run, we sample $\boldsymbol{\alpha}$ and $\boldsymbol{\varphi}$ from independent Rayleigh and uniform distributions respectively, as given by Eq. (2.5). To generate the time domain signal, we add Gaussian-distributed white noise with zero mean and variance given by $\sigma_t^2 = \sigma^2\Delta t$. Finally, we compute the periodogram of the signal following Eq. (2.7), dividing by σ^2 to produce the excess power in each frequency bin. The resulting normalised distribution of $p(\omega)$ for the Compton bin ($\omega = m$) and the sum/difference bins ($\omega = m \pm \omega_\oplus$) are in excellent agreement with our analytical result. We also show the

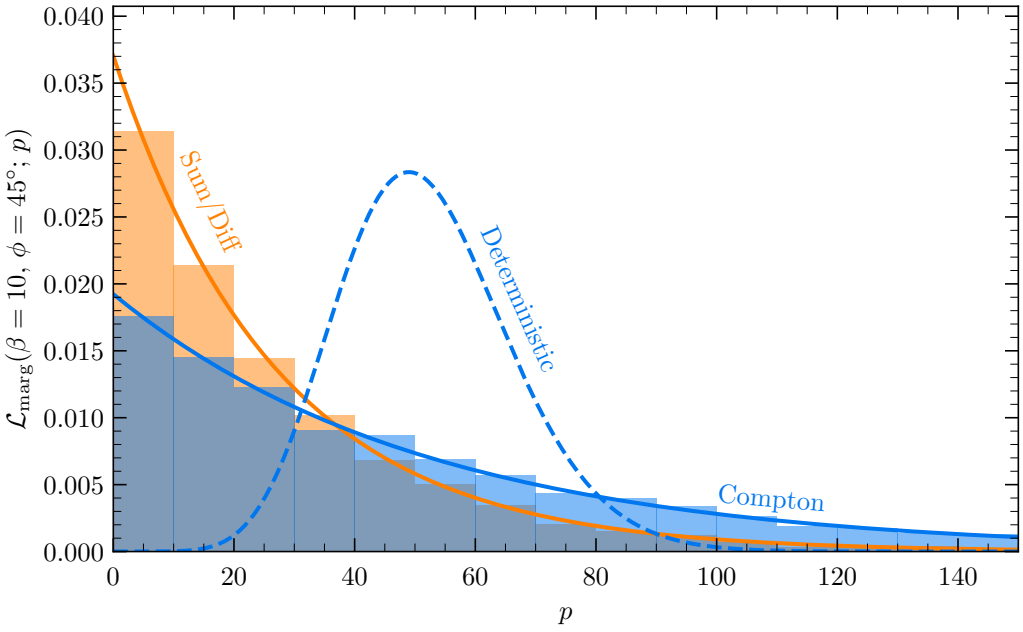


Figure 3: Example likelihoods for each of the three signal peaks once the stochastic variables have been marginalised over. The bars show the result of a numerical simulation of the noise-normalised periodogram values beginning from Eq. (2.6), while the solid lines show the analytical result of Eq. (3.2). Here, ϕ is the latitude of the experiment, p (a random variable) is the value of the measured excess power, and β is defined as per Eq. (2.8). Also shown as a dashed line is the deterministic result for the Compton peak, where the stochastic variable α_z^2 is set to its expectation value, $\langle \alpha_z^2 \rangle = 1$.

likelihood governing the deterministic result for the Compton peak: a non-central χ^2 with two degrees of freedom and non-centrality parameter given by the last term of Eq. (2.9). Without the nuisance parameter α_z^2 integrated out, we instead set it to its expectation value: $\langle \alpha_z^2 \rangle = 1$. We see that higher values of p are favoured in this case, which would ultimately lead to an overly aggressive constraint on β.

The full likelihood over all frequency space is then given by the product of the likelihoods in each frequency bin,

$$\mathcal{L}(\beta,\, \phi;\, \boldsymbol{p}) = \prod_{i=1}^{N_{\rm bins}} \mathcal{L}_{\rm marg}(\beta,\, \phi;\, p_i)\,, \tag{3.3}$$

where p_i represents the excess power density in the $i^{\rm th}$ frequency bin, $\boldsymbol{p}$ is the full data vector, and the product runs over all $N_{\rm bins}$ frequency bins. Ultimately, since our signal only manifests in three bins, it suffices for us to consider only those bins that could potentially contain a signal, and we may ignore all other bins. We can express the likelihood in this way because each bin is statistically uncorrelated, as we show in Appendix C. This is in

contrast with the analysis performed in Ref. [45], where a similar study was conducted in the case of the gradient of a scalar in the time domain. There, a complicated covariance matrix had to be computed to account for correlations in the signal at different times. In Fourier space, these covariances disappear. The power of performing this analysis in the frequency domain is thus not only that the signal is contained within a small number of bins, but also that these bins are statistically independent, which allows us to treat the statistics in a significantly simpler way.

Crucially, once the latitude of the experiment, ϕ, is fixed, the likelihood depends on the product of all experimental variables via the dimensionless parameter β. This means that we can set a more holistic limit that is independent of the specifics of an experiment. Once the form of $\mathcal{A}$ (which depends on both the experiment and the DM model), the observation time $T_{\rm obs}$, and the noise profile σ are known, the ensuing limit on β can be recast to one on the model parameters of interest. This makes our analysis, both the results and overall logic, as generally useful as possible.

3.2 Projected Exclusions

To derive our limits, we construct the one-sided log-likelihood-ratio test statistic, defined as

$$q_\beta \equiv \begin{cases} -2\ln\left[\frac{\mathcal{L}(\beta,\phi;\boldsymbol{p})}{\mathcal{L}(\hat{\beta},\phi;\boldsymbol{p})}\right] & \text{if} \quad \hat{\beta} \geq \beta \\ 0 & \text{else} \end{cases}, \tag{3.4}$$

where $\hat{\beta}$ is that value of β which maximises the likelihood given the observed data set $\boldsymbol{p}$, characterising the best-fit model. This statistic is defined as a piecewise function as we only expect excess signals to be disfavoured when excluding a value of β in a one-sided test. This corresponds to values of β greater than the best-fit value. Values below this are deemed under-fluctuations and considered consistent with observation. This statistic tells us how consistent the data are with a signal defined by β compared to the best-fit model, with zero representing perfect consistency and large values indicating high inconsistency.

The general idea is that we want to exclude those values of β that lead to excessive values of q_β. We do this by considering the distribution $f(q_\beta)$ that we expect to arise when many hypothetical experiments perform a measurement. Generating the $\alpha_{\rm conf}\%$ confidence level (CL) limit then depends on finding the value of the test statistic, $q_\beta^{\rm lim}$, for which an experiment has an $\alpha_{\rm conf}\%$ probability of attaining that value or below. That is, we solve for $q_\beta^{\rm lim}$ in

$$\int_0^{q_\beta^{\rm lim}} f(q_\beta)\,\mathrm{d}^3 q_\beta = \alpha_{\rm conf}\,. \tag{3.5}$$

From $q_\beta^{\rm lim}$, we then find that $\beta^{\rm lim}$ which gives us this value for the test statistic. This is our $\alpha_{\rm conf}\%$ CL limit on our parameter of interest, β.

Ultimately, we compute 90% CL limits ($\alpha_{\rm conf} = 0.90$) via a series of Monte Carlo (MC) simulations, following the above procedure in each MC run[8]. For a given choice of β, we

[8]While asymptotic formulae exist for computing exclusion limits, we have opted for an MC approach to ensure proper coverage [81]. Since we are following a hybrid frequentist-Bayesian approach, we found this to be an especially pertinent check.

begin by simulating the distribution $f(q_\beta)$. We do this by simulating 10^6 experiments, sampling the data p for each signal bin directly from the verified likelihoods given in Eq. (3.2). In each run, we find $\hat{\beta}$ and compute the distribution of q_β for a range of β and ϕ values. We then fit our distributions to the ansatz

$$f(q_\beta) = (1 - \varpi)\,\delta(q_\beta) + \varpi\,\chi^2(q_\beta;\, k = 1), \tag{3.6}$$

where $\varpi \in [0, 1]$ is a scale factor ensuring that the distribution is normalised to 1. This ansatz is inspired by the asymptotic result of Chernoff (where $\varpi = 1/2$), which itself is a limiting case of Wilk's theorem when the true value of β lies on the boundary of its domain (which is true in our case, since our background-only data set if defined by $\beta = 0$) [82, 83]. For each run, we find the best-fit value of ϖ. From Eq. (3.6), we can then invert Eq. (3.5) to find $q_\beta^{\rm lim}$. For the $\alpha_{\rm conf}$% CL limit, we have that

$$q_\beta^{\rm lim} = 2\left[\mathrm{Erf}^{-1}\left(1 + \frac{\alpha_{\rm conf} - 1}{\varpi}\right)\right]^2 . \tag{3.7}$$

In generating our distributions, we find a weak dependence on the chosen values of β and ϕ. However, this leads to a small change in the ultimate value of $q_\beta^{\rm lim}$. We take the mean value of it over our fits as its best estimator, yielding $q_\beta^{\rm lim} \simeq 2.43$, and use this throughout the rest of our study. Note that this is close to the asymptotically expected result of $q_\beta^{\rm lim} \simeq 2.71$ for a 1 d.o.f. problem [81]. We could have derived a similar result by integrating the resulting q_β histograms; however, we attain a good fit to Eq. (3.6), and it provides us with a closed-form solution for $q_\beta^{\rm lim}$, as per Eq. (3.7).

With $q_\beta^{\rm lim}$ at hand, we may derive the main result of this section, $\beta^{\rm lim}$. We once again follow an MC approach, generating 10^6 data sets consistent with a background-only observation (setting $\beta = 0$), and finding, for each hypothetical experiment, that value of β for which Eq. (3.4) returns $q_\beta = q_\beta^{\rm lim}$. This produces a distribution of limits, for which we take the median as our best estimator. We also produce the 1σ error bars on our limits by finding the $16^{\rm th}$- and $84^{\rm th}$-percentile of the distribution in $\beta^{\rm lim}$.

We show the 90% CL limit arising from our three-peak analysis in Fig. 4. Also shown are the corresponding results from two single-peak analyses focusing solely on the Compton and either one of the sum or difference peaks. These results follow the same MC procedure as above but take as the full likelihood only the Compton or the sum/difference likelihood given in Eq. (3.2). We see that the three-peak analysis produces a limit that is largely latitude-independent, rising slightly towards the pole. This is because the sensitivity axis at this latitude only has a component parallel to the Earth's rotation axis and is thus only able to pick out the Compton peak.

This latitude-independent limit is in contrast with the analyses that focus on only single peaks, which are both highly sensitive to where the experiment is placed. For the study focusing on the Compton peak, the constraining power is optimal at the pole, where all of the power is contained in the Compton frequency bin, and it rapidly declines towards the equator, where the Compton peak disappears. Note that this and the three-peak results join at this point, with no difference between the approaches. Conversely, for an

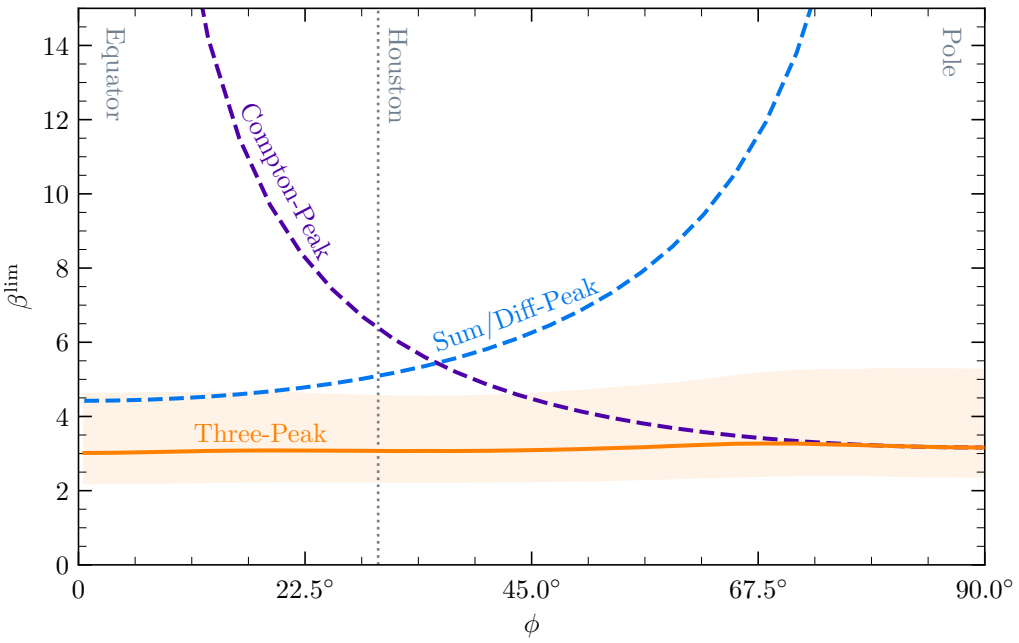


Figure 4: The 90% CL limits ($\beta^{\rm lim}$) on the dimensionless parameter $\beta \equiv \sqrt{\mathcal{A}^2 T_{\rm obs}/(2\sigma^2)}$ (see Eq. (2.8)) derived from our MC analysis . We show the results of our three-peak analysis and those of two single-peak analyses focusing on the Compton peak and on one of the sum or difference peaks. The shaded region indicates the 1σ error bar on our three-peak analysis. The dotted line indicates the latitude of Houston, which we use in Section 4. Our three-peak analysis generally provides a better/comparable limit to either of the two single-peak analyses and is largely latitude-independent.

analysis focusing on one of the sum or difference peaks, the situation is the opposite. In this case, the results of this and the three-peak methods do not converge since half the power is contained in a single one of the sum or difference peaks at the equator; the three-peak analysis captures all of this power, whereas the single-peak analysis misses half of the power. Thus, the strength of our analysis is that the constraining power is retained no matter where an experiment is placed, such that its latitude is rendered largely irrelevant from the viewpoint of constraining a ULDM signal.

We emphasize that the interpretation of Fig. 4 is as a set of exclusion lines whereby background pseudodata is generated and the assumed DM signal strength is constrained. The key point is that the level of this constraint depends on the assumption one makes on the nature of the DM signal given a non-detection. Taking this signal to be only a single peak in Fourier space then leads to constraints that are generally dependent on the latitude of the experiment, rapidly weakening towards latitude extremes. On the other hand, employing the full signal model consisting of three peaks yields stronger constraints that are almost independent of the experiment placement.

Throughout the above analysis, we assumed that the sensitivity axis pointed in the zenith direction. However, we can relax this assumption and consider what our results would look like if this axis pointed in some different direction, say for instance directions perpendicular to the zenith—namely, the East/West and North/South directions[9]. If North/South-pointing, all of the curves in Fig. 4 would be flipped about the line $\phi = 45°$. While the strongest limit for the Compton peak would now occur at the equator instead of the pole (and vice versa for both the sum and difference peaks), crucially we would still retain a largely latitude-independent constraint for our three-peak analysis. This is because, throughout the experiment, the directionality of the detector makes a cone, making it sensitive to the vector DM power in all the three directions. If, instead, the axis pointed towards the East/West, we would only see the sum and the difference peaks. This is because, throughout the experimental expedition, the directionality of the detector is restricted to lie on a plane (which would necessarily be perpendicular to the rotation axis of the Earth). Therefore, it is always insensitive to the power contained across the perpendicular direction, which is tied to the standalone Compton peak. One final possibility is when the directionality of the detector traces out a line throughout the experiment. This is only possible when it points parallel to the Earth's rotation axis (at any given latitude). In this case, we would naturally be oblivious to the Earth's rotation and hence to the sum and difference peaks, and we would only be able to resolve the Compton peak.

In summary, the best-case scenario is when the detector's sensitivity axis traces out a cone. In this case, we capture all the three peaks since we are sensitive to the vector DM power across all three directions (Earth's rotation axis and the two orthogonal directions).

4 Application to Accelerometer Studies

As an application of our analysis strategy, we consider a concrete sensor and DM model. As our sensor, we take the canonical optomechanical light cavity, which can be used to perform acceleration measurements by continuously measuring the distance between fixed and movable cavity mirrors. As our model, we consider 'dark photon' DM stemming from a gauged $U(1)_{B-L}$ symmetry, leading to wavelike DM in the ultralight regime that couples to the difference between baryon number, B, and lepton number, L. Gauging such a charge is popular in the context of particle physics, since it naturally leads to the introduction of right-handed neutrinos and, hence, can account for the non-zero neutrino masses [84–86]. For clarity, the Lagrangian reads

$$\mathcal{L} \supset -\frac{1}{4}A'^{\mu\nu}A'_{\mu\nu} - \frac{1}{2}m^2 A'^{\mu}A'_{\mu} - g_{B-L}j^{\mu}_{B-L}A'_{\mu}\,, \tag{4.1}$$

where $A'^{\mu\nu} \equiv \partial^{\mu}A'^{\nu} - \partial^{\nu}A'^{\mu}$ is the field strength tensor for the new field, m is the mass of the field, and j^{μ}_{B-L} is the new vector current under this model. This current is given by

$$j^{\mu}_{B-L} = \sum_f Q^f_{B-L}\bar{f}\gamma^{\mu}f\,, \tag{4.2}$$

[9]Here we assume that the sensitivity axis of the detector is locally fixed with respect to the zenith.

where the sum runs over all fermions in the SM and where Q^f_{B-L} is the $B-L$ charge of the fermion f. A multitude of studies have considered this combination and set limits or projections on $B-L$ coupled DM [35, 36, 38, 41, 42, 44].

However, those works that performed a Fourier space analysis did so by only focusing on the Compton peak. As we discussed in Section 3, such an analysis for an axial sensor is sub-optimal, as it fails to capture the full signal and therefore suffers from a signal loss at a range of latitudes. Moreover, ignoring the randomness of the nuisance variables leads to an overly aggressive constraint, as was illustrated in Fig. 3. Our more holistic three-peak strategy, which also considers this stochasticity, retains the full signal and is largely latitude-independent in its constraining power. Therefore, this choice of sensor and DM model makes for an excellent case study with which to showcase the improved constraining power of our method.

Furthermore, a proper vector treatment of the DM field in Fourier space, which includes the stochasticity of the ULDM field variables and the effect of the rotation of the Earth, has not been done. Ignoring the randomness of the nuisance variables leads to an overly aggressive constraint, as was also pointed out in Refs. [42, 79].

4.1 Recasting Generalised Limits onto $B-L$ Dark Matter

To recast our limits on β shown in Fig. 4 into one on the parameter of interest for this model, the gauge coupling strength g_{B-L}, we must define four quantities. Firstly, we must make clear what the quantity $\mathcal{A}$ is for this experiment, which will depend on both the model and the signal of interest for this sensor. Secondly, we must choose an observation time, $T_{\rm obs}$. Thirdly, we must elaborate on what the concrete noise profile, $\sigma(\omega)$, for this type of experiment is. Lastly, and least importantly following from our discussion above, we must choose a latitude for the experiment. Once these are known, Eq. (2.8) can be re-arranged for g_{B-L}, giving us our model- and experiment-specific 90% CL limit.

For $B-L$ coupled dark photon dark matter, the relevant signal is a differential acceleration. This is given by Eq. (2.6) in the time domain, with a now concrete choice for $\mathcal{A}$,

$$\mathcal{A} \equiv g_{B-L}\Delta_{ij}a_0\,. \tag{4.3}$$

Here, g_{B-L} is the gauge coupling strength of the model, Δ_{ij} is the differential $B-L$ charge per nucleon between materials i and j, given by

$$\Delta_{ij} \equiv \left|\frac{Z_i}{A_i} - \frac{Z_j}{A_j}\right|, \tag{4.4}$$

and $a_0 \equiv \sqrt{2\rho/3}\,u^{-1} \simeq 10^{12}\,\mathrm{m\,s^{-2}}$ is a characteristic acceleration imparted by the field to each nucleon (with u being the atomic mass unit). For most materials, $\Delta_{ij} \sim 0.1$, which we take in the following analysis [36]. Note that, for this particular model, $g \equiv g_{B-L}\Delta_{ij}/u$.

For our observation time, we take $T_{\rm obs} = 10T_\oplus$ to be firmly in the regime where the three peaks can be resolved. For light cavities, which may only be able to remain coherent over the scale of hours rather than days, such a runtime is optimistic. However, since our aim here is merely to showcase how our method can be used concretely and compare to

the works of Refs. [36, 38], we do not see this as an issue. Our strategy is general and can be applied to any axial sensor and vector-like DM model, and we have settled on this configuration only for the sake of argument; other sensor technologies, such a magnetically levitated sensors, do not have this issue. Moreover, multiple cavities or data-stacking techniques can be employed to mitigate this issue.

We model the background according to Refs. [36, 38]. Namely, we split the total expected background PSD σ^2, which we will write as S_{aa} as per convention, into a thermal, shot-noise, and back-action component,

$$S_{aa} = S_{aa}^{\rm Th} + S_{aa}^{\rm SN} + S_{aa}^{\rm BA} \,. \tag{4.5}$$

In what follows, we do not discuss the forms of these noise terms; we instead refer the reader to Ref. [52, 87] for a review on the topic. The thermal component is given by

$$S_{aa}^{\rm Th} \equiv \frac{4k_B T\gamma}{m_s} \,, \tag{4.6}$$

where γ represents the couplings between the sensor and the thermal bath of temperature T, m_s is the mass of the sensor, and k_B is Boltzman's constant. Typically, we parametrise the thermal coupling as $\gamma \equiv \omega_0/Q$, where ω_0 is the resonance frequency of the cavity and Q is its quality factor. The measurement-added noise terms—the shot-noise and back-action noise—are respectively given by

$$S_{aa}^{\rm SN}(\omega) \equiv \frac{\hbar\kappa L^2}{2\omega_L P_L} |\chi_c(\omega)|^{-2} |\chi_m(\omega)|^{-2} \,, \tag{4.7}$$

and

$$S_{aa}^{\rm BA}(\omega) \equiv \frac{2\hbar\omega_L P_L}{m_s^2 L^2 \kappa} |\chi_c(\omega)|^2 \,. \tag{4.8}$$

Here, κ is the cavity loss, which quantifies the efficiency of the optical modes of the cavity, L is the cavity length, ω_L is the angular frequency of the laser, and P_L is its power. The mechanical susceptibility is given by

$$\chi_m(\omega) \equiv \frac{1}{\omega_0^2 - \omega^2 + i\gamma\omega} \tag{4.9}$$

and the cavity susceptibility by

$$\chi_c(\omega) \equiv \frac{\sqrt{\kappa}}{i\omega - \kappa/2} . \tag{4.10}$$

Our choices for all of the above parameters except for the laser power, which we expand on below, are summarised in Table 1. These are in keeping with the choices made in Refs. [36, 38].

The choice of where to tune the laser power is critical to give us competitive limits for a wide range of dark matter masses. We have found that we can achieve excellent limits for low dark matter masses, which are of most relevance to our work, by tuning the laser power such that the back-action and shot-noise components are minimised at low

Quantity	**Value**
Sensor Mass (m_s)	10 mg
Bath Temperature (T)	10 mK
Quality Factor (Q)	10^9
Cavity Loss (κ)	10^6 Hz
Laser Wavelength (λ_L)	1.55 µm
Cavity Length (L)	10 cm

Table 1: The optomechanical cavity configuration we have assumed in this work.

frequencies. That is, by finding that P_L for which $\partial_{P_L}[S_{aa}^{\rm SN}(\omega \to 0) + S_{aa}^{\rm BA}(\omega \to 0)] = 0$ for a given choice of ω_0. The required laser power to achieve this is given by

$$P_L^{\rm min} = \frac{m_s \kappa^2 L^2 \omega_0^2}{8\omega_L} \,. \tag{4.11}$$

For the resonant frequencies we have considered, the laser power ranges from $P_L \sim 10^{-10}\,\mathrm{W}$ for $f_0 = 1\,\mathrm{Hz}$ to $P_L \sim 10^{-6}\,\mathrm{W}$ for $f_0 = 100\,\mathrm{Hz}$.

We note that this choice of power tuning is different from the strategies usually employed in other studies. Typically, the laser power is tuned so that the measurement-added noise is either minimised on resonance or, as LIGO implements it, well above resonance [88]. However, we found that both of these choices detriments the limit that we can draw at low masses, increasing the background at low frequencies beyond the thermal noise floor. For these other strategies to be beneficial at both the respective frequency targets and at low frequencies, the thermal noise would have to be significantly lower than that achieved with our choice of sensor mass, quality factor, and bath temperature.

In the treatment of our backgrounds, we have neglected seismic noise, which can become important at frequencies below $\sim 10\,\mathrm{Hz}$. Since we require the use of two materials to measure the differential acceleration peculiar to $B - L$ DM, we can envision constructing two sensors: one with a moveable mirror made of material i and another of material j. By subtracting their signals, we both isolate the differential acceleration signature and remove backgrounds common to both—this includes the seismic noise component [63]

Finally, we choose Houston as the location of our experiment, $\phi = 29.76°$. From Fig. 4, we find that $\beta^{\rm lim} \simeq 3.1$ for this latitude. However, we note that this information is almost unnecessary for the three-peak analysis since it is largely location-independent. We may then re-arrange Eq. (2.8) accounting for Eq. (4.3) to give us our limit on ultralight

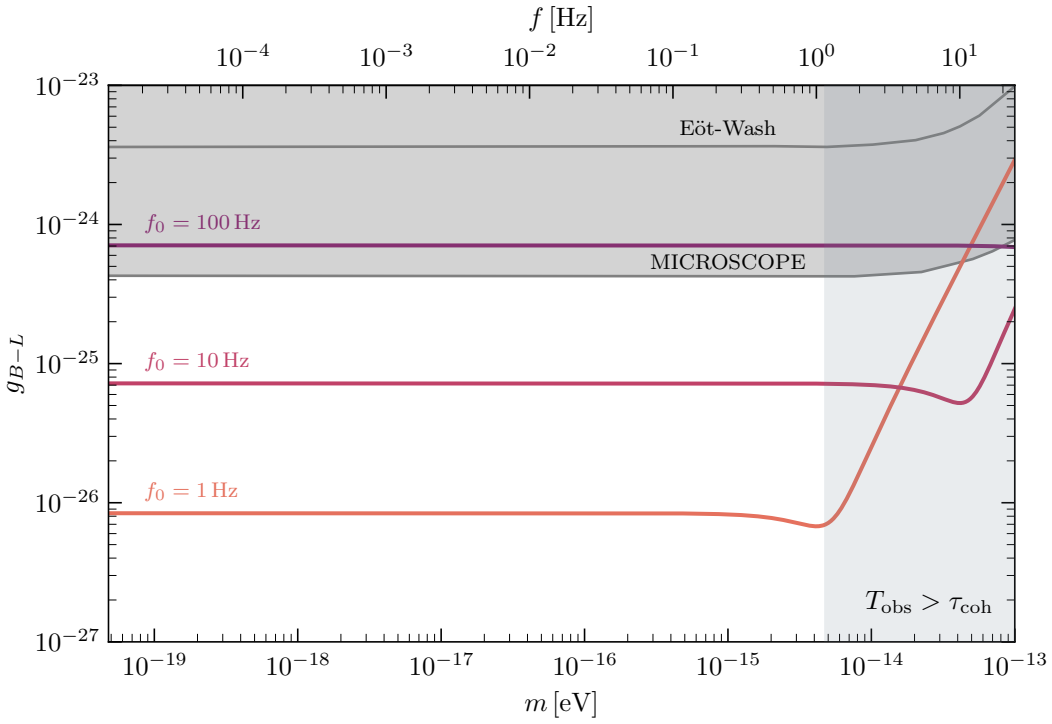


Figure 5: The 90% CL limits on the $B-L$ gauge coupling, g_{B-L}, for ultralight $B-L$ DM placed by an optomechanical cavity setup using our statistical framework. The limits using our three-peak analysis strategy (solid) for three resonance frequencies, $f_0 = 1\,\mathrm{Hz}$, $10\,\mathrm{Hz}$ and $100\,\mathrm{Hz}$ are shown. Existing bounds from MICROSCOPE [89] and Eöt-Wash [90] are shown in grey. The shaded region indicates where the observation time $T_{\mathrm{obs}} = 10T_{\oplus}$ becomes greater than the coherence time, where our framework is no longer valid. The top axis shows the Compton frequency for a given DM mass in Hz.

$B-L$-coupled DM,

$$g_{B-L} = \frac{\beta^{\mathrm{lim}}}{a_0 \Delta_{ij}} \sqrt{\frac{2S_{aa}}{T}} \tag{4.12}$$

We show our limits in Fig. 5 for three choices of resonance frequency: 1 Hz, 10 Hz and 100 Hz. For all but the last of these frequencies, we are able to exclude new regions of the UDLM $B-L$ parameter space, best excluded by the fifth-force satellite experiment MICROSCOPE [89] and torsion-balance experiment Eöt-Wash [90]. This showcases the power of such sensors in searching for this DM candidate, as was first pointed out in Ref. [63]. In a single-peak analysis focusing solely on the Compton peak, our limits would be weakened by approximately a factor of 2, as can be seen from Fig. 4. This difference becomes more dramatic for sensors located closer to the equator.

We only extend our limits to where they are appropriate. At the higher mass range, we are limited by keeping our observation time shorter than the coherence time, $T_{\mathrm{obs}} \ll \tau_{\mathrm{coh}} \simeq 10\,\mathrm{d}\,(5 \times 10^{-15}\,\mathrm{eV}/m)$. At the lower mass range, we must keep our observation time longer than a day (corresponding to $m \simeq 5 \times 10^{-20}$ eV) to be able to resolve the three

peaks $T_{\rm obs} \gtrsim 2\pi/\omega_\oplus$. This leads to the mass range $5 \times 10^{-20}\,{\rm eV} \lesssim m \lesssim 5 \times 10^{-15}\,{\rm eV}$ for where our study is valid.

We note that $\sigma(\omega)$, though mostly slowly varying in the frequency width $\Delta\omega = \omega_\oplus$, does exhibit a large gradient around the resonance frequency of the cavity. In the neighbourhood of this frequency, our assumption that $\sigma(\omega)$ does not vary greatly in the above range is incorrect, and a more careful analysis in which all three peaks take on different noise levels would have to be conducted for more representative limits. However, we do not expect that our limits would differ greatly from our calculation and, at any rate, would still smoothly join to the regimes on either side of the resonance frequency, where our assumption holds.

5 Future Directions

5.1 Longer Observation Times

In this work, we have focused on the wave vector DM signal within time scales much shorter than the coherence time, $\tau_{\rm coh} = 2\pi/mv_0^2 \simeq 50\,{\rm d}\,(10^{-15}\,{\rm eV}/m)$. This allowed us to treat the amplitudes and phases of the three different components of the vector to be constant random variables. Realistically, there would be modulations giving these random variables time dependence—corrections of the order $\mathcal{O}(t/\tau_{\rm coh})$. Simultaneously, there would be spatial variations/correlations due to the finite distance covered by the Earth/detector during the observation, leading to corrections of the order $\mathcal{O}(v_0 t/\ell_{\rm coh}) = \mathcal{O}(t/\tau_{\rm coh})$ again. For longer observation times, $T_{\rm obs} \gg \tau_{\rm coh}$, such modulations necessarily need to be taken into account. While we can easily generate the realistic time-series for such long time-scale signals (see top panel of Fig. 2), a more comprehensive treatment of how it affects our limits is left for future work.

5.2 Expanding the Mass Window

The detection scheme considered in this paper is one where the detector points in a specific fixed direction locally on Earth while rotating along with it. As noted above, in the short observation time scenario we are bounded from below by a day (corresponding to $m \simeq 5\times10^{-20}$ eV) and from above by the coherence time scale $\tau_{\rm coh} \simeq 10\,{\rm d}\,(5\times10^{-15}\,{\rm eV}/m)$ to be able to resolve the distinctive 3 peaks. To have a larger working window where we can neglect the previously mentioned corrections, the masses we can probe using this setup lie in the range $5 \times 10^{-20}\,{\rm eV} \lesssim m \lesssim 5 \times 10^{-15}\,{\rm eV}$. To expand this window towards higher masses, we need to push the lower bound coming from $T_{\rm obs} > 1\,{\rm d}$.

Instead of a fixed detector rotating with the Earth, a detector can also be made to rotate at an angular frequency faster than a day. For example, if $\omega_{\rm exp} \simeq 2\pi/(1\,{\rm min})$, then the detector needs to collect data for only a few minutes to be able to isolate the three peaks. With $\tau_{\rm coh} \simeq 15\,{\rm min}\,(5 \times 10^{-12}\,{\rm eV}/m)$, we can probe masses up to $m \simeq 5 \times 10^{-12}$ eV. Note that while the time signal would contain modulations due to Earth's rotation, the effects would be suppressed by $\mathcal{O}(\omega_\oplus/\omega_{\rm exp})$. Furthermore, in the frequency space, this modulation would split the three peaks at $\omega_{\rm left} = m - \omega_{\rm exp}$, $\omega_{\rm middle} = m$, and $\omega_{\rm right} = m + \omega_{\rm exp}$, into nine

peaks (each splitting into three). However, unless the frequency resolution $\Delta\omega$ becomes smaller than $\sim \omega_\oplus$, the experiment would not be able to resolve this splitting due to the Earth's rotation. Thus, we expect our whole analysis in this paper to carry forward, with $\omega_\oplus$ replaced by $\omega_{\rm exp}$ everywhere. Furthermore, such a setup would also be beneficial for the optomechanical light cavities we considered in Section 4, where their typical laser coherence times are of the order of hours and not days.

6 Conclusions

We have provided an analysis strategy for inferring the properties of ultralight vector dark matter from terrestrial experiments, taking into account the stochastic and vector nature of the field (see Fig. 1). Our main results are suited for observation times that are longer than a sidereal day, but shorter than the coherence time. They are as follows:

- We focused on the signal in Fourier space, deriving the power spectral density that such dark matter is expected to leave on an axial sensor that is sensitive to its oscillatory signal. Accounting for the rotation of the Earth, we found that the signal manifests as three peaks at definite frequencies but with random amplitudes (see Fig. 2).

- We derived the likelihoods in each of the signal-containing bins in Fourier space. We did this by considering the marginal likelihood after integrating out the six random variables exhibited by the ULDM signal in the coherent regime: the three Rayleigh amplitudes and the three uniformly distributed DM phases (see Eq. (3.2) and Fig. 3). We found that the general elliptical motion of the vector field afforded us a significantly simpler analysis in Fourier space than the linear polarization assumption since, in the former, all peaks become statistically uncorrelated.

- We drew exclusion limits on a generalised, dimensionless parameter that can be reinterpreted in the context of a concrete sensor setup and dark matter model. We did this via a series of log-likelihood ratio tests following a hybrid frequentist-Bayesian approach. Crucially, we found that, unlike analyses focusing on only a single peak, our approach retains constraining power for experimental setups at all latitudes. This is because we make use of the entire DM signal, which is distributed across all three peaks, instead of constraining ourselves to the signal in any one peak, which is dependent on the latitude of the experiment (see Fig. 4).

- We considered a specific sensor technology (the optomechanical light cavity) and dark matter model (ultralight dark matter stemming from a new gauged $U(1)_{B-L}$ symmetry) as a concrete application of our analysis strategy. We recast our general limit onto one on the gauge coupling of this model, g_{B-L}, finding that long-exposure cavities can rule out previously unexplored regions of the $B-L$ parameter space (see Fig. 5).

In this work, we have established a framework for future experimental efforts in the detection of ultralight vector dark matter. Novel direct-detection probes require an understanding of how the signal of ultralight vector dark matter behaves in our local neighborhood and manifests itself in a sensor. We hope that our work aids in (i) designing search strategies using emerging detector technologies that are not traditionally used for dark matter searches, and (ii) in understanding how well a given model can be tested in the context of calls for Big Science projects using quantum sensing [62].

Acknowledgments

We would like to thank Andrew Long for insightful discussions throughout this work, as well as John Carlton, Daniel Carney, Zhen Liu, and Yue Zhao for their valuable feedback. DA would like to thank Yunan Gao and Juehang Qin for helpful discussions regarding our statistical treatment. CT & DA are supported by the National Science Foundation under award 2046549. MA & MJ were partly supported by DOE grant DE-SC0021619, and MJ is currently supported by a Leverhulme Trust Research Project (RPG-2022-145).

References

[1] G. Bertone and D. Hooper, *History of dark matter*, *Rev. Mod. Phys.* **90** (2018) 045002 [1605.04909].

[2] K. Freese, *Status of Dark Matter in the Universe*, *Int. J. Mod. Phys.* **1** (2017) 325 [1701.01840].

[3] T.D. Brandt, *Constraints on MACHO Dark Matter from Compact Stellar Systems in Ultra-Faint Dwarf Galaxies*, *Astrophys. J. Lett.* **824** (2016) L31 [1605.03665].

[4] N. Dalal and A. Kravtsov, *Excluding fuzzy dark matter with sizes and stellar kinematics of ultrafaint dwarf galaxies*, *Phys. Rev. D* **106** (2022) 063517 [2203.05750].

[5] S. Hawking, *Gravitationally collapsed objects of very low mass*, *Mon. Not. Roy. Astron. Soc.* **152** (1971) 75.

[6] G.F. Chapline, *Cosmological effects of primordial black holes*, *Nature* **253** (1975) 251.

[7] W. Hu, R. Barkana and A. Gruzinov, *Cold and fuzzy dark matter*, *Phys. Rev. Lett.* **85** (2000) 1158 [astro-ph/0003365].

[8] P.H. Frampton, M. Kawasaki, F. Takahashi and T.T. Yanagida, *Primordial Black Holes as All Dark Matter*, *JCAP* **04** (2010) 023 [1001.2308].

[9] B. Carr, K. Kohri, Y. Sendouda and J. Yokoyama, *Constraints on primordial black holes*, *Rept. Prog. Phys.* **84** (2021) 116902 [2002.12778].

[10] B. Carr and F. Kuhnel, *Primordial Black Holes as Dark Matter: Recent Developments*, *Ann. Rev. Nucl. Part. Sci.* **70** (2020) 355 [2006.02838].

[11] S. Weinberg, *A New Light Boson?*, *Phys. Rev. Lett.* **40** (1978) 223.

[12] F. Wilczek, *Problem of Strong P and T Invariance in the Presence of Instantons*, *Phys. Rev. Lett.* **40** (1978) 279.

[13] L. Di Luzio, M. Giannotti, E. Nardi and L. Visinelli, *The landscape of QCD axion models*, *Phys. Rept.* **870** (2020) 1 [2003.01100].

[14] A. Arvanitaki, S. Dimopoulos, S. Dubovsky, N. Kaloper and J. March-Russell, *String Axiverse*, *Phys. Rev. D* **81** (2010) 123530 [0905.4720].

[15] A. Ringwald, *Axions and Axion-Like Particles*, in *49th Rencontres de Moriond on Electroweak Interactions and Unified Theories*, pp. 223–230, 2014 [1407.0546].

[16] L. Hui, J.P. Ostriker, S. Tremaine and E. Witten, *Ultralight scalars as cosmological dark matter*, *Phys. Rev. D* **95** (2017) 043541 [1610.08297].

[17] E.G.M. Ferreira, *Ultra-light dark matter*, *Astron. Astrophys. Rev.* **29** (2021) 7 [2005.03254].

[18] J. Jaeckel, *A force beyond the Standard Model - Status of the quest for hidden photons*, *Frascati Phys. Ser.* **56** (2012) 172 [1303.1821].

[19] M. Fabbrichesi, E. Gabrielli and G. Lanfranchi, *The Dark Photon*, 2005.01515.

[20] P.W. Graham, J. Mardon and S. Rajendran, *Vector Dark Matter from Inflationary Fluctuations*, *Phys. Rev. D* **93** (2016) 103520 [1504.02102].

[21] P. Agrawal, N. Kitajima, M. Reece, T. Sekiguchi and F. Takahashi, *Relic Abundance of Dark Photon Dark Matter*, *Phys. Lett. B* **801** (2020) 135136 [1810.07188].

[22] R.T. Co, A. Pierce, Z. Zhang and Y. Zhao, *Dark Photon Dark Matter Produced by Axion Oscillations*, *Phys. Rev. D* **99** (2019) 075002 [1810.07196].

[23] J.A. Dror, K. Harigaya and V. Narayan, *Parametric Resonance Production of Ultralight Vector Dark Matter*, *Phys. Rev. D* **99** (2019) 035036 [1810.07195].

[24] M. Bastero-Gil, J. Santiago, L. Ubaldi and R. Vega-Morales, *Vector dark matter production at the end of inflation*, *JCAP* **04** (2019) 015 [1810.07208].

[25] A.J. Long and L.-T. Wang, *Dark Photon Dark Matter from a Network of Cosmic Strings*, *Phys. Rev. D* **99** (2019) 063529 [1901.03312].

[26] E.W. Kolb and A.J. Long, *Completely dark photons from gravitational particle production during the inflationary era*, *JHEP* **03** (2021) 283 [2009.03828].

[27] R.T. Co, K. Harigaya and A. Pierce, *Gravitational waves and dark photon dark matter from axion rotations*, *JHEP* **12** (2021) 099 [2104.02077].

[28] P. Adshead, K.D. Lozanov and Z.J. Weiner, *Dark photon dark matter from an oscillating dilaton*, *Phys. Rev. D* **107** (2023) 083519 [2301.07718].

[29] D. Cyncynates and Z.J. Weiner, *Detectable, defect-free dark photon dark matter*, 2310.18397.

[30] O. Özsoy and G. Tasinato, *Vector dark matter, inflation and non-minimal couplings with gravity*, 2310.03862.

[31] M.A. Amin, M. Jain, R. Karur and P. Mocz, *Small-scale structure in vector dark matter*, *JCAP* **08** (2022) 014 [2203.11935].

[32] M. Gorghetto, E. Hardy, J. March-Russell, N. Song and S.M. West, *Dark photon stars: formation and role as dark matter substructure*, *JCAP* **08** (2022) 018 [2203.10100].

[33] M. Jain, M.A. Amin, J. Thomas and W. Wanichwecharungruang, *Kinetic relaxation and Bose-star formation in multicomponent dark matter*, *Phys. Rev. D* **108** (2023) 043535 [2304.01985].

[34] A. Pierce, K. Riles and Y. Zhao, *Searching for Dark Photon Dark Matter with Gravitational Wave Detectors*, *Phys. Rev. Lett.* **121** (2018) 061102 [1801.10161].

[35] L. Badurina et al., *AION: An Atom Interferometer Observatory and Network*, *JCAP* **05** (2020) 011 [1911.11755].

[36] D. Carney, A. Hook, Z. Liu, J.M. Taylor and Y. Zhao, *Ultralight dark matter detection with mechanical quantum sensors*, *New J. Phys.* **23** (2021) 023041 [1908.04797].

[37] Y. Michimura, T. Fujita, S. Morisaki, H. Nakatsuka and I. Obata, *Ultralight vector dark matter search with auxiliary length channels of gravitational wave detectors*, *Phys. Rev. D* **102** (2020) 102001 [2008.02482].

[38] J. Manley, M.D. Chowdhury, D. Grin, S. Singh and D.J. Wilson, *Searching for vector dark matter with an optomechanical accelerometer*, *Phys. Rev. Lett.* **126** (2021) 061301 [2007.04899].

[39] Y. Chen, M. Jiang, J. Shu, X. Xue and Y. Zeng, *Dissecting axion and dark photon with a network of vector sensors*, *Phys. Rev. Res.* **4** (2022) 033080 [2111.06732].

[40] A. Caputo, A.J. Millar, C.A.J. O'Hare and E. Vitagliano, *Dark photon limits: A handbook*, *Phys. Rev. D* **104** (2021) 095029 [2105.04565].

[41] M. Abe, P. Adamson, M. Borcean, D. Bortoletto, K. Bridges, S.P. Carman et al., *Matter-wave atomic gradiometer interferometric sensor (magis-100)*, *Quantum Science and Technology* **6** (2021) 044003.

[42] H. Nakatsuka, S. Morisaki, T. Fujita, J. Kume, Y. Michimura, K. Nagano et al., *Stochastic effects on observation of ultralight bosonic dark matter*, 2205.02960.

[43] J.W. Foster, N.L. Rodd and B.R. Safdi, *Revealing the Dark Matter Halo with Axion Direct Detection*, *Phys. Rev. D* **97** (2018) 123006 [1711.10489].

[44] LIGO Scientific, KAGRA, Virgo collaboration, *Constraints on dark photon dark matter using data from LIGO's and Virgo's third observing run*, *Phys. Rev. D* **105** (2022) 063030 [2105.13085].

[45] M. Lisanti, M. Moschella and W. Terrano, *Stochastic properties of ultralight scalar field gradients*, *Phys. Rev. D* **104** (2021) 055037 [2107.10260].

[46] L. Badurina, D. Blas and C. McCabe, *Refined ultralight scalar dark matter searches with compact atom gradiometers*, *Phys. Rev. D* **105** (2022) 023006 [2109.10965].

[47] L. Badurina, V. Gibson, C. McCabe and J. Mitchell, *Ultralight dark matter searches at the sub-Hz frontier with atom multigradiometry*, *Phys. Rev. D* **107** (2023) 055002 [2211.01854].

[48] L. Badurina, A. Beniwal and C. McCabe, *Super-Nyquist ultralight dark matter searches with broadband atom gradiometers*, *Phys. Rev. D* **108** (2023) 083016 [2306.16477].

[49] A.L. Miller and L. Mendes, *First search for ultralight dark matter with a space-based gravitational-wave antenna: LISA Pathfinder*, *Phys. Rev. D* **107** (2023) 063015 [2301.08736].

[50] Z. Ahmed et al., *Quantum Sensing for High Energy Physics*, in *First workshop on Quantum Sensing for High Energy Physics*, 3, 2018 [1803.11306].

[51] M.S. Safronova, D. Budker, D. DeMille, D.F.J. Kimball, A. Derevianko and C.W. Clark, *Search for new physics with atoms and molecules*, *Rev. Mod. Phys.* **90** (2018) 025008.

[52] J. Beckey, D. Carney and G. Marocco, *Quantum measurements in fundamental physics: a user's manual*, 2311.07270.

[53] D. Carney et al., *Mechanical Quantum Sensing in the Search for Dark Matter*, *Quantum Sci. Technol.* **6** (2021) 024002 [2008.06074].

[54] G. Higgins, S. Kalia and Z. Liu, *Maglev for Dark Matter: Dark-photon and axion dark matter sensing with levitated superconductors*, 2310.18398.

[55] C.G. Baker, W.P. Bowen, P. Cox, M.J. Dolan, M. Goryachev and G. Harris, *Optomechanical Dark Matter Direct Detection*, 2306.09726.

[56] E. Kilian et al., *Dark Matter Searches with Levitated Sensors*, 2401.17990.

[57] D.C. Moore and A.A. Geraci, *Searching for new physics using optically levitated sensors*, *Quantum Sci. Technol.* **6** (2021) 014008 [2008.13197].

[58] F. Monteiro, G. Afek, D. Carney, G. Krnjaic, J. Wang and D.C. Moore, *Search for composite dark matter with optically levitated sensors*, *Phys. Rev. Lett.* **125** (2020) 181102 [2007.12067].

[59] M. Blencowe, *Quantum electromechanical systems*, *Physics Reports* **395** (2004) 159.

[60] M. Aspelmeyer, T.J. Kippenberg and F. Marquardt, *Cavity optomechanics*, *Rev. Mod. Phys.* **86** (2014) 1391.

[61] O. Buchmueller et al., *Snowmass 2021: Quantum Sensors for HEP Science – Interferometers, Mechanics, Traps, and Clocks*, in *Snowmass 2021*, 3, 2022 [2203.07250].

[62] WINDCHIME collaboration, *Snowmass 2021 White Paper: The Windchime Project*, in *Snowmass 2021*, 3, 2022 [2203.07242].

[63] P.W. Graham, D.E. Kaplan, J. Mardon, S. Rajendran and W.A. Terrano, *Dark Matter Direct Detection with Accelerometers*, *Phys. Rev. D* **93** (2016) 075029 [1512.06165].

[64] M. Jain and M.A. Amin, *Polarized solitons in higher-spin wave dark matter*, *Phys. Rev. D* **105** (2022) 056019 [2109.04892].

[65] M.A. Fedderke, P.W. Graham, D.F.J. Kimball and S. Kalia, *Earth as a transducer for dark-photon dark-matter detection*, *Phys. Rev. D* **104** (2021) 075023 [2106.00022].

[66] PPTA collaboration, *High-precision search for dark photon dark matter with the Parkes Pulsar Timing Array*, *Phys. Rev. Res.* **4** (2022) L012022 [2112.07687].

[67] M.A. Fedderke, P.W. Graham, D.F. Jackson Kimball and S. Kalia, *Search for dark-photon dark matter in the SuperMAG geomagnetic field dataset*, *Phys. Rev. D* **104** (2021) 095032 [2108.08852].

[68] J. Frerick, J. Jaeckel, F. Kahlhoefer and K. Schmidt-Hoberg, *Riding the dark matter wave: Novel limits on general dark photons from LISA Pathfinder*, *Phys. Lett. B* **848** (2024) 138328 [2310.06017].

[69] C. Beaufort, M. Bastero-Gil, A. Catalano, D.-S. Erfani-Harami, O. Guillaudin, D. Santos et al., *Directional detection of meV dark photons with Dandelion*, 2310.16505.

[70] L. Sun, B.J.J. Slagmolen and J. Qin, *Search for ultralight vector dark matter with a Torsion Pendulum Dual Oscillator*, 2402.08935.

[71] H.-Y. Zhang, M. Jain and M.A. Amin, *Polarized vector oscillons*, *Phys. Rev. D* **105** (2022) 096037 [2111.08700].

[72] M. Jain, *Soliton stars in Yang-Mills-Higgs theories*, *Phys. Rev. D* **106** (2022) 085011 [2205.03418].

[73] M. Jain and M.A. Amin, *i-SPin: an integrator for multicomponent Schrödinger-Poisson systems with self-interactions*, *JCAP* **04** (2023) 053 [2211.08433].

[74] P. Arias, D. Cadamuro, M. Goodsell, J. Jaeckel, J. Redondo and A. Ringwald, *WISPy Cold Dark Matter*, *JCAP* **06** (2012) 013 [1201.5902].

[75] G. Alonso-Álvarez, T. Hugle and J. Jaeckel, *Misalignment \& Co.: (Pseudo-)scalar and vector dark matter with curvature couplings*, *JCAP* **02** (2020) 014 [1905.09836].

[76] B. Himmetoglu, C.R. Contaldi and M. Peloso, *Instability of anisotropic cosmological solutions supported by vector fields*, *Phys. Rev. Lett.* **102** (2009) 111301 [0809.2779].

[77] B. Himmetoglu, C.R. Contaldi and M. Peloso, *Ghost instabilities of cosmological models with vector fields nonminimally coupled to the curvature*, *Phys. Rev. D* **80** (2009) 123530 [0909.3524].

[78] M. Karciauskas and D.H. Lyth, *On the health of a vector field with (R A^2)/6 coupling to gravity*, *JCAP* **11** (2010) 023 [1007.1426].

[79] G.P. Centers et al., *Stochastic fluctuations of bosonic dark matter*, *Nature Commun.* **12** (2021) 7321 [1905.13650].

[80] E.J. Groth, *Probability distributions related to power spectra.*, *ApJS* **29** (1975) 285.

[81] G. Cowan, K. Cranmer, E. Gross and O. Vitells, *Asymptotic formulae for likelihood-based tests of new physics*, *Eur. Phys. J. C* **71** (2011) 1554 [1007.1727].

[82] H. Chernoff, *On the Distribution of the Likelihood Ratio*, *Ann. Math. Stat.* **25** (1954) 573.

[83] S. Algeri, J. Aalbers, K. Dundas Morå and J. Conrad, *Searching for new phenomena with profile likelihood ratio tests*, *Nature Rev. Phys.* **2** (2020) 245 [1911.10237].

[84] M.E. Peskin and D.V. Schroeder, *An Introduction to quantum field theory*, Addison-Wesley, Reading, USA (1995).

[85] L. Basso, A. Belyaev, S. Moretti and C.H. Shepherd-Themistocleous, *Phenomenology of the minimal B-L extension of the Standard model: Z' and neutrinos*, *Phys. Rev. D* **80** (2009) 055030 [0812.4313].

[86] S. Kanemura, T. Matsui and H. Sugiyama, *Neutrino mass and dark matter from gauged $U(1)_{B-L}$ breaking*, *Phys. Rev. D* **90** (2014) 013001 [1405.1935].

[87] A.A. Clerk, M.H. Devoret, S.M. Girvin, F. Marquardt and R.J. Schoelkopf, *Introduction to quantum noise, measurement, and amplification*, *Rev. Mod. Phys.* **82** (2010) 1155 [0810.4729].

[88] LIGO Scientific collaboration, *LIGO: The Laser interferometer gravitational-wave observatory*, *Rept. Prog. Phys.* **72** (2009) 076901 [0711.3041].

[89] MICROSCOPE collaboration, *MICROSCOPE Mission: Final Results of the Test of the Equivalence Principle*, *Phys. Rev. Lett.* **129** (2022) 121102 [2209.15487].

[90] T.A. Wagner, S. Schlamminger, J.H. Gundlach and E.G. Adelberger, *Torsion-balance tests of the weak equivalence principle*, *Class. Quant. Grav.* **29** (2012) 184002 [1207.2442].

[91] P. Mocz, M. Vogelsberger, V.H. Robles, J. Zavala, M. Boylan-Kolchin, A. Fialkov et al.,

Galaxy formation with BECDM – I. Turbulence and relaxation of idealized haloes, *Mon. Not. Roy. Astron. Soc.* **471** (2017) 4559 [1705.05845].

[92] F. Edwards, E. Kendall, S. Hotchkiss and R. Easther, *PyUltraLight: A Pseudo-Spectral Solver for Ultralight Dark Matter Dynamics*, *JCAP* **10** (2018) 027 [1807.04037].

[93] M. Jain, M.A. Amin and H. Pu, *Integrator for general spin-s Gross-Pitaevskii systems*, *Phys. Rev. E* **108** (2023) 055305 [2305.01675].

[94] P. Adshead and K.D. Lozanov, *Self-gravitating Vector Dark Matter*, *Phys. Rev. D* **103** (2021) 103501 [2101.07265].

A Equipartition between Longitudinal and Transverse Modes

The equation of motion for the field $\mathbf{\Psi}$ (written in Fourier space) is

$$i\dot{\Psi}^i_{\boldsymbol{k}} = \frac{k^2}{2m}\Psi^i_{\boldsymbol{k}} - (4\pi G m^2)\frac{1}{V}\sum_{\boldsymbol{p},\boldsymbol{q},\boldsymbol{\ell}} \delta_{\boldsymbol{k}+\boldsymbol{p}-\boldsymbol{q}-\boldsymbol{\ell}}\,|\boldsymbol{q}-\boldsymbol{p}|^{-2}\,\Psi^{j\,*}_{\boldsymbol{p}}\Psi^j_{\boldsymbol{q}}\Psi^i_{\boldsymbol{\ell}}\,. \tag{A.1}$$

Now, we wish to decompose the field into transverse and longitudinal pieces. Let us call them $\eta_{\boldsymbol{k}}$ and $\zeta_{\boldsymbol{k}}$. That is,

$$\eta^i_{\boldsymbol{k}} = \mathcal{P}^{ij}_{\boldsymbol{k}_\perp}\,\Psi^j_{\boldsymbol{k}} \qquad \text{and} \qquad \zeta^i_{\boldsymbol{k}} = \mathcal{P}^{ij}_{\boldsymbol{k}_{||}}\,\Psi^j_{\boldsymbol{k}}\,, \tag{A.2}$$

where

$$\mathcal{P}^{ij}_{\boldsymbol{k}_\perp} \equiv \left(\delta^{ij} - \frac{k^i k^j}{k^2}\right) \qquad \text{and} \qquad \mathcal{P}^{ij}_{\boldsymbol{k}_{||}} \equiv \frac{k^i k^j}{k^2} \tag{A.3}$$

are the two mutually exclusive projection matrices. Let us hit the above equation of motion by the transverse (longitudinal) projection operator to get the evolution for $\eta^i_{\boldsymbol{k}}$ ($\zeta^i_{\boldsymbol{k}}$). Also then split each $\Psi^i_{\boldsymbol{k}}$ into $\eta^i_{\boldsymbol{k}}$ and $\zeta^i_{\boldsymbol{k}}$. We get

$$\begin{aligned}
i\dot{\eta}^i_{\boldsymbol{k}} &= E_{\boldsymbol{k}}\eta^i_{\boldsymbol{k}} - (4\pi G m^2)\frac{1}{V}\sum_{\boldsymbol{p},\boldsymbol{q},\boldsymbol{\ell}} \delta_{\boldsymbol{k}+\boldsymbol{p}-\boldsymbol{q}-\boldsymbol{\ell}}\,|\boldsymbol{q}-\boldsymbol{p}|^{-2}\,(\eta^{n\,*}_{\boldsymbol{p}} + \zeta^{n\,*}_{\boldsymbol{p}})(\eta^n_{\boldsymbol{q}} + \zeta^n_{\boldsymbol{q}})(\mathcal{P}^{ij}_{\boldsymbol{k}_\perp}\eta^j_{\boldsymbol{\ell}} + \mathcal{P}^{ij}_{\boldsymbol{k}_\perp}\zeta^j_{\boldsymbol{\ell}}) \\
i\dot{\zeta}^i_{\boldsymbol{k}} &= E_{\boldsymbol{k}}\zeta^i_{\boldsymbol{k}} - (4\pi G m^2)\frac{1}{V}\sum_{\boldsymbol{p},\boldsymbol{q},\boldsymbol{\ell}} \delta_{\boldsymbol{k}+\boldsymbol{p}-\boldsymbol{q}-\boldsymbol{\ell}}\,|\boldsymbol{q}-\boldsymbol{p}|^{-2}\,(\eta^{n\,*}_{\boldsymbol{p}} + \zeta^{n\,*}_{\boldsymbol{p}})(\eta^n_{\boldsymbol{q}} + \zeta^n_{\boldsymbol{q}})(\mathcal{P}^{ij}_{\boldsymbol{k}_{||}}\eta^j_{\boldsymbol{\ell}} + \mathcal{P}^{ij}_{\boldsymbol{k}_{||}}\zeta^j_{\boldsymbol{\ell}})\,.
\end{aligned} \tag{A.4}$$

Notice that not only are the longitudinal and transverse pieces coupled to one another, but more importantly they source each other. Hence, we expect virialization between them due to such non-linear gravitational dynamics during DM halo formation, ultimately leading to equipartition of power amongst them. That is, 2/3 of the total power would be in the transverse sector, with the remaining 1/3 in the longitudinal sector.

Using codes based on the split-Fourier technique [73, 91–93], we have performed simulations of the Schrödinger -Poisson vector system [31, 64, 94] (physical space version of Eq. (A.1)):

$$i\frac{\partial}{\partial t}\mathbf{\Psi} = -\frac{1}{2m}\nabla^2\mathbf{\Psi} + m\,\Phi\,\mathbf{\Psi}\,, \qquad\qquad \nabla^2\Phi = 4\pi G m^2\,\mathbf{\Psi}^\dagger\mathbf{\Psi}\,, \tag{A.5}$$

with different initial conditions. Without loss of generality, we can parameterize the initial power spectrum by a single parameter Υ as

$$\langle\hat{\psi}^{i\,*}_{\boldsymbol{k}}\,\hat{\psi}^j_{\boldsymbol{p}}\rangle = \delta_{\boldsymbol{k},\boldsymbol{p}}\,\mathcal{F}_{\boldsymbol{k}}\left[\Upsilon\,\mathcal{P}^{ij}_{\boldsymbol{k}_\perp} + (1-2\Upsilon)\mathcal{P}^{ij}_{\boldsymbol{k}_{||}}\right]. \tag{A.6}$$

Here, $\mathcal{F}_{\boldsymbol{k}}$ is some arbitrary Fourier profile function (we shall take it to be a Gaussian in our simulations, such that the mean density is larger than the critical Jeans density so as to

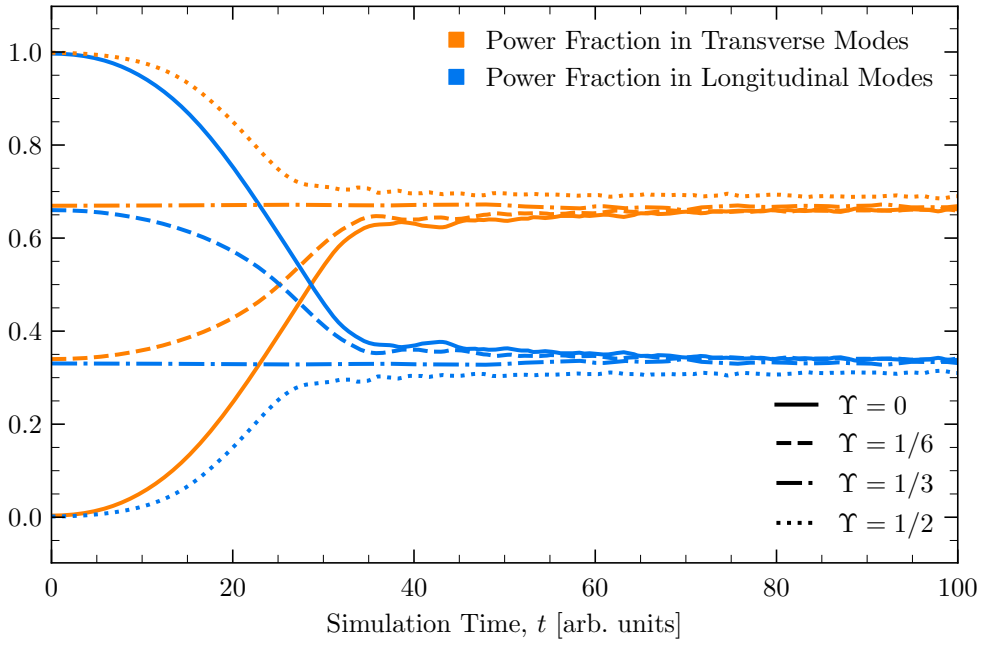


Figure 6: Evolution of the fractional powers in transverse and longitudinal modes around halo formation for four different simulations with initial conditions characterized by Υ: $\Upsilon = 0$ (solid), $\Upsilon = 1/6$ (dashed), $\Upsilon = 1/3$ (dot-dashed), and $\Upsilon = 1/2$ (dotted). The convergence of the fractional power in transverse modes towards 2/3 and that in longitudinal modes towards 1/3 demonstrates the ultimate equipartition of power.

form a halo). The parameter $\Upsilon \in [0, 1/2]$, with $\Upsilon = 0$ giving a longitudinal-only spectrum and $\Upsilon = 1/2$ giving a transverse-only spectrum. For $\Upsilon = 1/3$, we have equipartition.

To begin with, for every mode $\boldsymbol{k}$, we pick a 6-dimensional normal random variable, packaged as a 3-dimensional complex number $\hat{\boldsymbol{\epsilon}}_{\boldsymbol{k}}$, that is further restricted to lie uniformly on an S_5 so that it is unit normalized. That is, $\langle \hat{\epsilon}^{i*}_{\boldsymbol{k}} \hat{\epsilon}^{j}_{\boldsymbol{p}} \rangle = \delta_{\boldsymbol{k},\boldsymbol{p}}\, \delta^{ij}$. We then hit it with the transverse and longitudinal projection operators to get $\hat{\epsilon}^{i}_{\boldsymbol{k}_\perp} = \mathcal{P}^{ij}_{\boldsymbol{k}_\perp} \hat{\epsilon}^{j}_{\boldsymbol{k}}$ and $\hat{\epsilon}_{\boldsymbol{k}_{||}} = \mathcal{P}^{ij}_{\boldsymbol{k}_{||}} \hat{\epsilon}^{j}_{\boldsymbol{k}}$. With these, we construct the full transverse and longitudinal initial fields as

$$\{\eta^i(\boldsymbol{x}, 0), \zeta^i(\boldsymbol{x}, 0)\} = \int \frac{\mathrm{d}^3 k}{(2\pi)^3} \{\eta^i_{\boldsymbol{k}}(0), \zeta^i_{\boldsymbol{k}}(0)\}\, e^{-i\boldsymbol{k}\cdot\boldsymbol{x}} = \int \frac{\mathrm{d}^3 k}{(2\pi)^3} \sqrt{\mathcal{F}_{\boldsymbol{k}}}\, \{\hat{\epsilon}^i_{\boldsymbol{k}_\perp}, \hat{\epsilon}^i_{\boldsymbol{k}_{||}}\}\, e^{-i\boldsymbol{k}\cdot\boldsymbol{x}}\,, \tag{A.7}$$

with the full field being

$$\Psi^i(\boldsymbol{x}, 0) = \sqrt{\Upsilon}\, \eta^i(\boldsymbol{x}, 0) + \sqrt{1 - 2\Upsilon}\, \zeta^i(\boldsymbol{x}, 0)\,. \tag{A.8}$$

With this as the initial condition, we evolve the SP system (A.5). In Fig. 6 we present simulation results for various different initial conditions and different values of Υ.

B Derivation of Marginal Likelihood with Stochastic Field Amplitude

The full signal in time space is given by

$$\hat{\mathcal{S}}(t) = \text{signal}(t) + \hat{\mathcal{N}}(t)\,, \tag{B.1}$$

where $\hat{\mathcal{N}} \sim N(0, \sigma_t)$, with $\sigma_t^2 \equiv \sigma^2/\Delta t$ and σ^2 being the equivalent of the noise PSD in frequency space. From this, we get that the (two-sided) periodogram, $\mathcal{P}'$, normalised by the noise PSD is given by

$$\frac{\hat{\mathcal{P}}'}{\sigma^2} = \frac{\Delta t^2}{T}\frac{|\hat{\mathcal{S}}^2(\omega)|}{\sigma^2} = |\hat{X}_R + \text{signal}_R(\omega)|^2 + |\hat{X}_I + \text{signal}_I(\omega)|^2\,. \tag{B.2}$$

Here, both $\hat{X}_R$ and $\hat{X}_I$ are such that $\hat{X}_i \sim N(0, 1/\sqrt{2})$. The one-sided, noise-normalised periodogram, $\hat{\mathcal{P}}/\sigma^2$, therefore follows a non-central χ^2 distribution with non-centrality parameter

$$\begin{aligned}
\lambda &= \text{signal}_R^2(\omega) + \text{signal}_I^2(\omega) \\
&= \frac{\mathcal{A}^2 T}{8\,\sigma^2}\Big\{\cos^2\phi\left[\alpha_x^2 + \alpha_y^2 + 2\alpha_x\alpha_y\sin(\varphi_y - \varphi_x)\right]\delta_{\omega,s} \\
&\qquad + \cos^2\phi\left[\alpha_x^2 + \alpha_y^2 - 2\alpha_x\alpha_y\sin(\varphi_y - \varphi_x)\right]\delta_{\omega,d} \\
&\qquad + 4\sin^2\phi\,\alpha_z^2\delta_{\omega,m}\Big\}\,.
\end{aligned} \tag{B.3}$$

Introducing randomness in the parameters α's and φ's, with prior $\Pi'(\{\alpha_i, \varphi_i\})$, the marginalized likelihood is

$$\mathcal{L} = \int \mathrm{d}\alpha_x \mathrm{d}\alpha_y \mathrm{d}\alpha_z \mathrm{d}\varphi_x \mathrm{d}\varphi_y\, \Pi'(\varphi_x, \varphi_y, \alpha_x, \alpha_y, \alpha_z)\, e^{-(\lambda+p)/2} I_0(\sqrt{\lambda p})\,, \tag{B.4}$$

where I_0 is the modified Bessel function of the first kind. To evaluate the above integral, we first note that the prior is factorizable into that for α_z and for the set $\{\alpha_x, \alpha_y, \varphi_x, \varphi_y\}$. The latter 4 random variables (which correspond to the $\omega = s$ and $\omega = d$ peaks), can be redefined as two 2D random vectors $\boldsymbol{x}$ and $\boldsymbol{y}$ with relative angle $\pi/2 - (\varphi_x - \varphi_y)$, in order to give $\alpha_x^2 + \alpha_y^2 \pm 2\alpha_x\alpha_y\sin(\varphi_y - \varphi_x) \to |\boldsymbol{x} \pm \boldsymbol{y}|^2 = (x_1 \pm y_1)^2 + (x_2 \pm y_2)^2$. Here the subscript 1 and 2 correspond to the two components of the vectors, in the two directions of the 2D Euclidean space respectively. Since α's are Rayleigh distributed and φ's are uniformly distributed from $(0, 2\pi)$, the four variables $\{x_1, x_2, y_1, y_2\}$ are normally distributed with zero mean and variance equal to 1/2. Furthermore, we can now redefine x's and y's as $x_i + y_i = u_i$ and $x_i - y_i = v_i$ for $i = \{1, 2\}$, to get the following expression

$$\mathcal{L} \propto \int \mathrm{d}\alpha_z\, \Pi'(\alpha_z)\mathrm{d}u_1\mathrm{d}u_2\mathrm{d}v_1\mathrm{d}v_2\, \Pi(u_1, u_2, v_1, v_2)\, e^{-(\lambda+p)/2} I_0(\sqrt{\lambda p})\,. \tag{B.5}$$

with $\Pi(u_1, u_2, v_1, v_2) = e^{-(u_1^2+u_2^2+v_1^2+v_2^2)/2}$, $\Pi'(\alpha_z) = 2\alpha_z\, e^{-\alpha_z^2}$, and

$$\lambda = \frac{\mathcal{A}^2 T}{8\,\sigma^2}\Big\{\cos^2\phi\left[u_1^2 + u_2^2\right]\delta_{\omega,s} + \cos^2\phi\left[v_1^2 + v_2^2\right]\delta_{\omega,d} + 4\sin^2\phi\,\alpha_z^2\delta_{\omega,m}\Big\}\,. \tag{B.6}$$

Using the series representation of the Bessel function, together with Gamma function identities, the 5 random variables can be integrated out analytically. We arrive at the following marginalized (and normalized) likelihood:

$$\mathcal{L} = \frac{e^{-\frac{p}{2}\left(\frac{1}{1+X\delta_{\omega,s}}\right)} + e^{-\frac{p}{2}\left(\frac{1}{1+X\delta_{\omega,d}}\right)} + e^{-p\left(\frac{1}{2+Y\delta_{\omega,m}}\right)} - 2e^{-\frac{p}{2}}}{2(1+X\delta_{\omega,s}) + 2(1+X\delta_{\omega,d}) + (2+Y\delta_{\omega,m}) - 4}\,, \tag{B.7}$$

where

$$X = \frac{\mathcal{A}^2 T}{8\,\sigma^2}\cos^2\phi \qquad \text{and} \qquad Y = \frac{\mathcal{A}^2 T}{2\,\sigma^2}\sin^2\phi\,. \tag{B.8}$$

This likelihood can be split into three individual likelihoods for the sum/difference peaks and the Compton peak, as given in Eq. (3.2). The form of the likelihoods for the sum and difference peaks is equivalent.

C Covariance Matrix

To treat the total likelihood as the product of the individual likelihoods in each frequency bin, we must check that the covariance matrix is diagonal.

We will consider a signal-only analysis, discarding the noise, since the noise merely adds to the power and is uncorrelated between different frequency bins. We may write the values of the three peaks as

$$\begin{aligned}
\mathcal{P}_1 &= \frac{\mathcal{A}^2 T}{8}\left[\alpha_x^2 + \alpha_y^2 + 2\alpha_x\alpha_y\sin(\varphi_y - \varphi_x)\right]\cos^2\phi\,,\\
\mathcal{P}_2 &= \frac{\mathcal{A}^2 T}{8}\left[\alpha_x^2 + \alpha_y^2 - 2\alpha_x\alpha_y\sin(\varphi_y - \varphi_x)\right]\cos^2\phi\,,\\
\mathcal{P}_3 &= \frac{\mathcal{A}^2 T}{2}\alpha_z^2\sin^2\phi\,.
\end{aligned} \tag{C.1}$$

We wish to compute the quantity

$$\Sigma_{ij} \equiv \langle \mathcal{P}_i \mathcal{P}_j\rangle - \langle \mathcal{P}_i\rangle\langle \mathcal{P}_j\rangle\,. \tag{C.2}$$

We can do this using the expression for the raw moments,

$$\langle \alpha^n\rangle = 2^{n/2}\sigma^n\Gamma\left(1+\frac{n}{2}\right)\,, \tag{C.3}$$

where, for us, $\sigma = 1/\sqrt{2}$. Aside from this, we need to know that

$$\begin{aligned}
\langle \sin(\varphi_y - \varphi_x)\rangle &= 0\,,\\
\langle \sin^2(\varphi_y - \varphi_x)\rangle &= \frac{1}{2}\,.
\end{aligned} \tag{C.4}$$

We then get that

$$\begin{aligned}
\Sigma_{12} = \Sigma_{13} = \Sigma_{23} &= 0\,,\\
\Sigma_{11} = \Sigma_{22} &= \left(\frac{\sigma^2\mathcal{A}^2 T}{2}\cos^2\phi\right)^2 = \left(\frac{\mathcal{A}^2 T}{4}\cos^2\phi\right)^2\,,\\
\Sigma_{33} &= \left(\sigma^2\mathcal{A}^2 T\sin^2\phi\right)^2 = \left(\frac{\mathcal{A}^2 T}{2}\sin^2\phi\right)^2\,.
\end{aligned} \tag{C.5}$$

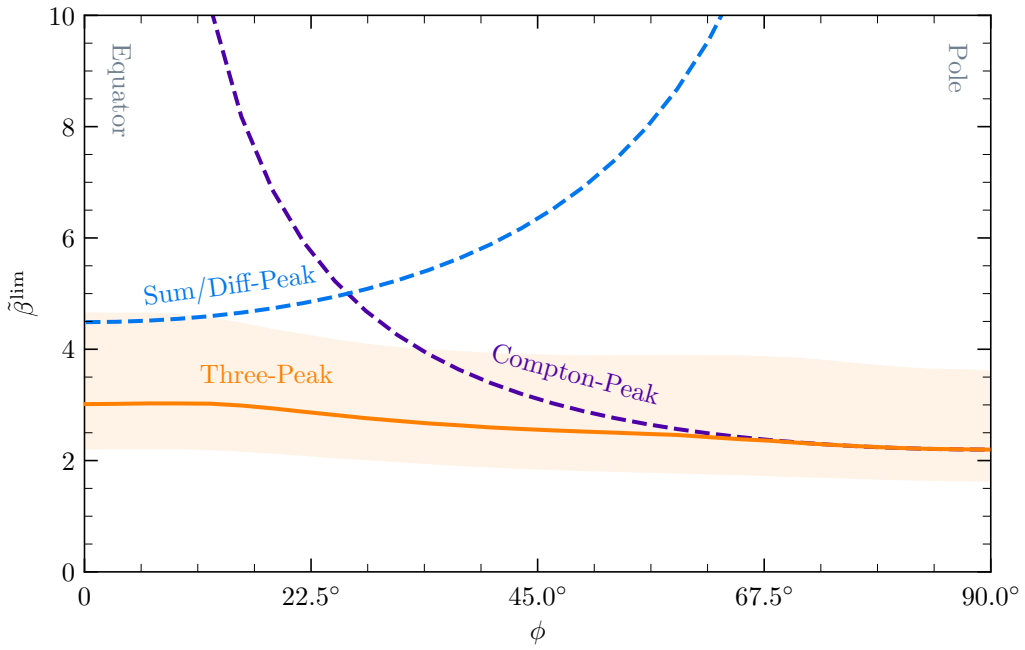


Figure 7: The 90% CL limits ($\tilde{\beta}^{\rm lim}$) on the dimensionless parameter $\tilde{\beta} \equiv \sqrt{\rho\, g_{\rm eff}^2\, \sigma_v^2\, T_{\rm obs}/\sigma_n^2}$ (see Eq. (D.2)) derived from our MC analysis (the same as in Fig. 4 but for the case of the gradient of a scalar). We show the results of our three-peak analysis and those of two single-peak analyses focusing on the Compton peak and on one of the sum or difference peaks. The shaded region indicates the 1σ error bar on our three-peak analysis. Our three-peak analysis generally provides a better/comparable limit to either of the two single-peak analyses and is largely latitude-independent.

Crucially, we get that the covariance between peaks is 0, allowing us to treat them as statistically independent and hence permitting us to express the total likelihood as the product of the individual likelihoods.

D The Case of the Gradient of a Scalar

In this case, there is a preferential direction because $\boldsymbol{\nabla} a$ points in the direction of the local DM velocity. Aligning the lab's working coordinate system such that this local velocity vector is parallel to the z axis, the amplitudes associated with the three different directions in Eq. (2.9) are not all the same. Effectively, there is an extra factor associated with the z direction, and the random signal in frequency space (c.f. Eq. (2.9)) takes the following

form

$$\tilde{\lambda}(\omega_n) = \frac{\tilde{\beta}^2}{4}\Big\{ \left[\alpha_x^2 + \alpha_y^2 + 2\alpha_x\alpha_y \sin(\varphi_y - \varphi_x)\right] \cos^2\phi\, \delta_{\omega_n,s} + \left[\alpha_x^2 + \alpha_y^2 - 2\alpha_x\alpha_y \sin(\varphi_y - \varphi_x)\right] \cos^2\phi\, \delta_{\omega_n,d} + 4\tilde{\gamma}\, \alpha_z^2 \sin^2\phi\, \delta_{\omega_n,m}\Big\}\,, \tag{D.1}$$

where (and following the notation of [45])

$$\tilde{\beta} \equiv \sqrt{\frac{\rho\, g_{\rm eff}^2\, \sigma_v^2\, T_{\rm obs}}{\sigma_n^2}} \qquad \text{and} \qquad \tilde{\gamma} \equiv 1 + \left(\frac{v_\odot}{\sigma_v}\right)^2 \simeq 2.1\,. \tag{D.2}$$

Proceeding similarly as in Appendix B, the marginalized likelihood is

$$\mathcal{L}' = \int \mathrm{d}\alpha_x \mathrm{d}\alpha_y \mathrm{d}\alpha_z \mathrm{d}\varphi_x \mathrm{d}\varphi_y\, \Pi'(\varphi_x, \varphi_y, \alpha_x, \alpha_y, \alpha_z)\, e^{-(p+\tilde{\lambda})/2} I_0(\sqrt{p\tilde{\lambda}})\,, \tag{D.3}$$

which we can evaluate by proceeding in the same fashion as in Appendix B; i.e. making redefinitions of the variables so they become independent and the integral becomes analytically tractable. We arrive at the following:

$$\mathcal{L}' = \frac{e^{-\frac{p}{2}\left(\frac{1}{1+X\delta_{\omega,s}}\right)} + e^{-\frac{p}{2}\left(\frac{1}{1+X\delta_{\omega,d}}\right)} + e^{-\frac{p}{2}\left(\frac{1}{1+Y\delta_{\omega,m}}\right)} - 2e^{-\frac{p}{2}}}{2(1+X\delta_{\omega,s}) + 2(1+X\delta_{\omega,d}) + 2(1+Y\delta_{\omega,m}) - 4}\,, \tag{D.4}$$

where

$$X = \frac{\tilde{\beta}^2}{4}\cos^2\phi \qquad \text{and} \qquad Y = \frac{\tilde{\beta}^2\tilde{\gamma}}{2}\sin^2\phi\,. \tag{D.5}$$

The overall result is that Y simply gets rescaled by $\tilde{\gamma}$.

Following the same MC analysis as outlined in Section 3, we show the 90% CL limits for the case of the gradient of a scalar in Fig. 7. The largest difference in this case is the increased constraining power of the Compton peak compared to the vector case shown in Fig. 4. This is because of the scaling that its amplitude receives by the factor $\tilde{\gamma} > 1$.